NONLINEAR MODELING, DYNAMIC ANALYSIS, AND

EXPERIMENTAL TESTING OF HYBRID SLIDING-ROCKING

BRIDGES

A Dissertation

by

MOHAMMAD SALEHI NAJAFABADI

Chair of Committee,	Petros Sideris
Committee Members,	Abbie B. Liel
	Joseph M. Bracci
	John B. Mander
	Mohammed E. Haque
Head of Department,	Robin L. Autenrieth

May 2020

Major Subject: Civil Engineering

ABSTRACT

Hybrid sliding-rocking (HSR) bridge columns were recently developed in the context of Accelerated Bridge Construction (ABC) for seismic regions. These columns incorporate end rocking joints, intermediate sliding joints, and unbonded posttensioning to introduce self-centering and energy dissipation into the substructure. This dissertation intends to further the overall understanding of the dynamic behavior of HSR columns, improve their seismic design, and examine their construction feasibility.

First, a modeling strategy is proposed to enable the nonlinear dynamic analysis of HSR columns. For this purpose, four finite element formulations are developed, namely: (1) a gradient inelastic force-based (FB) element formulation; (2) an HSR FB element formulation; (3) a continuous multi-node truss element formulation; and (4) a zero-length constraint element formulation. These element formulations are then implemented in an structural analysis software to validate the capability of the developed strategy in capturing the data from the past tests on HSR columns.

Once validated, the developed modeling strategy is used to evaluate the effects of several design variables on the seismic performance of HSR columns through multiple nonlinear static and time history analyses. The examined design variables directly/indirectly represent: (*i*) sliding joint distribution, (*ii*) coefficient of friction at sliding joints, (*iii*) duct and duct adaptor dimensions, and (*iv*) posttensioning system properties. Subsequently, a number of recommendations are made about the effective

design of HSR columns. The effects of vertical excitation and near-fault ground motions on the response of HSR columns are also examined, showing their minimal impacts.

The above computational investigations are followed by an extensive experimental program to validate the performance of HSR columns with improved design and to examine their actual response under various loading conditions. This program includes testing of four half-scale HSR columns under uniaxial lateral loading, combined uniaxial lateral and torsional loading, and biaxial lateral loading. The columns under uniaxial lateral loading are tested in both cantilever and fixed-fixed conditions. The test results show the low damageability of the HSR columns under displacements representing 950- and 2475-year earthquakes. Selected tests under uniaxial lateral loading are also simulated using the proposed modeling strategy and improvements are suggested accordingly.

DEDICATION

This dissertation is dedicated to my wonderful parents,

Esmaeil and Tahereh,

without their encouragement, none of my achievements would be possible,

and my lovely wife,

Samira,

for her endless support and patience during the last five years…

ACKNOWLEDGEMENTS

I would like to express my deepest gratitude to my advisor, Dr. Petros Sideris, for being such a tremendous academic mentor; for sure, this dissertation would not be achievable without his exceptional inspiration, extensive knowledge, and endless support throughout my Ph.D. studies. Likewise, my sincere thanks go to my co-advisor, Dr. Abbie Liel, for providing me with her valuable experience and guidance during the course of this research. I am also grateful to the other members of my advisory committee, Dr. Joseph Bracci, Dr. John Mander, and Dr. Mohammed Haque, for their invaluable comments on my research – their comments led to significant improvement of this dissertation.

Additionally, I would like to thank the personnel of the Structural and Materials Testing Laboratory at the Center for Infrastructure Renewal (CIR) at Texas A&M University, particularly, Mr. Charlie Droddy and Mr. Kirk Martin, for their substantial assistance with the various preparation and execution stages of the experimental testing program. The help from graduate students, Jakub Valigura, Mohammad Taghi Nikoukalam, Hareesh Reddy Goli, and Codi McKee, as well as undergraduate students, Janghwan Kim, Mark Stracener, Jacob Edge, and Fernando Ocon, with the construction of the test specimens, test setups assembly, and conducting the tests is also gratefully acknowledged.

Last but not least, I wish to extend my deepest thanks to my beloved family, in particular my parents, for their incredible support and encouragement during my entire life, and to my lovely wife, for her continuous patience and love during the last five years.

CONTRIBUTORS AND FUNDING SOURCES

Contributors

This work was supervised by an advisory committee consisting of Professors Petros Sideris (chair), Joseph Bracci, and John Mander from the Zachry Department of Civil and Environmental Engineering at Texas A&M University, Professor Mohammed Haque from the Department of Construction Science at Texas A&M University, and Professor Abbie Liel from the Department of Civil, Environmental, and Architectural Engineering at the University of Colorado-Boulder.

TABLE OF CONTENTS

LIST OF FIGURES

xv

xviii

xxii

xxiii

xxvi

xxvii

xxxiv

xl

xliii

LIST OF TABLES

1. INTRODUCTION

1.1. Problem Statement

According to the 2017 Infrastructure Report Card published by the American Society of Civil Engineers, in 2016, 39% of the bridges in the U.S. were more than 50 years old and 9.1% of them were structurally deficient – i.e. requiring significant maintenance, rehabilitation, or replacement. Replacing these bridges using conventional fabricated-in-place methods can, however, be too time-consuming and cause major mobility and safety issues. Contrarily, not only *Accelerated Bridge Construction* (ABC) methods substantially reduce construction time, traffic disruptions, lifecycle cost, and environmental impact at bridge sites, but they also improve the overall quality and long-term durability of bridges (Culmo 2011).

The primary ABC strategy is using prefabricated bridge elements and systems, such as precast concrete foundation, girders (usually prestressed), columns, and deck panels, which are cast offsite and transported to the bridge site at the time of installation. Such a strategy guarantees quality fabrication of concrete elements in a controlled environment without weather limitations. Also, the limited concrete pouring at the bridge construction site lowers its adverse impacts on its surrounding environment and increases the safety of workforce and the nearby community. Transportation, lifting, and installation of precast concrete elements can be further facilitated by fabricating those in the form of smaller segments and assembling them onsite, a technique referred to as *segmental bridge construction* (Figure 1-1). In this ABC technique, which is especially beneficial for the

construction of bridges of long spans and/or tall columns, precast concrete segments are often connected through a combination of (often bonded) posttensioning tendons and bonding agents (e.g. grout or epoxy resins) applied on their "match-cast" joints.

Figure 1-1. Precast concrete segmental bridge construction

Despite their vast application in the regions of low seismicity, fully precast concrete bridges are less commonly constructed in the regions of moderate to high seismicity. This is because, first, the seismic performances of various proposed precast concrete bridges are not as well-understood as cast-in-place systems', and second, there exists no straightforward standard procedure for the seismic design of such systems. The above facts particularly apply to bridge columns, which despite their crucial role in maintaining the stability of bridges, are expected to exhibit the highest level of nonlinearity among different bridge components.

In order to enable the use of precast concrete bridge columns in seismic regions, researchers have proposed various precast concrete column systems with acceptable seismic performances. One of the systems recently proposed in this context is the *hybrid sliding-rocking* (HSR) bridge column system (Sideris 2012; Sideris et al. 2014c; d). HSR columns are precast concrete segmental columns consisting of internal unbonded

posttensioning, end rocking joints, and intermediate sliding-dominant joints, providing these columns with significant self-centering and energy dissipation properties. A large number of quasi-static and shake table tests conducted on two HSR columns and a single-span HSR bridge specimen at the University at Buffalo have proved the seismic resilience of HSR columns (Sideris 2012; Sideris et al. 2014c; d). These tests demonstrated differences between the dynamic and quasi-static responses. Also, the effects of different earthquake excitations and various design variables on the dynamic response of HSR columns, which are essential in optimizing the system performance, have not been fully investigated. Evaluation of these subjects necessitates high-fidelity low-cost computational models that are capable of accurately predicting the dynamic response of HSR columns, while such computational models are not available. The current research aims to fill the above gaps by, first, developing the necessary tools for computational simulation of HSR columns; then, using those models to examine how the seismic performance of HSR columns is affected by different loading conditions and design variations; and eventually validate such design experimentally under a wide range of loading conditions, including torsional and bi-axial loading.

1.2. Background

1.2.1. Segmental Bridge Construction

Reportedly, the first precast concrete bridges were constructed in the 1940's in France (Podolny 1979; Figg and Pate 2004), but it took only less than five years until the first precast concrete segmental bridge in the U.S. was constructed (Muller 1975). The initial

motivation for building such bridges was reducing the challenges of casting concrete onsite (e.g. concrete casting in harsh weather conditions), while their further advantages, including their high quality, fast construction, minimal traffic disruptions, improved safety, and low lifecycle costs, have considerably increased their construction over the last few decades, mostly in low-seismicity areas (Freyermuth 1999; Figg and Pate 2004). The typical procedure of precast concrete segmental bridge construction is casting the bridge component segments in transportable sizes offsite, transporting them to the bridge site, and assembling those to get the final bridge product (NCHRP 2003; Culmo 2011). In order to gain sufficient shear transfer between adjacent bridge segments and to facilitate their alignments, they are usually "match-cast" and shear keys are provided at their joints. Filling the joints with epoxy resin and posttensioning are also the normal practice to achieve axial and flexural resistance at segment joints.

Despite the obvious benefits of segmental bridge construction, the presence of joints in various locations of segmental bridges – in comparison to conventional cast-in-place bridges – and the limited knowledge as to their seismic behavior have inhibited their vast construction in the areas of moderate to high seismicity. In order to change this view, over the last two decades, many attempts have been made by the researchers around the world to either understand the behavior of segmental bridges under excessive loading scenarios or devise new segmental bridge systems that sustain minimal damage under such loads. Because of the higher vulnerability of the bridge substructure to seismic damage than its superstructure, however, fewer studies have focused on the seismic aspects of precast concrete bridge superstructure systems (Geren and Tadros 1994; Holombo et al. 2000;

4

Megally et al. 2002b; Megally et al. 2003a; b; Megally et al. 2009; Veletzos and Restrepo 2009). Contrarily, studies on substructure systems are numerous.

1.2.2. Precast Concrete Columns for Seismic Regions

The precast concrete substructures systems developed for construction in seismic areas can be primarily categorized into two groups: (I) the systems whose column connections emulate the monolithic connectivity of cast-in-place RC columns with the foundation and bent cap; and (II) the systems that concentrate deformations in their column joints by allowing controlled rocking between their segments. Various connection details have been proposed to develop the first group of precast concrete columns, namely, using bar couplers (Matsumoto et al. 2008; Tazarv and Saiidi 2016a; b; Haber et al. 2017; Pantelides et al. 2017; Shim et al. 2017; Li et al. 2018) – Figure 1-2, grouted rebar ducts (Matsumoto et al. 2002; Matsumoto et al. 2008; Pang et al. 2010; Restrepo et al. 2011) – Figure 1-3, grouted rebar pocket (Hieber et al. 2005; Matsumoto et al. 2008) – Figure 1-4, and member socket (Lehman and Roeder 2012; Mehrsoroush and Saiidi 2016) – Figure 1-5. Although the behavior of this group of systems resembles conventional cast-in-place systems and their columns offer substantial energy dissipation due to the yielding of bonded longitudinal steel, they often suffer from major damage (e.g. bar buckling and concrete spalling/crushing) and large residual deformations during strong earthquakes, rendering their extensive repair/replacement necessary after earthquakes (Mander and Cheng 1997; Hewes and Priestley 2002; Kwan and Billington 2003a; Palermo et al. 2005a).
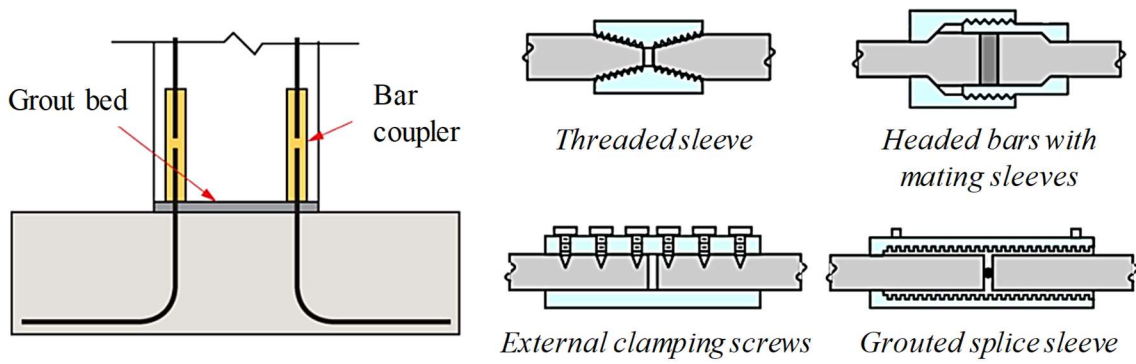
Figure 1-2. Typical bar coupler connection and coupler types (reprinted from Marsh et al. 2011)
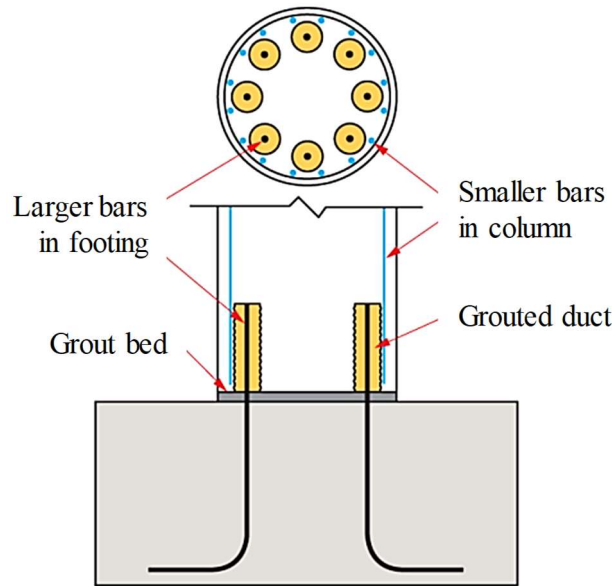
Figure 1-3. Grouted rebar duct connection (reprinted from Marsh et al. 2011)
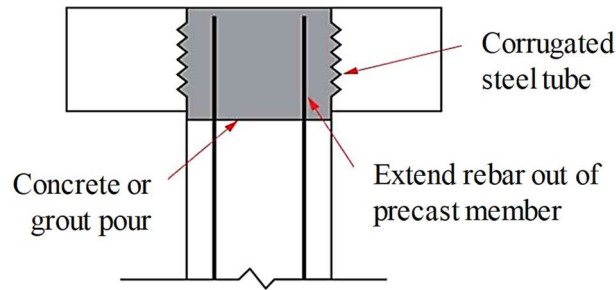
Figure 1-4. Grouted rebar pocket connection (reprinted from Marsh et al. 2011)
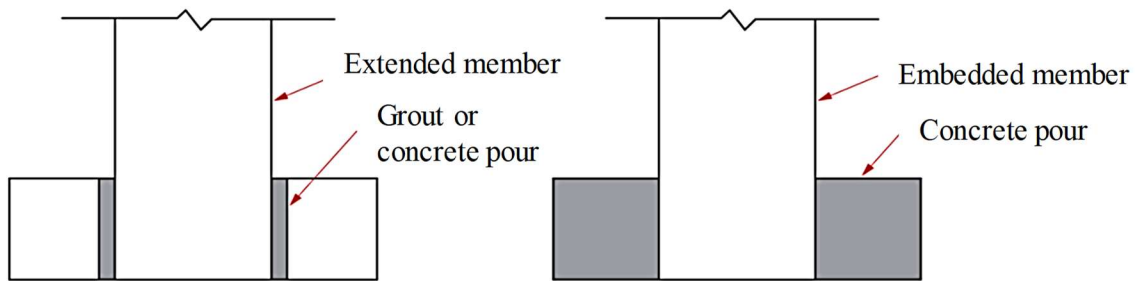
Figure 1-5. Member socket connection (reprinted from Marsh et al. 2011)

The second group of substructure systems are intended to improve the seismic performance of the first group by reducing their residual deformations and lowering their permanent damage, by confining plastic deformations and damage to their rocking joints. This goal is achieved by providing none or very limited amount of bonded longitudinal steel at column joints to avoid spread of tensile strains and residual curvature caused by steel yielding in the plastic hinge zones. Integrity and flexural resistance in such columns are instead provided mainly by gravity loads and unbonded posttensioning. The idea of pure rocking bridge piers (without posttensioning) was first investigated by McManus (1980), while one of the first reported applications of such a system was in a "stepping" rail bridge over Rangitikei River in New Zealand (Palermo et al. 2005a).

Posttensioned rocking bridge columns were initially introduced by Mander and Cheng (1997) as part of their Damage Avoidance Design (DAD) methodology. These columns consisted of end rocking joints and internal unbonded posttensioning tendons, while the rocking joint interfaces were armored by steel plates to protect them against compressive damage due to stress concentrations. Considering that the tendons were designed not to yield under expected loads, the main source of energy dissipation in these columns was the radiation damping resulting from the impacts at rocking joints. Cyclic tests on the proposed column up to 5% drift ratio showed their minimal damageability, while their equivalent damping ratios were estimated to be less than 5%.
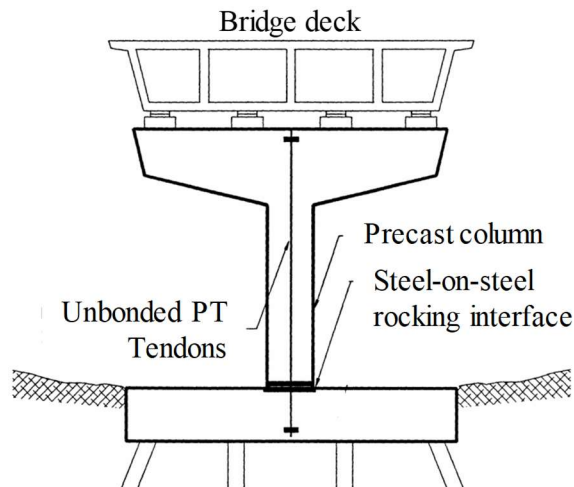
Figure 1-6. Rocking column design per DAD (reprinted from Mander and Cheng 1997)

Hewes and Priestley (2002) proposed a segmental column design, in which, instead of armoring the rocking interface via steel plates to mitigate compressive damage, they provided steel jacketing in the plastic hinge area. Large-scale column specimens with the

proposed design suffered from none or minimal strength degradation under cyclic lateral displacement with the maximum amplitude equivalent to 4% drift ratio. Larger displacements caused concrete crushing below the steel jacket toe, and in some cases, unexpected spalling right above the steel jackets. The hysteretic energy dissipation in all tested specimens were rather low, while using thinner steel jackets led to higher levels of energy dissipation due to the greater crushing resulted from lower level of confinement at compression toe.

Considering that the low energy dissipation of the aforementioned columns would increase their displacement demands compared to the systems with conventional columns (Kwan and Billington 2003b), Kwan and Billington (2003a) suggested utilizing fully/partially bonded longitudinal mild steel bars in addition to unbonded posttensioning steel to supplement the column's hysteretic energy dissipation. Analytical studies (Kwan and Billington 2003b; Ou et al. 2007; Jeong et al. 2008) and experiments (Palermo et al. 2007; Jeong et al. 2008; Wang et al. 2008; Ou et al. 2010; Davis et al. 2012; Thonstad et al. 2016; Cai et al. 2018) performed on the columns with such a design have shown the effectiveness of internal longitudinal mild steel in enhancing their energy dissipation properties.

In another study, to increase the hysteretic energy dissipation of unbonded posttensioned columns and reduce their damage, Billington and Yoon (2004) proposed building the column segments in the potential plastic hinge regions out of ductile fiber-reinforced cement-based concrete (DFRCC). Cyclic tests conducted on several small-scale column specimens with DFRCC and all-concrete segments showed that DFRCC

9

segments can significantly increase the energy dissipation of rocking columns up to a drift ratio of 3%. The DFRCC segments did not sustain any spalling and maintained their integrity even under 10% drift ratio. Shake table tests conducted on a column designed with a similar philosophy (using hybrid fiber-reinforced concrete at the column segment adjacent to the rocking joint, but armored with headed bars) by Trono et al. (2015) further confirmed the minimal damage of such columns under excessive drift ratios.

With the same purpose but an extended scope, Palermo et al. (2005a) introduced the concept of *hybrid* or "*controlled-rocking*" bridge pier systems, which were inspired by the building systems developed as part of the US-PRESSS (PREcast Seismic Structural System) Program (Priestley 1991; Stanton et al. 1991). These systems were suggested to increase the energy dissipation of rocking columns through either fully/partially bonded mild steel crossing the rocking joints or other internal/external energy dissipation devices at rocking joints (Figure 1-7). Several researches have investigated the quasi-static cyclic and pseudo-dynamic responses of columns with internal and external energy dissipaters, some of which are described in the following.

Chou and Chen (2006) investigated the effects of using external energy dissipaters on the cyclic response of concrete-filled steel tube segmental columns with unbonded posttensioning and dry joints. Due to the presence of steel tubes enclosing concrete segments, no longitudinal/transverse bars was used in these columns. The energy dissipaters employed in this study consisted of mild structural steel plates with reduced width in the middle and stiffeners at the ends. According to the cyclic force-displacement responses obtained from quasi-static tests on columns with and without dissipaters, the

energy dissipaters were found able to increase the equivalent damping ratio of the tested column about 50%. The energy dissipation devices, however, experienced early buckling (at a drift ratio of 0.6%) and fractured at a drift ratio of 4%, thereby decreasing the flexural strength of the tested column.
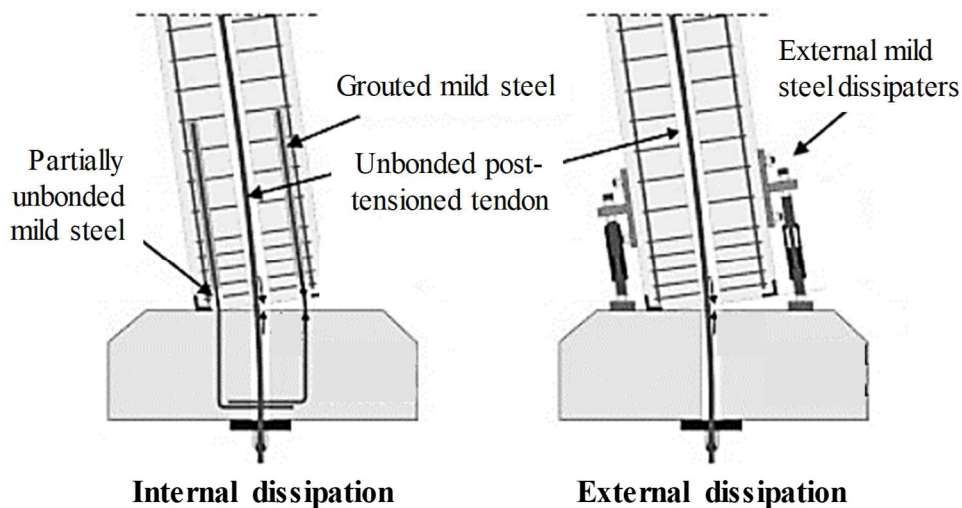
Figure 1-7. Columns with energy dissipaters (reprinted from Marriott et al. 2009)

Marriott et al. (2009) also evaluated the performance of hybrid columns with external energy dissipaters. The dissipaters proposed by these researchers consisted of machined mild steel bars with reduced diameter in the middle (to confine their yielding to a prescribed length), which were inserted in steel tubes filled with epoxy to avoid their buckling under compression. The advantage of these dissipaters was the possibility of their replacement upon their significant damage under unexpectedly large deformations. To protect the rocking joints against compressive damage, the columns tested in this study had steel-on-steel joint interface, as suggested by Mander and Cheng (1997). Under quasi-

static cyclic loading and up to a drift ratio of 3.5% (equivalent to MCE hazard level), the column specimens with the proposed design exhibited stable hysteretic responses and only flexural cracks.

In order to further validate the low damageability of the bridge columns designed per DAD (Mander and Cheng 1997), Solberg et al. (2009) tested a column with such a design and energy dissipation devices under bidirectional quasi-static and pseudo-dynamic loading. Posttensioned threaded rods were utilized in the shoe block design for the tested column as energy dissipation devices. Under quasi-static bidirectional loading and up to a drift ratio of 2%, the tested column experienced minimal damage, while during the pseudo-dynamic testing under a ground-motion representing MCE hazard, the column suffered from localized concrete crushing at the corners of its shoe block. The energy dissipation devices had very low contribution to the system's response and did not dissipate much energy.

Other than steel jacketing and rocking joint armoring to reduce damage in the neighborhood of rocking joints, some researchers have proposed use of unbonded posttensioned concrete-filled fiber-reinforced polymer (FRP) tube columns (Zhu et al. 2006; ElGawady et al. 2010; ElGawady and Sha'lan 2011). The advantages of FRP tubes are their corrosion resistance, their high strength-to-weight ratio, and their functionality as both longitudinal and transverse reinforcement. According to the quasi-static tests conducted on such columns (Zhu et al. 2006; ElGawady et al. 2010; ElGawady and Sha'lan 2011), although using FRP tubes could avoid the observable damage of rocking columns, even under drift ratios higher than 10%, the equivalent damping ratios of these columns

were as small as 3-6%. ElGawady et al. (2010) could increase the energy dissipation of their tested columns up to 50% by connecting the bottom column segment's toe to the foundation using steel angles as energy dissipater.

Guerrini et al. (2015) proposed a precast concrete bridge substructure consisting of high-performance concrete hollow-core columns enclosed between inside and outside steel shells, unbonded posttensioning bars, and internal mild steel dowel bars or external energy dissipation devices. The outside shell substituted the longitudinal and transverse reinforcement, while the inside shell created the hole in column and protected concrete from implosion. The external dissipaters used to construct the specimens tested in this study were similar to those by Marriott et al. (2009). Under cyclic lateral displacement, the two tested columns showed no considerable damage up to 3% of drift ratio, but crushing was observed at the mortar bed under columns for higher drift ratios. The self-centering capacity of the tested columns significantly dropped after the mortar crushing.

Moustafa and ElGawady (2018) proposed a segmental column design similar to that by Guerrini et al. (2015), but using GFRP tubes as outside shell and posttensioning strands instead of posttensioning bars. Two types of external energy dissipation devices were considered, namely, mild steel bars with a milled length in the middle and stiffened mild steel angles. The shake table test responses of two column specimens of the proposed design were compared with those of a monolithic RC column under various motions. The columns with proposed design were found minimally damaged and with less than 0.1% residual drift ratio under a base excitation equivalent to 250% design earthquake. Also, the energy dissipaters were very beneficial in reducing the displacement demands of

segmental columns, maintaining their drift ratio demands close to those of the monolithic RC column.

1.2.3. Hybrid Sliding-Rocking Bridge Columns

The hybrid sliding-rocking (HSR) bridge columns were introduced by Sideris (2012) and Sideris et al. (2014c; 2014d; 2015) as part of a precast concrete segmental bridge system for the regions of moderate to high seismicity. The HSR columns consisted of internal unbonded posttensioning tendons, end rocking joints, and intermediate sliding-dominant joints (from here on, called sliding joints) distributed uniformly along the height of column (Figure 1-8). Rocking between adjacent column segments was enabled by using no bonding agent or bonded steel at the joints. Sliding was facilitated by applying a thin layer of silicone material at the joint interfaces, while no shear keys were incorporated at any of the joints. The extent of sliding at sliding joints was controlled by the so-called duct adaptors, which were PVC ducts of larger diameter compared to the main tendon ducts passing the segments. Compared to the column designs briefly described in the previous section, HSR columns have several advantages: (*i*) friction at sliding joints provides these columns with a low-damage energy dissipation mechanism of high energy dissipation capacity, while the energy dissipation devices proposed in the literature may fracture due to large displacements or low-cycle fatigue and may require replacement after strong earthquakes; (*ii*) sliding joints act as a multi-level base isolation system, reducing both the base shear demand of the column and the displacements that need to be accommodated via rocking, thereby decreasing compressive damage at rocking joints; and (*iii*) torsional

14

sliding at the sliding joints premits accommodation of (limited) torsion in HSR columns without without any shear damage to column segments.
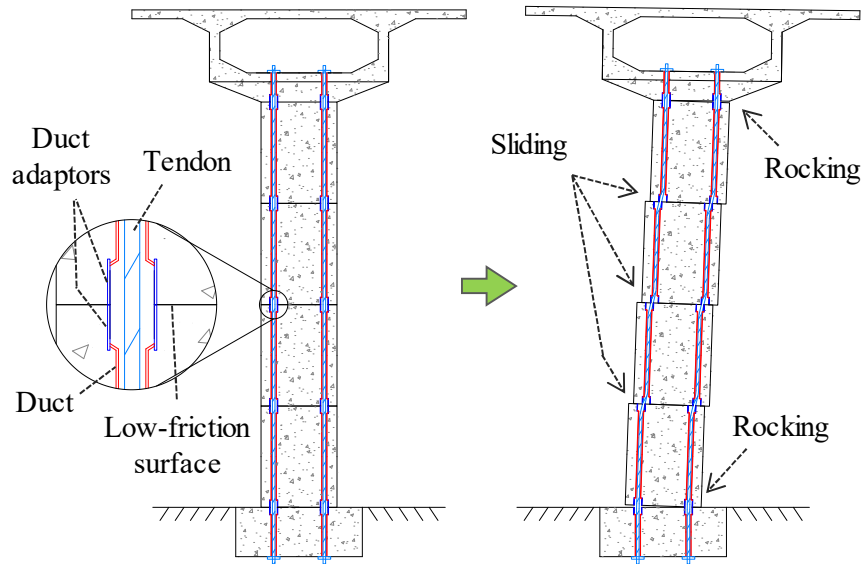
Figure 1-8. HSR column system

Duct-tendon interactions (Figure 1-9(a)) determine the response of a sliding joint under shear. The typical joint shear vs. sliding response of a sliding joint is depicted in Figure 1-9(b). As seen, the response of a sliding joint has three primary phases: (1) friction-only, (2) friction-bearing, and (3) ultimate sliding. In the first phase, the tendons are free to move within the ducts and the joint shear is primarily resisted via friction. In the second phase, however, the tendons have come in contact with the duct edges and contribute to the joint shear through their bearing reactions. The ultimate sliding is achieved when tendons get locked between the duct adaptor edges in the adjacent column

segments. Yet, this last phase is typically eliminated by design (Sideris et al. 2014d; Salehi et al. 2020).
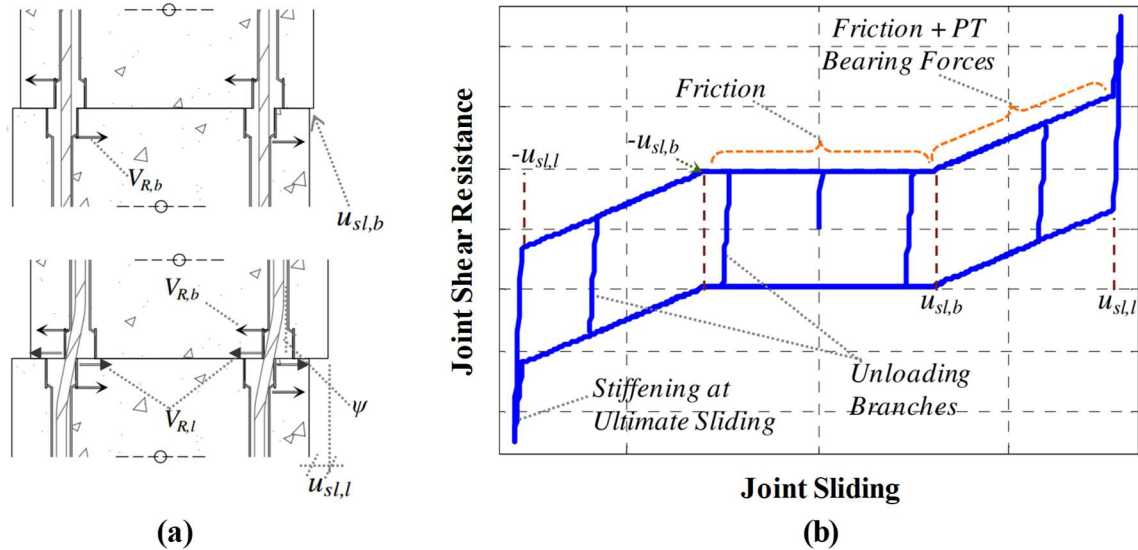
Figure 1-9. (a) Tendon-duct interactions; (b) joint shear vs. sliding response of sliding joints (reprinted from Sideris et al. 2014c; d)

Multiple shake table tests and two quasi-static cyclic tests were conducted on a large-scale single-span HSR bridge specimen with single-column bents (Figure 1-10(a)) and two large-scale HSR column specimens (Figure 1-10(b)), respectively, at the University at Buffalo. Under a base excitation corresponding to MCE hazard level, the HSR bridge specimen experienced a maximum drift ratio of 4.25% and a residual drift ratio of 1.42%, which was mainly due to residual sliding at sliding joints. During the shake table tests, sliding was mostly limited to the first sliding joint (above the bottom rocking joints), while all other sliding joints underwent almost zero sliding. The hysteretic energy dissipation created by sliding joints is obvious in column shear vs. displacement responses (Figure

1-11(a)). Under the MCE excitation, column damage appeared in the form of local concrete crushing and spalling at rocking joints and in the vicinity of the first sliding joint, respectively. According to the results of quasi-static cyclic tests, HSR columns had stable responses and limited damage up to a drift ratio of 3%, as a large portion of the imposed lateral displacement was accommodated by sliding at all sliding joints (Figure 1-11(b)). Concrete crushing and spalling at rocking joints and in the vicinity of sliding joints, respectively, started to occur at larger displacements. The equivalent damping ratios for the tested columns were found to be higher than 20% for the drift ratios as high as 5%, which mainly resulted from friction at sliding joints.

(a)   (b)
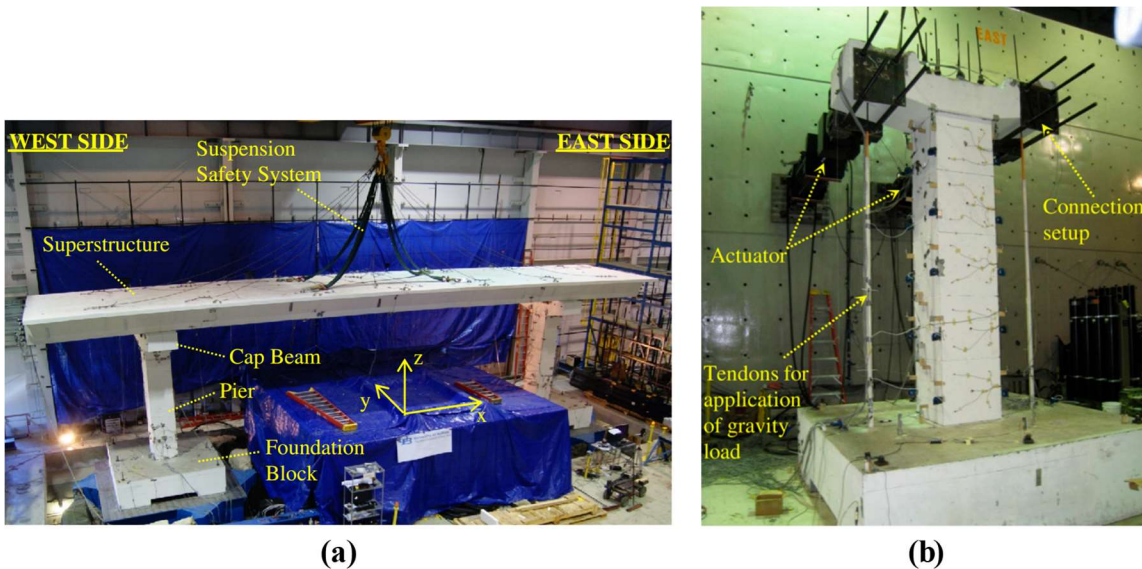
Figure 1-10. Past tests on HSR bridge and column specimens: (a) shake table test setup; (b) column test setup (reprinted from Sideris et al. 2014c; d)
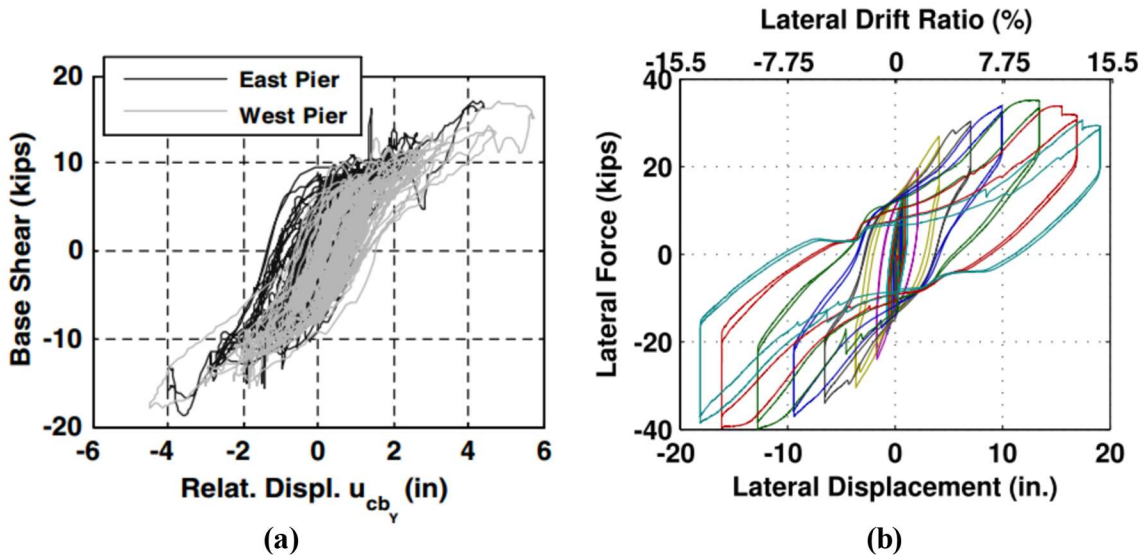
Figure 1-11. Sample column shear vs. displacement responses from: (a) shake table testing; (b) cyclic quasi-static testing (reprinted from Sideris et al. 2014c; d)

 Considering that HSR columns have several design variables specific to them (e.g. distribution of sliding joints, coefficient of friction, and duct adaptor height), Sideris et al. (2014d) proposed some analytically-derived design equations to facilitate their design based on their response under monotonic loading. These equations were intended to limit the compressive damage at the first joint, to guarantee sliding at the sliding-dominant joints before the column reaches its peak lateral load resistance, and to ensure that the sliding joints do not reach their ultimate sliding capacity subjecting the tendons to shearing. Sideris (2015) further investigated the effects of some of HSR column design variables through nonlinear static pushover analysis on 3D models in ABAQUS (DS 2010). Also, a capacity spectrum seismic design methodology was developed by Madhusudhanan and Sideris (2018) that would allow determination of seismic displacement demands of HSR columns using simplified nonlinear static analyses.

1.2.4. Computational Modeling of Rocking Columns

Although simulation of rocking columns using comprehensive three-dimensional finite element models could produce reasonably accurate response predictions, performing dynamic analysis using such models would be prohibitively time-consuming, thereby needing extensive computational resources. As a result, such sophisticated models have been merely used for static analysis of individual columns (Dawood et al. 2012; Dawood and ElGawady 2013). In order to enable dynamic analysis of rocking columns, such columns are usually modeled using less computationally expensive approaches, such as structural finite elements.

As reviewed in Section 1.2.1, the majority of rocking columns consist of two types of components, namely, concrete segment(s) and unbonded post-tensioning bars/tendons, which are in interaction with each other – i.e. rocking between concrete segment(s) and foundation/cap beam and bar/tendon-duct interactions. The concrete segments and unbonded bars/tendons are normally simulated via elastic/nonlinear beam-column elements and truss elements with initial strain, respectively. Also, if necessary, the interactions between the tendons and ducts can be modeled using zero-length gap elements. For modeling of rocking interactions between concrete segments and foundation/cap beam, however, various approaches have been adopted by researchers, which are summarized below.

Three primary strategies suggested in the literature to simulate rocking joints using two-node elements are: (1) using zero-length rotational springs (e.g. Palermo et al. 2007), (2) using multiple contact elements – the so-called Winker's spring method (e.g. Spieth et

al. 2004; Palermo et al. 2005b; Marriott et al. 2009; Wang et al. 2011), and (3) using elements with fiber sections (e.g. Shen et al. 2006; Perez et al. 2007; Weldon and Kurama 2007; 2012; Ameli and Pantelides 2017; Mantawy et al. 2019). In the first modeling strategy, the moment vs. rotation response of rocking joints is holistically represented via one or more zero-length springs (Figure 1-12(a)), which are calibrated using experimental data or more sophisticated simulation results. Such approaches may not capture the uplift induced at rocking joints, need a separate calibration for every given system, and, usually, do not account for axial-flexural interactions. In the second modeling strategy, a rocking joint is modeled through a series of zero-length axial springs or truss elements with no tensile strength (Figure 1-12(b)). If zero-length contact elements are used, their axial force vs. displacement response must represent a certain length of column, which is equal to the length of truss elements in the alternative approach, while this length is difficult to choose and physically interpret. Also, by using the first two strategies, damage spread over the rocking joint's neighborhood is not explicitly predictable. The third modeling strategy, which has a basis similar to the second one but is computationally more efficient, utilizes zero-length elements or finite-length force-based (FB) beam-column elements with fiber sections, in which the fiber section at rocking joint location comprises compression-only (no-tension) material models. In that sense, the normal strain distribution at rocking joints is assumed to be linear (principle of plane sections). Similar to the second type of models, if a zero-length element is used in these models, the material models constituting the fiber section must be appropriately calibrated. Because of the softening at rocking joints compared to their adjacent fiber sections that have tensile strength, the models using FB

20

beam-column elements can be impaired by the so-called strain localization phenomenon (Coleman and Spacone 2001). The strain localization is caused by the loss of strain field continuity under continuous stress field as softening starts at a cross-section, while the adjacent cross-sections unload. This phenomenon, which contradicts the experimental observations that show spread of damage over a finite length, has two implications for computational simulations: (1) lack of response objectivity (i.e. divergence of response with mesh refinement); and (2) solution algorithm instabilities and convergence failures.
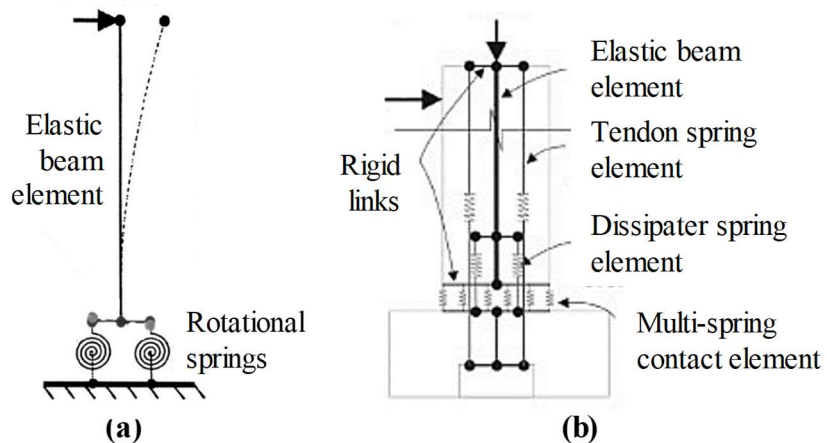
Figure 1-12. Modeling of rocking joints using: (a) rotational springs; (b) Winkler method (reprinted from Palermo et al. 2007; Marriott et al. 2009)

1.2.5. Computational Modeling of HSR Columns

In comparison with rocking-only columns, HSR columns have sliding at their intermediate joints, thereby making their modeling more challenging. The initial attempt in this direction was made by Sideris (2012), who employed the software SAP2000 (CSI 2009) to create a 3D model of a single-span HSR bridge using an extended form of the second

21

strategy described in Section 1.2.3, i.e. using no-tension slider contact elements to represent sliding-dominant joints. This model, however, suffered from rapid convergence failures of the numerical solution algorithm and response chattering, rendering this modeling approach impractical for analysis of HSR columns. As a result, more recently, Sideris (2015) built a 3D solid finite element model of an HSR column in the software ABAQUS (DS 2010). This model was capable of predicting the major mechanisms in HSR columns with acceptable accuracy and was validated using the data available from the quasi-static tests conducted by Sideris et al. (2014d). Even though this model was utilized to run several static analyses for a parametric study, it required very long analysis times and was found unsuitable for performing dynamic analysis on HSR columns.

1.3. Scope and Objectives

Based on the literature review provided in Section 1.2.3, there are several fundamental questions regarding the seismic response and design of HSR columns that yet need to be answered. These questions primarily include the following:

- Fundamental understanding of dynamic response properties of HSR columns: *How HSR columns behave under dynamic loads? How and why do the dynamic responses of HSR columns subjected to earthquake excitation differ from their responses under static lateral loading?* In past shake table tests (Sideris 2012; Sideris et al. 2014c), it was observed that only the lower sliding joints contributed to the response of HSR columns, whereas all of the sliding joints got activated under quasi-static loading. The reasons for such differences are not well understood, while predicting the dynamic response of HSR columns has been

22

challenging. Given the dynamic nature of seismic loads, it is of paramount importance, especially in the framework of Performance-Based Earthquake Engineering, to be able to evaluate the dynamic response of bridges with HSR columns under dynamic loads.

- Design of sliding joints: *How should HSR columns be designed to minimize their damage under seismic loads and allow their post-earthquake functionality?* The originally-designed HSR columns comprised several sliding joints uniformly distributed along their length, while their interfaces were merely covered with silicone-based material. According to the quasi-static tests performed on the original HSR columns, under lateral load, rocking at the bottom joint preceded the sliding at other joints. Under large displacements, concrete spalling was observed in the vicinity of sliding joints, indicating vulnerability of these joints to compressive stresses during joint sliding. Considering the foregoing, it is necessary to determine what is the minimum number of sliding joints needed to achieve the intended seismic performance of HSR columns, what their coefficient of friction should be, how they should be protected against the spalling observed in the original HSR columns, etc.

- Seismic performance assessment and design validation: *Is the new design of HSR columns effective in mitigating seismic damage? How do the HSR columns perform under seismic loads compared to rocking-only columns?* Computational modeling involves unavoidable simplifications and idealizations of various phenomena (e.g. friction properties and uniaxial constitutive laws) and

23

construction details. On the other side, the idealized conditions of an HSR column determined based on analyses cannot be accurately reproduced via an actual constructed system. Experimental tests provide the opportunity to investigate subtle phenomena that are missed/neglected in the computational models and quantify their effects on the response of constructed HSR columns. On a separate note, because of their resemblance to rocking-only columns, but their more involved design, it is also of interest to look into the benefits that HSR columns offer in terms of seismic performance, compared to rocking-only columns.

In order to answer the above questions, both computational and experimental investigations are requisite. Accordingly, the following major objectives are pursued in this dissertation:

1. Develop high-fidelity low-cost 2D and 3D finite element formulations to simulate the nonlinear dynamic response of HSR columns subjected to earthquake excitations;

2. Improve HSR column design through parametric studies evaluating the effects of major design variables of HSR columns on their seismic performance and provide recommendations on the construction of HSR columns;

3. Assess the seismic performance of HSR columns in reference to the earthquake excitations characteristics, including site-to-source distance and vertical excitation effects, and compare their seismic damageability with that of rocking-only columns;

4. Experimentally validate the improved design of HSR columns in terms of response properties under various loading conditions, damage avoidance capabilities, and rapid repair characteristics, and generate experimental data to further validate the computational models.

1.4. Dissertation Organization

The rest of dissertation consists of five chapters. In Chapter 2, a simplified finite element modeling strategy is proposed that enables the nonlinear static/dynamic analysis of HSR columns. The proposed modeling strategy includes novel finite element formulations that have been developed as part of this dissertation. Preliminary validation of the proposed modeling strategy via experimental data is included in the same chapter. In Chapter 3, the computational modeling strategy developed in Chapter 2 is used to perform numerous static and time-history analyses on several variations of HSR columns to identify and examine the effects of major design variables on their seismic performance. The effects of vertical and near-fault earthquake excitations on the response of HSR columns are also investigated in the same chapter. Chapter 3 further covers a comparison between the seismic performances of a HSR column and a rocking-only column of similar dimensions and lateral load resistance. The experimental program, including testing of four half-scale HSR column speciments, and the discussion of its results are covered in Chapter 4. In Chapter 5, the computational modeling strategy proposed in Chapter 2 is further validated through the simulation of the results of a number of the experimental tests discussed in Chapter 4. The summary and the primary conclusions are provided in Chapter 5.

2. COMPUTATIONAL MODELING[*]

This chapter is concerned with the computational modeling of HSR columns. The important mechanisms influencing the response of HSR columns are identified first. Next, a finite element configuration is proposed that allows accurate modeling of HSR columns and their nonlinear dynamic analysis. The proposed strategy makes use of a number of novel finite elements, whose formulations are derived herein. At the end of this chapter, the proposed modeling strategy is validated using the data from the past quasi-static cyclic and shake table tests on HSR columns (Sideris 2012; Sideris et al. 2014c; d).

2.1. Response Mechanisms and Challenges

According to Section 1.2.3, there are several mechanisms contributing to the response of HSR columns, which need to be simulated in order to be able to accurately capture their nonlinear response. These mechanisms are:

- *Sliding and friction at sliding joints:* Sliding, friction, and their relationship at sliding joints are among the most important determinants of the response of an HSR column. Therefore, they need to be explicitly modeled. The dependence of

[*] Parts of this chapter are reprinted with permission from:
- P. Sideris and M. Salehi (2016). "A Gradient Inelastic Flexibility-Based Frame Element Formulation." *Journal of Engineering Mechanics*, 142(7): 04016039
- M. Salehi and P. Sideris (2017). "Refined Gradient Inelastic Flexibility-Based Formulation for Members Subjected to Arbitrary Loading." *Journal of Engineering Mechanics*, 143(9): 04017090
- M. Salehi, P. Sideris, and A.B. Liel (2017). "Numerical Simulation of Hybrid Sliding-Rocking Columns Subjected to Earthquake Excitation." *Journal of Structural Engineering*, 143(11): 04017149

these phenomena on contact pressure can also significantly affect the response predictions of the finite models.

- *Rocking at all joints:* Although it is desired to only dominate the responses of the end joints, rocking can potentially occur at the sliding joints, too. Because of the separation and stress concentrations induced at the joints due to rocking, which is also increased by the elongation of the posttensioning tendons, rocking can substantially affect the response of HSR columns.

- *Tendon-duct interactions:* The bearing interactions between the ducts and the unbonded posttensioning tendons control the extent of sliding at sliding joints, influence the shear resistance at sliding joints, and affect the axial forces of the posttensioning tendons.

- *Material damage:* The damage-induced nonlinear responses of concrete (due to potential cracking and crushing), and high-strength prestressing steel (due to potential yielding and fracture) significantly affect the response of HSR columns under large displacements. Particularly, severe concrete damage at rocking joints and tendon yielding can result in major stiffness and strength degradation of an HSR column.

- *Axial-flexural interactions:* The coupling of flexural moment and axial force at the joints has substantial impact on the response of HSR columns. Specifically, flexure leads to tendon elongation, which in turn increases the axial force at the joints. Not only can the additional axial force intensify the compressive damage at the joints, but it can also affect the friction coefficient at sliding joints.

- *Geometric nonlinearities:* Under seismic loads, the geometry of an HSR column may considerably change due to sliding and rocking at its joints. The geometric changes can cause P-Delta effects, which usually increase the column damage and affect its dynamic response. In addition, sliding can create angle deviations along the tendons (i.e. deviations from their initially straight line geometry), which influence their bearing reactions on the ducts.

2.2. Proposed Modeling Strategy

In order to account for the important response mechanisms mentioned earlier, the finite element configuration demonstrated in Figure 2-1 is proposed to model an HSR column in two dimensions. Extension of this element configuration to three dimensions is straightforward. This modeling strategy employs four novel finite element formulations that are developed subsequently; these finite element formulations are:

- *Gradient inelastic (GI) beam-column element:* The GI beam-column element formulation is a two-node FB element formulation capable of capturing the softening response of precast concrete segments, without suffering from the strain localization issues. The FB formulation of this element allows its accurate predictions in the presence of nonlinear concrete and steel constitutive relations. The GI element formulation uses fiber sections and co-rotational geometric transformations to account for axial-flexural stress interactions and global geometric nonlinearities, respectively.

- *HSR element:* The HSR element formulation is also a two-node finite-length FB element formulation that can represent sliding/rocking joints and their close

28

vicinity. This element formulation combines the GI beam-column element formulation with a friction model at the sliding/rocking joint location – it is noted that, in reality, limited sliding can also occur at rocking joints. Both the section constitutive relations and the friction model in this element formulation utilize fiber discretization to capture axial-flexural interactions and the dependence of friction on the compressive stress distribution over the respective joint interface. Similarly to the GI element, the HSR element is formulated using co-rotational geometric transformations.

- *Multi-node continuous truss element:* A multi-node continuous truss element formulation can simulate an entire posttensioning tendon, wherein the prestressing is created via an initial strain. This element formulation is developed to enforce a constant axial strain over the full length of each posttensioning tendon, thus, equivalently, permitting the tendon to freely slide within the ducts. This formulation alleviates unrealistic tendon tensile stress concentrations in the vicinity of sliding and rocking joints, which lead to unrealistic predictions of premature tendon yielding and fracture. Co-rotational geometric transformations are also incorporated in the multi-node continuous truss element formulation.

- *Zero-length constraint element:* The two-node zero-length constraint element is intended to simulate the interaction of the unbonded posttensioning tendons with their ducts. This element formulation advances the zero-length element formulation available in the structural analysis software used in this research, i.e. OpenSees (McKenna et al. 2000), by incorporating co-rotational geometric

transformations to account for large rotations prevelant in the HSR columns. This formulation ensures that the tendons remain within the ducts in the deformed/rotated segment configuration.

The 2D versions of the above element formulations are fully discussed in the following sections. At the end of each section, the extension of the presented 2D formulation to three dimensions is briefly explained.

2.3. Developed Finite Element Formulations

2.3.1. Gradient Inelastic Beam-Column Element

The GI beam theory and a FB beam-column element formulation corresponding to it are developed herein. This element formulation aims to alleviate the strain localization issues, such as loss of responses objectivity and solution algorithm instabilities, caused by the strain field discontinuities predicted by the classical Navier's beam theory in the presence of softening cross-section response (Coleman and Spacone 2001; Valipour and Foster 2009; Sideris and Salehi 2016). This is achieved by generalizing the so-called strain gradient elasticity models (Mindlin 1964; Aifantis 1992; Polizzotto 2003) to inelastic beam problems. Further literature review on such models is found in Sideris and Salehi (2016) and Salehi and Sideris (2017). The GI beam theory and its numerical solution to develop a GI FB beam-column element formulation for two-dimensional modeling are discussed in the following. This section has adopted material from Sideris and Salehi (2016) and Salehi and Sideris (2017) with permission from ASCE.
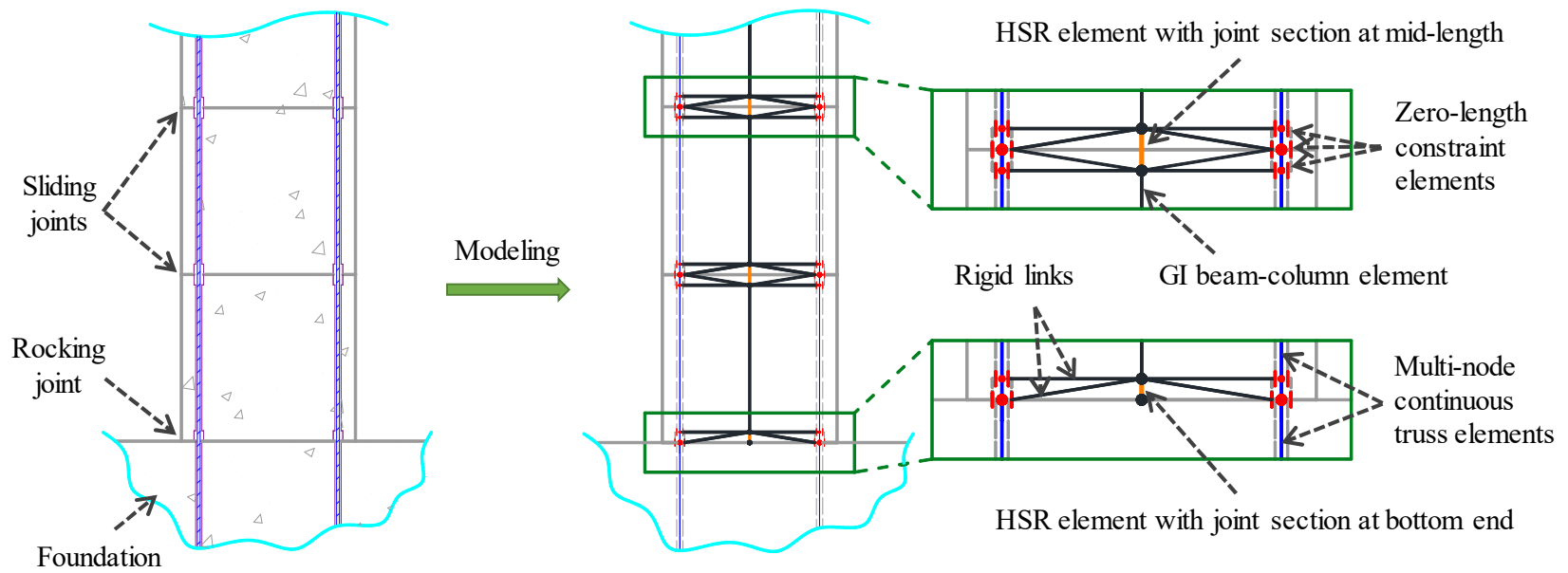
Figure 2-1. Proposed finite element configuration for modeling of HSR columns

Sliding joints

Rocking joint

Foundation

Modeling

HSR element with joint section at mid-length

Zero-length constraint elements

GI beam-column element

Rigid links

HSR element with joint section at bottom end

Multi-node continuous truss elements

31

2.3.1.1. Gradient Inelastic Beam Theory

The GI beam theory includes four sets of equations: (*i*) section strain-displacement equations, (*ii*) equilibrium equations, (*iii*) section constitutive relations, and (*iv*) nonlocality relations. The *section strain-displacement equations* employed herein adopt Navier's assumption of plane sections, which, for a two-dimensional beam, are expressed as:

$$
\begin{cases}
\varepsilon_o(x) = u_{o,x}(x) \\
\phi_o(x) = \theta_{,x}(x) \\
\gamma_o(x) = v_{o,x}(x) - \theta(x)
\end{cases}
\tag{2-1}
$$

where $\varepsilon_o(x)$, $\phi_o(x)$, and $\gamma_o(x)$ are the macroscopic axial strain, curvature, and shear strain at the location x along the beam reference axis, respectively (Figure 2-2(b)); and $u_o(x)$, $v_o(x)$, and $\theta(x)$ are the axial displacement, the transverse displacement, and the rotation of the cross section at the location x along the reference axis, respectively (Figure 2-2(a)), with $0 \le x \le L$, where L denotes the beam length. The subscript ",x" represents the first derivative with respect to x. The shear strain is assumed to be uniform over the member cross section, although any variations of it over the depth may be considered without loss of generality.

(a)   (b)
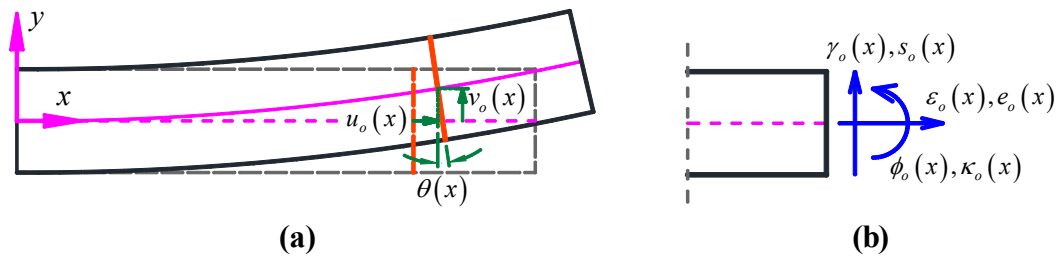
Figure 2-2. (a) Beam displacements; (b) section strains

32

The *equilibrium equations* refer to the undeformed configuration and do not consider dynamic effects and body loads, as shown below:

$$\begin{cases} N_{,x}(x) = 0 \\ V_{,x}(x) = 0 \\ M_{,x}(x) + V(x) = 0 \end{cases} \tag{2-2}$$

where $N(x)$, $V(x)$, and $M(x)$ are the axial force, the shear force, and the moment acting on the section located at x, respectively.

The *section constitutive relations*, which associate the section forces, $\vec{D}(x)$, with the material section strains, $\vec{d}^e(x)$, can be generically stated in vector form as:

$$\vec{D}(x) = \vec{f}_{ms}\left(\vec{d}^e(x)\right) \quad \text{with} \quad \begin{cases} \vec{D}(x) = \left[N(x) \quad M(x) \quad V(x) \right]^T \\ \vec{d}^e(x) = \left[e_o(x) \quad \kappa_o(x) \quad s_o(x) \right]^T \end{cases} \tag{2-3}$$

where $e_o(x)$, $\kappa_o(x)$, and $s_o(x)$ are the *material* section axial strain, curvature, and shear strain, while $\vec{f}_{ms}(.)$ is a function determined based on section dimensions and material constitutive laws. Through fiber discretization of cross sections, this function integrates normal/shear stress distributions over the cross section, determined from the respective cross section strain profiles via uniaxial material constitutive relations, to compute section forces, $\vec{D}(x)$ (Figure 2-3).
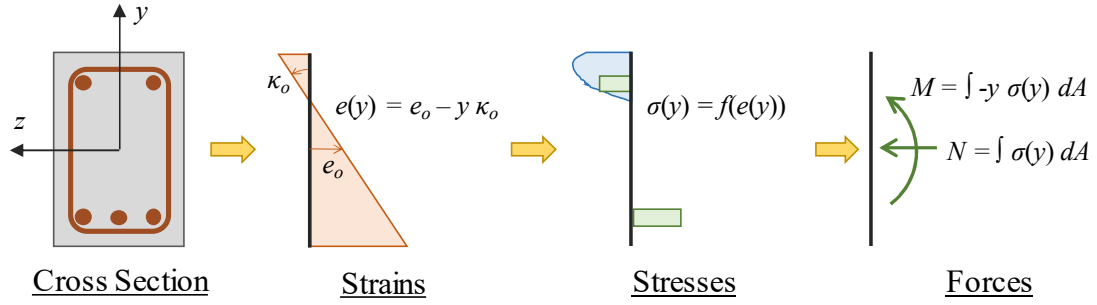
Figure 2-3. Section constitutive relations

The *nonlocality relations* are expressed in terms of the macroscopic and material section strains as:

$$\begin{cases} \dot{\vec{d}}(x)-\dfrac{1}{2}l_c^2\dot{\vec{d}}_{,xx}(x)=\dot{\vec{d}}^{\,e}(x) \\ \text{except for } \underbrace{\dot{\vec{d}}(x)=\dot{\vec{d}}^{\,e}(x)}_{\text{localization condition}} \text{ at } x=x_l \text{ with } \underbrace{\dot{W}_s(x_l)\le 0}_{\text{localization criterion}} \end{cases}$$

$(2\text{-}4)$

or, equivalently:

$$\dot{\vec{d}}(x)-\frac{1}{2}l_c^2\dot{\vec{d}}_{,xx}(x)H\left(\dot{W}_s(x)\right)=\dot{\vec{d}}^{\,e}(x)$$

$(2\text{-}5)$

with:

$$\begin{cases} \vec{d}(x)=\begin{bmatrix} \varepsilon_o(x) & \phi_o(x) & \gamma_o(x) \end{bmatrix}^T \\ \dot{W}_s(x_l)=\dfrac{1}{2}\dot{\vec{D}}(x_l)\cdot\dot{\vec{d}}^{\,e}(x_l) \end{cases}$$

$(2\text{-}6)$

where $\vec{d}(x)$ is the vector of macroscopic section strains, l_c is a characteristic length determining the extent of plasticity/damage spread upon their occurrence, and $\dot{W}_s(x_l)$ is the material section strain energy density rate at the localization location, x_l, and $H(.)$ is the Heaviside function. The overdot and the subscript ",*xx*" represent (time) rate and the

second derivative with respect to x, respectively. A negative value of $\dot{W}_s(x_l)$ represents softening response (Valanis 1985), while its zero value represents perfectly plastic response at the section, both of which lead to strain localization. Enforcing equal material and macroscopic section strain rates at x_l upon the occurrence of non-positive $\dot{W}_s(x_l)$ (as indicated in Eq. (2-4)) guarantees the boundedness of material section strains and the continuity of macroscopic section strains (obtained from time integration of the macroscopic section strain rates) upon strain localization. The two end BCs required to solve Eq. (2-4) are selected to be of the Dirichlet type, enforcing equal macroscopic and material section strain rates at the beam ends, $x = 0$ and L, i.e.:

$$\dot{\vec{d}}(0) = \dot{\vec{d}}^e(0), \quad \dot{\vec{d}}(L) = \dot{\vec{d}}^e(L) \tag{2-7}$$

The effects of 4th order nonlocality relations and other sets of BCs were investigated by Salehi and Sideris (2017).

2.3.1.2. Analytical Solution

A flexibility-based frame element formulation is obtained from the exact analytical solution of the refined GI beam theory. For the force BCs represented by the simply-supported reference beam of Figure 2-4, the equilibrium equations of Eq. (2-2) can be analytically solved for the section forces, $\vec{D}(x)$, as:

$$\vec{D}(x) = \left[b(x)\right]\vec{Q} \quad \text{with} \quad \begin{cases} \vec{Q} = \begin{bmatrix} Q_1 & Q_2 & Q_3 \end{bmatrix}^T \\ \left[b(x)\right] = \begin{bmatrix} 1 & 0 & 0 \\ 0 & x/L - 1 & x/L \\ 0 & -1/L & -1/L \end{bmatrix} \end{cases} \tag{2-8}$$

where $\vec{Q}$ is the vector of the end force BCs and $[b(x)]$ is the force shape function matrix.
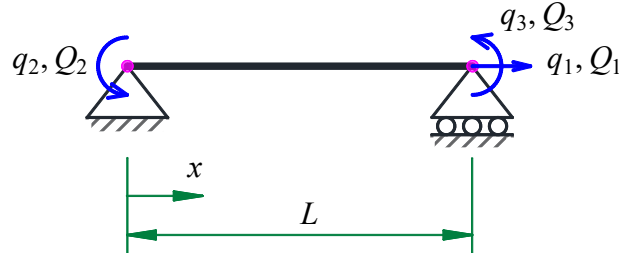
Figure 2-4. Simply-supported reference system for GI element formulation

Direct integration of the section strain-displacement equations yields a relationship between the end displacement BCs, $\vec{q}$ (Figure 2-4), and the macroscopic section strains (Figure 2-2(b)), $\vec{d}(x)$, as:

$$\vec{q} = \int_0^L \left[b(x) \right]^T \vec{d}(x) \, dx \quad \text{with} \quad \vec{q} = \begin{bmatrix} q_1 & q_2 & q_3 \end{bmatrix}^T \tag{2-9}$$

Assuming, for convenience of the subsequent derivations, that the solution of the selected nonlocality relations (Eq. (2-4)) with their BCs (Eq. (2-7)) has the generic form:

$$\dot{\vec{d}}(x) = \vec{f}_{nl}\left(\dot{\vec{d}}^e(x) \right) \tag{2-10}$$

where $\vec{f}_{nl}(.)$ represents the general solution function (which is not yet known), and after substituting Eq. (2-8) into Eq. (2-3), the system of equations below is obtained, which represents the analytical form of the *GI FB element formulation*:

$$\begin{cases} \left[b(x) \right] \vec{Q} - \vec{f}_{ms}\left(\dot{\vec{d}}^e(x) \right) = \vec{0} \\ \dot{\vec{q}} - \int_0^L \left(\left[b(x) \right]^T \dot{\vec{d}}(x) \right) dx = \vec{0} \end{cases} \tag{2-11}$$

For given end displacements, $\dot{\vec{q}}$, Eq. (2-11) is a system of two equations in two unknowns, namely, the end forces, $\dot{\vec{Q}}$, and the material section strain rates, $\dot{\vec{d}}^e(x)$. The macroscopic

36

section strain rates, $\dot{\vec{d}}(x)$, are explicitly computed from Eq. (2-10) for any material section

strain rates, $\dot{\vec{d}}^e(x)$, while the total material/macroscopic section strains used in Eq. (2-11)

are obtained from integration of $\dot{\vec{d}}(x)$ and $\dot{\vec{d}}^e(x)$ over time.

The tangent flexibility matrix, $[f_{el}]$, of the proposed FB frame element formulation

can be determined from Eq. (2-11) using chain rule differentiation, as:

$$[f_{el}] = \frac{\partial \vec{q}}{\partial \vec{Q}} = \int_0^L [b(x)]^T [k_{nl}(x)][k_{ms}(x)]^{-1}[b(x)] dx \qquad (2\text{-}12)$$

with:

$$\begin{cases} [k_{ms}(x)] = \left[\dfrac{\partial \vec{f}_{ms}}{\partial \vec{d}^e}(x)\right] \\[3mm] [k_{nl}(x)] = \left[\dfrac{\partial \vec{d}}{\partial \vec{d}^e}(x)\right] = \left[\dfrac{\partial \dot{\vec{d}}}{\partial \dot{\vec{d}}^e}(x)\right] \end{cases} \qquad (2\text{-}13)$$

where $[k_{ms}(x)]$ is the section tangent stiffness matrix, and $[k_{nl}(x)]$ is the derivative of the

macroscopic section strains, $\vec{d}(x)$, with respect to the material section strains, $\vec{d}^e(x)$.

2.3.1.3. Numerical Solution

Because the section constitutive relations (Eq. (2-3)) are nonlinear, and explicit analytical

solution (i.e., integration) of the nonlocality relations (Eq. (2-4)) for an arbitrary material

strain field is impractical, the FB formulation of Eq. (2-11) is spatially discretized into the

locations x_i, and is numerically solved at the discrete time instants t_k. In the spatially

discretized form, the section equilibrium equations (first of Eq. (2-11)) should be satisfied

at the discrete locations, x_i, (often called *integration points*) over the element length, while

the integral of the displacement compatibility equations (second of Eq. (2-11)) is

approximated by a weighted summation using the macroscopic section strains at the discrete locations, x_i. For a total of N integration points ($i = 1, 2,\dots , N$), the discretized form of Eq. (2-11) at a time instant, t_k, is expressed as:

$$\begin{cases} \left[b(x_1) \right] \vec{Q}_k - \vec{f}_{ms}\left(\vec{d}_k^e(x_1) \right) = \vec{0} \\ \left[b(x_2) \right] \vec{Q}_k - \vec{f}_{ms}\left(\vec{d}_k^e(x_2) \right) = \vec{0} \\ \quad\vdots \qquad\qquad \vdots \qquad\qquad \vdots \\ \left[b(x_N) \right] \vec{Q}_k - \vec{f}_{ms}\left(\vec{d}_k^e(x_N) \right) = \vec{0} \\ \vec{q}_k - \sum_{i=1}^{N} w_i \left[b(x_i) \right]^T \vec{d}_k(x_i) = \vec{0} \end{cases} \qquad (2\text{-}14)$$

where the subscript k represents values at the time instant t_k, and w_i is the integration weight at x_i, determined based on a selected numerical integration rule, such that $\sum_{i=1}^{N} w_i = L$. It is noted that $x_1 = 0$ and $x_N = L$, while $[b(x_i)]$ and w_i are time invariant.

A solution to the nonlocality relations at the time instant t_k can be obtained in a discretized form by enforcing the nonlocality relations at the N integration points (discrete locations) and replacing the spatial derivatives with their finite difference approximations. Using a 2nd order accurate finite difference approximation for the second spatial derivative, the discretized form of the 2nd order nonlocality relation (Eq. (2-4)) at the ith integration point, x_i, (and at t_k) becomes:

$$\dot{\vec{d}}_k(x_i) - \frac{1}{2} l_c^2 \left(\frac{\dot{\vec{d}}_k(x_{i+1}) - 2\dot{\vec{d}}_k(x_i) + \dot{\vec{d}}_k(x_{i-1})}{(\Delta x)^2} \right) = \dot{\vec{d}}_k^e(x_i) \qquad (2\text{-}15)$$

where Δx is the spacing between adjacent integration points, which are assumed to be equally-spaced. Enforcing the end Dirichlet BCs of Eq. (2-7) yields:

$$\dot{\bar{d}}_k(x_1)=\dot{\bar{d}}_k^e(x_1), \quad \dot{\bar{d}}_k(x_N)=\dot{\bar{d}}_k^e(x_N) \tag{2-16}$$

whose combination with Eq. (2-15) yields:

$$\dot{\bar{d}}_{tot,k}=\left[H_k\right]^{-1}\dot{\bar{d}}_{tot,k}^e \quad \text{with} \quad \begin{cases} \dot{\bar{d}}_{tot,k}^e=\left[\dot{\bar{d}}_k^{e\,T}(x_1) \quad \dot{\bar{d}}_k^{e\,T}(x_2) \quad \cdots \quad \dot{\bar{d}}_k^{e\,T}(x_N)\right]^T \\[2mm] \dot{\bar{d}}_{tot,k}=\left[\dot{\bar{d}}_k^{T}(x_1) \quad \dot{\bar{d}}_k^{T}(x_2) \quad \cdots \quad \dot{\bar{d}}_k^{T}(x_N)\right]^T \end{cases} \tag{2-17}$$

where the vectors $\dot{\bar{d}}_{tot,k}^e$ and $\dot{\bar{d}}_{tot,k}$ include the material and macroscopic section strain rates

at all integration points, respectively. $[H_k]$ is a $3N \times 3N$ matrix, defined as:

$$\left[H_k\right]=\begin{bmatrix} [I_3] & [O_3] \\ B_c[I_3] & A_c[I_3] & B_c[I_3] \\ & \ddots & \ddots & \ddots \\ & & B_c[I_3] & A_c[I_3] & B_c[I_3] \\ & & & [O_3] & [I_3] \end{bmatrix} \quad \text{with} \quad \begin{cases} A_c=1+\left(\dfrac{l_c}{\Delta x}\right)^2 \\[4mm] B_c=-\dfrac{1}{2}\left(\dfrac{l_c}{\Delta x}\right)^2 \end{cases} \tag{2-18}$$

where $[I_3]$ and $[O_3]$ are 3×3 identity and zero matrices, respectively, and A_c and B_c are

constants. Eq. (2-17) is the spatially discretized form (at t_k) of Eq. (2-10), which represents

the generic form of the solution of the nonlocality relations. Total section strains at t_k are

obtained via time integration of Eq. (2-17) using an implicit time discretization for the

strain rates as: $\dot{\bar{d}}_{tot,k}=\bar{d}_{tot,k}-\bar{d}_{tot,k-1}$ and $\dot{\bar{d}}_{tot,k}^e=\bar{d}_{tot,k}^e-\bar{d}_{tot,k-1}^e$. The *localization condition*

(second of Eq. (2-4)) is implemented at localization locations (i.e., integration points, x_i,

experiencing softening at the time instant, t_k) by replacing the corresponding rows of $[H_k]$

with zeros, except for the diagonal elements, which are replaced with unities. This

operation introduces instantaneous changes (temporal discontinuities) in $[H_k]$, which do

not propagate to the total strains, due to the rate form of Eq. (2-17). Localization locations

are identified via the *localization criterion* (second of Eq. (2-4)), which is applied to all

integration points, x_i. The discretized form of the localization criterion of Eq. (2-6) at x_i and t_k reads:

$$\dot{W}_s\left(x_i, t_k\right) = \frac{1}{2}\left(\vec{D}_k\left(x_i\right) - \vec{D}_{k-1}\left(x_i\right)\right) \cdot \left(\dot{\vec{d}}_k^e\left(x_i\right) - \dot{\vec{d}}_{k-1}^e\left(x_i\right)\right) \le 0 \qquad (2\text{-}19)$$

The spatially discretized form of the GI FB frame element formulation of Eq. (2-14) at t_k can be rearranged into two matrix equations, as:

$$\begin{cases} \left[B_Q\right]\vec{Q}_k - \vec{F}_{ms}\left(\vec{d}_{tot,k}^e\right) = \vec{0} \\ \vec{q}_k - \left[B_q\right]\vec{d}_{tot,k} = \vec{0} \end{cases} \qquad (2\text{-}20)$$

with:

$$\left[B_Q\right] = \begin{bmatrix} \left[b\left(x_1\right)\right] \\ \left[b\left(x_2\right)\right] \\ \vdots \\ \left[b\left(x_N\right)\right] \end{bmatrix}_{3N \times 3} \quad, \quad \vec{F}_{ms}\left(\vec{d}_{tot,k}^e\right) = \begin{Bmatrix} \vec{f}_{ms}\left(\vec{d}_k^e\left(x_1\right)\right) \\ \vec{f}_{ms}\left(\vec{d}_k^e\left(x_2\right)\right) \\ \vdots \\ \vec{f}_{ms}\left(\vec{d}_k^e\left(x_N\right)\right) \end{Bmatrix}_{3N \times 1} \qquad (2\text{-}21)$$

and:

$$\left[B_q\right] = \begin{bmatrix} w_1\left[b\left(x_1\right)\right]^T & w_2\left[b\left(x_2\right)\right]^T & \cdots & w_N\left[b\left(x_N\right)\right]^T \end{bmatrix}_{3 \times 3N} \qquad (2\text{-}22)$$

where $\vec{F}_{ms}(.)$ is the vector of the internal section forces, which are function of the material section strains, $\vec{d}_{tot,k}^e$, $[B_Q]$ is the discretized force shape function matrix, and $[B_q]$ is the integration weights matrix. Note that $[B_Q]$ and $[B_q]$ are time invariant.

For given displacement BCs at t_k, $\vec{q}_k$, the force BCs, $\vec{Q}_k$, and the material section strains, $\vec{d}_{tot,k}^e$, can be computed from Eq. (2-20), through a Newton-Raphson iterative solution scheme, as:

$$\left\{ \begin{array}{c} \vec{Q}_k \\ \vec{d}^{\,e}_{tot,k} \end{array} \right\}_{j+1} = \left\{ \begin{array}{c} \vec{Q}_k \\ \vec{d}^{\,e}_{tot,k} \end{array} \right\}_j -$$

$$\left[\begin{array}{cc} \left[B_Q \right]_{3N \times 3} & -\left[K_{ms,k} \right]_{3N \times 3N} \\ \left[0 \right]_{3 \times 3} & -\left(\left[B_q \right]\left[K_{nl,k} \right] \right)_{3 \times 3N} \end{array} \right]_j^{-1} \left\{ \begin{array}{c} \left[B_Q \right]\vec{Q}_k - \vec{F}_{ms}\left(\vec{d}^{\,e}_{tot,k} \right) \\ \vec{q}_k - \left[B_q \right]\vec{d}_{tot,k} \end{array} \right\}_j \qquad (2\text{-}23)$$

with:

$$\left[K_{ms,k} \right] = \left[\begin{array}{cccc} \left[k_{ms,k}\left(x_1 \right) \right] & \left[0 \right] & \cdots & \left[0 \right] \\ \left[0 \right] & \left[k_{ms,k}\left(x_2 \right) \right] & \cdots & \left[0 \right] \\ \vdots & \vdots & \ddots & \vdots \\ \left[0 \right] & \left[0 \right] & \cdots & \left[k_{ms,k}\left(x_N \right) \right] \end{array} \right] \qquad (2\text{-}24)$$

where $[K_{ms,k}]$ is the total tangential section stiffness matrix at t_k, and:

$$\left[K_{nl,k} \right] = \left[H_k \right]^{-1} \qquad (2\text{-}25)$$

The element tangential flexibility matrix at t_k can be computed, in accordance with Eq. (2-12), as:

$$\left[f_{el,k} \right]_{3 \times 3} = \frac{\partial \vec{q}_k}{\partial \vec{Q}_k} = \left[B_q \right]\left[H_k \right]^{-1}\left[K_{ms,k}\left(x \right) \right]^{-1}\left[B_Q \right] \qquad (2\text{-}26)$$

2.3.1.4. Co-rotational Transformations

The co-rotational geometric transformations used in the GI element formulation are in accordance with those of de Souza (2000), so the respective equations are not presented herein. The 2D transformation process is graphically described in Figure 2-5. The first and the second coordinate systems utilized in this transformation are the *global* and the *local* coordinate systems. Both the global and local systems are associated with the initial position/orientation of the (undeformed) element. The third coordinate system is the co-rotated local coordinate system, which is translated/rotated with the element, as the

element deforms and translates/rotates in the 2D space, so that its x-axis always passes from the element ends. For given nodal displacements in the global system, p_i (i = 1, 2, …, 6), their local counterparts, $\bar{q}_i$ (i = 1, 2, …, 6), are obtained via a constant rotation transformation. The transformation of the six local nodal displacements to the three co-rotated local nodal displacements, q_j (j = 1, 2, 3), includes two steps: (*a*) rotation, and (*b*) removal of the rigid-body displacements/rotations (generating a simply-supported reference beam, similar to Figure 2-4). Transformation of the co-rotated nodal forces, Q_j, obtained from the element formulation, to the local forces, $\bar{Q}_i$, is performed by first extending the three statically independent forces to six dependent ones (using the equilibrium equations) and then rotating them into the initial local coordinate system. The local forces are then transformed to their global counterparts, P_i, by a constant rotation transformation.

2.3.1.5. Evaluation

In order to evaluate the ability of the GI FB element formulation to generate objective responses, it is used to simulate the cantilever prismatic column shown in Figure 2-6(a), once with zero l_c (representing classical beam element) and once with a non-zero l_c. For the latter case, the characteristic length, l_c, representing the equivalent plastic hinge length, is selected to be 40 cm. The column is subjected to a lateral monotonic displacement and a constant vertical load. The column is 2 m tall and has a square cross section of the depth 40 cm. The vertical load is constant and equal to 5,000 kN.
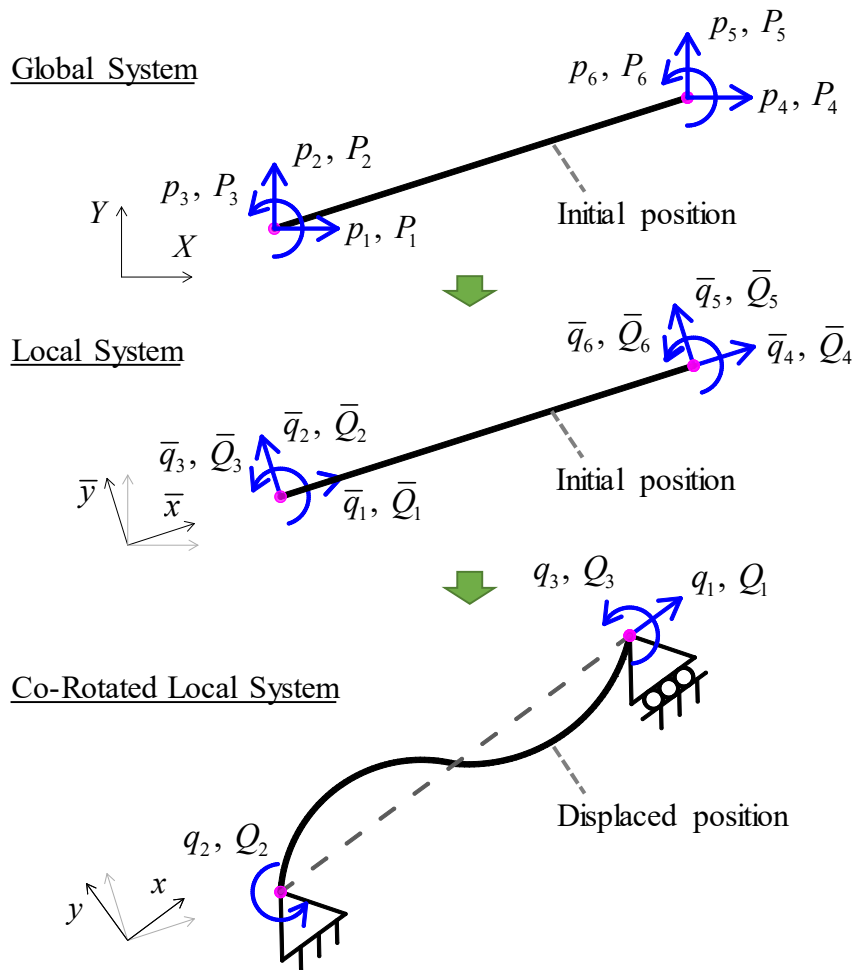
Figure 2-5. Co-rotational transformations for GI element formulation (Salehi and Sideris 2018)

The softening normal stress vs. strain response of Figure 2-6(b) is considered for the column material, which has an elastic modulus of 200 GPa, and a yield strength of 400 MPa. The peak strength of 450 MPa is obtained at a strain of 3%, resulting in a post-elastic-to-elastic stiffness ratio of 9×10^{-3}. Beyond the peak stress, the material response deteriorates linearly reaching a value of 45 MPa at a strain of 6%. Beyond this point, the stress increases slightly with the strain through a small stiffness that results in a residual-

to-elastic stiffness ratio of 9×10^{-5}. The shear stress vs. shear strain response is independent of the normal stress vs. normal strain response and remains linear elastic with a shear modulus of 76.9 GPa, representing a Poisson's ratio of 0.3. The cross-section is discretized into fibers of 1 cm × 1 cm, resulting in a total of 1600 fibers, which is deemed sufficient for the purposes of this examination. Trapezoidal method is employed for the integration of section strain-displacement equations (i.e. in third of Eqs. (2-21)).
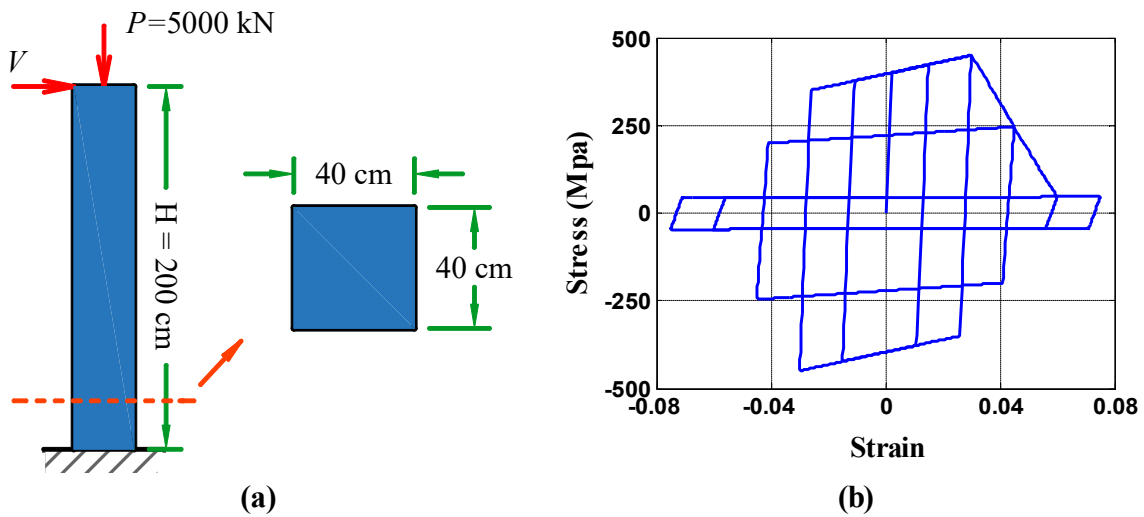
Figure 2-6. Evaluation of GI element: (a) column dimensions; (b) cyclic stress-strain response of selected material

The force vs. displacement curves for the GI FB formulation with $l_c = 0$ (local formulation) and the GI FB formulation with $l_c = 40$ cm, for an increasing number of (equally spaced) integration points, N, are compared in Figure 2-7. It is observed that the force vs. displacement curves for the local formulation become progressively more abrupt in the deteriorating branch with the number of integration points, N, and deterioration

starts at progressively smaller lateral displacements. On the contrary, the force vs. displacement curves for the GI FB formulation with non-zero l_c converge to a single solution with the number of integration points, N, thereby providing objective response. It is noticed that, for the chosen numerical integration method (i.e. trapezoidal rule), mesh convergence is achieve for a large enough N that yields $l_c / \Delta x \geq 3$.
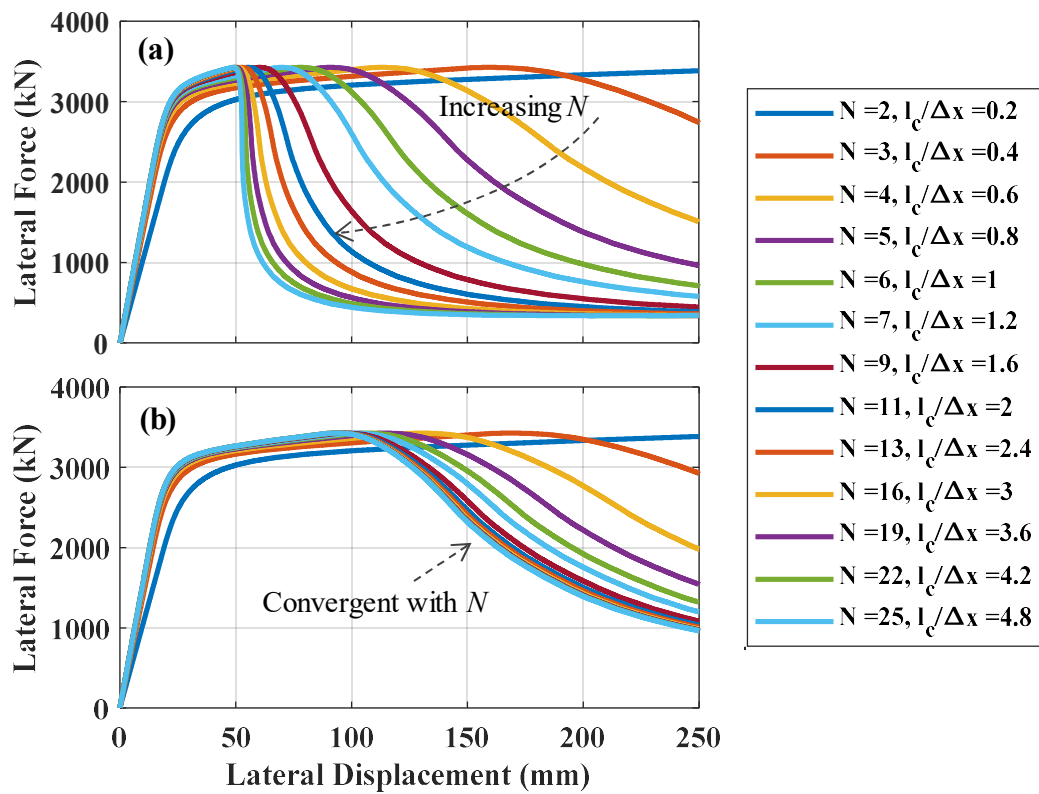
Figure 2-7. Evaluation of GI element – lateral force vs. displacement responses for various number of IPs, N, and: (a) $l_c = 0$; (b) $l_c = 40$ cm (note that when $l_c = 0$, $l_c / \Delta x$ equals 0 for all N values)

The macroscopic curvature distributions obtained from the GI FB element formulations with zero and non-zero l_c ($l_c = 40$ cm) for various number of IPs, N, are

compared in Figure 2-8. The curvature distributions of the local FB formulation (i.e. when $l_c = 0$) exhibit an increasingly localized response with N, resulting in progressively larger curvatures at the column's bottom end. The macroscopic curvature distributions of the GI formulation converge to a single continuous curvature field along the element length. In this case, the converged macroscopic curvature at the column's bottom section at the peak lateral displacement of 250 mm is about 0.5 rad/m.
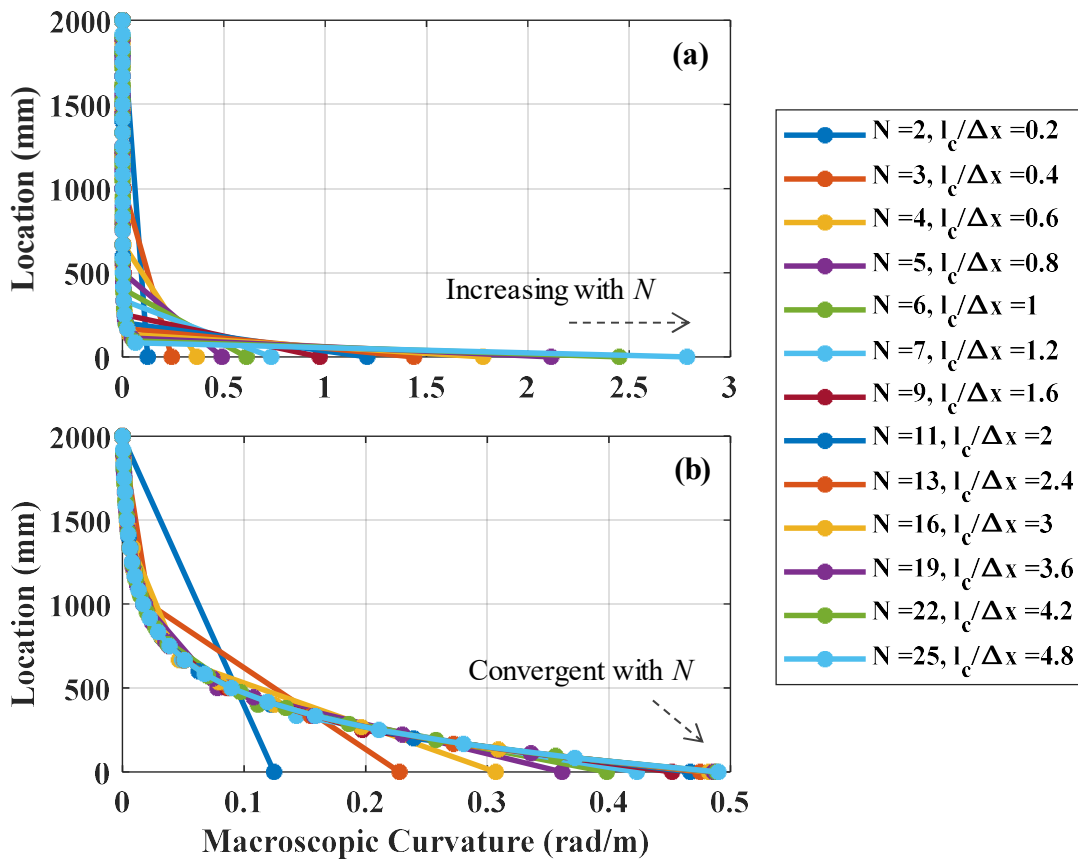
Figure 2-8. Evaluation of GI element – macroscopic curvature distributions for various number of IPs, N, and: (a) $l_c = 0$; (b) $l_c = 40$ cm (note that when $l_c = 0$, $l_c / \Delta x$ equals 0 for all N values)

2.3.1.6. Extension to 3D

Extension of the gradient inelastic beam theory presented earlier to three diemensions is very straightforward, even though deriving the co-rotational geometric transformations for a 3D element can be challenging. Here, however, only the 3D version of the beam theory is described. The numerical solution of the resulting equations is similar to that provided in the previous sections. Moreover, 3D co-rotational transformations applicable to the 3D GI element formulation can be found in de Souza (2000).

In three dimensions, the macroscopic and material section strain components increase into 6 components, as shown in Figure 2-9(a). These components include one axial strain, two shear strains, two flexural curvatures, and one torsional curvature. Consistently, the cross section displacement/rotation components increase to six, including an axial displacement, u, two transverse displacements, v_o and w_o, two rotations, θ_y and θ_z, and one twist, θ_x. Accordingly, the strain-displacement equations in 2D (Eqs. (2-1)) are changed into:

$$
\begin{cases}
\varepsilon_o(x) = u_{o,x}(x) \\
\gamma_y(x) = v_{o,x}(x) - \theta_z(x) \\
\gamma_z(x) = w_{o,x}(x) + \theta_y(x)
\end{cases}
\quad \text{and} \quad
\begin{cases}
\phi_y(x) = \theta_{y,x}(x) \\
\phi_z(x) = \theta_{z,x}(x) \\
\phi_x(x) = \theta_{x,x}(x)
\end{cases}
\tag{2-27}
$$

Likewise, the section forces are six in 3D, as shown in Figure 2-9(b). Accordingly, in the absence of body forces, the force equilibrium equations are supplemented as:

$$
\begin{cases}
N_{,x}(x) = 0 \\
V_{y,x}(x) = 0 \\
V_{z,x}(x) = 0
\end{cases}
\quad \text{and} \quad
\begin{cases}
M_{y,x}(x) - V_z(x) = 0 \\
M_{z,x}(x) + V_y(x) = 0 \\
T_{,x}(x) = 0
\end{cases}
\tag{2-28}
$$

where V_y and V_z denote the shear force components in y and z directions, respectively; M_y and M_z denote the moment components about y- and z-axes, respectively; and T denotes the torsion (about x-axis).

The section constitutive relations are changed from Eqs. (2-3) into:

$$\vec{D}(x) = \vec{f}_{ms}\left(\vec{d}^{\,e}(x)\right) \quad \text{with}$$

$$\begin{cases} \vec{D}(x) = \begin{bmatrix} N(x) & V_y(x) & V_z(x) & M_y(x) & M_z(x) & T(x) \end{bmatrix}^T \\ \vec{d}^{\,e}(x) = \begin{bmatrix} e_o(x) & s_y(x) & s_z(x) & \kappa_y(x) & \kappa_z(x) & \kappa_x(x) \end{bmatrix}^T \end{cases} \tag{2-29}$$
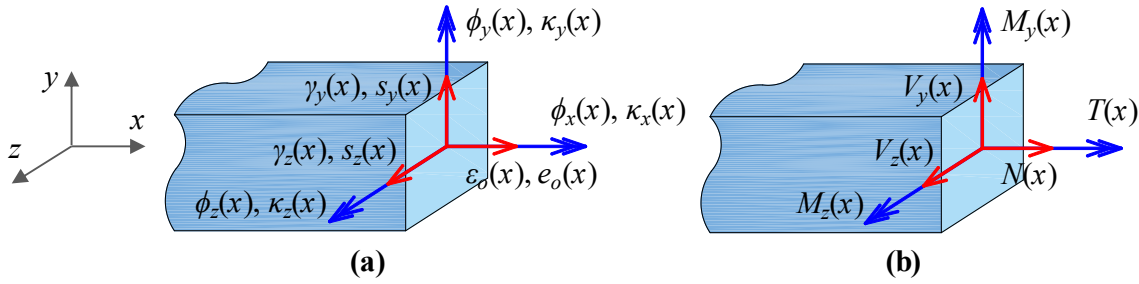
Figure 2-9. (a) Section strains in 3D; (b) section forces in 3D

The nonlocality relations and their boundary conditions remain identical to Eqs. (2-4) and (2-7), respectively, while the vector of macroscopic section strains defined in Eqs. (2-6) changes into:

$$\vec{d}(x) = \begin{bmatrix} \varepsilon_o(x) & \gamma_y(x) & \gamma_z(x) & \phi_y(x) & \phi_z(x) & \phi_x(x) \end{bmatrix}^T \tag{2-30}$$

2.3.2. HSR Element

This section is partly reprinted from Salehi et al. (2017) with permission from ASCE. The proposed HSR element is essentially a two-node GI beam element with a sliding joint

located somewhere along its length. The formulation of the HSR element combines a GI FB formulation that accounts for material deformations and joint rocking, with a hysteretic friction model that accounts for joint sliding-friction response (Figure 2-10). Rocking is considered within the GI FB formulation through section constitutive relations with zero tensile strength at sliding/rocking joints. Apart from eliminating strain localization issues and providing response objectivity, use of the GI FB element formulation also offers improved stability and convergence properties of the numerical solution (Sideris and Salehi 2016), and prediction of the section strain field in the vicinity of joints (damage propagation), which has not been possible with the other FB formulations (Salehi et al. 2017).
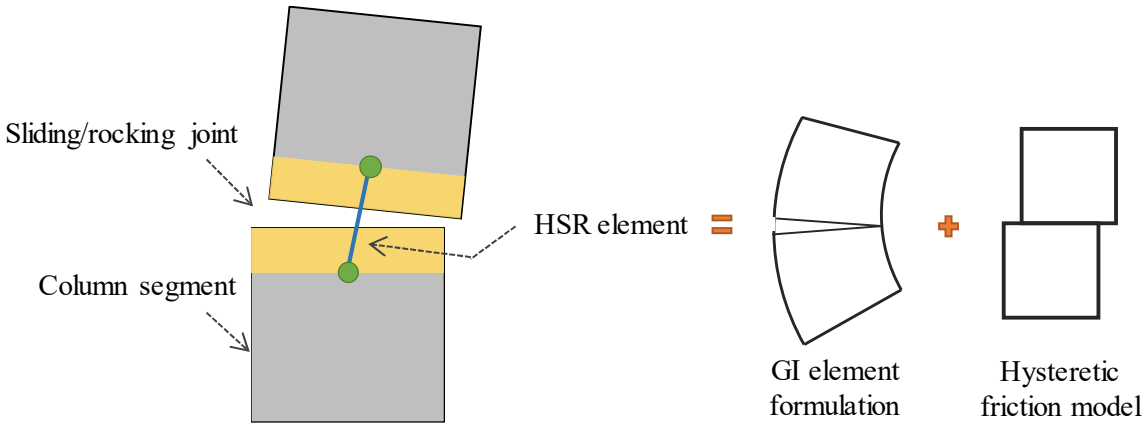
Figure 2-10. Concept of HSR element formulation

2.3.2.1. System of Equations

The system of equations in the HSR element formulation consists of those of the GI beam-column element formulation (Section 2.3.1) with some simplification and a hysteretic

friction model. The condensed set of equations from the GI element formulation include Eqs. (2-1), (2-2), and (2-3), i.e.:

$$
\begin{cases}
\text{Equilibrium equations:} & \begin{cases} N_{,x}(x) = 0 \\ V_{,x}(x) = 0 \\ M_{,x}(x) + V(x) = 0 \end{cases} \\
\text{Section strain-displacement equations:} & \begin{cases} \varepsilon_o(x) = u_{o,x}(x) \\ \phi_o(x) = \theta_{,x}(x) \\ \gamma_o(x) = v_{o,x}(x) - \theta(x) \end{cases} \\
\text{Section constitutive relations:} & \vec{D}(x) = \vec{f}_{ms}\left(\vec{d}^e(x)\right)
\end{cases}
\tag{2-31}
$$

As well as the nonlocality relations in their total form, rather than rate form, i.e.:

$$
\vec{d}(x) - \frac{1}{2} l_c^2 \vec{d}_{,xx}(x) = \vec{d}^e(x)
\tag{2-32}
$$

Similar to the GI element formulation (Eq. (2-7)), the two BCs needed to solve Eq. (2-31) are selected to be of Dirichlet type, expressed as:

$$
\vec{d}(0) = \vec{d}^e(0), \ \vec{d}(L) = \vec{d}^e(L)
\tag{2-33}
$$

Although Eqs. (2-32) and (2-33) ensure the continuity of macroscopic section strain distributions along the element, an additional measure – enforced as an BC – is needed to bound the material section strains and provide objective force vs. displacement response during strain localization. Because the only section along the HSR element (other than the end sections) which may experience strain localization is the joint section, an additional Dirichlet BC is permanently enforced at the joint location, x_j, as:

$$
\vec{d}(x_j) = \vec{d}^e(x_j)
\tag{2-34}
$$

The nonlocality relations and their BCs (Eqs. (2-33) and (2-34)) do not need to be in rate form, because softening is not expected to occur at an arbitrary location along the element length, but it can only occur at the joint location (because its zero tensile strength makes it weaker than its adjacent sections).

The friction force, V_{fr}, at the joint location is obtained by integrating the frictional stresses, $\tau_{fr}(y)$, where y denotes the location on the cross section, over the cross section area, A, as:

$$V_{fr} = \int_A \tau_{fr}(y)\,dA \tag{2-35}$$

The hysteretic model used here to compute frictional stress, $\tau_{fr}(y)$, for a given sliding, u_{sl}, is essentially a uniaxial plasticity model with a constant loading/unloading stiffness, k_{fr}, and a yield/bounding surface defined as the product of the coefficient of friction, μ, and the normal contact stress, $\sigma(x_j, y)$, which is negative in compression. The coefficient of friction is taken to be pressure-dependent, i.e. $\mu = f_\mu(\sigma(y))$, in accordance with the experimental findings by Sideris (2012) and Reddy Goli (2019). Accordingly, the hysteretic model can be mathematically expressed as:

$$\dot{\tau}_{fr}(y) = k_{fr}\dot{u}_{sl} \quad \text{with} \quad \left|\tau_{fr}(y)\right| < f_\mu\left(\sigma(x_j, y)\right)\left|\sigma(x_j, y)\right| \tag{2-36}$$

It is noted that sliding, u_{sl}, at all points over the joint cross section is assumed to be constant and the contact stress is always non-positive, $\sigma(y) \leq 0$. Overall, Eqs. (2-35) and (2-36) can be presented as:

$$V_{fr} = f_{fr}\left(u_{sl}, k_{sl}, \sigma(x_j, y)\right) \tag{2-37}$$

In order to complete the system of equations, the shear force equilibrium at the joint location, x_j, yields:

$$V_{fr} = V(x_j) \tag{2-38}$$

2.3.2.2. Analytical Solution

The proposed HSR element formulation is obtained by solving Eqs. (2-31) thru (2-38). Solution to the equations of the GI beam theory requires six BCs, namely, three end displacements and three end forces. As opposed to the simply-supported reference system used in the solution of the GI beam-column element formulation (Figure 2-4), here, these BCs are chosen in accordance with the cantilever reference system shown in Figure 2-11. Solving the force equilibrium equations (first of Eq. (2-31)), analytically, for the section forces, $\vec{D}(x)$, yields:

$$\vec{D}(x) = [b(x)]\vec{Q} \quad \text{with} \quad [b(x)] = \begin{bmatrix} 1 & 0 & 0 \\ 0 & 1 & L-x \\ 0 & 0 & 1 \end{bmatrix} \tag{2-39}$$

where, similar to Eq. (2-8), $[b(x)]$ is the matrix of the section force shape functions, $\vec{Q}$ is the vector of end force BCs (Figure 2-11), and L is the element length. In addition, solving the shear force equilibrium at the HSR joint (Eq. (2-38)) yields:

$$V_{fr} = [b_{fr}]\vec{Q} \quad \text{with} \quad [b_{fr}] = [0 \quad 0 \quad 1] \tag{2-40}$$

where $[b_{fr}]$ is the matrix of the friction force shape function.
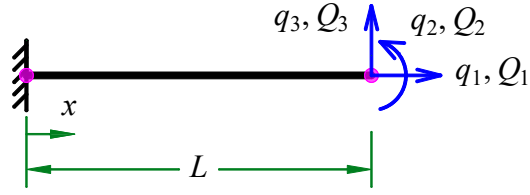
Figure 2-11. Cantilever reference system for HSR element formulation

According to Figure 2-12, the total end displacements, $\vec{q}$, of the HSR element (Figure 2-11) are determined as the sum of the end displacements obtained from the GI beam theory, $\vec{q}_{GI}$, i.e. those associated with material deformations and joint rocking, and the end displacements resulting from the joint sliding, $\vec{q}_{sl}$; in other words:

$$\vec{q} = \vec{q}_{GI} + \vec{q}_{sl} \tag{2-41}$$

By the direct integration of the macroscopic section strain-displacement equations (second of Eq. (2-31)), $\vec{q}_{GI}$ is given by:

$$\vec{q}_{GI} = \int_0^L \left[b(x) \right]^T \vec{d}(x) dx \quad \text{with} \quad \vec{q}_{GI} = \left[q_{GI,1} \quad q_{GI,2} \quad q_{GI,3} \right]^T \tag{2-42}$$

The end displacements due to joint sliding, $\vec{q}_{sl}$, are determined as (see Figure 2-12):

$$\vec{q}_{sl} = \left[b_{fr} \right]^T u_{sl} \quad \text{with} \quad \vec{q}_{sl} = \left[q_{sl,1} \quad q_{sl,2} \quad q_{sl,3} \right]^T \tag{2-43}$$

By assuming that the solution of the nonlocality relation (Eq. (2-32)) along with its BCs (Eqs. (2-33) and (2-34)) has the form:

$$\vec{d}(x) = \vec{f}_{nl}\left(\vec{d}^e(x) \right) \tag{2-44}$$

and substituting the third of Eqs. (2-31) into Eq. (2-39), Eq. (2-37) into Eq. (2-40), and Eqs. (2-42) and (2-43) into Eq. (2-41), the final system of equations is obtained as:

53

$$\begin{cases} \left[b(x) \right] \vec{Q} - \vec{f}_{ms}\left(\vec{d}^{e}(x) \right) = \vec{0} \\ \left[b_{fr} \right] \vec{Q} - f_{fr}\left(u_{sl}, k_{fr}, \sigma\left(x_j, y \right) \right) = \vec{0} \\ \vec{q} - \int_0^L \left[b(x) \right]^T \vec{f}_{nl}\left(\vec{d}^{e}(x) \right) dx - \left[b_{fr} \right]^T u_{sl} = \vec{0} \end{cases} \qquad (2\text{-}45)$$
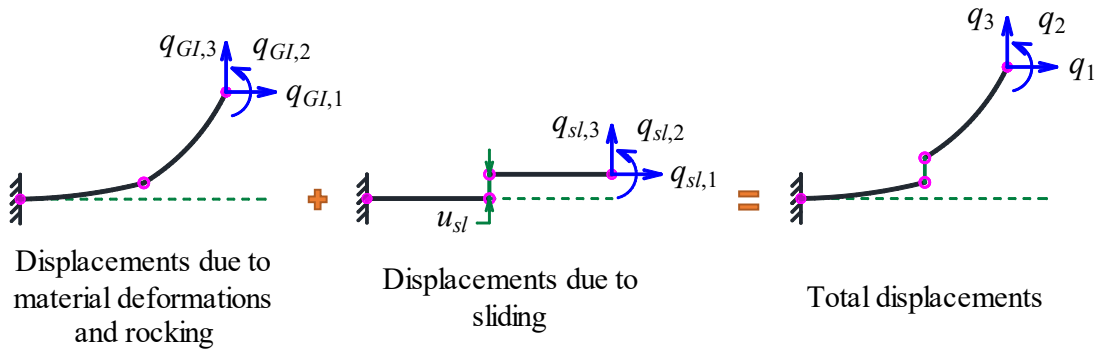
Figure 2-12. Compatibility of displacements for HSR element formulation

The first of Eqs. (2-45) represents the GI beam equilibrium and constitutive relations; the second of Eqs. (2-45) represents the shear force equilibrium and hysteretic friction model at the joint location; and the third of Eqs. (2-45) represents the displacement compatibility, accounting for contributions from material deformations, joint rocking, and joint sliding. For any given end displacements, $\vec{q}$, Eqs. (2-45) constitute a system of three equations in three unknowns, namely, $\vec{Q}$, $\vec{d}^{e}(x)$, and u_{sl}.

The element tangent flexibility matrix, $[f_{el}]$, is determined by using the chain rule and Eqs. (2-45), as:

$$[f_{el}] = \frac{\partial \vec{q}}{\partial \vec{Q}}$$

$$= \int_0^L [b(x)]^T [k_{nl}(x)][k_{ms}(x)]^{-1}[b(x)]dx + [b_{fr}]^T K_{fr}^{-1}[b_{fr}]$$

(2-46)

with:

$$\begin{cases} [k_{ms}(x)] = \left[\frac{\partial \vec{f}_{ms}}{\partial \vec{d}^e}(x) \right] \\ [k_{nl}(x)] = \left[\frac{\partial \vec{f}_{nl}}{\partial \vec{d}^e}(x) \right] \\ K_{fr} = \frac{\partial f_{fr}}{\partial u_{sl}} \end{cases}$$

(2-47)

where $[k_{ms}(x)]$ is the section tangent stiffness matrix, $[k_{nl}(x)]$ is the derivative of $\vec{d}(x)$ with respect to $\vec{d}^e(x)$, and K_{fr} is the tangent frictional stiffness.

2.3.2.3. Numerical Solution

Because the section constitutive relations ($\vec{f}_{ms}(.)$ from the third of Eq. (2-31)) and frictional constitutive relations ($f_{fr}(.)$ from Eq. (2-37)) are nonlinear, and the nonlocality relations (Eq. (2-32)) do not accept closed-form solution for arbitrary material strain distributions, Eqs. (2-45) need to be solved numerically. For this purpose, the element is discretized into N integration points along its length, which represent monitored cross-sections. The first of Eqs. (2-45) should be satisfied at all discrete IPs, while the second of Eqs. (2-45) should be satisfied at the joint location, x_j. Also, the integral in the third of Eqs. (2-45) is substituted by a weighted summation of the integrand values at the IP locations. The resulting discretized form of Eqs. (2-45) is expressed as:

$$
\begin{cases}
\left[b(x_1)\right]\vec{Q} - \vec{f}_{ms}\left(\vec{d}^e(x_1)\right) = \vec{0} \\
\left[b(x_2)\right]\vec{Q} - \vec{f}_{ms}\left(\vec{d}^e(x_2)\right) = \vec{0} \\
\quad\vdots \qquad\qquad \vdots \qquad\qquad \vdots \\
\left[b(x_N)\right]\vec{Q} - \vec{f}_{ms}\left(\vec{d}^e(x_N)\right) = \vec{0} \\
\left[b_{fr}\right]\vec{Q} - f_{fr}\left(u_{sl}, k_{fr}, \sigma(x_j, y)\right) = \vec{0} \\
\vec{q} - \sum_{i=1}^{N} w_i \left[b(x_i)\right]^T \vec{f}_{nl}\left(\vec{d}^e(x_i)\right) - \left[b_{fr}\right]^T u_{sl} = \vec{0}
\end{cases}
\tag{2-48}
$$

where x_i and w_i are the x-coordinate and the integration weight of the ith IP ($i = 1, 2, \ldots ,$ N), respectively, computed in accordance with a selected numerical integration method, with $\sum_{i=1}^{N} w_i = L$. Considering that the element length, L, can be smaller than l_c, which reduces the effectiveness of the nonlocality relations in spreading the damage, in such a condition (i.e. if $L < l_c$), the integration weights, w_i, are multiplied by l_c/L. The joint location, x_j, should always match one of the selected IP locations. Also, the first and last IPs should always be located at the element ends, i.e. $x_1 = 0$ and $x_N = L$.

Eq. (2-48) still requires the solution, $\vec{f}_{nl}\left(\vec{d}^e(x_i)\right)$, of the nonlocality relations (Eq. (2-32)), which can be obtained in a discretized form, by enforcing them at each IP location, and replacing the derivative with a 2nd order accurate central difference approximation. The resulting discretized form of the nonlocality relations of Eq. (2-32) at the ith IP location is:

$$
\vec{d}(x_i) - \frac{1}{2}l_c^2 \left(\frac{\vec{d}(x_{i+1}) - 2\vec{d}(x_i) + \vec{d}(x_{i-1})}{(\Delta x)^2} \right) = \vec{d}^e(x_i)
\tag{2-49}
$$

where Δx is the distance between any two adjacent IPs, which are considered to be equally-spaced. Combining Eq. (2-49) with the end BCs of Eqs. (2-33) and the additional BC of Eq. (2-34) for the joint location, yields:

$$\vec{d}_{tot} = [H]^{-1}\,\vec{d}_{tot}^{\,e} \quad \text{with} \quad \begin{cases} \vec{d}_{tot} = \left[\vec{d}^{\,T}(x_1) \quad \vec{d}^{\,T}(x_2) \quad \cdots \quad \vec{d}^{\,T}(x_N)\right]^T \\ \vec{d}_{tot}^{\,e} = \left[\vec{d}^{\,e\,T}(x_1) \quad \vec{d}^{\,e\,T}(x_2) \quad \cdots \quad \vec{d}^{\,e\,T}(x_N)\right]^T \end{cases} \tag{2-50}$$

where $\vec{d}_{tot}^{\,e}$ and $\vec{d}_{tot}$ are vectors including the material and macroscopic section strains, respectively, at all IP locations. Moreover, $[H]$ is a $3N$-by-$3N$ matrix, defined as:

$$[H] = \begin{bmatrix} [I_3] & [O_3] & & & & & & & \\ B_c[I_3] & A_c[I_3] & B_c[I_3] & & & & & & \\ & \ddots & \ddots & \ddots & & & & & \\ & & B_c[I_3] & A_c[I_3] & B_c[I_3] & & & & \\ & & & [O_3] & [I_3] & [O_3] & & & \\ & & & & B_c[I_3] & A_c[I_3] & B_c[I_3] & & \\ & & & & & \ddots & \ddots & \ddots & \\ & & & & & & B_c[I_3] & A_c[I_3] & B_c[I_3] \\ & & & & & & & [O_3] & [I_3] \end{bmatrix} \begin{matrix} IP_1 \\ IP_2 \\ \vdots \\ IP_{j-1} \\ IP_j \\ IP_{j+1} \\ \vdots \\ IP_{N-1} \\ IP_N \end{matrix} \tag{2-51}$$

where A_c and B_c are constants identical to those in Eqs. (2-18).

Utilizing Eq. (2-50), Eqs. (2-48) can be condensed into a matrix form:

$$\begin{cases} [B_Q]\vec{Q} - \vec{F}_{ms}\left(\vec{d}_{tot}^{\,e}\right) = \vec{0} \\ [b_{fr}]\vec{Q} - f_{fr}\left(u_{sl}, k_{fr}, \sigma(x_j, y)\right) = \vec{0} \\ \vec{q} - [B_q][H]^{-1}\vec{d}_{tot}^{\,e} - [b_{fr}]^T u_{sl} = \vec{0} \end{cases} \tag{2-52}$$

where $\vec{F}_{ms}$, $[B_Q]$, and $[B_q]$ are defined according to Eqs. (2-21). The final system of equations (Eqs. (2-52)) can be solved by using Newton-Raphson iterative solution algorithm, as:

$$
\left\{ \begin{array}{c} \vec{Q} \\ u_{sl} \\ \vec{d}^{\,e}_{tot} \end{array} \right\}_{k+1} = \left\{ \begin{array}{c} \vec{Q} \\ u_{sl} \\ \vec{d}^{\,e}_{tot} \end{array} \right\}_{k} -
$$

$$
\begin{bmatrix} \left[B_Q \right]_{3N \times 3} & \left[0 \right]_{3N \times 1} & -\left[K_{ms} \right]_{3N \times 3N} \\ \left[b_{fr} \right]_{1 \times 3} & -K_{fr} & \left[0 \right]_{1 \times 3N} \\ \left[0 \right]_{3 \times 3} & -\left[b_{fr} \right]^T_{3 \times 1} & -\left[B_q \right]\left[H \right]^{-1}_{3 \times 3N} \end{bmatrix}^{-1}_{k} \left\{ \begin{array}{c} \left[B_Q \right]\vec{Q} - \vec{F}_{ms}\left(\vec{d}^{\,e}_{tot} \right) \\ \left[b_{fr} \right]\vec{Q} - f_{fr}\left(u_{sl}, ... \right) \\ \vec{q} - \left[B_q \right]\left[H \right]^{-1} \vec{d}^{\,e}_{tot} - \left[b_{fr} \right]^T u_{sl} \end{array} \right\}_{k} \tag{2-53}
$$

where k is the iteration number, and $[K_{ms}]$ is the matrix including tangent section stiffness

matrices (for all IP locations) on its diagonal, formed as:

$$
\left[K_{ms} \right] = \begin{bmatrix} \left[k_{ms}\left(x_1 \right) \right] & \left[0 \right] & \cdots & \left[0 \right] \\ \left[0 \right] & \left[k_{ms}\left(x_2 \right) \right] & \cdots & \left[0 \right] \\ \vdots & \vdots & & \vdots \\ \left[0 \right] & \left[0 \right] & \cdots & \left[k_{ms}\left(x_N \right) \right] \end{bmatrix} \tag{2-54}
$$

Accordingly, the element tangent flexibility matrix, $[f_{el}]$, can be numerically

computed per Eq. (2-46), as:

$$
\left[f_{el} \right] = \frac{\partial \vec{q}}{\partial \vec{Q}} = \left[B_q \right]\left[K_{ms} \right]^{-1}\left[B_Q \right] + \left[b_{fr} \right]^T K_{fr}^{-1}\left[b_{fr} \right] \tag{2-55}
$$

2.3.2.4. Co-Rotational Transformations

Similar geometric transformations to those described in Section 2.3.1.4 for the GI element

formulation are necessary to transform the global nodal displacements and forces into the

co-rotated local system, and vice versa (Figure 2-13). The co-rotated local (basic)

coordinate system used for the HSR element formulation should, however, agree with the

cantilever reference system according to which the nodal displacement and force BCs

were defined (Figure 2-11). That is, herein, the basic coordinate system translates/rotates

with its origin rotationally and translationally constrained to the element's first node.
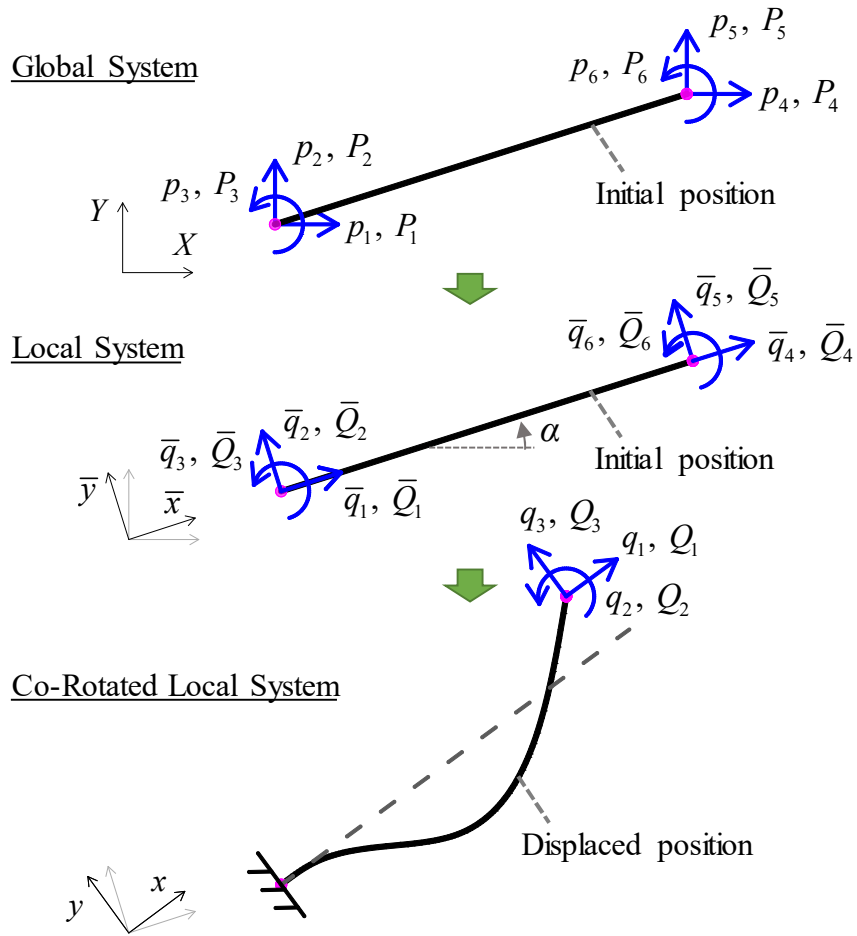
Figure 2-13. Co-rotational transformations for HSR element formulation

According to Figure 2-13, the relationships between the global nodal displacement vector, $\vec{p}$, and its local counterparts, $\vec{\overline{q}}$, is:

$$\vec{\overline{q}} = \left[T_{rot}(\alpha) \right] \vec{p} \quad \text{with} \quad \begin{cases} \vec{p} = \begin{bmatrix} p_1 & p_2 & p_3 & p_4 & p_5 & p_6 \end{bmatrix}^T \\ \vec{\overline{q}} = \begin{bmatrix} \overline{q}_1 & \overline{q}_2 & \overline{q}_3 & \overline{q}_4 & \overline{q}_5 & \overline{q}_6 \end{bmatrix}^T \end{cases} \quad (2\text{-}56)$$

where α is the angle that the local reference axes make with the global reference axes (which is constant), and $[T_{rot}(\theta)]$ is a simple rotation transformation matrix, expressed as:

$$[T_{rot}(\theta)] = \begin{bmatrix} \cos\theta & \sin\theta & 0 & 0 & 0 & 0 \\ -\sin\theta & \cos\theta & 0 & 0 & 0 & 0 \\ 0 & 0 & 1 & 0 & 0 & 0 \\ 0 & 0 & 0 & \cos\theta & \sin\theta & 0 \\ 0 & 0 & 0 & -\sin\theta & \cos\theta & 0 \\ 0 & 0 & 0 & 0 & 0 & 1 \end{bmatrix} \qquad \text{(2-57)}$$

with θ = rotation angle.

The basic nodal displacement vector, $\vec{q}$, is found by, first, rotating the local nodal displacements, $\vec{\bar{q}}$, to align with the basic coordinate axes (attached to the first node), and second, eliminating the parts of the displacements/rotations induced by rigid-body motion. Accordingly, $\vec{q}$ is obtained from $\vec{\bar{q}}$ as:

$$\vec{q} = [T_{lb,q}][T_{rot}(\bar{q}_3)]\vec{\bar{q}} - \vec{q}_{rot} \quad \text{with} \quad \vec{q}_{rot} = L \begin{Bmatrix} 1 - \cos\bar{q}_3 \\ 0 \\ \sin\bar{q}_3 \end{Bmatrix} \qquad \text{(2-58)}$$

where L is the initial length of the element and:

$$[T_{lb,q}] = \begin{bmatrix} -1 & 0 & 0 & 1 & 0 & 0 \\ 0 & 0 & -1 & 0 & 0 & 1 \\ 0 & -1 & 0 & 0 & 1 & 0 \end{bmatrix} \qquad \text{(2-59)}$$

After the basic nodal forces, $\vec{Q}$, are obtained from the element formulation for the basic nodal displacements, $\vec{q}$, resulted from Eq. (2-58), they can be transferred to the local coordinate system. For this purpose, in the first step, the three Q_j components (j = 1, 2, 3) are extended to extended to six components, using the force equilibrium equations for the cantilever reference system (Figure 2-11). In the second step, the resulting six components

are rotated to align with the local axes, generating the local nodal forces, $\vec{\bar{Q}}$. The above two steps are mathematically expressed as:

$$\vec{\bar{Q}} = \left[T_{rot}\left(\bar{q}_3\right)\right]^T \left[T_{lb,Q}\right]^T \vec{Q} \quad \text{with} \quad \vec{\bar{Q}} = \begin{bmatrix} \bar{Q}_1 & \bar{Q}_2 & \bar{Q}_3 & \bar{Q}_4 & \bar{Q}_5 & \bar{Q}_6 \end{bmatrix}^T \quad (2\text{-}60)$$

where:

$$\left[T_{lb,Q}\right] = \begin{bmatrix} -1 & 0 & q_3 & 1 & 0 & 0 \\ 0 & 0 & -1 & 0 & 0 & 1 \\ 0 & -1 & -L-q_1 & 0 & 1 & 0 \end{bmatrix} \quad (2\text{-}61)$$

Subsequently, the local nodal force vector, $\vec{\bar{Q}}$, can be transformed into its global counterpart, $\vec{P}$, via a rotation transformation, as:

$$\vec{P} = \left[T_{rot}\left(-\alpha\right)\right]\vec{\bar{Q}} = \left[T_{rot}\left(\alpha\right)\right]^T \vec{\bar{Q}}$$

$$\text{with} \quad \vec{P} = \begin{bmatrix} P_1 & P_2 & P_3 & P_4 & P_5 & P_6 \end{bmatrix}^T \quad (2\text{-}62)$$

Using the above transformations and the chain rule, the element tangent stiffness matrix in the global coordinate system, $[K_{el}]$, can be obtained from the element's flexibility matrix in the basic coordinate system, $[f_{el}]$ (Eq. (2-55)). By definition, $[K_{el}]$ equals the derivative of the global nodal force vector, $\vec{P}$, to the global nodal displacement vector, $\vec{p}$, which is:

$$\left[K_{el}\right] = \frac{\partial \vec{P}}{\partial \vec{p}} = \frac{\partial \vec{P}}{\partial \vec{\bar{Q}}} \frac{\partial \vec{\bar{Q}}}{\partial \vec{Q}} \frac{\partial \vec{Q}}{\partial \vec{q}} \frac{\partial \vec{q}}{\partial \vec{\bar{q}}} \frac{\partial \vec{\bar{q}}}{\partial \vec{p}} \quad (2\text{-}63)$$

where:

$$
\begin{cases}
\dfrac{\partial \vec{P}}{\partial \vec{\bar{Q}}} = \left[T_{rot}\left(\alpha\right) \right]^{T} \\[2ex]
\dfrac{\partial \vec{\bar{Q}}}{\partial \vec{\bar{Q}}} = \left[T_{rot}\left(\bar{q}_{3}\right) \right]^{T} \left[T_{lb,Q} \right]^{T} \\[2ex]
\dfrac{\partial \vec{\bar{Q}}}{\partial \vec{q}} = \left[f_{el} \right]^{-1} \\[2ex]
\dfrac{\partial \vec{q}}{\partial \vec{\bar{q}}} = \left[T_{lb,q} \right] \left(\dfrac{\partial \left[T_{rot}\left(\bar{q}_{3}\right) \right]}{\partial \vec{q}} \vec{\bar{q}} + \left[T_{rot}\left(\bar{q}_{3}\right) \right] \right) - \dfrac{\partial \vec{q}_{rot}}{\partial \vec{\bar{q}}} \\[2ex]
\dfrac{\partial \vec{\bar{q}}}{\partial \vec{p}} = \left[T_{rot}\left(\alpha\right) \right]
\end{cases}
\tag{2-64}
$$

According to Eqs. (2-57) and (2-58), the two unknown terms in the fourth of Eqs. (2-64) are also found as:

$$
\begin{aligned}
\frac{\partial \left[T_{rot}\left(\bar{q}_{3}\right) \right]}{\partial \vec{\bar{q}}} \vec{\bar{q}} &= \sum_{i=1}^{6} \frac{\partial \left[T_{rot}\left(\bar{q}_{3}\right) \right]}{\partial \bar{q}_{i}} \bar{q}_{i} \\[2ex]
&= \begin{bmatrix}
-\sin\bar{q}_{3} & \cos\bar{q}_{3} & 0 & 0 & 0 & 0 \\
-\cos\bar{q}_{3} & -\sin\bar{q}_{3} & 0 & 0 & 0 & 0 \\
0 & 0 & 0 & 0 & 0 & 0 \\
0 & 0 & 0 & -\sin\bar{q}_{3} & \cos\bar{q}_{3} & 0 \\
0 & 0 & 0 & -\cos\bar{q}_{3} & -\sin\bar{q}_{3} & 0 \\
0 & 0 & 0 & 0 & 0 & 0
\end{bmatrix} \bar{q}_{3}
\end{aligned}
\tag{2-65}
$$

and:

$$
\frac{\partial \vec{q}_{rot}}{\partial \vec{\bar{q}}} = L \begin{bmatrix}
0 & 0 & \sin\bar{q}_{3} & 0 & 0 & 0 \\
0 & 0 & 0 & 0 & 0 & 0 \\
0 & 0 & \cos\bar{q}_{3} & 0 & 0 & 0
\end{bmatrix}
\tag{2-66}
$$

2.3.2.5. Evaluation

The mesh convergence of the proposed HSR element formulation's responses needs to be evaluated. For this purpose, this element formulation is used to simulate a reinforced

concrete column with a rocking joint at its mid-length, as depicted in Figure 2-14(a). The

column is under a constant vertical load of $P = 288$ kips ($= 0.1f'_cA_g$) and a monotonically

increasing lateral displacement δ. The column is modeled as shown in Figure 2-15, where

an HSR element with a length of 1 ft is used in the middle of the column height to represent

the rocking joint and two GI elements represent the remaining length of the column. Both

element formulations use the composite Simpson's integration rule to integrate strain-

displacement equations (i.e. in the last of Eqs. (2-48)). The value of l_c for the GI elements

is taken as 24 in. (= cross section depth) and each GI element has 5 IPs, leading to a $l_c/\Delta x$

> 1.5, sufficient to ensure response objectivity (Salehi and Sideris 2016; 2017).
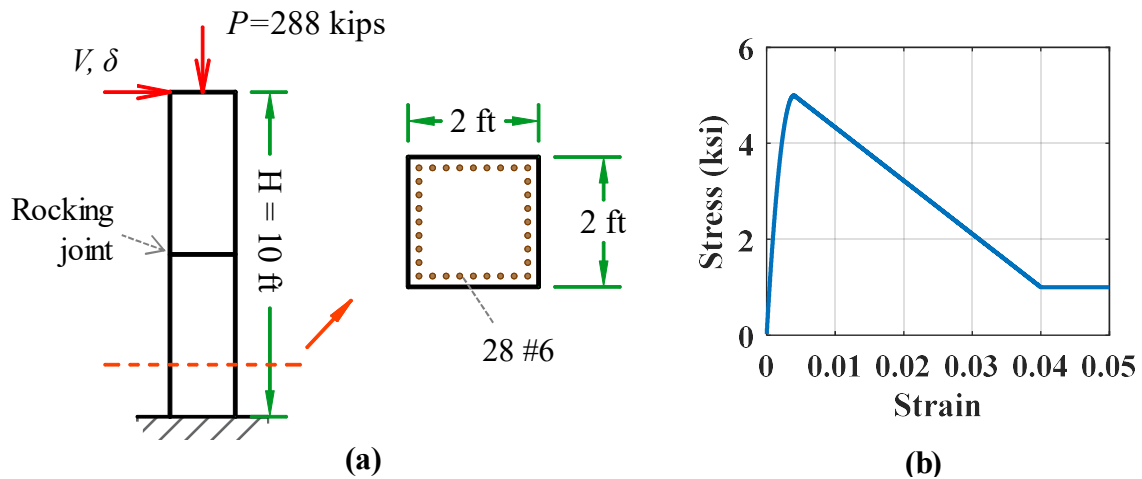
Figure 2-14. Evaluation of HSR element: (a) column dimensions; (b) stress-strain backbone curve of concrete material

Each cross section is discretized into 48 layers of concrete material with the stress-

strain backbone curve shown in Figure 2-14(b) (Scott et al. 1982), and, if not at the rocking

joint, steel fibers of bilinear behavior. The modulus of elasticity, yield stress, and strain

63

hardening ratio for the steel material are chosen to be 29,000 ksi, 68 ksi, and 1%. The fiber section at the rocking joint location (corresponding to the middle IP in the HSR element) does not include any steel fibers. The value of l_c for the HSR element remains constant in all analyses and it equals half of the cross section depth, i.e. 12 in.
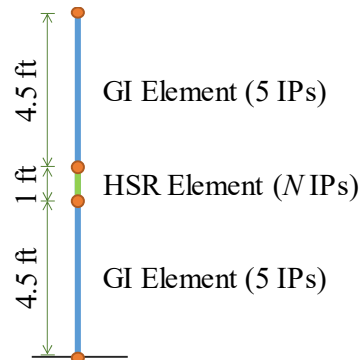
Figure 2-15. Evaluation of HSR element: model description

The lateral force (V) vs. displacement (δ) responses obtained from the model with various number of IPs used in the HSR element formulation, N, are compared in Figure 2-16(a). It is observed that for the values of N resulting in $l_c/\Delta x \geq 2$ the responses remain very similar, while for the case with $l_c/\Delta x = 1$ the predicted strength deterioration is less severe. Likewise, the macroscopic curvature distributions generated by the HSR element formulation with different N values become very close as $l_c/\Delta x$ exceeds 2 (Figure 2-16(b)). It is noted that the maximum curvature (predicted at the rocking joint location) does not increase by N, which would be the case if strain localization was not alleviated.
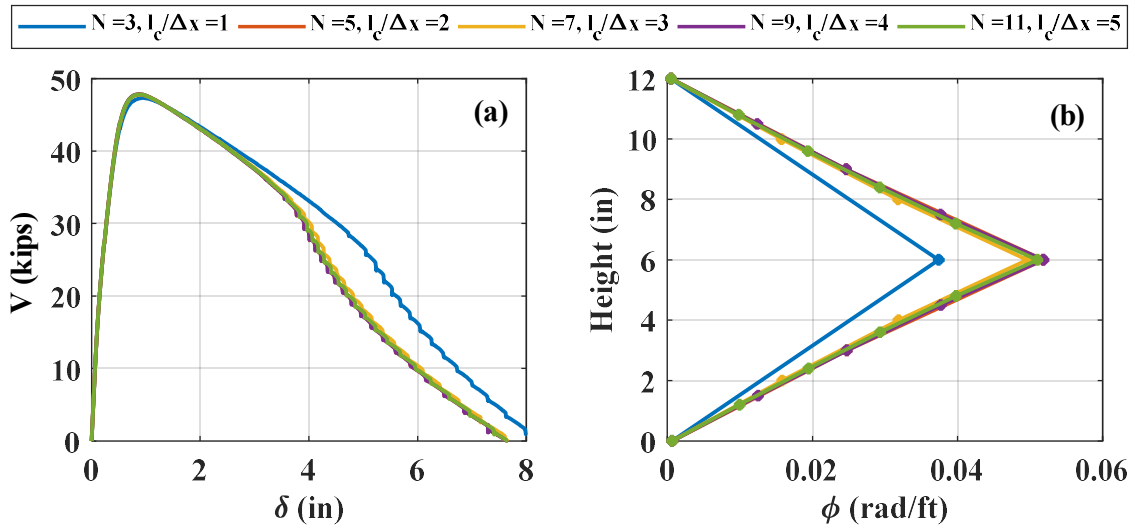
Figure 2-16. Evaluation of HSR element: (a) *V-δ* responses; (b) macroscopic curvature distributions

2.3.2.6. Extension to 3D

The basic HSR element formulation is also easily extendable to three dimensions, but it requires the friction model used in this formulation to be of bidirectional type – i.e. generating the firctional stresses considering the sliding components in both transverse directions – and its co-rotational geometric transformations to refer to 3D – the latter may be somewhat complicated to derive. In the following, the system of equations for such an element formulation are described and a bidirectional friction model that has been found effective by the author is introduced.

For the 3D HSR element formulation, the section strain-displacement equations, equilibrium equations, and section constitutive relations are identical to those for the 3D gradient inelastic beam theory, i.e. Eqs. (2-27) thru (2-29). The nonlocality relations and

their associated boundary conditions remain the same as Eqs. (2-31) thru (2-34), while the vector of macroscopic section strains is extended to that of Eq. (2-30).

In the 3D HSR element formulation, the sliding components increase from one to three (Figure 2-17(a)), i.e. two translational components along y- and z-axes, denoted by v_{sl} and w_{sl}, respectively, and one torsional, denoted by θ_{sl}. The joint friction force components also increase to three, including two shear forces, $V_{fr,y}$ and $V_{fr,z}$, and a torsion, T_{fr}. Accordingly, the friction model in the 3D element formulation should relate the friction force vector, $\vec{F}_{fr}$, to the sliding vector, $\vec{d}_{sl}$, as:

$$\vec{F}_{fr} = \vec{f}_{fr}\left(\vec{d}_{sl}, \sigma\left(x_j, y, z\right)\right) \quad \text{with} \quad \begin{cases} \vec{F}_{fr} = \begin{bmatrix} V_{fr,y} & V_{fr,z} & T_{fr} \end{bmatrix}^T \\ \vec{d}_{sl} = \begin{bmatrix} v_{sl} & w_{sl} & \theta_{sl} \end{bmatrix}^T \end{cases} \tag{2-67}$$

The friction force components are obtained by integrating the frictional stresses in the two transverse directions, i.e. $\tau_{fr,y}$ and $\tau_{fr,z}$, over the joint area (Figure 2-17(b)), as:

$$\begin{cases} V_{fr,y} = \int_A \tau_{fr,y}\left(y,z\right) dA \\ V_{fr,z} = \int_A \tau_{fr,y}\left(y,z\right) dA \\ T_{fr} = \int_A \left(y\tau_{fr,z}\left(y,z\right) - z\tau_{fr,y}\left(y,z\right)\right) dA \end{cases} \tag{2-68}$$

The frictional stresses at any location (y,z) over the joint area are dependent on both sliding component at that location, while their resultant should be in the direction of sliding. In order to generate frictional stresses with such quality, the bidirectional friction model employed here matches that proposed by Constantinou et al. (1990), which is based on the plasticity model originally developed by Wen (1989). According to this model:

$$\left\{ \begin{array}{c} \tau_{fr,y} \\ \tau_{fr,z} \end{array} \right\} = \mu \left\langle -\sigma \right\rangle \left\{ \begin{array}{c} Z_y \\ Z_z \end{array} \right\} \tag{2-69}$$

where Z_y and Z_z are dimensionless variables determining the hysteresis of the frictional stresses in the y and z directions and μ is the coefficient of friction, which may be dependent on pressure and velocity. These variables are computed in accordance with the following differential equations:

$$\begin{cases} \dot{Z}_y = \dfrac{1}{\eta}\left(A\dot{v}_{sl} - \beta\left|\dot{v}_{sl}Z_y\right|Z_y - \gamma\dot{v}_{sl}Z_y^2 - \beta\left|\dot{w}_{sl}Z_z\right|Z_y - \gamma\dot{w}_{sl}Z_yZ_z \right) \\ \dot{Z}_z = \dfrac{1}{\eta}\left(A\dot{w}_{sl} - \beta\left|\dot{w}_{sl}Z_z\right|Z_z - \gamma\dot{w}_{sl}Z_z^2 - \beta\left|\dot{v}_{sl}Z_y\right|Z_z - \gamma\dot{v}_{sl}Z_yZ_z \right) \end{cases} \tag{2-70}$$

where A, β, and γ are dimensionless constants influencing the initial stiffness and the shape of transition from elastic to plastic branches, while η is a displacement constant. The values of these constants are determined by calibration based on experimental data, but $A/(\beta + \gamma)$ must be 1, so that the Z parameters vary between -1 and 1.
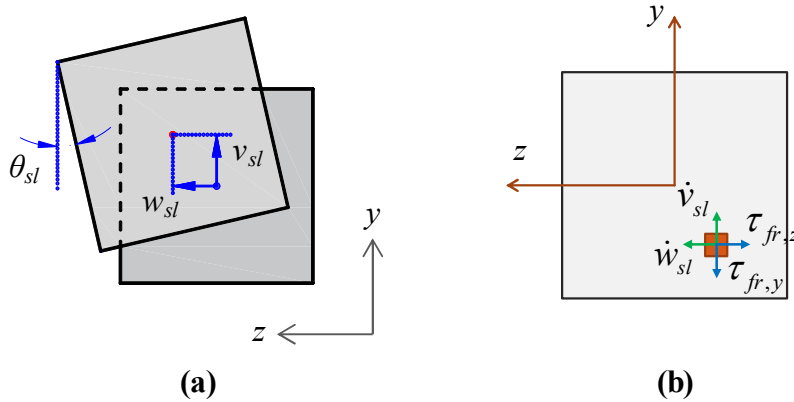
Figure 2-17. (a) Joint sliding components; (b) sliding rates and frictional stresses

In terms of displacement compatibility equations, a similar equation to Eq. (2-41) for 2D element formulation holds for the 3D version, too (see Figure 2-18).
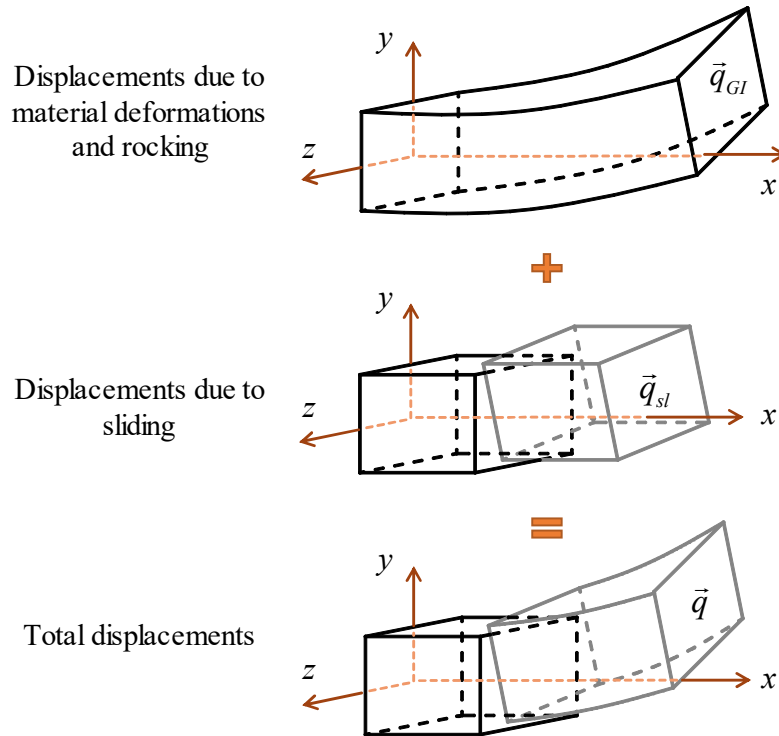
Figure 2-18. Compatibility of displacements for 3D HSR element formulation

2.3.3. Continuous Multi-Node Truss Element

This section is based on Salehi et al. (2020). The continuous multi-node truss element simulates unbonded tendons via a series of truss sub-elements, which share the same axial strain (and stress) over their entire length. This axial strain is computed as the total tendon elongation (i.e. sum of the elongations of all sub-elements) divided by the initial total tendon length (i.e. sum of the initial lengths of all sub-elements). This formulation addresses erroneously predicted strain concentrations that lead to predictions of premature

tendon yielding/fracture at individual short elements in the vicinity of rocking/sliding joints when tendons are modeled using individual truss elements. However, this formulation does not account for the friction between tendons and the ducts, and thus, cannot predict axial force variations along a tendon's length. Physically, within this formulation, all the intermediate (as opposed to the boundary/end) nodes of the continuous multi-node truss element can be thought of as frictionless rings through which the tendon slides (Figure 2-19).
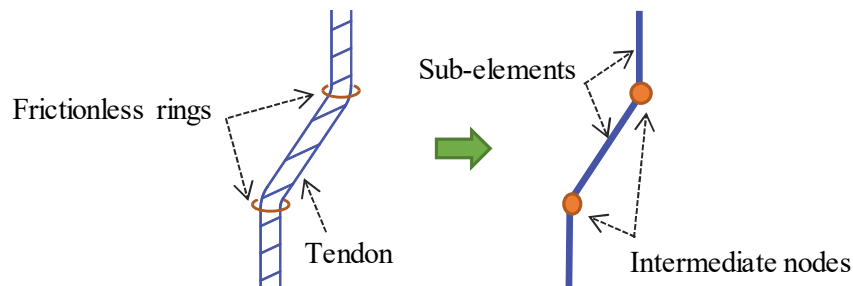
Figure 2-19. Concept of multi-node continuous truss element

2.3.3.1. Basic Equations

Each continuous multi-node truss element can include any number of nodes, which result in sub-elements of arbitrary lengths and initial orientations (Figure 2-20(a)). Each sub-element is essentially a truss element that can only sustain axial forces. All sub-elements sustain the same axial strain, ε_t, obtained as:

$$\varepsilon_t = \sum_{i=1}^{N} u_i \Big/ \sum_{i=1}^{N} L_i \quad \text{with} \quad u_i = l_i - L_i \tag{2-71}$$

where u_i, L_i, and l_i are the axial deformation, the initial length, and the current length of the ith sub-element (i = 1, 2, …, N), respectively, while N is the total number of sub-elements.

Having obtained ε_t, the axial force, F_t, which is the same for all sub-elements, can subsequently be determined as:

$$F_t = A_t \sigma_t (\varepsilon_t)$$

(2-72)

where A_t is the cross section area, which is the same for all sub-elements, and $\sigma_t(\varepsilon_t)$ is the axial stress, which is obtained from a selected material model as a function of the axial strain, ε_t, and its history.
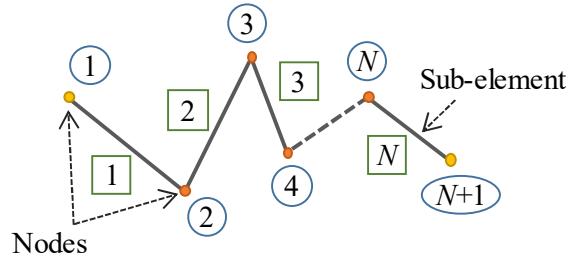
Figure 2-20. Continuous multi-node truss element configuration

The tangent axial stiffness of the ith sub-element is obtained as:

$$k_i = \frac{\partial F_t}{\partial u_i} = A_t \frac{\partial \sigma_t}{\partial \varepsilon_t} \frac{\partial \varepsilon_t}{\partial u_i} = A_t E_{tan} \bigg/ \sum_{i=1}^{N} L_i$$

(2-73)

where E_{tan} is the tangent elasticity modulus obtained from the material model. As expected, it is clear per Eq. (2-73) that k_i is equal for all the sub-elements, i.e. $k_i = k_t$ for i = 1, 2, …, N.

70

2.3.3.2. Co-Rotational Computations

The initial length of each sub-element, L_i, is determined from the initial coordinates of the nodes of that sub-element at the beginning of the analysis, while the current length, l_i, is calculated according to the updated locations of the truss nodes at each analysis step. Denoting the initial and current coordinates of the jth node (j = 1, 2, …, N+1) as $\vec{X}_j$ and $\vec{x}_j$, respectively, the corresponding lengths are obtained as:

$$L_i = \left\| \vec{X}_{i+1} - \vec{X}_i \right\| \quad \text{and} \quad l_i = \left\| \vec{x}_{i+1} - \vec{x}_i \right\| \tag{2-74}$$

where $\|.\|$ represents the Euclidean norm. It is noted that the current coordinates of the jth node, $\vec{x}_j$, are determined as:

$$\vec{x}_j = \begin{Bmatrix} x_{j,1} \\ x_{j,2} \end{Bmatrix} = \begin{Bmatrix} X_{j,1} + p_{j,1} \\ X_{j,2} + p_{j,2} \end{Bmatrix} \tag{2-75}$$

with $x_{j,1}$ and $x_{j,2}$ being the horizontal and vertical coordinates in $\vec{x}_j$, respectively; $X_{j,1}$ and $X_{j,2}$ being the horizontal and vertical coordinates in $\vec{X}_j$, respectively; and $p_{j,1}$ and $p_{j,2}$ being the horizontal and vertical global nodal displacements of the jth node.

In order to obtain the nodal reactions for the entire multi-node element, first, the nodal reactions for each sub-element are obtained, and then, they are used to assemble the entire element's global nodal force vector, $\vec{P}$. The global nodal force vector for the ith sub-element, $\vec{P}_i^{sub}$, can be obtained from the force equilibrium at its two end nodes in the sub-element's deformed configuration, neglecting the axial force in the other truss sub-elements. According to Figure 2-21:

$$\vec{P}_i^{sub} = \begin{Bmatrix} P_{i,1}^{sub} \\ P_{i,2}^{sub} \\ P_{i,3}^{sub} \\ P_{i,4}^{sub} \\ P_{i,5}^{sub} \\ P_{i,6}^{sub} \end{Bmatrix} = \vec{t}_{bg} F_t \quad \text{with} \quad \vec{t}_{bg} = \begin{Bmatrix} -c_i \\ -s_i \\ 0 \\ c_i \\ s_i \\ 0 \end{Bmatrix} \tag{2-76}$$

where c_i and s_i are the direction cosine and sine of the ith sub-element, obtained as:

$$\begin{cases} c_i = \cos\theta_i = \left(x_{i+1,1} - x_{i,1}\right)/l_i \\ s_i = \sin\theta_i = \left(x_{i+1,2} - x_{i,2}\right)/l_i \end{cases} \tag{2-77}$$
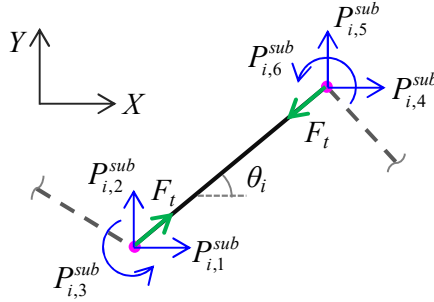
Figure 2-21. Global nodal forces for a truss sub-element

Accordingly, the vector of global nodal reactions for the jth node, $\vec{P}_j$, is found as:

$$\vec{P}_j = \begin{Bmatrix} P_{j,1} \\ P_{j,2} \\ P_{j,3} \end{Bmatrix} = \begin{cases} \begin{bmatrix} P_{1,1}^{sub} & P_{1,2}^{sub} & P_{1,3}^{sub} \end{bmatrix}^T & j=1 \\ \begin{bmatrix} P_{j-1,4}^{sub}+P_{j,1}^{sub} & P_{j-1,5}^{sub}+P_{j,2}^{sub} & P_{j-1,6}^{sub}+P_{j,3}^{sub} \end{bmatrix}^T & 2 \le j \le N \\ \begin{bmatrix} P_{N,4}^{sub} & P_{N,5}^{sub} & P_{N,6}^{sub} \end{bmatrix}^T & j=N+1 \end{cases} \tag{2-78}$$

The element's tangent stiffness matrix in the global coordinate system is also assesmbled using the sub-element's tangent stiffness matrices in the global system. The global tangent stiffness matrix for the ith subelement, $[K_i^{sub}]$, is computed as:

$$\left[K_i^{sub}\right] = \frac{\partial \vec{P}_i^{sub}}{\partial \vec{p}_i^{sub}} \quad \text{with} \quad \vec{p}_i^{sub} = \begin{bmatrix} p_{i,1} & p_{i,2} & p_{i,3} & p_{i+1,1} & p_{i+1,2} & p_{i+1,3} \end{bmatrix}^T \quad (2\text{-}79)$$

where $\vec{p}_i^{sub}$ contains the global nodal displacements of the ith subelement. Per Eq. (2-76), Eq. (2-79) gives:

$$\left[K_i^{sub}\right] = \vec{t}_{bg} \frac{\partial F_t}{\partial \vec{p}_i^{sub}} + \frac{\partial \vec{t}_{bg}}{\partial \vec{p}_i^{sub}} F_t \quad (2\text{-}80)$$

The partial derivative in the first term on the right-hand side of Eq. (2-80) can be determined per Eqs. (2-71) and (2-72), as:

$$\frac{\partial F_t}{\partial \vec{p}_i^{sub}} = A_t \frac{\partial \sigma_t}{\partial \varepsilon_t} \frac{\partial \varepsilon_t}{\partial \left(\sum\limits_{m=1}^{N} u_m\right)} \frac{\partial \left(\sum\limits_{m=1}^{N} u_m\right)}{\partial \vec{p}_i^{sub}} \quad \text{with} \quad \begin{cases} \dfrac{\partial \sigma_t}{\partial \varepsilon_t} = E_t \\[2ex] \dfrac{\partial \varepsilon_t}{\partial \left(\sum\limits_{m=1}^{N} u_m\right)} = \dfrac{1}{\sum\limits_{m=1}^{N} L_m} \end{cases} \quad (2\text{-}81)$$

where E_t is the tangent modulus resulting from the material model. The last partial derivative in Eq. (2-81) is determined per Eq. (2-71), as follows:

$$\frac{\partial \left(\sum\limits_{m=1}^{N} u_m\right)}{\partial \vec{p}_i^{sub}} = \frac{\partial l_{tot}}{\partial \vec{p}_i^{sub}} = \begin{bmatrix} \dfrac{\partial l_{tot}}{\partial p_{i,1}} & \dfrac{\partial l_{tot}}{\partial p_{i,2}} & \dfrac{\partial l_{tot}}{\partial p_{i,3}} & \dfrac{\partial l_{tot}}{\partial p_{i+1,1}} & \dfrac{\partial l_{tot}}{\partial p_{i+1,2}} & \dfrac{\partial l_{tot}}{\partial p_{i+1,3}} \end{bmatrix} \quad (2\text{-}82)$$

with l_{tot} being equal to $\sum\limits_{m=1}^{N} l_m$. According to Eqs. (2-74), (2-75), and (2-77):

$$\frac{\partial l_{tot}}{\partial \vec{p}_i^{\,sub}} = \begin{bmatrix} \dfrac{\partial l_{tot}}{\partial p_{i,1}} & \dfrac{\partial l_{tot}}{\partial p_{i,2}} & \dfrac{\partial l_{tot}}{\partial p_{i,3}} & \dfrac{\partial l_{tot}}{\partial p_{i+1,1}} & \dfrac{\partial l_{tot}}{\partial p_{i+1,2}} & \dfrac{\partial l_{tot}}{\partial p_{i+1,3}} \end{bmatrix}$$

$$= \begin{cases} \begin{bmatrix} -c_i & -s_i & 0 & c_i - c_{i+1} & s_i - s_{i+1} & 0 \end{bmatrix} & i = 1 \\[2mm] \begin{bmatrix} c_{i-1} - c_i & s_{i-1} - s_i & 0 & c_i - c_{i+1} & s_i - s_{i+1} & 0 \end{bmatrix} & 1 < i < N \\[2mm] \begin{bmatrix} c_{i-1} - c_i & s_{i-1} - s_i & 0 & c_i & s_i & 0 \end{bmatrix} & i = N \end{cases} \tag{2-83}$$

The partial derivative in the second term on the right-hand side of Eq. (2-80) can be determined per Eqs. (2-76) and (2-77), as:

$$\frac{\partial \vec{t}_{bg}}{\partial \vec{p}_i^{\,sub}} = \begin{bmatrix} \dfrac{\partial \vec{t}_{bg}}{\partial p_{i,1}} & \dfrac{\partial \vec{t}_{bg}}{\partial p_{i,2}} & \dfrac{\partial \vec{t}_{bg}}{\partial p_{i,3}} & \dfrac{\partial \vec{t}_{bg}}{\partial p_{i+1,1}} & \dfrac{\partial \vec{t}_{bg}}{\partial p_{i+1,2}} & \dfrac{\partial \vec{t}_{bg}}{\partial p_{i+1,3}} \end{bmatrix}$$

$$= \frac{1}{l_i} \begin{bmatrix} 1 - c_i^2 & -s_i c_i & 0 & c_i^2 - 1 & s_i c_i & 0 \\ -s_i c_i & 1 - s_i^2 & 0 & s_i c_i & s_i^2 - 1 & 0 \\ 0 & 0 & 0 & 0 & 0 & 0 \\ c_i^2 - 1 & s_i c_i & 0 & 1 - c_i^2 & -s_i c_i & 0 \\ s_i c_i & s_i^2 - 1 & 0 & -s_i c_i & 1 - s_i^2 & 0 \\ 0 & 0 & 0 & 0 & 0 & 0 \end{bmatrix} \tag{2-84}$$

Obviously, because the truss sub-elements cannot withstand moment, the elements of the stiffness matrix associated with the rotational DOFs are zeros (see Eq. (2-84)).

2.3.3.3. Evaluation

In order to evaluate the capability of the proposed multi-node continuous truss element in enforcing uniform axial force along the entire length of an unbonded tendon, the responses of the three models demonstrated in Figure 2-22 under the displacement δ applied at its horizontally free end are compared. As indicated in the figures, Models 1, 2, and 3 consist of one two-node truss element, three two-node truss elements, and one multi-node truss element, respectively. The cross sectional area for all elements is 1.4 cm^2 and the material

is assumed to be bilinear, with the modulus of elasticity of 196.5 GPa, the yield strength

of 1.67 GPa, and a post-yield hardening ratio of 1%.
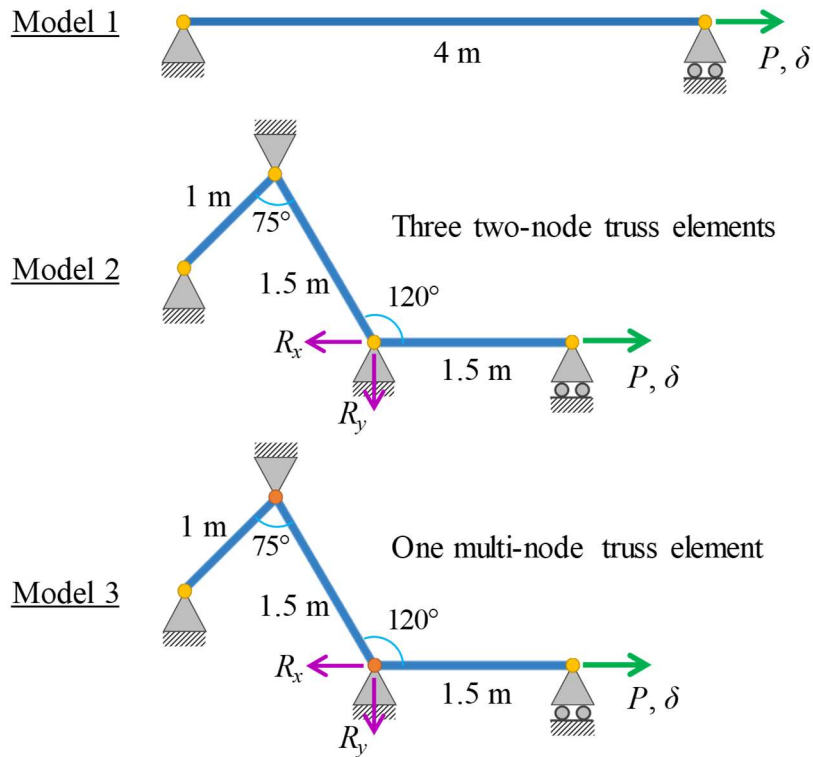
Figure 2-22. Evaluation of multi-node truss element: compared models

A monotonically increasing displacement is applied as δ in all three models and the

values of the force P and the reactions R_x and R_y (only available in Models 2 and 3) are

monitored. The P-δ responses are compared in Figure 2-23. As expected, Model 2 with

two-node truss elements exhibits an earlier yielding, because it does not allow propagation

of the elongation from the horizontal element to the two oblique elements. However,

Model 3 have a similar response to that of Model 1 with one two-node truss element of

the same total length (4 m), confirming the ability of the multi-node truss element in enforcing a constant strain over all sub-elements.
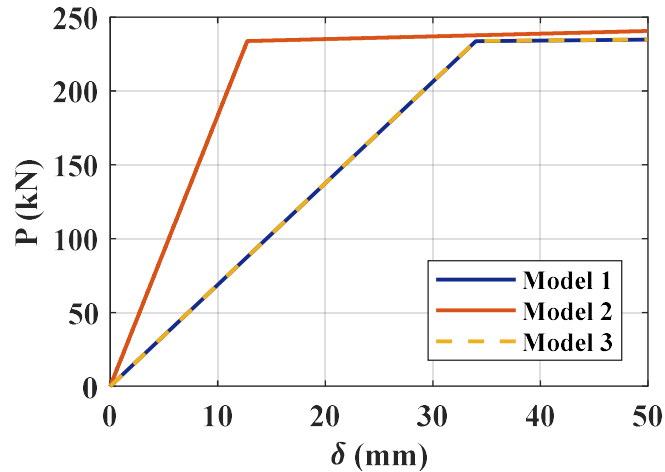
Figure 2-23. Evaluation of multi-node truss element: *P-δ* responses

The above results are further supported by the reactions, R_x and R_y, predicted by Models 2 and 3 (Figure 2-24). Comparing the *P-δ* (Figure 2-23) and R_x-δ (Figure 2-24) responses obtained from Model 3 indicates that *P* has completely transformed into the horizontal reaction, R_x, transferring no force to the adjacent two-node truss element. This is why the vertical reaction, R_y, remains zero for any δ. On the contrary, according to the predicted reactions R_x and R_y, Model 3 with a multi-node truss element is found capable of producing constant axial force over all its sub-elements, irrespective of their orientations. At the yielding point (*P* = 234 kN), for example, R_x and R_y are equal to 117 kN and 203 kN, respectively, which correspond with their expected analytical values, i.e. *P* (1 – cos 60°) and *P* sin 60°, respectively.
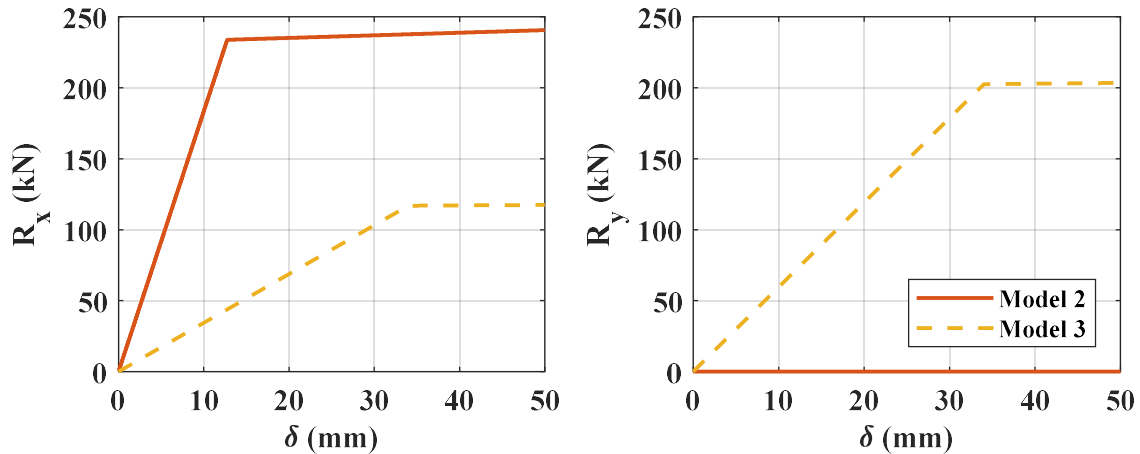
Figure 2-24. Evaluation of multi-node truss element: R_x-δ and R_y-δ responses

2.3.3.4. Extension to 3D

Extending the discussed formulation to three dimensions is straightforward, although the co-rotational transformations become slightly more complicated. The basic equations defining the element state remain the same as Eqs. (2-71) thru (2-73). The geometric transformations can be derived similarly to the derivation provided for the 2D element formulation, but it is not provided herein.

2.3.4. Zero-Length Constraint Element

The zero-length constraint element is developed to represent the interactions of the tendons with their ducts, while accounting for large rotations. Updating the geometry in this element formulation is important, because the predicted response of HSR columns can be considerably affected by the rotations of the ducts due to rocking (see Figure 2-25). The propoposed formulations ensures that the tendons will remain within the ducts in the deformed/rotated segment configuration. The proposed element formulation simultaneously applies three independent constraints between its two end nodes, namely:

77

(*i*) longitudinal constraint; (*ii*) transverse constraint; and (*iii*) rotational constraint (Figure 2-26).
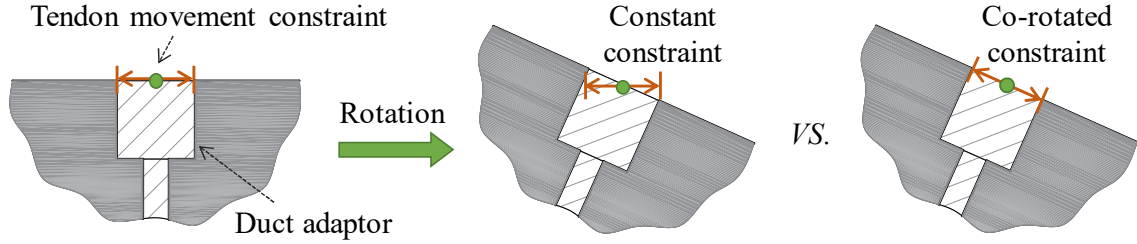
Figure 2-25. Effect of rotation on elements with constant and updated geometry

2.3.4.1. Basic Equations

The concept of the proposed zero-length constraint element is schematically depicted in Figure 2-26. The basic nodal forces, Q_i, (i = 1,2,3) are obtained from uniaxial constraint functions, as:

$$\vec{Q} = \begin{Bmatrix} Q_1 \\ Q_2 \\ Q_3 \end{Bmatrix} = \begin{Bmatrix} f_l(q_1) \\ f_t(q_2) \\ f_r(q_3) \end{Bmatrix} \tag{2-85}$$

where f_t, f_l, and f_r represent the transverse, longitudinal, and rotation constraint functions, respectively. In accordance with Eq. (2-85), the element's tangent stiffness matrix in its co-rotated local (basic) system, $[k_{el}]$, is obtained as:

$$[k_{el}] = \frac{\partial \vec{Q}}{\partial \vec{q}} = \begin{bmatrix} \partial f_l(q_1)/\partial q_1 & 0 & 0 \\ 0 & \partial f_t(q_2)/\partial q_2 & 0 \\ 0 & 0 & \partial f_r(q_3)/\partial q_3 \end{bmatrix} \tag{2-86}$$

The elements of the stiffness matrix of Eq. (2-86) are generated by the constraint functions.
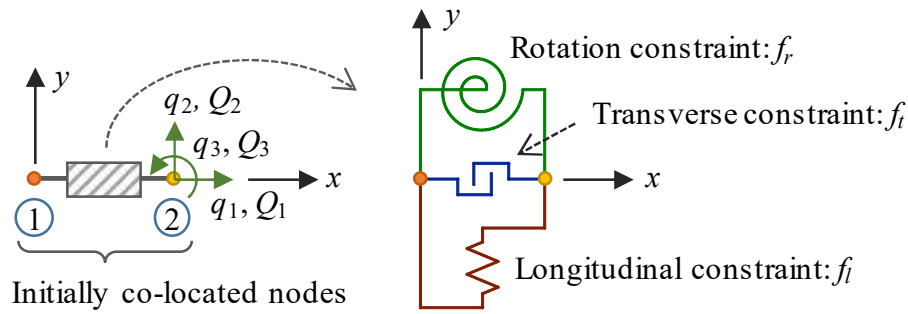
Figure 2-26. Concept of zero-length constraint element

2.3.4.2. Co-rotational Transformations

Considering that the basic reference system for the constraint element translates/rotates with its first node (node 1 in Figure 2-26), the co-rotational transformations employed here are similar to those discussed for the HSR element (see Section 2.3.2.4 and Figure 2-13). As a result, Eqs. (2-56) thru (2-66) are also applicable here, except the initial length of the element, L, is zero for the constraint element and $[f_{el}]^{-1}$ in Eqs. (2-64) is equal to $[k_{el}]$ from Eq. (2-86).

2.3.4.3. Extension to 3D

The 3D zero-length constraint element formulation provides six constraints between the nodes it connects, namely, three enforced to the displacements along the element's three basic coordinate axes and three enforced to the rotations around those axes (Figure 2-27(a)). As a result, in its basic system, the 3D element formulation involves six nodal displacements and six corresponding nodal forces, as shown in Figure 2-27(b).
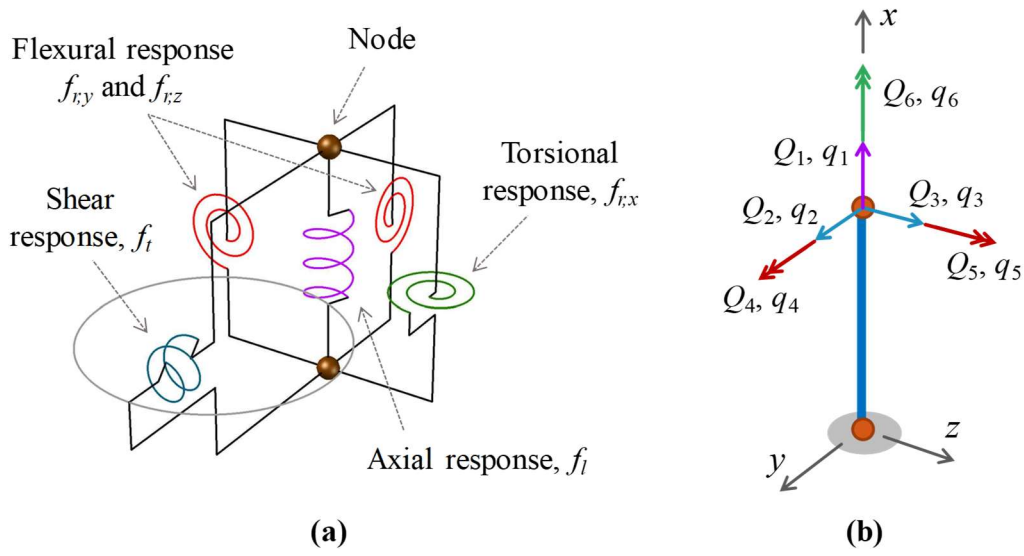
Figure 2-27. 3D zero-length constraint element: (a) concept; (b) reference system

The constraints on the two transverse relative displacements of the nodes can be coupled, e.g. to constrain the movement of the tendons within a circular boundary. With such a transverse displacement constraint, the basic nodal forces can be obtained as:

$$\vec{Q} = \begin{Bmatrix} Q_1 \\ Q_2 \\ Q_3 \\ Q_4 \\ Q_5 \\ Q_6 \end{Bmatrix} = \begin{Bmatrix} f_l(q_1) \\ \dfrac{q_2}{\sqrt{q_2^2 + q_3^2}} f_t\left(\sqrt{q_2^2 + q_3^2}\right) \\ \dfrac{q_3}{\sqrt{q_2^2 + q_3^2}} f_t\left(\sqrt{q_2^2 + q_3^2}\right) \\ f_{r,y}(q_4) \\ f_{r,z}(q_5) \\ f_{r,x}(q_6) \end{Bmatrix} \tag{2-87}$$

where f_t and f_l represent the transverse and longitudinal constraint constitutive functions, respectively, and $f_{r,x}$, $f_{r,y}$, and $f_{r,z}$ denote the constitutive functions constraining the rotations around x-, y-, and z-axes, respectively. The above equations ensure that the transverse forces produced by this formulation are in the same directions as the transverse

80

displacemets. In the context of tendon-duct interactions, this means that the bearing forces emerging due to the tendons contact with their ducts remain normal to the duct edges.

2.4. Preliminary Validation

The element formulations developed earlier are implemented in the open-source structural analysis program OpenSees (McKenna et al. 2000) to allow their use in combination with a large library of other element formulations, material models, and analysis methods available in this program. For the preliminary validation of the proposed modeling strategy and the developed element formulations in combination together, they are used to simulate two large-scale experiments conducted at the University at Buffalo (Sideris 2012; Sideris et al. 2014c; d), i.e. a quasi-static test on a single-column HSR pier, and a shake table test on a single-span bridge with two single-column HSR piers. The following sections discussing these validation examples have been extracted from Salehi et al. (2017).

2.4.1. Description of HSR Column Specimens

The HSR column specimens consisted of five precast concrete segments, a cap-beam and a foundation block, which were post-tensioned together with eight internal unbonded tendons (Figure 2-28). The tendons were seven-wire monostrands conforming to Gr. 270 per ASTM A416/A416M (ASTM 2010) with a diameter of 0.6 in. The ducts had a diameter of 0.9 in., while the duct adaptors, used at both ends of the column segments, had interior diameter of 1.375 in. and height of 1.5 in. No duct adaptors were used in the cap beam and the foundation block. All HSR joints included a thin layer of silicone material to achieve a target coefficient of friction of 0.08 to 0.1 (Sideris 2012; Sideris et

al. 2014d). The 28-day nominal strength of the concrete material was 5 ksi, while the mild

reinforcing steel conformed to Gr. 60 per ASTM A615/A615M (ASTM 2009). The

longitudinal mild reinforcement of the column segments was comprised of #3 straight bars

that provided a volumetric ratio of 0.025. The transverse reinforcement of the column

segments consisted of #3 closed ties in each wall, providing volumetric reinforcement

ratios of 0.0198 and 0.014 in the wall-parallel and wall-normal directions, respectively.

Further reinforcement details can be found in Sideris (2012).

2.4.2. Modeling of Column Specimen

All analyses are conducted in two dimensions and using an element configuration similar

to Figure 2-1, considering only the responses in the lateral and vertical directions. The

value of l_c for the HSR elements is taken as 0.8 times cross section depth. The column

cross section is discretized into fibers/layers of approximate width of 0.625 in., as

demonstrated in Figure 2-29. The stress-strain backbone curves considered for different

materials are shown in Figure 2-30(a-c). The constitutive model by Mattock (1979) for the

posttensioning tendons is calibrated in accordance with Sideris et al. (2014b). For the mild

reinforcing steel, the Giuffré-Menegotto-Pinto model (Giuffrè and Pinto 1970) is used

with a strain hardening ratio of 1%, while the confined and unconfined concrete are

simulated using the Modified Kent and Park model (Scott et al. 1982). Based on the test

data from Sideris (2012), the measured strength of the unconfined concrete was 5.7 ksi,

while the estimated strength and ultimate strain of the confined concrete were 7.75 ksi and

0.041, respectively (Sideris et al. 2014d). At the HSR joints, all material models used for

the cross section fibers have zero tensile strength.
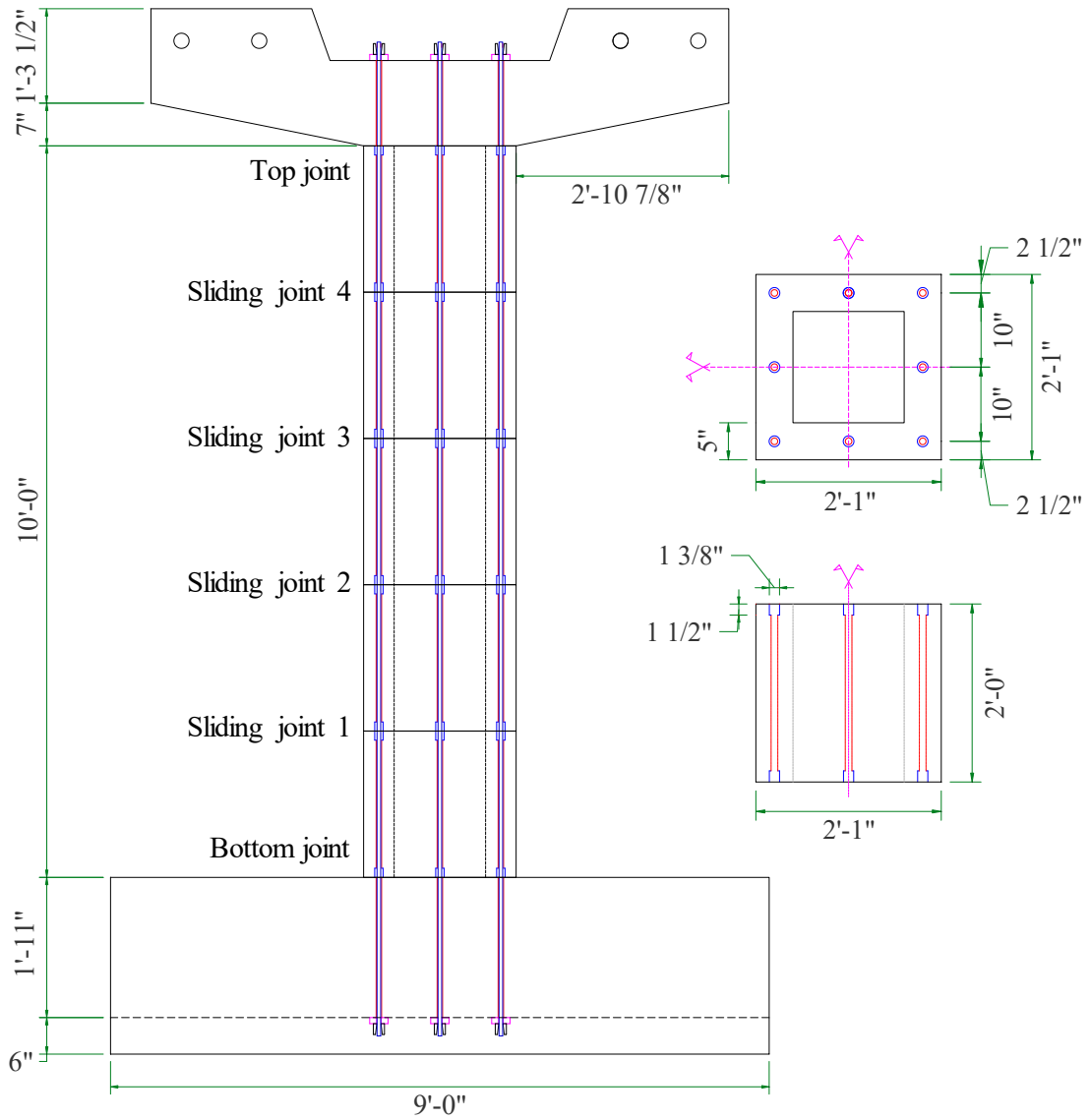
Figure 2-28. Dimensions of tested HSR column specimen
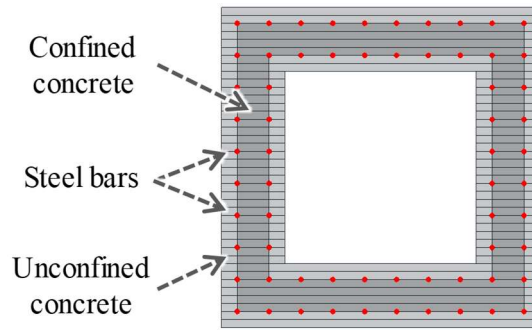
Figure 2-29. Fiber discretization of column cross sections

Variation of coefficient of friction with contact pressure/stress is considered to be in accordance with a hyperbolic function and calibrated based on the test data (Figure 2-30(d)). The function used for this purpose is:

$$\mu = \mu_{max} - \left(\mu_{max} - \mu_{min}\right)\tanh\left(\alpha p\right) \tag{2-88}$$

where μ is the coefficient of friction, μ_{max} is the maximum coefficient of friction (at zero pressure), μ_{min} is the minimum coefficient of friction (at infinite pressure), α is a calibration constant, and p is the contact pressure (positive in compression and zero in tension). The values used herein are: $\mu_{max} = 0.22$, $\mu_{min} = 0.085$, and $\alpha = 0.0022$ psi^{-1}.

The force reaction of the gap elements between the tendons and ducts or duct adaptors is zero prior to engaging the gap, and increases linearly (with high stiffness) with the gap "violation". Inelasticity or damage at the contact of ducts and duct adaptors is not considered.
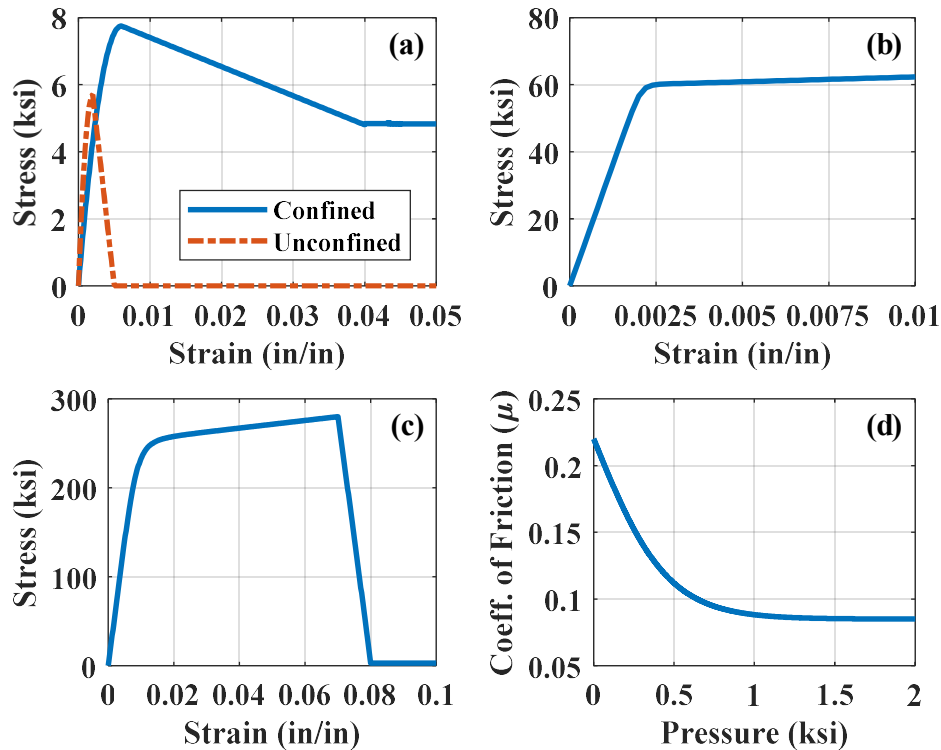
Figure 2-30. (a) Stress-strain backbone curves for concrete; (b) stress-strain backbone curve for mild steel; (c) stress-strain backbone curve for prestressing steel; (d) coefficient of friction vs. contact pressure at sliding joints

2.4.3. Simulation of Quasi-Static Cyclic Test

The quasi-static test setup is shown in Figure 2-31. In this test, the initial posttensioning was 20 kips per tendon. The total gravity load of 44 kips was applied through two external tendons, each having a PT force of 18 kips, plus the weight of the actuators and the connection setup, which was approximated as 8 kips. The test specimen was subjected to a displacement-controlled lateral loading protocol, including symmetric double cycles of increasing amplitude. The peak drift ratio was 14.9%.
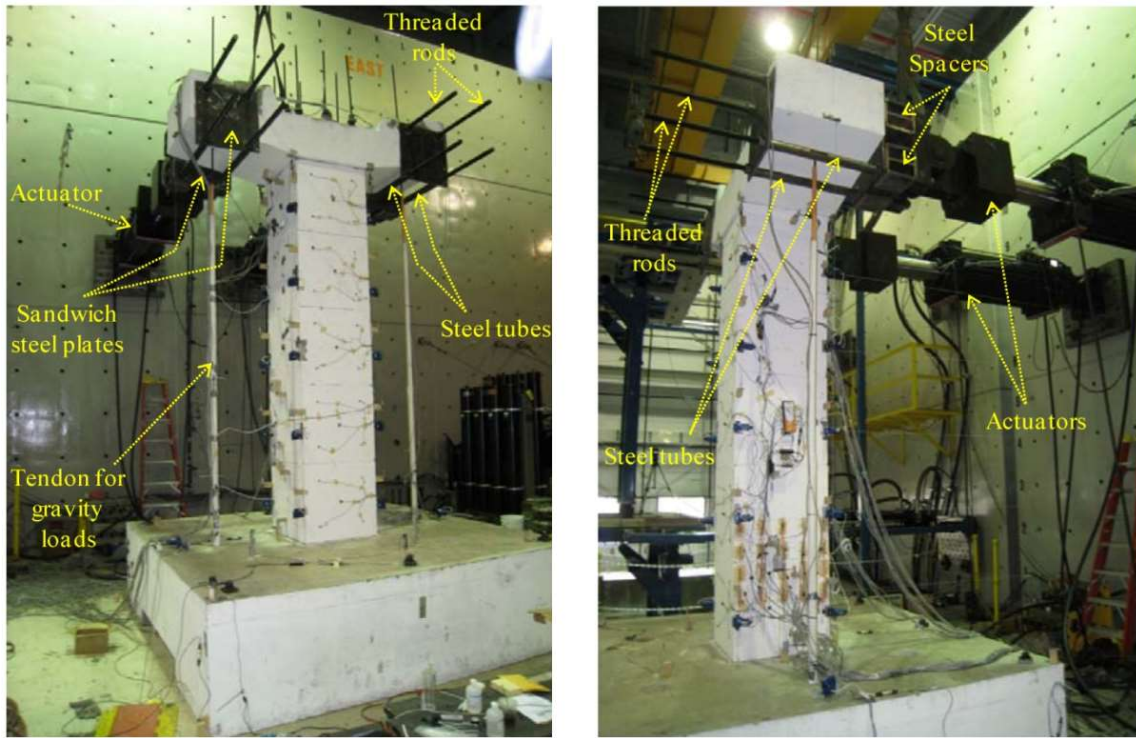
Figure 2-31. Setup for quasi-static loading of HSR column specimens (Sideris 2012)

In the generated model, the gravity tendons are simulated by truss elements, while the weight of the actuators and the lateral load are applied at the location of the swivel, as shown in Figure 2-32. The distance of the swivel from the column centerline is estimated to be 30 in.

Comparisons between computational and experimental data in terms of the lateral force vs. lateral displacement response is shown in Figure 2-33. The model accurately predicts the lateral strength in both directions, including the softening observed with the increasing displacement amplitudes. However, residual displacements are underestimated for cycles with larger displacement amplitudes. This underestimation is due to drops in the lateral force upon displacement/load reversals indicative of friction-type effects, which

are not captured by the model. The cause of those drops is undetermined; consideration of two potential causes, namely, the friction between the tendons and the ducts/duct adaptors, and the friction in the actuator swivels, were not found to significantly improve the predictions. However, as shown later, such friction-type drops did not appear in the shake table tests.
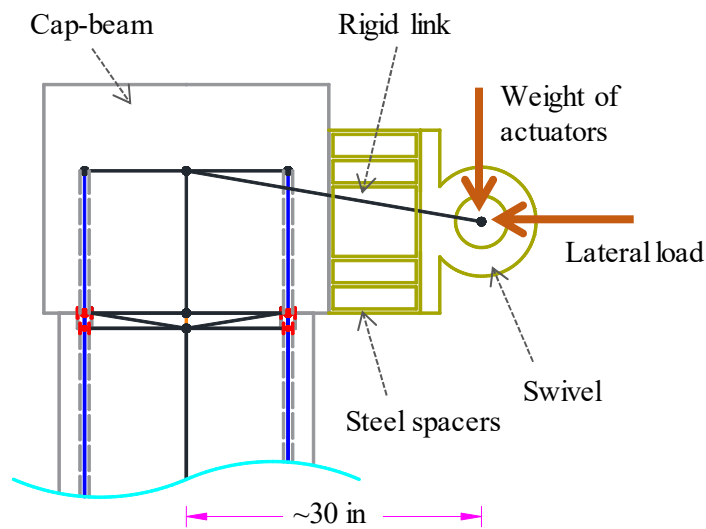
Figure 2-32. Simulation of quasi-static cyclic test: location of applied loads

The model accurately predicts residual posttensioning forces (Figure 2-34); however, it overestimates peak PT forces by 20%. This overestimation of the peak PT forces could have resulted from the larger rocking rotation demands predicted by the model at the bottom end of the column (Figure 2-35), due to the smaller joint sliding amplitudes predicted by the model under large applied displacements (as shown subsequently). Another reason for the posttensioning overestimation by the model is its inability to

simulate the bearing damage to the ducts, which could reduce the elongation of the tendons under large rotations.
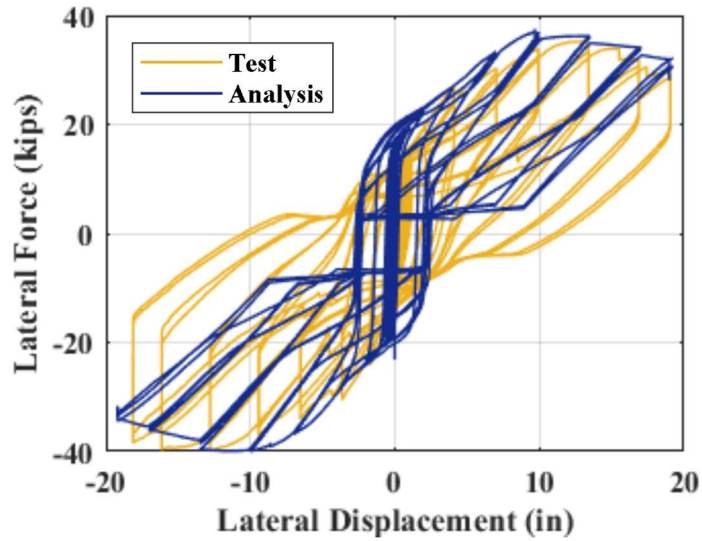
Figure 2-33. Simulation of quasi-static cyclic test: lateral force vs. lateral displacement responses
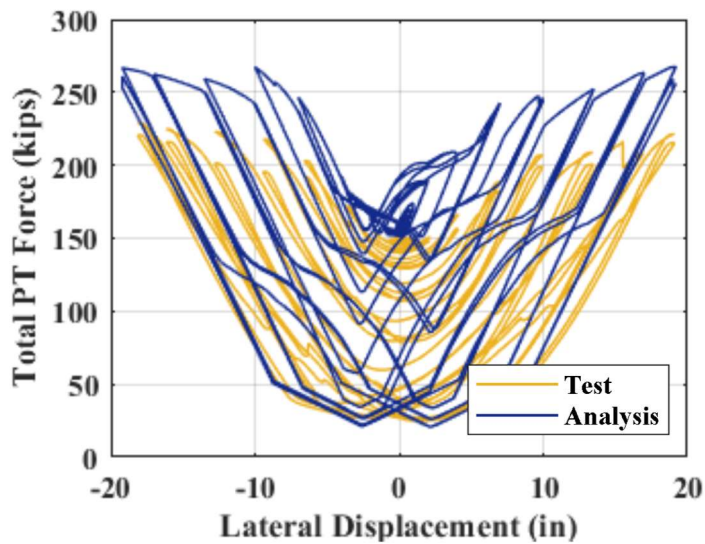
Figure 2-34. Simulation of quasi-static cyclic test: total PT force vs. lateral displacement responses
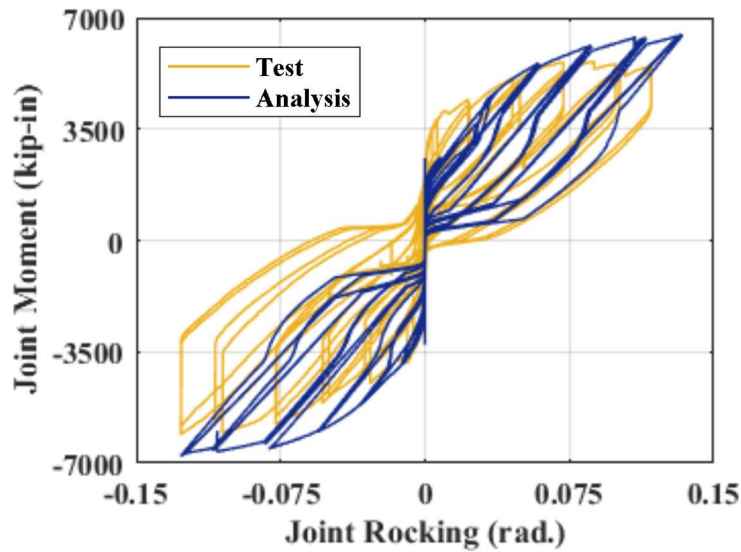
Figure 2-35. Simulation of quasi-static cyclic test: bottom joint moment vs. rotation responses

A comparison between computational and experimental joint shear vs. sliding responses for all joints is shown in Figure 2-36. The model's capability of simulating joint sliding is obvious from these results. However, peak sliding values are underestimated, because the concrete damage caused by the bearing of PT tendons on the connection between ducts and duct adaptors (Sideris 2012) is not simulated. Moreover, during the actual test, concrete compressive damage at the bottom joint introduced significant debris at the sliding interface, resulting in a different sliding behavior compared to the joints above, which is difficult to accurately capture by the HSR element. Due to the uncertainty in the frictional properties introduced by such debris, Sideris et al. (2014d) recommended that sliding should always be restrained in the end rocking joints.
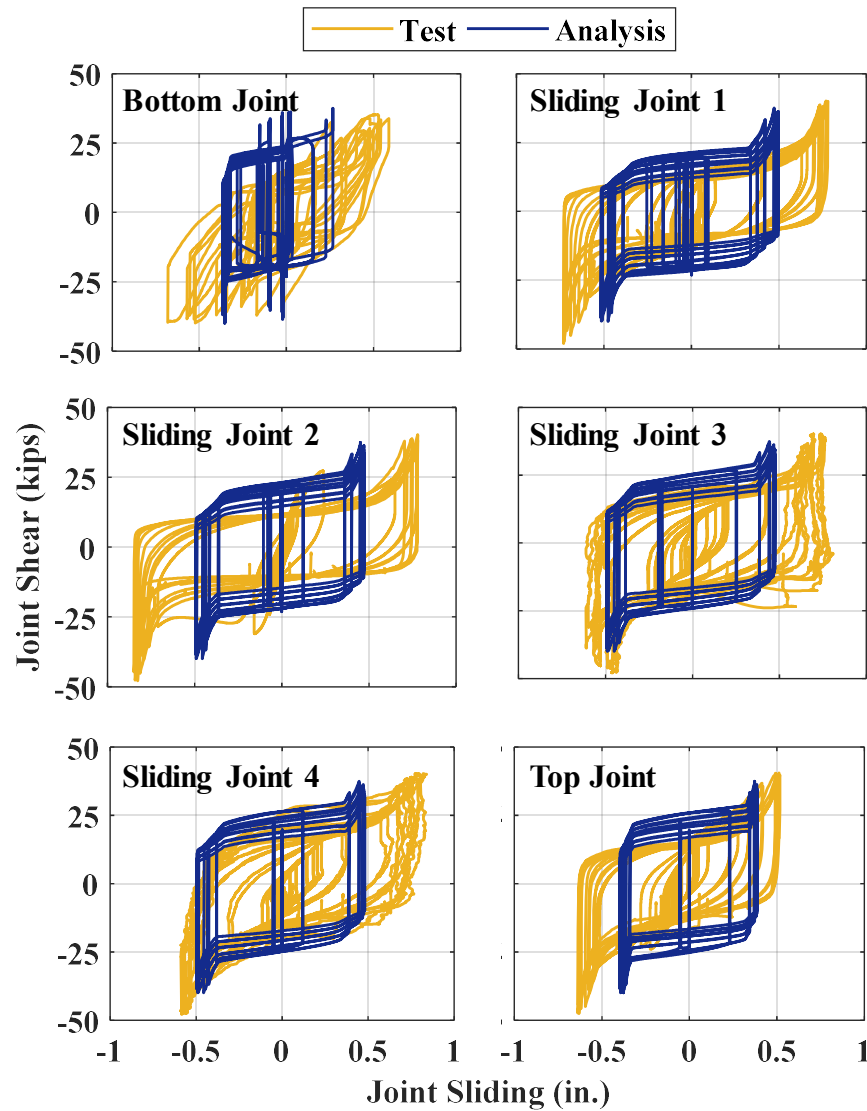
Figure 2-36. Simulation of quasi-static cyclic test: joint shear vs. sliding responses

2.4.4. Simulation of Shake Table Test

The shake table test setup is shown in Figure 2-37. The superstructure was supported on the cap beams through simple contact, and sliding was prevented via dry concrete-on-concrete friction. The bridge specimen – including several variations (Sideris et al. 2015) – was subjected to nearly 145 tests. For the test considered in this examination

(ABC_S1_SC_M2_YZ per Sideris (2012)), the input motion was the base excitation from the 1979 Imperial Valley earthquake, recorded at the Delta station. The horizontal components of the originally recorded motion were scaled to represent 2.4 times the maximum considered earthquake (MCE) hazard level, while the vertical component was scaled to represent 3.6 times the MCE hazard level. The initial posttensioning load prior to this test was almost 15 kips per tendon.
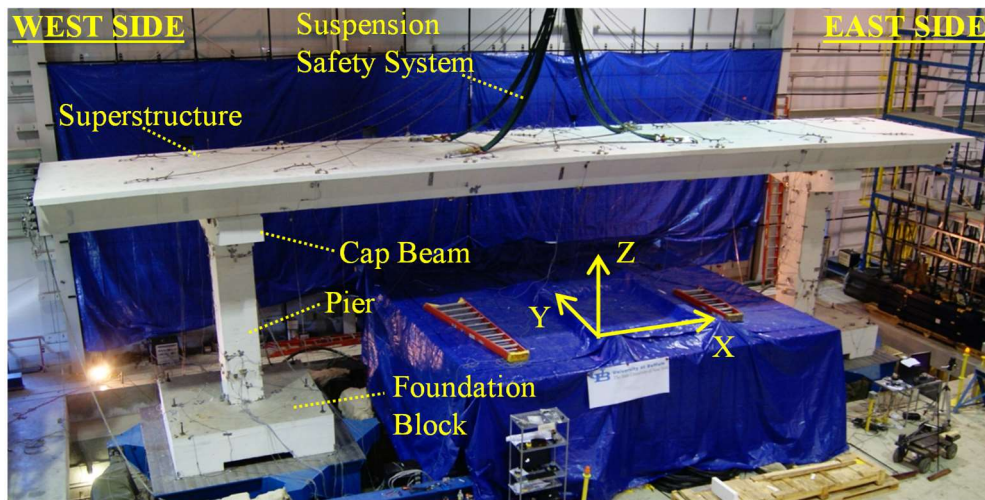
Figure 2-37. Setup for shake table testing of HSR column specimens (Sideris 2012)

In accordance with this test, the simulation is conducted using the lateral and vertical ground motion components (y-z directions, per Figure 2-37) and using one out of the two HSR piers supporting half of the superstructure weight. The superstructure-to-cap-beam connectivity is represented by two HSR elements, while the superstructure's seismic mass (34 kips) and mass moment of inertia (303 kip-ft^2) are assigned to a node located at the centroid of the superstructure cross section (Figure 2-38). To maintain consistency with

the experimental response, the dynamic analysis is performed using the acceleration time histories recorded on the shake table (Figure 2-39). The inherent damping is modeled using the Rayleigh method, considering a critical damping ratio of 3% to the first and the second modes of vibration. This value of the damping ratio is smaller than the values reported by Sideris et al. (2015), which also accounted for small joint sliding (hysteretic energy dissipation) activated during white noise tests (Sideris 2012).
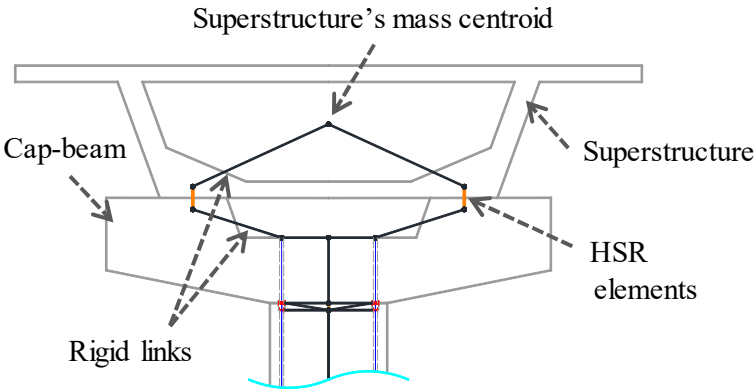
Figure 2-38. Simulation of shake table test: modeling of superstructure-to-cap-beam connection
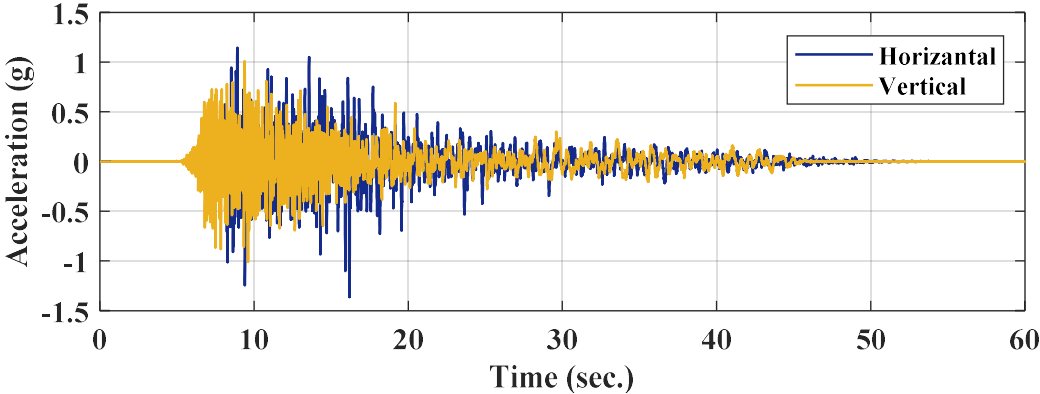
Figure 2-39. Simulation of shake table test: base acceleration time histories

The lateral displacement of the superstructure relative to the foundation obtained from the analysis is compared with the corresponding experimental data in Figure 2-40. The analysis predictions are in good agreement with the test data, both in terms of peak amplitudes and frequency content. The peak positive displacement obtained from the analysis is only 5% less than the corresponding experimental value, while the peak negative displacement is almost identical to the corresponding experimental value. The predicted residual displacement is almost zero, in accordance with the experimental data. However, towards the end of the motion, the experimental response has larger displacement amplitude and decays more slowly than the simulated response, which has much smaller displacements and decays more rapidly. This response results from the accumulated damage at the bottom joint during prior testing, which cannot be captured by this analysis, as it only considers a single motion and starts from undamaged conditions.
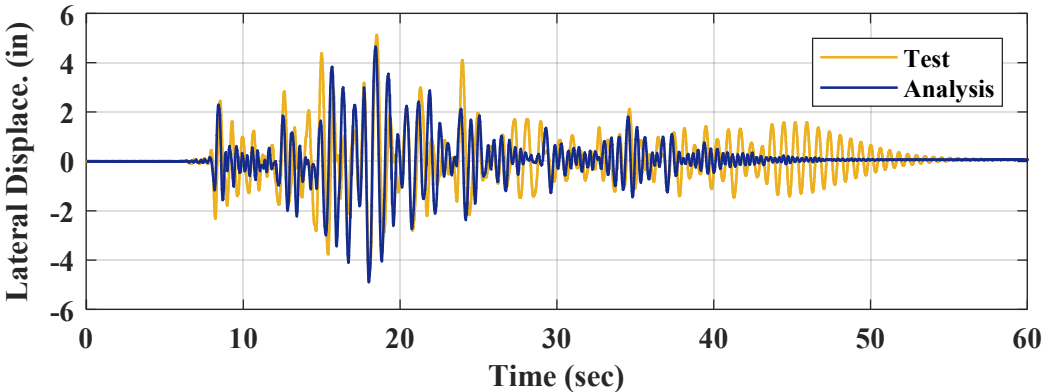
Figure 2-40. Simulation of shake table test: lateral displacement time histories

As a result, the model accurately captures, both in terms of peak responses and frequency content, the portion of the system response associated with the large joint

93

sliding and rocking (i.e., first 35 seconds in Figure 2-40) driven by the high intensity part of the applied ground motion (Figure 2-39). However, it does not capture the (flexible) elastic response towards the end of the motion (i.e., between 45 and 55 seconds in Figure 2-40), because the accumulated stiffness deterioration from prior testing is not accounted for in the simulation. This is also demonstrated by a comparison of the period of the first lateral mode, which was 0.36 sec for the test specimen prior to this test, as opposed to 0.28 sec. predicted by the model.

The column base shear vs. cap beam's lateral displacement responses obtained from the test and the analysis are in good agreement (Figure 2-41) in terms of the predicted peak base shear and peak displacement. However, the test specimen is more flexible (in the elastic range), because of the accumulated damage at the bottom joint during prior testing.
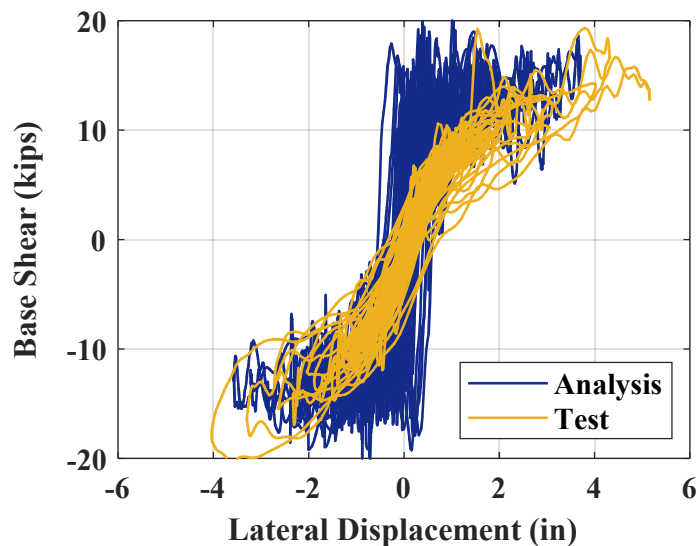
Figure 2-41. Simulation of shake table test: lateral force vs. lateral displacement responses

In addition, according to Figure 2-42, the predicted peak PT forces are up to 20% larger than the peak PT forces recorded during testing, which is consistent with the stiffer behavior of the simulated column observed in Figure 2-41.
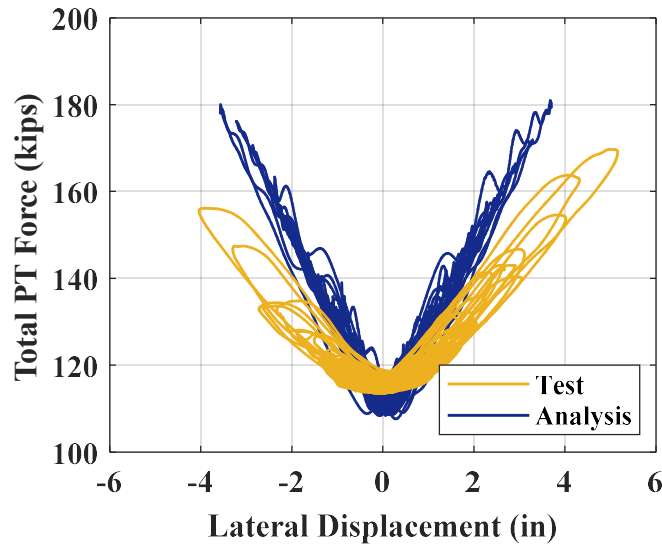
Figure 2-42. Simulation of shake table test: total PT force vs. lateral displacement responses

The joint shear vs. sliding responses obtained from the analysis are compared with those from experiments in Figure 2-43. The joint responses obtained from the analysis for the three instrumented joints (bottom joint, sliding joint 1, and top joint per Figure 2-28) match the corresponding experimental responses reasonably well. The peak sliding values recorded through the simulation closely resemble those measured during the test, but the simulation overestimated the peak negative joint sliding at sliding joint 1. The simulation also predicted that, under dynamic loading, only the two lower joints undergo considerable

sliding, while the third joint from the bottom exhibits minor sliding, which is in agreement with experimental observations (Sideris 2012).
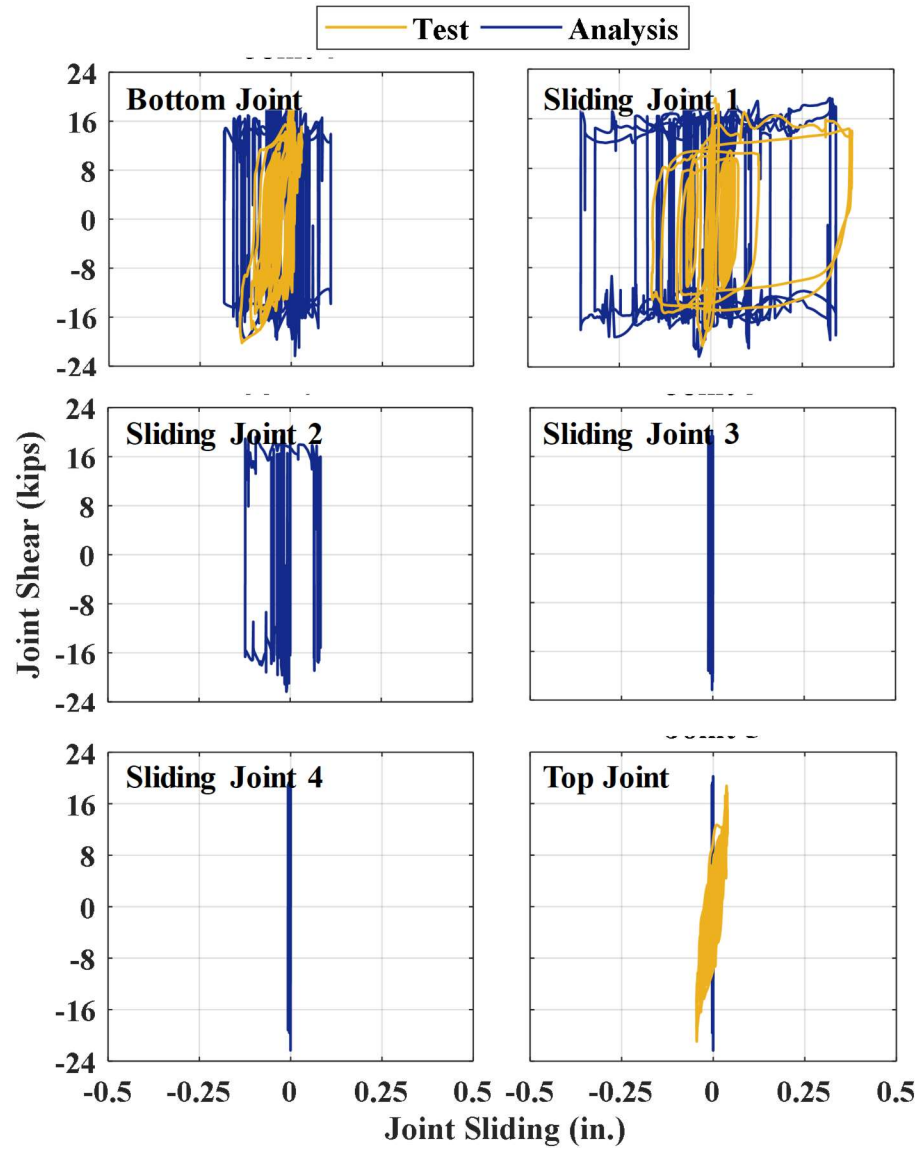
Figure 2-43. Simulation of shake table test: joint shear vs. sliding responses

3. COMPUTATIONAL INVESTIGATIONS

This chapter aims to evaluate the seismic performance of HSR columns through computational simulations. The more specific objectives of this chapter are:

1. Evaluate the effects of various design variables on the response of HSR columns, identify the more important variables, and provide design recommendations;

2. Examine the effects of vertical and near-fault earthquake excitations on the response of HSR columns;

3. Compare the seismic performance of an HSR column with a rocking-only column of similar design.

In order to achieve these objectives, first, a reference HSR pier design is selected and its modeling details are described. Various design variables that can affect the response of an HSR column are then identified and their effects are evaluated through quasi-static and time history analyses. The results of these examinations are used as a basis to make recommendations for the effective low-damage design of HSR columns. The effects of vertical excitation on the performance of HSR columns are examined by comparing the responses of the reference column subjected to horizontal excitation components with its responses under both horizontal and vertical excitation components. Likewise, two ensembles of near-fault motions with and without velocity pulses are applied to the an HSR column to evaluate the changes in its performance with respective to its performance under far-field ground motions. In the last section of this chapter, considering the developed design recommendations, the design details of the reference HSR column are

modified and its seismic performance under far-field motions is compared with the seismic performance of a similar column without sliding joints – i.e. a rocking-only column.

3.1. Reference HSR Pier

The reference bridge pier consists of a cantilever single-column HSR column (Figure 3-1). The dimensions and material properties of the reference pier are selected to be very close to those of the specimens tested by Sideris et al. (2014c; 2014d). The column itself is 10 ft tall, while the distance from the column's top rocking joint to the superstructure's centroid is 2.5 ft. The column has a 25 in. by 25 in. square cross-secton with a 15 in. by 15 in. square hole in it, while its reinforcement details are as described in Section 2.4.1. Eight unbonded post-tensioning monostrands of diameter 0.6 in. pass the walls of the column cross-section. For earthquake excitation in the transverse (and vertical) direction, this specimen is representative of piers away from the abutments, as is the case for the piers considered by Sideris et al. (2014c; 2014d), which represented the piers of the middle span of a five-span bridge.

The initial post-tensioning force in each tendon is 20 kips. The superstructure's weight supported by the column is 38 kips (also representing the seismic mass) and its mass moment of inertia is 10 kip-ft-sec.[2]. The nominal compressive strength of concrete, f'_c, is 5 ksi and the reinforcing mild steel and the tendons' high-strength steel conform to Grade 60 per ASTM A615/A615M (ASTM 2018a) and Grade 270 per ASTM A416/A416M (ASTM 2018b), respectively. The variation of the coefficient of friction with contact pressure at the sliding joints is assumed to be of the hyperbolic form of Eq. (2-88), which is identified as friction model 2 in Figure 3-2. The rest of the construction

details, such as duct and duct adaptor dimensions, vary depending on the design variables whose effects are investigated.
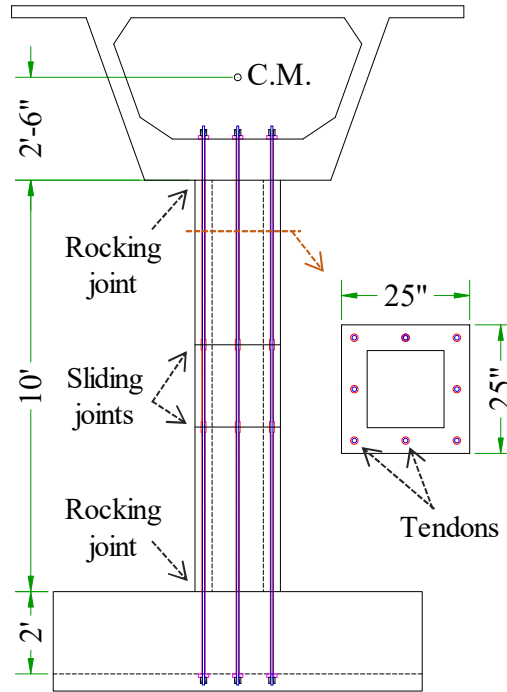
Figure 3-1. Reference HSR pier dimensions
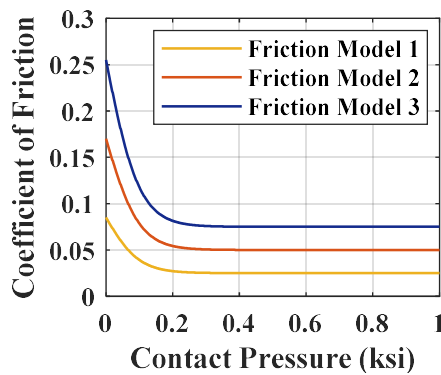
Figure 3-2. Considered variations of coefficient of friction with contact pressure

3.2. Finite Element Modeling

The finite element modeling of the reference column and its variations that will be analyzed throughout the subsequent sections is carried out as described in Section 2.4.2 for the preliminary validation of the modeling approach proposed in Chapter 2. The only differences are in the material model utilized herein to represent confined concrete, which follows the Mander model (Mander et al. 1988) instead of the Modified Kent and Park model (Scott et al. 1982), as well as the mild steel's yield strength, which is taken as its expected value, i.e. 68 ksi (Caltrans 2013). Inherent damping is modeled through an Enhanced Rayleigh damping model (Salehi and Sideris 2020), considering 3% critical damping ratios at the first and second modal periods. All analyses are performed in OpenSees (McKenna et al. 2000).

3.3. Ground Motion Selection and Scaling

Three groups of earthquake ground motions are used to perform the time history analyses in the subsequent sections: (1) far-field, (2) near-fault without velocity pulse, and (3) near-fault with velocity pulse. Each group consists of 10 motions (Table 3-1) picked from the ground motion ensembles of FEMA P695 (FEMA 2009) such that the main statistical properties of the spectral accelerations of the selected ground motions over the period range of 0.2-1.0 sec. are close to those for the entire ground motion ensembles of FEMA P695 (Figure 3-3).

Table 3-1. Selected ground motions for time history analyses

No	Earthquake			Recording Station		Horizontal Component
	Name	Year	M	Name	Owner	
Far-Field						
1	Northridge	1994	6.7	Beverly Hils - Mulhol	USC	279
2	Northridge	1994	6.7	Canyon Country-WLC	USC	000
3	Duzce,Turkey	1999	7.1	Bolu	ERD	000
4	Hector Mine	1999	7.1	Hector	SCSN	000
5	Imperial Valley	1979	6.5	Delta	UNAMUCSD	262
6	Imperial Valley	1979	6.5	El Centro Array #11	USGS	230
7	Kobe, Japan	1995	6.9	Nishi-Akashi	CUE	000
8	Kobe, Japan	1995	6.9	Shin-Osaka	CUE	000
9	Kocaeli, Turkey	1999	7.5	Duzce	ERD	270
10	Kocaeli, Turkey	1999	7.5	Arcelik	KOERI	000
Near-Fault without Velocity Pulse						
1	Imperial Valley-06	1979	6.5	Bonds Corner	USGS	323
2	Imperial Valley-06	1979	6.5	Chihuahua	UNAMUCSD	233
3	Nahanni, Canada	1985	6.8	Site 1	-	160
4	Loma Prieta	1989	6.9	Corralitos	CDMG	038
5	Cape Mendocino	1992	7	Cape Mendocino	CDMG	260
6	Northridge-01	1994	6.7	LA - Sepulveda VA	USGS/VA	122
7	Chi-Chi, Taiwan	1999	7.6	TCU067	CWB	285
8	Chi-Chi, Taiwan	1999	7.6	TCU067	CWB	015
9	Chi-Chi, Taiwan	1999	7.6	TCU084	CWB	271
10	Denali, Alaska	2002	7.9	TAPS Pump Sta. #10	CWB	289
Near-Fault with Velocity Pulse						
1	Imperial Valley-06	1979	6.5	El Centro Array #7	USGS	233
2	Irpinia, Italy-01	1980	6.9	Sturno	ENEL	313
3	Loma Prieta	1989	6.9	Saratoga - Aloha	CDMG	038
4	Erzican, Turkey	1992	6.7	Erzincan	-	122
5	Landers	1992	7.3	Lucerne	SCE	329
6	Northridge-01	1994	6.7	Rinaldi Receiving Sta	DWP	032
7	Northridge-01	1994	6.7	Sylmar - Olive View	CDMG	032
8	Chi-Chi, Taiwan	1999	7.6	TCU065	CWB	272
9	Chi-Chi, Taiwan	1999	7.6	TCU102	CWB	008
10	Duzce, Turkey	1999	7.1	Duzce	ERD	172
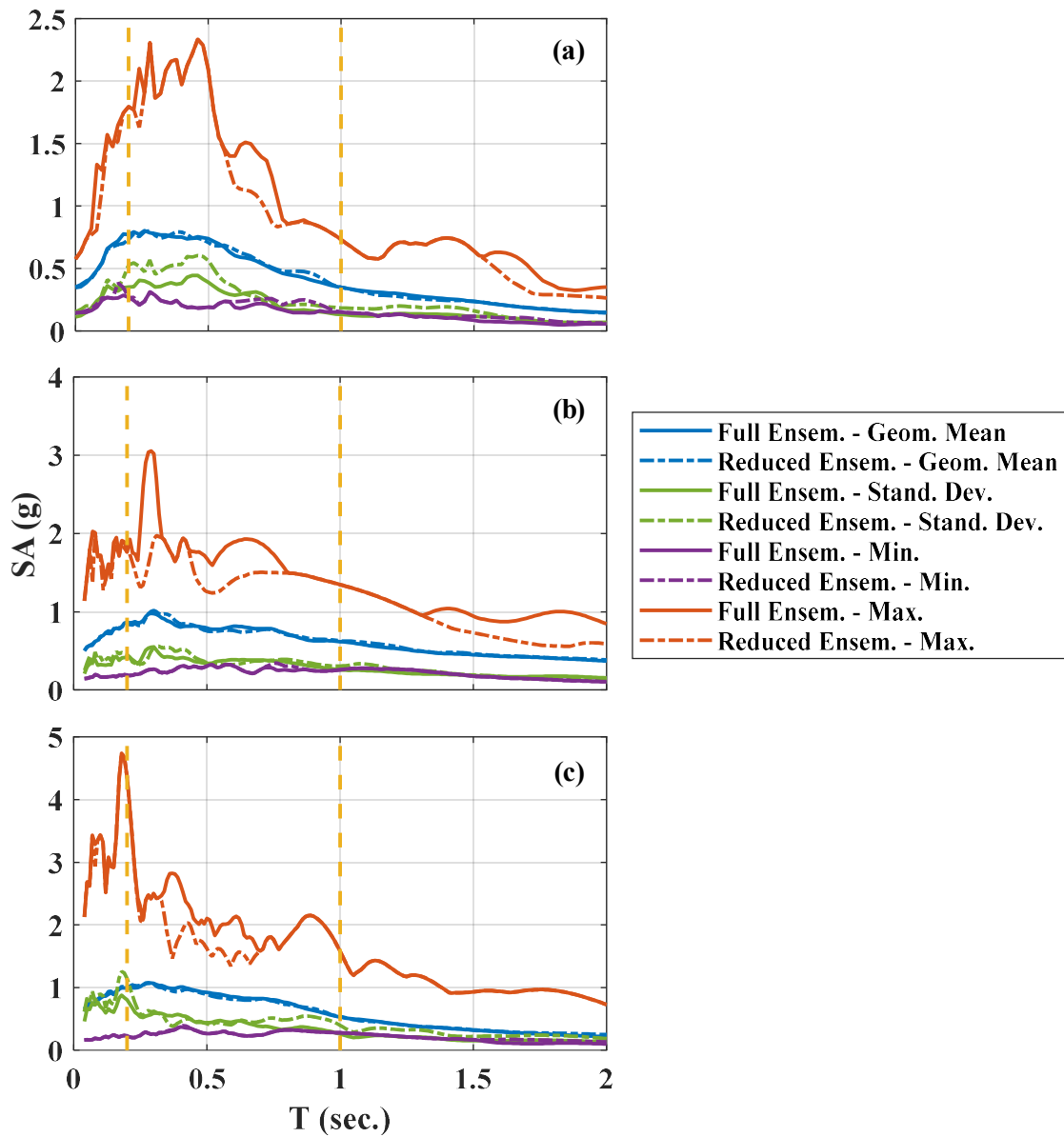
Figure 3-3. Comparison of statistical properties of full FEMA P695 ground motion ensembles and reduced ensembles: (a) far-field; (b) near-fault without velocity pulse; (c) near-fault with velocity pulse

Depending on the examination purposes, the ground motions are scaled to two or three hazard levels: (I) design earthquake or DE (1000-yr event per AASHTO (2014)); (II) maximum considered earthquake or MCE (2475-yr event), obtained by multiplying

the DE spectral accelerations by 1.5; and (III) double MCE, obtained by multiplying the MCE spectral accelerations by 2. The DE hazard level refers to a site of moderate seismicity in California considered in the design of the reference column, with the short- and long-period spectral acceleration coefficients of $S_S = 0.625$ and $S_1 = 0.36$, respectively, in prototype domain (Sideris 2012). Scaling the motions to represent the DE hazard level is achieved by multiplying all acceleration records by a single factor, such that their geometric mean response spectral accelerations are not less than the design spectral accelerations over a period range of $0.5T_1$ to $2T_1$ (Figure 3-4), where T_1 equals the reference pier's first modal period (~ 0.25 sec. in model domain). This approach is similar to that proposed by ASCE 7-10 (ASCE 2010).
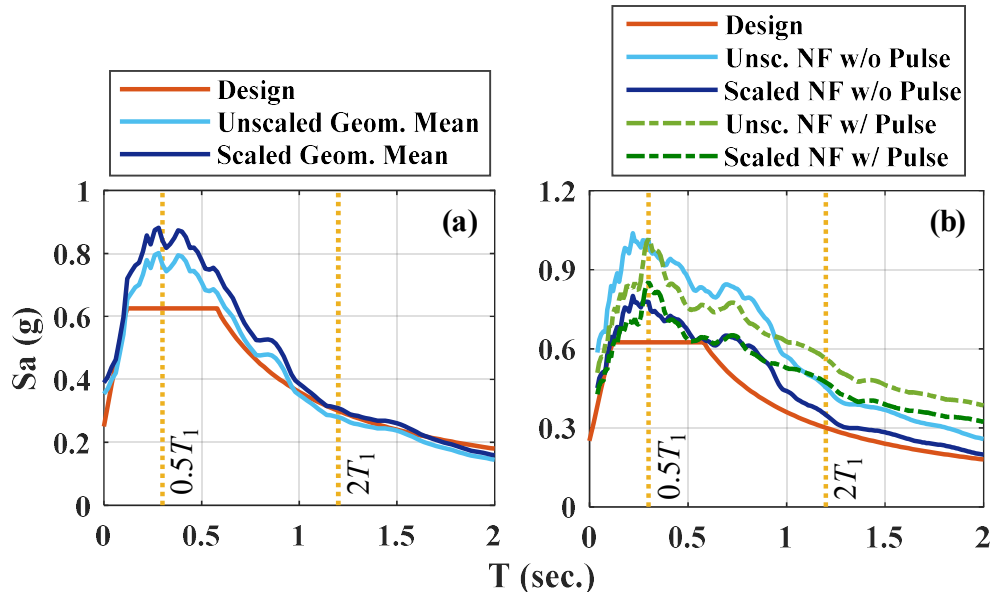
Figure 3-4. Comparison of unscaled and scaled geometric mean response acceleration spectra with design spectrum in prototype domain: (a) for far-field motions; (b) for near-fault motions

In accordance with the similitude analysis from Sideris (2012), the acceleration values and time step size of all accelerograms are further multiplied by the similitude factors of 2.388 and 0.419, respectively. In all analyses, each ground motion is followed by 15 seconds of zero acceleration to ensure the system comes to rest before residual deformations are recorded.

3.4. Evaluation of Effects of Design Variables

Before looking into the effects of major design variables on the response of HSR columns, it is necessary to identify those. For this reason, it is important to first understand the mechanics of the sliding joints. The shear-sliding response of an isolated sliding joint includes three stages (see Figure 3-5):

I.   *Friction-only stage:* At this stage, tendons can almost freely move sideways within the ducts and the joint shear is almost exclusively resisted by the friction force. The joint shear resistance in this stage equals the friction present at the joint, which is also equal to the *incipient sliding shear, V_{is}*, i.e. the shear at which sliding starts. The value of V_{is} can be approximated as:

$$V_{is} = \mu\left(N_g + N_{PT0}\right)\text{sgn}\left(\dot{u}_{sl}\right) \tag{3-1}$$

where μ, N_g, N_{PT0}, and $\dot{u}_{sl}$ are the coefficient of friction at the joint interface, total gravity load, total initial post-tensioning force, and sliding velocity, respectively, and sgn(.) represents the sign function. Among these parameters, μ can change with pressure and sliding velocity (depending on the material utilized at joint interface).
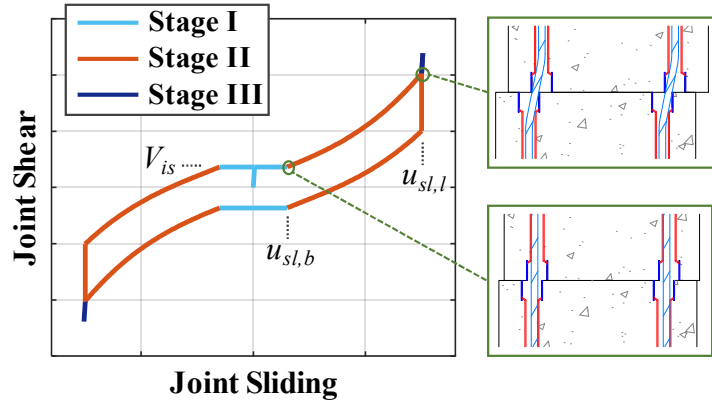
Figure 3-5. Typical shear vs. sliding response of an HSR joint

II.   *Friction-bearing stage:* At this stage, tendons have come in contact with ducts and the applied shear is resisted by both friction and the emerged tendon bearing forces (Figure 3-6). The sliding value at which the bearing forces initiate, termed *incipient bearing sliding amplitude*, $u_{sl,b}$, is equal to $D_d - D_{PT}$, where D_d and D_{PT} are the duct and tendon diameters, respectively (Figure 3-6). During this stage, the total shear resisted by an HSR joint, V, can be approximated as:

$$V = \mu \left(N_g + N_{PT} \right) \mathrm{sgn}\left(\dot{u}_{sl} \right) + N_{PT} \sin \psi \qquad (3\text{-}2)$$

with the total tendon forces, N_{PT}, assuming elastic response, obtained as:

$$N_{PT} = N_{PT0} + 2h_{da} \left(\frac{1}{\cos \psi} - 1 \right) \left(\frac{EA}{L} \right)_{PT} \qquad (3\text{-}3)$$

where $(EA/L)_{PT}$ represents the total tendons axial stiffness, ψ is the tendon deviation angle, and h_{da} is the duct adaptor height (see Figure 3-6). Per Sideris et al. (2014d), ψ is given by the following relationship:

$$\tan \psi = \frac{\left\langle |u_{sl}| - u_{sl,b} \right\rangle}{2h_{da}} \operatorname{sgn}(u_{sl}) \tag{3-4}$$

According to Eqs. (3-2) thru (3-4), the duct adaptor height, h_{da}, is a major construction detail that can control the level of sliding recentering (due to bearing forces) and peak achievable sliding.

III. *Ultimate stage*: At this stage, in case the bearing forces between the tendons and ducts allow and no shear keys exist, tendons come in contact with the duct adaptors at the interface of the sliding joint and the *nominal sliding capacity*, $u_{sl,l}$ ($= D_{da} - D_{PT}$), is reached. No further sliding is possible thereafter, except due to tendon and duct adaptor deformations. In this stage, as long as the tendons do not fracture, the joint shear continues to increase (Sideris et al. 2014d).
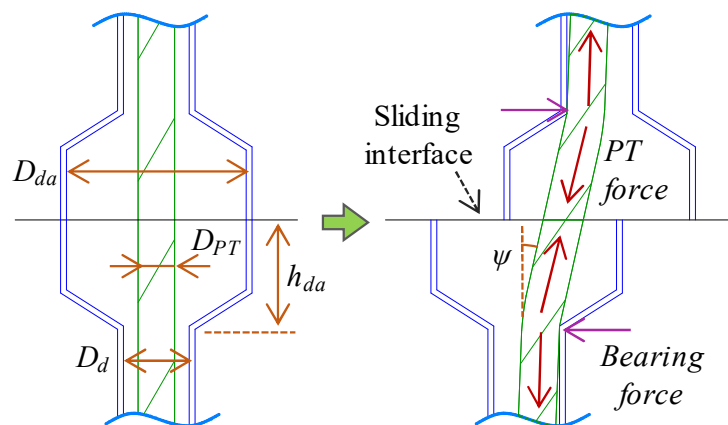
Figure 3-6. Duct and duct adaptor dimensions and tendon bearing forces

The response of an HSR column under lateral loading combines the response characteristics of a rocking-only column with the shear-sliding response of a number of

HSR joints, while both rocking and sliding continuously affect one another. The typical responses of a cantilever HSR column subjected to monotonic and cyclic lateral loading are schematically shown in Figure 3-7(a) and (b), respectively. Considering the above description of the sliding joints response and the respective equations, it is clear that several variables can influence the response of HSR columns, including: (*i*) column cross section dimensions and material properties; (*ii*) posttensioning tendons' dimensions, mechanical properties, and initial force; (*iii*) duct and duct adaptor dimensions; and (*iv*) coefficient of friction at sliding joints. However, these variables are too specific and had better be combined into a few more general and meaningful variables. Such major design variables are identified as follows.
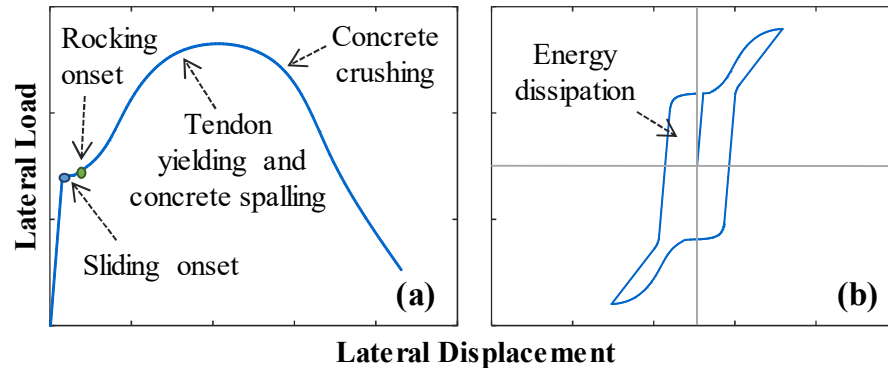
Figure 3-7. Typical force-displacement response of an HSR column: (a) under monotonic displacement; (b) under cyclic displacement

Per Sideris et al. (2014d), HSR columns should be designed so that joint sliding initiates before the column's ultimate lateral strength is reached, i.e. the ratio of the base shear at joint sliding initiation (incipient sliding base shear) over the ultimate lateral

strength should be smaller than unity. Herein, this ratio is referred to as the *incipient sliding base shear ratio*, R_{is}. The ratio of the base shear at which rocking starts, i.e. when decompression starts, over the peak base shear is also referred to as the *incipient rocking base shear ratio*, R_{ir}. These two ratios can be considered as two major variables affecting the behavior of HSR columns, as their values characterize how dominant each response mechanism (i.e. rocking and sliding) is.

In addition, according to Sideris et al. (2014d) and Madhusudhanan and Sideris (2018), within an HSR column design, sliding joints should ideally not reach their nominal sliding capacity, $u_{sl,l}$, because they could subject the tendons to shearing forces and local inelastic deformations. Avoiding such shearing is possible because, for large enough duct adaptor diameters, D_{da}, the joint shear required to reach $u_{sl,l}$ exceeds the column's lateral strength, which makes $u_{sl,l}$ unattainable. Therefore, the *peak achievable sliding capacity*, $u_{sl,peak}$, which is herein defined as the joint sliding obtained under monotonically applied lateral loading when the column reaches its peak lateral strength, should be smaller than $u_{sl,l}$. The peak achievable sliding capacity is dependent on the joint stiffness against sliding induced by bearing contact with the tendons, which is impacted by h_{da} and D_{da} (see Eqs. (3-2) and (3-4)). Thus, for a given D_{da}, different values of h_{da} can be used to obtain different values of $u_{sl,peak}$, all being smaller than $u_{sl,l}$. As a result of the above explanation, the peak achievable sliding capacity, $u_{sl,peak}$, can also be examined as a major design variable reflecting several more specific variables.

The incipient bearing sliding amplitude, $u_{sl,b}$, represents the joint sliding amplitude at which bearing reactions initiate and affects both the energy dissipation at the sliding joints

and the residual joint sliding. The extent of this variable relative to the peak achievable

sliding capacity, $u_{sl,peak}$, can also be a design variable to be evaluated.

Finally, another design requirement recognized by Sideris et al. (2014d) is that

compression damage should be avoided at the interface of sliding joints, which results in

a minimum distance of the sliding joints from the column ends, i.e. the locations of peak

flexural demands. However, it is not clear if the locations of sliding joints over the

permissible region has significant effect on the response of HSR columns. Additionally,

experimental observations (Sideris 2012) have shown that sliding may not propagate

substantially beyond two sliding joints, making the effective number of sliding joints a

design unknown. Considering the above points, the number and distribution of sliding

joints over the column height are also examined as major design variables.

In order to examine the effects of the above design variables, a total of 18 variation

of the reference HSR column (Figure 3-1) are analyzed. The construction details of these

design variations, which are listed in Table 3-2, are selected such that each group of those

are primarily different in terms of the major design variable of interest. The time history

analyses of this section are conducted with ground acceleration applied only in the

transverse direction (i.e. using only horizontal components), while the ground motions

used here are the far-field ensemble in Table 3-1. The performance of column variations

are quantified in terms of peak and residual deck displacements, peak and total residual

joint sliding (sum of residual sliding absolute values), peak concrete cover and core strains

(recorded at the extreme fibers in the cover and core regions of the column cross section),

peak base shear, and peak tendon strain obtained from time history analyses.

Table 3-2. HSR column design variations

Examined Design Variable	No. of Sliding Joints	Location of Sliding Joints†	Friction Model‡	D_d (in)	D_{da} (in)	h_{da} (in)	Tot. $u_{sl,b}$ (in)	Tot. $u_{sl,l}$ (in)	Tot. $u_{sl,peak}$ (in)	R_{is}	R_{ir}
Location of sliding joint	2	Bottom	2	0.9	1.6	4.5	0.6	2	1.4	0.36	0.32
	2	Mid-height	2	0.9	1.6	4.5	0.6	2	1.4	0.36	0.32
	2	Top	2	0.9	1.6	4.5	0.6	2	1.4	0.35	0.32
	2	Top-bottom	2	0.9	1.6	4.5	0.6	2	1.4	0.35	0.31
Number of sliding joints	1	Mid-height	2	1.2	2.6	9	0.6	2	1.4	0.37	0.32
	2	Mid-height	2	0.9	1.6	4.5	0.6	2	1.4	0.36	0.32
	3	Mid-height	2	0.8	1.3	3	0.6	2	1.4	0.36	0.32
Incipient slid. base shear ratio, R_{is}	2	Mid-height	1	0.9	1.6	1.5	0.6	2	1.1	0.18	0.32
	2	Mid-height	2	0.9	1.6	2.5	0.6	2	1.1	0.36	0.32
	2	Mid-height	3	0.9	1.6	9	0.6	2	1.1	0.58	0.32
Tot. incipient bearing slid. amplitude, $\Sigma u_{sl,b}$	2	Mid-height	2	0.75	1.6	6.25	0.3	2	1.4	0.37	0.32
	2	Mid-height	2	0.9	1.6	4.5	0.6	2	1.4	0.36	0.32
	2	Mid-height	2	1.05	1.6	3	0.9	2	1.4	0.37	0.32
	2	Mid-height	2	1.2	1.6	1.25	1.2	2	1.4	0.37	0.32
Total peak achievable slid. capacity, $\Sigma u_{sl,peak}$	2	Mid-height	1	0.9	1.6	0.6	0.6	2	0.7	0.36	0.32
	2	Mid-height	1	0.9	1.6	2.4	0.6	2	1	0.37	0.32
	2	Mid-height	1	0.9	1.6	4.8	0.6	2	1.4	0.37	0.32
	2	Mid-height	1	0.9	1.6	7.2	0.6	2	1.8	0.37	0.32

† See Figure 3-8
‡ See Figure 3-2

3.4.1. Sliding Joint Distribution

3.4.1.1. Location of Sliding Joints

The effect of the location of sliding joints on the seismic performance of HSR columns is evaluated by considering the reference HSR pier (Figure 3-1) with four sliding joint distributions depicted in Figure 3-8. All of the selected joint distributions consider two sliding joints: (I) located close to the bottom end of the column, (II) centered in the column's mid-height, (III) located close to the top end of the column, and (IV) located close to the bottom and top ends of the column. The friction model considered for the material at sliding joints is friction model 2 per Figure 3-2, leading to a friction coefficient of . For all joint distributions, D_d, D_{da}, and h_{da} are taken as 0.9, 1.6, and 4.5 in., respectively (Table 3-2). These values result in an incipient bearing sliding amplitude, $u_{sl,b}$, and a nominal sliding capacity, $u_{sl,l}$, of 0.3 in. and 1 in., respectively, per sliding joint.
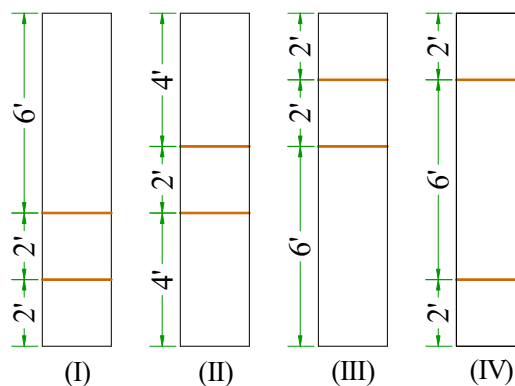
Figure 3-8. Effects of sliding joint locations: examined sliding joint distributions

As demonstrated by the variations of total joint sliding with lateral displacement obtained from the pushover analyses (Figure 3-9(b)), all four designs exhibit the same

total peak achievable sliding capacity, $\Sigma u_{sl,peak}$, of 1.4 in., which equals 70% of their total nominal sliding capacity, $\Sigma u_{sl,l}$ (= 2 in.). All designs have nearly identical lateral load vs. displacement responses under monotonic lateral loading (Figure 3-9(a)) and cyclic lateral loading (Figure 3-10), with minor difference obtained for the column with joint distribution IV.
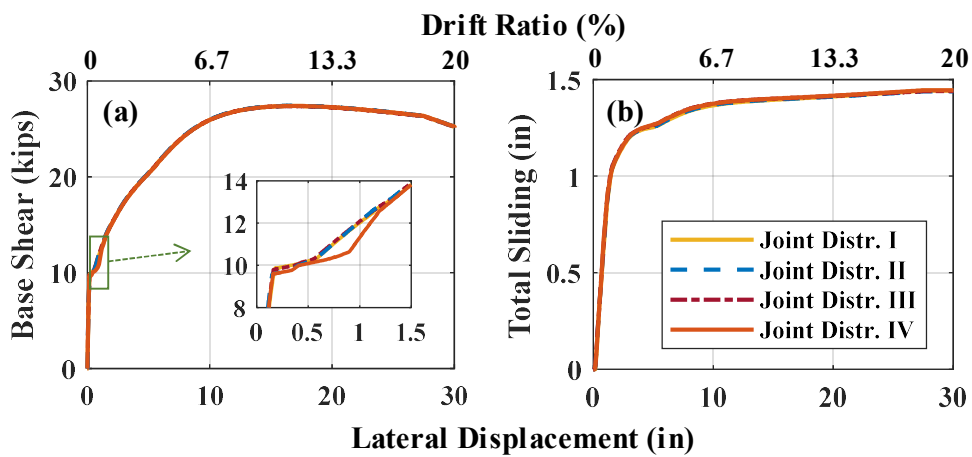
Figure 3-9. Effects of sliding joint locations on pushover analysis results: (a) base shear vs. lateral displacement; (b) total sliding vs. lateral displacement
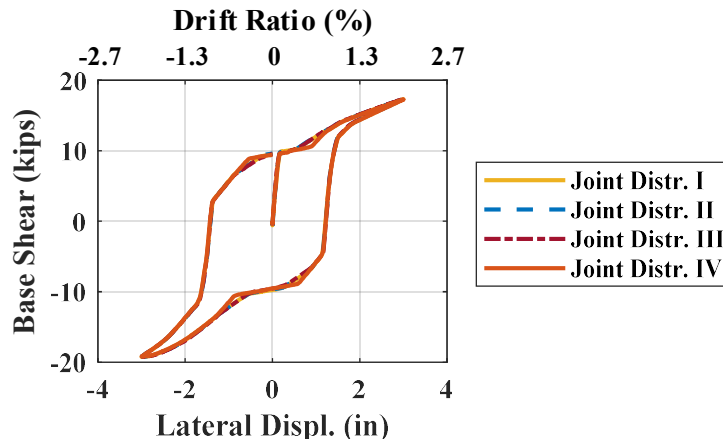
Figure 3-10. Effects of sliding joint locations on base shear vs. lateral displacement response under cyclic loading

The nonlinear time history analysis results obtained under DE and MCE excitation intensities are summarized through the boxplots displayed in Figure 3-11. Each boxplot demonstrates the variation of the respective demands via their median, minimum and maximum, and 1st and 3rd quartiles. All joint distributions yield similar responses for both seismic intensities, mostly because of the high mass of the superstructure relative to the mass of the column segments, which results in the response being dominated by the first mode. Yet, joint distribution I results in slightly lower overall peak cover and core strains (Figure 3-11(c, d)), which increase as the location of sliding joints moves higher, i.e. for distributions II and III. Indeed, no spalling is observed for distribution I, unlike all other distributions – note that here, the spalling strain was taken as 0.005 (Berry and Eberhard 2003). This behavior is attributed to the slightly lower coefficient of friction for distribution I as a result of the slightly higher pressure at the sliding joints close to the bottom end of the column, which results in slightly earlier onset of sliding. For all analyses, peak tendon strains barely exceed 0.5% (Figure 3-11(e)), thereby remaining far below the yield strain of 0.86%. Based on the above observations, locating sliding joints toward the lower end of the column (or closer to the location of high flexural demand) may very slightly improve the overall system performance. According to Figure 3-12(a), the sliding at none of the joints reached its nominal maximum capacity, $u_{sl,l}$.
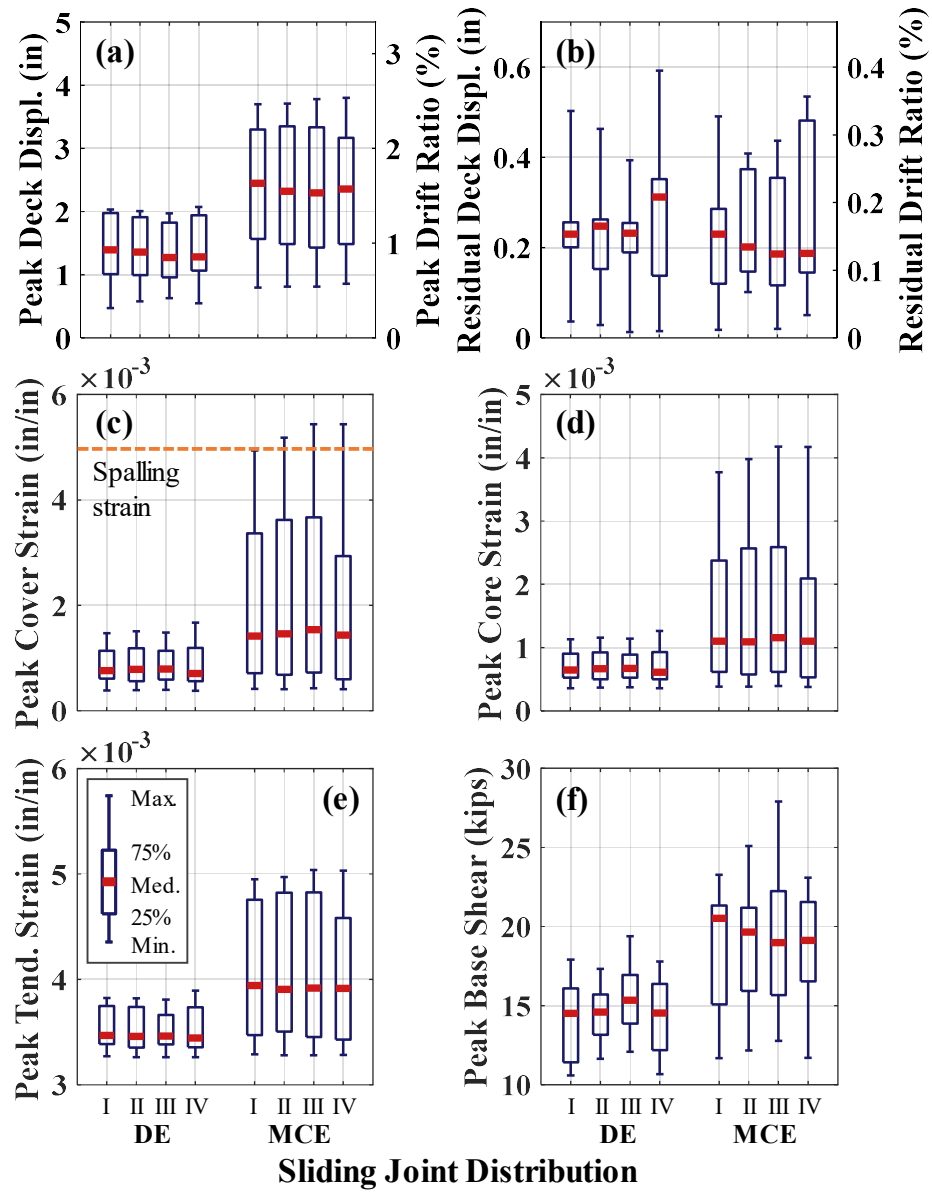
Figure 3-11. Effects of sliding joint locations on time history analysis results: (a) peak deck displacement; (b) residual deck displacement; (c) peak cover concrete strain; (d) peak core concrete strain; (e) peak tendon strain; (f) peak base shear

114
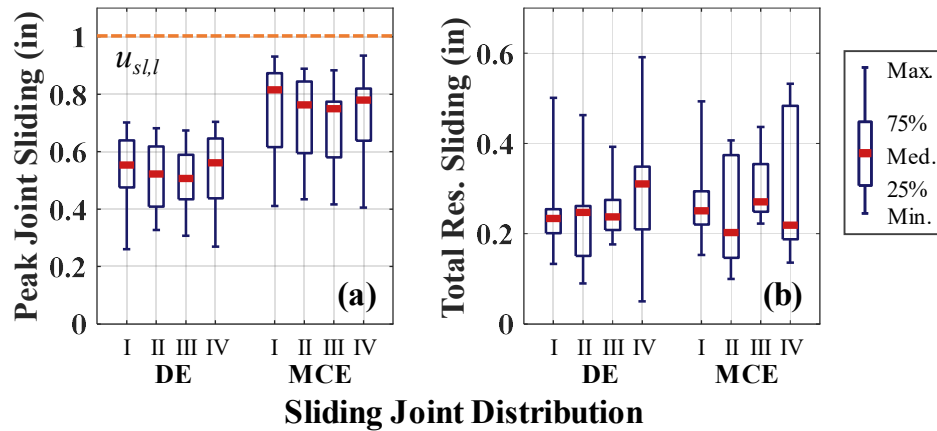
Figure 3-12. Effects of sliding joint locations on time history analysis results: (a) peak joint sliding; (b) total residual displacement

3.4.1.2. Number of Sliding Joints

The effect of the number of sliding joints on the seismic performance of HSR columns is evaluated through the joint distributions depicted in Figure 3-13 with 1, 2, and 3 sliding joints centered at the column mid-height. The duct and duct adaptor dimensions for each column are chosen such that the total $u_{sl,b}$, the total $u_{sl,l}$, and the total $u_{sl,peak}$ are the same for all joint distributions (Table 3-2); these values are 0.6 in., 2 in., and 1.4 in., respectively. Note that the total peak achievable sliding capacity, $\Sigma u_{sl,peak}$, is obtained via pushover analysis (Figure 3-14(b)) and is mainly controlled by h_{da}. That said, values of h_{da} are adjusted (see Table 3-2) such that $\Sigma u_{sl,peak}$ is constant and 30% smaller than the total $u_{sl,l}$, thereby ensuring that tendon shear damage is avoided. The friction model used in all cases is friction model 2 per Figure 3-2.
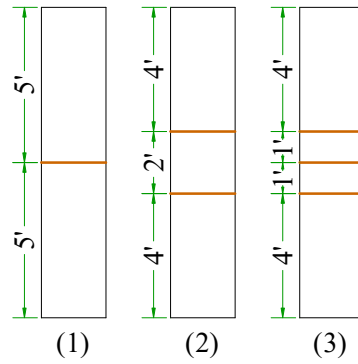
Figure 3-13. Effects of number of sliding joints: examined sliding joint distributions

All three designs with different number of sliding joints exhibit similar response under both monotonic and cyclic lateral load (Figure 3-14(a) and Figure 3-15). Yet, even though the total $u_{sl,b}$ is the same for all three designs, tendon bearing starts at a lower displacement in columns with more sliding joints (Figure 3-14(a)), due to their lower $u_{sl,b}$ per joint and the sequential sliding initiation from lower to higher joints, resulting from the lower coefficient of friction at lower joints due to their higher contact pressure.
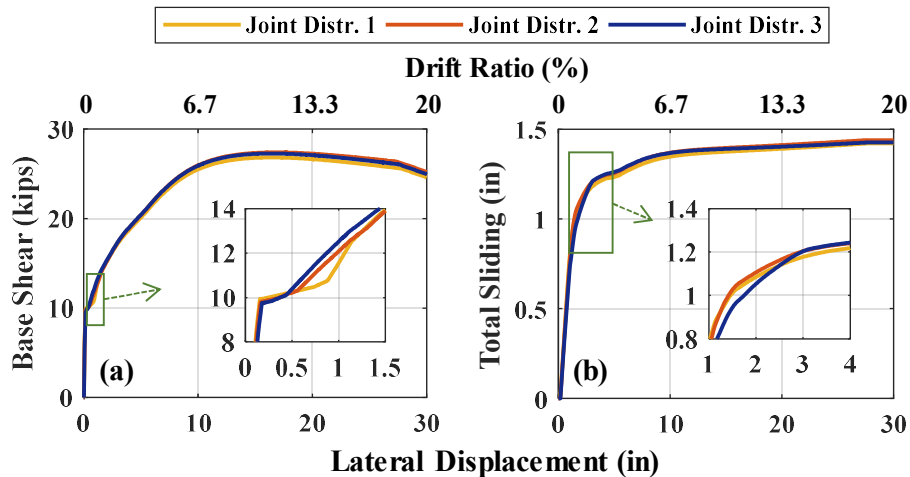
Figure 3-14. Effects of number of sliding joints on pushover analysis results: (a) base shear vs. lateral displacement; (b) total sliding vs. lateral displacement

116
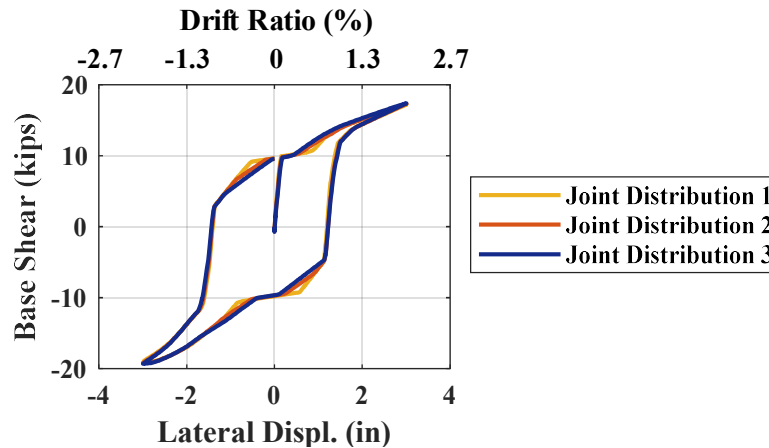
Figure 3-15. Effects of number of sliding joints on base shear vs. lateral displacement response under cyclic loading

The results of the time history analyses on the HSR columns with the three different number of sliding joints show that peak deck displacements, peak tendon strains, and peak cover and core concrete strains are practically unaffected by the number of joints (Figure 3-16). However, the residual deck displacements (Figure 3-16(b)) and total residual joint sliding values (Figure 3-17(b)) decrease with the number of joints. This is mainly because, for larger number of sliding joints, the same total sliding amplitude is shared between more joints, for which bearing forces initiate at smaller sliding amplitudes. This finding is in agreement with the pushover curves in Figure 3-14(a), where larger sliding is observed after the sliding initiation and before rocking initiation in the column with one sliding joint. Likewise, it is noticed that the peak base shear values slightly increase with the number of sliding joints (Figure 3-16(f)). Despite these small changes, peak residual drifts remain negligible (< 0.2%) for all of the considered joint distributions (Figure 3-13), which makes the effect of the number of sliding joints on the seismic performance of HSR columns inconsequential.
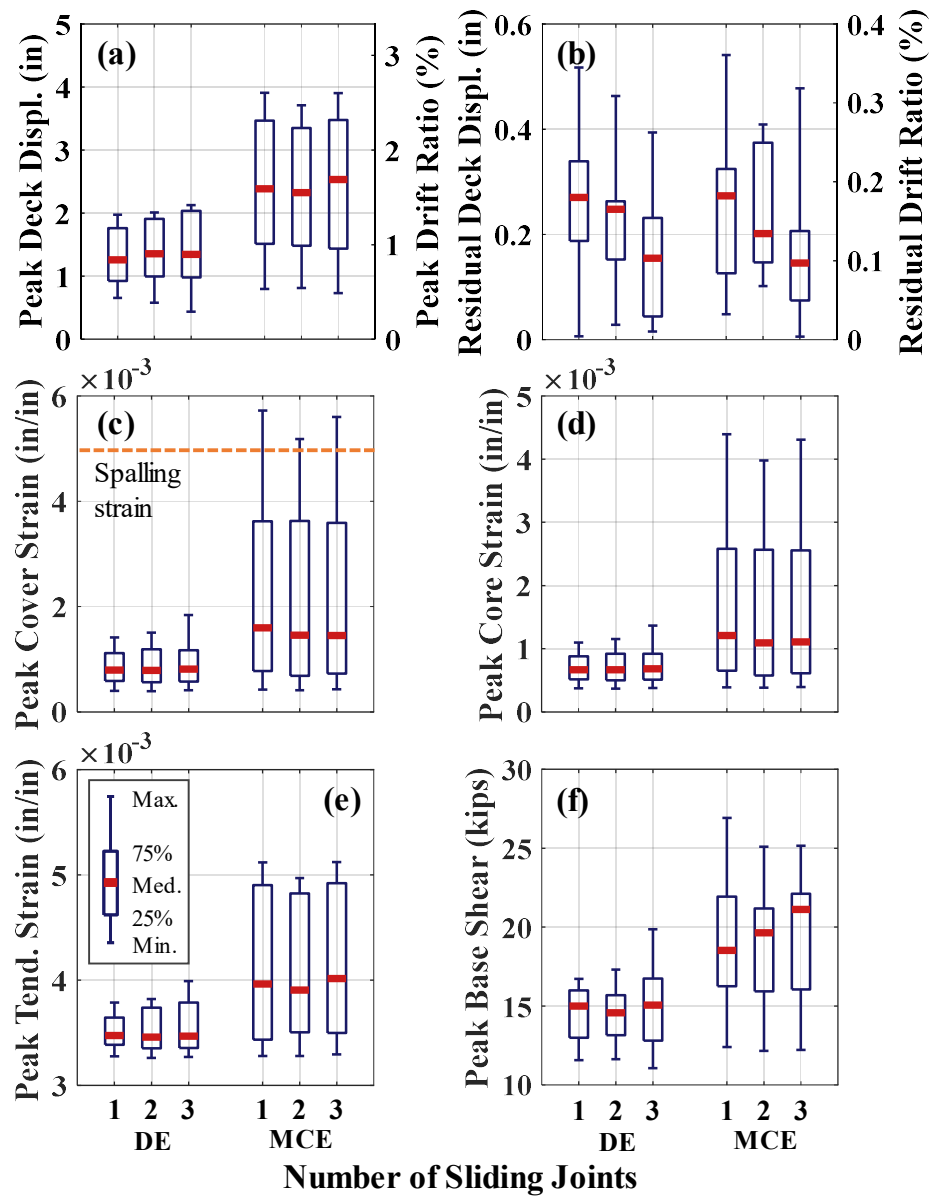
Figure 3-16. Effects of number of sliding joints on time history analysis results: (a) peak deck displacement; (b) residual deck displacement; (c) peak cover concrete strain; (d) peak core concrete strain; (e) peak tendon strain; (f) peak base shear
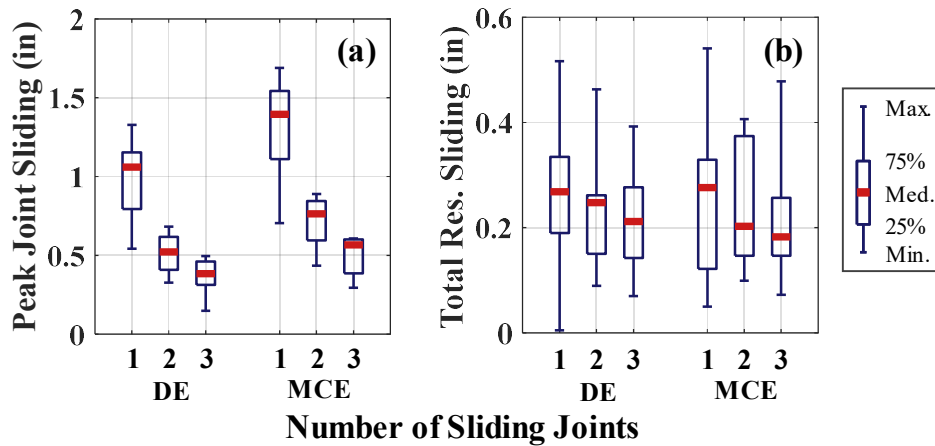
Figure 3-17. Effects of number of sliding joints on time history analysis results: (a) peak joint sliding; (b) total residual displacement

3.4.2. Incipient Sliding Base Shear Ratio

For given initial posttensioning and gravity load, the incipient sliding base shear ratio, R_{is}, primarily depends on the coefficient of friction at the sliding joints (see Eq. (3-1). Analyses are conducted for the reference HSR column (Figure 3-1) with three variations of the coefficient of friction with contact pressure obtained by multiplying the friction coefficients determined by friction model 2 of the reference column by 0.5, 1, and 1.5 (friction models 1 through 3 in Figure 3-2). In order to obtain similar total peak achievable sliding capacities, $\Sigma u_{sl,peak}$, a different value of h_{da} is selected for each friction model (Table 3-2), resulting in $\Sigma u_{sl,peak}$ of about 1.1 in. for all three column designs (Figure 3-18(b)). The resulting R_{is} obtained via pushover analysis (Figure 3-18(a)) when friction models 1, 2 and 3 are considered for the sliding joints include 0.18, 0.36, and 0.58, respectively. The R_{ir} is about 0.32 for all of the three column designs. Thus, the three values of R_{is} represent three cases: (*i*) joint sliding initiates prior to joint rocking initiation

($R_{is} < R_{ir}$), (*ii*) joint sliding initiates slightly after joint rocking initiation ($R_{is} \approx R_{ir}$), and

(*iii*) joint sliding initiates well after joint rocking initiation ($R_{is} > R_{ir}$).
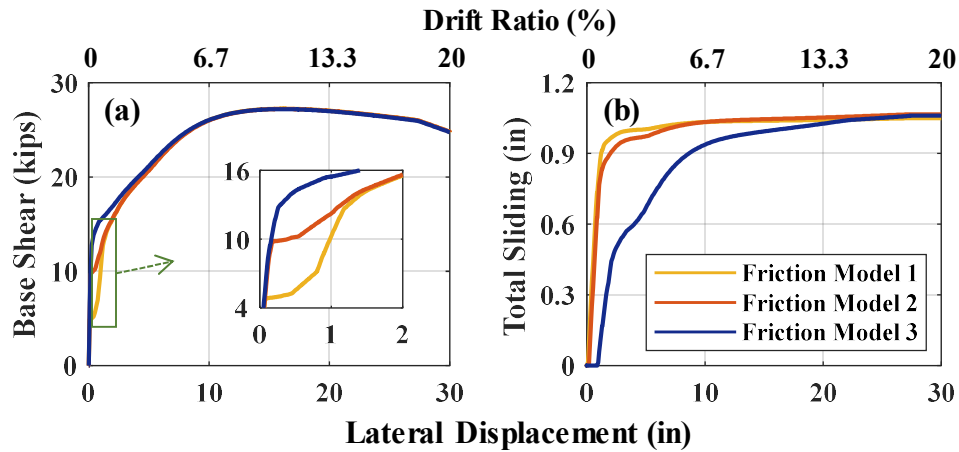
Figure 3-18. Effects of incipient sliding base shear ratio on pushover analysis results: (a) base shear vs. lateral displacement; (b) total sliding vs. lateral displacement

Although the total $u_{sl,peak}$ is nearly the same for all friction models, the joint sliding

for the column with friction model 3 (where $R_{is} > R_{ir}$) reaches this extent under much

larger lateral displacement (Figure 3-18(b)) compared to the columns with the other two

friction models. This slow progression of joint sliding results from the progressively

increasing post-tensioning forces due to joint rocking, which requires progressively larger

joint shear forces to overcome the frictional resistance. Under symmetric cyclic loading

(Figure 3-19), the hysteretic response of the HSR column is fairly symmetric for R_{is} close

to or smaller than R_{ir} (i.e. using friction models 1 and 2), but not for R_{is} larger than R_{ir} (i.e.

using friction model 3). For the latter case, higher joint sliding is observed during

unloading and reloading in the opposite direction, mainly due to post-tensioning losses occurring during initial loading.
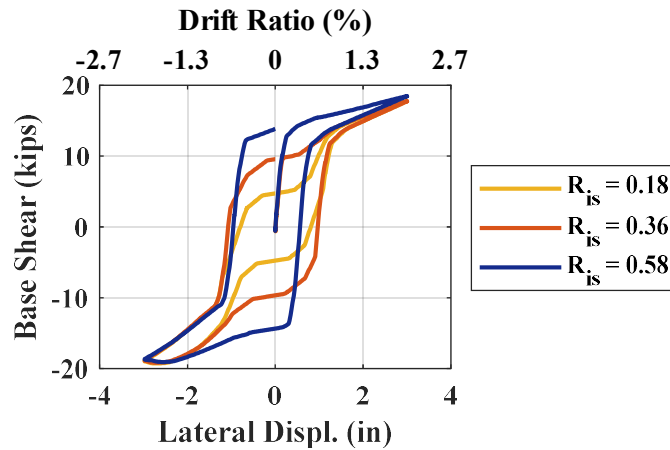
Figure 3-19. Effects of incipient sliding base shear ratio on base shear vs. lateral displacement response under cyclic loading

The seismic demands predicted by the time history analyses are displayed in Figure 3-20. For both hazard levels, the lowest peak displacement demands, peak concrete cover and core strains, and peak tendon strains are obtained for the column with $R_{ir} \approx R_{is} = 0.36$ (i.e. using friction model 2). These findings can be justified by the energy dissipation capabilities of each column, which are reflected in the effective damping ratios, ξ_{eff}, of each system computed via an equivalent system linearization for different peak displacement amplitudes (e.g. Sideris et al. 2014d; Madhusudhanan and Sideris 2018) and demonstrated in Figure 3-21. According to this graph, for $R_{ir} >> R_{is} = 0.18$, ξ_{eff} is large only at low drift ratios (< 1%), for which the response is dominated by major joint sliding and limited rocking at the bottom. However, for $R_{ir} << R_{is} = 0.58$, ξ_{eff} is large only at higher

drift ratios (> 1.5%), for which the response is dominated by rocking at the bottom rocking joint and joint sliding slowly increases with the peak drift ratio. For $R_{ir} \approx R_{is} = 0.36$, ξ_{eff} nearly envelops the other two curves providing the highest damping ratio in nearly the entire drift ratio range, and clearly in the range from 0.5% to 1.5%, which covers the seismic demands of the examined columns (see Figure 3-20(a)).

The lowest residual deck displacements were predicted for $R_{is} = 0.18$ (Figure 3-20(b)), because of the lower friction, and thus, the higher sliding restoration ability of the posttensioning tendons. This result is in agreement with the cyclic responses displayed in Figure 3-19. According to (Figure 3-22(b)), even the total residual sliding is lower for the column of friction model 2 compared to the columns of lower and higher friction coefficients at their sliding joints (i.e. friction models 1 and 3). This interesting finding illustrates the reduced effectiveness of the tendons' bearing reactions in restoring sliding when the coefficient of friction is relatively large (e.g. for friction model 3). It is further observed in Figure 3-22(a) that the variation of the peak joint sliding obtained for the column of higher coefficient of friction at its sliding joints is larger compared to the variation of the peak sliding values in other two columns. This is because, in that case, the shear required to initiate sliding is larger at the joints, making the peak sliding more dependent on ground motions.
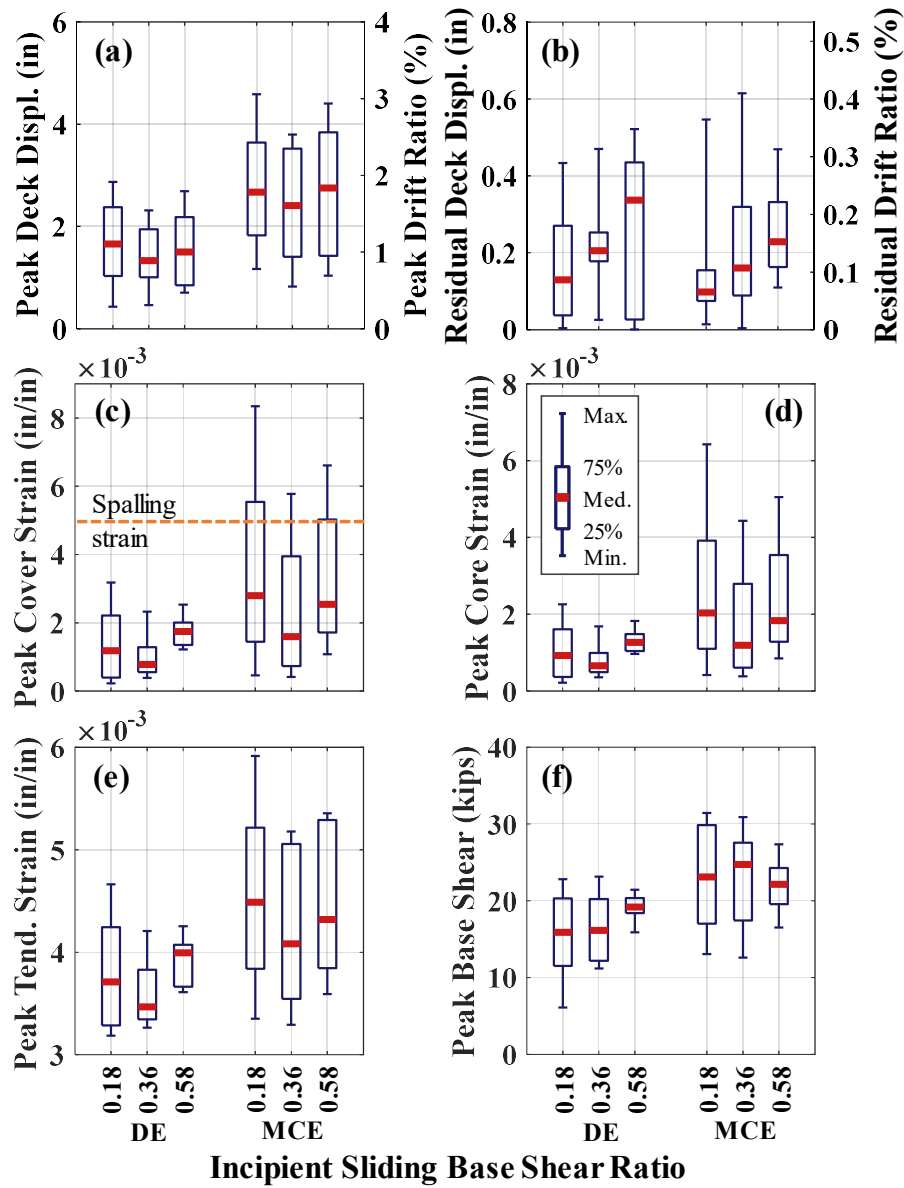
Figure 3-20. Effects of incipient sliding base shear ratio on time history analysis results: (a) peak deck displacement; (b) residual deck displacement; (c) peak cover concrete strain; (d) peak core concrete strain; (e) peak tendon strain; (f) peak base shear
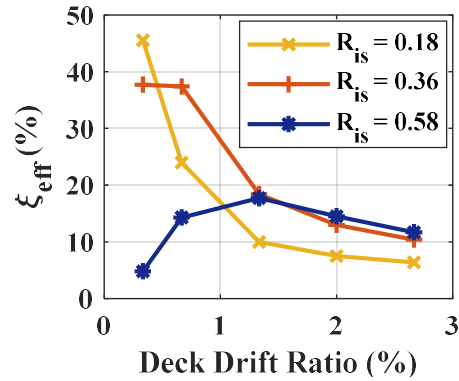
Figure 3-21. Effects of incipient sliding base shear ratio: variation of effective damping ratio with applied deck drift ratio obtained from cyclic analyses
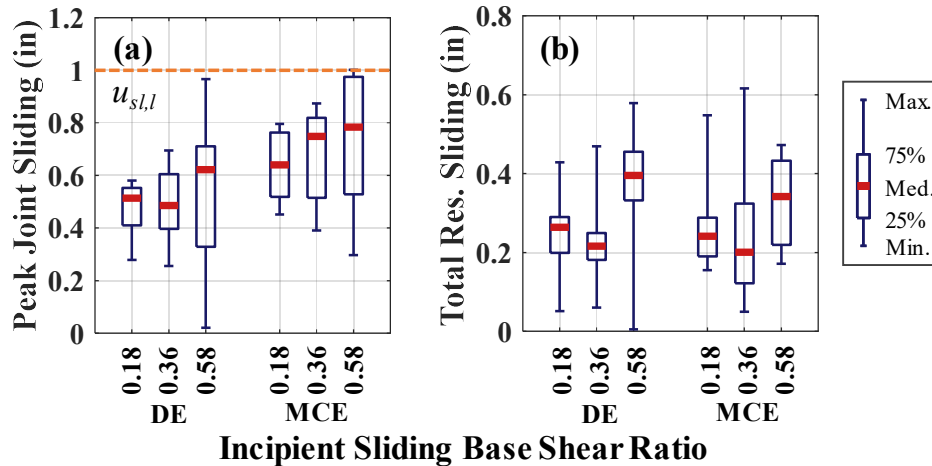
Figure 3-22. Effects of incipient sliding base shear ratio on time history analysis results: (a) peak joint sliding; (b) total residual displacement

3.4.3. Incipient Bearing Sliding Amplitude

The incipient bearing sliding amplitude, $u_{sl,b}$, of a sliding joint represents the portion of its peak achievable sliding capacity, $u_{sl,peak}$, for which no tendon bearing forces have emerged. This parameter can potentially influence the energy dissipation of HSR columns under low displacement demands and their residual joint sliding. For the reference HSR column

of Figure 3-1, four values of total $u_{sl,b}$ varying from 0.3 in. to 1.2 in. are considered, spanning a range of 20% to 85% of $u_{sl,peak}$. The selected values of $u_{sl,b}$ are obtained by varying the duct diameter, D_d (Table 3-2). The duct adaptor diameter, D_{da}, is the same for all designs and equals 1.6 in., resulting in a $u_{sl,l}$ of 1 in. per sliding joint. The same total $u_{sl,peak}$ of 1.4 in., i.e. 70% of the total $u_{sl,l}$, is achieved for all designs (Figure 3-23(b)) by varying the duct adaptor height, h_{da} (Table 3-2).
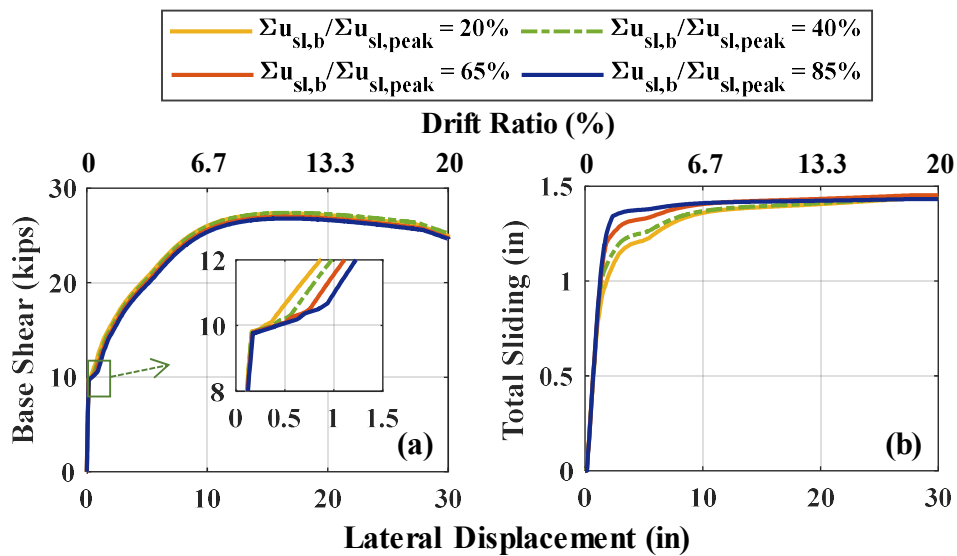
Figure 3-23. Effects of incipient bearing sliding amplitude on pushover analysis results: (a) base shear vs. lateral displacement; (b) total sliding vs. lateral displacement

The pushover analyses show that the lower the value of $u_{sl,b}$ is, the earlier rocking initiates (Figure 3-23(a)) and the more slowly sliding progresses with lateral displacement (Figure 3-23(b)). According to the cyclic analyses, for lower drift ratios (up to 2%), energy dissipation slightly increases with $u_{sl,b}$. Specifically, the effective damping ratios, ξ_{eff}, obtained from the cyclic responses of Figure 3-24, i.e. for a drift ratio of 2%, are 15.7%,

125

16%, 16.7%, and 17.1% for $\Sigma u_{sl,b}/ \Sigma u_{sl,peak}$ of about 20%, 40%, 65%, and 85%, respectively.
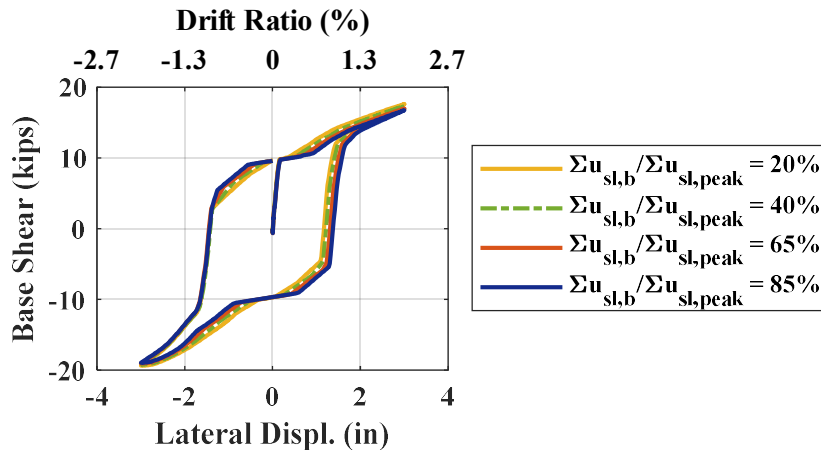
Figure 3-24. Effects of incipient bearing sliding amplitude on base shear vs. lateral displacement response under cyclic loading

Time history analysis results show that the peak deck displacements (Figure 3-25(a)) and peak tendon and concrete strains (Figure 3-25(c-e)) are mostly unaffected by the values of $u_{sl,b}$, particularly for the DE hazard level. For the MCE hazard level, the material strain demands slightly decrease with $u_{sl,b}$. The residual deck drift ratios are, however, lower for the two lower values of $u_{sl,b}$ compared to the two higher values of $u_{sl,b}$ (Figure 3-25(b)). Considering these findings, a balanced value of $u_{sl,b}$ appears to be around 50% of $u_{sl,peak}$. Comparing Figure 3-25(b) with Figure 3-26(b), there is an obvious correlation between the residual deck displacements and total residual joint sliding values, showing the major contribution of joint sliding to the recorded residual deck displacements.
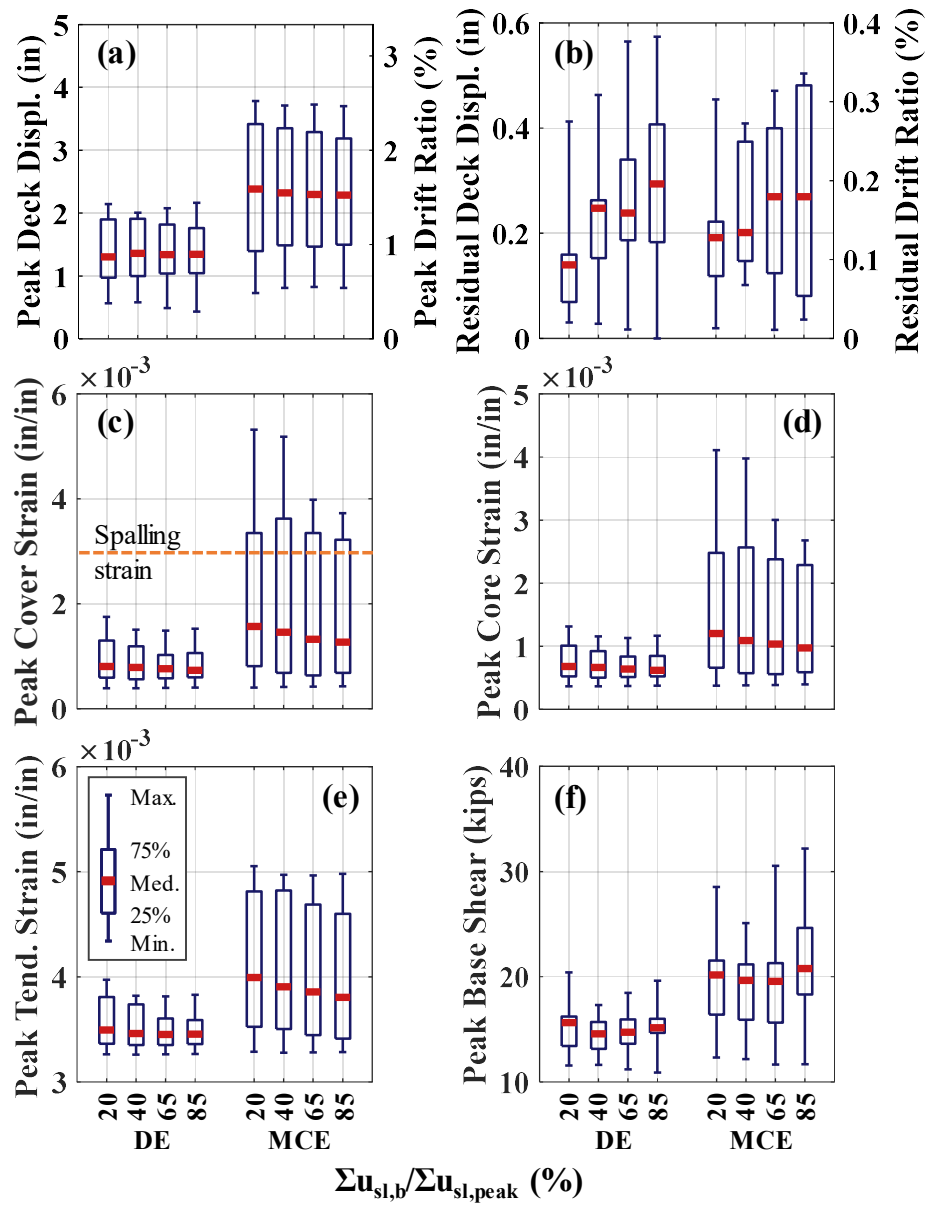
Figure 3-25. Effects of incipient bearing sliding amplitude on time history analysis results: (a) peak deck displacement; (b) residual deck displacement; (c) peak cover concrete strain; (d) peak core concrete strain; (e) peak tendon strain; (f) peak base shear
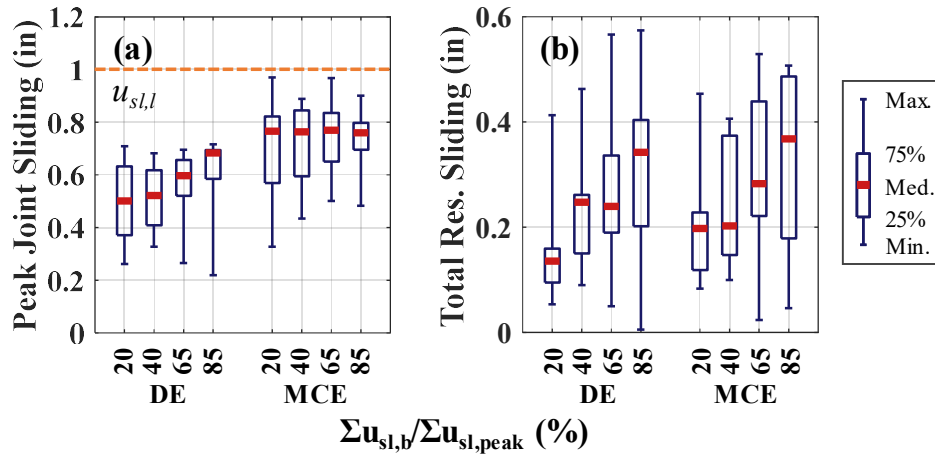
Figure 3-26. Effects of incipient bearing sliding amplitude on time history analysis results: (a) peak joint sliding; (b) total residual displacement

3.4.4. Peak Achievable Sliding Capacity

The peak achievable sliding capacity, $u_{sl,peak}$, controls the portion of the total displacement of the HSR columns sustained through joint sliding and affects their energy dissipation capacity, their damageability (through rocking), and their self-centering capabilities. For the reference HSR column (Figure 3-1), four different duct adaptor heights, h_{da}, are considered (Table 3-2), resulting in $\Sigma u_{sl,peak}$ of 0.7, 1.0, 1.4, and 1.8 in. (Figure 3-27(b)).

Monotonic pushover analyses show that the lateral strength is practically unaffected by $\Sigma u_{sl,peak}$ (Figure 3-27(a)). The responses of the compared HSR column variations under a displacement cycle of drift ratio of 2% (Figure 3-28) indicate a considerable expansion of the hysteresis loops with $\Sigma u_{sl,peak}$, which results in a significant increase of the corresponding effective damping ratios, ξ_{eff}. According to Figure 3-29, ξ_{eff} increases from 10% to 20% as $\Sigma u_{sl,peak}/H_{deck}$ increases from 0.5% to 1.2%. Also, as expected, the residual joint sliding increases with $\Sigma u_{sl,peak}$ (Figure 3-28).

128
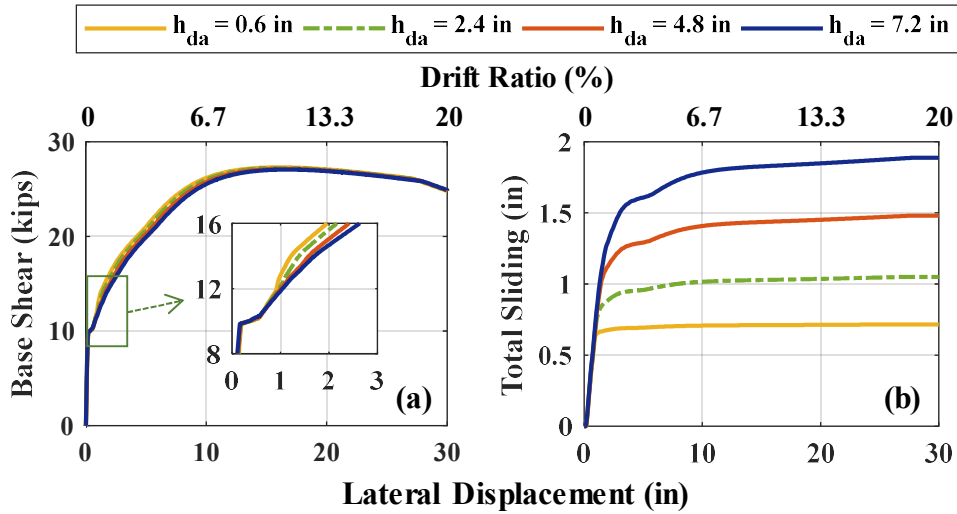
Figure 3-27. Effects of peak achievable sliding capacity on pushover analysis results: (a) base shear vs. lateral displacement; (b) total sliding vs. lateral displacement
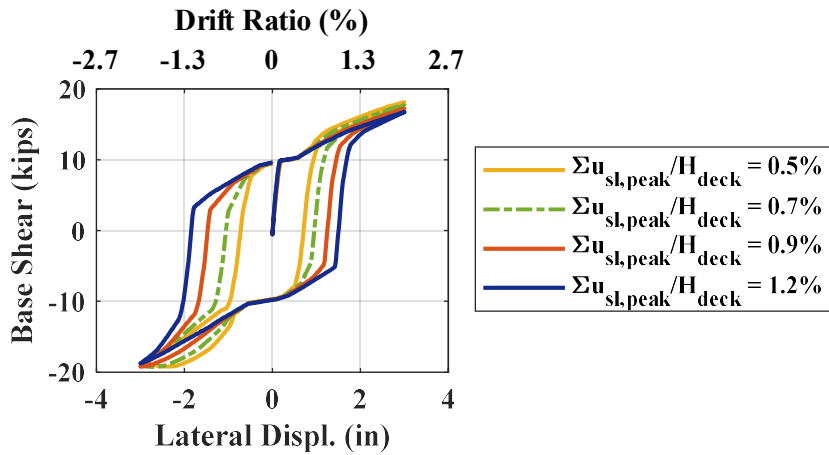
Figure 3-28. Effects of peak achievable sliding capacity on base shear vs. lateral displacement response under cyclic loading
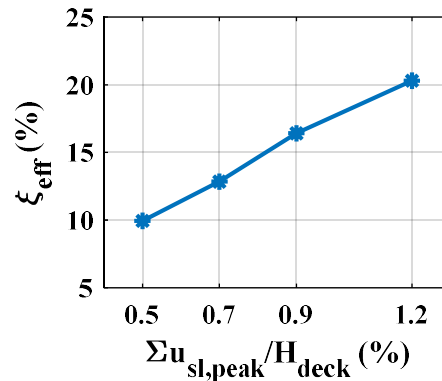
Figure 3-29. Effects of peak achievable sliding capacity on effective damping ratio obtained from cyclic analyses with 2% drift ratio amplitude

Time history analyses show that peak deck displacements slightly decrease with $\Sigma u_{sl,peak}$ (Figure 3-30(a)) due to the higher energy dissipation achieved for higher joint sliding capacities, while residual deck displacements and total residual joint sliding slightly increase with $\Sigma u_{sl,peak}$ (Figure 3-30(b) and Figure 3-31(b)). The reduction of peak strains in concrete cover, concrete core, and tendons as well as peak base shear with $\Sigma u_{sl,peak}$ is more significant (Figure 3-30(c-f)). This is because increasing $\Sigma u_{sl,peak}$ lowers the contribution of rocking to the column displacement, thereby reducing the elongation of the tendons and concrete compressive damage at the bottom end of the column. Based on the observed responses, it is reasonable to design $\Sigma u_{sl,peak}$ to account for at least 75% of the column design displacement demand to ensure that concrete (and tendon) damage is alleviated.
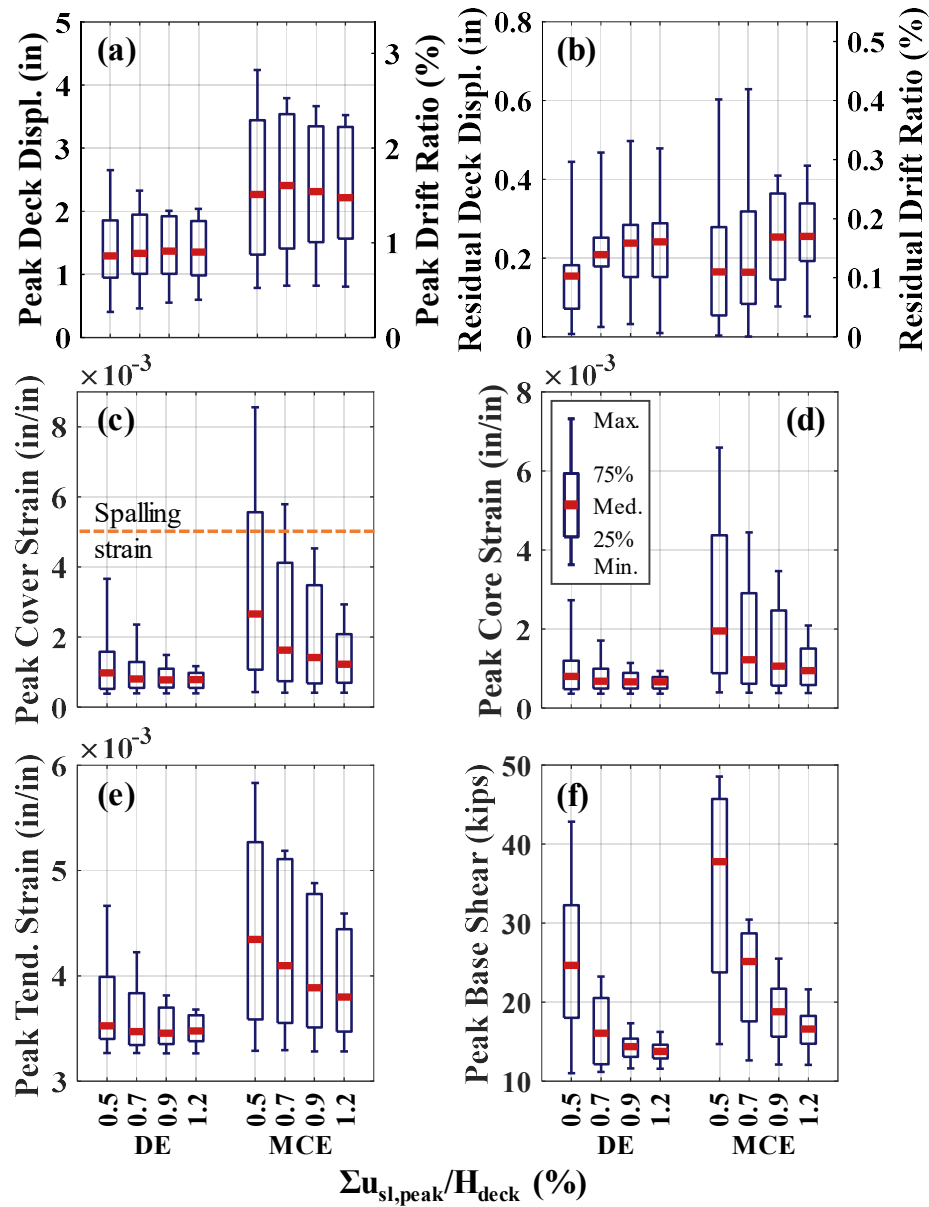
Figure 3-30. Effects of peak achievable sliding capacity on time history analysis results: (a) peak deck displacement; (b) residual deck displacement; (c) peak cover concrete strain; (d) peak core concrete strain; (e) peak tendon strain; (f) peak base shear
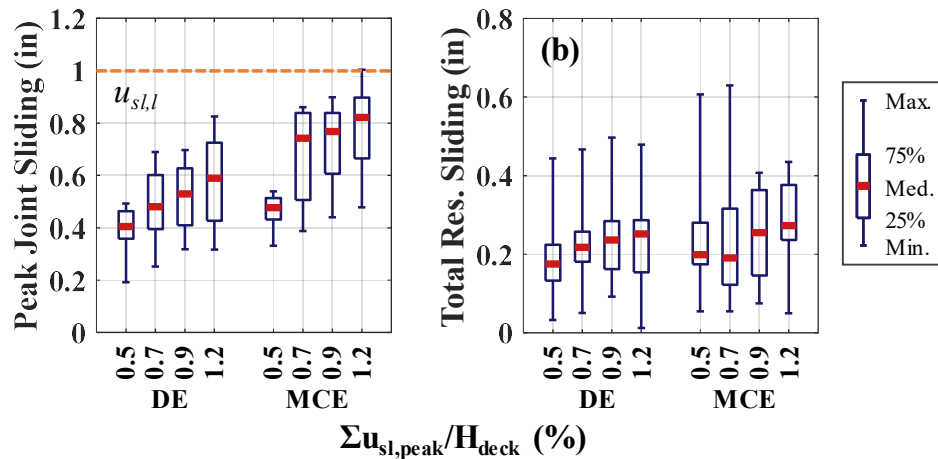
Figure 3-31. Effects of peak achievable sliding capacity on time history analysis results: (a) peak joint sliding; (b) total residual sliding

3.4.5. Design Recommendations

According to the findings of the prior sections on the effects of various design variables on the seismic performance of HSR columns, the following component-level design recommendations can be made:

- The number and location of sliding joints was found not to significantly affect the performance of HSR columns; yet, sliding joints closer to the bottom end of column, i.e. the location of high flexural demands, were found slightly lower damage, thereby being preferred. The sliding joints should still maintain a minimum distance from the end rocking joints, per Sideris et al. (2014d), to ensure that compressive strains at the sliding joints remain sufficiently low and damage at their interfaces and adjacent to those is avoided. Sliding joints closer to the bottom end of column may be easier to inspect, too. The number of sliding joints, when they are close to each other, was found to be of inconsequential

effect on the performance of HSR columns. Thus, no more than one or two sliding joints are recommended per HSR column. This is also in agreement with Sideris et al. (2014c), who observed that joint sliding is difficult to propagate to more than two sliding joints in HSR columns with sparsely spaced sliding joints over their entire height. A lower number of sliding joints is further expected to reduce the initial and inspection costs of HSR columns over their lifetime (Valigura 2019).

- The coefficient of friction at the sliding joints and the column dimensions should be selected such that the incipient sliding base shear ratio, R_{is}, is nearly identical to the incipient rocking base shear ratio, R_{ir}. This combination maximizes the energy dissipation and the effective damping ratio of the system, thereby limiting the seismic demands and imposed damage. Lower or higher R_{is} result in lower damping and larger demands and damage. Per Sideris et al. (2014d), the incipient sliding base shear should be lower than the peak strength, i.e. $R_{is} < 1$, which is already integrated in the above condition, i.e. $R_{is} \approx R_{ir}$, because $R_{ir} \approx 0.3$ to 0.5 for typical rocking columns.

- The incipient bearing sliding amplitude, $u_{sl,b}$, has a small influence on the performance of HSR columns. Yet, a reasonable value of $u_{sl,b}$ appears to be around 50% of $u_{sl,peak}$, for which both the peak concrete strains and the system residual deformations remain low. Thus, the duct diameter, D_d, should be selected to generate such value of $u_{sl,b}$ ($= D_d - D_{PT}$).

- The duct adaptor height, h_{da}, should be selected such that the total peak achievable sliding capacity, $\Sigma u_{sl,peak}$, accounts for at least 75% the lateral displacement demand of the HSR column at the design earthquake to effectively reduce concrete (and tendon) damage. The displacement demand can be estimated using the capacity spectrum design method by Madhusudhanan and Sideris (2018) or time history analyses. To prevent potential tendon bearing damage and shearing at the joint interface (Sideris et al. 2014d; Madhusudhanan and Sideris 2018), the duct adaptor diameter, D_{da}, should be large enough, so that $u_{sl,l}$ exceeds $u_{sl,peak}$ at all sliding joints. A $u_{sl,peak}$ equal to 70% of $u_{sl,l}$ was found reasonable in this study. In reference to the column dimensions, $u_{sl,l}$ is suggested not to exceed 20-25% of the wall thickness and 4-5% of the cross-section diameter to ensure column stability in the deformed configuration. Yet, larger values could be possible, as dictated by individual designs.

3.5. Evaluation of Effects of Vertical Excitation

Understanding the effects of vertical component of earthquake shaking on the response of HSR columns is of paramount importance, because of the presence of unbonded post-tensioning tendons and the absence of any bonding at the interface of sliding joints. For this purpose, time history analyses are conducted on the reference HSR column of Figure 3-1 with two sliding joints at the mid-height with 2-ft spacing using the far-field ground motion set from Table 3-1. For the sliding joints, D_d, D_{da}, and h_{da} are taken as 0.9 in., 2.1 in., and 4.5 in., leading to a nominal sliding capacity, $u_{sl,l}$, of 1.5 in. per sliding joint. The motions are scaled to the DE, MCE, and double MCE hazard levels. The third hazard level

is herein employed to generate extremely strong vertical excitations on the HSR columns. The vertical acceleration components are scaled using the same scale factors used for the horizontal ones and have a horizontal to vertical PGA ratio ranging from 0.98 to 4.06.

According to the time history analysis results (Figure 3-32), the seismic demands are barely influenced by the vertical component of the ground motions at all hazard levels considered. This is because the largest portion of the compressive stress (~ 80% in static conditions) in all joints is contributed by the unbonded post-tensioning, whereas the contribution of the gravity load and the vertical component of the earthquake excitation, even for high intensities, remains small. This observation is in agreement with the findings of Sideris (2015), who observed, through equivalent quasi-static pushover analyses, that the influence of the vertical component of the seismic load on the response of a HSR column with similar properties was small. From a dynamics perspective, it is also worth noting that large vertical accelerations appear for short time intervals and are not sufficient to cause structural instabilities. However, the resulting variations of the joint shear due to friction change with contact pressure result in small variations of the column's lateral response. Occasionally, upward accelerations contribute to the re-centering of the joint sliding by decreasing the joint friction and increasing tendon dowel forces (Sideris 2012), which is apparent in the residual displacements and total residual sliding values obtained for the DE hazard level (Figure 3-32(b) and Figure 3-33(b)).
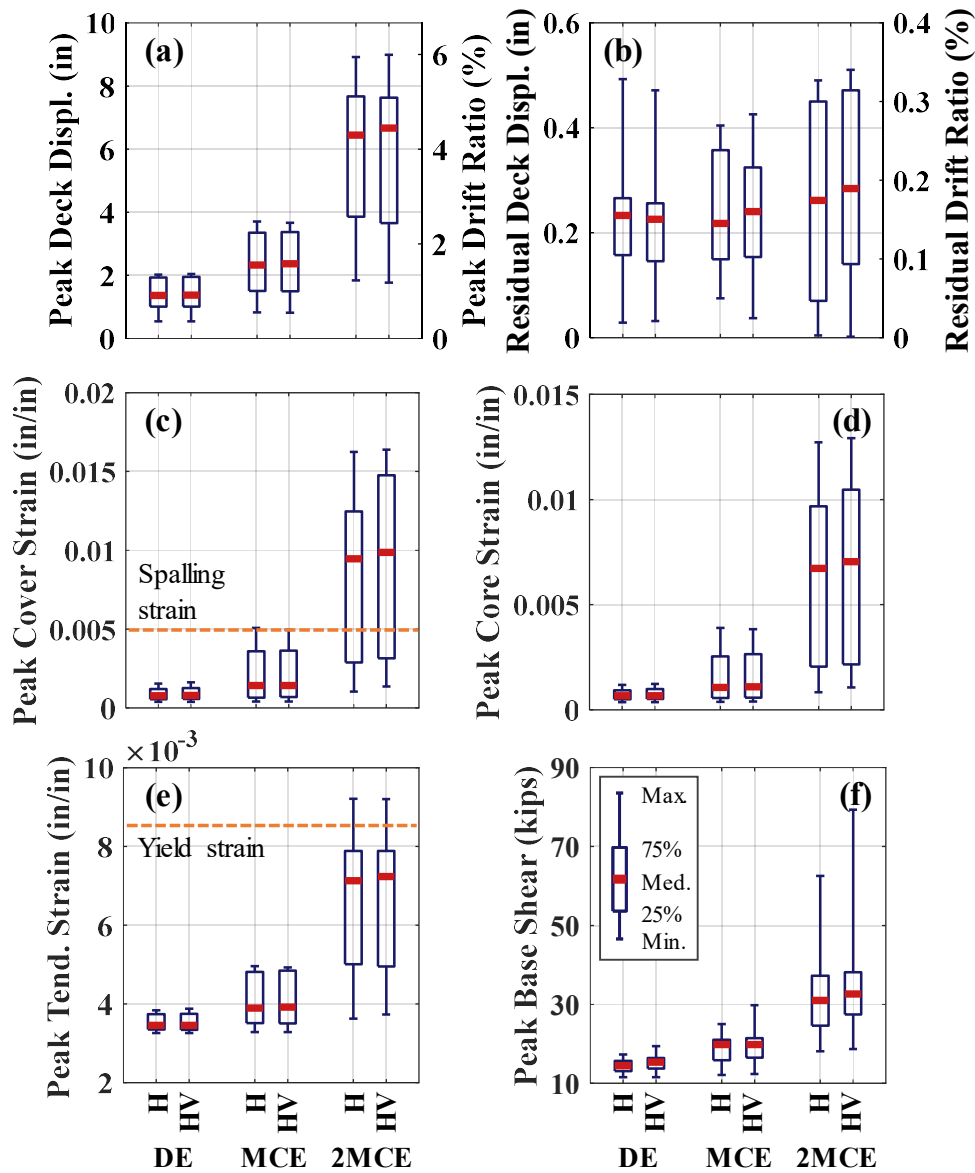
Figure 3-32. Effects of vertical excitation on time history analysis results: (a) peak deck displacement; (b) residual deck displacement; (c) peak cover concrete strain; (d) peak core concrete strain; (e) peak tendon strain; (f) peak base shear (H = horizontal excitation; HV = simultaneous horizontal and vertical excitation)
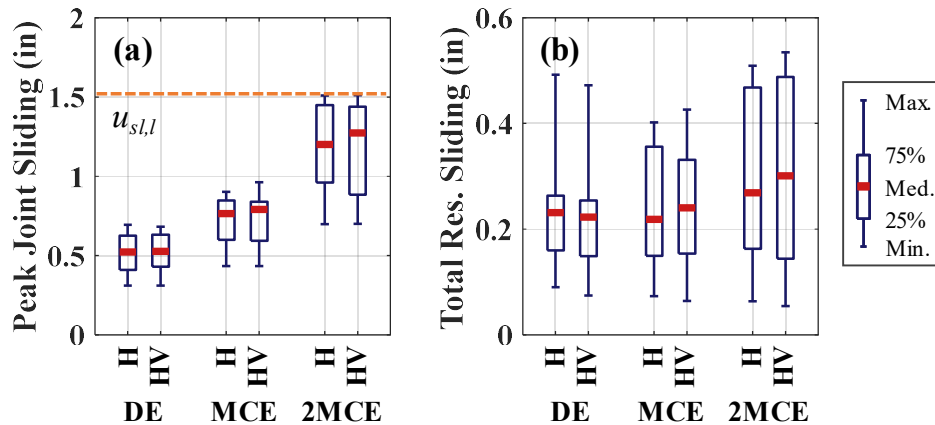
Figure 3-33. Effects of vertical excitation on time history analysis results: (a) peak joint sliding; (b) total residual sliding (H = horizontal excitation; HV = simultaneous horizontal and vertical excitation)

3.6. Evaluation of Effects of Near-Fault Motions

Considering their different frequency content and the existence of potential velocity pulses compared to far-field motions, near-fault motions with and without velocity pulses can potentially impact the performance of HSR columns. In order to explore their possible influence, the reference column of Figure 3-1 with the same sliding joint distribution used in the previous section is subjected to the horizontal components of all three ground motion sets of Table 3-1 scaled to DE and MCE hazard levels. The duct and duct adaptor dimensions and the variation of coeffiecient of friction with contact pressure remained similar to those considered in the previous section.

The results of the time history analyses are summarized through the boxplots of Figure 3-35 and Figure 3-34. It is observed that near-fault motions without pulses do not increase the seismic demands, especially peak concrete and tendon strains as well as peak base shear (Figure 3-35(c-f)). If having velocity pulses, near-fault motions result in almost

equal and/or slightly larger median seismic demands for the DE and MCE levels, respectively (Figure 3-35). The variations of the demands obtained under the near-fault motions with velocity pulse is, however, signficantly higher, particularly when they are scaled to the MCE hazard level. Overall, these observations demonstrate the capability of HSR columns to withstand both far-field and near-fault motions with limited damage, as well as their low sensitivity to site-to-source distance effects. Such versatility of the HSR columns is the result of the sliding joints, which can help the system endure high-intensity intervals of motions with limited damage.
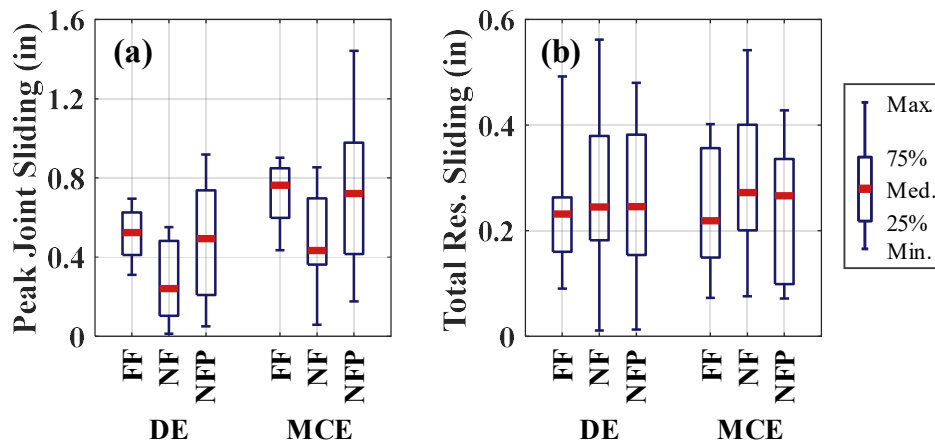
Figure 3-34. Effects of near-fault ground motions on time history analysis results: (a) peak joint sliding; (b) total residual sliding (FF = far-field motions; NF = near-fault motions without pulse; NFP = near-fault motions with pulse)
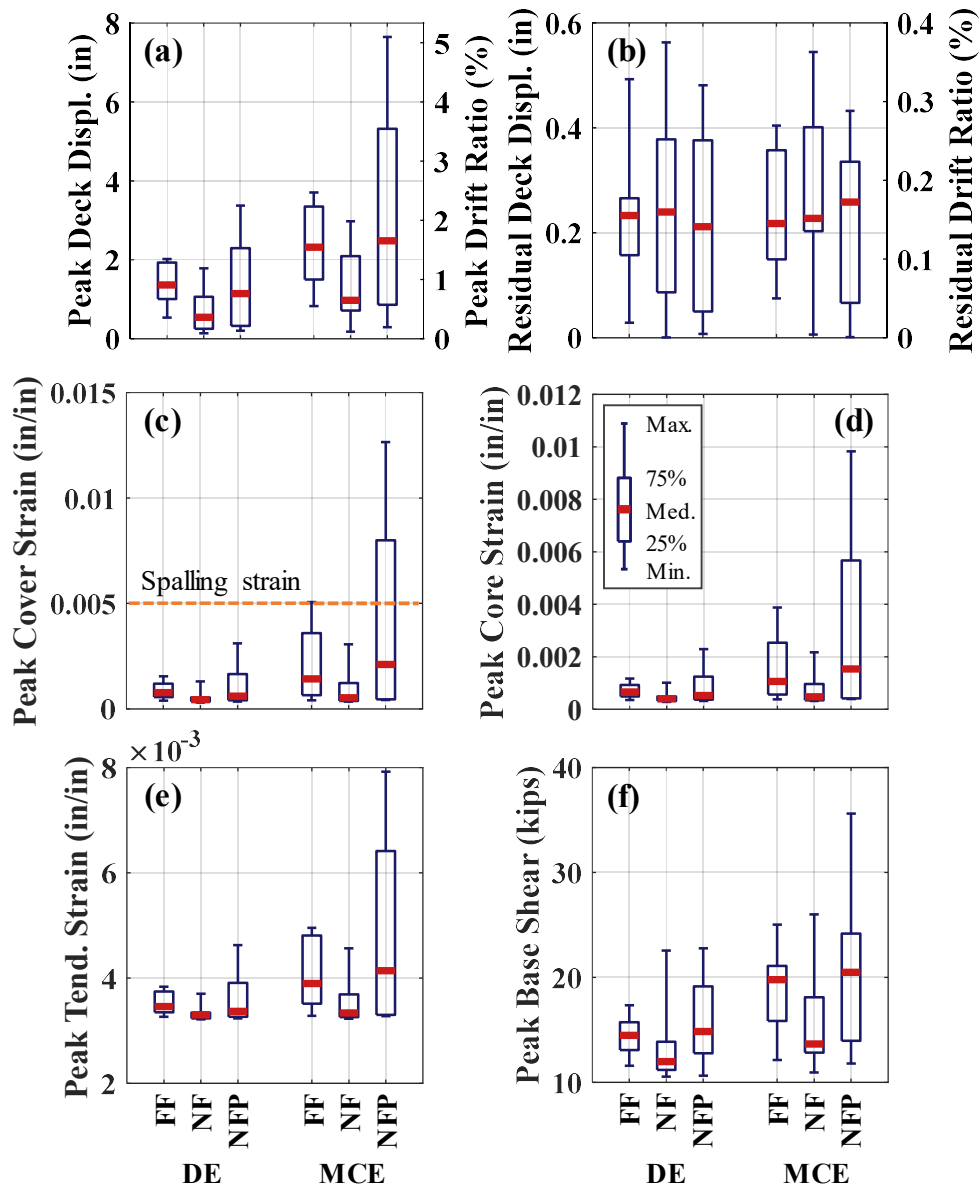
Figure 3-35. Effects of near-fault ground motions on time history analysis results: (a) peak deck displacement; (b) residual deck displacement; (c) peak cover concrete strain; (d) peak core concrete strain; (e) peak tendon strain; (f) peak base shear (FF = far-field motions; NF = near-fault motions without pulse; NFP = near-fault motions with pulse)

3.7. Comparison with Rocking-Only Column

The objective of this section is to examine how an HSR column's performance compares with a rocking-only column of similar design. Such comparison allows understanding the pros and cons of HSR columns with respect to typical rocking columns in terms of seismic demands. For this purpose, the response of the reference HSR column (Figure 3-1) with the following construction details is compared with that of a rocking-only column of identical dimensions and material properties. Two sliding joints are considered with 2-ft spacings from the bottom rocking joint of the HSR column. According to the design recommendations provided earlier, for the HSR column examined herein, the total peak achievable sliding capacity, $\Sigma u_{sl,peak}$, is taken as 1.4 in., which is close to the predicted displacement demand for the column under DE hazard. The total incipient bearing sliding amplitude, $\Sigma u_{sl,b}$, and the total nominal sliding capacity, $\Sigma u_{sl,l}$, are set at half of $\Sigma u_{sl,peak}$, i.e. 0.7 in., and 30% higher than $\Sigma u_{sl,peak}$, i.e. 1.8 in., respectively. The above conditions are obtained by $D_d = 0.95$ in., $D_{da} = 1.8$ in., and $h_{da} = 4$ in. Furthermore, friction model 2 (Figure 3-2) is maintained to achieve $R_{is} \approx R_{ir}$.

According to the pushover analysis results, the two columns have nearly identical peak lateral strength (Figure 3-36(a)). However, due to the joint sliding, damage (i.e. concrete spalling, tendon yielding, and concrete crushing) is delayed until higher displacements for the HSR column. Under cyclic loading, the HSR column exhibits significantly larger hysteretic energy dissipation (Figure 3-36(b)) compared to the rocking-only column, but lower self-centering capabilities. It is noted, though, that the

residual displacement in the HSR column is exclusively caused by residual joint sliding, which is recoverable.
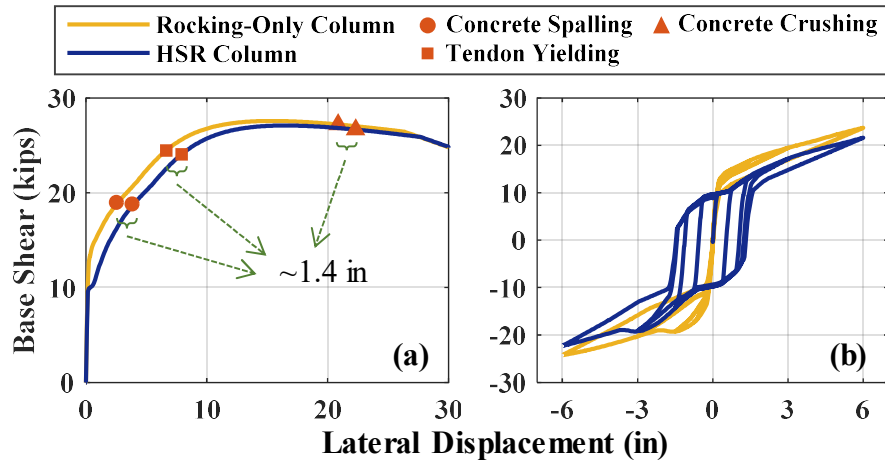
Figure 3-36. Comparison with rocking-only column: (a) pushover lateral force-displacement responses; (b) cyclic lateral force-displacement responses

The deck centroid displacement time histories obtained from the time history analyses of the bridge piers with the two columns subjected to a single ground motion are compared in Figure 3-37. The horizontal and vertical components of the far-field ground motion 1 in Table 3-1 scaled to the DE hazard level was used for this purpose. According to Figure 3-37, the peak total lateral displacements obtained for the HSR column are at least 25% smaller than those obtained for the rocking-only column. Particularly when the total joint sliding, which does not correspond to damage, is subtracted from the deck displacements, the resulting peak deck displacements values do not exceed 35% of those predicted for the rocking-only column. This significant decrease in the displacement demand accommodated through rocking translates into a significant decrease in the damage at the

HSR column's bottom rocking joint compared to the rocking-only column's bottom joint. As seen in the displacement time histories, the energy dissipation provided by the HSR column due to friction (see Figure 3-38(a)) significantly speeds up the dissipation of the HSR column vibrations, unlike the rocking-only column, for which vibration remain large for much longer durations.
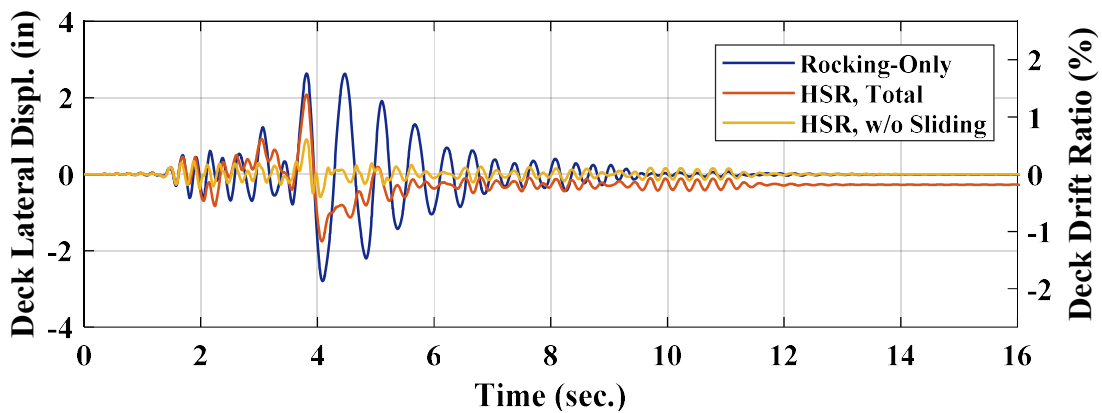
Figure 3-37. Comparison with rocking-only column – single time history analysis results: deck centroid displacement time histories

The base shear vs. lateral deck displacement responses of the two columns obtained from the same analyses are demonstrated in Figure 3-38(a). Clearly, the maximum base shear of the rocking-only column is higher than that of the HSR column by more than 85%, inducing higher moment (and shear) demands in the foundation. Per Figure 3-38(b), the total tendon forces in the HSR column remain up to 15% lower than those in the rocking-only column, even for the same column displacements. This finding is primarily attributed to the smaller rocking (at the bottom end of the column) in the presence of joint

sliding. Moreover, joint sliding results in a much slower variation/increase of the tendons

elongation, and thus, their forces, compared to joint rocking.
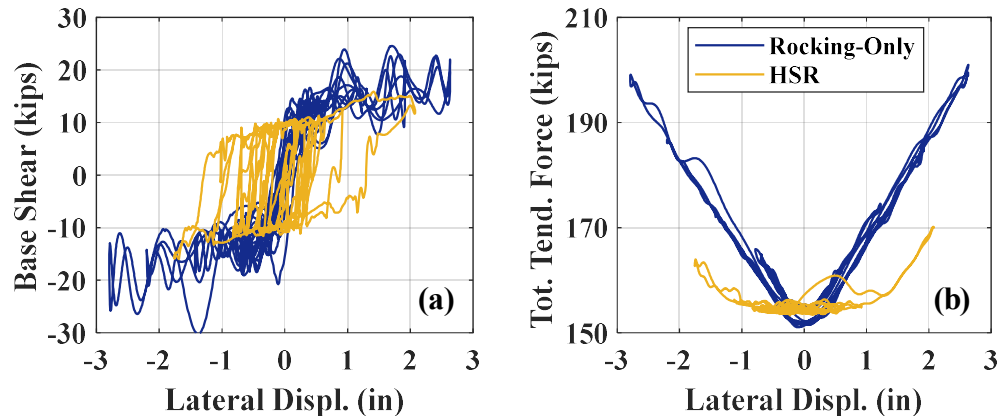
Figure 3-38. Comparison with rocking-only column – single time history analysis results: (a) hysteretic lateral force-displacement responses; (b) total PT force vs. lateral displacement responses

Multiple time history analyses are performed on both bridge piers under the far-field

ground motion ensemble (Table 3-1) scaled to the DE, MCE, and double-MCE hazard

levels and considering both the horizontal and vertical components of the motions. The

results show that, for all intensity levels, peak deck displacements are in general smaller

for the HSR column compared to the rocking-only column (Figure 3-39(a)). This finding

is mainly attributed to the higher energy dissipation of the HSR column relative to the

rocking-only column, due to the frictional response of its sliding joints.
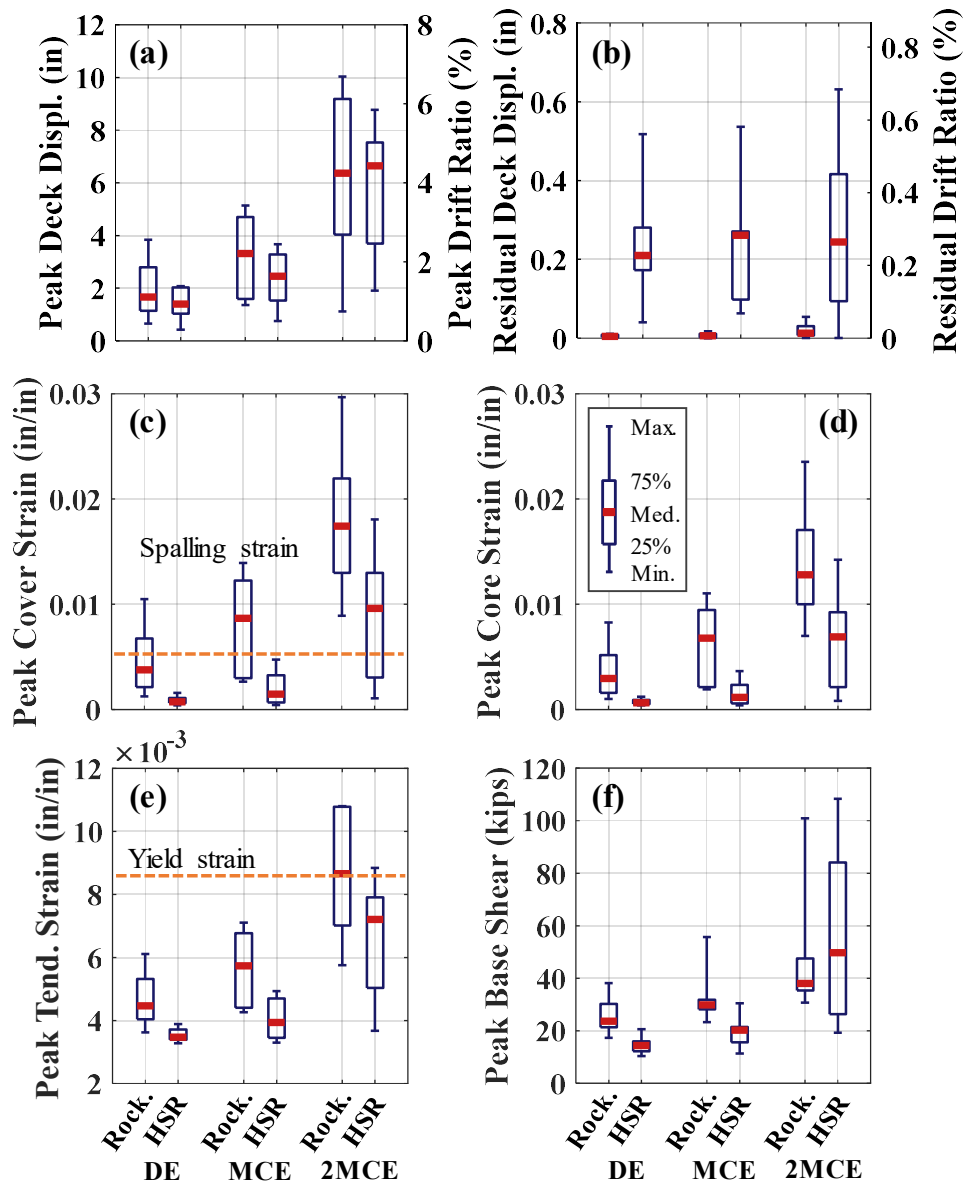
Figure 3-39. Comparison with rocking-only column – multiple time history analysis results: (a) peak displacement; (b) residual displacement; (c) peak cover concrete strain; (d) peak core concrete strain; (e) peak tendon strain; (f) peak base shear

The residual deck drift ratios remain small (median values < 0.3%) for the HSR column, and nearly zero for the rocking-only column (Figure 3-39(b)). A comparison of the total residual joint sliding values (Figure 3-40(b)) and the residual deck displacements

144

predicted for the HSR column (Figure 3-39(b)) reveals that the residual deck displacements have resulted from the residual joint sliding rather than column damage. Hence, such residual displacements can be eliminated by re-setting the sliding joints.
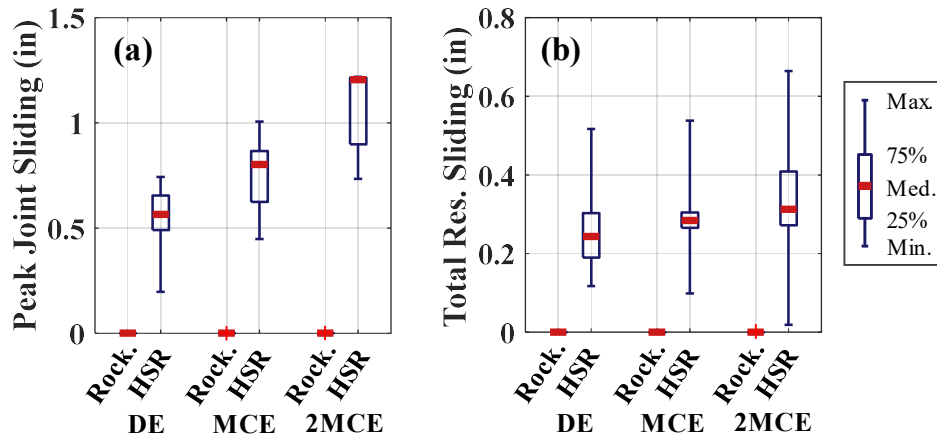
Figure 3-40. Comparison with rocking-only column – multiple time history analysis results: (a) peak joint sliding; (b) total residual sliding

The above observation is further confirmed by the much lower peak concrete and tendon strains in the HSR column compared to those predicted for the rocking-only column (Figure 3-39(c-e)). The rocking-only column sustains spalling for some of the ground motions at the DE hazard level, for most of the ground motions at the MCE hazard level, and for all of the motions at double-MCE hazard level (Figure 3-39(c)). The HSR column, on the other hand, exhibits concrete spalling only for some of the ground motions scaled to the double-MCE hazard level (Figure 3-39(c)). Similarly, for all earthquake intensities, peak tendon strains are lower for the HSR column compared to the rocking-only column, which experiences tendon yielding under half of the motions scaled to the

double-MCE hazard level (Figure 3-39(e)). The tendons in the HSR column, however, only yield in one instance.

The peak base shear demand for the HSR column is up to 50% smaller than that for the rocking-only column under the DE and MCE hazard levels (Figure 3-39(f)); this is because joint sliding controls the dynamic inertial forces more efficiently and causes a much smaller increase to the base shear, compared to rocking. According to Figure 3-40(a), as desired, the peak sliding at each joint remains below the nominal sliding capacity, $u_{sl,l}$ (i.e. 1.2 in.) for the DE and MCE hazard levels, but its median increases to $u_{sl,l}$ under very high-intensity motions, i.e. those representing the double-MCE hazard.

4. EXPERIMENTAL INVESTIGATIONS

This chapter is concerned with an extensive experimental program on HSR columns designed in accordance with the findings of the analytical investigations (Chapter 3). The objectives of the experimental testing program are:

- Evaluate the constructibility of HSR columns with the properties required based on the findings of the analytical investigations of Chapter 3 to improve their seismic behavior;

- Assess the overall performance of HSR columns with improved design under simulated seismic loads;

- Examine the effects of various loading and boundary conditions, including torsional loading, biaxial loading, and rotationally fixed top end connection, on the response of HSR columns;

- Produce sufficient experimental data to further validate and improve the finite element formulations and modeling strategy proposed in Chapter 2.

In order to achieve the above objectives, in the following sections, an HSR column is designed as part of a highway bridge in a highly seismic region and four half-scale specimens with that design are tested under various loading and boundary conditions. The loading conditions consist of uniaxial lateral loading, torsional loading, and biaxial loading. The boundary conditions include free and fixed top end rotation. The loading protocols consist of both quasi-static and dynamic loading applied in the form of displacement time histories of various shapes and amplitudes.

4.1. Prototype Bridge

The HSR column specimens are assumed to be part of the single-column bents adjacent to the middle span of the fictitious five-span bridge studied by Megally et al. (2002a), depicted in Figure 4-1. The bridge is symmetric and its interior and exterior spans are each 100 ft and 75 ft long, respectively. In the prototype bridge, the height of deck centroid from column footings was 25 ft, but no information was provided about the substructure (i.e. cap beam and column dimensions). Therefore, in this study, the height of the columns supporting the superstructure is assumed to be 20 ft.

4.2. Similitude Analysis

Due to the limitations of the laboratory equipment (e.g. capacity of the cranes and stroke and force capacity of actuators – Table 4-5) and construction cost, the column specimens need to be smaller than their actual size. Considering the above limitations and after a few iterations, the length scale factor, S_L, is chosen as 2, leading to 10 ft tall columns.

Because the testing program includes dynamic loading protocols, per similitude analysis rules, scale factors for three fundamental dimensions need to be arbitrarily selected, while the rest of scale factors are computed accordingly. Other than the length scale factor, S_L, which was set at 2, the other two basic scale factors are chosen to be those of density and modulus of elasticity, i.e. S_ρ and S_E, respectively. These scale factors are taken as unity, because the materials (e.g. steel and concrete) used to build the test specimens are desired to be similar to those in the actual structure. The remaining important scale factors are found in accordance with the above three basic scale factors and are summarized in Table 4-1.
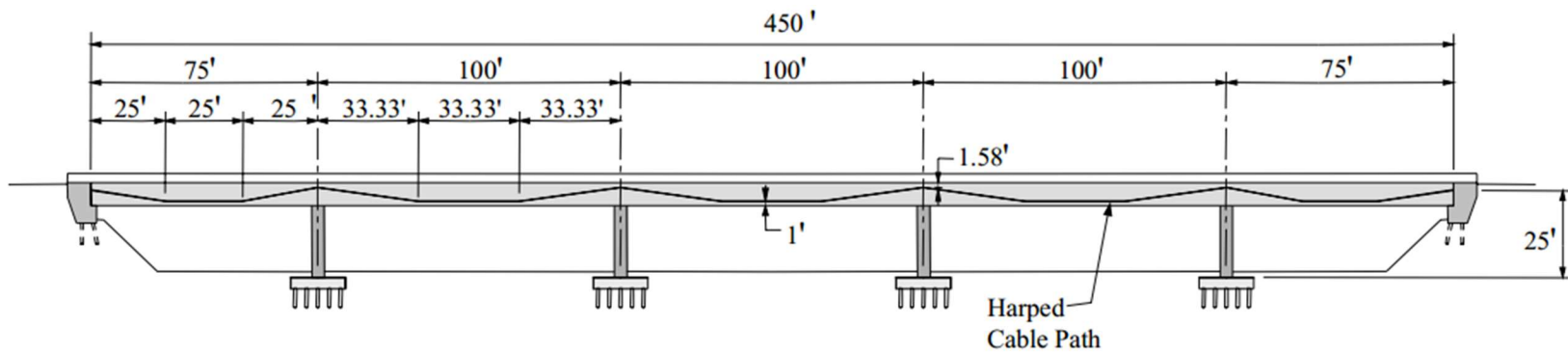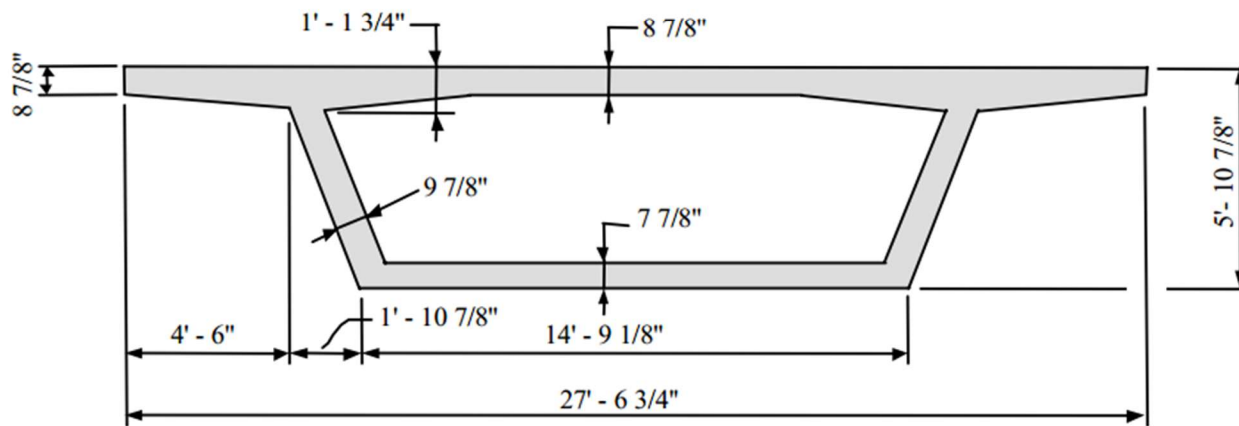
Figure 4-1. Prototype bridge: (a) elevation; (b) deck cross section (Megally et al. 2002a)

149

Table 4-1. Dependent similarity scale factors

Dimension	Notation	Relationship	Scale Factor
Area	S_A	S_L^2	4
Volume	S_V	S_L^3	8
Mass	S_m	$S_V S_\rho$	8
Force	S_F	$S_A S_E$	4
Moment	S_M	$S_F S_L$	8
Weight	S_W	S_F	4
Stress	S_σ	S_E	1
Acceleration	S_a	S_F/S_m	0.5
Time	S_t	$(S_L/S_a)^{0.5}$	2
Gravity Acceleration	S_g	S_a	0.5

It is observed that the scale factor for gravity acceleration, S_g, needs to be equal to 0.5 in order to uphold the similarity. Even though it is impractical to double the acceleration of gravity in the lab environment, this will not affect the actual loading states generated during testing, because gravity loads will be applied through hydraulic actuators, which will explicitly account for the actual loads that would be generated into this scaled up (by a factor of 2) gravitational field. The only distortion arises in the axial force variation over the height of the column due to the self-weight of the column segments, which is deemed insignificant, compared to the weight of the superstructure.

4.3. Design of Column Specimens

The testing program includes four column specimens of identical design. The design was carried out in accordance with the AASHTO LRFD Bridge Design Specifications (AASHTO 2014), the AASHTO Guide Specifications for LRFD Seismic Bridge Design

(AASHTO 2011), the Precast Prestressed Bridge Design Manual (PCI 2003), and the findings of Chapter 3 investigating the effective design of sliding joints in HSR columns.

For convenience and to avoid any inconsistency with design codes, the column specimens are designed in the model domain. That is, the column dimensions and properties are determined for the force effects first obtained in the prototype domain and then scaled down to the model domain according to the similarity scale factors of Table 4-1.

Assuming that the substructure is connected to the superstructure through an integral bent cap, the column's top end is assumed to be rotationally constrained to the superstructure. It is noted that slider/elastomeric bearings are redundant between the bents and the superstructure in HSR bridges, as lateral movement will be undertaken by sliding at the column joints. Because the prototype bridge is a five-span bridge and the selected bent is far from the abutments, the column is assumed to act as a cantilever in the plane normal to the bridge's longitudinal axis (Figure 4-2(b)).
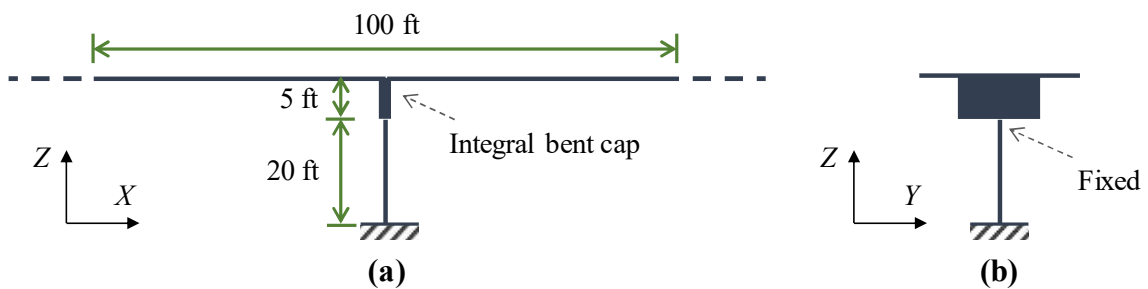
Figure 4-2. Bridge part considered in design: (a) in the longitudinal plane; (b) in the transverse plane

This procedure used here for the design of HSR columns is illustrated in Figure 4-3. According to the flowchart, in the first step of design, the AASHTO LRFD Bridge Design Specifications is used to determine the dimensions of the cross section and the steel reinforcement of the column as a normal posttensioned precast concrete column (with no sliding) under calculated force effects (after they were scaled down into model domain). For the column specimens designed here, the AASHTO Guide Specifications for LRFD Seismic Bridge Design is also used to check the reinforcement limits to ensure the columns have sufficient ductility (e.g. to ensure the sufficiency of concrete confinement and to avoid early rebar buckling near rocking joints). In addition, the Precast Prestressed Bridge Design Manual is used to determine the prestress losses in order to check the concrete stress and posttensioning load limits.

Once the column cross section dimensions and steel reinforcement are chosen, the design variables related to sliding joints are preliminarily selected based on reasonable predictions of the displacement demand of the column (e.g. by elastic analysis) and its estimated lateral load carrying capacity. These design variables include number of sliding joints and their locations, coefficient of friction at sliding joints, diameter and height of duct adaptors, and duct diameter. Using these preliminarily selected details, a 2D finite element model of the column is built in OpenSees per the modeling strategy proposed in Chapter 2 and it is utilized to determine the designed column's displacement demands and maximum lateral load resistance. The displacement demands are obtained via Capacity Spectrum method (Madhusudhanan and Sideris 2018) or multiple time history analyses, while the column's load capacity is predicted using nonlinear pushover analysis. The

displacement demand and lateral load carrying capacity of the column are then used in an iterative process (the loop between steps 3 and 4 in Figure 4-3) to adjust the design variables associated with the sliding joints, until an effective design is achieved.

Step 1: Choose cross section dimensions and design mild steel reinforcement and posttensioning system

- *According to AASHTO LRFD Bridge Design Specifications*
- *Assuming zero sliding*

Step 2: Make preliminary choices for number and location of sliding joints, duct and duct adaptor dimensions, and coefficient of friction at sliding joints

- *Assuming reasonable displacement demand*
- *Using design forces as column load carrying capacity*
- *According to findings of Chapter 3*

Step 3: Estimate displacement demand under design earthquake and calculate lateral load resistance capacity of column

- *By Capacity Spectrum method or time history analyses*

Step 4: Adjust number and location of sliding joints, duct and duct adaptor dimensions, and coefficient of friction at sliding joints

- *According to findings of Chapter 3*

Figure 4-3. General procedure for design of HSR columns

The above process is described with more details, yet briefly, in the following sections. More details regarding the design of the column dimensions and steel reinforcement in the absence of sliding are provided in Appendix A.

4.3.1. Force Effects

The design loads considered for the design of the HSR column specimens are dead load, live load, secondary loads, and earthquake loads. The load combinations used to control the sufficiency of the designed column correspond to the limits states Service I, Strength I, and Extreme Event I (AASHTO 2014).

4.3.1.1. Service Loads

The total dead load supported by the column in model domain is 207 kips. Considering two design lanes on the bridge deck, the maximum vertical live load on the column in model domain is found equal to 92 kips. Additionally, the maximum moment at the column's bottom end due to the live loads on the deck equals 47 kip-ft in model domain.

4.3.1.2. Seismic Loads

The prototype bridge is assumed to be located in a highly seismic region in Los Angeles County, California (Figure 4-4(a)). According to the AASHTO LRFD Bridge Design Specifications and assuming the site class is B, the design response spectrum for this location is determined to be as displayed in Figure 4-4(b) – in this figure, C_{sm} denotes the elastic seismic response coefficient; PGA represents the peak ground acceleration; S_S and S_1 stand for the short-period and long-period response spectral acceleration coefficients, respectively; and F_{pga}, F_a, and F_v are site factors, which equal unity for the site class B. It is noted that the AASHTO LRFD Bridge Design Specifications defines the design earthquake as a seismic hazard with 7% probability of exceedance in 75 years (or a return period of approximately 1000 years). Since $0.5 < S_{D1}$, the bridge lies in Seismic Zone 4

per AASHTO LRFD Bridge Design Specifications, which represents the regions of very high seismicity.
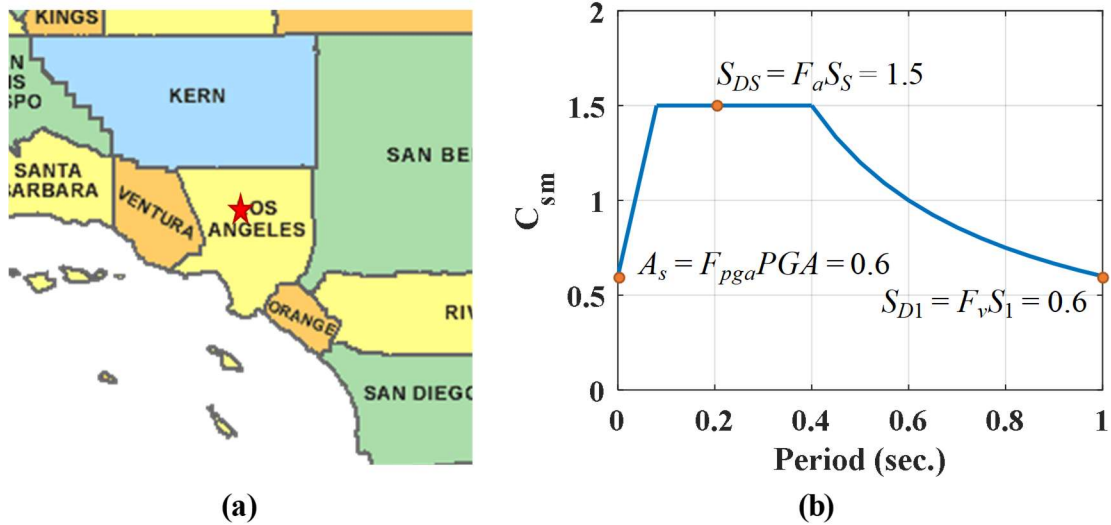
Figure 4-4. (a) Bridge location; (b) design response spectrum in prototype domain

Given the prototype bridge is an essential multi-span bridge located in the Seismic Zone 4, according to the AASHTO LRFD Bridge Design Specifications, the earthquake force effects shall be obtained by time history analysis. However, assuming that the bridge is long enough to allow its design in model domain considering only one span, a single-mode elastic analysis method is deemed adequate. The values of C_{sm} obtained by this approach for the longitudinal and transverse directions are 1.5 and 1.18. In order to intensify the inelastic response of the column specimens tested here, the response modification factor, R, is taken as 8. Accordingly, the modified C_{sm} values are 0.188 and 0.148 for the longitudinal and transverse directions, respectively. The earthquake force

effects obtained using these seismic response coefficients and scaled down to suite the model domain are summarized in Table 4-2.

Table 4-2. Earthquake force effects for column in model domain

Direction	Longitudinal			Transverse		
Force Effect	N (kips)	V (kips)	M (kip-ft)	N (kips)	V (kips)	M (kip-ft)
Value	0	±41	±206	0	±33	±405

4.3.2. Design of Column with Zero Sliding

The cross section of the column specimens is chosen to be hollow and circular. The nominal compressive strength of concrete, f'_c, is chosen to be 5 ksi and the Grade 60 steel (ASTM 2018a) is selected for both longitudinal and transverse reinforcement of the column segments. The prestressing steel is also chosen to be of Grade 270 (ASTM 2018b).

After several iterations and considering all the possible load combinations specified by the AASHTO LRFD Bridge Design Specifications, the cross section with the dimensions and reinforcement details demonstrated in Figure 4-5 was found to provide adequate strength and meet the requirements of both AASHTO LRFD Bridge Design Specifications and AASHTO Guide Specifications for LRFD Seismic Bridge Design. As seen, the column cross section has an inside dimeter of 2 ft and an outside diameter of 3 ft, resulting in an aspect ratio of 4.17 (= H/D, with H = 12.5 ft and D = 3 ft). The clear cover concrete (from concrete surface to the outside of the transverse reinforcement) is taken as 0.75 in. The longitudinal reinforcement consists of 32 #4 bars, leading to a longitudinal steel ratio of 1.1%. The transverse reinforcement comprises two #3 spirals on

the inside and outside surfaces of the hollow column segments with 3-in pitch, providing a volumetric transverse reinforcement ratio of 1.6%. Moreover, the unbonded posttensioning steel consists of eight monostrands of 0.6 in. diameter, which is equivalent to a prestressing steel ratio (A_{ps}/A_g, where A_{ps} and A_g denote the total prestressed steel area and the cross section gross area, respectively) of 0.3%. The posttensioning of each strand after all losses (at the time of testing) is selected to be 18 kips.
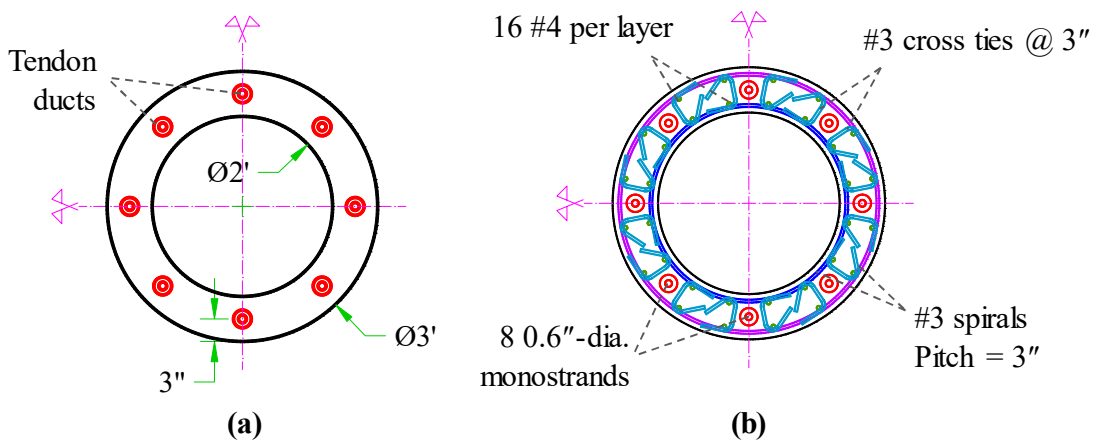
Figure 4-5. Designed cross section for column specimens: (a) dimensions; (b) reinforcement details

Given the initial posttensioning forces, the sum of gravity loads (including 100% dead load and 50% of maximum live load) and posttensioning applied to the column specimens at the time of testing equals 397 kips, being equivalent to 14% of the nominal compressive strength of the cross section (P/f'_cA_g). The axial load vs. moment interaction diagram achieved by simplified calculations for the designed column along with the most critical axial force-bending moment combination is shown in Figure 4-6.
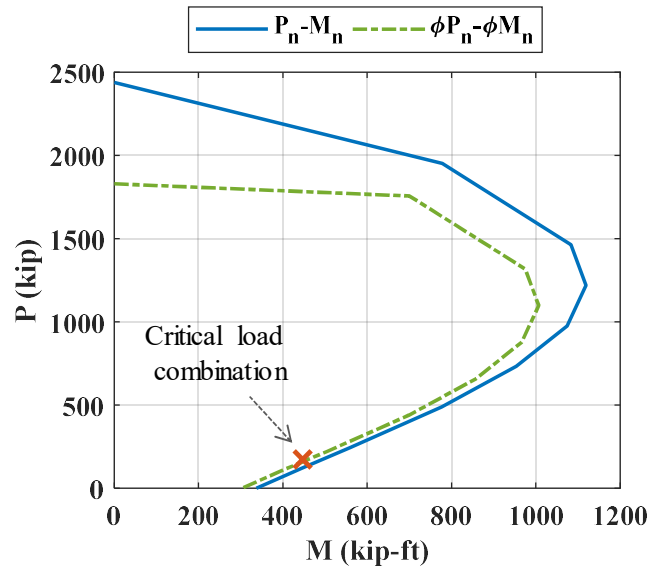
Figure 4-6. Axial load vs. moment interaction diagram for designed column

4.3.3. Design of Sliding Joints

According to the general design procedure of Figure 4-3, after the column with zero sliding is designed, the parameters exclusive to HSR columns need to be specified through an iterative process. These parameters are: (1) coefficient of friction at sliding joints; (2) sliding joint distribution (i.e. number and location); and (3) duct and duct adaptor dimensions. In the following, the way each of these parameters are selected for the column specimens is discussed.

4.3.3.1. Coefficient of Friction

According to the design recommendations made in Section 3.4.2, compressive damage at the rocking joints can be significantly reduced by selecting the incipient sliding base shear, V_{is}, close to the incipient rocking base shear, V_{ir}. Once the column dimensions and steel reinforcement are selected (Step 1 in Figure 4-3), V_{ir} can be estimated with an acceptable

accuracy, either by hand calculations or nonlinear pushover analysis. Having estimated V_{ir}, one may set V_{is} (Eq. (3-1)) equal to V_{ir} and approximate the desirable coefficient of friction at sliding joints, μ_{des}, as:

$$\mu_{des} = \frac{V_{ic}}{N_g + N_{PT0}} \tag{4-1}$$

where N_g and N_{PT0} are the gravity and initial PT loads, respectively. Clearly, the values of coefficient of friction achievable by various materials appropriate for use at sliding joints (e.g. steel and PTFE) are discrete and cannot be arbitrarily chosen. As a result, when μ_{des} is calculated via Eq. (4-1), a material with a close coefficient of friction needs to be selected and the coefficient of friction achievable by that material shall be used during the remainder of the design process.

Herein, in order to determine the incipient rocking base shear, V_{ir}, the column with prevented sliding was modeled using a strategy similar to that proposed for HSR columns (see Chapter 2). According to the pushover analysis of this model, the value of V_{ir} was predicted to be close to 18 kips. As a result, substituting the values of V_{ir} (18 kips), N_g (253 kips), and N_{PT0} (144 kips) in Eq. (4-1) yields $\mu_{des} = 0.045$. Note that N_g was considered as the total dead load plus half the maximum design live load supported by the column. Based on the low value of μ_{des}, a suitable material for the sliding joint interfaces has to be of PTFE basis, as further explained in Section 4.6.1.5.

4.3.3.2. Sliding Joint Distribution

According to the analytical studies discussed in Section 3.4.1, the impact of the distribution of sliding joints on the performance of HSR columns is inconsequential and

one to two sliding joints are sufficient, so long as they are far enough from the rocking joints (i.e. locations of maximum flexure). Accordingly, for the test specimens, the number of sliding joints is set at two and they are decided to be 3 ft (equal to column's outside diameter) apart. Per simplified equations similar to those derived by Sideris et al. (2014d), the minimum distance of the sliding joints from the rocking joints to prevent compressive damage at the sliding joints was found to be less than 18 in. In those equations, the maximum compressive stress allowed at the sliding joints to avoid damage was taken as 2.5 ksi, which is the compressive strength of the glass-filled PTFE material used to fabricate the sliding joints (see Section 4.6.1.5). Despite the calculated minimum distance, however, to ensure no damage will occur to the sliding joints, the distance of the first sliding joint from the bottom rocking joint is chosen as 3 ft. The final joint distribution selected for the HSR column specimens is depicted in Figure 4-7.
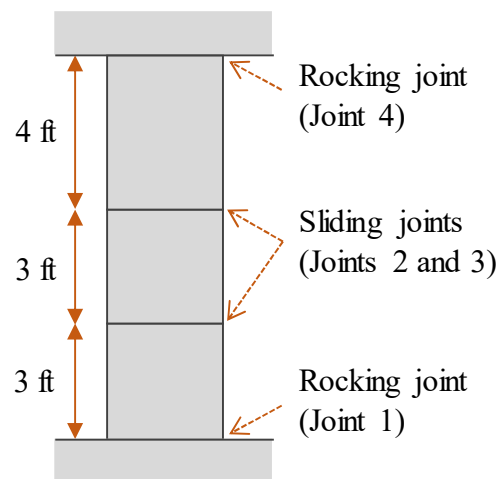
Figure 4-7. Selected joint distribution for column specimens

4.3.3.3. *Duct and Duct Adaptor Dimensions*

First, it must be noted that the ducts and duct adaptors in the column specimens will be made out of PVC pipes. As a result, the selected duct and duct adaptor diameters need to be among the PVC pipe sizes available in the market. According to Section 3.4.5, the duct and duct adaptor dimensions are recommended to be selected such that:

- The total peak achievable sliding capacity, $\Sigma u_{sl,peak}$, of the HSR column is at least 75% the column's displacement demand under design earthquake;

- The total nominal sliding capacity, $\Sigma u_{sl,l}$, is sufficiently larger than $\Sigma u_{sl,peak}$;

- The incipient bearing sliding capacity, $u_{sl,b}$, at each joint is almost half its $u_{sl,peak}$.

Note that, due to gradual changes in the design recommendations with the progress of the project, not all of the above points are met herein. After a number of iterations and by estimating the displacement demand under the design earthquake through the Capacity Spectrum Design method (Madhusudhanan and Sideris 2018), the dimensions of the ducts and duct adaptors are chosen as in Table 4-3. These dimensions lead to total $u_{sl,b}$ and total $u_{sl,l}$ equal to 0.44 in. (= 0.3% drift ratio) and 2.9 in. (= 1.9% drift ratio), respectively.

Table 4-3. Selected duct and duct adaptor dimensions

Component	Diameter (in)	Height (in)	Nominal PVC Pipe Size
Duct	0.82	-	3/4 in.
Duct Adaptor	2.05	4.5	2 in.

4.3.4. Final Design Check

In order to ensure that the above sliding joint design (i.e. coefficient of friction, and duct and duct adaptor dimensions) meets the design objectives and it can eventually avoid the column damage under design earthquake, the column specimen with above design is simulated through the approach proposed in Chapter 2 and is analyzed under both quasi-static monotonic loading and multiple earthquake excitations. In the model, the lengths of the tendons passing through the column footing and superstructure are assumed to be 21 in. and 59 in., respectively (equal to their values in the test setups – see Section 4.5). Moreover, the expected unconfined concrete strength, f'_c, is taken as 1.3 times the design value, i.e. 6.5 ksi, to recognize the typical conservative concrete mixture design and the possible strength gain with age (AASHTO 2011; Caltrans 2013).

4.3.4.1. Pushover Analysis

The pushover base shear vs. lateral displacement response predicted by the model is shown in Figure 4-8(a). In this figure, the points at which rocking starts, cover concrete spalling occurs, and tendon yielding initates are also indicated by different markers. Per Berry and Eberhard (2003), the spalling strain limit for circular cross sections of spiral transverse reinforcement is chosen as 0.008. According to Figure 4-8(a), as desired per the design recommendations of Chapter 3, the incipient sliding and rocking base shear values are acceptably close for the designed HSR column specimen. The column does not exhibit concrete spalling until a lateral displacement of 5.8 in. (drift ratio of 3.9%). The tendons start yielding at a lateral displacement of 8.0 in. (drift ratio of 5.3%), which is slightly before the column's strength deterioration begins (i.e. at a drift ratio of 6%). The maximum

lateral load resistance of the column is predicted to be slightly above 44 kips, which is about 20% larger than the design base shear (see Figure 4-6).

As seen in Figure 4-8(b), the total peak achievable sliding capacity, $\Sigma u_{sl,peak}$, is 2.4 in., which is 17% smaller than the total nominal maximum sliding capacity of the column, $\Sigma u_{sl,l}$, i.e. 2.9 in. Although the duct adaptor diameter could be increased in order to ensure that the tendons are not prone to shearing, it is decided to keep them of 2 in. diameter to experimentally investigate their potential damage.
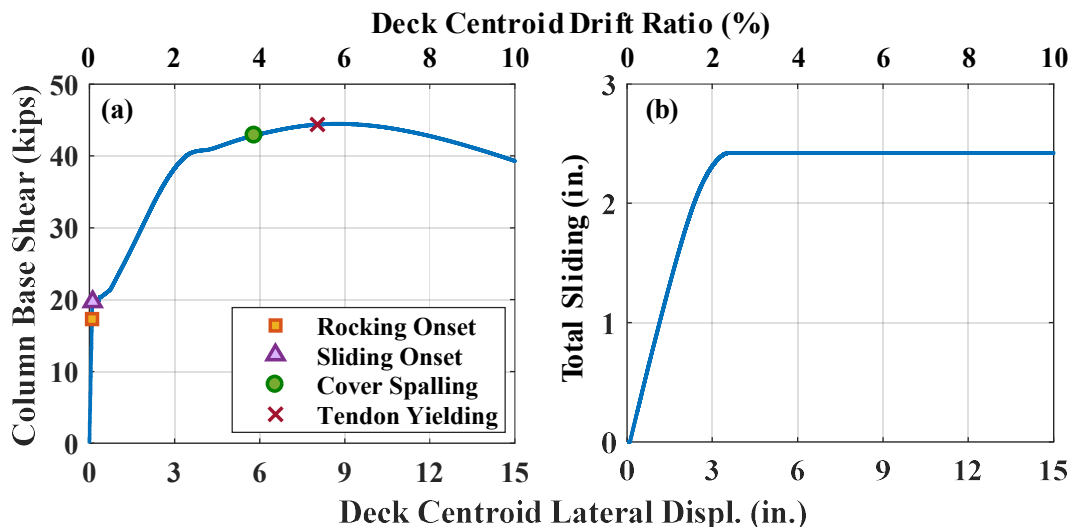
Figure 4-8. Pushover analysis results: (a) column's base shear vs. lateral displacement response; (b) total joint sliding vs. lateral displacement

4.3.4.2. Time History Analyses

Similarly to the pushover analysis, the time history analyses are performed in model domain, where all variables are scaled accordingly (per Table 4-1). The same 10 horizontal earthquake acceleration records selected from the far-field ground motion ensemble of

FEMA P695 (FEMA 2009) listed in Table 3-1 are considered for the time history analyses.

The ground motions are all scaled using the same factor such that the square root of the

sum of the squares of the differences of the median spectral accelerations from the design

spectral accelerations (Figure 4-4(b)) over the period range of $0.5T_1$ to $2T_1$ is minimized –

T_1 is the period of the pier's first mode in transverse direction. By eigenvalue analysis of

the pier model (including the mass and mass moment of inertia of the superstructure's

segment supported by the column), T_1 is found to be close to 0.35 sec. (in the model

domain). Since the time scale factor is 2 (Table 4-1), the median spectral acceleration error

minimization is carried out for a period range of 0.35-1.4 sec. in the prototype domain, as

shown in Figure 4-9. The scale factor obtained throug this approach is 1.5.
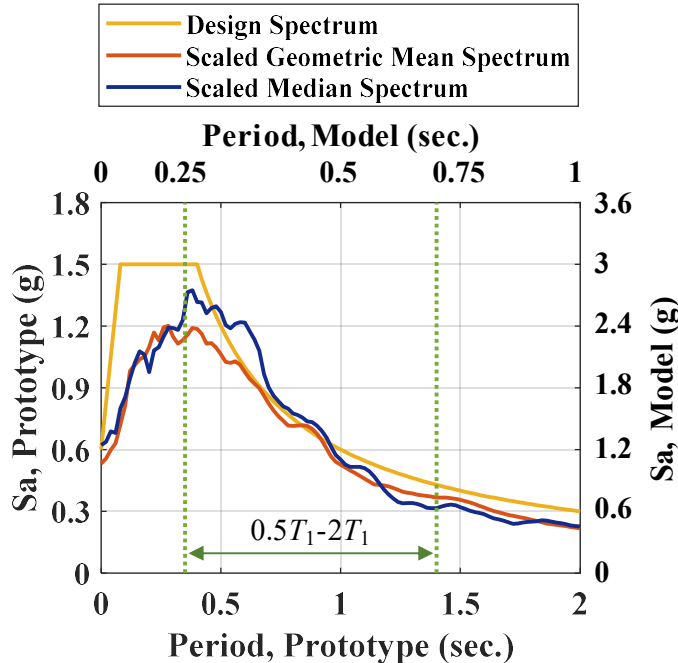
Figure 4-9. Median and geometric mean response acceleration spectra of scaled ground motions vs. design acceleration spectrum

164

The maximum deck centroid displacement demands and total sliding values predicted by the time history analyses of the HSR column specimen are shown in Figure 4-10(a). The mean and median of the peak deck displacement demands are 2.22 in. and 2.09 in., respectively, which are equivalent to drift ratios 1.48% and 1.39%, respectively. As seen in the same figure, the above displacement demands are mostly accommodated by joint sliding. Per Figure 4-10(b), except for one ground motion that causes cover spalling at the bottom rocking joint, no considerable concrete damage is predicted in the column. The peak tendon strains also remain well below the tendons' yield strain, i.e. ~0.085. The above results illustrate the effectiveness of the HSR column specimen's design.

4.4. Preliminary Design of Test Setups

As pointed out earlier, the four column specimens are to be tested under four different loading/boundary conditions, which are summarized in Table 4-4. In order to produce the loads in different directions (longitudinal and transverse) simultaneously and to restrain the rotation of the column's top end in Phase III, three test setups with different configurations of hydraulic actuators and control algorithms are designed. However, because all specimens are identical and use the same loading beam and foundation block, the loading beam, i.e. the beam through which the loads are transferred to the column's top end, and the foundation block, which supports the column and the vertical actuators and anchors the PT tendons, require to be designed such that they can accomodate all actuator configurations and remain undamaged under the applied loads.
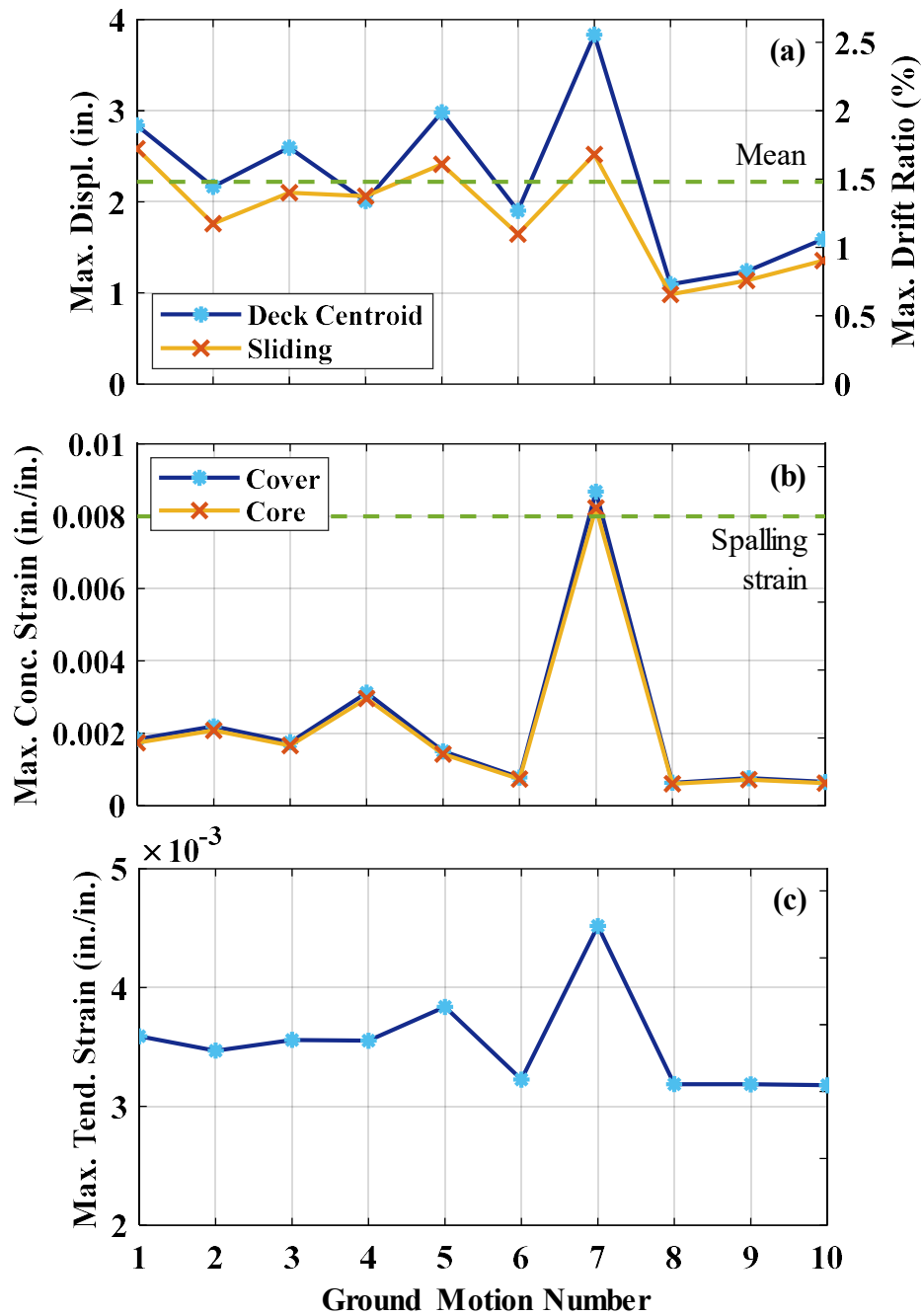
Figure 4-10. Time history analysis results: (a) maximum deck displacement and total sliding; (b) peak concrete strain; (c) peak tendon strain

Table 4-4. Phases of testing

Phase	I	II	III	IV
Loading	Uniaxial lateral	Torsional + uniaxial lateral	Uniaxial lateral	Biaxial lateral
Top End Rotation	Free	Free	Fixed	Free

The restrictions that need to be accounted for while designing the setups are: (*i*) dimensions of the column specimens, (*ii*) accessibility considerations (e.g. possibility of access to the tendon anchors under the foundation block and connecting the hydraulic actuators to the loading beam and the foundation block), (*iii*) the actuators' dimensions, and (*iv*) the hole grids on the reaction wall and the strong floor. The information of the hydraulic actuators employed for the tests is provided in Table 4-5. The hole grids on the reaction wall and the strong floor of the Structural and Materials Testing Laboratory at the Center for Infrastructure Renewal (CIR) are shown in Figure 4-11.

Table 4-5. Information of hydraulic actuators

Actuators	Application	Minimum Length	Dynamic Stroke	Tension Capacity	Compression Capacity
MTS 244.51S	Horizontal loading	144.5 in.	30 in.	220 kip	220 kip
MTS 201.90G2	Vertical loading	132.5 in.	20 in.	400 kip	590 kip
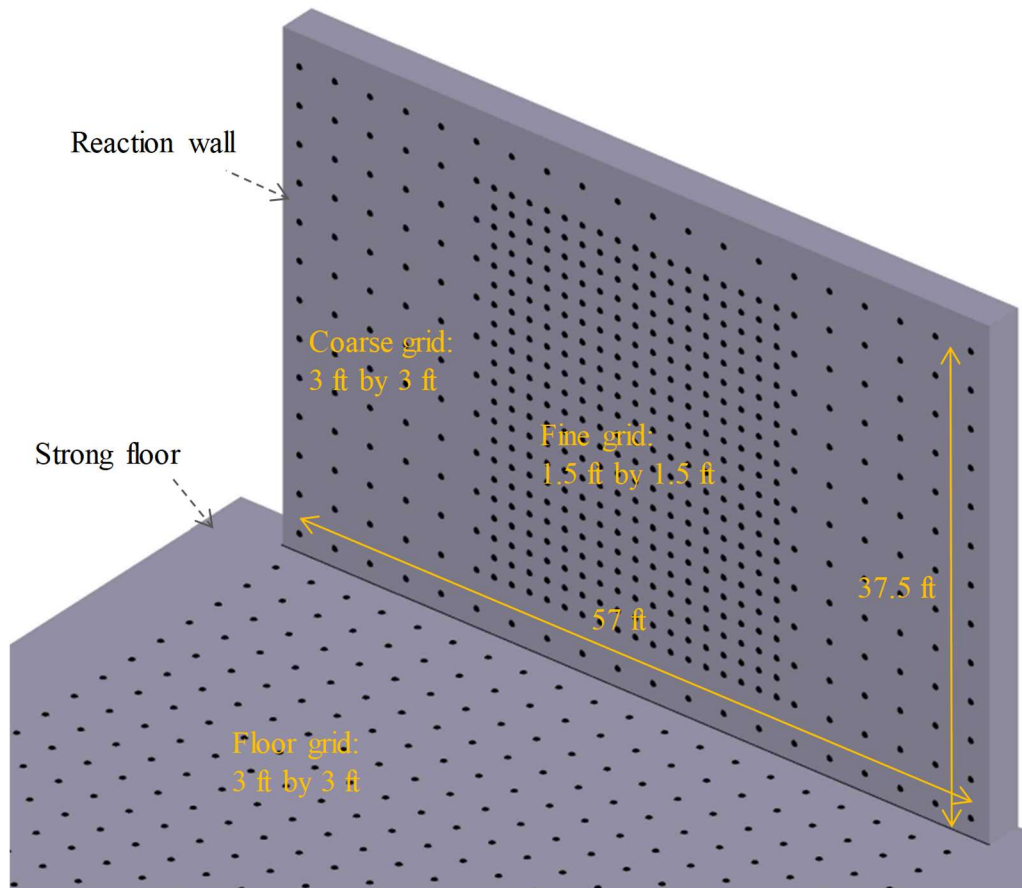
Figure 4-11. Hole grids on reaction wall and strong floor

Given the foregoing, three test setups are designed, one for Phases I and II (Setup A, Figure 4-12), one for Phase III (Setup B, Figure 4-13), and one for Phase IV (Setup C, Figure 4-14). In Phase I (Setup A), two 220-kip actuators and two 590-kip actuators are utilized to apply identical horizontal displacements and identical vertical loads, respectively. In Phase II (Setup A), the two 590-kip actuators maintain identical loads, while the 220-kip actuators apply different displacements producing desired lateral displacement and torsional roation (twist). In Phase III (Setup B), the horizontal load is applied via a single 220-kip actuator, whereas the 590-kip actuators apply the vertical

168

loads such that their displacements are identical (to ensure zero rotation at the top end) and the total vertical load remains equal to the target value. Finally, the horizontal loads in Setup C are applied by the two 220-kip actuators, which are initially perpendicular to each other, and identical vertical loads are applied by the two 590-kip actuators. Further information about the test setups and the actuators' control systems used in each of them is found in the separate sections dedicated to each Phase.
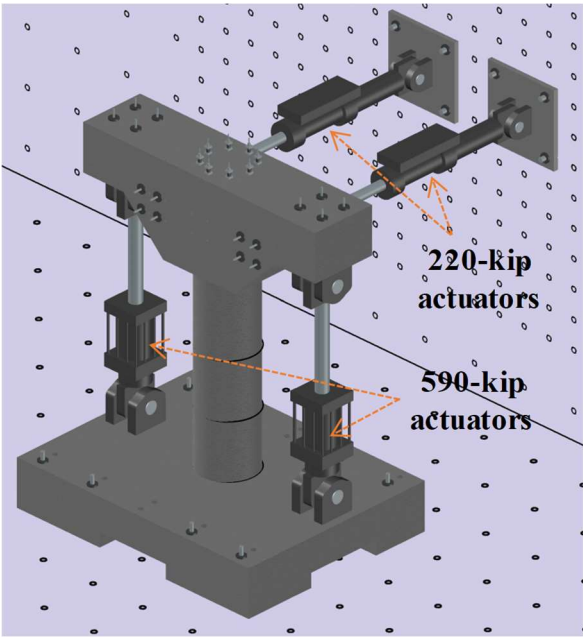
Figure 4-12. Setup A
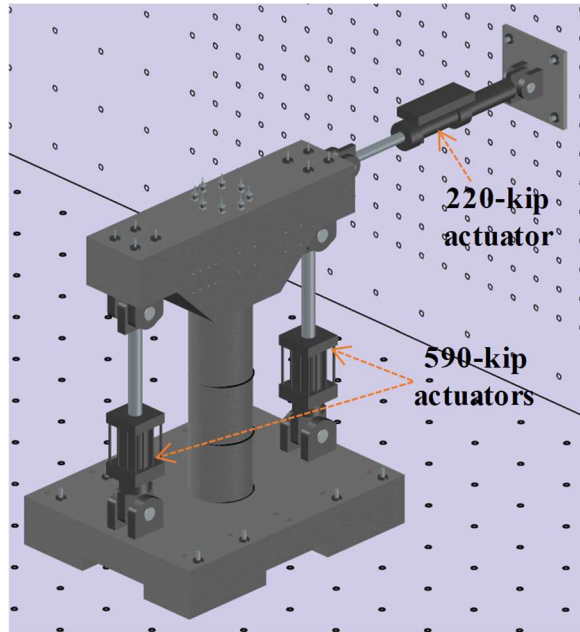
Figure 4-13. Setup B
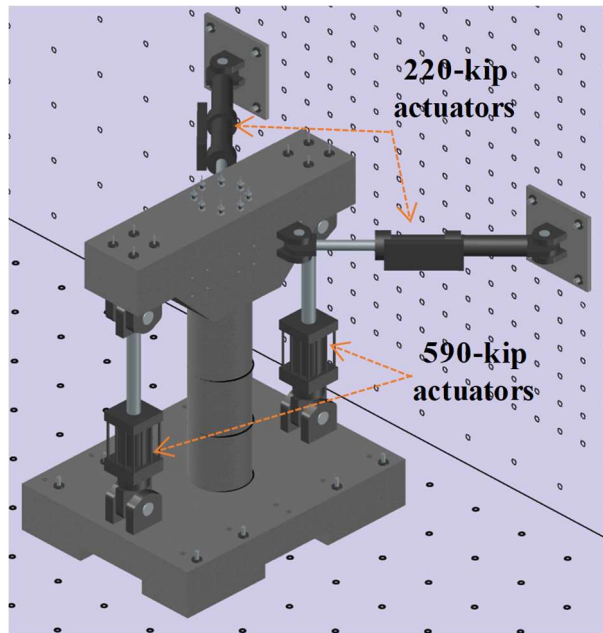
Figure 4-14. Setup C

4.5. Design of Loading Beam and Foundation Block

In order to avoid any damage in them, the loading beam and the foundation block were designed for the most adverse loading scenarios imposed to those during all the planned tests, doubled in magnitudes. Using capacity design, the expected moment capacity of the column specimens was calculated (using expected material strengths) and was used to compute the maximum shear and the maximum loads applied by the actuators to the loading beam and the foundation in different configurations. Both the loading beam and the foundation block were designed using concrete with nominal strength of 5 ksi and reinforcing steel of Grade 60 (ASTM 2018a).

The foundation block was designed such that it has enough clear space underneath to allow access to the bottom end of the threaded rods connecting the vertical actuators to the foundation and the tendon anchors. The minimum and maximum depths of foundation are 1'-9" and 2'-6", respectively, while it is 14' long and 10'-10" wide (Figure 4-15). For simplicity, the foundation block was designed as a two-way slab. The reinforcement details of the foundation are found in Appendix B.

Given the lengths of the vertical actuators and to allow the application of horizontal loads at a height matching the centroid of superstructure in the prototype domain, i.e. 2.5 ft above the column top in model domain, the depth of the loading beam in the middle had to be relatively large (4 ft-11 in.) compared to the beam's length (14 ft) – Figure 4-16. Because of this and the fact that several forces will be applied to it at various locations and in different directions (i.e. the horizontal and vertical forces of the actuators, the axial force and moment of column specimens, and the tendon reactions), the loading beam was

designed by the strut-and-tie method. The reinforcement details of the loading beam are found in Appendix B.
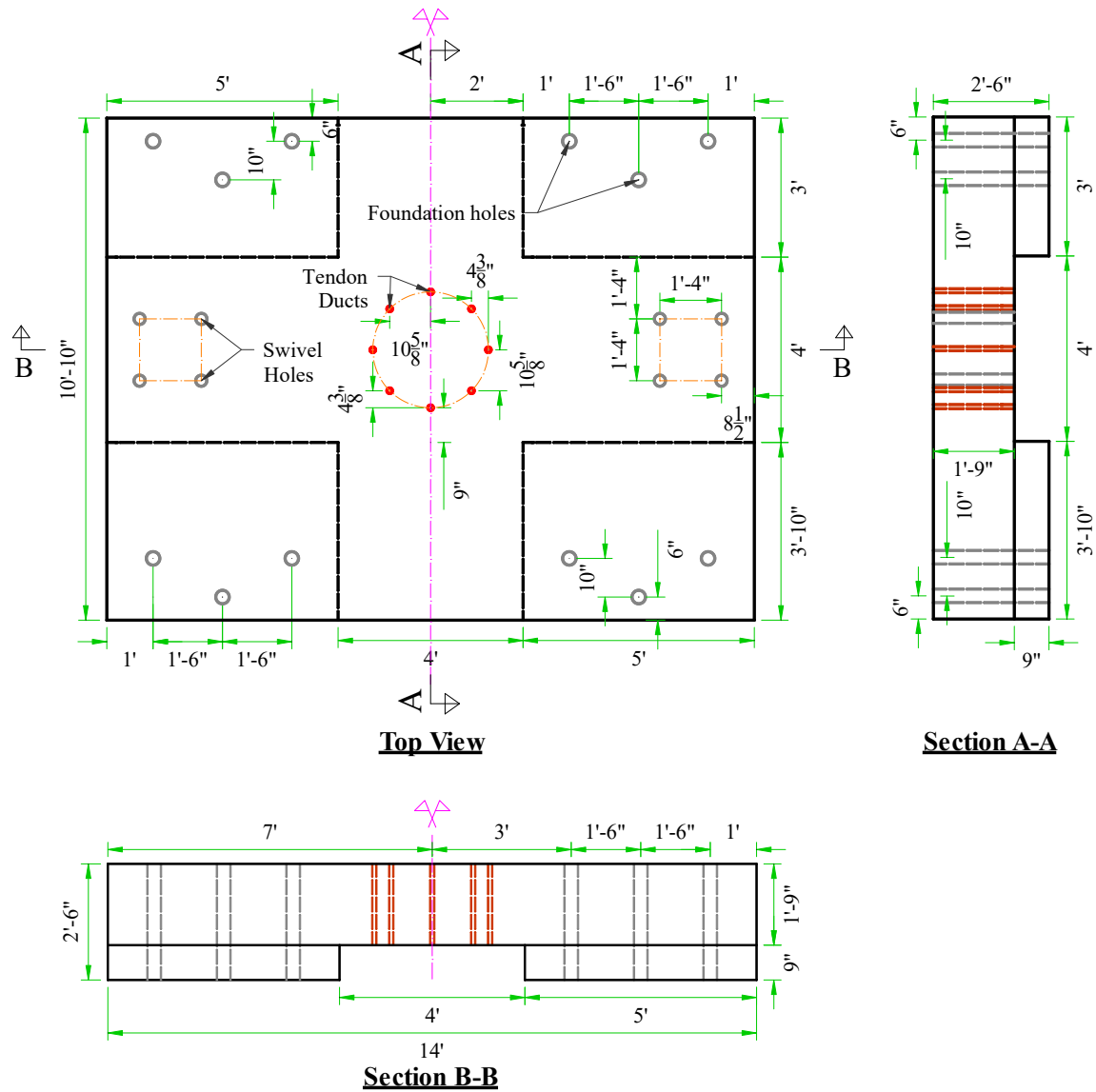
Figure 4-15. Dimensions of foundation block
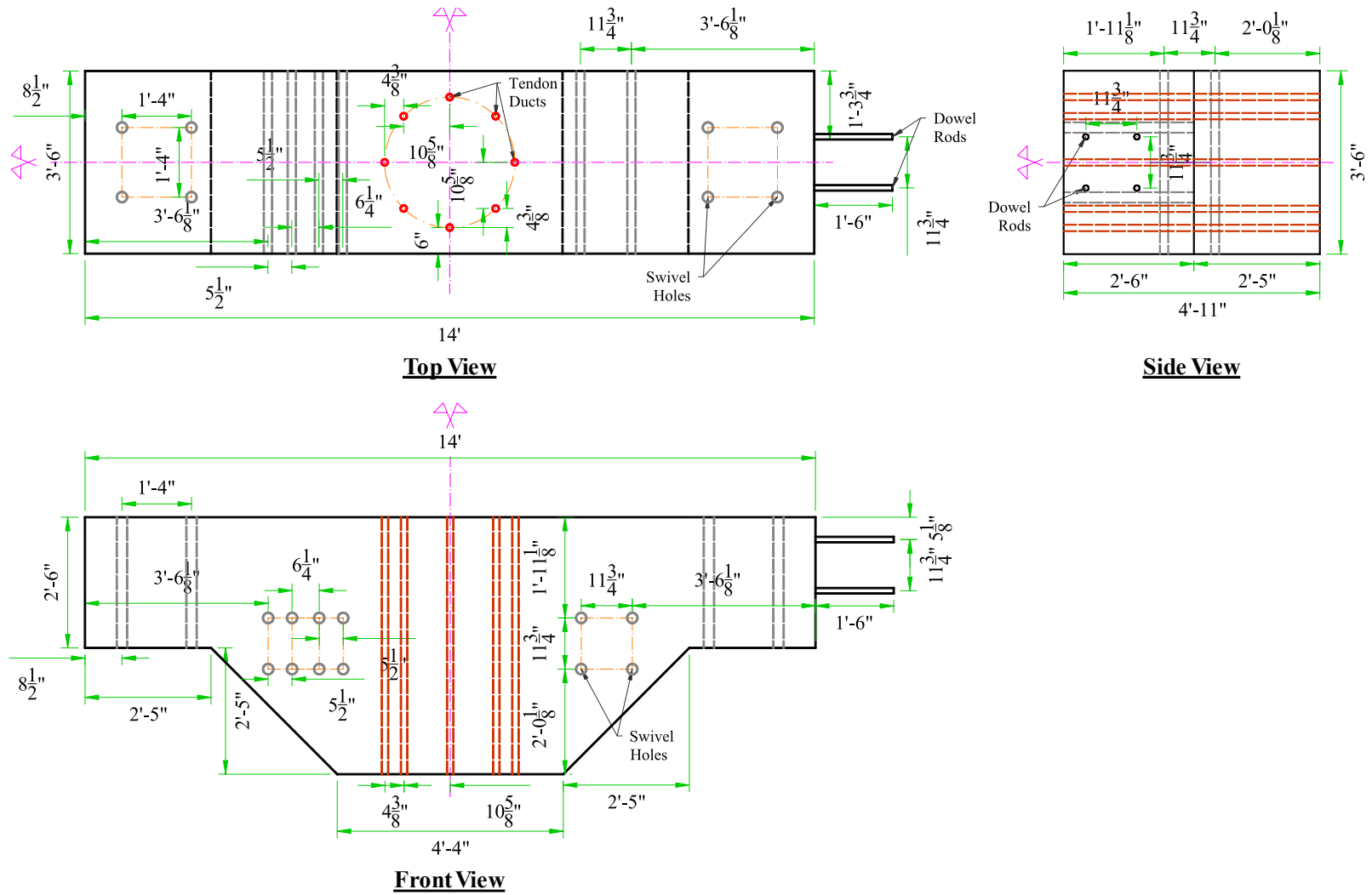
Figure 4-16. Dimensions of loading beam

173

4.6. Fabrication of Specimens

All the test specimens were built in the Structural and Materials Testing Laboratory at the CIR. The fabrication process for each of the components is briefly described in the following sections.

4.6.1. Column Segments

4.6.1.1. Steel Reinforcement Cage

The steel cages were built using a frame made out of wood to ensure the longitudinal bars are in their correct locations. The frame consisted of two plywood sheets with hole patterns matching the rebar arrangement and four vertical boards connecting them. Figure 4-17 shows the process of making the steel cage of a column segment.

Figure 4-17. Building reinforcement cages for column segments

4.6.1.2. Ducts and Duct Adaptors

Schedule 40 PVC pipes were used to make the tendon ducts and duct adaptors. The nominal sizes of the pipes used for the ducts and duct adaptors were 3/4 in. and 2 in.,

respectively. The average inside diameters for the 3/4-in. and 2-in. PVC pipes are 0.82 in. and 2.05 in., respectively. The duct adaptors were connected to the ducts via PVC reducer couplings and PVC cement (Figure 4-18).
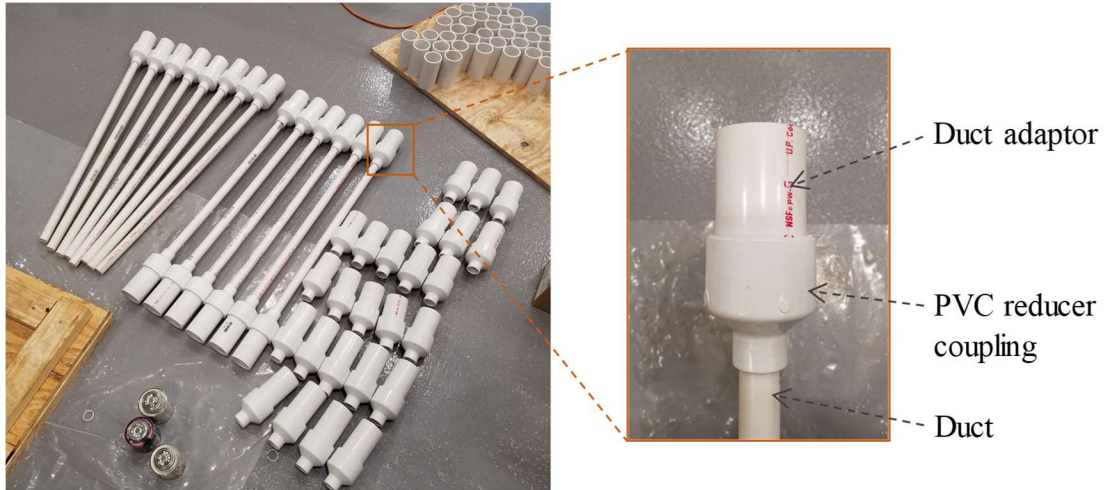
Figure 4-18. Ducts and duct adaptors made of PVC pipes and fittings

4.6.1.3. *Formwork*

Although using steel forms for casting the column segments would be more convenient, due to cost considerations, special cardboard tubes and wood were used to make the forms. That is, the form for each column segment needed to be built using two concentric tubes with different diameters, supported by a group of plywoods underlying those and a number of boards outside them.

In order to ensure the roundedness of the cross sections and the concentricity of the two tubes at the bottom end, and to hold the ducts in their right locations at the bottom end, the supporting plate of each form was built via three layers of plywood (Figure 4-19).

A ring was cut out of the topmost layer such that it supports the walls of the two form tubes inside it. Also, eight holes were drilled in the middle layer to hold the ducts in their right locations. The bottommost layer was used to seal the holes.

Figure 4-19. Column segment formwork: bottom plate

After the bottom plate was ready, the inner tube was connected to it using two pieces of board extending up to the top of the tube. To reduce the probability of its implosion due to concrete pressure, the inner tube was also braced inside at two heights (Figure 4-20(a)). A circular cap cut out of plywood was then pushed into the inner tube from the top to maintain its roundedness at the top end (Figure 4-20(b)). The steel cage and the ducts were subsequently placed in their positions (Figure 4-20(c) and (d)). The ducts were then tied to the steel cage by wire to hold them in their right locations (Figure 4-20(d)). Finally, the outer tube was placed and a supporting wooden frame was built outside it (Figure 4-20(e)).
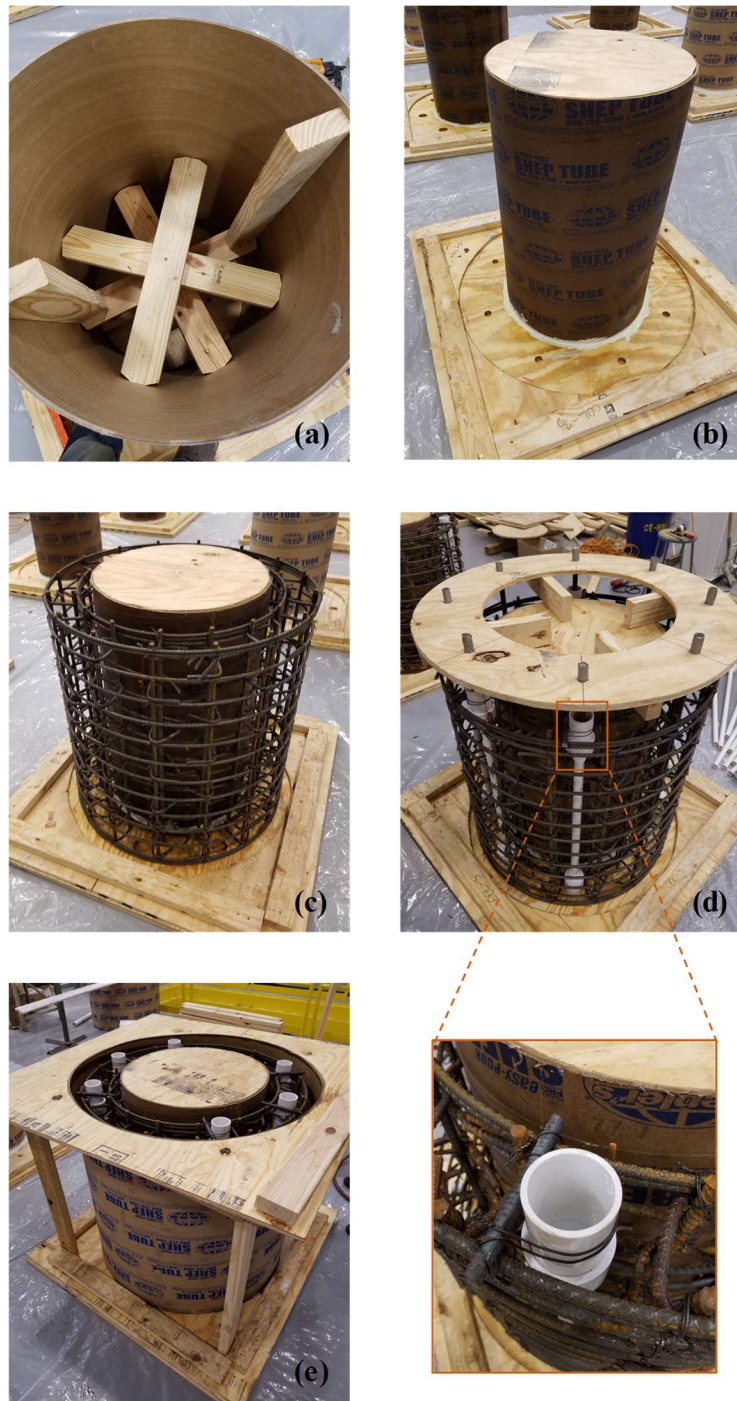
Figure 4-20. Column segment formwork: (a) internal braces; (b) placing inner tube and its cap; (c) placing steel cage; (d) placing ducts and their connection to steel cage; (e) placing outer tube and connection of support frame

In order to be able to lift the column segments by crane, two lifting sockets were embedded at each of the two opposite sides of each column segment, in which hoist rings could be screwed. Each lifting socket was fabricated by welding a bolt to a coupling nut (Figure 4-21). Before the concrete casting was completed, the sockets were temporarily connected to the outside form tubes using other bolts. The thread size of the coupling nuts used here was 1"-8.
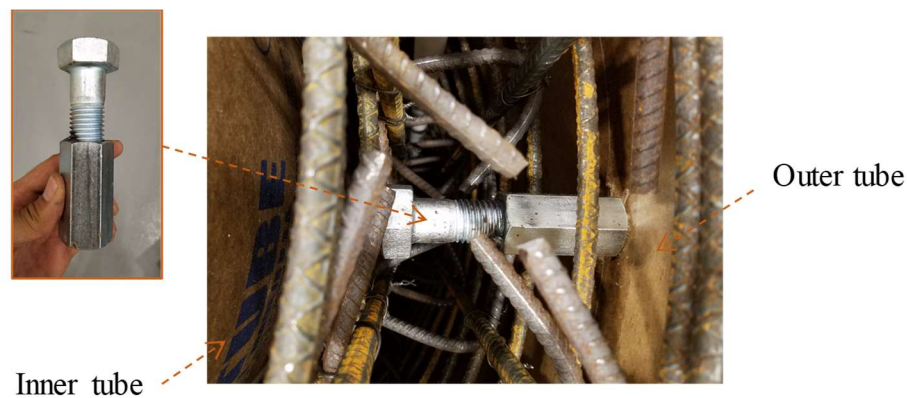
Figure 4-21. Column segment formwork: connection of lifting sockets

It is worth mentioning that the exterior form tubes used to cast the column specimens tested in Phases I and III had an inside diameter of almost 37 in. rather than 36 in. for the remaining two column specimens. The outside diameters of the interior form tubes used to cast all column segments were close to 22.5 in. instead of 24 in. considered in the design. These discrepancies from the original design resulted from discrepancies between ordered and actually received formwork tubes.

4.6.1.4. Concrete Casting

Concrete was mixed and delivered via two trucks by a local company (Figure 4-22(a)). The concrete mixture was designed by the company itself and was requested to have a nominal strength of 4.5 ksi so that its actual strength does not exceed 6 ksi. In addition, due to the small cover considered for the column segments and to ensure sufficient compaction of the concrete, the maximum aggregate size was chosen to be 3/8 in. and a superplasticizer was used in the concrete mixture. The column specimens tested in Phases II and III were cast using the first concrete batch and the other two column specimens were cast using the second concrete batch.

A few photos from the concrete casting process are provided in Figure 4-22. The forms were removed after 72 hours, but the curing was continued for another week by keeping the segments moist. Among the 12 cast segments, two segments were found of large voids in their bottom parts, which had been caused by inadequate compaction (as a result of unexpectedly low workability of the provided fresh concrete). These segments were the bottom and the top segments of the column specimen tested in Phase II and were repaired using non-shrink 8-ksi grout two days after the forms were removed. The repair process is described in Appendix C.

The concrete compressive strengths obtained for the column specimens after 28 days from casting and on the days of testing are listed in Table 4-6. These values were obtained by testing 4"-by-8" cylinders per ASTM C39/C39M (ASTM 2018c). Note that the concrete cylinders were kept in a curing room with 100% humidity before they were tested.

179

Figure 4-22. Casting of column segments: (a) ready mixed concrete delivery by truck; (b) pouring concrete in forms; (c) compaction by vibrator; (d) surface finishing; (e) covering forms for curing

Table 4-6. Concrete compressive strengths

Column Specimen ID			1	2	3	4
Testing Phase			III	II	IV	I
Concrete Batch			A	A	B	B
Compressive Strength (ksi)	After 28 Days	Sample 1	5.67	5.67	4.99	4.99
		Sample 2	5.80	5.80	5.44	5.44
		Sample 3	5.91	5.91	5.45	5.45
		Sample 4	5.79	5.79	5.21	5.21
		Average	5.79	5.79	5.27	5.27
	Day of Testing	Sample 1	7.07	7.78	7.57	7.18
		Sample 2	7.82	7.15	7.53	7.08
		Sample 3	7.55	7.98	7.55	7.38
		Average	7.48	7.64	7.55	7.21

4.6.1.5. Sliding Joints

According to Section 4.3.3.1, the sliding joints were required to have a coefficient of friction as low as 0.05. In order to achieve such a low coefficient of friction, the sliding joint interfaces were made of a polytetrafluoroethylene (PTFE)-based material. While virgin (unfilled) PTFE could provide lower coefficients of friction at low pressures and high sliding velocities (Mokha et al. 1988; 1990), it suffers from large deformations under large pressures, leading to the so-called plowing phenomenon (Figure 4-23), and has limited wear resistance (Khoddamzadeh et al. 2009; Golchin et al. 2012). Even though the plowing issues can be partly avoided by selecting a material other than PTFE for the opposite sliding surface, e.g. mirror-finished stainless steel (Mokha et al. 1988; Hwang et al. 1990; Mokha et al. 1990; Bondonet and Filiatrault 1997), its low wear resistance has led to the introduction of additives to PTFE, such as glass fibers (Golchin et al. 2012; Ala et al. 2016). In addition to increasing the wear resistance of sliding bearing pads, glass-

filled PTFE has a higher modulus of elasticity compared to unfilled PTFE and allows using the same material for both sliding surfaces.
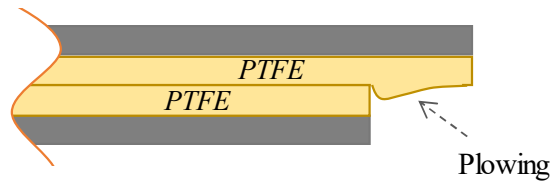
Figure 4-23. Plowing of unfilled PTFE under high pressure

Given the foregoing, the material selected for the fabrication of sliding joint interfaces was 25% glass-filled PTFE. The information of the glass-filled PTFE provided by the manufacturer is found in Appendix D. Per the product manufacturer, the compressive strength of this material is up to 2.5 ksi, thereby making it suitable for the application in HSR columns. With this material, there was no need to use a different material (e.g. steel) for the opposite sliding surface. The only problem with this material was that, in the unlubricated (dry) condition and under the initial pressure present at the sliding joints here (~700 psi), it could only provide a coefficient of friction as low as 0.11 (Reddy Goli 2019). As a result, in order to reduce its coefficient of friction, during the assembly of the column specimens, the installed PTFE pads had to be covered by some type of grease. The grease used here was a multipurpose PTFE-based grease, whose information is found in Appendix D.

An important quality requisite for the sliding joints was surface evenness, because an uneven surface could lead to stress concentrations, unexpected sliding twist, and the deviation of column segments from their desired vertical orientation. However, since the

182

column segment surfaces were finished manually in the laboratory, they were not perfectly even and needed to be ground. In order to further improve the contact between the sliding surfaces at the sliding joints, the glass-filled PTFE pads were decided to be first bonded to thin structural carbon steel substrates. The steel substrates were then bonded to the appropriate end surfaces of the column segments. This approach would also reinforce the concrete adjacent to the sliding joints against compressive damage.

The glass-filled PTFE material used here was supplied in the form of 2 ft by 4 ft 1/8-in. thick sheets. Thus, two halves of the circular pads required to cover each sliding joint surface were cut out of each sheet (Figure 4-24). Cutting the sheets into full circular pads would result in excessive waste. In addition, the 1/8-in. thick carbon steel plates conformed with ASTM A36/A36M specifications (ASTM 2014) and were cut by plasma at a local steel shop. The holes on the steel plates were slightly oversized (diameter = 2.875 in.) to provide some tolerance for the accidental duct movements during the casting of the column segments.
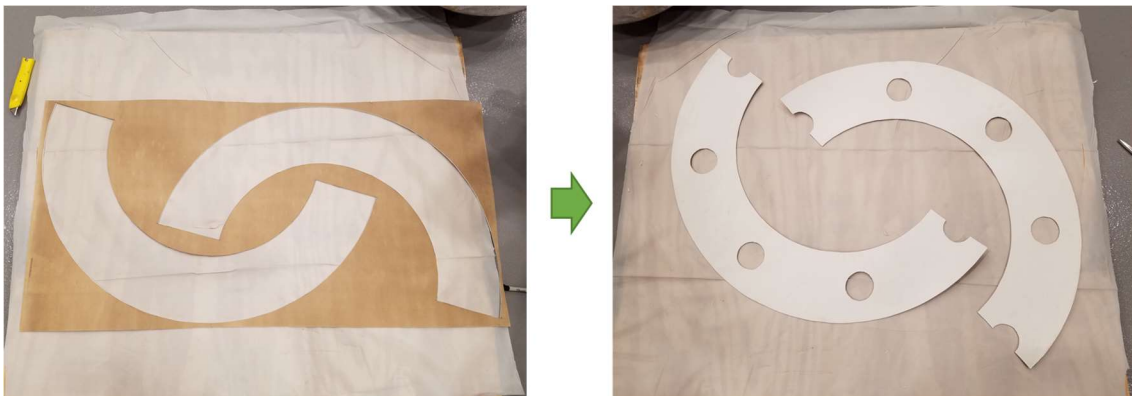
Figure 4-24. Cutting glass-filled PTFE pads

The epoxy used for bonding all the layers was the same and had a high resistance against compression, shear, and peeling. This epoxy was selected after its quality was validated through testing of smaller material specimens (Reddy Goli 2019). Further information about the employed epoxy is found in Appendix D.

(1) Sanding and degreasing of steel
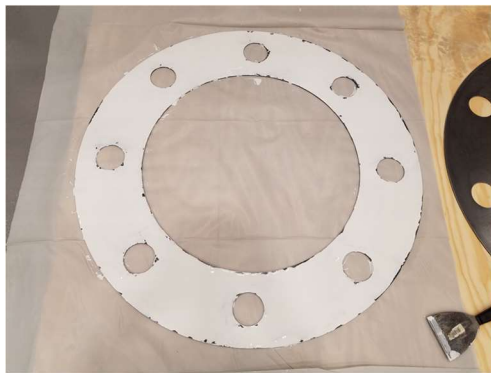
(2) Application of epoxy on steel plate

(3) Positioning pre-cleaned PTFE and pressing using weights

Figure 4-25. Bonding PTFE pad on steel plate

The process of bonding the sliding interface materials to each other and then on the column segments is displayed in Figure 4-25 and Figure 4-26, respectively. Before the epoxy application, all the surfaces were fully cleaned from dust and grease, using acetone.

It is noted that, given the low surface energy of PTFE-based materials, one side of the glass-filled PTFE sheets was chemically etched (by the manufacturer) to enhance their bonding to other materials. After each PTFE pad was bonded on a steel plate, they were not disturbed for a minimum of 12 hours, before they could be attached to the column segments. Steel weights were used to impose pressure on different layers during bonding.

(1) Grinding and removing dust by compressed air

(2) Application of epoxy on concrete surface

(3) Positioning pre-cleaned PTFE and pressing using weights

(4) Polishing final PTFE surface

Figure 4-26. Bonding PTFE-steel bundle on concrete

4.6.2. Loading Beam

The steel reinforcement cage for the loading beam was assembled on a frame, as shown in Figure 4-27(a). The final built cage is shown in Figure 4-27(b). The wooden formwork was fully built before the cage was inserted in it (Figure 4-28). A circular piece of plywood with a diameter of 37.5 in. and a thickness of 0.25 in. was attached inside the formwork to create an indentation at the contact location of the column specimens. This indentation acts as a shear key to prevent excessive sliding between the column specimens and the loading beam. All the holes necessary to connect the actuators to the loading beam and passing the tendons through it were created by PVC pipes of appropriate sizes.

In order to be able to connect the horizontal actuator to the loading beam in Setup B, four dowel rods with a thread size of 1.25"-7 were inserted in the loading beam (Figure 4-28 and Figure 4-29). These rods were anchored inside the concrete using two sets of nuts and washers along their 20 in. of embedded length.

Figure 4-27. Steel cage for loading beam: (a) assembly; (b) completed cage

The concrete used to cast the loading beam was mixed at a local company and was delivered by one truck (Figure 4-30). The nominal compressive strength of the concrete was 8 ksi (larger than the 5-ksi strength considered in its design). The formwork was removed after more than a week from concrete pouring, while the concrete surface was maintained wet during this period. The photo in Figure 4-31 shows the cast loading beam after the form removal.

Figure 4-28. Formwork of loading beam before concrete casting
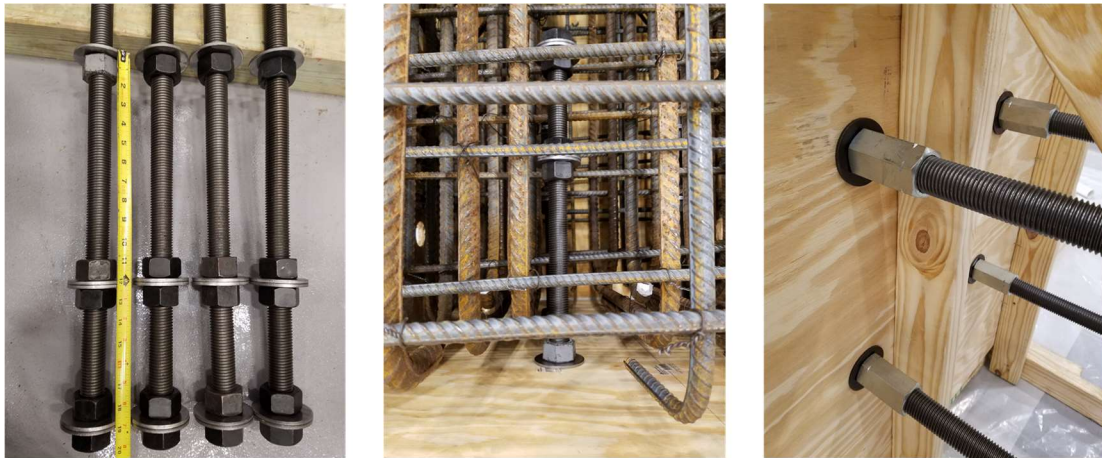
Figure 4-29. Dowel rods in loading beam formwork for connection of horizontal actuator in Setup B

Figure 4-30. Concrete casting of loading beam

Figure 4-31. Loading beam after form removal

4.6.3. Foundation Block

Similar to the loading beam, the reinforcement cage for the foundation block was assembled on a frame (Figure 4-32). After placing the reinforcement cage inside the

189

wooden formwork made for casting the foundation block, PVC pipes and four U-shaped #8 bars were inserted in the cage to to create the necessary connection holes and to allow lifting, respectively (Figure 4-33). Moreover, a ring-shaped 0.5-in. thick plywood with outside and inside diameters of 37.5 in. and 22 in., respectively, was connected to the top of the formwork to create an indentation on the foundation surface, where the column specimens will sit (Figure 4-33). This ring would hold the foundation tendon ducts in their proper locations, while the indentation would serve as a shear key.
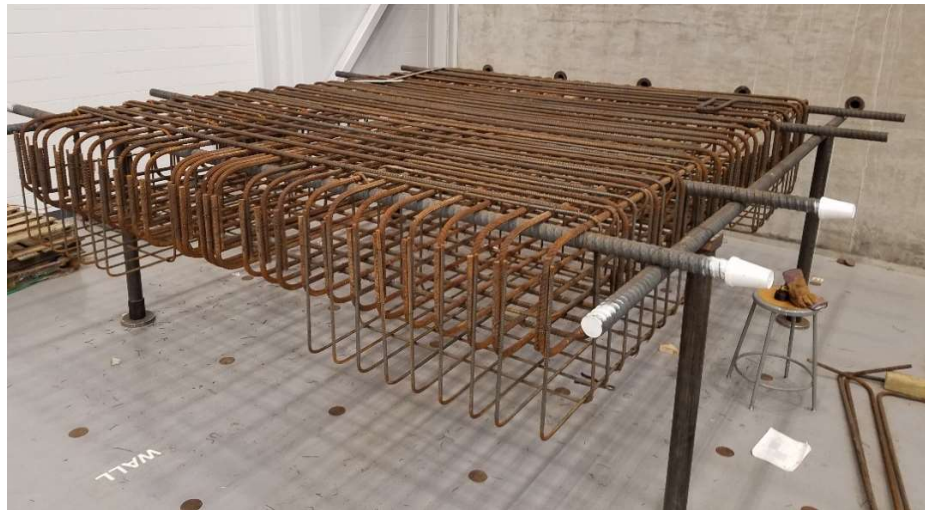
Figure 4-32. Assembly of steel cage for foundation block

The concrete used to cast the foundation was also mixed at a local company and was delivered by two trucks (Figure 4-34). The nominal 28-day compressive strength of the concrete was 8 ksi (larger than the 5-ksi strength considered in its design). The form was removed after a week of curing. The foundation block after the form was removed is shown in Figure 4-35.

190

Plywood for indentation

PVC pipes

Lifting hoop

Figure 4-33. Formwork of foundation block before concrete casting

Figure 4-34. Concrete casting of foundation block
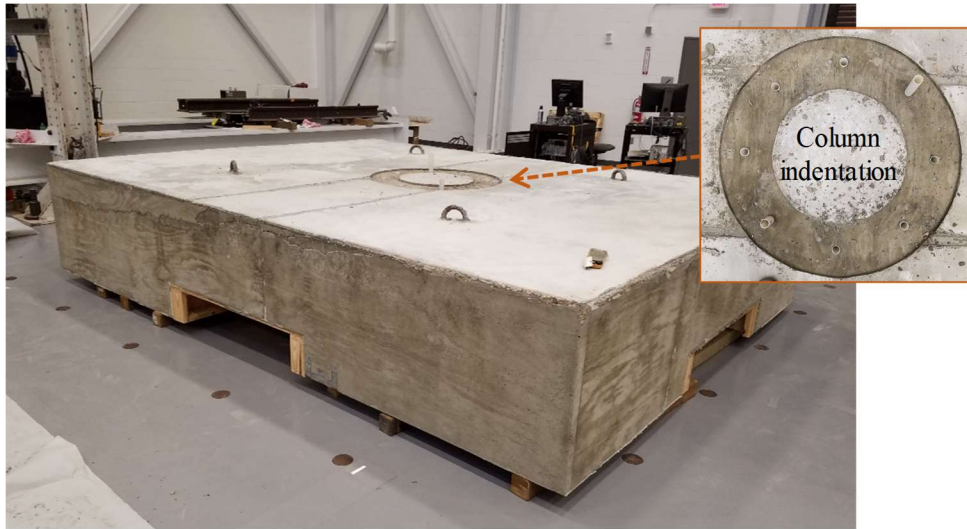
Figure 4-35. Foundation block after form removal

4.7. Testing

As mentioned before, the testing program comprises four Phases, each aiming to investigate the effects of certain loading/boundary conditions on the response of HSR columns. In each Phase, one of the four constructed column specimens is tested under a large number of static and dynamic loading protocols. In selected tests in Phases I to III, the effect of variable vertical loading is also examined. The detailed information and the results of all Phases are presented in the following sections.

4.7.1. Phase I: Cantilever Column under Uniaxial Lateral Loading

4.7.1.1. Test Setup

The test setup designed for Phase I is Setup A (Figure 4-12), where two vertical 590-kip actuators are used to apply the vertical load and two horizontal 220-kip actuators are used to apply the same horizontal displacement. The plan view, front view, and side view of this setup are provided in Figure 4-36, Figure 4-37, and Figure 4-38, respectively. The

center-to-center distance between the horizontal actuators was 6 ft (Figure 4-36), while the center-to-center distance between the vertical actuators was 11 ft-3 in. The clear distance between the loading beam and the reaction wall was chosen as 13 ft-5 in., so that the horizontal actuators could apply close to 15 in. of lateral displacement (10% drift ratio) in both the positive and negative directions. The height of the lateral load application point from the foundation surface (bottom end of the column specimen) was 12 ft-6 in., which coincides with the centroid of the superstructure in the model domain – recall that this height in the prototype bridge was 25 ft.
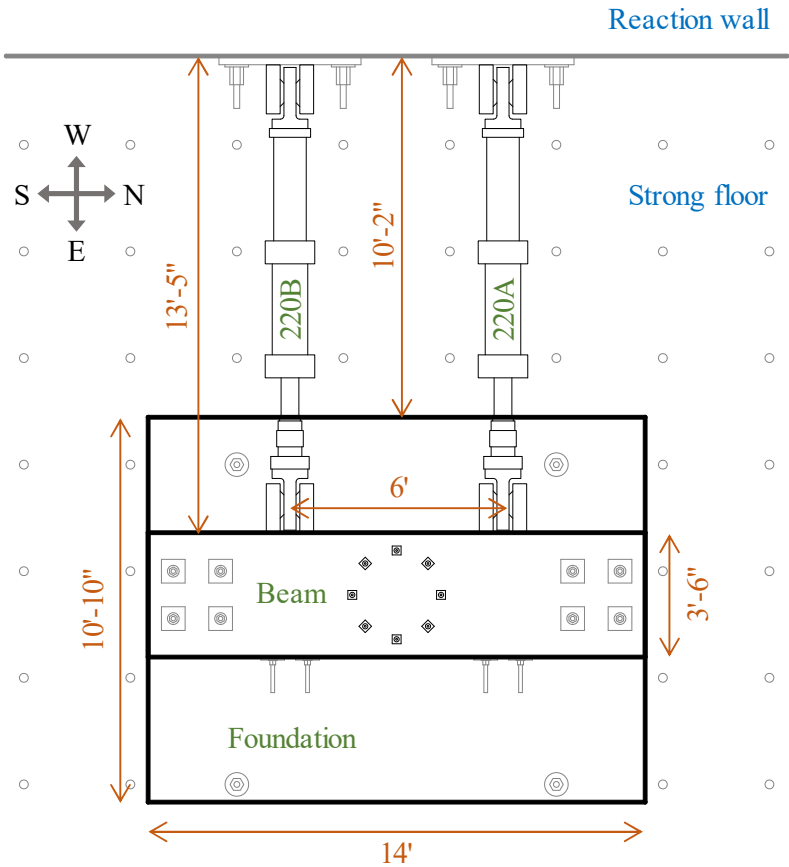
Figure 4-36. Setup A: plan view
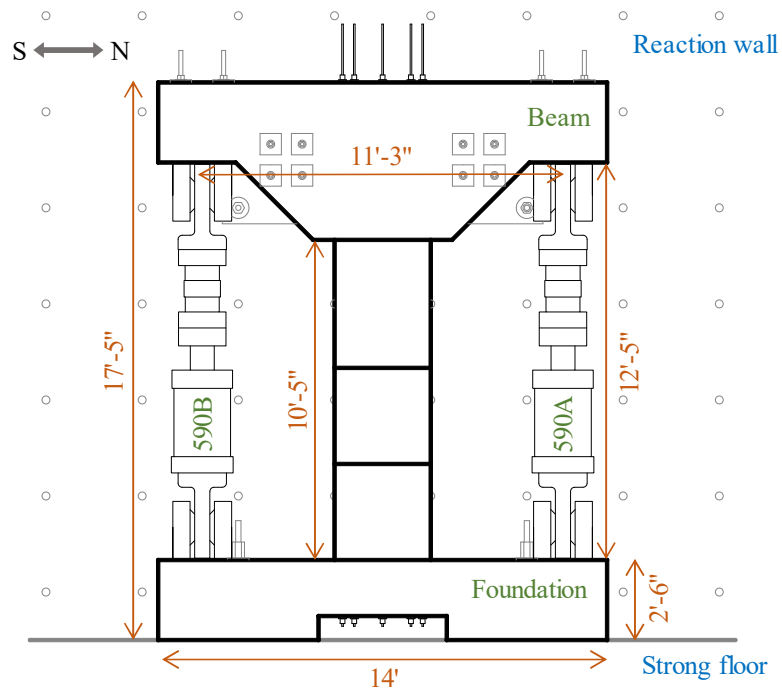
Figure 4-37. Setup A: front view
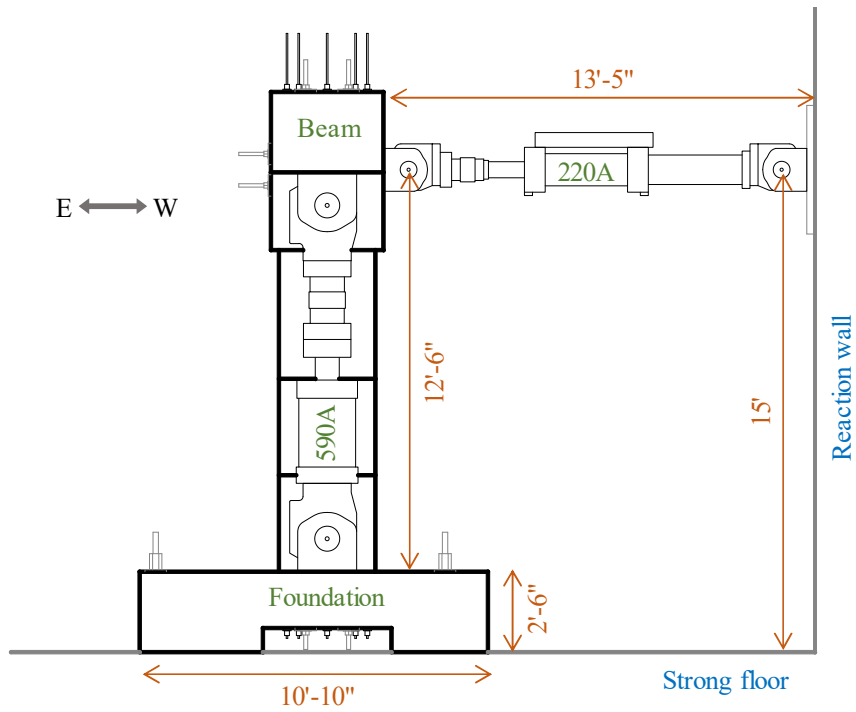
Figure 4-38. Setup A: side view

194

The setup assembly began with placing the foundation block on 2-ft deep steel beams to allow passing the tendons through the ducts inside the foundation block and installing the anchors and the tendon load cells at the bottom end of the tendons (Figure 4-39(a, b)). The tendon load cells, which were made in-house (see Appendix E for their design and fabrication details), were placed between two 4 in. by 4 in. by 1 in. steel plates and their bundles were positioned between the tendon anchors (each comprising a barrel chuck and a 3-part wedge) and the foundation surface (Figure 4-40). The foundation block was then moved to its appropriate location via a crane (Figure 4-39(c)) and was connected to the strong floor using four prestressed DYWIDAG Threadbars (Figure 4-39(d)).
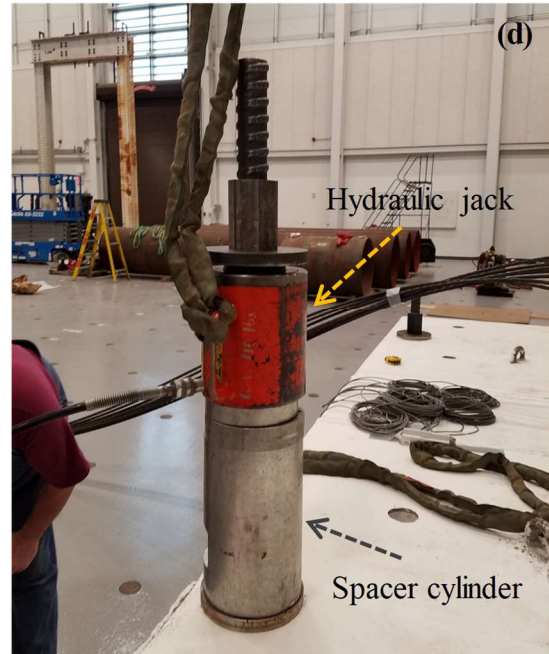
Figure 4-39. Preparation of foundation block: (a) passing tendons; (b) installation of anchors and tendon load cells under foundation; (c) moving foundation with crane; (d) connection of foundation to strong floor
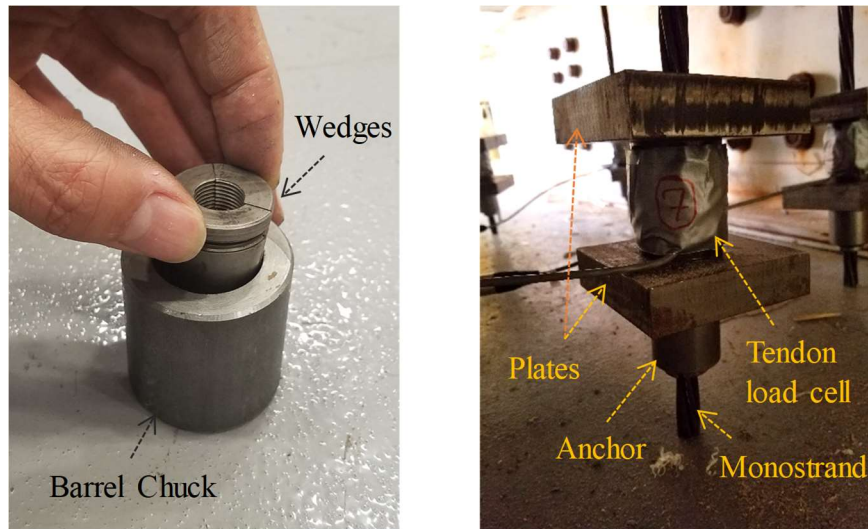
Figure 4-40. Configuration of tendon anchors and load cells

After the foundation block was secured on the floor, the column segments were stacked on the foundation one by one (Figure 4-41), while each sliding joint surface was covered by sufficient amount of grease before the next segment was placed atop it. The loading beam, to which the vertical actuators had been connected earlier, was placed on the column specimen subsequently (Figure 4-42 and Figure 4-43). Once the loading beam was on the column, the top anchors and load cells were installed on top of the loading beam (Figure 4-44) and the tendons were prestressed using a hydraulic monostrand posttensioning jack.

Figure 4-41. Column assembly

Figure 4-42. Moving loading beam and placing it on column
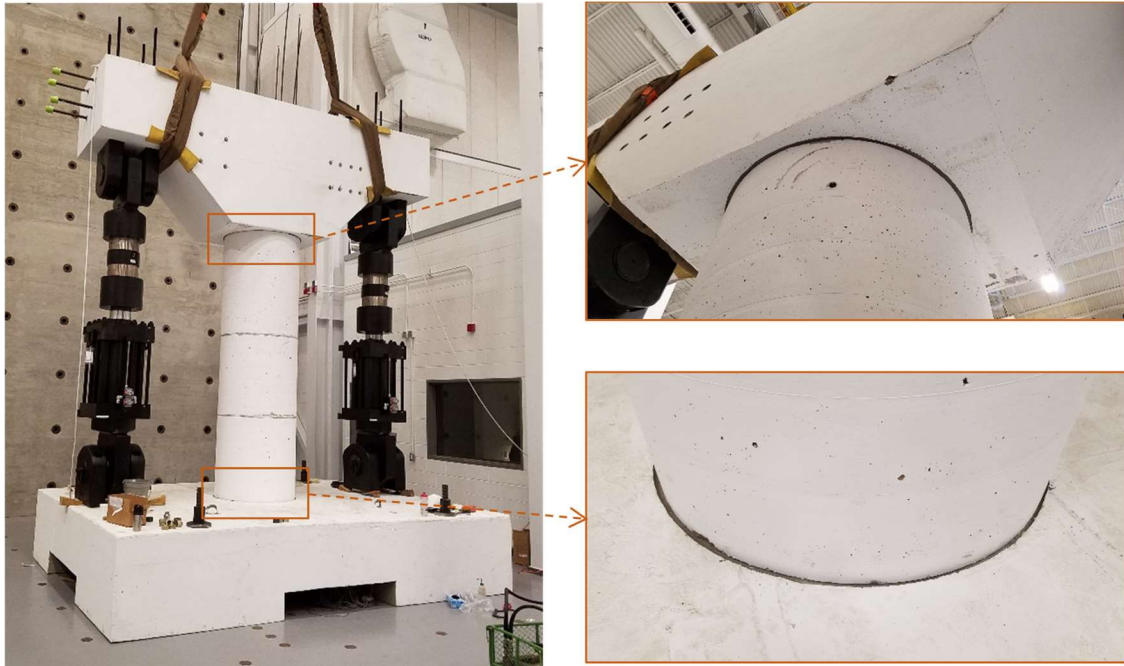
Figure 4-43. Assembled column specimen

Figure 4-44. Tendon anchors and load cells above loading beam

When the column specimen was prestressed, the bottom swivels of the vertical actuators were connected to the foundation block via torqued threaded rods. Subsequently, the horizontal actuators were first connected to the reaction wall and then to the loading beam by torqued threaded rods. A 3-in thick 4'-by-4' steel plate was used to connect each horizontal actuator to the reaction wall using four DYWIDAG Threadbars (Figure 4-45), which were prestressed by a hydraulic jack later on.
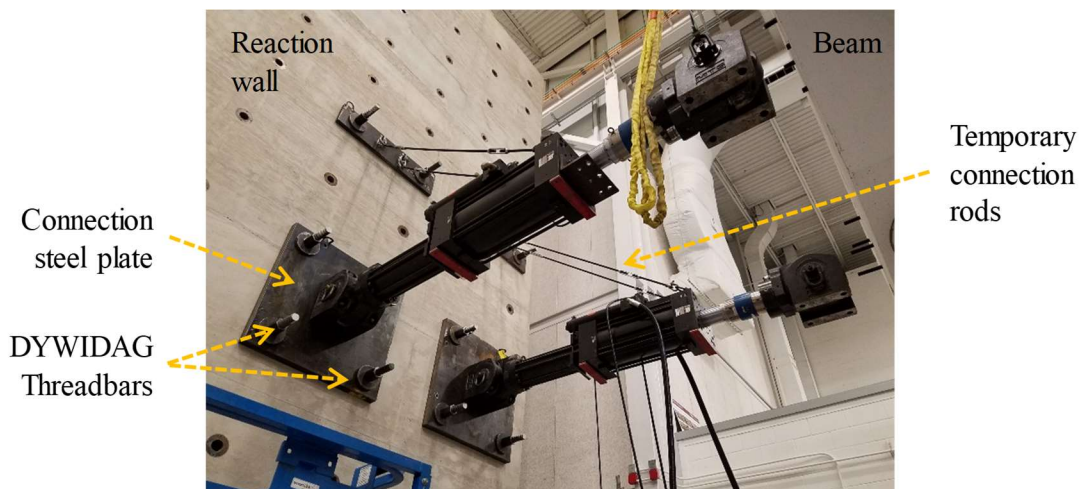
Figure 4-45. Temporary connection of horizontal actuators to reaction wall before connecting those to loading beam

4.7.1.2. Instrumentation

Other than the actuator load cells, a total of 79 sensors were used to measure the displacements and the tendon forces (Figure 4-46). The number and type of the sensors used in this test setup are listed in Table 4-7.
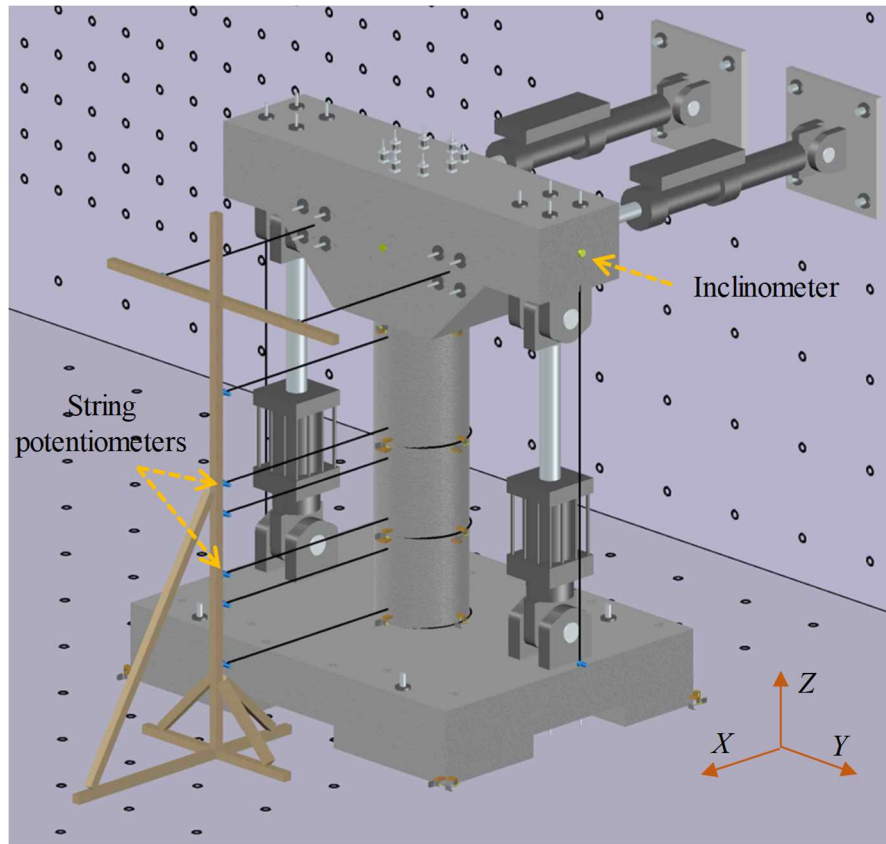
Figure 4-46. General arrangement of sensors in Phase I

Table 4-7. Type and number of sensors used in Phase I

Type	String Potentiometer	LVDT	Tendon Load Cell	Inclinometer
Number	40	12	16	3

The absolute displacements of the column segments in the lateral direction (west-east direction per Figure 4-36) were measured by two string potentiometers per column segment. These string potentiometers were attached along a wooden post positioned on the floor in front of the column and their string ends were connected to the column segments (see Figure 4-46). The information of these string potentiometers is presented in Table 4-8.

Table 4-8. String pots measuring column segment displacements in Phase I

ID	Stroke (in.)	Measurement Point
SP-S1-B	4	Bottom segment, bottom
SP-S1-T	12	Bottom segment, top
SP-S2-B	12	Middle segment, bottom
SP-S2-T	25	Middle segment, top
SP-S3-B	25	Top segment, bottom
SP-S3-T	50	Top segment, top

The rocking and sliding at the column joints are measured in/around both horizontal directions (X and Y directions per Figure 4-46) using LVDTs and string potentiometers (Figure 4-47). For the bottom rocking joint, four string potentiometers located next to the four quadrants of the column cross section measured the sliding and four others measured the rocking. For the top rocking joint, the same number of string potentiometers measured the sliding, whereas only two string potentiometers on the east and west quadrats measured the rocking. For each sliding joint, four string potentiometers and four LVDTs were employed to measure sliding and rocking, respectively. The list of the sensors used adjacent to the column joints is found in Table 4-9.

The displacements and rotations of the loading beam were measured through string potentiometers and inclinometers, respectively. The loading beam's lateral displacement (along X-axis per Figure 4-46) was measured via two string potentiometers connected to the wooden post (Figure 4-46). The vertical displacement of the loading beam was, however, measured with respect to the foundation block, using two string potentiometers attached to the two sides of the foundation (Figure 4-46). Three inclinometers were also

used to measure the rotations of the loading beam around the two horizontal axes (*X*- and *Y*-axes per Figure 4-46). These sensors are listed in Table 4-10.
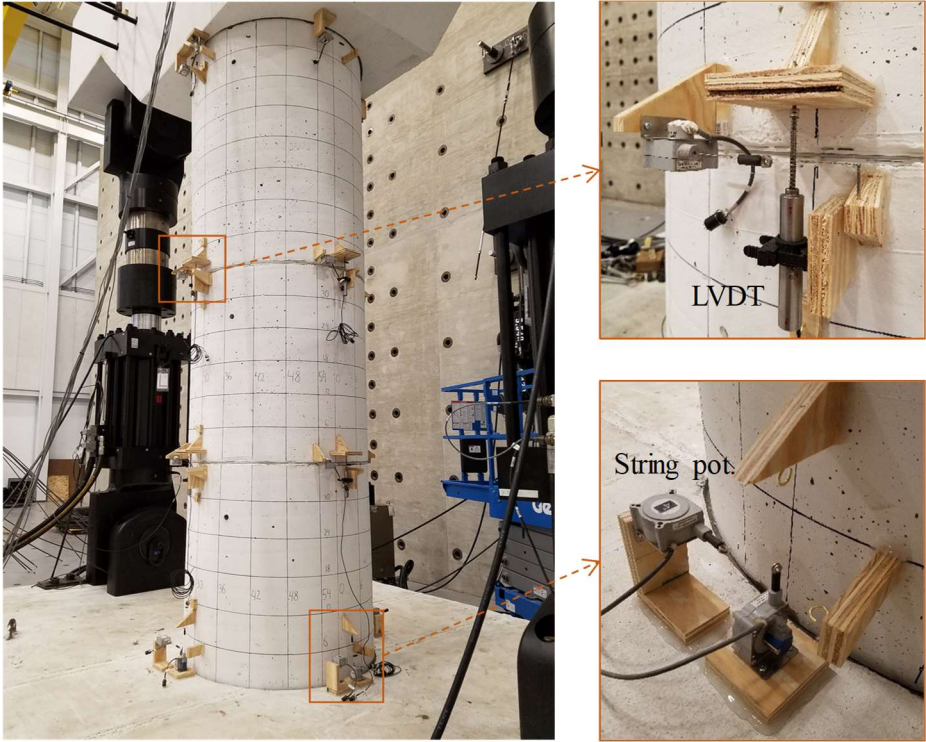
Figure 4-47. Instrumentation of column joints

Table 4-9. Sensors measuring joint sliding/rotation in Phase I

ID	Type	Stroke (in)	Location	Measurement
SP-J0-N-H	String pot.	4	Bottom joint - north	Sliding
SP-J0-S-H	String pot.	4	Bottom joint – south	Sliding
SP-J0-E-H	String pot.	4	Bottom joint – east	Sliding
SP-J0-W-H	String pot.	4	Bottom joint – west	Sliding
SP-J0-N-V	String pot.	12	Bottom joint – north	Separation
SP-J0-S-V	String pot.	12	Bottom joint – south	Separation
SP-J0-E-V	String pot.	12	Bottom joint – east	Separation
SP-J0-W-V	String pot.	12	Bottom joint – west	Separation
SP-J1-N-H	String pot.	4	Sliding joint 1 – north	Sliding
SP-J1-S-H	String pot.	4	Sliding joint 1 – south	Sliding
SP-J1-E-H	String pot.	4	Sliding joint 1 – east	Sliding
SP-J1-W-H	String pot.	4	Sliding joint 1 – west	Sliding
LV-J1-N-V	LVDT	1	Sliding joint 1 – north	Separation
LV-J1-S-V	LVDT	1	Sliding joint 1 – south	Separation
LV-J1-E-V	LVDT	1	Sliding joint 1 – east	Separation
LV-J1-W-V	LVDT	1	Sliding joint 1 – west	Separation
SP-J2-N-H	String pot.	4	Sliding joint 2 – north	Sliding
SP-J2-S-H	String pot.	4	Sliding joint 2 – south	Sliding
SP-J2-E-H	String pot.	4	Sliding joint 2 – east	Sliding
SP-J2-W-H	String pot.	4	Sliding joint 2 – west	Sliding
LV-J2-N-V	LVDT	1	Sliding joint 2 – north	Separation
LV-J2-S-V	LVDT	1	Sliding joint 2 – south	Separation
LV-J2-E-V	LVDT	1	Sliding joint 2 – east	Separation
LV-J2-W-V	LVDT	1	Sliding joint 2 – west	Separation
SP-J3-N-H	String pot.	4	Top joint - north	Sliding
SP-J3-S-H	String pot.	4	Top joint – south	Sliding
SP-J3-E-H	String pot.	4	Top joint – east	Sliding
SP-J3-W-H	String pot.	4	Top joint – west	Sliding
SP-J3-E-V	String pot.	4	Top joint – east	Separation
SP-J3-W-V	String pot.	4	Top joint – west	Separation

Table 4-10. Sensors measuring loading beam displacements/rotations in Phase I

ID	Type	Range	Location	Measurement
SP-CP-F-L	String pot.	50 (in.)	Front face – left actuator loading point	X displacement
SP-CP-F-R	String pot.	50 (in.)	Front face – right actuator loading point	X displacement
SP-CP-B-L	String pot.	12 (in.)	South side	Z displacement
SP-CP-B-R	String pot.	12 (in.)	North side	Z displacement
IN-CP-LS-C	Inclinometer	20°	South face	Y rotation
IN-CP-RS-C	Inclinometer	20°	North face	Y rotation
IN-CP-F-C	Inclinometer	20°	Front face	X rotation

Sliding and rotation of the foundation block with respect to the strong floor were measured using string potentiometers and LVDTs attached to its four corners (Figure 4-48). The LVDTs measured the foundation's separation from the floor (uplift), while the string potentiometers measured its sliding in the two horizontal directions. The information of these sensors is summarized in Table 4-11.
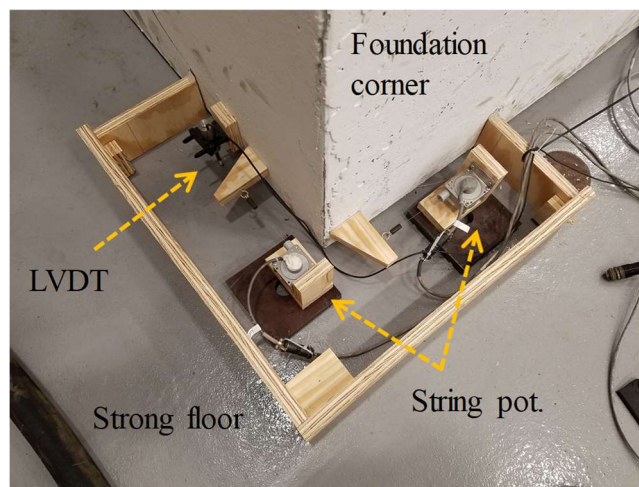
Figure 4-48. Instrumentation of foundation block

Table 4-11. Sensors measuring foundation displacements in Phase I

ID	Type	Stroke (in)	Location	Measurement
SP-FN-N-L-H	String pot.	4	NE corner	X sliding
SP-FN-N-R-H	String pot.	4	NW corner	X sliding
SP-FN-S-L-H	String pot.	4	SE corner	X sliding
SP-FN-S-R-H	String pot.	4	SW corner	X sliding
SP-FN-W-L-H	String pot.	4	SW corner	Y sliding
SP-FN-W-R-H	String pot.	4	NW corner	Y sliding
LV-FN-W-L-V	LVDT	0.5	SW corner	Separation
LV-FN-W-R-V	LVDT	0.5	NW corner	Separation
SP-FN-E-L-H	String pot.	4	SE corner	Y sliding
SP-FN-E-R-H	String pot.	4	NE corner	Y sliding
LV-FN-E-L-V	LVDT	0.5	SE corner	Separation
LV-FN-E-R-V	LVDT	0.5	NE corner	Separation

Table 4-12. Tendon load cells in Phase I

ID	Location	Tendon Map
LC-TN-C-1	Loading beam – E	
LC-TN-C-2	Loading beam – SE	
LC-TN-C-3	Loading beam – S	
LC-TN-C-4	Loading beam – SW	
LC-TN-C-5	Loading beam – W	
LC-TN-C-6	Loading beam – NW	
LC-TN-C-7	Loading beam – N	
LC-TN-C-8	Loading beam – NE	
LC-TN-F-1	Foundation – E	
LC-TN-F-2	Foundation – SE	
LC-TN-F-3	Foundation – S	
LC-TN-F-4	Foundation – SW	
LC-TN-F-5	Foundation – W	
LC-TN-F-6	Foundation – NW	
LC-TN-F-7	Foundation – N	
LC-TN-F-8	Foundation – NE	

In order to measure the tendon forces, two tendon load cells were used at the two ends of each tendon, where they were anchored (Figure 4-39(b) and Figure 4-44). The tendon load cells were fabricated in the laboratory and each of them could measure more than 100 kips of load (see Appendix E). The IDs of these load cells along with their locations are listed in Table 4-12. In Figure 4-49, the final setup with all the sensors used in Phase I is displayed.
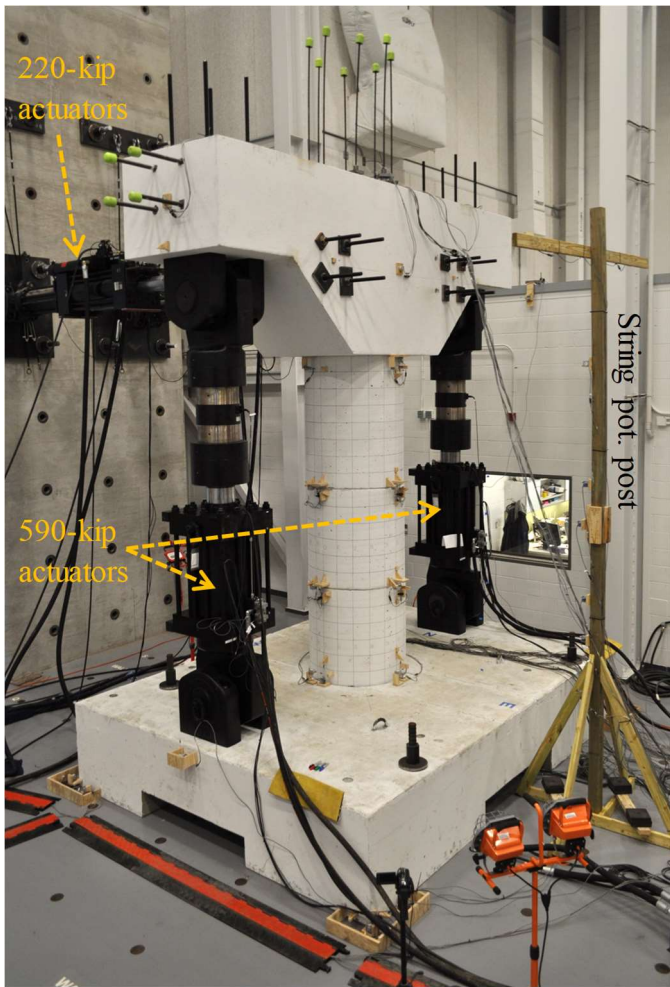
Figure 4-49. Completed test setup for Phase I

4.7.1.3. Data Acquisition and Processing

The sensors data was acquired via two SCXI-1001 chassis manufactured by National Instruments. The minimum and maximum sampling rates were 64 and 1652 samples per second, respectively. The latter sampling rate was only used during the tests under fast loading (Loading Sets 3 and 5, as described in Section 4.7.1.4). The acquired data is processed in two stages before it can be interpreted. In the first stage (data cleaning), the noise within the digital signals recorded by the DAQ system is reduced; and in the second stage (post-processing), based on the geometry of the test setup, mathematical operations are performed on the cleaned data to obtain response parameters interpretable to structural engineers (e.g. column drift ratio, column shear, and joint sliding/rocking).

Here, the data cleaning of the acquired data is carried out using a low-pass zero-phase Butterworth filter in Matlab (MathWorks 2019). The cutoff frequencies used for the signals obtained from different types of sensors were different and chosen in accordance with the Fourier amplitude spectra of the signals prior to loading (i.e. in steady state).

In the post-processing, the response parameters considered for this phase were:

- $\Delta_{bm,X}$: The lateral displacement (i.e. in X direction per Figure 4-46) of the loading point on the loading beam (equivalent to the superstructure centroid in the prototype bridge) relative to the foundation block's top surface;

- $u_{sl,X,j}$: The jth joint's sliding in the lateral direction (i.e. in X direction per Figure 4-46), with j = 1, 2, 3, and 4 from bottom to top;

- $\theta_{r,Y,j}$: The jth joint's rocking (rotation) around Y-axis (Figure 4-46);

- $V_{col,X}$: The column's base shear in the transverse direction (i.e. in X direction per Figure 4-46);

- $M_{jnt,Y,j}$: The jth joint's moment about Y-axis (Figure 4-46);

- N_{col}: The axial force on the column (i.e. excluding the column weight);

- N_{PT}: The total posttensioning force in the tendons;

- $M_{PT,Y}$: The posttensioning-induced moment about Y-axis (Figure 4-46) on the loading beam.

Selected response parameters are demonstrated in Figure 4-50. For example, as indicated in the figure, the loading beam's lateral displacement with respect to the foundation block must be computed by subtracting the lateral displacement caused by the foundation rotation, $\theta_{fnd,Y}$, and sliding, $u_{fnd,X}$, i.e. $H_o\theta_{fnd,Y} + u_{fnd,X}$, from the absolute displacements measured by the string potentiometers (with respect to the strong floor) attached to the post (Figure 4-46).

The joint sliding and joint rocking parameters (e.g. $u_{sl,X,j}$ and $\theta_{r,Y,j}$) are obtained by solving a minimization problem involving the relative displacement data obtained from the string potentiometers and the LVDTs attached at the four quadrants of the joint sections. According to Figure 4-51, the relationships between the sliding components at the jth joint and the horizontal displacements measured around the joint section are:

$$\vec{u}_j = \left[D_{sl}\right]\vec{u}_{sl,j} \tag{4-2}$$

with:

$$\begin{cases} \vec{u}_j = \begin{bmatrix} u_{S,j} & u_{E,j} & u_{N,j} & u_{W,j} \end{bmatrix}^T \\ \vec{u}_{sl,j} = \begin{bmatrix} u_{sl,X,j} & u_{sl,Y,j} & \theta_{sl,j} \end{bmatrix}^T \end{cases} \quad \text{and} \quad [D_{sl}] = \begin{bmatrix} 1 & 0 & d_S \\ 0 & 1 & d_E \\ 1 & 0 & -d_N \\ 0 & 1 & -d_W \end{bmatrix} \tag{4-3}$$

where $u_{sl,Y,j}$ and $\theta_{sl,j}$ are the joint sliding in Y direction and rotational sliding (around Z-axis per Figure 4-46); $u_{S,j}$, $u_{E,j}$, $u_{N,j}$, and $u_{W,j}$ are the measured displacements at the south, east, north, and west quadrants, respectively; and d_S, d_E, d_N, and d_W are the corresponding distances from the measurement points to the cross section center. From Eq. (4-2), the joint sliding components can be found as:

$$\vec{u}_{sl,j} = \left([D_{sl}]^T [D_{sl}] \right)^{-1} [D_{sl}]^T \vec{u}_j \tag{4-4}$$
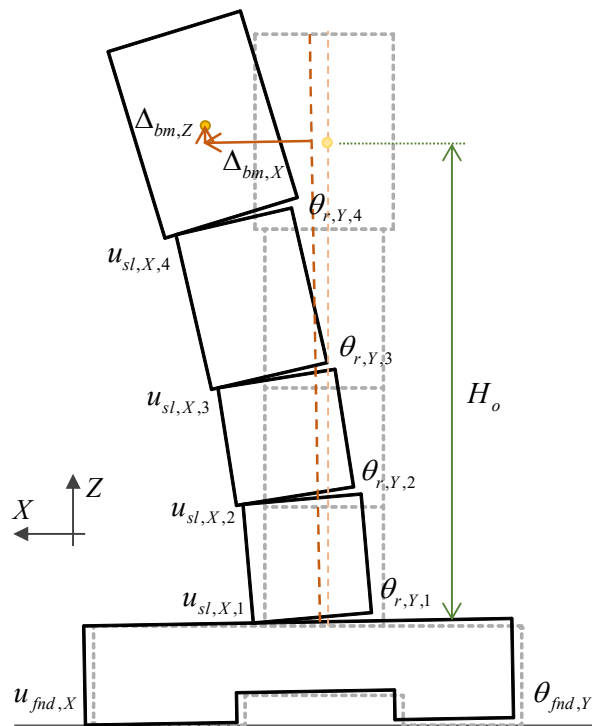
Figure 4-50. Column displacements

210
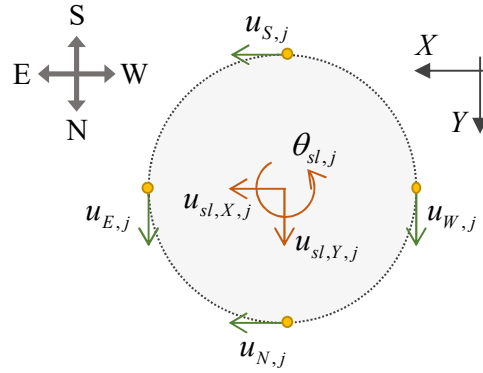
Figure 4-51. Determination of sliding components at a joint

Likewise, the relationship between the rocking (rotation) components and the vertical displacements measured by the sensors at the jth joint is found to be:

$$\vec{w}_{r,j} = \left([D_r]^T [D_r] \right)^{-1} [D_r]^T \vec{w}_j \tag{4-5}$$

with:

$$\begin{cases} \vec{w}_{r,j} = \begin{bmatrix} w_{r,j} & \theta_{r,X,j} & \theta_{r,Y,j} \end{bmatrix}^T \\ \vec{w}_j = \begin{bmatrix} w_{S,j} & w_{E,j} & w_{N,j} & w_{W,j} \end{bmatrix}^T \end{cases} \quad \text{and} \quad [D_{sl}] = \begin{bmatrix} 1 & -d_S & 0 \\ 1 & 0 & -d_E \\ 1 & d_N & 0 \\ 1 & 0 & d_W \end{bmatrix} \tag{4-6}$$

where $w_{r,j}$ and $\theta_{r,X,j}$ are the separation/uplift at the joint center and the rotation around X-axis (i.e. south-north axis), respectively. Also, $w_{S,j}$, $w_{E,j}$, $w_{N,j}$, and $w_{W,j}$ are the adjacent segments' relative vertical displacements measured at the south, east, north, and west quadrants, respectively. It is noted that the displacement and rotation components of the foundation block can be computed using equations similar to Eqs. (4-2) through (4-6).

The column's shear, $V_{col,X}$, moment, $M_{col,Y}$, and axial force, N_{col}, are computed per equilibrium equations and accounting for the geometry changes during the tests, as

211

depicted in Figure 4-52. Accordingly, assuming $\sin \theta \approx \theta$, $\cos \theta \approx 1$, and $\theta^2 \approx 0$ for very small values of θ, which is the case for the present test setup (all rotations < 0.1 rad), the above response parameters can be approximated as:

$$
\begin{cases}
V_{col,X} \simeq -F_{act,h} + F_{act,v}\theta_{act,Y} \\
M_{col,Y} \simeq -F_{act,h}h_{bm} - \left(F_{act,v} + 2W_{act,v}\right)\left(\Delta_{bm,X} - d_{act,v}\theta_{bm,Y}\right) \\
\qquad + F_{act,v}\theta_{act,Y}\left(h_{bm} - d_{act,v}\right) + 2W_{act,h}\left(d_{act,h} - \Delta_{bm,X}\right) \\
\qquad - W_{bm}\Delta_{bm,C,X} + M_{PT,Y} \\
N_{col} \simeq W_{bm} + 2W_{act,v} + 2W_{act,h} + F_{act,v} + N_{PT}
\end{cases}
\tag{4-7}
$$

where W_{bm}, $W_{act,v}$, and $W_{act,h}$ denote the weights of the loading beam (~ 27.5 kips), part of the vertical actuators (~ 2.5 kips), and part of the horizontal actuators (~ 2.5 kips), respectively; $F_{act,h}$ and $F_{act,v}$ equal the total forces applied by the horizontal and vertical actuators, respectively; $d_{act,h}$ and $d_{act,v}$ are the horizontal and vertical distances between the pins of the horizontal and vertical actuator swivels on the loading beam and the beam's desired loading point (i.e. 12.5 ft above the foundation), respectively (Figure 4-52; $d_{act,h} =$ 30.5 in. and $d_{act,v} = 13.25$ in.); and $\Delta_{bm,C,X}$ represents the horizontal displacement of the centroid of the loading beam. In addition, h_{bm} is the current height of the beam's loading point, i.e. $H_o + \Delta_{bm,Z}$, and $\theta_{act,Y}$ represents the vertical actuator's rotation around Y-axis, which is obtained as:

$$
\theta_{act,Y} \simeq \frac{\left(\Delta_{bm,X} - d_{act,v}\theta_{bm,Y}\right)}{l_{act,v}}
\tag{4-8}
$$

where $l_{act,v}$ is the current length of the vertical actuators (assuming it is equal for both actuators), measured as the distance between the swivel pins – the value of this variable is obtained from the initial length and the displacement measurements of the actuators. It is

worth noting that, ideally, in the computation of column shear, $V_{col,X}$, (first of Eqs. (4-7)) when the loading condition is not quasi-static, the inertia forces need to be considered, too. However, computation of the inertia forces requires reliable acceleration data, which could not be achieved via the sensors used in the test setup.
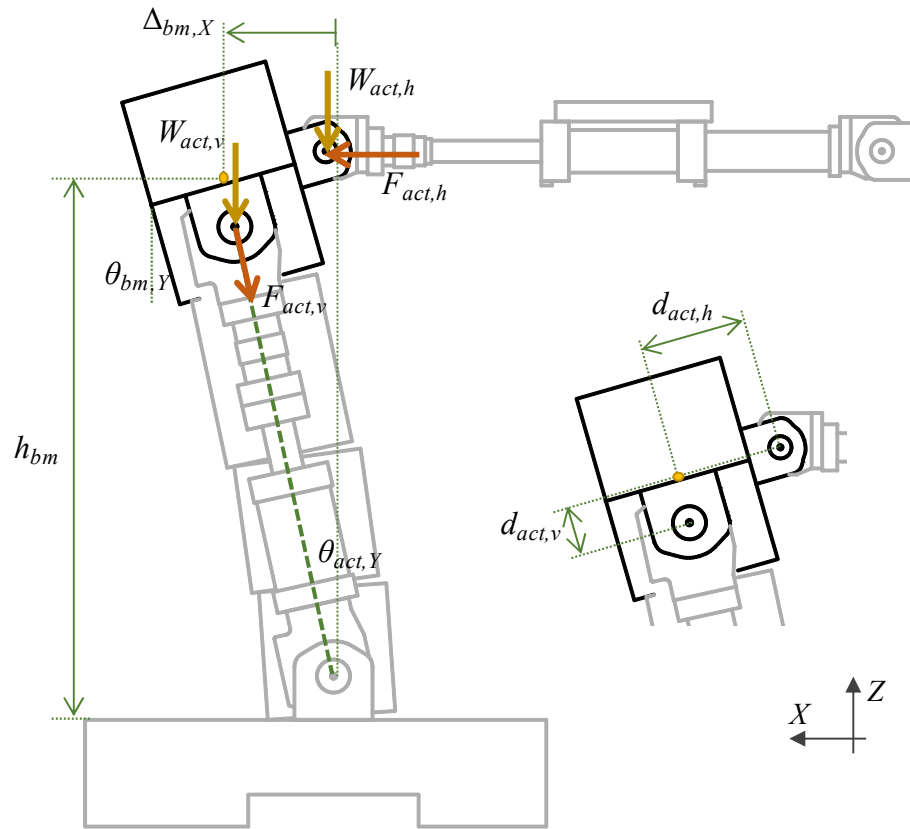
Figure 4-52. Actuator forces on the loading beam in Phase I

Finally, the total posttensioning force, N_{PT}, and the moment acting on the loading beam due to the posttensioning, $M_{PT,Y}$, are computed as:

$$\begin{cases} N_{PT} = \sum_{i=1}^{8} F_{PT,i} \\ M_{PT,Y} = -\sum_{i=1}^{8} x_{PT,i} F_{PT,i} \end{cases} \qquad (4\text{-}9)$$

where $F_{PT,i}$ and $x_{PT,i}$ denote the axial force in the ith strand and its distance from Y-axis, respectively. The strand forces eventually used were those obtained from the load cells on the top of the loading beam, because the data obtained from the majority of the load cells located under the foundation block was suspicious (or incompatible with the expected forces).

4.7.1.4. Loading Protocols

In Phase I, the column specimen was subjected to a total of 28 tests under various loading protocols, which are divided into six Loading Sets. The characteristics of these Loading Sets are summarized in Table 4-13. In all cases, the vertical actuators were force-controlled and they applied identical forces, whereas the horizontal actuators were displacement-controlled and applied identical displacements.

Table 4-13. Loading Sets in Phase I

Loading Set	Number of Protocols	Max. Drift Ratio (%)	Lateral Displacement	Vertical Load
1	3	4	Cyclic	Constant
2	3	2	Cyclic	Cyclic
3	7	2	Cyclic	Constant
4	3	4	Cyclic	Constant
5	10	4.9	Arbitrary	Constant
6	2	8	Cyclic	Constant

The loading protocols within different Loading Sets and their objectives are explained in the following. The loading protocol IDs in this Phase start with "HSR4_UN_CNT_S*n*," where 4 is the ID of the cast column specimen, "UN" stands for uniaxial loading, "CNT" stands for cantilever state, and the letter "*n*" after "S" is Loading Set number. The letters following this nomenclature are specific to each Loading Set, giving further information about the loading protocol.

4.7.1.4.1. Loading Set 1

The first Loading Set aimed to evaluate the general performance of the HSR column specimen under constant vertical load and cyclic lateral displacements representing certain seismic hazard levels.

The vertical load consisted of 100% dead load (207 kips) and 50% maximum live load (46 kips) on the column, resulting in a total of 253 kips. From this amount, approximately, 27.5 kips, 5 kips, and 5 kips are contributed by the weights of the loading beam, the horizontal actuators, and the vertical actuators, respectively. As a result, the total load applied by the vertical actuators was 215.5 kips – note that the loads applied by the vertical actuators did not vary with the loading beam's displacement, so the vertical load on the loading beam would slightly decrease when the actuators were inclined. This descrease is small, because the peak actuator inclination was small (< 0.1 radians). The cyclic lateral loading protocol in each test included six full symmetric ramp cycles. Each two consecutive cycles had an identical amplitude, while the displacement amplitude for every pair of cycles was 33% larger than the previous pair's (Figure 4-53). The displacement rate in all cycles was constant and less than 0.05 in./sec. (drift ratio rate of

0.03% /sec.). The maximum lateral displacement amplitudes (d_{max} in Figure 4-53) used in the three loading protocols of this Loading Set corresponded to three seismic hazard levels, namely, earthquakes with 950-year return period (5% probability of exceedance in 50 years), earthquakes with 2475-year return period (2% probability of exceedance in 50 years), and earthquakes with much longer return period (much less than 1% probability of exceedance in 50 years).
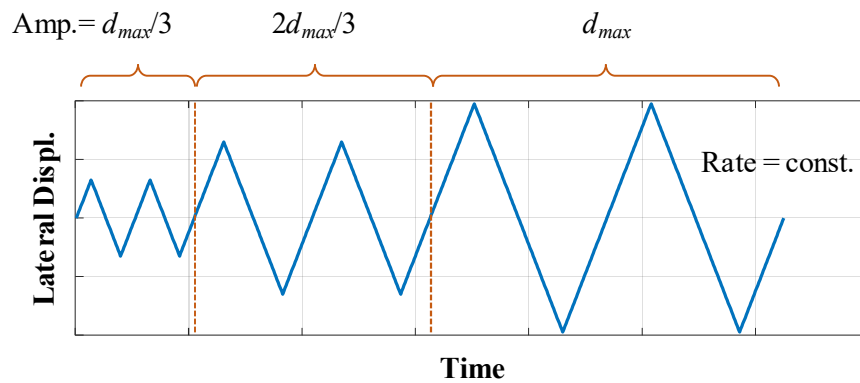
Figure 4-53. Lateral displacement time histories in Loading Set 1, Phase I

The peak displacement demands for the first two hazard levels were computed as the median of the peak lateral displacement demands predicted for the column by multiple nonlinear time history analyses. For the last hazard level, double the displacement demand for the second hazard level was considered. The analyses were conducted using a 2D OpenSees model created for the column specimen, according to the modeling strategy proposed in Chapter 2 and accounting for the superstructure mass and mass moment of inertia. The ground motions used for the analyses related to each hazard level were selected and scaled to match the Conditional Mean Spectra developed for the prototype

bridge location (Valigura 2019). The parameters defining the three loading protocols in

Loading Set 1 are summarized in Table 4-14.

Table 4-14. Loading protocols in Loading Set 1 from Phase I

No	ID	Max. Drift Ratio (%)
1	HSR4_UN_CNT_S1_DR_1_3	1.3
2	HSR4_UN_CNT_S1_DR_2	2
3	HSR4_UN_CNT_S1_DR_4	4

4.7.1.4.2. Loading Set 2

The loading protocols in Loading Set 2 were intended to investigate the effects of variable

vertical loading on the response of the HSR column specimen. Furthermore, the data

obtained from the respective tests will be employed to validate the computational

modeling strategy proposed in Chapter 2.

Loading Set 2 included three loading protocols. All loading protocols consisted of

three consecutive lateral displacement sinusoid cycles with a constant amplitude of 3 in.

(equivalent to 2% drift ratio) and a frequency of 1/240 Hz. The variation of the applied

vertical load, $F_{act,v}$, in each loading protocol followed three consecutive sinusoidal

functions with variable amplitude and constant frequency, expressed as:

$$F_{act,v}(t) = 215.5 + 215.5 R_F \sin\left(2\pi\left(R_f \frac{1}{240}\right)t\right) \quad \text{(kips)} \qquad (4\text{-}10)$$

where t denotes time and ranges from 0 to 240 sec. for each function; R_F is the ratio of the

sinusoid amplitude to the reference vertical load (i.e. 215.5 kips), which takes the values

0.1, 0.2, and 0.3; and R_f is the ratio of the vertical load variation frequency to the frequency

of the sinusoidal lateral displacement (1/240 Hz), which remains constant during each loading protocol. The values of R_f for the three protocols of Loading Set 2 are 1, 2, and 3. The loading protocols of this Loading Set are summarized in Table 4-15 and their pertinent vertical load time histories are depicted in Figure 4-54.

Table 4-15. Loading protocols in Loading Set 2 from Phase I

No	ID	Vertical Load to lateral Displacement Frequency Ratio, R_f
4	HSR4_UN_CNT_S2_V2H_1	1
5	HSR4_UN_CNT_S2_V2H_2	2
6	HSR4_UN_CNT_S2_V2H_3	3
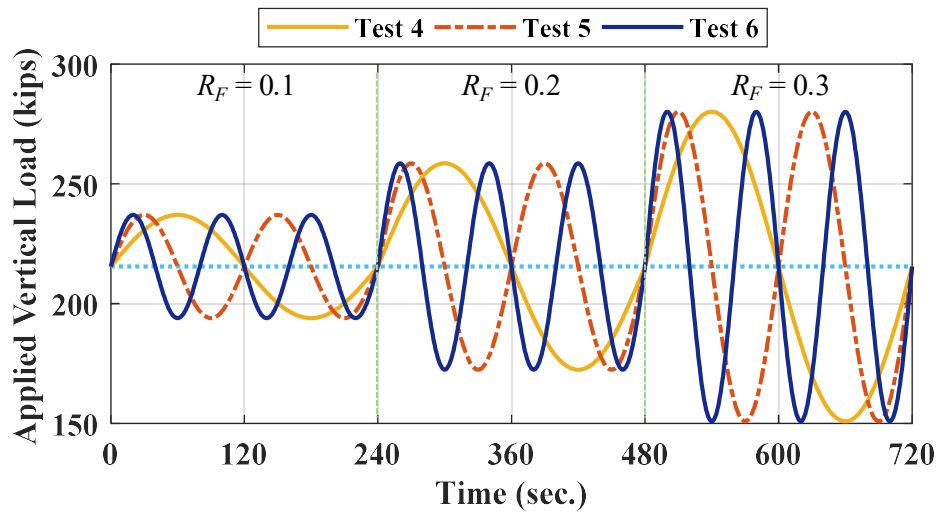
Figure 4-54. Applied vertical load time histories in Loading Set 2, Phase I

218

4.7.1.4.3. Loading Set 3

The objective of Loading Set 3 was to examine the effects of lateral displacement rate on the response of the HSR column specimen. Potential changes in the joint sliding and rocking due to the change in lateral displacement rate were of particular interest.

In all seven loading protocols of this Loading Set, the total vertical load remained constant and equal to that in Loading Set 1, i.e. 253 kips, which requires the vertical load applied by the actuators to be equal to 215.5 kips. The lateral displacement was applied in the form of a sinusoid cycle with the constant amplitude of 3 in. (2% drift ratio), while the sinusoid frequency was altered in each loading protocol to obtain certain peak displacement rates. The displacement rates selected for this purpose were 2, 4, 6, 8, 10, 14, and 18 in./sec., which were equal to the drift ratio rates 1.33%, 2.67%, 4%, 5.33%, 6.67%, 9.33%, and 12% per sec., respectively. The loading protocols of this Loading Set are listed in Table 4-16 and their displacement time histories are shown in Figure 4-55.

Table 4-16. Loading protocols in Loading Set 3 from Phase I

No	ID	Max. Displacement Rate (in./sec.)	Max. Drift Ratio Rate (%/sec.)
7	HSR4_UN_CNT_S3_Vmx_2	2	1.33
8	HSR4_UN_CNT_S3_Vmx_4	4	2.67
9	HSR4_UN_CNT_S3_Vmx_6	6	4
10	HSR4_UN_CNT_S3_Vmx_8	8	5.33
11	HSR4_UN_CNT_S3_Vmx_10	10	6.67
12	HSR4_UN_CNT_S3_Vmx_14	14	9.37
13	HSR4_UN_CNT_S3_Vmx_18	18	12
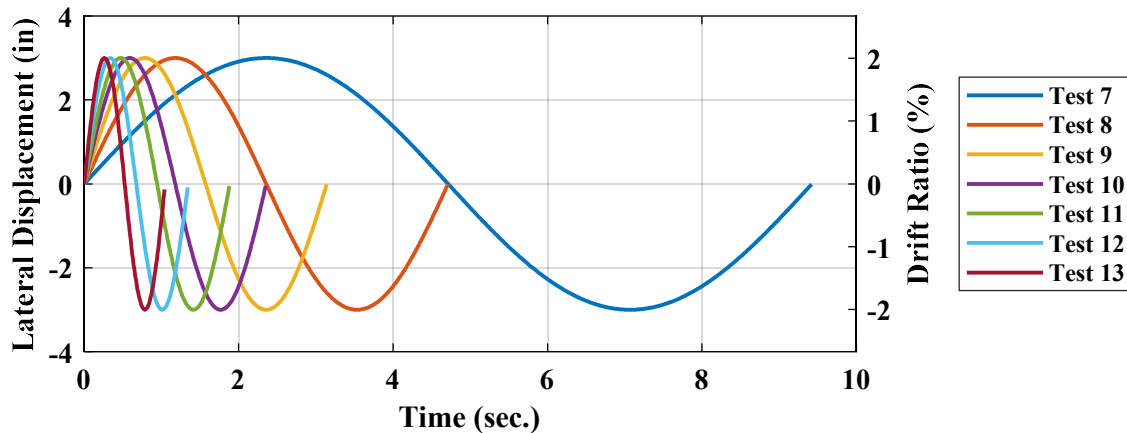
Figure 4-55. Lateral displacement time histories in Loading Set 3, Phase I

4.7.1.4.4. Loading Set 4

This Loading Set is exactly similar to Loading Set 1 and aims to assess the effectiveness of a common RC column repair method in repairing the HSR columns (Valigura 2019). After the first three Loading Sets, the first column segment was repaired by concrete patching and CFRP wrapping, and by restoring the posttensioning forces in three tendons to above 16 kips. The repair was performed to satisfy the needs of another component of the research project, which was conducted by Valigura (2019) and focused on the life-cycle assessment of HSR columns. The repair procedure is illustrated in Appendix F and in Valigura (2019). The loading protocols in this Loading Set are summarized in Table 4-17.

Table 4-17. Loading protocols in Loading Set 4 from Phase I

No	ID	Max. Drift Ratio (%)
14	HSR4_UN_CNT_S4_DR_1_3	1.3
15	HSR4_UN_CNT_S4_DR_2	2
16	HSR4_UN_CNT_S4_DR_4	4

4.7.1.4.5. Loading Set 5

The purpose of this Loading Set was to examine the response of the HSR column specimen under fast arbitrary uniaxial lateral displacement time histories, similar to those induced by earthquakes.

This Loading Set consisted of 10 loading protocols with arbitrary lateral displacement time histories of different peak displacements. Among these procedures, six involved constant vertical load and the remaining four involved arbitrary vertical load time histories. The displacement and vertical load time histories were obtained from the same 2D analyses performed to predict the peak lateral displacement demands of the column specimen for the design of the loading protocols in Loading Set 1. However, in order to ensure that the displacement time histories could be produced by the available hydraulic equipment, the raw displacement time histories obtained from the analyses were lengthened (slowed down) to keep the displacement rate below 8 in./sec., which was the capacity of the hydraulic system and actuators. The vertical load variation rate was also maintained below 40 kips/sec. Further details of the loading protocols are found in Table 4-18.

Table 4-18. Loading protocols in Loading Set 5 from Phase I

No	ID	Ground Motion	Max. Drift Ratio (%)	Max. Vertical Load (kips)
17	HSR4_UN_CNT_S5_H_GM_1	5% in 50 yr, GM 7	1.70	253
18	HSR4_UN_CNT_S5_H_GM_2	5% in 50 yr, GM 16	1.18	253
19	HSR4_UN_CNT_S5_H_GM_3	2% in 50 yr, GM 9	2.32	253
20	HSR4_UN_CNT_S5_H_GM_4	2% in 50 yr, GM 13	2.53	253
21	HSR4_UN_CNT_S5_H_GM_5	1% in 50 yr, GM 12	3.64	253
22	HSR4_UN_CNT_S5_H_GM_6	1% in 50 yr, GM 13	4.89	253
23	HSR4_UN_CNT_S5_HV_GM_1	5% in 50 yr, GM 7	1.70	293
24	HSR4_UN_CNT_S5_HV_GM_2	5% in 50 yr, GM 16	1.18	291
25	HSR4_UN_CNT_S5_HV_GM_3	2% in 50 yr, GM 9	2.32	304
26	HSR4_UN_CNT_S5_HV_GM_4	2% in 50 yr, GM 13	2.53	301

The displacement time histories for the first six loading protocols (i.e. those with constant vertical load) are shown in Figure 4-56. The displacement time histories for the last four loading protocols (i.e. those with variable vertical load) are shown in Figure 4-57. Note that these displacement time histories were slightly different from those in the first four loading protocols, because the numerical simulations used to generate those were performed by applying both horizontal and vertical excitation components to the column. The longer durations of the last four displacement time histories compared to the first four were also to keep the maximum force variation rate below 40 kips/sec. The time histories of the vertical load applied by the actuators in the last four loading protocols are displayed in Figure 4-58. It is noted that the total vertical load also includes parts of the actuators weights and the full loading beam weight, whose sum was about 37.5 kips.
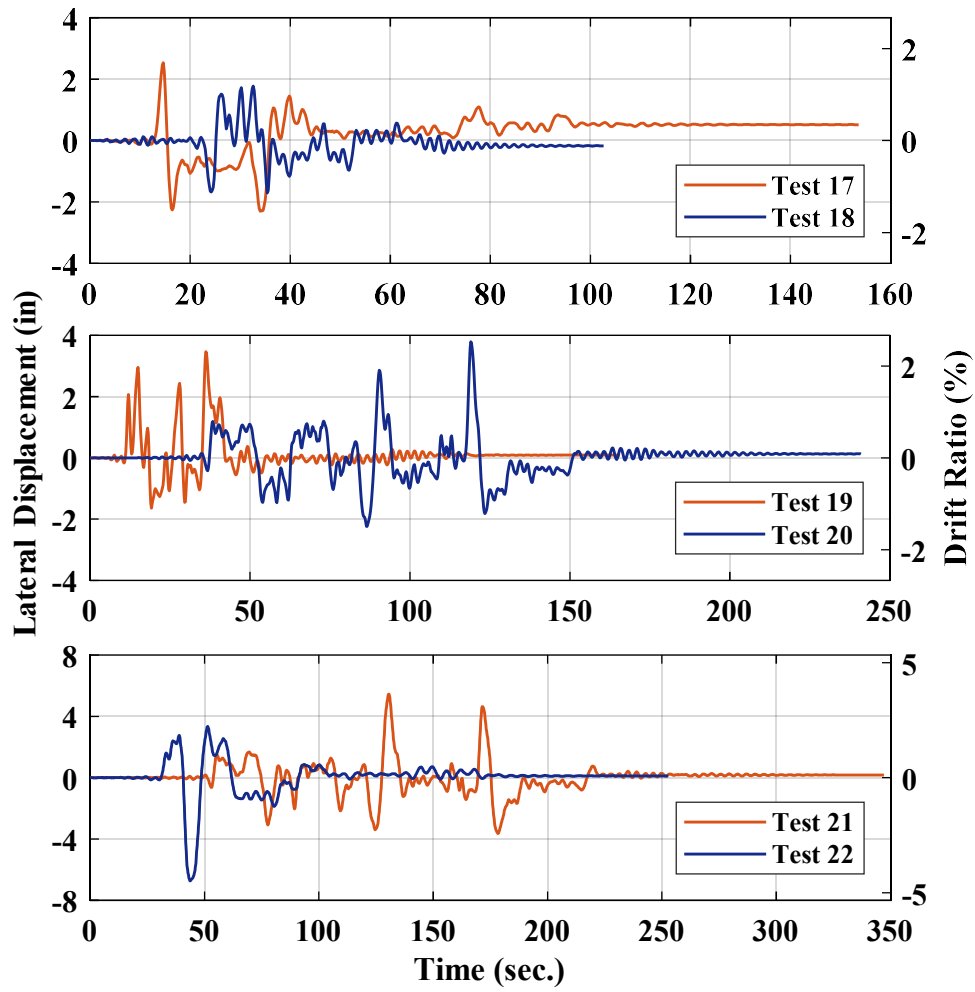
Figure 4-56. Lateral displacement time histories for loading protocols of constant vertical load in Loading Set 5, Phase I
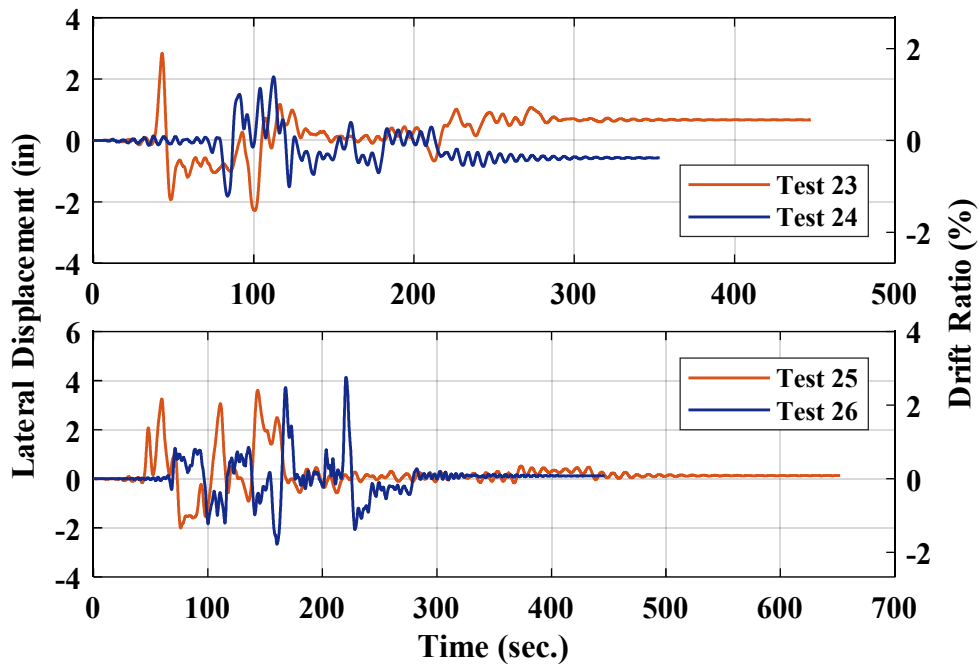
Figure 4-57. Lateral displacement time histories for loading protocols of variable vertical load in Loading Set 5, Phase I

4.7.1.4.6. Loading Set 6

The last Loading Set intended to evaluate the performance of the designed HSR column under extreme drift ratios up to 8%. Of particular interest in these tests was the level of damage to the rocking joint, sliding joint interfaces, ducts, and tendons.

A total of two loading protocols were considered in this Loading Set, both imposing a constant vertical load of 253 kips and a sinusoidal lateral displacement of two identical cycles. The displacement amplitudes for the first and the second loading protocols were 9 in. and 12 in., amounting to 6% and 8% drift ratios, respectively. The frequency of the sinusoidal functions in both loading protocols was 0.002 Hz. These loading protocols are listed in Table 4-19.
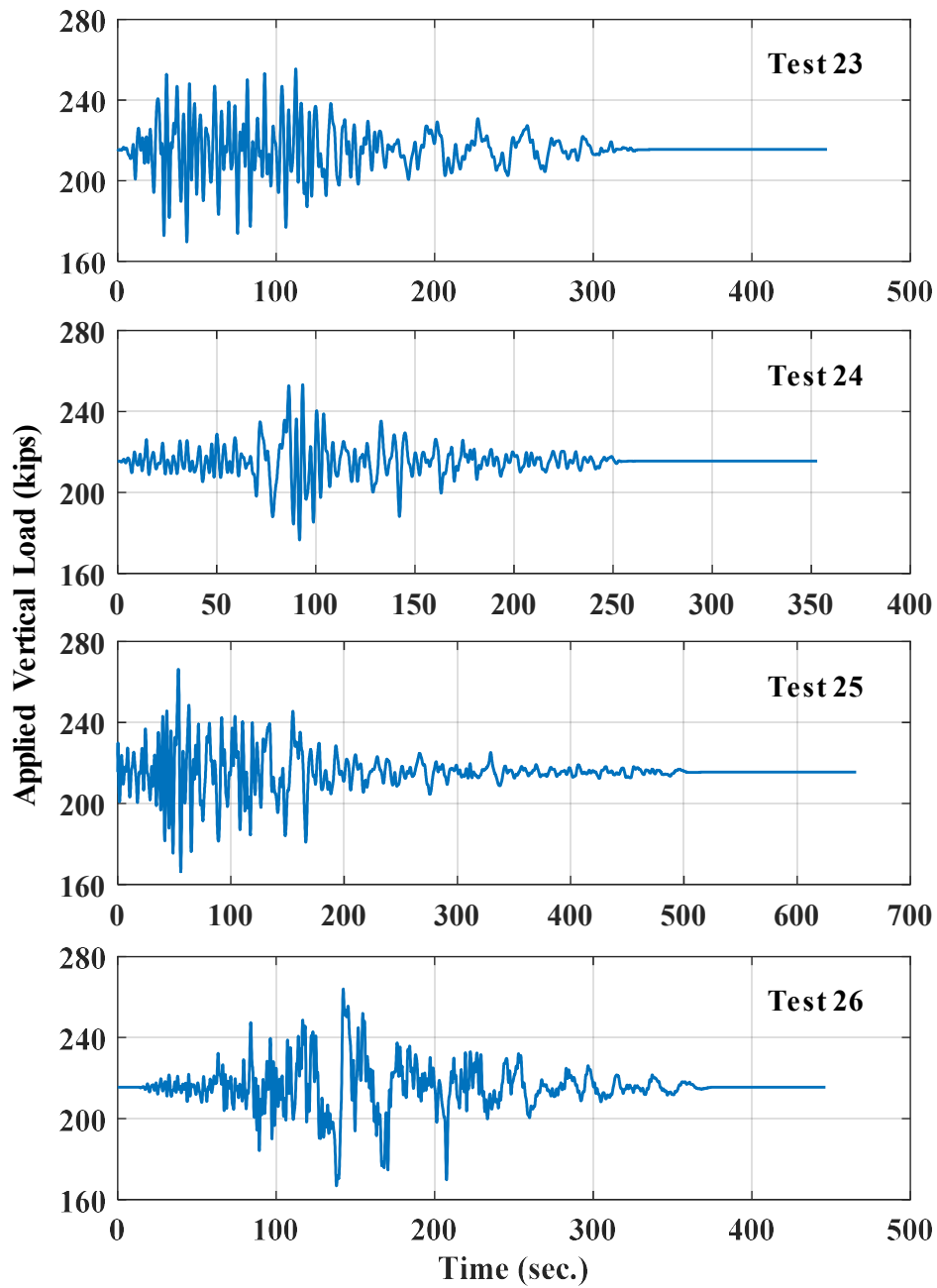
Figure 4-58. Applied vertical load time histories f or loading protocols of variable vertical load in Loading Set 5, Phase I

Table 4-19. Loading protocols in Loading Set 6 from Phase I

No	ID	Max. Drift Ratio (%)
27	HSR4_UN_CNT_S6_DR_6	6
28	HSR4_UN_CNT_S6_DR_8	8

4.7.1.5. Results and Discussion

4.7.1.5.1. Initial Vertical Load Application

Once the vertical load was applied for the first time, some diagonal hairline cracks appeared at the bottom segment of the column, which were marked. The state of the bottom segment at this point is displayed in Figure 4-59. The exact cause of these cracks is unknown. However, it is believed that these cracks were caused by stress concentrations resulting from potential unevenness of the joints surfaces. Additionally, the initial states of the sliding joints (Joints 2 and 3 per Figure 4-7) are shown in Figure 4-60 and Figure 4-61.
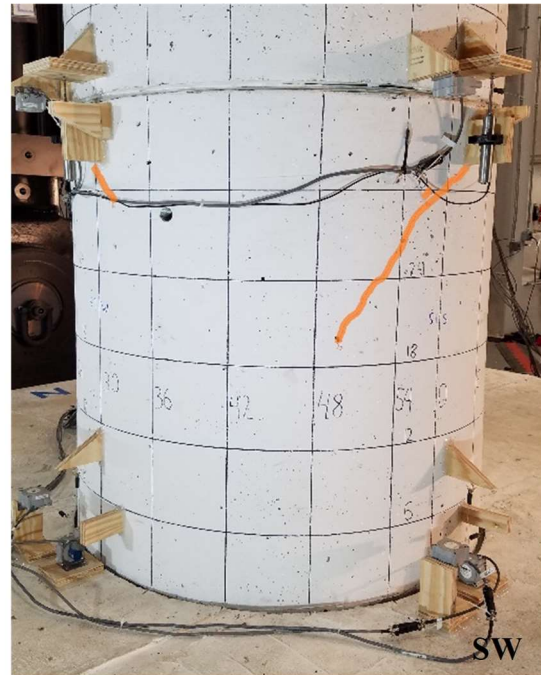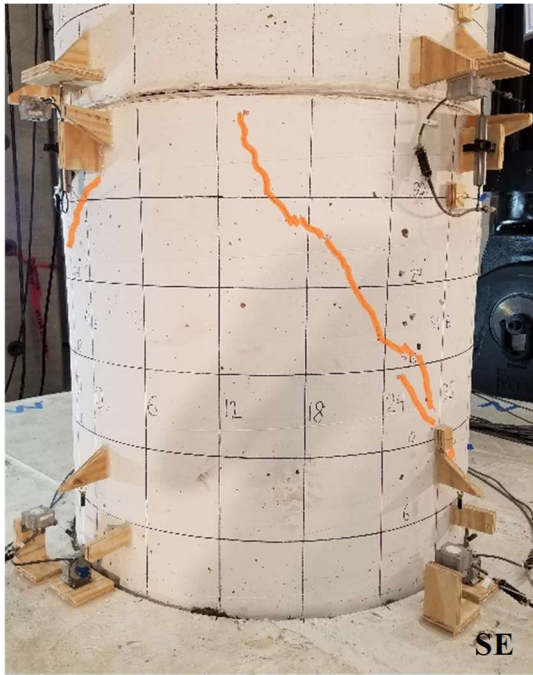
Figure 4-59. Phase I, initial vertical load application: hairline cracks on bottom column segment
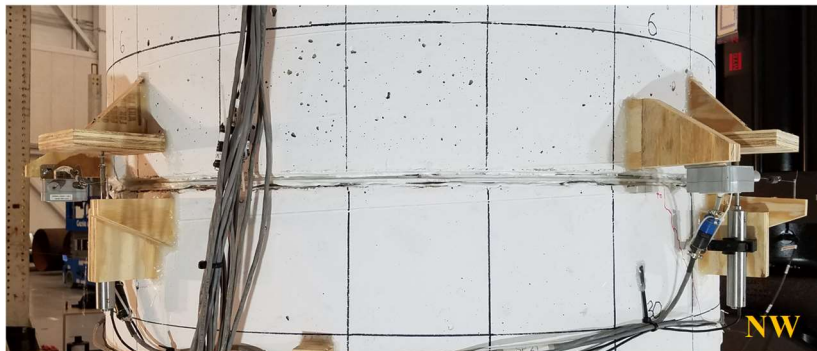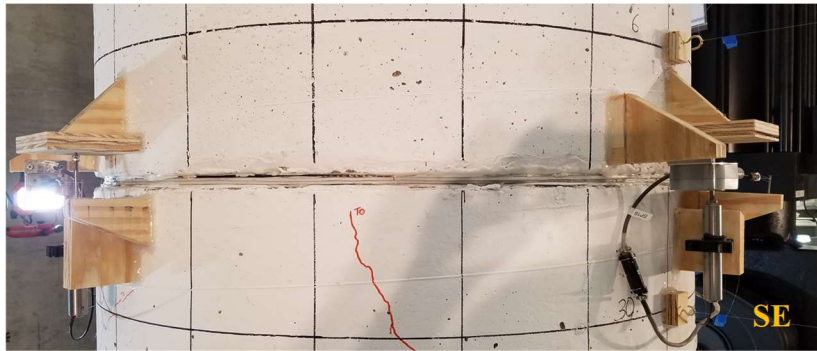
Figure 4-60. Phase I, initial state of first sliding joint (Joint 2)

Figure 4-61. Phase I, initial state of second sliding joint (Joint 3)

4.7.1.5.2. Results from Loading Set 1

The base shear vs. lateral displacement response of the column specimen under the loading protocol HSR4_UN_CNT_S1_DR_1_3 (with a maximum drift ratio of 1.3%) is shown in Figure 4-62. As seen, the column dd not exhibit any sliding during the first two and half cycles, because of the considerable breakaway friction at the sliding joints. However, near the second peak of the third cycle (first cycle with peak drift ratio of 0.87%), at a drift ratio close to 0.3% (and at negative base shear), the sliding started (appearing in Figure 4-62 as an abrupt drop in base shear magnitude). Sticking also occurred in the following loading path in the positive direction, but the breakaway friction became very small and sliding seemed continuous (i.e. without sticking phase). After sliding initiation, the response was fairly stable and each two cycles are nearly identical, implying minimal cyclic deterioration.

The average residual displacements (the mean of the displacements at which base shear becomes zero in unloading and reloading) corresponding to the peak displacement amplitudes of 0.65, 1.3, and 1.95 in. were 0.18, 1.04, and 1.49 in., respectively. In terms of drift ratio, these values amount to 0.1%, 0.7%, and 1%, respectively. However, the residual displacements were mainly caused by the residual sliding, as discussed subsequently.
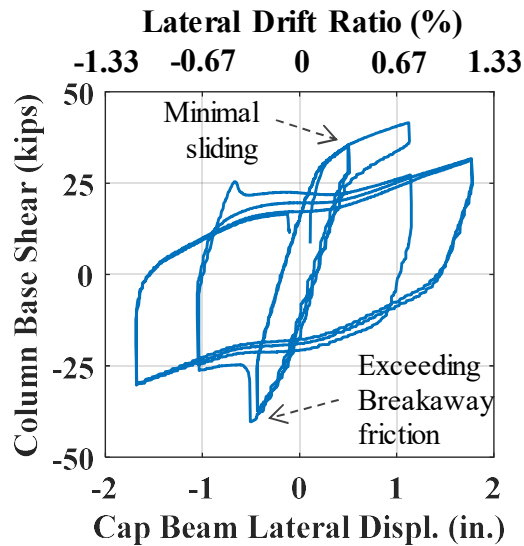
Figure 4-62. Phase I, loading protocol HSR4_UN_CNT_S1_DR_1_3: base shear vs. lateral displacement response

The resulting time histories of the sliding in X direction (loading direction) for all four column joints are shown in Figure 4-63. It is observed that sliding occurred only in the first sliding joint (Joint 2). Due to the inevitable difference in the breakaway friction values of the two sliding joints, both joints could not start to slide at the same time. On the other hand, when one sliding joint entered its slipping phase, the base shear decreased and the second joint would not get activated unless the base shear became large enough to overcome the breakaway friction present at that joint – note that the breakaway friction became even larger with the increase in posttensioning forces with the lateral displacement (Figure 4-69). The maximum sliding at Joint 2 equaled 1.40 in. and 1.43 in. in the positive and negative X-directions, respectively. According to Figure 4-64, this extent of sliding comprised up to 84% of the imposed lateral displacement in the last two cycles, which had a maximum recorded displacement amplitude of 1.77 in. That said, only less than 20% of

231

the displacement demand required to be accommodated through rocking and material

deformations, reducing the column's damage.
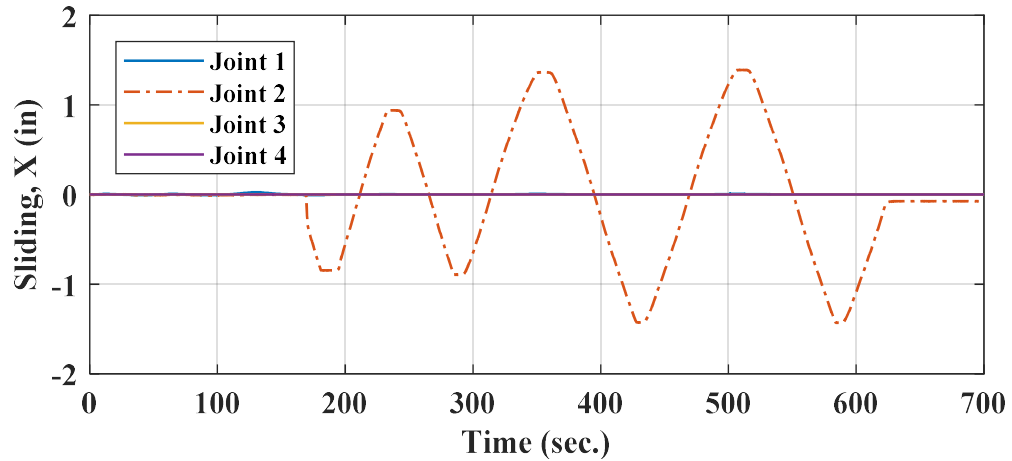
Figure 4-63. Phase I, loading protocol HSR4_UN_CNT_S1_DR_1_3: joint sliding time histories in *X* direction
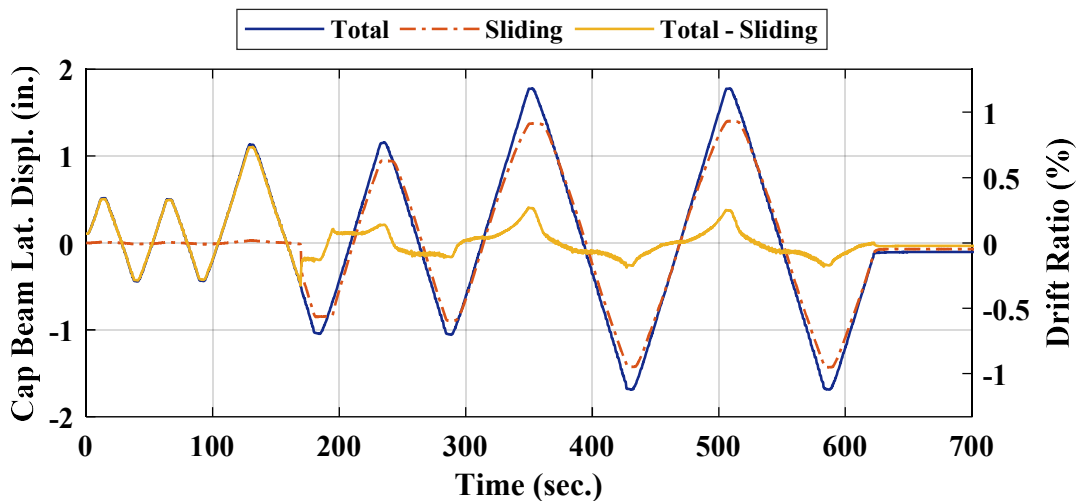
Figure 4-64. Phase I, loading protocol HSR4_UN_CNT_S1_DR_1_3: time histories of lateral displacement components

The join shear vs. sliding responses of all the column joints in X direction are demonstrated in Figure 4-65. The residual sliding values for the two groups of sliding cycles are 0.91 in. and 1.35 in., which constitute at least 85% of the respective total residual displacements reported earlier, i.e. 1.04 in. and 1.49 in., respectively. This means that the existing residual displacements are not caused by the column damage, but can be eliminated using appropriate equipment. At this level of loading, the response at Joint 2 is almost symmetric, even though the friction appears to depend on the accumulated sliding.
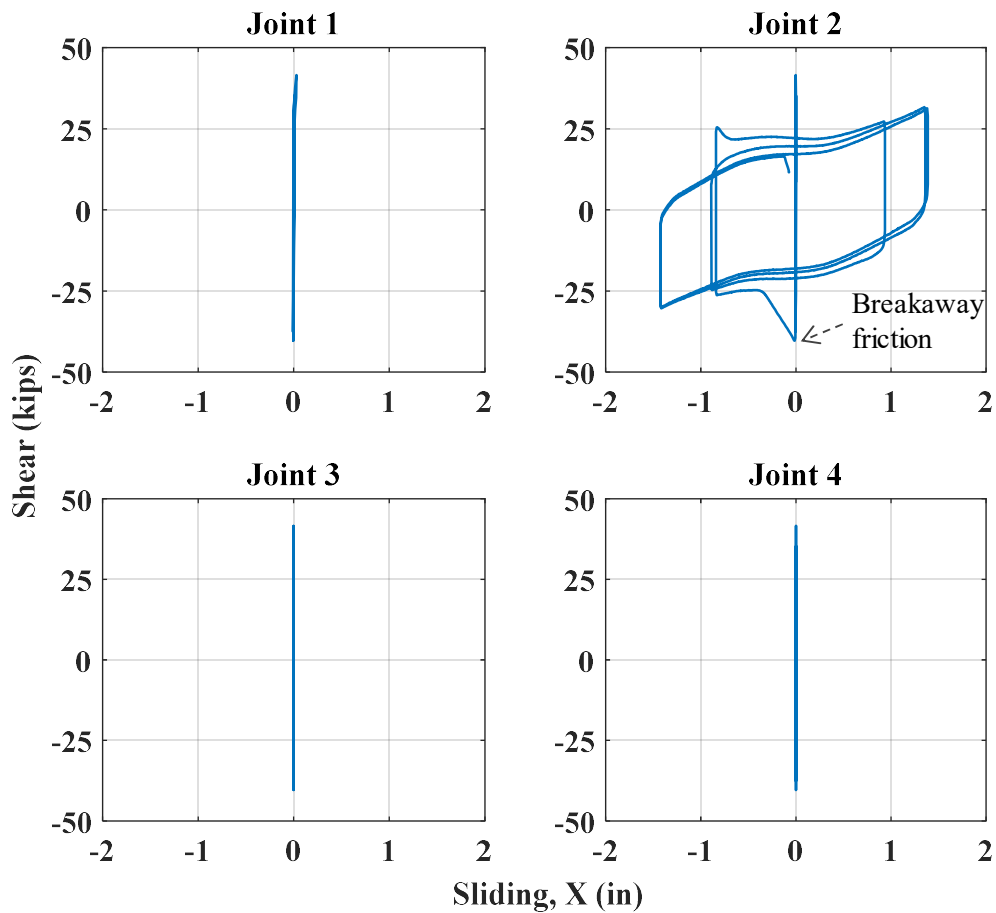
Figure 4-65. Phase I, loading protocol HSR4_UN_CNT_S1_DR_1_3: joint shear vs. sliding responses in X direction

The ratio of the joint shear to the axial force at Joint 2 is plotted against the accumulated sliding in Figure 4-66. Even though the shear force is the sum of both the friction force at the joint interface and the tendon bearing forces, the ratio of the shear force to the axial force can be a good representative of the variation of the average coefficient of friction, especially under low displacement demands, where no significant rocking is present. On the other hand, the accumulated sliding often controls the reduction of the breakaway friction. According to Figure 4-66, it is observed that during about 16 in. of accumulated sliding, the average coefficient of friction decreased by 25% (from 0.057 to 0.042).
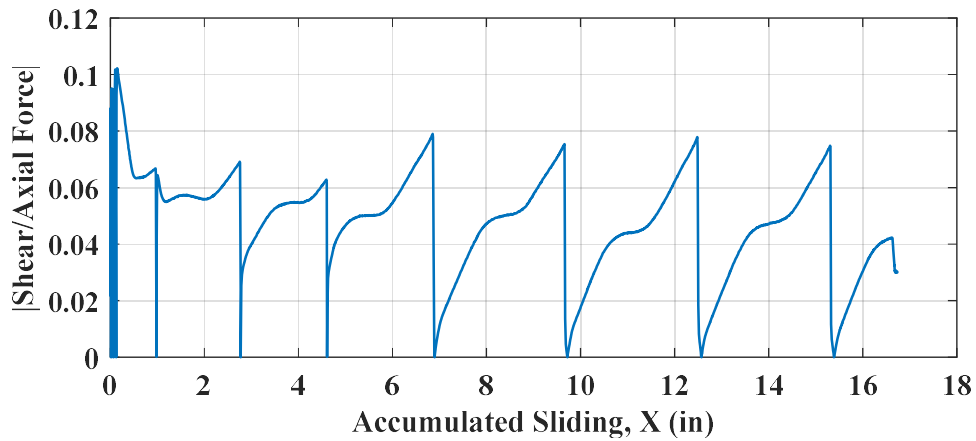
Figure 4-66. Phase I, loading protocol HSR4_UN_CNT_S1_DR_1_3: shear to axial force ratio vs. accumulated sliding

The moment vs. rocking responses of all the joints are shown in Figure 4-67. As expected, the lowest joint (Joint 1) had the maximum rocking, but the rocking at the other joints was also non-zero. The response at Joint 1 had the typical shape of the response of undamaged rocking columns, with minimal hysteretic energy dissipation. The moment-

234

rotation behavior of the first sliding joint (Joint 2) can be attributed to the relatively low modulus of elasticity of the PTFE material (about 100 ksi) and its polymer-like nonlinear viscous behavior. The second sliding joint (Joint 3) had the lowest extent of recorded rocking, even compared to Joint 4, even though the moment at that joint was higher than that at Joint 4. This finding is justified by the sticky nature of the grease existing between the segments at that joint and the fact that no sliding occurred there to eliminate it.
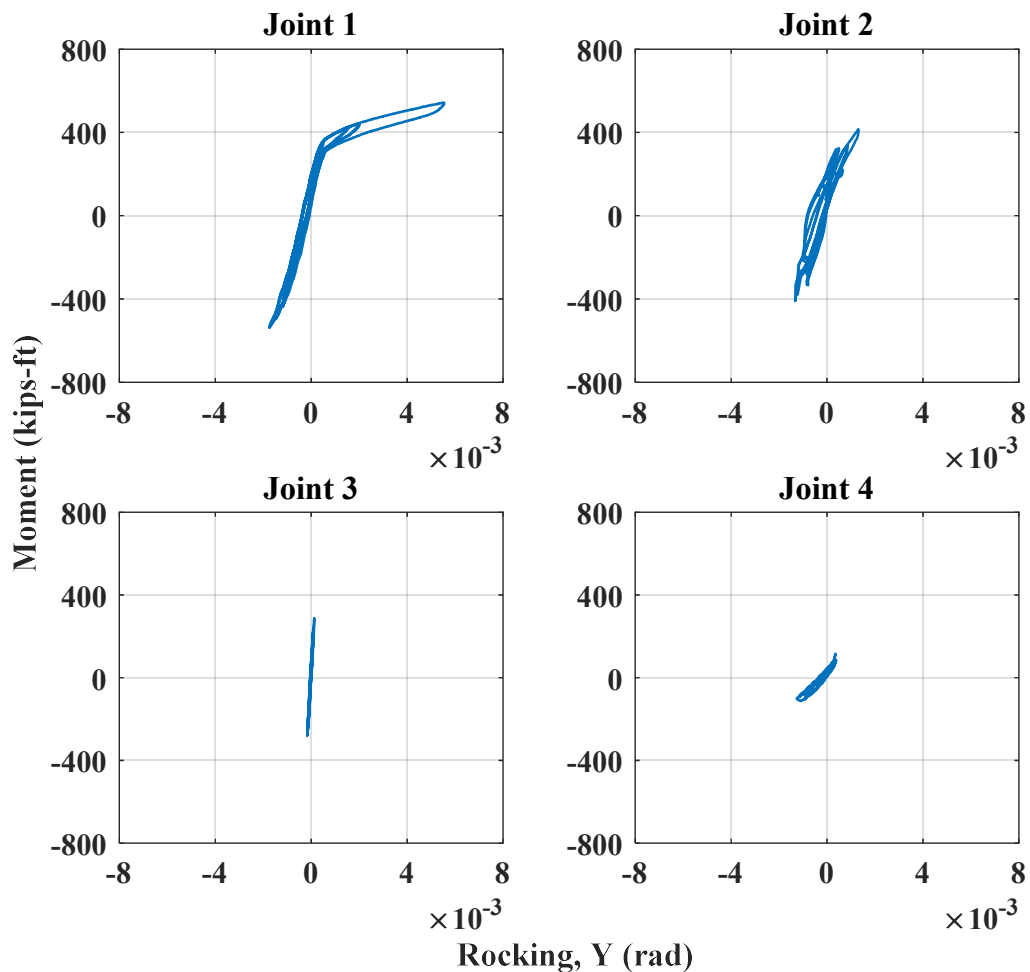
Figure 4-67. Phase I, loading protocol HSR4_UN_CNT_S1_DR_1_3: joint moment vs. rocking around *Y*-axis

The variation of the forces in the posttensioning strands with time and the loading beam's lateral displacement are displayed in Figure 4-68 and Figure 4-69, respectively. It is observed that the initial total PT force was close to 141 kips, i.e. about 2% lower than the design value (144 kips). The sliding initiation is found capable of reducing the PT forces by reducing the rocking motion, and thus, the tendons' elongation. During the test, the PT force in none of the tendons exceeded 22 kips, which is much less than their nominal yield strength (~53 kips). The total PT loss was about 2 kips, i.e. less than 1.5%.
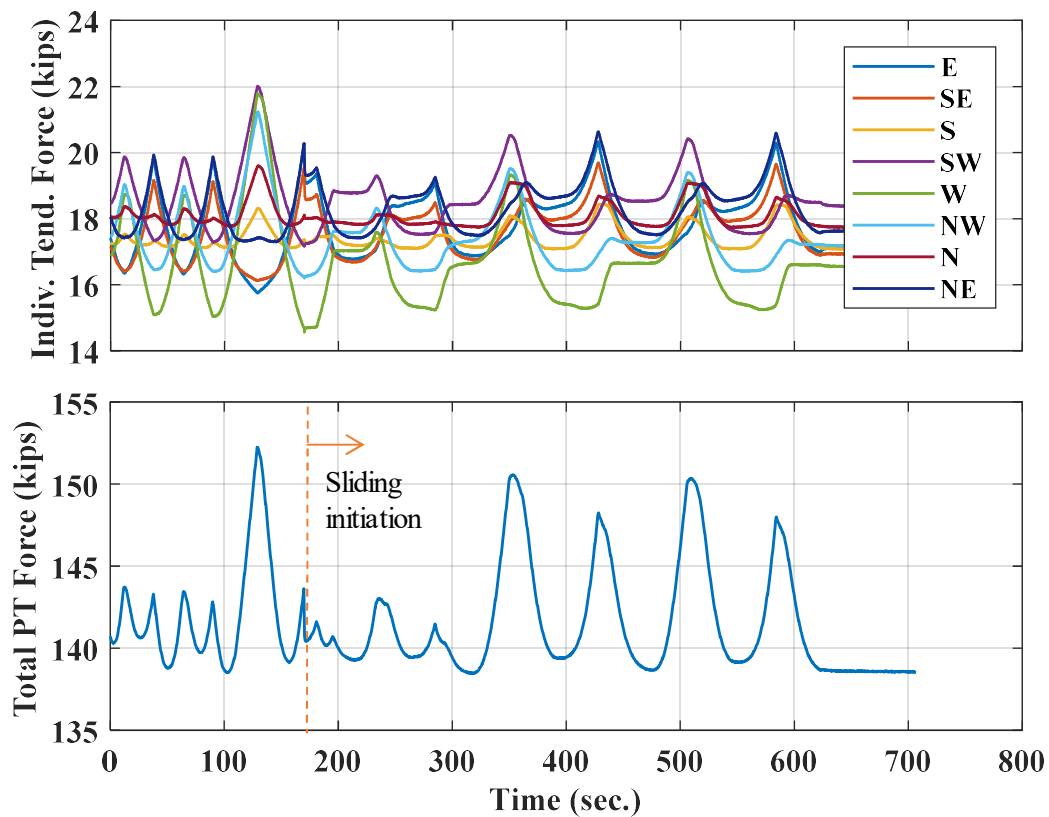
Figure 4-68. Phase I, loading protocol HSR4_UN_CNT_S1_DR_1_3: time histories of posttensioning forces
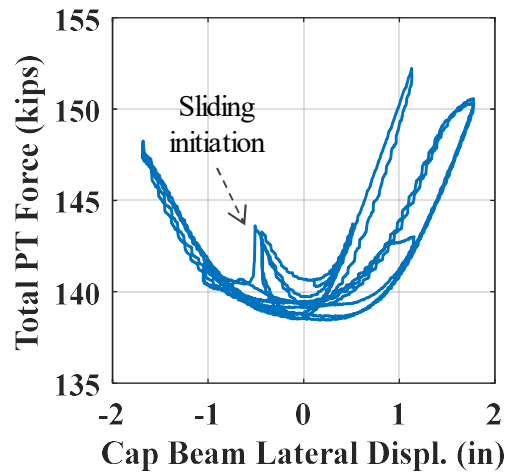
Figure 4-69. Phase I, loading protocol HSR4_UN_CNT_S1_DR_1_3: total PT force vs. lateral displacement

The visible damage of the loading protocol HSR4_UN_CNT_S1_DR_1_3 on the column specimen appeared in the form of new hairline cracks and the growth of the previous cracks on the bottom column segment (Figure 4-70). No cracks were observed on the upper two segments and no damage was detected around the sliding joints.

The base shear vs. lateral displacement response of the column under the next loading protocol, i.e. HSR4_UN_CNT_S1_DR_2, is demonstrated in Figure 4-71. The desired maximum drift ratio in this test was 2%. The breakaway friction in this test was about 33 kips, which is 17% less than that in the first test (~40 kips, Figure 4-62). This discrepancy happened due to the prior sliding at the joint (Reddy Goli 2019). The hysteretic response was again stable, with minimal cyclic deterioration.
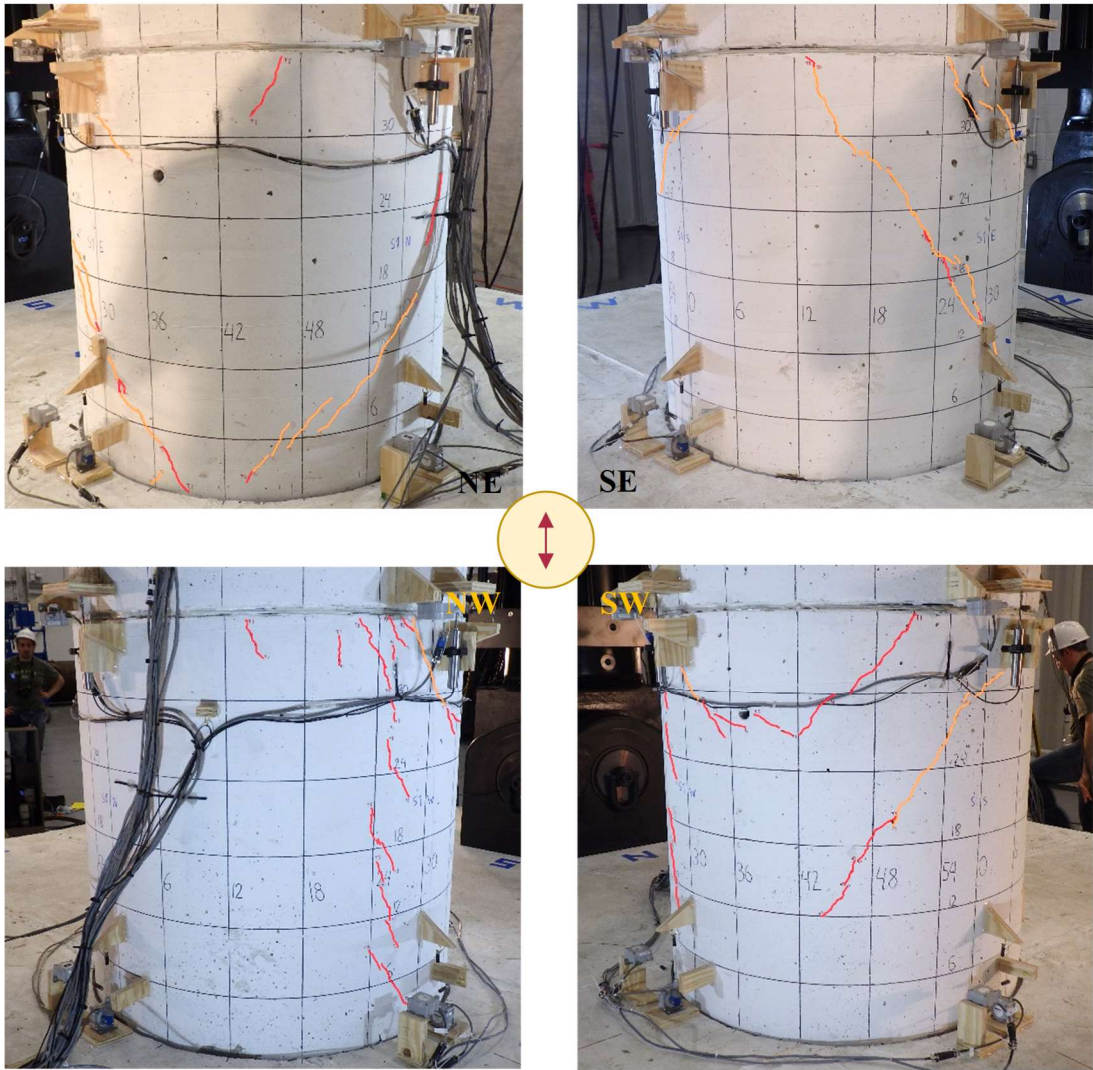
Figure 4-70. Phase I, loading protocol HSR4_UN_CNT_S1_DR_1_3: distribution of cracks on bottom segment after test
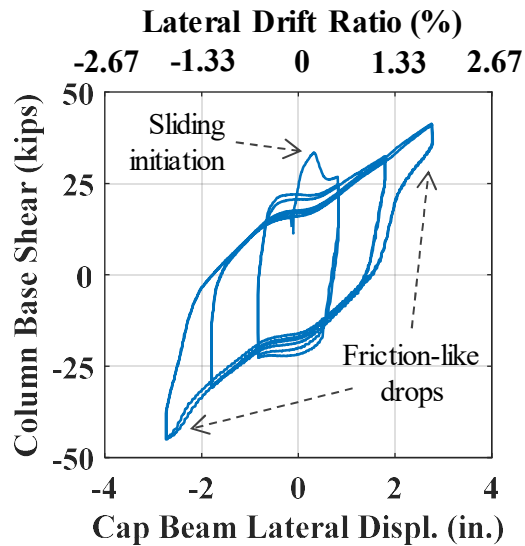
Figure 4-71. Phase I, loading protocol HSR4_UN_CNT_S1_DR_2: base shear vs. lateral displacement response

The column response was dominated by rocking as the lateral displacement in any direction exceeded 2 in. (1.33% drift ratio). This is because no further sliding at the first sliding joint (Joint 2) was possible and, similar to the prior test, the second sliding joint (Joint 3) did not exhibit sliding (Figure 4-72). It is worth noting that, even though the base shear went over 40 kips (the base shear required in the previous test to overcome the sticking phase of the first sliding joint), the second sliding joint was not expected to exhibit sliding. The reason for this is that the breakaway friction generally increases with the axial load on the column, which itself increases with lateral displacement due to the elongation of the posttensioning tendons.

In Figure 4-71, the base shear reduction with the number of cycles in the displacements close to zero (where sliding is the dominant mode of response) is due to the dependence of the coefficient of friction on the accumulated sliding travel distance after

friction breakaway. The average residual displacement during the last two displacement cycles in this test was about 1.64 in. (1.1% drift ratio), which was mainly caused by residual sliding (Figure 4-73).
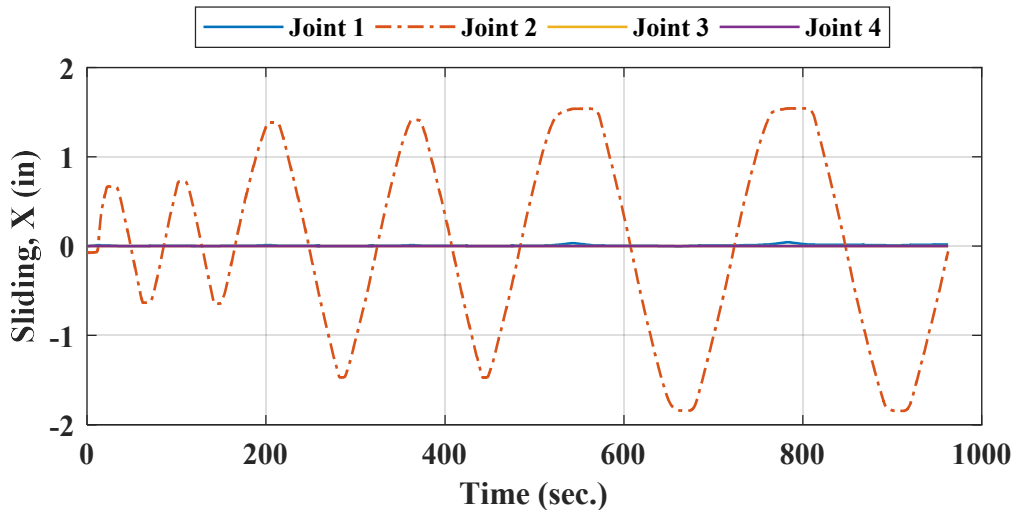
Figure 4-72. Phase I, loading protocol HSR4_UN_CNT_S1_DR_2: joint sliding time histories in *X* direction

Another important observation made in Figure 4-71 is the friction-like base shear drops at the peak displacements when the rocking behavior is dominant. These drops are associated with the friction between the tendons and their ducts, especially during the rocking motion. In order to further probe into this, the variations of the south tendon's end forces (obtained from the top and bottom load cells) with lateral displacement are compared. According to Figure 4-74, during loading phases, the force at the bottom end of the tendon was up to 1 kip larger than the force at its top end. Contrarily, during the unloading phases, the bottom end's force became smaller than the top end's. These

observations indicate that the presence of friction between the tendons and the ducts and its direction change as the column rocked back and forth (see Figure 4-75). As a result of these friction forces, the tendons resistance increased with the column's rotation and vice versa, leading to similar changes in the moment resistance and the base shear of the column specimen.
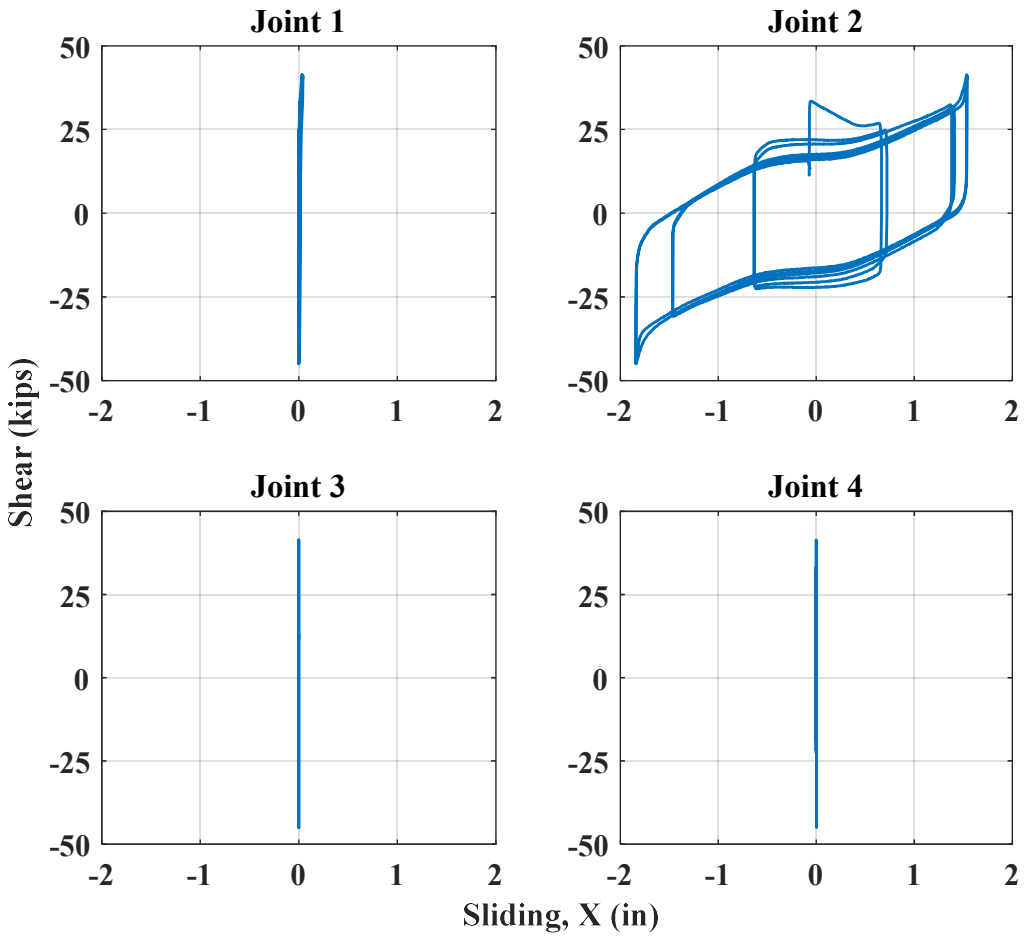
Figure 4-73. Phase I, loading protocol HSR4_UN_CNT_S1_DR_2: joint shear vs. sliding responses in *X* direction
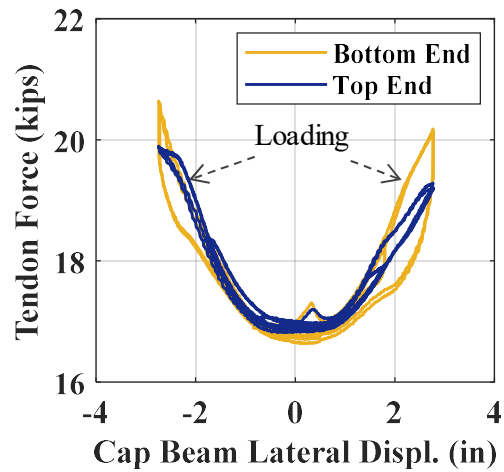
Figure 4-74. Phase I, loading protocol HSR4_UN_CNT_S1_DR_2: south tendon end forces vs. lateral displacement
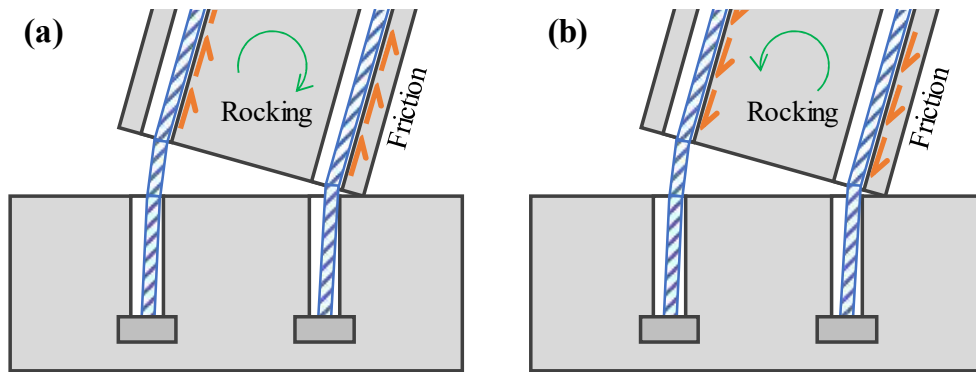
Figure 4-75. Friction between tendons and their ducts: (a) during loading; (b) during unloading

The maximum joint sliding values achieved in the positive and negative X directions for Joint 2 were 1.54 in. and 1.84 in., respectively, (Figure 4-72) which are both higher than the designed nominal sliding capacity of the sliding joints, i.e. 1.45 in.; this discrepancy is attributed to the oversized holes on the steel plates and the PTFE pads used at the sliding joints as well as the indentation of the PVC pipes due to the tendons bearing.

The difference between the maximum sliding values achieved in the opposite directions could be resulted from the unwanted misalignment of the ducts at the sliding joint.

The time histories of the loading beam's lateral displacement and the total joint sliding, along with their difference (displacement induced by rocking and material deformations), are compared in Figure 4-76. According to this graph, for the highest displacement demand in this test, up to 67% of the required displacement could be accommodated by sliding. It is also noted that the sliding time history has only a negligible time lag compared to the imposed displacement time history.
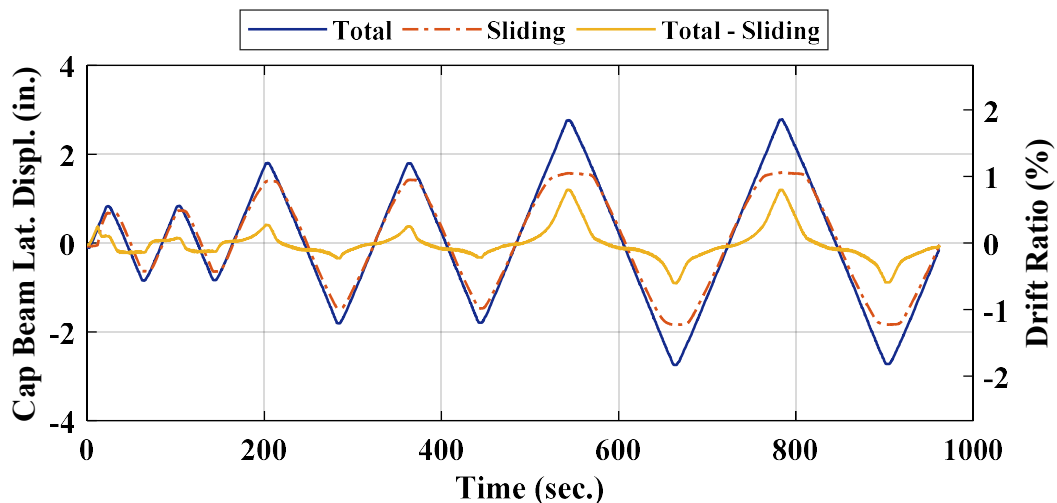
Figure 4-76. Phase I, loading protocol HSR4_UN_CNT_S1_DR_2: time histories of lateral displacement components

The joint shear vs. sliding responses of all of the column joints are displayed in Figure 4-73. Because of the duct misalignments, the hysteresis obtained for the first sliding joint (Joint 2) is not fully symmetric, but it is stable. The friction reduction with the number of sliding cycles is also clear in Figure 4-73, which is also illustrated through the graph in

243

Figure 4-77 showing the ratio of the joint shear to the axial force with respect to the accumulated sliding. Similar to the data shown in Figure 4-66 for the test under loading protocol HSR4_UN_CNT_S1_DR_1_3, the coefficient of friction seems to have decreased from about 0.06 in the initial cycles to 0.04 in the last cycle. This comparison implies that the primary cause of such reduction in coefficient of friction was the gradual changes in the grease material rather than the PTFE surface.
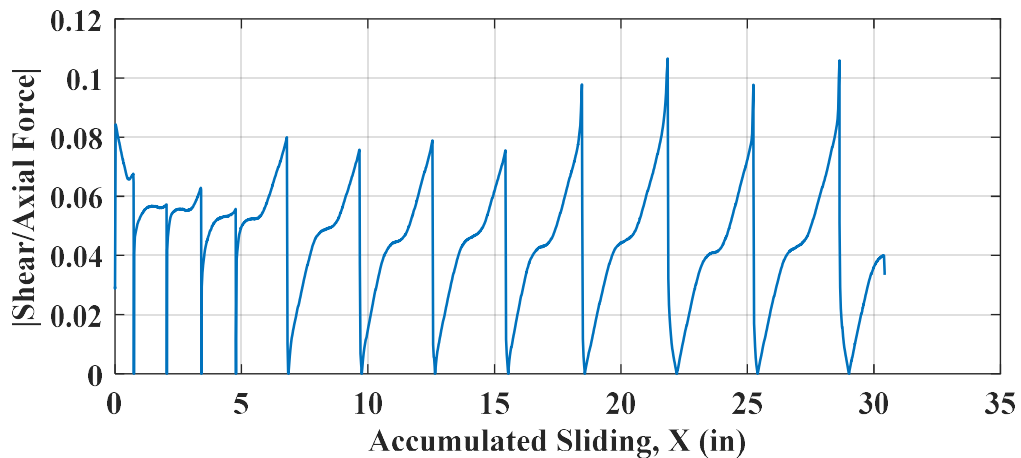
Figure 4-77. Phase I, loading protocol HSR4_UN_CNT_S1_DR_2: shear to axial force ratio vs. accumulated sliding

The joints' moment vs. rocking responses are presented in Figure 4-78. Similar to the previous test, no significant deterioration is observed in the response of the bottommost joint (Joint 1), where the maximum rocking is expected. The irregular shape of the hysteresis obtained for the first sliding joint (Joint 2) could have been caused by the unwanted sliding-induced movements of the LVDTs used to measure the relative vertical displacements of the column segments with respect to each other (Figure 4-47), the

nonlinear behavior of the PTFE material under compression, and the combined rocking-sliding interactions of the segments. Compared to other joints, the second sliding joint (Joint 3) exhibited the lowest relative rotation, while larger rotation is observed at the loading beam with respect to the top column segment under smaller moment. This is again justified by the presence of sticky grease at Joint 3, while Joint 4 was dry.
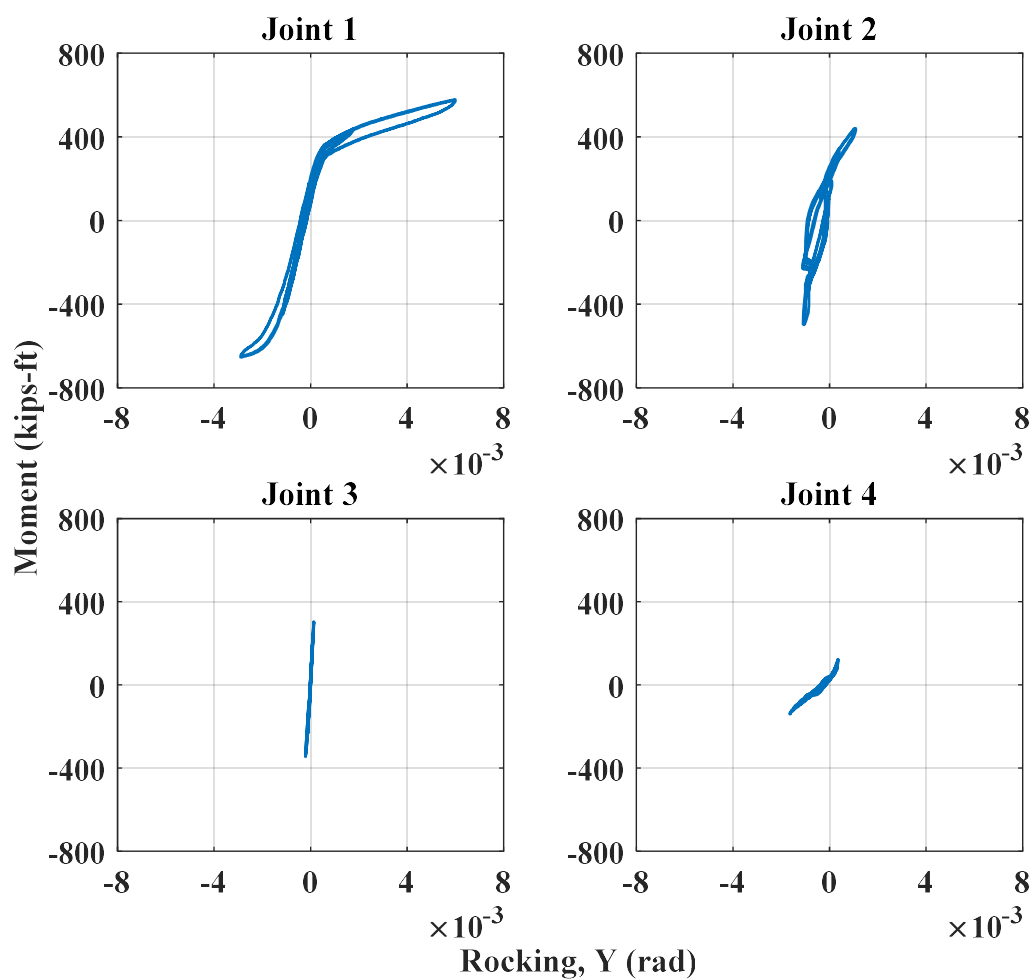
Figure 4-78. Phase I, loading protocol HSR4_UN_CNT_S1_DR_2: joint moment vs. rocking responses around *Y*-axis

The PT force time histories of the individual tendons and their sum are demonstrated in Figure 4-80. In addition, the total PT force is plotted against the loading beam's lateral displacement in Figure 4-79. Similar to the previous test, none of the strands experienced yielding under the imposed cyclic displacement (Figure 4-80). The strands passing the east and west quadrants of the column cross section (the farthest strands from the neutral axis) underwent the maximum forces, i.e. 24 kips and 23.3 kips, respectively, which are both less than 50% their nominal yield strength. The total PT loss during this test was found to be about 1%, implying minimal damage to the strands and the column, even though Joint 2 reached its nominal sliding capacity.
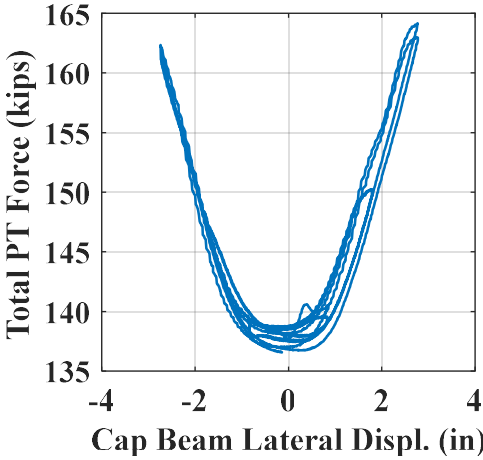
Figure 4-79. Phase I, loading protocol HSR4_UN_CNT_S1_DR_2: total PT force vs. lateral displacement
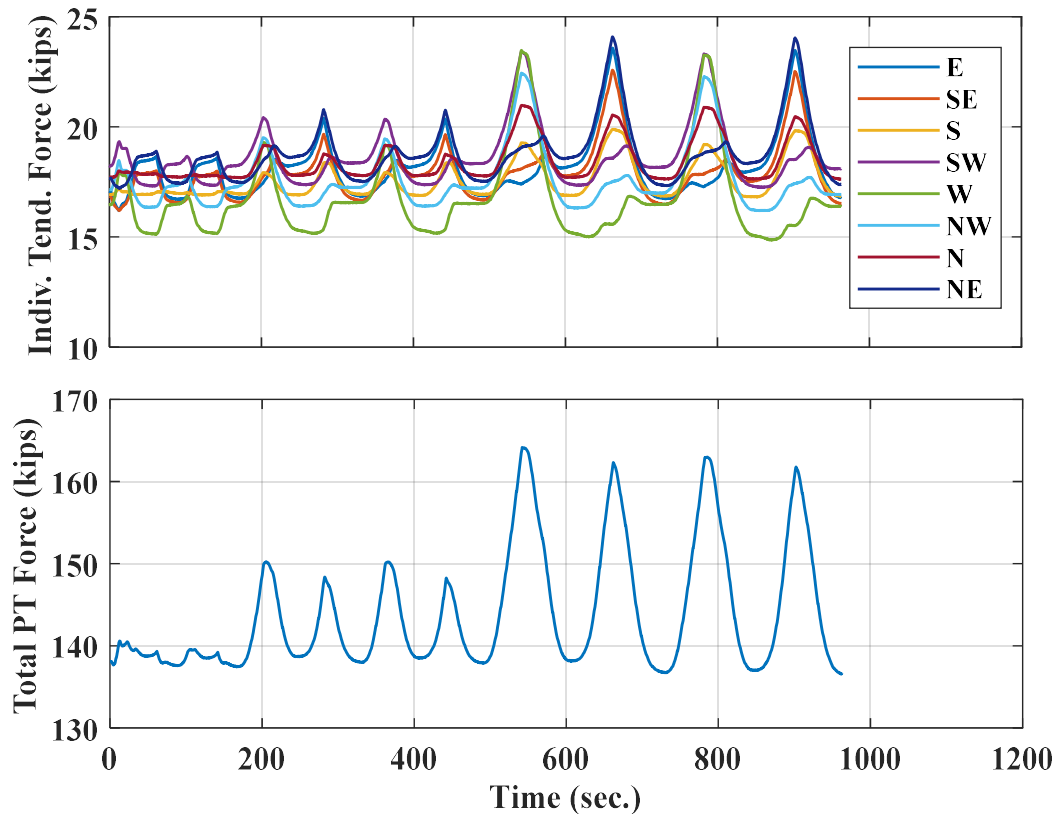
Figure 4-80. Phase I, loading protocol HSR4_UN_CNT_S1_DR_2: time histories of posttensioning forces

As expected, given that a large portion of the displacement imposed to the column was accommodated through sliding, the additional column damage with respect to the previous test was minimal. The new hairline cracks emerged on the surface of the bottom segment are marked in the photos shown in Figure 4-81. No damage was noticed around the sliding joint interfaces (e.g. separation of PTFE from the steel plate or PTFE wearing).

247
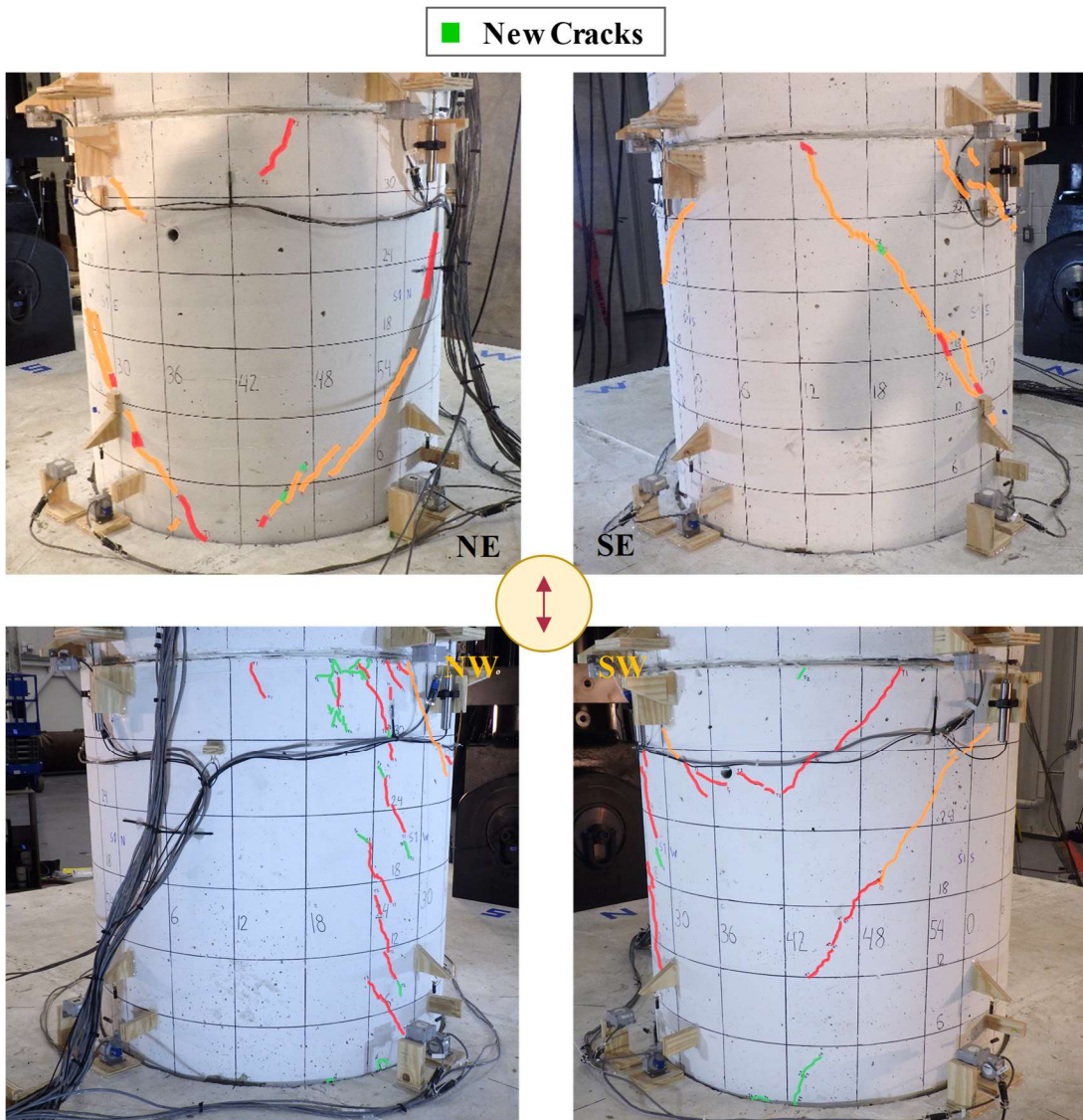
Figure 4-81. Phase I, loading protocol HSR4_UN_CNT_S1_DR_2: distribution of cracks on bottom segment after test

The base shear vs. lateral displacement response of the column under the loading protocol HSR4_UN_CNT_S1_DR_4 (peak drift ratio = 4%) is depicted in Figure 4-82. The base shear required to initiate sliding was 28.5 kips, which is almost 14% lower than that in the previous test (33 kips). This difference can be associated with both the PT loss

(Figure 4-88) and the reduction of coefficient of friction at the first sliding joint due to its previous sliding history. The second sliding joint did not exhibit sliding in this test, too (Figure 4-83).
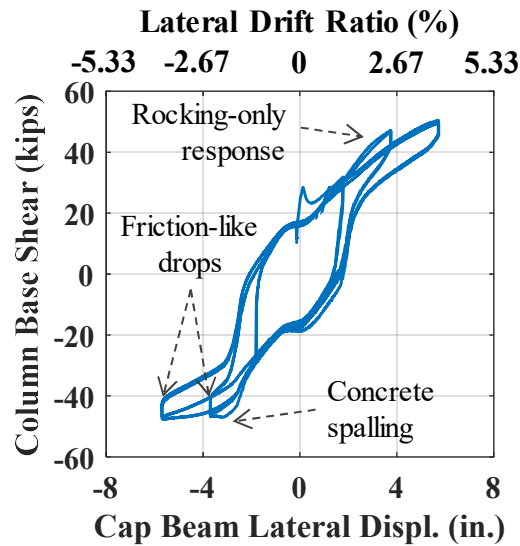
Figure 4-82. Phase I, loading protocol HSR4_UN_CNT_S1_DR_4: base shear vs. lateral displacement response
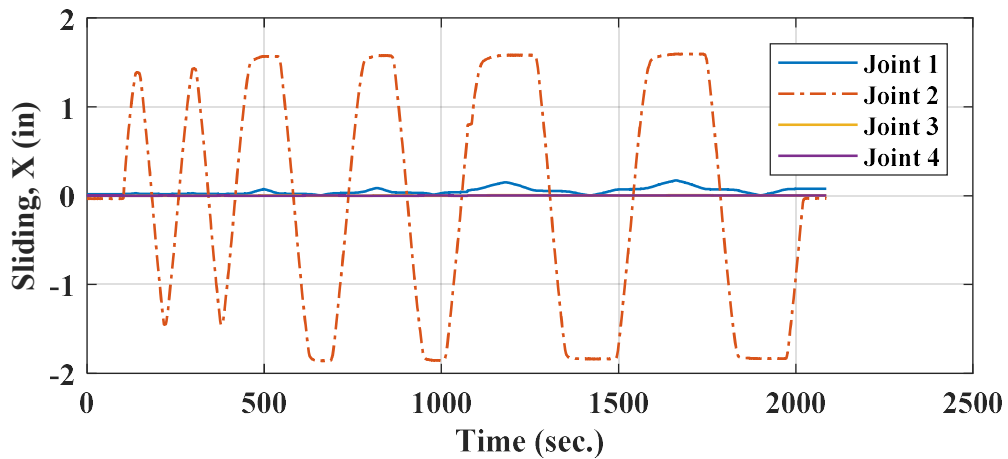
Figure 4-83. Phase I, loading protocol HSR4_UN_CNT_S1_DR_4: joint sliding time histories in *X* direction

249

Similarly to the previous test, base shear drops are observed at the load reversals, which mainly resulted from the friction forces between the tendons and their ducts (see Figure 4-75). The evidence of the direction change of the friction forces with the load reversals is found in the variations of the south tendon's end forces with lateral displacement as shown in Figure 4-84. As seen, the force at the bottom end of that specific tendon droped up to 3-4 kips at load reversals, particularly when rocking was dominant.
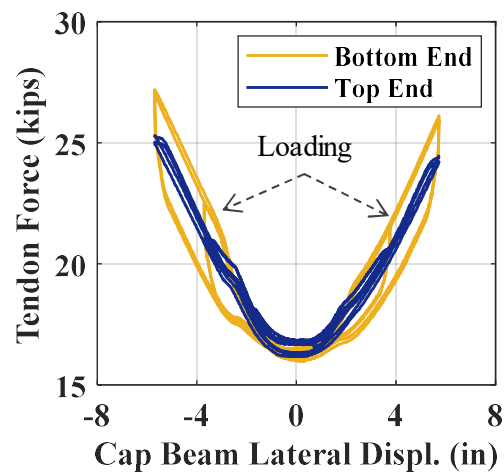
Figure 4-84. Phase I, loading protocol HSR4_UN_CNT_S1_DR_4: south tendon end forces vs. lateral displacement

While the column did not exhibit noticeable strength/stiffness deterioration during the first two and half cycles, its strength had a slight drop near the first negative displacement peak from the third cycle with a drift ratio amplitude of 2.67%. This strength drop, which was followed by stiffness deterioration in the following cycles in the same direction, resulted from small concrete spalling at the lower part of the west face of the bottom column segment (Figure 4-90). The stiffness and strength deteriorations observed near the

positive displacement peaks of the last two cycles were also caused by limited concrete spalling on the opposite side, i.e. the lower part of the east face of the bottom column segment (Figure 4-90). It should be noted that the concrete spalling could be delayed if the second sliding joint (Joint 3) had exhibited sliding.

In spite of the concrete damage, the maximum shear values emerged in the column when subjected to the highest displacement demands (i.e. 6 in.) in the positive and negative directions were 50.5 kips and 48 kips, respectively, indicating the symmetry of the column's response. The average of the residual lateral displacements in the two directions during the last two cycles were found to be close to 1.95 in. (equal to 1.3% drift ratio), about 84% of which was contributed by the residual sliding (Figure 4-85).

The sliding time histories for all the column joints are displayed in Figure 4-83. Very small sliding (less than 0.2 in.) is observed at the bottom rocking joint (Joint 1), which could be due to the effect of rocking on the measurements (see also Figure 4-85), but the second sliding joint (Joint 3) did not exhibit any sliding. After the first two displacement cycles, the first sliding joint (Joint 2) reached its maximum sliding capacity in both directions. The maximum sliding in both directions remained almost constant thereafter, though, which implies no cyclic damage to the ducts. The difference between the maximum sliding achieved in the two opposite directions (+1.6 in. and -1.84 in.), which is more obvious in Figure 4-85, is attributed to the duct misalignments and measurement errors. Because that there was zero sliding at the second sliding joint (Joint 3), up to 69% of the total lateral displacement was accommodated through rocking (Figure 4-86).
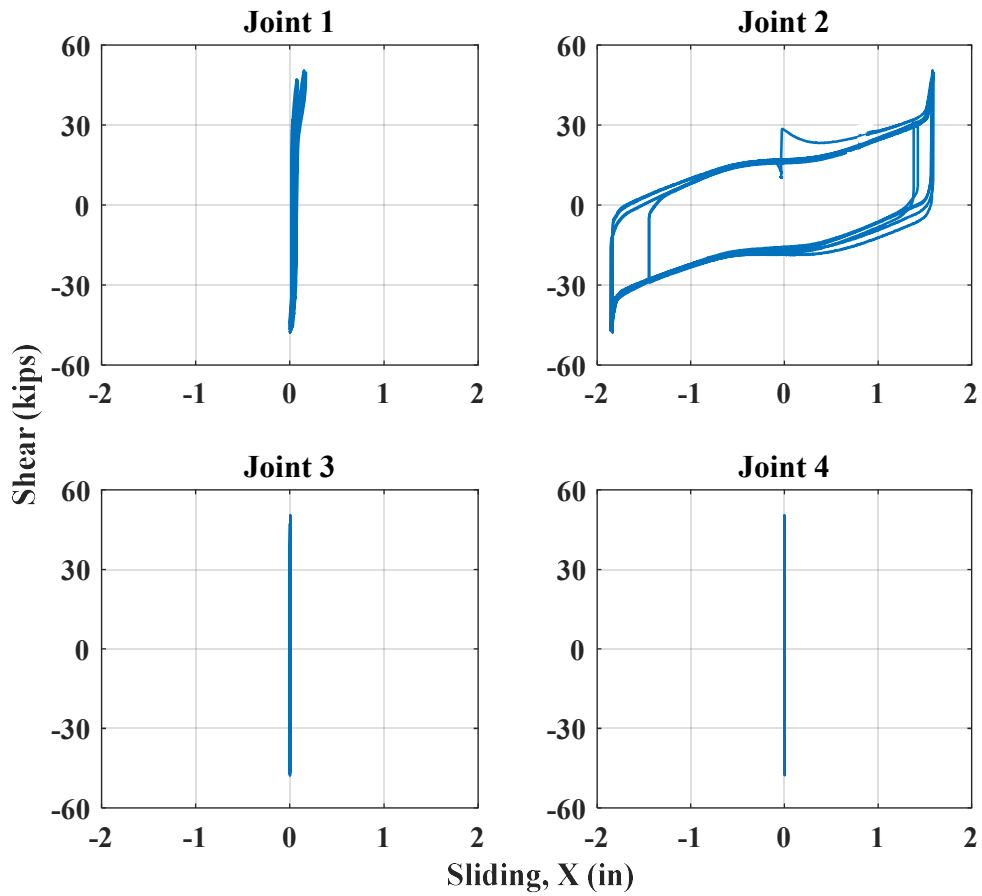
Figure 4-85. Phase I, loading protocol HSR4_UN_CNT_S1_DR_4: joint shear vs. sliding responses in *X* direction
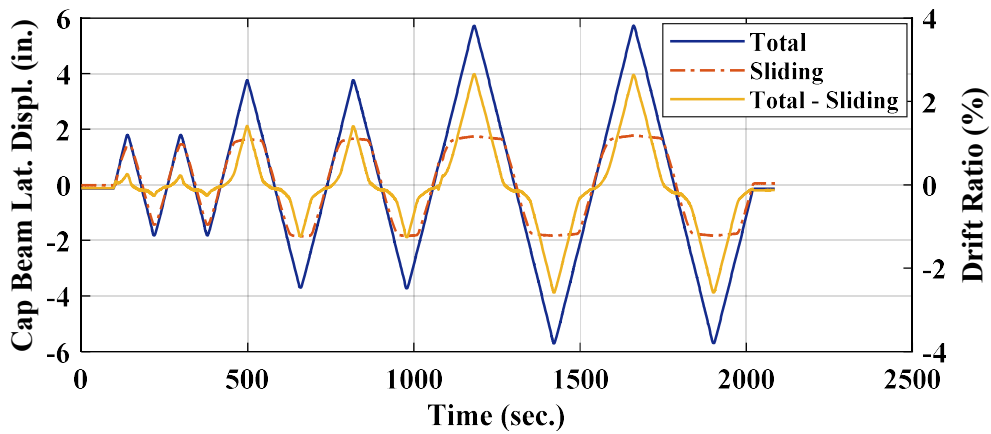
Figure 4-86. Phase I, loading protocol HSR4_UN_CNT_S1_DR_4: time histories of lateral displacement components

252

The moment vs. rocking responses of the joints during this test are shown in Figure 4-87. Although the maximum rocking values for Joint 1 during the first four displacement cycles were similar in both directions, after a more severe concrete spalling occurred on the west side of the column than its east side (Figure 4-90), the rocking in the negative direction exceeded that in the positive direction by 20%. The measured rocking in the upper joints was less than a tenth of the rocking at the bottom rocking joint (Joint 1).
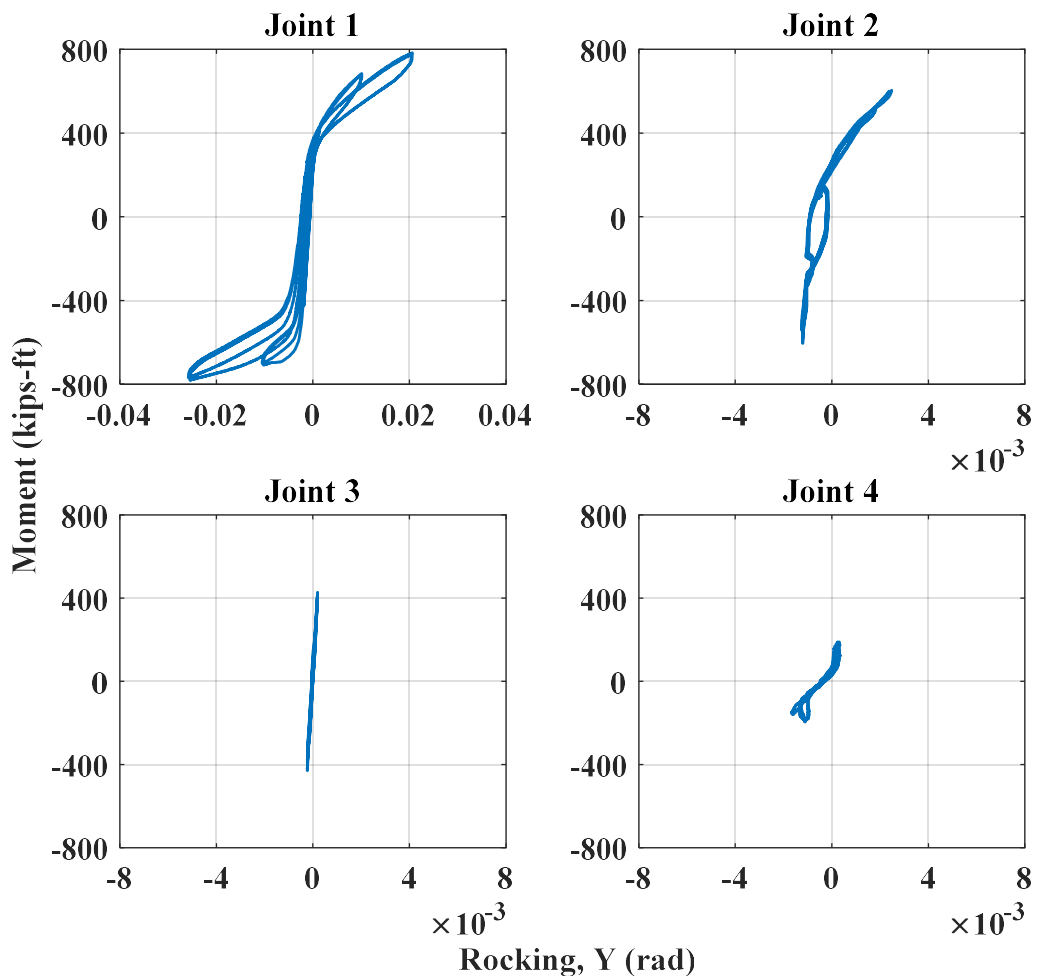
Figure 4-87. Phase I, loading protocol HSR4_UN_CNT_S1_DR_4: joint moment vs. rocking responses around *Y*-axis

The variation of the individual tendon forces and the total posttensioning force with time are demonstrated in Figure 4-88. As expected, the tendons on the east and west sides of the column cross section sustained the largest forces at the displacement peaks in the negative and positive directions, respectively, but none of them yielded. The maximum PT forces in those tendons were, however, very close. Particularly during the last two displacement cycles, mainly due to the concrete damage near the bottom rocking joint, a gradual loss is observed in the total PT force. The total PT loss during this test was 8%, which is mainly associated with the movement of the wedge inside the barrel chucks under large tendon forces (Sideris et al. 2014a).
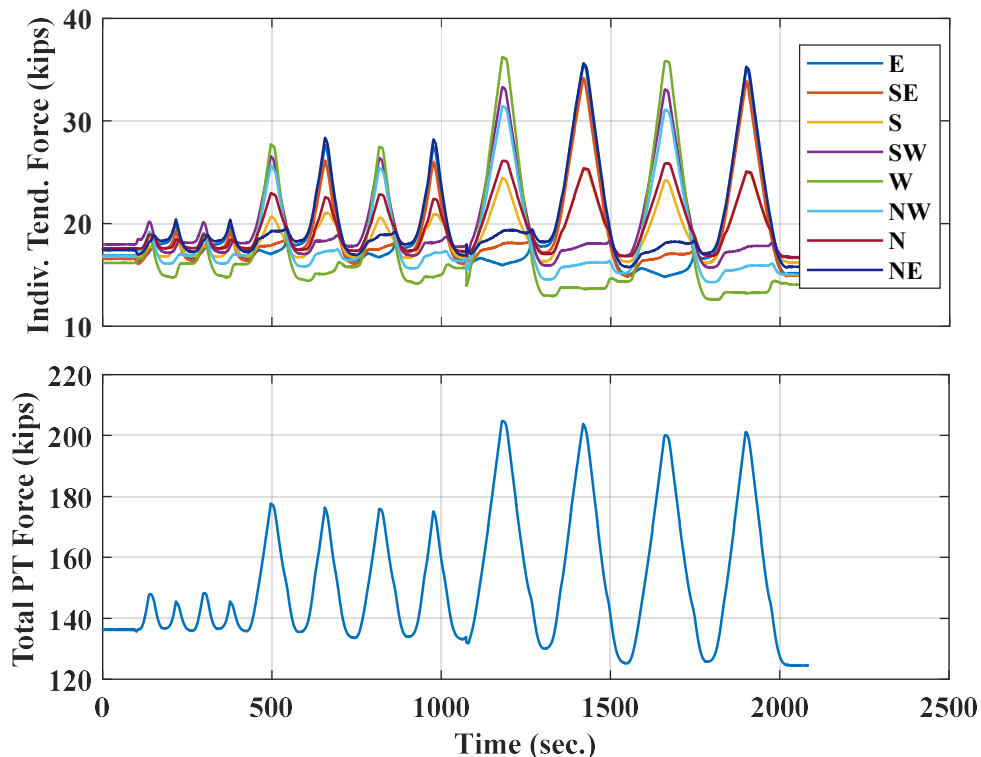
Figure 4-88. Phase I, loading protocol HSR4_UN_CNT_S1_DR_4: time histories of posttensioning forces
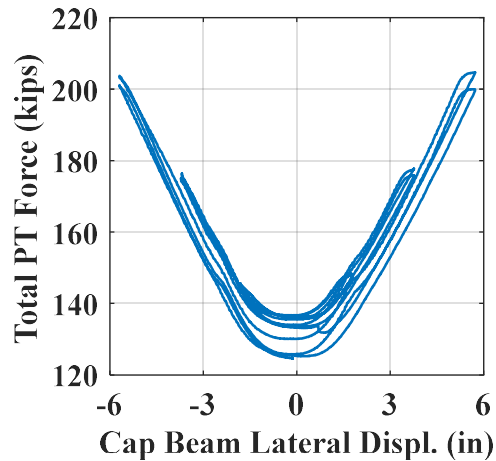
Figure 4-89. Phase I, loading protocol HSR4_UN_CNT_S1_DR_4: total PT force vs. lateral displacement

After the test was completed, the majority of the new cracks were concentrated in the bottom segment, especially close to the compression toes on the east and west sides (Figure 4-90). Slight spalling was also observed under the first sliding joint, on the west side (Figure 4-91). This damage was caused by the compressive stress concentration near the west edge of the sliding surface on the bottom segment, caused by rocking at this joint and surface unevenness. The depth of the spalled concrete on the west side of the bottom column segment was about 3/4 in. and it spread up to 6 in. above the rocking joint. On the east side, the depth of the spalled concrete was lower, but the spalling spread up to 10 in. above the rocking joint. The first hairline cracks on the upper segments were also observed after this test (Figure 4-92).
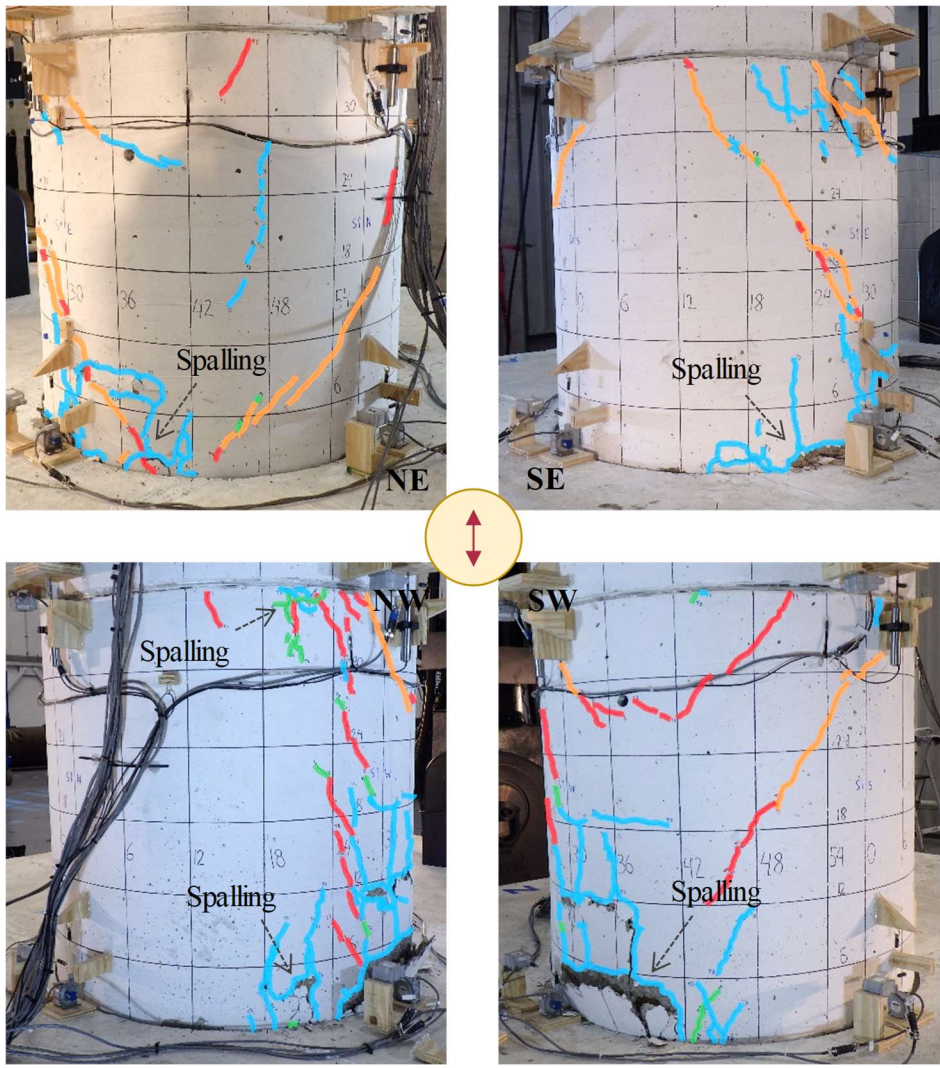
Figure 4-90. Phase I, loading protocol HSR4_UN_CNT_S1_DR_4: distribution of cracks on bottom segment after test
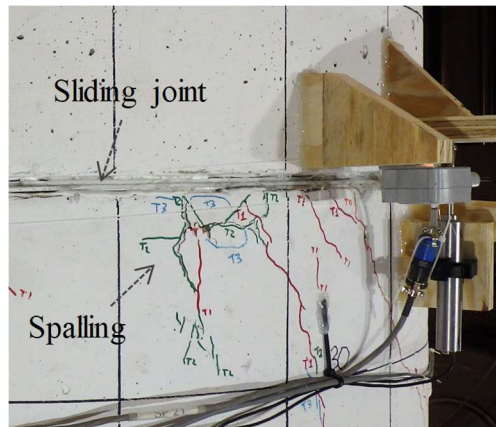
Figure 4-91. Phase I, loading protocol HSR4_UN_CNT_S1_DR_4: slight spalling below first sliding joint on west side
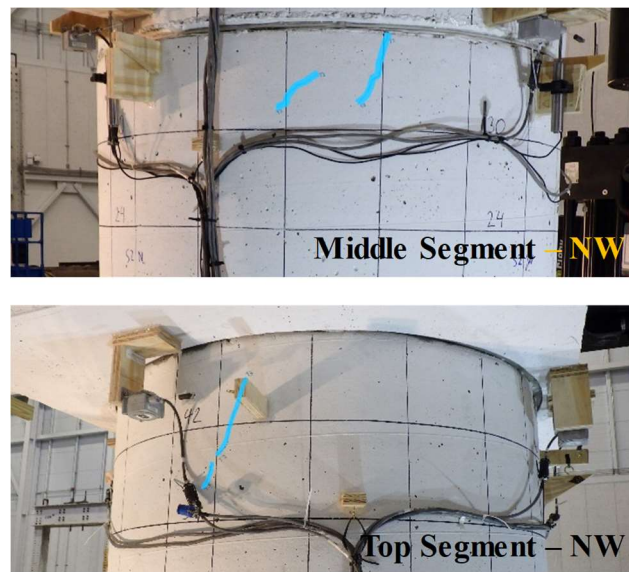
Figure 4-92. Phase I, loading protocol HSR4_UN_CNT_S1_DR_4: cracks on middle and top segments after test

The complete hysteretic response of the column specimen under the loading cycles of Loading Set 1 with increasing amplitudes (i.e. drift ratios 0.43%, 0.87%, 1.3%, 2%, 2.67%, and 4%) is demonstrated in Figure 4-93. Note that the response cycles with

intermediate displacement amplitudes that were lower than the maximum amplitude experienced by the column in prior loading protocols are not included in the plot.
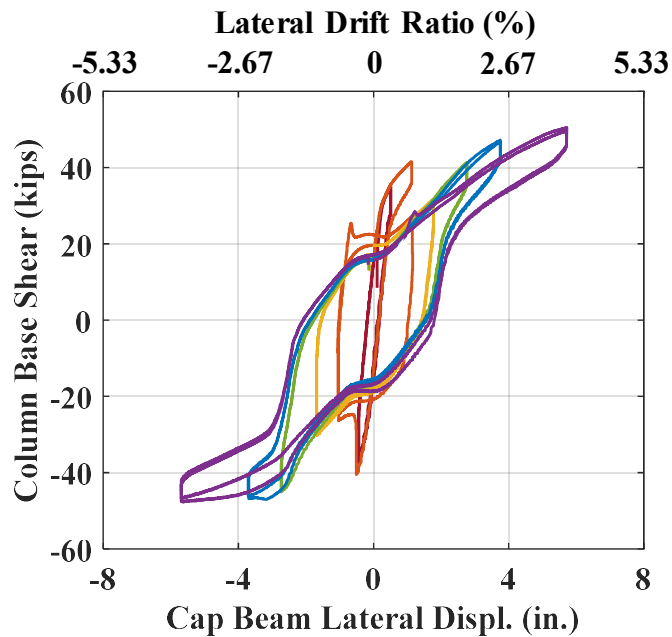
Figure 4-93. Phase I, Loading Set 1: complete base shear vs. displacement response of column under displacement cycles of increasing amplitude

In order to understand the general trend of the responses of the HSR column specimen under various peak drift ratio demands, the effective viscous damping ratios and the residual drift ratios obtained during different displacement cycles imposed to the column in Loading Set 1 are compared. From the base shear vs. lateral displacement response of the column under a given displacement cycle, the effective viscous damping ratio, ζ_{eff}, and the residual displacement, Δ_{res}, can be estimated as (Figure 4-94):

$$\begin{cases} \zeta_{\textit{eff}} = \dfrac{E_d}{2\pi K_{\text{sec}} \Delta_{\max}^2} \\[4mm] \Delta_{\textit{res}} = \dfrac{\Delta_{\textit{res}}^+ - \Delta_{\textit{res}}^-}{2} \end{cases} \quad \text{with} \quad \begin{cases} E_d = \displaystyle\int V d\Delta \\[3mm] \Delta_{\max} = \dfrac{\Delta_{\max}^+ - \Delta_{\max}^-}{2} \\[4mm] K_{\text{sec}} = \dfrac{V_{\max}^+ - V_{\max}^-}{\Delta_{\max}^+ - \Delta_{\max}^-} \end{cases} \tag{4-11}$$

where E_d is the energy dissipated during the considered cycle; K_{sec} is the column's secant stiffness; Δ_{res}^- and Δ_{res}^+ are the residual displacements in the negative and positive directions, respectively; V and Δ represent base shear and lateral displacement, respectively; Δ_{max}^- and Δ_{max}^+ are the peak displacements achieved in the negative and positive directions, respectively; and V_{max}^- and V_{max}^+ are the base shear values corresponding to Δ_{max}^- and Δ_{max}^+, respectively.
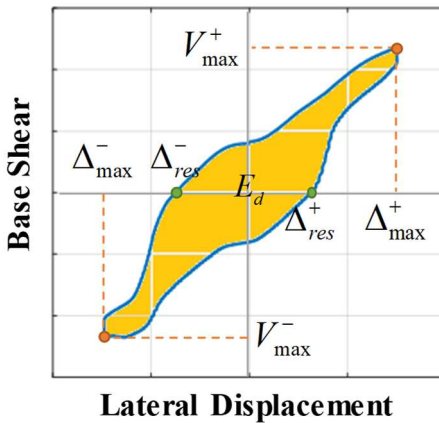
Figure 4-94. Response parameters used to obtain effective damping ratio and residual displacement

The effective damping ratios and residual drift ratios obtained per Eqs. (4-11) for various peak drift ratios considered for the displacement cycles in Loading Set 1 are

compared in Figure 4-95. The maximum effective damping ratio is achieved for a peak drift ratio of 0.87%. The effective damping ratio decreases with the peak drift ratio after the above value, as the activated sliding joint reaches its maximum sliding capacity.

The residual drift ratio increased with the peak drift ratio, while the maximum residual drift ratio (for a peak drift ratio of 4%) was 1.3%. According to Figure 4-95, the largest portion of the residual drift ratios was contributed by the residual joint sliding. For example, for a peak drift ratio of 4%, almost 85% of the total residual drift ratio was contributed by residual joint sliding.
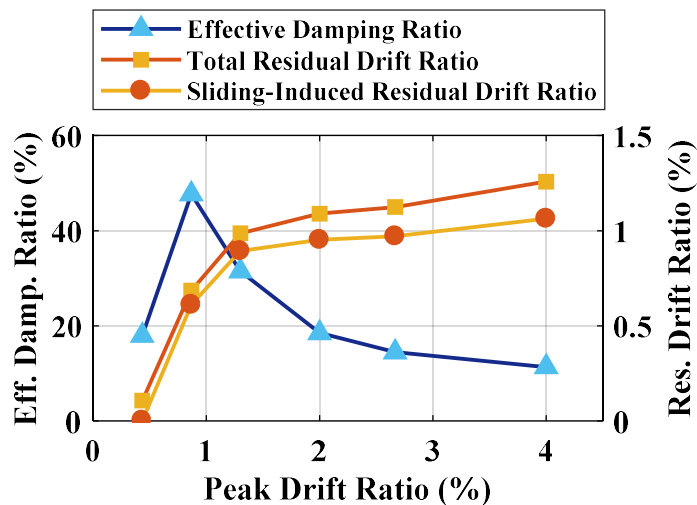
Figure 4-95. Phase I, Loading Set 1: variation of effective damping ratio and residual drift ratio with peak drift ratio

The variations of peak and residual total sliding with peak drift ratio are also shown in Figure 4-96. It is observed that for the peak drift ratios lower than 1.3%, the residual sliding values equaled the peak sliding values. For larger drift ratios, however, the peak sliding remained almost constant with the increase of peak drift ratio, but the residual

sliding values were up to 13% smaller. This finding indicates the slight, yet existent, sliding self-centering capability of the tendons. For the peak drift ratio of 4%, although the peak sliding remains similar to that for the lower peak drift ratios, the residual sliding slightly increases; this can be attributed to the larger posttensioning loss in the cycle of 4% drift ratio amplitude (Figure 4-97) and the damage of the tendons ducts under bearing forces.
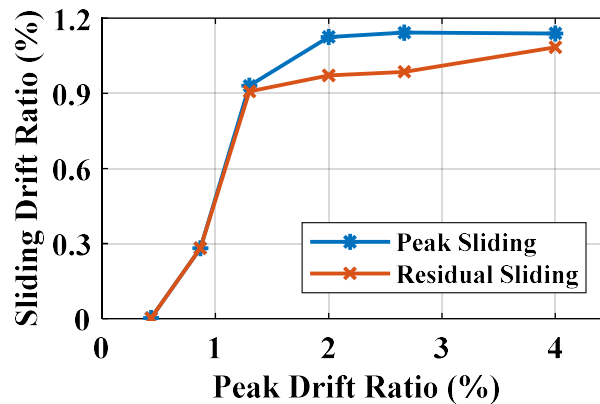
Figure 4-96. Phase I, Loading Set 1: variation of peak and residula sliding with peak drift ratio

The recorded total posttensioning force at the end of each pair of displacement cycles with the same peak drift ratio and their respective calculated losses are plotted against the peak drift ratio in Figure 4-97. As expected, the PT loss was small for the drift ratios less than 2%, because the sliding capacity at the first sliding joint was large enough to prevent the column from large rocking motions and the resulting PT losses. However, as the peak drift ratio became larger, the PT losses increased (e.g. more than 6% for 4% peak drift ratio). The observed trend in the PT losses is believed not to be specific to the HSR

261

columns and is mainly caused by the wedge setting in the anchorage hardware as the PT

forces increase. That said, such losses may not generally be an indicator of tendons'

yielding or localized damage.
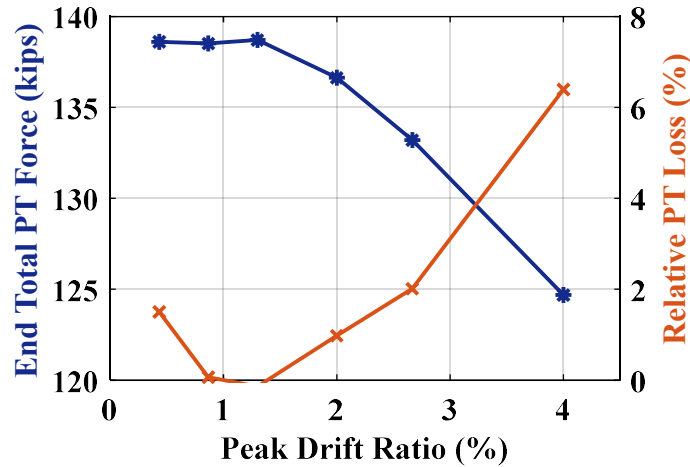
Figure 4-97. Phase I, Loading Set 1: variation of end total PT force and PT loss with peak drift ratio

4.7.1.5.3. Results from Loading Set 2

The variations of the column's axial force with time in the three tests conducted under

the loading protocols of Loading Set 2 (Table 4-15) are demonstrated in Figure 4-98. It

is noted that the computed axial force includes the vertical load applied by actuators,

supported components' weights, and posttensioning forces. Clearly, the maximum axial

forces were higher when the peaks of the displacement cycles and the positive peaks of

the applied vertical load cycles coincided, as the posttensioning forces reached their

maximum at the displacement peaks. Per Figure 4-98, the maximum axial force imposed

to the column specimen under these loading protocols was about 456 kips (= 0.16 $f'_c A_g$).

According to Figure 4-99, the column bases shear is observably affected by the column's axial force variation, particularly because the friction force at the first sliding joint depended on the pressure existing at the joint. It is noted that the effect of axial force on the friction force is two-fold, as its increase can both heighten the frictional stresses by increasing the contact pressure and lower the frictional stresses by decreasing the coefficient of friction (due to its pressure-dependence). As a result of this, although the combined effect was the friction increase in the tested HSR column specimen, the relative increase observed in the column base shear was not proportionate to the relative increase in the axial forces, but was lower.
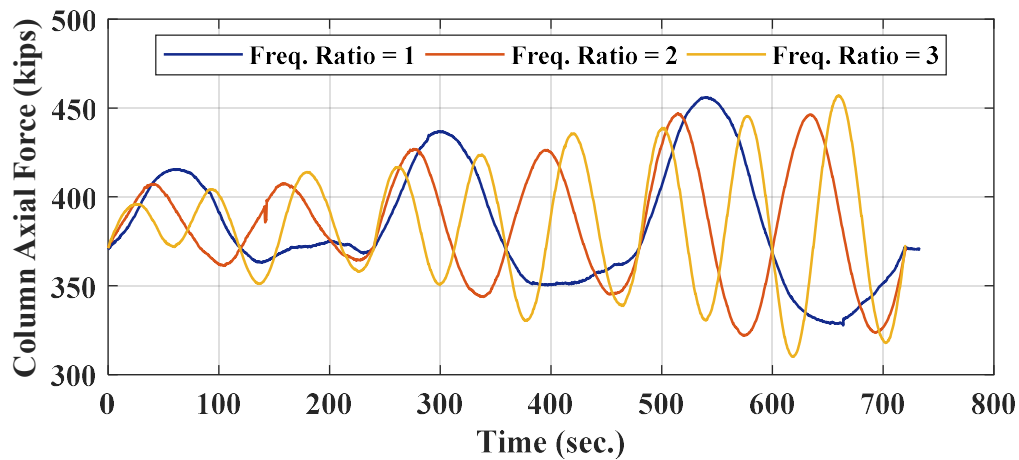
Figure 4-98. Phase I, Loading Set 2: time histories of column axial force

The time histories of the sliding at Joint 2 and the rocking at Joint 1 obtained under Loading Set 2 are shown in Figure 4-100(a) and (b), respectively. It is observed that the axial force variation, regardless of its relative frequency, had minimal effect on the sliding and rocking responses of the column joints. This is mainly because the maximum

263

amplitude of load variation was less than 20% of the total vertical load on the column. According to Figure 4-100(b) and for loading protocol HSR4_UN_CNT_S2_V2H_1 (Frequency Ratio = 1), when the force applied by the vertical actuators was 30% lower than its reference value, the maximum rocking of the column at its bottom joint increased only about 8% compared to the respective value when the load applied by the vertical actuators was 20% lower than its reference value.
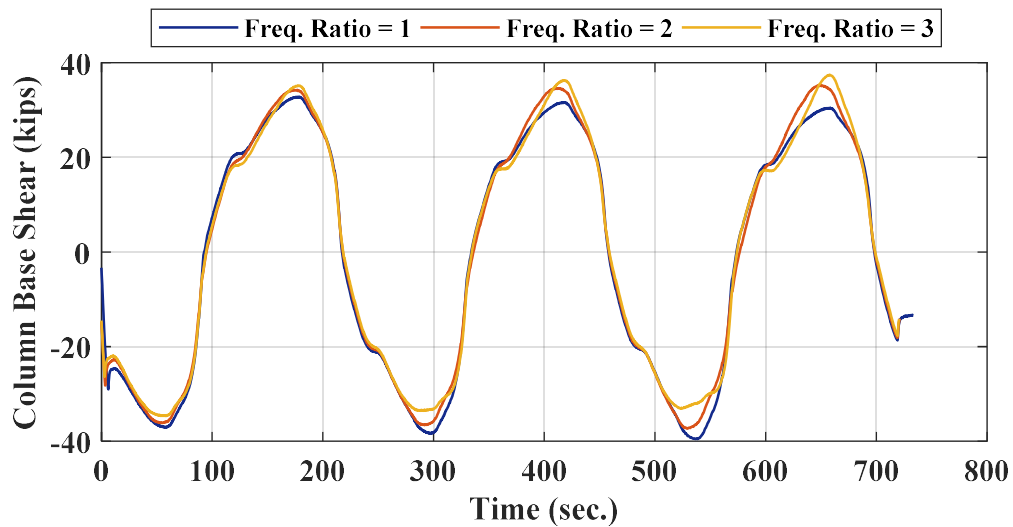
Figure 4-99. Phase I, Loading Set 2: time histories of column base shear

During the three tests conducted under Loading Set 2, only a few new hairline cracks appeared on the surface of the bottom column segment and the concrete spalling started in Loading Set 1 did not grow. Around the sliding joints, however, small amounts of grease were observed to have been pressed out of the sliding joints (Figure 4-101). The amount of this grease on the east and west sides of the first sliding joint was higher, because the sliding had helped with the grease expelling.
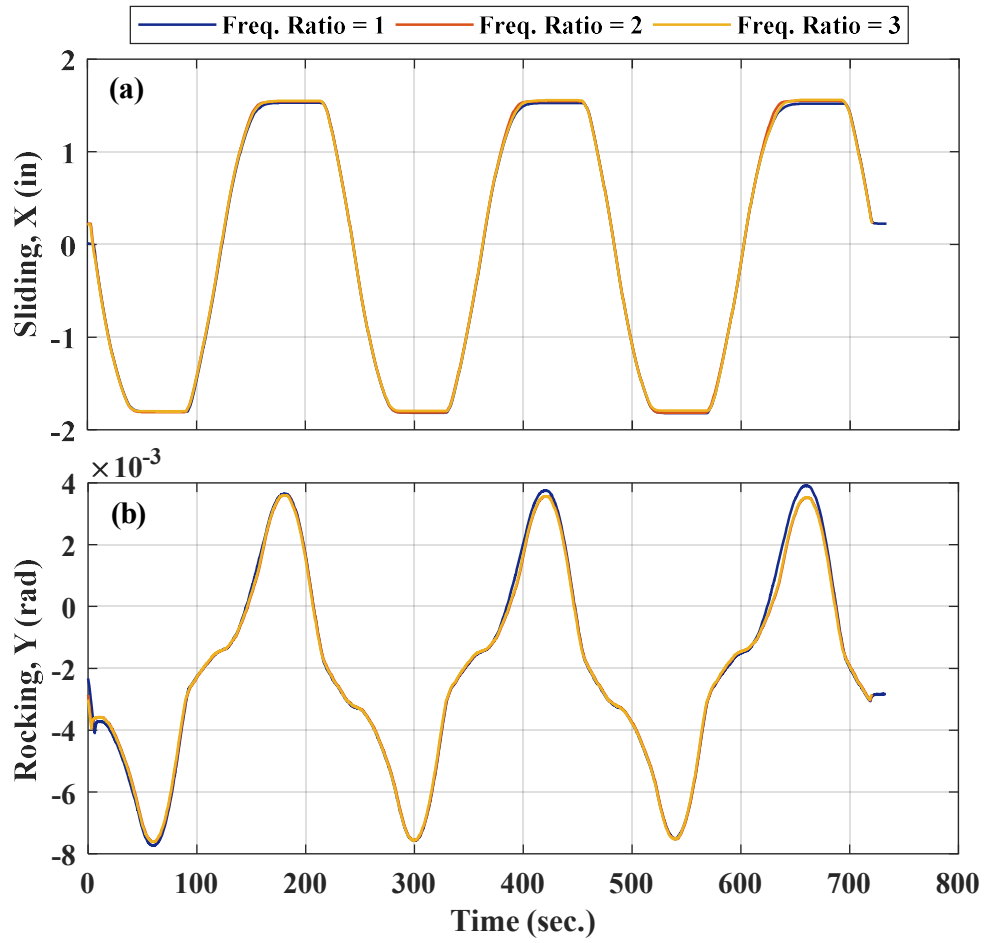
Figure 4-100. Phase I, Loading Set 2: (a) sliding time histories for Joint 2; (b) rocking time histories for Joint 1
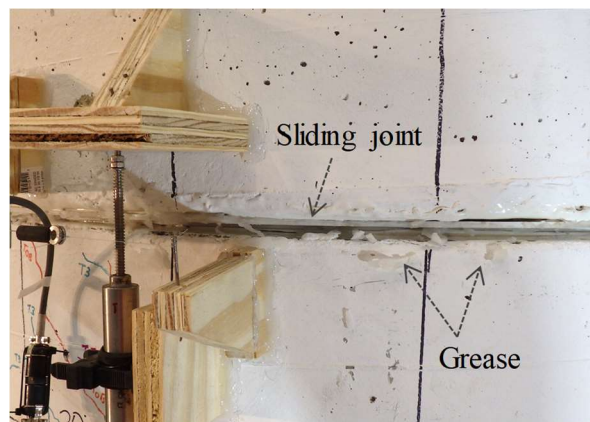
Figure 4-101. Phase I, Loading Set 2: grease pressed out of first sliding joint

4.7.1.5.4. Results from Loading Set 3

The loading beam displacement time histories achieved during the tests under the last three loading protocols in Loading Set 3 (Table 4-16) did not acceptably resemble the controller displacement commands, so the respective data is not discussed here. The maximum horizontal acceleration applied to the loading beam in the remaining tests was 0.055g, whose resulting inertia force is deemed negligible.

Figure 4-102(a) and Figure 4-102(b) show the column base shear vs. lateral displacement responses and the total posttensioning force vs. lateral displacement responses obtained from the tests under the loading protocols of Loading Set 3, respectively. The breakaway friction and maximum base shear values are found minimally affected by the displacement rate (Figure 4-102(a)). The shapes of hysteresis curves are, however, slightly changed with the increase in displacement rate.
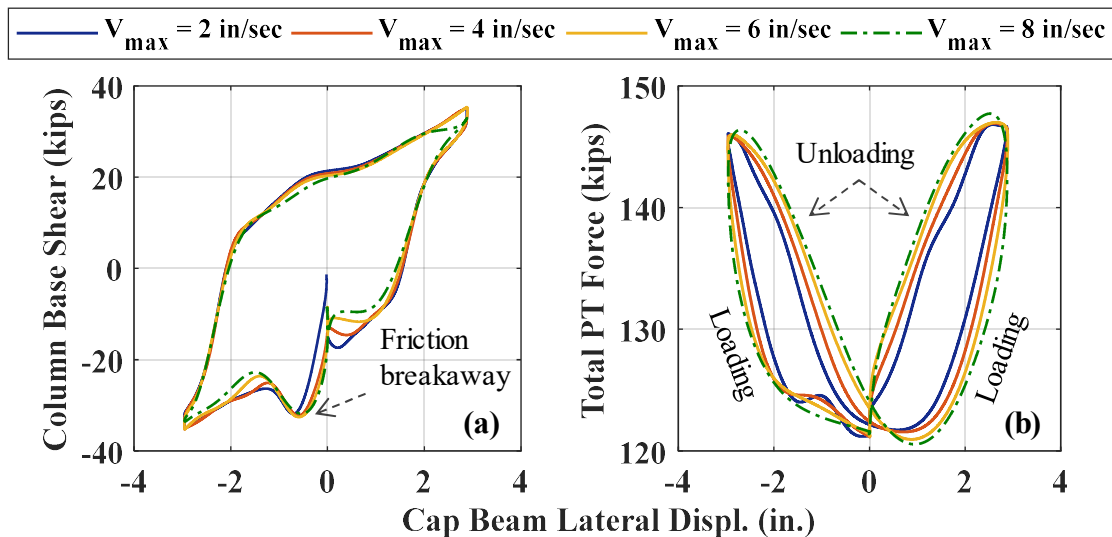
Figure 4-102. Phase I, Loading Set 3: (a) column base shear vs. lateral displacement responses; (b) total PT force vs. lateral displacement responses

266

According to Figure 4-102(b), the posttensioning forces seem to have been more affected by the displacement rate. That is, on the loading paths in both positive and negative directions, the higher the displacement rate was, the smaller the total posttensiong force became. In the unloading paths, contrarily, the posttensioning forces increased with displacement rate. In spite of these trends, which can be attributed to the higher friction between the tendons and the ducts under faster movements, the maximum recorded PT forces were very close.

In terms of joint siding, regardless of the displacement rate, only the first sliding joint (Joint 2) was activated in the above tests. The column base shear vs. sliding responses of the first sliding joint obtained under the loading protocols of the maximum displacement rates 2 thru 8 in./sec. are compared in Figure 4-103(a). As seen, there is no discernible difference between the maximum sliding values. The same finding is true for the maximum rocking achieved at the bottom rocking joint (Joint 1), as shown in Figure 4-103(b). These results imply the minimal effect of the displacement rates as high as considered here (i.e. 8 in./sec.) on the responses of the sliding and rocking joints.

The column's visible damage was not considerably increased and only a few new hairline cracks appeared on the outside surfaces of the bottom and the top column segments. Also, because of the fast movement of the column, small parts of the concrete spalled in Loading Set 1 fell off the bottom segment (e.g. see Figure 4-104). After the tests, small amounts of PTFE debris were identified around the first sliding joint (Figure 4-105), which had probably resulted from the PTFE wearing due to repeated sliding.
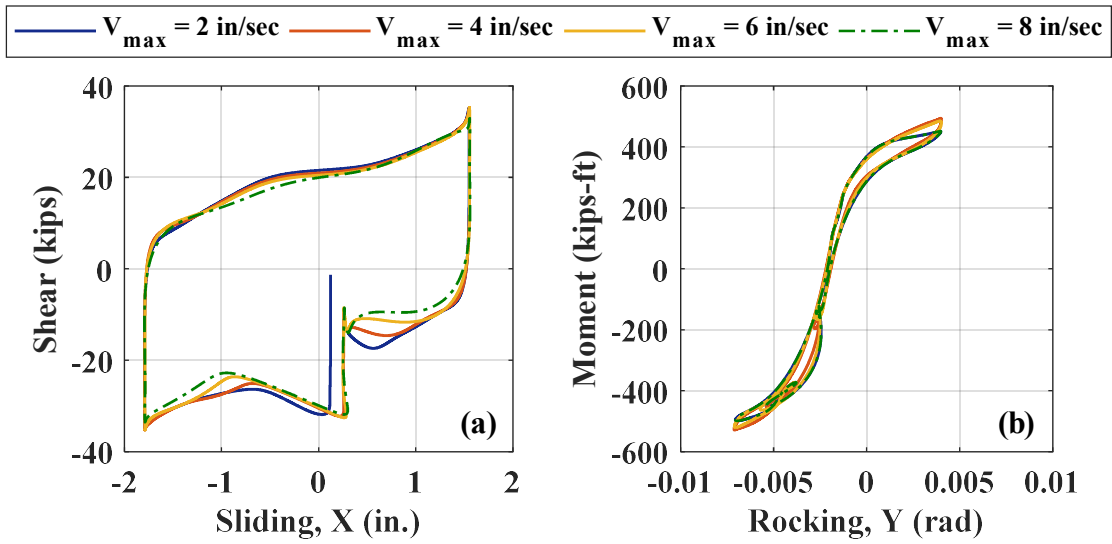
Figure 4-103. Phase I, Loading Set 3: (a) shear vs. sliding responses in *X direction* for Joint 2; (b) moment vs. rocking responses around *Y*-axis for Joint 1

Figure 4-104. Phase I, Loading Set 3: spalled concrete below Joint 2 on west side
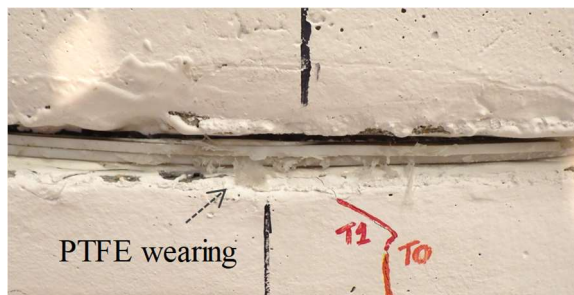
Figure 4-105. Phase I, Loading Set 3: evidence of PTFE wearing at Joint 2

268

4.7.1.5.5. Results from Loading Set 4

A mentioned earlier in Section 4.7.1.4.4, the HSR column specimen was repaired after Loading Set 3 was completed. Some photos from the repaired column are displayed in Figure 4-106, while further details about the concrete repair are found in Appendix F. A detailed evaluation of the effectiveness of the repair method is found in Valigura (2019) and Valigura et al. (2020).
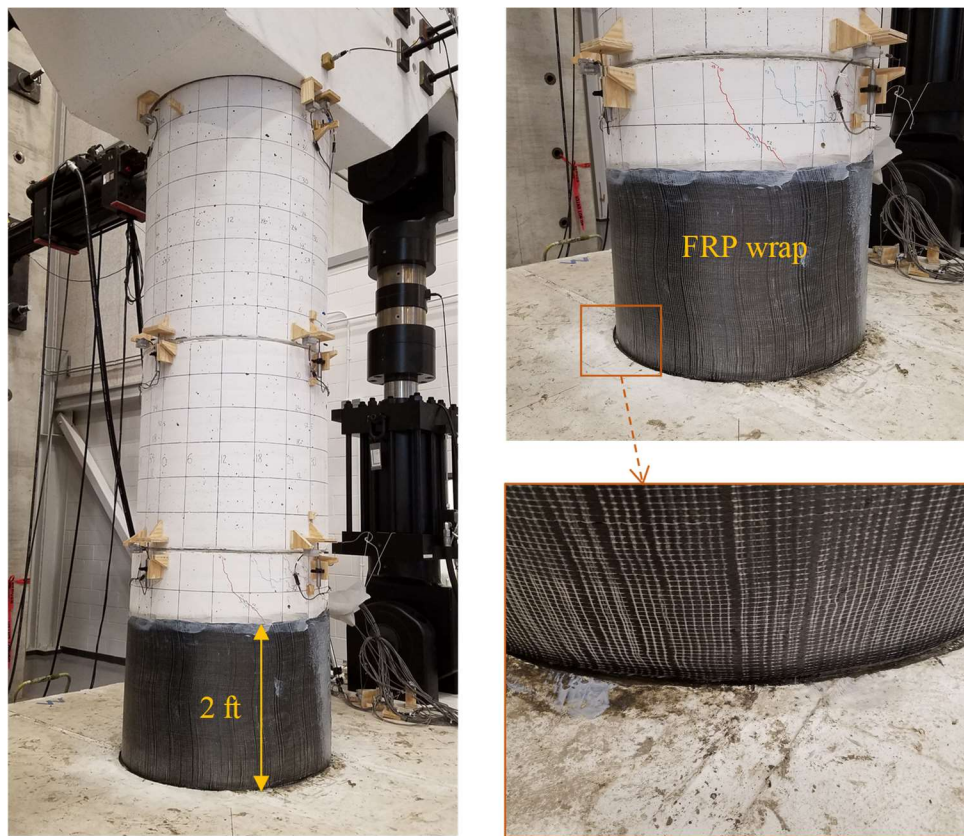
Figure 4-106. Repaired column after Loading Set 3

Here, only the hysteretic responses of the column under the cyclic lateral displacement profiles of Loading Sets 1 and 4, i.e. before and after repair, are compared

(Figure 4-107). Note that the loading in the post-repair tests was started in the negative X direction, i.e. the opposite of the loading direction in the tests in Loading Set 1. The second sliding joint (Joint 3) remained without sliding during the repeated tests, too. According to the graphs displayed in Figure 4-107, in general, the repair method was able to restore the column's original response. The breakaway friction in the repaired column was more than 50% smaller than that in the original column. This is because the grease at the first sliding joint had lost its stickiness due to the many sliding cycles that it had experienced before the new tests. The friction in all the three post-repair tests was also lower than that in the pre-repair tests, mainly because the total posttensioning force before the new tests was 131 kips, as opposed to the initial posttensioning of 141 kips before conducting the tests in Loading Set 1. Slight cyclic stiffness degradation is clear in the last cycle of loading protocol HSR4_UN_CNT_S4_DR_2 and the fourth and sixth cycles of loading protocol HSR4_UN_CNT_S4_DR_4. Such degradation occurred because, while no concrete spalling was possible in the presence of the CFRP wrap, concrete at the segment toes could sustain plastic deformation under the excessive compressive stresses caused by rocking.
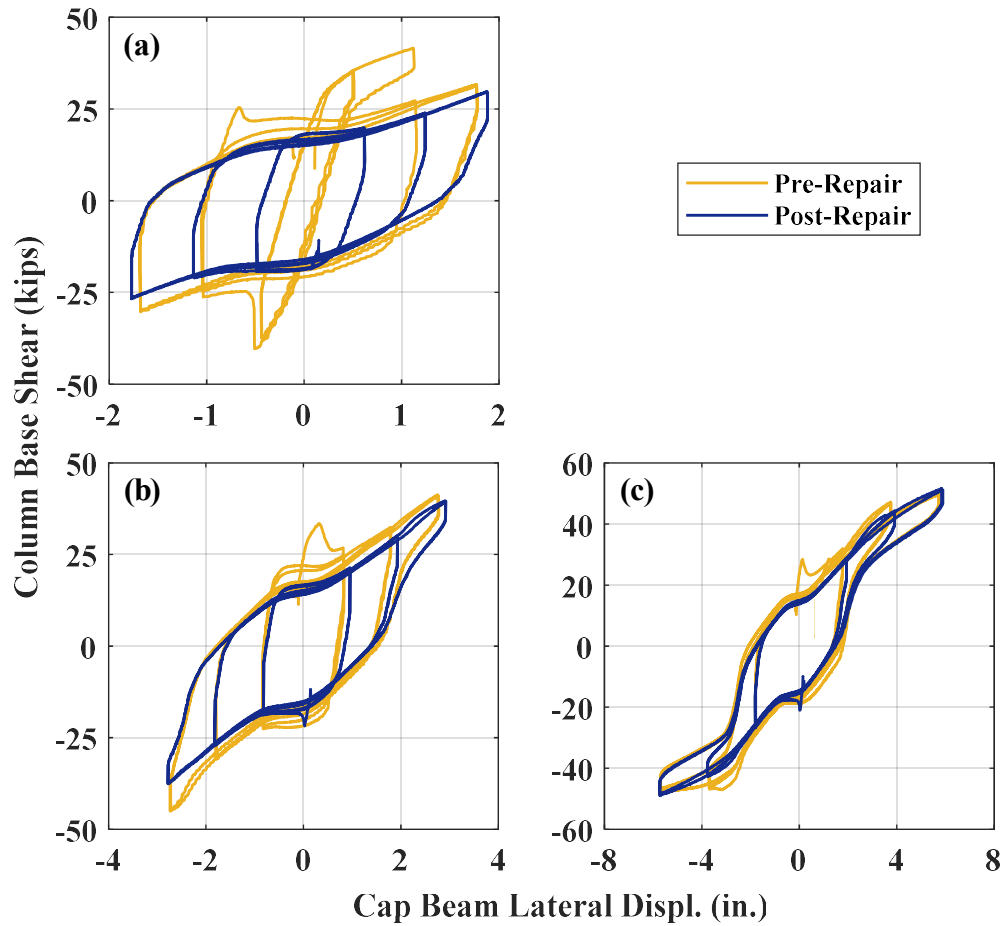
Figure 4-107. Phase I, Loading Set 4 – column base shear vs. lateral displacement responses under loading protocols: (a) HSR4_UN_CNT_S4_DR_1_3; (b) HSR4_UN_CNT_S4_DR_2; (c) HSR4_UN_CNT_S4_DR_4

No new cracks were observed on the column segment surfaces after Loading Set 4. An interesting observation was slippage of grout patch under the CFRP wrap on the west side of the bottom segment during these tests (Figure 4-108), which had occurred due to the low bond between the patch and the original concrete.
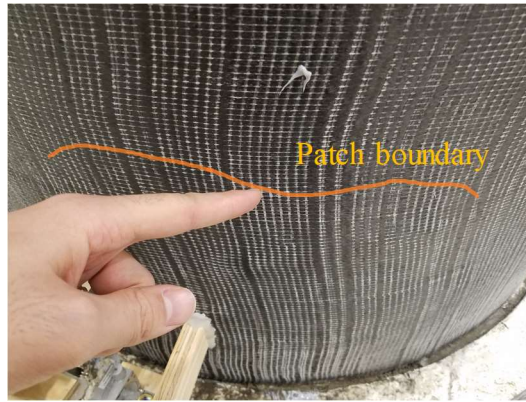
Figure 4-108. Phase I, Loading Set 4: slippage of grout patch under CFRP wrap on west side of bottom column segment

4.7.1.5.6. Results from Loading Set 5

Neglecting the inertia forces, the column base shear vs. lateral displacement responses obtained during the six tests with constant applied vertical load (tests 17-22 in Table 4-18) are shown in Figure 4-109. The second sliding joint (Joint 3) did not get activated during these tests. According to Figure 4-109, all the responses were dominated by the sliding-friction response of the first sliding joint and were similar in shape, without significant cyclic deterioration from one test to the next one. Some rocking also occurred under the last four loading protocols (i.e. HSR4_UN_CNT_S5_H_GM_3 thru 6), which corresponded to the higher hazard levels with 2% and 1% probability of exceedance in 50 years. It is observed in Figure 4-110, which juxtaposes all the plots in Figure 4-109, that the hysteretic responses are enclosed in similar envelopes, except a slightly larger maximum sliding was achieved in the positive direction for the test under HSR4_UN_CNT_S5_H_GM_6 – this additional sliding can be an indicator of damage to the ducts/duct adaptors in the vicinity of Joint 2 and/or PT losses.
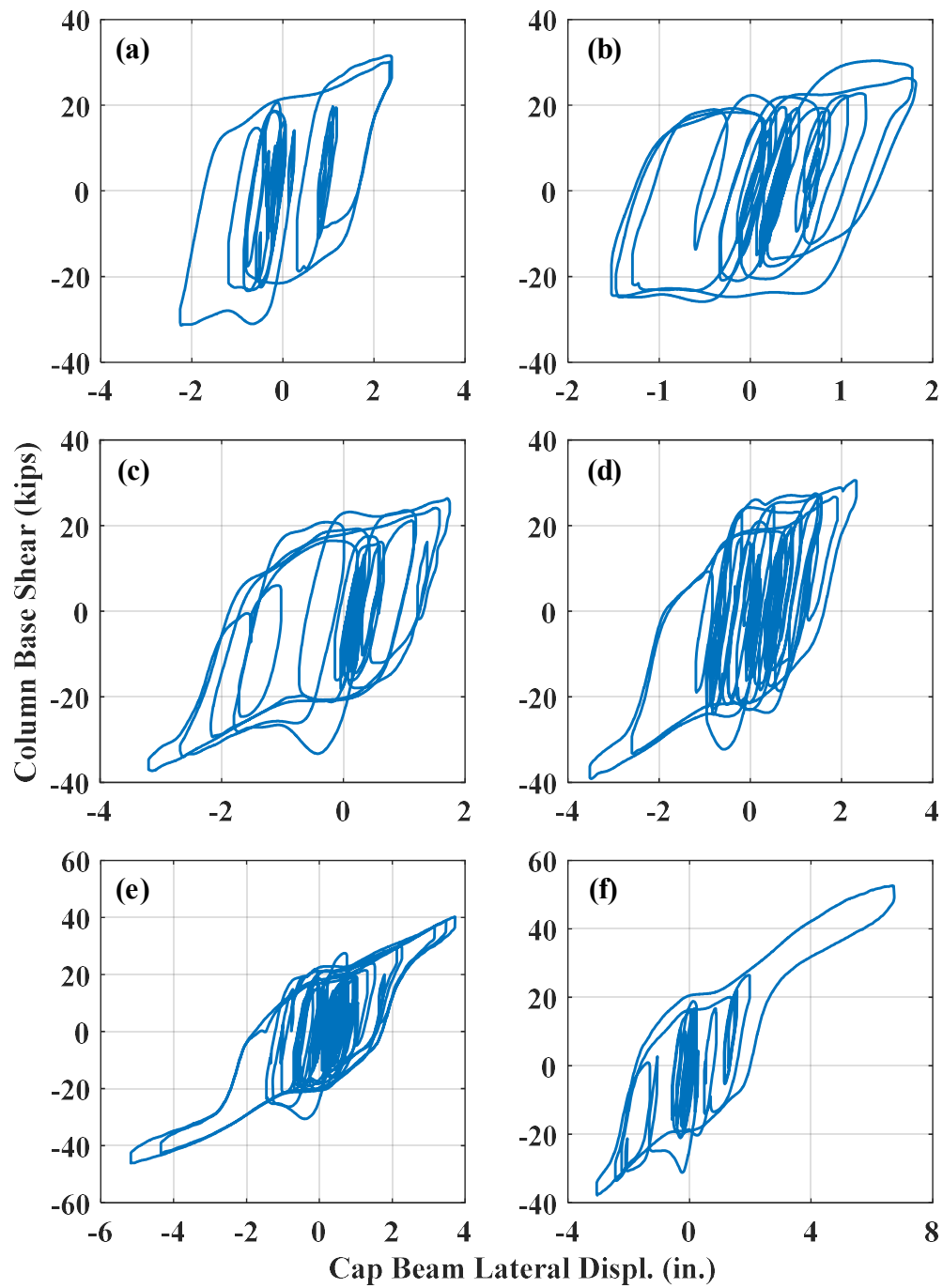
Figure 4-109. Phase I, Loading Set 5: column base shear vs. lateral displacement responses obtained under loading protocols HSR4_UN_CNT_S5_H_GM_ (a) 1; (b) 2; (c) 3; (d) 4; (e) 5; (f) 6
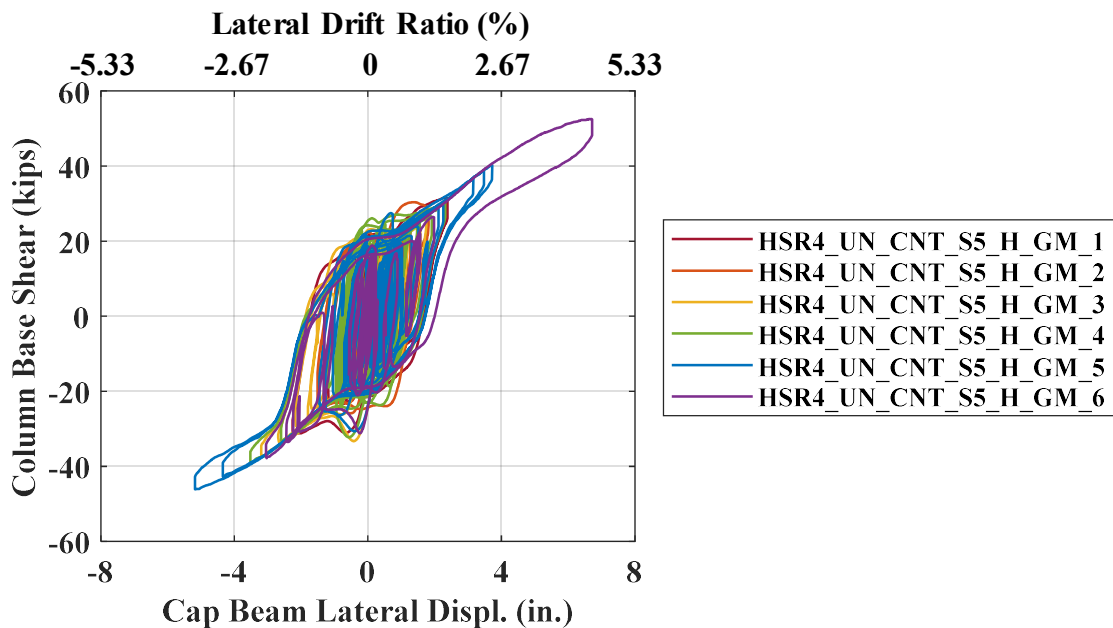
Figure 4-110. Phase I, Loading Set 5: column base shear vs. lateral displacement responses obtained under loading protocols HSR4_UN_CNT_S5_H_GM_1 thru HSR4_UN_CNT_S5_H_GM_6

The time histories of the loading beam's lateral displacement and total sliding achieved during the tests under the same loading protocols are compared in Figure 4-111 and Figure 4-112. The joint sliding is found to have closely followed and accommodated a major portion of the imposed lateral displacement. Due to the stick-slip nature of friction mechanism, the sliding time history exhibited a smoother variation (i.e. unable to accommodate high frequency motions with small amplitudes). In turn, the low-amplitude high-frequency variations were primarily accommodated through rocking. It is also worth noting that, if the second sliding joint (Joint 3) had experienced sliding, the rocking at the bottom joint (Joint 1) would have become even smaller, thereby lowering the risk of concrete and tendon damage.
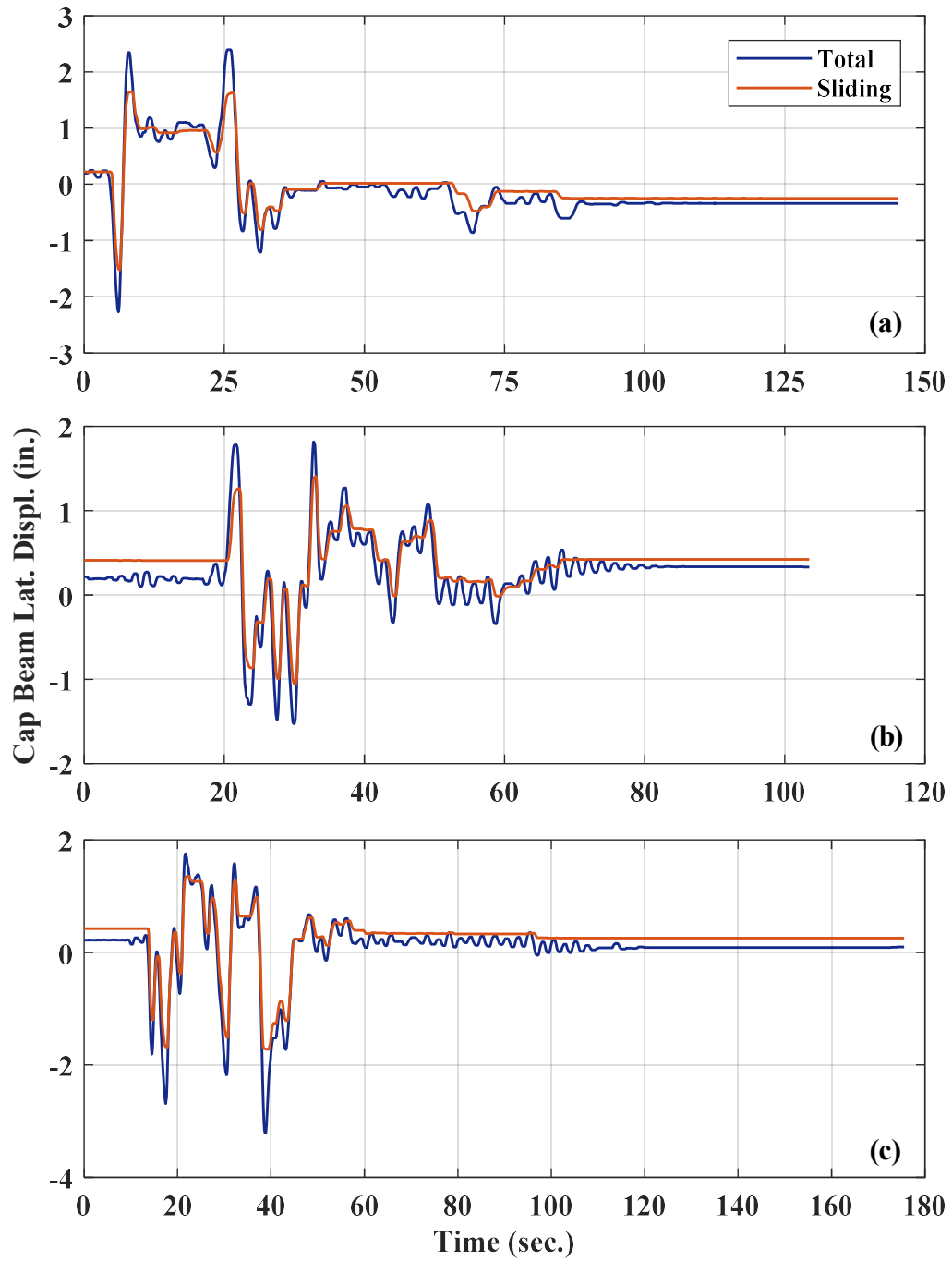
Figure 4-111. Phase I, Loading Set 5: total lateral displacement and sliding time histories under loading protocols: (a) HSR4_UN_CNT_S5_H_GM_1; (b) HSR4_UN_CNT_S5_H_GM_2; (c) HSR4_UN_CNT_S5_H_GM_3

275
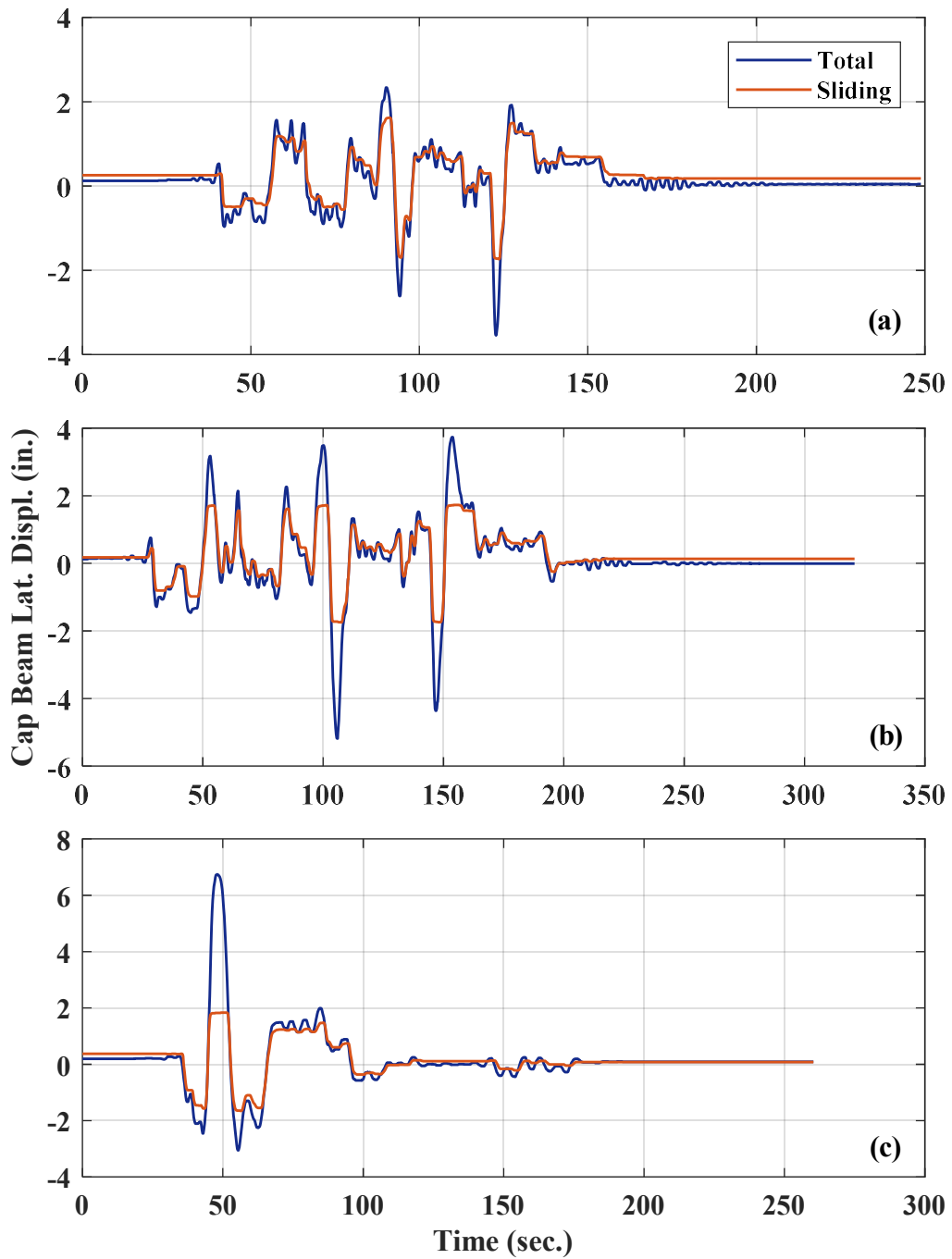
Figure 4-112. Phase I, Loading Set 5 – total lateral displacement and sliding time histories under loading protocols: (a) HSR4_UN_CNT_S5_H_GM_4; (b) HSR4_UN_CNT_S5_H_GM_5; (c) HSR4_UN_CNT_S5_H_GM_6

276

The time histories of the energies dissipated through the entire system, sliding, and rocking, under the same loading protocols (i.e. HSR4_UN_CNT_S5_H_GM_1 thru HSR4_UN_CNT_S5_H_GM_6) are demonstrated in Figure 4-113 and Figure 4-114. According to the plotted results, the energy dissipation resulted from the sliding constituted 81%, 79%, 82%, 76%, 79%, and 71% of the total energy dissipated during loading protocols HSR4_UN_CNT_S5_H_GM_1 thru 6, respectively. The energy dissipated through rocking, however, merely comprised 4%, 5%, 4%, 5%, 6%, and 12% of the total dissipated energy during loading protocols HSR4_UN_CNT_S5_H_GM_1 thru 6, respectively.
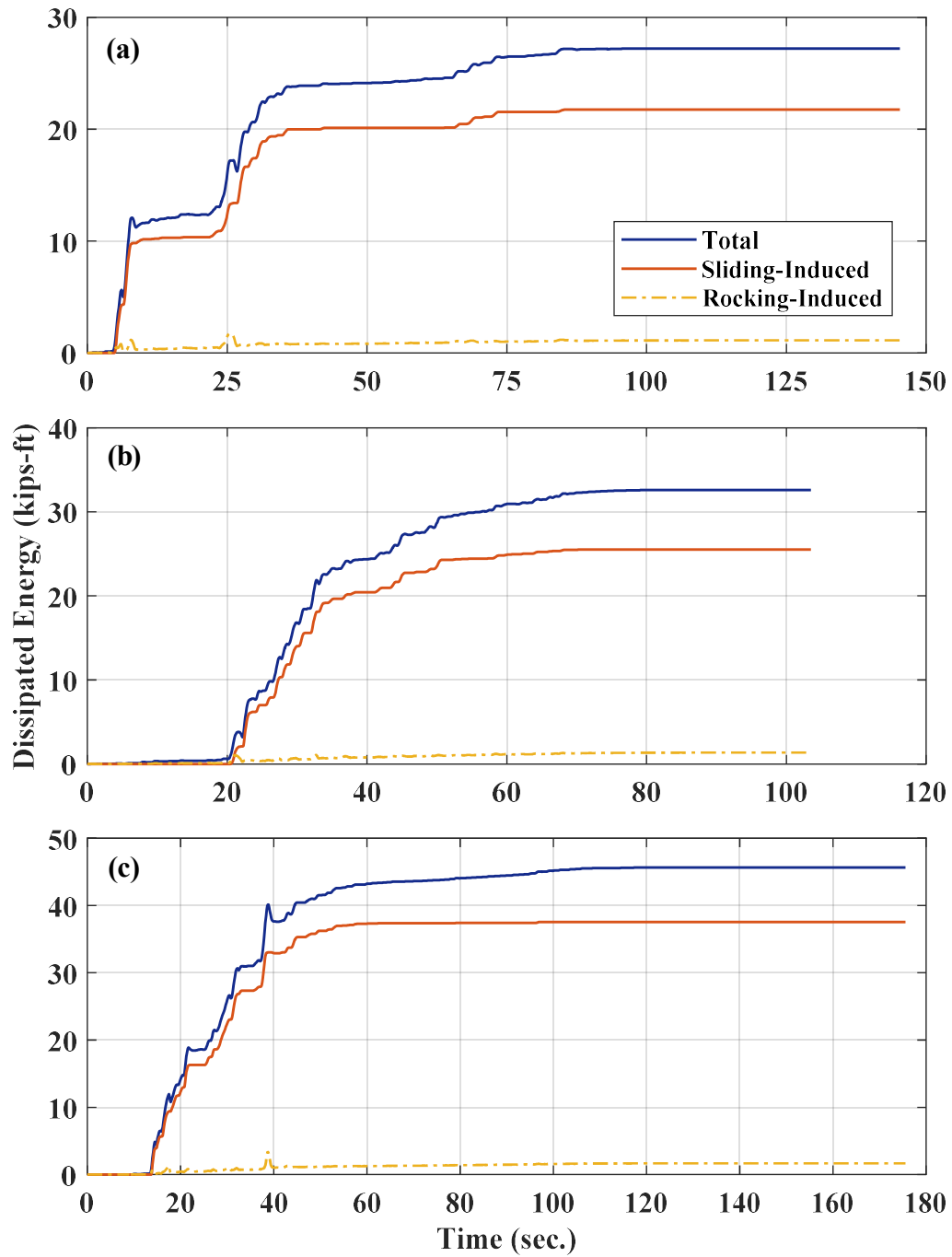
Figure 4-113. Phase I, Loading Set 5 – dissipated energy time histories under loading protocols: (a) HSR4_UN_CNT_S5_H_GM_1; (b) HSR4_UN_CNT_S5_H_GM_2; (c) HSR4_UN_CNT_S5_H_GM_3
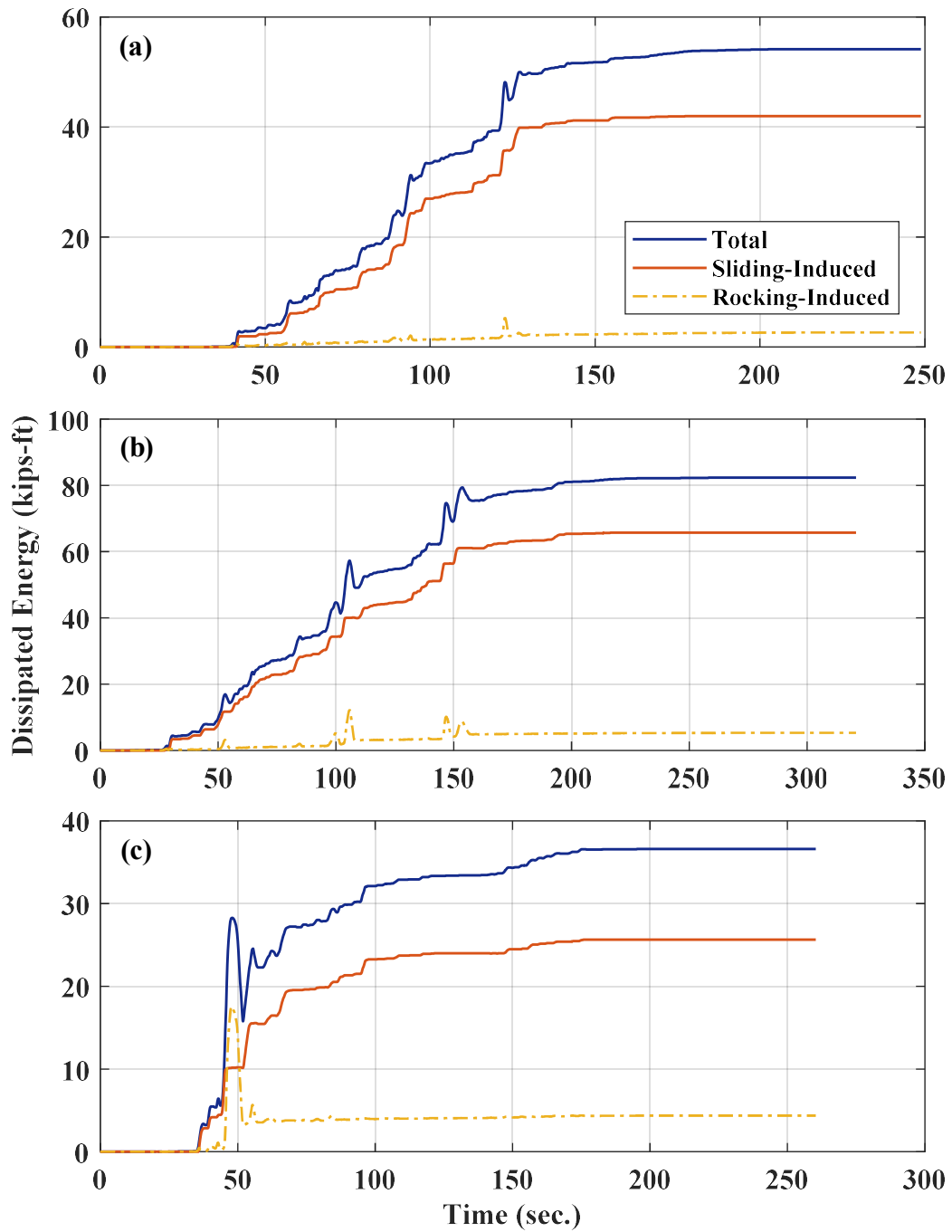
Figure 4-114. Phase I, Loading Set 5: dissipated energy time histories under loading protocols: (a) HSR4_UN_CNT_S5_H_GM_4; (b) HSR4_UN_CNT_S5_H_GM_5; (c) HSR4_UN_CNT_S5_H_GM_6

The tendon force time histories achieved under the same loading protocols are shown in Figure 4-116 and Figure 4-117. According to these plots, none of the tendons reached their yield strength (i.e. about 52 kips), although they could yield locally, especially at locations close to the first sliding joint due to its repeated bending. The variation of the total posttensioning force and the PT losses with the application of the above loading protocols is demonstrated in Figure 4-115. As seen, the PT losses during the first five tests in this Loading Set were only about 0.5% per test. The sixth test (under loading protocol HSR4_UN_CNT_S5_H_GM_6) caused the maximum PT loss of about 1.3%, which was mainly due to the large rocking motion experienced by column in that test (see Figure 4-109(f) and Figure 4-117(c)). Overall, these findings indicate the minimal cyclic deterioration and damageability of the repaired HSR column specimen under arbitrary loading representing real/realistic earthquake-induced displacement time histories.
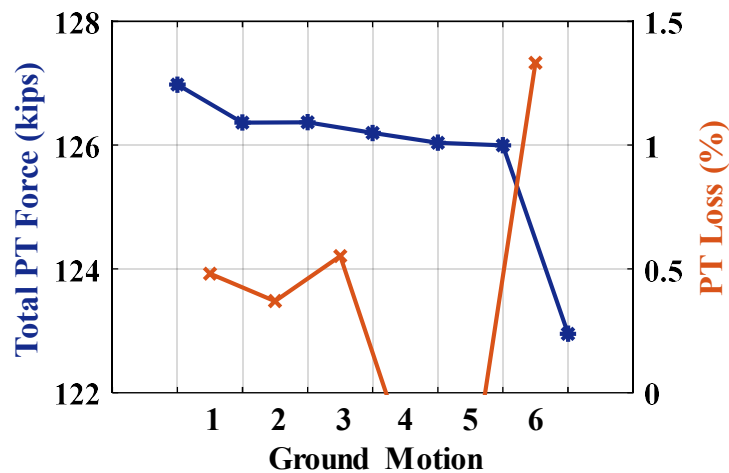
Figure 4-115. Phase I, Loading Set 5: posttensioning force change under loading protocols HSR4_UN_CNT_S5_H_GM_1 thru HSR4_UN_CNT_S5_H_GM_6
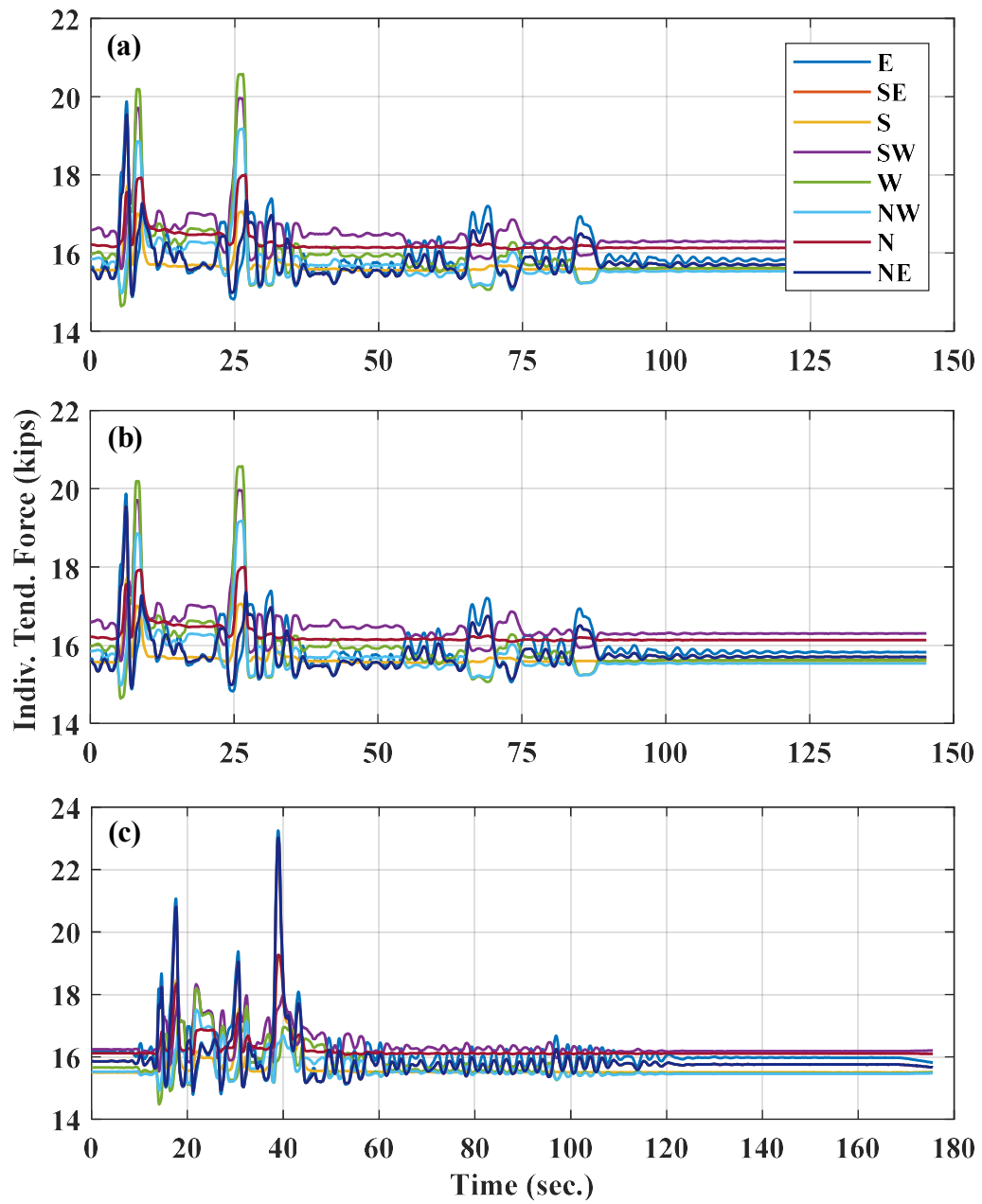
Figure 4-116. Phase I, Loading Set 5: tendon PT force time histories under loading protocols: (a) HSR4_UN_CNT_S5_H_GM_1; (b) HSR4_UN_CNT_S5_H_GM_2; (c) HSR4_UN_CNT_S5_H_GM_3
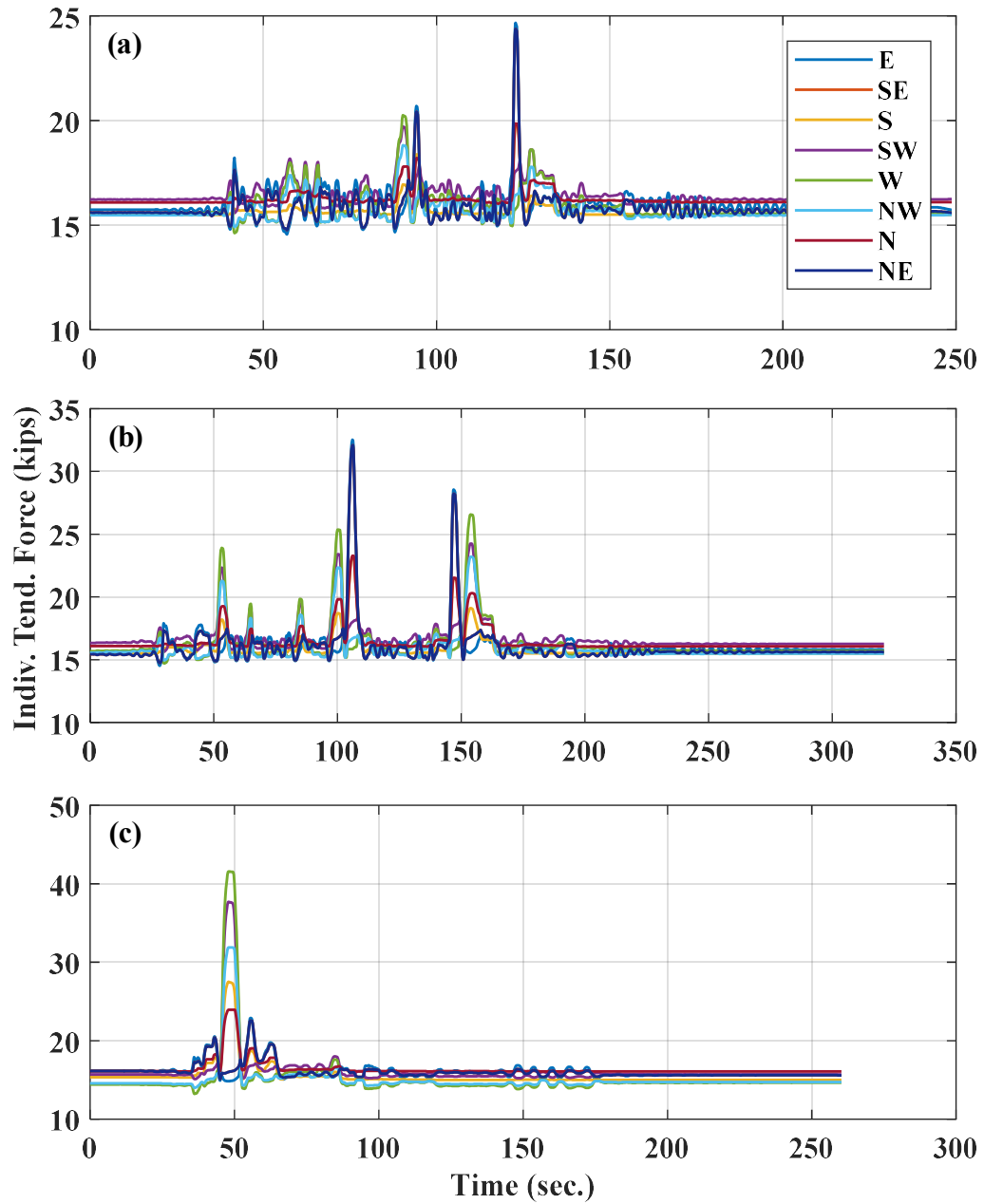
Figure 4-117. Phase I, Loading Set 5: tendon PT force time histories under loading protocols: (a) HSR4_UN_CNT_S5_H_GM_4; (b) HSR4_UN_CNT_S5_H_GM_5; (c) HSR4_UN_CNT_S5_H_GM_6

In order to examine the effects of variable vertical loading on the column responses under arbitrary lateral displacement, the hysteretic force-displacement responses of the column specimen under loading protocols HSR4_UN_CNT_S5_HV_GM_1 through HSR4_UN_CNT_S5_HV_GM_4 are compared with those obtained under loading protocols HSR4_UN_CNT_S5_H_GM_1 through HSR4_UN_CNT_S5_H_GM_4, respectively. As shown in Figure 4-118, the variable vertical load in the loading protocols HSR4_UN_CNT_S5_HV_GM_1 thru HSR4_UN_CNT_S5_HV_GM_4 only slightly affected the hysteretic responses. The dominance of sliding behavior over the rocking behavior is also still clear in the results.

During the 10 tests conducted under the loading protocols of Loading Set 5, only a few more cracks appeared on the bottom column segment. No visible damage was found in the CFRP wrap and it remained intact. The patch under the first sliding joint on the west side of the bottom column segment also gradually debonded from its underlying surface and fell off during the loading protocol HSR4_UN_CNT_S5_H_GM_6 (Figure 4-119). In addition, further evidence of PTFE wearing at the first sliding joint was observed at different corners of the joint (Figure 4-119), which was caused by the large number of sliding cycles experienced by the sliding joint during these tests and the tests before that.
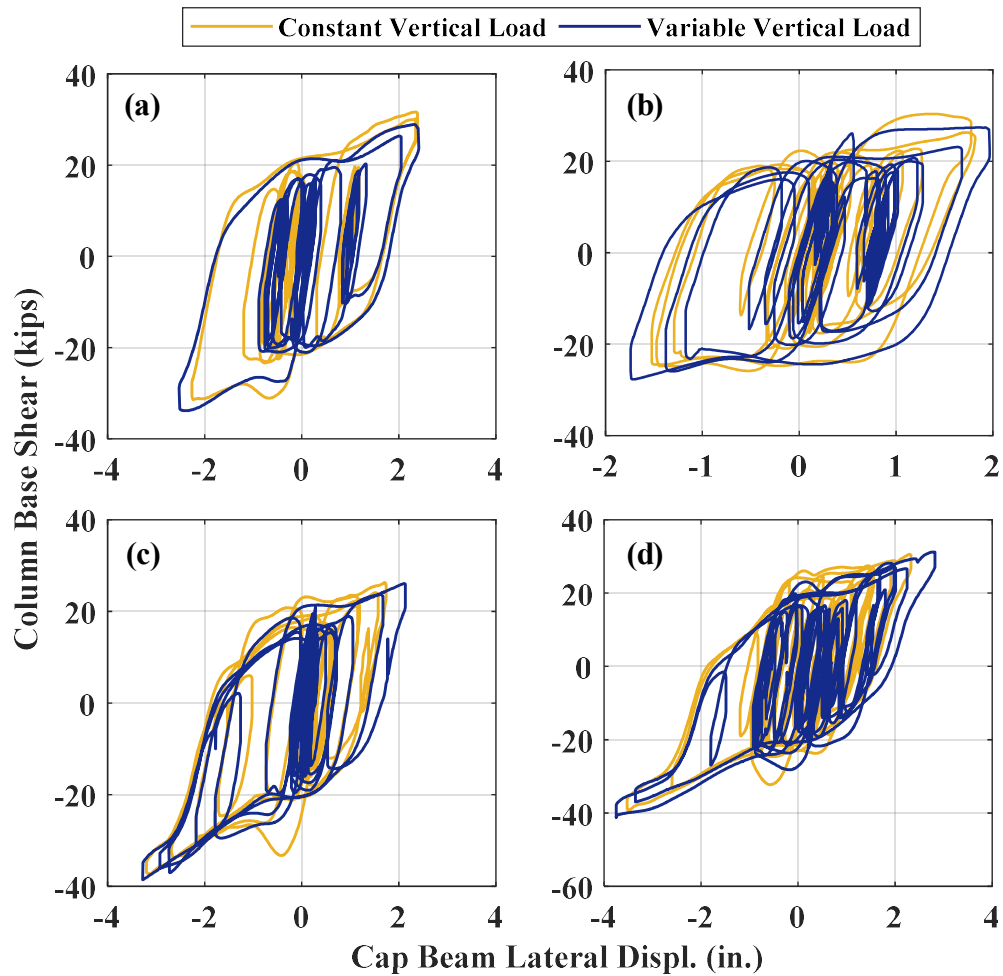
Figure 4-118. Phase I, Loading Set 5: column base shear vs. lateral displacement responses obtained under loading protocols: (a) HSR4_UN_CNT_S5_HV_GM_1; (b) HSR4_UN_CNT_S5_HV_GM_2; (c) HSR4_UN_CNT_S5_HV_GM_3; (d) HSR4_UN_CNT_S5_HV_GM_4
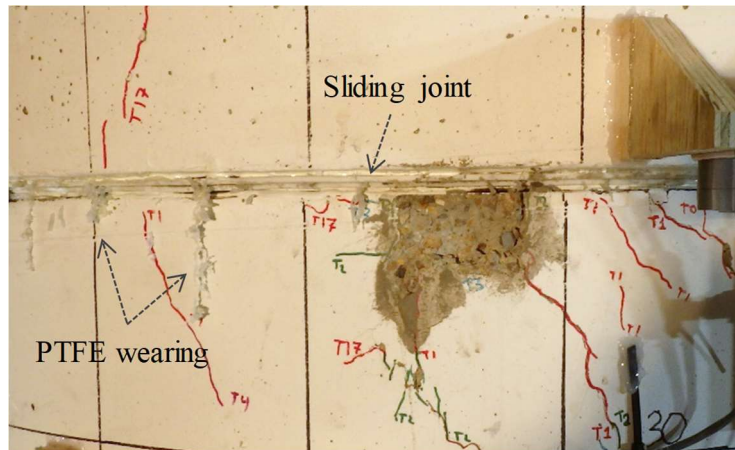
Figure 4-119. Phase I, Loading Set 5: spalling of grout patch and PTFE wearing on west side of first sliding joint

4.7.1.5.7. Results from Loading Set 6

Because of the additional confinement of the bottom segment provided by the CFRP wrap, the results of the tests in this Loading Set are not fully representative of the response of the originally designed HSR column (i.e. without any external confinement means). However, these tests could still help to evaluate the damageability of the sliding joints, ducts, and tendons under extremely large lateral displacements. It is noted that, because the concrete damage at the bottom rocking joint was reduced by the extra confinement, the damage to the tendons and the sliding joints could be more than that when the rocking joint suffered from concrete crushing and significant PT losses were resulted. In other words, when rocking joint is confined to prevent damage, larger demands are to be observed in the PT tendons.

The base shear vs. lateral displacement response of the column specimen under the loading protocol HSR4_UN_CNT_S6_DR_6 (6% peak drift ratio) is demonstrated in

Figure 4-120. There is no softening observed in the response, but the significant reduction in the slope of the curve close to the displacement peaks in the first cycle suggest the concrete damage at the compression toes (i.e. the east and west quadrants of the first column segment's bottom end) and the yielding of some of the tendons. This resulting damage in the first cycle becomes more apparent in the second cycle, where the friction force at the first sliding joint (no sliding occurred at the second sliding joint – Figure 4-121) and the column's stiffness were noticeably lower. The average residual displacement during this test was 1.95 in., which amounts to 1.3% drift ratio and about 85% of it was due to the residual sliding at Joint 2 (Figure 4-121).
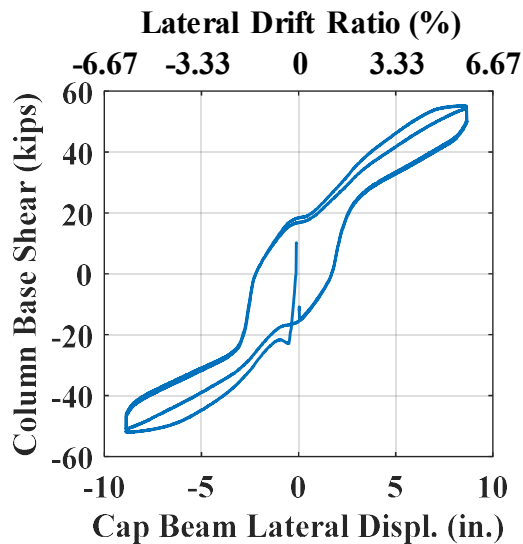
Figure 4-120. Phase I, loading protocol HSR4_UN_CNT_S6_DR_6: base shear vs. lateral displacement response

According to Figure 4-121, no sliding was recorded at the second two joints (Joints 3 and 4), while the bottom rocking joint experienced very small sliding. The maximum

286

sliding values achieved at Joint 2 in both cycles were identical, showing minimal damage to the ducts and duct adaptors during this test. The average residual sliding was 1.66 in. (equivalent to 1.1% drift ratio). This value is very close to the residual sliding reported after Test 3 (under the loading protocol HSR4_UN_CNT_S1_DR_4), implying the minimal damage of the ducts and duct adaptors within the 23 other tests conducted between these tests.
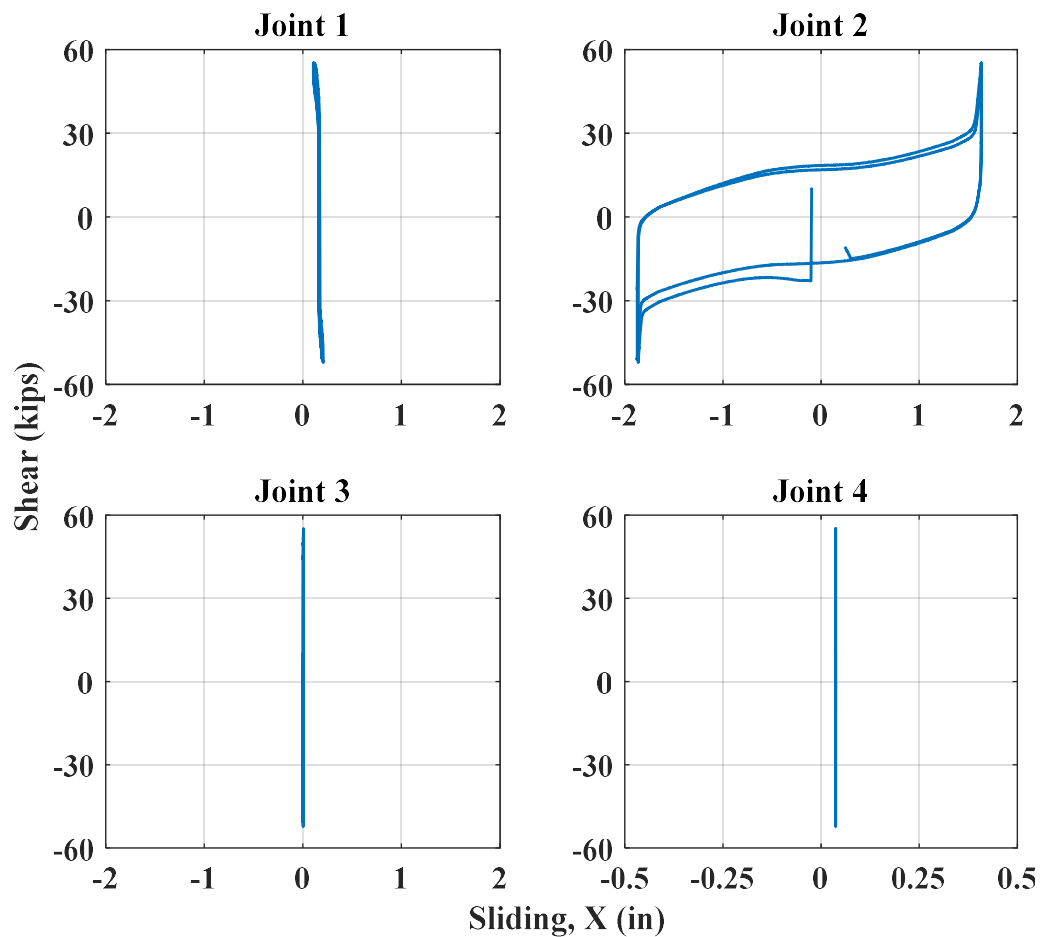
Figure 4-121. Phase I, loading protocol HSR4_UN_CNT_S6_DR_6: joint shear vs. sliding responses in *X* direction

The zero rotation at zero moment observed in the moment vs. rocking response of Joint 1 (Figure 4-122) demonstrates the effectiveness of the additional confinement by the CFRP wrap and unbonded posttensioning in ensuring the column's rocking self-centering, even under such large displacements. Aside from Joint 1, Joint 2 (the first sliding joint) also experienced rocking, but it was less than a tenth of the rocking at Joint 1.
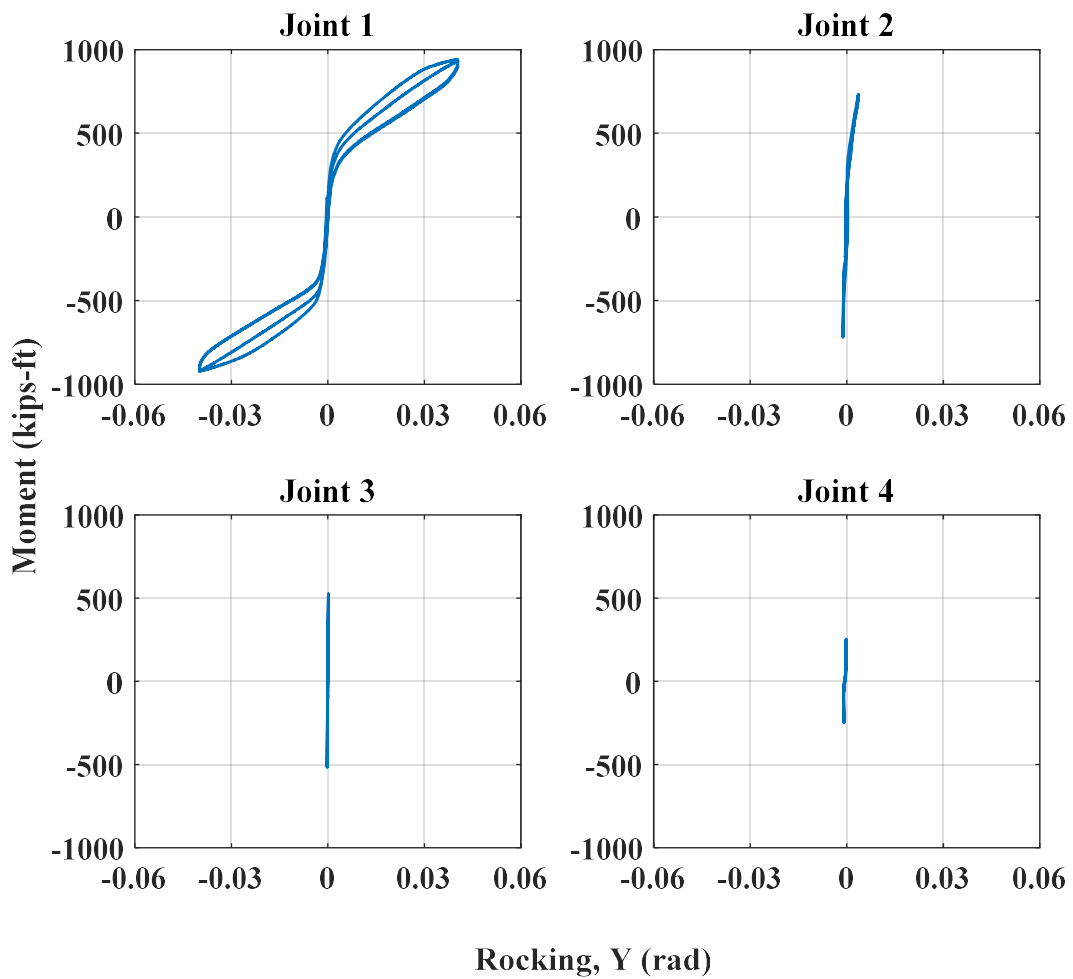
Figure 4-122. Phase I, loading protocol HSR4_UN_CNT_S6_DR_6: joint moment vs. rocking responses around *Y*-axis

The time histories of the tendon forces and the total posttensioning force are presented in Figure 4-124 and the variation of total PT force with lateral displacement is shown in Figure 4-123. The maximum force was recorded for the tendon located at the west side of the cross section, which was about 48.5 kips. Even though this force is less than the nominal yield strength of the strand (~ 52 kips), because of the local bending deformations of the west strand in the vicinity of the sliding joint, it could have yielded at this point. The same is true for the east-side strand and the four other strands next to these two strands, which is one of the reasons why there were significant PT losses in some of these strands (e.g. 34%, 33%, and 31% in the west, northwest, and east strands). The other reason for the losses is the further slippage of the strand wedges in the anchorage devices. The total PT loss during this test is found to be 19%.
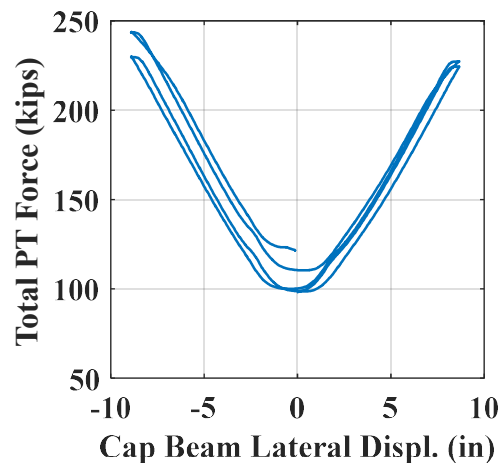
Figure 4-123. Phase I, loading protocol HSR4_UN_CNT_S6_DR_6: total PT force vs. lateral displacement
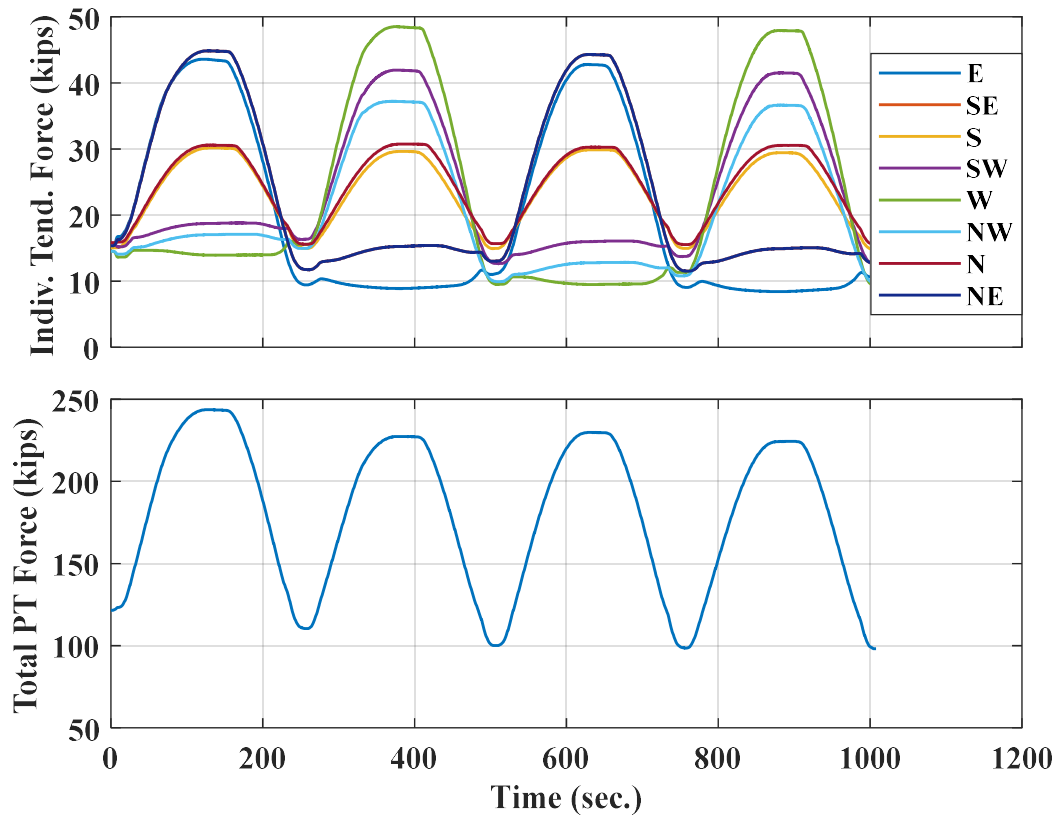
Figure 4-124. Phase I, loading protocol HSR4_UN_CNT_S6_DR_6: time histories of posttensioning forces

The extra damage observed after this test was some new cracks and the growth of some old cracks on the bottom segment surface, particularly on the east and west sides and under the first sliding joint (Figure 4-125). The cracks near the west side of the joint were significantly widened. These cracks indicate the large compressive stresses developing at the east and west corners of the sliding joint under such large displacement demands, particularly because the sliding at the respective joint would reduce the contact area between the segments.

Figure 4-125. Phase I, loading protocol HSR4_UN_CNT_S6_DR_6: observed new cracks on bottom column segment after test

The second displacement cycle of the last loading protocol in Loading Set 6 (i.e. HSR4_UN_CNT_S6_DR_8, with 8% peak drift ratio) was not completed because of the instability of one of the horizontal hydraulic actuators. Naturally, this test was more

destructive than the prior one and caused softening in the column's force-displacement response (Figure 4-126). The maximum values of the base shear resisted by the column in the positive and negative directions were 54 and 52 kips, respectively. During the first cycle and near the displacement peaks in both directions, a wire from each of the southwest and northeast strands fractured (see Figure 4-128 and Figure 4-139). The fracture of the wires caused about 6% sudden drops in the column's strength in both directions.
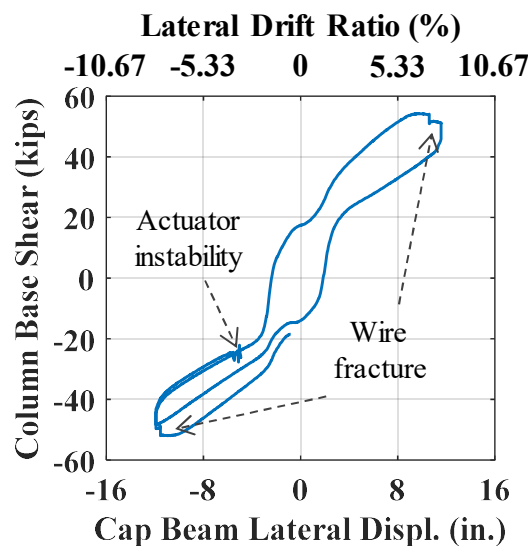
Figure 4-126. Phase I, loading protocol HSR4_UN_CNT_S6_DR_8: base shear vs. lateral displacement response

As seen in Figure 4-127, similar to all of the previous tests, no sliding was observed in the second sliding joint (Joint 2). This finding indicates that the grease used at the sliding joints created an undesirably large breakaway friction at the joints with the 25% glass-filled PTFE sliding surfaces. If the second sliding joint (Joint 3) had exhibited sliding, the additional sliding could have reduced the tendons' elongation, thereby avoiding the wire

fractures. However, such a large breakaway friction had not been predicted during the column design and fabrication.
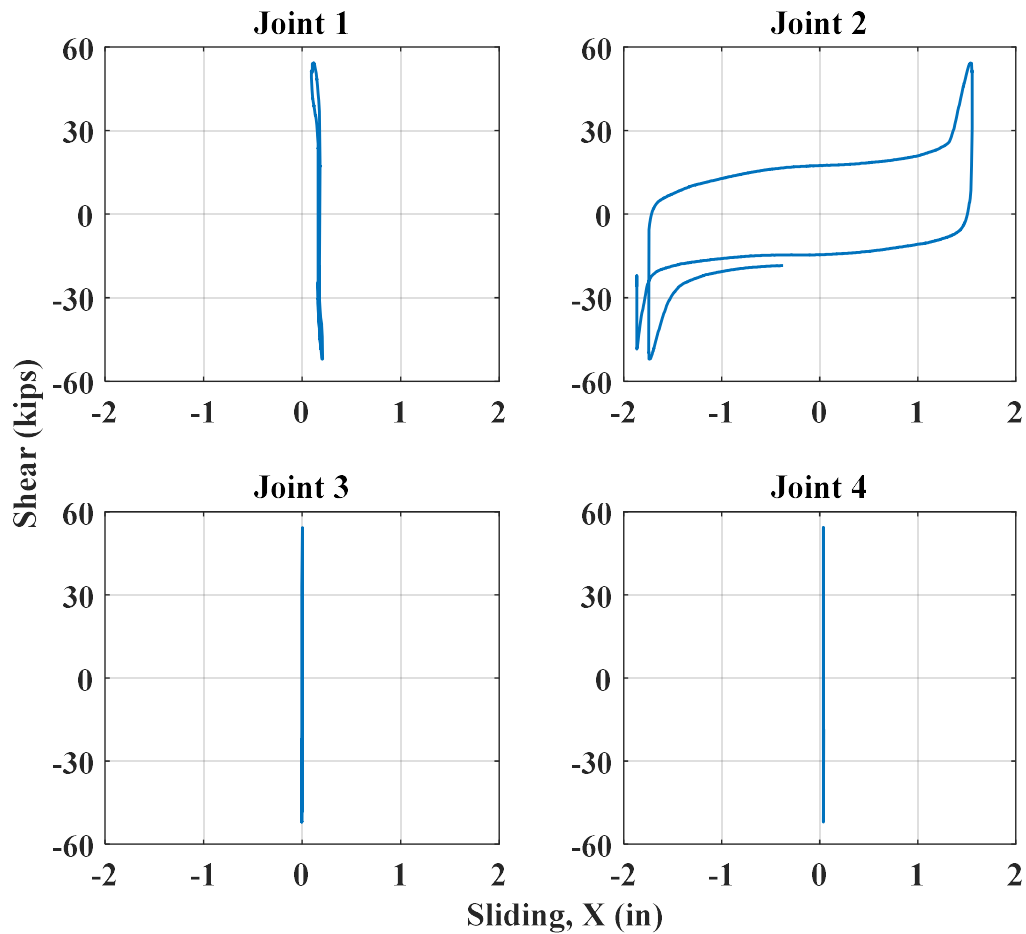
Figure 4-127. Phase I, loading protocol HSR4_UN_CNT_S6_DR_8: joint shear vs. sliding responses in *X* direction

Figure 4-128 shows the tendon force time histories obtained during the last test, while the data for the SE strand was removed due to the respective load cell's malfunction. The wire fractures in the northeast and southwest strands are evident in Figure 4-128. These fractures caused more than 20% PT losses in those strands. It is also observed that the east

293

and west strands certainly yielded during this test, as they became slack (i.e. carried almost zero axial force) after the first displacement peaks in the negative and positive directions, respectively.
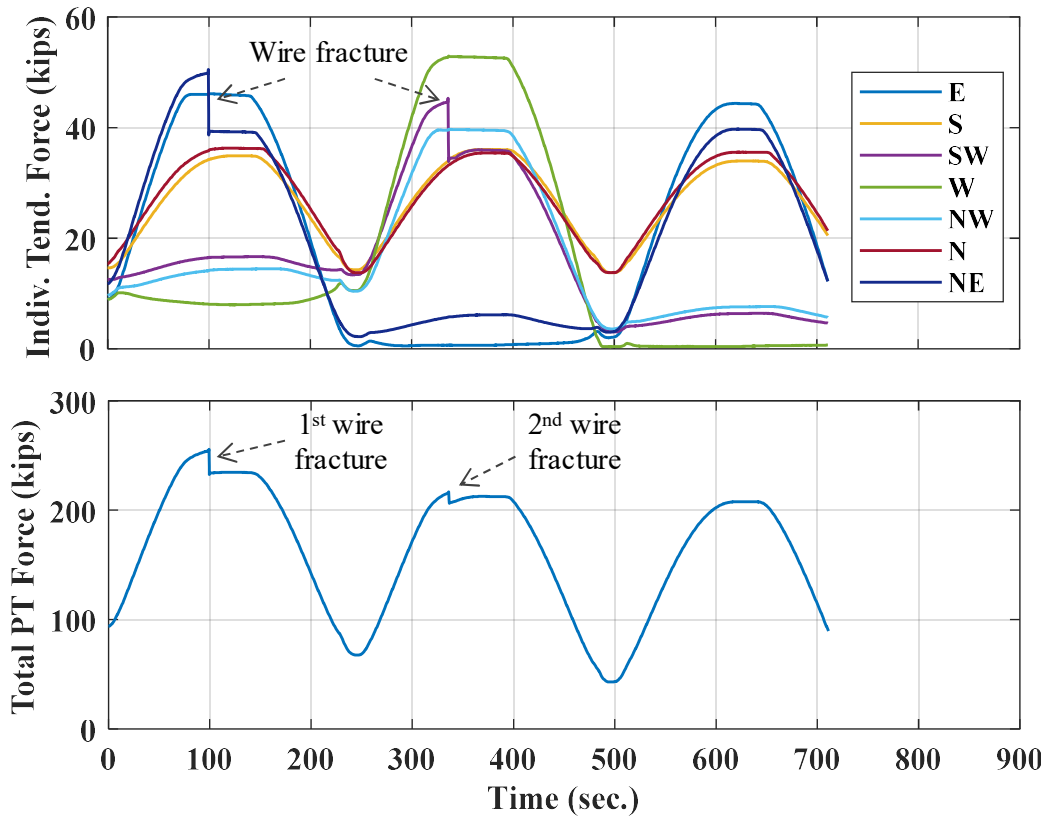
Figure 4-128. Phase I, loading protocol HSR4_UN_CNT_S6_DR_8: time histories of posttensioning forces

The visible damage caused by this test was again limited to some new cracks on the bottom segment (Figure 4-129). As mentioned earlier, during this test, two popping sounds were heard near the displacement peaks in the two directions, which were found later on to have been caused by the fracture of one wire from each of the SW and NE strands

(discussed later). Further damage inspection of the column specimen after all the tests is presented in the next section.
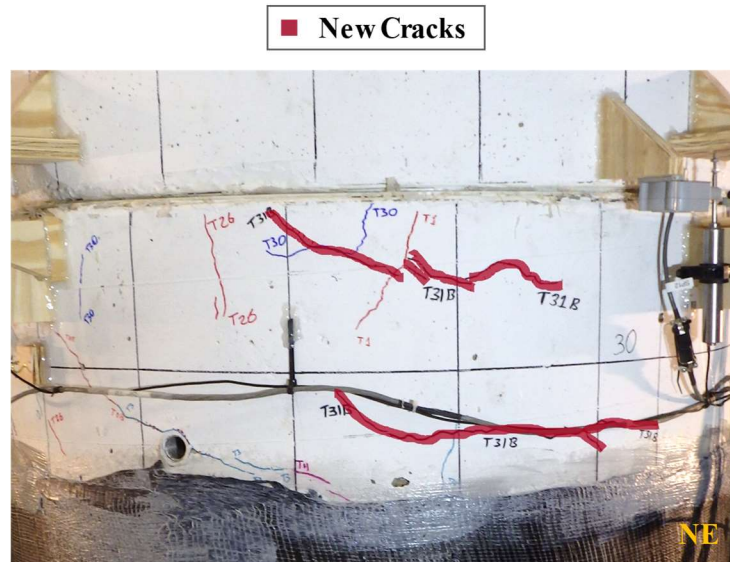
Figure 4-129. Phase I, loading protocol HSR4_UN_CNT_S6_DR_8: observed new cracks on bottom segment after test

The complete hysteretic response of the repaired HSR column specimen obtained by over-plotting its responses under loading protocols HSR4_UN_CNT_S4_DR_1_3, HSR4_UN_CNT_S4_DR_2, HSR4_UN_CNT_S4_DR_4, HSR4_UN_CNT_S6_DR_6, and HSR4_UN_CNT_S6_DR_8 is displayed in Figure 4-130. Note that in this graph, only the force-displacement loops of increasing amplitudes are plotted. According to this figure, the maximum load resistance of the repaired column in the positive and negative directions were 55 kips and 52 kips, respectively, which occurred at a drift ratio range of 5.5-6%. Based on the shape of unloading and reloading branches and the absence of major concrete damage, the observed stiffness and strength deteriorations were primarily caused

295

by the yielding of the tendons and P-Delta effects. It is worth mentioning that, in case no additional confinement had been provided via the CFRP wrap, most likely, the column's softening response would have been dominated by the concrete spalling/crushing.
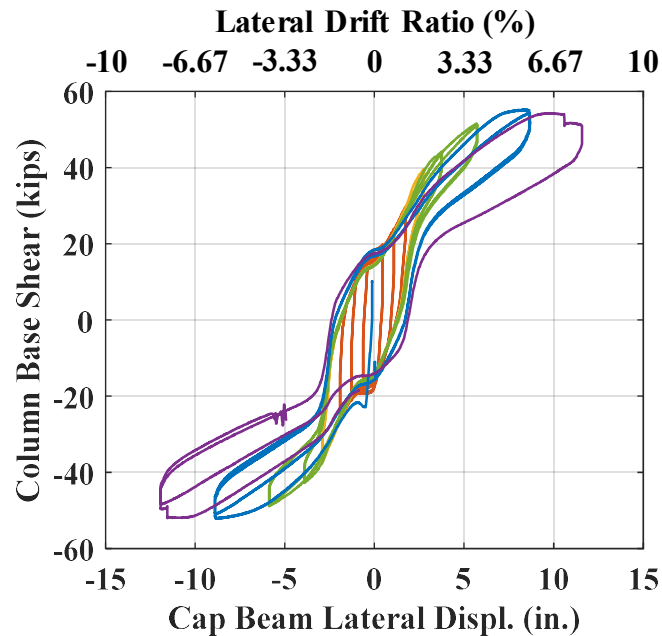
Figure 4-130. Phase I: complete hysteretic response of repaired column

4.7.1.6. Final Damage Inspection

4.7.1.6.1. Overall Column Damage

After the completion of Phase I, the sensors were removed from the column and the external damage was inspected once again. The photos in Figure 4-132 show the final state of the east and west sides of the column specimen. The residual sliding observed at the first sliding joint remained in the column after the actuator instability during the last test (HSR4_UN_CNT_S6_DR_8). According to the photos, the column remained fully stable,

and because of the CFRP wrapping of the bottom segment, no major damage is observed in the plastic hinge region of the column.

4.7.1.6.2. Column Segments

Photos from the inside of the bottom column segment after removing the top two segments are shown in Figure 4-131. It is observed that the damage inside this segment, which underwent the maximum axial stresses, was limited to a number of horizontal and vertical cracks on the east and west sides of the top region. These cracks could have been caused by the high bearing forces imposed to the ducts by the tendons in the direction of lateral loading (i.e. east-west direction).
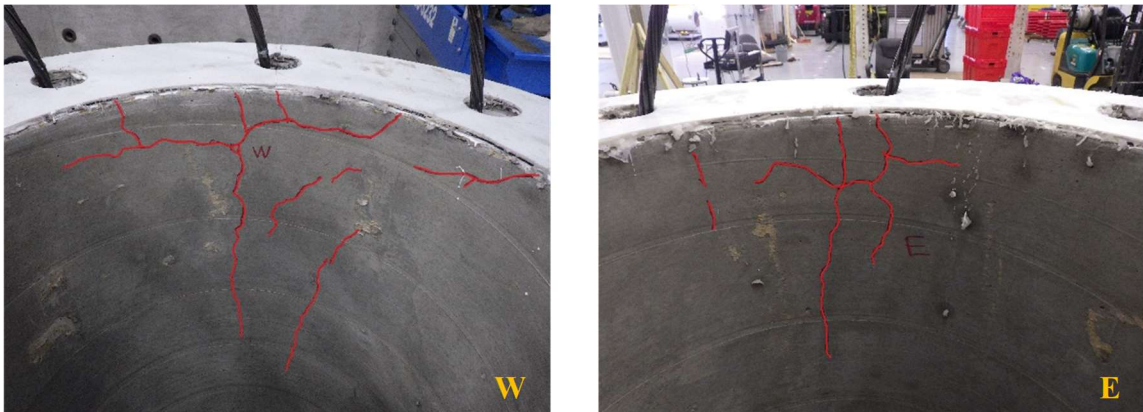
Figure 4-131. Phase I, final damage inspection: cracks inside of bottom segment
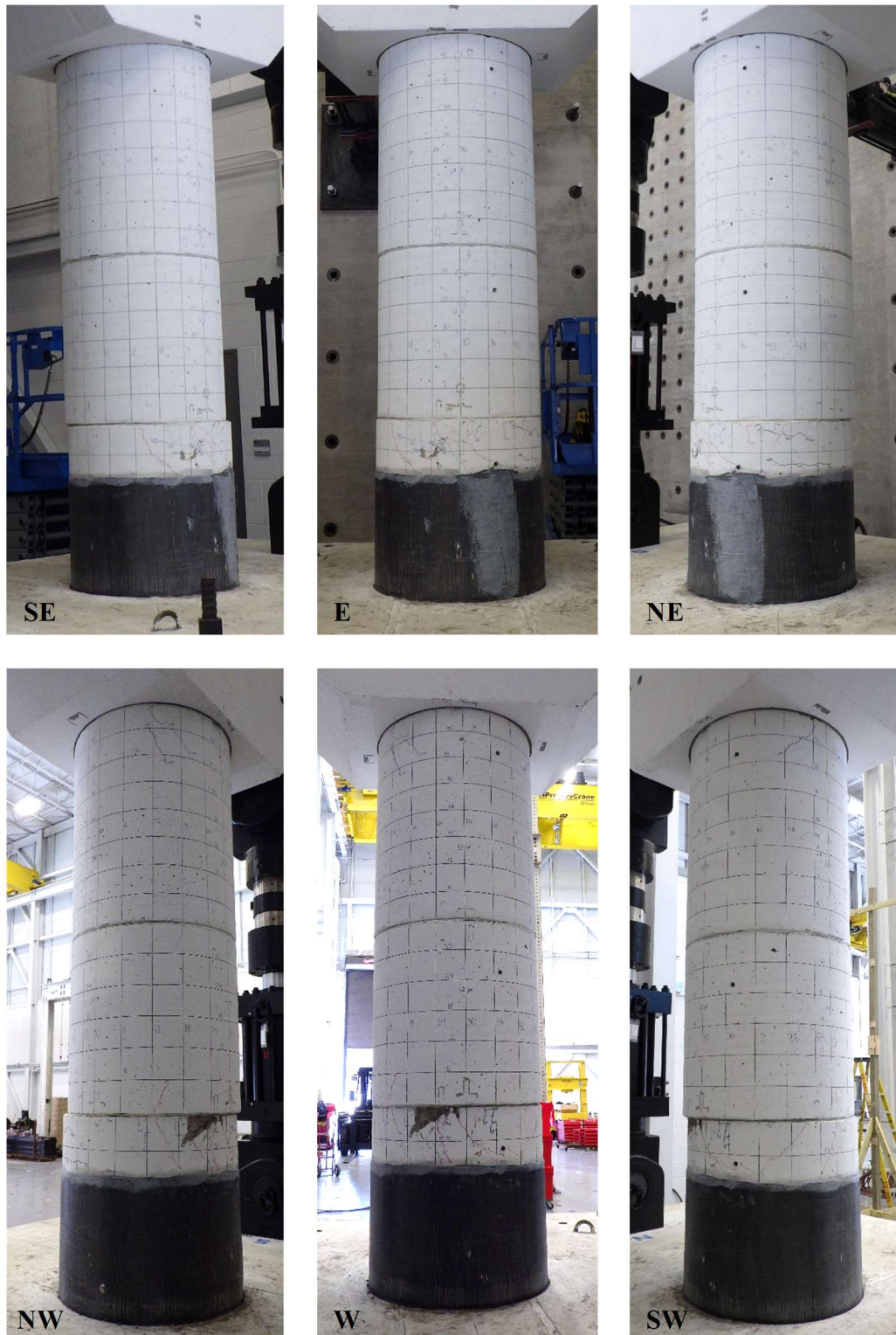
Figure 4-132. Phase I, final damage inspection: column elevation

The bottom surface of the same column segment after disassembly is displayed in Figure 4-133. Per this figure, the additional confinement provided by the CFRP wrap was very effective in avoiding the concrete compressive damage at the bottom rocking joint and only the patching at the east and west compression toes suffered from crushing. According to Figure 4-134, the top surface of the bottom segment, which was one of the sliding surfaces in the first sliding joint, did not have any significant damage, too. Slight wearing was observed on the glass-filled PTFE pad, but it was not visibly deformed or broken. There was minimal grease left on the surface, but it looked smoother than it originally was. The PVC pipes and fittings were also found effective in avoiding the concrete damage due to the tendons' bearing, even though there were indentations observed on the edges of the duct adaptors and the ducts.

Figure 4-133. Phase I, final damage inspection: bottom surface of bottom segment
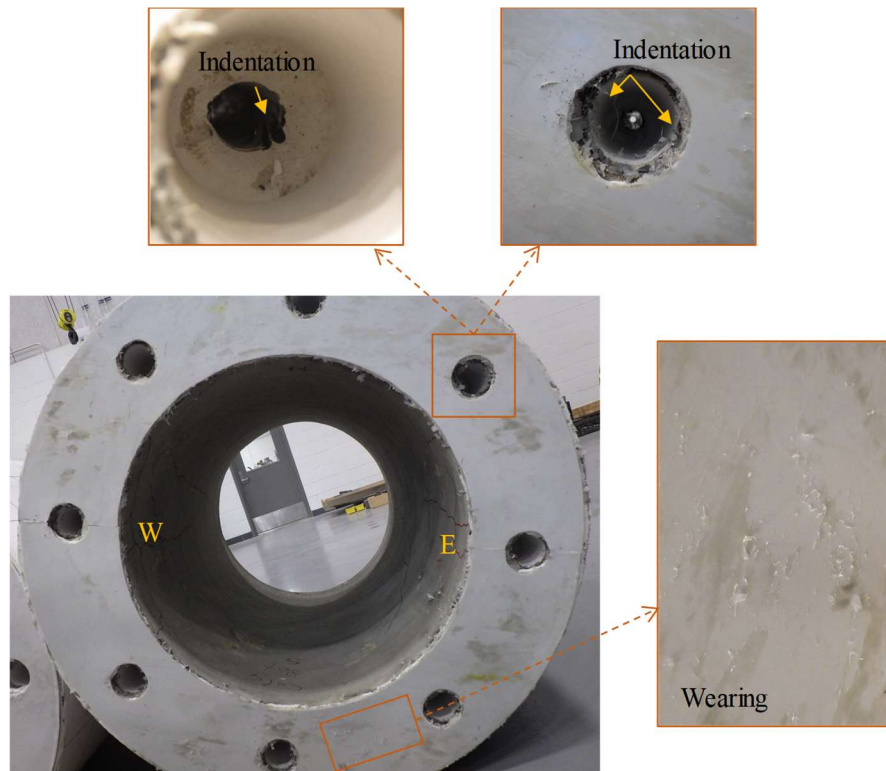
Figure 4-134. Phase I, final damage inspection: top surface of bottom segment

Similar to the top surface of the bottom segment, the bottom surface of the second segment (i.e. the top sliding surface of the first sliding joint) had not sustained any damage except slight wearing (Figure 4-135). Indentations similar to those in the bottom segment ducts were observed in the ducts of the middle segment. Such indentations provide the reason why the measured sliding values were larger than the nominal sliding capacity at the first sliding joint (Joint 2). The top surface of the same segment, which constituted the lower surface of the second sliding joint, had not experienced any sliding, so it was fully undamaged and still covered by a large amount of grease (Figure 4-136). No damage was found on any of the top and bottom surfaces of the top column segment, too (Figure 4-137).
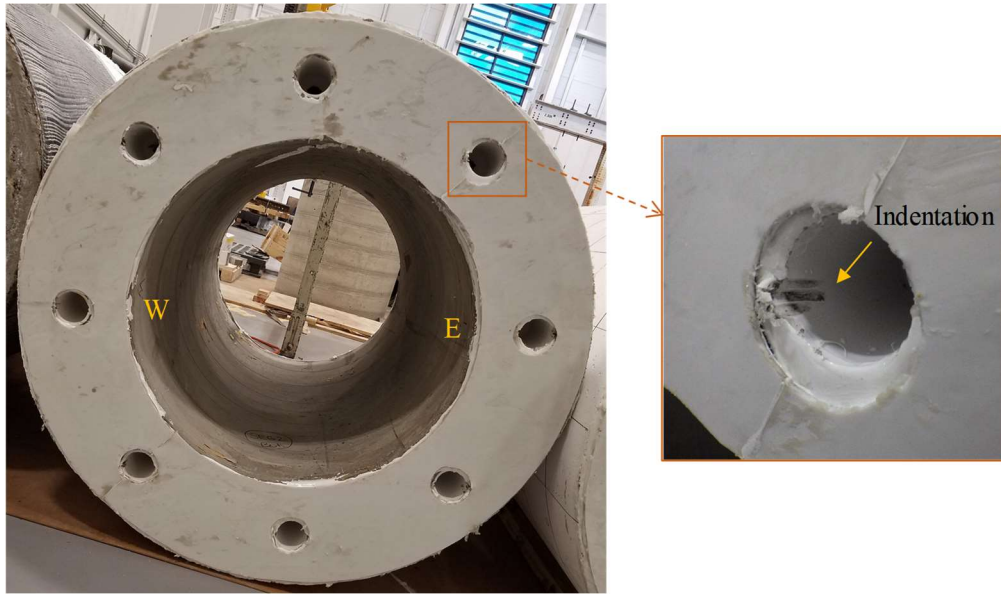
Figure 4-135. Phase I, final damage inspection: bottom surface of middle segment
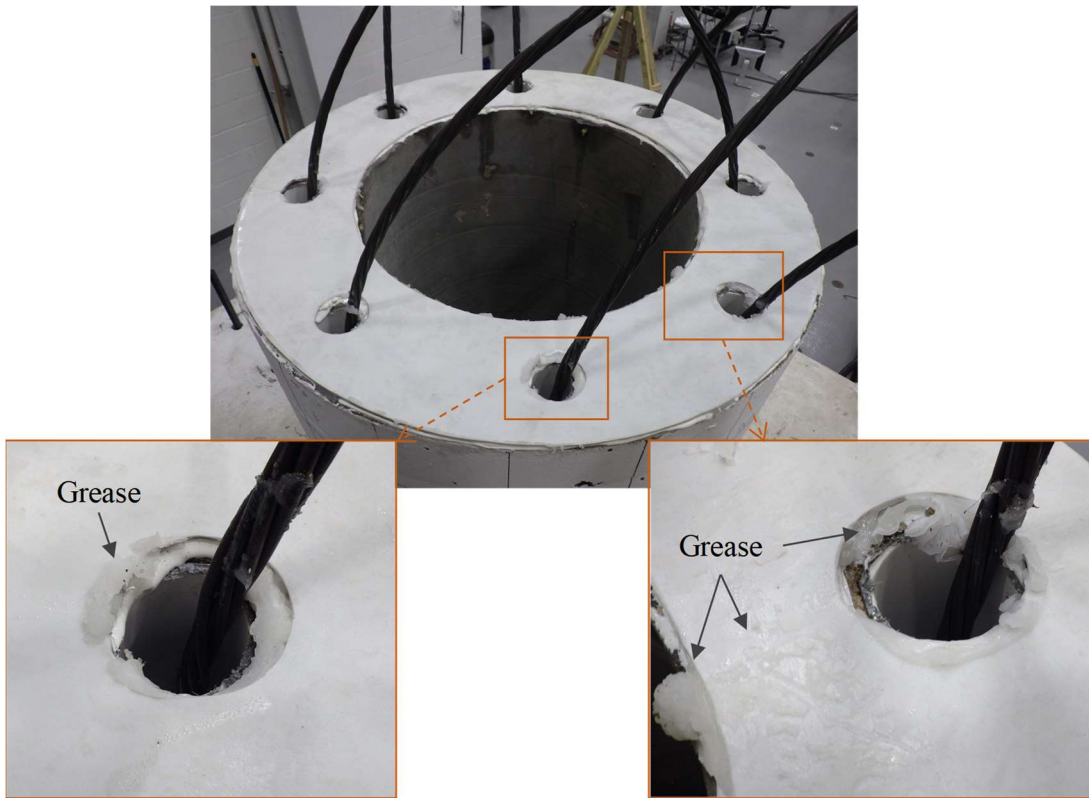
Figure 4-136. Phase I, final damage inspection: top surface of middle segment
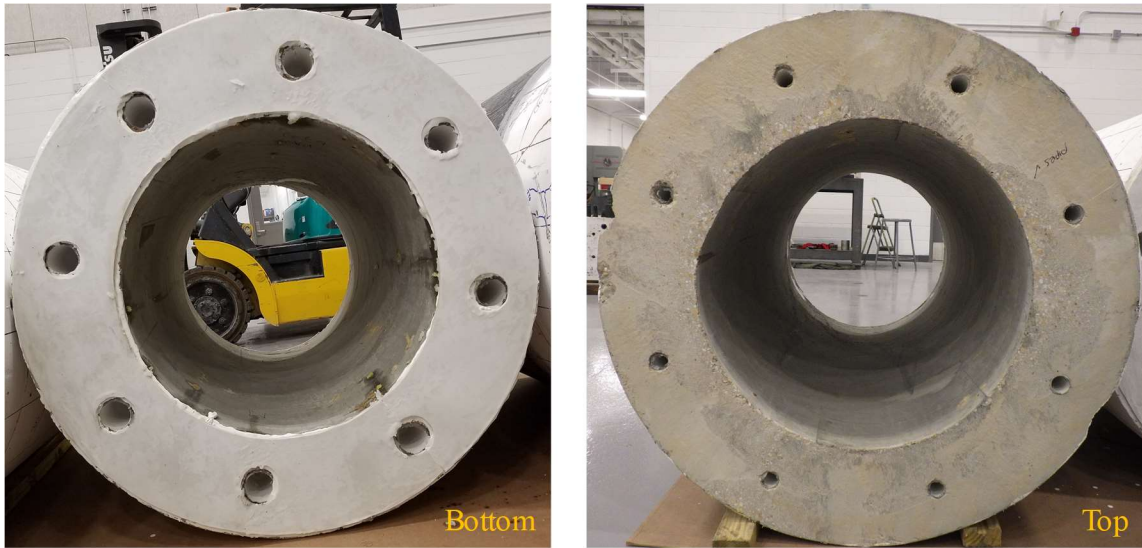
Figure 4-137. Phase I, final damage inspection: end surfaces of top segment

4.7.1.6.3. Posttensioning Tendons

The extracted tendons after the column disassembly are shown in Figure 4-138. It is observed that some of the tendons had sustained localized plastic bending at the bottom rocking joint, and particularly, above and below the first sliding joint. Despite the excessively large drift ratios applied to this column, no wires were broken or locally dented in the neighborhood of the first sliding joint, indicating that the PVC pipes and fittings could protect the tendons against such damage – therefore, no shear keys were necessary. However, one wire from each of the strands located at the southwest and the northeast of the column cross section had fractured at their lower end anchors (Figure 4-139), not in the vicinity of the sliding joints. This finding further demonstrates the adverse impact of the anchor wedges on the tendon wires (Sideris et al. 2014a).
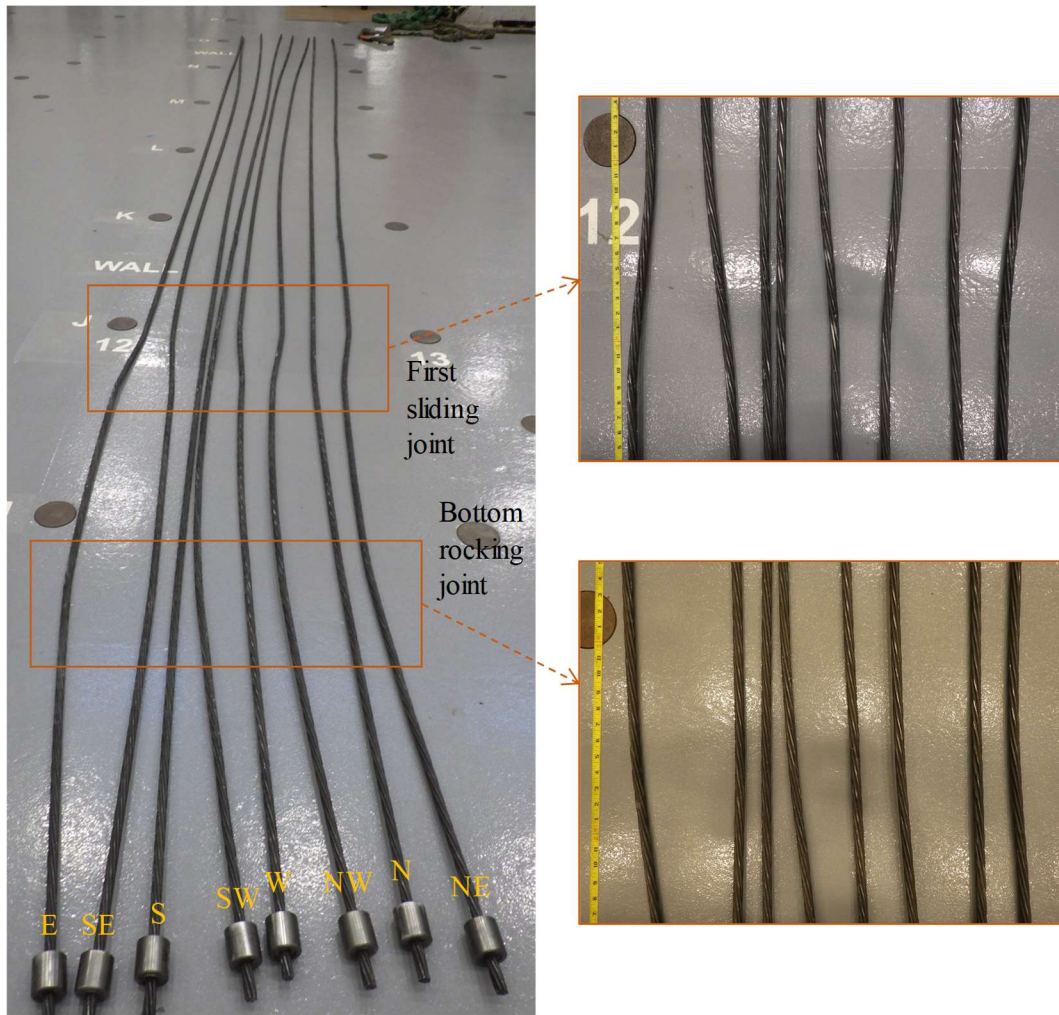
Figure 4-138. Phase I, final damage inspection: posttensioning tendons
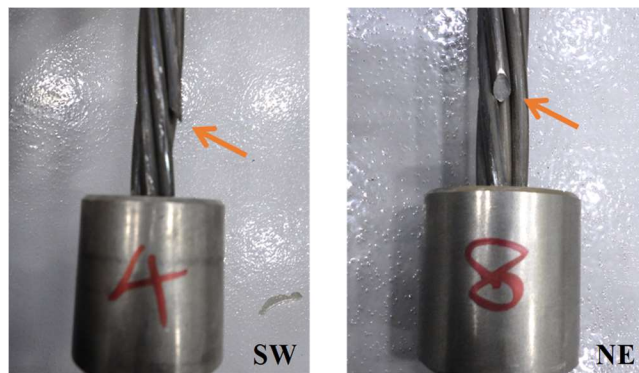
Figure 4-139. Phase I, final damage inspection: fractured wires near anchors

4.7.1.6.4. Foundation

The damage to the foundation was negligible and the edge of the recessed area had remained almost undamaged. Some grout debris was found on the foundation surface, which was easily removed before the next setup was assembled.
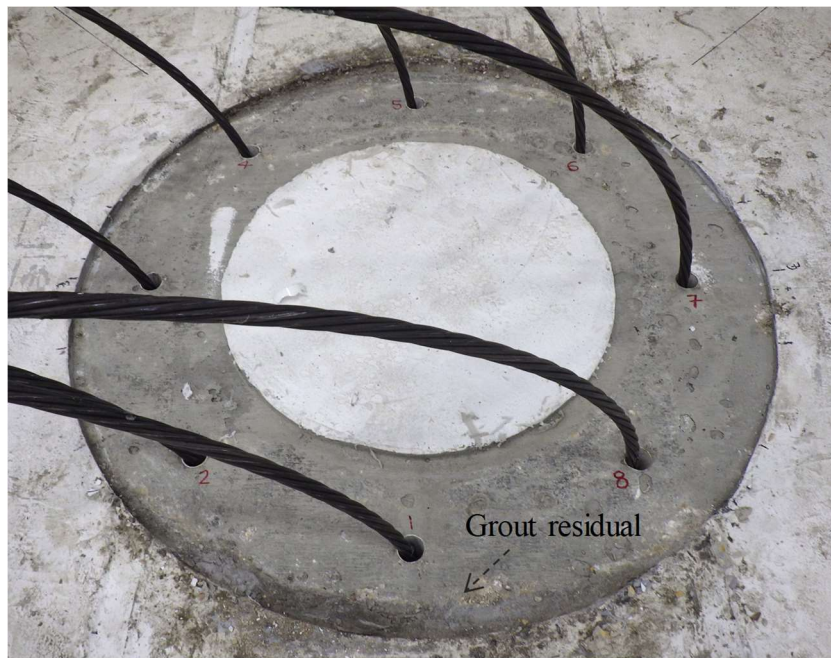
Figure 4-140. Phase I, final damage inspection: foundation recessed area

4.7.2. Phase II: Cantilever Column under Combined Torsional and Uniaxial Lateral Loading

4.7.2.1. Test Setup

Similar to Phase I, Setup A (Figure 4-12) was used to run the tests in Phase II. The plan view, front view, and the side view of this setup are the same as those shown in Figure 4-36, Figure 4-37, and Figure 4-38, respectively, except for the locations of the horizontal

actuators 220A and 220B, which were swapped. Further information about the test setup and its assembly can be found in Section 4.7.1.1. During the assembly process, the bottom east edge of the first column segment was slightly damaged (Figure 4-141). In addition, the column segments slightly slid on each other, leading to some initial sliding before the tests start, which was difficult to eliminate without the column's reassembly.

Figure 4-141. Bottom column segment damage caused during test setup assembly

4.7.2.2. Instrumentation

The instrumentation in Phase II was similar to that in Phase I (Section 4.7.1.2), yet some of the sensors used in Phase I were not used here and the arrangement of some of the sensors was slightly different. A total of 66 sensors (aside from those in the actuators) were used here, whose types and numbers are summarized in Table 4-20.

Table 4-20. Type and number of sensors used in Phase II

Type	String Potentiometer	LVDT	Tendon Load Cell
Number	39	11	16

The general arrangement of the sensors in this Phase is demonstrated in Figure 4-142. Because of their low accuracy, in this Phase, inclinometers were removed from the loading beam. Instead, to allow the measurement of the loading beam rotation around Y-axis, an additional string potentiometer was used to measure the lateral displacement of a point 2 ft lower than the loading point of the horizontal actuators (i.e. 10.5 ft above the foundation surface). All other sensors were, however, connected in a similar arrangement to that discussed in Section 4.7.1.2 for Phase I.
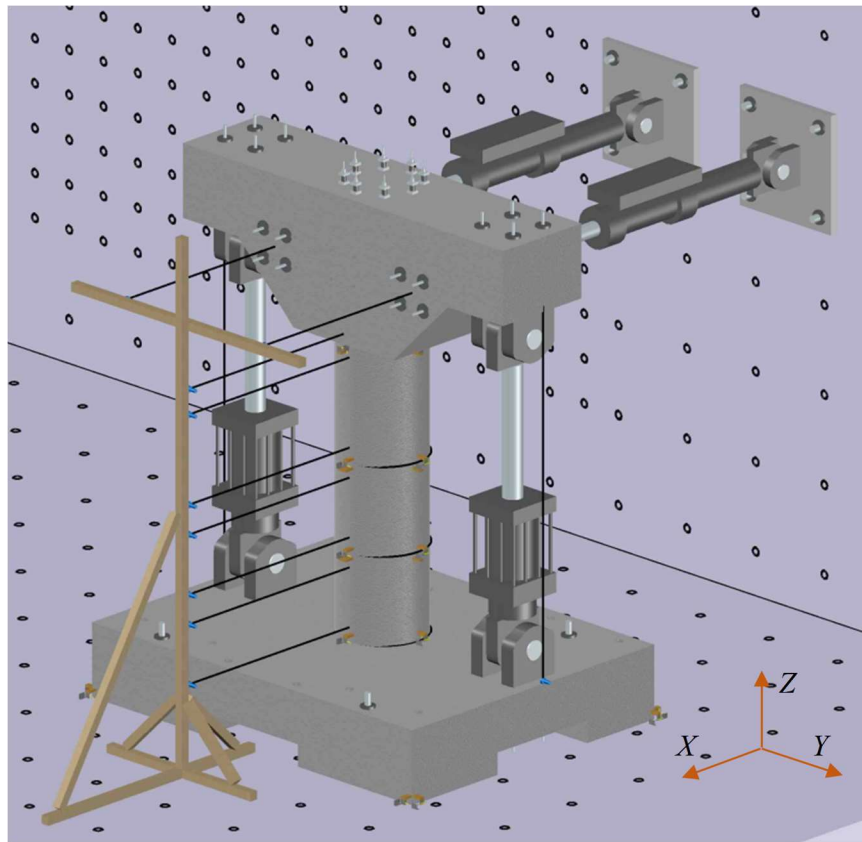
Figure 4-142. General arrangement of sensors in Phase II

The sensors used to measure the segment displacements and the joint responses were the same as those in Phase I (Table 4-21 and Table 4-23). The sensors measuring the loading beam's displacements and the foundation block's displacements are listed in Table 4-24 and Table 4-22, respectively. The tendon load cells used in this Phase were identical to those in Phase I (Table 4-25).

Table 4-21. String pots measuring column segment displacements in Phase II

ID	Stroke (in.)	Measurement Point
SP-S1-B	4	Bottom segment, bottom
SP-S1-T	12	Bottom segment, top
SP-S2-B	12	Middle segment, bottom
SP-S2-T	25	Middle segment, top
SP-S3-B	25	Top segment, bottom
SP-S3-T	50	Top segment, top

Table 4-22. Sensors measuring foundation displacements in Phase II

ID	Type	Stroke (in)	Location	Measurement
SP-FN-N-L-H	String pot.	4	NE corner	X sliding
SP-FN-N-R-H	String pot.	4	NW corner	X sliding
SP-FN-S-L-H	String pot.	4	SE corner	X sliding
SP-FN-W-L-H	String pot.	4	SW corner	Y sliding
SP-FN-W-R-H	String pot.	4	NW corner	Y sliding
LV-FN-W-L-V	LVDT	0.5	SW corner	Separation
LV-FN-W-R-V	LVDT	0.5	NW corner	Separation
SP-FN-E-R-H	String pot.	4	NE corner	Y sliding
LV-FN-E-R-V	LVDT	0.5	NE corner	Separation

Table 4-23. Sensors measuring joint sliding/rotation in Phase II

ID	Type	Stroke (in)	Location	Measurement
SP-J0-N-H	String pot.	4	Bottom joint - north	Sliding
SP-J0-S-H	String pot.	4	Bottom joint – south	Sliding
SP-J0-E-H	String pot.	4	Bottom joint – east	Sliding
SP-J0-W-H	String pot.	4	Bottom joint – west	Sliding
SP-J0-N-V	String pot.	12	Bottom joint – north	Separation
SP-J0-S-V	String pot.	12	Bottom joint – south	Separation
SP-J0-E-V	String pot.	12	Bottom joint – east	Separation
SP-J0-W-V	String pot.	12	Bottom joint – west	Separation
SP-J1-N-H	String pot.	4	Sliding joint 1 – north	Sliding
SP-J1-S-H	String pot.	4	Sliding joint 1 – south	Sliding
SP-J1-E-H	String pot.	4	Sliding joint 1 – east	Sliding
SP-J1-W-H	String pot.	4	Sliding joint 1 – west	Sliding
LV-J1-N-V	LVDT	1	Sliding joint 1 – north	Separation
LV-J1-S-V	LVDT	1	Sliding joint 1 – south	Separation
LV-J1-E-V	LVDT	1	Sliding joint 1 – east	Separation
LV-J1-W-V	LVDT	1	Sliding joint 1 – west	Separation
SP-J2-N-H	String pot.	4	Sliding joint 2 – north	Sliding
SP-J2-S-H	String pot.	4	Sliding joint 2 – south	Sliding
SP-J2-E-H	String pot.	4	Sliding joint 2 – east	Sliding
SP-J2-W-H	String pot.	4	Sliding joint 2 – west	Sliding
LV-J2-N-V	LVDT	1	Sliding joint 2 – north	Separation
LV-J2-S-V	LVDT	1	Sliding joint 2 – south	Separation
LV-J2-E-V	LVDT	1	Sliding joint 2 – east	Separation
LV-J2-W-V	LVDT	1	Sliding joint 2 – west	Separation
SP-J3-N-H	String pot.	4	Top joint - north	Sliding
SP-J3-S-H	String pot.	4	Top joint – south	Sliding
SP-J3-E-H	String pot.	4	Top joint – east	Sliding
SP-J3-W-H	String pot.	4	Top joint – west	Sliding
SP-J3-E-V	String pot.	4	Top joint – east	Separation
SP-J3-W-V	String pot.	4	Top joint – west	Separation

Table 4-24. String pots measuring loading beam displacements in Phase II

ID	Stroke (in)	Location	Measurement
SP-CP-F-L	50	Front face – left actuator loading point	X displacement
SP-CP-F-R	50	Front face – right actuator loading point	X displacement
SP-CP-F-C	50	Front face – 2 ft below actuators loading point	X displacement
SP-CP-B-L	4	South side	Z displacement
SP-CP-B-R	4	North side	Z displacement

Table 4-25. Tendon load cells in Phase II

ID	Location	Tendon Map
LC-TN-C-1	Loading beam – E	
LC-TN-C-2	Loading beam – SE	
LC-TN-C-3	Loading beam – S	
LC-TN-C-4	Loading beam – SW	
LC-TN-C-5	Loading beam – W	
LC-TN-C-6	Loading beam – NW	
LC-TN-C-7	Loading beam – N	
LC-TN-C-8	Loading beam – NE	
LC-TN-F-1	Foundation – E	
LC-TN-F-2	Foundation – SE	
LC-TN-F-3	Foundation – S	
LC-TN-F-4	Foundation – SW	
LC-TN-F-5	Foundation – W	
LC-TN-F-6	Foundation – NW	
LC-TN-F-7	Foundation – N	
LC-TN-F-8	Foundation – NE	

4.7.2.3. Data Acquisition and Processing

The sensors' data was acquired and cleaned (from noise) as explained for Phase I (see Section 4.7.1.3). Compared to Phase I, here, the post-processing of the data is more challenging, because the loading beam has large rotations around the vertical axis (Z-axis per Figure 4-142). In this Phase, the following response parameters were of interest:

- $\Delta_{bm,X}$: The lateral displacement (i.e. in X direction per Figure 4-142) of the loading point on the loading beam (equivalent to the superstructure centroid in the prototype bridge) relative to the foundation block's top surface;

- $\theta_{bm,Z}$: The torsional rotation (twist) of the loading beam relative to the foundation block (i.e. around Z-axis per Figure 4-142);

- $u_{sl,X,j}$: The jth joint's sliding in the lateral direction (i.e. in X direction per Figure 4-142), with j = 1, 2, 3, and 4 from bottom to top;

- $\theta_{sl,j}$: The jth joint's torsional sliding (i.e. rotation around vertical axis);

- $\theta_{r,Y,j}$: The jth joint's rocking (rotation) around Y-axis (Figure 4-142);

- $V_{col,X}$: The column's base shear in the transverse direction (i.e. in X direction per Figure 4-142);

- T_{col}: The column's torsion (torsional moment);

- $M_{jnt,Y,j}$: The jth joint's moment about Y-axis (Figure 4-142);

- N_{col}: The axial force on the column (i.e. excluding the column weight);

- N_{PT}: The total posttensioning force in the tendons;

- $M_{PT,Y}$: The posttensioning-induced moment about Y-axis (Figure 4-142) on the loading beam.

The displacement parameters can be obtained from the geometry of the setup and the displacements measured by the sensors. The sliding and rocking components at the column joints are found using Eqs. (4-2) thru (4-6). According to Figure 4-143, the column internal forces can be determined as:

$$\begin{cases}
V_{col,X} \simeq -F_{act,h1} - F_{act,h2} + F_{act,v1,X} + F_{act,v2,X} \\
M_{col,Y} \simeq -\left(F_{act,h1} + F_{act,h2}\right)h_{bm} + 2W_{act,h}\left(d_{act,h} - \Delta_{bm,X}\right) \\
\qquad -\left(F_{act,v1} + W_{act,v}\right)\left(\Delta_{bm,X} + b_{act,v}\theta_{bm,Z} - d_{act,v}\theta_{bm,Y}\right) \\
\qquad -\left(F_{act,v2} + W_{act,v}\right)\left(\Delta_{bm,X} - b_{act,v}\theta_{bm,Z} - d_{act,v}\theta_{bm,Y}\right) \\
\qquad +\left(F_{act,v1,X} + F_{act,v2,X}\right)\left(h_{bm} - d_{act,v}\right) \\
\qquad -W_{bm}\Delta_{bm,C,X} + M_{PT} \\
N_{col} \simeq W_{bm} + 2W_{act,v} + 2W_{act,h} + F_{act,v1} + F_{act,v2} + N_{PT} \\
T_{col} \simeq -F_{act,h1}\left(b_{act,h} + d_{act,h}\theta_{bm,Z}\right) + F_{act,h2}\left(b_{act,h} - d_{act,h}\theta_{bm,Z}\right) \\
\qquad +\left(F_{act,v1,X} - F_{act,v2,X}\right)b_{act,v}
\end{cases} \qquad (4\text{-}12)$$

with:

$$\begin{cases}
F_{act,v1,X} = F_{act,v1}\theta_{act,Y1} \\
F_{act,v2,X} = F_{act,v2,X}\theta_{act,Y2}
\end{cases} \qquad (4\text{-}13)$$

where the numbers 1 and 2 in the subscripts indicate the actuator to which the variables refer – for example, $F_{act,h1}$ refers to the total force applied by the horizontal actuator 220A. Additionally, $b_{act,v}$ and $b_{act,h}$ represent the initial horizontal distances of the loading points of the vertical and horizontal actuators from the center of loading beam, respectively (see Figure 4-143; $b_{act,v}$ = 5'-7.5" and $b_{act,h}$ = 3').
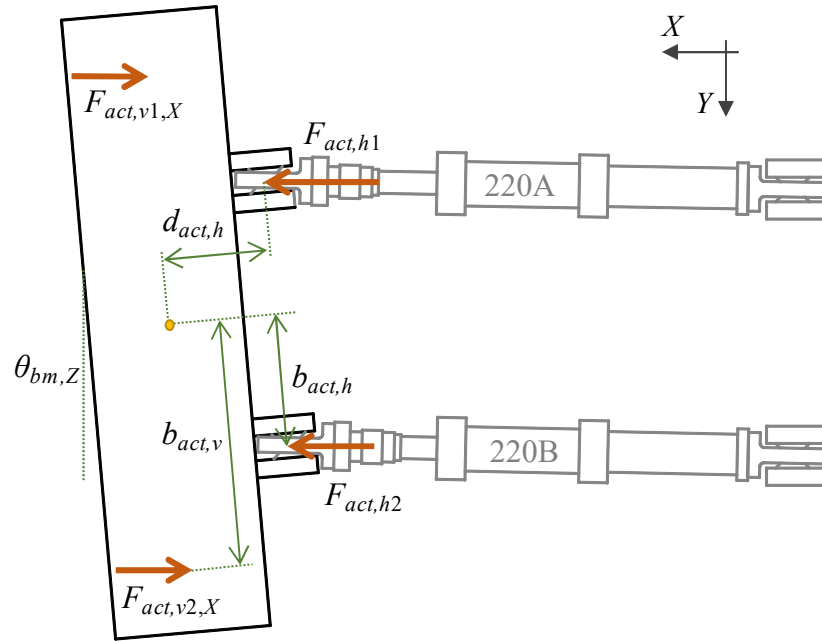
Figure 4-143. Actuator forces acting on loading beam in *XY* plane, Phase II

4.7.2.4. Loading Protocols

In Phase II, a total of 30 tests were conducted on the column specimen in the form of seven

Loading Sets, as summarized in Table 4-26. In all of these tests, equal forces were applied

by the vertical actuators under force control. However, both horizontal actuators were

displacement-controlled and their displacement commands were determined depending on

the desired loading beam's lateral displacement, $\Delta_{bm,X}$, and twist, $\theta_{bm,Z}$. Assuming the

rotations were very small ($\sin \theta \approx \theta$, $\cos \theta \approx 1$, and $\theta^2 \approx 0$), the displacements of the

horizontal actuators 1 and 2 (220A and 220B per Figure 4-143), denoted by $\Delta_{act,h1}$ and

$\Delta_{act,h1}$, respectively, for given $\Delta_{bm,X}$ and $\theta_{bm,Z}$ were computed as:

$$\begin{cases} \Delta_{act,h1} = \Delta_{bm,X} + \theta_{bm,Z} b_{act,h} \\ \Delta_{act,h2} = \Delta_{bm,X} - \theta_{bm,Z} b_{act,h} \end{cases} \tag{4-14}$$

The objectives of the seven Loading Sets considered in this Phase and their respective loading protocols are described in the following sections. The nomenclature for the loading protocol IDs in this Phase start with "HSR2_TU_CNT_Sn," where 2 is the ID of the column specimen as identified during the casting process, "TU" stands for combined torsional and uniaxial loading, "CNT" stands for cantilever state, and the letter "n" after "S" represents the Loading Set number. The letters following the above letters are specific to each Loading Set, giving further information about the loading protocol.

Table 4-26. Loading Sets in Phase II

Loading Set	Number of Protocols	Max. Drift Ratio (%)	Max. Twist (rad)	Lateral Displacement	Twist	Vertical Load
1	2	0	0.09	None	Cyclic	Constant
2	3	0	0.09	None	Cyclic	Cyclic
3	4	0	0.09	None	Cyclic	Constant
4	9	4	0.08	Cyclic	Cyclic	Constant
5	9	5.2	0.055	Arbitrary	Arbitrary	Constant
6	2	8	0.08	Cyclic	Cyclic	Constant
7	1	10	0	Cyclic	None	Constant

4.7.2.4.1. Loading Set 1

The objective of this Loading Set was to examine the response of the HSR column specimen subjected to pure torsion and constant vertical load. For this reason, the horizontal actuators' displacement commands in this Loading Set were produced using zero $\Delta_{bm,X}$ and non-zero $\theta_{bm,Z}$ in Eqs. (4-14).

In the loading protocols of Loading Set 1, the load applied by each vertical actuator equaled 107.75 kips, leading to a total external vertical load of 253 kips on the column. This value includes the weights of the loading beam and actuators and is equivalent to 100% dead load plus 50% maximum live load imposed to the column based on the design code. In each loading protocol, four consecutive sinusoidal twist cycles were applied to the column, with the amplitudes and the periods of the first two cycles being smaller than the second two cycles'. The loading protocols in this Loading Set are listed in Table 4-27 and their respective twist time histories are shown in Figure 4-144 – twist ratio is the ratio of total twist to the loading point's height. Note that twist amplitudes were limited to 0.09 rad, based on the capability of the swivels to undertake out of plane rotation.
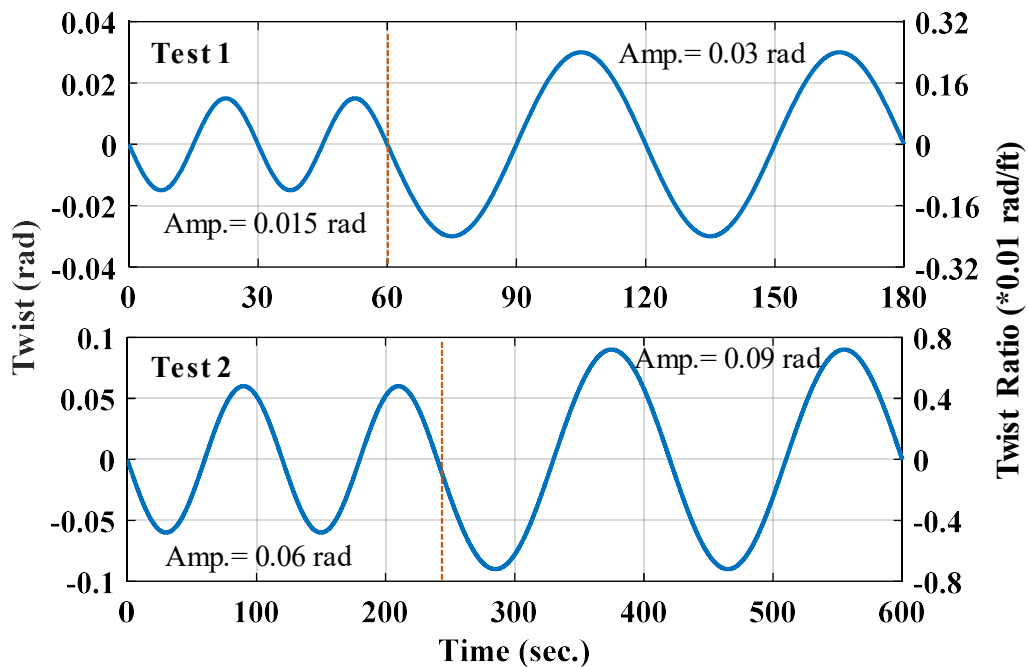
Figure 4-144. Twist time histories in Loading Set 1, Phase II

Table 4-27. Loading protocols in Loading Set 1 from Phase II

No	ID	Max. Twist (rad)
1	HSR2_TU_CNT_S1_TW_3	0.03
2	HSR2_TU_CNT_S1_TW_9	0.09

4.7.2.4.2. Loading Set 2

In this Loading Set, the effects of variable vertical loading on the torsional response of the column specimen were of interest. Similar to Loading Set 1, in Loading Set 2, only pure twist was imposed to the column, while the vertical load was cyclically changed.

Three loading protocols were considered, in all of which twist was applied in the form of three sinusoidal cycles of constant amplitude and frequency of 0.09 rad and 1/120 Hz, respectively. Similar to Loading Set 2 in Phase I, the total load applied by the vertical actuators in every loading protocol consisted of three consecutive sinusoidal functions of constant frequencies but increasing amplitudes, expressed as:

$$F_{act,v}(t) = 215.5 + 253 R_F \sin\left(2\pi \left(R_f \frac{1}{120} \right) t \right) \quad \text{(kips)} \tag{4-15}$$

In Eq. (4-15), t varied from 0 to 120 sec. for each of the loading protocols. The values of R_F for these three functions were 0.1, 0.2, and 0.3. The ratio of the frequency of the cyclic vertical load to the frequency of the cyclic twist, R_f, equaled 1, 2, and 3 for the three loading protocols. The described loading protocols are listed in Table 4-28 and the time histories of the applied vertical loads for these protocols are compared in Figure 4-145.

Table 4-28. Loading protocols in Loading Set 2 from Phase II

No	ID	Vertical Load to Displacement Frequency Ratio
3	HSR2_TU_CNT_S2_V2H_1	1
4	HSR2_TU_CNT_S2_V2H_2	2
5	HSR2_TU_CNT_S2_V2H_3	3
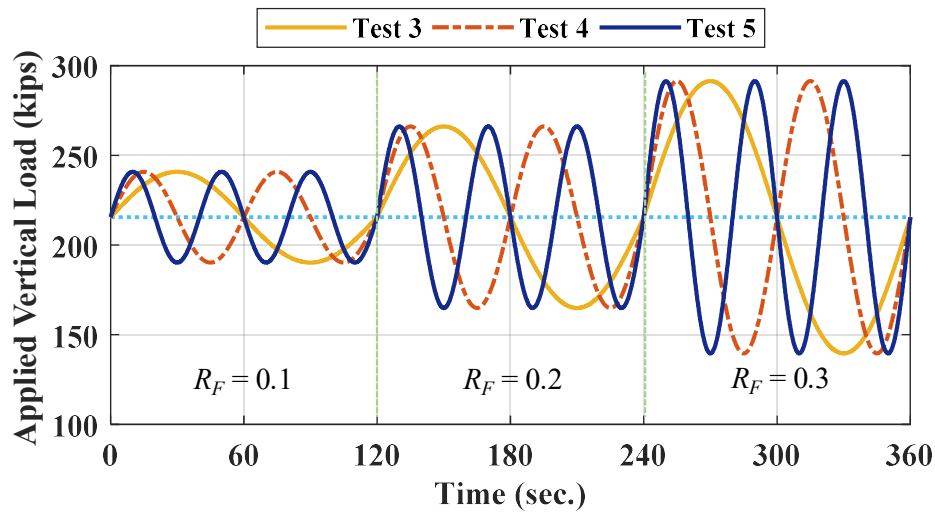
Figure 4-145. Applied vertical load time histories in Loading Set 2, Phase II

4.7.2.4.3. Loading Set 3

This Loading Set aimed to investigate the impact of twist rate on the behavior of the HSR column specimen, particularly its joint sliding. In each loading protocol of Loading Set 3, a full sinusoidal cycle of pure twist with an amplitude of 0.09 rad and a different maximum twist rate was applied to the column, while the vertical load remained constant. For all four protocols herein, the total load applied by the vertical actuators was equal to 215.5 kips. Contrarily, the frequency of the applied twist sinusoid varied for each loading protocol to achieve various peak twist rates of 0.05, 0.1, 0.15, and 0.2 rad/sec. (see Figure 4-146). The list of the loading protocols in Loading Set 3 is presented in Table 4-29.

316

Table 4-29. Loading protocols in Loading Set 3 from Phase II

No	ID	Max. Twist Rate (rad/sec.)
6	HSR2_TU_CNT_S3_TR_5	0.05
7	HSR2_TU_CNT_S3_TR_10	0.1
8	HSR2_TU_CNT_S3_TR_15	0.15
9	HSR2_TU_CNT_S3_TR_20	0.2
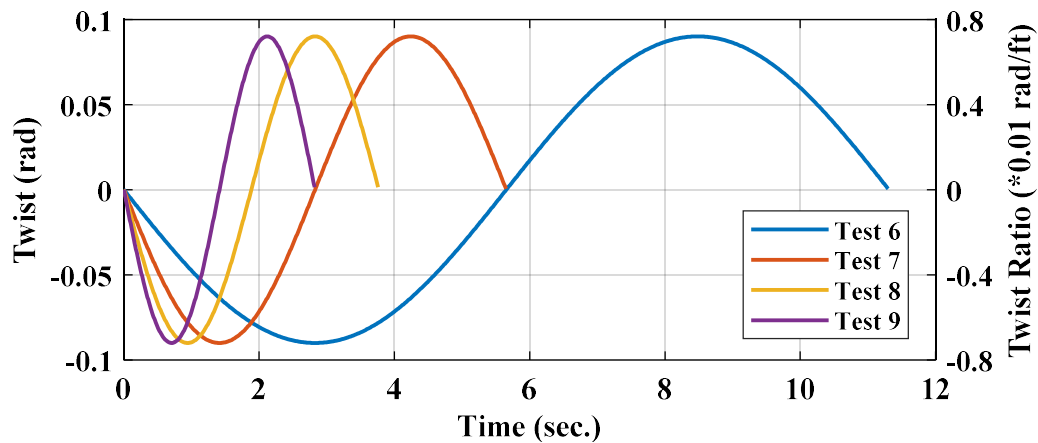
Figure 4-146. Twist time histories in Loading Set 3, Phase II

4.7.2.4.4. Loading Set 4

The loading protocols in Loading Set 4 included the simultaneous application of cyclic lateral displacement and cyclic twist to investigate their combined effect on the performance of HSR columns. Of particular interest were the effects of such loading on the response of sliding joints and the column damage modes.

This Loading Set comprised nine loading protocols. In all of the protocols, the load applied by the vertical actuators was kept constant and equal to 215.5 kips, leading to a total external vertical load of 253 kips on the column. In each loading protocol, the lateral displacement was applied in the form of eight full sinusoidal cycles with constant

317

amplitude and frequency, while a different amplitude was considered for each group of three loading protocols. These lateral displacement amplitudes corresponded to the peak drift ratios from the three earthquake hazard levels considered in Loading Set 1 in Phase I, namely, 1.3%, 2%, and 4%. The twist time history for each loading protocol included 13 sinusoid cycles of constant amplitude, but variable frequency. The frequencies of the twist cycles in every loading protocol consisted of 0.5, 1, 2, and 3 times the frequency of the lateral displacement cycles in the same loading protocol.

Table 4-30. Loading protocols in Loading Set 4 from Phase II

No	ID	Max. Drift Ratio (%)	Max. Twist (rad)
10	HSR2_TU_CNT_S4_DR_1_3_T2D_0_5	1.3	0.0065
11	HSR2_TU_CNT_S4_DR_1_3_T2D_1	1.3	0.013
12	HSR2_TU_CNT_S4_ DR_1_3_T2D_2	1.3	0.026
13	HSR2_TU_CNT_S4_ DR_2_T2D_0_5	2	0.01
14	HSR2_TU_CNT_S4_ DR_2_T2D_1	2	0.02
15	HSR2_TU_CNT_S4_ DR_2_T2D_2	2	0.04
22	HSR2_TU_CNT_S4_ DR_4_T2D_0_5	4	0.02
23	HSR2_TU_CNT_S4_ DR_4_T2D_1	4	0.04
24	HSR2_TU_CNT_S4_ DR_4_T2D_2	4	0.08

For each of the above-mentioned three lateral displacement amplitudes, three levels of twist were considered. The twist level was characterized by the ratio of the twist amplitude to the lateral drift ratio amplitude, denoted by R_A. The amplitude ratios used here were 0.5, 1, and 2. Table 4-30 summarizes the loading protocols in this Loading Set and Figure 4-147, Figure 4-148, and Figure 4-149 show their corresponding drift ratio and twist time histories. It is noted that the reason why the last three loading protocols in Table

4-30 are numbered 22-24 instead of 16-18 is that, because of some actuator tuning issues, those three tests had to be run after the first six tests in Loading Set 5 (Table 4-31).
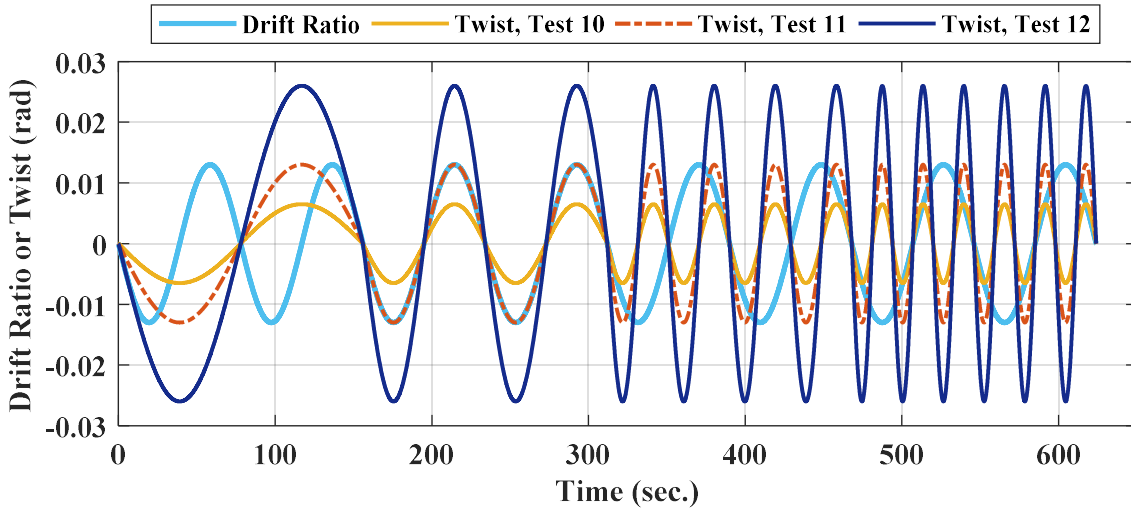
Figure 4-147. Drift and twist time histories for tests 10-12, Loading Set 4, Phase II
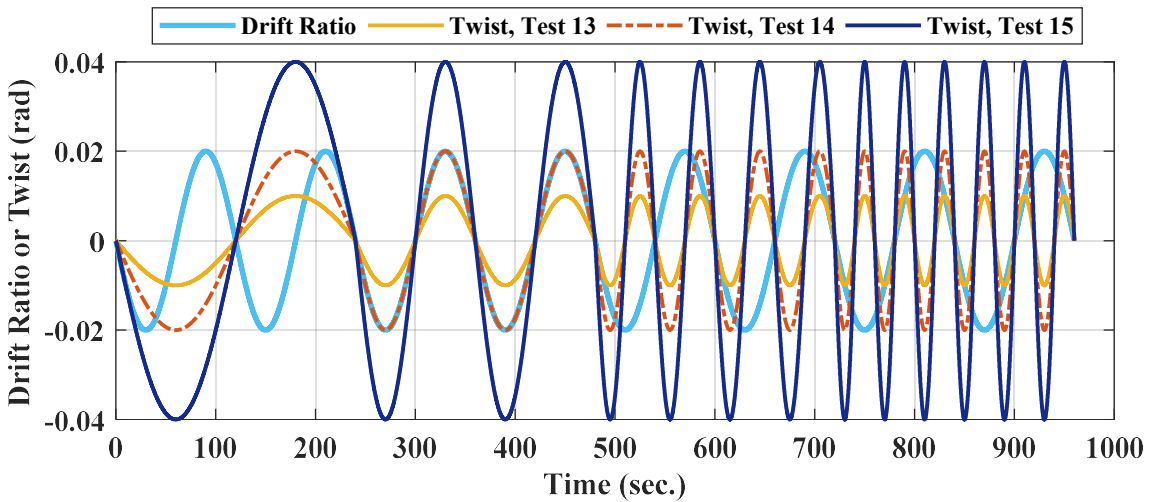
Figure 4-148. Drift and twist time histories for tests 13-15, Loading Set 4, Phase II
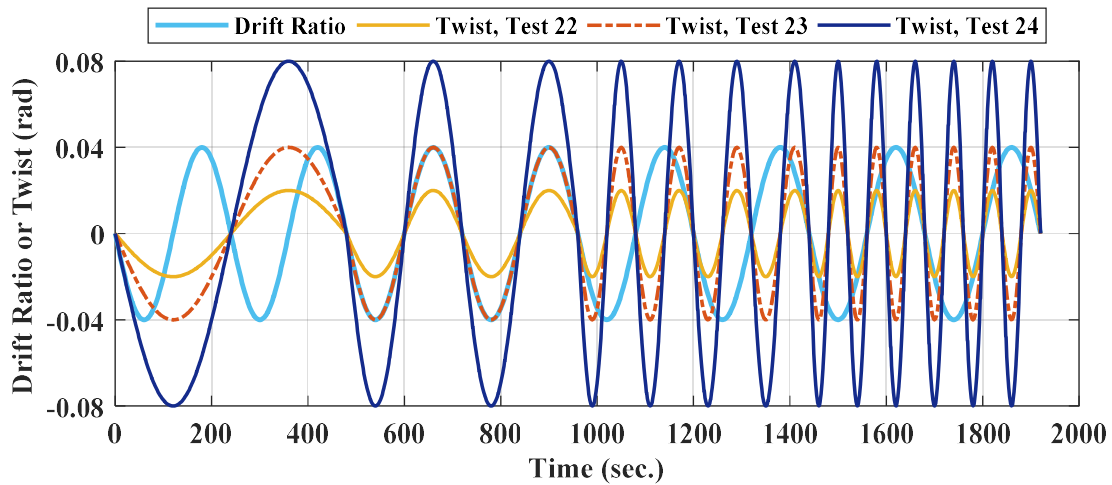
Figure 4-149. Drift and twist time histories for tests 22-24, Loading Set 4, Phase II

4.7.2.4.5. Loading Set 5

The loading protocols of Loading Set 5 comprised arbitrary lateral displacement and twist time histories in conjunction with constant vertical load. The results of the tests under these loading protocols would enable investigating the response of HSR columns, especially their joints, under arbitrary displacement and twist time histories.

In all the loading protocols, the total load applied by the vertical actuators remained equal to 215.5 kips. The lateral displacement and twist time histories were, however, generated by running time history analyses using a 3D OpenSees model of a pier including the column specimen. Since the developed model did not have the full superstructure simulated, the superstructure's horizontal mass component was assigned to a point with 3 inches of eccentricity with respect to the centerline of the column so that the column experiences sufficient twist. The time histories were obtained under six ground motions, two from the 5%-in-50-years ensemble, two from the 2%-in-50-years ensemble, and two from the 1%-in-50-years ensemble.

320

In order to be able to apply the resulting displacement time histories with a rate producible by the available hydraulics, the durations of the time histories was increased such that the maximum displacement rate for each actuator did not exceed 8 in./sec. Moreover, for one motion per hazard level, two loading protocols were considered, one with the lateral displacement and twist time histories directly obtained from the analysis, and one with the same lateral displacement time history but doubled twist time history.

Given the foregoing, a total of nine loading protocols (three per hazard level) constituted Loading Set 5 (Table 4-31). The time histories of the drift ratio and the twist applied to the column specimen through some of these loading protocols are demonstrated in Figure 4-150 and Figure 4-151 – note that the time histories of the tests 18, 21, and 27 were similar to those shown for the tests 17, 20, and 26, respectively, except their twist magnitudes were double.

Table 4-31. Loading protocols in Loading Set 5 from Phase II

No	ID	Ground Motion	Max. Drift Ratio (%)	Max. Twist (rad)
16	HSR2_TU_CNT_S5_5in50_GM_7	5% in 50 yr, GM 7	1.71	0.018
17	HSR2_TU_CNT_S5_5in50_GM_16	5% in 50 yr, GM 16	1.10	0.016
18	HSR2_TU_CNT_S5_5in50_GM_16_2	5% in 50 yr, GM 16	1.10	0.032
19	HSR2_TU_CNT_S5_2in50_GM_9	2% in 50 yr, GM 9	2.26	0.033
20	HSR2_TU_CNT_S5_2in50_GM_13	2% in 50 yr, GM 13	2.14	0.028
21	HSR2_TU_CNT_S5_2in50_GM_13_2	2% in 50 yr, GM 13	2.14	0.055
25	HSR2_TU_CNT_S5_1in50_GM_12	1% in 50 yr, GM 12	5.18	0.033
26	HSR2_TU_CNT_S5_1in50_GM_13	1% in 50 yr, GM 13	3.44	0.026
27	HSR2_TU_CNT_S5_1in50_GM_13_2	1% in 50 yr, GM 13	3.44	0.052
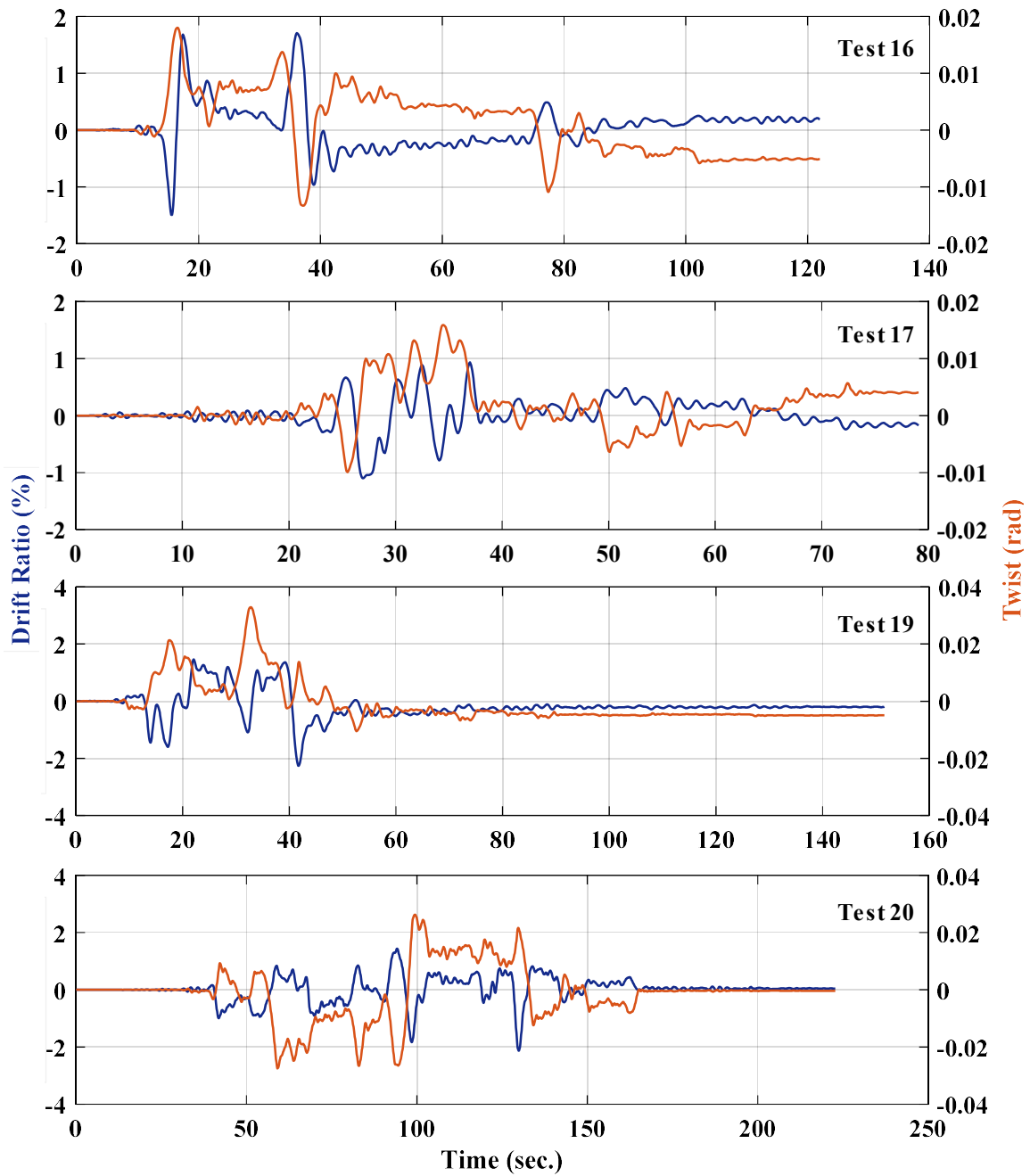
Figure 4-150. Drift and twist time histories for tests 16, 17, 19, and 20, Loading Set 5, Phase II
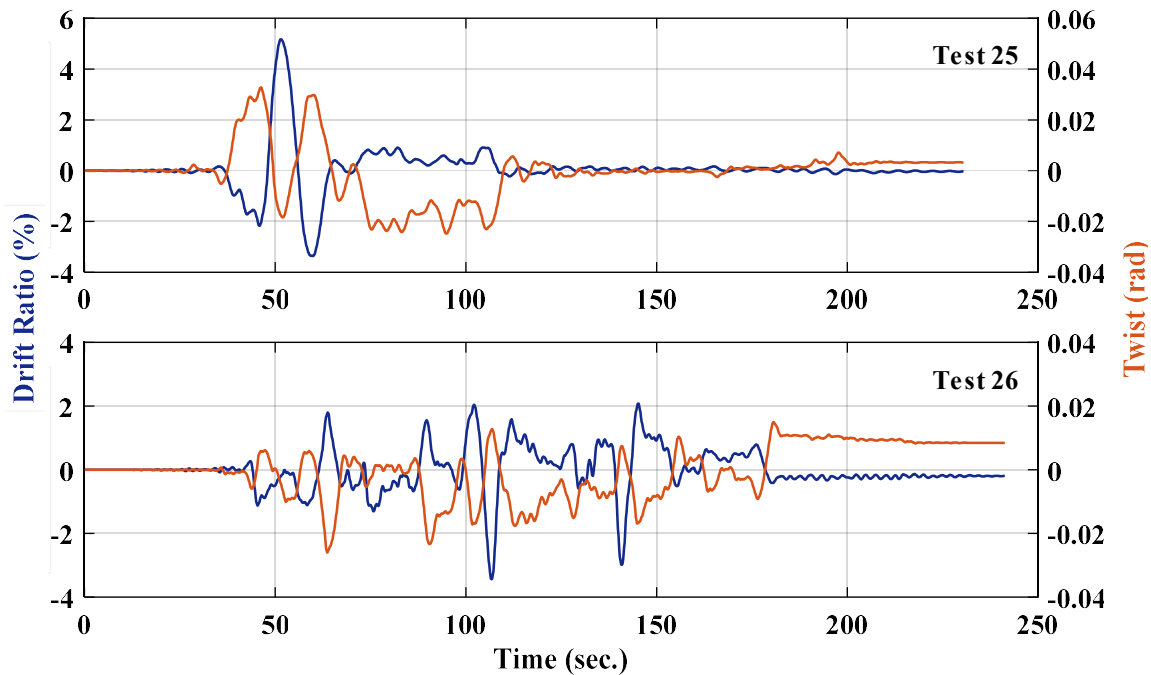
Figure 4-151. Drift and twist time histories for tests 25-26, Loading Set 5, Phase II

4.7.2.4.6. Loading Set 6

This Loading Set was intended to evaluate the response of the HSR column specimen and its damage subjected to the combined effects of excessive lateral displacement and twist.

Similarly to the previous three Loading Sets, in this Loading Set, the total load applied by the vertical actuators was constant and equal to 215.5 kips. Both lateral displacement and twist were, however, applied through sinusoidal functions similar to those in Loading Set 4. Each loading protocol consisted of eight lateral displacement cycles of constant amplitude and frequency, along with 13 twist cycles of constant amplitude and variable frequency. In this Loading Set, only three loading protocols with two lateral displacement amplitudes were considered. The peak displacement amplitudes corresponded to 6% and 8% peak drift ratios, whereas the twist amplitude in each loading protocol was equal to

323

the drift ratio amplitude – e.g. 0.06 rad for the procedure with 6% of drift ratio amplitude. The loading protocols of this Loading Set are summarized in Table 4-32 and their corresponding drift ratio and twist time histories are displayed in Figure 4-152.

Table 4-32. Loading protocols in Loading Set 6 from Phase II

No	ID	Max. Drift Ratio (%)	Max. Twist (rad)
28	HSR2_TU_CNT_S6_DR_6	6	0.06
29	HSR2_TU_CNT_S6_DR_8	8	0.08
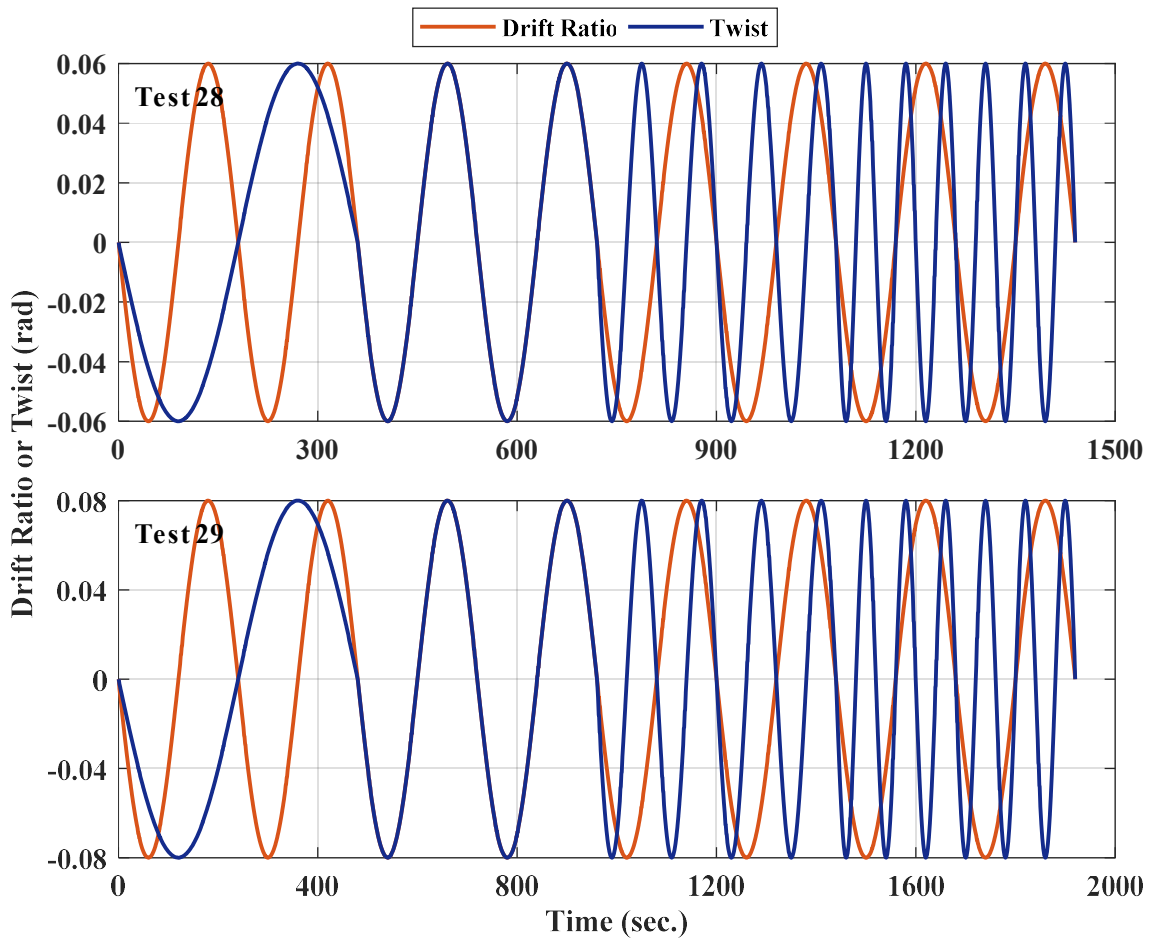
Figure 4-152. Drift ratio and twist time histories in Loading Set 6, Phase II

4.7.2.4.7. Loading Set 7

The last Loading Set consisted of one loading protocol imposing the maximum lateral displacement achievable by the horizontal actuators to the column specimen. For that reason, no twist was applied in this loading protocol. The applied displacement profile consisted of two sinusoid cycles of the same amplitude (equal to 15 in., amounting to 10% drift ratio). The ID for this procedure is HSR2_TU_CNT_S7_DR_10.

4.7.2.5. Results and Discussion

4.7.2.5.1. Results from Loading Set 1

The torsion vs. twist response of the column obtained under the first pure twist loading protocol, i.e. HSR2_TU_CNT_S1_TW_3 is demonstrated in Figure 4-153. As seen, there was a breakaway friction at the sliding joints, but considering the high torsional strength of the column segments compared to the torsion required to cause rotational sliding at the sliding joints, sliding started very soon after the loading started. The torsion required to overcome the breakaway friction was almost 70 kip-ft, which reduced to almost 40 kip-ft (i.e. 40% decrease) in both directions after sliding initiation. This reduction occurred with a faster rate at the beginning and became less significant as the accumulated rotational sliding increased.

Based on the obtained hysteretic response (Figure 4-153), the column did not exhibit any rotational sliding restoration capability at this twist level (i.e. the residual twist was equal to the peak twist in each cycle). This was because the torsion resisted through friction at the sliding joints was much higher than the opposite torsion created by the bearing of the tendons against the ducts upon rotational sliding. It is noted that, during

sliding, the torsional (tangent) stiffness significantly decreased, as hardening could only be achieved through the bearing of the tendons against the ducts.
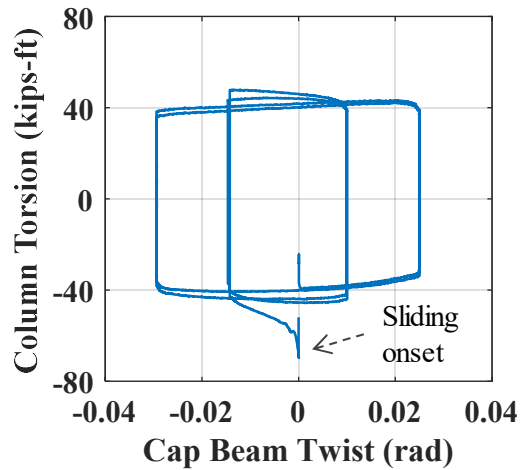
Figure 4-153. Phase II, loading protocol HSR2_TU_CNT_S1_TW_3: torsion vs. twist response

According to Figure 4-154, during the same test, only the first sliding joint (Joint 2) underwent sliding and the other joints remained without relative rotational displacement. The reason why the second sliding joint was not activated was that the maximum twist in this test was smaller than the maximum rotational sliding capacity of one sliding joint, i.e. 0.096 rad. Given the very high torsional stiffness of the column segments, the rotational sliding time history at Joint 2 nearly matches the total twist time history imposed to the loading beam (Figure 4-144).
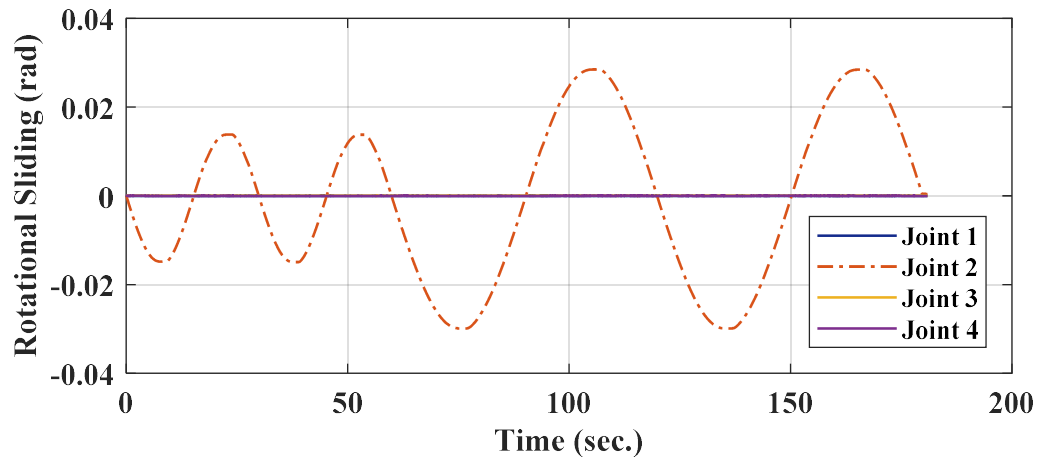
Figure 4-154. Phase II, loading protocol HSR2_TU_CNT_S1_TW_3: time histories of joint rotational sliding

The torsion vs. rotational sliding responses of all joints are also displayed in Figure 4-155. The slope variation observed in the sliding joint response (Figure 4-155(b)) leading to the curved edges of the hysteresis loops could be justified by the increase of coefficient of friction with sliding velocity (Reddy Goli 2019).

To understand the potential effects of rotational sliding on the tendon forces, Figure 4-156 shows the variation of the total posttensiong force with the loading beam twist. According to this figure, the total PT force was minimally affected by the rotational sliding at the first sliding joint. This wass because the elongation caused in the tendons by the rotational sliding at the sliding joint was very small compared to the total tendon lengths.
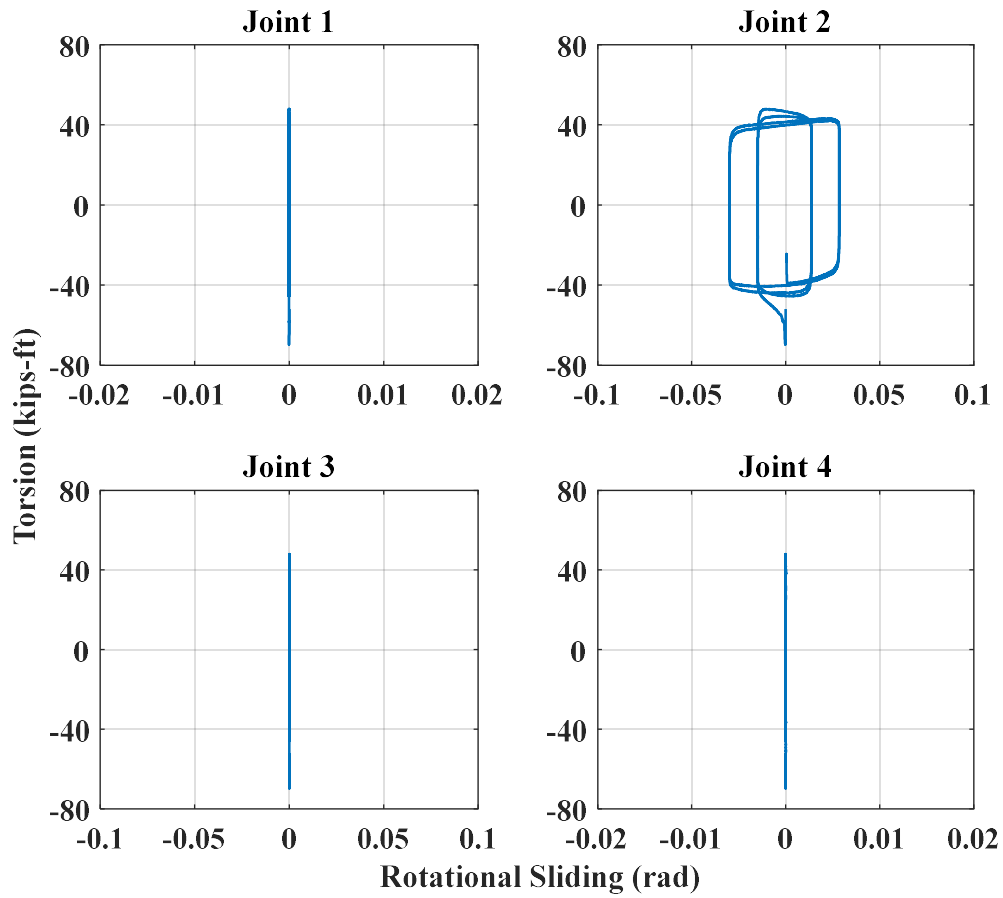
Figure 4-155. Phase II, loading protocol HSR2_TU_CNT_S1_TW_3: joint torsion vs. rotational sliding responses
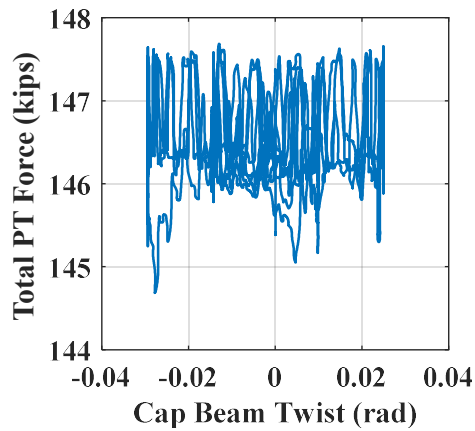
Figure 4-156. Phase II, loading protocol HSR2_TU_CNT_S1_TW_3: total PT force vs. loading beam twist response

328

The damage observed on the column surface after the first test was limited to a few diagonal hairline cracks on its bottom segment (Figure 4-158) and its top segment (Figure 4-157). The cause of these cracks, most of which had appeared on the column surface before the torsion application, has not been identified. However, because of their very small widths (less than 0.01 in.), these cracks ar considered inconsequential to the column's structural performance.
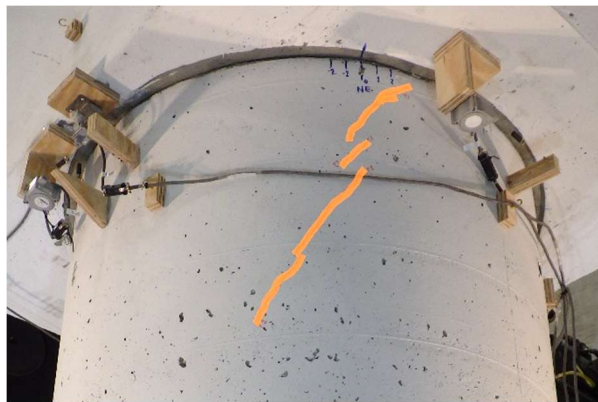
Figure 4-157. Phase II, loading protocol HSR2_TU_CNT_S1_TW_3: cracks on northeast side of top segment after test
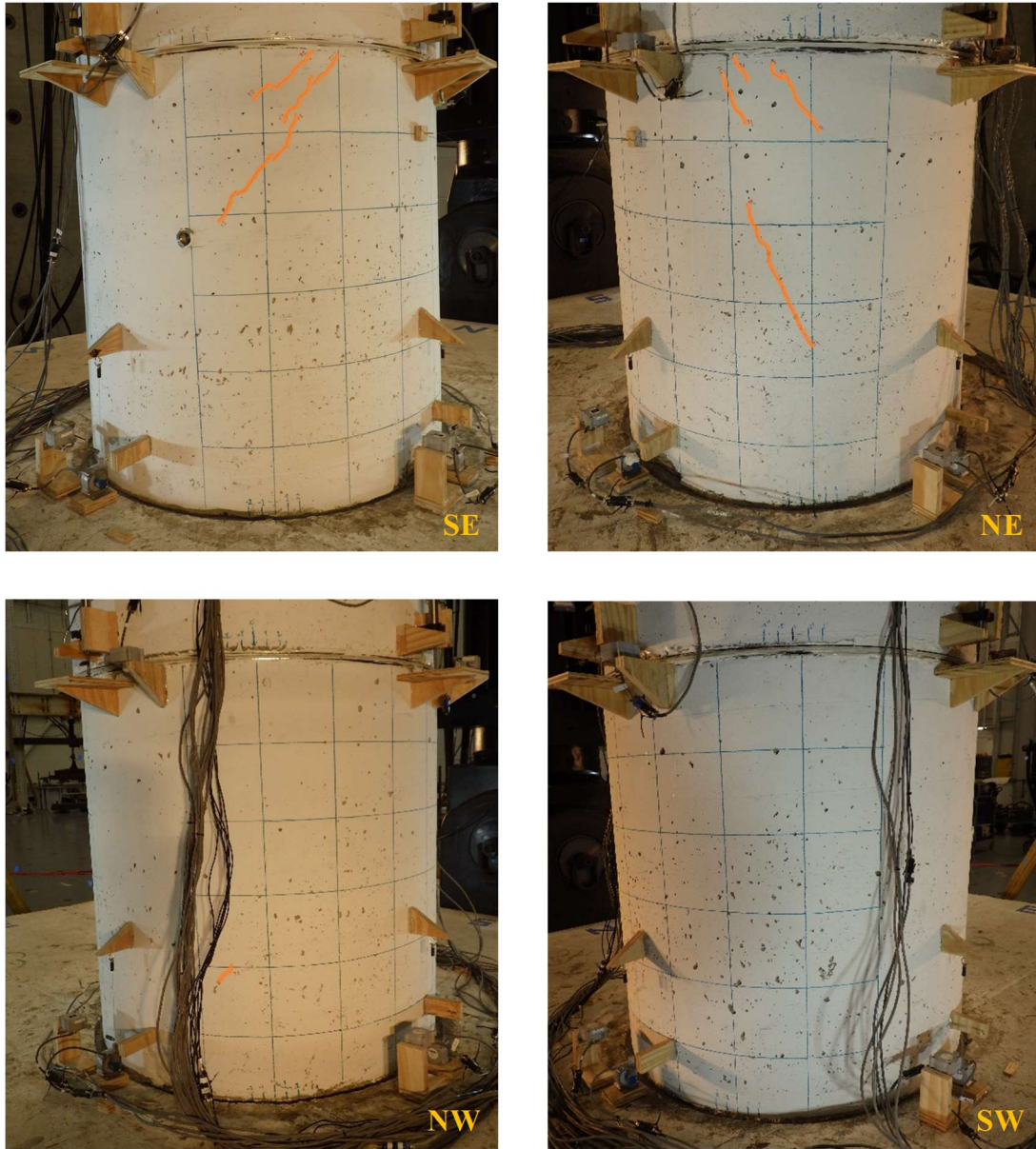
Figure 4-158. Phase II, loading protocol HSR2_TU_CNT_S1_TW_3: distribution of cracks on bottom segment after test

The column's torsion vs. twist response under the second loading protocol in Loading Set 1, i.e. HSR2_TU_CNT_S1_TW_9, is shown in Figure 4-159. The torsion required to overcome the breakaway friction at the first sliding joint was almost 89 kip-ft, i.e. 27%

larger than that in the first test. The breakaway friction in the first test was lower because, due to a technical error, loading protocol HSR2_TU_CNT_S1_TW_3 had to be repeated in the first test and the data presented earlier belonged to the repeated test. The maximum torsion values resisted by the column under the maximum twist of 0.09 rad in the positive and negative directions were 70 kip-ft and 53 kip-ft, respectively. The difference between these values could be due to the initial duct misalignments at the sliding joints and the unevenness of the sliding surfaces. Note that the unevenness at the sliding joint surfaces could result in the rotational sliding around an axis other than the column's central axis (see Figure 4-160, where sliding components in X and Y directions are non-zero). The residual twist values in the column were equal to the peak applied twist, demonstrating the column's inability to provide torsional self-centering. It is noted that the entire residual twist resulted from the residual sliding at the sliding joints (see Figure 4-161) and did not represent permanent damage to the column.
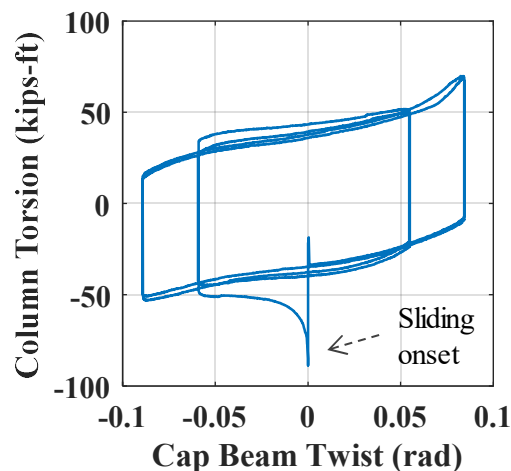
Figure 4-159. Phase II, loading protocol HSR2_TU_CNT_S1_TW_9: torsion vs. twist response
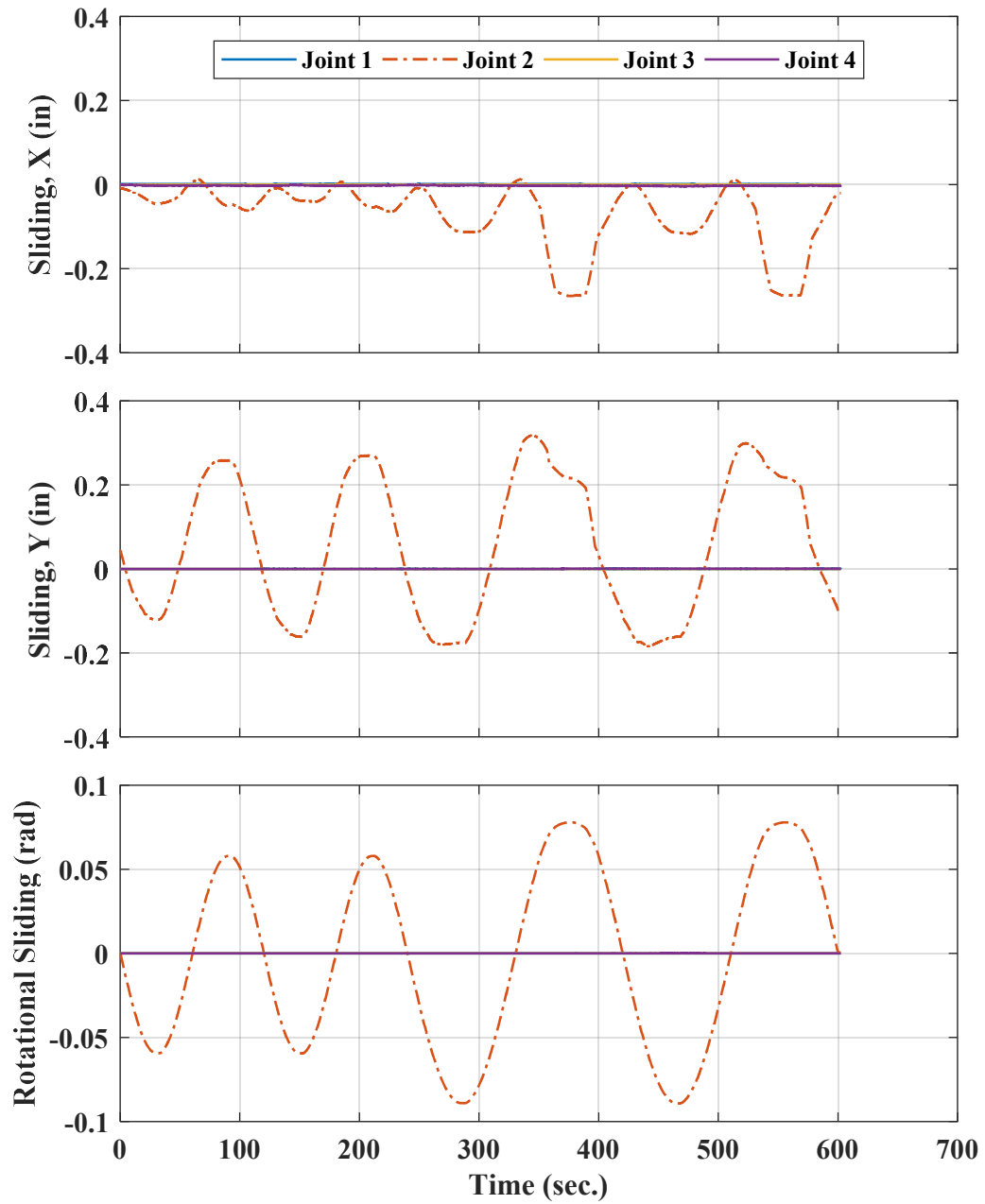
Figure 4-160. Phase II, loading protocol HSR2_TU_CNT_S1_TW_9: time histories of joint sliding components
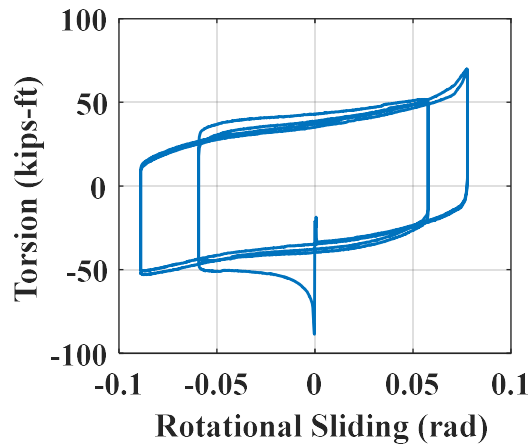
Figure 4-161. Phase II, loading protocol HSR2_TU_CNT_S1_TW_9: torsion vs. rotational sliding response of Joint 2

In this test also, the joint sliding was confined to the first sliding joint (Joint 2, Figure 4-160), which could fully accommodate the imposed twist. As observed in Figure 4-160, however, Joint 2 had also experienced considerable non-rotational sliding (e.g., up to 0.3 in. in *Y* direction), which may indicate potential unevenness of the joint interface and/or misalignment of the ducts. In addition, there was a small difference between the maximum rotational sliding achieved in the positive and negative directions under the twist cycle of 0.09 rad amplitude (less than 0.08 rad and almost 0.09 rad, respectively). According to Figure 4-161 that shows the torsion variation with rotational sliding at Joint 2, the residual rotational sliding at the only activated sliding joint in this test almost equaled the peak rotational sliding in each cycle. The decrease in the coefficient of friction with the sliding travel is also clear in this graph.

The variations of tendon forces with time are compared in Figure 4-162. The noise in the data obtained from one of the load cells (used for the east tendon) was significant, but the trends are still clear. The fact that not all the tendon forces increased at the same twist

333

values is because of the eccentric rotational sliding at the first sliding joint, as mentioned earlier. The total PT force increased only less than 5% at the twist peak of 0.09 rad, implying that the the HSR column's twist cannot damage the tendons. The total PT loss was also negligible (about 0.3%).
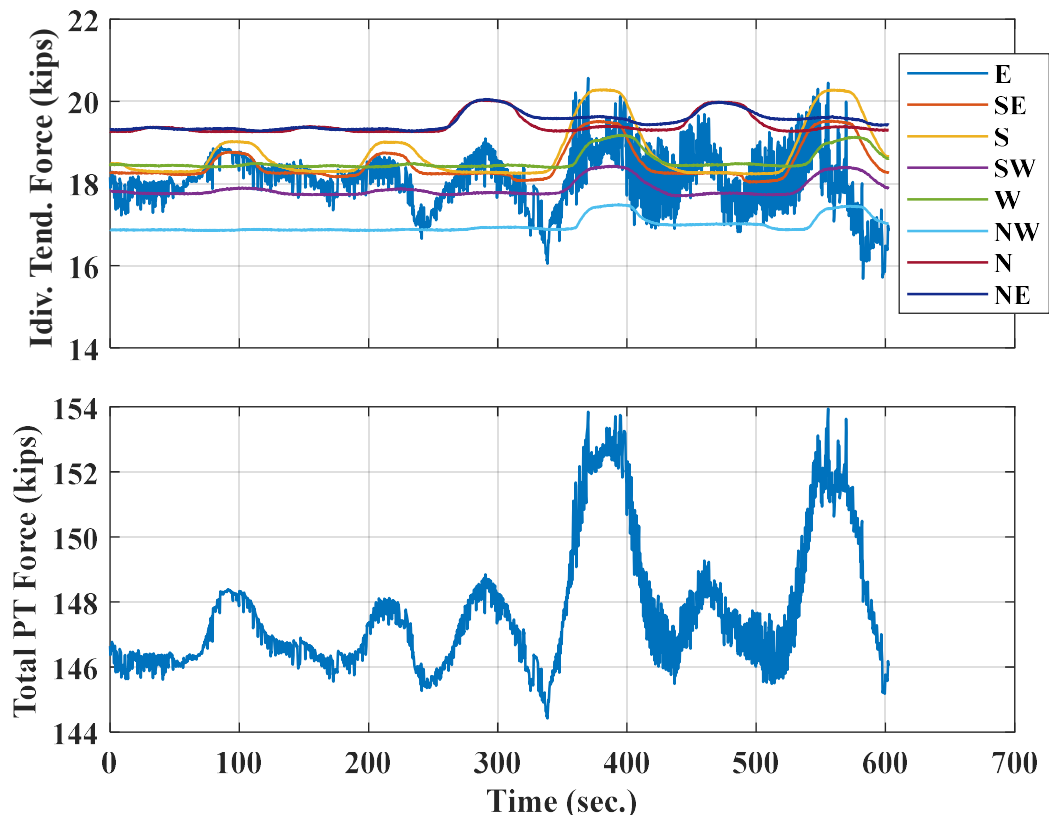
Figure 4-162. Phase II, loading protocol HSR2_TU_CNT_S1_TW_9: time histories of tendon forces
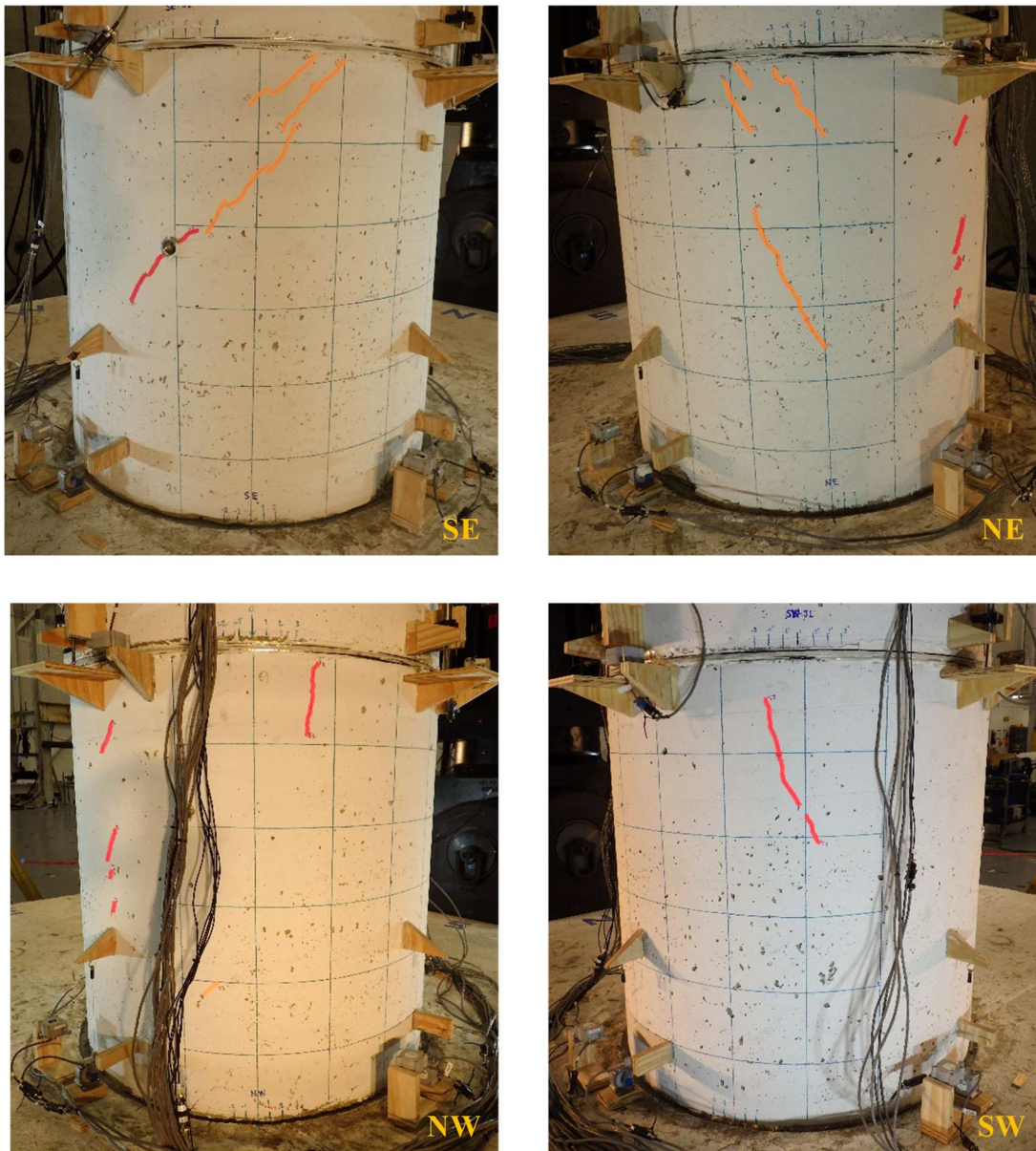
Figure 4-163. Phase II, loading protocol HSR2_TU_CNT_S1_TW_9: distribution of cracks on bottom segment after test

The new cracks appeared on the column's bottom and top segments during this test are shown in Figure 4-163 and Figure 4-164, respectively. All these cracks were hairline

335

cracks and no cracks were observed on the middle segment. Considering that cracks with comparable orientation had also appeared on the segments surfaces during the initial tests in Phase I, these cracks may not necessarily be associated with the torsion-induced shear stresses in the current test, as the extent of torsion resisted by the column in this test was not high enough to cause shear cracking.
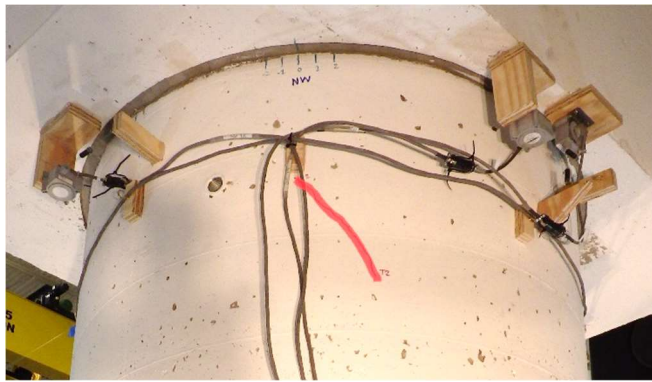
Figure 4-164. Phase II, loading protocol HSR2_TU_CNT_S1_TW_9: cracks on northwest side of top segment after test

4.7.2.5.2. Results from Loading Set 2

The time histories of the total axial force acting on the column during the three tests of Loading Set 2 are shown in Figure 4-165. The data obtained from the east tendon load cell during the test under loading protocol HSR2_ TU_CNT_S2_V2H_1 was corrupted, which is why the corresponding total force time history (i.e. the line labeled as Freq. Ratio = 1 in the figure) has a lower average than the other two (384 kips vs. 397 kips).

The column torsion time histories obtained through the three tests with various vertical to horizontal cyclic load frequency ratios are compared in Figure 4-166.

According to these results, the effect of the variable vertical load on the column's torsion is found insignificant, regardless of the frequency ratio, because the externally applied vertical load only accounts for 20% of the total pressure over the sliding joint interfaces. Additionally, after the tests in Loading Set 2, no considerable increase/growth of cracks was observed on the column segments (Figure 4-167).
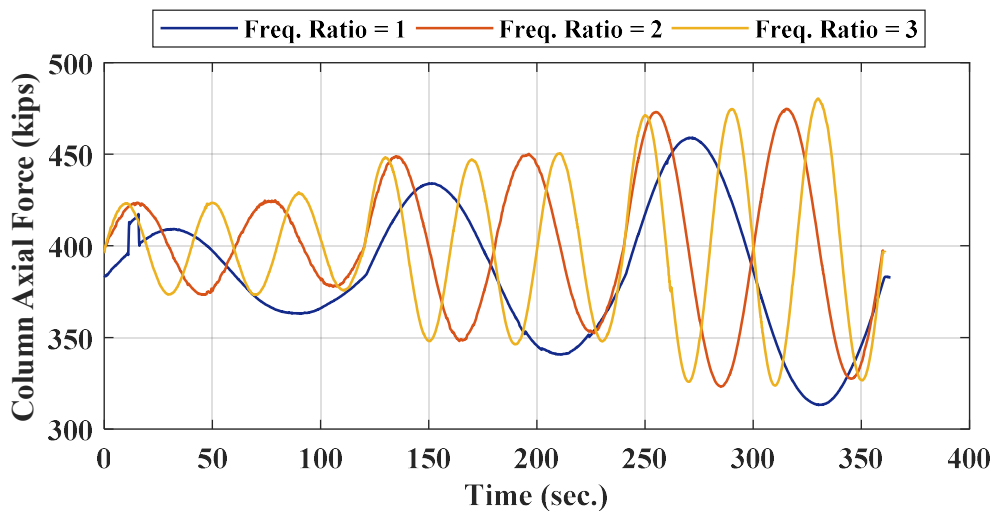
Figure 4-165. Phase II, Loading Set 2: time histories of column axial force
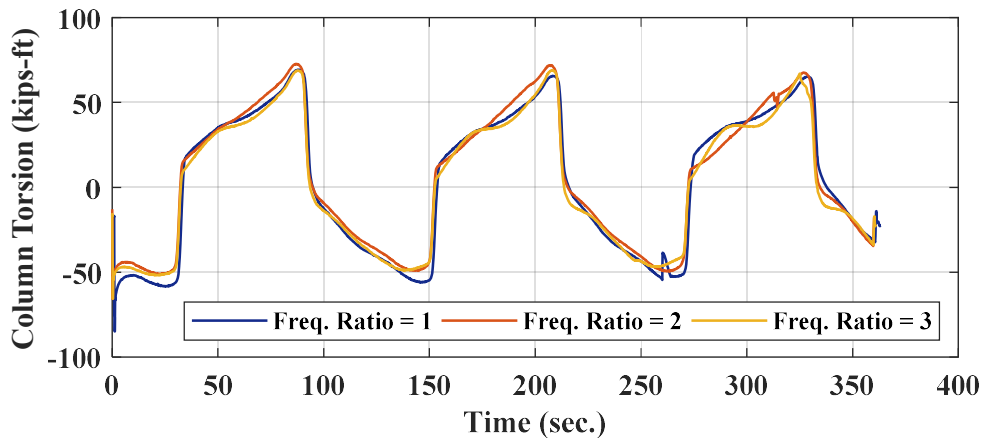
Figure 4-166. Phase II, Loading Set 2: time histories of column torsion

337
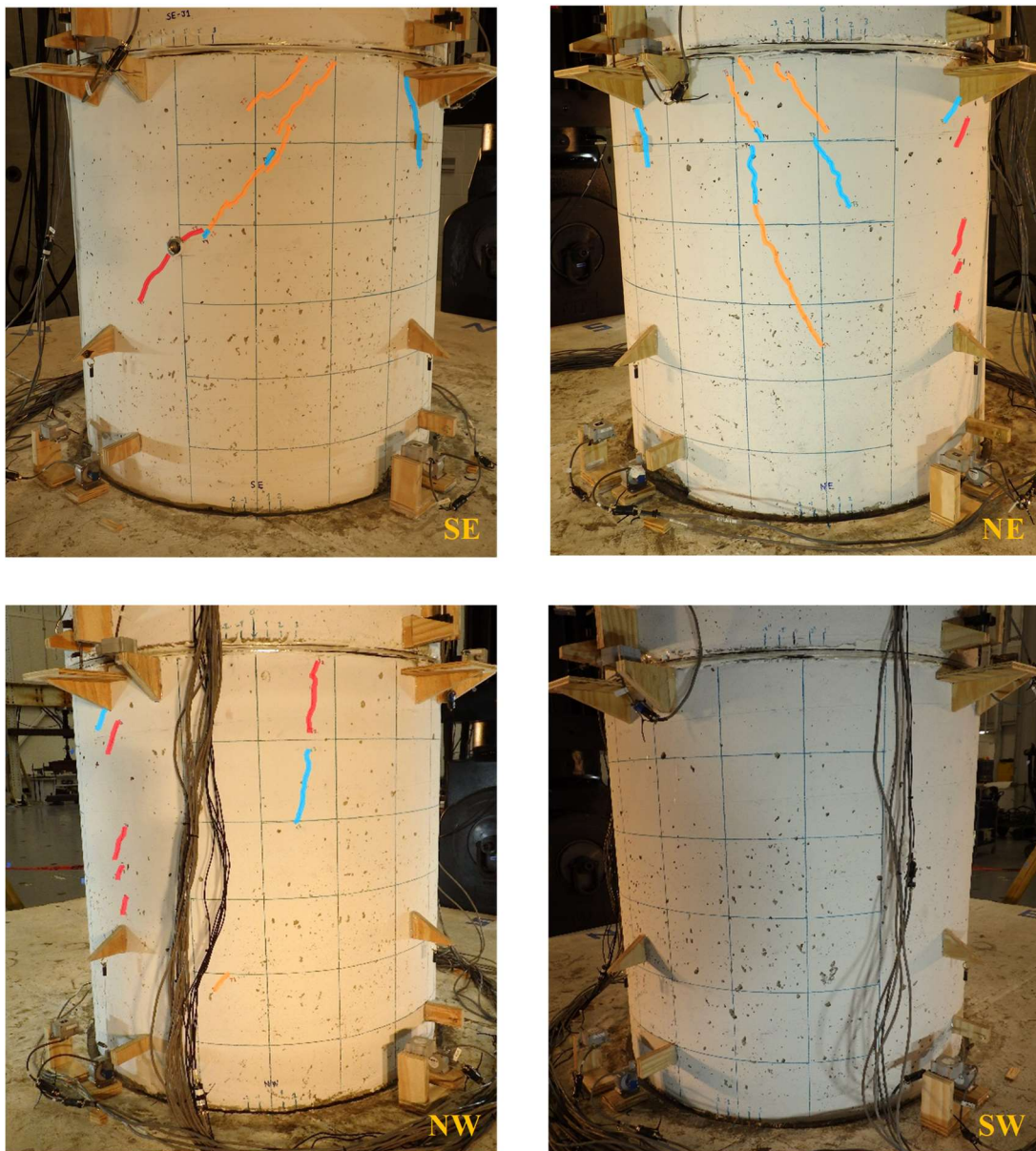
Figure 4-167. Phase II, Loading Set 2: distribution of cracks on bottom segment after tests

4.7.2.5.3. Results from Loading Set 3

The column specimen's torsion vs. twist responses obtained from the tests in Loading Set 3 (for various twist rates) are compared in Figure 4-168(a). No significant difference is observed in the responses, except for an increase in the torsion at the beginning of loading with the twist rate. The potential sources of this increase include the increase of breakaway friction with velocity and the inertia of the loading beam. During these tests, the second sliding joint (Joint 3) still exhibited zero sliding, whereas the first sliding joint (Joint 2) accommodated almost the entire twist imposed to the column (Figure 4-168(b)). Per Figure 4-168(b), the dependence of friction coefficient on sliding velocity (over the examined range) is found insignificant.
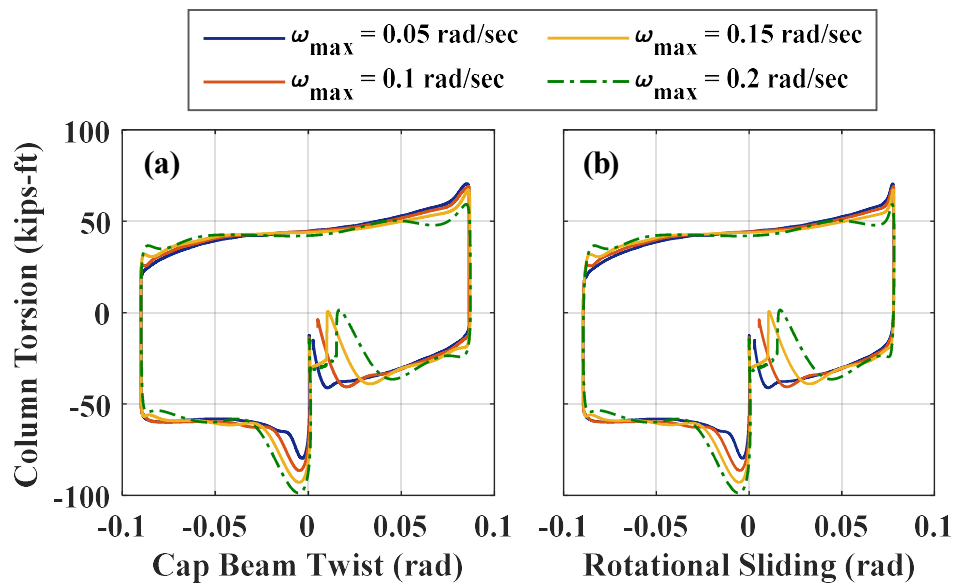
Figure 4-168. Phase II, Loading Set 3: (a) column torsion vs. twist responses; (b) joint torsion vs. rotational sliding responses of Joint 2

The extra damage caused to the column during this Loading Set was a slight growth of some of the previous hairline cracks on the column segments.

4.7.2.5.4. Results from Loading Set 4

The time histories of the loading beam's lateral displacement and twist measured during the first three loading protocols of Loading Set 4 with a maximum drift ratio of 1.3% (HSR2_TU_CNT_S4_DR_1_3_T2D_0_5, HSR2_TU_CNT_S4_DR_1_3_T2D_1, and HSR2_TU_CNT_S4_DR_1_3_T2D_2, with the twist to drift ratio amplitude ratios of 0.5, 1, and 2, respectively) are displayed in Figure 4-169. Although the obtained lateral displacement time histories closely resemble the desired time histories, the measured twist time histories are slightly different (see Figure 4-147). The observed differences could be due to the post-processing assumptions and the loading beam's motion in the Y direction – note that a full control over the planar motion of the loading beam would require an additional horizontal actuator normal to the other two.

The base shear vs. lateral displacement responses of the HSR column specimen achieved under the above loading protocols are demonstrated in Figure 4-170. Based on the plotted results, the larger the twist amplitude was, the more significant the base shear variation with lateral displacement became. This result was predictable, because the friction force at the sliding joint depends on the frictional stresses over the entire sliding joint, while depending on the translational and rotational sliding components, the distributions of frictional stresses over the joint area varies. Moreover, the bearing forces caused by the tendons on the ducts change with the rotational sliding at the sliding joints, thereby affecting the joint resistance, and consequently the base shear.
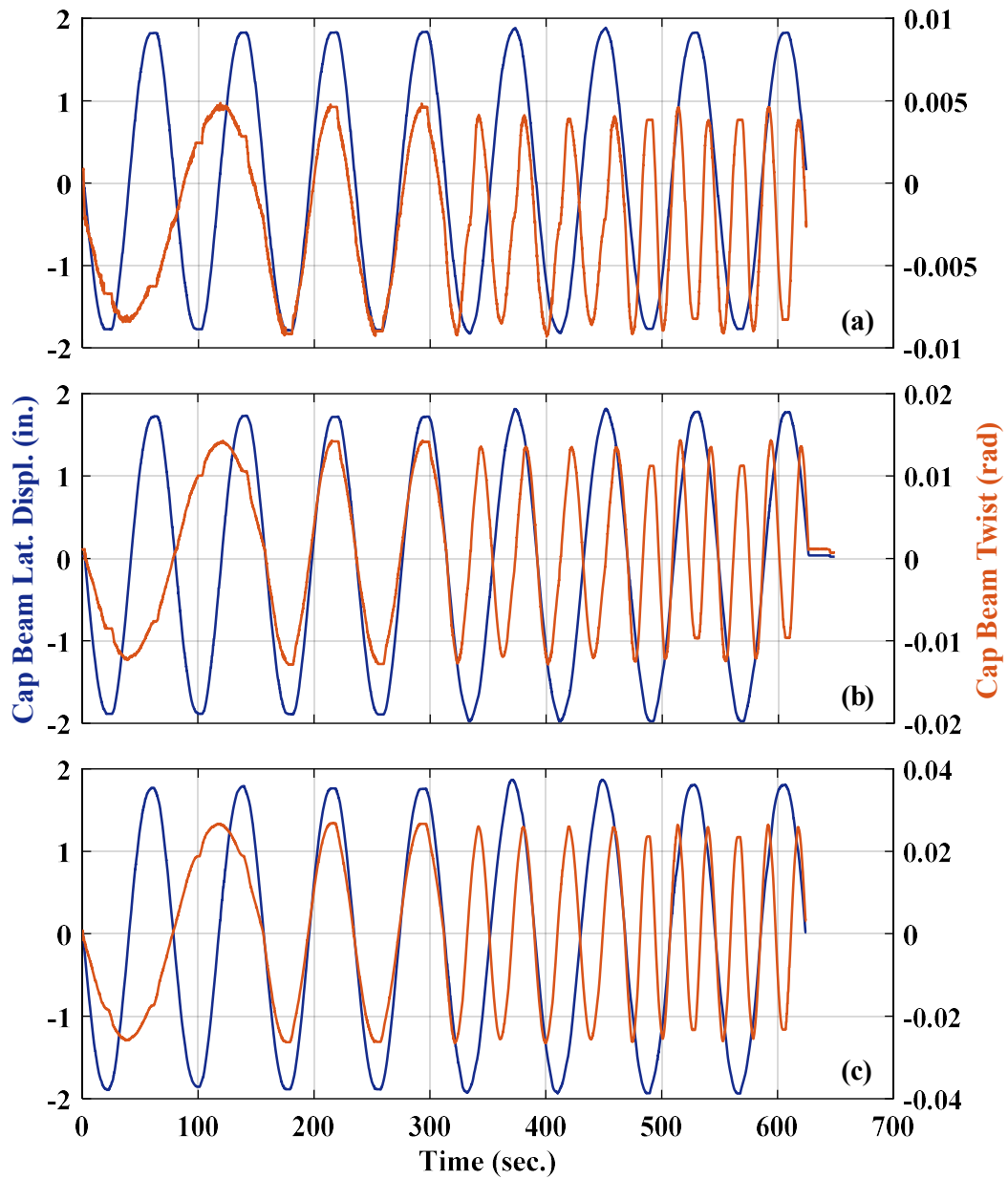
Figure 4-169. Phase II, Loading Set 4: beam lateral displacement and twist time histories under loading protocols: (a) HSR2_TU_CNT_S4_DR_1_3_T2D_0_5; (b) HSR2_TU_CNT_S4_DR_1_3_T2D_1; (c) HSR2_TU_CNT_S4_DR_1_3_T2D_2
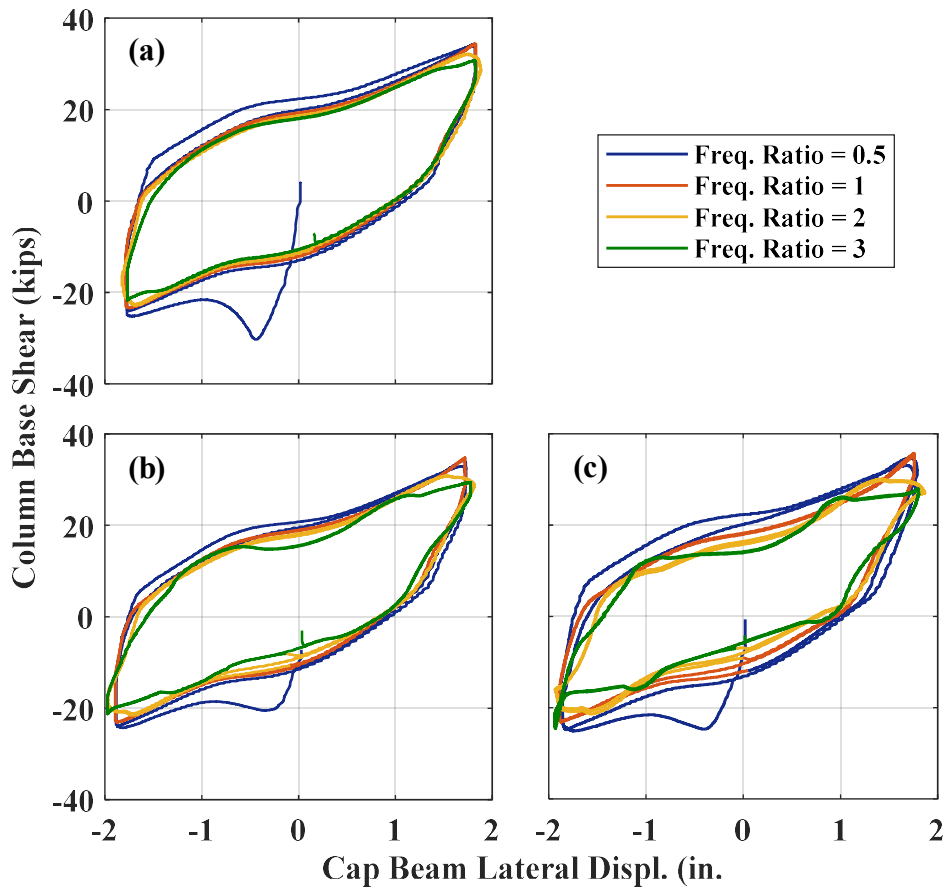
Figure 4-170. Phase II, Loading Set 4: base shear vs. lateral displacement responses under loading protocols: (a) HSR2_TU_CNT_S4_DR_1_3_T2D_0_5; (b) HSR2_TU_CNT_S4_DR_1_3_T2D_1; (c) HSR2_TU_CNT_S4_DR_1_3_T2D_2

According to Figure 4-170, for all the three tests examined here, the base shear values corresponding to similar lateral displacement in the positive and negative directions were different. The cause of the difference between the negative and positive base shear values corresponding to the same absolute displacement value is not fully clear. The effect of twist amplitude on the peak base shear values is found insignificant, but in-phase lateral displacement and twist cycles resulted in the highest peak base shear values (i.e. for the frequency ratio of 1 – also see Figure 4-171(a)).
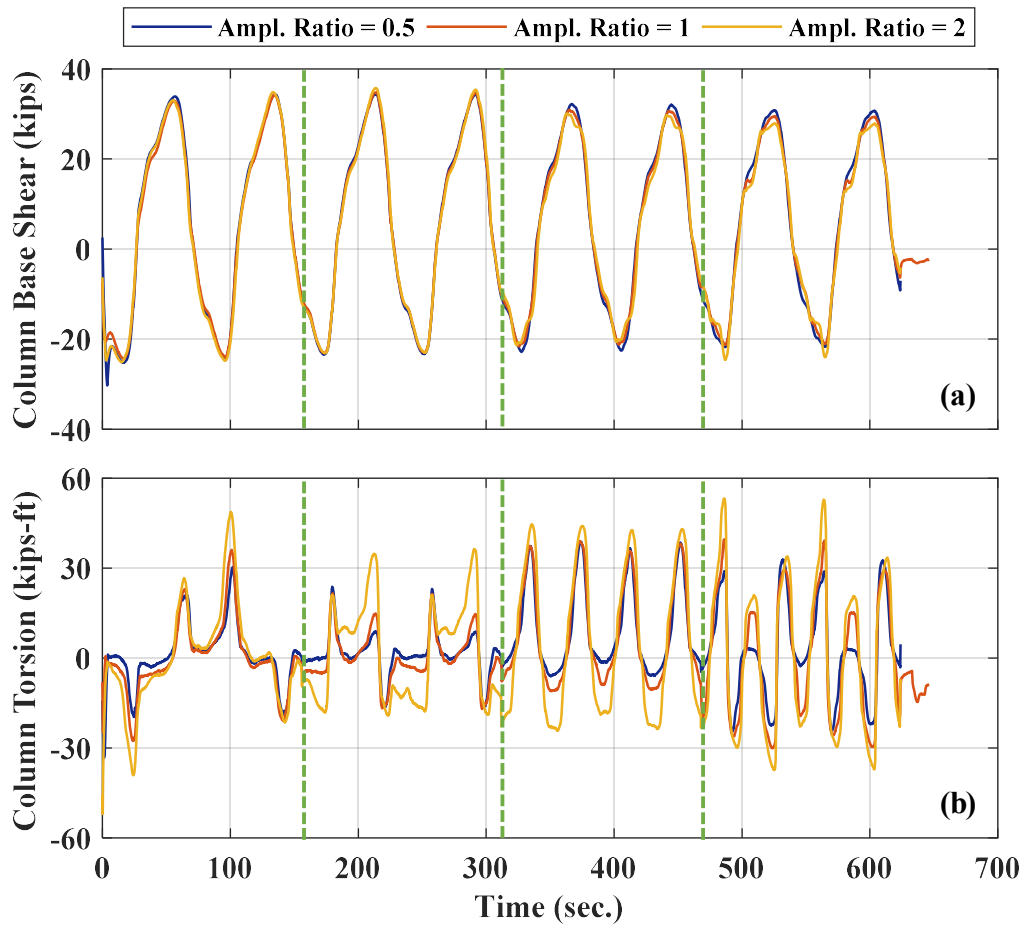
Figure 4-171. Phase II, Loading Set 4, loading protocols of maximum drift ratio of 1.3%: (a) column base shear time histories; (b) column torsion time histories

The torsion vs. twist responses and the torsion time histories of the column under the above-mentioned loading protocols are shown in Figure 4-172 and Figure 4-171(b), respectively. The torsion range is not significantly different from the range of torsion resisted by the column under pure twist (see Figure 4-153). As expected, according to Figure 4-172, the hysteretic torsion-twist responses of the column under combined uniaxial and torsional loading are not of a simple shape, as opposed to those achieved under pure torsion (Figure 4-153). According to Figure 4-171(b), the peak torsion values

343

were expectedly increased with the twist amplitude, but the relationship between the twist-to-displacement frequency ratio and the peak torsion is less clear. Depending on whether the peaks of lateral displacement and twist coincide or not and their amplitude ratio, the torsion peaks occurred in a direction opposite to the twist direction or not at the peak twists (e.g. compare the cycles of various frequency ratios in Figure 4-172), because the torsion produced via the tendon bearing forces could exceed that due to the friction at the joint interface or vice versa.

Similar to the previous tests, during the tests with the maximum drift ratio of 1.3%, only the first sliding joint (Joint 2) experienced sliding. The time histories of the sliding in X direction and rotational sliding measured for Joint 2 during the same tests are compared in Figure 4-173. For all of these tests, the maximum sliding achieved in X direction was slightly larger than 1.5 in. and it occurred in the negative direction (Figure 4-173(a). For the current level of lateral displacement and twist, the effect of column twist on the achievable sliding in the direction of lateral loading (X direction), irrespective of frequency ratio, was found minimal. Even though the other joints did not exhibit any sliding, the recorded rotational sliding time histories for Joint 2 (Figure 4-173(b)) do not fully follow the recorded beam twist time histories (Figure 4-169).This is because of the errors in the rotational sliding measurements, the initial misalignment of the ducts (which caused an offset in the computed sliding components), and the initial sliding existing at the sliding joints before the testing started.
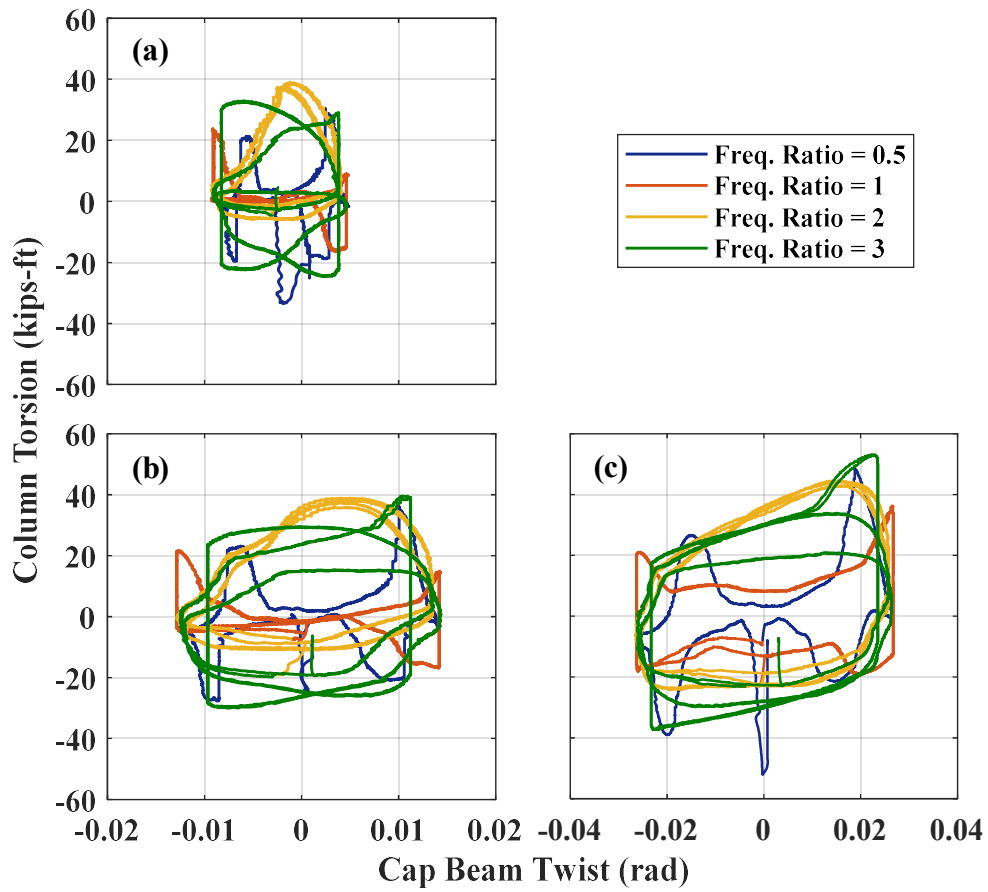
Figure 4-172. Phase II, Loading Set 4: column torsion vs. twist responses under loading protocols: (a) HSR2_TU_CNT_S4_DR_1_3_T2D_0_5; (b) HSR2_TU_CNT_S4_DR_1_3_T2D_1; (c) HSR2_TU_CNT_S4_DR_1_3_T2D_2
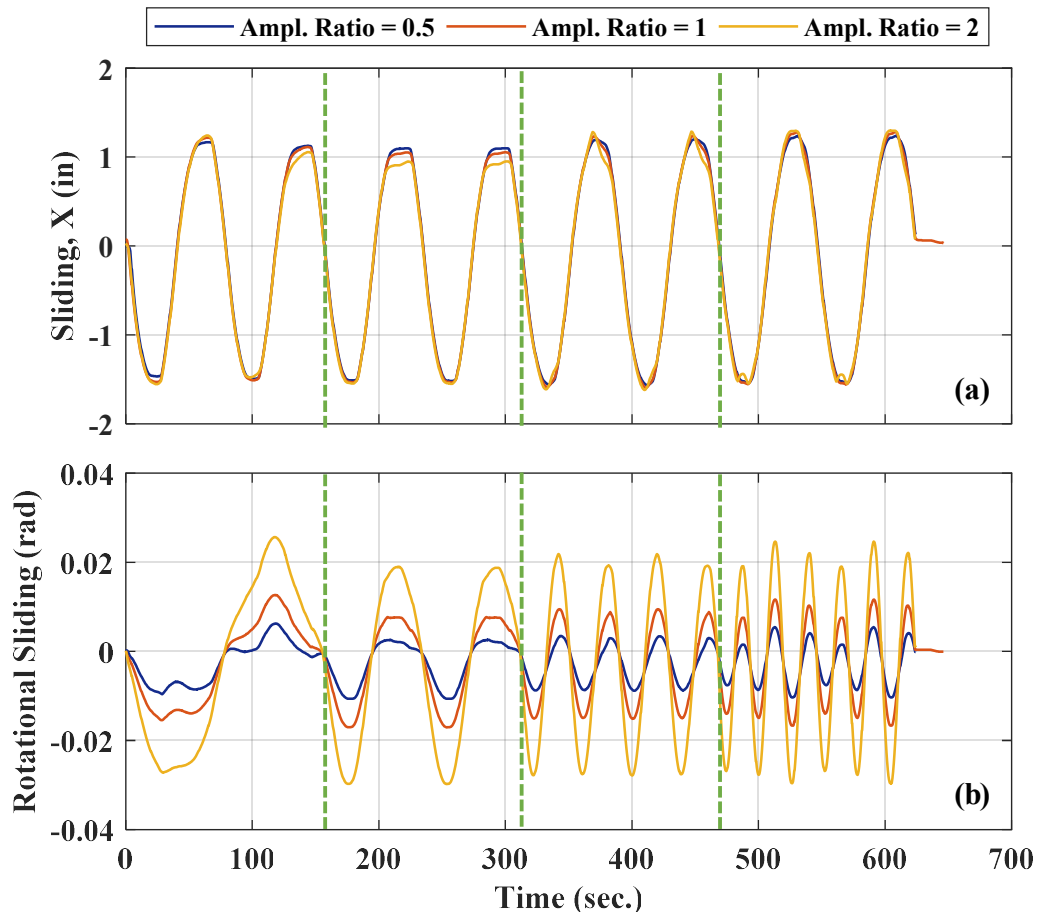
Figure 4-173. Phase II, Loading Set 4, loading protocols of maximum drift ratio of 1.3%: (a) time histories of sliding at Joint 2 in X direction; (b) time histories of rotational sliding at Joint 2

The rocking around Y-axis at Joint 1 (Figure 4-174) was higher when the column was laterally displaced in the positive X direction, because the sliding joint accommodated less sliding in that direction (Figure 4-173(a)). In addition, discrepancies are observed in the peak rocking values obtained under different twist-to-displacement amplitude and frequency ratios (Figure 4-174). Specifically, the larger the amplitude ratio was, the larger the differences caused by the frequency ratio became. The rocking at the first sliding joint

346

(Joint 2) was less than half of that at Joint 1 and its peak was minimally affected by the twist-to-displacement amplitude and frequency ratios.
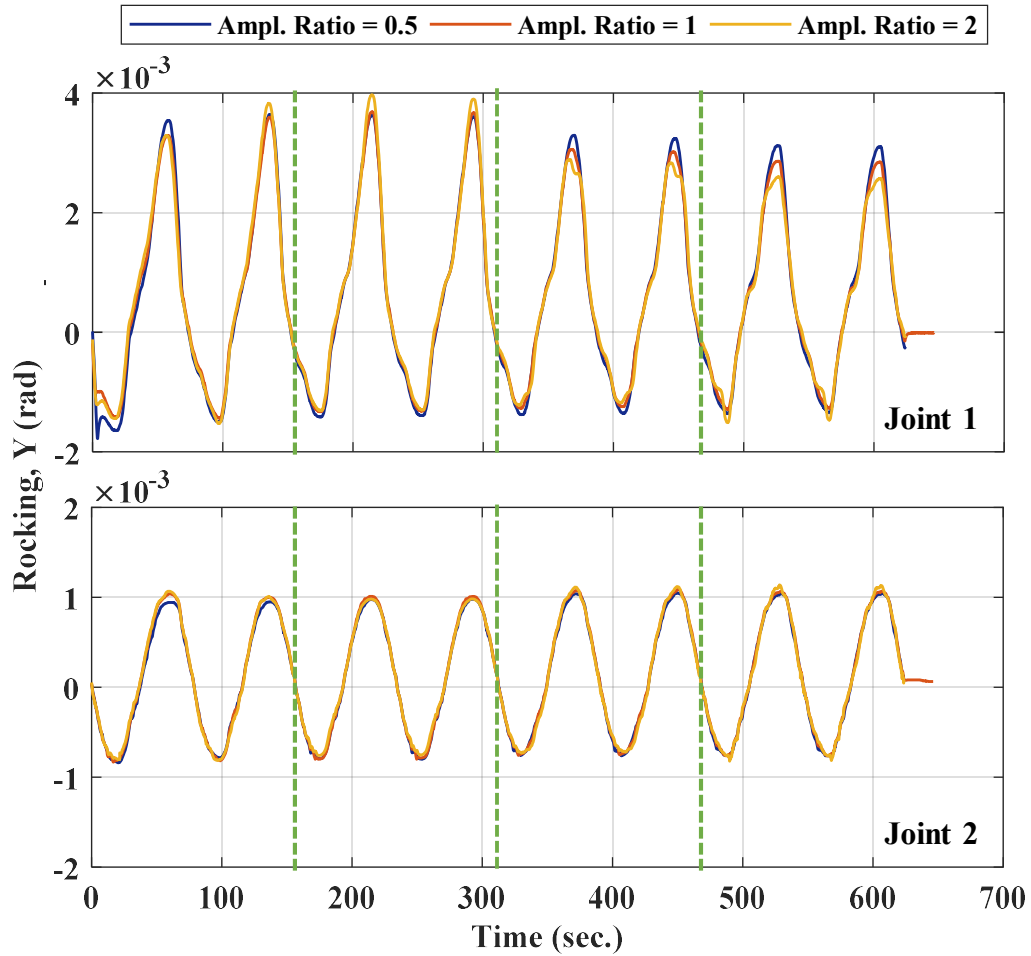
Figure 4-174. Phase II, Loading Set 4, loading protocols of maximum drift ratio of 1.3%: time histories of rocking around *Y*-axis at bottom two joints

The time histories of total PT forces measured during the three tests are compared in Figure 4-175 – note that the load cell used to measure the force in the east tendon was defective, so its data was omitted. As seen, lateral displacement had the dominant effect on the tendon forces. In none of the tests, the tension in a tendon exceeded 50% of its yield

strength. The total PT losses in all three tests were very small (less than 1%) and the twist amplitude had no impact on the PT loss.
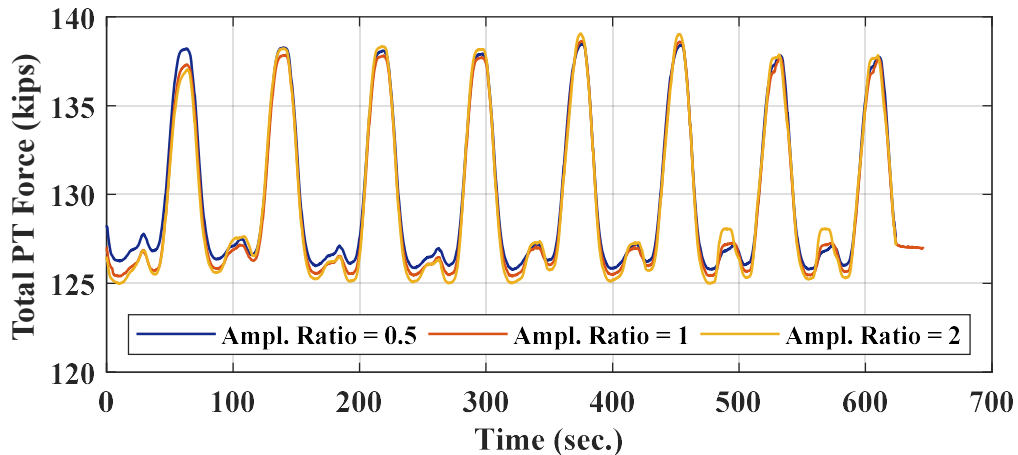
Figure 4-175. Phase II, Loading Set 4, loading protocols of maximum drift ratio of 1.3%: time histories of total PT force

The propagation of cracks on the bottom column segment during the same tests (HSR2_TU_CNT_S4_DR_1_3_T2D_0_5, HSR2_TU_CNT_S4_DR_1_3_T2D_1, and HSR2_TU_CNT_S4_DR_1_3_T2D_2 with constant peak drift ratio and various twist amplitudes) is displayed in Figure 4-176. Although some of the hairline cracks from the previous tests under pure torsion grew and some new cracks appeared during the first two tests, no additional damage was induced during the third test with the largest twist amplitude. During these tests, only a couple of hairline cracks appeared near the joints on the top two column segments. In comparison with the crack distribution observed on the bottom segment of the column specimen tested under pure uniaxial lateral displacement

of the same amplitude in Phase I (Figure 4-70), here, the number and extent of cracks appeared on the bottom column segment were similar (or slightly higher).
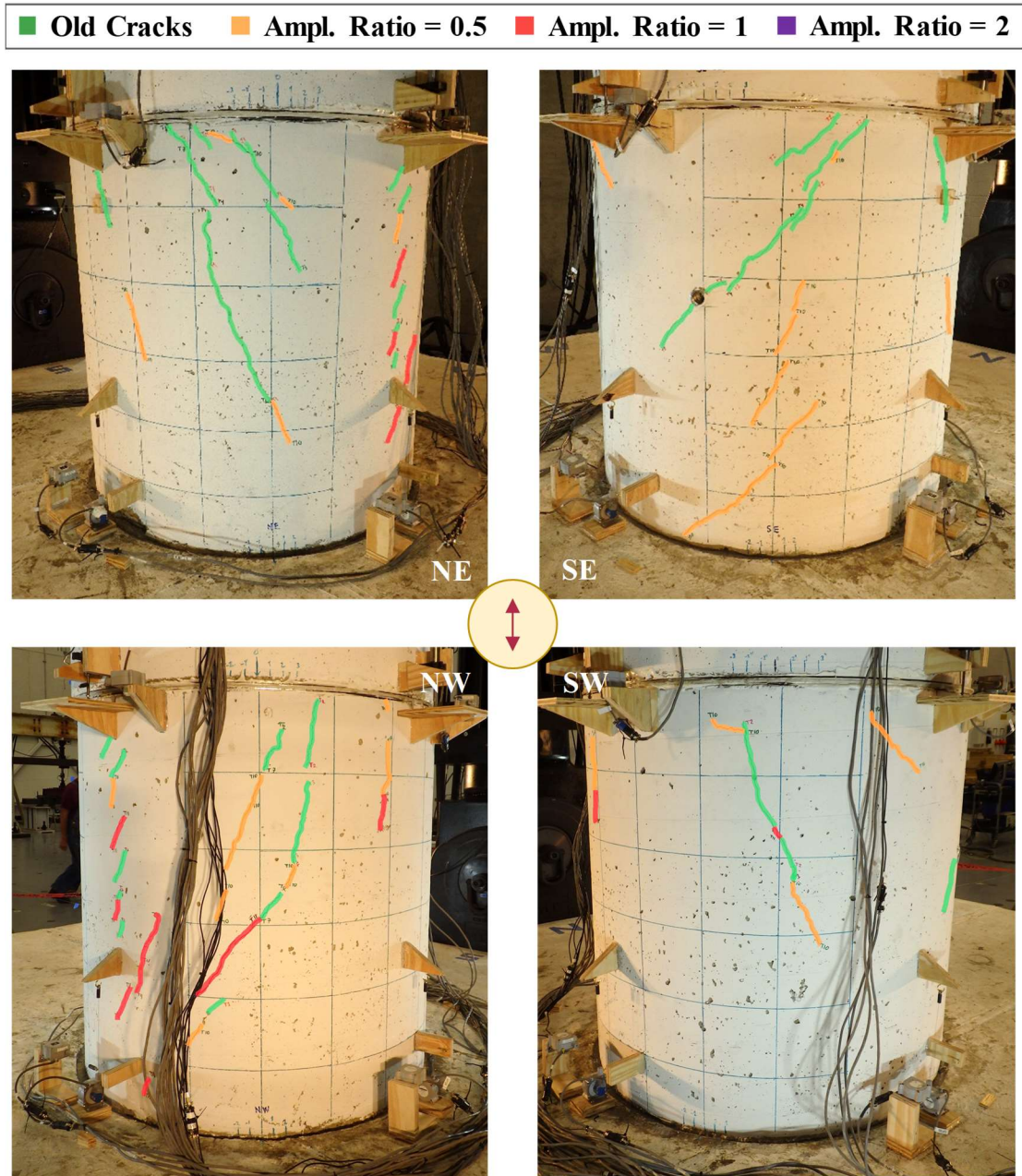
Figure 4-176. Phase II, Loading Set 4, loading protocols of maximum drift ratio of 1.3%: crack propagation with twist to drift ratio amplitude ratio

The lateral displacement and twist time histories of the loading beam achieved during the second three tests in Loading Set 4 (HSR2_TU_CNT_S4_DR_2_T2D_0_5, HSR2_TU_CNT_S4_DR_2_T2D_1, and HSR2_TU_CNT_S4_DR_2_T2D_2), with the same peak drift ratio of 2%, but different twist amplitude ratios, are displayed in Figure 4-177. Similarly to the prior three tests, the lateral displacement time histories were close to the desired time histories, but the twist time histories were slightly different, particularly in the cycles with higher twist frequencies.

The hysteretic base shear vs. lateral displacement responses obtained from the above-mentioned tests are compared in Figure 4-178. Similarly to the results of the tests under 1.3% peak drift ratio (Figure 4-170), the deviation of the column specimen's response under combined torsional and uniaxial lateral loading from that under uniaxial lateral loading increased with the twist amplitude and frequency.
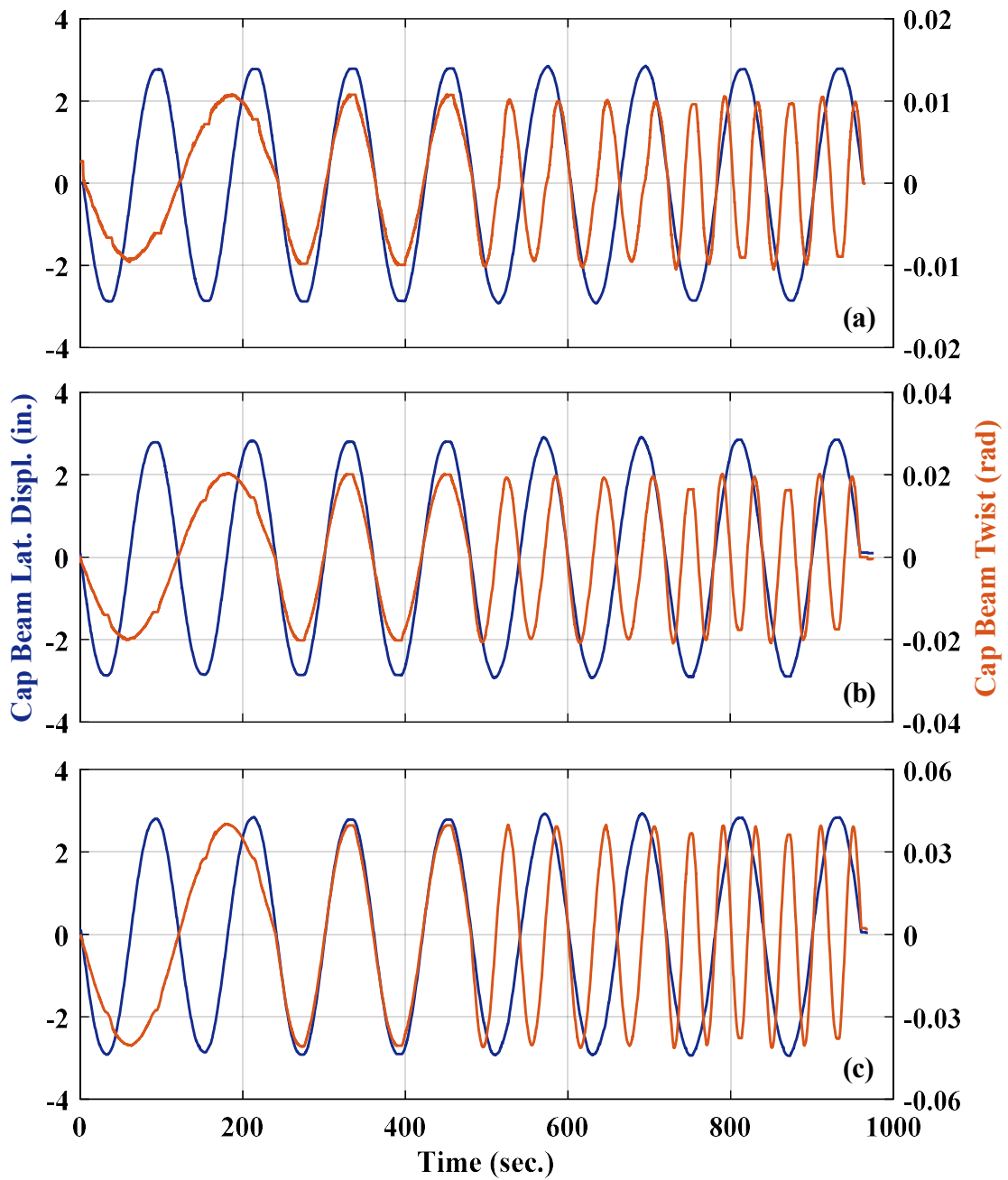
Figure 4-177. Phase II, Loading Set 4: beam lateral displacement and twist time histories under loading protocols: (a) HSR2_TU_CNT_S4_DR_2_T2D_0_5; (b) HSR2_TU_CNT_S4_DR_2_T2D_1; (c) HSR2_TU_CNT_S4_DR_2_T2D_2
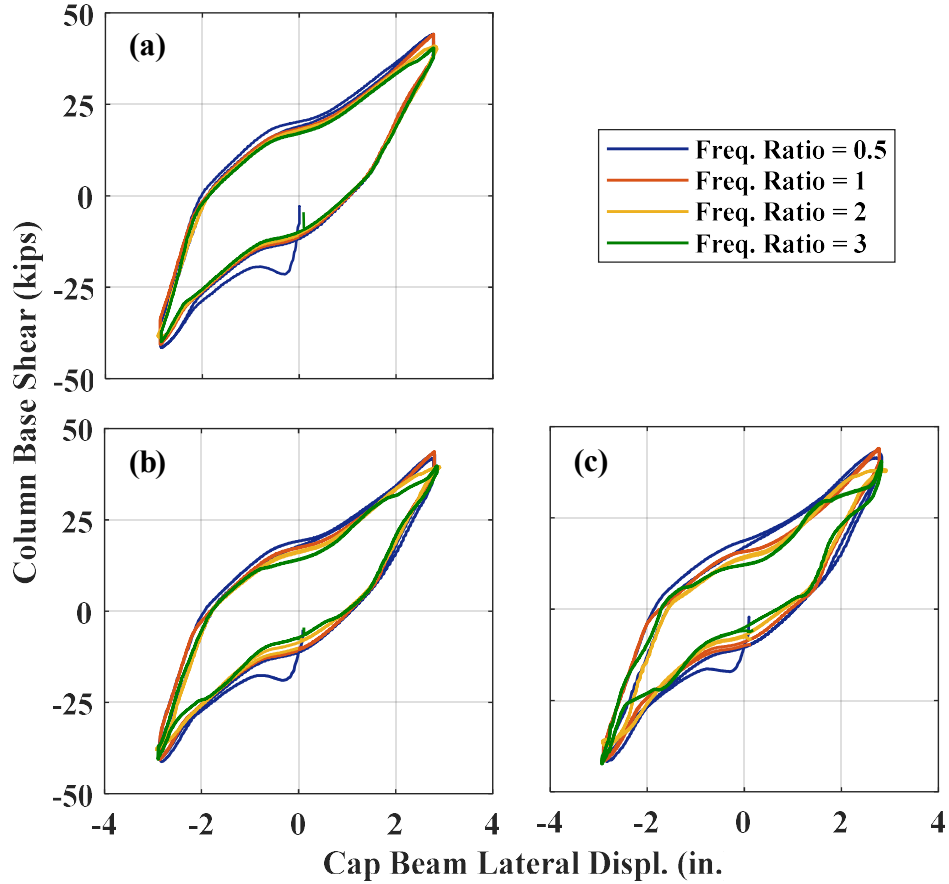
Figure 4-178. Phase II, Loading Set 4: base shear vs. lateral displacement responses under loading protocols: (a) HSR2_TU_CNT_S4_DR_2_T2D_0_5; (b) HSR2_TU_CNT_S4_DR_2_T2D_1; (c) HSR2_TU_CNT_S4_DR_2_T2D_2

According to Figure 4-179(a), the peak base shear resisted by the column specimen changed negligibly and less than 15% with the cyclic twist amplitude and frequency, respectively. The torsion vs. twist responses of the column under the same loading protocols are displayed in Figure 4-180. Based on these responses, the peak torsion values were influenced by both the twist amplitude and the twist-to-displacement frequency ratio. Specifically, larger twist amplitude led to larger torsion for all twist frequencies, whereas

352

the effect of the ratio of twist frequency to lateral displacement frequency was less

noticeable (see Figure 4-179(b) for a better comparison).
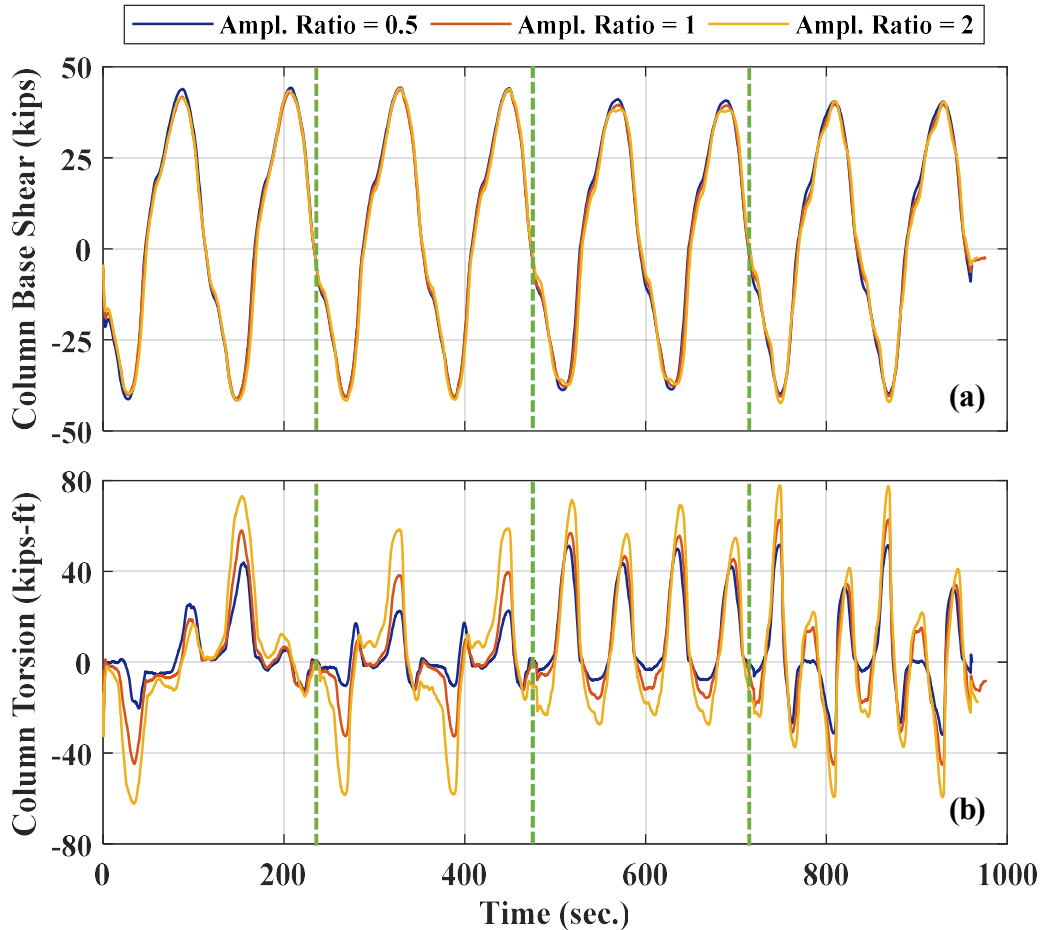
Figure 4-179. Phase II, Loading Set 4, loading protocols of maximum drift ratio of 2%: (a) column base shear time histories; (b) column torsion time histories

The first sliding joint (Joint 2) was the only joint experiencing sliding within all the

three tests with the peak drift ratio of 2%. The time histories of the sliding in X direction

and rotational sliding at this joint obtained from the above tests are compared in Figure

4-181. The peak sliding in X direction was only slightly affected by the twist amplitude

353

ratio (Figure 4-181(a)) and it reached 1.5 in. and 2 in. in the positive and negative directions, respectively. Considering that the other joints had no sliding and the column segments could not have experienced noticeable torsional deformation, the time histories of the loading beam's twist (Figure 4-177) and the joint's rotational sliding (Figure 4-181(b)) were expected to be identical.
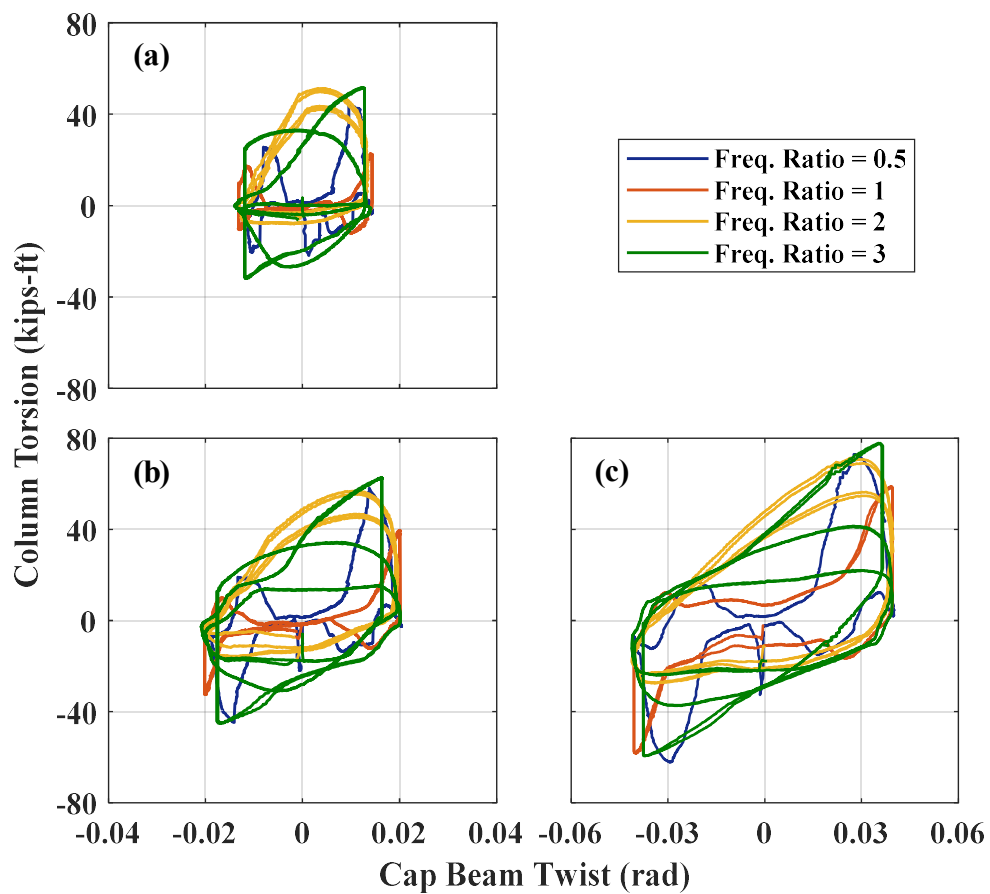
Figure 4-180. Phase II, Loading Set 4: column torsion vs. twist responses under loading protocols: (a) HSR2_TU_CNT_S4_DR_2_T2D_0_5; (b) HSR2_TU_CNT_S4_DR_2_T2D_1; (c) HSR2_TU_CNT_S4_DR_2_T2D_2
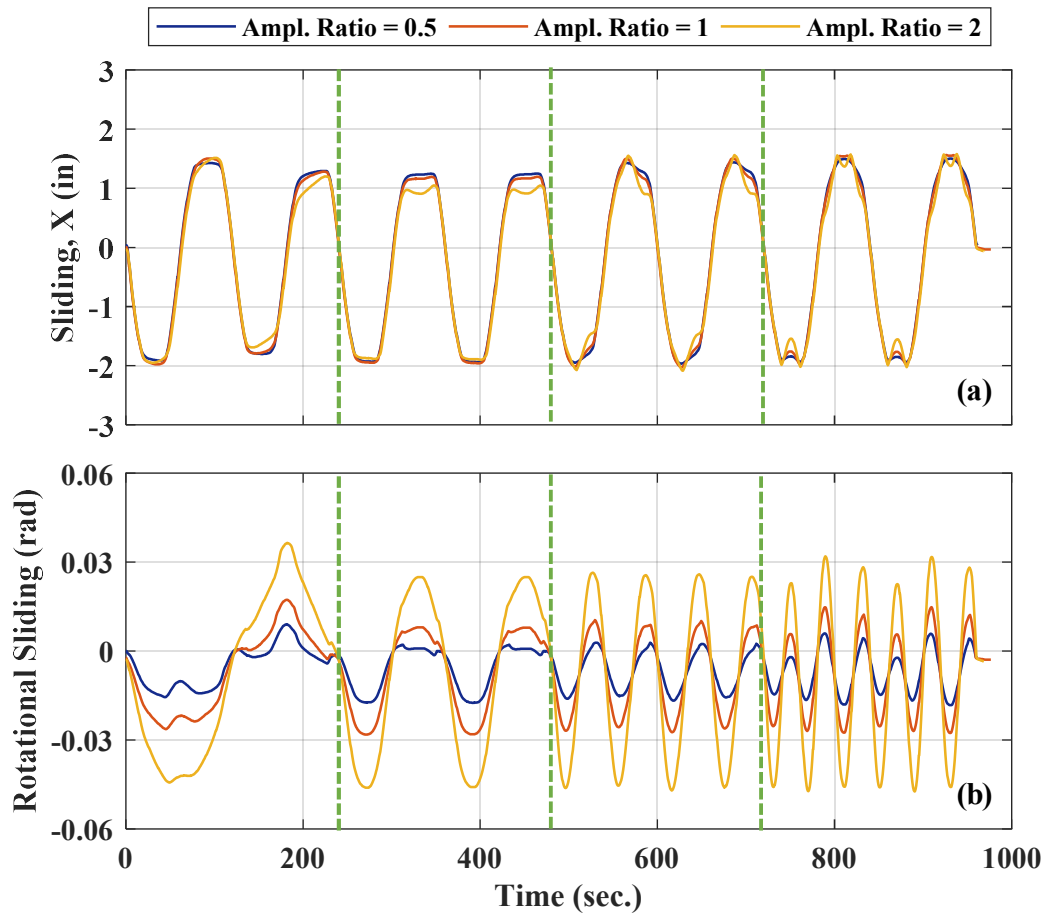
Figure 4-181. Phase II, Loading Set 4, loading protocols of maximum drift ratio of 2%: (a) time histories of sliding at Joint 2 in *X* direction; (b) time histories of rotational sliding at Joint 2

The time histories of the rocking around *Y*-axis at Joint 1 obtained during the same three tests are compared in Figure 4-182. It is observed that rocking was more sensitive to the twist-to-displacement frequency ratio rather than the twist amplitude. In fact, when the twist and lateral displacement peaks coincided (e.g. for the second pair of lateral displacement cycles, where the twist frequency equaled the lateral displacement's), the rocking slightly increased. In contrast, when twist was zero at the lateral displacement peak (e.g. during the third pair of lateral displacement cycles, where the frequency of the

twist cycles was double the frequency of the lateral displacement cycles), the peak rocking slightly decreased.
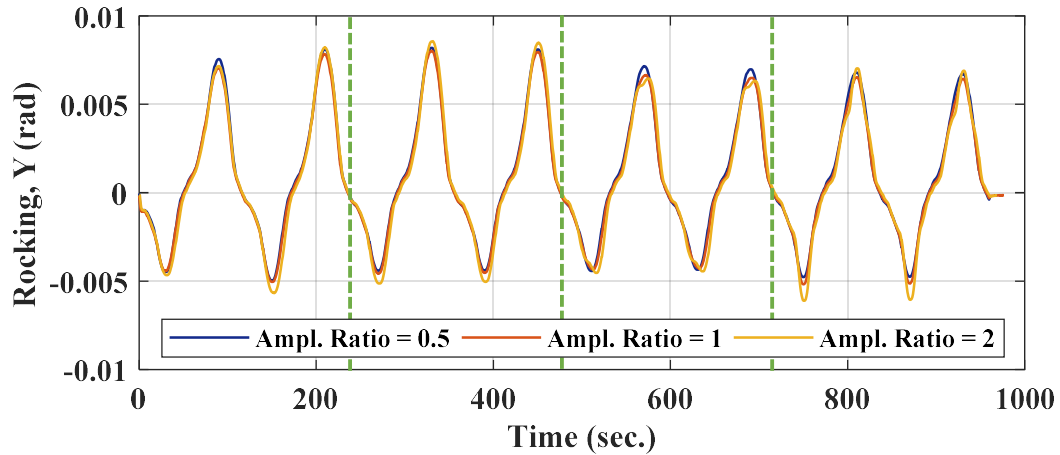
Figure 4-182. Phase II, Loading Set 4, loading protocols of maximum drift ratio of 2%: time history of rocking around *Y*-axis at Joint 1

The total PT force time histories computed without the data from the east tendon's load cell are compared in Figure 4-183. The PT forces were not considerably influenced by the twist amplitude. In addition, the total PT losses in the tests under loading protocols HSR2_TU_CNT_S4_DR_2_T2D_0_5, HSR2_TU_CNT_S4_DR_2_T2D_1, and HSR2_TU_CNT_S4_DR_2_T2D_2 were 1.3%, 0.4%, and 1.1%, respectively.
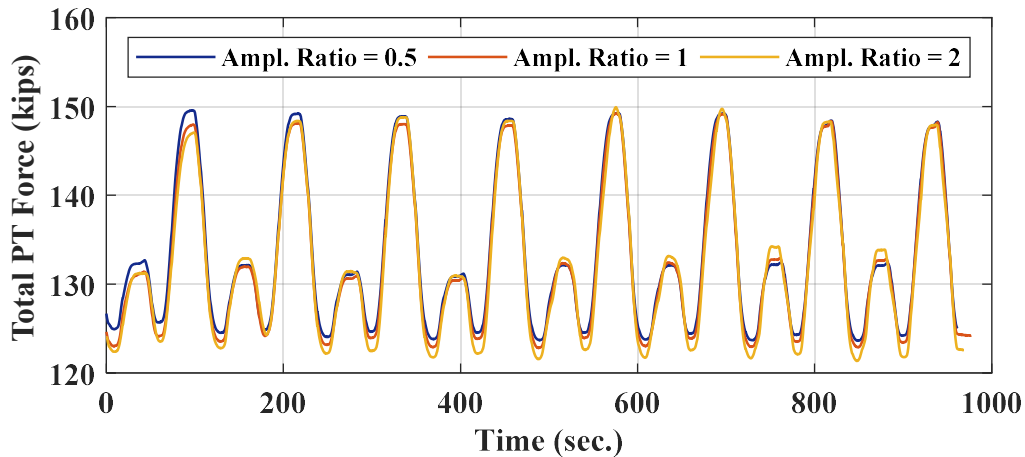
Figure 4-183. Phase II, Loading Set 4, loading protocols of maximum drift ratio of 2%: time histories of total PT force

The crack propagation over the bottom segment of the column during the above three tests is shown in Figure 4-184. All of the new cracks were hairline cracks. In general, the cracks started with a diagonal orientation on the north and south sides of the column segment and became almost vertical below the sliding joint on the east and west sides of the segment. No concrete spalling or sliding joint interface damage was observed after these tests. Similarly to the previous tests with 1.3% maximum drift ratio, only a couple of hairline cracks appeared on the upper two segments. Compared to the cracks reported for the bottom segment of the column specimen tested in Phase I under pure uniaxial lateral displacement of the same amplitude (Figure 4-81), the crack population on the bottom segment of the new column specimen was slightly larger, but none of the cracks were wide. Note that this increase in population could be the outcome of the larger number of prior tests performed on this column specimen compared to those for the column specimen tested in Phase I.

357
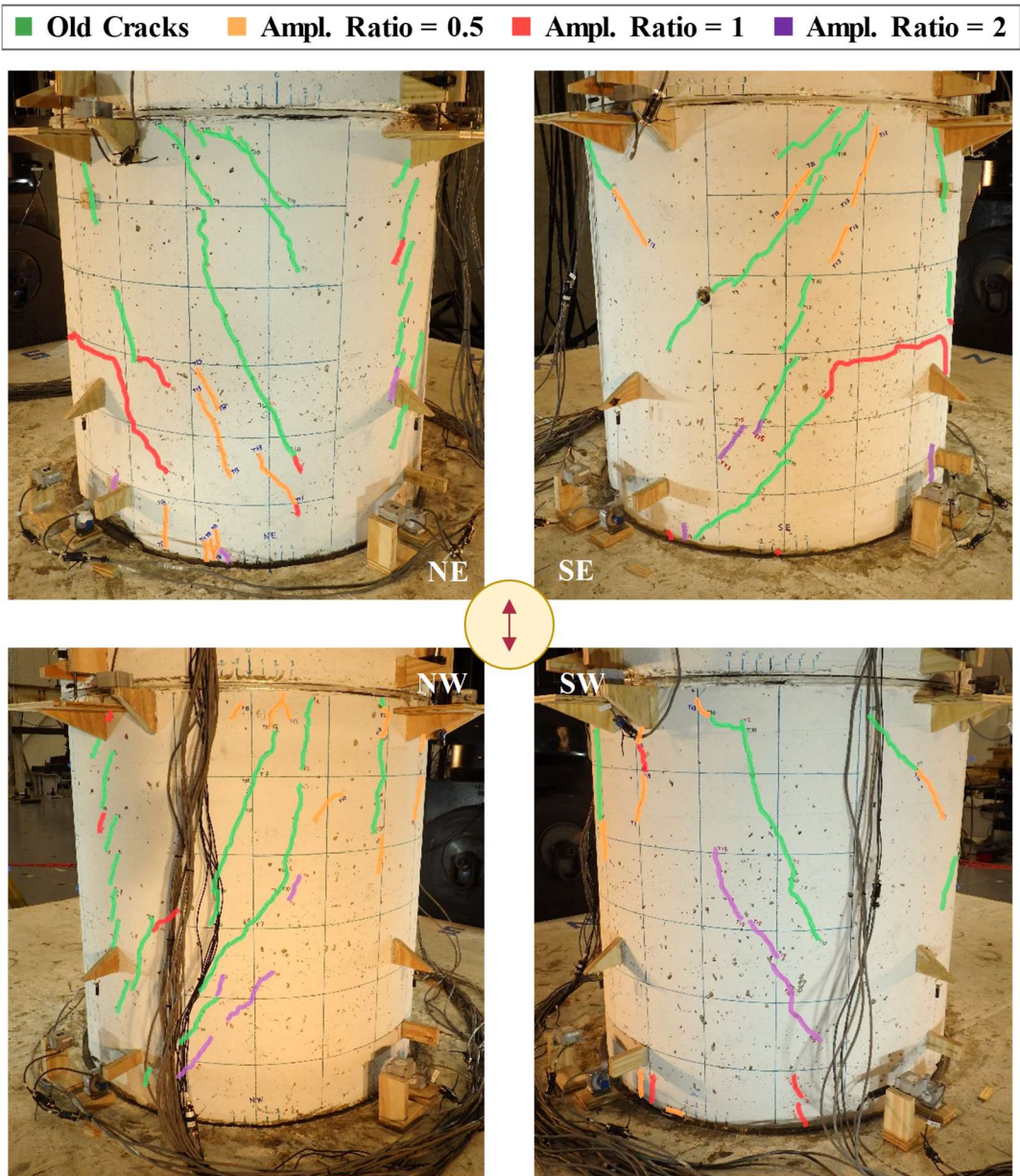
Figure 4-184. Phase II, Loading Set 4, loading protocols of maximum drift ratio of 2%: crack propagation with twist-to-drift ratio amplitude ratio

The lateral displacement and twist time histories produced during the last three tests in Loading Set 4 with a peak drift ratio of 4% (HSR2_TU_CNT_S4_DR_4_T2D_0_5, HSR2_TU_CNT_S4_DR_4_T2D_1, and HSR2_TU_CNT_S4_DR_4_T2D_2) are

shown in Figure 4-185. These time histories closely resemble the desired time histories (Figure 4-149).
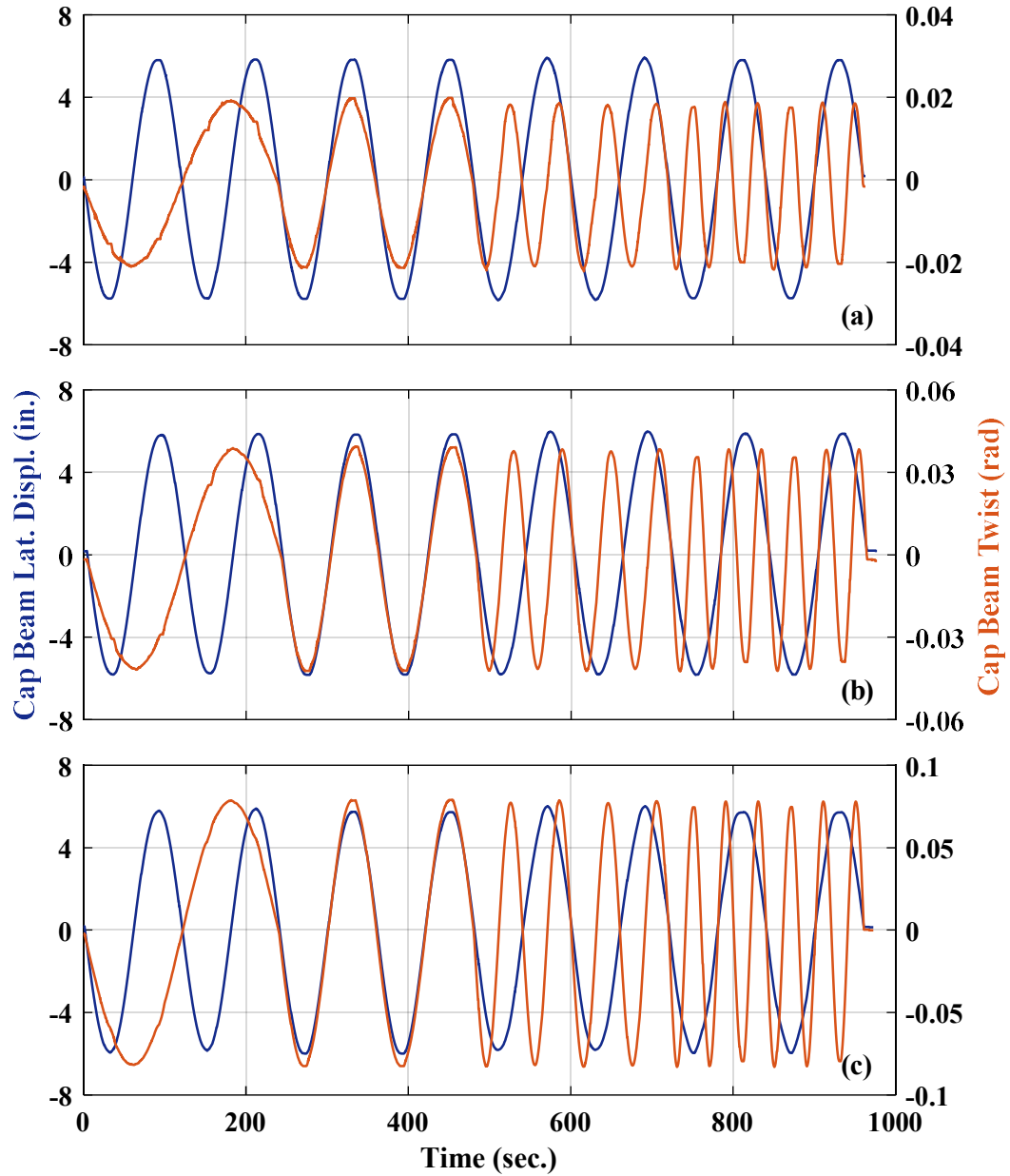
Figure 4-185. Phase II, Loading Set 4: beam lateral displacement and twist time histories under loading protocols: (a) HSR2_TU_CNT_S4_DR_4_T2D_0_5; (b) HSR2_TU_CNT_S4_DR_4_T2D_1; (c) HSR2_TU_CNT_S4_DR_4_T2D_2

The base shear vs. lateral displacement hysteretic responses obtained from the three tests are shown in Figure 4-186. The compression toes on both east and west sides of the bottom column segment sustained concrete spalling near the peaks of the first lateral displacement cycle in loading protocol HSR2_TU_CNT_S4_DR_4_T2D_0_5. The concrete spalling was less severe on the east side, as it was already damaged since the column assembly (Figure 4-141) and there was less compressive stress on the edge. The stiffness degradation in the positive direction due to this damage is clear in Figure 4-186(a). No further significant cyclic deterioration is seen in none of the test results thereafter.

Comparing the hysteretic responses of the column under the above three loading protocols, it is observed that the column experienced less total sliding and more rocking motion during the first test (Figure 4-186(a)) compared to the other two (Figure 4-186(b) and (c)). This was because the second sliding joint became active (Figure 4-187) near the sixth lateral displacement peak in the second test (Figure 4-188(b)), whose twist amplitude was double the first test's. This indicates that at that point the combined shear and torsion got large enough to overcome the breakaway friction at Joint 3, even if the posttensioning forces had increased due to the column's rocking motion.
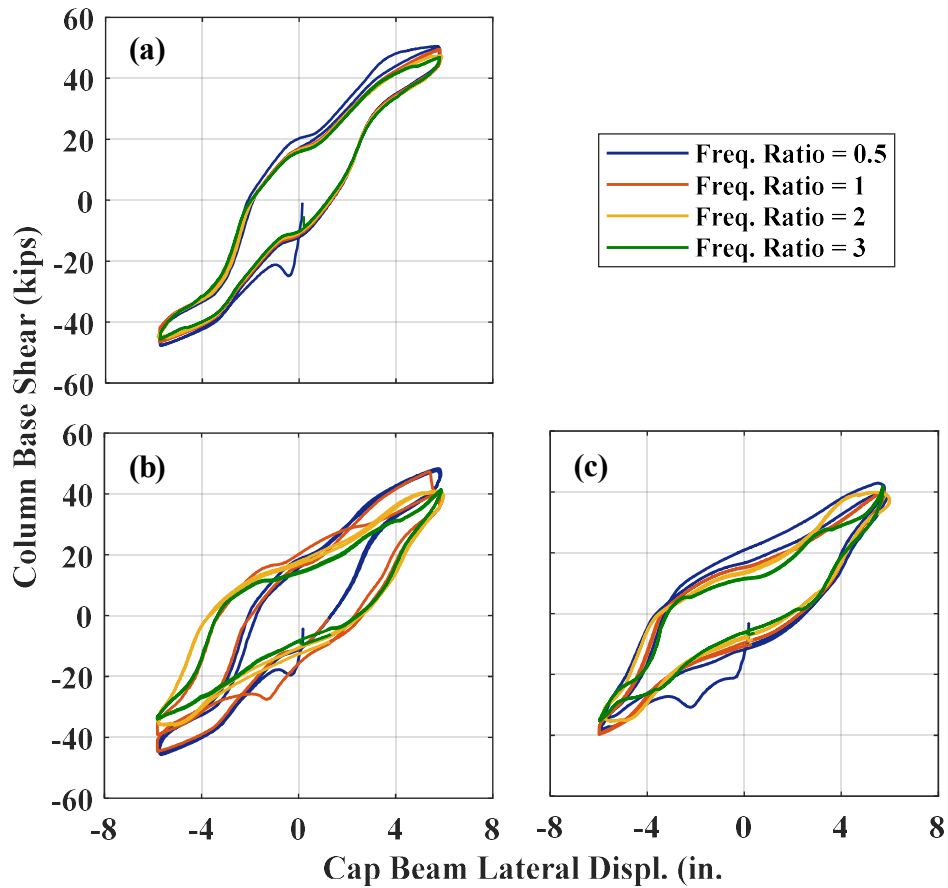
Figure 4-186. Phase II, Loading Set 4: base shear vs. lateral displacement responses under loading protocols: (a) HSR2_TU_CNT_S4_DR_4_T2D_0_5; (b) HSR2_TU_CNT_S4_DR_4_T2D_1; (c) HSR2_TU_CNT_S4_DR_4_T2D_2

The additional sliding provided by the second sliding joint led to a significant increase in the column's energy dissipation, which is represented by the area inside the hysteretic loops (compare Figure 4-186(b) and (c) with Figure 4-186(a)). The column's residual displacement increased with the additional sliding, too. That is, while the average residual drift ratio in the first test (HSR2_TU_CNT_S4_DR_4_T2D_0_5) was 1.1%, it increased to 2.2% and 1.9% in the second and the third tests, respectively.
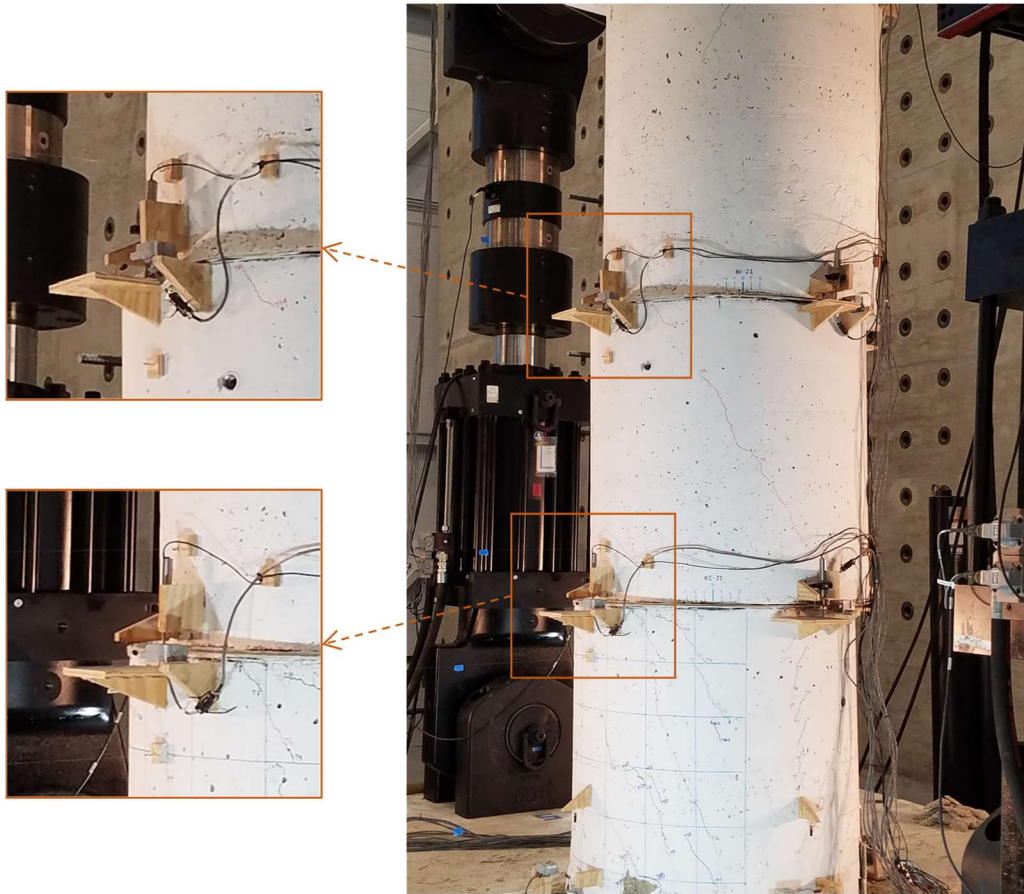
Figure 4-187. Phase II, loading protocol HSR2_TU_CNT_S4_DR_4_T2D_1: simultaneous sliding at both sliding joints

The time histories of the sliding in X direction at Joints 2 and 3 are demonstrated in Figure 4-188. In the second test (with the amplitude ratio of 1), the activation of the second sliding joint (Joint 3) did not visibly affect the peak sliding achieved at the first sliding joint (Joint 2). The sliding time histories of the two joints were almost in-phase, i.e. their peaks and reversals occurred almost concurrently. The peak sliding values at Joint 2 were only slightly larger than those achieved at Joint 3. Specifically, during the last two tests discussed herein, the peak positive sliding values at Joints 2 and 3 were 1.63 in. and 1.6

in., respectively, and the peak negative sliding values at Joints 2 and 3 were 2.15 in. and 1.95 in., respectively.
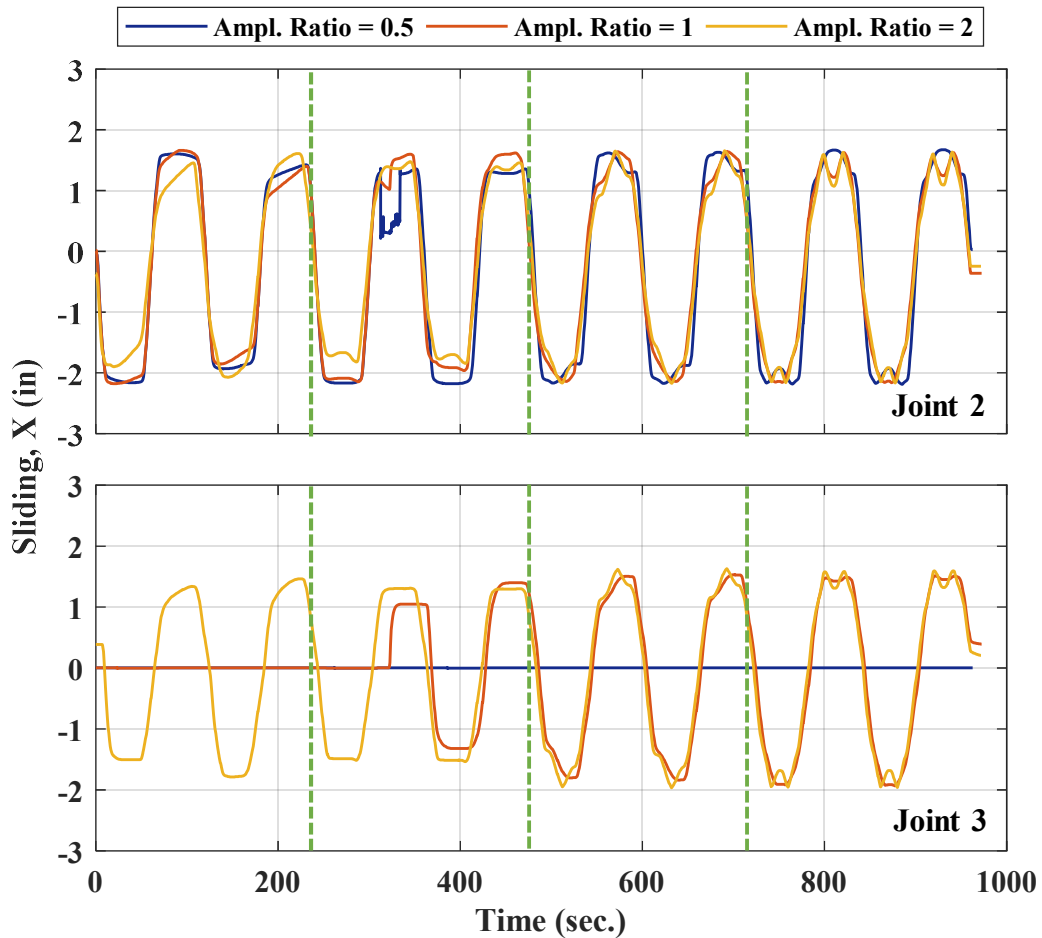
Figure 4-188. Phase II, Loading Set 4, loading protocols of maximum drift ratio of 4%: time histories of joint sliding in X direction

The torsion vs. twist responses of the column specimen under the same three tests are compared in Figure 4-190. The impact of the sliding at Joint 3 is less discernible in the plots presented in this figure, but according to the torsion time histories compared in Figure 4-189(b), the additional sliding lowered the torsion demand on the column

specimen. This is justified by the fact that the contribution of the tendons' bearing reactions to the torsional moment and stiffness is reduced as sliding capacity increases. The observations made for the torsion-twist responses of the first six tests in Loading Set 4 are valid here, as well. It is further seen in Figure 4-189(a) that the peak base shear decreased with the onset of sliding at the second sliding joint, while the amplitude and frequency of the twist cycles relative to the frequency of the lateral displacement cycles minimally affected the peak base shear values.
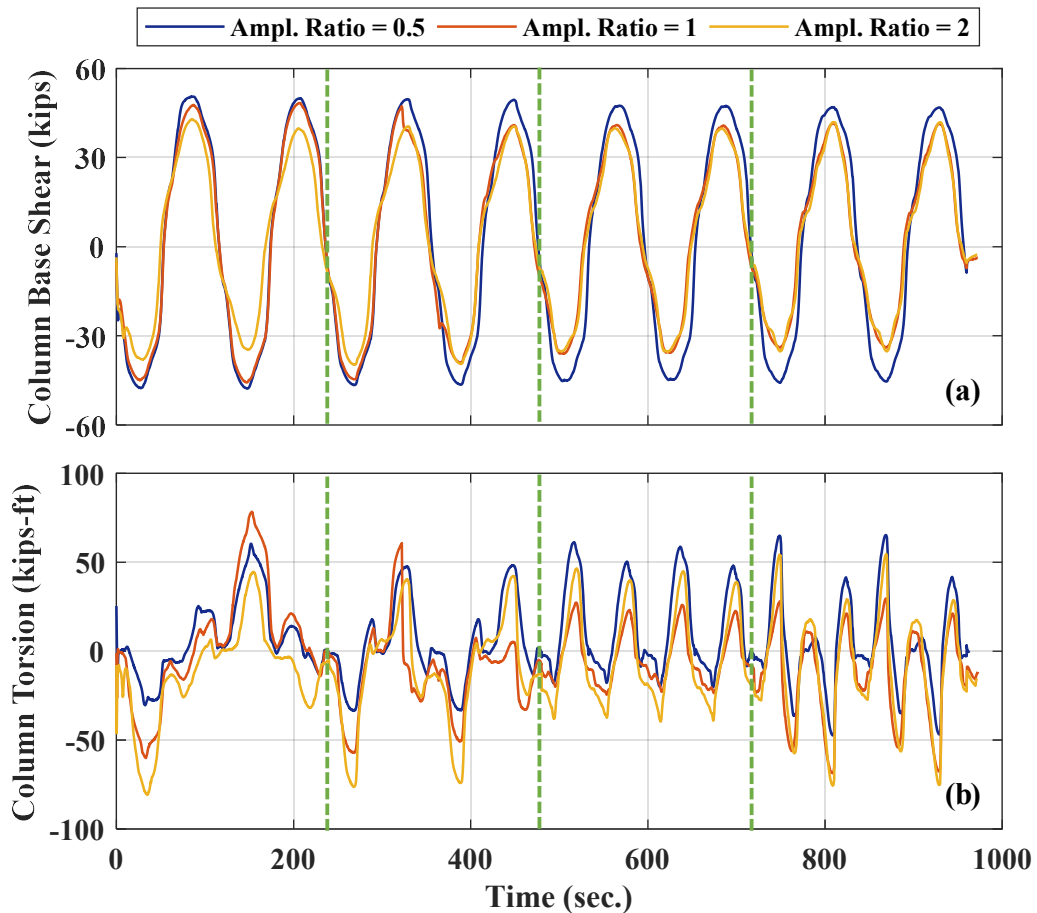
Figure 4-189. Phase II, Loading Set 4, loading protocols of maximum drift ratio of 4%: (a) column base shear time histories; (b) column torsion time histories
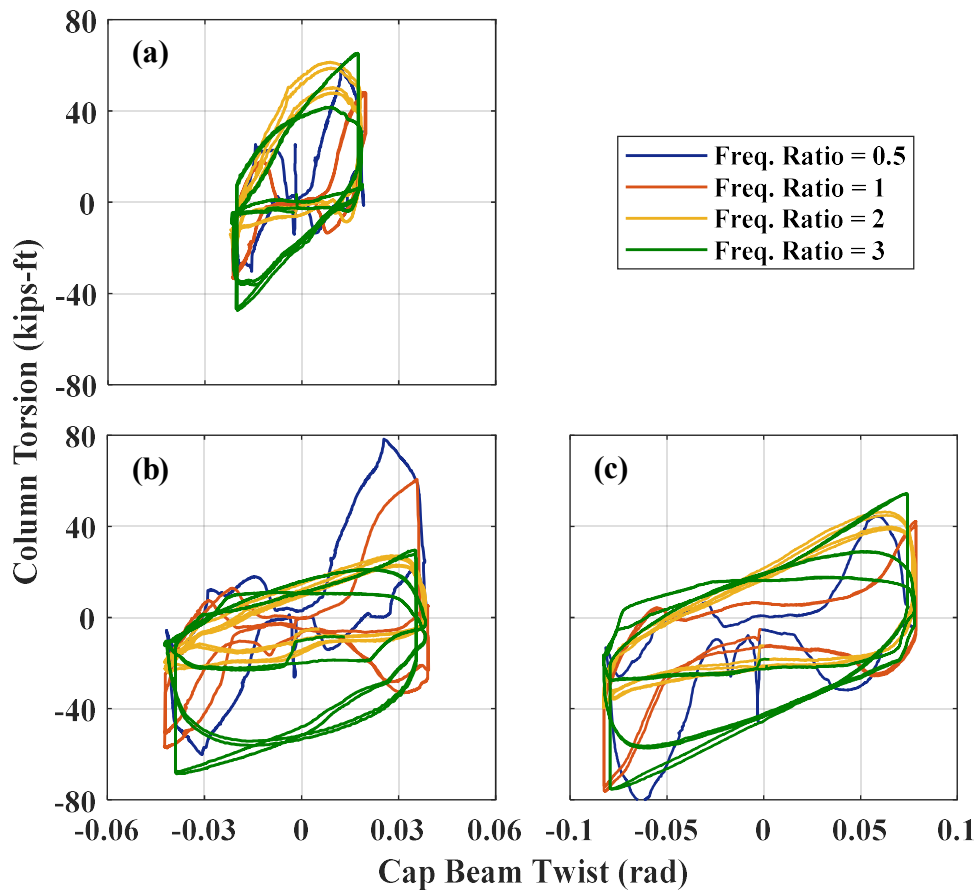
Figure 4-190. Phase II, Loading Set 4: column torsion vs. twist responses under loading protocols: (a) HSR2_TU_CNT_S4_DR_4_T2D_0_5; (b) HSR2_TU_CNT_S4_DR_4_T2D_1; (c) HSR2_TU_CNT_S4_DR_4_T2D_2

According to Figure 4-191, the sliding initiation at Joint 3 led to the realignment of the ducts in the middle segment with respect to the ducts in the bottom and top segments. Note that the top column segment was placed on the middle segment with an initial negative twist with respect to it. This fact led to positive and negative offsets in the relative rotational sliding measurements at the two sliding joints, respectively (see Figure 4-192). During the latter two tests, the peak relative rotational sliding achieved at the first sliding

joint was slightly larger than that at the second sliding joint, but they were both close to

half of the total twist imposed to the column at any time instant.
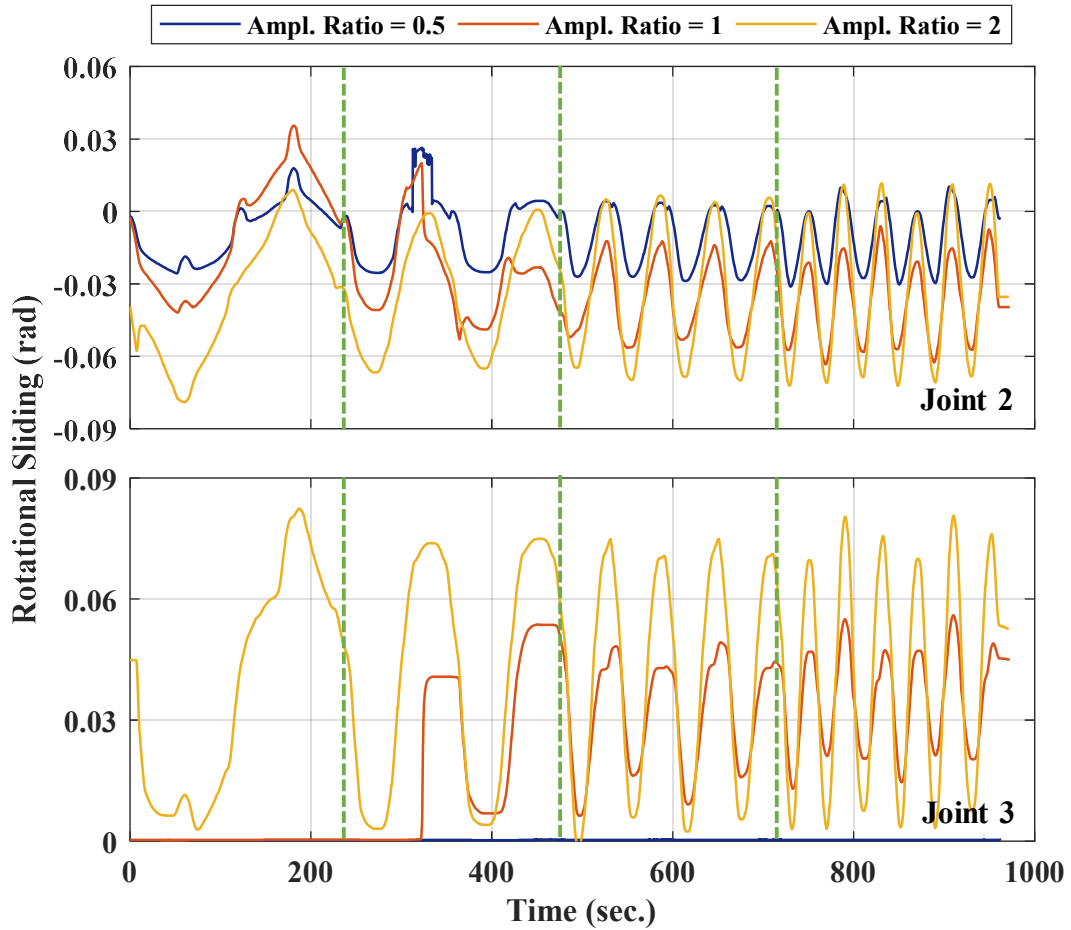
Figure 4-191. Phase II, Loading Set 4, loading protocols of maximum drift ratio of 4%: time histories of rotational joint sliding
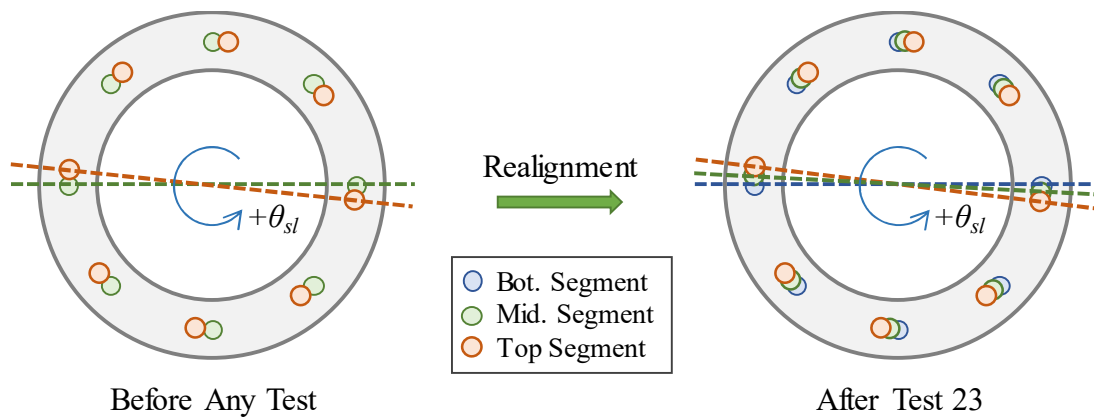
Figure 4-192. Realignment of middle segment ducts

The rocking time histories of Joint 1 (where the maximum moment occurred) measured during the above tests are also compared in Figure 4-193. It is observed that the sliding at Joint 3 could reduce the maximum rocking at the bottom joint by 29%. This is because the lateral displacement that would be accommodated through rocking decreased as a result of the additonal joint sliding capacity provided by Joint 3. Similarly to the previous tests with smaller peak drift ratios, however, the effect of twist frequency on the peak rocking was insignificant.

During the tests discussed here, the maximum posttensioning force was recorded in the west tendon, which was less than 70% its yield strength. The time histories of the sum of the PT forces of all tendons except the east one (because of its load cell deficiency) are displayed in Figure 4-194. Per this figure, by the end of the first test (amplitude ratio = 0.5), the total PT loss was close to 7%, which was primarily caused by the wedge setting in the barrel chucks. As expected, the second sliding joint's activation in the last two tests of Loading Set 4 resulted in a decrease of the peak total PT forces up to 7%. Despite this

decrease in the posttensioning forces, the total losses during the second two tests were 6% and 3%, respectively.
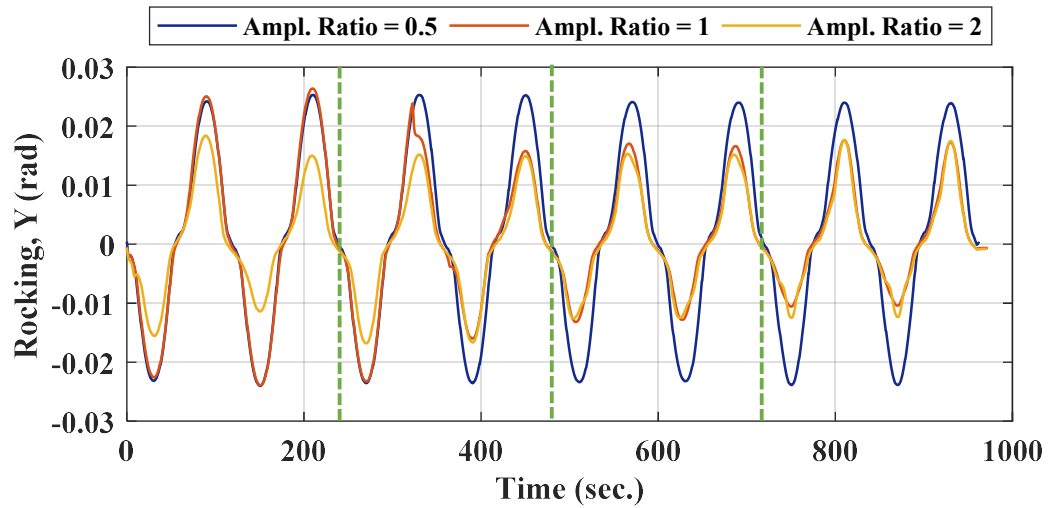
Figure 4-193. Phase II, Loading Set 4, loading protocols of maximum drift ratio of 4%: time history of rocking around *Y*-axis at Joint 1
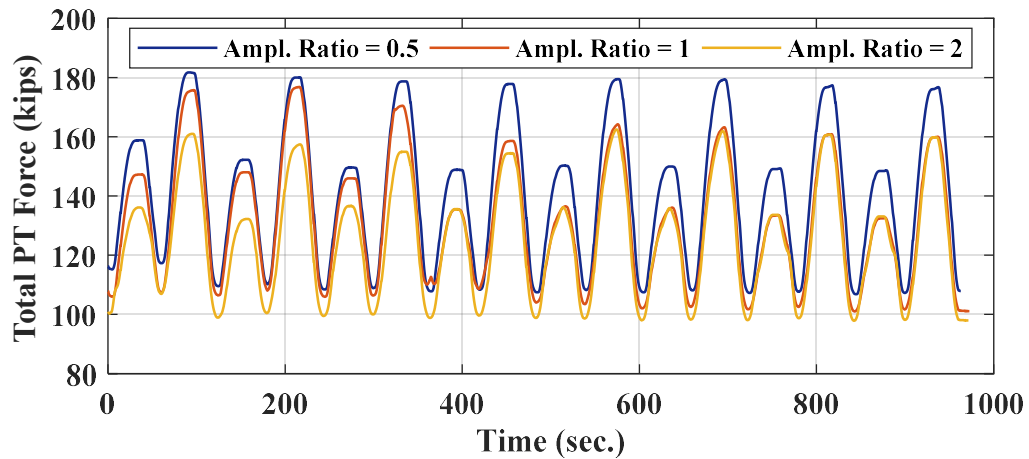
Figure 4-194. Phase II, Loading Set 4, loading protocols of maximum drift ratio of 4%: time histories of total PT force

The cracks emerged on the surface of the bottom column segment during the last three tests of Loading Set 4 are marked in the photos of Figure 4-195. As seen, most of the previous cracks extended, while some of the initially thin cracks near the segment toes at the bottom joint were widened and new vertical (compressive) cracks appeared on the east and west faces of the segment – i.e. where maximum compressive stresses emerged. New vertical and horizontal cracks also appeared on the east and west sides of the segment, right below the first sliding joint. Similar to the wide cracks observed in Phase I (Figure 4-90), these cracks were caused by the large compressive stresses on the west and east quadrants of the sliding surface on the top of the bottom segment. During the above tests, a few hairline cracks also appeared on the surfaces of the top two segments.

As mentioned earlier, when the column's drift ratio reached almost 4% in the negative and positive directions for the first time, the west and east sides of the column's bottom segment sustained concrete spalling, respectively (Figure 4-195). The concrete spalling region was slightly expanded by the repetition of the lateral displacement cycles in the three tests (Figure 4-196 and Figure 4-197). The final depths of concrete spalling on the east and west sides of the segment were close to 9 in. and 12 in., respectively, which resemble the depths of concrete spalling measured after the test of similar peak drift ratio in Phase I (i.e. under loading protocol HSR4_UN_CNT_S1_DR_4; Figure 4-90).
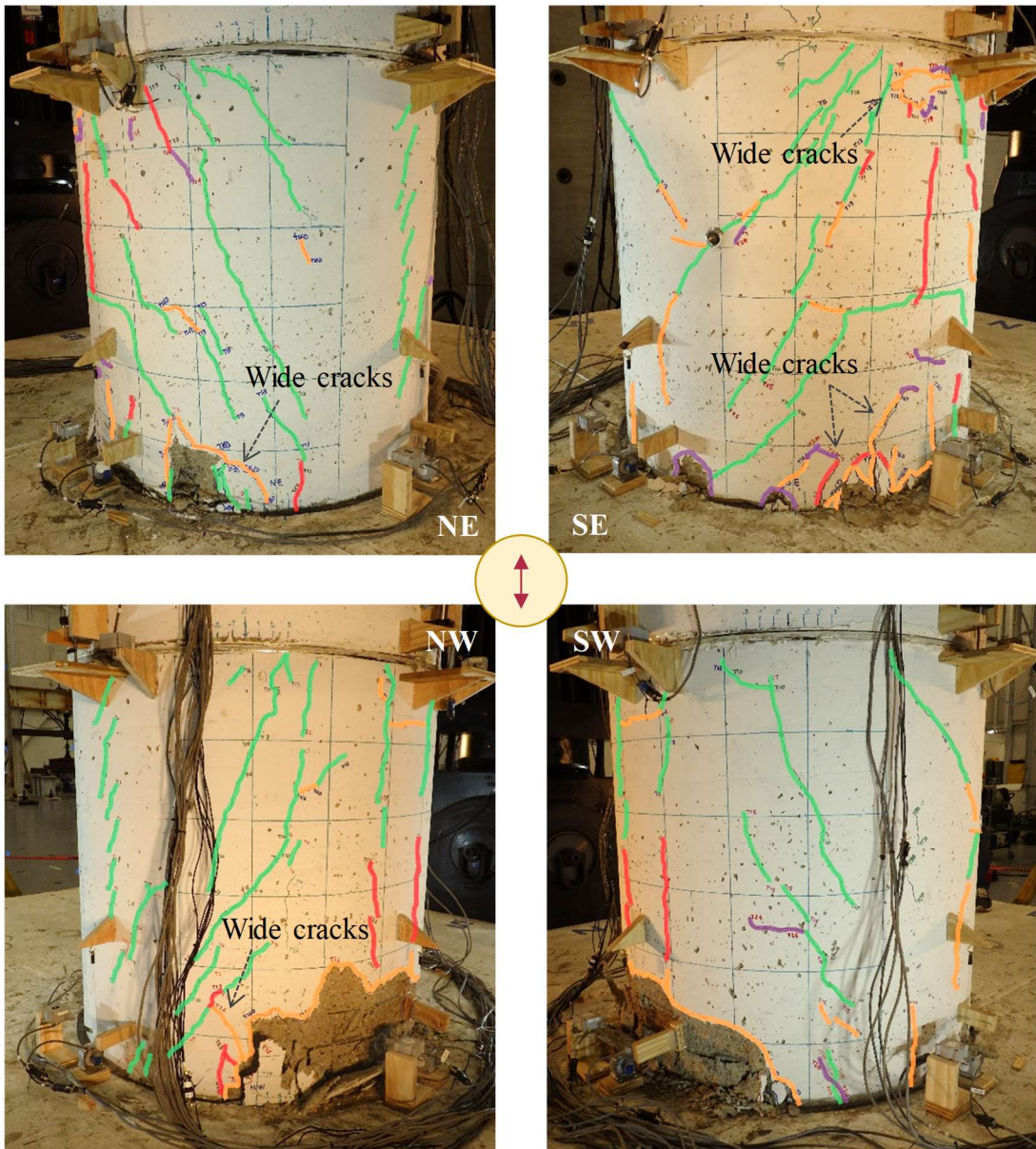
Figure 4-195. Phase II, Loading Set 4, loading protocols of maximum drift ratio of 4%: crack propagation with twist-to-drift ratio amplitude ratio

Figure 4-196. Phase II, Loading Set 4, concrete spalling near east segment toe after tests under loading protocols: (a) HSR2_TU_CNT_S4_DR_4_T2D_0_5; (b) HSR2_TU_CNT_S4_DR_4_T2D_1; (c) HSR2_TU_CNT_S4_DR_4_T2D_2
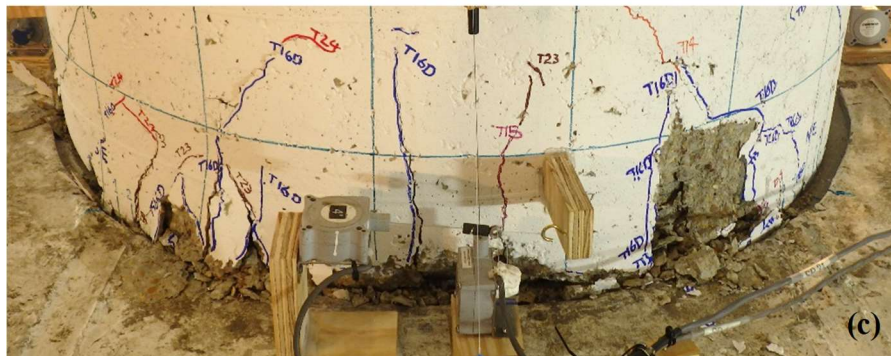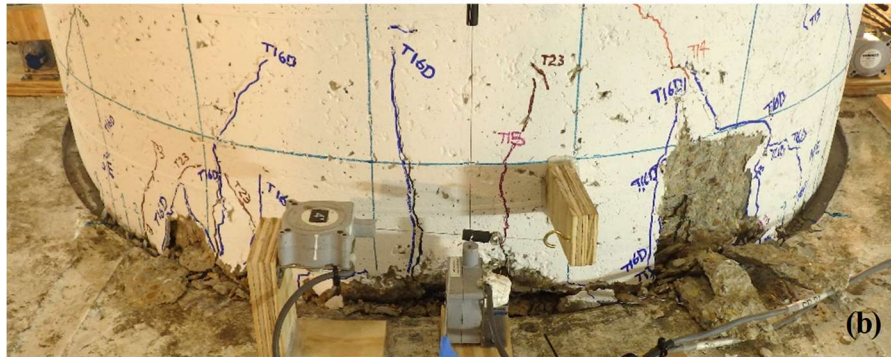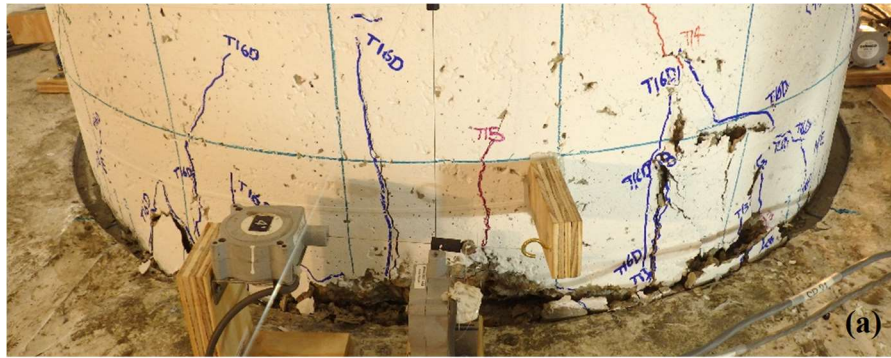
Figure 4-197. Phase II, Loading Set 4, concrete spalling near west segment toe after tests under loading protocols: (a) HSR2_TU_CNT_S4_DR_4_T2D_0_5; (b) HSR2_TU_CNT_S4_DR_4_T2D_1; (c) HSR2_TU_CNT_S4_DR_4_T2D_2

4.7.2.5.5. Results from Loading Set 5

The base shear vs. lateral displacement and torsion vs. twist responses of the column specimen under the arbitrary loading protocols generated by the time history analyses under the three ground motions of 5% probability of exceedance in 50 years are shown in Figure 4-198. Note that these tests were conducted prior to the tests 22-24 per Table 4-30, so only the first sliding joint was active in those. As seen, the base shear vs. lateral displacement responses were governed by the friction-sliding mechanism at the first sliding joint and the responses did not exhibit rocking at this displacement level. This fact becomes more evident when the time histories of the total lateral displacement and total sliding are compared (Figure 4-199). According to these time histories, at least 55% of the lateral displacement imposed to the column specimen during the above tests was accommodated via joint sliding.

Comparing the responses of the column under loading protocols HSR2_TU_CNT_S5_5in50_GM_16 and HSR2_TU_CNT_S5_5in50_GM_16_2, which had identical lateral displacement time histories but the twist applied through the latter was double the former's, indicates the minimal effect of the increased twist on the maximum base shear (Figure 4-198(c) vs. (b)) and torsion (Figure 4-198(f) vs. (e)) undergone by the column specimen.

The maximum sliding values achieved at the first sliding joint (the only sliding joint activated in the tests so far) equaled 1.45 in. and 1.55 in. in the positive and negative directions, respectively, which both occurred during the test under loading protocol HSR2_TU_CNT_S5_5in50_GM_7 (Figure 4-199(a)). These values are just slightly lower

than the sliding values obtained under the same lateral displacements but applied in a quasi-static condition (e.g. see the results for test 13, Figure 4-181).
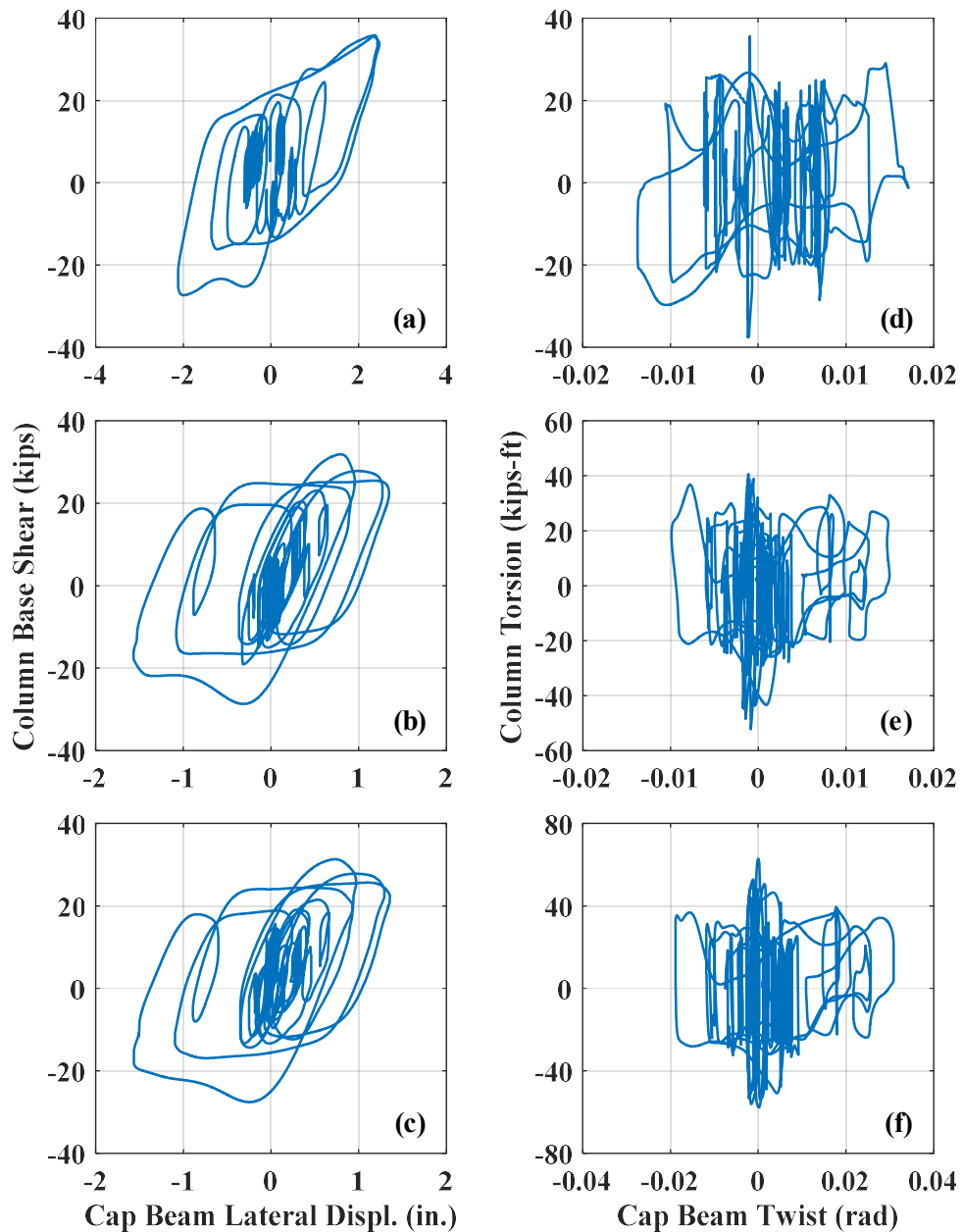
Figure 4-198. Phase II, Loading Set 5: column base shear vs. lateral displacement and torsion vs. twist responses under: (a, d) HSR2_TU_CNT_S5_5in50_GM_7; (b, e) HSR2_TU_CNT_S5_5in50_GM_16; (c, f) HSR2_TU_CNT_S5_5in50_GM_16_2
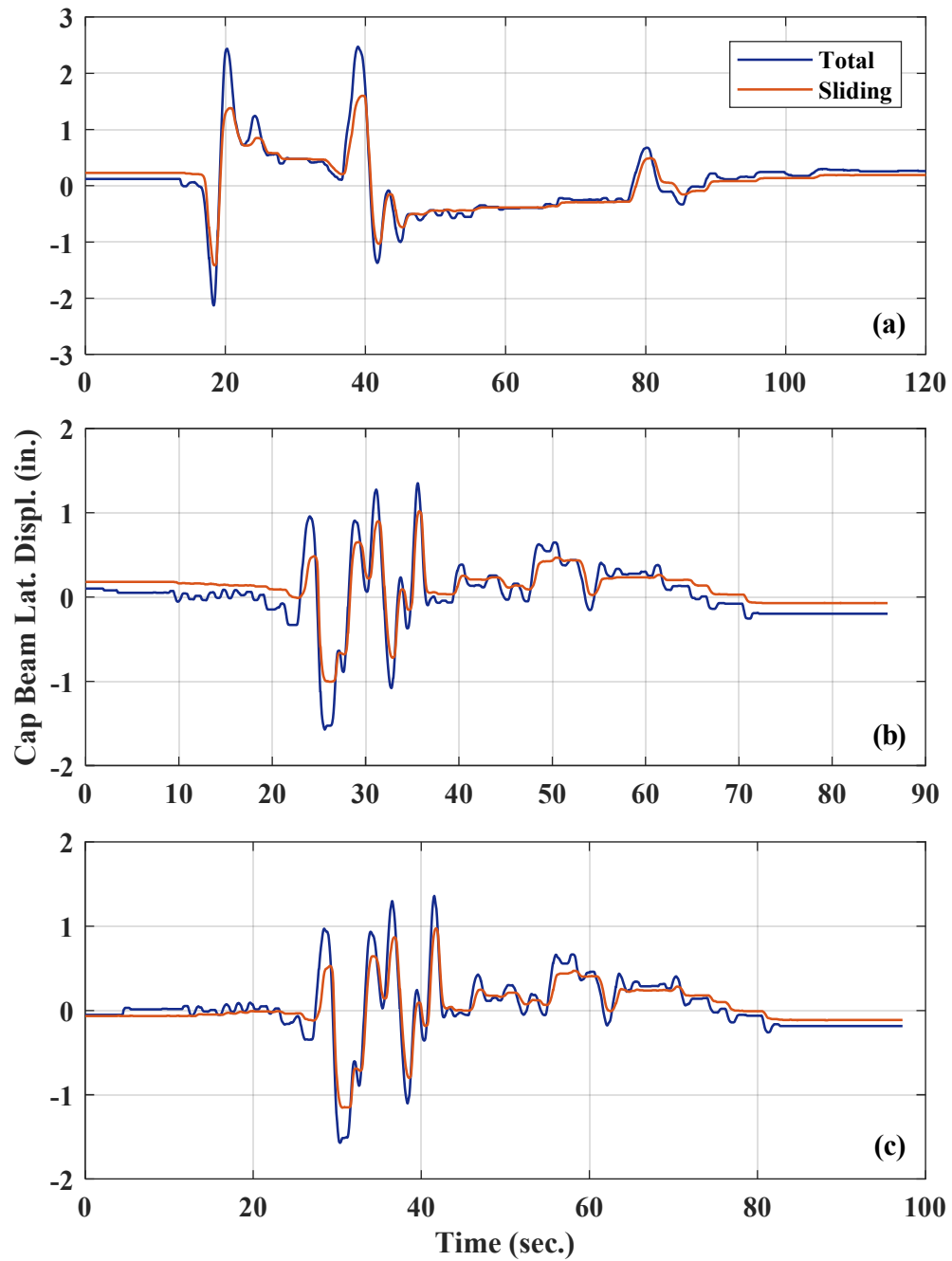
Figure 4-199. Phase II, Loading Set 5: total lateral displacement and sliding time histories under loading protocols: (a) HSR2_TU_CNT_S5_5in50_GM_7; (b) HSR2_TU_CNT_S5_5in50_GM_16; (c) HSR2_TU_CNT_S5_5in50_GM_16_2

In terms of twist accommodation, the first sliding joint was able to accommodate at least 70% of the total twist imposed to the column (Figure 4-200). It is noted that, considering that the column segments had very large torsional stiffness compared to the sliding joints, this percentage is believed to have been much closer to 100% in reality. The observed discrepancy is attributed to the measurement inaccuracies.

The total energy dissipated by the column system and its contributing components during the above tests are plotted against time in Figure 4-201. It is observed that, in these tests, the energy dissipated through sliding (both rotational and translational) constituted between 78% and 88% of the total energy dissipated through the HSR column. From these amounts, only 8-29% was dissipated through rotational sliding, while the remainder was dissipated through the translational sliding. Doubling the twist magnitude in the test under loading protocol HSR2_TU_CNT_S5_5in50_GM_16_2 relative to the test under loading protocol HSR2_TU_CNT_S5_5in50_GM_16, changes the energy dissipation percentages by translational and rotational sliding from 67% and 11% (Figure 4-201(b)), respectively, to 58% and 29%, respectively (Figure 4-201(c)). This, however, should not be interpreted as a reduction in the energy dissipation due to translational sliding, but in fact, the total energy dissipation was increased by the increase of twist.
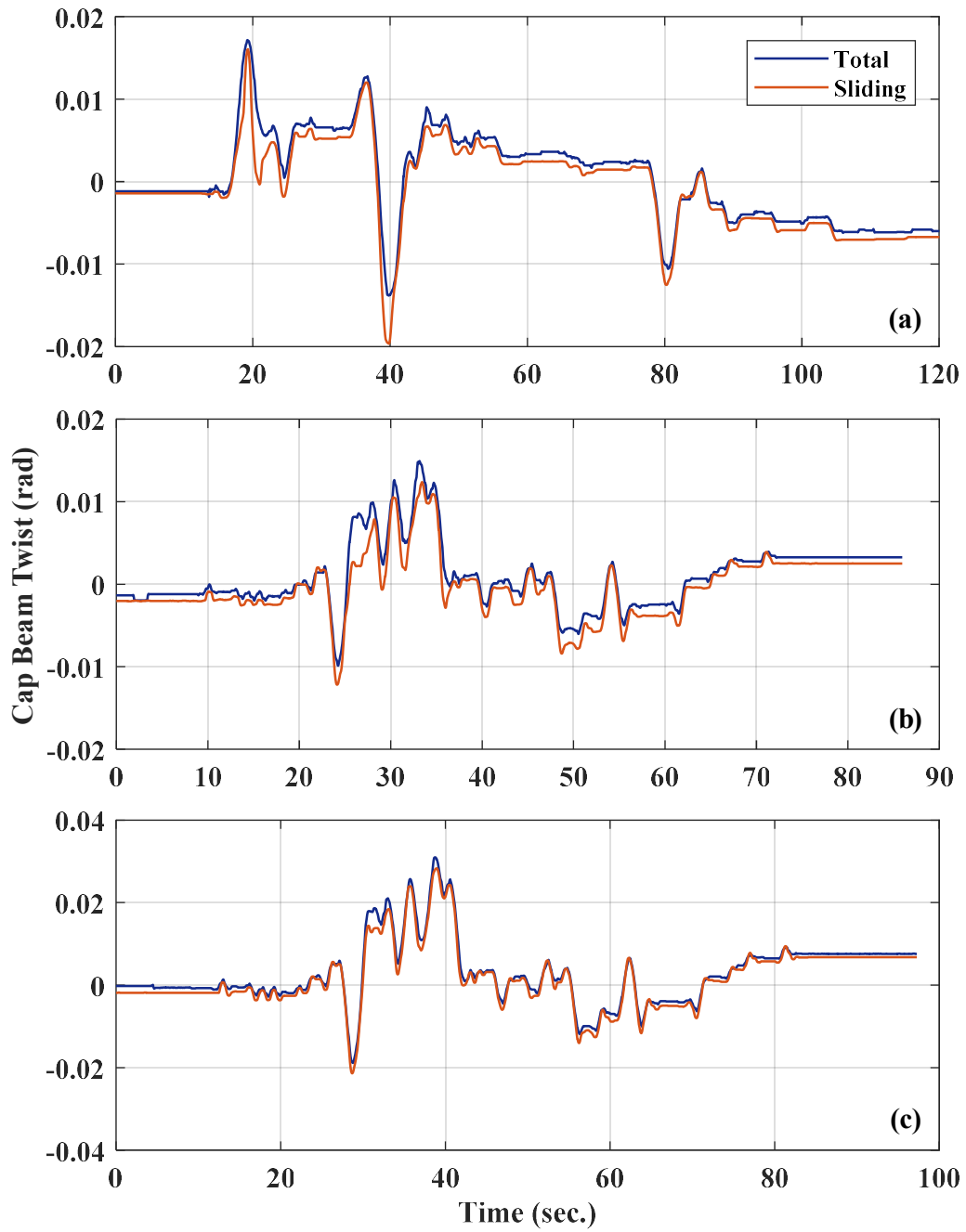
Figure 4-200. Phase II, Loading Set 5: total twist and rotational sliding time histories under loading protocols: (a) HSR2_TU_CNT_S5_5in50_GM_7; (b) HSR2_TU_CNT_S5_5in50_GM_16; (c) HSR2_TU_CNT_S5_5in50_GM_16_2
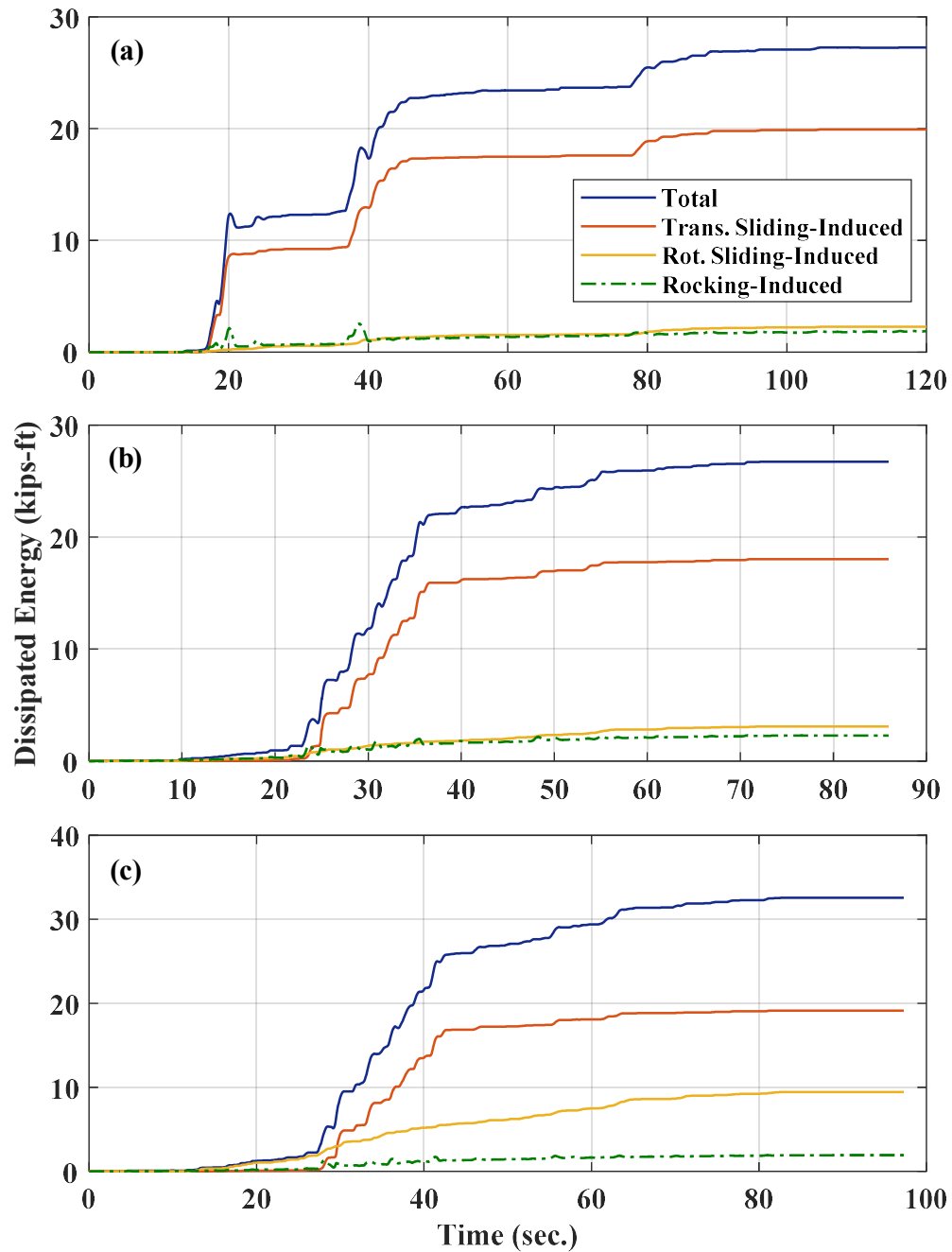
Figure 4-201. Phase II, Loading Set 5: dissipated energy time histories under loading protocols: (a) HSR2_TU_CNT_S5_5in50_GM_7; (b) HSR2_TU_CNT_S5_5in50_GM_16; (c) HSR2_TU_CNT_S5_5in50_GM_16_2

The hysteretic responses achieved through the tests under loading protocols representing 2%-in-50-years ground motions (i.e. HSR2_TU_CNT_S5_2in50_GM_9, HSR2_TU_CNT_S5_2in50_GM_13, and HSR2_TU_CNT_S5_2in50_GM_13_2) are shown in Figure 4-202. The responses exhibited both sliding and rocking mechanisms, even though the sliding mechanism is more evident. The maximum base shear withstood by the column specimen under a lateral displacement close to 3 in. was 40 kips, which resembles the corresponding value obtained through the quasi-static tests (e.g. test 13, Figure 4-178).

According to Figure 4-203, the joint sliding closely followed the lateral displacement imposed to the column without time lag, though it could not accommodate the displacement variations of higher frequency. The maximum sliding achieved under the largest lateral displacement applied to the column through these tests (~3.25 in.) was about 1.85 in., thereby leaving only 1.4 in. (= 0.9% drift ratio) to be accommodated through rocking.

The twist applied to the column was also primarily accommodated by the first sliding joint (Figure 4-204), particularly because the maximum twist applied to the column (less than 0.06 rad) was much smaller than the maximum rotational sliding that could be provided by each sliding joint (more than 0.1 rad).
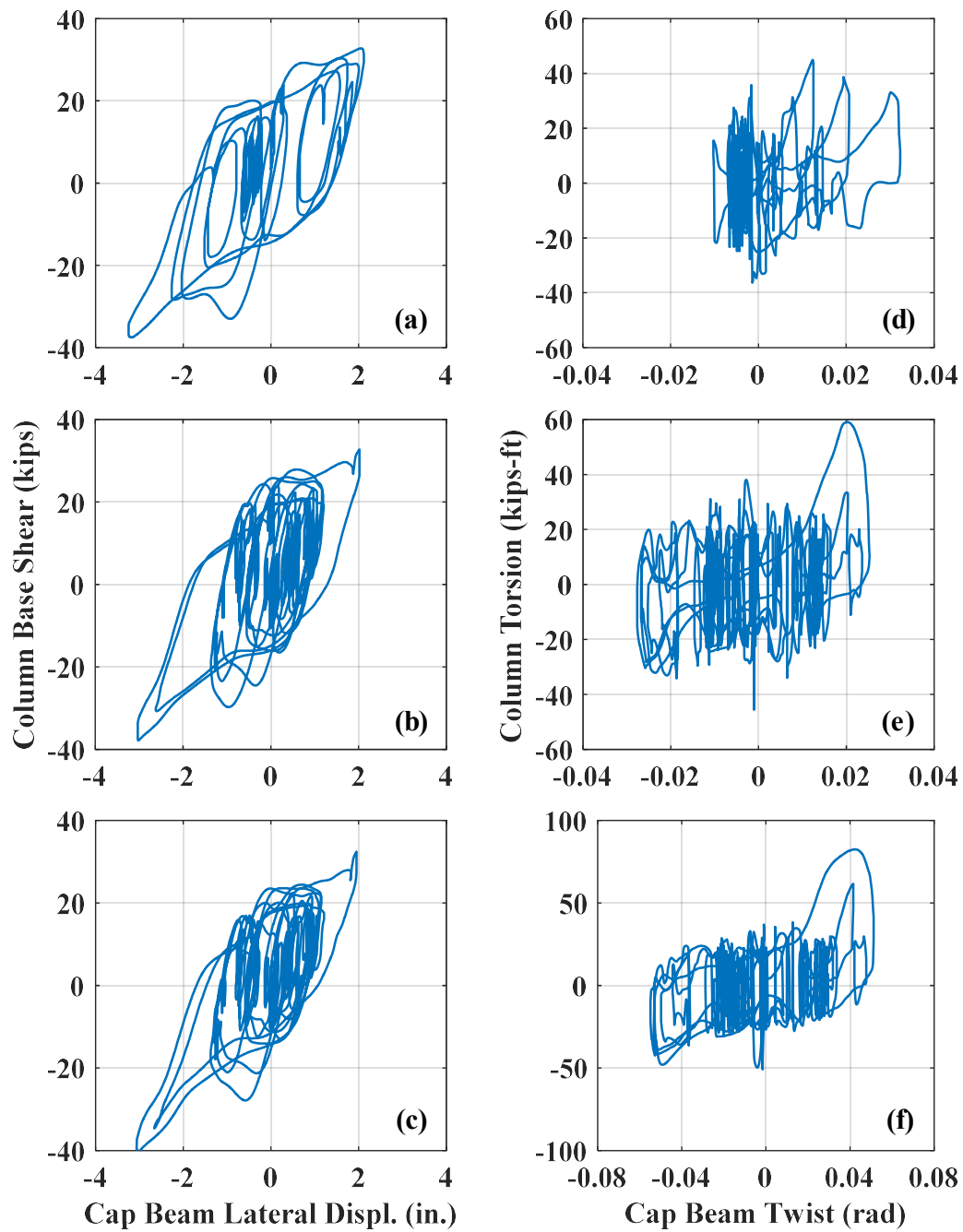
Figure 4-202. Phase II, Loading Set 5: column base shear vs. lateral displacement and torsion vs. twist responses under: (a, d) HSR2_TU_CNT_S5_2in50_GM_9; (b, e) HSR2_TU_CNT_S5_2in50_GM_13; (c, f) HSR2_TU_CNT_S5_2in50_GM_13_2
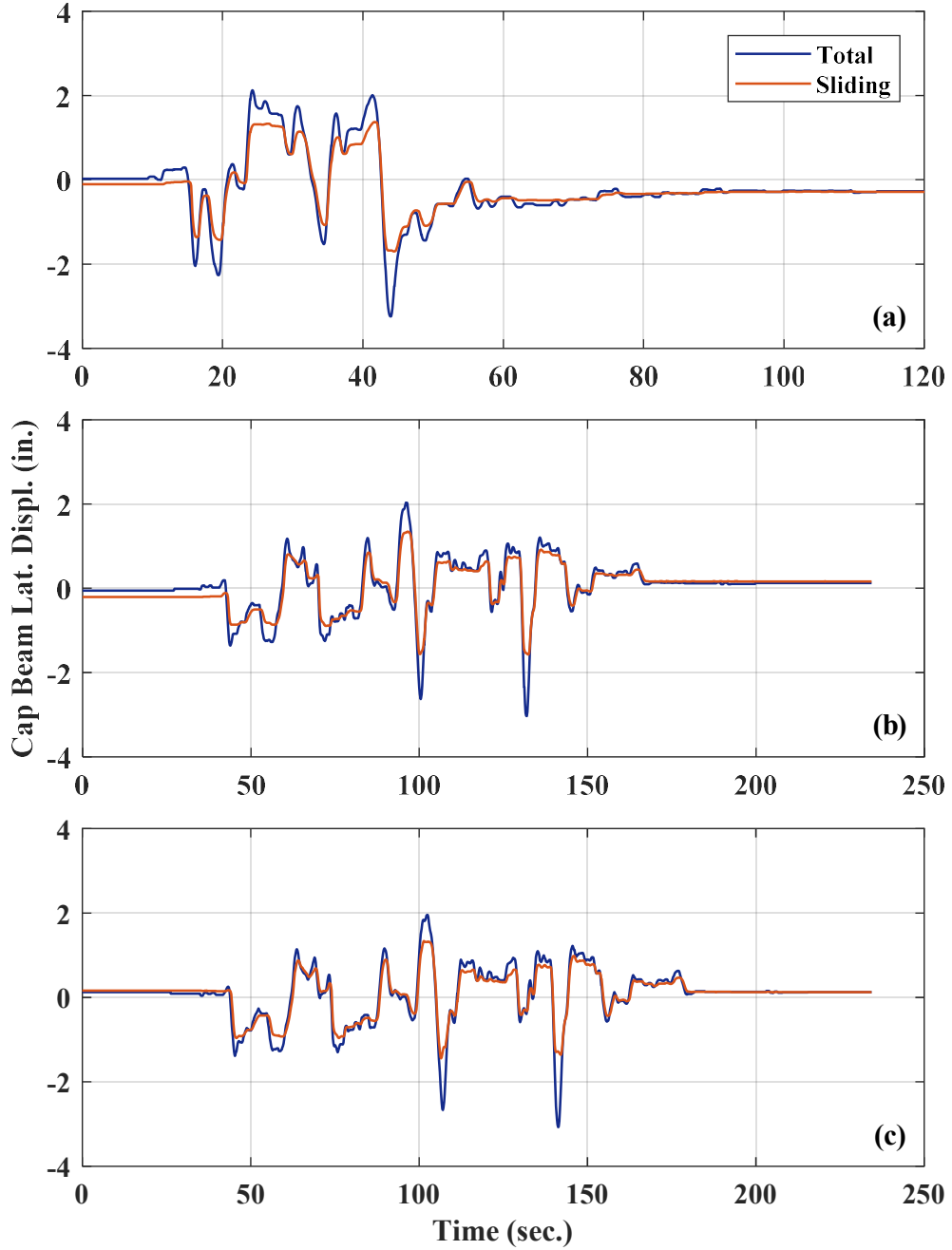
Figure 4-203. Phase II, Loading Set 5: total lateral displacement and sliding time histories under loading protocols: (a) HSR2_TU_CNT_S5_2in50_GM_9; (b) HSR2_TU_CNT_S5_2in50_GM_13; (c) HSR2_TU_CNT_S5_2in50_GM_13_2
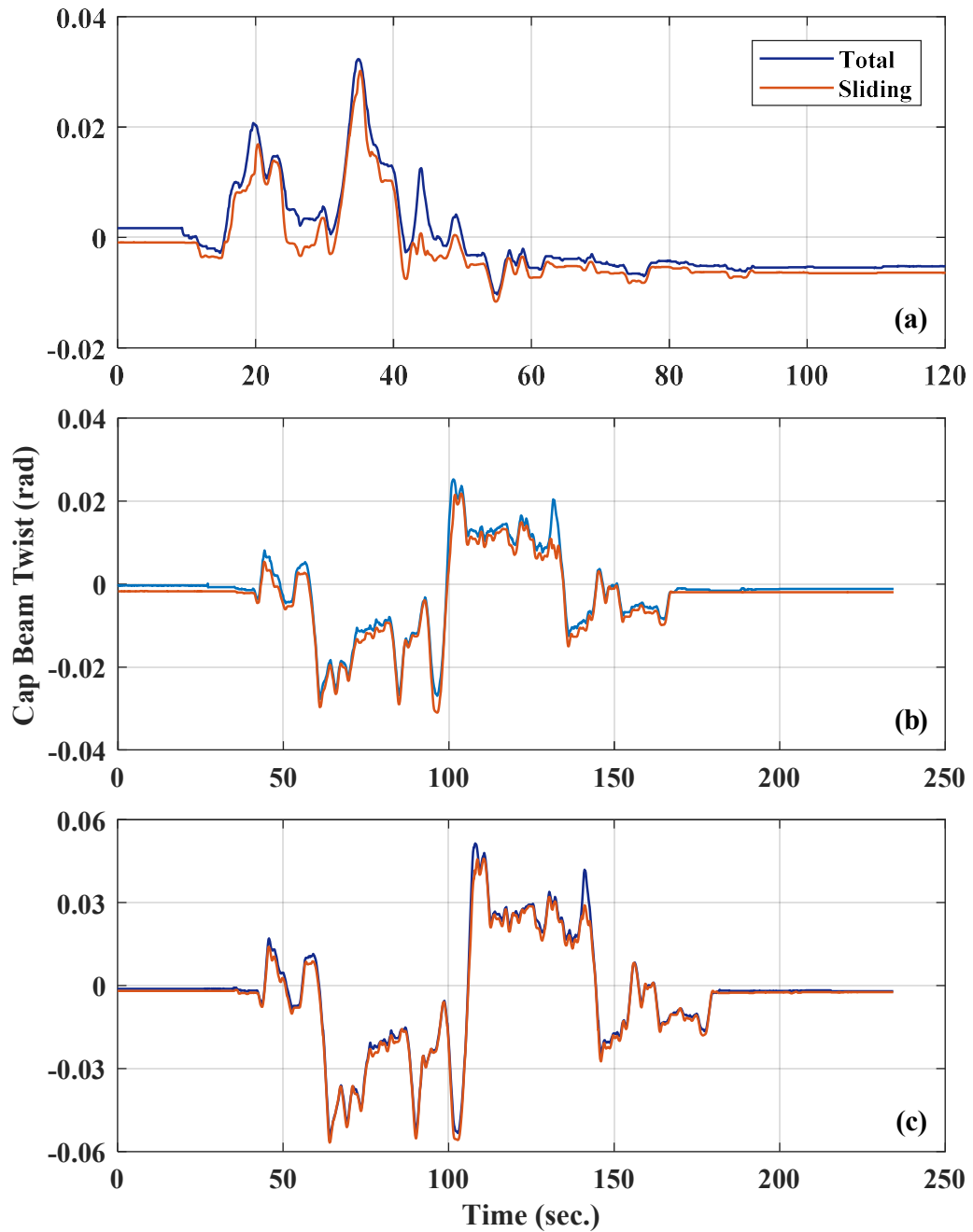
Figure 4-204. Phase II, Loading Set 5: total twist and rotational sliding time histories under loading protocols: (a) HSR2_TU_CNT_S5_2in50_GM_9; (b) HSR2_TU_CNT_S5_2in50_GM_13; (c) HSR2_TU_CNT_S5_2in50_GM_13_2

The base shear vs. lateral displacement and column torsion vs. twist responses of the last three tests in Loading Set 5 (i.e. tests 25-27 per Table 4-31) are displayed in Figure 4-205. As pointed out earlier in Section 4.7.2.4, these tests were conducted after the tests 22-24 from Loading Set 4, during which the second sliding joint became active. This means that in these tests, the breakaway friction at the second sliding joint (Joint 3) had reduced relative to the previous tests in this Loading Set and it could contribute to the column's overall response. Due to the additional joint sliding capacity, the hysteretic responses of the column specimen obtained from these tests exhibited larger energy dissipation capability (i.e. the area enclosed by the hysteretic loops was considerably larger).

The loading beam's lateral displacement and total sliding time histories are compared in Figure 4-206. As seen, there was no discernible phase lag between the displacement and sliding time histories and the sliding joints could accommodate at least 45% of the total lateral displacement applied to the column. According to Figure 4-207, however, the majority of the sliding was provided by the first sliding joint (Joint 2), because the breakaway friction for the second sliding joint (Joint 3) was still higher. That said, Joint 3 seems to have contributed to the response only when the sliding at Joint 2 had already got close enough to its maximum capacity.
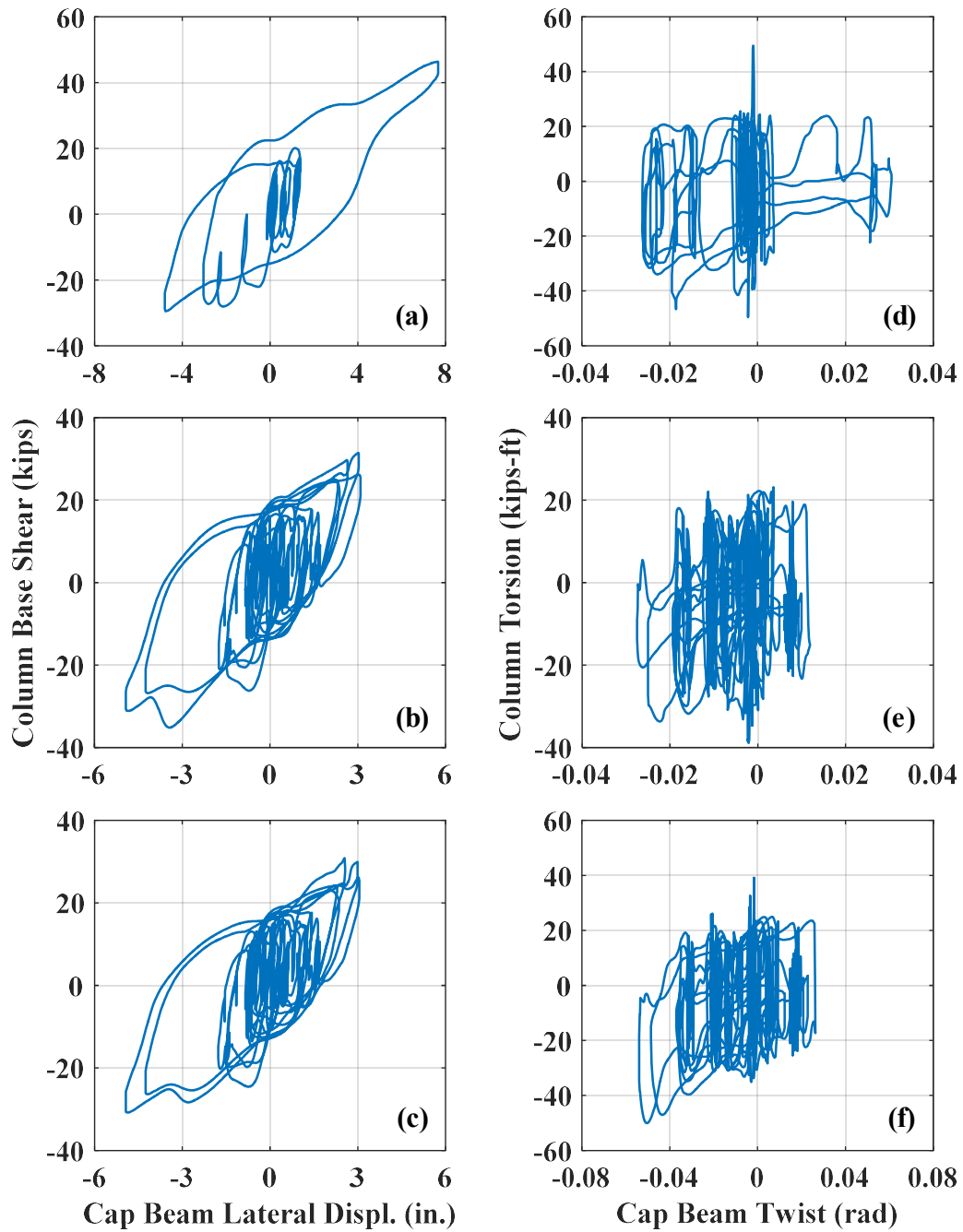
Figure 4-205. Phase II, Loading Set 5: column base shear vs. lateral displacement and torsion vs. twist responses under: (a, d) HSR2_TU_CNT_S5_1in50_GM_12; (b, e) HSR2_TU_CNT_S5_1in50_GM_13; (c, f) HSR2_TU_CNT_S5_1in50_GM_13_2

384
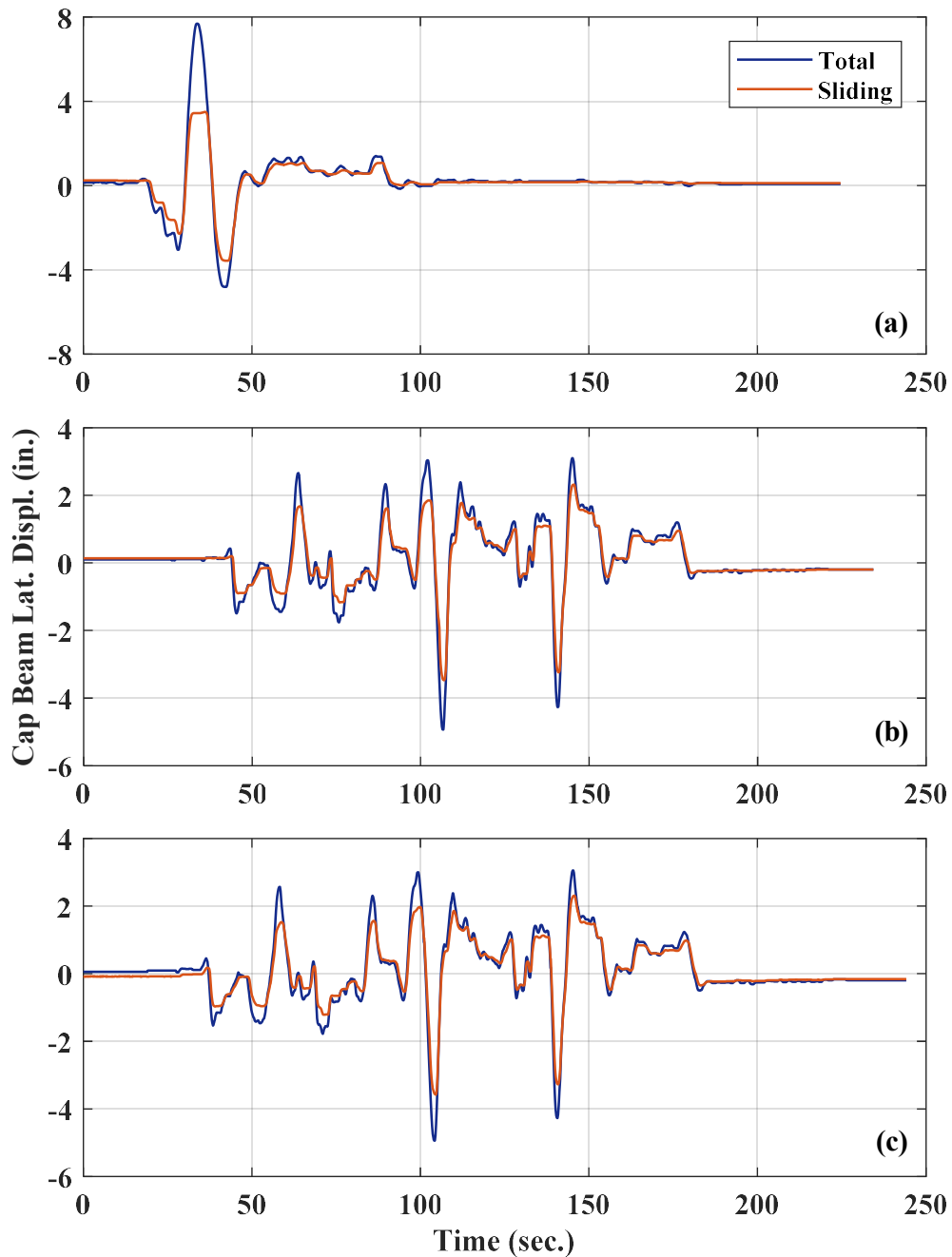
Figure 4-206. Phase II, Loading Set 5: total lateral displacement and sliding time histories under loading protocols: (a) HSR2_TU_CNT_S5_1in50_GM_12; (b) HSR2_TU_CNT_S5_1in50_GM_13; (c) HSR2_TU_CNT_S5_1in50_GM_13_2
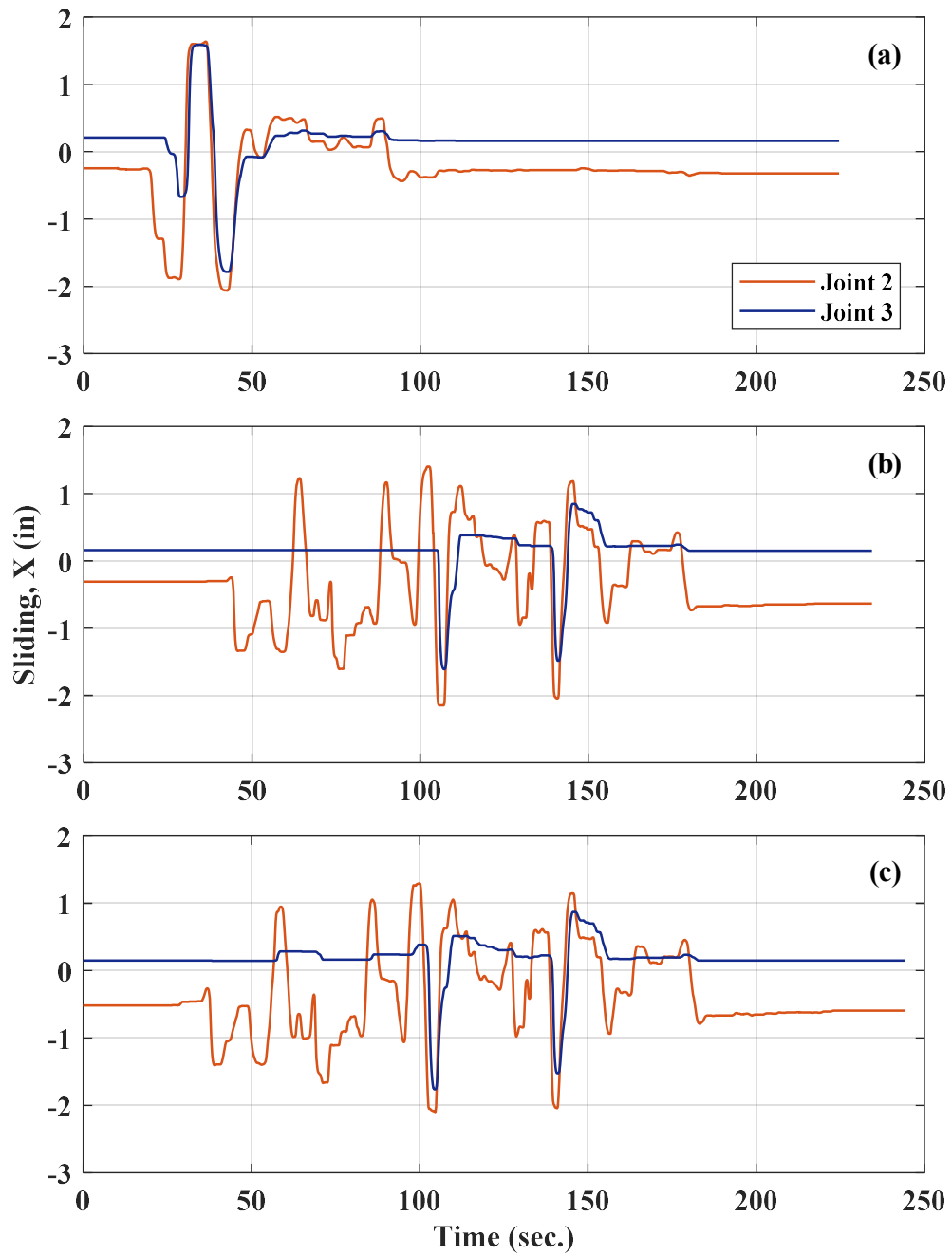
Figure 4-207. Phase II, Loading Set 5: time histories of joint sliding in *X* direction under loading protocols: (a) HSR2_TU_CNT_S5_1in50_GM_12; (b) HSR2_TU_CNT_S5_1in50_GM_13; (c) HSR2_TU_CNT_S5_1in50_GM_13_2

A significant portion of the applied twist was also accommodated by the sliding at the two sliding joints (Figure 4-208), particularly Joint 2 (Figure 4-209). Comparing the time histories of the joint sliding in X direction (Figure 4-207) and the rotational sliding (Figure 4-209) in all three tests, naturally, both the rotational and translational sliding started at the same time instants.
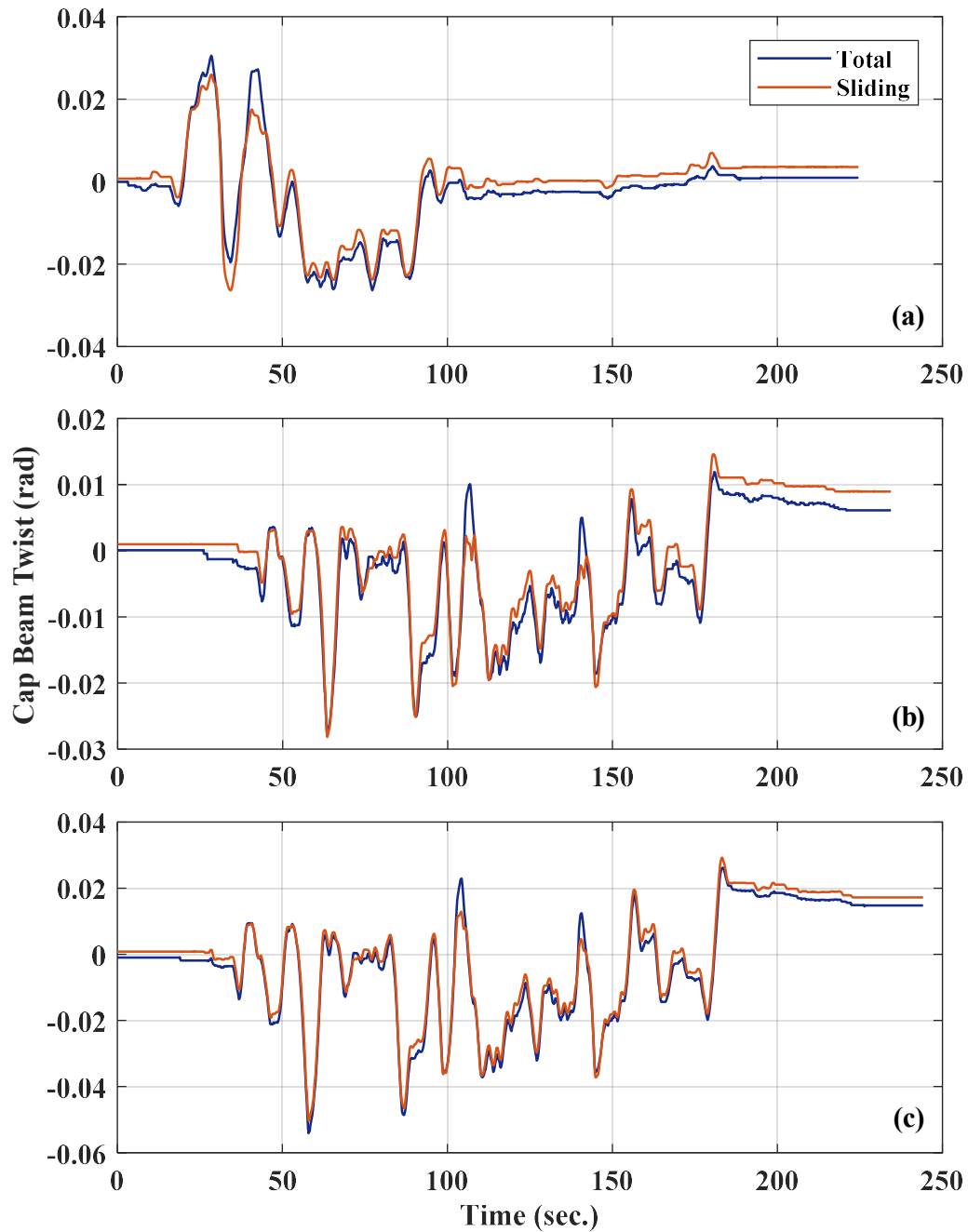
Figure 4-208. Phase II, Loading Set 5: total twist and rotational sliding time histories under loading protocols: (a) HSR2_TU_CNT_S5_1in50_GM_12; (b) HSR2_TU_CNT_S5_1in50_GM_13; (c) HSR2_TU_CNT_S5_1in50_GM_13_2
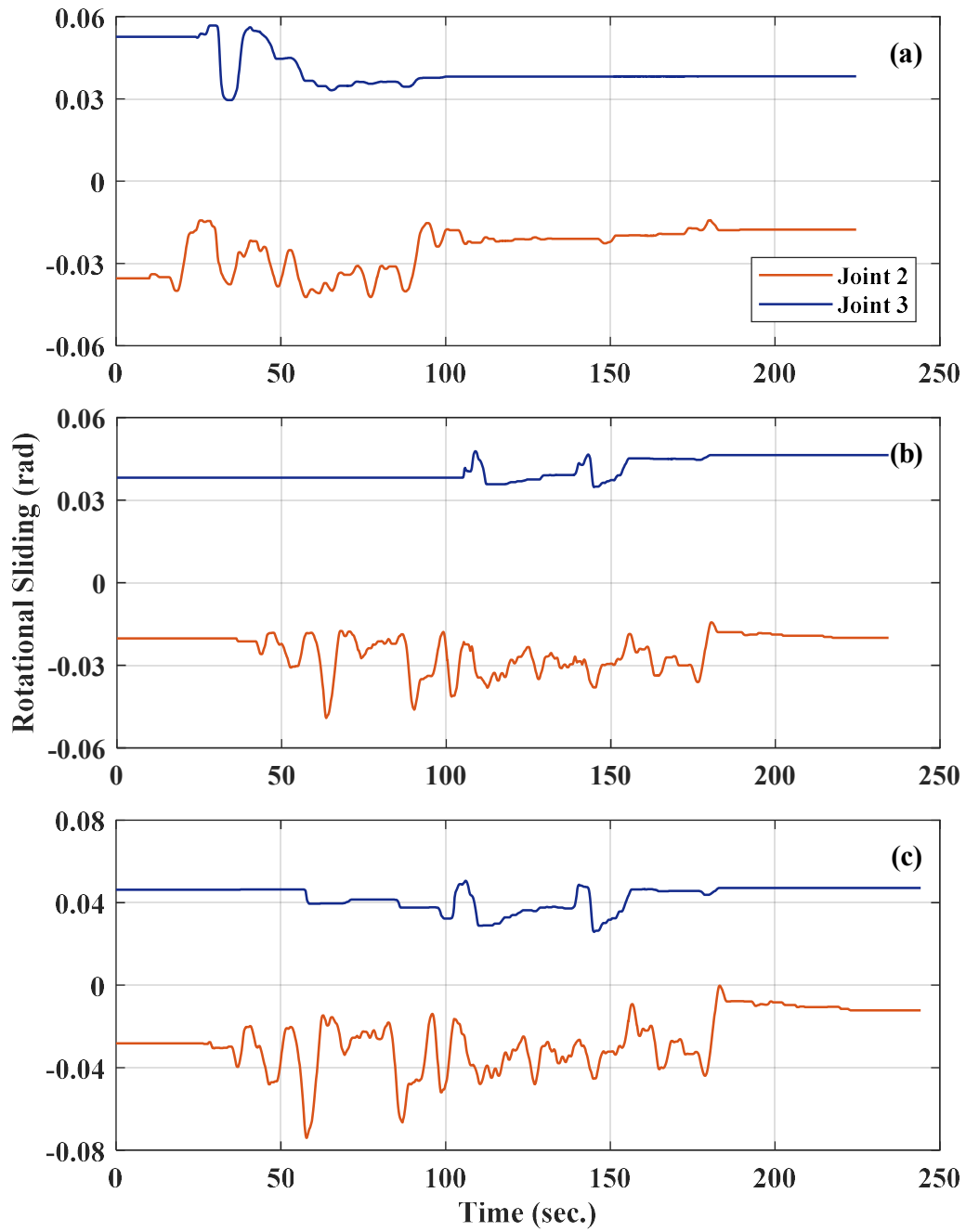
Figure 4-209. Phase II, Loading Set 5: joint rotational sliding time histories under loading protocols: (a) HSR2_TU_CNT_S5_1in50_GM_12; (b) HSR2_TU_CNT_S5_1in50_GM_13; (c) HSR2_TU_CNT_S5_1in50_GM_13_2

In none of the nine tests of Loading Set 5, the tendons exceeded 45% their yield strength, even though they might have sustained local damages in the vicinity of sliding joints due to bearing reactions and bending. The relative PT losses occurred during the tests in Loading Set 5 are shown in Figure 4-210. Because of its deficiency, the data obtained from the east tendon load cell was excluded in the calculation of the total PT forces, so the actual losses are predicted to have been slightly higher. Moreover, it must be noted that the PT losses were calculated based on the PT forces at the end of each loading protocol, regardless of the residual lateral displacement and twist; this is why the losses computed for the 5th and the 6th tests in this Loading Set are negative (Figure 4-210). Overall, the maximum PT loss in this Loading Set belonged to the first test (HSR2_TU_CNT_S5_5in50_GM_7), which equaled 2.1%. The PT losses for the rest of the tests ranged from 0% to 1.6%, which are deemed relatively low. The damage caused by the tests in Loading Set 5 was limited to a few hairline cracks on the bottom segment.
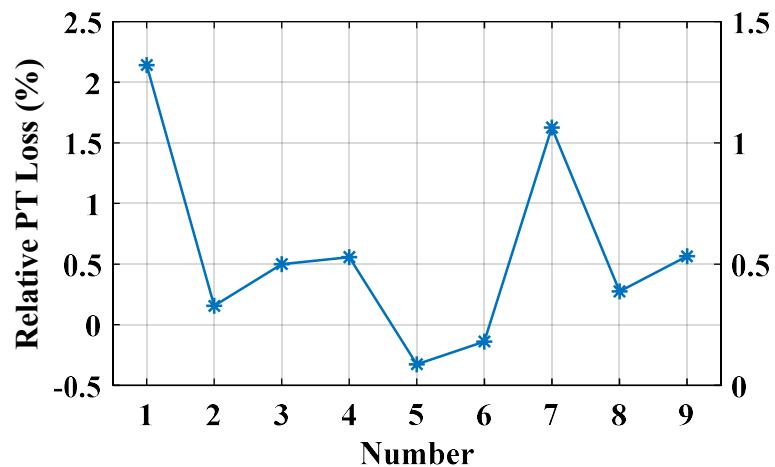
Figure 4-210. Phase II, Loading Set 5: relative PT loss vs. test number

4.7.2.5.6. Results from Loading Set 6

The column base shear-lateral displacement response obtained under loading protocol HSR2_TU_CNT_S6_DR_6 is displayed in Figure 4-211. Even under the larger peak drift ratio of 6% applied to the column specimen, it did not exhibit in-cycle softening. The maximum values of the base shear resisted by the column specimen in the positive and negative directions were 48 kips and 43 kips, respectively, which are higher than the values obtained under loading protocol HSR2_TU_CNT_S4_DR_4_T2D_1 after the second sliding joint became active (i.e. 43 kips and 40 kips in the positive and negative directions, respectively). However, according to Figure 4-212, the column sustained 4% strength drop after the first lateral displacement cycle. This cyclic deterioration, which was probably caused by the growth of concrete spalling near the bottom segment toes (Figure 4-218) and PT losses (Figure 4-217), was not observed in the rest of the cycles.
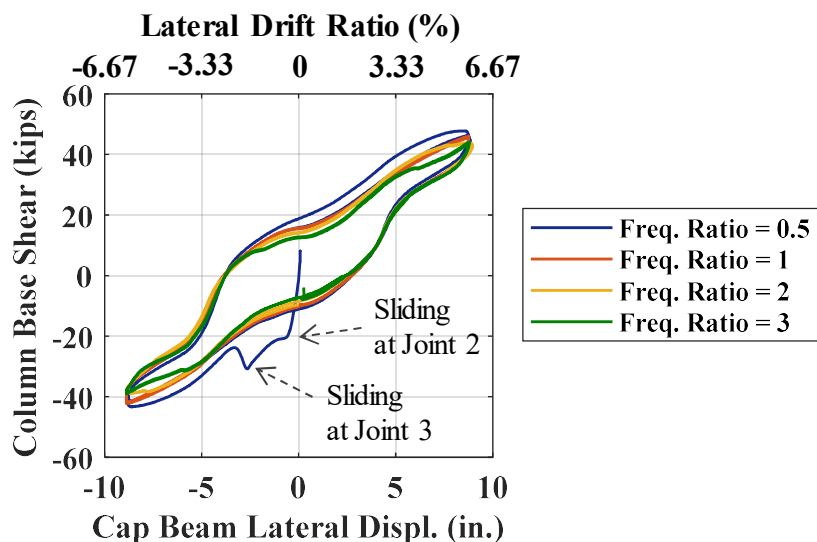
Figure 4-211. Phase II, loading protocol HSR2_TU_CNT_S6_DR_6: base shear vs. lateral displacement response

391
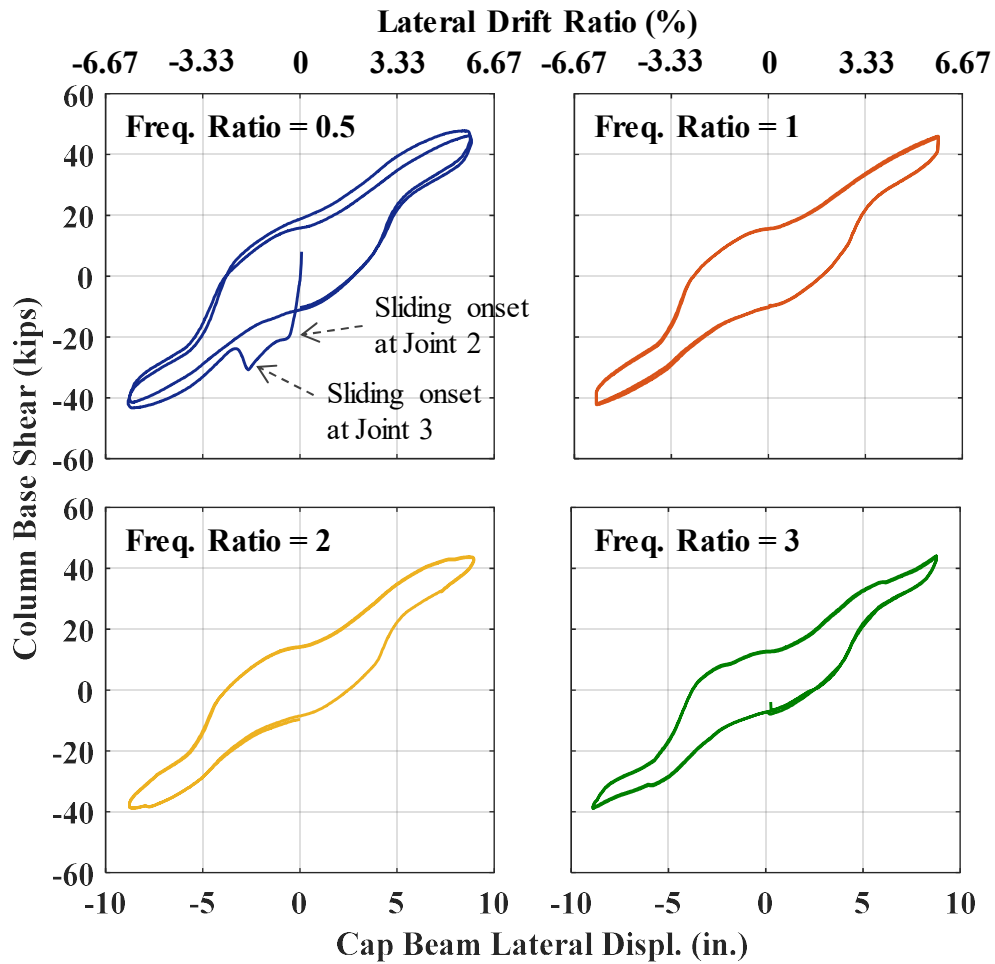
Figure 4-212. Phase II, loading protocol HSR2_TU_CNT_S6_DR_6: different cycles of base shear vs. lateral displacement response

The residual drift ratios in all displacement cycles were similar and equal to 1.8% and 2.6% in the positive and negative directions, respectively. However, 77% and 93% of the residual displacements in the positive and negative directions, respectively, were caused by the residual sliding at the sliding joints (Figure 4-213). That said, the residual drift ratios caused by the column damage (i.e. excluding the residual sliding) in the positive and negative directions were only 0.4% and 0.2%, which are considered very small.
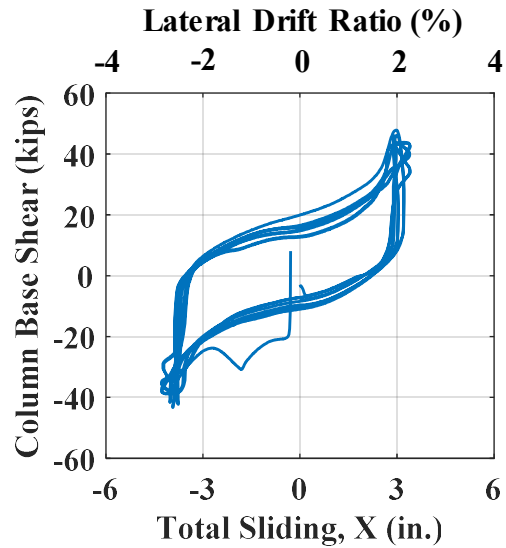
Figure 4-213. Phase II, loading protocol HSR2_TU_CNT_S6_DR_6: base shear vs. total sliding response

The effect of the twist-to-displacement frequency ratio on the column's hysteresis loops is explored through Figure 4-212. It is observed that, for the chosen displacement and twist amplitudes (peak twist = peak drift ratio), the larger the frequency ratio became, the smaller the area underneath the hysteresis loop got – i.e. lower energy dissipation.

The friction force at the sliding joints also decreased with the number of cycles, mainly due to the gradual posttensioning loss (Figure 4-217), which is also noticed in Figure 4-213. However, the values of the peak base shear resisted by the column in both directions were minimally affected by the frequency ratio and the number of cycles. This is because at that point, the sliding joints would reach their maximum capacities and the base shear would not be affected by the friction extent anymore.

The moment vs. rocking response of the bottommost joint of the column (Joint 1), where the maximum moment occurred, is demonstrated in Figure 4-214. The maximum

rocking values measured during all eight lateral displacement cycles and in both directions are found to be very close. While minor cyclic deterioration is observed in the response, the posttensioning system was capable of restoring the rotation at the bottom joint (Joint 1) to less than 0.003 rad (less than 0.2 degrees).
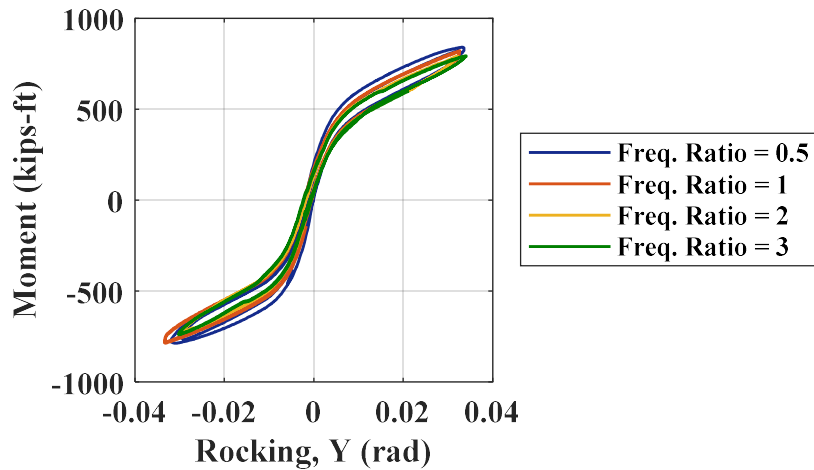
Figure 4-214. Phase II, loading protocol HSR2_TU_CNT_S6_DR_6: moment vs. rocking response at Joint 1

The complete torsion vs. twist response of the column specimen under the same loading protocol is shown in Figure 4-215, whereas parts of this response from each pair of lateral displacement cycles are compared in Figure 4-216. The larger (by 36%) peak values of the torsion in the negative direction compared to its values in the positive direction (Figure 4-215) may be attributed to the initial duct misalignments, particularly because there was a negative rotational sliding at Joint 3 before the testing started (see Figure 4-192). In addition, it is observed in Figure 4-216 that the frequency ratio could

394

noticeably change the hysteresis loop's shapes, but the torsion demands were primarily affected by the peak twist.
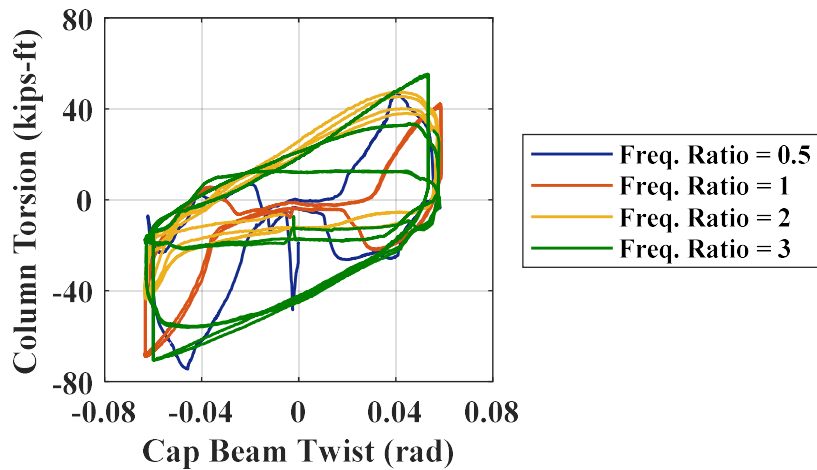
Figure 4-215. Phase II, loading protocol HSR2_TU_CNT_S6_DR_6: column torsion vs. twist response

According to Figure 4-217, none of the tendons lost their full posttensioning, but it is predicted that some of the tendons could have yielded during this test – note that the PT forces reported herein were measured by the load cells at the top end of the strands, while due to friction, the tendon forces at the bottom end could generally become larger (see Figure 4-75). The total posttensioning force at the beginning of this test was 102 kips, which is 30% lower than its initial value before any test was executed on the column specimen. The total PT loss under the current loading protocol was half the total loss caused during the last 27 tests (i.e. 15%). Not only does this extent of posttensioning loss imply the significant damage caused to the bottom rocking joint, but it also implies the

potential yielding of some of the tendons and further wedge setting at the anchorage hardware.
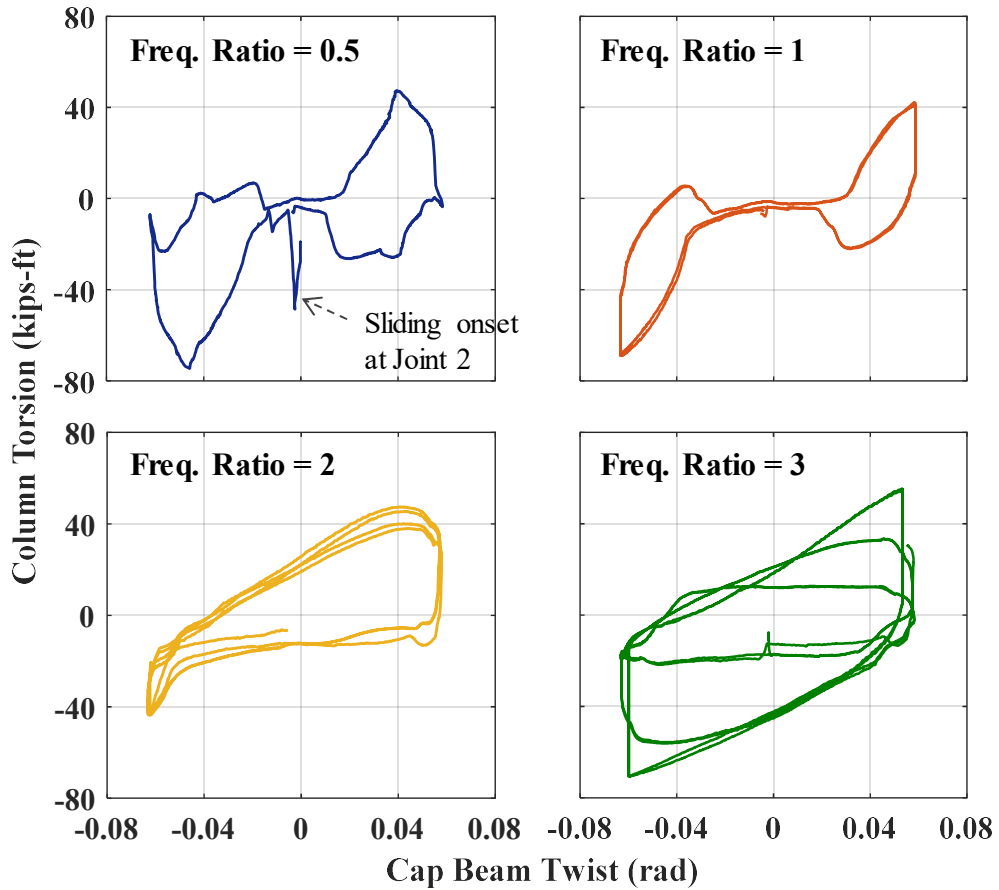
Figure 4-216. Phase II, loading protocol HSR2_TU_CNT_S6_DR_6: different cycles of column torsion vs. twist response
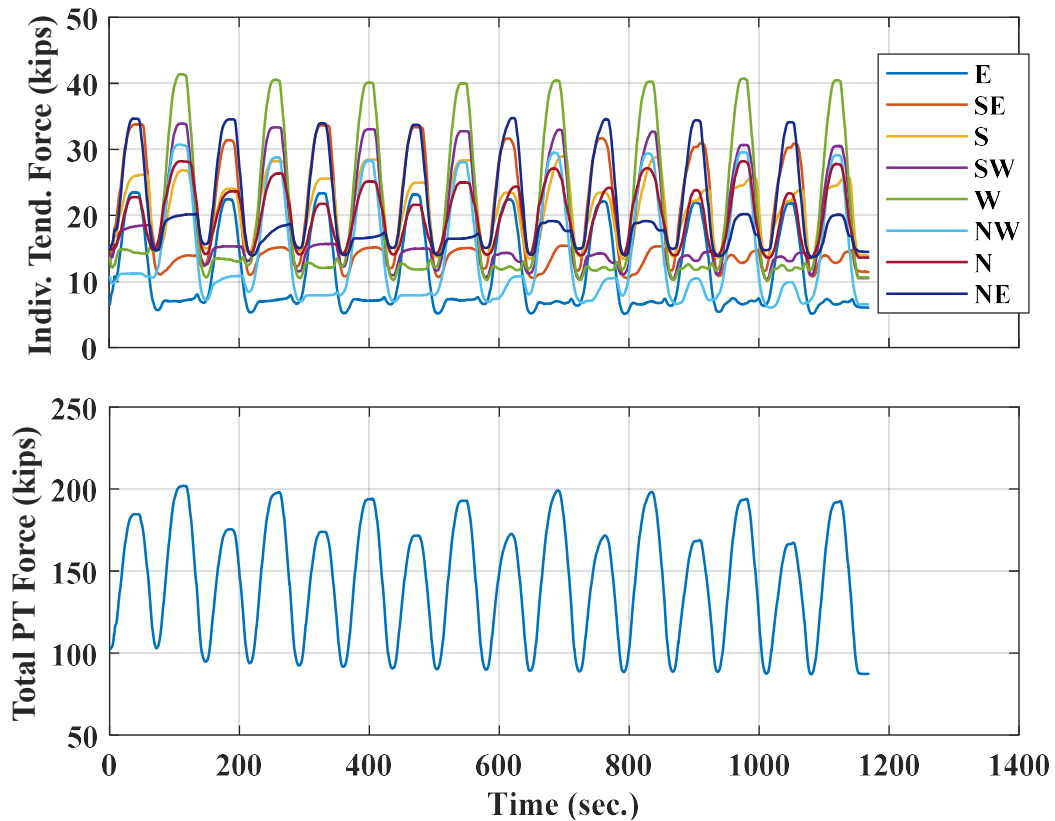
Figure 4-217. Phase II, loading protocol HSR2_TU_CNT_S6_DR_6: time histories of posttensioning forces

The additional column damage observed on the outside of the column was mainly confined to the bottom column segment, and in particular, in the vicinity of the west and east compression toes (Figure 4-218). In those regions, the cover concrete completely spalled and the spiral rebar and some of the longitudinal bars were exposed. More limited concrete spalling was also observed on the north and south quadrants of the bottom rocking joint (Figure 4-219), indicating the spread of large compressive strains toward the center of the column cross section and their destructive interaction with the torsion-induced shear strains. No new cracks appeared on the upper two segments.
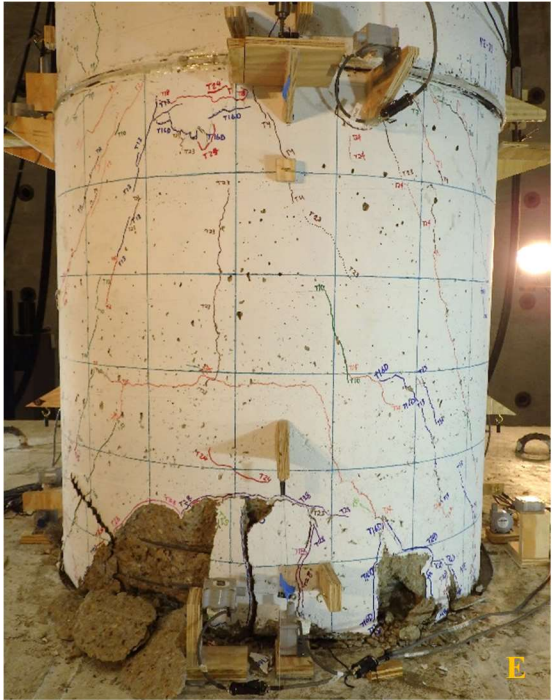
Figure 4-218. Phase II, loading protocol HSR2_TU_CNT_S6_DR_6: concrete damage on east and west sides of bottom segment
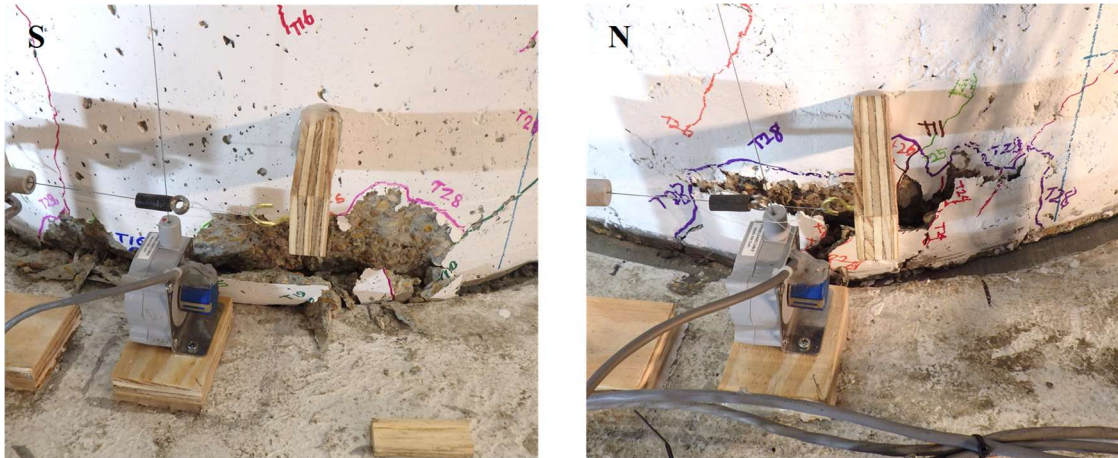
Figure 4-219. Phase II, loading protocol HSR2_TU_CNT_S6_DR_6: concrete damage on south and north sides of bottom rocking joint

The column's response obtained from the second test in Loading Set 6 (i.e. under loading protocol HSR2_TU_CNT_S6_DR_8) is demonstrated in Figure 4-220. It is obvious that, under the large deformations induced by the simultaneous application of 8% peak drift ratio and the peak twist of 0.08 rad (see Figure 4-222), the column specimen suffered from significant strength and stiffness degradation. According to Figure 4-223, near the peaks of the first lateral displacement cycle (at the drift ratios of 6.5% and 7.2% in the positive and negative directions, respectively), the column specimen experienced in-cycle softening for the first time. The average peak base shear under the applied loading was 44 kips, which is slightly smaller than that achieved in the previous test with a peak drift ratio of 6% (i.e. 46 kips, Figure 4-202), indicating that the column's response was within its post-peak range. Similarly to the previous test, a decrease in the friction force (base shear near zero lateral displacement) is observed in the response (see also Figure 4-221), which was mainly caused by the posttensioning losses (Figure 4-227).
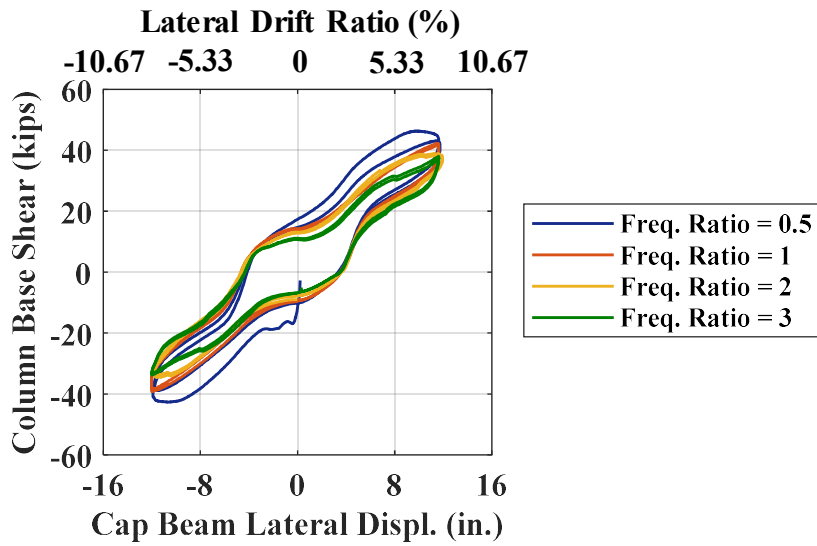
Figure 4-220. Phase II, loading protocol HSR2_TU_CNT_S6_DR_8: base shear vs. lateral displacement response
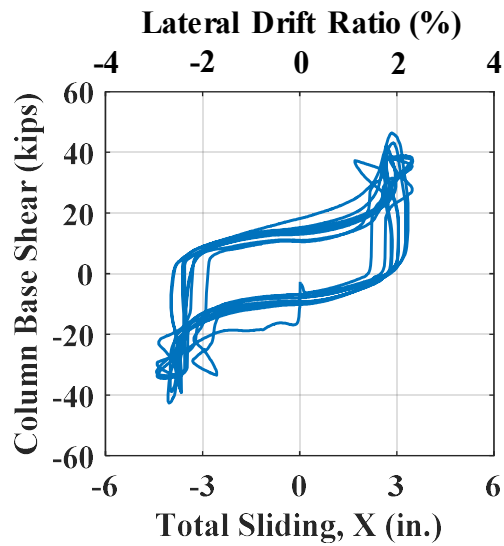
Figure 4-221. Phase II, loading protocol HSR2_TU_CNT_S6_DR_8: base shear vs. total sliding response
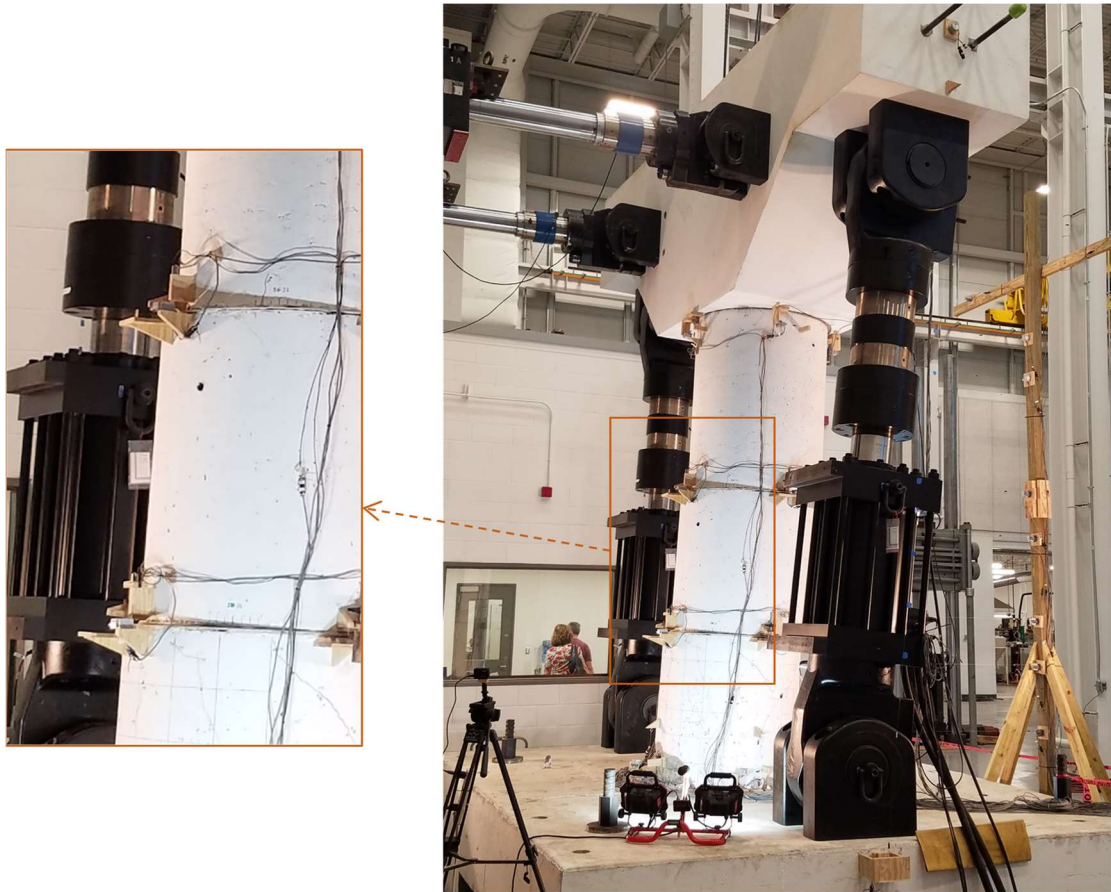
Figure 4-222. Phase II, loading protocol HSR2_TU_CNT_S6_DR_8: column deformation during test

The effect of the twist cycles on the column's base shear vs. lateral displacement response is illustrated through Figure 4-223. As seen in Figure 4-212 for the previous test, larger frequency ratios led to narrower lateral force-displacement hysteresis loops, but wider torsion-twist hysteresis loops (Figure 4-224).
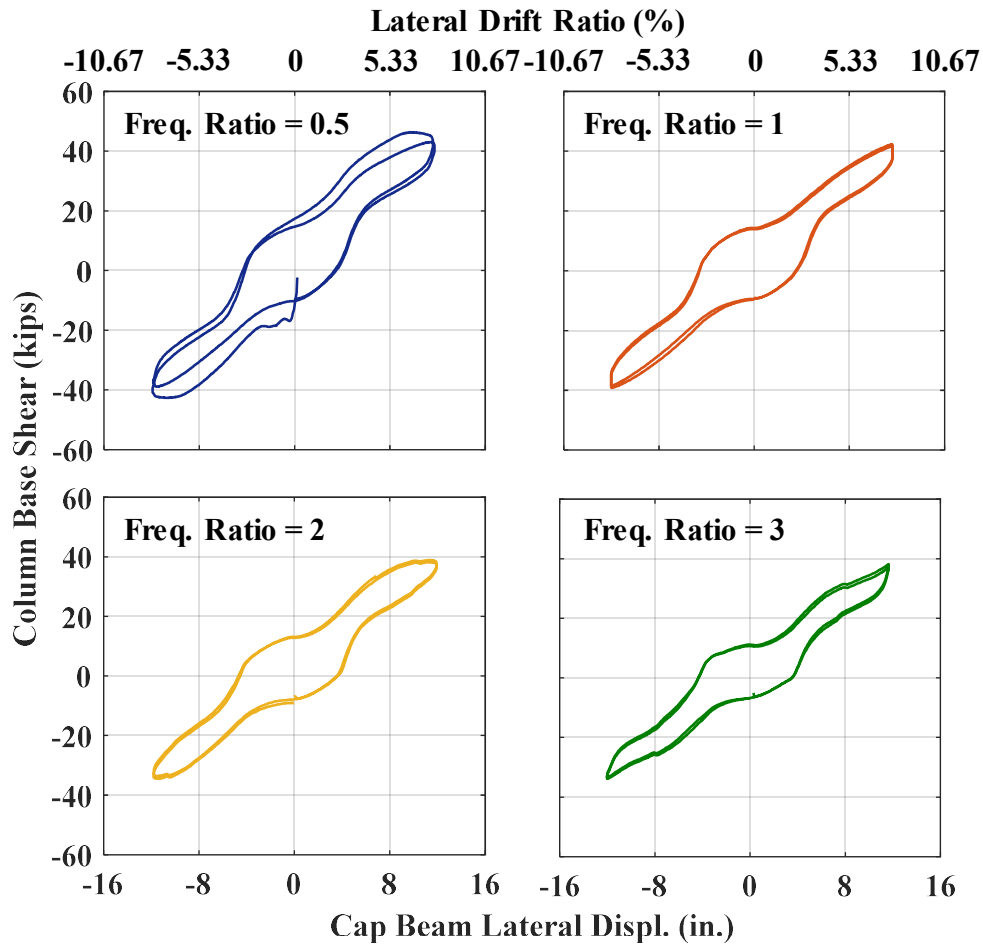
Figure 4-223. Phase II, loading protocol HSR2_TU_CNT_S6_DR_8: different cycles of base shear vs. lateral displacement response

The moment vs. rocking response at the bottom rocking joint of the HSR column specimen is shown in Figure 4-225. Compared to the response obtained in the previous test (Figure 4-214), there is a more severe stiffness and moment strength degradation observed here. However, the residual rotation at the bottom end of the column was still very small, i.e. 0.006 rad (0.34 degrees), thereby proving the efficacy of the designed posttensioning system in avoiding unrecoverable residual deformations.
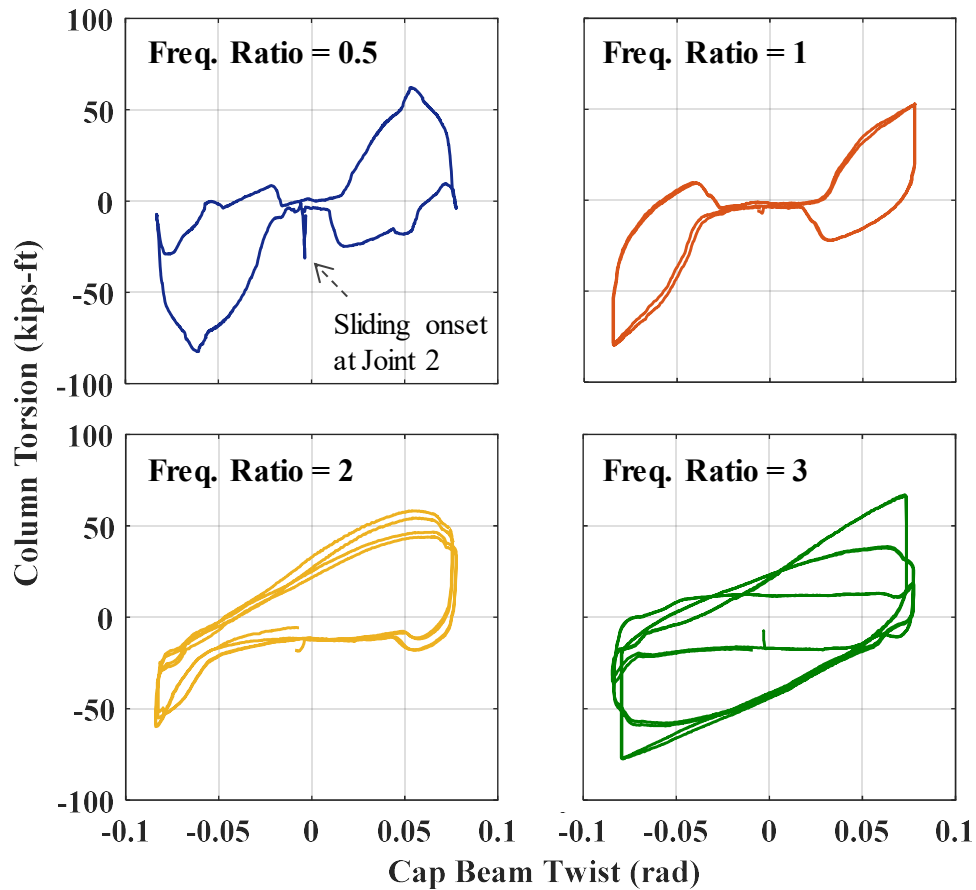
Figure 4-224. Phase II, loading protocol HSR2_TU_CNT_S6_DR_8: different cycles of column torsion vs. twist response

The general shape of the torsion-twist hysteresis loops obtained in this test (Figure 4-226) resemble those obtained in the previous test (Figure 4-215) and those in Loading Set 4. Compared to the previous test, the maximum torsion was increased by only 7% (from 75 kip-ft to 80 kip-ft), even though the peak twist increased by more than 30% (from 0.06 rad to 0.08 rad).
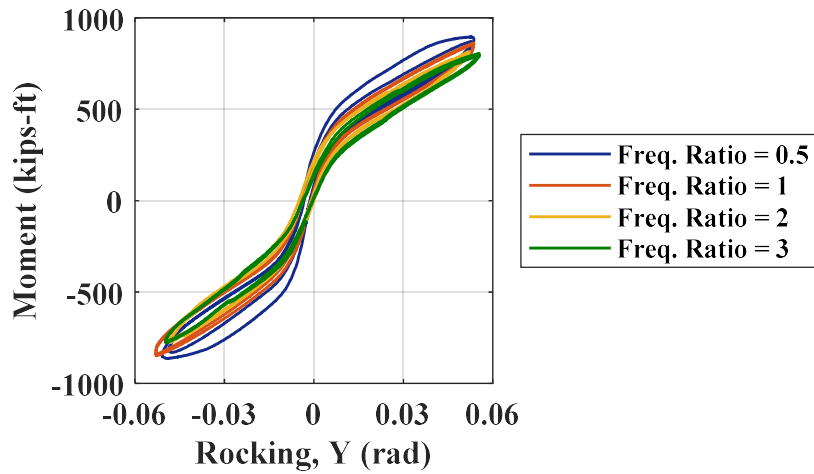
Figure 4-225. Phase II, loading protocol HSR2_TU_CNT_S6_DR_8: moment vs. rocking response at Joint 1
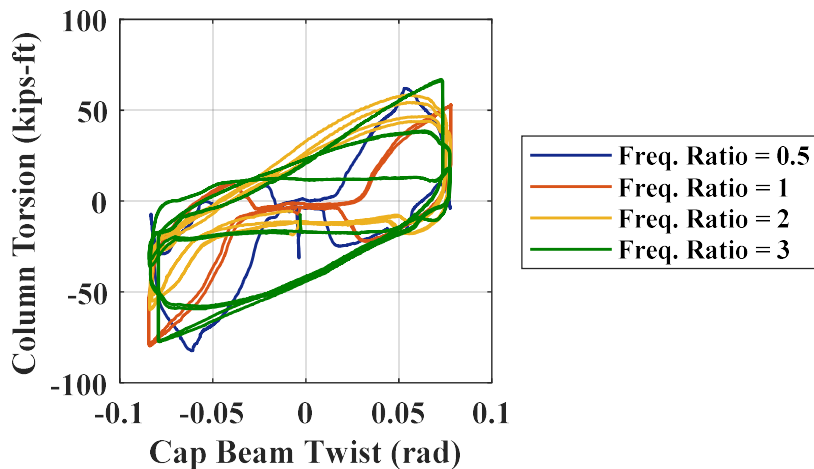
Figure 4-226. Phase II, loading protocol HSR2_TU_CNT_S6_DR_8: column torsion vs. twist response

The variations of individual tendon forces and their sum with time are shown in Figure 4-227. The tendons located on the east, west, southeast, and southwest are predicted to have locally yielded, as they lost the majority of their prestressing. In addition, one of the wires of the north strand broke near the second peak of the fifth lateral displacement cycle.

Per subsequent inspections, this fracture had occurred at the duct-to-duct-adaptor connection point above the first sliding joint (Figure 4-248). The location of this fracture indicates that the low cyclic fatigue of the tendons under localized bending could lead to their premature fracture. The total posttensioning loss as a result of this test was about 56%, leading to a remaining total PT force of 38 kips in the column.
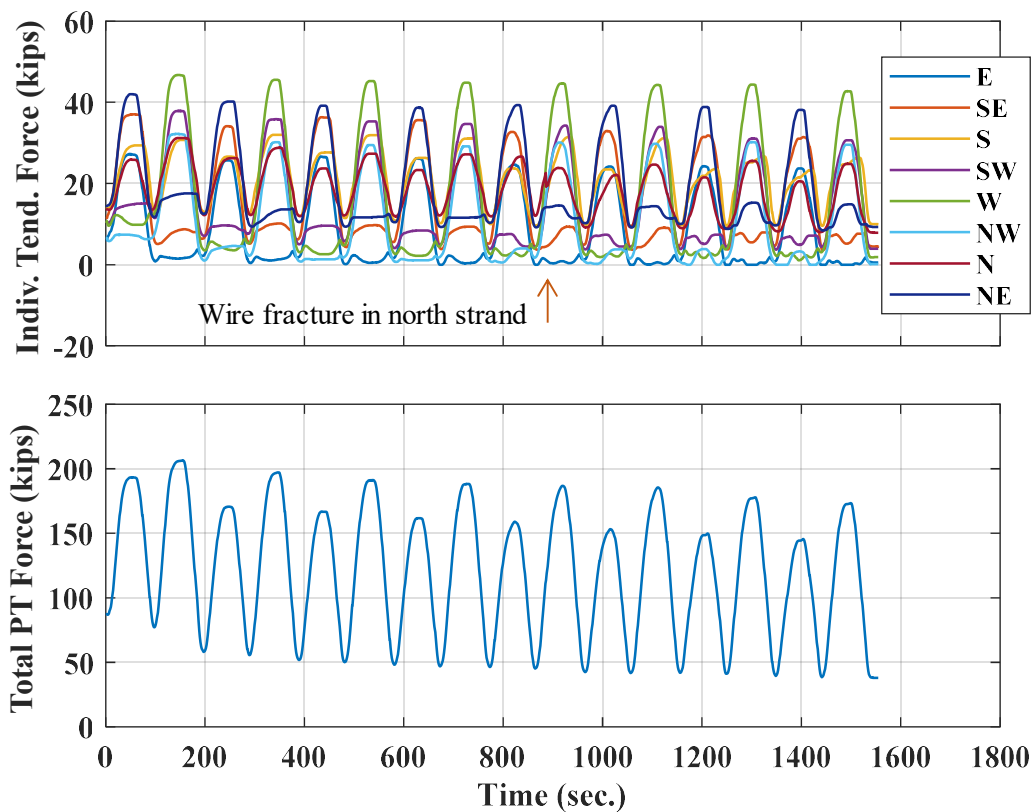
Figure 4-227. Phase II, loading protocol HSR2_TU_CNT_S6_DR_8: time histories of posttensioning forces

During the test under loading protocol HSR2_TU_CNT_S6_DR_8, the concrete spalling further propagated sideways toward the south and north quadrants of the bottom

rocking joint (Figure 4-228). The concentration of damage at the bottom end of the column

prevented the appearance of new cracks and the growth of the older cracks on the surface

of the upper two segments.
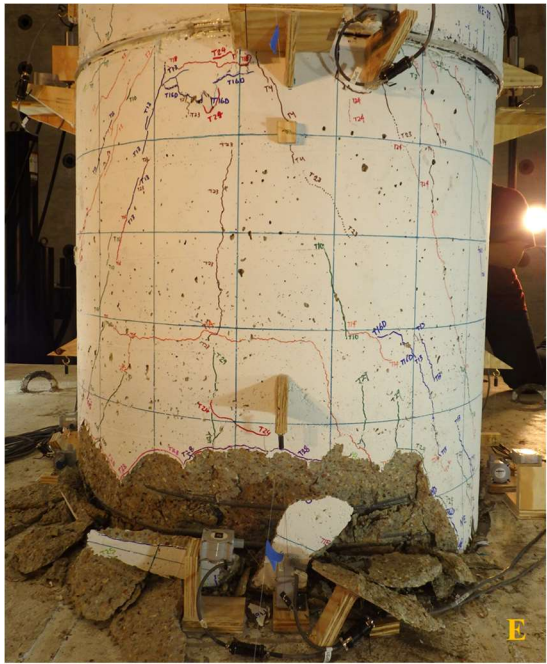
Figure 4-228. Phase II, loading protocol HSR2_TU_CNT_S6_DR_8: concrete damage on bottom segment

4.7.2.5.7. Results from Loading Set 7

As described in Section 4.7.2.4.7, the last Loading Set to test the column specimen in Phase II included only one loading protocol, i.e. HSR2_TU_CNT_S7_DR_10, which imposed two full sinusoidal lateral displacement cycles of 15-in. amplitude (equivalent to 10% drift ratio) and zero twist to the column. A photo from the column's deformed shape at one of the negative displacement peaks is displayed in Figure 4-229.
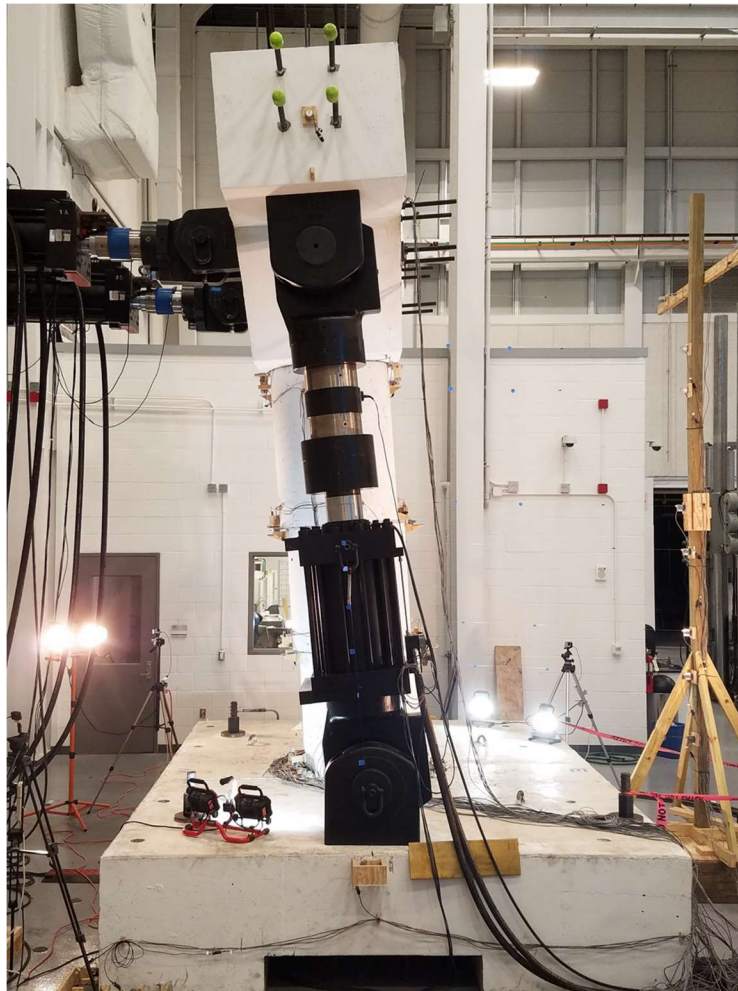
Figure 4-229. Phase II, loading protocol HSR2_TU_CNT_S7_DR_10: column deformation under a drift ratio of 10%

The column's base shear vs. lateral displacement and moment vs. rocking responses achieved under the above loading protocol are shown in Figure 4-230(a) and Figure 4-230(b), respectively. The column's post-sliding stiffness and strength were noticeably lower than those obtained in the previous test (Figure 4-220). Specifically, the peak base shear achieved here was close to 37 kips in both directions, which is on average 16% less than the peak base shear values achieved in the previous test.

The average residual displacement was greater than 5 in., amounting to 3.4% drift ratio (Figure 4-230(a)). According to Figure 4-231, the residual sliding (3.8 in.) constituted up to 75% of the residual displacement, though. That said, the residual displacement caused by the concrete damage in the bottom segment was still less than 1%. This finding is additionally substantiated by the relatively low residual rotation at the bottom rocking joint, i.e. 0.004 rad (Figure 4-230(b)).
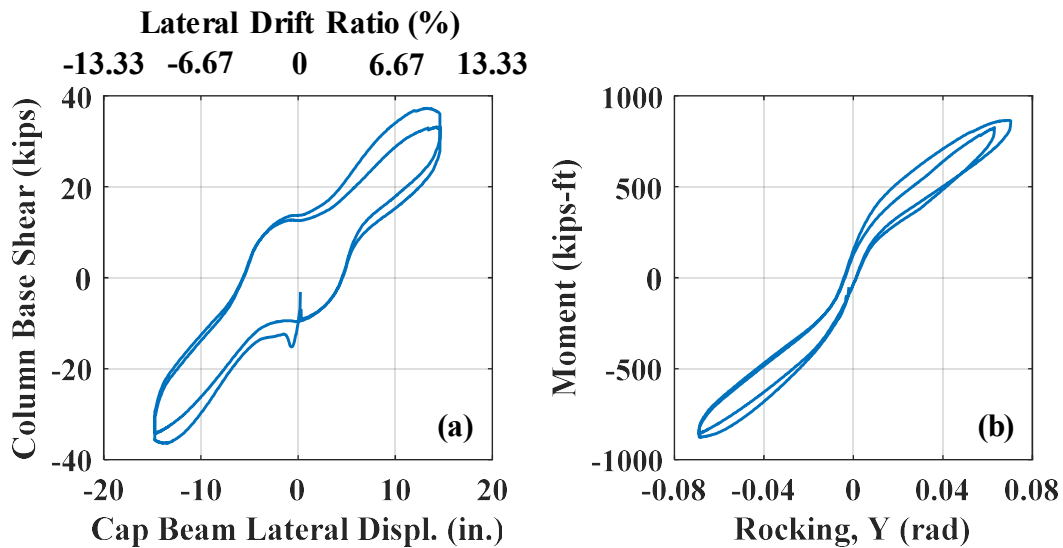
Figure 4-230. Phase II, loading protocol HSR2_TU_CNT_S7_DR_10: (a) base shear vs. lateral displacement; (b) moment vs. rocking at Joint 1
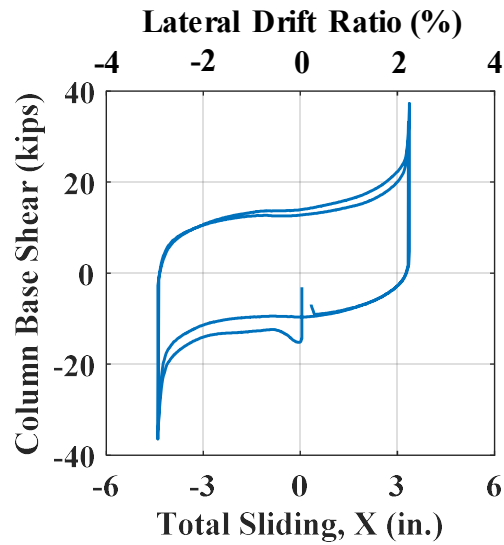
Figure 4-231. Phase II, loading protocol HSR2_TU_CNT_S7_DR_10: base shear vs. total sliding response

According to Figure 4-232, although none of the strands were completely lost and still contributed to the lateral load resistance of the column upon its rocking, most of them (all except the north, south, and northeast strands) had undergone considerable plastic deformation such that they would be nearly slack at zero rocking. The total PT loss during this test was 21%.
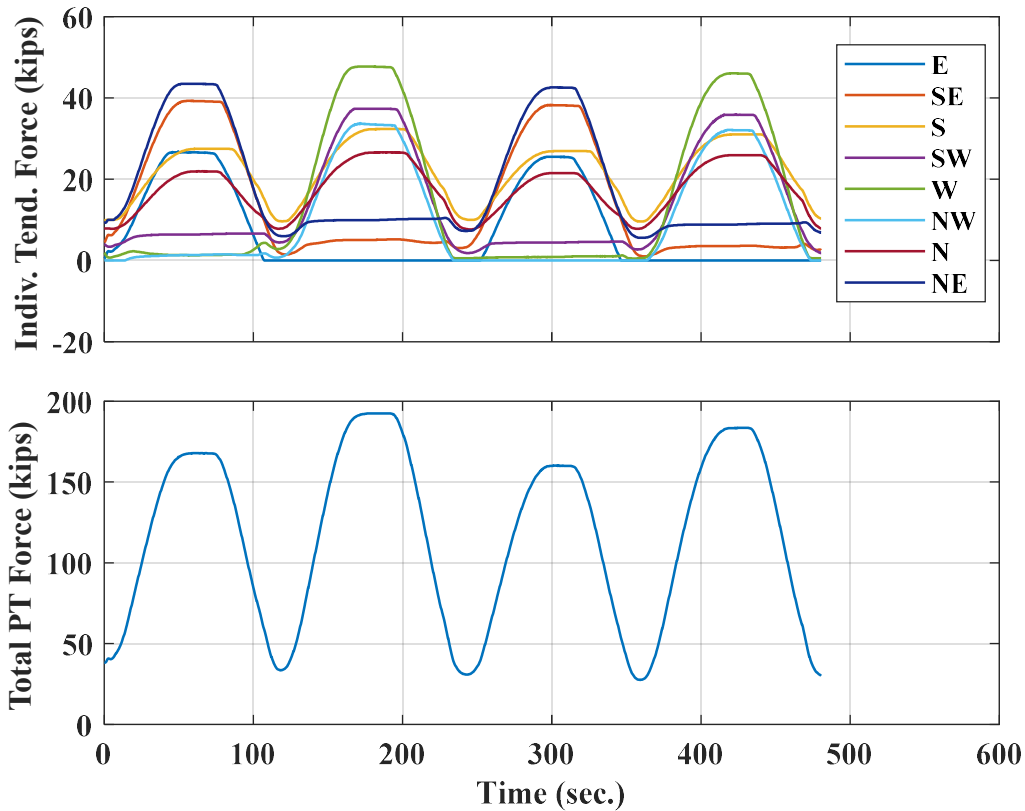
Figure 4-232. Phase II, loading protocol HSR2_TU_CNT_S7_DR_10: time histories of posttensioning forces

The damage in the bottom column segment caused by the last test in Phase II can be seen in Figure 4-233, Figure 4-234, and Figure 4-235. Concrete damage included further concrete spalling around the bottom rocking joint and toward the middle of the bottom segment on the east face, as well as concrete crushing near the compression toes. Some of the longitudinal bars located on the east and west of the cross section had buckled and the 90-degree hooks at the ends of some of the cross ties had slightly bent back. Additionally, because of the concrete crushing, the bottom turns of the spiral at the compression toes had bent up (see Figure 4-240).

411
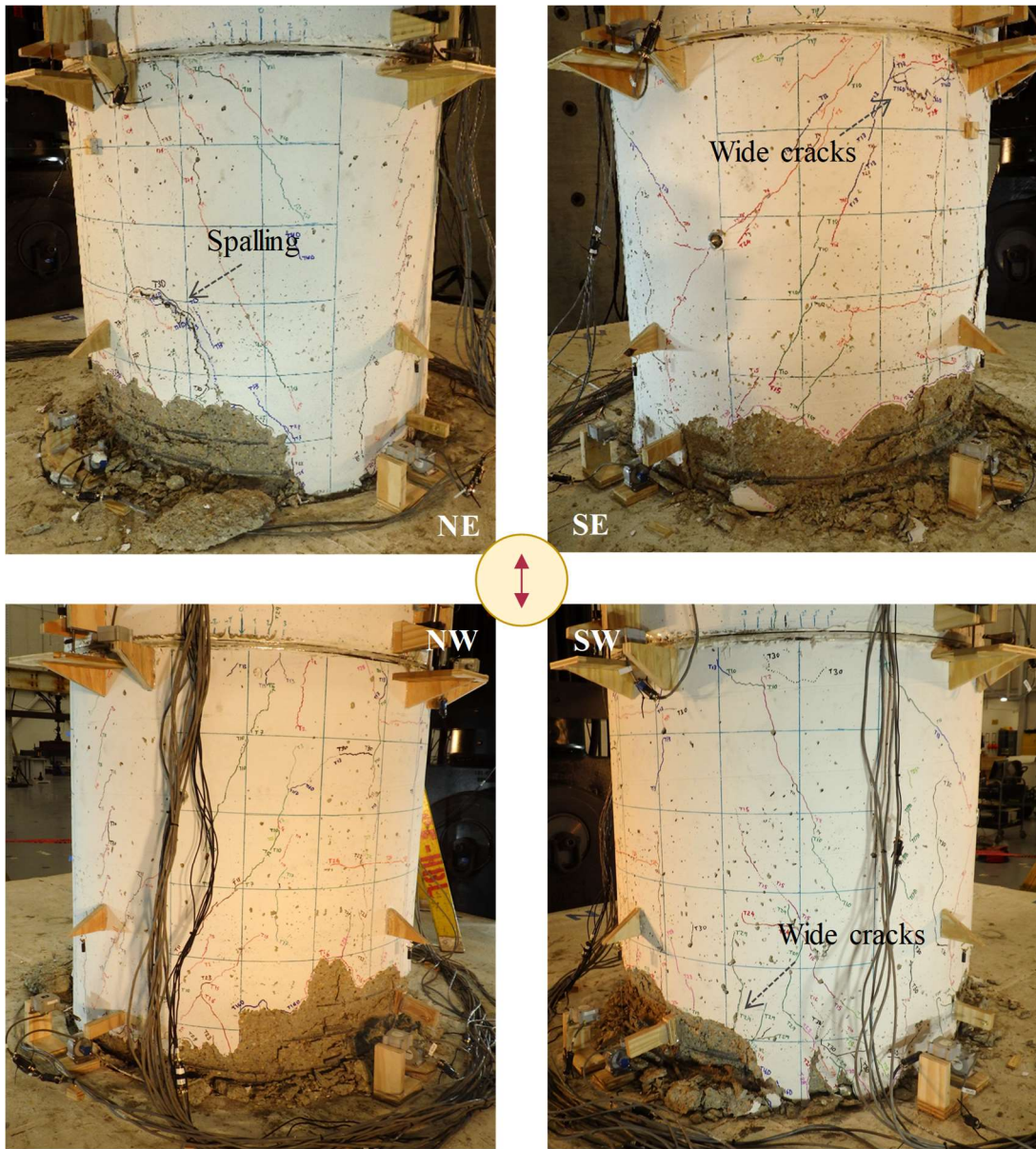
Figure 4-233. Phase II, loading protocol HSR2_TU_CNT_S7_DR_10: damage on bottom column segment
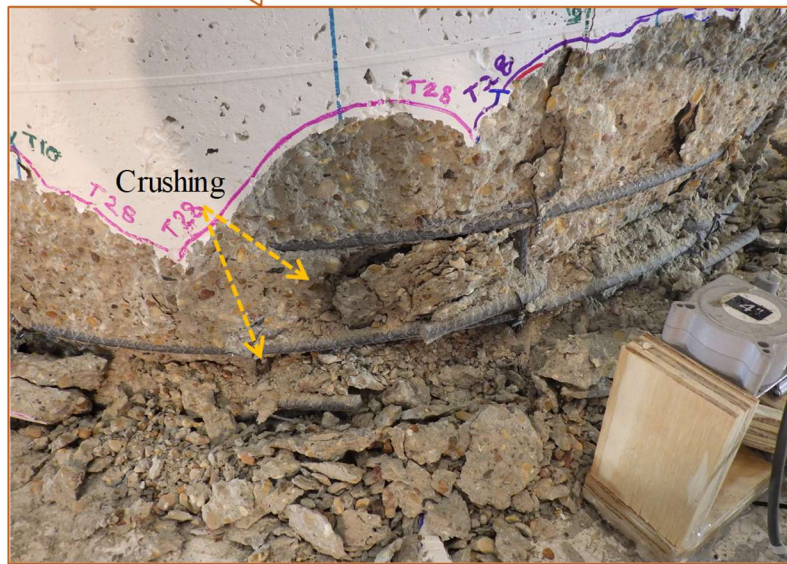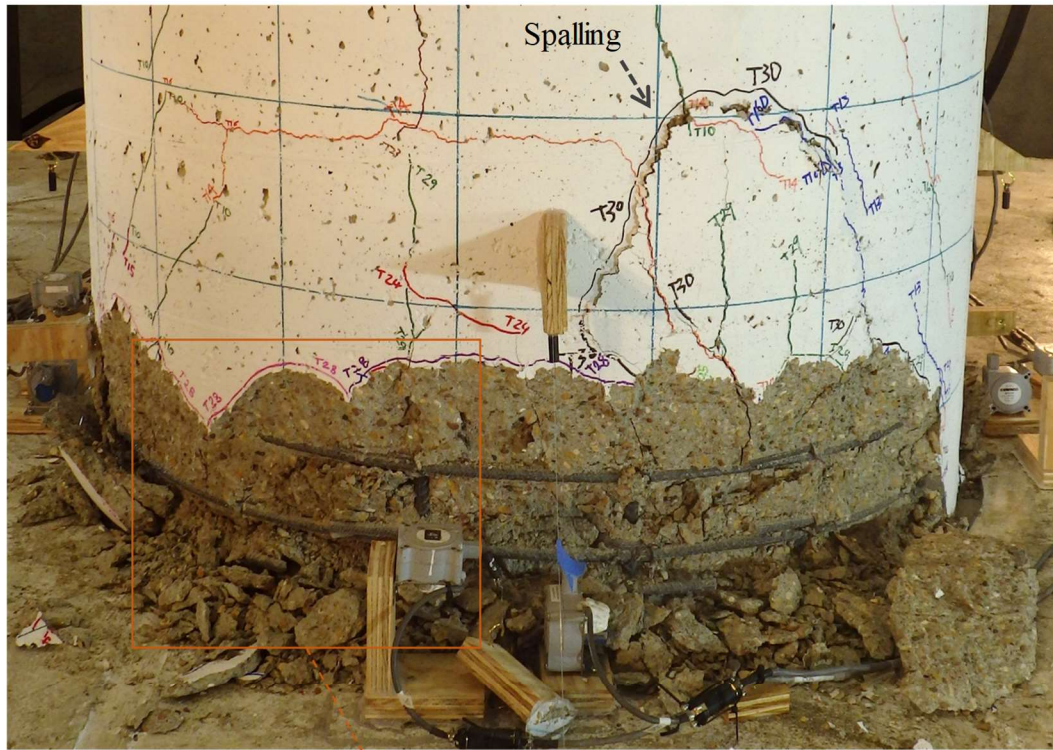
Figure 4-234. Phase II, loading protocol HSR2_TU_CNT_S7_DR_10: concrete damage on east side of bottom segment
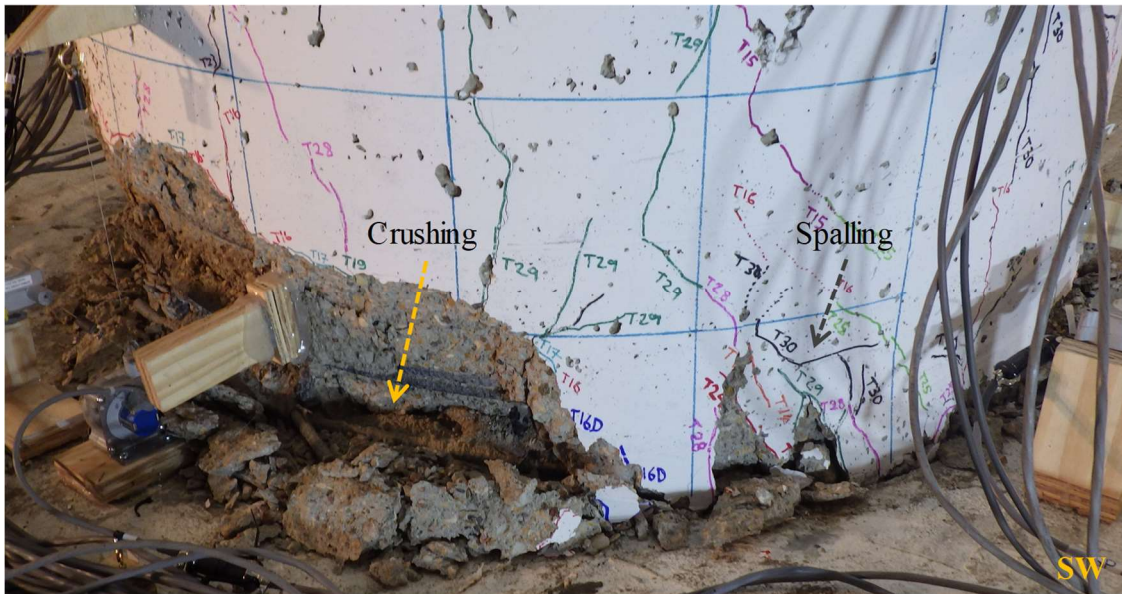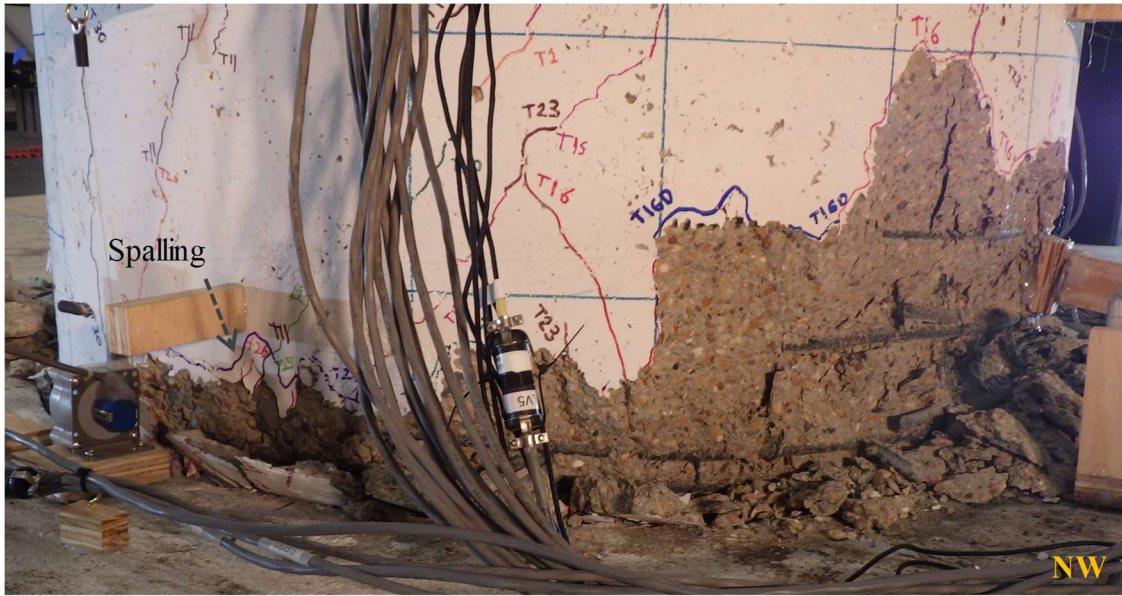
Figure 4-235. Phase II, loading protocol HSR2_TU_CNT_S7_DR_10: concrete damage on west side of bottom segment

To better examine the strength and stiffness deterioration of the column specimen under cyclic load, the HSR column's lateral force-displacement responses obtained during the first two lateral displacement cycles of each of the tests under loading protocols

414

HSR2_TU_CNT_S4_DR_1_3_T2R_0.5,   S4_DR_2_T2R_0.5,   S4_DR_4_T2R_0.5,

S6_DR_6, S6_DR_8, and S7_DR_10 are over-plotted in Figure 4-236. It is observed that

the maximum lateral load resistance of the column (~49 kips) occurred during the first

displacement cycle of 4% peak drift ratio, when only the first sliding joint was active.

Thereafter, the column's lateral load resistance degraded until it reached 76% of the

maximum lateral load resistance, i.e. 37 kips, at a drift ratio of 10%. This degradation

resulted from several intermediate tests as described in the previous section. In addition,

the increase in the residual displacement with the peak drift ratio due to the concrete

damage at the bottom rocking joint, the ducts damage due to the tendons bearing reactions,

and posttensioning loss is evident in the hysteretic loops.
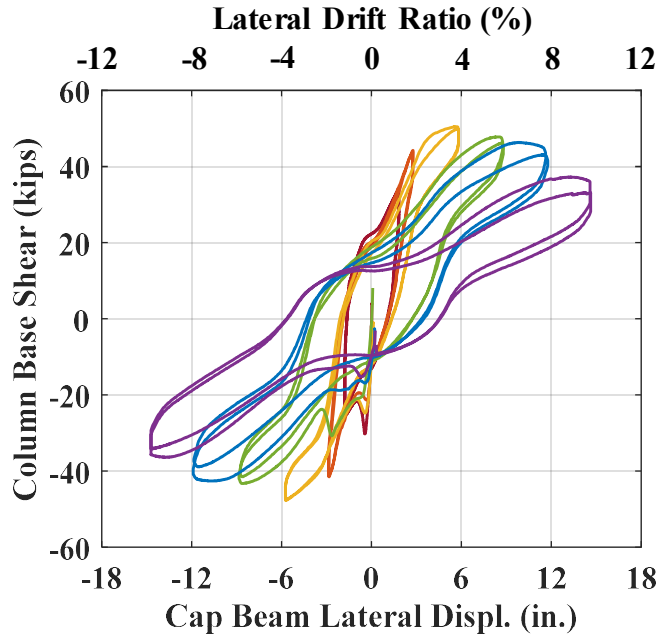
Figure 4-236. Phase II: aggregated base shear vs. lateral displacement response

4.7.2.6. Final Damage Inspection

4.7.2.6.1. Overall Column Damage

After the last test was done, the instrumentation was removed and the spalled concrete and other debris were removed. Photos taken from the east and west sides of the entire column are shown in Figure 4-237. As seen, the column's integrity was maintained by the remaining prestressing force and the major damage was confined to the lower half of the bottom column segment.

Figure 4-237. Phase II, final damage inspection: east and west sides of column

According to Figure 4-238, almost the entire edge of the bottom column segment in contact with foundation was significantly damaged. Particularly, considerable amounts of concrete core were lost near the east and west segment toes, leaving up to 2 in. deep voids in the column core (Figure 4-239). The longitudinal bars and the spiral reinforcement had also been noticeably engaged during the rocking motion of the column, leading to the buckling of some of the longitudinal bars and bending of the spiral reinforcement (Figure 4-240).

Figure 4-238. Phase II, final damage inspection: concrete damage around bottom rocking joint
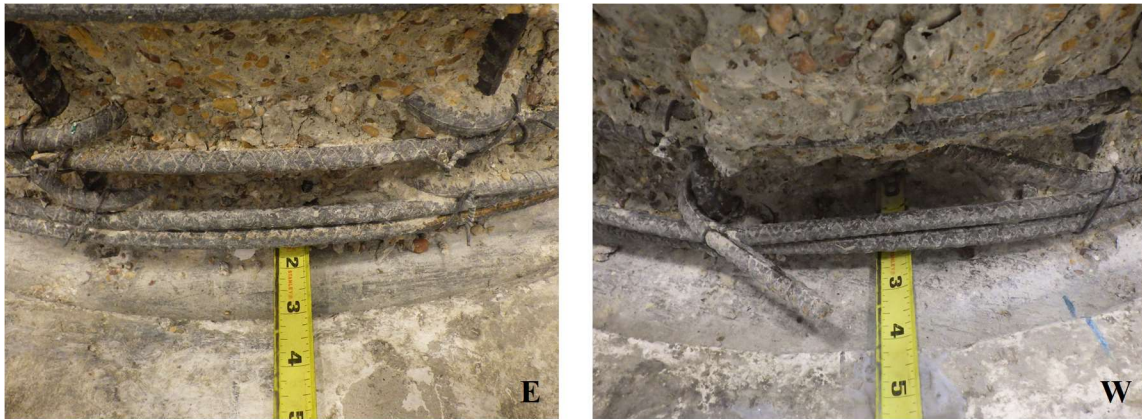
Figure 4-239. Phase II, final damage inspection: core concrete loss at bottom segment toes
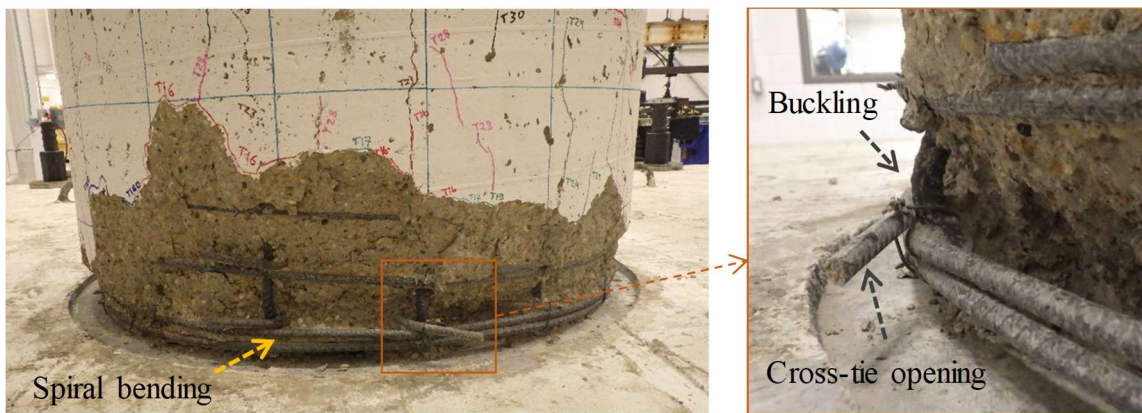
Figure 4-240. Phase II, final damage inspection: rebar buckling, spiral bending, and cross-tie opening on west side of bottom rocking joint

4.7.2.6.2. Column Segments

The bottom column segment had sustained the majority of damage, particularly near the bottom rocking joint, where the maximum compressive stresses occurred. As seen in Figure 4-241, the concrete damage had spread to the inside cover of the segment. Specifically, on the east and west sides (i.e. farther from the neutral axis), considerable concrete spalling had occurred.

418
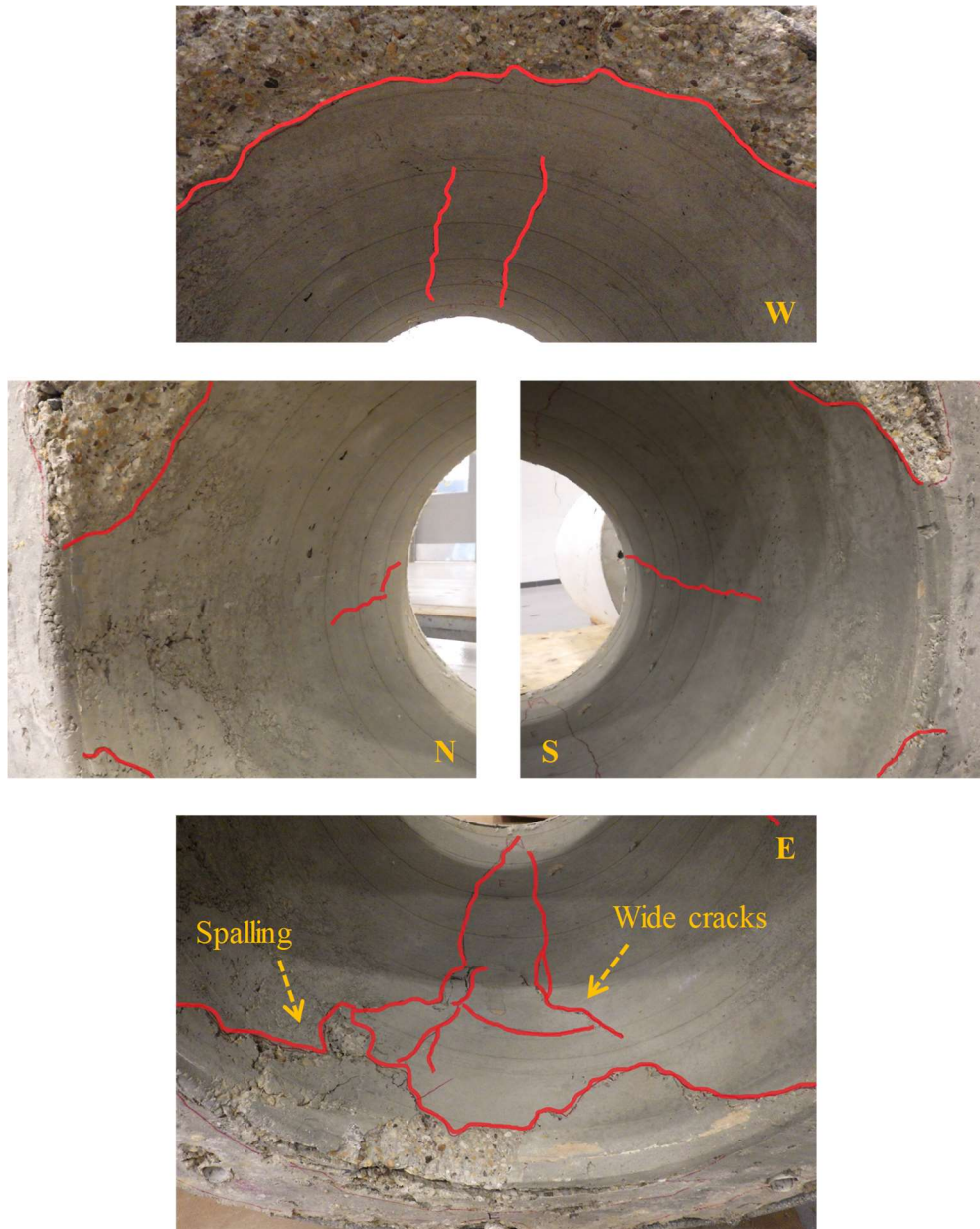
Figure 4-241. Phase II, final damage inspection: cracks inside of bottom segment

At the bottom surface of the same segment, the end turns of the spiral along the entire outside perimeter of the cross section had been completely exposed (Figure 4-243). The buckled longitudinal bars on the west side of the rocking joint are also seen in Figure 4-242. As explained in Section 4.6.1.4, the lower segment had been repaired after the concrete casting, which could have contributed to the significant damage observed at the rocking joint.
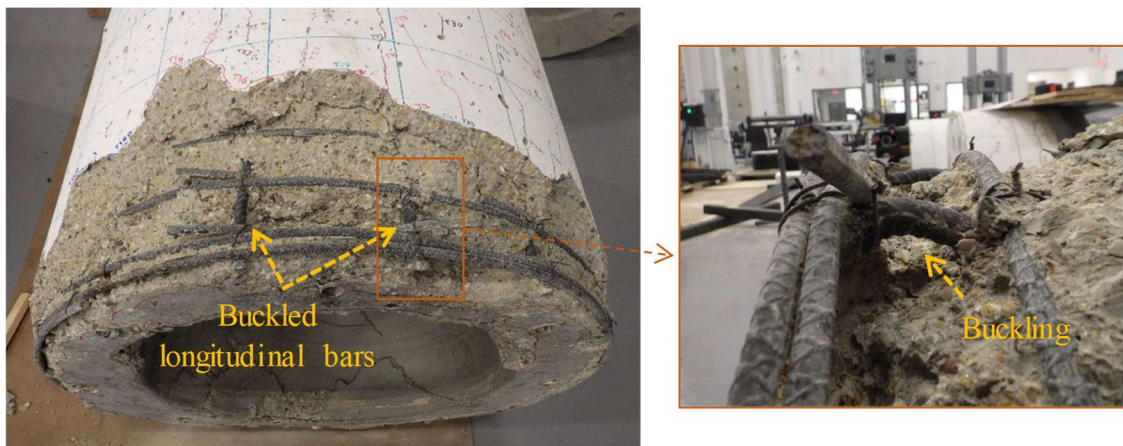
Figure 4-242. Phase II, final damage inspection: longitudinal rebar buckling on west side of bottom segment

Figure 4-243. Phase II, final damage inspection: bottom surface of bottom segment

As for the bottom segment's top sliding surface (Figure 4-244), it had suffered from limited wearing, resulted from the excessive number of sliding cycles that the first sliding joint had experienced. In addition, indentations were evident on the edges of the ducts and duct adaptors, which had been caused by the large bearing reactions of the tendons in the direction of lateral loading. However, the damage was limited to the PVC pipes and the PTFE adjacent to the duct perimeter.
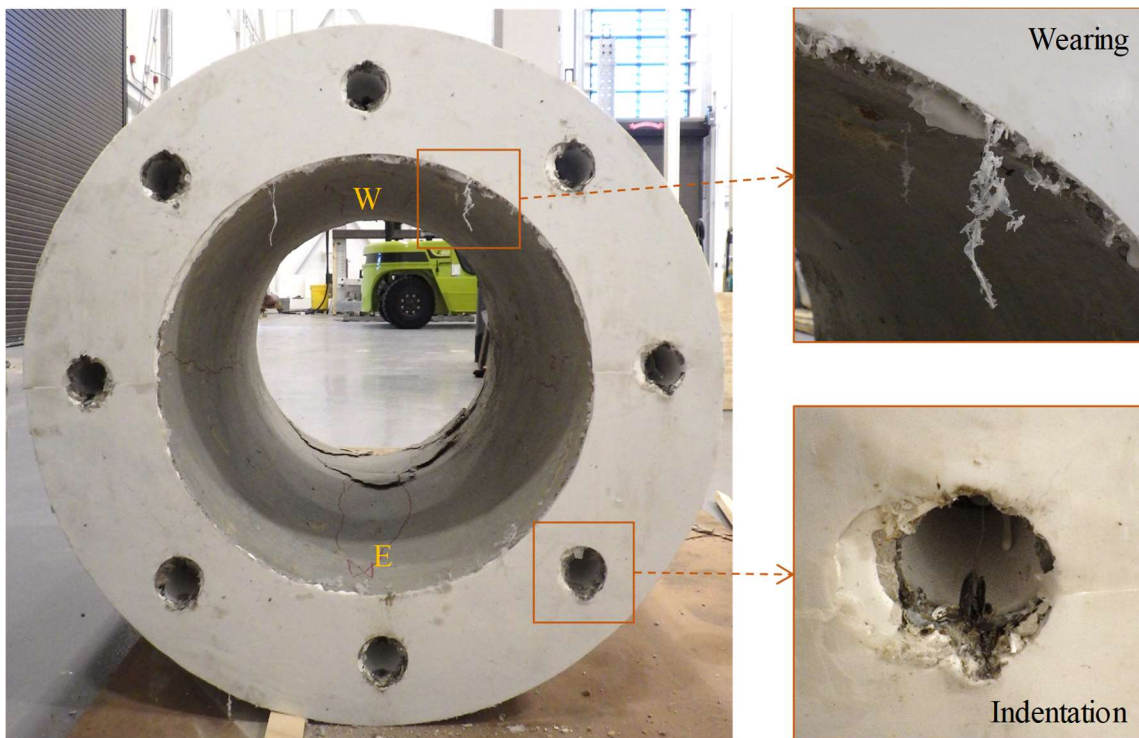
Figure 4-244. Phase II, final damage inspection: top surface of bottom segment

The middle segment was expectedly much less damaged than the bottom segment and no sign of wide cracks or concrete spalling could be found on its surface. Some diagonal hairline cracks had appeared on the south and north surfaces inside the segment (Figure

4-245). Even though they were only on those two sides, these cracks may be attributed to the torsion-induced shear strains.
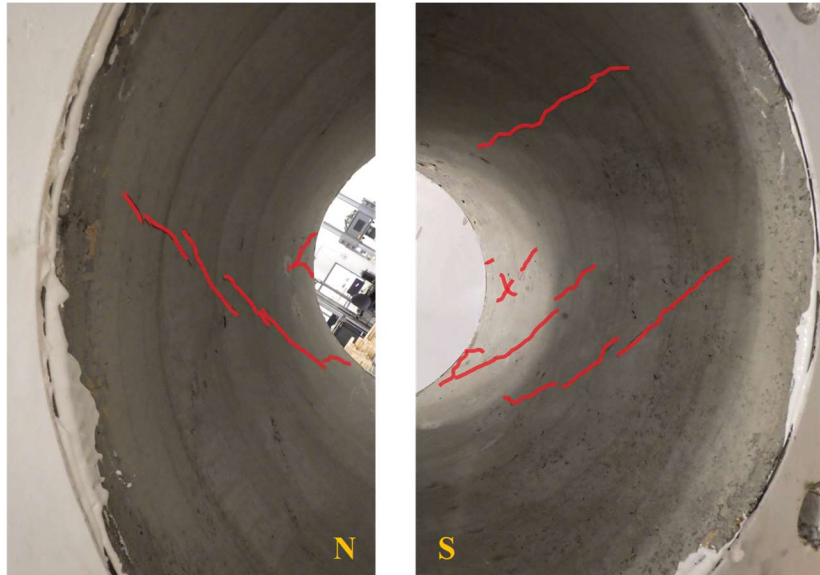
Figure 4-245. Phase II, final damage inspection: cracks inside of middle segment

Similarly to the top surface of the bottom segment, PVC pipe indentation and PTFE wearing were the only visible damage observed on the two end surfaces of the middle segment (Figure 4-246). Here also, the indentations had been created only at the east and west quadrants of the duct adaptors, i.e. in the direction of lateral loading.

Inside the top segment, only a couple of short vertical hairline cracks had appeared on the lower parts of the south and north surfaces. Photos from the end surfaces of the top segment are displayed in Figure 4-247. The bottom (sliding) surface did not show any sign of wearing, but bearing-induced indentations could be seen on the duct adaptor edges.
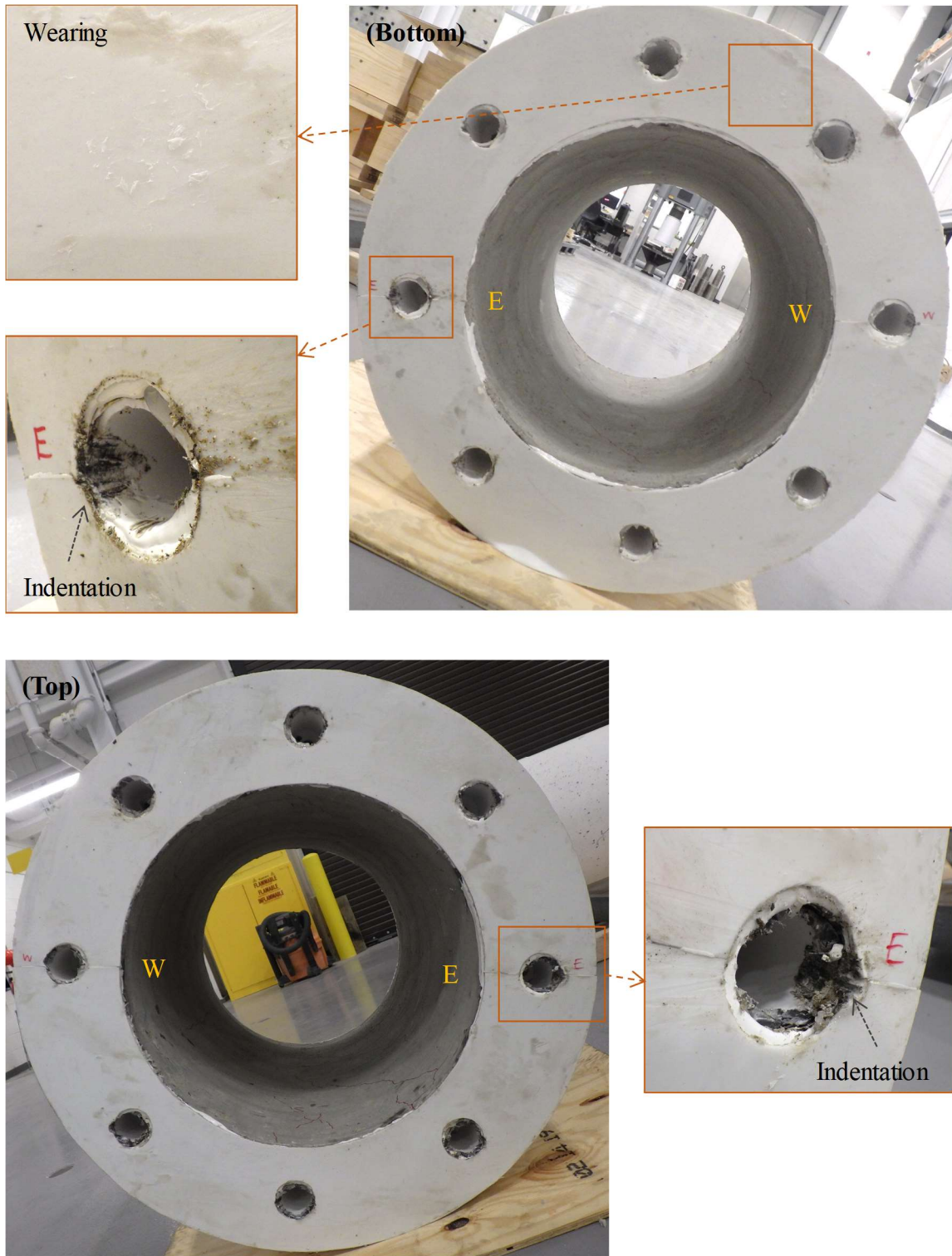
Figure 4-246. Phase II, final damage inspection: end surfaces of middle segment
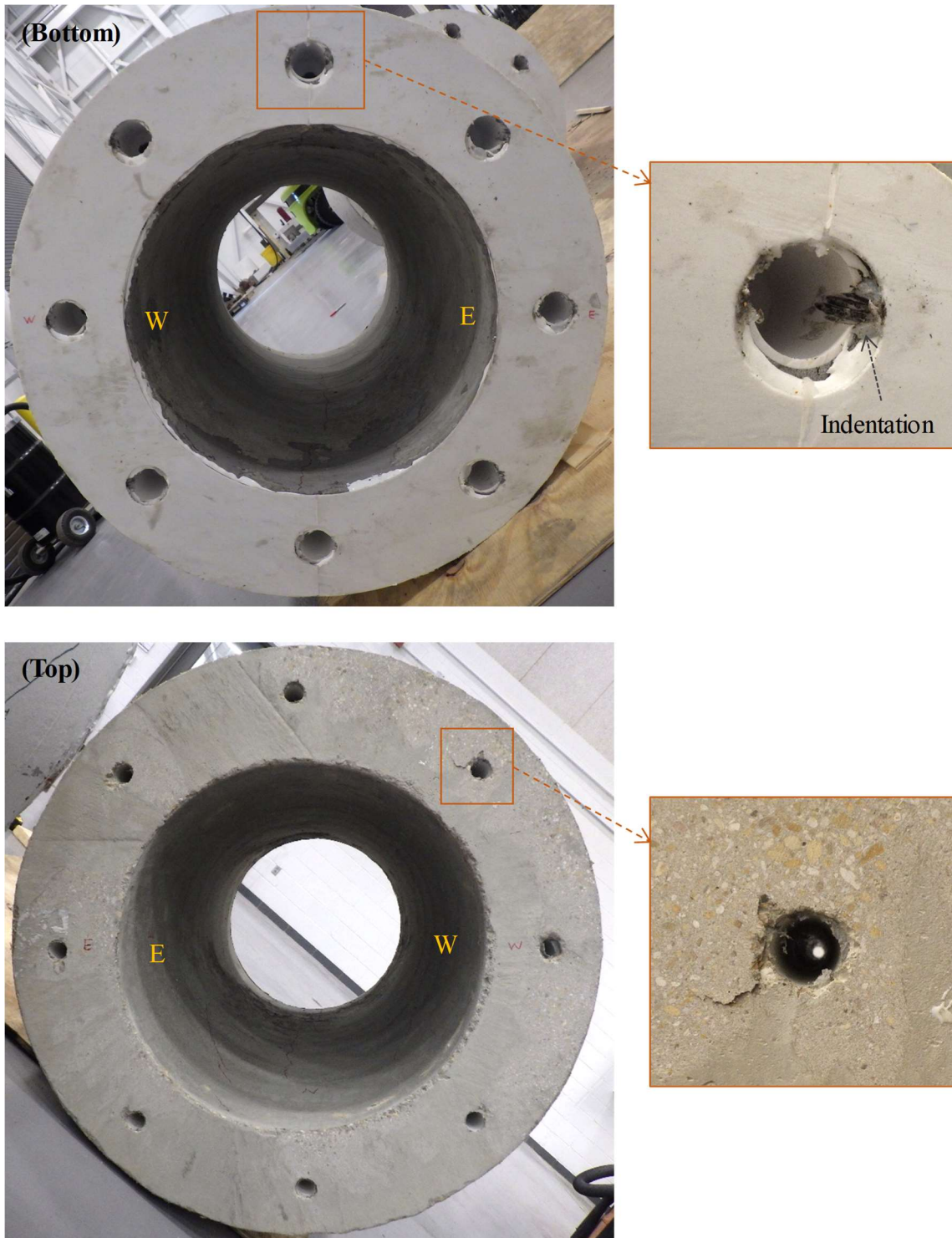
Figure 4-247. Phase II, final damage inspection: end surfaces of top segment

4.7.2.6.3. Posttensioning Tendons

Photos taken from the posttensioning strands after their removal from the column ducts are displayed in Figure 4-248. As was the case for the strands used in the column specimen tested in Phase I (see Figure 4-138), the strands had locally bent and deformed at the locations where they would contact the duct edges (below and above the sliding joints). The low-cycle fatigue of the north strand above the first sliding joint had led to the fracture of one of its wires. There was, however, no sign of damage at the heights where the sliding joint interfaces were located. This finding proves that no shear keys are necessary to prevent potential shearing of the strands, in accordance with the intended design objectives described in Chapter 3.
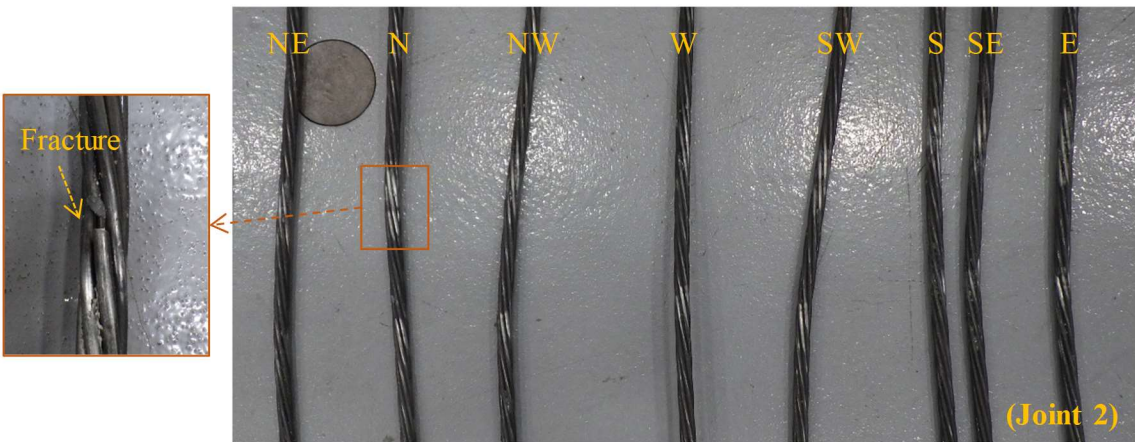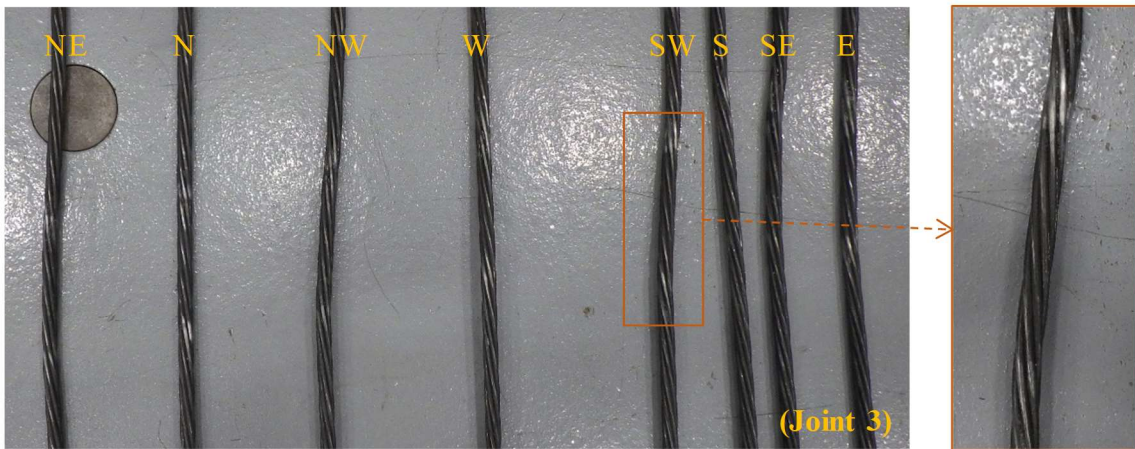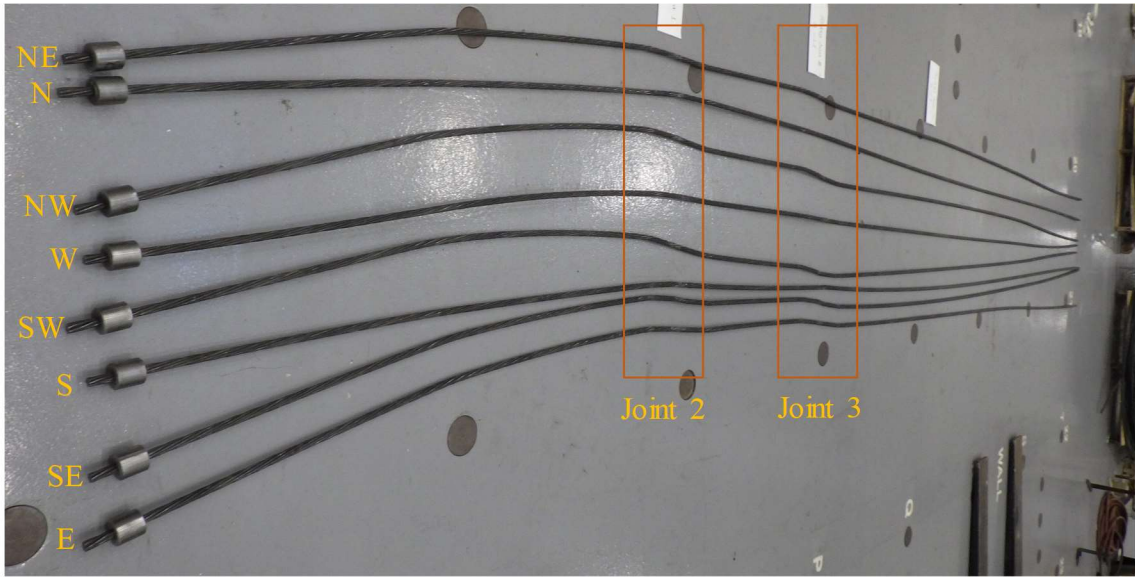
Figure 4-248. Phase II, final damage inspection: posttensioning tendons

4.7.3. Phase III: Fixed-Fixed Column under Uniaxial Lateral Loading

4.7.3.1. Test Setup

The test setup designed for Phase III was Setup B (Figure 4-13), wherein the two 590-kip actuators and one 220-kip actuator were employed to apply the vertical loads and lateral displacement, respectively. In order to provide a fixed constraint at the top end of the column, the loading beam had to be prevented from rotating in the plane of loading (Figure 4-250). This was achieved by setting the displacement command of one of the 590-kip actuators (590A) equal to the displacement output of the other 590-kip actuator (590B). At the same time, the sum of the forces applied by the two vertical actuators was set equal the desired total external vertical load on the column. This condition was achieved in the controller by enforcing an equality condition between a variable defined as the sum of the forces of the two vertical actuators and the desired total vertical load. The above control algorithm required the actuators 590A and 590B to be in displacement- and force-controlled modes, respectively, while the time history of the sum of their forces was the only input given to the controller by the operator.

The schematic 2D views of the test setup are shown in Figure 4-249, Figure 4-251, and Figure 4-250. The clear distance between the reaction wall and the loading beam was 13 ft-6 in. so that half of the maximum stroke of the horizontal actuator (i.e. 30 in.) could be used in each direction (Figure 4-249). The height of the horizontal loading point from the foundation surface was 14 ft, i.e. 1 ft-6 in. above the equivalent height of the superstructure centroid (Figure 4-250).

428

Figure 4-249. Setup B: plan view

Figure 4-250. Setup B: side view
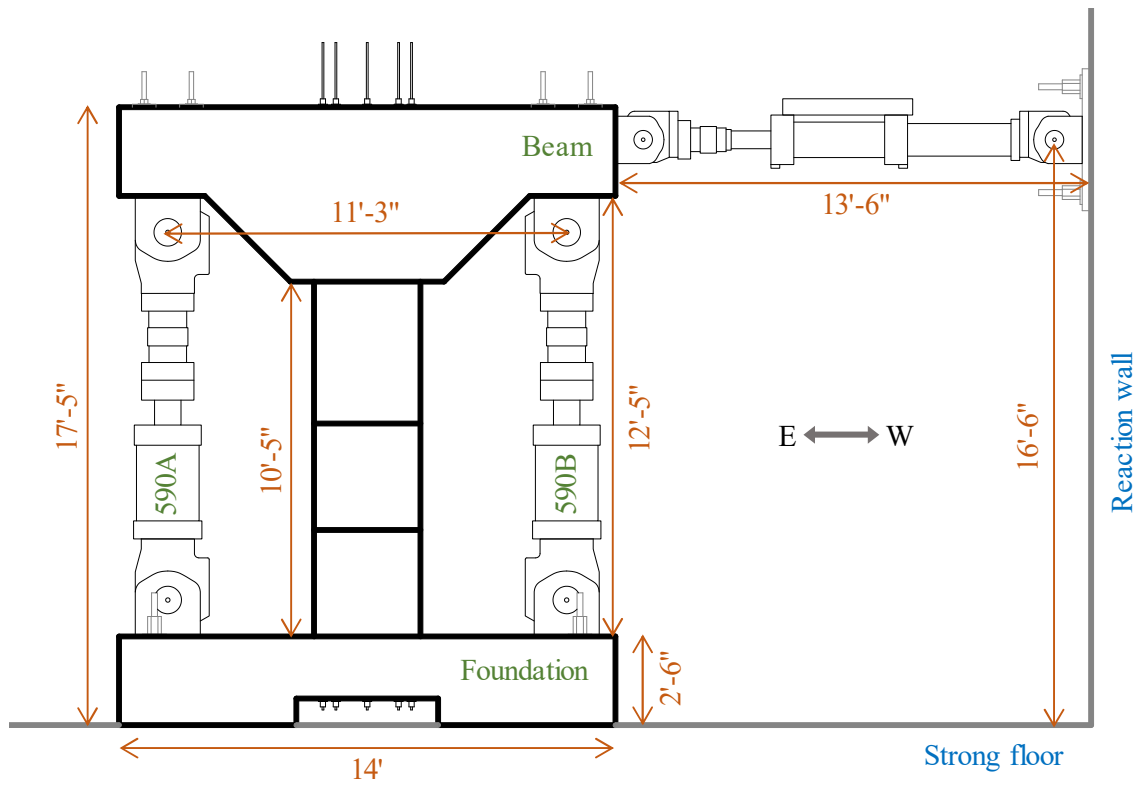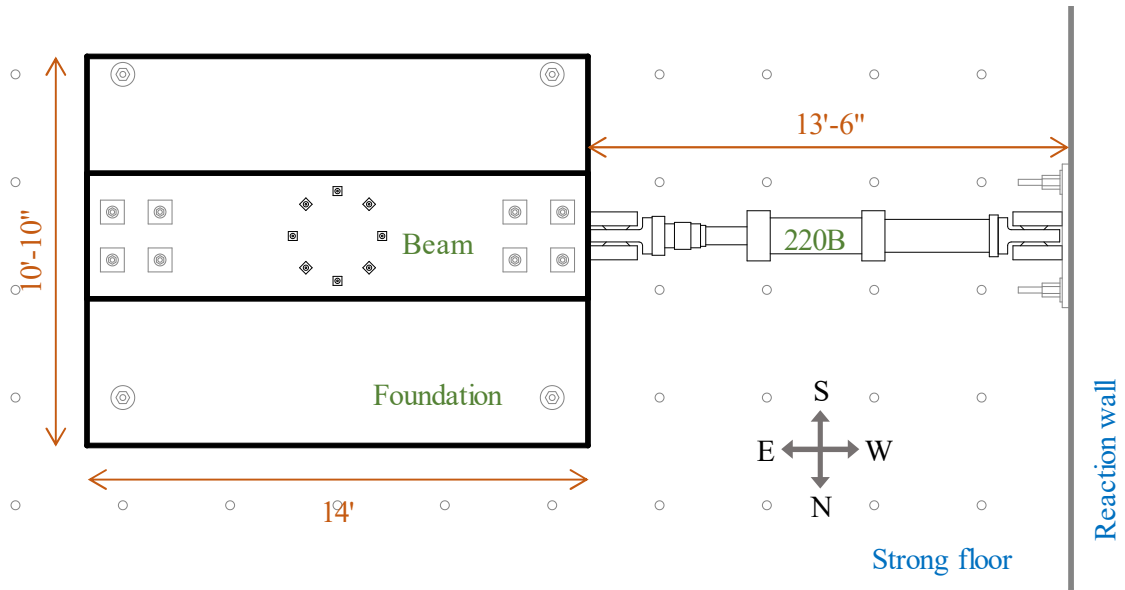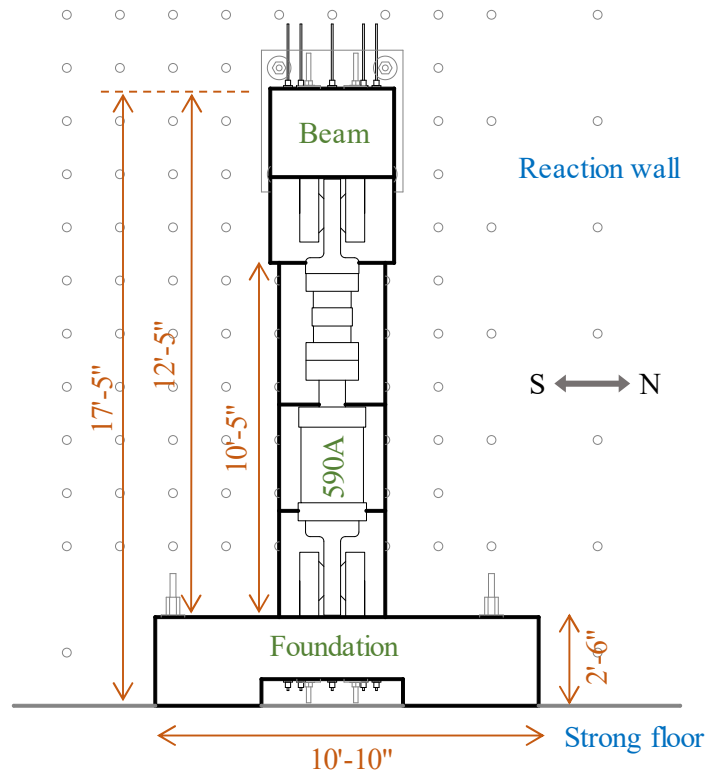
Figure 4-251. Setup B: front view

The assembly process of Setup B nearly resembled the process for Setup A explained in Section 4.7.1.1. The vertical actuators, however, needed to rotate 90 degrees about their axis with respect to the loading beam so that their swivels could accommodate large rotations in the plane of motion (Figure 4-250). The photos in Figure 4-252 show the way that the loading beam with the new orientation of the vertical actuators was lifted from the floor using two cranes. In addition, to avoid unwanted sliding at the sliding joints while the loading beam was placed on the column specimen, the segments were held together by ratchet straps, as seen in Figure 4-253.
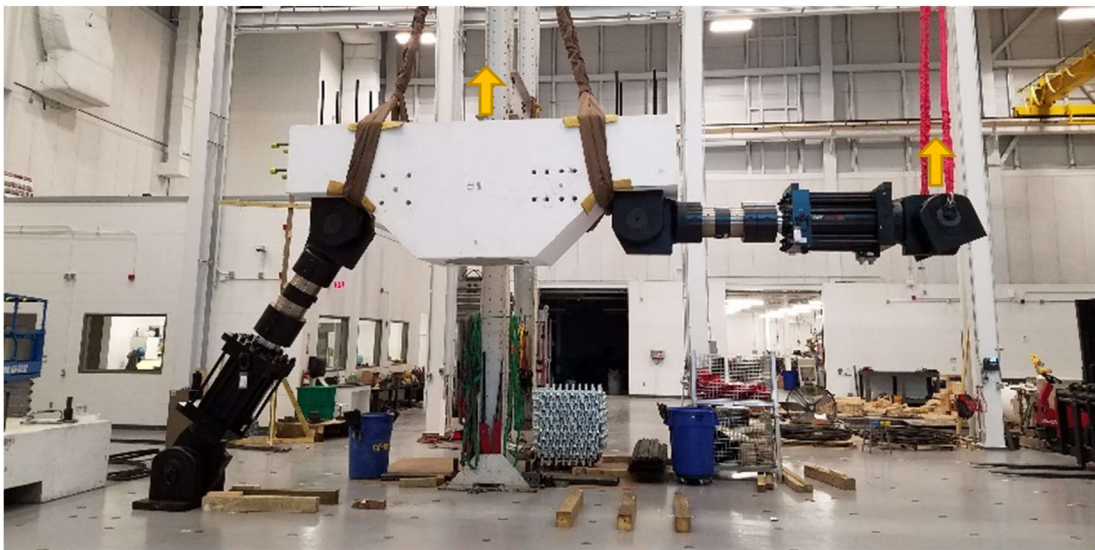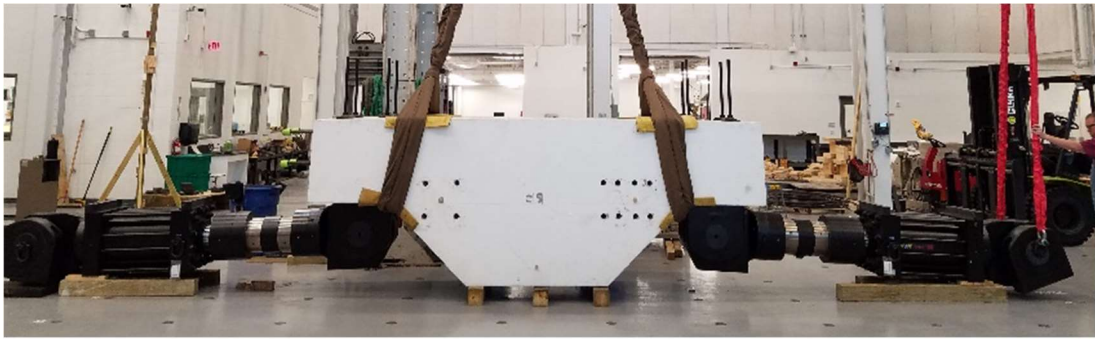
Figure 4-252. Lifting of loading beam before its placement on column

Figure 4-253. Prevention of accidental sliding at sliding joints using ratchet straps

4.7.3.2. Instrumentation

The instrumentation for Setup B resembled that of Setup A in Phase II (Section 4.7.1.2) with small changes. Instead of using one post, two posts were used to enable measuring both in-plane and out-of-plane displacements/rotations of the loading beam (Figure 4-254). Also, in this setup, due to its geometry, no string potentiometers could be used/fitted to measure the displacements of the column segments in loading direction (X direction per Figure 4-254). The total number of the sensors used in this setup was 74 (Table 4-33).

Table 4-33. Type and number of sensors used in Phase III

Type	String Potentiometer	LVDT	Tendon Load Cell
Number	37	11	16
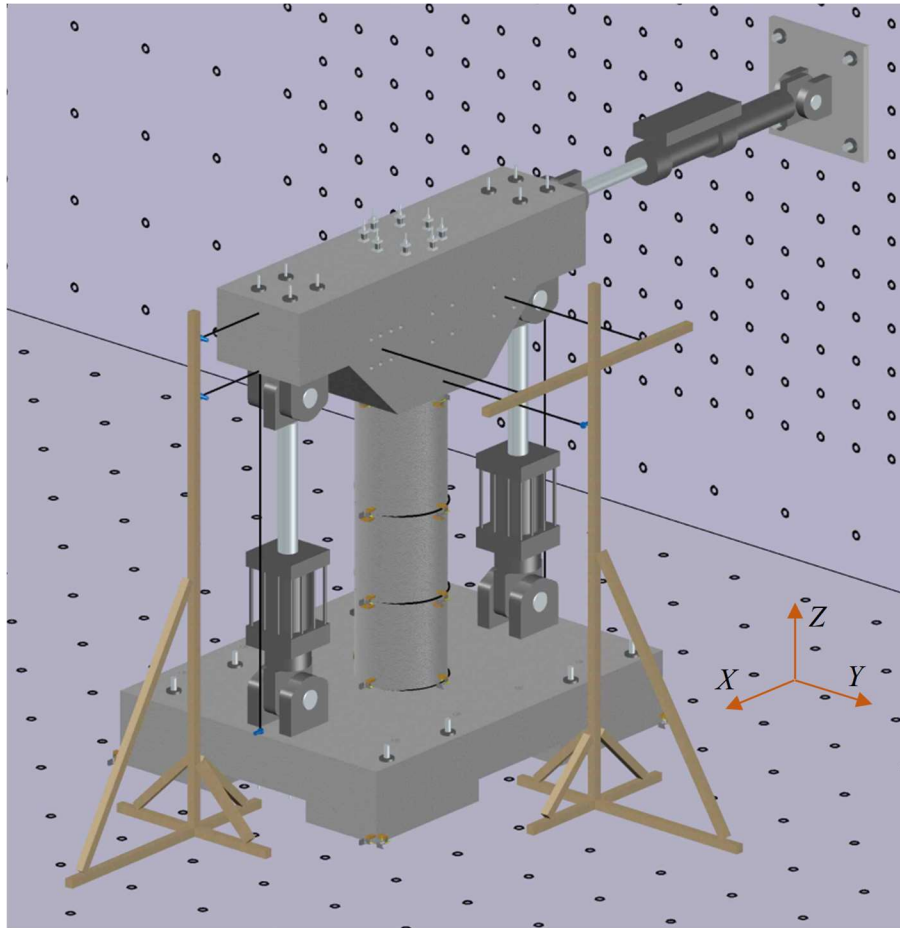
Figure 4-254. General arrangement of sensors in Phase III

The sensors used to measure the relative displacements of the column segments at the joints were similar to those in Phase I (Table 4-34). The lists of the sensors employed here to measure the displacements of the loading beam and foundation block are presented in Table 4-35 and Table 4-37, respectively. The tendon load cells are also as listed in Table 4-36. A photo from the completed test setup for Phase III is displayed in Figure 4-255.

Table 4-34. Sensors measuring joint sliding/rotation in Phase III

ID	Type	Stroke (in)	Location	Measurement
SP-J0-N-H	String pot.	4	Bottom joint - north	Sliding
SP-J0-S-H	String pot.	4	Bottom joint – south	Sliding
SP-J0-E-H	String pot.	4	Bottom joint – east	Sliding
SP-J0-W-H	String pot.	4	Bottom joint – west	Sliding
SP-J0-N-V	String pot.	12	Bottom joint – north	Separation
SP-J0-S-V	String pot.	12	Bottom joint – south	Separation
SP-J0-E-V	String pot.	12	Bottom joint – east	Separation
SP-J0-W-V	String pot.	12	Bottom joint – west	Separation
SP-J1-N-H	String pot.	4	Sliding joint 1 – north	Sliding
SP-J1-S-H	String pot.	4	Sliding joint 1 – south	Sliding
SP-J1-E-H	String pot.	4	Sliding joint 1 – east	Sliding
SP-J1-W-H	String pot.	4	Sliding joint 1 – west	Sliding
LV-J1-N-V	LVDT	1	Sliding joint 1 – north	Separation
LV-J1-S-V	LVDT	1	Sliding joint 1 – south	Separation
LV-J1-E-V	LVDT	1	Sliding joint 1 – east	Separation
LV-J1-W-V	LVDT	1	Sliding joint 1 – west	Separation
SP-J2-N-H	String pot.	4	Sliding joint 2 – north	Sliding
SP-J2-S-H	String pot.	4	Sliding joint 2 – south	Sliding
SP-J2-E-H	String pot.	4	Sliding joint 2 – east	Sliding
SP-J2-W-H	String pot.	4	Sliding joint 2 – west	Sliding
LV-J2-N-V	LVDT	1	Sliding joint 2 – north	Separation
LV-J2-S-V	LVDT	1	Sliding joint 2 – south	Separation
LV-J2-E-V	LVDT	1	Sliding joint 2 – east	Separation
LV-J2-W-V	LVDT	1	Sliding joint 2 – west	Separation
SP-J3-N-H	String pot.	4	Top joint - north	Sliding
SP-J3-S-H	String pot.	4	Top joint – south	Sliding
SP-J3-E-H	String pot.	4	Top joint – east	Sliding
SP-J3-W-H	String pot.	4	Top joint – west	Sliding
SP-J3-E-V	String pot.	4	Top joint – east	Separation
SP-J3-W-V	String pot.	4	Top joint – west	Separation

Table 4-35. String pots measuring loading beam displacements in Phase III

ID	Stroke (in)	Location	Measurement
SP-CP-F-T	50	East face – 14.5 ft above foundation surface	X displacement
SP-CP-F-B	50	East face – 12.5 ft above foundation surface	X displacement
SP-CP-S-C	4	North face – center, 10.5 ft above foundation surface	Y displacement
SP-CP-S-L	12	North face – 3 ft to the left of center, 12.5 ft above foundation surface	Y displacement
SP-CP-S-R	12	North face – 3 ft to the right of center, 12.5 ft above foundation surface	Y displacement
SP-CP-B-L	4	East side	Z displacement
SP-CP-B-R	4	West side	Z displacement

Table 4-36. Tendon load cells in Phase III

ID	Location	Tendon Map
LC-TN-C-1	Loading beam – E	
LC-TN-C-2	Loading beam – SE	
LC-TN-C-3	Loading beam – S	
LC-TN-C-4	Loading beam – SW	
LC-TN-C-5	Loading beam – W	
LC-TN-C-6	Loading beam – NW	
LC-TN-C-7	Loading beam – N	
LC-TN-C-8	Loading beam – NE	
LC-TN-F-1	Foundation – E	
LC-TN-F-2	Foundation – SE	
LC-TN-F-3	Foundation – S	
LC-TN-F-4	Foundation – SW	
LC-TN-F-5	Foundation – W	
LC-TN-F-6	Foundation – NW	
LC-TN-F-7	Foundation – N	
LC-TN-F-8	Foundation – NE	

Table 4-37. Sensors measuring foundation displacements in Phase III

ID	Type	Stroke (in)	Location	Measurement
SP-FN-N-L-H	String pot.	4	NE corner	X sliding
SP-FN-N-R-H	String pot.	4	NW corner	X sliding
SP-FN-S-L-H	String pot.	4	SE corner	X sliding
SP-FN-S-R-H	String pot.	4	SW corner	X sliding
SP-FN-W-R-H	String pot.	4	NW corner	Y sliding
LV-FN-W-L-V	LVDT	0.5	SW corner	Separation
LV-FN-W-R-V	LVDT	0.5	NW corner	Separation
SP-FN-E-L-H	String pot.	4	SE corner	Y sliding
LV-FN-E-L-V	LVDT	0.5	SE corner	Separation

Figure 4-255. Completed test setup for Phase III

4.7.3.3. Data Acquisition and Processing

The sensors' data was acquired and cleaned (from noise) similarly to Phase I (see Section 4.7.1.3), while the maximum sampling rate was 512 samples per second. Post-processing methods similar to those discussed for the previous Phases (Sections 4.7.1.3 and 4.7.2.3) were used to obtain meaningful response parameters out of the raw data obtained from the sensors. The main response parameters of interest in Phase III included:

- $\Delta_{bm,X}$: The lateral displacement (i.e. in X direction per Figure 4-254) of the loading point on the loading beam (equivalent to the superstructure centroid in the prototype bridge) relative to the foundation block's top surface;

- $u_{sl,X,j}$: The jth joint's sliding in the lateral direction (i.e. in X direction per Figure 4-254), with $j = 1, 2, 3$, and 4 from bottom to top;

- $\theta_{r,Y,j}$: The jth joint's rocking (rotation) around Y-axis (Figure 4-254);

- $V_{col,X}$: The column's base shear in the transverse direction (i.e. in X direction per Figure 4-254);

- $M_{jnt,Y,j}$: The jth joint's moment about Y-axis (Figure 4-254);

- N_{col}: The axial force on the column (i.e. excluding the column weight);

- N_{PT}: The total posttensioning force in the tendons.

The joint response parameters (i.e. sliding and rocking components) were obtained from Eqs. (4-2) thru (4-6). However, according to Figure 4-256, the column's forces were computed according to the equations below:

$$\begin{cases} V_{col,X} \simeq -F_{act,h} + \left(F_{act,v1} + F_{act,v2}\right)\theta_{act,Y} \\ M_{col,Y} \simeq -F_{act,h}\left(h_{bm} + d_{act,h}\right) + W_{act,h}\left(b_{act,h} - \Delta_{bm,X}\right) \\ \qquad - F_{act,v1}\left(b_{act,v} + \Delta_{bm,X}\right) + F_{act,v2}\left(b_{act,v} - \Delta_{bm,X}\right) \\ \qquad + \left(F_{act,v1} + F_{act,v2}\right)\theta_{act,Y}\left(h_{bm} - d_{act,v}\right) - W_{bm}\Delta_{bm,X} + M_{PT} \\ N_{col} \simeq W_{bm} + 2W_{act,v} + W_{act,h} + F_{act,v1} + F_{act,v2} + N_{PT} \end{cases} \qquad (4\text{-}16)$$

where all variables are of similar definitions to those in Eqs. (4-7) and (4-12), but $b_{act,h}$

and $d_{act,h}$ equal 7 ft-9½ in. and 18 in., respectively.
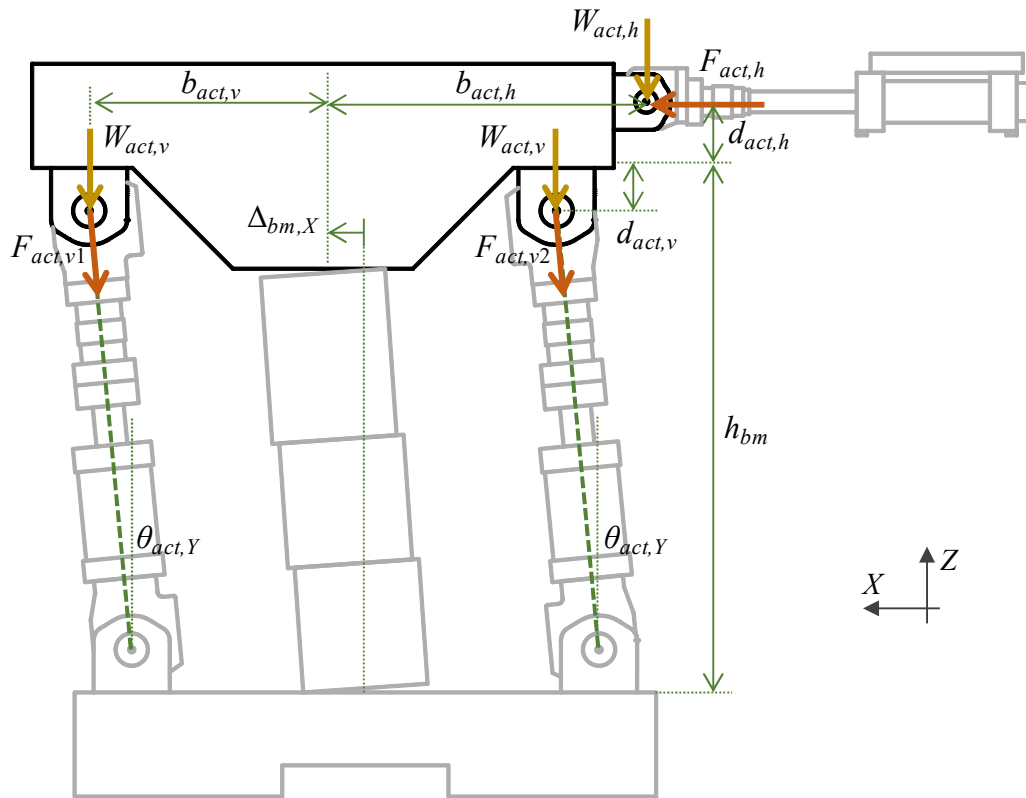
Figure 4-256. Actuator forces acting on loading beam in Phase III

438

4.7.3.4. Loading Protocols

A total of 16 loading protocols were used to perform the tests in Phase III. These loading protocols were categorized into five Loading Sets, as summarized in Table 4-38 and described in the following sections.

The nomenclature for the loading protocol IDs in Phase III start with "HSR1_UN_FXD_Sn," where 1 is the ID of the cast column specimen, "UN" stands for uniaxial loading, "FXD" stands for fixed-fixed state, and the letter "n" after "S" represents Loading Set number. The letters following the above letters are specific to each Loading Set, giving further information about the loading protocol.

Table 4-38. Loading Sets in Phase III

Loading Set	Number of Protocols	Max. Drift Ratio (%)	Lateral Displacement	Vertical Load
1	3	3	Cyclic	Constant
2	3	2	Cyclic	Cyclic
3	4	2	Cyclic	Constant
4	4	2.5	Arbitrary	Constant
5	2	6	Cyclic	Constant

4.7.3.4.1. Loading Set 1

This Loading Set involved three loading protocols of cyclic lateral displacement and constant vertical load. The purpose of these loading protocols was to examine the behavior and damageability of HSR columns in fixed-fixed condition and under displacement demands corresponding to selected earthquake hazard levels.

The loading protocols in this Loading Set were mapped to those of Loading Set 1 in Phase I and referred to the same hazard levels, but their displacement amplitudes were different. The total load applied by the vertical actuators was equal to 218 kips, resulting in a total gravity load of 253 kips on the column (i.e. including the weight of the loading beam and actuators). This amount of external vertical load represented 100% dead load plus 50% maximum design live load. The lateral displacement time history applied in each loading protocol included three pairs of ramp cycles, with each pair having a different amplitude (Figure 4-53). The displacement rate for all loading protocols was equal to 0.05 in./sec, corresponding to a drift ratio rate of 0.03% /sec. The maximum amplitudes, i.e. those of the last pairs of cycles in each loading protocol, were taken as the peak displacement demands of the column specimen under the seismic hazards of 5% and 2% probability of exceedance in 50 years, whereas that last/third loadinf protocol used a peak drift ratio twice as large as the one referring to the 2% in 50 years hazard. The peak displacement demands for the first two hazard levels were the medians peak displacement demands (Table 4-39) obtained by running multiple time history analyses on the column's 2D simulation model. The ground motion excitations selected for this purpose are found in Valigura (2019).

Table 4-39. Loading protocols in Loading Set 1 from Phase III

No	ID	Max. Drift Ratio (%)
1	HSR1_UN_FXD_S1_DR_1_1	1.1
2	HSR1_UN_FXD_S1_DR_1_5	1.5
3	HSR1_UN_FXD_S1_DR_3	3

4.7.3.4.2. Loading Set 2

This Loading Set also resembled Loading Set 2 of Phase I and it was intended to evaluate the response of HSR columns under simultaneous cyclic lateral displacement and cyclic vertical loading.

Three loading protocols with the same lateral displacement time histories but different vertical load time histories were considered. The applied lateral displacement consisted of three full sinusoidal cycles of amplitude 3 in. (equivalent to 2% drift ratio) and frequency 1/240 Hz. The load applied by the vertical actuators in each loading protocol consisted of three consecutive sets of cycles, each following the function below:

$$F_{act,v}(t) = 218 + 253 R_F \sin\left(2\pi\left(R_f \frac{1}{240}\right)t\right) \quad \text{(kips)} \tag{4-17}$$

where R_F equaled 0.1, 0.2, and 0.3 for the three sets of cycles; R_f was the ratio of vertical load frequency to lateral displacement frequency, which varied for each loading protocol; and t ranged from 0 to 240 sec., resulting in 1, 2, and 3 vertical load cycles for R_f equal to 1, 2, and 3, respectively. The loading protocols of Loading Set 2 are listed in Table 4-40. The applied vertical load time histories for the three loading protocols considered here are demonstrated in Figure 4-257.

Table 4-40. Loading protocols in Loading Set 2 from Phase III

No	ID	Vertical Load to Displacement Frequency Ratio
4	HSR1_UN_FXD_S2_V2H_1	1
5	HSR4_UN_CNT_S2_V2H_2	2
6	HSR4_UN_CNT_S2_V2H_3	3
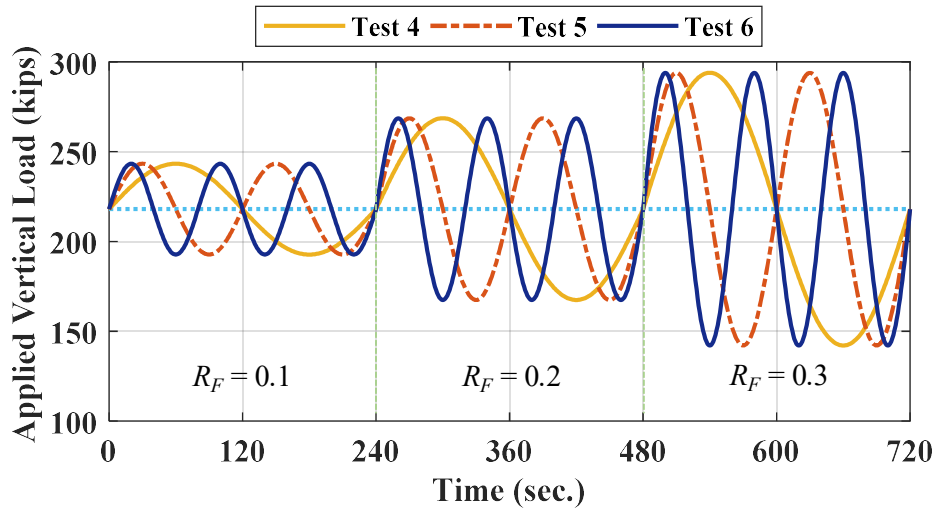
Figure 4-257. Applied vertical load time histories in Loading Set 2, Phase III

4.7.3.4.3. Loading Set 3

The objective of this Loading Set is to examine the effect of fast lateral loading on the response of HSR columns in a fixed-fixed condition.

Similar to Loading Set 2 of Phase I, in this Loading Set, the sum of the loads applied by the vertical actuators remained constant and equal to 218 kips. The lateral displacement was, however, applied in the form of one full sinusoid cycle with an amplitude of 3 in. (2% drift ratio). The frequency of the sinusoid changed for each loading protocol, depending on the desired peak displacement rate (Figure 4-258). The loading protocols considered in this Loading Set are summarized in Table 4-41.

Table 4-41. Loading protocols in Loading Set 3 from Phase III

No	ID	Max. Displacement Rate (in./sec.)
7	HSR1_UN_FXD_S3_Vmx_2	2
8	HSR1_UN_ FXD_S3_Vmx_4	4
9	HSR1_UN_ FXD_S3_Vmx_6	6
10	HSR1_UN_ FXD_S3_Vmx_8	8
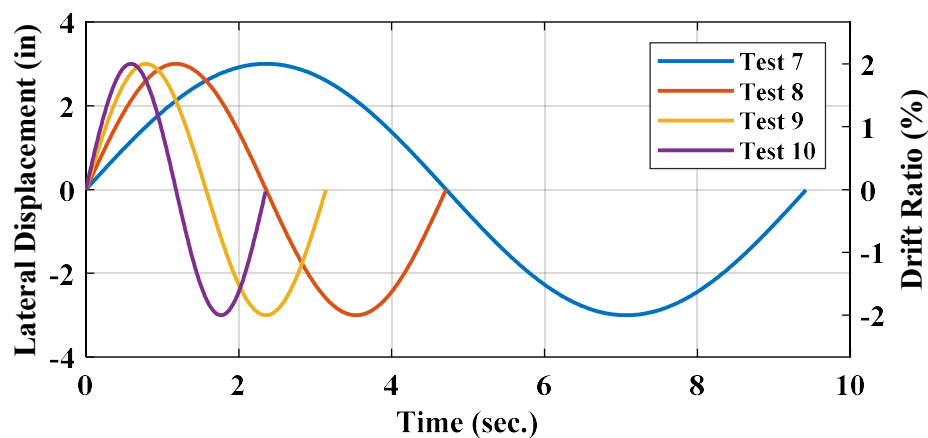
Figure 4-258. Lateral displacement time histories in Loading Set 3, Phase III

4.7.3.4.4. Loading Set 4

This Loading Set aimed to investigate the response of the fixed-fixed HSR column specimen under arbitrary lateral displacement and constant vertical load.

The constant load applied by the vertical actuators was 218 kips. A total of four loading protocols were considered for this Loading Set, whose lateral displacement time histories were obtained from the time history analysis of the column under four ground motions representing 5% and 2% probability of exceedance in 50 years (Valigura 2019). Compared to the original displacement time histories achieved from the analyses, the time histories used here were lengthened in time (slowed down) to keep the displacement rate

443

below 8 in./sec. (the maximum displacement rate safely achievable by the available hydraulics). Table 4-42 lists the loading protocols in this Loading Set. The displacement time histories applied through the above loading protocols are demonstrated in Figure 4-259.

Table 4-42. Loading protocols in Loading Set 4 from Phase III

No	ID	Ground Motion	Max. Drift Ratio (%)
11	HSR1_UN_FXD_S4_5in50_GM_7	5% in 50 yr, GM 7	1.70
12	HSR1_UN_FXD_S4_5in50_GM_16	5% in 50 yr, GM 16	1.18
13	HSR1_UN_FXD_S4_2in50_GM_9	2% in 50 yr, GM 9	2.32
14	HSR1_UN_FXD_S4_2in50_GM_13	2% in 50 yr, GM 13	2.53
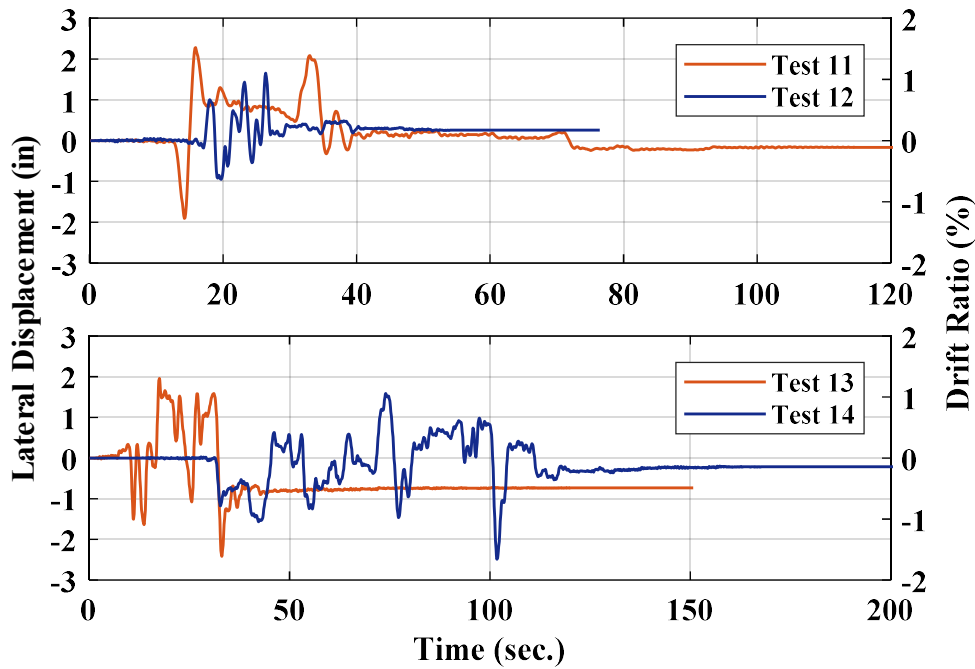
Figure 4-259. Displacement time histories in Loading Set 4, Phase III

4.7.3.4.5. Loading Set 5

In this final Loading Set, the column was subjected to excessively large lateral displacements to explore its behavior and damages towards failure.

Two loading protocols were considered, both with the constant vertical load of 218 kips. The lateral displacement time history in each loading protocol comprised two sinusoidal cycles of the same amplitude and frequency, while the maximum drift ratio rate was limited to 0.1% to produce a quasi-static loading condition. The loading protocols considered here are listed in Table 4-43.

Table 4-43. Loading protocols in Loading Set 5 from Phase III

No	ID	Max. Drift Ratio (%)
15	HSR1_UN_FXD_S5_DR_4	4
16	HSR1_UN_FXD_S5_DR_6	6

4.7.3.5. Results and Discussion

4.7.3.5.1. Initial Vertical Load Application

A few diagonal hairline cracks appeared on the bottom and middle column segments after the first time that the vertical loads were applied. The cause of these cracks is believed to have been potential stress variations or concentrations at the joints due to their potentially uneven surfaces. The distributions of these cracks on the bottom and middle column segments are seen in Figure 4-260 and Figure 4-261, respectively.
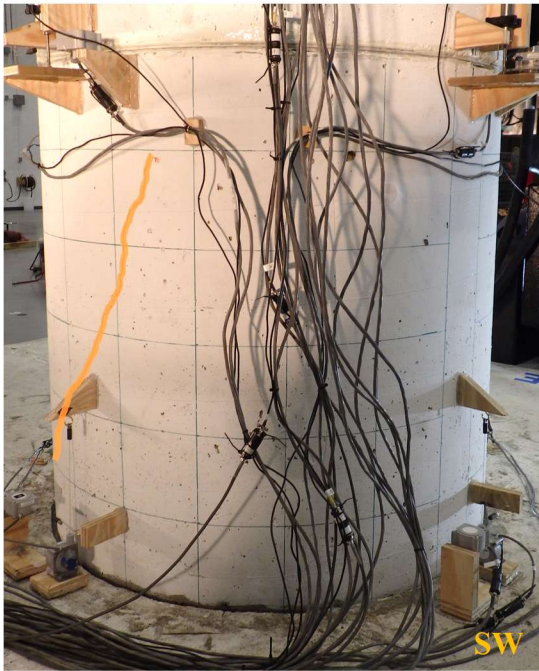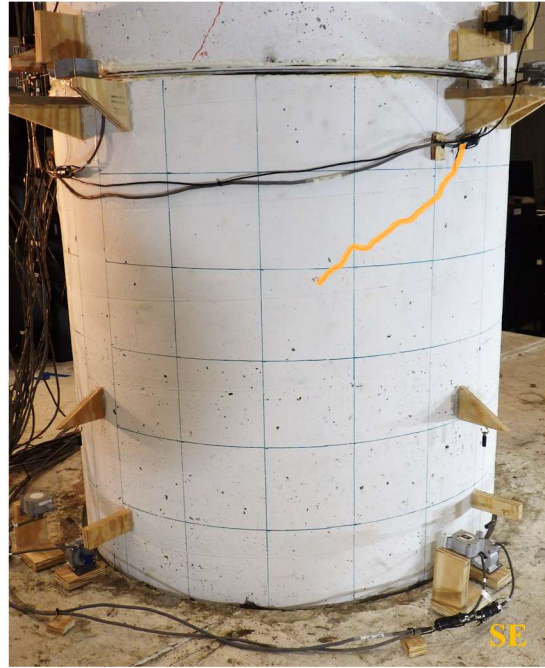
Figure 4-260. Phase III, initial vertical load application: hairline cracks on bottom column segment

446
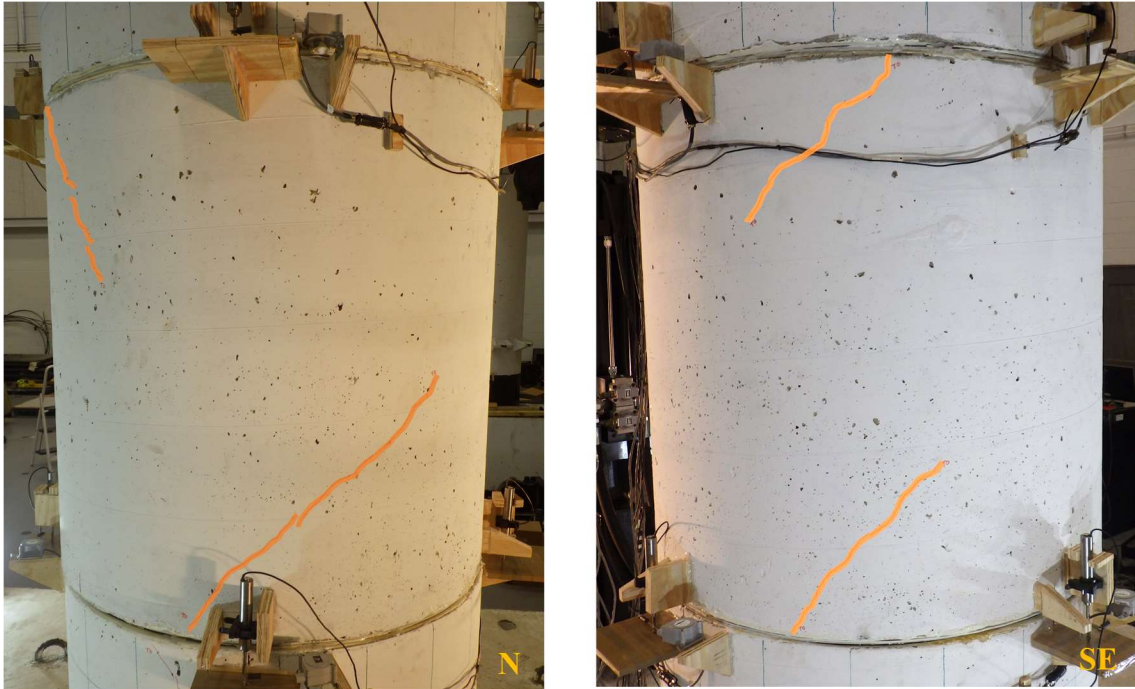
Figure 4-261. Phase III, initial vertical load application: hairline cracks on middle column segment

4.7.3.5.2. Results from Loading Set 1

The base shear vs. lateral displacement response of the column specimen under the first loading protocol in Loading Set 1, i.e. HSR1_UN_FXD_S1_DR_1_1, with a peak drift ratio of 1.1% representing 950-year seismic hazard, is demonstrated in Figure 4-262. Note that the lateral displacement application started in the negative *X*-direction. As seen, since the sliding joints had not experienced sliding before this test, the breakaway friction was quite large (with a frictional resistant exceeding 70 kips) and the column underwent 0.3 in. of lateral displacement before sliding initiated.
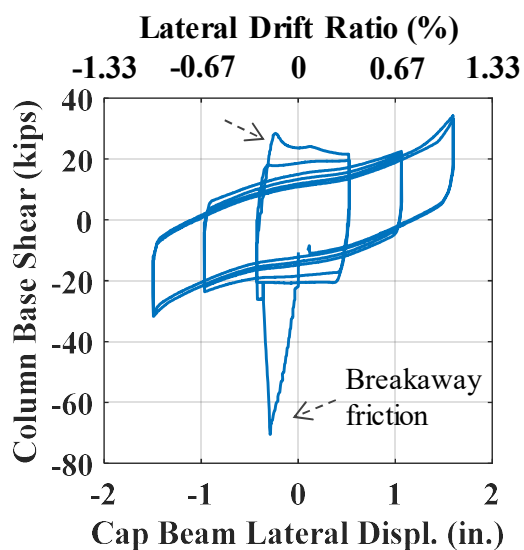
Figure 4-262. Phase III, loading protocol HSR1_UN_FXD_S1_DR_1_1: base shear vs. lateral displacement response

Contrary to the previous two Phases, in this Phase, sliding started at the second sliding joint (Joint 3) instead of the first sliding joint (Figure 4-264). This event is justified by the fact that the flexural moment generated at the second sliding joint was higher than that of the first sliding joint (Figure 4-266), thereby leading to a lower coefficient of friction at the second sliding joint due to its pressure dependence. Once the breakaway friction was overcome, the base shear abruptly reduced to 30% of that resistance (about 21 kips). According to Figure 4-262, the sliding joint went into the sticking phase once again after the first lateral displacement reversal, but the breakaway friction was much smaller this time (28 kips). Similarly to the previously tested columns, the coefficient of friction gradually decreased with the total sliding travel distance.

As shown in Figure 4-263, considering that the maximum applied displacement was 1.65 in., sliding at the second sliding joint was enough to accommodate almost the entire

displacement. Per Figure 4-262, the residual displacements corresponding to the maximum displacement amplitude in the positive and negative directions were equal to 1.2 in. and 1.1 in., respectively. These residual displacements, which are equivalent to 0.8% and 0.7% of drift ratio, respectively, were primarily caused by the residual sliding at the second sliding joint (Joint 3, Figure 4-264).
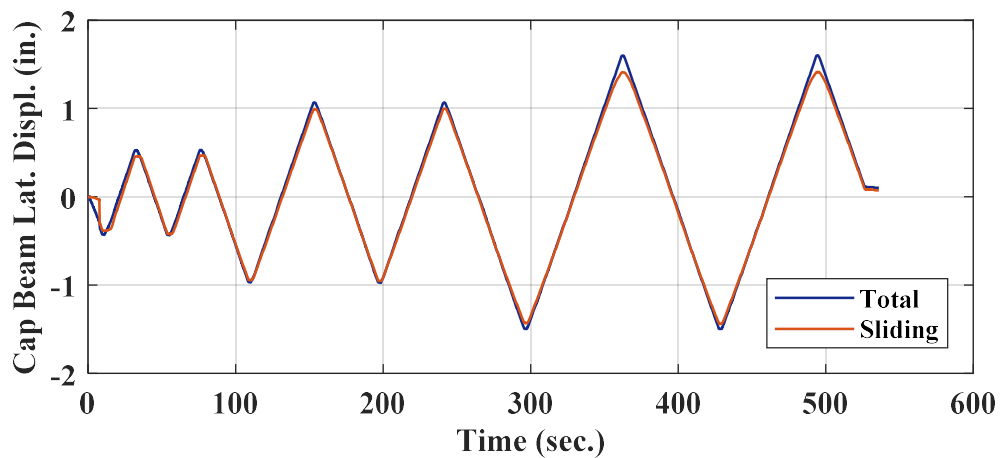
Figure 4-263. Phase III, loading protocol HSR1_UN_FXD_S1_DR_1_1: time histories of total lateral displacement and sliding

Per Figure 4-264, which displays the column shear vs. joint sliding responses, during this test, the maximum sliding achieved at Joint 2 was slightly larger than 1.4 in. in both directions. The residual joint sliding during the last displacement cycle was almost 1.1 in. in both directions, i.e. comprising at least 92% of the residual displacement values reported earlier.
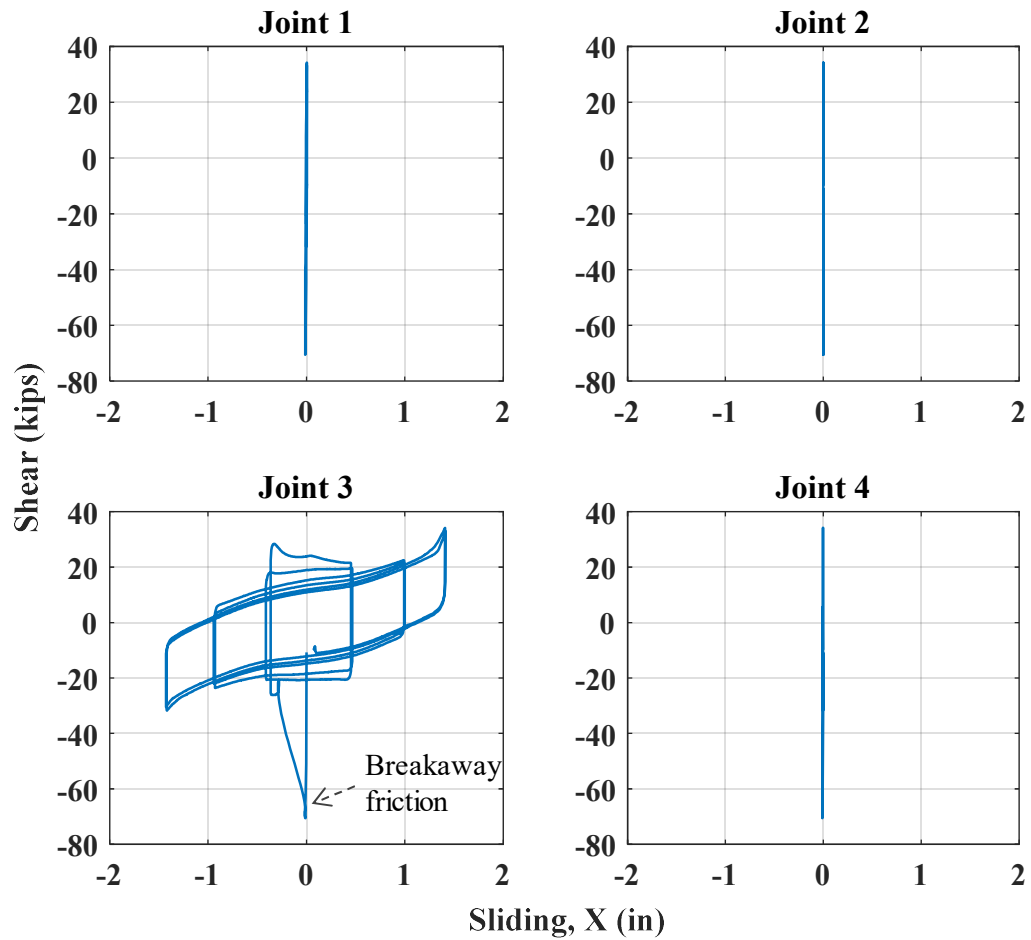
Figure 4-264. Phase III, loading protocol HSR1_UN_FXD_S1_DR_1_1: joint shear vs. sliding responses in *X* direction

In order to examine the variation of coefficient of friction with the accumulated sliding traveling at Joint 3, the ratio of the base shear to the column's axial force is plotted against the accumulated sliding in Figure 4-265. The accumulated traveling appears to control the reduction of the breakaway friction coefficient (Reddy Goli 2019). Based on this graph, the static coefficient of friction was about 0.18 and it decreased to about 0.03 after 20 in. of sliding travel distance.
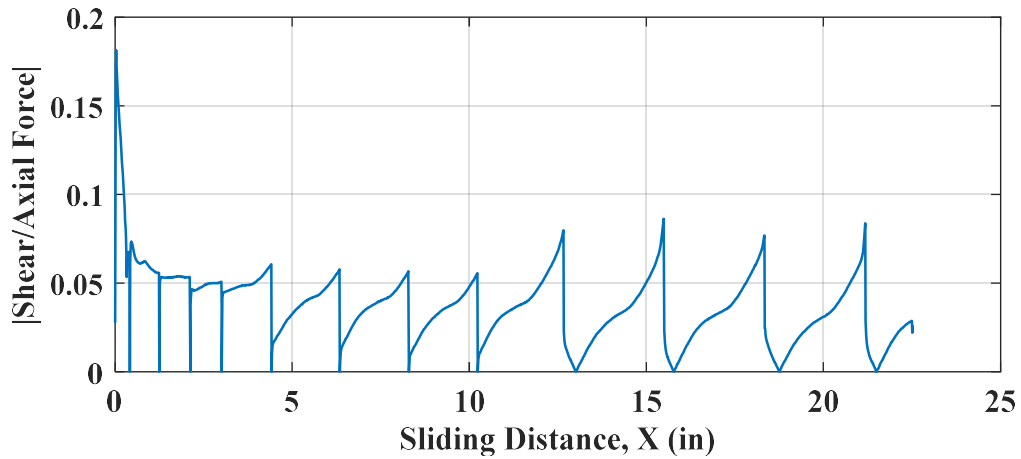
Figure 4-265. Phase III, loading protocol HSR1_UN_FXD_S1_DR_1_1: shear to axial force ratio vs. accumulated sliding

The moment and rocking time histories obtained at the column joints are compared in Figure 4-266. According to Figure 4-266(a), the maximum moment occurred at the topmost join (Joint 4), while the rocking measured at the second sliding joint (Joint 3) was higher than that at Joint 4 – Figure 4-266(b). This most likely happened because, even though the moment at Joint 4 was higher, the stiffness and strength of that joint against rotation was higher than those of Joint 3 with the PTFE material, in particular as the contact area at Joint 3 decreased with sliding. Moreover, the rotations at the sliding joints computed on the basis of the data obtained from the LVDTs (see Figure 4-47) were not very reliable, because the LVDTs tended to rotate with joint sliding. The rocking at the bottom rocking joint (Joint 1) was also relatively higher than that at Joint 4, whereas the first sliding joint that experienced no sliding had very small moment and rocking. Note that, regardless of the comparisons made above, the extent of rocking achieved during this test was quite small at all joints (less than 0.2 degrees).

451
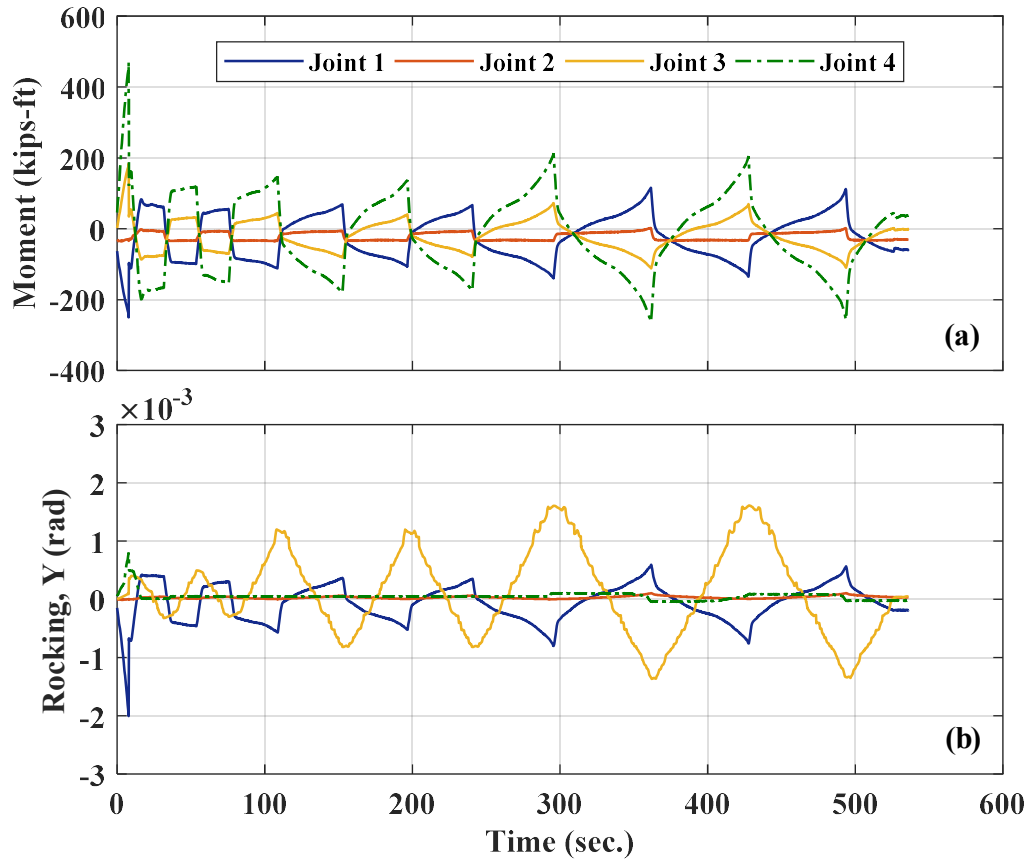
Figure 4-266. Phase III, loading protocol HSR1_UN_FXD_S1_DR_1_1: (a) time histories of joints moment; (b) time histories of joints rocking

The time histories of the posttensioning forces in individual tendons and their total are demonstrated in Figure 4-267 and the variation of the total PT force with lateral displacement is shown in Figure 4-268. It is observed that the initial tendon forces were about 6% smaller than their design-targeted values (i.e. 18 kips per tendon), which may be attributed to the PTFE material's creep.

As seen in Figure 4-267, because of the zero rotation of the loading beam, all the tendons' forces changed with lateral displacement consistently. Although in an ideal fixed-fixed HSR column the posttensioning forces of all the tendons should change equally,

452

here, the tendons did not have equal elongations. This is because of duct misalignments, tendon-duct friction differences, and tendon load cell measurement errors.

The maximum PT force increase in every tendon was less than 15% and the PT forces did not exceed 37% of the tendons' yield strength. The observed PT increases were mainly induced by the sliding at Joint 3. In addition, the total PT loss during this test was very small (less than 1%), which is in agreement with the low extent of posttensioning increase in the tendons.
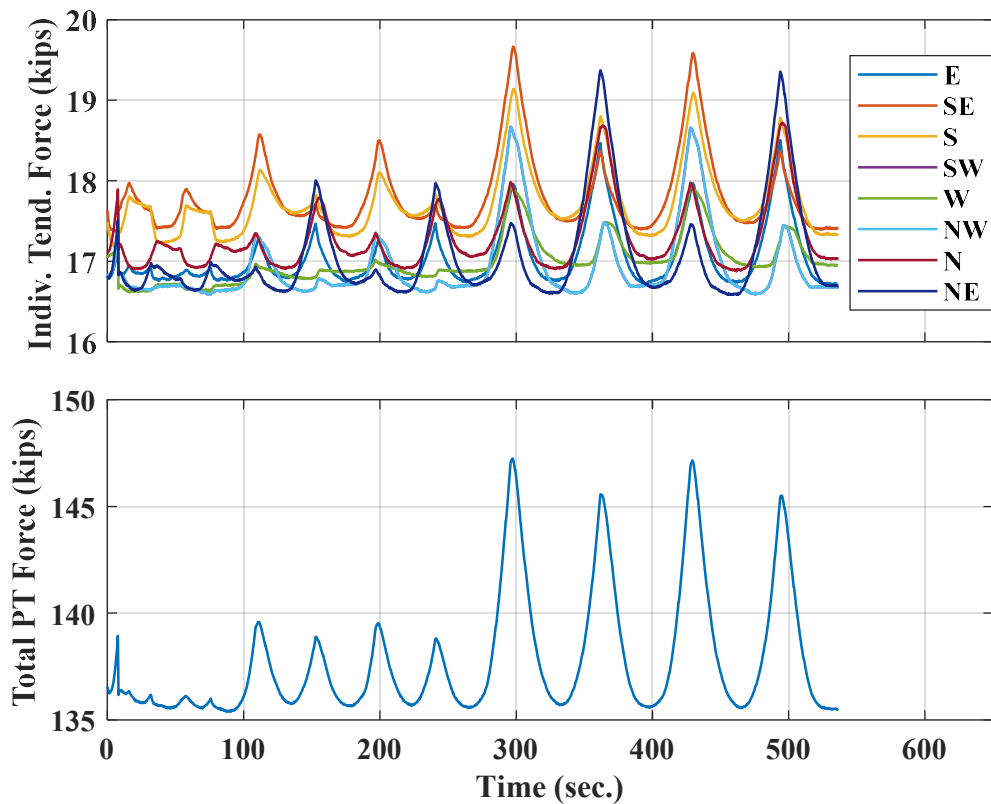
Figure 4-267. Phase III, loading protocol HSR1_UN_FXD_S1_DR_1_1: time histories of posttensioning forces
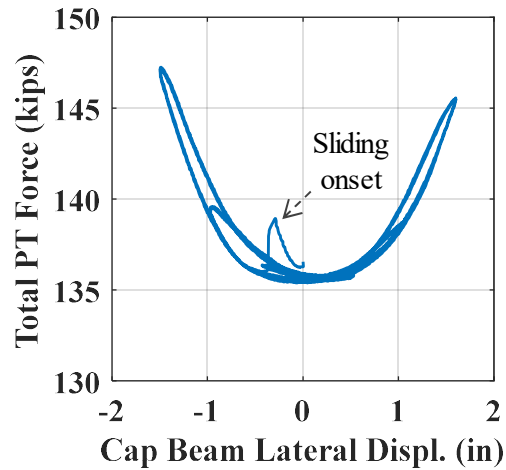
Figure 4-268. Phase III, loading protocol HSR1_UN_FXD_S1_DR_1_1: total PT force vs. lateral displacement response

The column specimen's force-displacement response obtained under loading protocol HSR1_UN_FXD_S1_DR_1_5, with a peak drift ratio of 1.5% and representing the 2475-year seismic hazard, is shown in Figure 4-269. The breakaway friction force was 35 kips (equivalent to an average coefficient of friction of 0.09 over the joint interface), which was almost half of that observed in the previous test (i.e. 70 kips). In this test, similar to the previous test, only the second sliding joint (Joint 3) experienced sliding (Figure 4-271), even though less than 75% of the total applied displacement could be accommodated via this joint (Figure 4-270). This means that the remainder of the imposed lateral displacement was accommodated through rocking and material deformations.
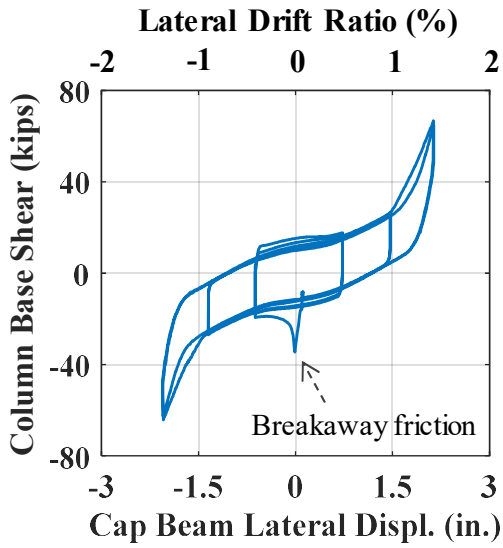
Figure 4-269. Phase III, loading protocol HSR1_UN_FXD_S1_DR_1_5: base shear vs. lateral displacement response
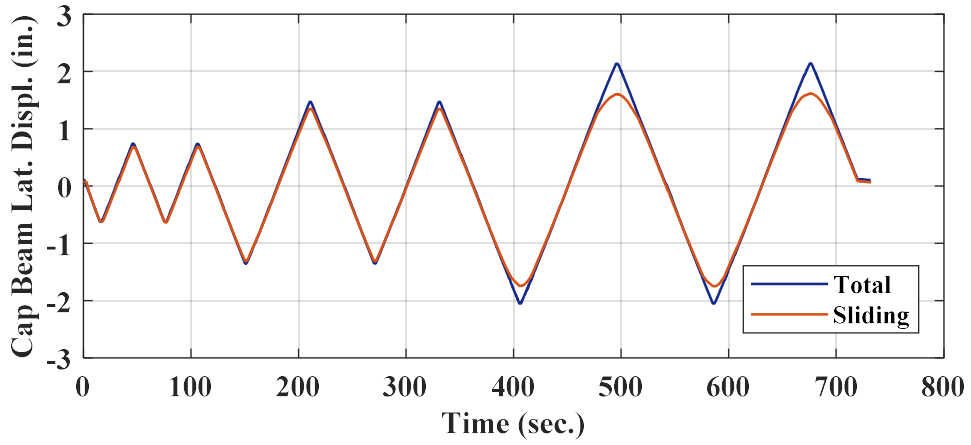
Figure 4-270. Phase III, loading protocol HSR1_UN_FXD_S1_DR_1_5: time histories of total lateral displacement and sliding

455
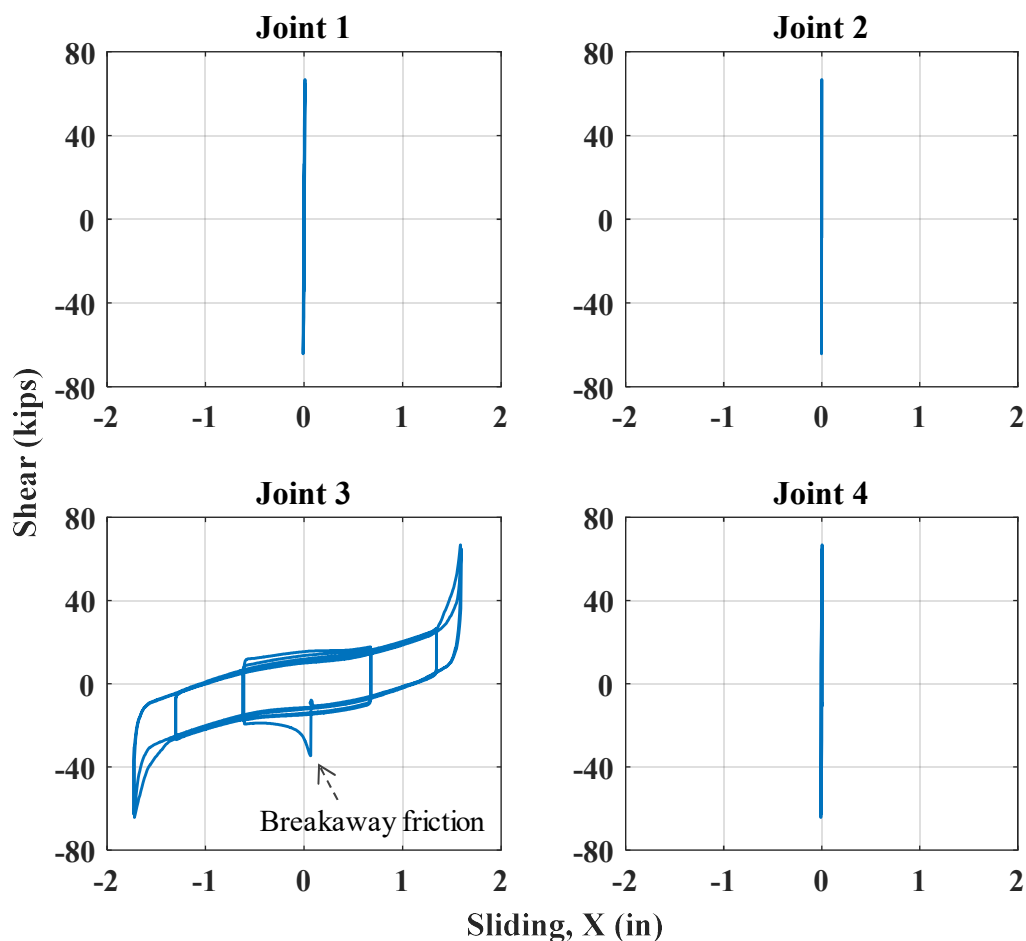
Figure 4-271. Phase III, loading protocol HSR1_UN_FXD_S1_DR_1_5: joint shear vs. sliding responses in *X* direction

The significant hardening observed in Figure 4-269 resulted from the tendon bearing reactions at Joint 3, particularly because, during the last two displacement cycles, the sliding at that joint had exceeded its nominal maximum sliding capacity, i.e. 1.45 in. (see the response of Joint 3 in Figure 4-271). A cyclic stiffness deterioration is also observed during the last two cycles, which can be associated with the PT losses and the bearing-induced duct damages caused in the first cycle of the maximum amplitude. The hysteretic

response was almost symmetric and the maximum base shear in both directions was close to 65 kips.

According to Figure 4-269, the maximum residual displacements in the positive and negative directions were 1.2 in. and 1.1 in., respectively, which were unchanged compared to the values obtained during the first test. From these values, however, about 95% was caused by the residual sliding at the active sliding joint (Joint 3, Figure 4-271), which does not represent permanent damage.

The time histories of the joints' moment and rocking obtained during the same test are compared in Figure 4-272. According to Figure 4-272(a), the minimum and maximum moments occurred at Joints 2 and 4, respectively. The moment signs indicate that the inflection point of the column (where moment was zero) fell somewhere along the middle segment's height and close to the first sliding joint (Joint 2). In terms of rocking, however, its maximum occurred between the two upper segments, i.e. at Joint 3 (Figure 4-272(b)). This unexpected result is justified by the lower stiffness of the PTFE material than concrete, reduced overlapping contact area with sliding, as well as the sliding-induced errors in the data obtained from the LVDTs measuring the relative vertical displacements of the segments at the sliding joints. The higher rotation at the bottom rocking joint (Joint 1) compared to the top rocking joint (Joint 4) results ftom its potentially lower moment capacity.
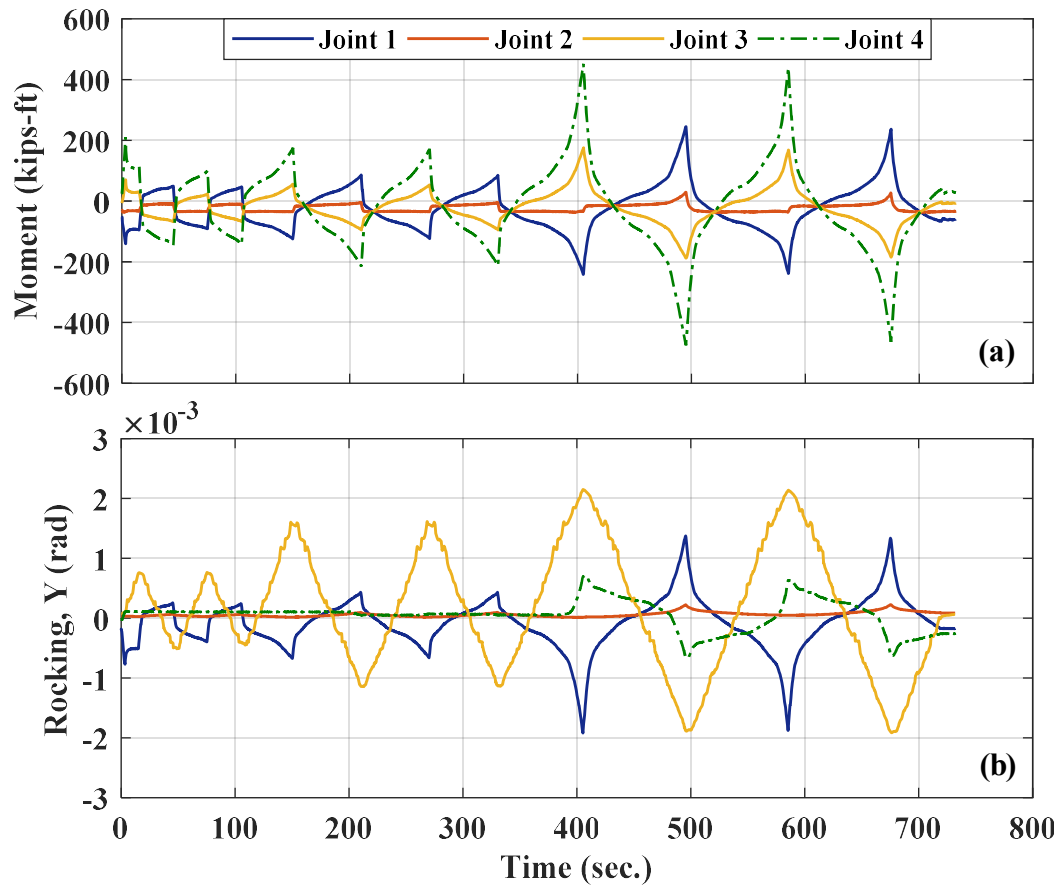
Figure 4-272. Phase III, loading protocol HSR1_UN_FXD_S1_DR_1_5: (a) time histories of joints moment; (b) time histories of joints rocking

The time histories of the tendon forces are displayed in Figure 4-273. As seen, the tendon forces varied consistently and the maximum posttensioning force increase in the tendons ranged from 2.4 kips to 4.1 kips at the maximum applied displacement. According to Figure 4-274, the maximum total PT force created in the column was 158 kips that occurred at the negative peak displacement. In addition, similarly to the previous test, the PT loss in this test was found to be less than 1%.
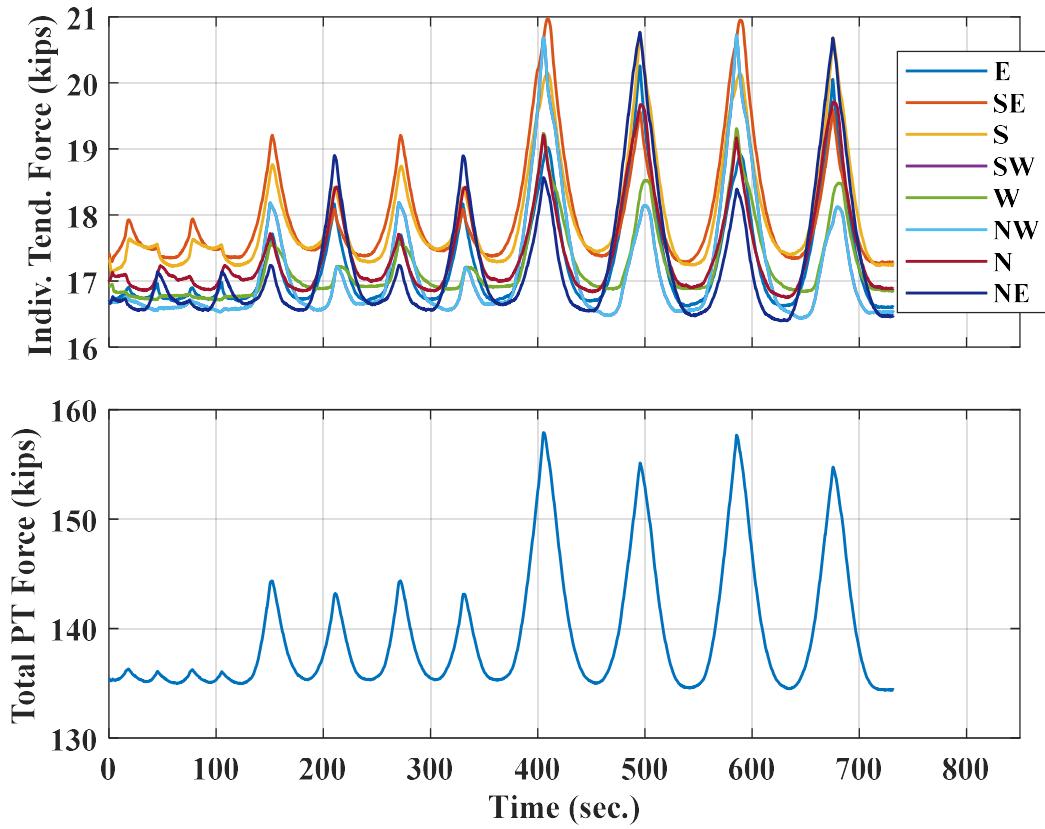
Figure 4-273. Phase III, loading protocol HSR1_UN_FXD_S1_DR_1_5: time histories of posttensioning forces
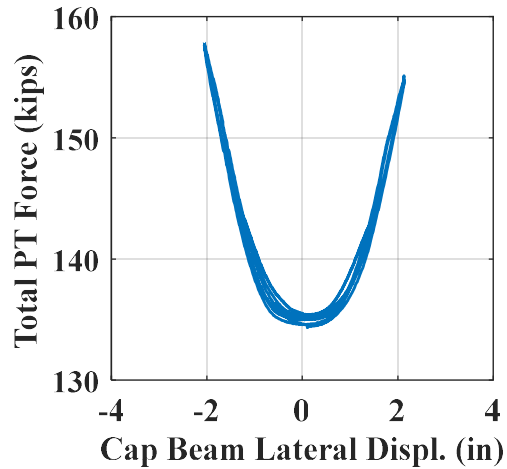
Figure 4-274. Phase III, loading protocol HSR1_UN_FXD_S1_DR_1_5: total PT force vs. lateral displacement response

459

The last test in Loading Set 1 was conducted under loading protocol HSR1_UN_FXD_S1_DR_3, with a maximum lateral displacement of 4.5 in. (resulting in a peak drift ratio of 3%). Due to a technical problem, this test was run in two separate runs, one including only the first four displacement cycles and the second one including the remaining two displacement cycles. The pause between the two test runs led to discontinuities in the responses and an undesirable change in the rotation of the loading beam around Y-axis.

The lateral force-displacement response of the column specimen under the above loading protocol is shown in Figure 4-275(a). As expected, the response exhibited several base shear extrema, after sliding initiated at each sliding joint. According to Figure 4-276, the first sliding joint became active for the first time near the fifth displacement peak – i.e. the first peak of the first cycle of 3-in. amplitude. The breakaway friction for the first sliding joint was 93 kips (Joint 2, Figure 4-277), which is 23 kips larger than the breakaway friction at the second sliding joint (Joint 3) measured during the first test (under loading protocol HSR1_UN_FXD_S1_DR_1_1, Figure 4-264). The larger breakaway frictional resistance is the result of the higher posttensioning forces under larger lateral displacement. The rest of base shear extrema occurred due to stick-slip transitions at the sliding joints.
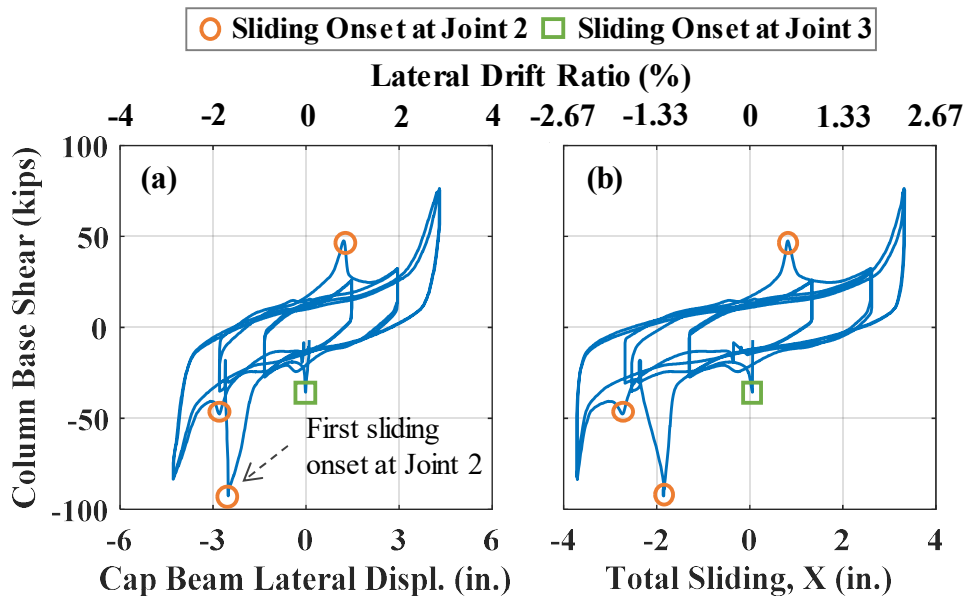
Figure 4-275. Phase III, loading protocol HSR1_UN_FXD_S1_DR_3: (a) base shear vs. lateral displacement response; (b) base shear vs. total sliding response
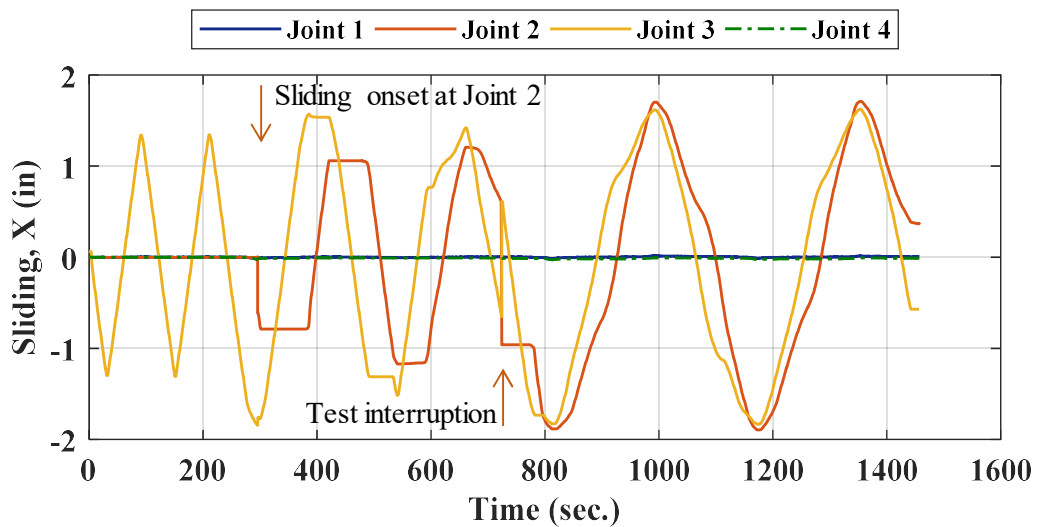
Figure 4-276. Phase III, loading protocol HSR1_UN_FXD_S1_DR_3: time histories of joint sliding in *X* direction

461
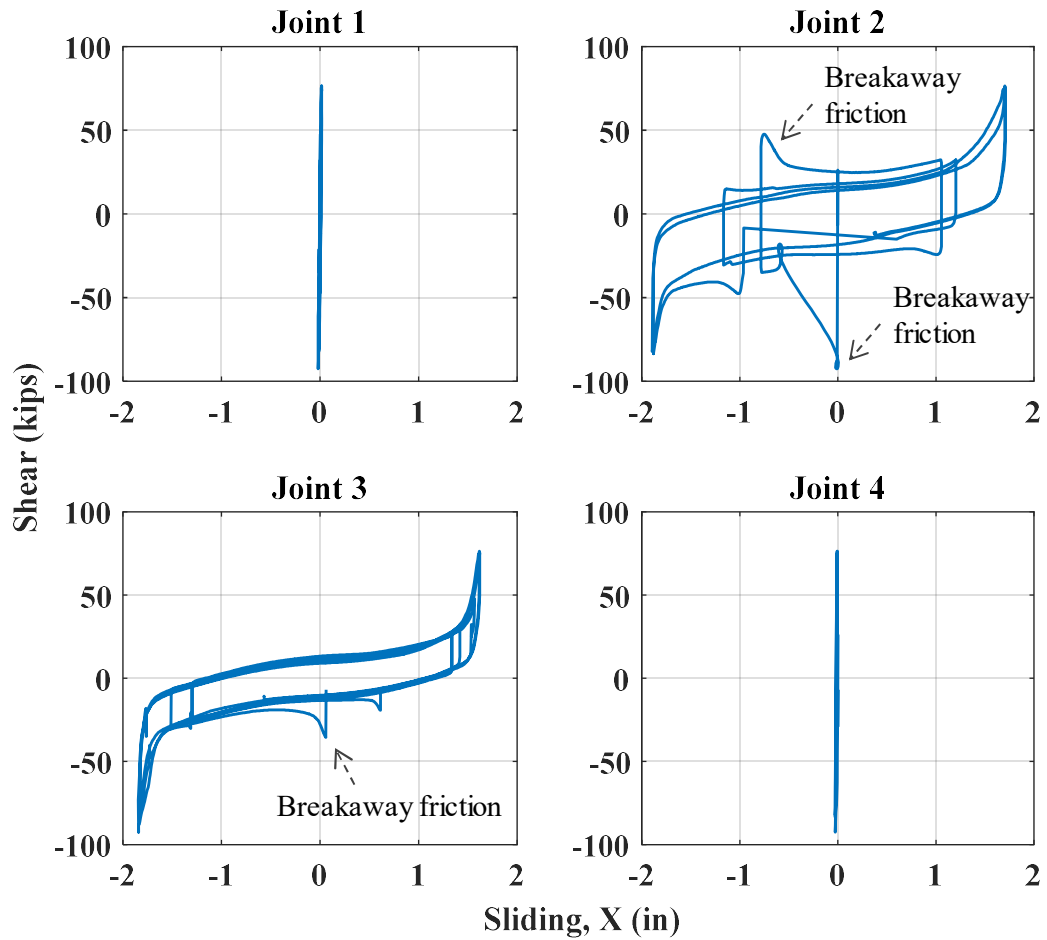
Figure 4-277. Phase III, loading protocol HSR1_UN_FXD_S1_DR_3: joint shear vs. sliding responses in *X* direction

Nonetheless, the column's hysteretic response (Figure 4-275(a)) during the last displacement cycles looks symmetric and the maximum base shear values resisted by the column in the negative and positive directions were less than 10% different (83 kips and 76 kips, respectively). The maximum residual displacement values obtained in the negative and positive loading directions were 2.4 in. and 2.75 in., respectively, which are equivalent to the drift ratios of 1.6% and 1.8%, respectively. According to Figure 4-276(b),

the corresponding residual joint sliding values were 2.55 in. and 2.4 in., which are slightly larger than and 87% of the residual displacement values, respectively.

Per Figure 4-276, in this test, the majority of sliding was accommodated by the second sliding joint (Joint 3) and the first sliding joint (Joint 2) was activated merely when Joint 3 reached a large enough sliding that would develop large enough shear to overcome the breakaway friction at Joint 2. This fact led to a noticeable phase lag between the sliding responses of the two sliding joints, making them oppositely signed at some time periods. However, the peak sliding values achieved in both sliding joints were close to 1.85 in. in the negative *X*-direction. It is also observed that, despite the fact that the final lateral displacement applied to the column was zero, the corresponding joint sliding values were almost +0.4 in. and -0.6 in. at Joints 3 and 4, respectively – the final state of the column segments at the end of the test is displayed in Figure 4-278.

It is observed from Figure 4-277 that the friction force at Joint 2 was higher than that at Joint 3 during the entire loading. This resulted from the fact that the second sliding joint (Joint 3) had traveled a larger sliding distance by the time this test was run, and thus, its coefficient of friction had decreased.
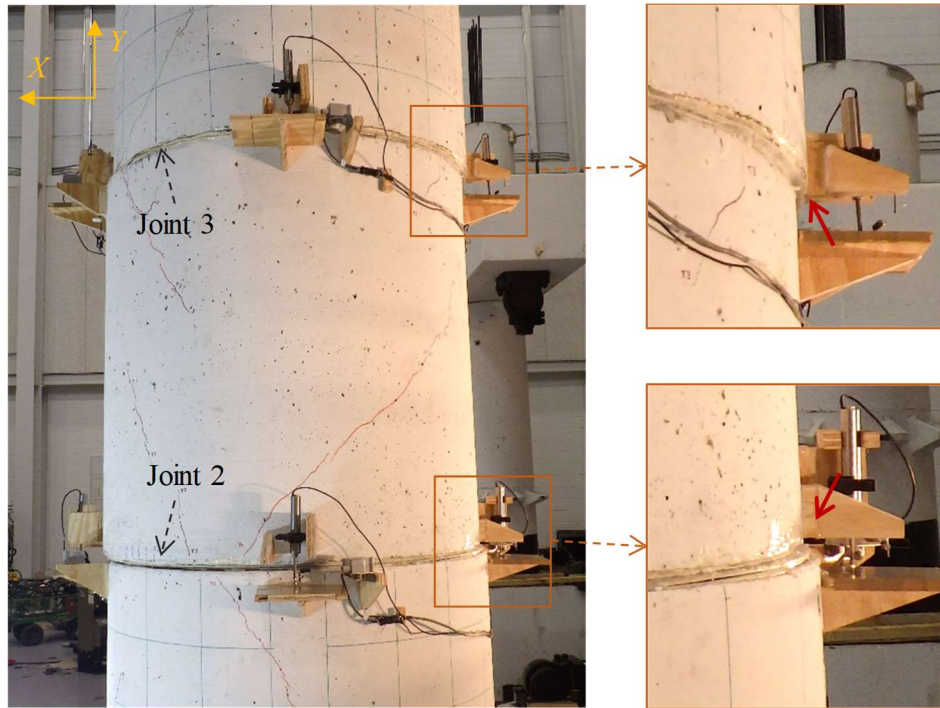
Figure 4-278. Phase III, loading protocol HSR1_UN_FXD_S1_DR_3: final states of sliding joints after test

Per Figure 4-279, similarly to the previous two tests, the maximum moment happened at the top rocking joint (Joint 4) and the inflection point (zero moment) fell along the middle column segment. After the pause in the testing caused by the aforementioned technical problem, a constant positive residual moment close to 100 kip-ft was formed at the top end of the column, thereby making the moment values over the entire column height vary around that instead of zero. The rocking values computed for the sliding joints seem unreliable, because their signs do not necessarily agree with the signs of the moments and they seem to follow the sliding responses. This observation implies that the data obtained from the LVDTs was severely affected by the joints' sliding. For the rocking

joints, however, as was the case in the previous test, the relative rotation at the bottom

rocking joint is larger than the relative rotation at the top rocking joint.
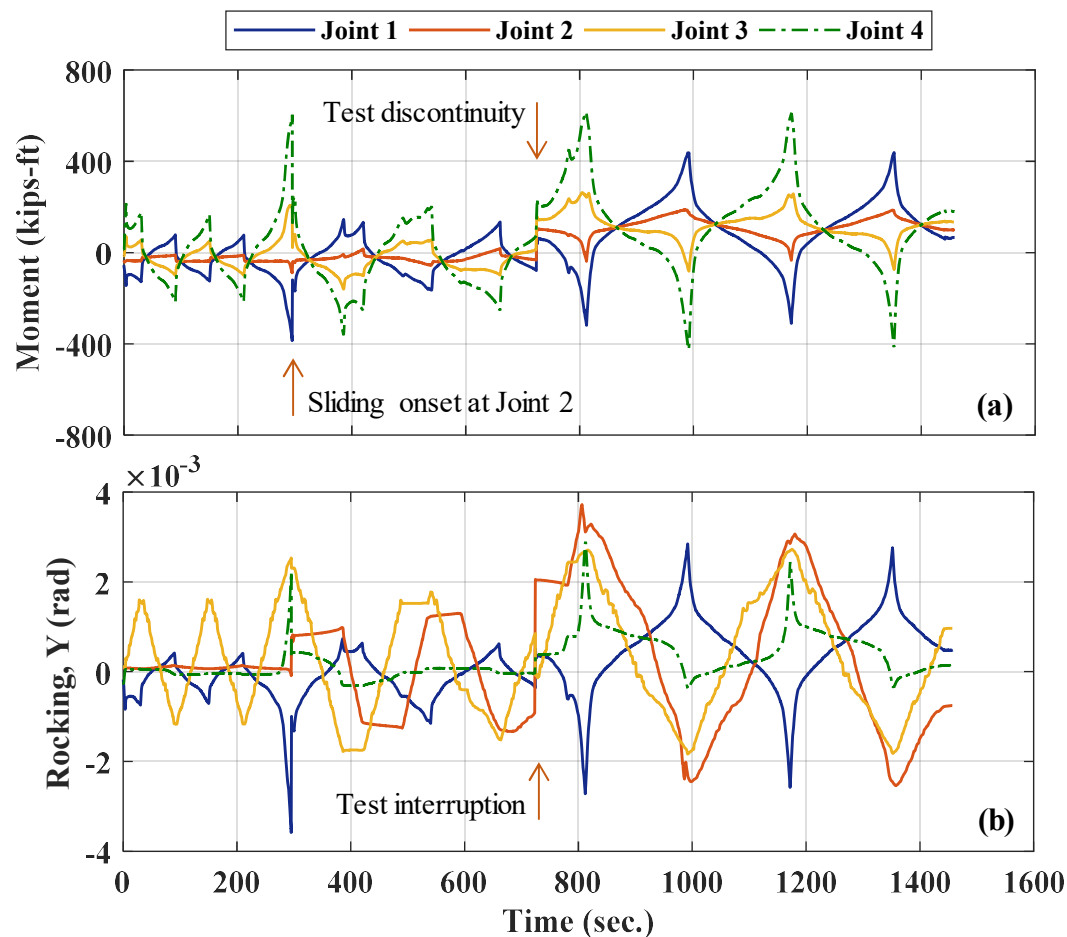
Figure 4-279. Phase III, loading protocol HSR1_UN_FXD_S1_DR_3: (a) time histories of joints moment; (b) time histories of joints rocking

The time histories of the tendon forces obtained during this test are shown in Figure 4-280. The maximum achieved tendon force was near 26 kips, i.e. 50% less than the strands nominal yield strength. According to Figure 4-281, sliding at the first sliding joint (Joint 2) could pause the increase in the posttensioning forces for some time intervals, but

yet the rocking motion of the column segments led to 41% and 27% posttensioning increases at the negative and positive peak displacements, respectively. The 14% difference between the total PT force increases in the negative and positive directions can be associated with the duct misalignments and the variations of friction between the tendons and their ducts. The total PT loss during this test was less than 3%.
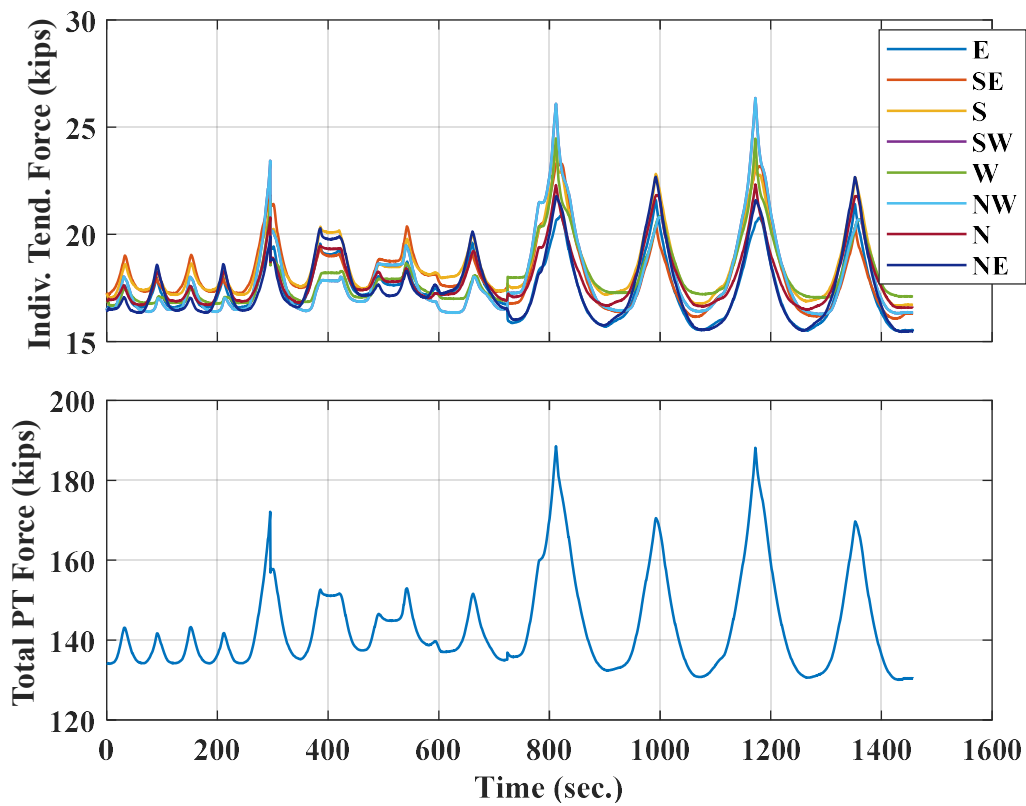
Figure 4-280. Phase III, loading protocol HSR1_UN_FXD_S1_DR_3: time histories of posttensioning forces
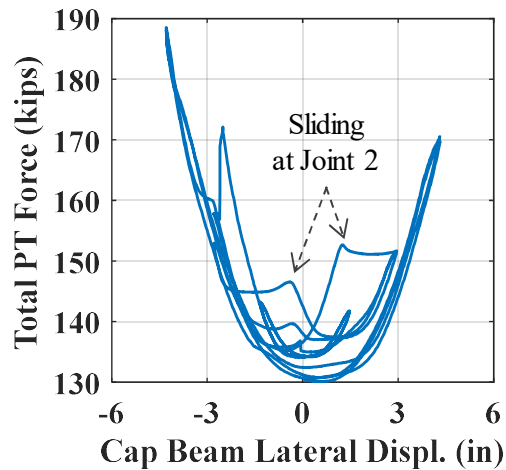
Figure 4-281. Phase III, loading protocol HSR1_UN_FXD_S1_DR_3: total PT force vs. lateral displacement response

The lateral force-displacement hysteresis loops obtained from the tests under the displacement cycles of Loading Set 1 with increasing displacement amplitudes are overplotted in Figure 4-282. It is clear from the graph that the friction forces gradually reduced during the initial cycles, but, except for the extrema induced by the breakaway friction at the sliding joints, the column's overall response was almost symmetric and repeatable.

The variations of the effective damping ratio and residual drift ratio (see Eqs. (4-11)) with the peak drift ratio are demonstrated in Figure 4-283. According to the results shown, the maximum effective damping ratio, i.e. 57%, was resulted at the lowest peak drift ratio applied to the column specimen, i.e. 0.37%. When only one sliding joint was active (i.e. for drift ratios < 2%), the effective damping ratio significantly decreased with the peak drift ratio, from close to 60% for a peak drift ratio of 0.37% to close to 10% for a peak drift ratio of 1.5%. As sliding at the first sliding joint (Joint 2) initiated for the peak drift

ratio of 2%, the effective damping ratio increased again, but it decreased to one third (i.e. 10%) at the peak drift ratio of 3%.
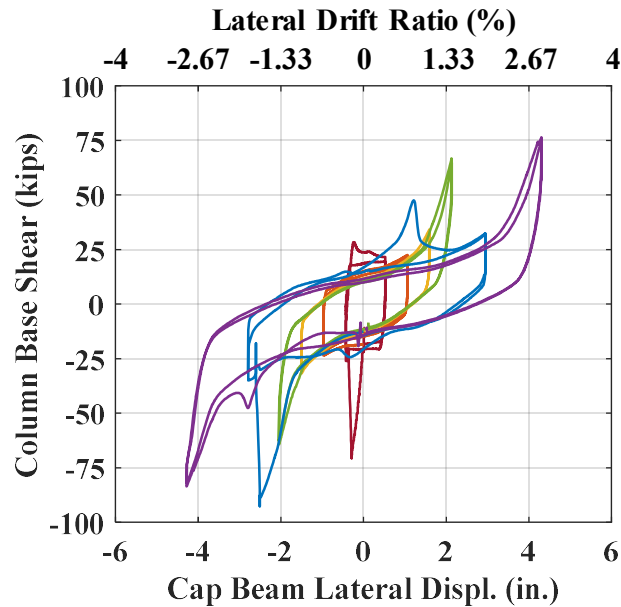
Figure 4-282. . Phase III, Loading Set 1: complete base shear vs. displacement response of column under displacement cycles of increasing amplitude
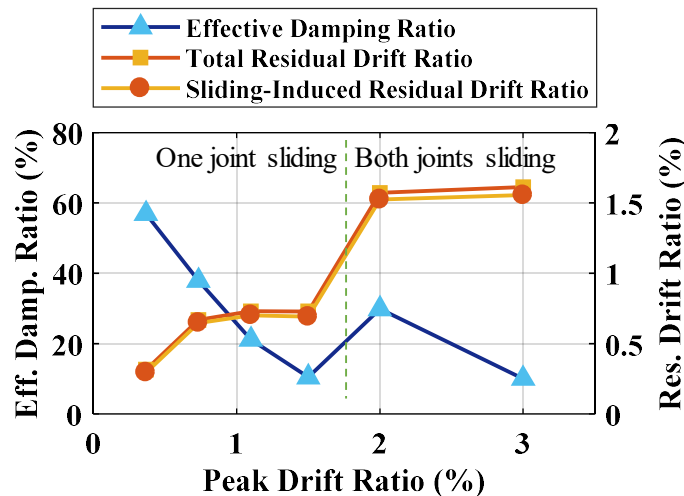
Figure 4-283. Phase III, Loading Set 1: variation of effective damping ratio and residual drift ratio with peak drift ratio

468

The least residual displacement occurred for the peak drift ratio of 0.37% and it was close to 0.31%, i.e. only slightly less than the maximum applied displacement. The residual displacement became almost constant (close to 0.7%) under the displacement cycles with peak drift ratios less than 1.5%, as the residual sliding remained almost the same. With the activation of the first sliding joint (Joint 2) as the peak drift ratio exceeded 2%, both the residual sliding and the residual displacements got more than double (i.e. more than 1.5% in terms of drift ratio). It is noted that, while the residual drift ratios were large relative to the peak applied drift ratios, the residual sliding constituted more than 95% of those values, so they could be recovered.

The distribution of cracks appeared on the bottom two segments after the three tests in Loading Set 1 are shown in Figure 4-284 and Figure 4-285. Only two hairline cracks were visible on the top segment. All of the cracks caused during the first two tests and the majority of the cracks caused during the third test were hairline cracks, and most of these cracks were caused during the third test. Moreover, after the third test (under loading protocol HSR1_UN_FXD_S1_DR_3 with a peak drift ratio of 3%), as shown in Figure 4-286, wide cracks and slight shallow spalling were observed near the east and west tendon ducts below the first sliding joint (Joint 2) and the northeast tendon duct below the second sliding joint (Joint 3). These wide cracks as well as epoxy damage on the northeast of Joint 3 (Figure 4-286) indicates the high normal stresses generated by rocking and the significance of the tendon bearing forces formed on the edges of the duct adaptors at the sliding joints as the two sliding joints reached their maximum sliding capacities during the third test.
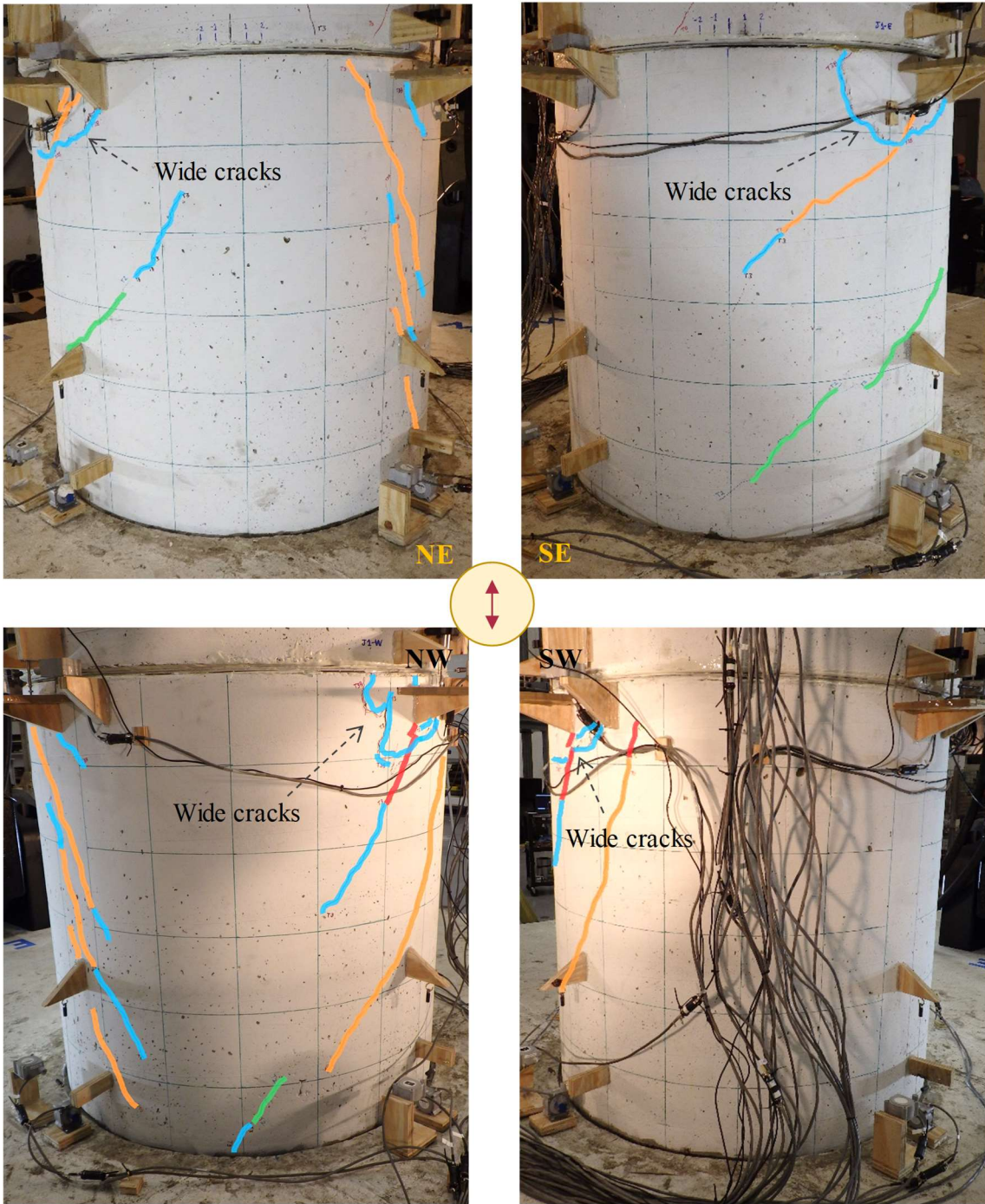
Figure 4-284. Phase III, Loading Set 1: distribution of cracks on bottom segment

470
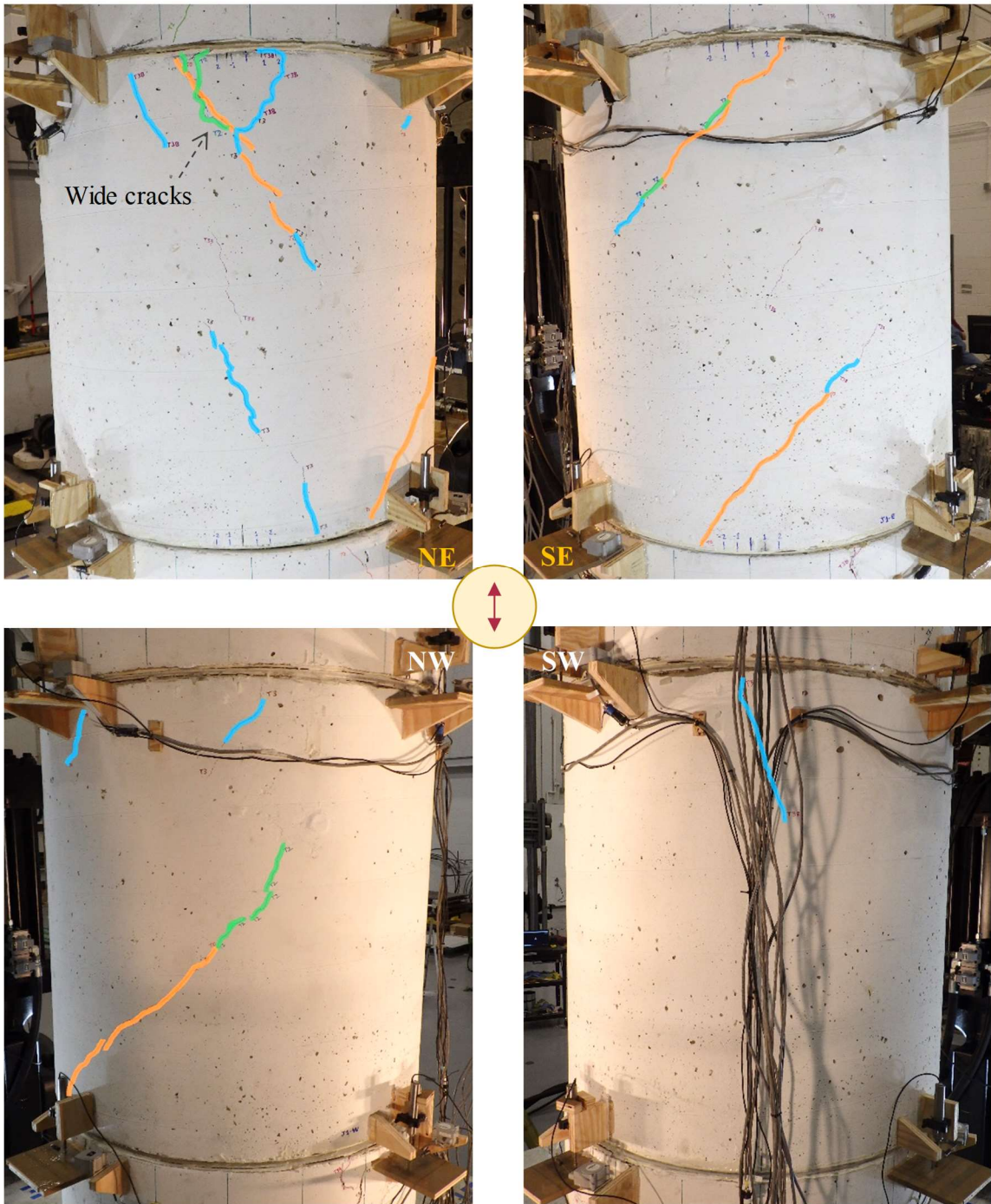
Figure 4-285. Phase III, Loading Set 1: distribution of cracks on middle segment

471
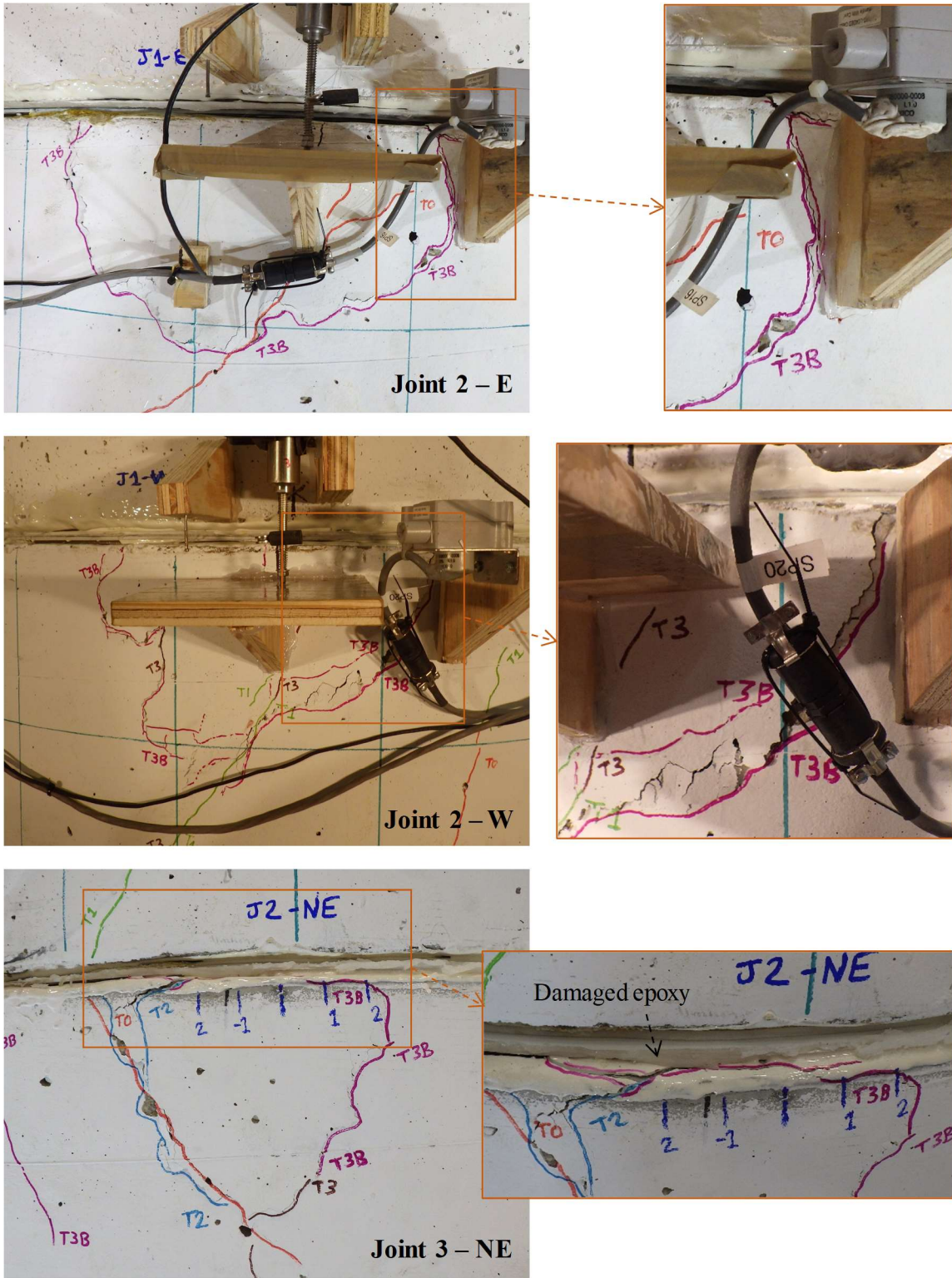
Figure 4-286. Phase III, Loading Set 1: concrete damage around sliding joints

472

The fact that the damage was mostly concentrated around the sliding joints rather than the rocking joints is the implication of the low extent of rocking at the end rocking joints (top and bottom of the column), as the friction at the sliding joints was considerably smaller than the incipient rocking base shear in a fixed-fixed condition.

4.7.3.5.3. Results from Loading Set 2

The time histories of the total axial force and the shear resisted by the column specimen during the three tests in Loading Set 2 are compared in Figure 4-287. As shown, the column base shear was only slightly affected by the amount of applied vertical load, and the base shear only slightly increased with axial force.

The effect of variable vertical load on the rocking of Joint 1 is illustrated through Figure 4-288. According to this figure, the change in the extent of rocking with the vertical load's frequency and amplitude was less than 20%, where increase in the frequency and amplitude of the vertical load variation led to larger changes. These changes are mainly observed in the positive direction because of the asymmetry caused by the residual negative moment at the column's top end induced by the discontinuity/interruption in the test during the third loading protocol of Loading Set 1 (see Figure 4-279).

The time histories of the sliding at the sliding joints are compared in Figure 4-289. It is observed that the variable vertical loading, irrespective of its frequency and amplitude, did not significantly change the maximum sliding achieved at the sliding joints, except during the very first displacement half cycle. Even this finding could have been due to the variations in the breakaway friction and not necessarily the vertical load variation.

473
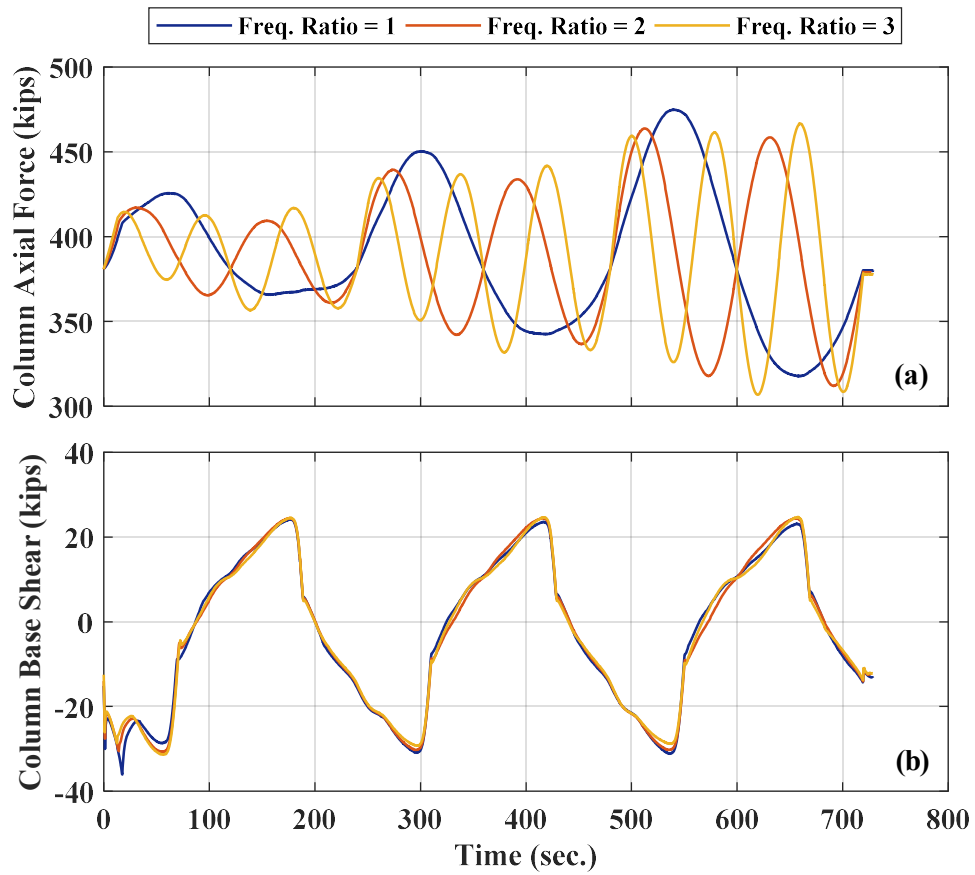
Figure 4-287. Phase III, Loading Set 2: (a) column axial force time histories; (b) column base shear time histories
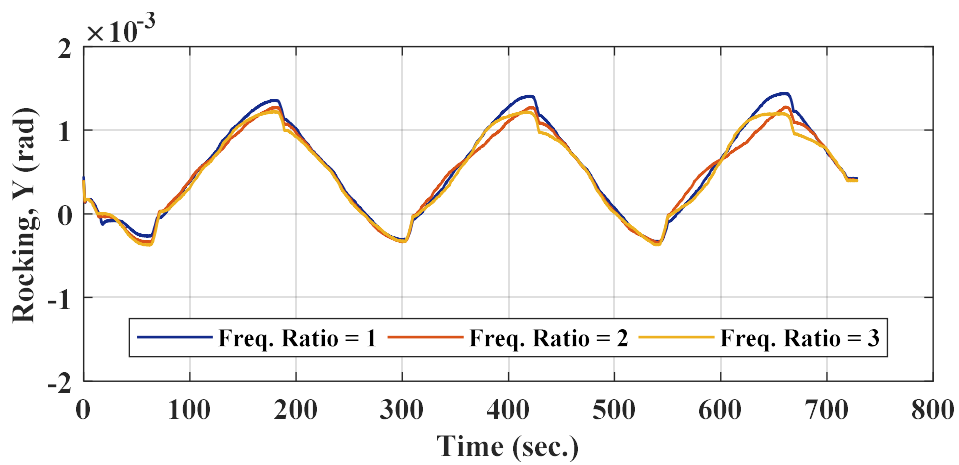
Figure 4-288. Phase III, Loading Set 2: time histories of rocking at Joint 1 around *Y*-axis

474
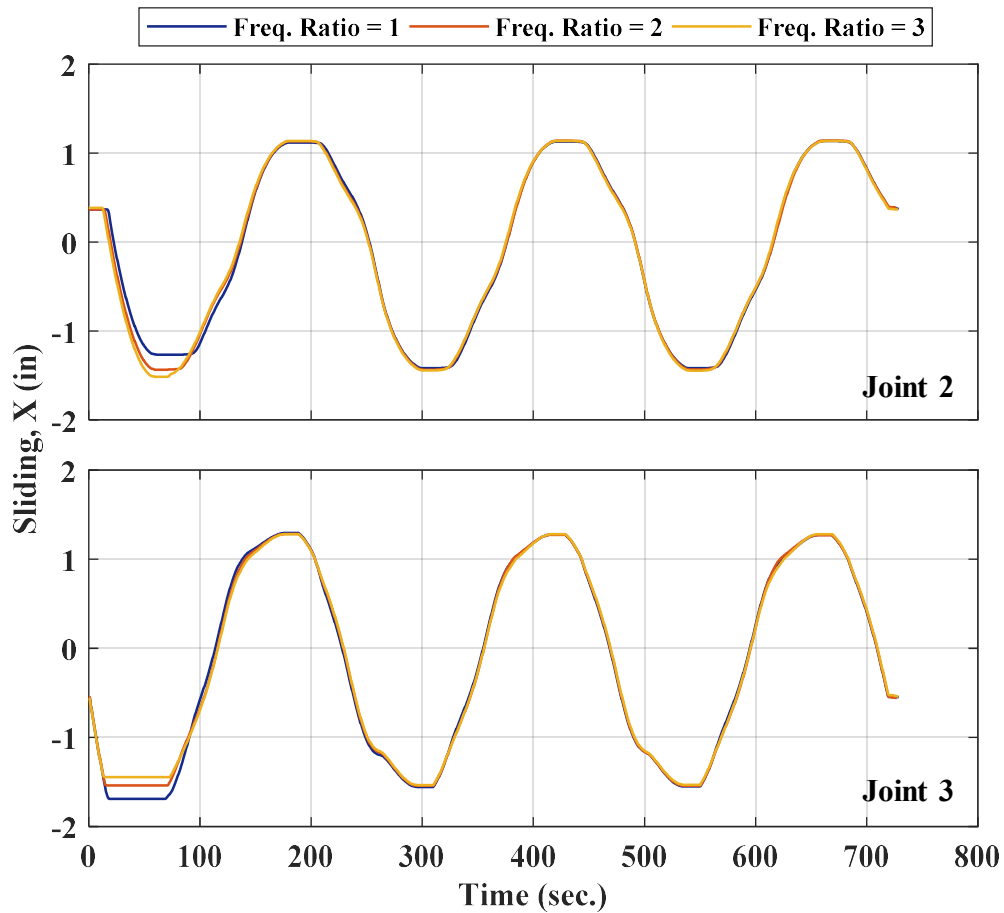
Figure 4-289. Phase III, Loading Set 2: time histories of joints sliding in *X* direction

As for the column damage, the three tests in Loading Set 2 resulted in the slight growth and appearance of a few hairline cracks on the bottom column segment.

4.7.3.5.4. Results from Loading Set 3

The column specimen's lateral force vs. displacement responses and the total posttensioning force vs. displacement responses obtained under single sinusoid displacement cycles with different maximum displacement rates (Table 4-41) are compared in Figure 4-290(a) and (b), respectively. According to Figure 4-290(a), the column's overall response did not considerably change with the increase of displacement

rate, even though slight changes due to the inertia effects are observed. The maximum posttensioning forces changed minimally, too (Figure 4-290(b)). In contrast, the posttensioning force variation with displacement seems to be more visibly affected by the displacement rate, implying the dependence of the tendon-duct friction on the velocity.
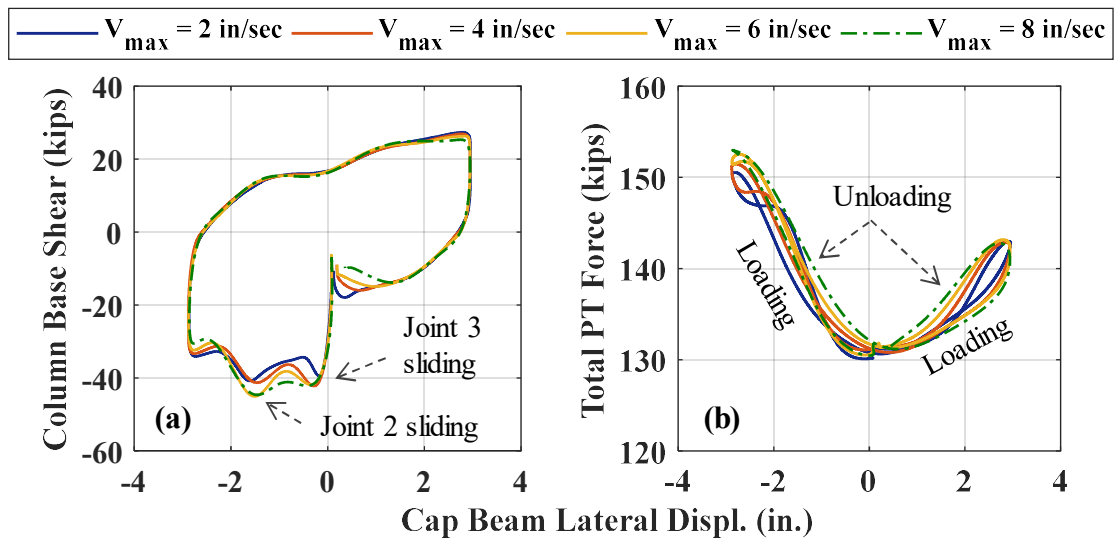
Figure 4-290. Phase III, Loading Set 3: (a) base shear vs. lateral displacement responses; (b) total posttensioning force vs. lateral displacement responses

The joint shear vs. sliding responses of the sliding joints (Joints 2 and 3) obtained from the same tests are demonstrated in Figure 4-291. As seen, regardless of the maximum displacement rate, the maximum sliding values obtained for each joint in the two directions were almost constant. It is also observed that, the joints returned to almost the same positions at the end of all tests, showing the repeatability of the column specimen's response. No further damage to the column specimen was observed after the three tests in Loading Set 3.
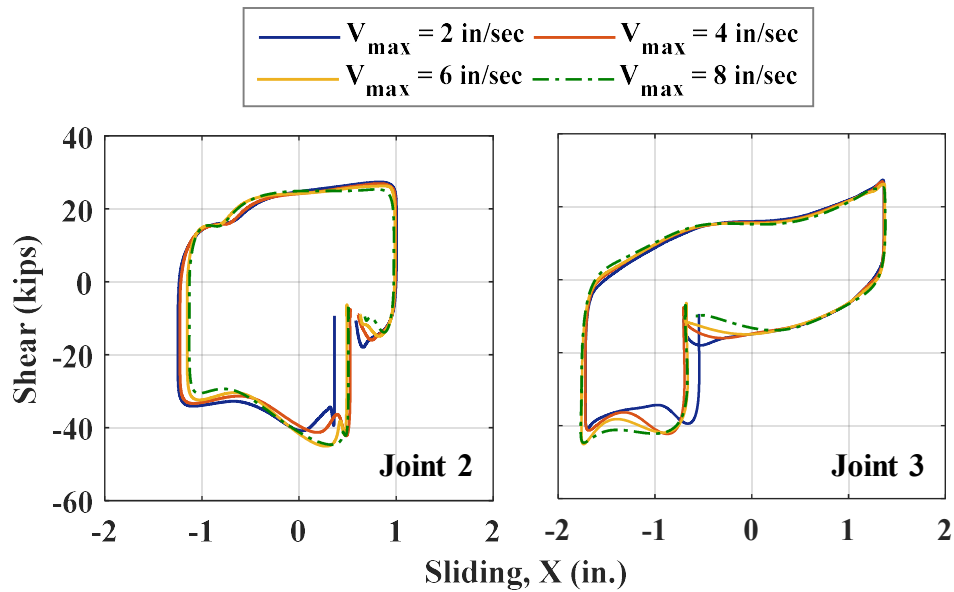
Figure 4-291. Phase III, Loading Set 3: joint shear vs. sliding responses of sliding joints

4.7.3.5.5. Results from Loading Set 4

The hysteretic force-displacement responses obtained from the four tests conducted under the loading protocols of Loading Set 4, which include earthquake-induced motions, are shown in Figure 4-292. In all tests, the column's response was dominated by sliding (Figure 4-293), although the second sliding joint (Joint 3) had the most contribution (Figure 4-294). This is because, in the majority of these tests, the peak lateral displacements were low enough not to make the first sliding joint (Joint 2) start sliding.

According to Figure 4-293, the joints' sliding closely followed the applied displacement time history, because the base shear required to create rocking motion at the end joints of the fixed-fixed column was much higher than that required to initate sliding at the sliding joints. Unlike the sliding joints in the cantilever column, which could not accommodate high-frequency low-amplitude displacement variation (Figure 4-111 and

477

Figure 4-112), the sliding joints of the fixed-fixed HSR column were found to be capable of doing that.
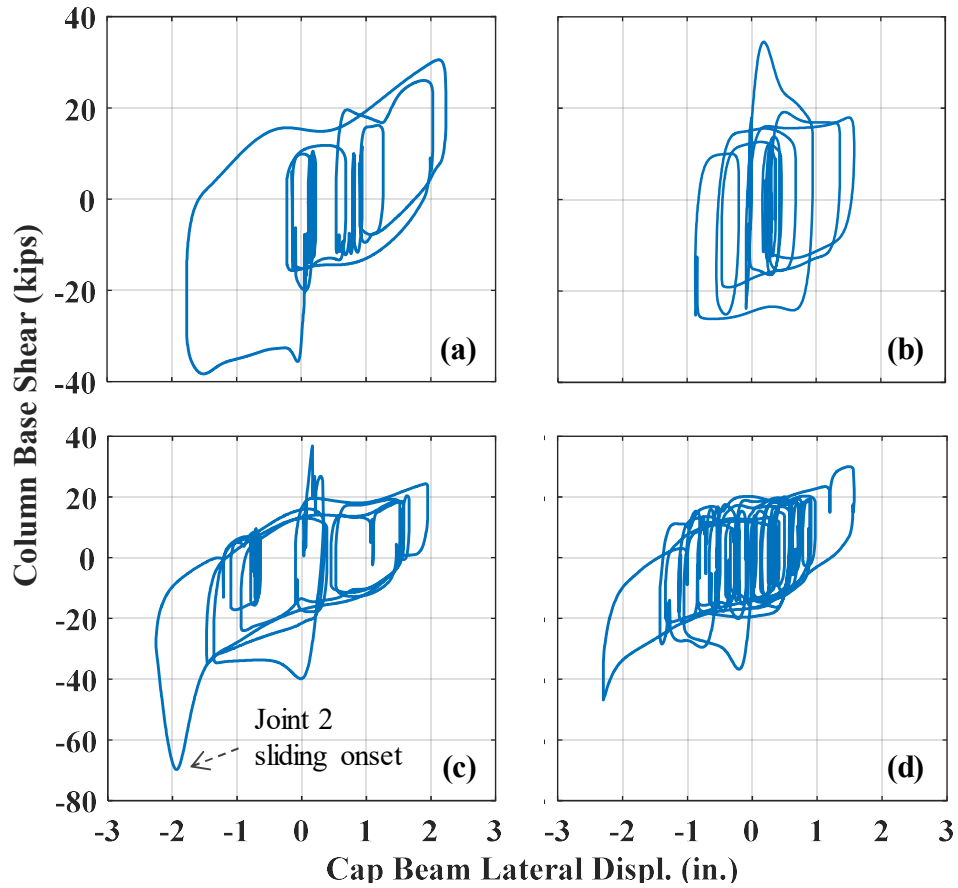
Figure 4-292. Phase III, Loading Set 4 – column base shear vs. lateral displacement responses obtained under: (a) HSR1_UN_FXD_S4_5in50_GM_7; (b) HSR1_UN_FXD_S4_5in50_GM_16; (c) HSR1_UN_FXD_S4_2in50_GM_9; (d) HSR1_UN_FXD_S4_2in50_GM_13
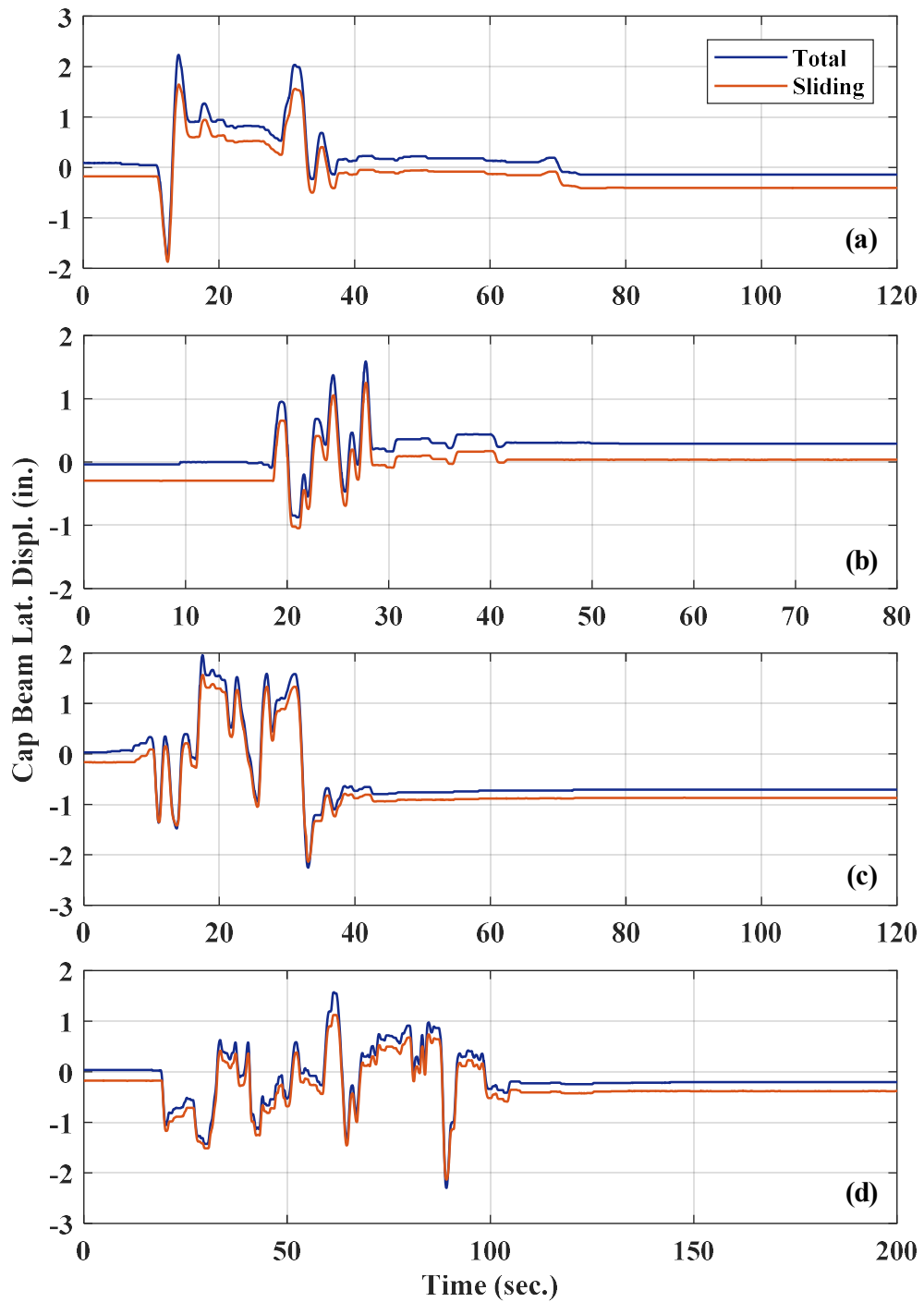
Figure 4-293. Phase III, Loading Set 4: lateral displacement and total sliding time histories obtained under HSR1_UN_FXD_S4_ (a) 5in50_GM_7; (b) 5in50_GM_16; (c) 2in50_GM_9; (d) 2in50_GM_13
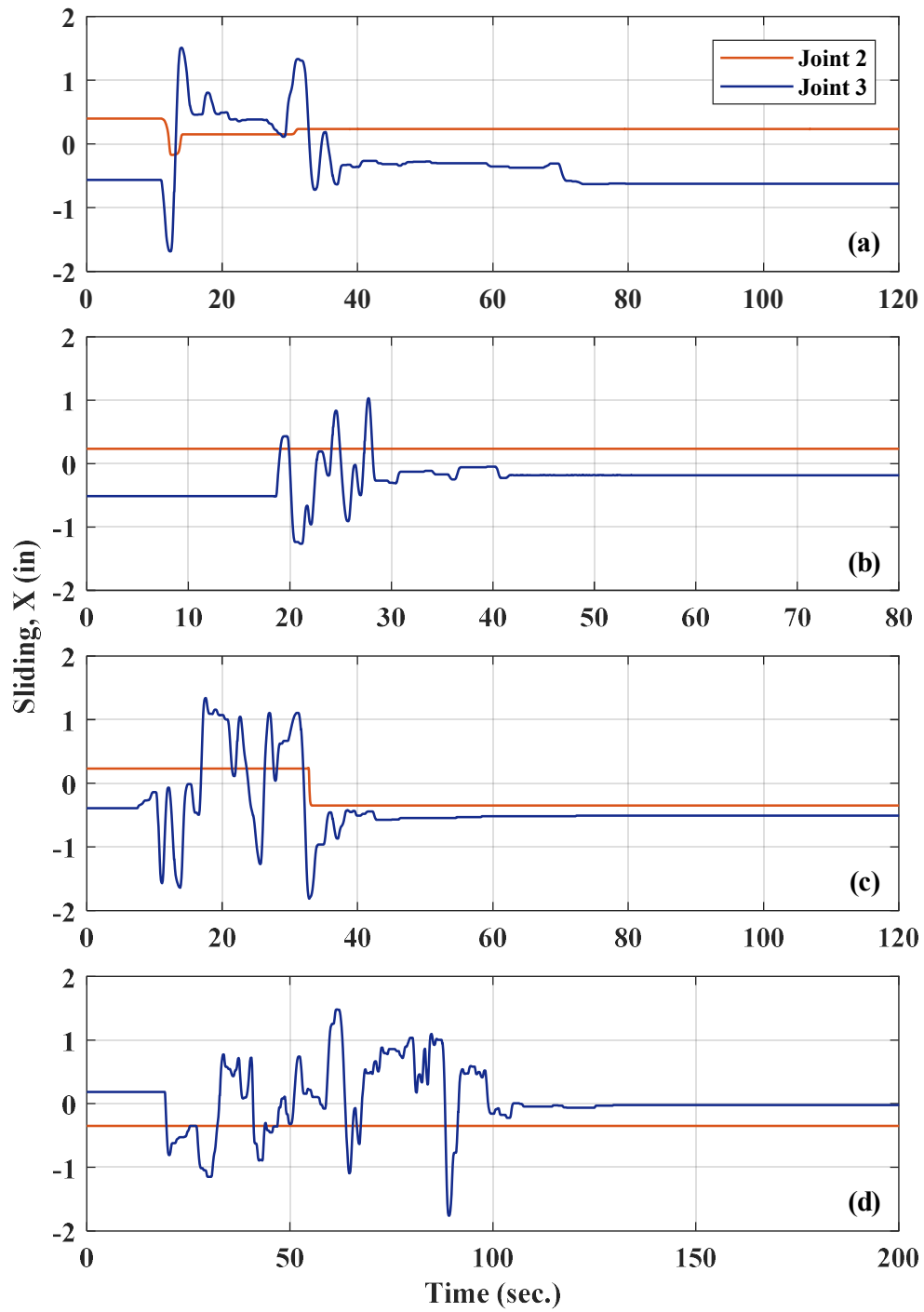
Figure 4-294. Phase III, Loading Set 4: joint sliding time histories obtained under HSR1_UN_FXD_S4_ (a) 5in50_GM_7; (b) 5in50_GM_16; (c) 2in50_GM_9; (d) 2in50_GM_13

According to Figure 4-295, more than 93% of the energy dissipated by the column specimen was through joint sliding, while less than 3% was contributed by the rocking joints. The very low contribution of the rocking joints to the total dissipated energy indicates the low damage at those joints.

No extra damage (e.g. cracks) occurred to the column during the tests under the four loading protocols in Loading Set 4.

4.7.3.5.6. Results from Loading Set 5

The column specimen's base shear vs. lateral displacement response under the first loading protocol in Loading Set 5, i.e. HSR1_UN_FXD_S5_DR_4, are shown in Figure 4-296(a). The extent of column's deformation under 4% drift ratio can be seen in Figure 4-298. Due to the sliding limitation, within a lateral displacement range of almost -4 in. to +4 in., the column's response was clearly governed by the sliding joints. Under larger displacements, however, more that 30% of lateral displacement was accommodated by rocking (Figure 4-297).

According to Figure 4-296(a), the maximum base shear resisted by the column while sliding at the joints continued was less than 40 kips, whereas it increased to about 120 kips (200% larger) with less than 2 in. increase in the displacement in both directions. Comparing the responses obtained under the first and the second displacement cycles, the column's rocking-induced hardening began at slightly larger displacements in the second cycle. This was resulted from the damage caused by the tendons' large bearing reactions on the duct adaptors and the adjacent concrete (see Figure 4-306 and Figure 4-307).
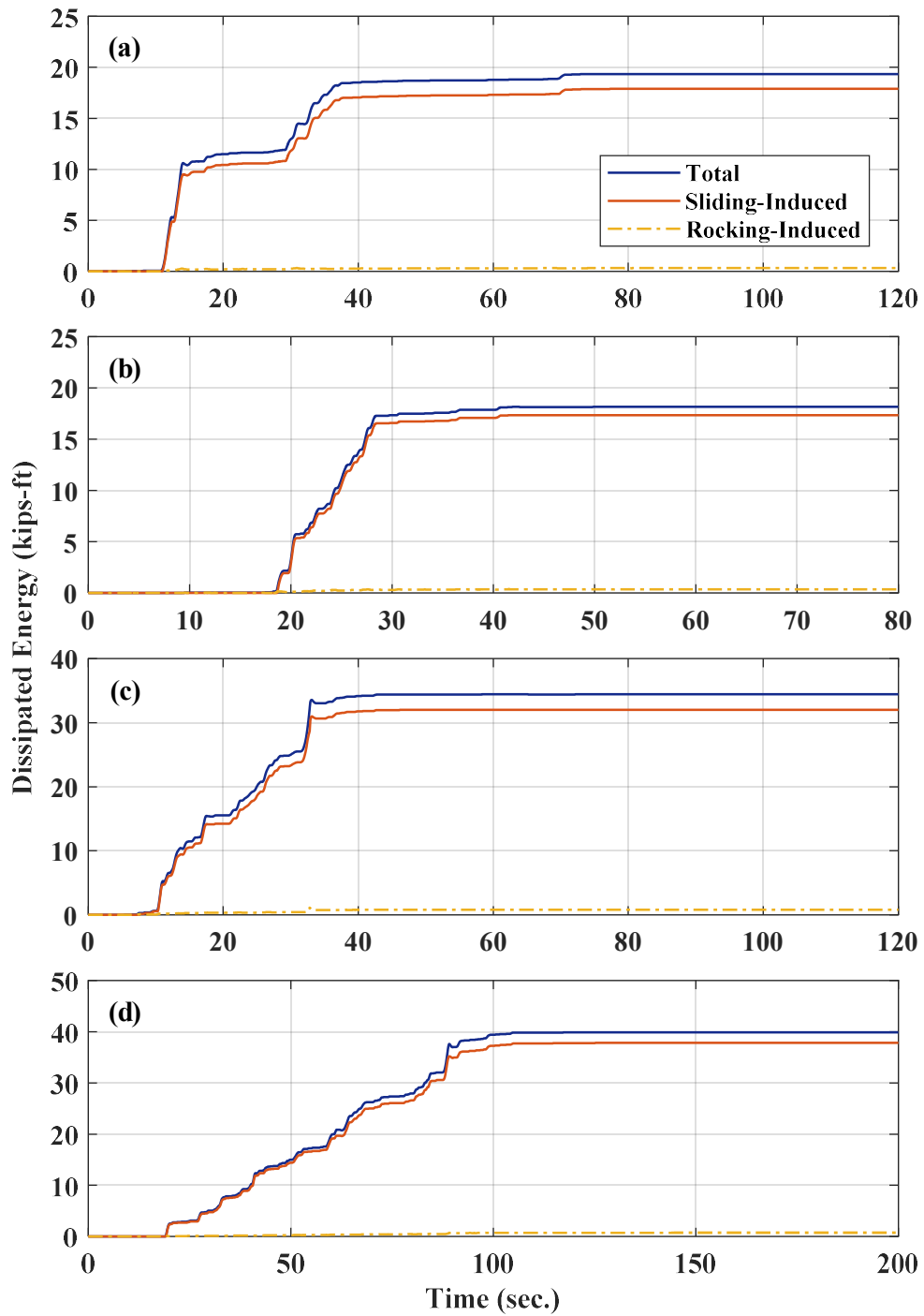
Figure 4-295. Phase III, Loading Set 4: dissipated energy time histories obtained under HSR1_UN_FXD_S4_ (a) 5in50_GM_7; (b) 5in50_GM_16; (c) 2in50_GM_9; (d) 2in50_GM_13

482
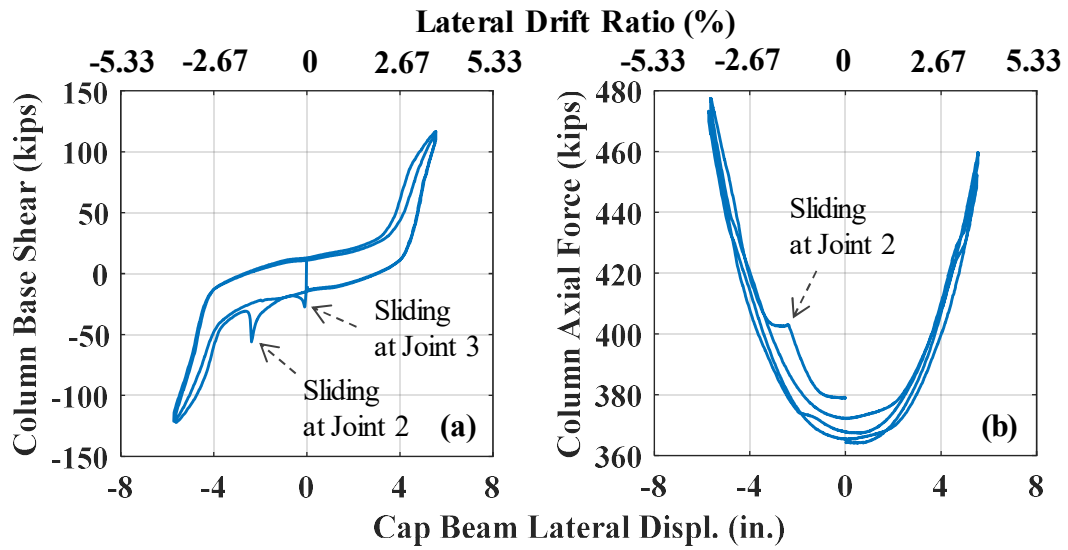
Figure 4-296. Phase III, loading protocol HSR1_UN_FXD_S5_DR_4: (a) column base shear vs. lateral displacement response; (b) column axial force vs. lateral displacement response
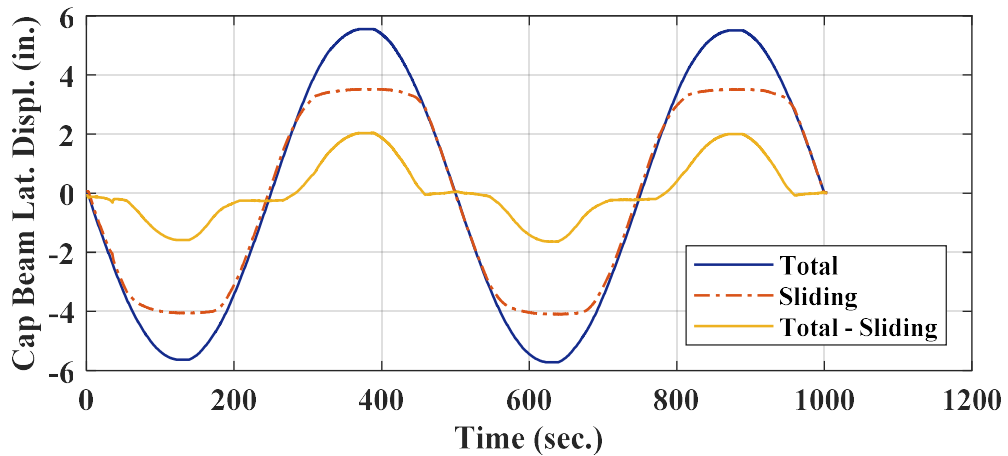
Figure 4-297. Phase III, loading protocol HSR1_UN_FXD_S5_DR_4: time histories of lateral displacement components

483
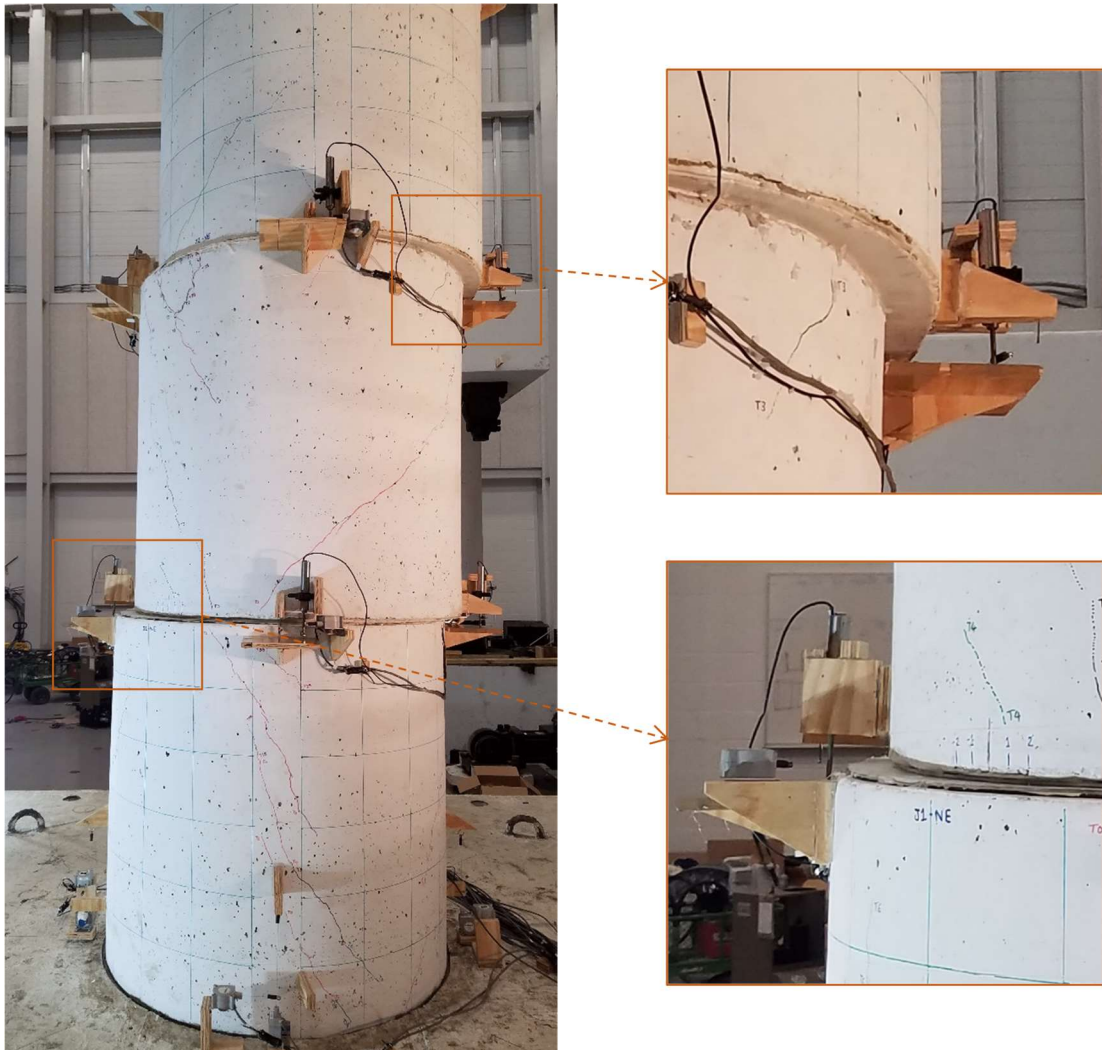
Figure 4-298. Phase III, loading protocol HSR1_UN_FXD_S5_DR_4: column deformation under drift ratio of 4%

Per Figure 4-296(a), the average residual displacement was less than 2.9 in. (less than 2% drift ratio), out of which about 95% was comprised by residual sliding (Figure 4-299). The effective damping ratio computed on the basis of the second force-displacement cycle was 7.3%, indicating the low energy dissipation capacity of the fixed-fixed HSR column when the incipient sliding base shear is much lower than the maximum load resistance of

the column. In addition, according to Figure 4-296(b), as long as joint sliding continued (i.e. for lateral displacements smaller than 4 in.), the increase in the column's axial force remained less than 15%. However, as the sliding joints reached their maximum sliding capacities, the axial force increased up to 30%.

The joints' shear vs. sliding responses are demonstrated in Figure 4-299. According to the results shown, similarly to the previous tests, the rocking joints (Joints 1 and 4) experienced negligible sliding. The maximum sliding at the sliding joints was 2 in. (0.55 in. larger than the nominal sliding capacity per joint, i.e. 1.45 in.). The difference observed between the values of the maximum sliding achieved in the two opposite directions is justified by the initial duct misalignments. The effects of the bearing-induced concrete damages in the east and west sides of Joint 2 and the east side of Joint 3 (see Figure 4-306 and Figure 4-307) on the response of the two sliding joints close to their sliding peaks are obvious.

Based on the sliding time histories presented in Figure 4-300, sliding initiated at Joint 3 (the upper sliding joint) and later propagated to Joint 2. It is also observed that there was a phase lag between the sliding responses, as they did not reach their peaks and reversal points at the same times and there were some pauses in the sliding of Joint 3 – because of sliding initiation at Joint 2, and probably in some cases, duct misalignments.

The moment vs. rocking responses of the bottom and top rocking joints (Joints 1 and 4, respectively) are demonstrated in Figure 4-301. As seen, the stiffness of Joint 1 against rotation was found to be lower than that of Joint 4, while it also exhibited slight cyclic deterioration. Given its bilinear shape, the moment-rotation response of Joint 4 was close

to the response of an ideal post-tensioned rocking rigid body, whereas Joint 1 had a more nonlinear response. This could be partly justified by the higher axial force present at the bottom joint compared to the top joint, as the column itself weighed about 7 kips. The moment at which both of these joints are predicted to have undergone separation (i.e. where the curve slope suddenly changes) is slightly more than 500 kip-ft.
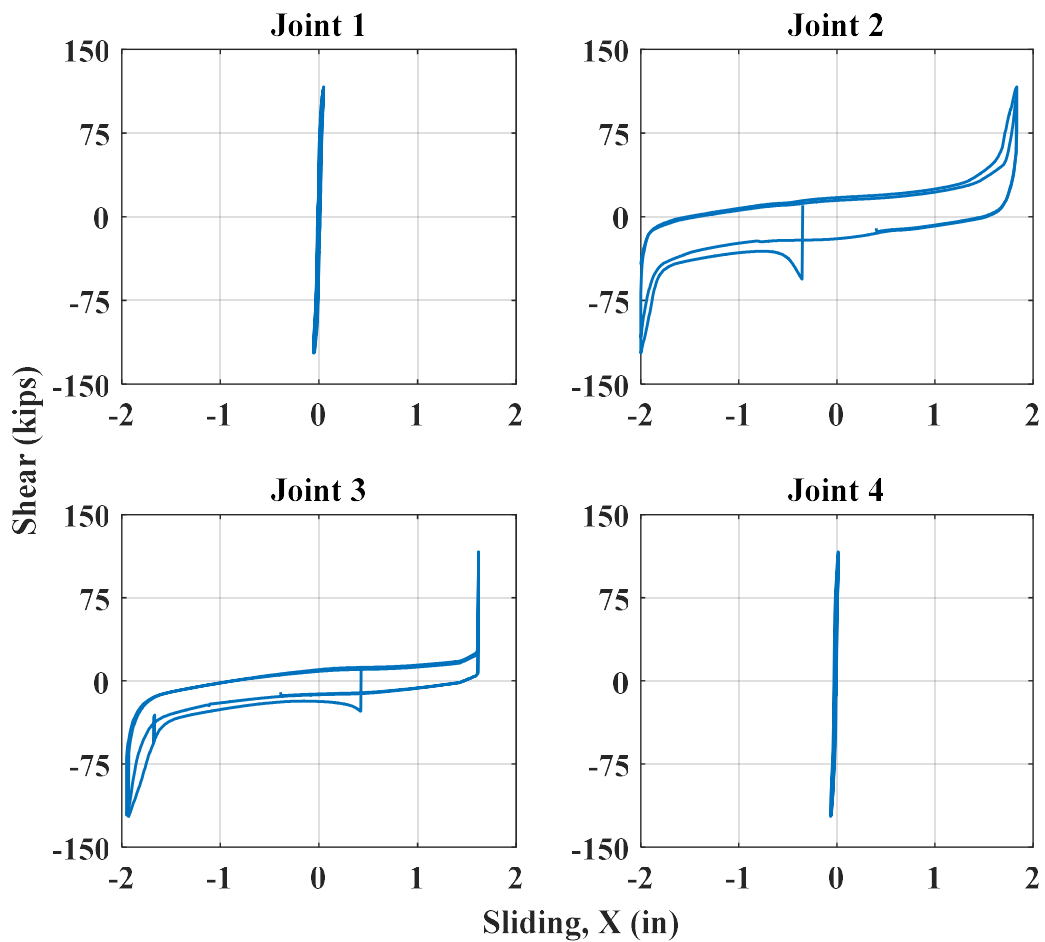
Figure 4-299. Phase III, loading protocol HSR1_UN_FXD_S5_DR_4: joint shear vs. sliding responses in *X* direction
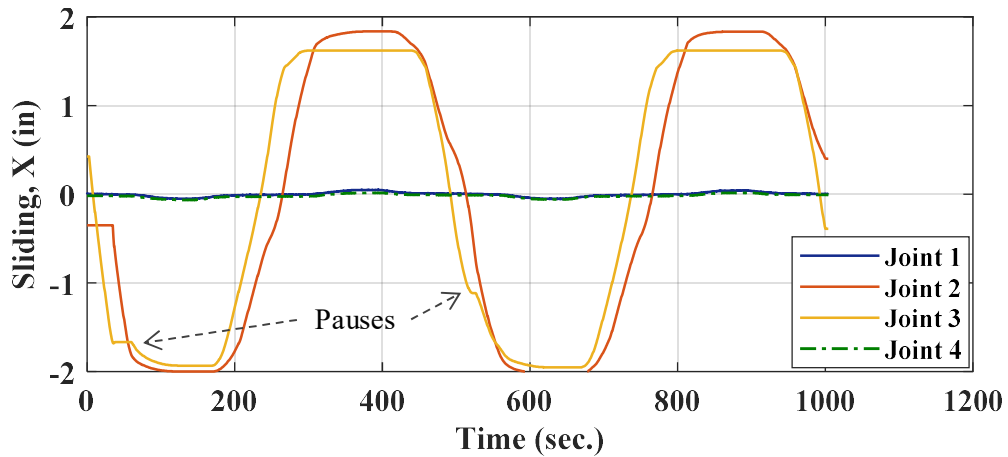
Figure 4-300. Phase III, loading protocol HSR1_UN_FXD_S5_DR_4: time histories of joint sliding in *X* direction
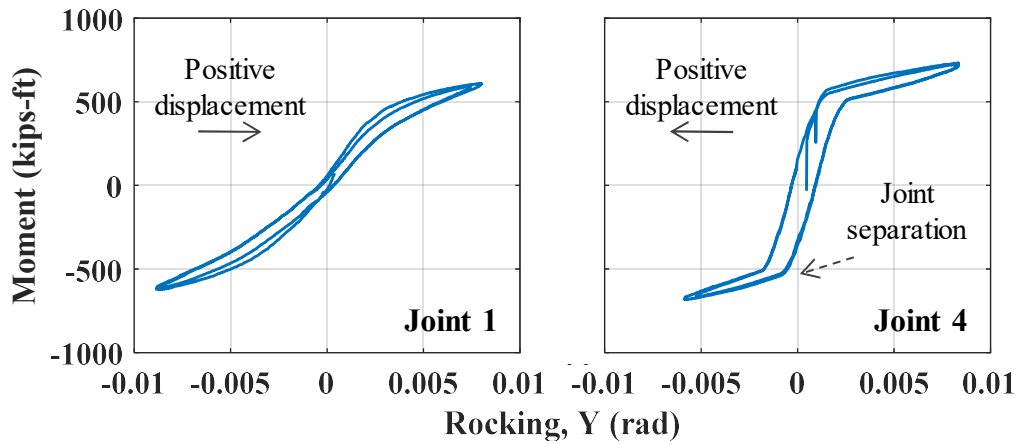
Figure 4-301. Phase III, loading protocol HSR1_UN_FXD_S5_DR_4: moment vs. sliding responses of rocking joints

According to Figure 4-302, the maximum force generated in the posttensiong tendons was about 34 kips, which is much smaller than their yield strength (i.e. about 53 kips). However, the total PT loss resulted through this test was about 12%, implying local yielding of the tendons in the vicinity of the sliding joints and slippage in their anchors. As seen in Figure 4-303, the larger posttensioning increase resulted under the negative

lateral displacement compared to that under the positive displacement may be associated with the duct misalignments, which could have caused higher elongation in the west, northwest, and southwest tendons when the column was pulled in the negative direction. Note that a very similar trend was observed in the previous tests' results (e.g. see Figure 4-281).
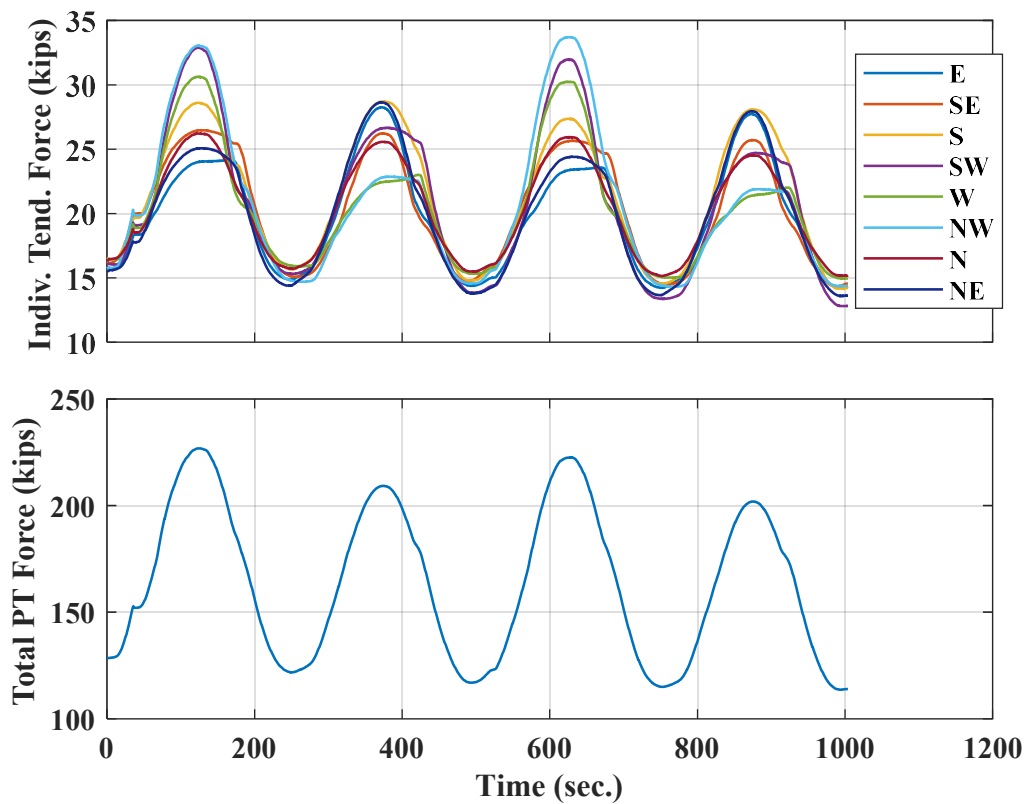
Figure 4-302. Phase III, loading protocol HSR1_UN_FXD_S5_DR_4: time histories of posttensioning forces
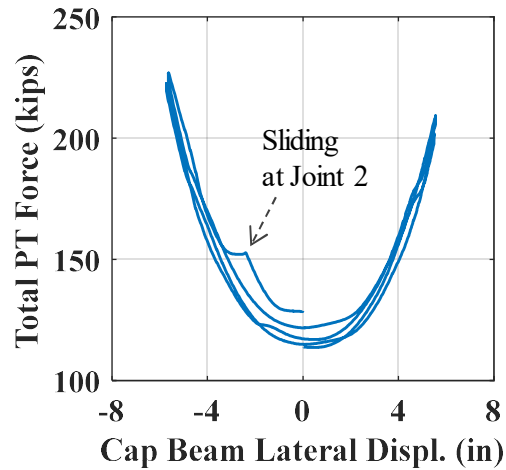
Figure 4-303. Phase III, loading protocol HSR1_UN_FXD_S5_DR_4: total PT force vs. lateral displacement

The condition of the east and west sides of the column specimen (facing the positive and negative displacement directions, respectively) after the test are shown in Figure 4-304 and Figure 4-305, respectively. The major damage observed outside the column was the concrete cone failures primarily caused by the tendon bearing reactions on the duct adaptors close to the east and west sides of the sliding joints and also the normal stress concetrations during rocking. Specifically, on the east side (Figure 4-306), these failures occurred adjacent to east duct adaptor below Joint 2 as well as adjacent to the east and northeast duct adaptors below Joint 3, whereas on the west side (Figure 4-307), they occurred adjacent to the west duct adaptor below Joint 2 and adjacent to the west duct adaptor above Joint 3. As seen in the close-up photos, the concrete cones were pushed out due to the tendon bearing reactions on the edges of the duct adaptors. The heights and widths of the failure planes reached 12 in. and 8 in., respectively. It is noted that, even though the cone failures happened during the first displacement cycle, the separated

489

concrete cones fell off near the second two displacement peaks. The new cracks that appeared on the surfaces of the column segments during this test were only a few diagonal hairline cracks.
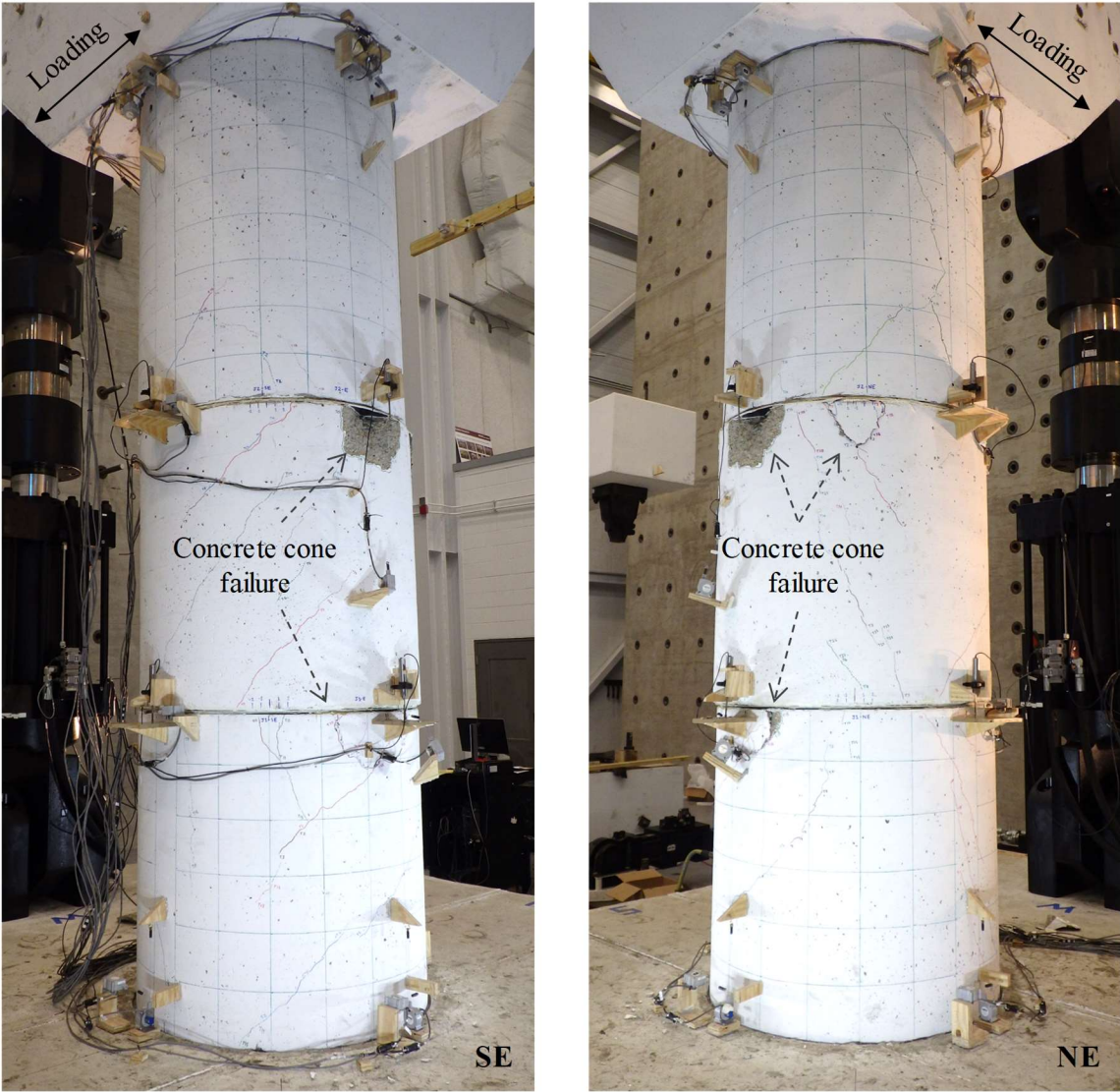
Figure 4-304. Phase III, loading protocol HSR1_UN_FXD_S5_DR_4: condition of east side of column specimen after test
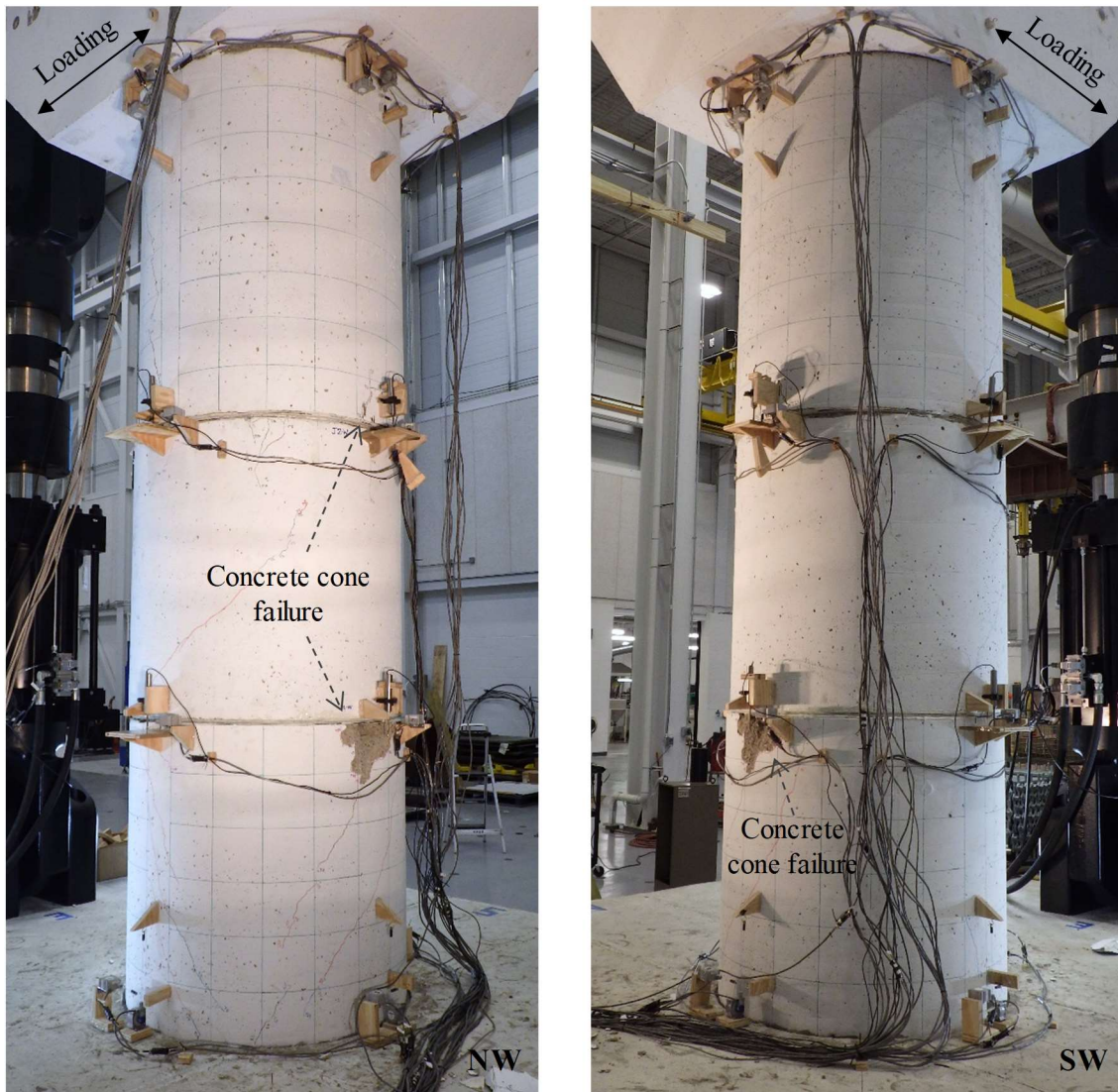
Figure 4-305. Phase III, loading protocol HSR1_UN_FXD_S5_DR_4: condition of west side of column specimen after test

(Joint 2 - E)

(Joint 3 – NE)

Steel plate

Duct adaptor

J2-NE
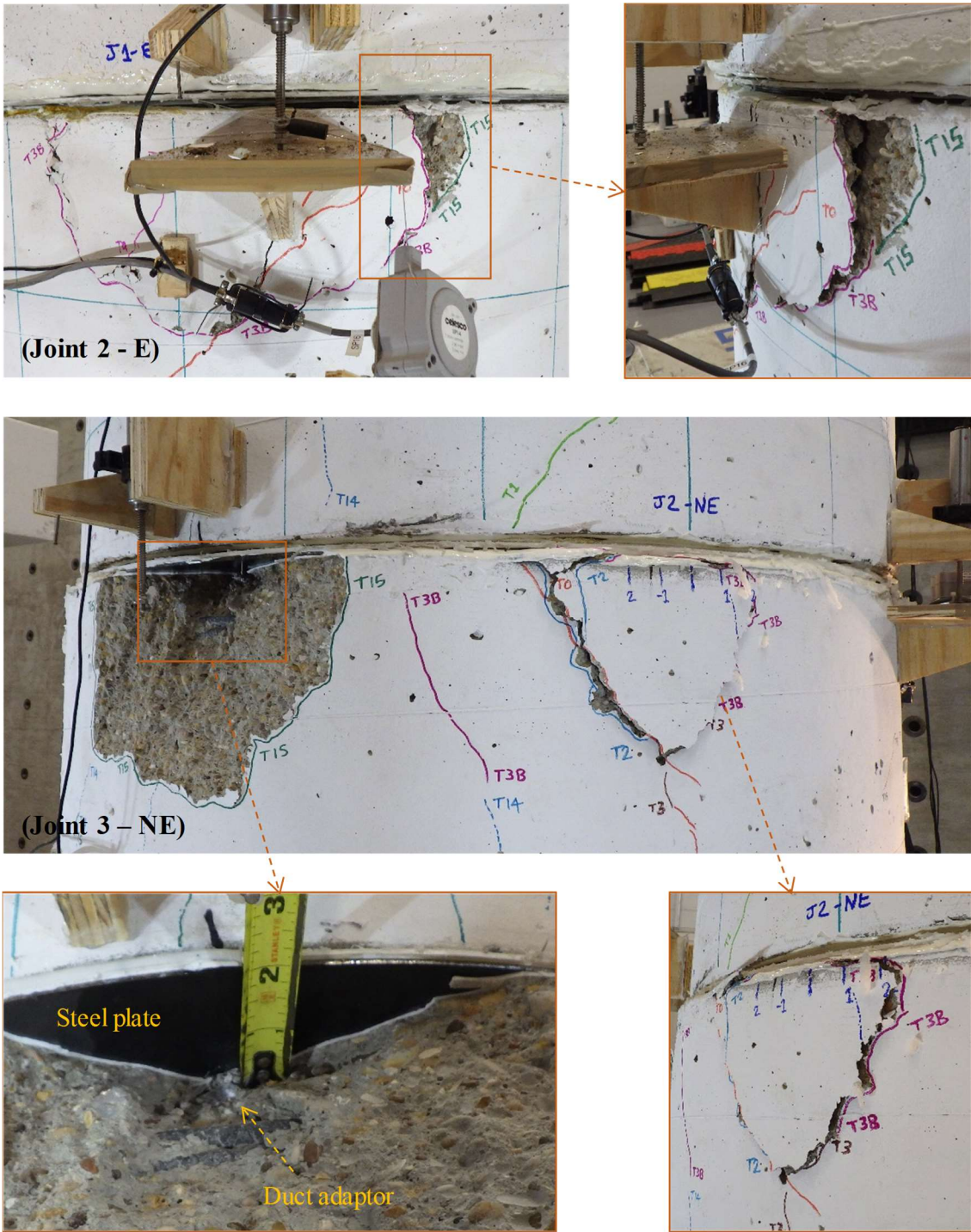
Figure 4-306. Phase III, loading protocol HSR1_UN_FXD_S5_DR_4: concrete damage adjacent to sliding joints, east side of column
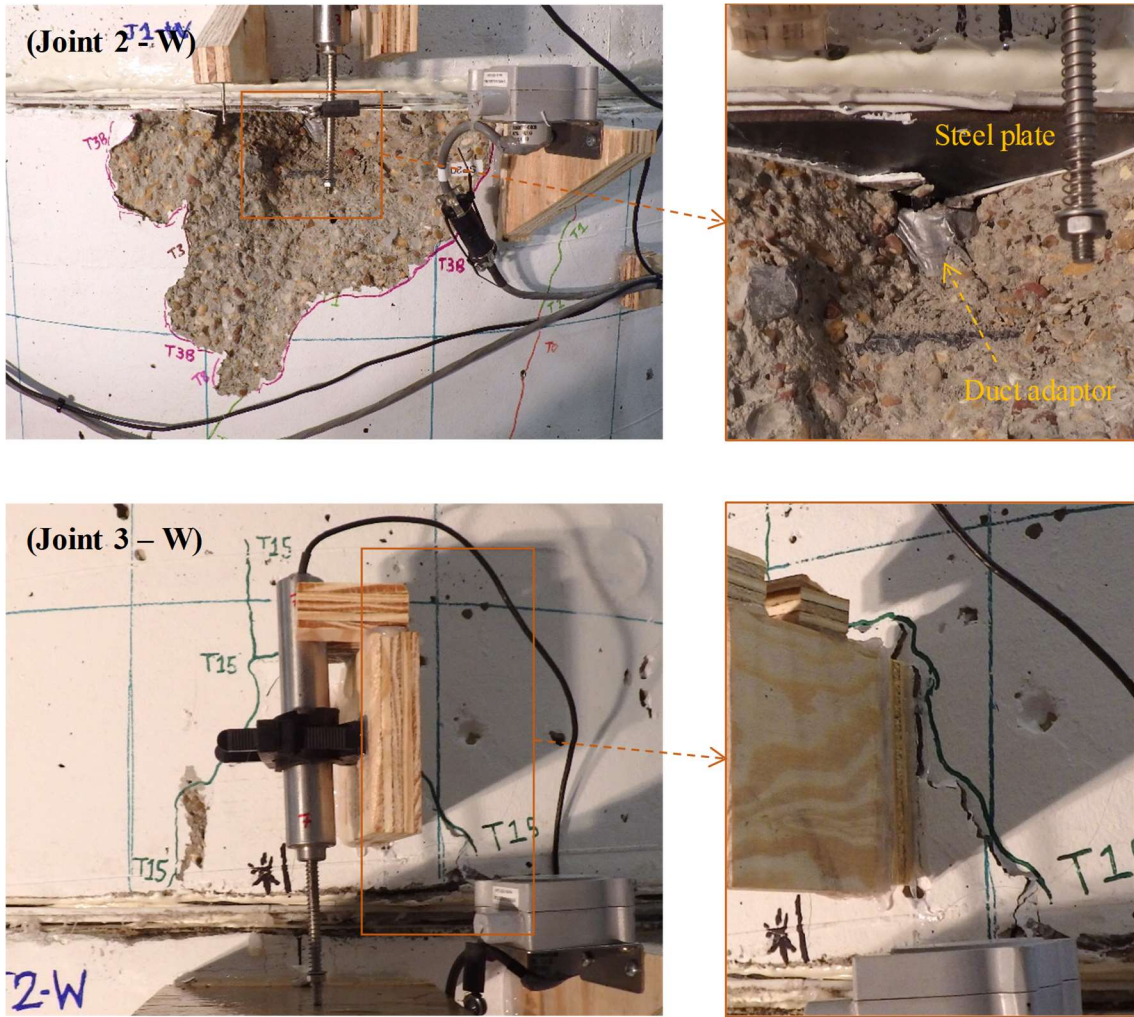
Figure 4-307. Phase III, loading protocol HSR1_UN_FXD_S5_DR_4: concrete damage adjacent to sliding joints, west side of column

The column specimen's lateral force-displacement response obtained during the last test in Phase III (under loading protocol HSR1_UN_FXD_S5_DR_6) with a peak drift ratio of 6% is shown in Figure 4-308(a). During this test, because of the rotational sliding caused at sliding joints by construction imperfections and duct misalignments as well as the tendons' unequal PT forces, the column experienced significant twist (up to 0.09 rad) under positive lateral displacement (see Figure 4-309(b)). Note that when the lateral

displacement was negative, the horizontal actuator pulled the loading beam toward the reaction wall, so almost no accidental twist was generated in the respective time intervals. The accidental twist, which is somewhat observable in a photo taken at the second positive peak displacement of this test (Figure 4-310), did not allow the positive peak displacement values to reach their target value, i.e. 9 in., thereby creating an asymmetry in the column specimen's hysteretic response (Figure 4-308(a)).
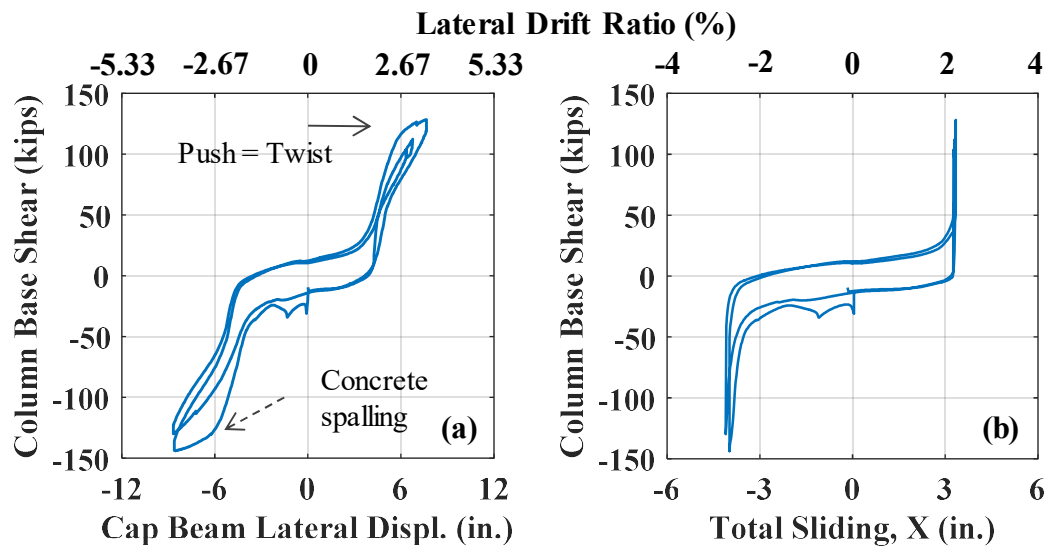
Figure 4-308. Phase III, loading protocol HSR1_UN_FXD_S5_DR_6: (a) column base shear vs. lateral displacement response; (b) column base shear vs. total sliding

Mainly because of the concrete spalling adjacent to the compression toes of the bottom and top segments (see Figure 4-317 and Figure 4-318), the column exhibited in-cycle and cyclic deterioration at the lateral displacements close to 6 in. (equivalent to 4% drift ratio). The maximum base shear resisted by the column in the negative direction was about 144 kips, while it was lower in the positive direction because of the loading beam's

494

twist. The average residual displacement and drift ratio were 3.75 in. and 2.5%, respectively, nearly 85% of which was caused by residual sliding (Figure 4-308(b)).
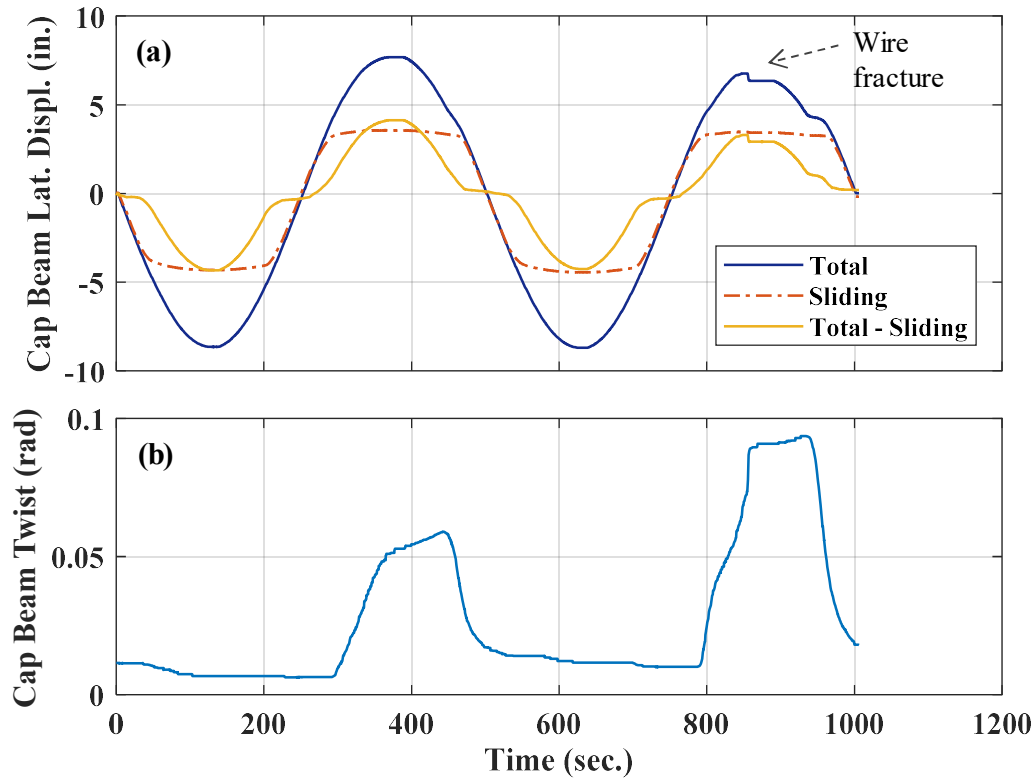
Figure 4-309. Phase III, loading protocol HSR1_UN_FXD_S5_DR_6: (a) time histories of lateral displacement components; (b) loading beam's twist time history

According to Figure 4-309(a), during this test, the joint sliding and all other mechanisms accommodated almost equal fractions of the maximum lateral displacement imposed to the column specimen. Comparing the time histories of the total sliding and the loading beam's twist (Figure 4-309(b)), it can be deduced that the loading beam's twist increased when the joint sliding in the positive X direction stopped. Moreover, the fracture

of two wires from the southwest strand during the second half-cycle (Figure 4-314) led to an increase in the twist observed in the last half-cycle.
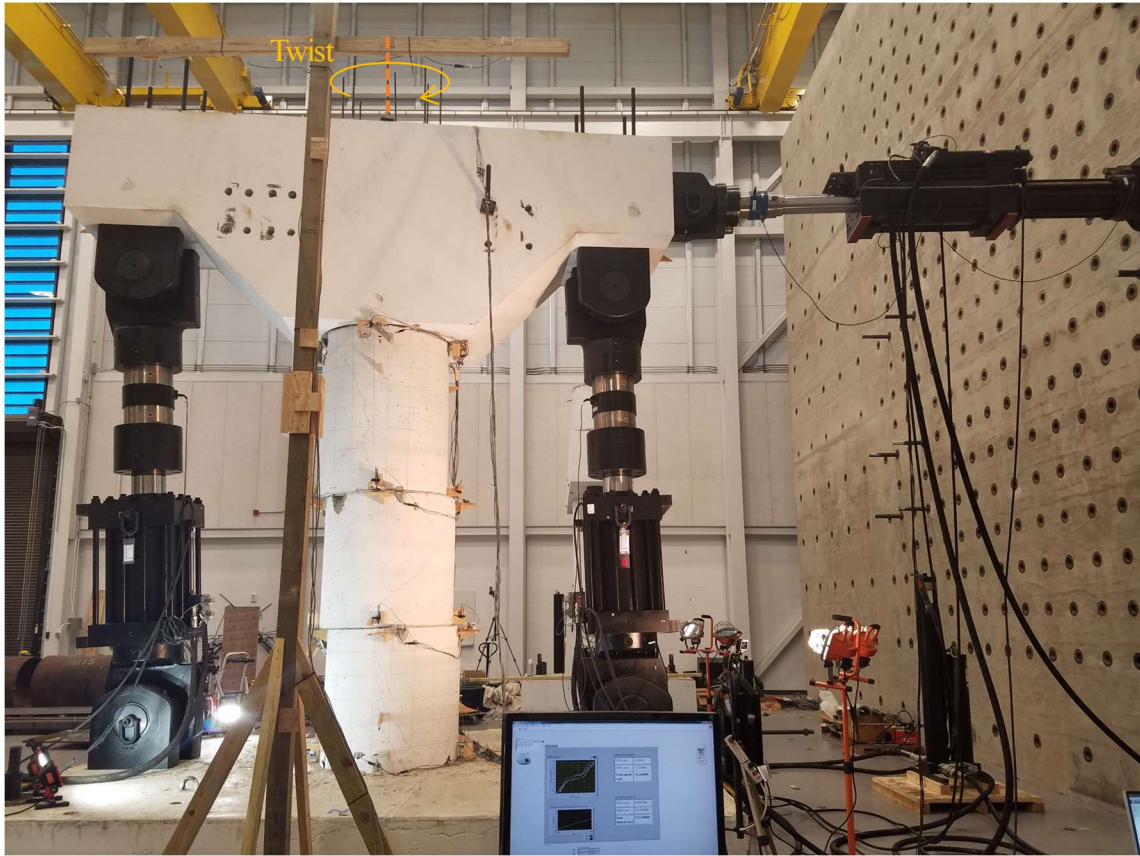
Figure 4-310. Phase III, loading protocol HSR1_UN_FXD_S5_DR_6: loading beam's accidental twist under peak positive lateral displacement

The joints' shear-sliding responses are demonstrated in Figure 4-311 and the sliding time histories of the joints are compared in Figure 4-312. As opposed to the previous tests, during this test, the rocking joints exhibited very small sliding (less than 0.2 in. in each direction) – part of the computed values could be due to rocking-induced measurement errors, though. The shear-sliding responses of the sliding joints also show signs of damage

to the duct adaptors, particularly on the west side of Joint 3, which were verified in the damage inspection following the test (see Figure 4-319 thru Figure 4-321) and after the column disassembly (see Section 4.7.3.6).
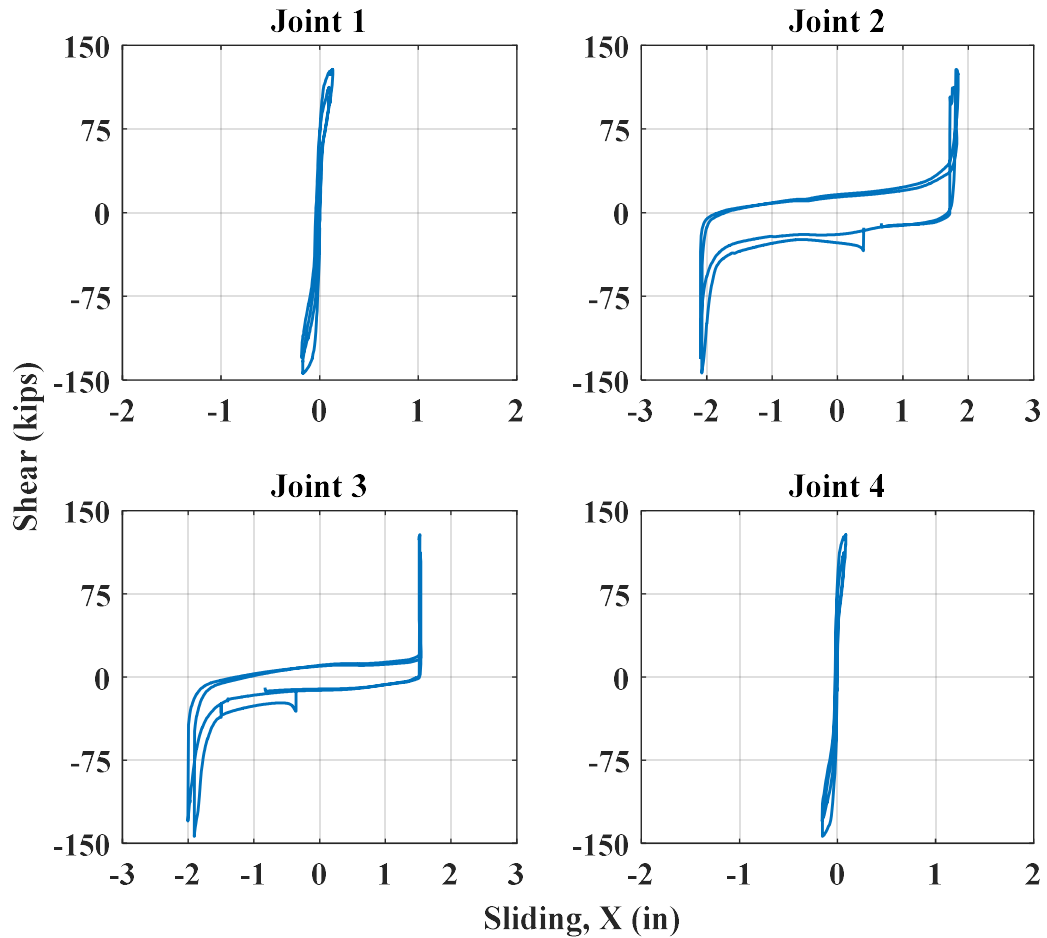
Figure 4-311. Phase III, loading protocol HSR1_UN_FXD_S5_DR_6: joint shear vs. sliding responses

The moment vs. rocking responses of the rocking joints are displayed in Figure 4-313. The maximum rocking achieved at both bottom and top rocking joints at the negative peak displacement was 0.03 rad, while at the positive peak displacement (which was lower than

the negative one because of the loading beam's twist), this value was lower (about 0.025 rad). Consistently with the rocking measurements, the maximum moment computed for the bottom rocking joint (Joint 1) was 750 kip-ft and it occurred when the column was pulled in the negative X direction. The maximum moment computed for the top rocking joint was, however, about 900 kip-ft, which also occurred when the first negative displacement peak was reached. The concrete spalling at both rocking joints (Figure 4-317 and Figure 4-318), however, significantly reduced their moment strengths during the second displacement cycle.
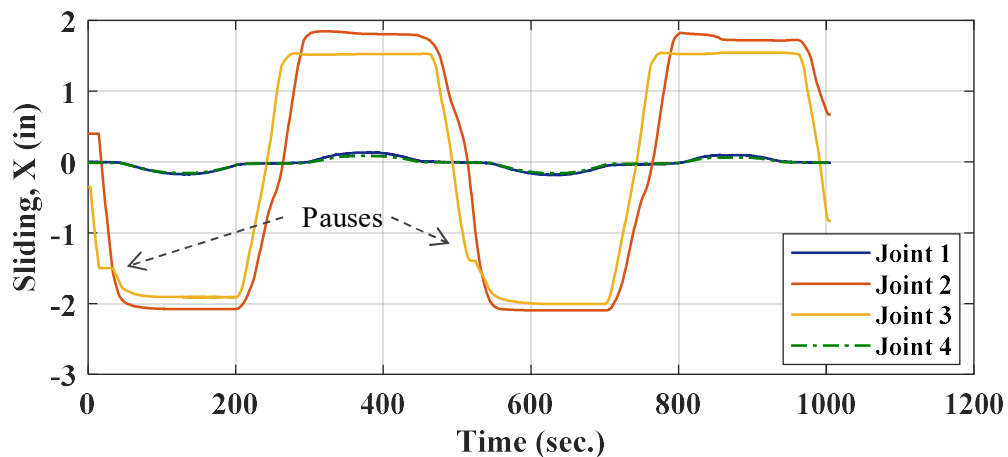
Figure 4-312. Phase III, loading protocol HSR1_UN_FXD_S5_DR_6: time histories of joint sliding in X direction
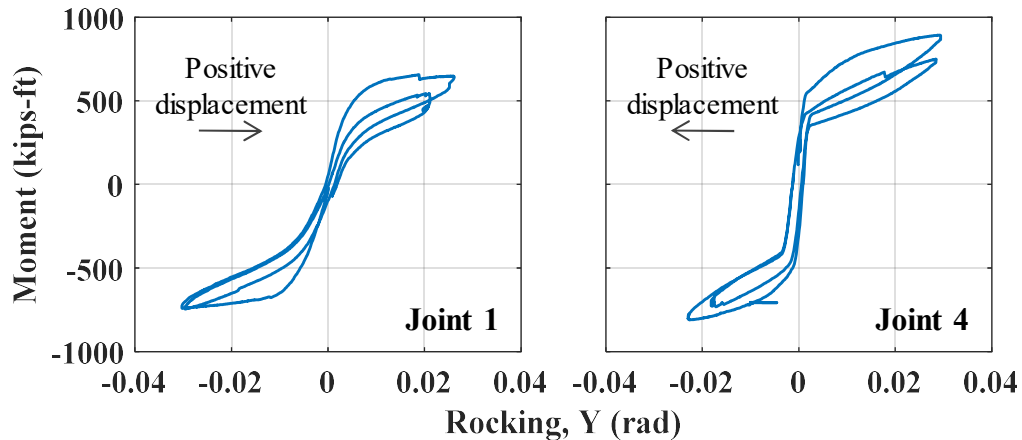
Figure 4-313. Phase III, loading protocol HSR1_UN_FXD_S5_DR_6: moment vs. sliding responses of rocking joints

The time histories of the tendon forces recorded during this test are shown in Figure 4-314. According to the individual tendon force time histories, the maximum measured tendon force, i.e. 51 kips, belonged to the southwest and northwest strands. While it is less than the nominal yield strength of the tendons (~53 kips), this force could potentially have caused yielding in parts of these tendons. Other tendons could also have experienced local yielding along their lengths, especially due to their bending at the locations where they came in contact with the duct edges (i.e. adjacent to the sliding joints).

It is also observed in Figure 4-314 that a total of nine wires fractured in this test, four from the southwest strand, one wire from the west strand, and four from the south strand (see Figure 4-328). The locations of all the wire fractures coincided with the top ends of the duct adaptors above the second sliding joint (Joint 3) and none of the wires fractured under the first displacement peak, even though the total PT force became maximum at that displacement peak. These facts imply that the wire fractures were mainly caused by the local yielding and the low-cycle fatigue of the strand wires due to their bending. As a

result of the wire fractures and yielding of the strands, the total PT loss in this test was about 49% – the final total posttensioning load was only 58 kips.
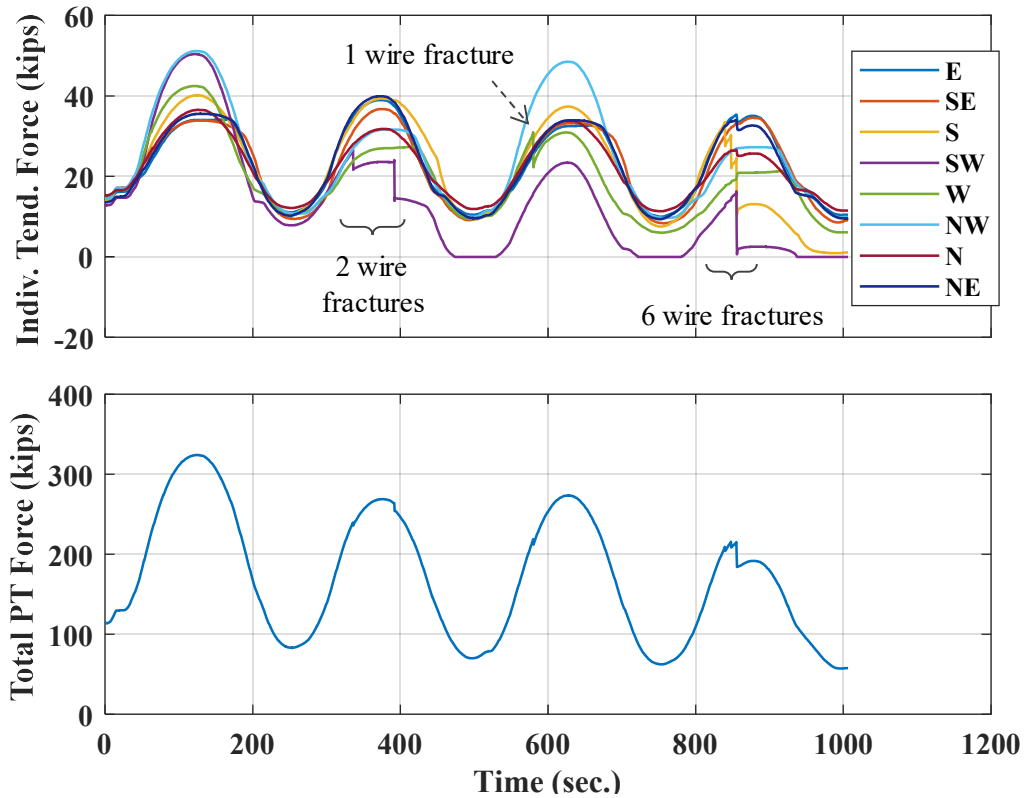
Figure 4-314. Phase III, loading protocol HSR1_UN_FXD_S5_DR_6: time histories of posttensioning forces

The last test resulted in many cracks, major concrete spalling close to the rocking joints, as well as new concrete cone failures adjacent to the sliding joints (Figure 4-315 and Figure 4-316). The cracks were mostly vertical (compressive cracks) and appeared on the bottom and top segments. The concrete spalling near the rocking joints initiated during the first cycle, when the loading beam was displaced close to 9 in. (i.e. 6% drift ratio), and it slightly grew during the second cycle.
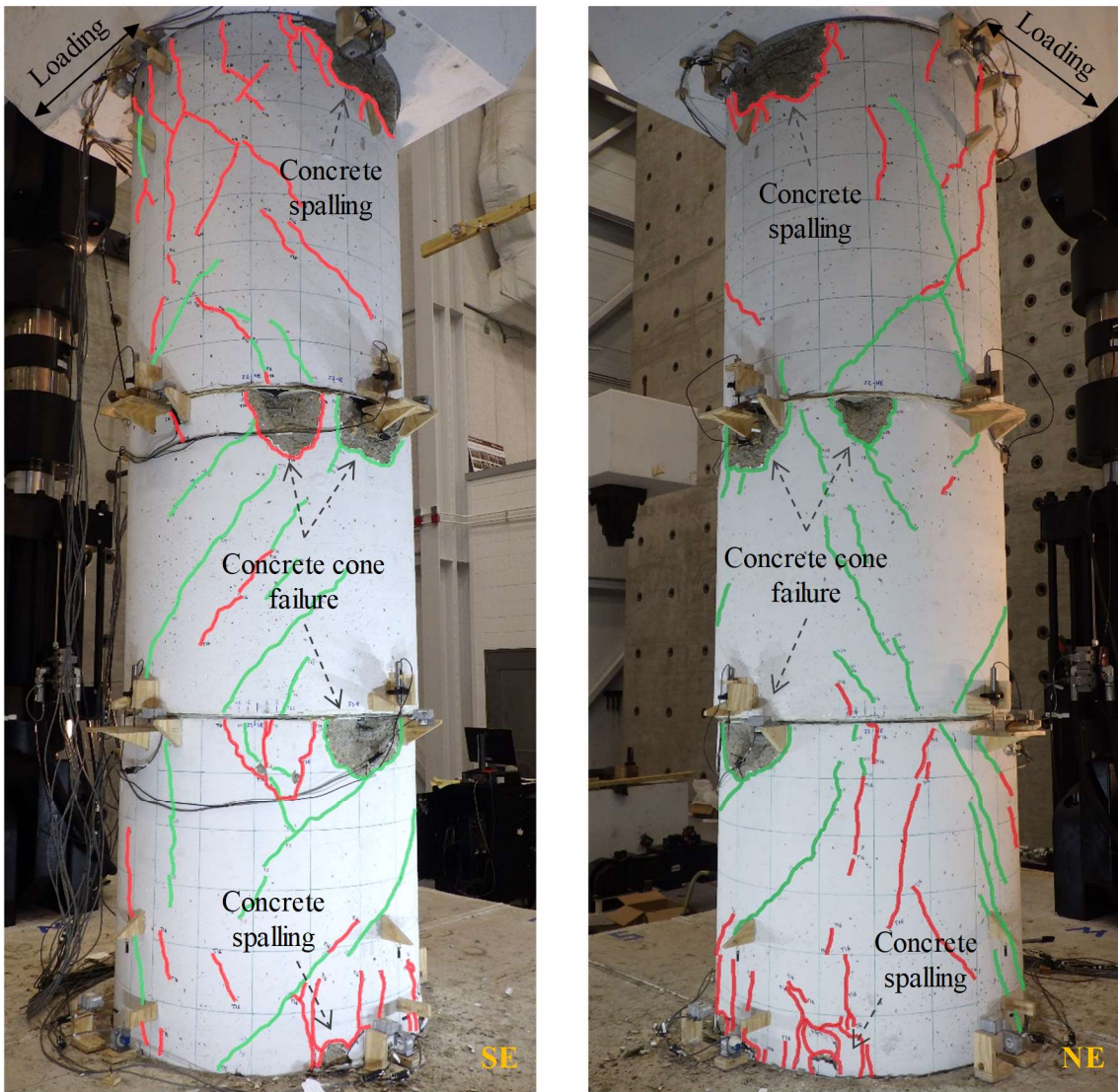
Figure 4-315. Phase III, loading protocol HSR1_UN_FXD_S5_DR_6: condition of east side of column specimen after test
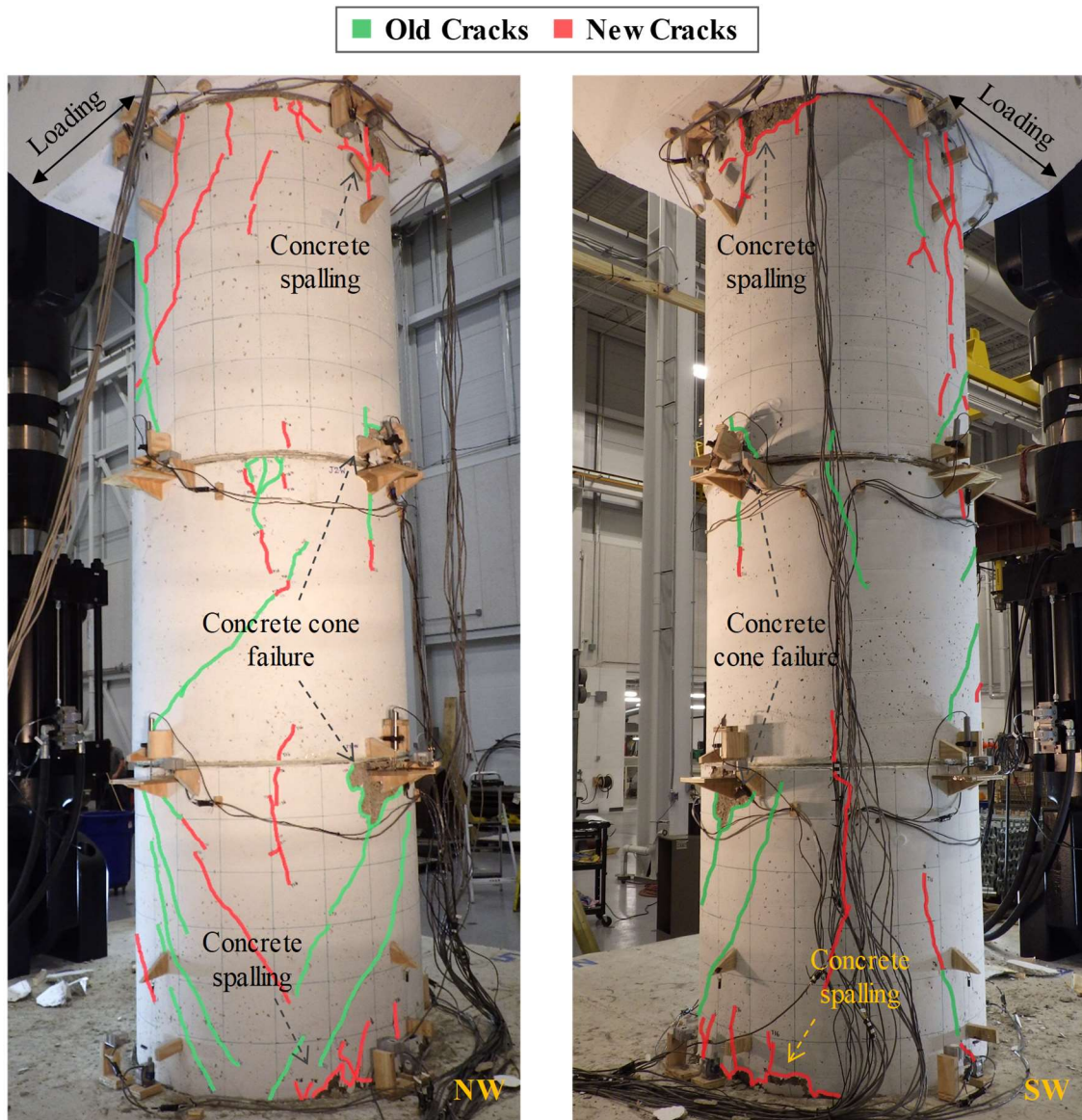
Figure 4-316. Phase III, loading protocol HSR1_UN_FXD_S5_DR_6: condition of west side of column specimen after test

According to Figure 4-317 and Figure 4-318, concrete spalling near the top rocking joint was more significant and spread by 10 in. from the joint, whereas the concrete spalling near the bottom rocking joint extended only up to 6 in. Due to the higher moment imposed to the top rocking joint than the bottom one (Figure 4-313), the concrete spalling

near the top joint was deep enough to expose the transverse reinforcement, as opposed to the spalling near the bottom joint, which was relatively shallow.
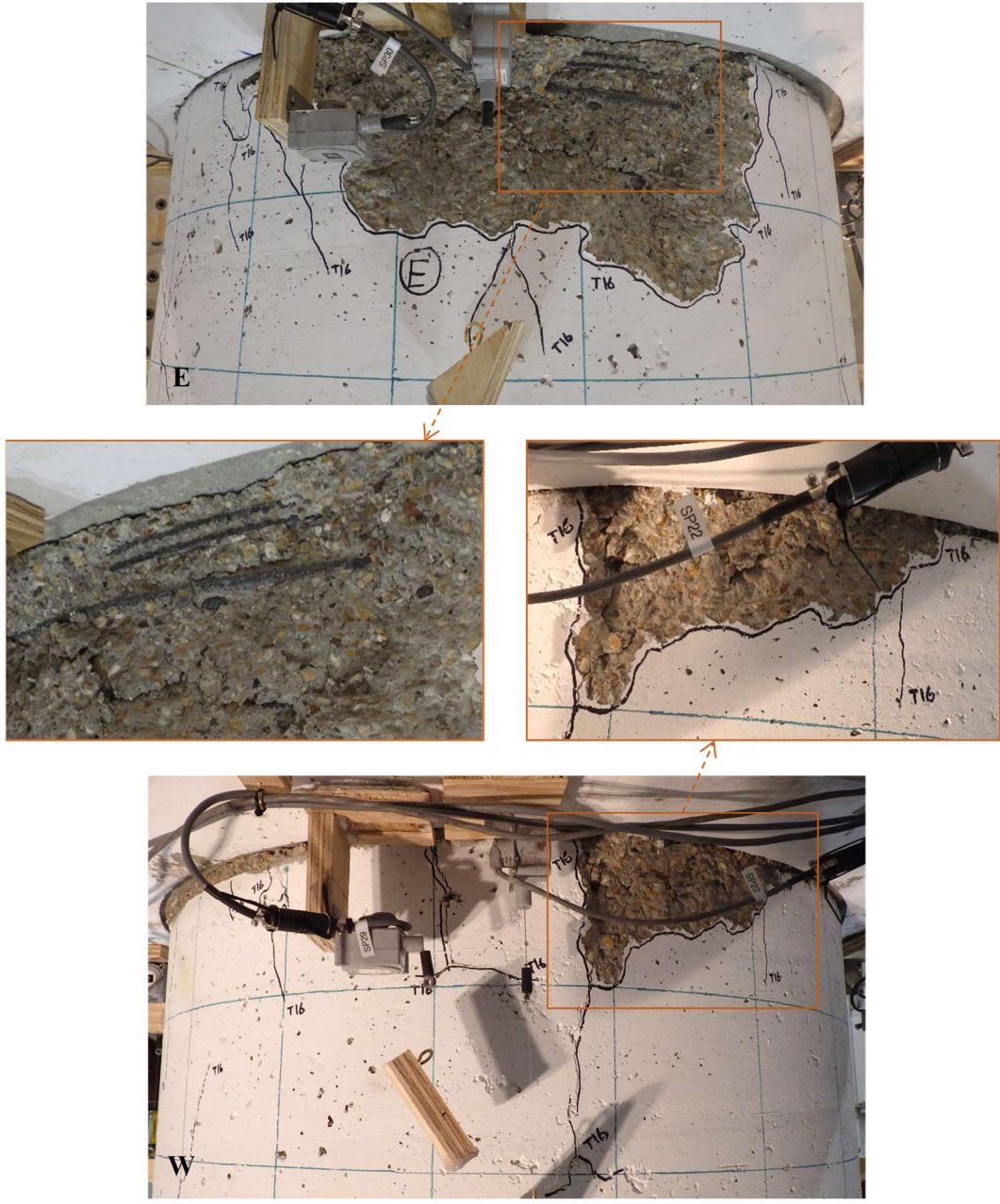
Figure 4-317. Phase III, loading protocol HSR1_UN_FXD_S5_DR_6: concrete damage near top rocking joint
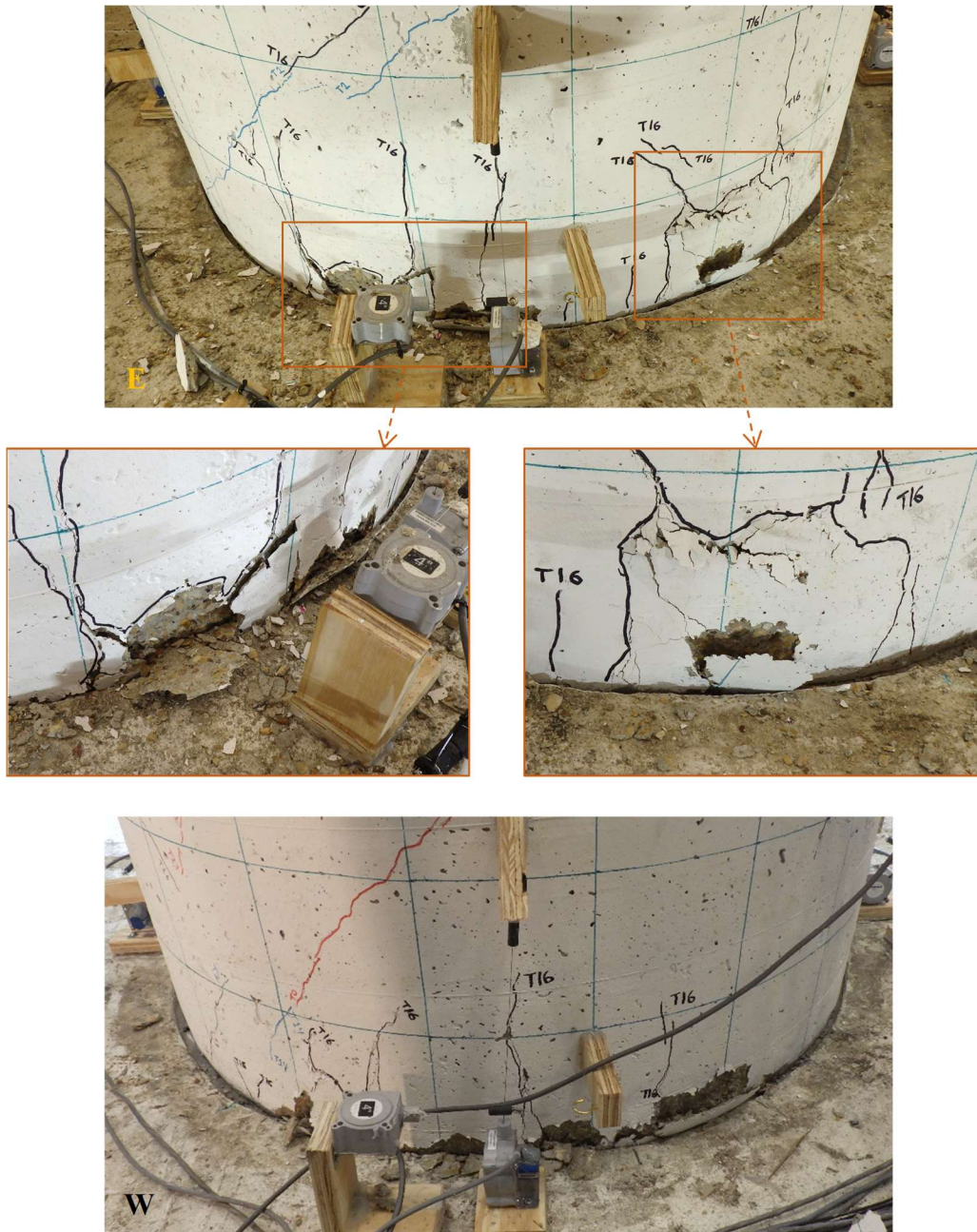
Figure 4-318. Phase III, loading protocol HSR1_UN_FXD_S5_DR_6: concrete damage near bottom rocking joint

As seen in Figure 4-319, Figure 4-320, and Figure 4-321, the new concrete cone

failures due to the bearing of the tendons occurred near the southeast duct adaptors below

504

the two sliding joints (Joints 2 and 3). Close to the duct adaptors where the concrete was already damaged, the steel plate covering the concrete segment end surfaces had locally bent and in some cases torn under the strands' excessive bearing reactions.
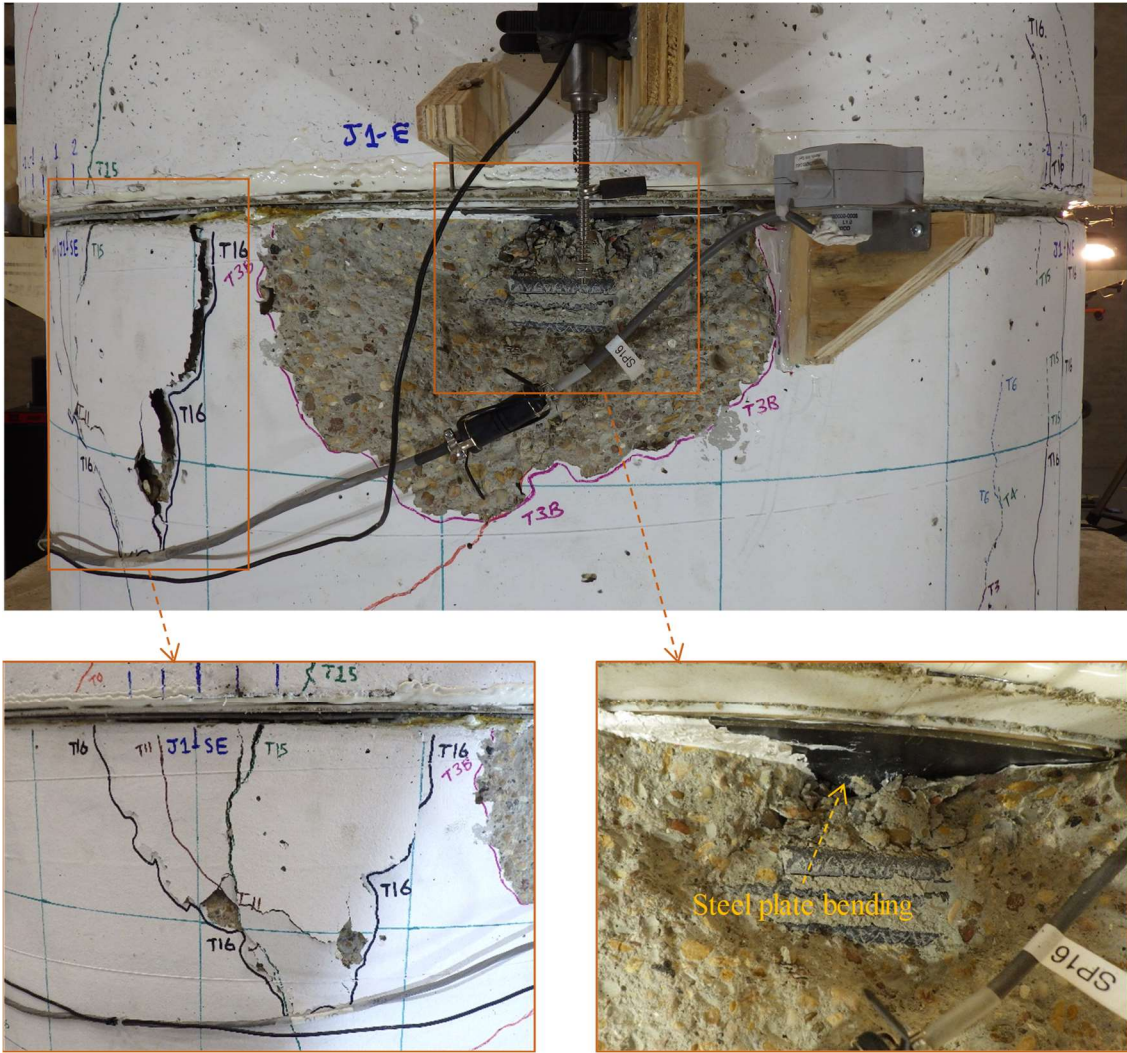
Figure 4-319. Phase III, loading protocol HSR1_UN_FXD_S5_DR_6: concrete damage on east of Joint 2
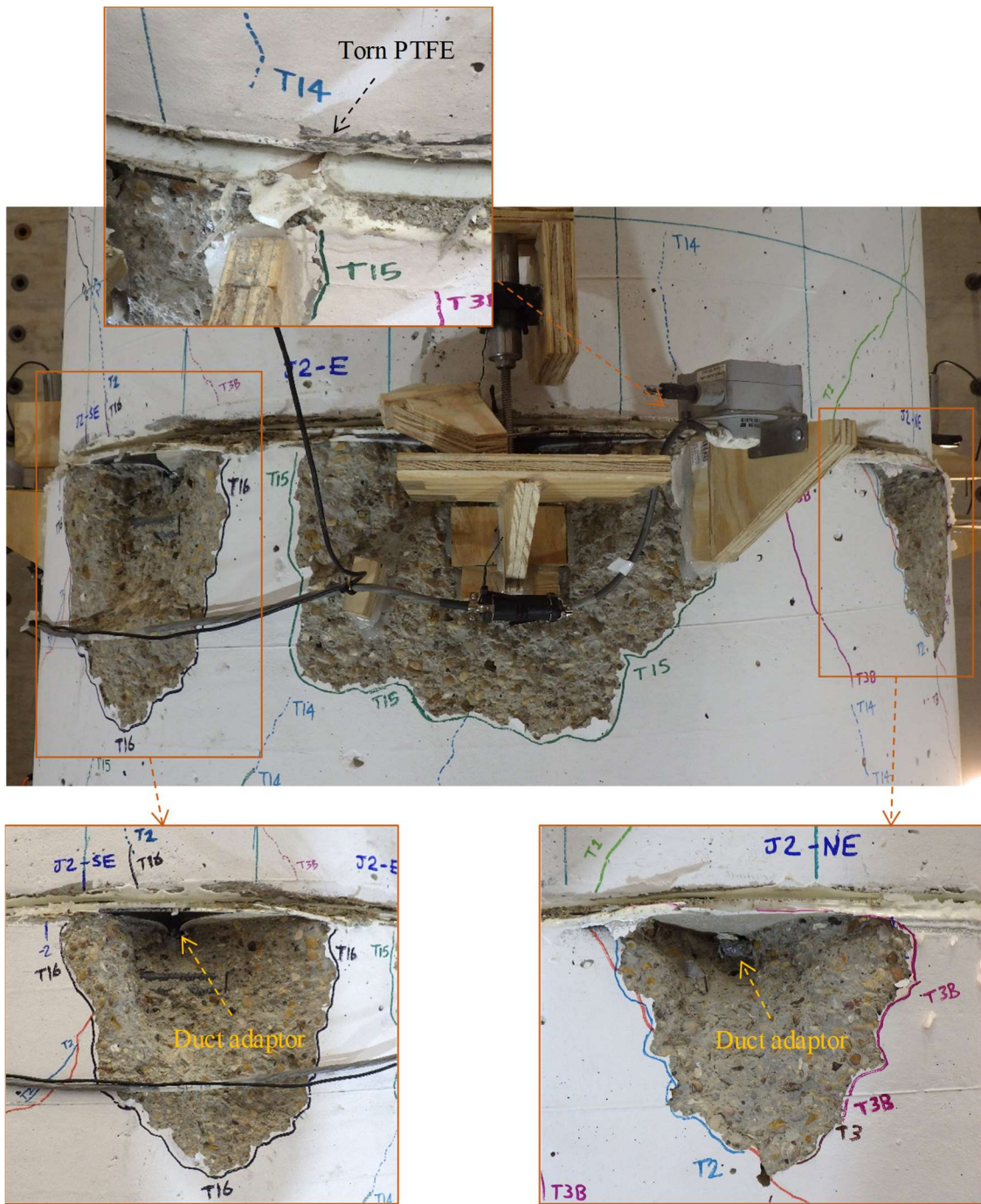
Figure 4-320. Phase III, loading protocol HSR1_UN_FXD_S5_DR_6: concrete damage on east of Joint 3
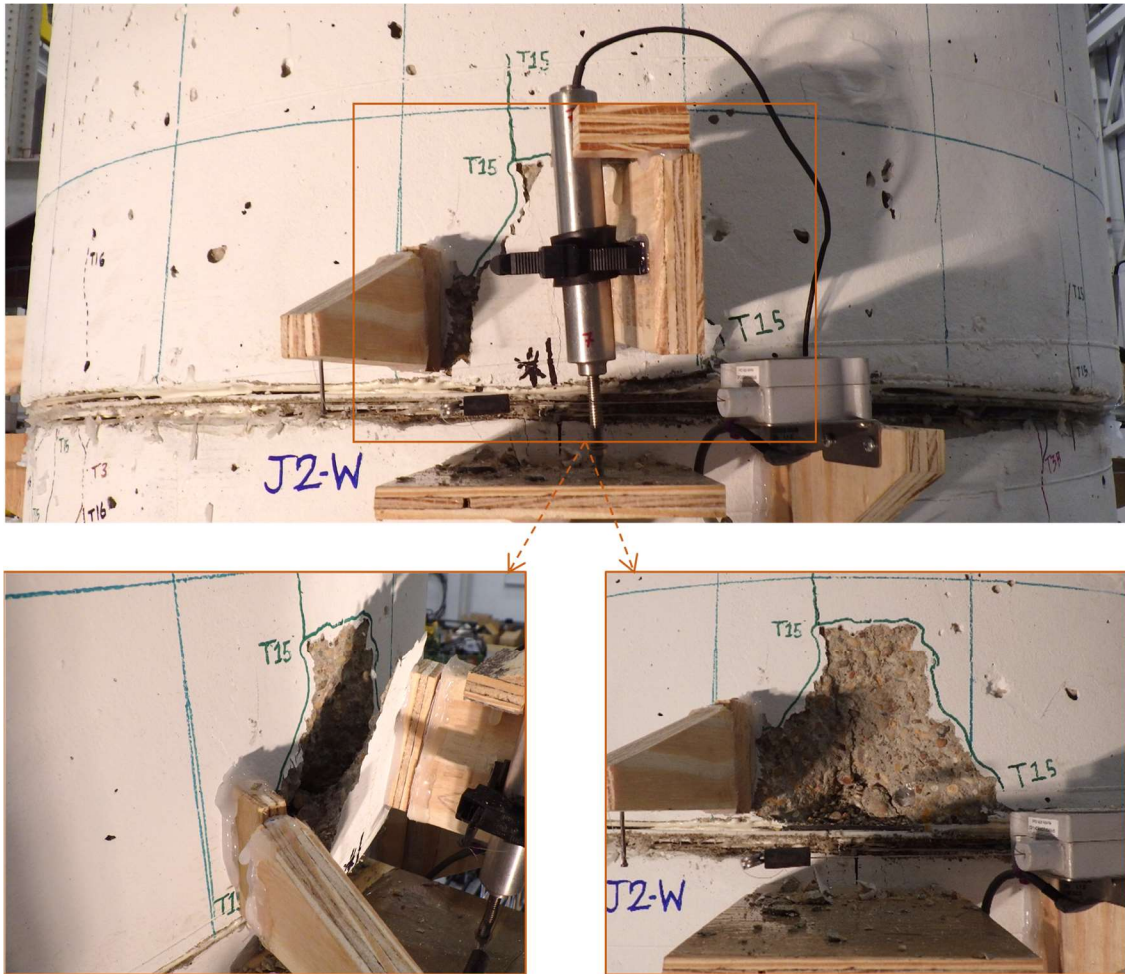
Figure 4-321. Phase III, loading protocol HSR1_UN_FXD_S5_DR_6: concrete damage on west of Joint 3

4.7.3.6. Final Damage Inspection

4.7.3.6.1. Overall Column Damage

Photos taken from the four sides of the full column after all the tests were completed and the sensors were removed are displayed in Figure 4-322. As seen, although the column was subjected to 16 successful tests and up to 6% drift ratio, it did not lose its integrity and the major damages were confined to the vicinity of the joints.
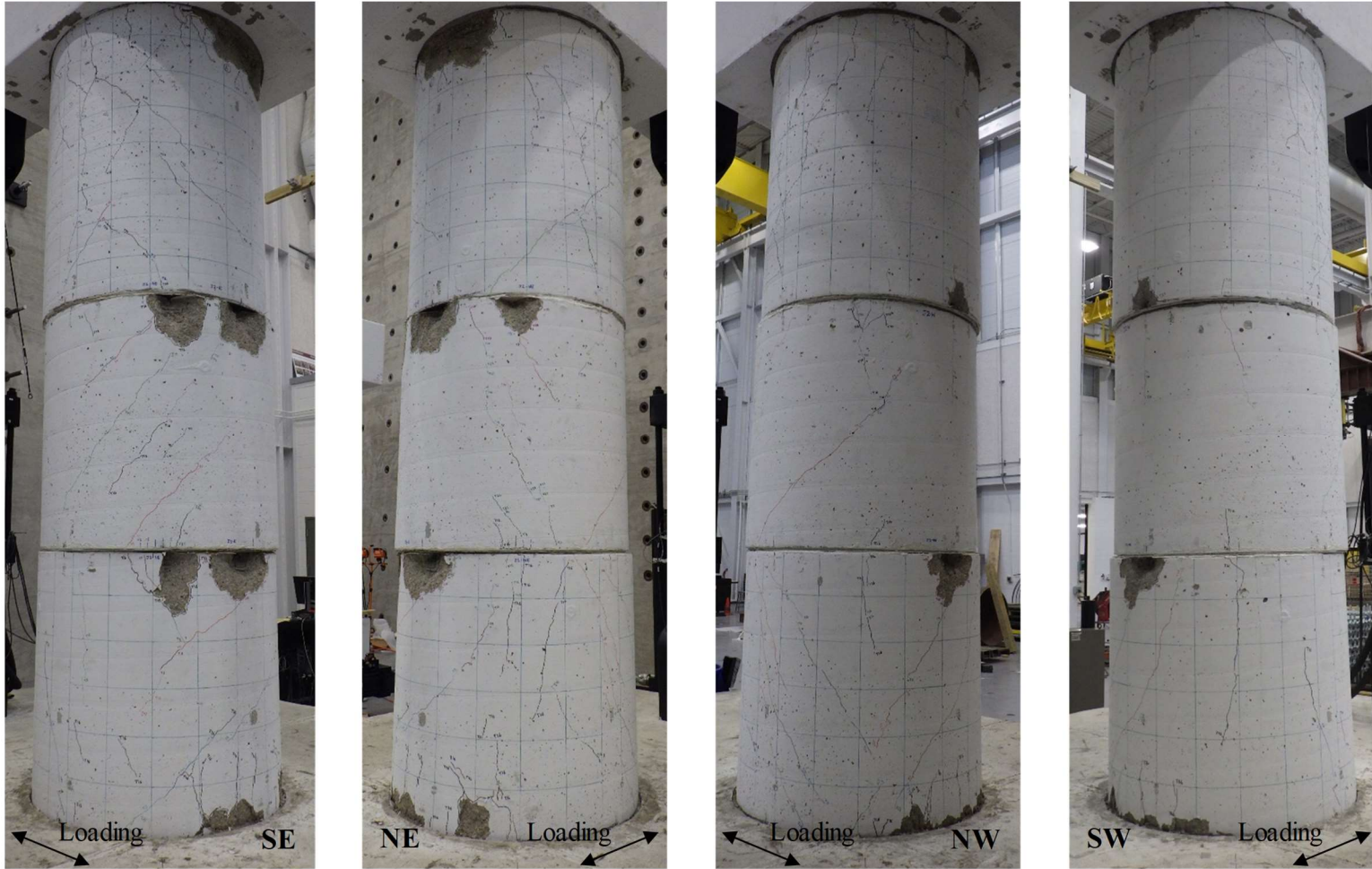
Figure 4-322. Phase III, final damage inspection: four sides of column specimen

508

4.7.3.6.2. Column Segments

After the column was disassembled, the segments' surfaces and the joints were inspected for additional damage. All the column segments were damaged, mainly externally and close to the sliding and rocking joints. Photos from the interior surface of the bottom segment are shown in Figure 4-323. According to these photos, concrete cone failures similar to those observed outside the segment, adjacent to the east and west quadrants of the first sliding joint (Figure 4-306 and Figure 4-307), had also occurred close to the east and west duct adaptors inside the segment. Vertical (compressive) cracks were also found on the same sides of the segment's central hole, extending from the top toward the bottom end of the column. No further damage was visible on the interior surface of the bottom segment.
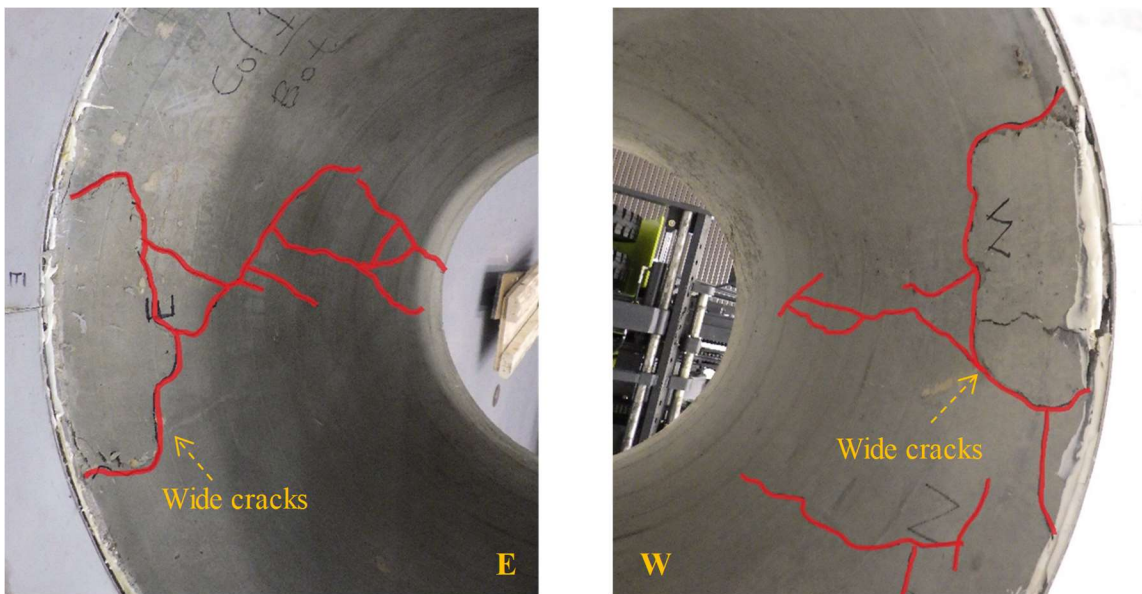
Figure 4-323. Phase III, final damage inspection: damage inside bottom segment

The final conditions of the bottom segment's ends are also displayed in Figure 4-324. The compressive concrete damage at the bottom end of the segment (Joint 1) was limited to the spalling observed from outside and no sign of core concrete crushing was found. However, as predicted on the basis of the concrete cone failures observed outside, the indentations on the PVC ducts and the bearing damage to the PTFE pads in the vicinity of the duct adaptors were rather significant. Although such damage did not visibly affect the coefficient of friction at the sliding joints, it did increase the maximum sliding capacity of the joints up to 35%. Additionally, evidence of limited PTFE wearing was found on the PTFE surface.

Per Figure 4-325, which shows the top and bottom surfaces of the middle segment, the joints damage consisted of duct and duct adaptor indentations and PTFE tearing. The PTFE damage was particularly significant at the west and east sides of the west and east duct adaptors, close to which the concrete cone failures had occurred. Such damage was obviously caused by the extra freedom of the strands to move in those duct adaptors upon sliding. As seen in Figure 4-325(b), a small piece of the PTFE pad on the east side of the top surface was also torn during the last test in this Phase (i.e. under loading protocol HSR1_UN_FXD_S5_DR_6 – see Figure 4-320). The cause of this damage is unclear, as nothing was found on the bottom surface of the top segment that could have torn the PTFE covering the top surface of the middle segment (Figure 4-326(a)). No sign of concrete damage was found inside the middle segment.

Similar vertical cracks to those found inside the bottom segment, but thinner and fewer in number, were observed inside the top segment (Figure 4-327).

510
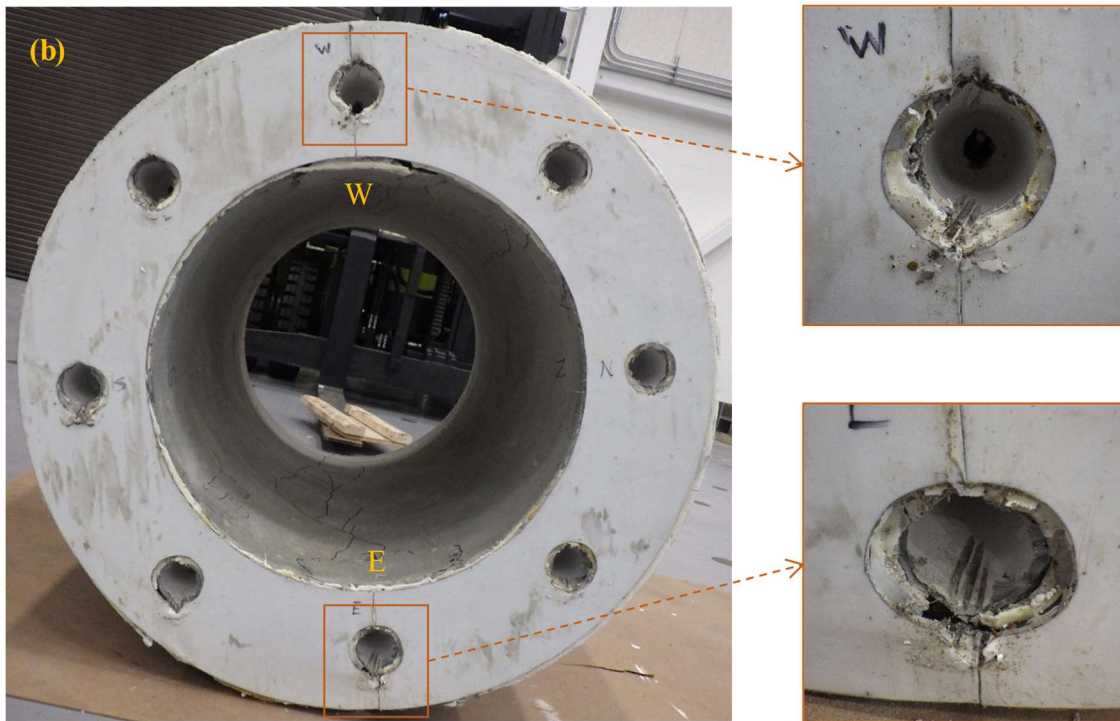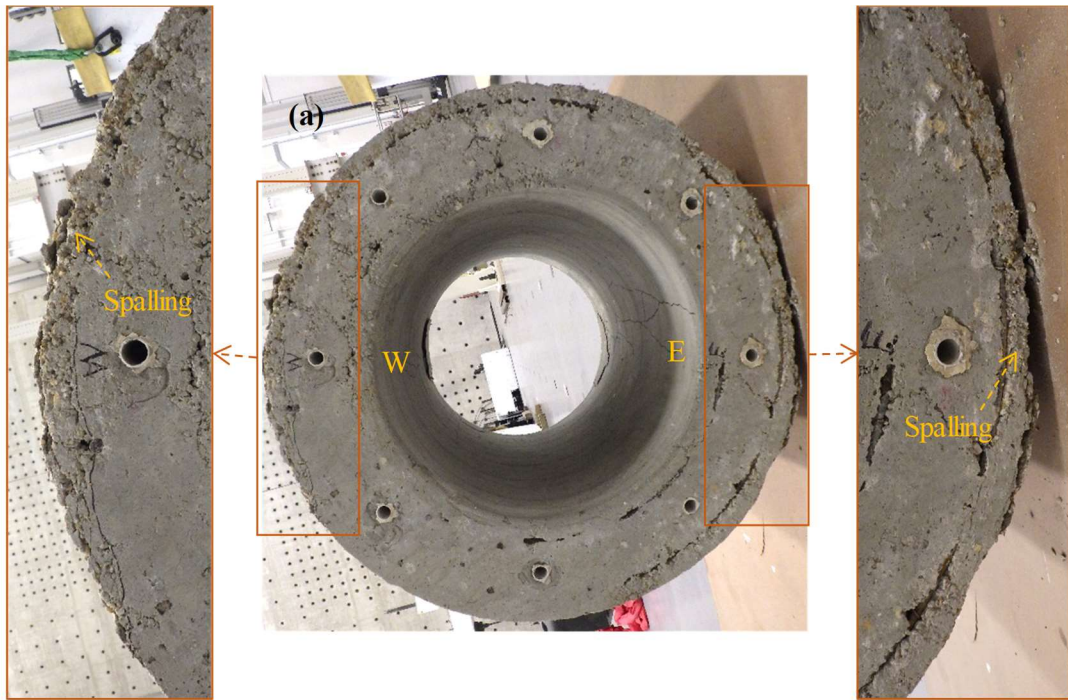
Figure 4-324. Phase III, final damage inspection, bottom segment: (a) bottom end; (b) top end

511

Figure 4-325. Phase III, final damage inspection, middle segment: (a) bottom end; (b) top end

512
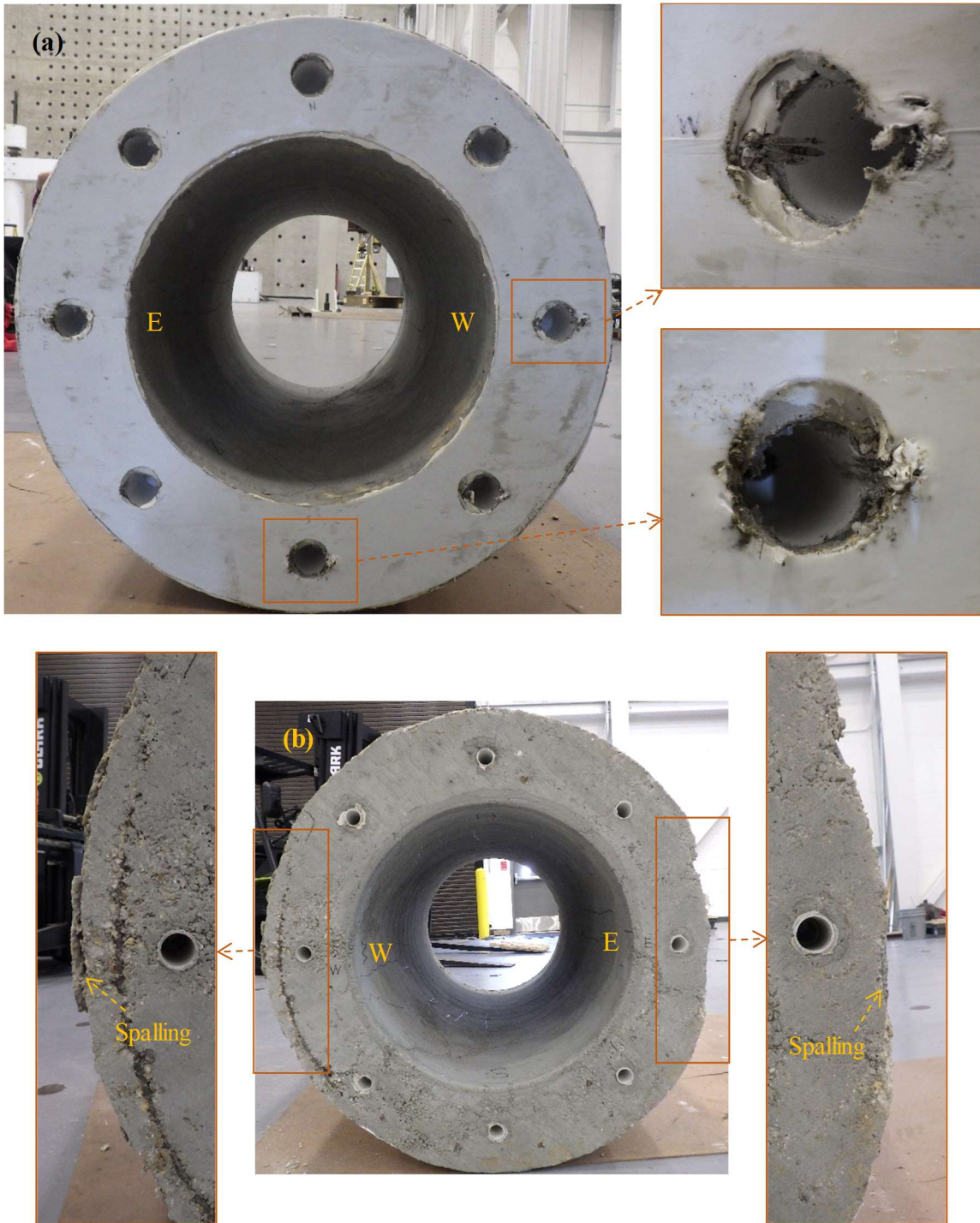
Figure 4-326. Phase III, final damage inspection, top segment: (a) bottom end; (b) top end

513
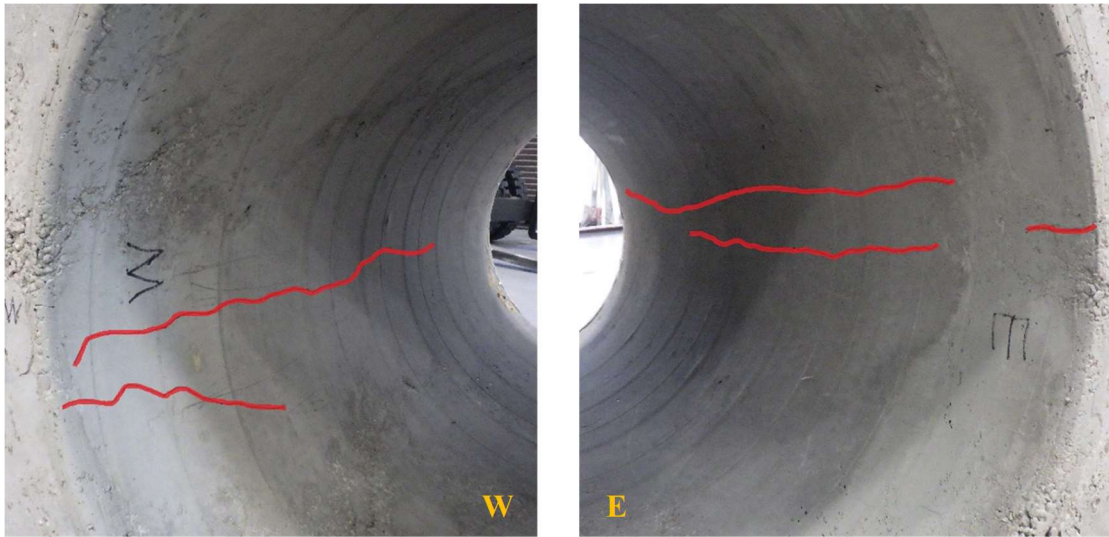
Figure 4-327. Phase III, final damage inspection: cracks inside top segment

4.7.3.6.3. Posttensioning Tendons

The deformed posttensioning tendons are shown in Figure 4-328. As was the case for the previous two column specimens tested in Phases I and II, the tendons had plastically bent above and below the sliding joints at the duct-to-duct adaptor connection (not at the sliding joint interface). The cyclic bending of the tendons had led to the local yielding and fracture of some of the wires. All the fractures had occurred above the second sliding joint (Joint 3), most probably because that joint experienced the majority of sliding throughout the tests in this Phase. No plastic deformation was observed over the tendon lengths crossing the rocking joints, though.
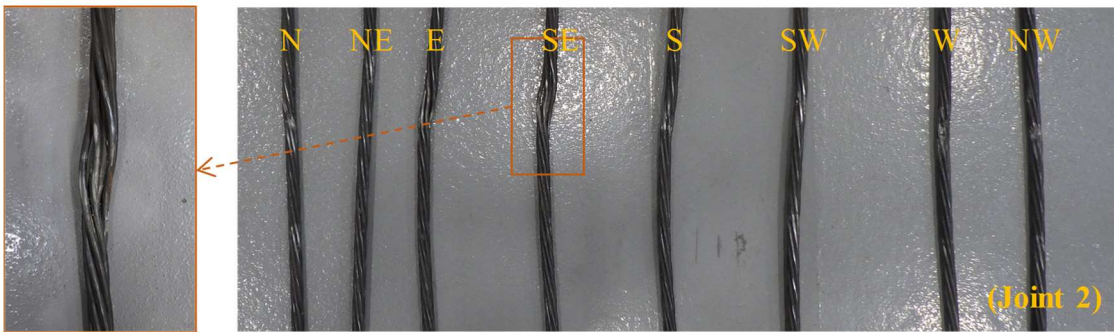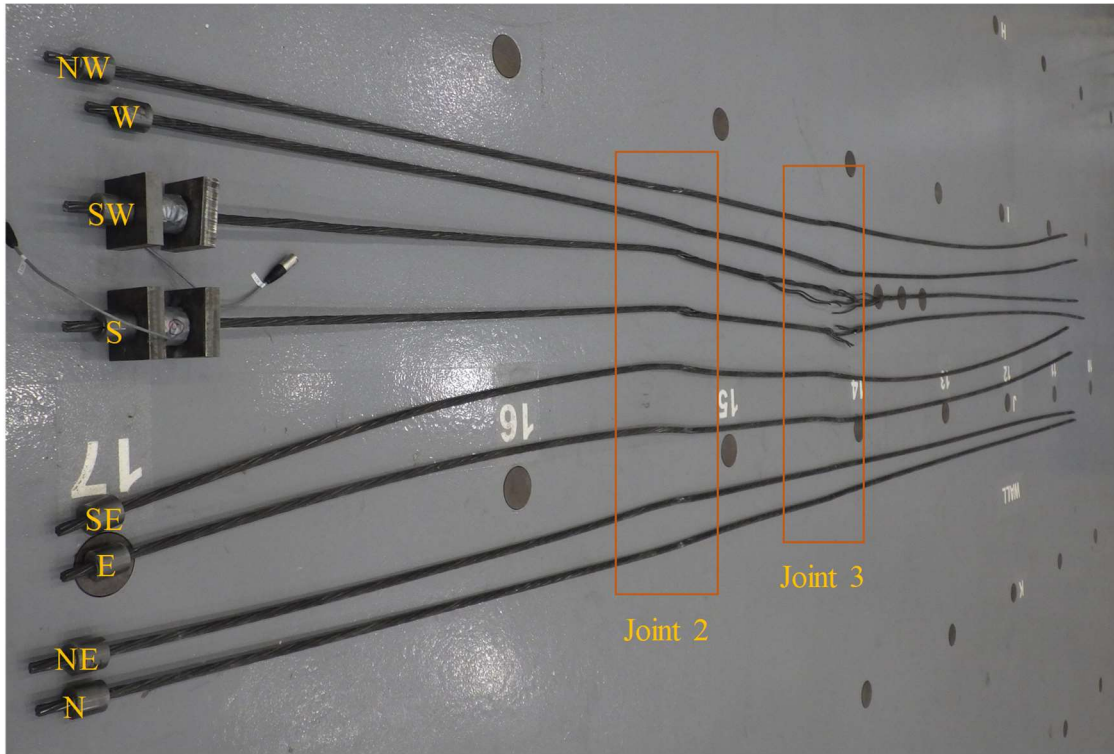
Figure 4-328. Phase III, final damage inspection: posttensioning tendons

4.7.4. Phase IV: Cantilever Column under Biaxial Lateral Loading

4.7.4.1. Test Setup

The test setup in this Phase was Setup C, which was schematically depicted in Figure 4-14. In this setup, two vertical 590-kip actuators were used to apply the vertical load and two 220-kip horizontal actuators connected to the loading beam at 45° angles were used to apply the lateral displacement in two normal directions. In order to provide almost free rotation at the top end of the column, both vertical actuators were force-controlled and applied identical forces. That is, upon the loading beam's rotation around the *Y*-axis (Figure 4-331), one of the vertical actuators would retract and the other one would extend. Each horizontal actuator was controlled separately from the other one using its own displacement command, while the displacement commands were computed such that a desired movement of the loading beam in the horizontal plane was achieved.

The plane view of the test setup is demonstrated in Figure 4-329. The location of the column with respect to the wall and the locations of the horizontal actuators' connection points on the wall and the loading beam were selected such that the horizontal actuators made 45° angles with the loading beam's longitudinal axis and their axes intersected at the column's vertical centerline. In this configuration, the clear distance of the loading beam from the reaction wall was 4 ft-6 in. and each of the horizontal actuators could retract by up to 9 in. and extend up to 21 in. – note that the total stroke of each horizontal actuator was 30 in.
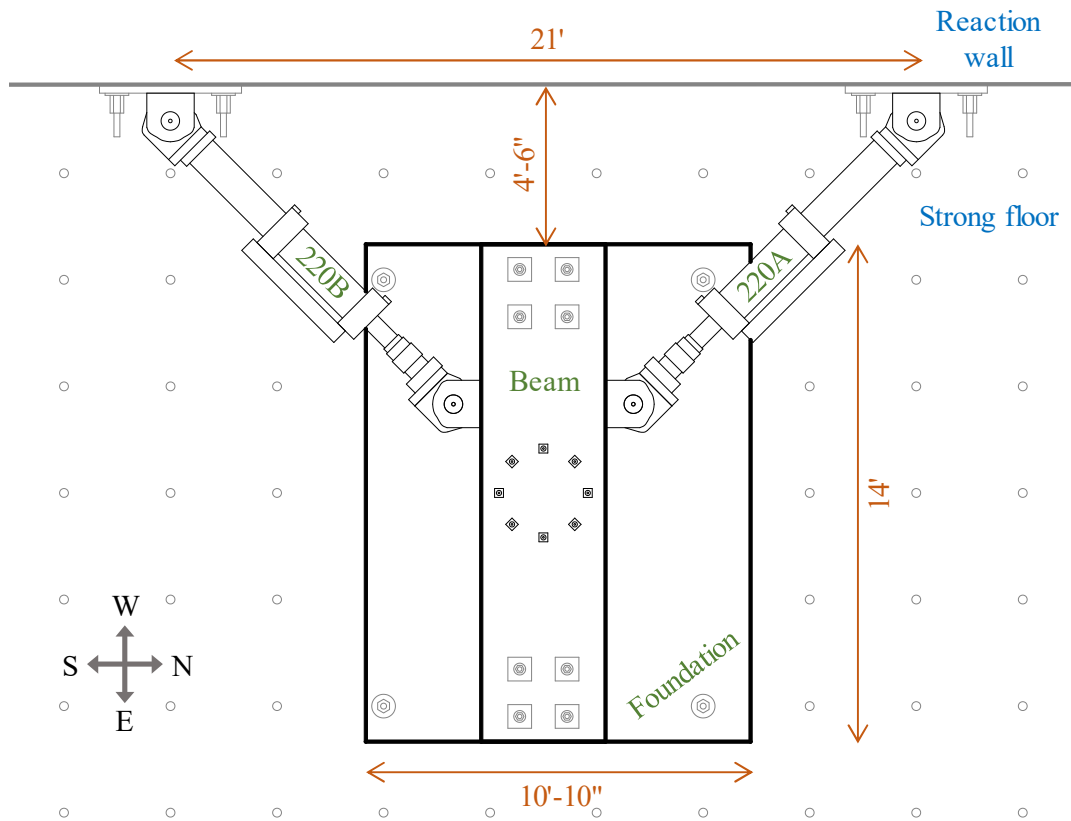
Figure 4-329. Setup C: plan view

Assembling the column specimen was carried out exactly as described for Phase III (Section 4.7.3.1). After the loading beam was mounted atop the column specimen and the column was posttensioned, the horizontal actuators were first connected to the loading beam and then to the reaction wall. The horizontal actuators had to be connected to the loading beam while they were normal to the beam because, in the rotated orientation, two of the rods connecting the swivels to the loading beam could not be accessed for torquing. Also, since the two swivels on both sides of the loading beam were connected via the same rods passing though both swivels, the two actuators had to be connected to the loading beam at the same time. For this purpose, considering that only one of the cranes could be

517

used above the loading beam, one of the horizontal actuators had to be first mounted on a temporary scaffold, while the second one was hung from the crane (Figure 4-330).
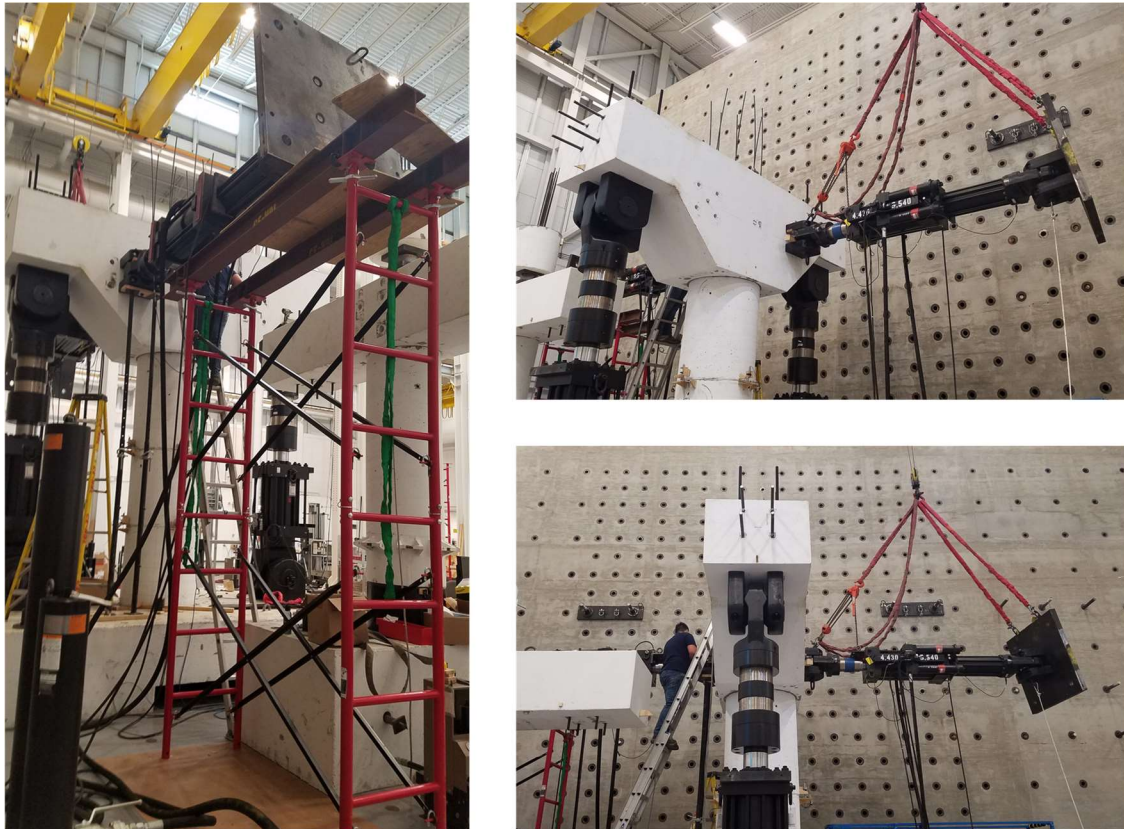
Figure 4-330. Connection of horizontal actuators to loading beam

4.7.4.2. Instrumentation

The general arrangement of the sensors used to measure the displacements of the concrete components and the forces in Phase IV is depicted in Figure 4-331. A total of 52 sensors aside from the actuators' load cells were utilized in this setup (Table 4-44).

Table 4-44. Type and number of sensors used in Phase III

Type	String Potentiometer	LVDT	Tendon Load Cell
Number	33	11	8
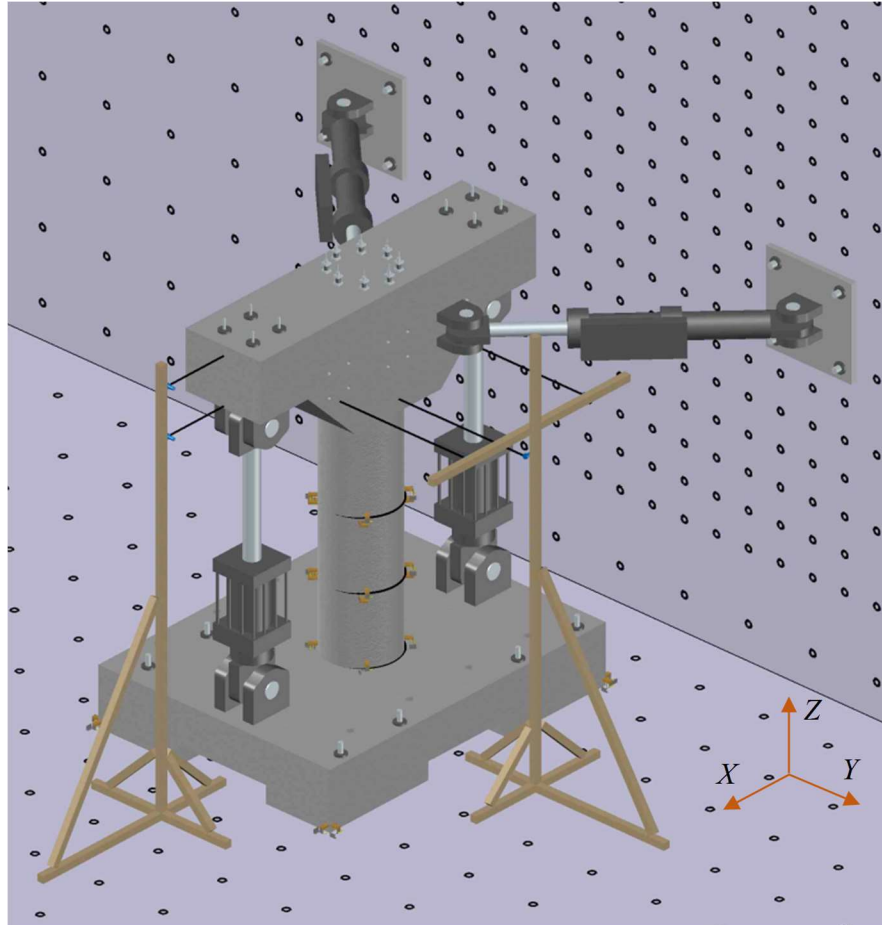
Figure 4-331. General arrangement of sensors in Phase IV

The sensors used to measure the relative displacements at the column joints were the same as those used in the previous three Phases, as listed in Table 4-45. The sensors used to measure the displacements of the loading beam and the foundation block are listed in Table 4-46 and Table 4-47, respectively. Only eight tendon load cells were used in this

setup, which were located on the top of the loading beam (Table 4-48). A photo from the completed test setup is displayed in Figure 4-332.

Table 4-45. Sensors measuring joint sliding/rotation in Phase IV

ID	Type	Stroke (in)	Location	Measurement
SP-J0-N-H	String pot.	4	Bottom joint - north	Sliding
SP-J0-S-H	String pot.	4	Bottom joint – south	Sliding
SP-J0-E-H	String pot.	4	Bottom joint – east	Sliding
SP-J0-W-H	String pot.	4	Bottom joint – west	Sliding
SP-J0-N-V	String pot.	12	Bottom joint – north	Separation
SP-J0-S-V	String pot.	12	Bottom joint – south	Separation
SP-J0-E-V	String pot.	12	Bottom joint – east	Separation
SP-J0-W-V	String pot.	12	Bottom joint – west	Separation
SP-J1-N-H	String pot.	4	Sliding joint 1 – north	Sliding
SP-J1-S-H	String pot.	4	Sliding joint 1 – south	Sliding
SP-J1-E-H	String pot.	4	Sliding joint 1 – east	Sliding
SP-J1-W-H	String pot.	4	Sliding joint 1 – west	Sliding
LV-J1-N-V	LVDT	1	Sliding joint 1 – north	Separation
LV-J1-S-V	LVDT	1	Sliding joint 1 – south	Separation
LV-J1-E-V	LVDT	1	Sliding joint 1 – east	Separation
LV-J1-W-V	LVDT	1	Sliding joint 1 – west	Separation
SP-J2-N-H	String pot.	4	Sliding joint 2 – north	Sliding
SP-J2-S-H	String pot.	4	Sliding joint 2 – south	Sliding
SP-J2-E-H	String pot.	4	Sliding joint 2 – east	Sliding
SP-J2-W-H	String pot.	4	Sliding joint 2 – west	Sliding
LV-J2-N-V	LVDT	1	Sliding joint 2 – north	Separation
LV-J2-S-V	LVDT	1	Sliding joint 2 – south	Separation
LV-J2-E-V	LVDT	1	Sliding joint 2 – east	Separation
LV-J2-W-V	LVDT	1	Sliding joint 2 – west	Separation
SP-J3-N-H	String pot.	4	Top joint - north	Sliding
SP-J3-S-H	String pot.	4	Top joint – south	Sliding
SP-J3-E-H	String pot.	4	Top joint – east	Sliding
SP-J3-W-H	String pot.	4	Top joint – west	Sliding
SP-J3-E-V	String pot.	4	Top joint – east	Separation
SP-J3-W-V	String pot.	4	Top joint – west	Separation

Table 4-46. String pots measuring loading beam displacements in Phase IV

ID	Stroke (in)	Location	Measurement
SP-CP-F-T	50	East face – 14.5 ft above foundation surface	X displacement
SP-CP-F-B	50	East face – 12.5 ft above foundation surface	X displacement
SP-CP-S-C	25	North face – center, 10.5 ft above foundation surface	Y displacement
SP-CP-S-L	25	North face – 3 ft to the left of center, 140 in above foundation surface	Y displacement
SP-CP-S-R	25	North face – 3 ft to the right of center, 140 in above foundation surface	Y displacement

Table 4-47. Sensors measuring foundation displacements in Phase IV

ID	Type	Stroke (in)	Location	Measurement
SP-FN-N-L-H	String pot.	4	NE corner	X sliding
SP-FN-E-R-H	String pot.	4	NE corner	Y sliding
LV-FN-E-R-V	LVDT	0.5	NE corner	Separation
LV-FN-E-L-V	LVDT	0.5	SE corner	Y sliding
SP-FN-S-R-H	String pot.	4	SW corner	X sliding
SP-FN-W-L-H	String pot.	4	SW corner	X sliding
LV-FN-W-L-V	LVDT	0.5	NW corner	Separation

Table 4-48. Tendon load cells in Phase IV

ID	Location	Tendon Map
LC-TN-C-1	Loading beam – E	
LC-TN-C-2	Loading beam – SE	
LC-TN-C-3	Loading beam – S	
LC-TN-C-4	Loading beam – SW	
LC-TN-C-5	Loading beam – W	
LC-TN-C-6	Loading beam – NW	
LC-TN-C-7	Loading beam – N	
LC-TN-C-8	Loading beam – NE	
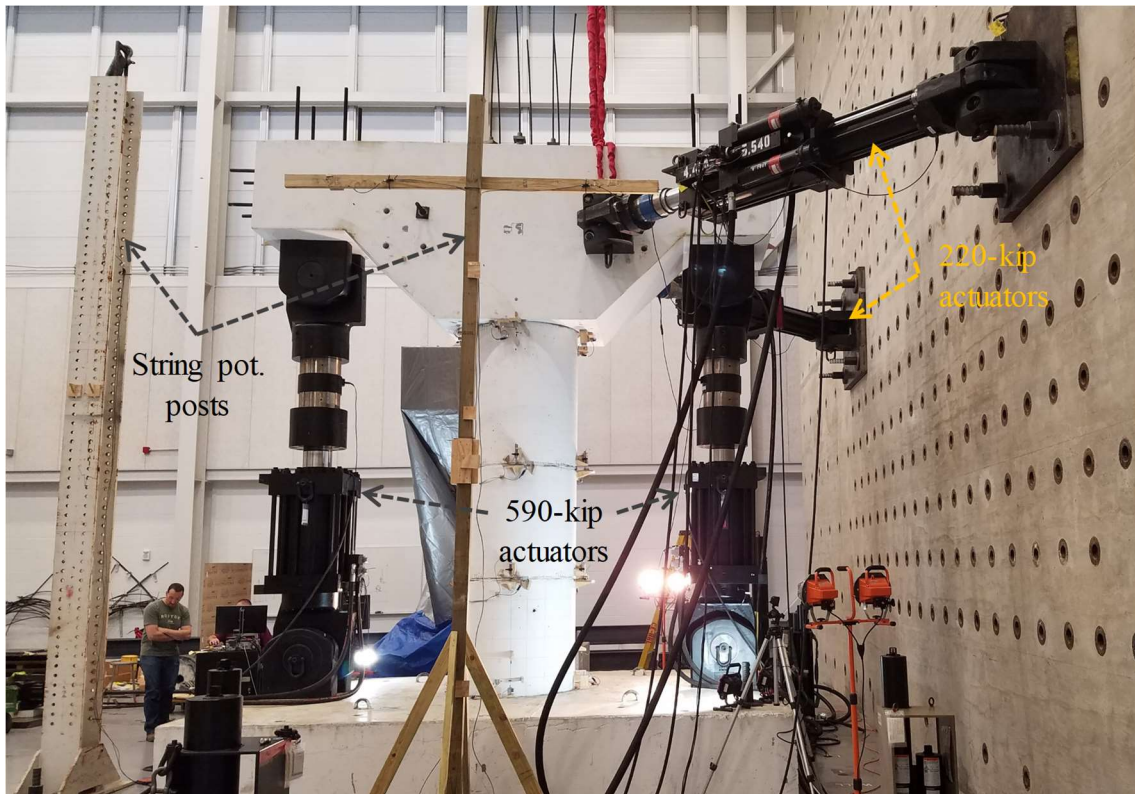
Figure 4-332. Complete test setup for Phase IV

4.7.4.3. Data Acquisition and Processing

The sensors' data was acquired and cleaned (from noise) similarly to Phase I (see Section 4.7.1.3), whereas the maximum sampling rate used in Phase IV was 128 data points per second, because no fast loading was applied to the column in this Phase. Similarly to the previous Phases, the data obtained from the DAQ during the tests in this Phase needed to be processed to achieve interpretable column responses. The noise filtering was performed as explained in Section 4.7.1.3 for Phase I. Considering that all components moved in three directions in this Phase, the response parameters listed in Section 4.7.1.3 for the cantilever column specimen subjected to unaixial lateral loading were increased into:

- $\Delta_{bm,X}$: The longitudinal displacement (i.e. in X direction per Figure 4-331) of the loading beam's reference point (corresponding to the superstructure centroid in the prototype bridge) relative to the foundation block's top surface;

- $\Delta_{bm,Y}$: The transverse displacement (i.e. in Y direction per Figure 4-331) of the loading beam's reference point relative to the foundation block's top surface;

- $u_{sl,X,j}$: The jth joint's sliding in the longitudinal direction (i.e. in the X direction per Figure 4-331), with $j = 1, 2, 3$, and 4 from bottom to top;

- $u_{sl,Y,j}$: The jth joint's sliding in the transverse direction (i.e. in the Y direction per Figure 4-331), with $j = 1, 2, 3$, and 4 from bottom to top;

- $\theta_{r,Y,j}$: The jth joint's rocking around Y-axis (Figure 4-331);

- $\theta_{r,X,j}$: The jth joint's rocking around X-axis (Figure 4-331);

- $V_{col,X}$: The column's base shear in the longitudinal direction (i.e. in X direction per Figure 4-331);

- $V_{col,Y}$: The column's base shear in the transverse direction (i.e. in Y direction per Figure 4-331);

- $M_{jnt,Y,j}$: The jth joint's moment about Y-axis (Figure 4-331);

- $M_{jnt,X,j}$: The jth joint's moment about X-axis (Figure 4-331);

- N_{col}: The axial force on the column (i.e. excluding the column weight);

- N_{PT}: The total posttensioning force in the tendons;

- $M_{PT,Y}$: The posttensioning-induced moment on the loading beam about Y-axis.

- $M_{PT,X}$: The posttensioning-induced moment on the loading beam about X-axis.

The joint response parameters were obtained through Eqs. (4-2) through (4-6). Because of the large changes in the orientations of the strings of the string potentiometers during the tests in this Phase, the loading beam's displacements were determined by solving a nonlinear least-squares problem including the lengths of the strings at each time step. This approach is briefly decribed as follows.

Lets assume that $\vec{\Delta}_{bm}$ and $\vec{\Theta}_{bm}$ denote the vectors of translational displacements and rotations, respectively, of the loading beam's reference point at an arbitrary time instant. By further assuming that the loading beam is rigid, the displacements of any point p on the loading beam, $\vec{\Delta}_p$, can be determined as:

$$\vec{\Delta}_p = \vec{\Delta}_{bm} + \vec{\Theta}_{bm} \times \vec{r}_p \quad \text{with} \quad \begin{cases} \vec{\Delta}_p = \begin{bmatrix} \delta_{p,X} & \delta_{p,Y} & \delta_{p,Z} \end{bmatrix}^T \\ \vec{\Delta}_{bm} = \begin{bmatrix} \delta_{bm,X} & \delta_{bm,Y} & \delta_{bm,Z} \end{bmatrix}^T \\ \vec{\Theta}_{bm} = \begin{bmatrix} \theta_{bm,X} & \theta_{bm,Y} & \theta_{bm,Z} \end{bmatrix}^T \end{cases} \tag{4-18}$$

where $\vec{r}_p$ is the constant position vector of the point p with respect to the loading beam's reference point in a reference system attached to the loading beam, i.e. $\vec{r}_p = \vec{X}_{p,o} - \vec{X}_{bm,o}$, where $\vec{X}_{p,o}$ and $\vec{X}_{bm,o}$ represent the initial positions of point p and the loading beam's reference point (Figure 4-333); $\delta_{p,X}$, $\delta_{p,Y}$, and $\delta_{p,Z}$ are the respective point's displacements in X-, Y-, and Z-directions; $\delta_{bm,Z}$ is the vertical displacement of the loading beam's reference point; and $\theta_{bm,X}$, $\theta_{bm,Y}$, and $\theta_{bm,Z}$ are the rotations of the loading beam around X-, Y-, and Z-axes, respectively. Having its displacement, $\vec{\Delta}_p$, at each time instant, the location vector of the point p, $\vec{X}_p$, is found as:

$$\vec{X}_p = \vec{X}_{p,o} + \vec{\Delta}_p \tag{4-19}$$

Let's now assume that each point p represents the moving end of a string potentiomenter and its other end, p', which is located on the fixed wooden post, has the position vector $\vec{X}_{p'}$. Then, the current and initial lengths of the string, denoted by L_p and $L_{p,o}$, respectively, can be determined as:

$$L_p = \left\| \vec{X}_p - \vec{X}_{p'} \right\| \quad \text{and} \quad L_p = \left\| \vec{X}_{p,o} - \vec{X}_{p'} \right\| \tag{4-20}$$

Moreover, $L_p = L_{p,o} + \Delta L_p$, where ΔL_p is the length change (i.e. string potentiometer's measurement). Eqs. (4-18) thru (4-20) can be condensed into the equation below, relating the displacement measurement of the string potentiometer connected to the point p on the loading beam, ΔL_p, to the displacements and the rotations of the loading beam's reference point ($\vec{\Delta}_{bm}$ and $\vec{\Theta}_{bm}$, respectively):

$$\Delta L_p = \left\| \vec{X}_{p,o} - \vec{X}_{p'} + \vec{\Delta}_{bm} + \vec{\Theta}_{bm} \times \vec{r}_p \right\| - L_{p,o} \tag{4-21}$$
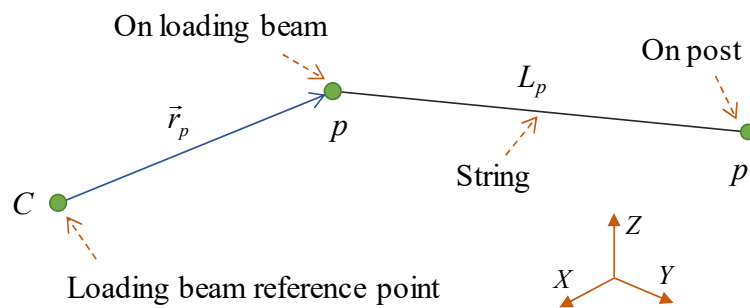
Figure 4-333. Relationship between loading beam displacements and string potentiometer measurement

Given the number of unknowns in Eq. (4-21) is six (the displacement and rotation components of the loading beam), data from 6 potentiometers is needed. To obtain a system of six equations in six unknowns, similar equations were considered for all of the five string potentiometers whose string ends were connected to the loading beam (Table 4-46) as well as the east vertical actuator. The resulting six equations were solved using the nonlinear least-squares solution algorithm of Matlab (MathWorks 2019). Once the loading beam's displacements and rotations were obtained from the above procedure, they were further corrected to eliminate the effects of the foundation displacements and rotations.

After the loading beam's displacements and rotations were determined for each time instant, the current coordinates of the pins of the actuator swivels connected to the loading beam were computed. Using these coordinates and knowing the coordinates of the swivel pins on the other ends of the actuators, the force components acting on each pin on the loading beam were determined. The column forces (i.e. axial force, shear components, and moment components) were then computed via the equilibrium equations including all the force components acting on the column-loading-beam system (i.e. actuator forces and component weights) and the coordinates of the displaced swivel pins and loading beam's centroid.

4.7.4.4. Loading Protocols

A total of 13 tests were conducted on the HSR column specimen in Phase IV. These tests were performed using the loading protocols categorized in four Loading Sets, as summarized in Table 4-49. The loads applied via the vertical actuators in all Loading Sets

were identical and equal to 215.5 kips, whose sum with the weights of the loading beam and the actuators equaled 253 kips – this value equaled the full design dead load plus half the design live load acting on the column in model domain (see Section 4.7.1.4.1).

Table 4-49. Loading Sets in Phase IV

Loading Set	Number of Protocols	Max. Drift Ratio (%)	Horizontal Displacement	Vertical Load
1	3	4	Cyclic	Constant
2	4	2	Cyclic	Constant
3	5	4.2	Arbitrary	Constant
4	1	6	Cyclic	Constant

The nomenclature for the IDs of the loading protocols in Phase IV starts with "HSR1_BI_CNT_Sn," in which 1 is the column specimen ID from the casting process, "BI" stands for biaxial, "CNT" stands for cantilever, and n is the Loading Set number.

In order to apply certain displacement components to the loading beam in X and Y directions through the horizontal actuators, their displacement commands were computed in accordance with the geometry of the system in the XY-plane (Figure 4-334). Considering that only two horizontal actuators were used in this test setup, it could not be guaranteed that the loading beam would remain unrotated (i.e. without twist), but the horizontal actuators' displacements were determined with such an assumption. The displacements of the horizontal actuators 220A and 220B, denoted by $\Delta_{act,h1}$ and $\Delta_{act,h1}$, respectively, were obtained as:

$$\begin{cases} \Delta_{act,h1} = L_A - L_o \\ \Delta_{act,h2} = L_B - L_o \end{cases} \tag{4-22}$$

where L_A and L_B are the actuators' current lengths and L_o is their initial length (at zero horizontal displacements). Per Pythagorean theorem, for given loading beam displacement components $\Delta_{bm,X}$ and $\Delta_{bm,Y}$, the required actuator lengths could be computed as (see Figure 4-334):

$$\begin{cases} L_A = \sqrt{\left(a + \Delta_{bm,X}\right)^2 + \left(a - \Delta_{bm,Y}\right)^2} \\ L_B = \sqrt{\left(a + \Delta_{bm,X}\right)^2 + \left(a + \Delta_{bm,Y}\right)^2} \end{cases} \tag{4-23}$$

where a is the initial distance of the actuators' end pins along either X- or Y-axes, which equaled 95.5 in.
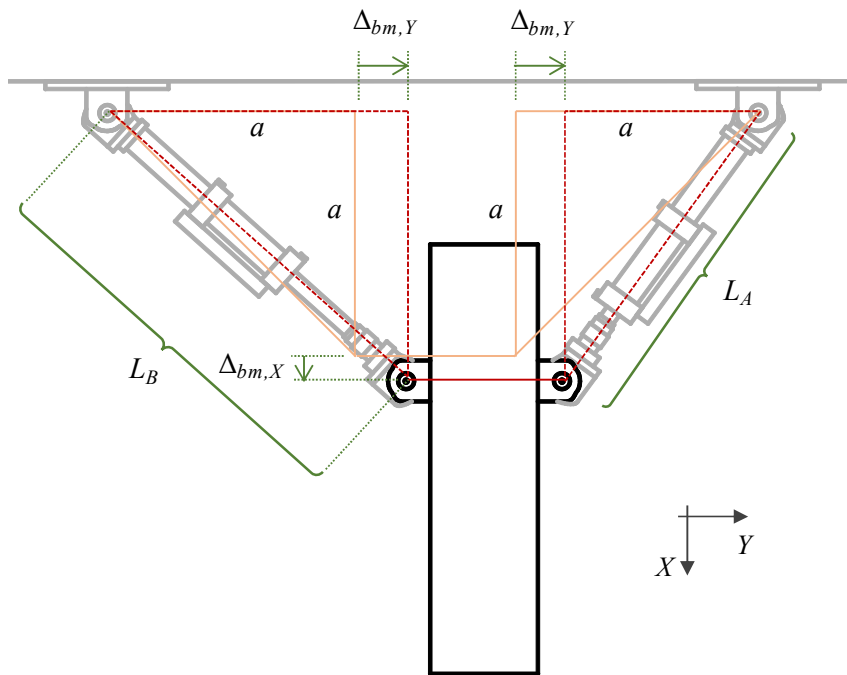
Figure 4-334. Determination of displacements of horizontal actuators

528

4.7.4.4.1. Loading Set 1

The loading protocols in Loading Set 1 aimed to examine the general performance of the HSR column specimen under biaxial lateral displacement time histories with maximum drift ratios representing three seismic hazard levels. The chosen hazard levels represented earthquakes with 5% probability of exceedance in 50 years (design earthquake), 2% probability of exceedance in 50 years (maximum considered earthquake), and much smaller probability of exceedance in 50 years (associated with a drift ratio demand twice as large as that obtained from the maximum considered earthquake). Because the column would be tested with a free top rotation, the peak drift ratios considered for the loading protocols in this Loading Set were the same as those used in Loading Set 1 in Phase I, i.e. 1.3%, 2%, and 4%. Each loading protocol consisted of six biaxial displacement cycles with a clover-shaped path in the XY-plane, while each of the three pairs of cycles had the same displacement amplitude. The displacement amplitudes of the three cycle pairs in each loading protocol equaled 1/3, 2/3, and 3/3 of the peak drift ratio corresponding to the selected hazard level (Figure 4-335 and Figure 4-336).

Table 4-50. Loading protocols in Loading Set 1 from Phase IV

No	ID	Max. Drift Ratio (%)
1	HSR3_BI_CNT_S1_DR_1_3	1.3
2	HSR3_ BI_CNT _S1_DR_2	2
3	HSR3_ BI_CNT _S1_DR_4	4

The displacement components for the first leaf of the clover-shaped path (in the first quadrant of the graph in Figure 4-335) were defined through the equations below (Marriott et al. 2011):

$$\begin{cases} \Delta_X = r(t)\cos\theta(t) \\ \Delta_Y = r(t)\sin\theta(t) \end{cases} \quad \text{with} \quad r(t) = R\sin 2\theta(t) \qquad (4\text{-}24)$$

where R is the maximum total displacement and θ varies linearly over time from 0 to $\pi/2$. The displacement components for other leaves are found using similar equations, but different θ ranges. While here θ changed with a constant rate, the duration of loading was chosen such that the maximum displacement rate in each direction would not exceed 0.1 in./sec. Note that the three selected peak drift ratios determined R, not the maximum displacements in each of the horizontal directions; therefore, the peak drift ratios in X and Y directions were smaller than the selected peak drift ratios for each loading protocol.
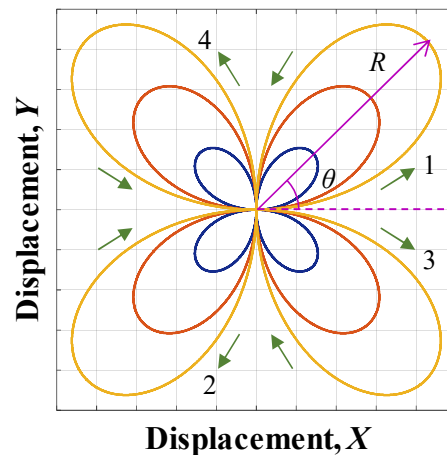
Figure 4-335. Clover-shaped biaxial displacement path used in Loading Set 1, Phase IV
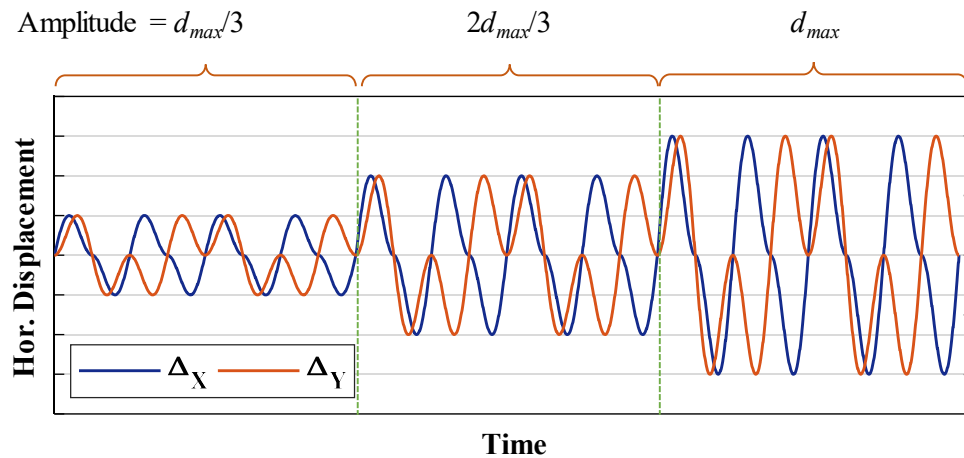
Figure 4-336. Horizontal displacement time histories in Loading Set 1, Phase IV

4.7.4.4.2. Loading Set 2

The second Loading Set consisted of four loading protocols with the constant maximum drift ratio of 2%, but different biaxial displacement paths. This Loading Set was mainly intended to produce sufficient data that could be used to validate the 3D HSR column computational models in the future. The loading paths chosen here were butterly-shaped, spiral-shaped, wave-shaped, and orbital-shaped, as shown in Figure 4-337. The loading protocols considered here are listed in Table 4-51. The first three loading paths consisted of two cycles. In the second cycles in the butterfly- and wave-shaped patters, the X and Y displacement components were swapped with one another. In the second cycle of the spiral-shaped pattern, the displacement component time histories were reversed and the Y component was multiplied by -1.

531
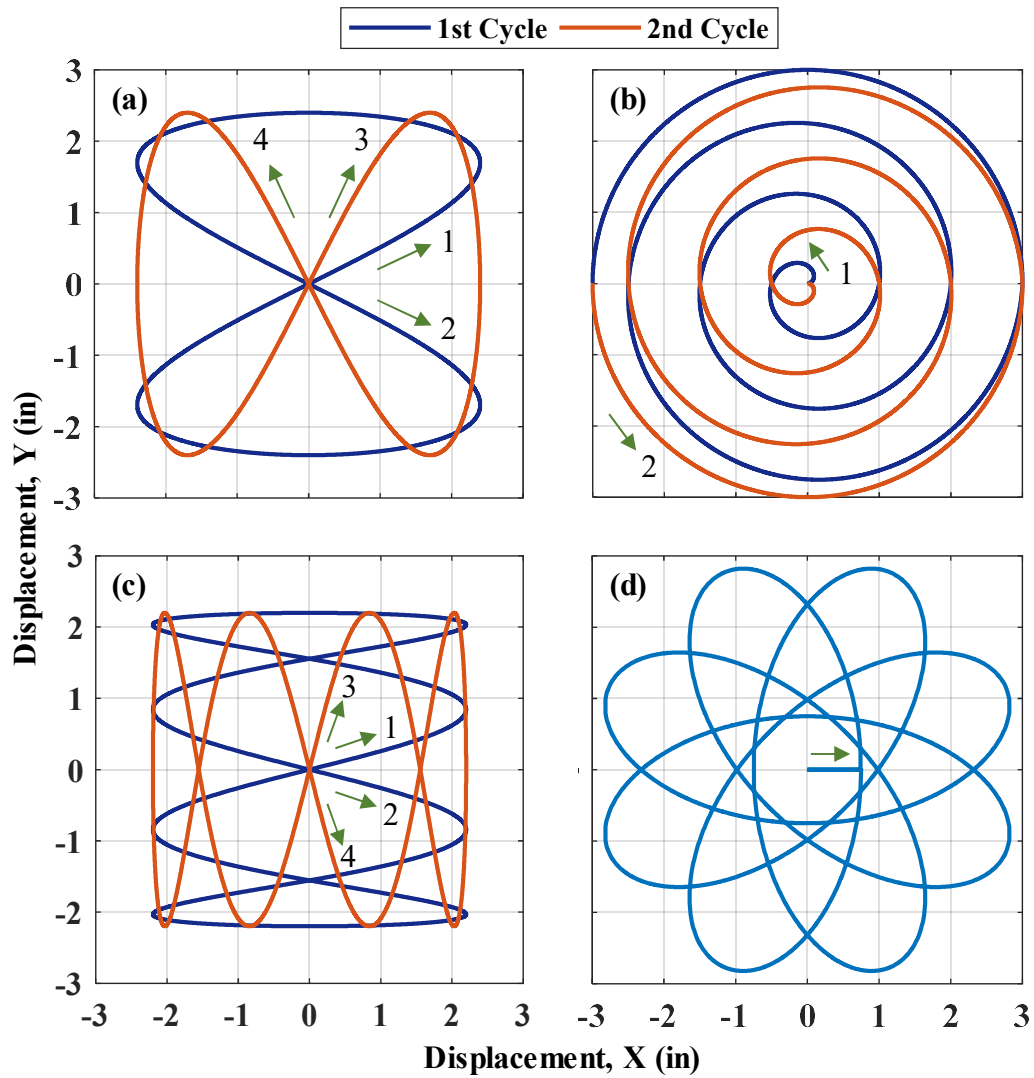
Figure 4-337. Biaxial displacement paths in Loading Set 2, Phase IV: (a) butterfly-shaped; (b) spiral-shaped; (c) wave-shaped; (d) orbital-shaped

Table 4-51. Loading protocols in Loading Set 2 from Phase IV

No	ID	Displacement Pattern Shape
4	HSR3_BI_CNT_S2_BTRF	Butterfly
5	HSR3_ BI_CNT _S2_SPRL	Spiral
6	HSR3_ BI_CNT _S2_WAVE	Wave
7	HSR3_ BI_CNT _S2_ORBT	Orbital

The first cycle of the butterfly-shaped path was mathematically expressed as:

$$\begin{cases} \Delta_X(t) = r(t)\sin 2\theta(t) \\ \Delta_Y(t) = r(t)\sin\theta(t) \end{cases} \quad \text{with} \quad r(t) = R\sin 2\theta(t) \tag{4-25}$$

where θ ranges from 0 to 2π and R is equal to 0.8 times the desired maximum horizontal displacement. Also, the wave-shaped path was expressed as:

$$\begin{cases} \Delta_X(t) = r(t)\sin 4\theta(t) \\ \Delta_Y(t) = r(t)\sin\theta(t) \end{cases} \quad \text{with} \quad r(t) = R\sin 2\theta(t) \tag{4-26}$$

where R equals 0.73 times the desired maximum horizontal displacement and the variation of θ is the same as for the butterfly-shaped pattern. The first cycle of the spiral-shaped pattern was defined as:

$$\begin{cases} \Delta_X(t) = r(t)\cos\theta(t) \\ \Delta_Y(t) = r(t)\sin\theta(t) \end{cases} \quad \text{with} \quad r(t) = R\frac{\theta(t)}{2m\pi} \tag{4-27}$$

where m is the number of turns in the spiral (here selected as 3) and θ varies from 0 to $2m\pi$ with a constant rate. In addition, the orbital pattern was expressed as:

$$\begin{cases} \Delta_X(t) = a(t)\cos\alpha(t) - b(t)\sin\alpha(t) \\ \Delta_Y(t) = a(t)\sin\alpha(t) + b(t)\cos\alpha(t) \end{cases} \quad \text{with} \quad \begin{cases} a(t) = a_o\cos\theta(t) \\ b(t) = b_o\sin\theta(t) \end{cases} \tag{4-28}$$

where a and b are the maximum and minimum values of the horizontal displacement achievable during the orbital motion; θ ranges from 0 to $2m\pi$ with a constant rate, where m is the number of orbits (here selected as 4); and α varies between 0 and 2π with a constant rate equal to m times the change rate of θ.

4.7.4.4.3. Loading Set 3

Loading Set 3 included five loading protocols with arbitrary biaxial displacement time histories. The purpose of these loading protocols was to examine the response of HSR columns under biaxial displacement histories that more realistically represent the earthquake loads. The displacement time histories were obtained from the time history analysis of the cantilever HSR column's finite element model under the horizontal acceleration components of four scaled ground motions representing earthquakes with 5%, 2%, and 1% probability of exceedance in 50 years. The loading protocols and the information of the earthquake records (Valigura 2019) used to produce the displacement time histories are summarized in Table 4-52 and their respective displacement time histories are demonstrated in Figure 4-338 and Figure 4-339. The planar motion paths of the loading beam resulting from those displacement time histories are also shown in Figure 4-340 and Figure 4-341.

Table 4-52. Loading protocols in Loading Set 3 from Phase IV

No	ID	Ground Motion	Max. Drift Ratio (%)
8	HSR3_ BI_CNT_S3_5in50_GM_7	5% in 50 yr, GM 7	1.7
9	HSR3_ BI_CNT_S3_5in50_GM_16	5% in 50 yr, GM 16	1.6
10	HSR3_ BI_CNT_S3_2in50_GM_9	2% in 50 yr, GM 9	2.6
11	HSR3_ BI_CNT_S4_2in50_GM_13	2% in 50 yr, GM 13	3.3
12	HSR3_ BI_CNT_S4_1in50_GM_13	1% in 50 yr, GM 12	4.2
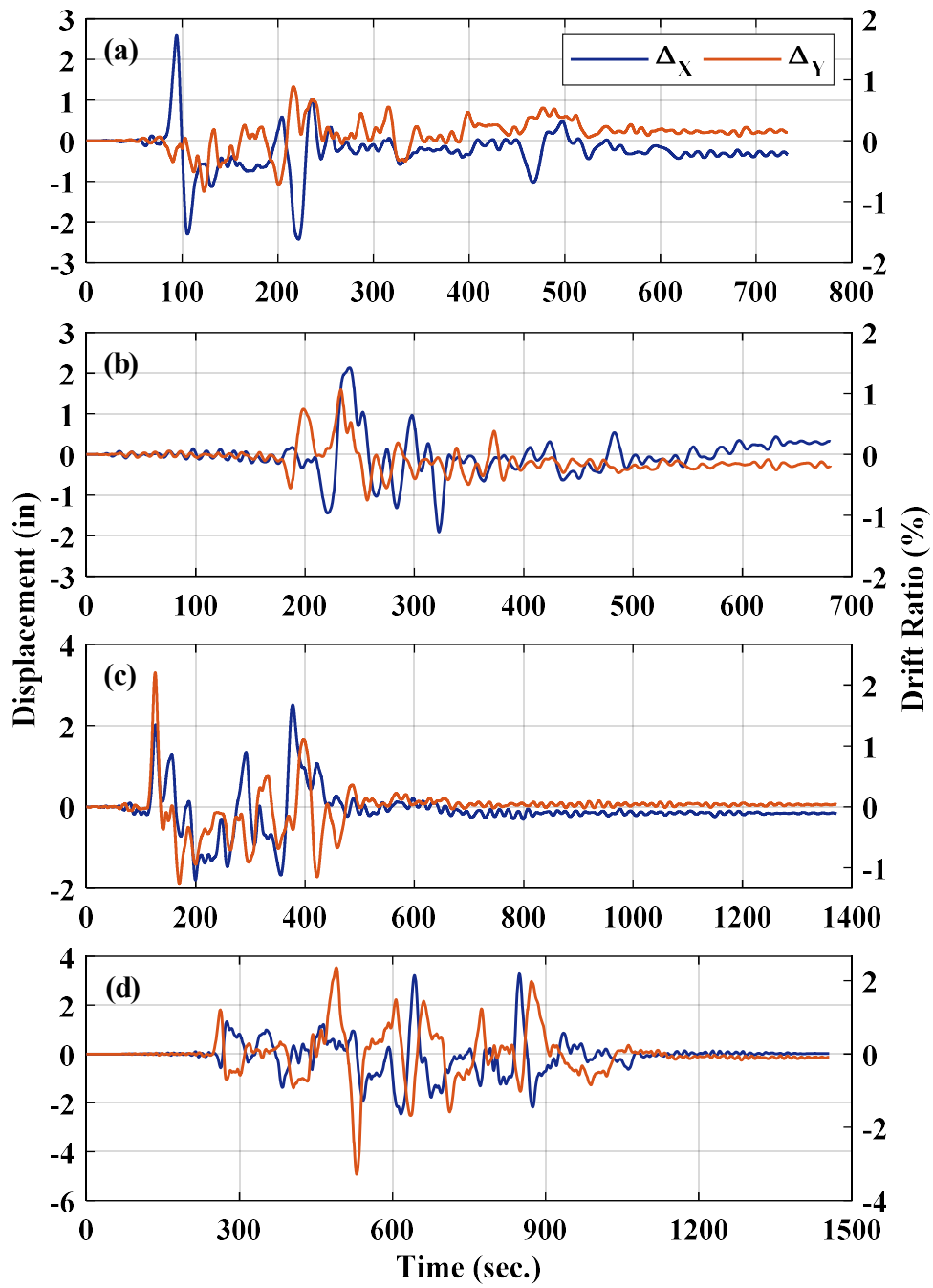
Figure 4-338. Displacement time histories in Loading Set 3, Phase IV: (a) test 8; (b) test 9; (c) test 10; (d) test 11

535
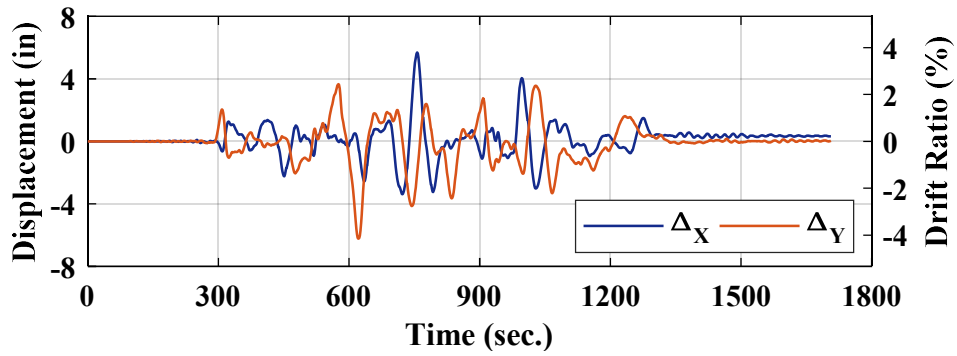
Figure 4-339. Displacement time histories in Loading Set 3, Phase IV: test 12
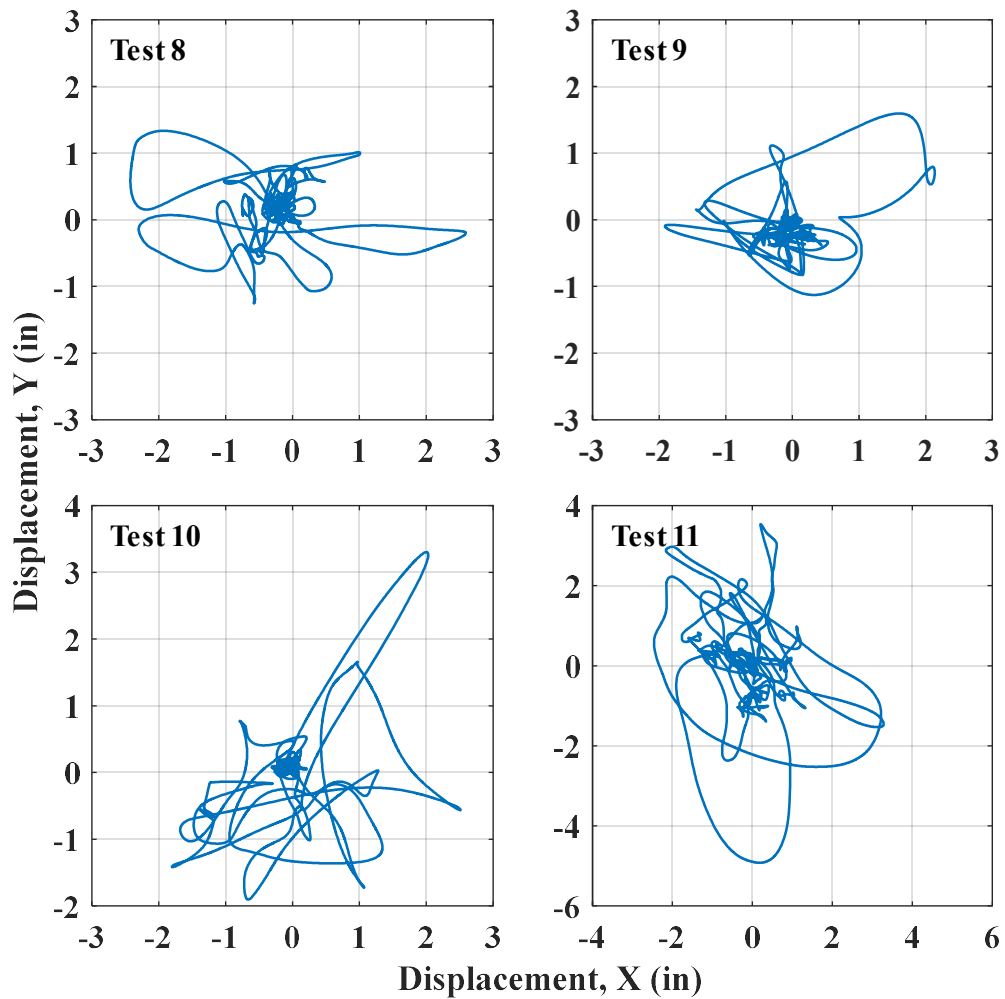
Figure 4-340. Planar motion paths of loading beam in Loading Set 3, Phase IV: tests 8-11

536
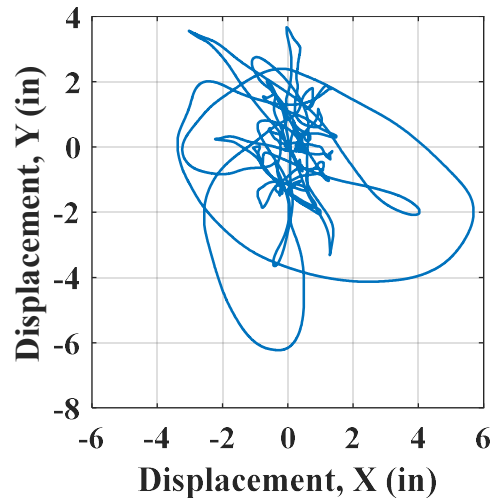
Figure 4-341. Planar motion paths of loading beam in Loading Set 3, Phase IV: test 12

4.7.4.4.4. Loading Set 4

Similar to the last Loading Set in the last three Phases, Loading Set 4 was aimed to evaluate the response and damage states of the HSR column specimen under extreme displacement demands. Because of the limitations of the swivel rotation and the stroke of the employed hydraulic actuators as well as safety considerations, the maximum achievable horizontal displacement in Phase IV was 9 in. in the diagonal direction. As a result, the single loading protocol considered in Loading Set 4 consisted of a two-cycle clover-shaped biaxial displacement path with a constant amplitude of 9 in., equivalent to a 6% drift ratio (Figure 4-342).
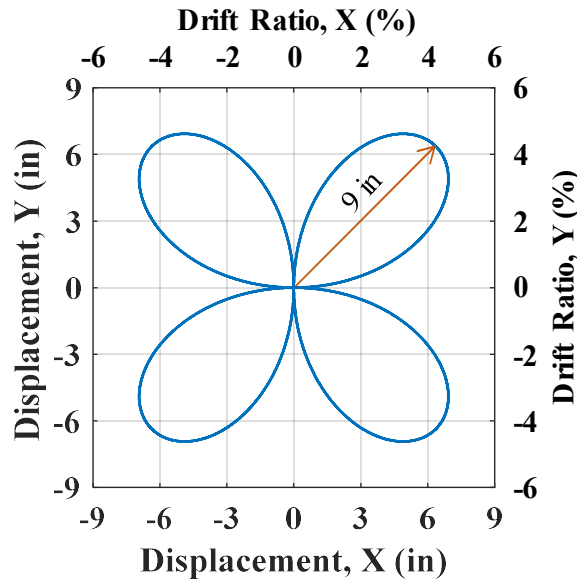
Figure 4-342. Biaxial displacement path in Loading Set 4, Phase IV

4.7.4.5. Results and Discussion

4.7.4.5.1. Results from Loading Set 1

Due to the geometry of the test setup and the lack of a third horizontal hydraulic actuator to enable the full control of the planar motion of the loading beam, the displacement time histories obtained during the tests were not identical to the desired displacement time histories. This was particularly more observable for the loading protocols with lower displacement demands.

The desired and achieved loading beam displacement paths in the test under the loading protocol HSR3_BI_CNT_S1_DR_1_3 are compared in Figure 4-343. According to the graph, the achieved motion was somewhat asymmetric and the peak lateral displacement (in the positive *Y* direction) was about 17% smaller than its target value, i.e. 1.5 in. Such differences were the result of the loading beam's unwanted twist (Figure

4-344(c)), potential inaccuracies in the loading commands (e.g. not accounting for out of plane motion) and potential inaccuracies in the measurements.
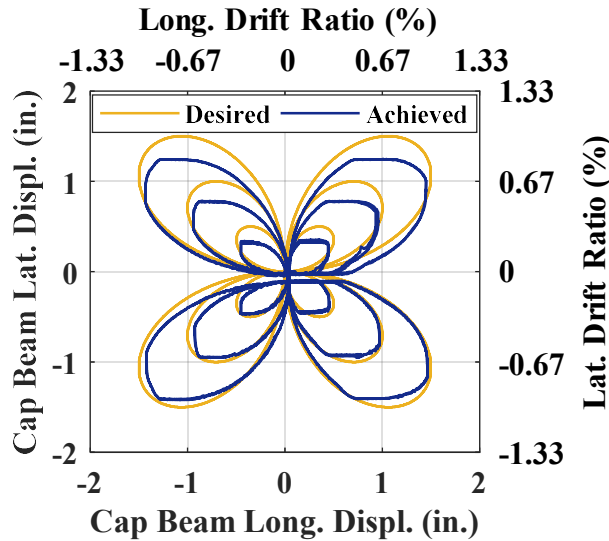
Figure 4-343. Phase IV, loading protocol HSR3_BI_CNT_S1_DR_1_3: comparison of achieved and desired loading beam's displacement paths

According to Figure 4-344, in the very first test in this Phase, joint sliding initiated prior to the first displacement peak from the third cycle, i.e. the first cycle of amplitude 1.3 in. (0.87% drift ratio). The sliding occurred only at the first sliding joint (Joint 2, Figure 4-348 and Figure 4-349). Comparing the loading beam's displacement and total joint sliding time histories in Figure 4-344(a) and (b), it is obvious that the column's response was dominated by joint sliding, as at least 50% of the horizontal displacement imposed to the column was provided by the joint sliding. Small phase lags are also observed between the beam displacement and sliding time histories, especially in the longitudinal (X) direction.
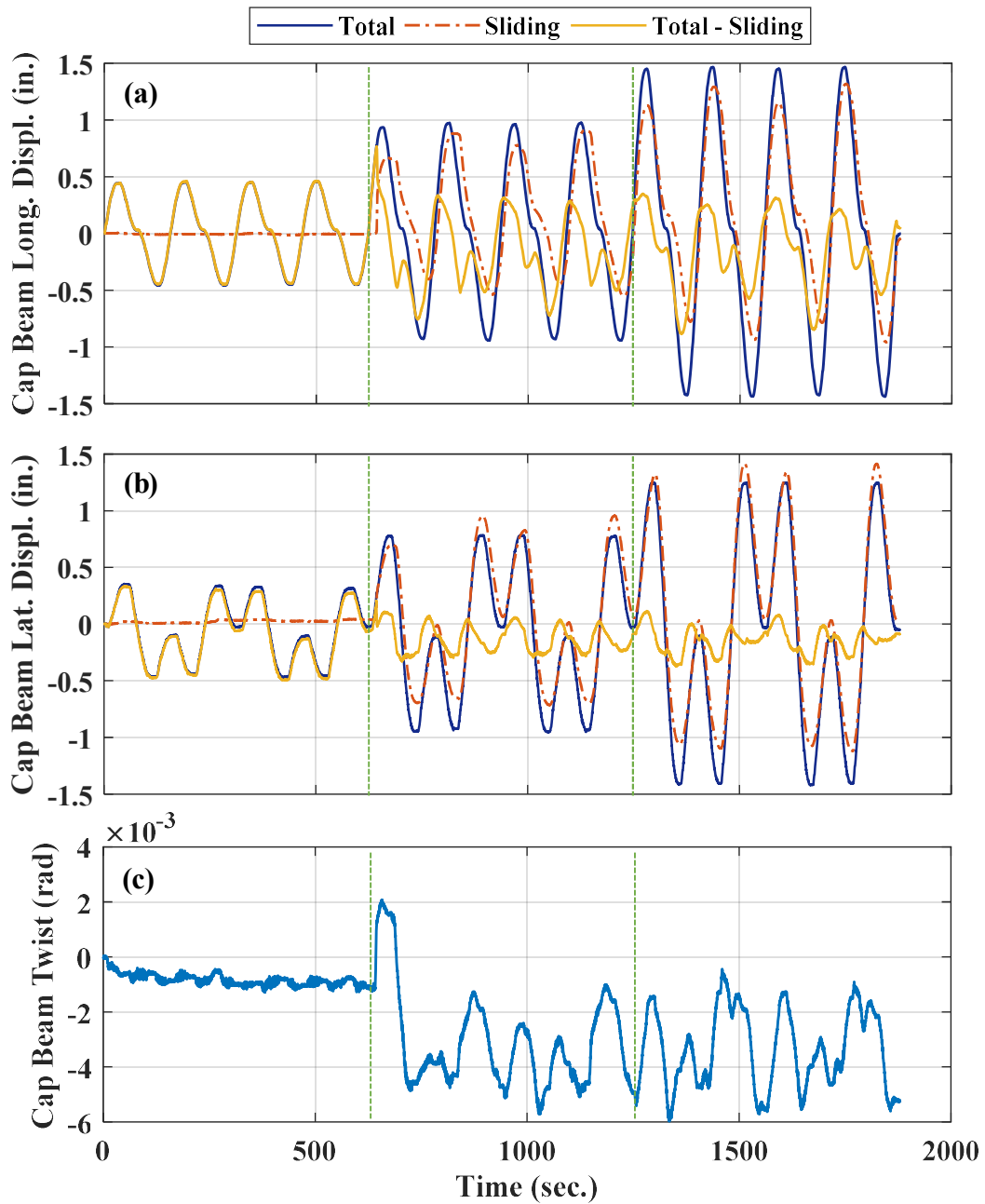
Figure 4-344. Phase IV, loading protocol HSR3_BI_CNT_S1_DR_1_3: time histories of loading beam's: (a) longitudinal displacement components; (b) lateral displacement components; (c) twist

The contribution of sliding to the applied displacement in the negative X direction was considerably lower than that in the opposite direction, resulting in a larger fraction of

540

displacement peaks that required to be accommodated through rocking (Figure 4-344(a)). The maximum sliding achieved in the negative and positive *X* directions were 0.95 in. and 1.32 in., respectively, while they were 1.12 in. and 1.42 in. in the negative and positive *Y* directions, respectively; all these values are yet smaller than the maximum nominal achievable sliding in any direction, i.e. 1.45 in. The inequality of the maximum sliding values achieved in four directions, which is more apparent in Figure 4-345, could be justified by the tendon ducts' misalignment and the potential measurement and data post-processing errors. After sliding initiated, the sliding paths achieved during each pair of the displacement cycles are found repeatable (Figure 4-345), implying minimal damage to the column specimen.
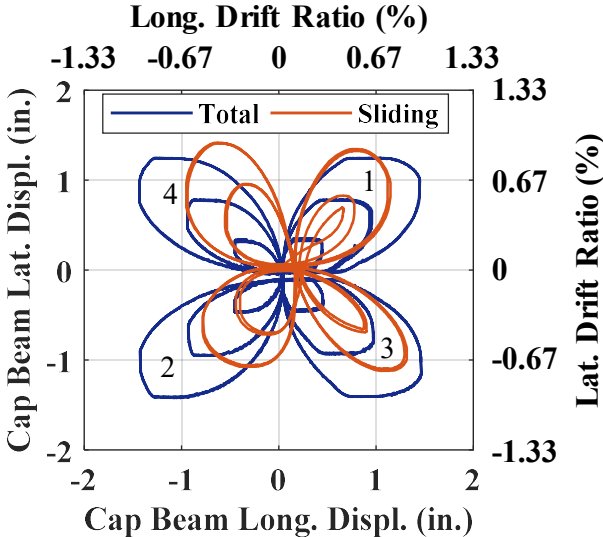
Figure 4-345. Phase IV, loading protocol HSR3_BI_CNT_S1_DR_1_3: comparison of loading beam's displacement path and sliding path at Joint 2

The column specimen's base shear vs. displacement responses obtained in the two horizontal directions under the same loading protocol are shown in Figure 4-346. Considering that the displacement time histories applied in the longitudinal (X) and lateral (Y) directions were different (see Figure 4-344(a) and (b)), the hysteretic responses did not fully resemble. The maximum base shear values in this tests were obtained before the joint sliding initiation (i.e. under pure rocking), which were 22 kips and 35 kips in the longitudinal and lateral directions, respectively. The reason for the 37% smaller maximum base shear in the longitudinal direction than its lateral counterpart is not clear, but it could be attributed to the test setup's asymmetry in the two directions.
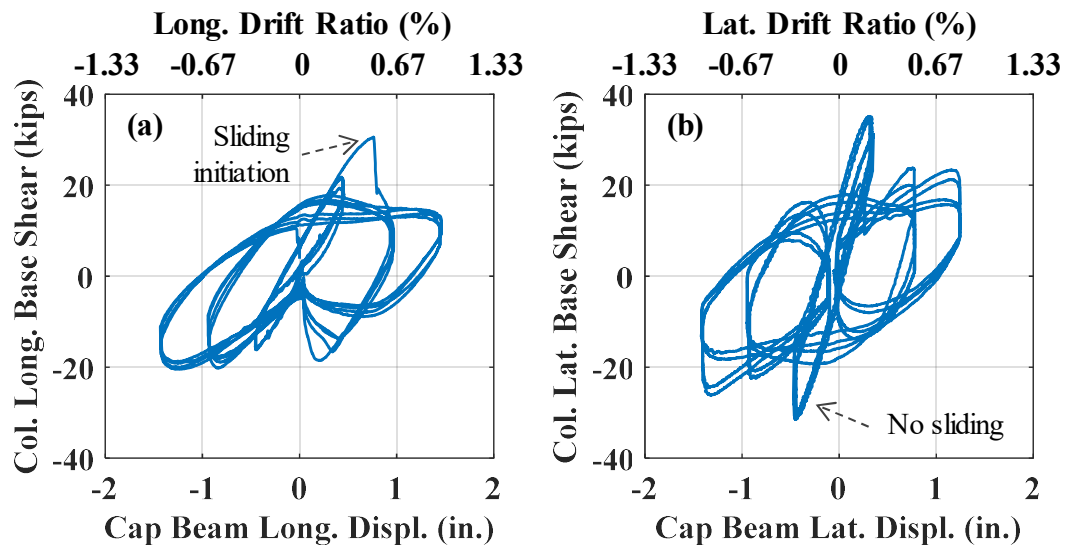
Figure 4-346. Phase IV, loading protocol HSR3_BI_CNT_S1_DR_1_3 – column base shear vs. horizontal displacement responses in: (a) X direction; (b) Y direction

With the onset of joint sliding in the column, the effect of sliding direction change on the values of the base shear components is evident in Figure 4-347. According to this

figure, the peak total base shear (magnitude) values corresponding to the same total displacement peaks but in various directions were less than 23% different. The total base shear at which sliding started at Joint 2 was almost 37 kips – this value is consistent with the incipient sliding base shear of the column tested in Phase I (i.e. 40 kips, Figure 4-62). With the start of sliding, as expected, the column's total base shear significantly decresed. The residual displacements (the largest of the two values in the negative and positive directions) corresponding to the last displacement peak were 1.25 in. and 1.17 in. in *X* and *Y* directions, respectively. These values equal less than 0.85% drift ratio.
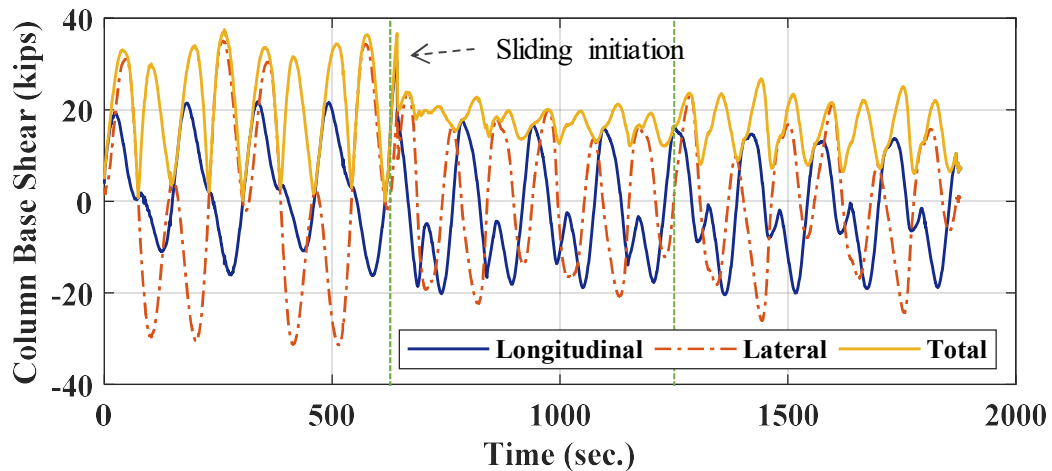
Figure 4-347. Phase IV, loading protocol HSR3_BI_CNT_S1_DR_1_3: time histories of column base shear components and total base shear

The joints' shear vs. sliding responses in the *X* and *Y* directions are demonstrated in Figure 4-348 and Figure 4-349, respectively. As mentioned earlier, only the first sliding joint (Joint 2) exhibited sliding and the rest of the joints experienced almost no sliding. The dependence of the friction components on the sliding direction is evident in the shapes

of the hysteretic responses of Joint 2. More specifically, it is observed in the above results that the joint shear components in each direction dropped to almost zero as the sliding path became normal to the respective direction and the loading beam's displacement was small enough such that the response was friction-dominant (see Figure 4-345). This was because the friction force and sliding increment/rate vectors are generally of the same direction and the friction force component normal to the sliding's instantaneous direction is zero.
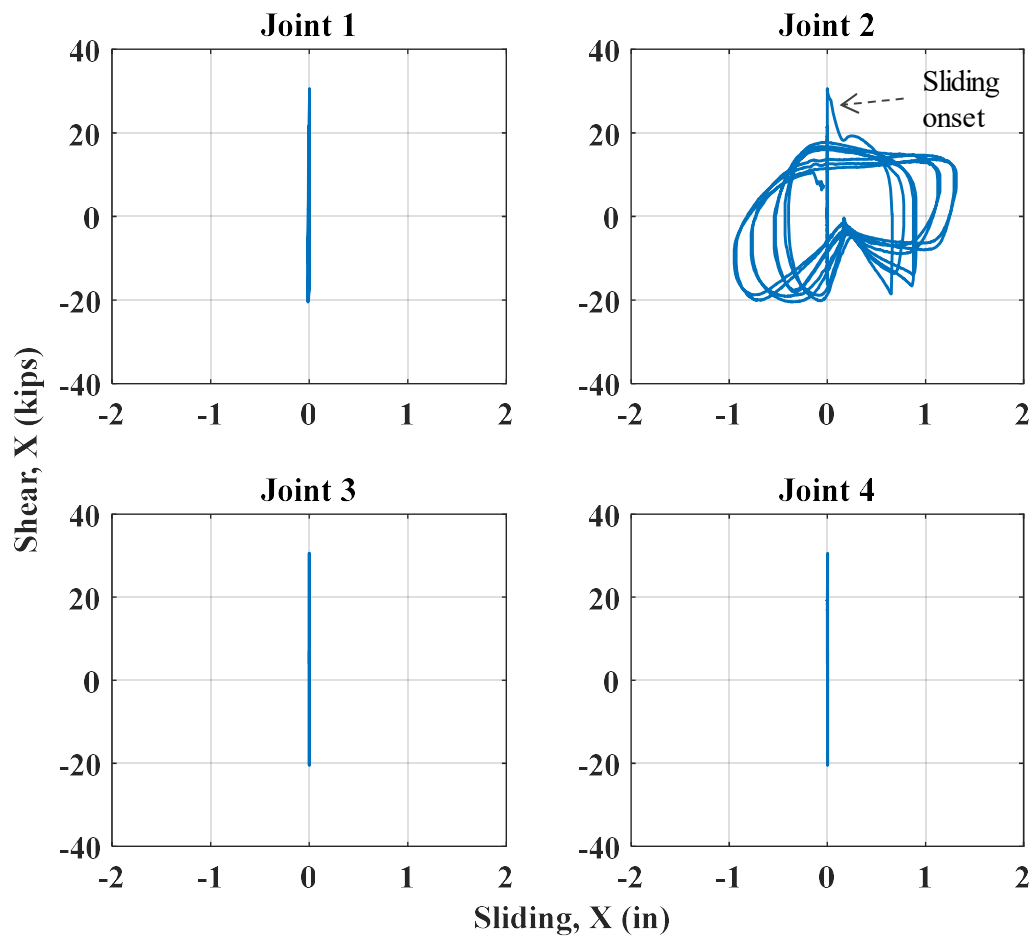
Figure 4-348. Phase IV, loading protocol HSR3_BI_CNT_S1_DR_1_3: joint shear vs. sliding responses in *X* direction
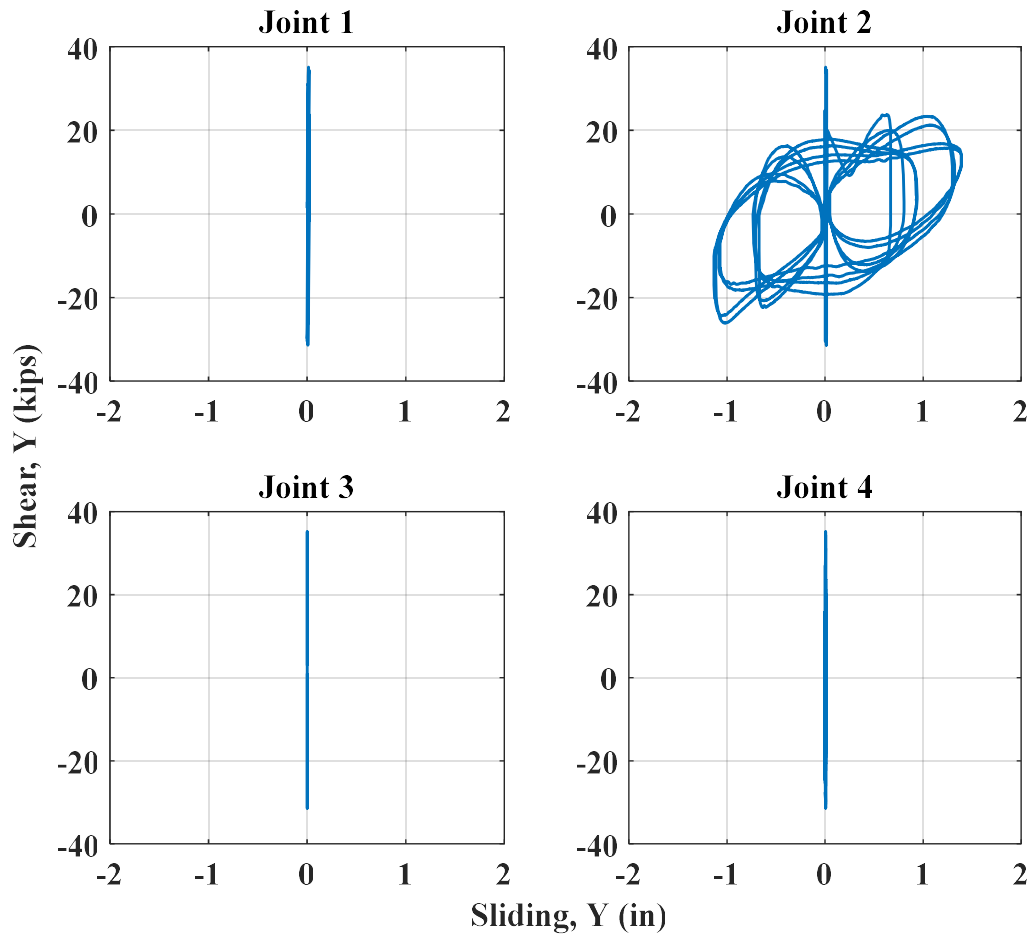
Figure 4-349. Phase IV, loading protocol HSR3_BI_CNT_S1_DR_1_3: joint shear vs. sliding responses in *Y* direction

The time histories of the column's base moment components computed according to the data recorded in this test are shown in Figure 4-350. Consistently with the base shear time histories presented in Figure 4-347, the peak base moments about the *X*- and *Y*-axes were observably different. As explained before, the difference between these values can be attributed to the test setup's asymmetry, the variation of material properties over the column volume, the potential lack of cross section symmetry, and the potential unevenness of the joint surfaces. The maximum total moment withstood by the column under the

applied loading protocol was 470 kip-ft, which occurred during the first two cycles of horizontal displacement, when no sliding happened and rocking was maximum. Even though the peak drift ratio increased in the subsequent displacement cycles, because of the joint sliding, the maximum moment at the column base dropped by 23%, thereby reducing the compressive strain demands at the bottom rocking joint.
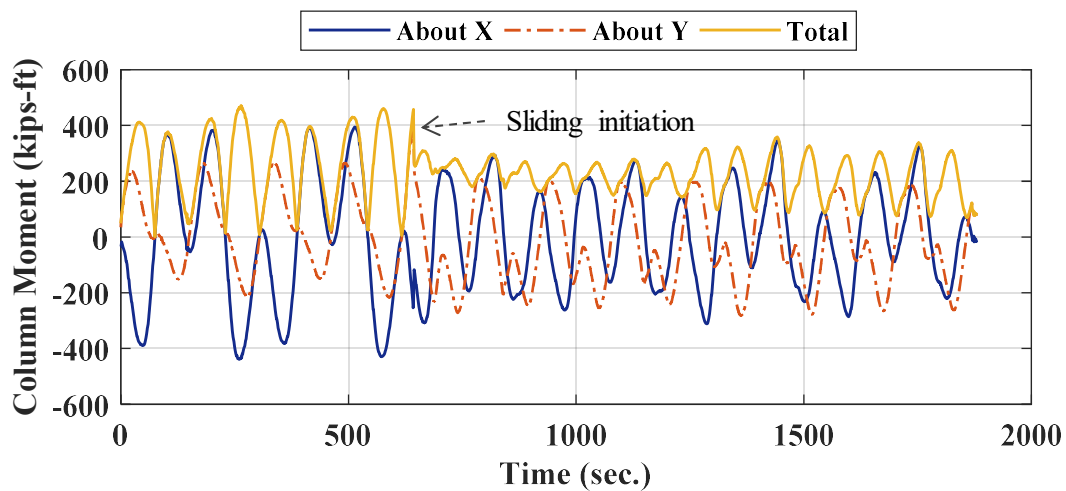
Figure 4-350. Phase IV, loading protocol HSR3_BI_CNT_S1_DR_1_3: column base moment time histories

The time histories of the individual tendon forces recorded during the same test as well as their sum are demonstrated in Figure 4-351. The initial posttensioning existing in the column before the start of horizontal loading was 136 kips, i.e. about 6% lower than the design value (144 kips). This posttensioning loss could have happened due to the PTFE/epoxy creep at the sliding joints.

As expected, the tendon forces increased with the peak drift ratio, as the maximum values of the total PT forces during the first and the last two displacement cycles were 136

546

kips and 144 kips, respectively. This is also obvious in Figure 4-352, showing the variation of total PT force with the loading beam's horizontal displacement. The maximum individual tendon force during the test was less than 21 kips, i.e. less than 40% of the strands yield strength. The individual tendons' PT losses ranged from 4% to 7%, whereas the total posttensioning loss was less than 6%.
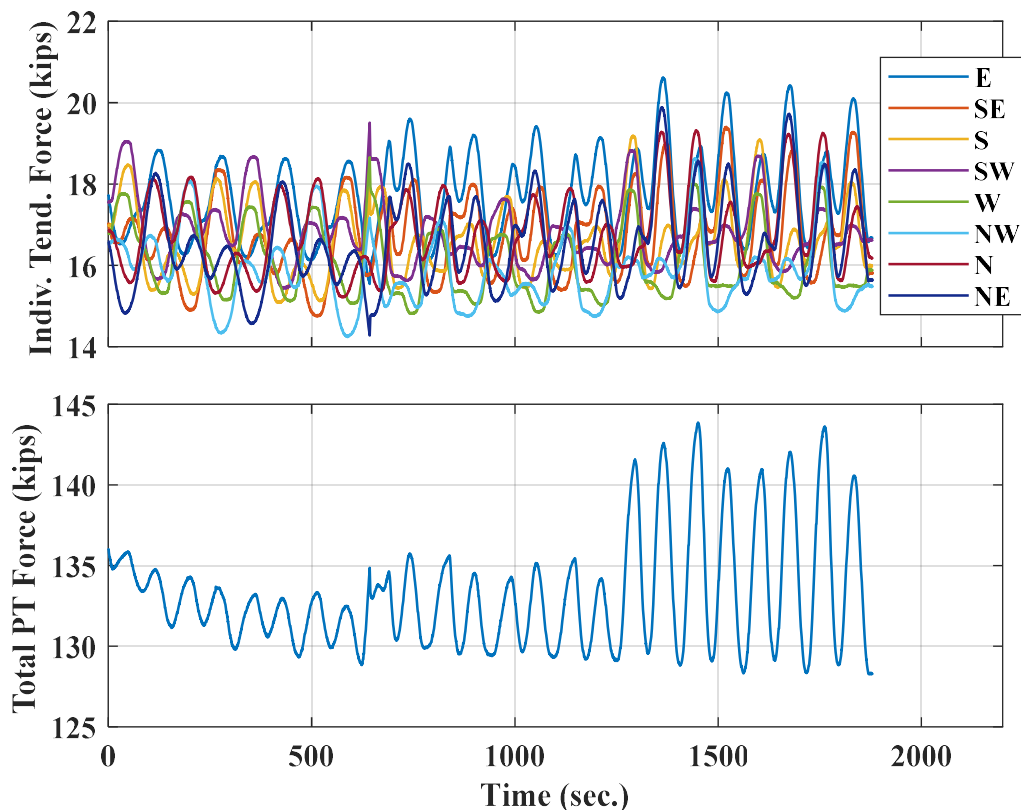
Figure 4-351. Phase IV, loading protocol HSR3_BI_CNT_S1_DR_1_3: time histories of posttensioning forces
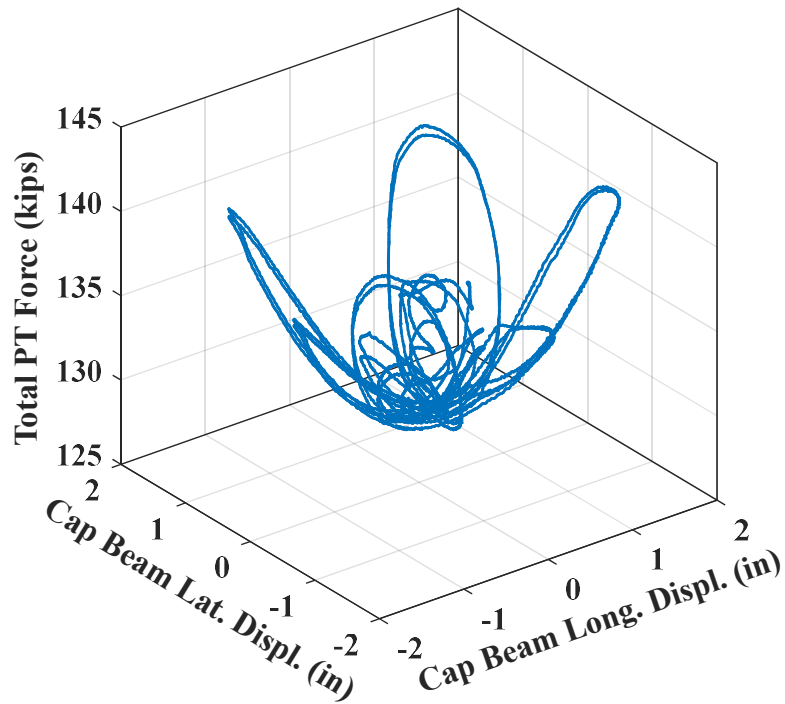
Figure 4-352. Phase IV, loading protocol HSR3_BI_CNT_S1_DR_1_3: total PT force vs. loading beam horizontal displacements

The visible damage sustained by the column segments under the first loading protocol was limited to several cracks (mostly hairline) on the surface of the bottom segment (Figure 4-353), slight spalling near the south compression toe at the bottom joint (Figure 4-354), and a couple of diagonal cracks on the middle segment (Figure 4-355). The majority of the cracks on the bottom segment were horizontal and appeared on the east and west sides of the segment, extending up toward the sliding joint. Given their pattern and orientations, these cracks could not be compressive cracks. The fact that the cracks had propagated from the sliding joint back to the sliding joint along arc-shaped paths imply that they had probably occurred due to the stress variations/concenterations caused by the unevenness of the first sliding joint interface.

548
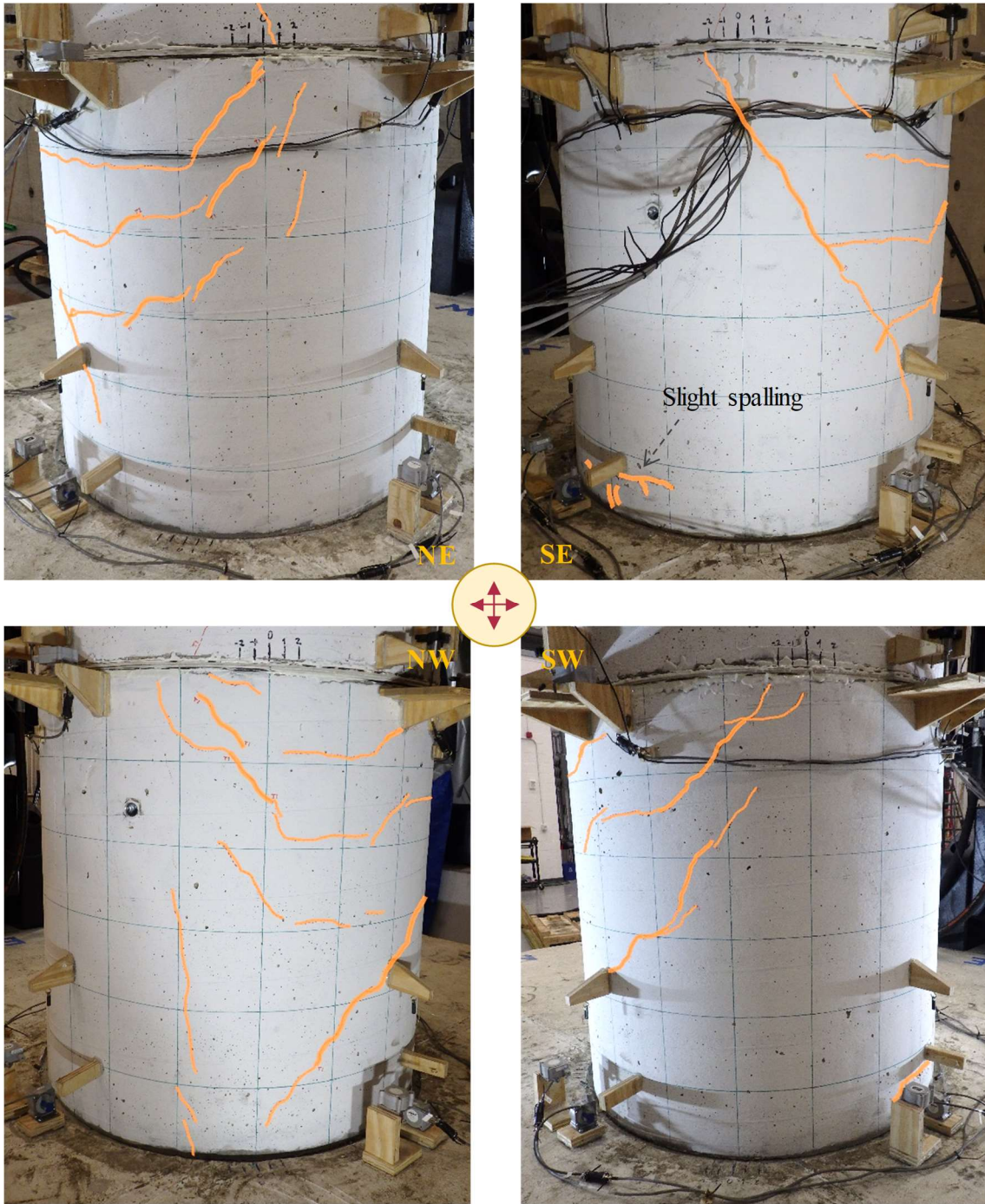
Figure 4-353. Phase IV, loading protocol HSR3_BI_CNT_S1_DR_1_3: distribution of cracks on bottom segment

549

Figure 4-354. Phase IV, loading protocol HSR3_BI_CNT_S1_DR_1_3: slight spalling near south quadrant of bottom rocking joint

NE NW
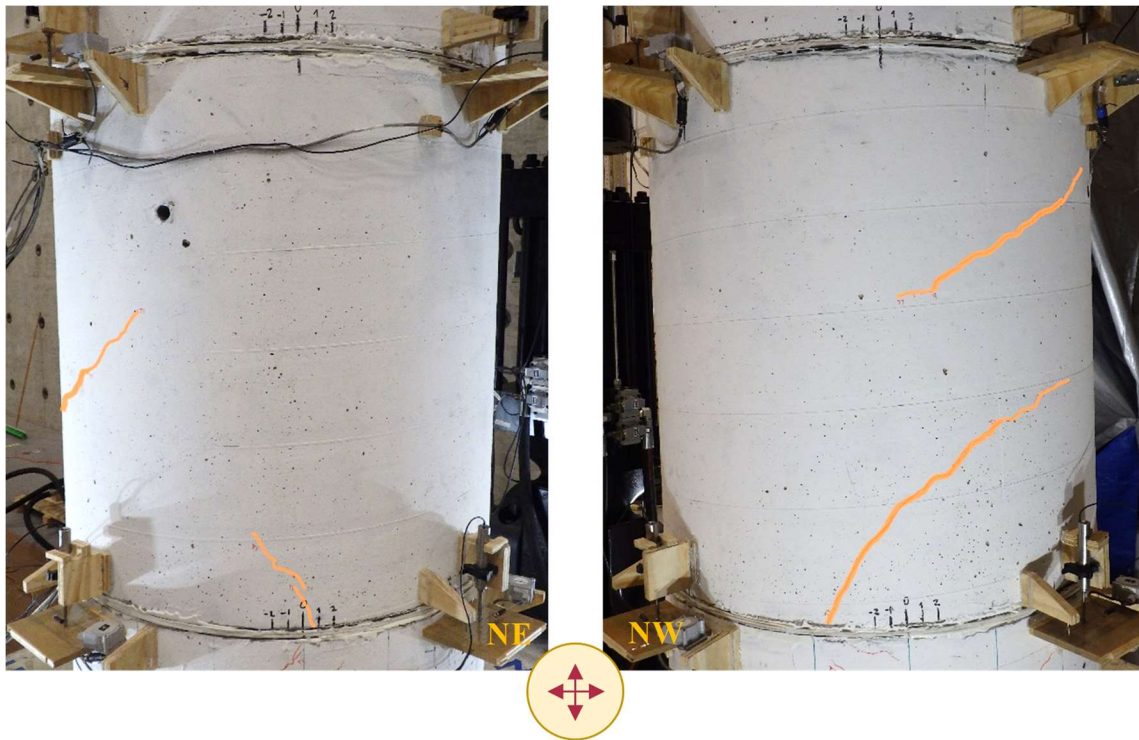
Figure 4-355. Phase IV, loading protocol HSR3_BI_CNT_S1_DR_1_3: distribution of cracks on middle segment

The loading beam's horizontal displacement path achieved under loading protocol HSR3_BI_CNT_S1_DR_2 is compared with the desired path in Figure 4-356. It is observed that the achieved displacement components are slightly smaller than the desired

displacement components, especially in the lateral (*Y*) direction. The maximum
displacement achieved in the negative and positive *Y* directions were 2.1 in. and 2 in.,
respectively, whereas the desired values were both equal to 2.3 in. As mentioned earlier,
the failure to precisely achieve the desired displacement paths is associated with the
loading beam's unwanted twist which was not accounted for in the horizontal actuators'
displacement commands.
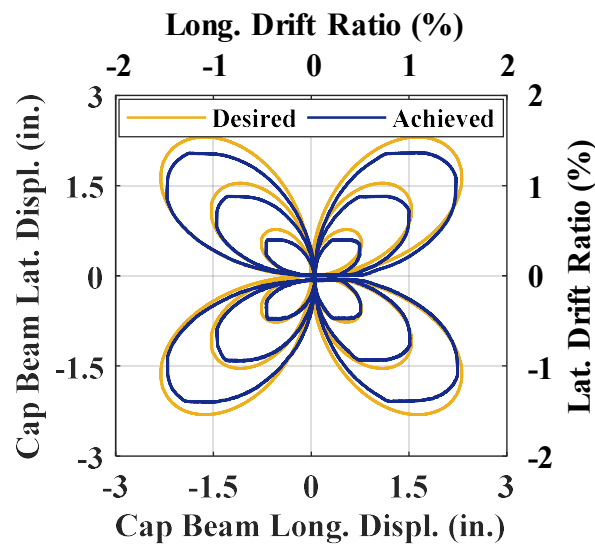
**Figure 4-356. Phase IV, loading protocol HSR3_BI_CNT_S1_DR_2: comparison of
achieved and desired loading beam's displacement paths**

According to Figure 4-357, at least 49% and 63% of the horizontal displacements
applied to the loading beam in the longitudinal and lateral directions, respectively, were
accommodated through joint sliding. Similar to the previous test, sliding was confined to
the first sliding joint (Joint 2) in this test (see Figure 4-361 and Figure 4-362), as the shear
force in the column did not become large enough to overcome the breakaway friction at

551

the second sliding joint (Joint 3). Otherwise, the displacement demands could have been fully accommodated through joint sliding.
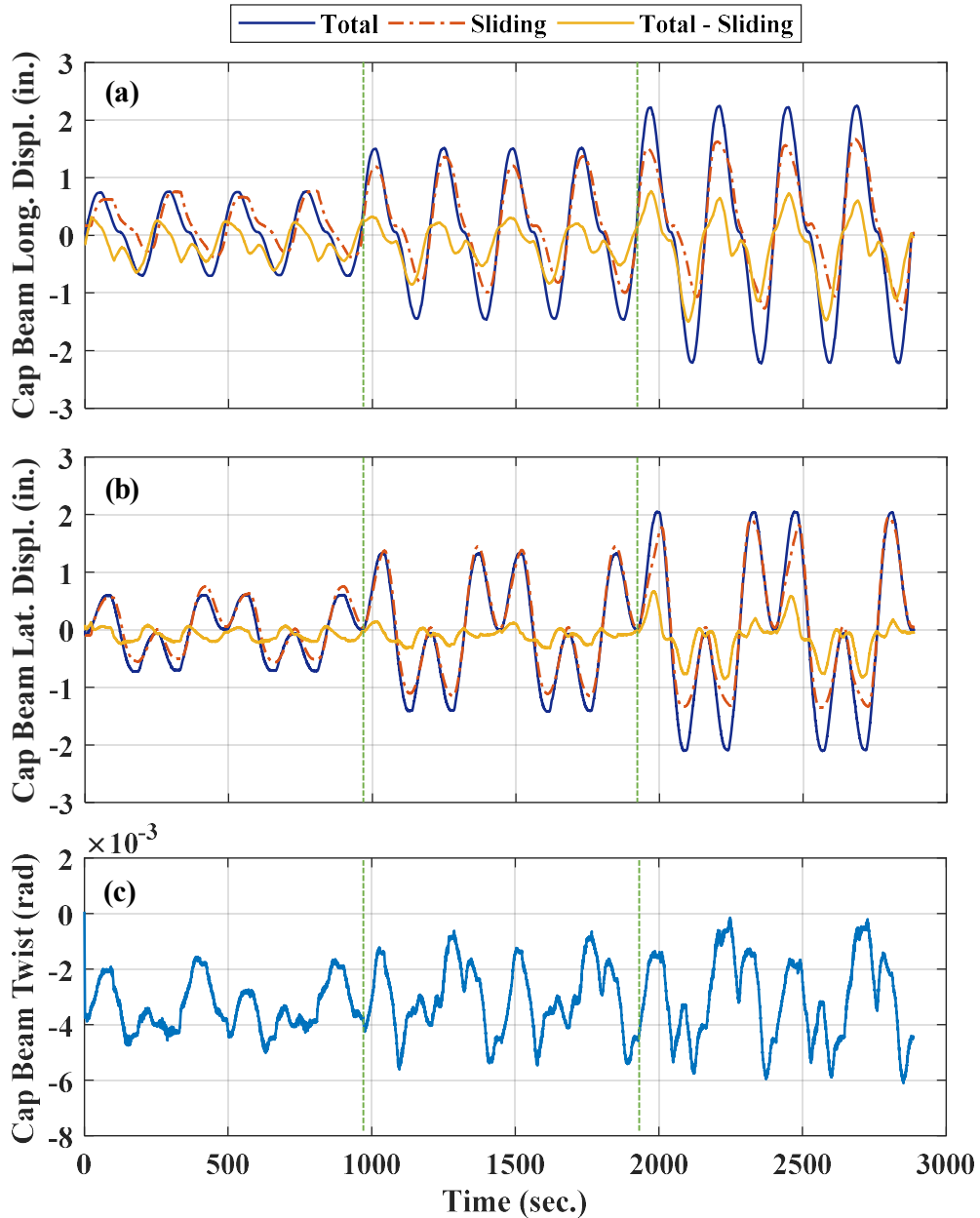
Figure 4-357. Phase IV, loading protocol HSR3_BI_CNT_S1_DR_2: time histories of loading beam's: (a) longitudinal displacement components; (b) lateral displacement components; (c) twist

It is also observed in Figure 4-357 that the sliding peaks in each direction did not necessarily coincide with the displacement peaks in the same direction. This could be justified by the presence of friction between the tendons and the ducts and the initial duct misalignments. According to Figure 4-358, the minimum sliding was achieved in the southwest direction, which was also the case for the previous test (Figure 4-345). The fact that the maximum sliding values in different directions were different is attributed to the initial duct misalignments, giving the tendons different amounts of space to move in various directions. The maximum twist recorded during this test was quite small (0.006 rad = 0.34 degrees).
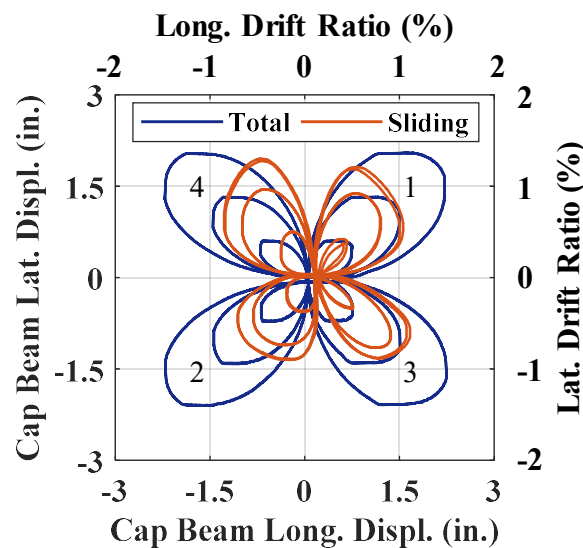
Figure 4-358. Phase IV, loading protocol HSR3_BI_CNT_S1_DR_2: comparison of loading beam's displacement path and sliding path at Joint 2

The column specimen's base shear vs. displacement responses in the two horizontal directions under the same loading protocol are shown in Figure 4-359. Due to the previous

553

sliding at Joint 2, the breakaway friction at that joint was considerably lower than that recorded during the first test. The hardening character of the responses indicates the effect of the tendons bearing against the ducts.
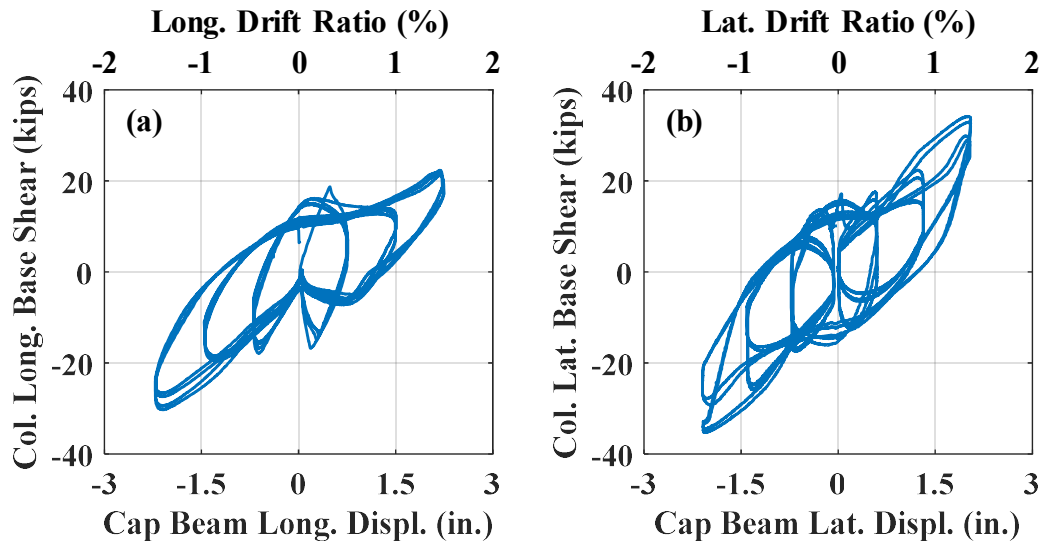
Figure 4-359. Phase IV, loading protocol HSR3_BI_CNT_S1_DR_2 – column base shear vs. horizontal displacement responses in: (a) *X* direction; (b) *Y* direction

It is also observed that, for equal peak lateral displacements, the corresponding base shear values could be different, which shows the significant effect of the loading path and the tendon-duct friction on the responses – note that equal lateral displacements were obtained on each pair of the clover leaves (Figure 4-356), but the corresponding longitudinal displacements and the path leading to those displacements were different.

Another important observation in accordance with Figure 4-359, which is consistent with the first test's results (Figure 4-346), was that the maximum base shear values in the longitudinal (*X*) direction were smaller than those in the lateral (*Y*) direction. Specifically,

the maximum base shear values obtained in the negative and positive Y directions were 35 kips and 34 kips, respectively (Figure 4-359(b)), while the maximum base shear values achieved in the negative and positive X directions were 30 kips and 22 kips, respectively (Figure 4-359(a)). The considerably lower longitudinal base shear in the positive X direction is believed to have been induced by a small gap observed between the first two column segments over the east part of the lower sliding joint interface, resulting in a flexural stiffness reduction in the positive X direction.

The average residual displacement values determined on the basis of the hysteretic responses shown in Figure 4-359 were 1.28 in. and 1.23 in. in X and Y directions, respectively. Major portions of these residual displacements (up to 99%) were caused by the residual sliding at Joint 2 (Figure 4-361 and Figure 4-362).
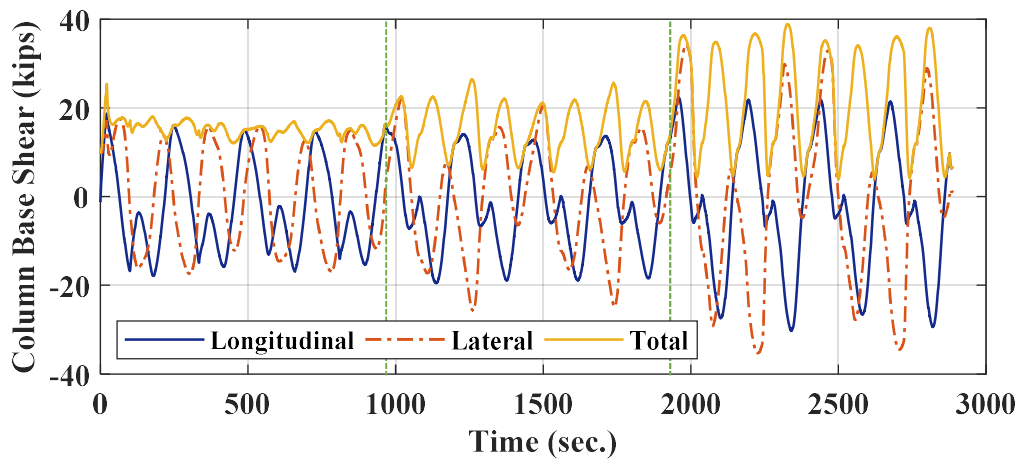
Figure 4-360. Phase IV, loading protocol HSR3_BI_CNT_S1_DR_2: time histories of column base shear components and total base shear

The maximum total base shear was almost 39 kips, which occurred during the fifth displacement cycle with a peak drift ratio of 2% (Figure 4-360). In terms of cyclic deterioration, the responses obtained during the two cycles per displacement amplitude appeared to be very similar, implying no cyclic damage in the column specimen.
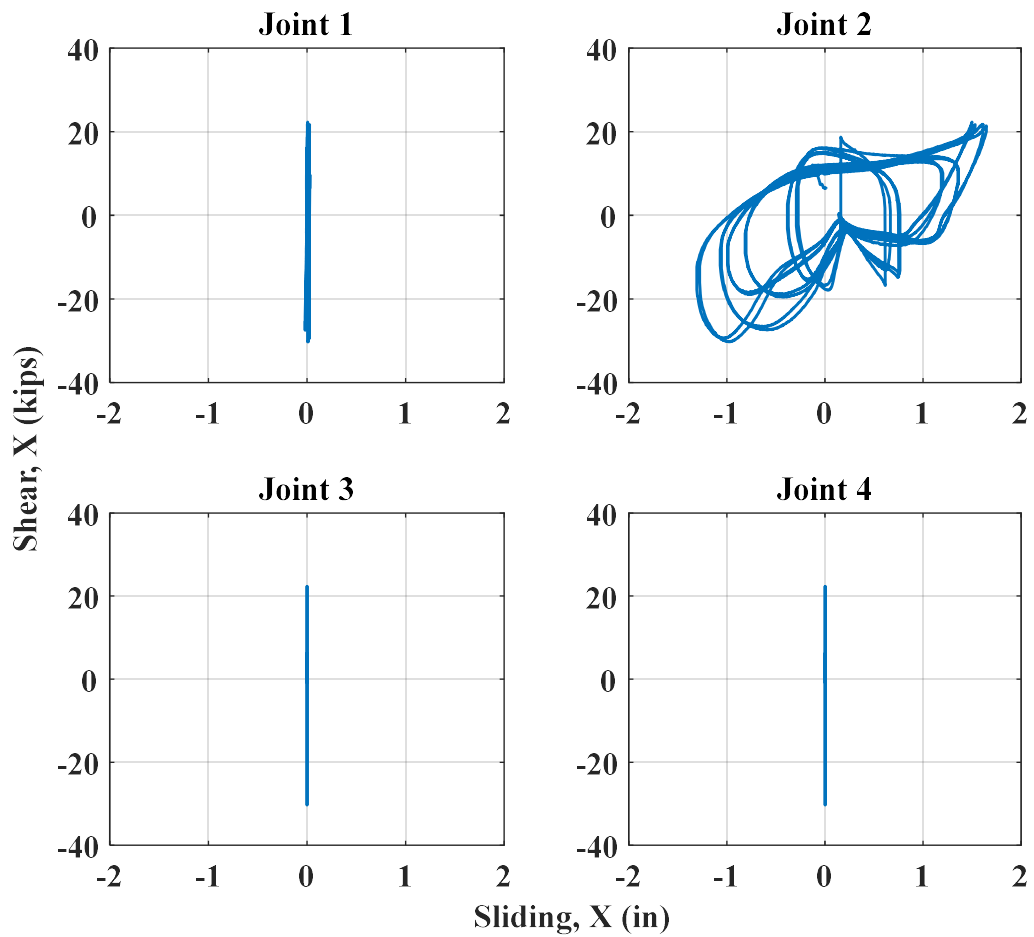
Figure 4-361. Phase IV, loading protocol HSR3_BI_CNT_S1_DR_2: joint shear vs. sliding responses in *X* direction
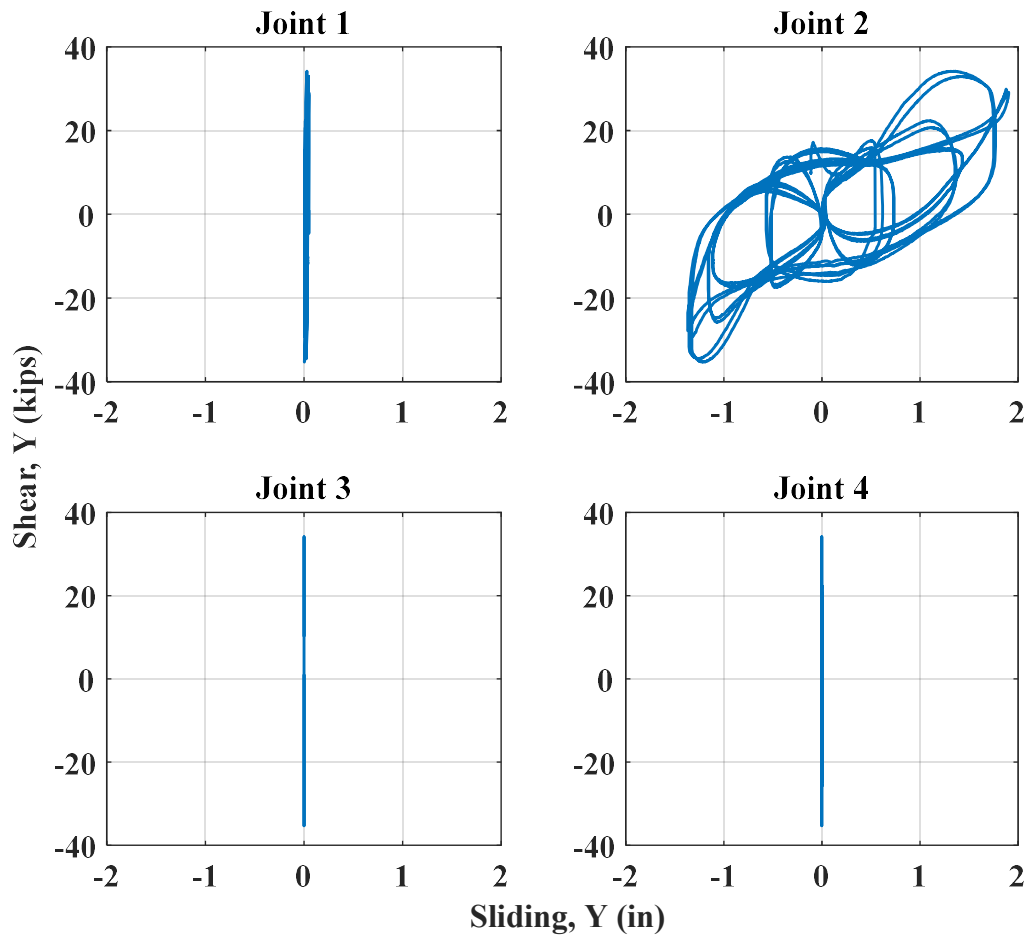
Figure 4-362. Phase IV, loading protocol HSR3_BI_CNT_S1_DR_2: joint shear vs. sliding responses in *Y* direction

Per Figure 4-361 and Figure 4-362, the joint sliding primarily occurred at Joint 2. The maximum sliding achieved at Joint 2 in the negative and positive longitudinal (*X*) directions were 1.3 in. and 1.6 in., respectively, whereas the maximum sliding values in the negative and positive lateral (*Y*) directions were 1.4 in. and 1.9 in., respectively. Some of these values are smaller than the nominal sliding capacity of each joint (~1.45 in.) and some are larger, implying the initial misalignment of the tendon ducts. In addition, the similarity of the maximum sliding values achieved during the two cycles of each

557

displacement amplitude show that the duct adaptors were not significantly damaged by the tendons' bearing reactions during this test.

The variations of the moment components at the column base around the *X*- and *Y*-axes and their resultant with time are compared in Figure 4-363. The maximum moment created at the column's bottom end about the *Y*-axis under the horizontal displacement in the positive *X* direction was 305 kip-ft, which was 27% lower than that under the horizontal displacement in the negative direction (~ 420 kip-ft). In contrast, the maximum negative moment value obtained about the *X*-axis is only 2% smaller than its positive counterpart (~ 470 kip-ft). As explained for the difference of the maximum negative and positive base shear values in the *X* direction observed earlier (Figure 4-359), the large difference in the maximum neagative and positive moment values about the *Y*-axis is justified by the imperfect contact between the bottom and the middle column segments toward the east side of the first sliding joint, compromising the flexural stiffness of the column under positive longitudinal displacement. The larger rocking observed at the bottom rocking joint around the *X*-axis compared to that around *Y*-axis is another proof for the above fact (Figure 4-364).
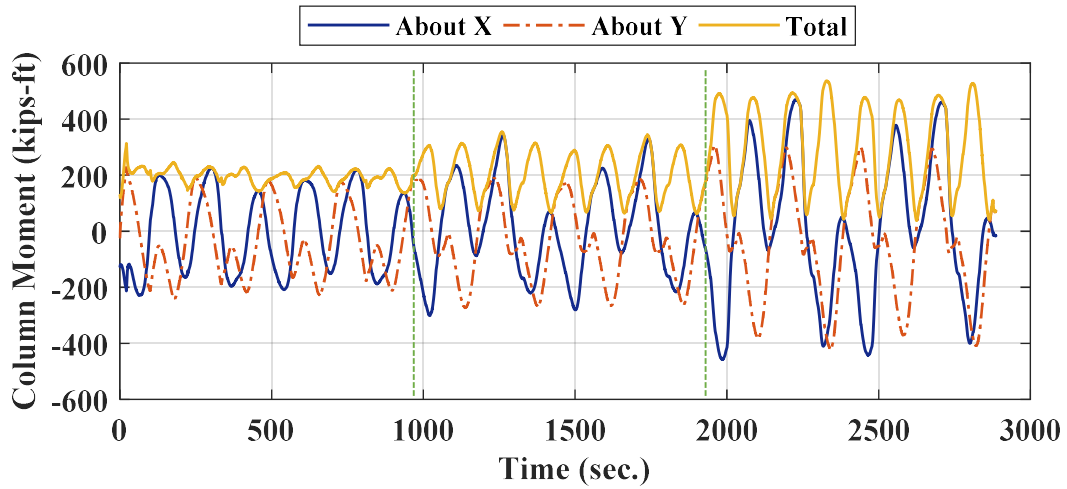
Figure 4-363. Phase IV, loading protocol HSR3_BI_CNT_S1_DR_2: column base moment time histories
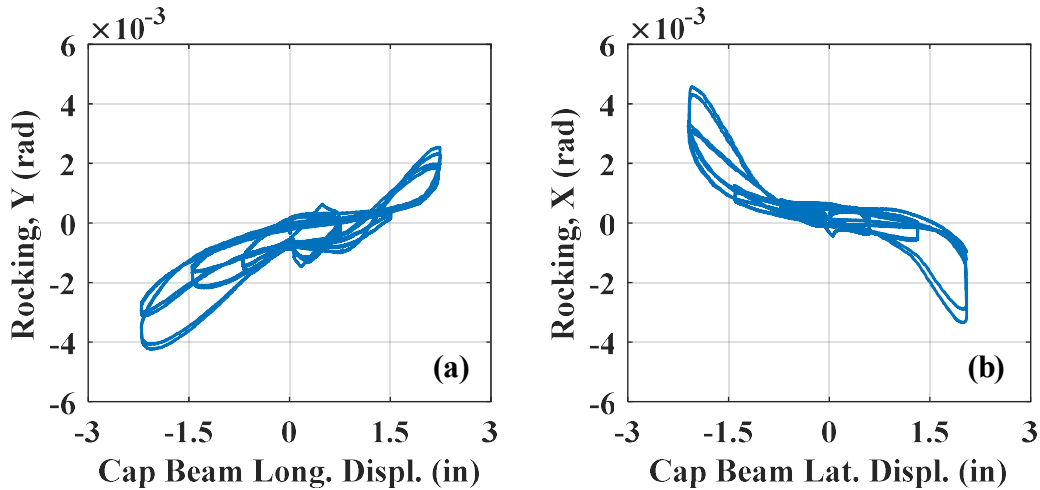
Figure 4-364. Phase IV, loading protocol HSR3_BI_CNT_S1_DR_2 – bottom joint response: (a) rocking around *Y*-axis vs. displacement in *X* direction; (b) rocking around *X*-axis vs. displacement in *Y* direction

On average, the tendon forces increased by 23% under the maximum drift ratio of 2%, but they still remained far below their yielding point – the maximum tendon force was about 24 kips (Figure 4-365). The total posttensioning loss resulted after this test was

559

less than 3%, which primarily occurred during the last two displacement cycles (i.e. with the maximum drift ratio imposed in this test). According to Figure 4-366, as expected, there was a direct relationship between the total PT force and the total imposed horizontal displacement, irrespective of its direction.
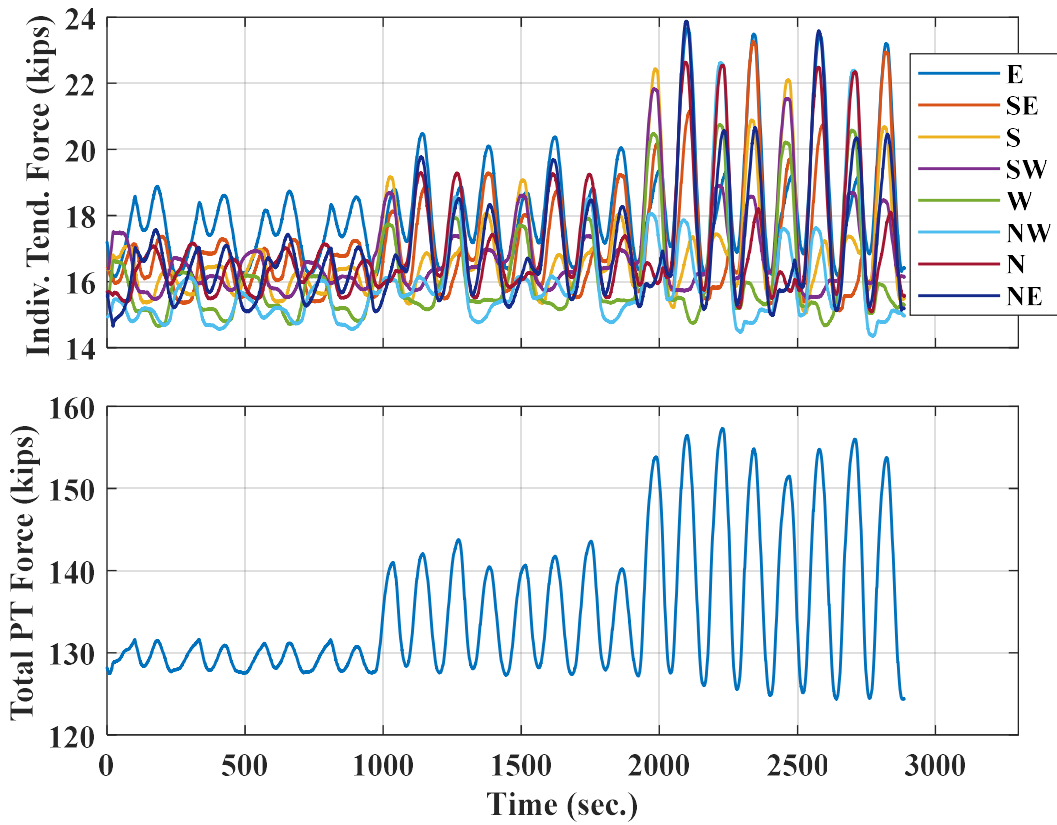
Figure 4-365. Phase IV, loading protocol HSR3_BI_CNT_S1_DR_2: time histories of posttensioning forces
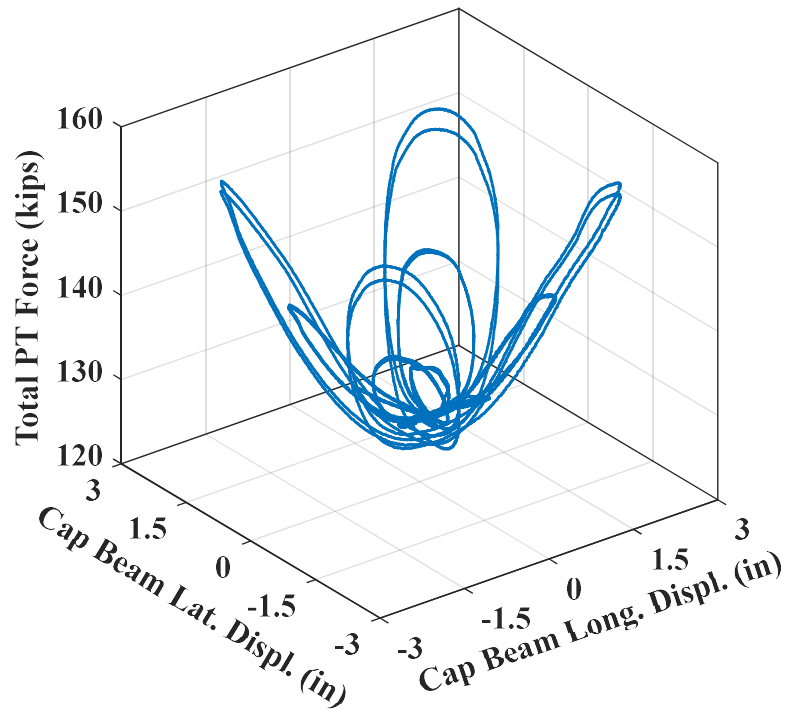
Figure 4-366. Phase IV, loading protocol HSR3_BI_CNT_S1_DR_2: total PT force vs. loading beam horizontal displacements

After the above test, no significant damage was observed, except for some new hairline cracks on the bottom segment (Figure 4-367) and very shallow concrete spalling at two spots near the bottom two joints (Figure 4-368). The spalling near the sliding joint (Figure 4-368(a)) was most likely caused by the stress concentrations/variations due to the unevenness of the sliding interface. The spalling near the south quadrant of the bottom rocking joint (Figure 4-368(b)) can, however, be associated with the extra axial load emerging in the column when the column was pushed toward southeast (on the third clover leaf in Figure 4-358) compared to other directions (seen the total PT force time history in Figure 4-365). No additional cracks were observed on the top two segments.
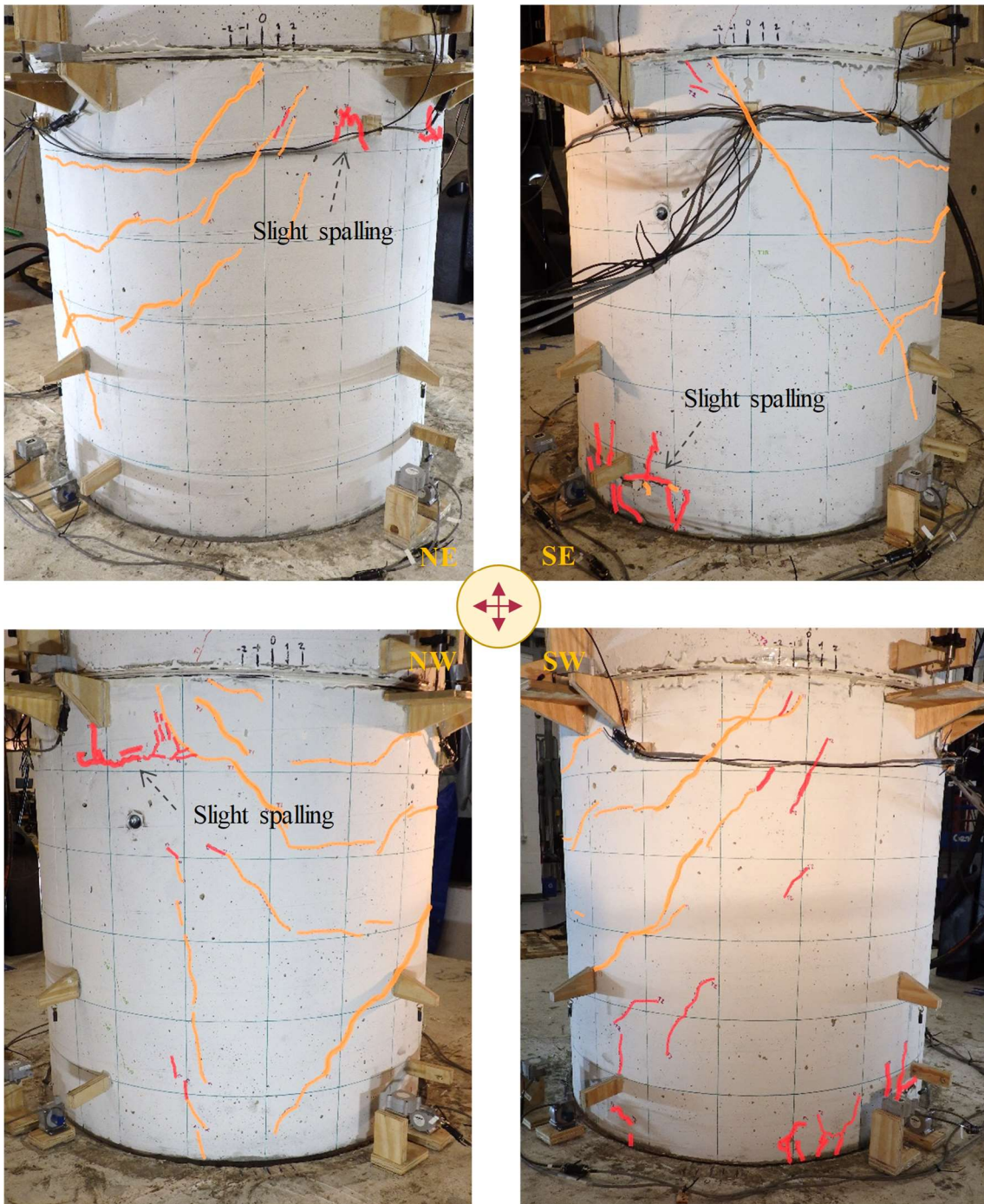
Figure 4-367. Phase IV, loading protocol HSR3_BI_CNT_S1_DR_2: distribution of cracks on bottom segment
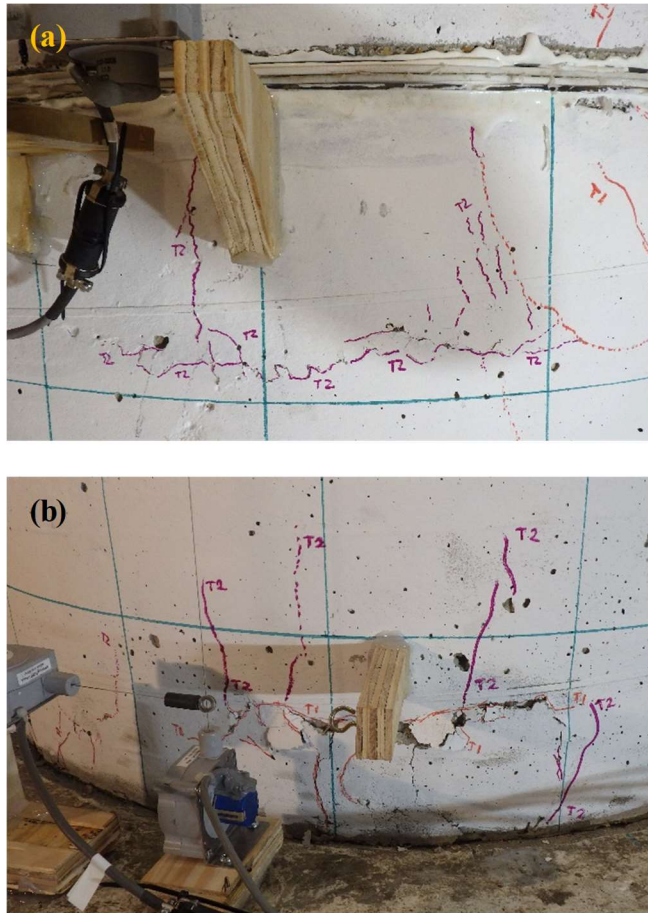
Figure 4-368. Phase IV, loading protocol HSR3_BI_CNT_S1_DR_2: shallow spalling: (a) below Joint 2, north quadrant; (b) above Joint 1, south qudrant

The achieved loading beam displacement path under the loading protocol HSR3_BI_CNT_S1_DR_4 is compared with the respective target path in Figure 4-369. The achieved displacement components in the longitudinal (X) and lateral (Y) directions were slightly smaller than their desired values, but the paths were close in shape and the cycles of the same amplitude were almost identical. The maximum displacement values obtained in the X and Y directions were 4.55 in. and 4.25 in., respectively, while the desired peak displacement in each direction was 4.6 in.
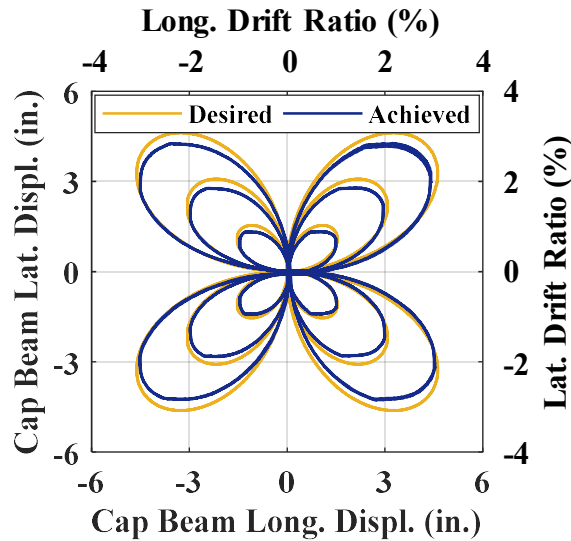
Figure 4-369. Phase IV, loading protocol HSR3_BI_CNT_S1_DR_4: comparison of achieved and desired loading beam's displacement paths

According to the horizontal displacement and total sliding time histories compared in Figure 4-370, the applied displacements were dominantly accommodated through rocking. During the last two biaxial displacement cycles with the maximum amplitude, a maximum of 52% of the applied displacement was in the form of sliding. Similar to the previous two tests, only the first sliding joint became active, so the second sliding joint did not exhibit any sliding (see Figure 4-374 and Figure 4-375). As seen in Figure 4-371, because of duct misalignments, the sliding was minimum in the southwest direction (on the 2nd clover leaf). The maximum twist remained below 0.007 rad (~ 0.4 degrees) during this test (Figure 4-370(c)).
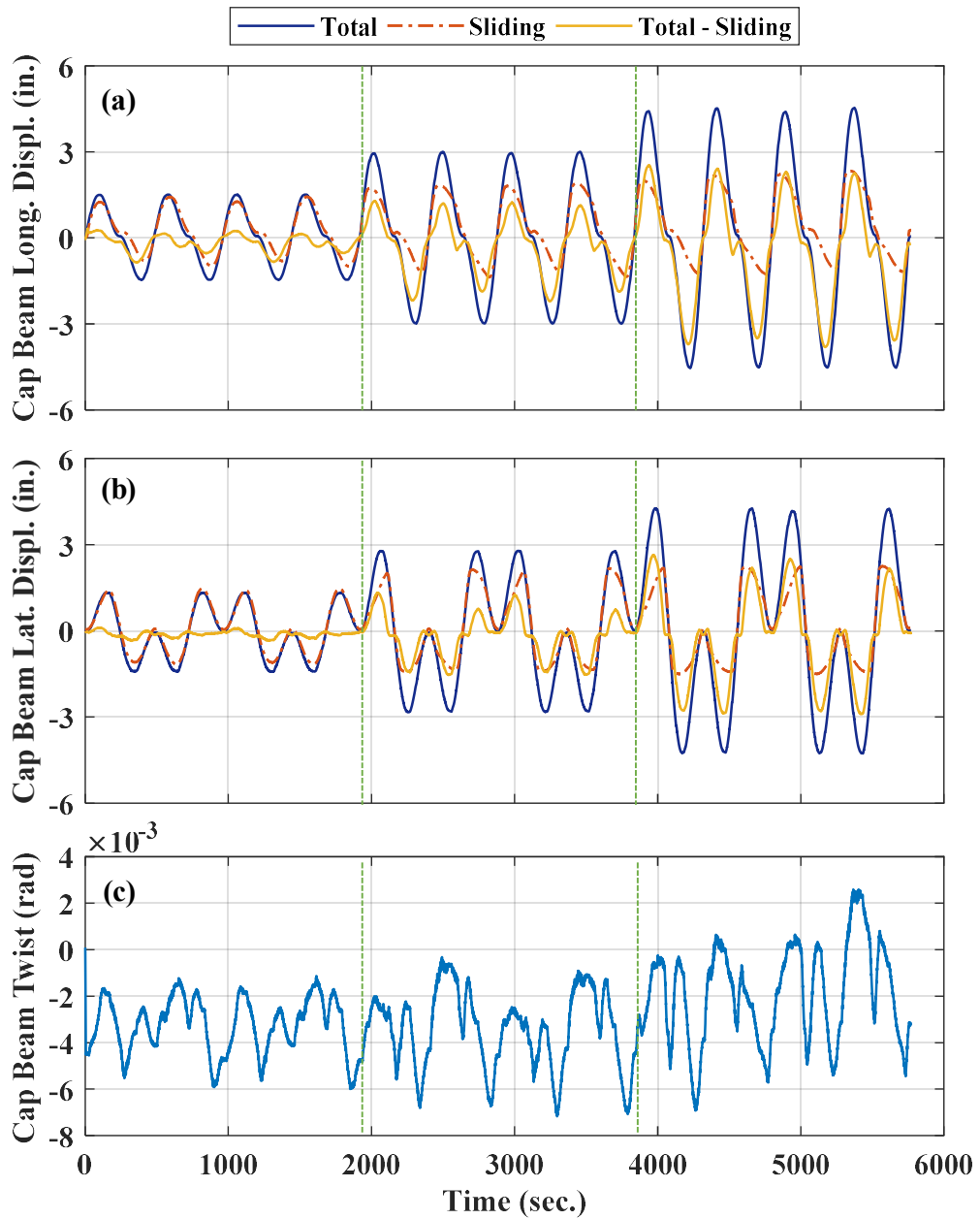
Figure 4-370. Phase IV, loading protocol HSR3_BI_CNT_S1_DR_4: time histories of loading beam's: (a) longitudinal displacement components; (b) lateral displacement components; (c) twist

565
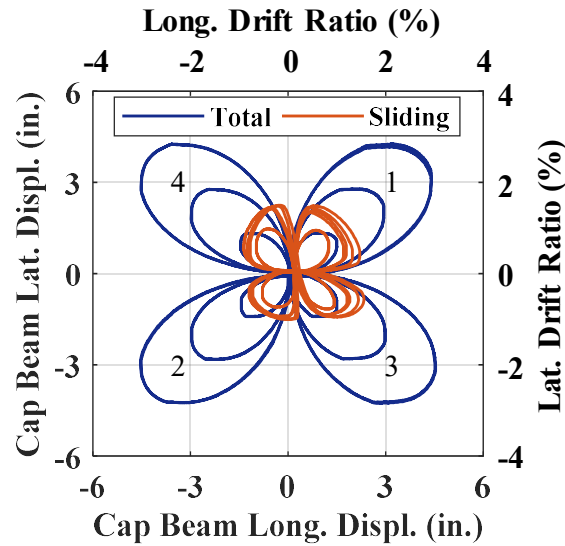
Figure 4-371. Phase IV, loading protocol HSR3_BI_CNT_S1_DR_4: comparison of loading beam's displacement path and sliding path at Joint 2

The column base shear vs. displacement responses in the two horizontal directions are shown in Figure 4-372. It is noted that, similarly to the respective results for the previous tests, the base shear values corresponding to a single displacement value in a direction could be different from each other in two different time instants, as the column's resistance is dependent on both displacement components as well as the displacement path; for example, the base shear in the X direction was different for the same longitudinal displacement but various lateral displacement values, or for the same longitudinal and lateral displacements, but on the 1st and the 4th clover leaves shown in Figure 4-371.

The maximum base shear values obtained in the negative and positive X directions and the negative and positive Y directions (at the peak displacements in those directions) were 33, 34, 36, and 37 kips, respectively (Figure 4-372). The closeness of these values

demonstrates the higher response symmetry of the column specimen under large displacement demands, regaldless of the sliding joint imperfections.
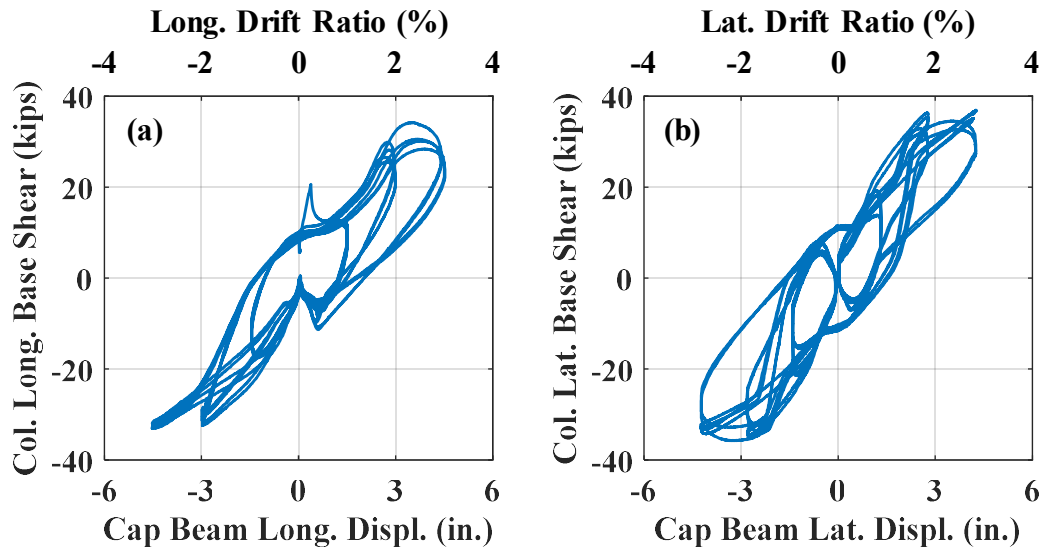
Figure 4-372. Phase IV, loading protocol HSR3_BI_CNT_S1_DR_4 – column base shear vs. horizontal displacement responses in: (a) *X* direction; (b) *Y* direction

Some strength deterioration is observed in the column specimen's hysteretic responses, particularly during the last two cycles (with maximum 4% drift ratio). This strength deterioration, which is better seen in the total base shear vs. displacement response depicted in Figure 4-373, was caused by the concrete spalling near the bottom rocking joint (see Figure 4-382) and the significant posttensioning loss that occurred during the fifth displacement cycle (the first cycle with 4% drift ratio amplitude, Figure 4-379).
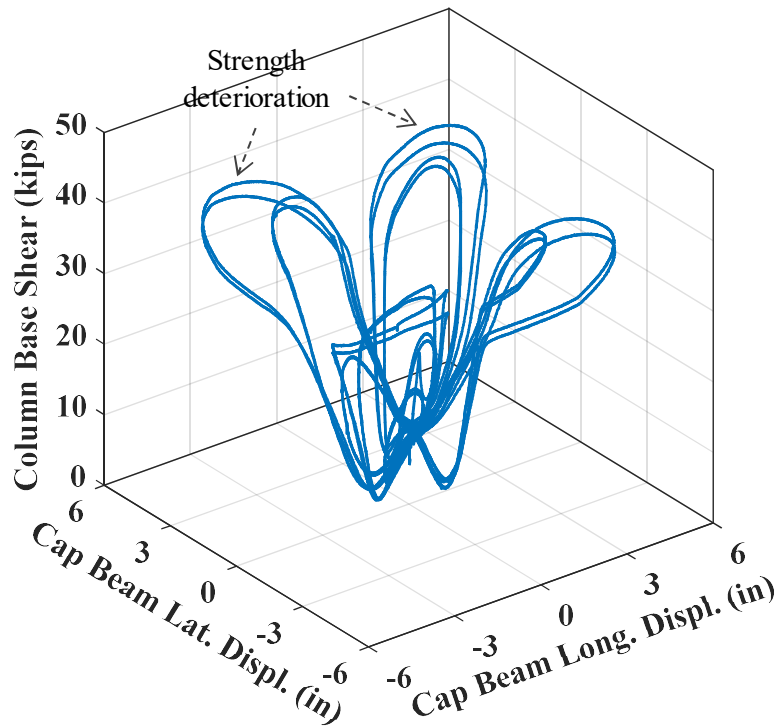
Figure 4-373. Phase IV, loading protocol HSR3_BI_CNT_S1_DR_4: total column base shear vs. beam horizontal displacement components

The maximum residual displacements along the X- and Y-axes were found to be 2 and 1.65 in., respectively. These residual displacements, which are equivalent to the residual drift ratios 1.3% and 1.1%, respectively, were primarily induced by the residual sliding at Joint 2 (see Figure 4-374 and Figure 4-375).

Some sliding was recorded at the bottom rocking joint, in particular in the positive X direction (by 0.45 in.), but no sliding was observed at Joints 3 and 4 (Figure 4-374 and Figure 4-375). The bottommost joint's sliding seems to have occurred due to the bottom segment's gradual walking eastward.
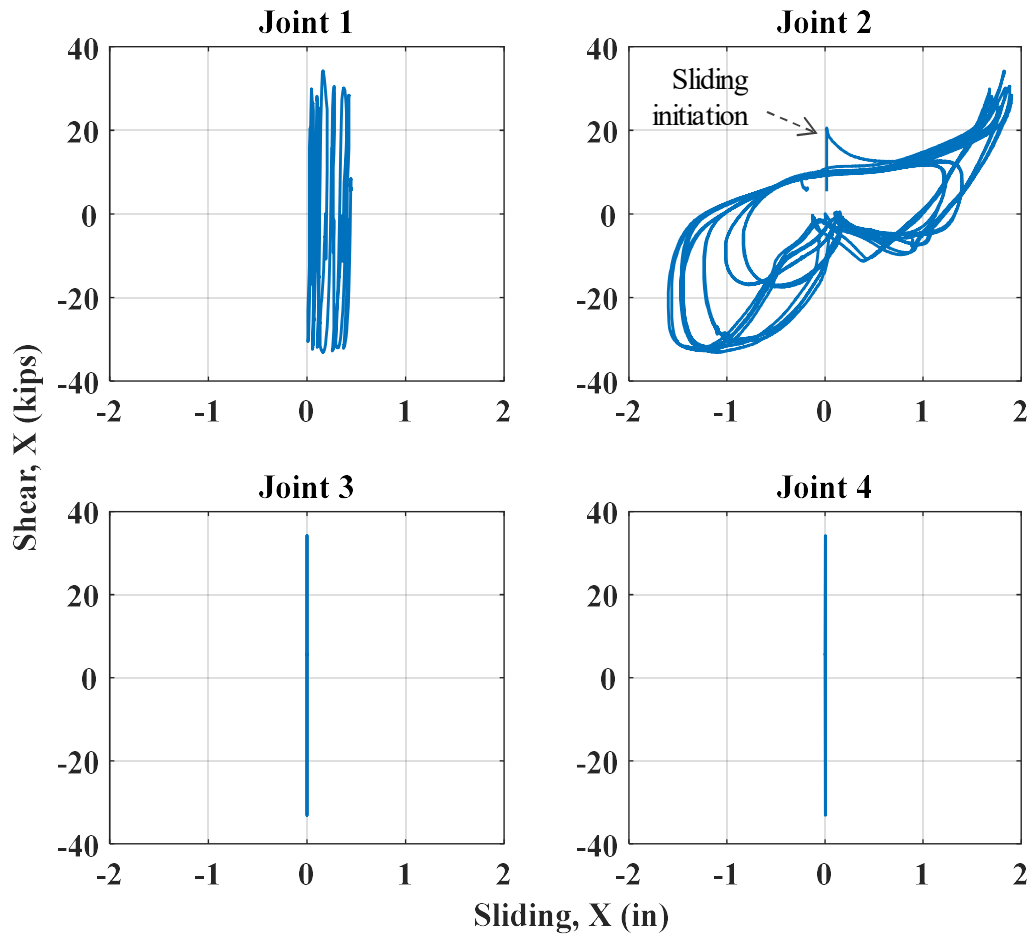
Figure 4-374. Phase IV, loading protocol HSR3_BI_CNT_S1_DR_4: joint shear vs. sliding responses in *X* direction

According to Figure 4-374, the breakaway friction at the first sliding joint (Joint 2) was similar to that in the previous test under loading protocol HSR3_BI_CNT_DR_2, i.e. 20 kips. The achieved sliding at Joint 2 is also overplotted with its design-based sliding capacity in Figure 4-376. The peak sliding values achieved at Joint 2, in the *X* and *Y* directions, were 1.9 in. and 2.2 in., respectively. These values are about 15% larger than those achieved in the prior test (with 2% peak drift ratio). Considering that the nominal maximum sliding capacity of the sliding joint was merely 1.45 in. and the oversized holes

on the steel plates and the PTFE pads at the sliding joint could only slightly increase the maximum achievable sliding capacity, it can be deduced that the maximum sliding increase in this test resulted from the duct adaptors damage.
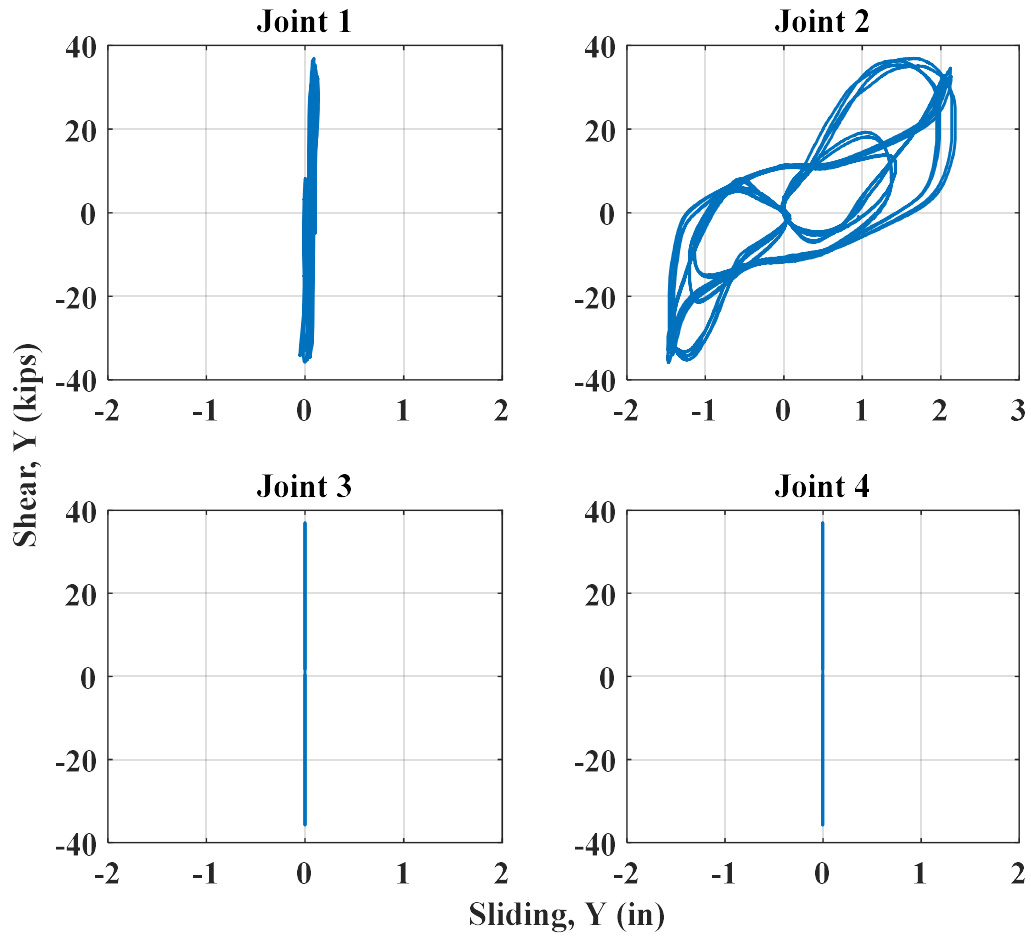
Figure 4-375. Phase IV, loading protocol HSR3_BI_CNT_S1_DR_4: joint shear vs. sliding responses in *Y* direction
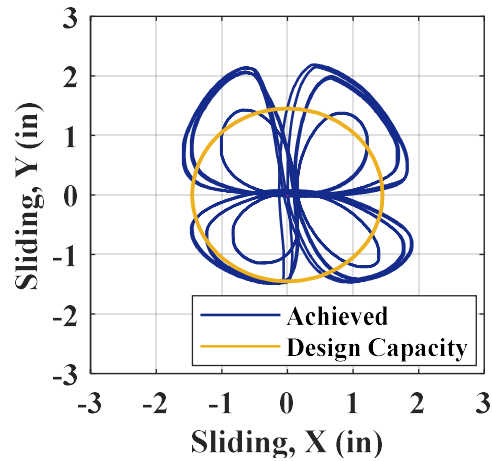
Figure 4-376. Phase IV, loading protocol HSR3_BI_CNT_S1_DR_4: comparison of achieved sliding with design-based sliding capacity at Joint 2

According to Figure 4-377, the values of the column's base moment about the two horizontal axes at similar peak displacements were close. It is also seen that the maximum values of the total moment resisted by the column during the second two pairs of displacement cycles with the peak drift ratios of 2.67% and 4% were nearly similar (510-580 kips). This was because, during the last two cycles (with 4% peak drift ratio), the bottom rocking joint sustained some damage, reducing the flexural stiffness of the column during rocking.

The variation of the rocking components at the bottom rocking joint with respect to the loading beam displacements are displayed in Figure 4-378. Consistently with the results of the previous test (Figure 4-364), the extent of rocking around the X-axis under lateral displacement (in the Y direction) was somewhat larger than that around the Y axis under longitudinal displacement (in X direction). The main reason for this is probably the higher flexibility of the first sliding joint and measurement inaccuracies. It is also observed

that, depending on the achievable extent of sliding in the direction of loading, the rocking

values varied for the same maximum displacement values, particularly around the *X*-axis

(Figure 4-378(b)).
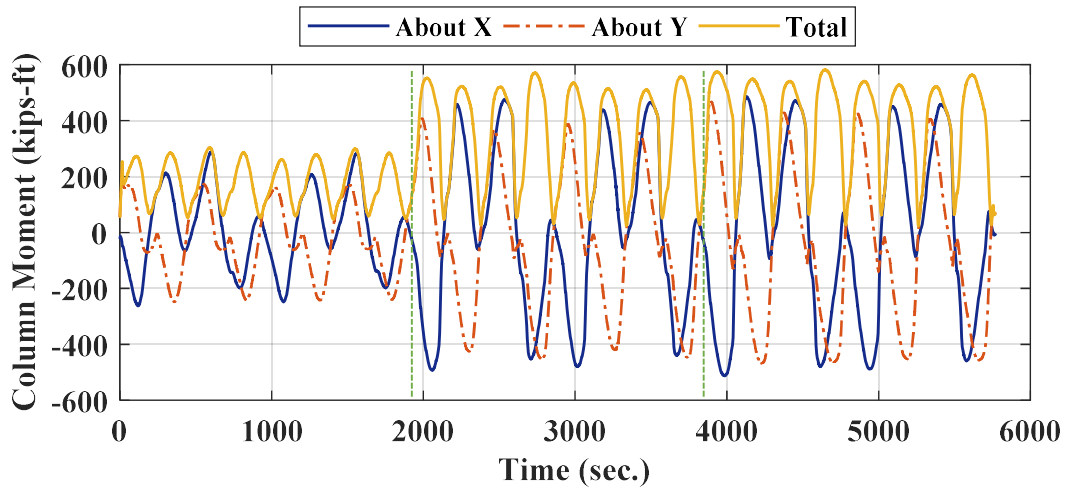
Figure 4-377. Phase IV, loading protocol HSR3_BI_CNT_S1_DR_4: column base moment time histories
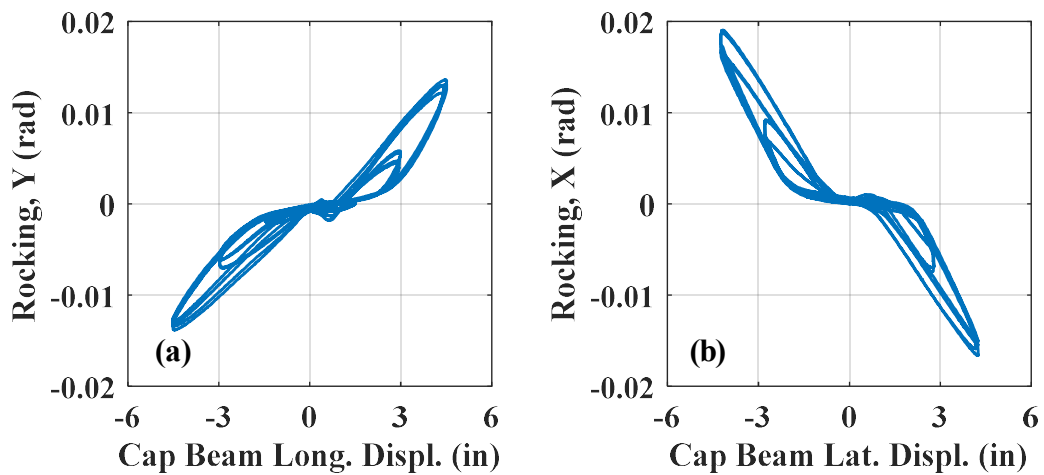
Figure 4-378. Phase IV, loading protocol HSR3_BI_CNT_S1_DR_4 – bottom joint response: (a) rocking around *Y*-axis vs. displacement in *X* direction; (b) rocking around *X*-axis vs. displacement in *Y* direction

572

The individual tendons' posttensioning force time histories along with the time history of their sum are displayed in Figure 4-379. According to Figure 4-380, at larger displacements (e.g. above 2 in.), there seems to have been an almost linear relationship between the total PT force and the displacement demand, as rocking became the primary source of the column's lateral displacement. Maximum recorded tendon force during this test was about 37 kips, which belonged to the northeast strand and was obtained when the column was pushed in the southwest direction up to 6 in. (4% drift ratio). Even though 37 kips is 30% lower than the strand's yield strength, i.e. ~ 53 kips, the combined effect of axial force and the local bending of the strands could have led to localized yielding of some of the strand wires.

This localized yielding of the strands as well as the concrete damage in the bottom column segment and anchor wedge slippage in the barrel chucks were the primary causes of the large posttensioning loss observed in Figure 4-379. Specifically, during the second and the third pairs of displacement cycles (of peak drift ratios 2.67% and 4%, respectively), the total PT losses were 5% and 14%, respectively.
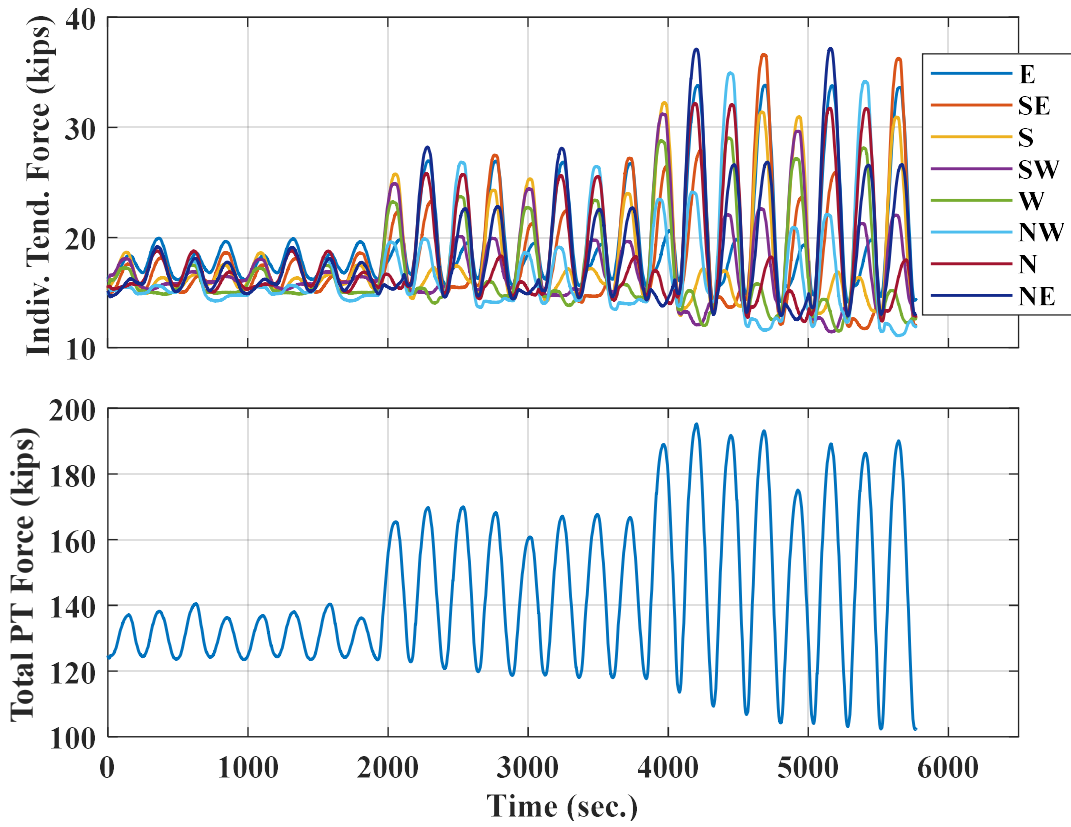
Figure 4-379. Phase IV, loading protocol HSR3_BI_CNT_S1_DR_4: time histories of posttensioning forces
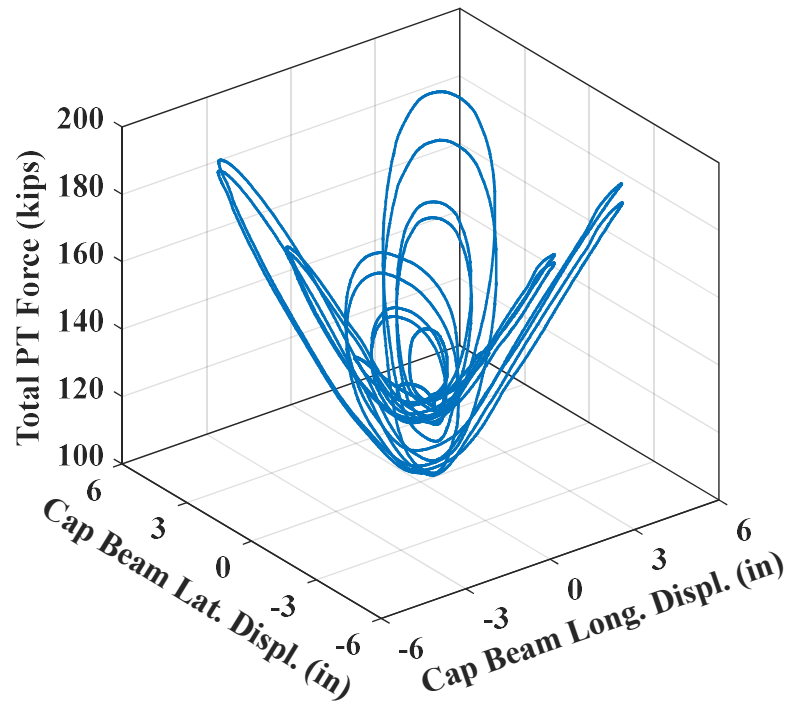
Figure 4-380. Phase IV, loading protocol HSR3_BI_CNT_S1_DR_4: total PT force vs. loading beam horizontal displacements

The concrete damage was confined to the bottom segment, consisting of concrete spalling above the rocking joint and wide vertical (compressive) cracks propagating toward the top of the segment (Figure 4-381 and Figure 4-382). The depth of concrete spalling was not large enough to expose the reinforcing steel, but it extended up to 10 inches above the rocking joint. The crack widths reached 1 mm (< 0.05 in.) at some locations and the majority of those occurred on the north face of the column. The spalled concrete was mostly seen at the northeast, northwest, southeast, and southwest corners of the column, where the maximum compressive stresses were caused under the clover-shaped displacement path applied to the column in this test.
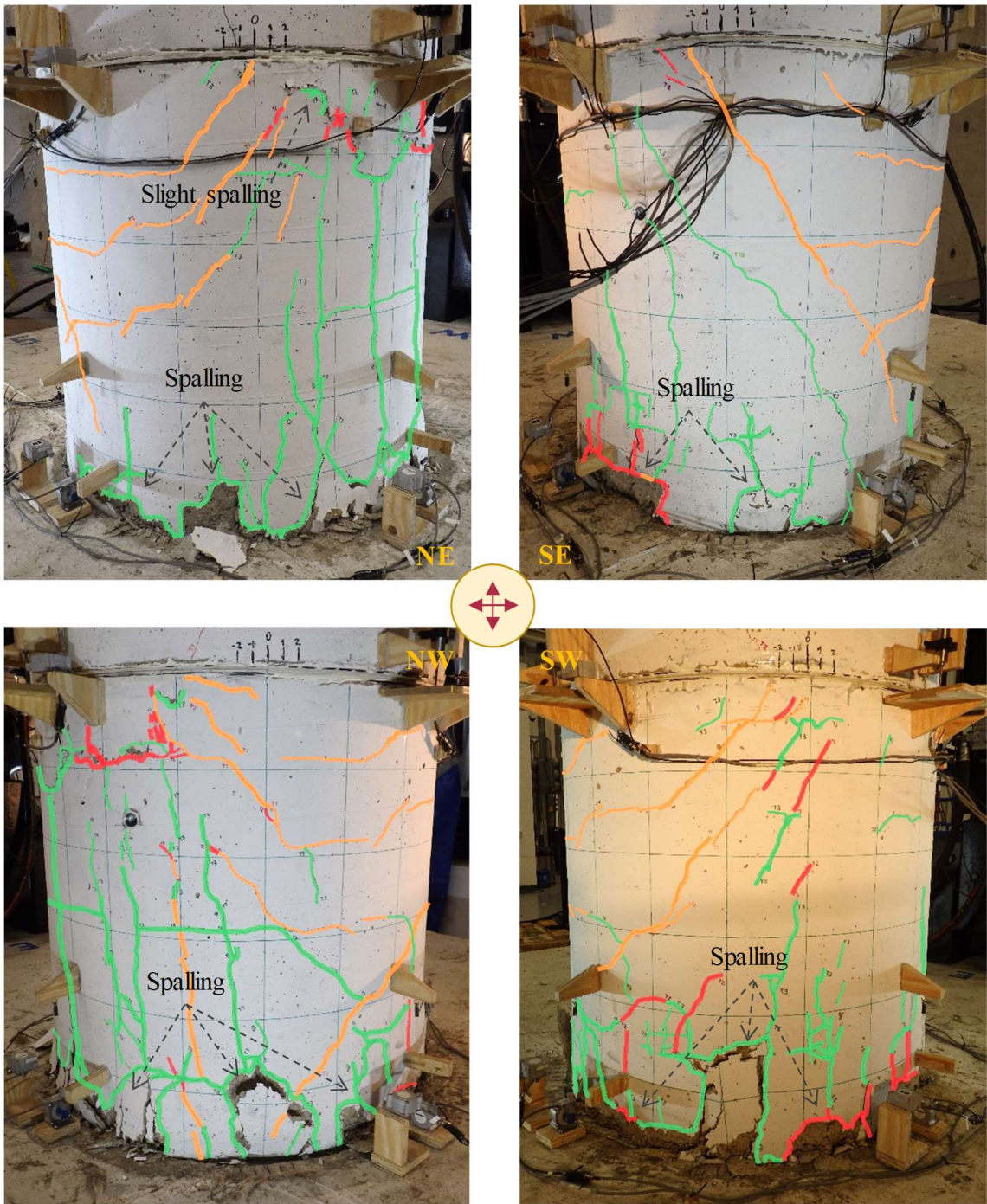
Figure 4-381. Phase IV, loading protocol HSR3_BI_CNT_S1_DR_4: distribution of cracks on bottom segment
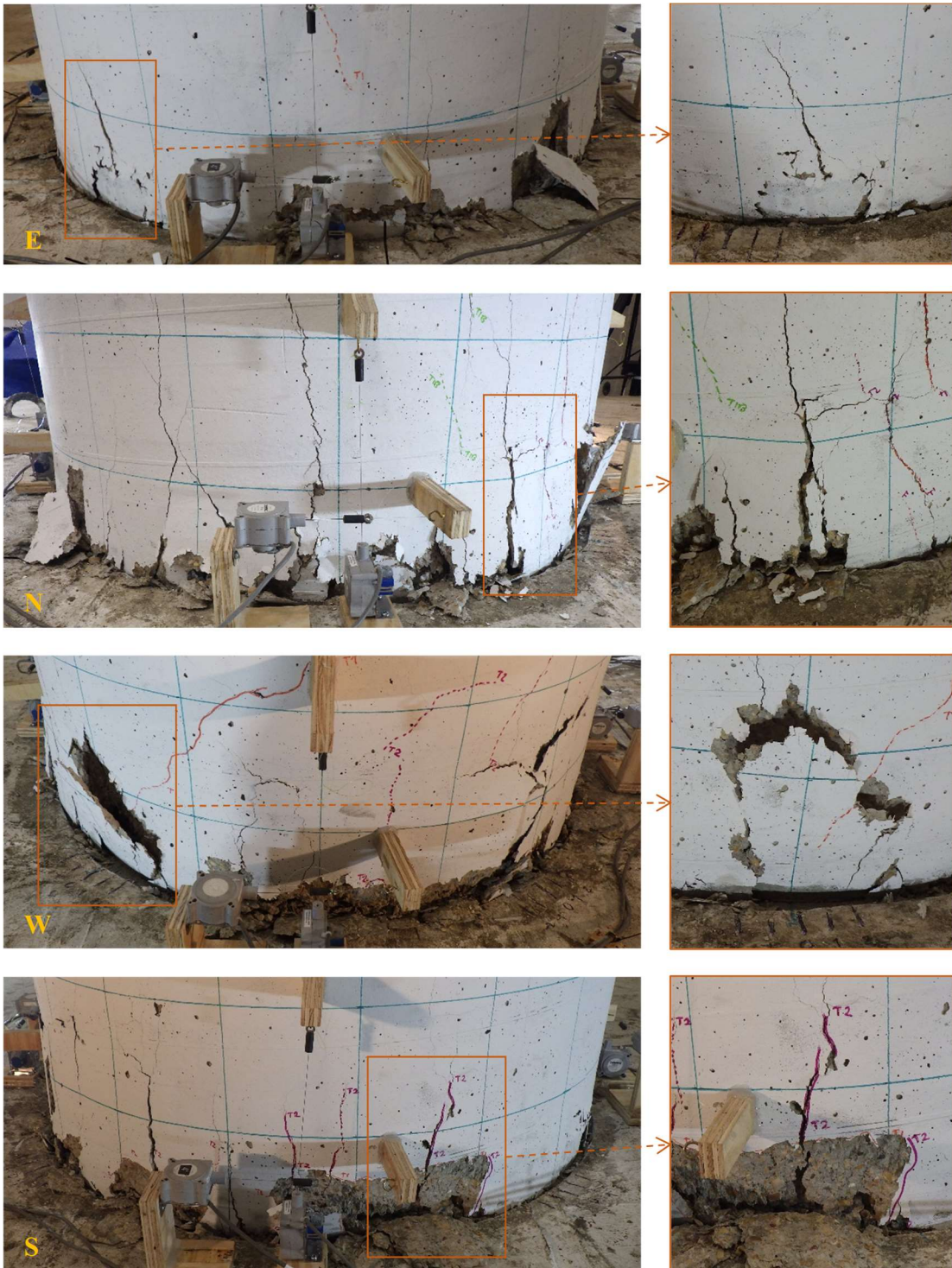
Figure 4-382. Phase IV, loading protocol HSR3_BI_CNT_S1_DR_4: concrete damage around bottom rocking joint

The column specimen's shear-displacement responses obtained in the last three tests with increasing displacement amplitude are summarized in Figure 4-383. In this figure, the responses obtained along two normal axes with 45-degree angles with the *X*- and *Y*-axes (i.e. in the SW-NE and SE-NW directions per Figure 4-329) are shown. The cycles shown in Figure 4-383(a) are those achieved when the applied displacement time history followed the first two leaves of the clover-shaped displacement path, while the cycles shown in Figure 4-383(b) are those obtained under the displacement time histories of the remaining two leaves.

The distinct features of the HSR column responses, e.g. frictional energy dissipation for small displacements, tendon bearing-induced hardenining, and rocking-induced stiffness decrease, are evident in the responses of the column in both directions. The responses are also almost symmetric. The maximum base shear withstood by the column in the four directions ranged from 38 kips to 41 kips. Slight softening behavior is observed close to the maximum displacement applied to the column, i.e. 6 in. (4% drift ratio). The maximum residual displacements along both selected axes were less than 1.7 in., which equals 1.1% of drift ratio. It is noted that these residual displacements were mainly caused by the residual sliding at Joint 2 and could be recovered if needed.

The variation of total PT force and its losses with peak drift ratio were also determined based on the previous test results – the computed parameters are demonstrated in Figure 4-384. The initial total PT force in the respective column specimen (before the first test was run) was 136 kips. It is observed that the posttensioning losses generally increased with the displacement demand, as the rocking contribution to the lateral displacement

578

increased. The PT loss went up to 13% during the displacement cycles with the peak drift ratio of 4%. The accumulated total PT loss during all the displacement cycles applied within the three tests was about 25%.
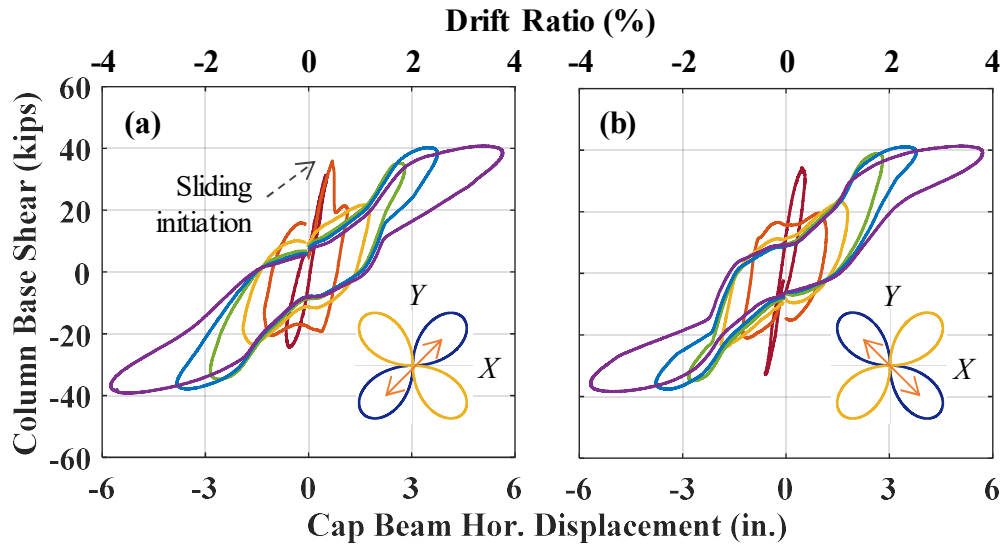
Figure 4-383. Phase IV, Loading Set 1 – column base shear vs. horizontal displacement responses: (a) in SW-NE direction; (b) in SE-NW direction
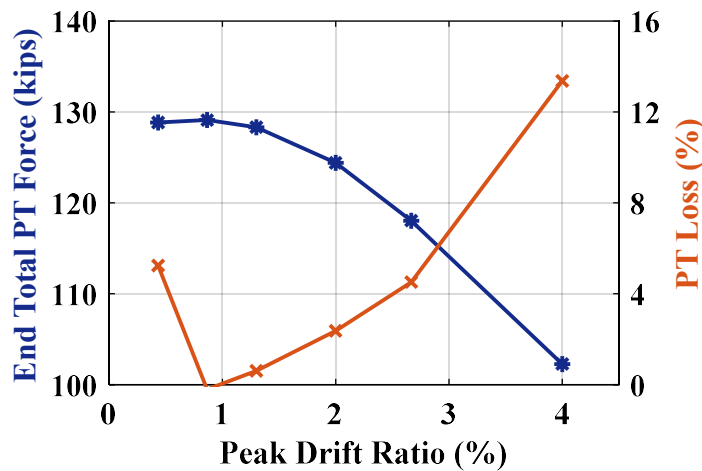
Figure 4-384. Phase IV, Loading Set 1: variation of end total PT force and PT loss with peak drift ratio

579

4.7.4.5.2. Results from Loading Set 2

The biaxial displacement paths obtained during the tests under the four loading protocols of Loading Set 2 along with the corresponding sliding paths of Joint 2 are shown in Figure 4-385. Note that only Joint 2 exhibited sliding in these tests, because the base shear did not get large enough to overcome the static friction at Joint 3. As it was the case in the previous three tests, the loading beam's displacement components in the two horizontal directions did not fully match the desired displacement components, but were acceptably close. According to the plotted results, the maximum sliding achieved in the positive X and Y directions were over 35% larger than those achieved in the negative directions. This was an implication of the initial misalignments between the bottom and middle column segments' ducts.

The base shear vs. displacement responses of the column in the X and Y directions obtained from the four tests of Loading Set 2 are compared in Figure 4-386 and Figure 4-387. Given the friction-sliding character of the responses at lower displacements, the impact of the displacement path on the shear responses is obvious. As expected, even though the maximum total horizontal displacement applied to the column in all of the above tests was 3 in. (= 2% drift ratio), the maximum base shear values in the X and Y directions obtained under the selected displacement paths were different because their maximum displacement values were achieved in various directions. For each displacement path, the maximum base shear components achieved in the the positive and negative X- and Y-directions were close, while the minimum base shear was obtained in the positive X direction. As discussed earlier, the lower stiffness of the column specimen in that

direction could be associated with the incomplete contact between the bottom and the

middle segments at Joint 2.
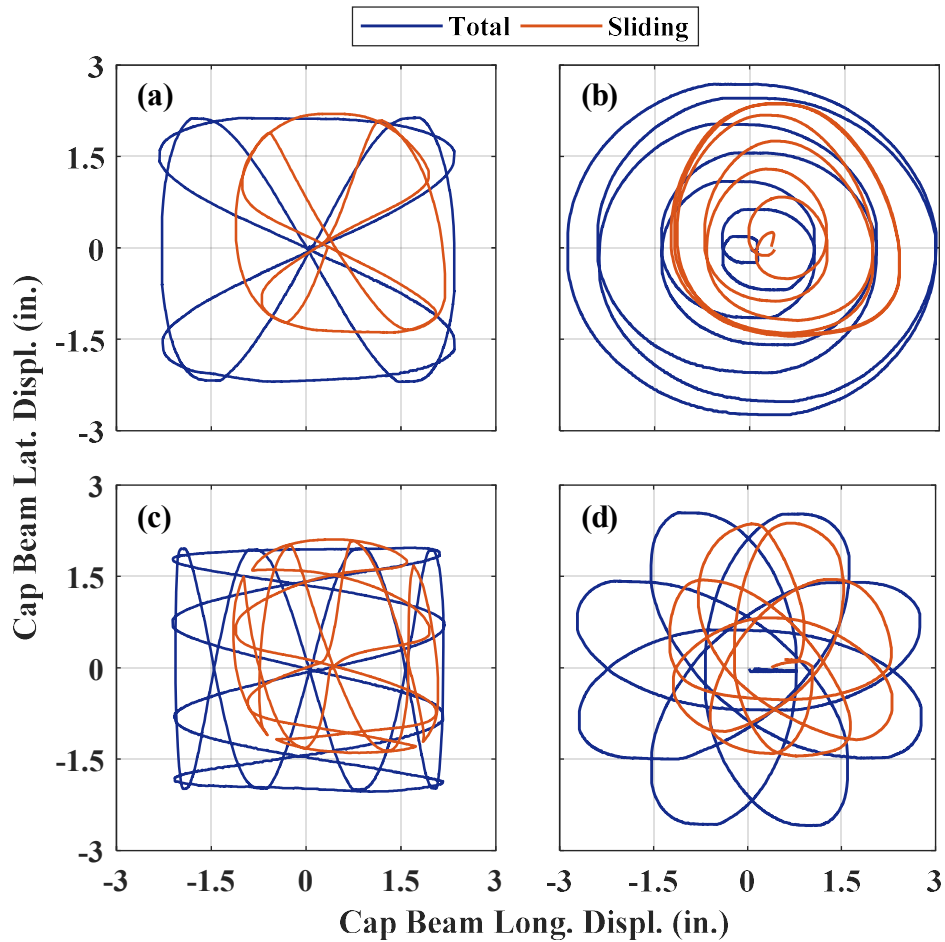
Figure 4-385. Phase IV, Loading Set 2 – comparison of loading beam's displacement path and sliding path at Joint 2 under loading protocols: (a) HSR3_BI_CNT_S2_BTRF; (b) HSR3_BI_CNT_S2_SPRL; (c) HSR3_BI_CNT_S2_WAVE; (d) HSR3_BI_CNT_S2_ORBT
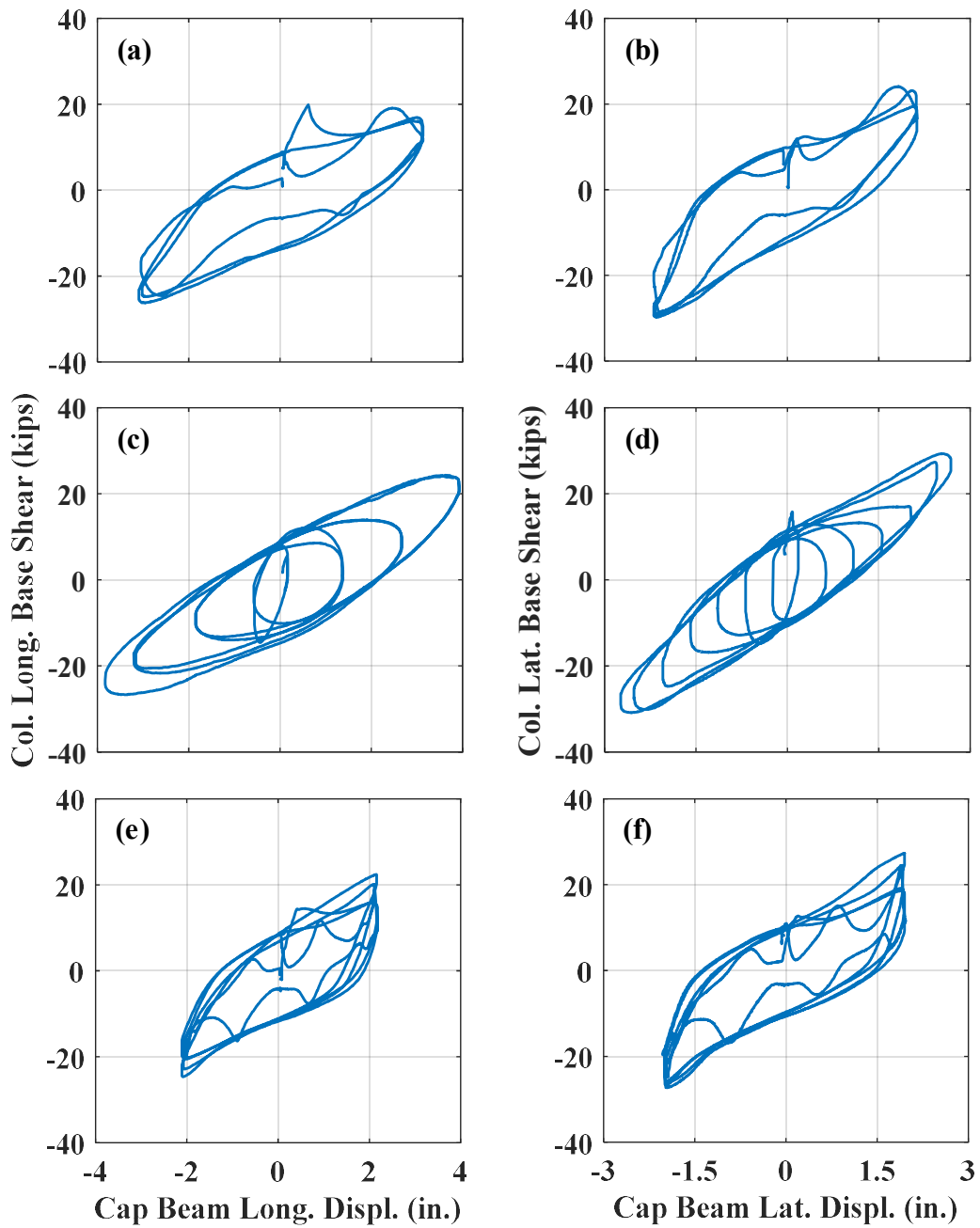
Figure 4-386. Phase IV, Loading Set 2 – column base shear vs. horizontal displacement responses under loading protocols: (a, b) HSR3_BI_CNT_S2_BTRF; (c, d) HSR3_BI_CNT_S2_SPRL; (e, f) HSR3_BI_CNT_S2_WAVE
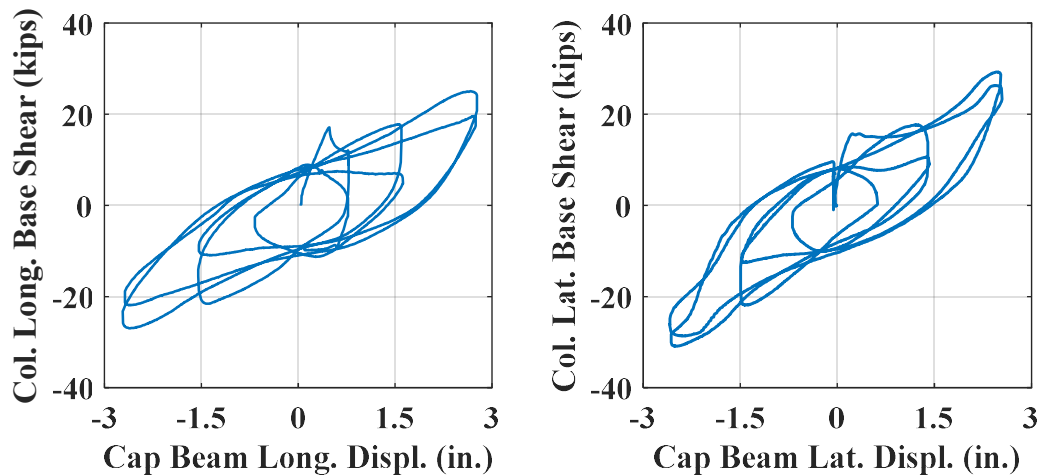
Figure 4-387. Phase IV, Loading Set 2: column base shear vs. horizontal displacement responses under loading protocol HSR3_BI_CNT_S2_ORBT

The variations of the total PT force with the loading beam's horizontal displacement achieved through the four tests in Loading Set 2 are also displayed in Figure 4-388. The peak total PT forces recorded during the tests under loading protocols HSR3_BI_CNT_S2_BTRF, HSR3_BI_CNT_S2_SPRL, HSR3_BI_CNT_S2_WAVE, and HSR3_BI_CNT_S2_ORBT were 135 kips, 136 kips, 132 kips, and 133 kips, respectively, which are relatively close. Since the column specimen had previously experienced double the peak displacement applied in Loading Set 2, the total PT losses resulted from the tests in this Loading Set were relatively small (ranged between 0 and 1.4%).

The additional column damage as a result of the loading protocols of Loading Set 2 was limited to the growth of a few hairline cracks on the surface of the bottom column segment and the appearance of a couple of more hairline cracks on the middle column segment. The orientation of these cracks seemed random.

583
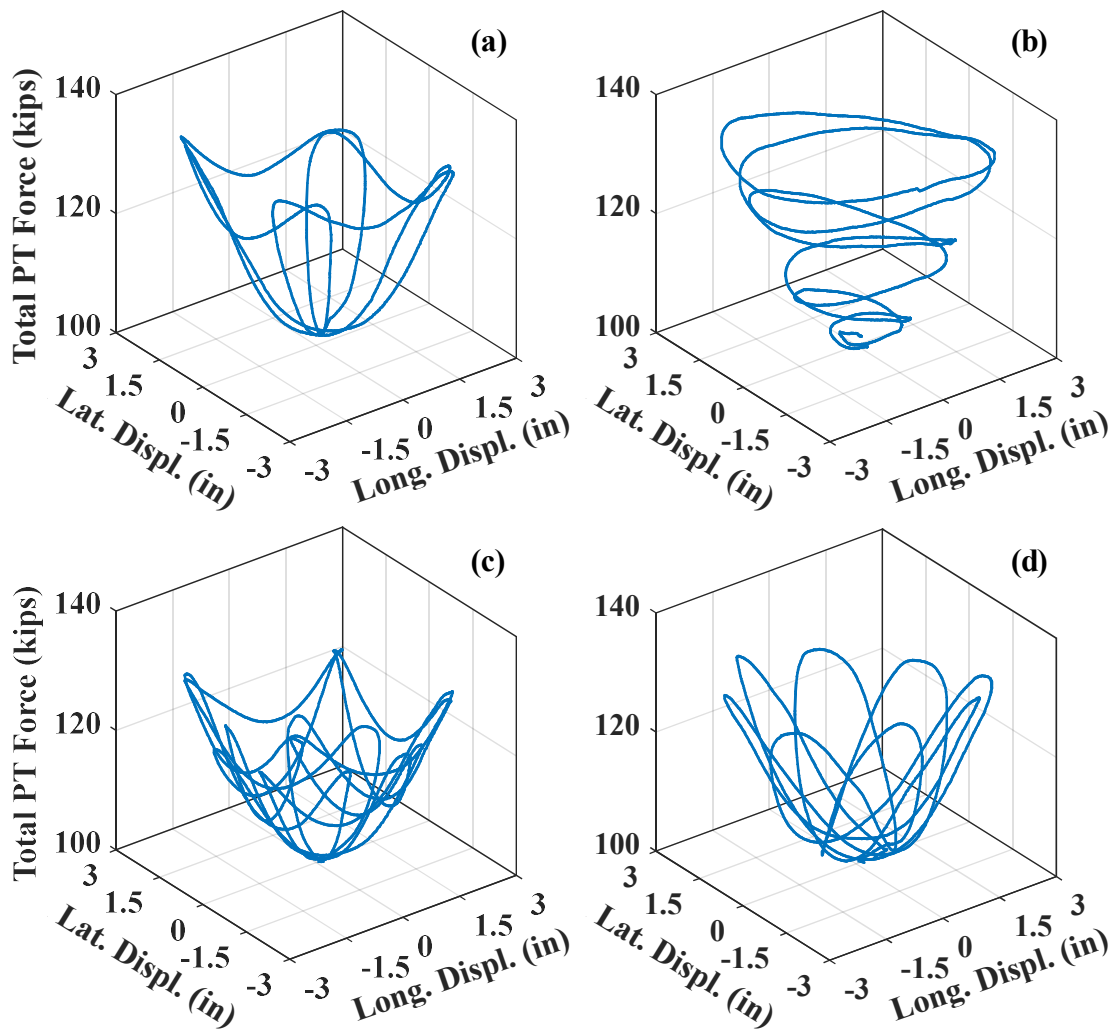
Figure 4-388. Phase IV, Loading Set 2 – total PT force vs. loading beam horizontal displacements under loading protocols: (a) HSR3_BI_CNT_S2_BTRF; (b) HSR3_BI_CNT_S2_SPRL; (c) HSR3_BI_CNT_S2_WAVE; (d) HSR3_BI_CNT_S2_ORBT

4.7.4.5.3. Results from Loading Set 3

During the tests using the loading protocols of Loading Set 3, the only activated sliding

joint was Joint 2. The loading beam's path in the *XY*-plane and the biaxial sliding path of

Joint 2 achieved during the tests under the above loading protocols are shown in Figure

4-389. Joint sliding accommodated a significant portion of the displacement applied to the column in all of these tests, particularly the first two with displacement demands less than the maximum sliding capacity of Joint 2. Larger portions of the displacement imposed to the column under loading protocols HSR3_BI_CNT_S3_2in50_GM_13 and HSR3_BI_CNT_S3_1in50_GM_13 were provided through the column's rocking, as the displacement demands in some directions exceeded 6 in. The time histories of the sliding components in the X and Y directions are also displayed in Figure 4-390 and Figure 4-391.
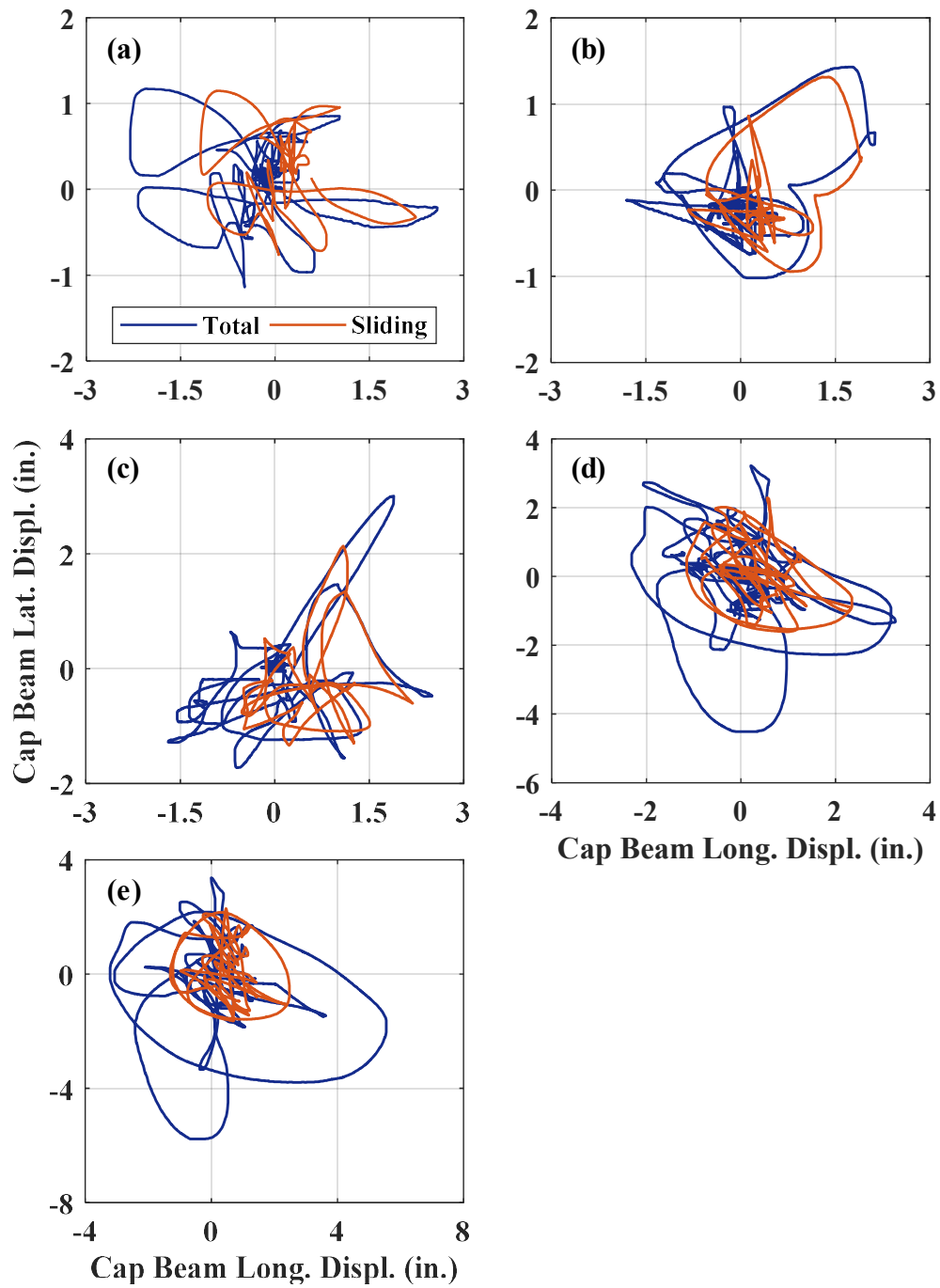
Figure 4-389. Phase IV, Loading Set 3 – comparison of beam displacement and sliding at Joint 2 under loading protocols HSR3_BI_CNT_S3_: (a) 5in50_GM_7; (b) 5in50_GM_16; (c) 2in50_GM_9; (d) 2in50_GM_13; (e) 1in50_GM_13
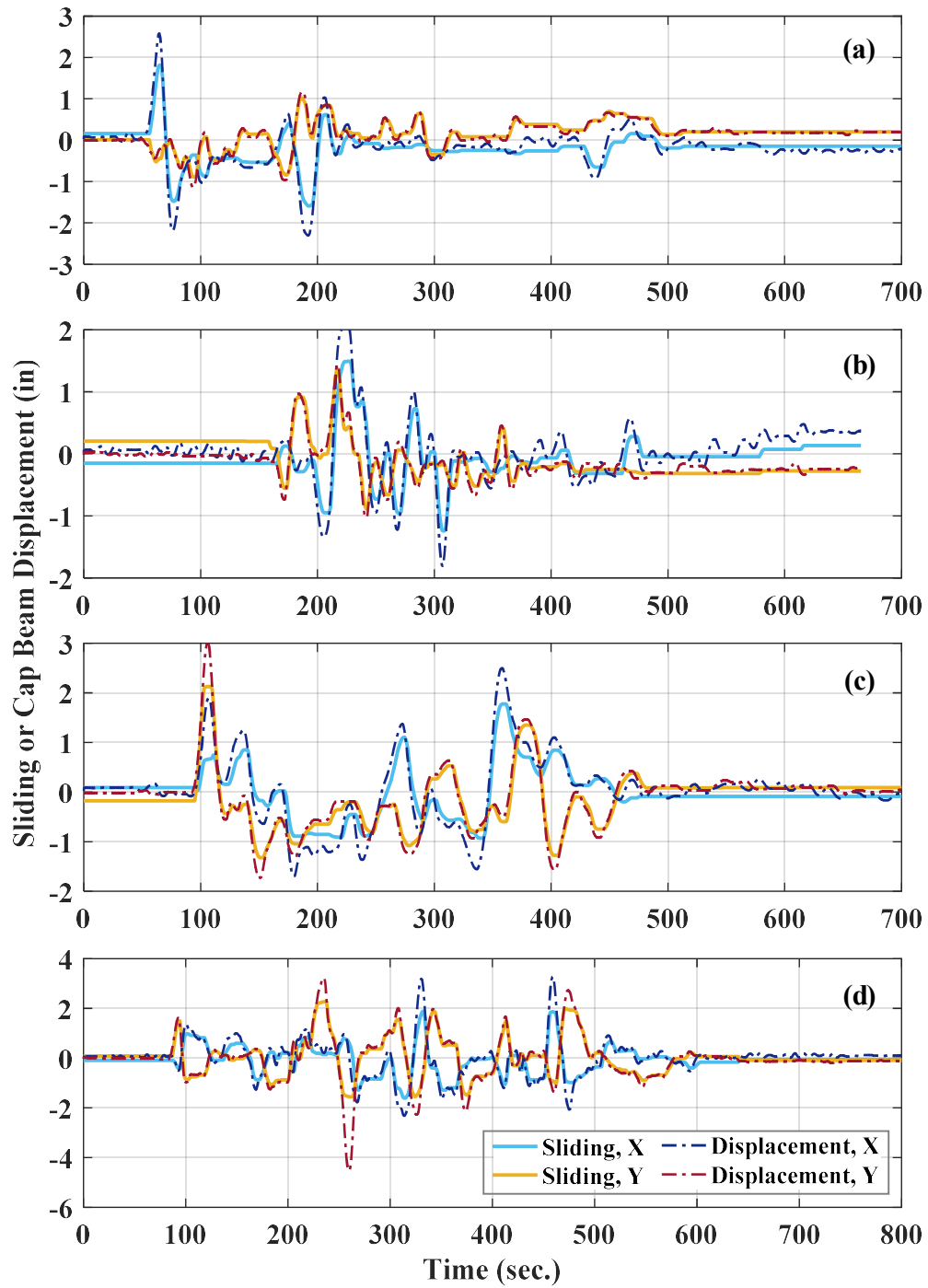
Figure 4-390. Phase IV, Loading Set 3 – time histories of loading beam displacement and sliding at Joint 2 under loading protocols HSR3_BI_CNT_S3_: (a) 5in50_GM_7; (b) 5in50_GM_16; (c) 2in50_GM_9; (d) 2in50_GM_13

587
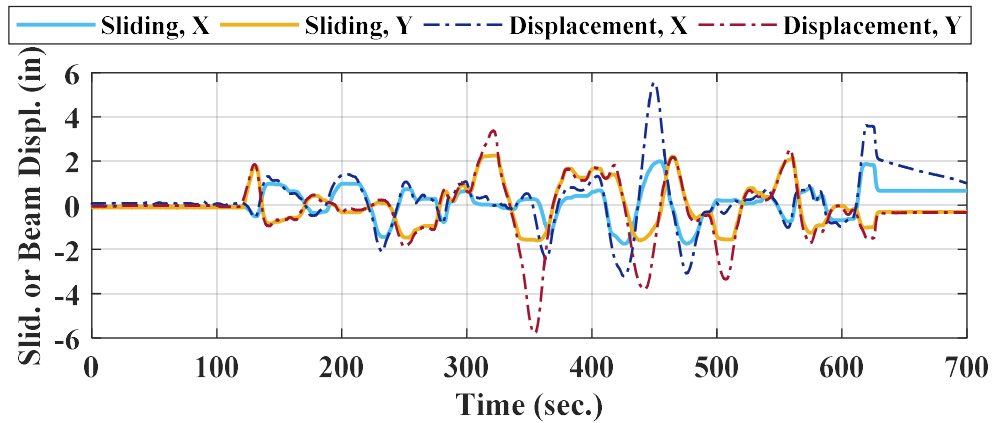
Figure 4-391. Phase IV, loading protocol HSR3_BI_CNT_S3_1in50_GM_13: sliding time histories at Joint 2

The hysteretic force-displacement responses of the column under the same loading protocols, in the two horizontal directions, are shown in Figure 4-392, Figure 4-393, and Figure 4-394. Note that the maximum displacement rate in these tests was less than 1 in./sec., so the inertia effects were neglected while determining the base shear values. The significance of the energy dissipation resulted from the friction at the first sliding joint is obvious in all of the hysteretic responses. The rocking motion in the tests under the last two loading protocols of Loading Set 3 was more apparent (Figure 4-393(c,d) and Figure 4-394), as Joint 2 had reached its sliding capacity and the shear at Joint 3 did not overcome its breakaway friction.
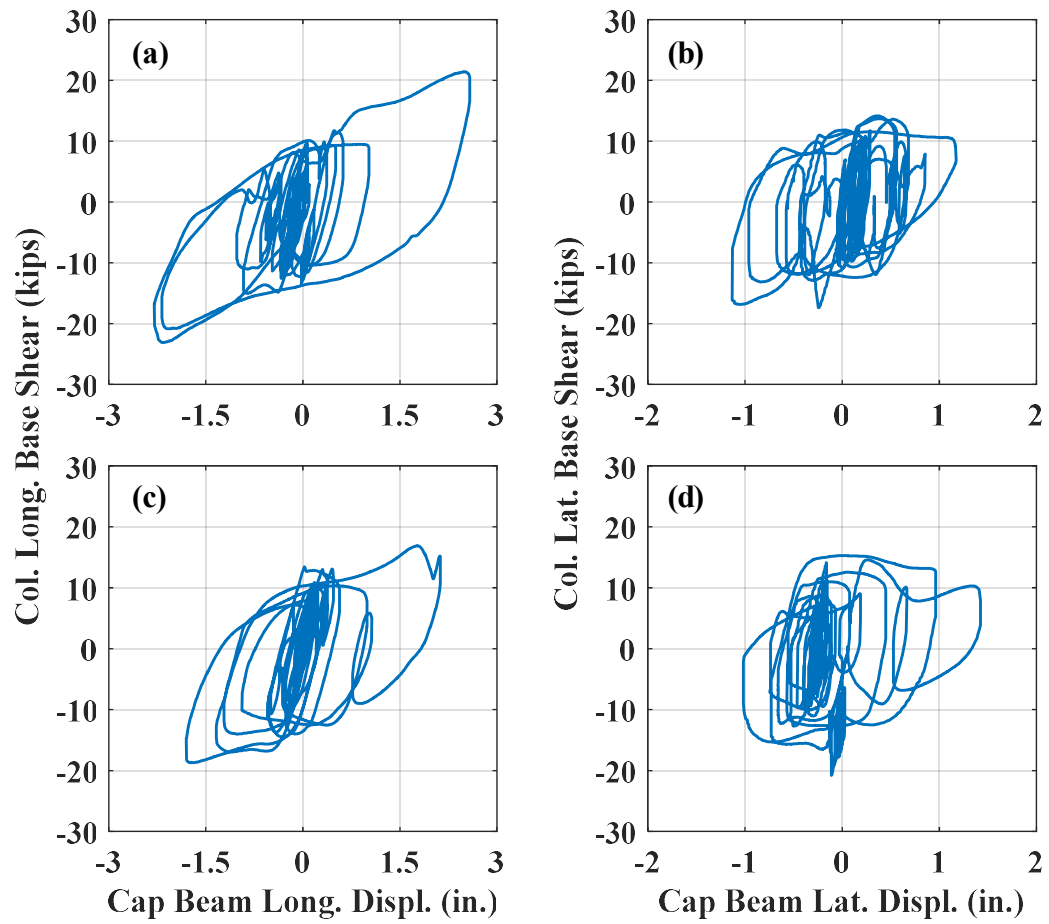
Figure 4-392. Phase IV, Loading Set 3 – column base shear vs. displacement responses under loading protocols: (a, b) HSR3_BI_CNT_S3_5in50_GM_7; (c, d) HSR3_BI_CNT_S3_5in50_GM_16
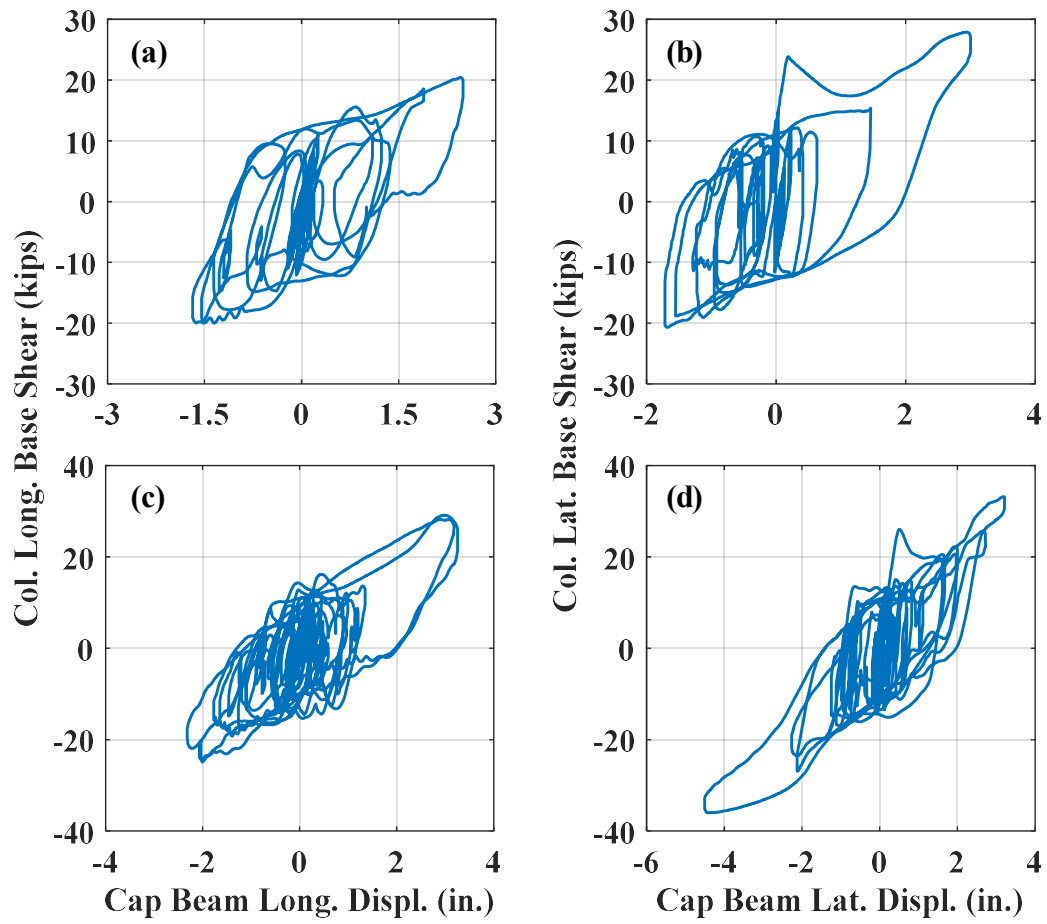
Figure 4-393. Phase IV, Loading Set 3 – column base shear vs. displacement responses under loading protocols: (a, b) HSR3_BI_CNT_S3_2in50_GM_9; (c, d) HSR3_BI_CNT_S3_2in50_GM_13
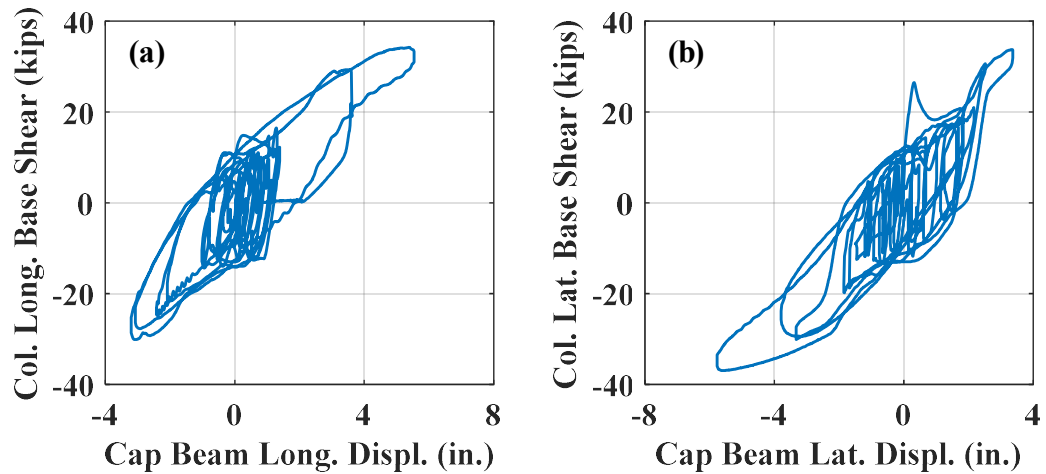
**Figure 4-394. Phase IV, loading protocol HSR3_BI_CNT_S3_1in50_GM_13 –
column base shear vs. displacement responses in: (a) *X* direction; (b) *Y* direction**

The time histories of the energy dissipated through the rocking at the bottom rocking joint and the sliding at all joints along with the total dissipated energy are compared in Figure 4-395 and Figure 4-396. According to the displayed results, the contribution of rocking to the total energy dissipation did not exceed 5%, 10%, and 16% for the tests under the applied displacement time histories corresponding to the seismic hazards with the 5%, 2%, and 1% probability of exceedence in 50 years, respectively. The higher value of the rocking-induced energy dissipation at higher displacement levels resulted from the higher compressive damage at the bottom rocking joint. A much higher percentage of the total energy dissipation was, however, provided through sliding. Specifically, the sliding-induced energy dissipation in the first four tests constituted about 80% of the total energy dissipation, whereas this amount for the last test was 73%.
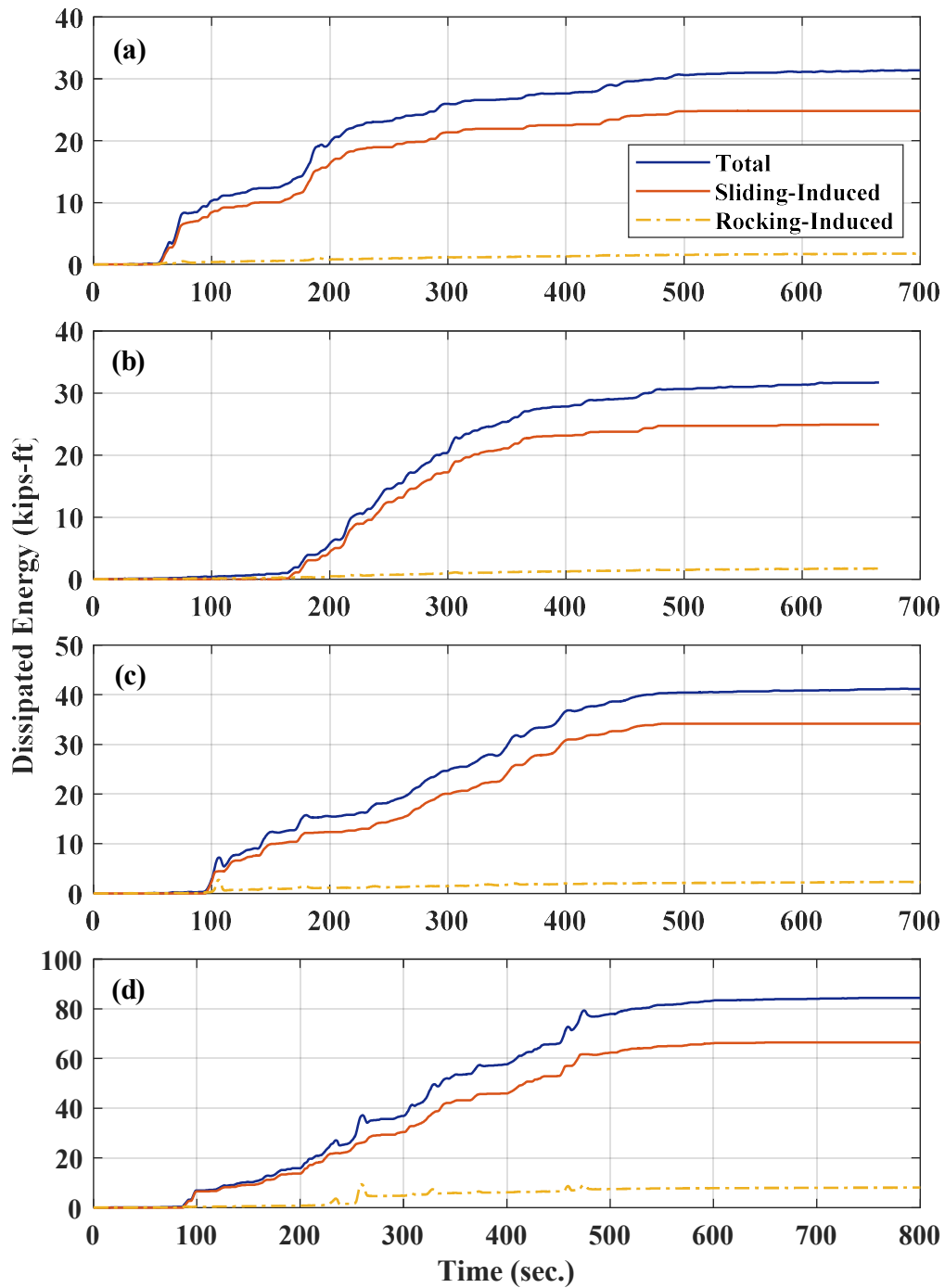
Figure 4-395. Phase IV, Loading Set 3 – dissipated energy time histories under loading protocols HSR3_BI_CNT_S3_ : (a) 5in50_GM_7; (b) 5in50_GM_16; (c) 2in50_GM_9; (d) 2in50_GM_13

592
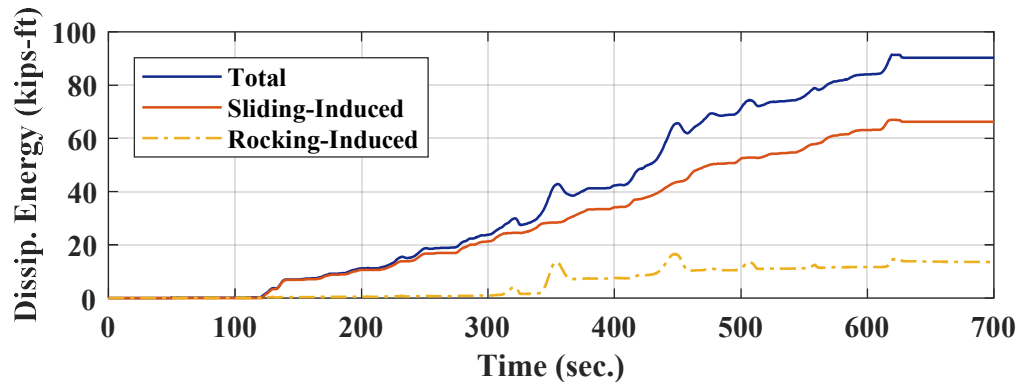
Figure 4-396. Phase IV, loading protocol HSR3_BI_CNT_S3_1in50_GM_13: dissipated energy time histories

No further damage other than minor growth of existing cracks was observed on the surface of the column after the first three tests in this Loading Set. The last two tests under loading protocols HSR3_BI_CNT_S3_2in50_GM_13 and HSR3_BI_CNT_S3_1in50_GM_13, however, slightly increased the concrete spalling near the bottom rocking joint (Figure 4-397). The concrete spalling near the east, north, and southwest corners of the rocking joint exposed the transverse reinforcement. It is noted that the concrete at these spots had already spalled during the earlier test under loading protocol HSR3_BI_CNT_S1_DR_6, but the spalled concrete had not completely come off.
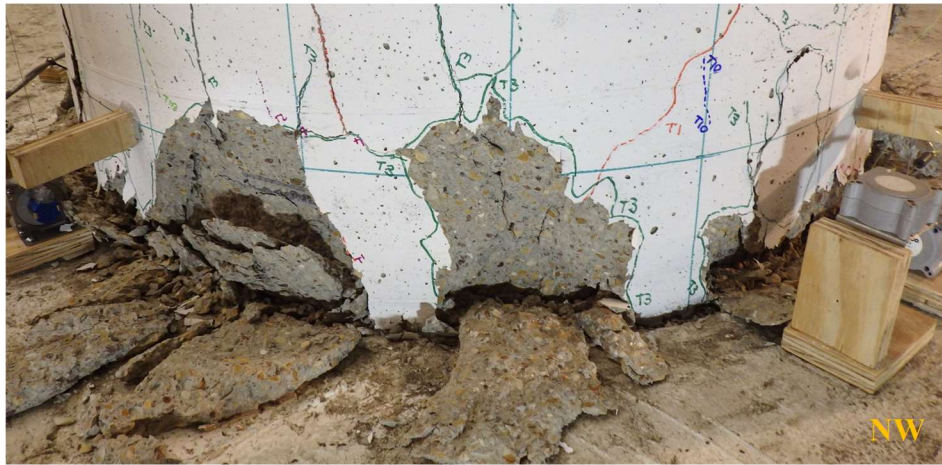
Figure 4-397. Phase IV, Loading Set 3: damage spread above bottom rocking joint

594

4.7.4.5.4. Results from Loading Set 4

Per Section 4.7.4.4.4, Loading Set 4 included only one loading protocol with 6% maximum drift ratio, i.e. HSR3_BI_CNT_S4_DR_6. The loading beam's displacement path obtained from the column's testing under this loading protocol is shown in Figure 4-398. The maximum longitudinal and lateral displacements (i.e. in X and Y directions, respectively) achieved in this test were 6.9 in. and 6.4 in., respectively, while the targeted value in each direction was 6.9 in. The maximum horizontal displacement (in diagonal direction) was 8.7 in. (5.8% drift ratio), which is close enough to the target value of 9 in. (6% drift ratio).
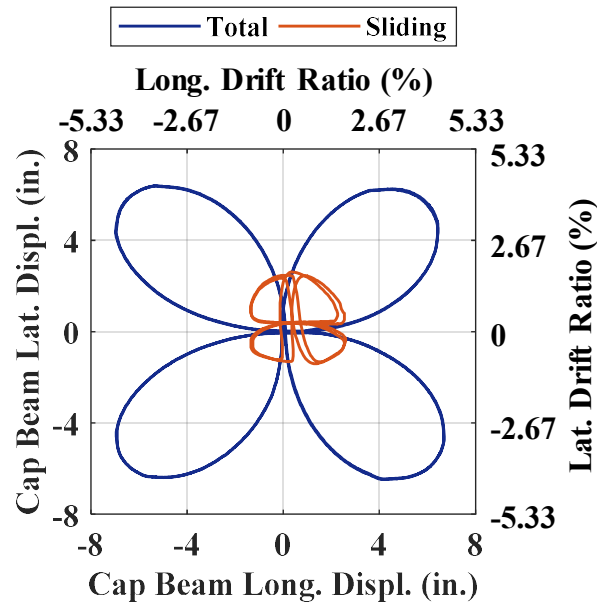
Figure 4-398. Phase IV, loading protocol HSR3_BI_CNT_S4_DR_6: comparison of loading beam's planar motion and sliding at Joint 2

In Figure 4-398, the sliding path at Joint 2 is also plotted, while the other sliding joint (Joint 3) did not exhibit sliding (Figure 4-400). Comparing the total applied displacement components with the sliding components indicates the significance of the rocking motion imposed to the HSR column specimen in this last test.

According to the time histories of the loading beam displacement components and total sliding components plotted in Figure 4-399(a) and (b), the maximum sliding achieved in the negative and positive X directions were 1.4 in. and 2.6 in., respectively. In the negative and positive Y directions, the maximum sliding values were 1.3 in. and 2.5 in., respectively. The larger extent of the maximum sliding values in the positive directions is the result of, first, the duct misalignments, and second, the sliding at Joint 1 (bottom rocking joint) in the positive X and Y directions (see Figure 4-400). In particular, sliding at Joint 1 reached over 0.5 in. in the positive X direction, though part of it could be due to measurement inaccuracies. Based on Figure 4-399(c), the loading beam's twist (rotation around Z-axis) was mostly lower than 0.01 rad (~ 0.6 degrees).
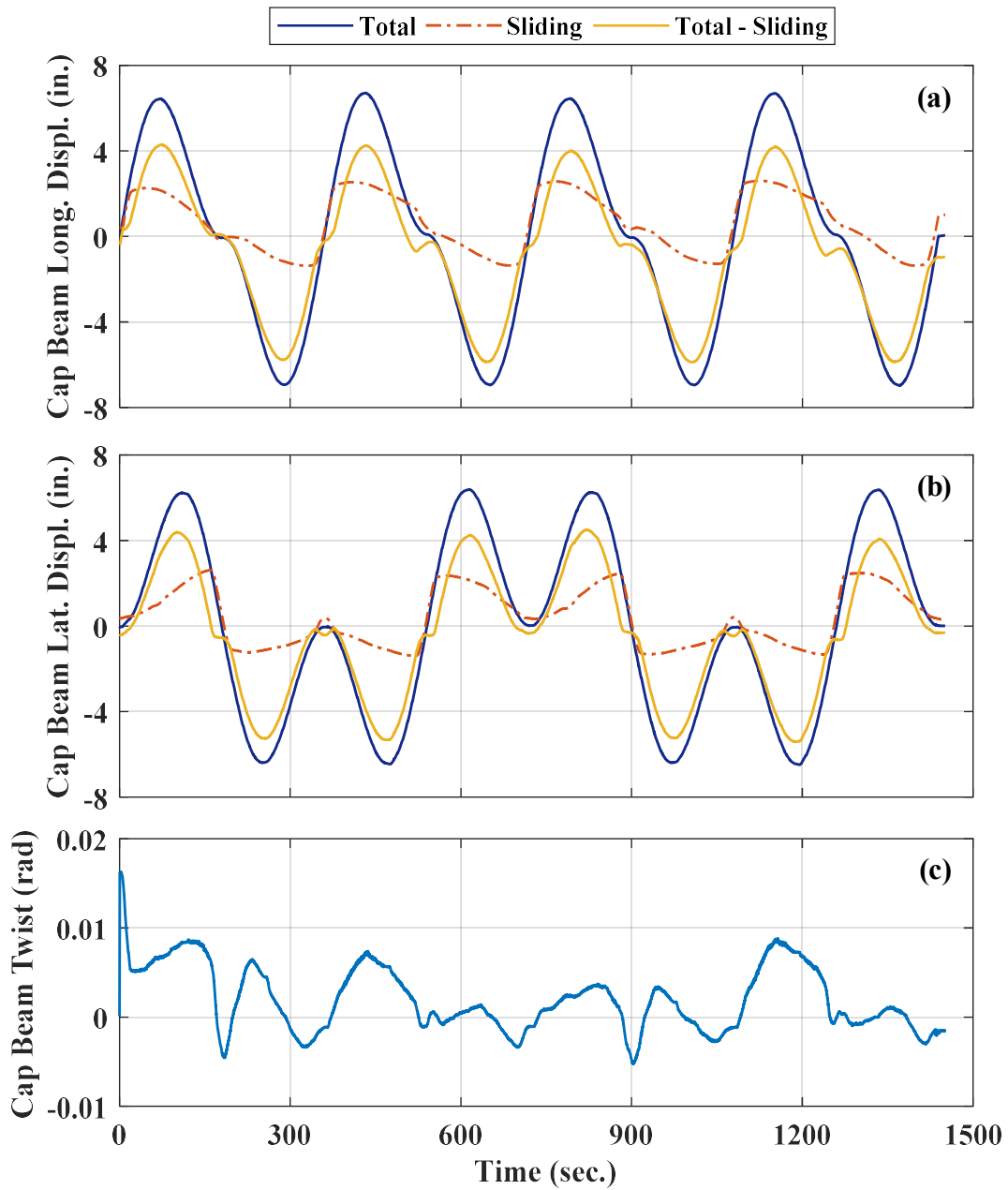
Figure 4-399. Phase IV, loading protocol HSR3_BI_CNT_S4_DR_6: time histories of loading beam's: (a) longitudinal displacement components; (b) lateral displacement components; (c) twist

597
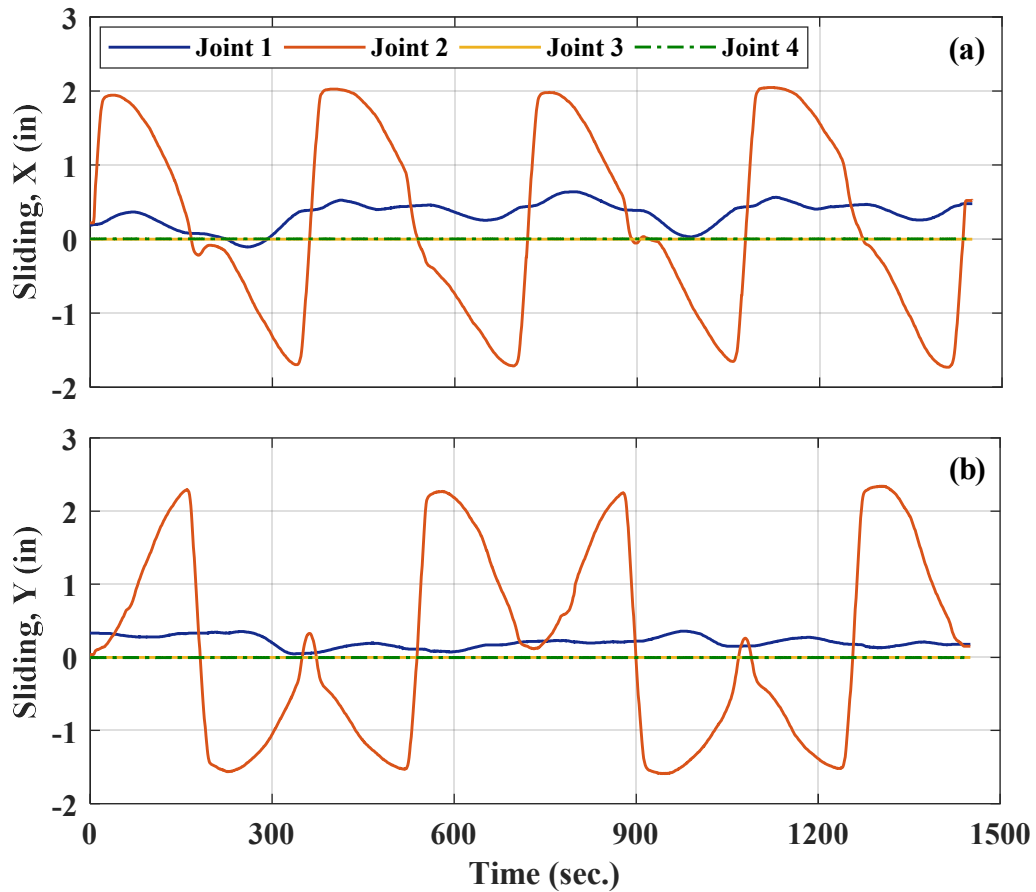
Figure 4-400. Phase IV, loading protocol HSR3_BI_CNT_S4_DR_6 – joint sliding time histories: (a) in *X* direction; (b) in *Y* direction

The base shear vs. displacement responses of the column in the *X* and *Y* directions are demonstrated in Figure 4-401(a) and (b), respectively. Per these responses, the column exhibited some cyclic deterioration, as the hysteretic loops did not repeat. The strength deterioration is better observed in Figure 4-402, where the total base shear is plotted against the horizontal displacement components. The total base shear values corresponding to the peak displacements achieved in four different directions in this test ranged from 36 kips to 40 kips. This range reduced to 34-36 kips during the second

598

displacement cycle, with a maximum of 11% strength drop in the SW direction. The deterioration occurred due to both increased concrete damage (Figure 4-407) and posttensioning losses (Figure 4-405).
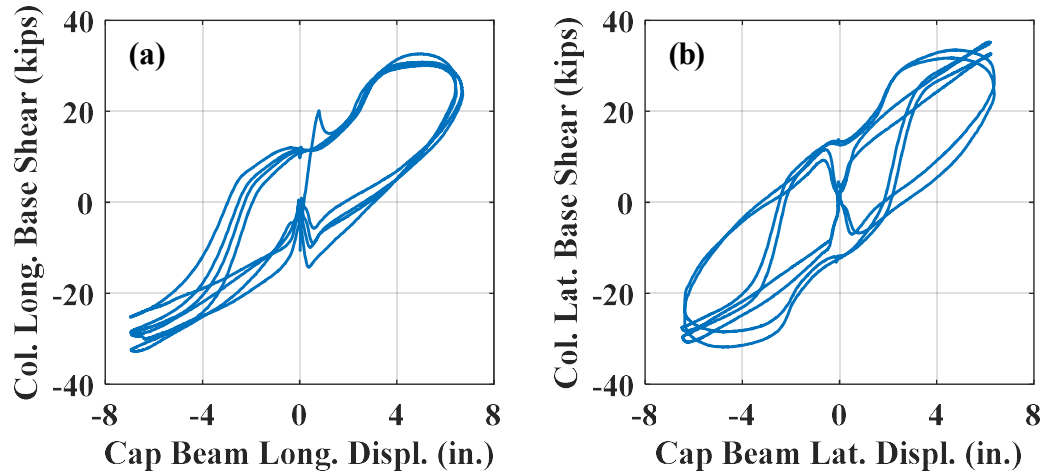
Figure 4-401. Phase IV, loading protocol HSR3_BI_CNT_S4_DR_6 – column base shear vs. horizontal displacement responses in: (a) *X* direction; (b) *Y* direction

The column's rocking at the bottom end around the *X*- and *Y*-axes are plotted against the lateral and longitudinal displacements in Figure 4-403. It is observed in the graphs that there was some negative residual rotations at the bottom joint before this test started. The maximum rotation recorded at the bottom end was 0.036 rad (~ 2 degrees) around the *X*-axis. This amount of rotation by itself could provide about 5.4 in. of lateral displacement 150 in. above the foundation (i.e. at the equivalent height of the superstructure centroid).
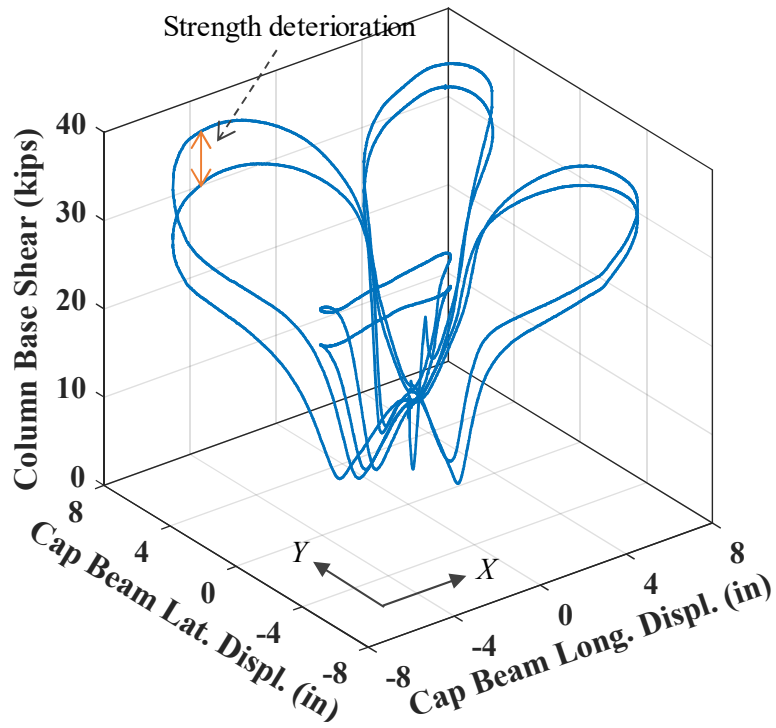
Figure 4-402. Phase IV, loading protocol HSR3_BI_CNT_S4_DR_6: total column shear vs. horizontal displacement response
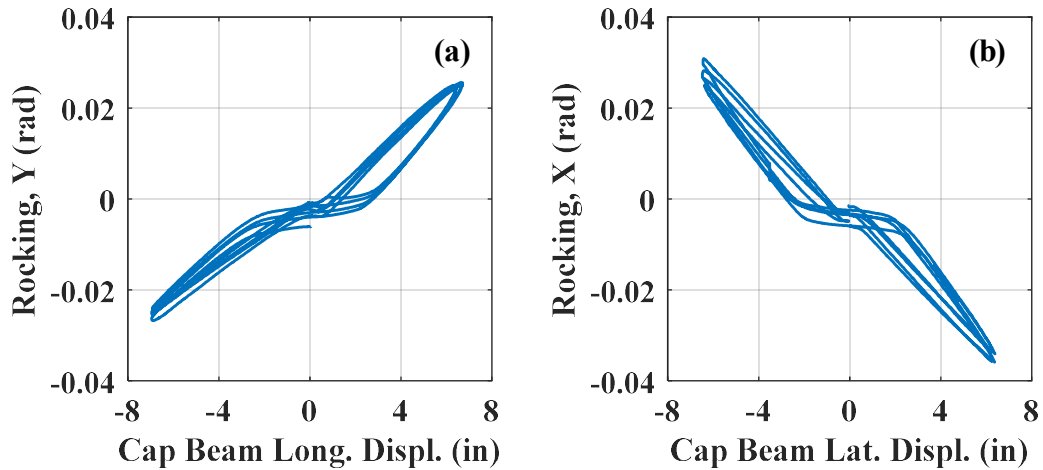
Figure 4-403. Phase IV, loading protocol HSR3_BI_CNT_S4_DR_6 – bottom joint response: (a) rocking around *Y*-axis vs. displacement in *X* direction; (b) rocking around *X*-axis vs. displacement in *Y* direction

According to Figure 4-404, the maximum total rocking at the bottom rocking joint (Joint 1) happened when the column was pulled in the northwest direction (i.e. negative X displacement and positive Y displacement). This finding is in agreement with the severe concrete damage and bar buckling observed near the northwest corner of the rocking joint (see Figure 4-413). It is also observed in Figure 4-404 that, due to the column damage during the first displacement cycle, the biaxial rocking response achieved in the first cycle was not repeated during the second cycle.
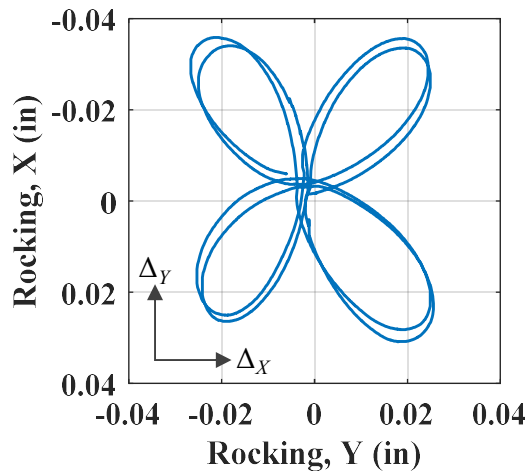
Figure 4-404. Phase IV, loading protocol HSR3_BI_CNT_S4_DR_6: rocking around X-axis vs. rocking around Y-axis for Joint 1

The posttensioning tendon force time histories obtained from the last test are presented in Figure 4-405. Because of the local flexural deformations imposed to the strands in the vicinity of the first sliding joint (Joint 2), the maximum tendon forces of close to 50 kips was an indication of potential yielding in some of the strands. This hypothesis is further supported by the significant PT force losses during this test, reaching

a total of 40%. Another certain cause of such a large posttensioning loss was the severe concrete damage in the bottom column segment (Figure 4-407). The gradual total PT force loss with the applied displacements in the two horizontal directions is obvious in Figure 4-406.
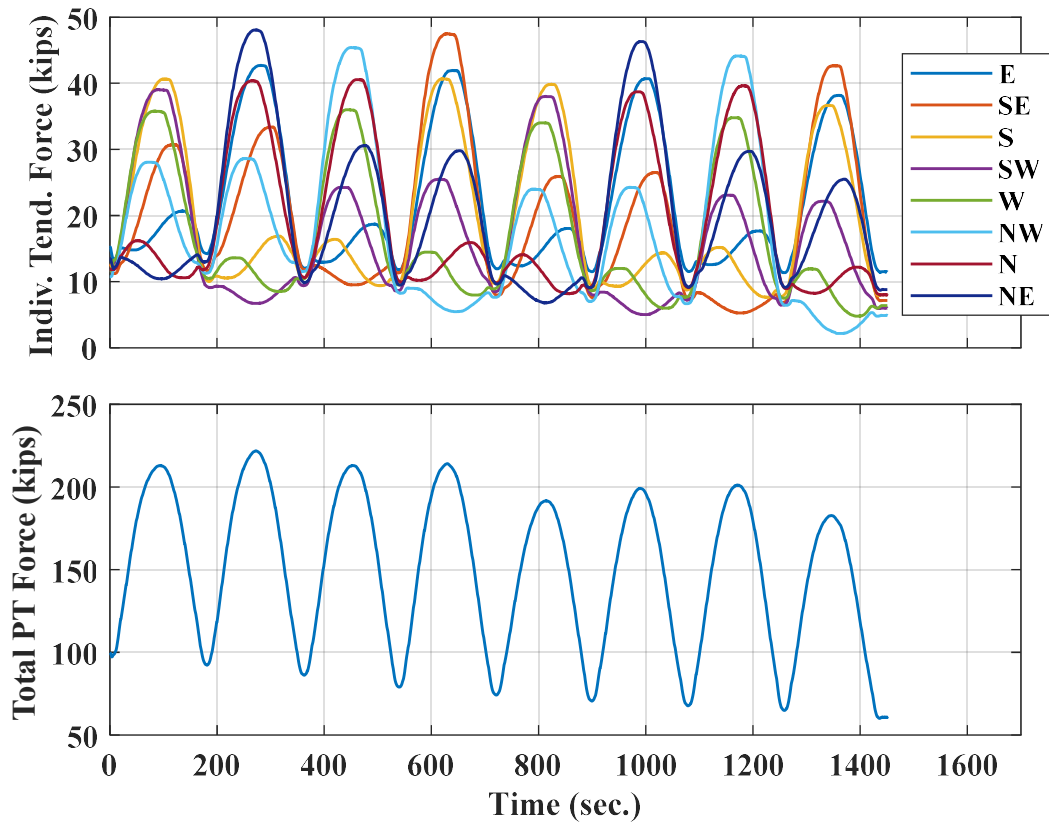
Figure 4-405. Phase IV, loading protocol HSR3_BI_CNT_S4_DR_6: time histories of posttensioning forces
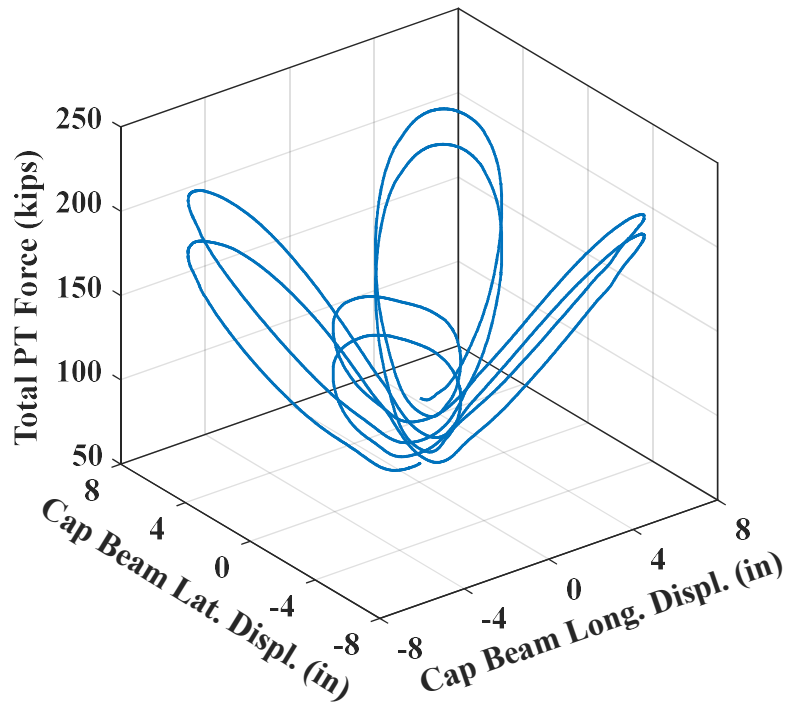
Figure 4-406. Phase IV, loading protocol HSR3_BI_CNT_S4_DR_6: total PT force vs. loading beam horizontal displacements

The majority of the damage caused in the column during this test occurred in the bottom column segment. This damage consisted of lengthening and widening of existing (from previous tests) cracks, generation of new cracks, and severe concrete spalling all around the entire segment. The cover concrete (~ 0.75 in. deep) over a large height of the segment (exceeding 30 in. on the north face) was lost, exposing the transverse steel reinforcement. The shallow concrete spalling that emerged below the first sliding joint (Joint 2) during the earlier tests had also expanded after this test (Figure 4-408). Adjacent to the rocking joint interface, the core concrete was also slightly damaged, while some of the longitudinal bars had slightly buckled at the four corners of the column cross section toward which the column was displaced the most (see Section 4.7.4.6).
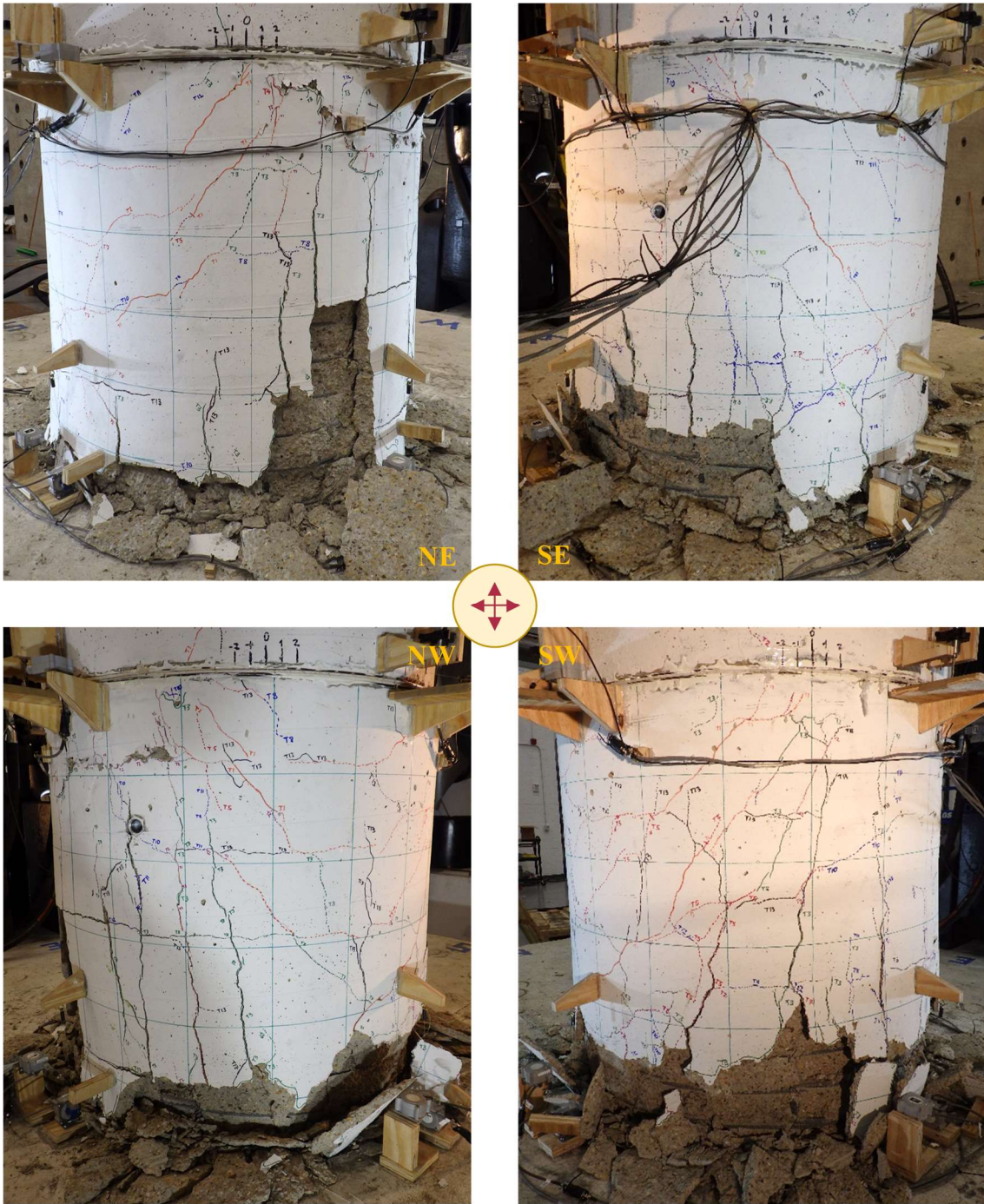
Figure 4-407. Phase IV, loading protocol HSR3_BI_CNT_S4_DR_6: damage outside bottom column segment
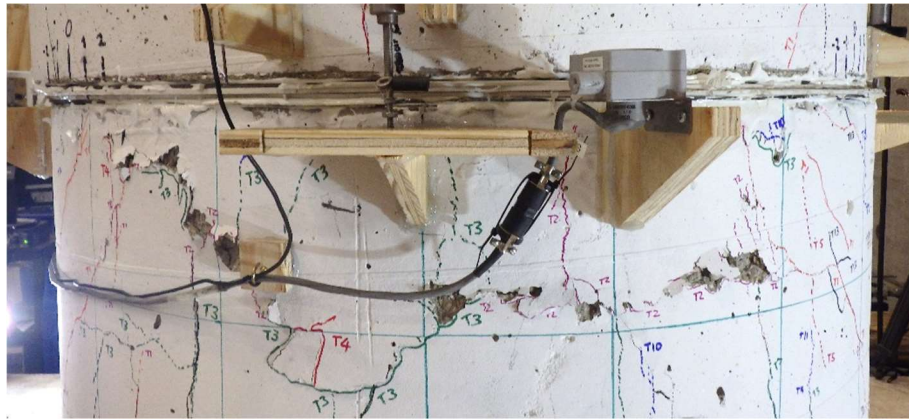
Figure 4-408. Phase IV, loading protocol HSR3_BI_CNT_S4_DR_6: extended shallow concrete spalling below Joint 2, north side

The full hysteretic responses of the column in the two normal directions SW-NE and SE-NW (per Figure 4-329) were obtained from the results of the tests under protocols HSR3_BI_CNT_S1_DR_1_3, HSR3_BI_CNT_S1_DR_2, HSR3_BI_CNT_S1_DR_4, and HSR3_BI_CNT_S4_DR_6 (Figure 4-409). Clearly, the tests run between the third test and the last one could have affected the response of the column under the last loading protocol, but still the aggregated hysteretic responses are informative. It is observed that the column's softening behavior started as its drift ratio exceeded 3.5%, although it did not progress fast. Insignificant cyclic strength deterioration appeared in the responses for the drift ratios above 2%. There was a gradual increase in the residual displacement with the applied displacement, which was caused by the damage at the bottom rocking joint, the posttensioning losses, and the duct adaptors bearing damage. The maximum residual displacements in the SW-NE and SE-NW directions were found to be 2.7 in. (1.8% drift ratio) and 3 in. (2% drift ratio), respectively, 75% of which was induced by the residual sliding at the bottom two joints.
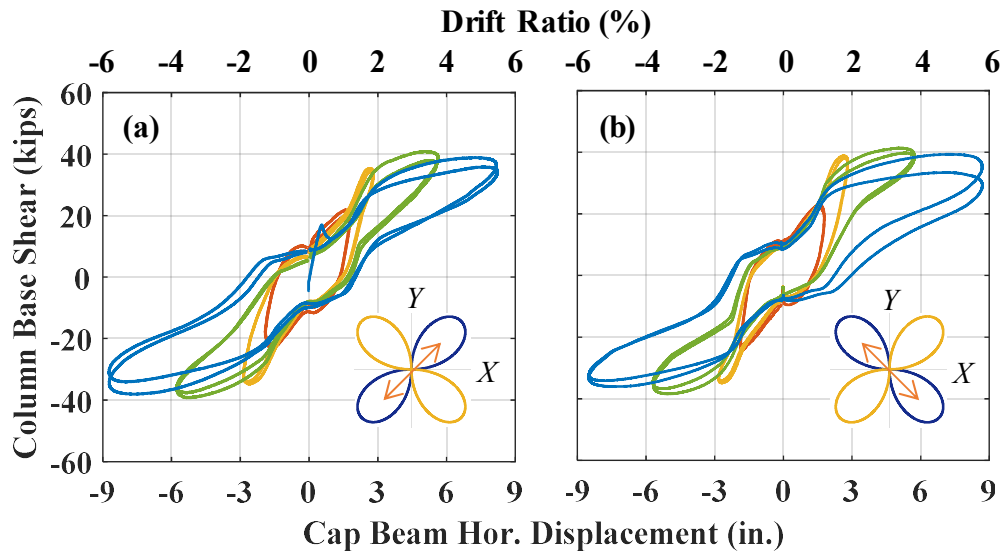
Figure 4-409. Phase IV – complete hysteretic responses of column: (a) in SW-NE direction; (b) in SE-NW direction

4.7.4.6. Final Damage Inspection

4.7.4.6.1. Overall Column Damage

Photos from four sides of the column specimen, taken after the removal of the instrumentation and concrete debris, are displayed in Figure 4-410. The column had not lost its integrity and was still stable under axial load. The extent/height of concrete spalling on the outside surface of the bottom column segment is provided in the photos (Figure 4-410). It is observed that the height of concrete spalling along the cross section circumference was not uniform (see also Figure 4-412). Specifically, the minimum and maximum heights of concrete spalling occurred on the north (> 30 in.) and east faces (< 12 in.) of the bottom segment. Consistently with the processed data (Figure 4-400), almost 0.5 in. of residual sliding was also identified at each of the lower two joints (Joints 1 and 2), as shown in Figure 4-411.
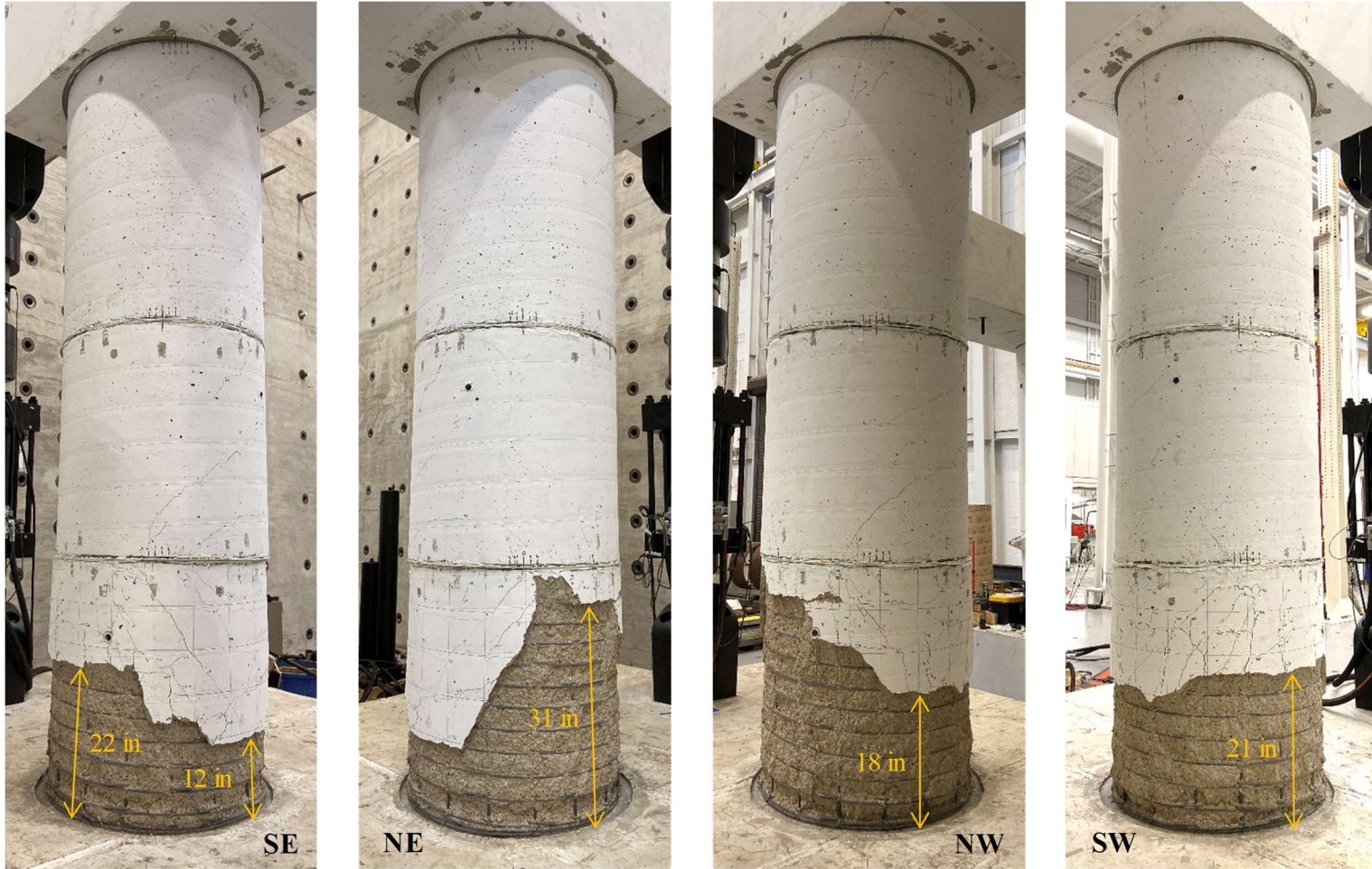
Figure 4-410. Phase IV, final damage inspection: four sides of column specimen

Figure 4-411. Phase IV, final damage inspection: residual joint sliding

4.7.4.6.2. Column Segments

The four faces of the bottom column segment after the spalled concrete was removed are shown in Figure 4-412. Some close-up views from the bottom part of the segment are also displayed in Figure 4-413. As seen, the cover concrete was completely lost over the spalling area, exposing the transverse reinforcement and the lower lengths of the longitudinal bars. Three of the longitudinal bars close to the northwest, southwest, and southeast corners of the cross section had slightly buckled, leading to the outward bending

of their bracing cross-ties (Figure 4-413). Such observations show the contribution of the longitudinal rebar to the rocking columns' lateral strength.
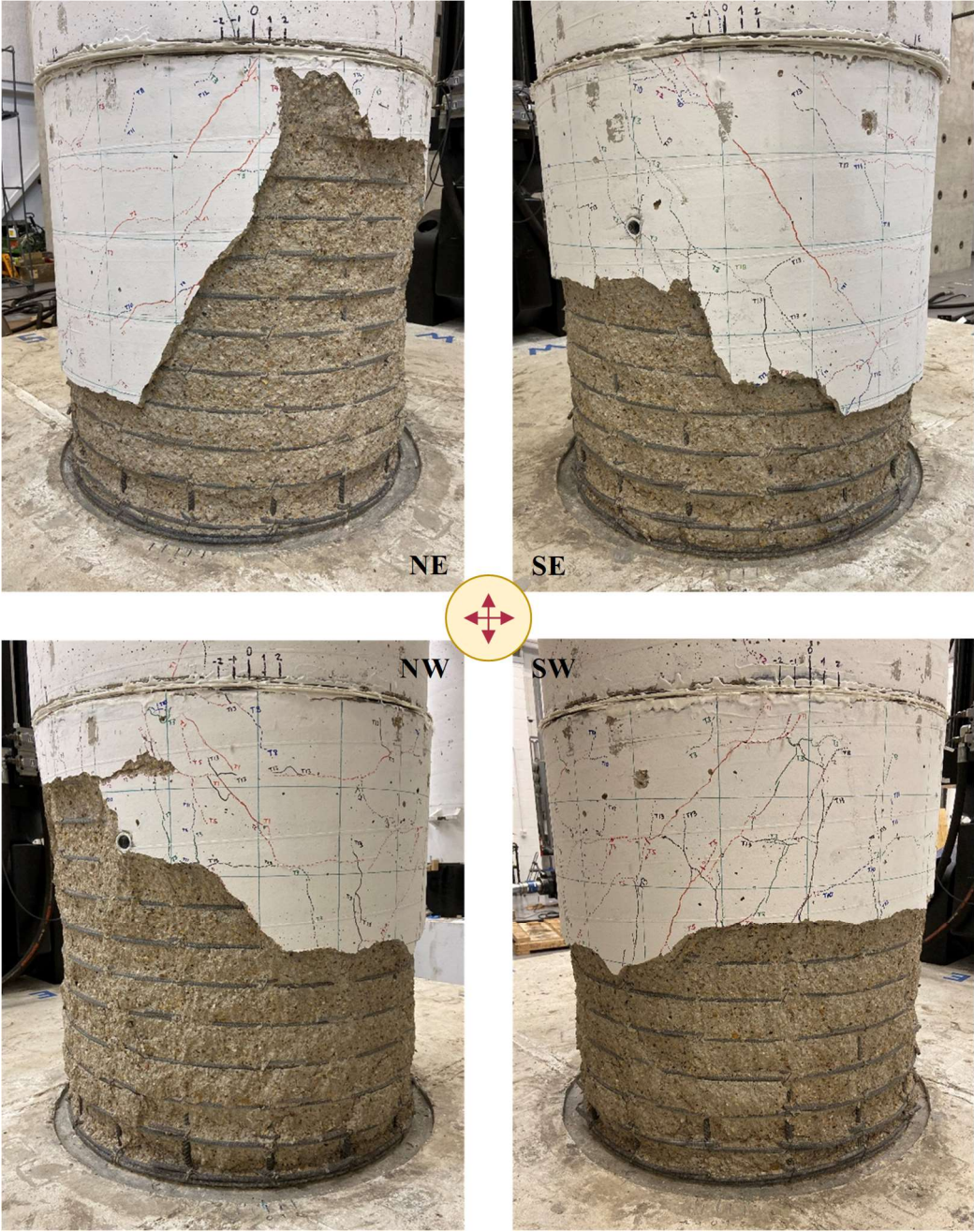
Figure 4-412. Phase IV, final damage inspection: bottom column segment
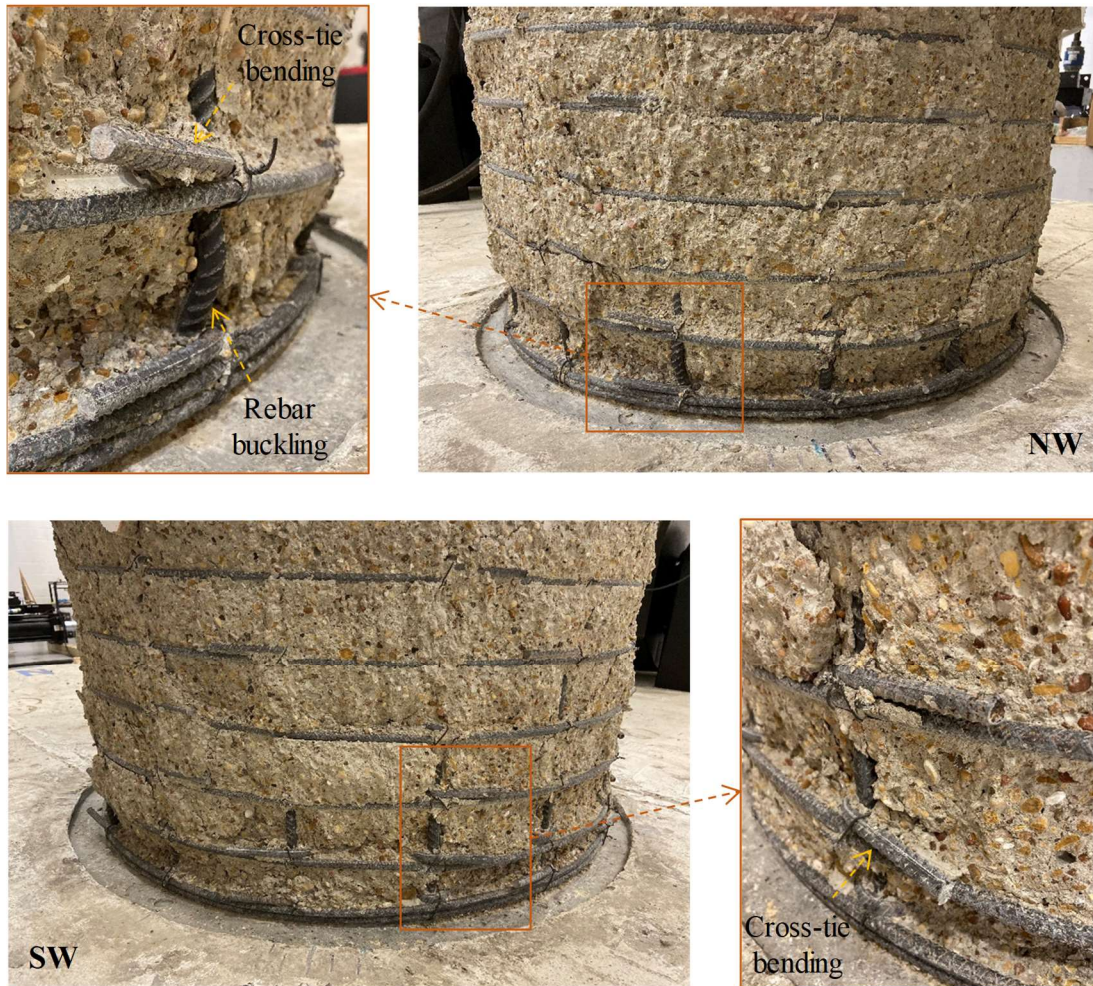
Figure 4-413. Phase IV, final damage inspection: longitudinal rebar buckling and cross-tie bending

Once the loading beam was taken off the top of the column, the inside surfaces of each of the column segments were inspected before they were lifted. The top and middle bottom segments had some minor hairline cracks, but the inside cover of the bottom segment had sustained some spalling, too (Figure 4-414). The spalling was more severe on the northwest and southwest sides of the interior surface and had propagated up to 18

in. from the bottom end on the southwest side. It is noted that longitudinal rebar buckling was observed at the same corners of the cross section (Figure 4-413).

As seen in a photo taken from one of the duct adaptors on the top of the bottom segment after the removal of the top two segments (Figure 4-415(a)), the repeated rubbing of the strands on the duct adaptors' inside surfaces due to the biaxial sliding at Joint 2 had damaged the PVC pipes, reaching the concrete. The debris resulted from the PVC and concrete damage at the duct adaptors had slipped down the column segment ducts and through the foundation ducts (Figure 4-415(b)). The strands had also slightly indented the edges of the PTFE pads at some points, but the damage was not severe (Figure 4-415(a)).
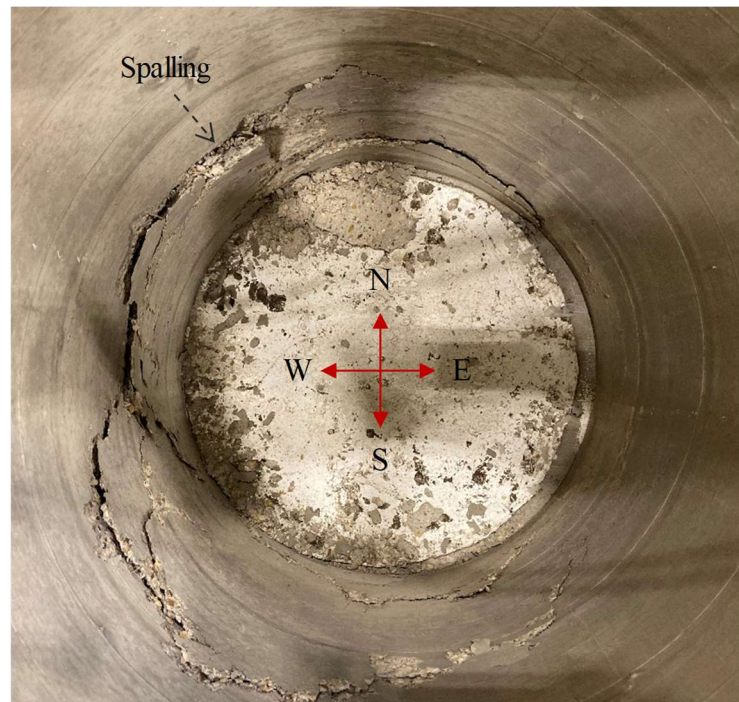
Figure 4-414. Phase IV, final damage inspection: concrete damage inside bottom column segment
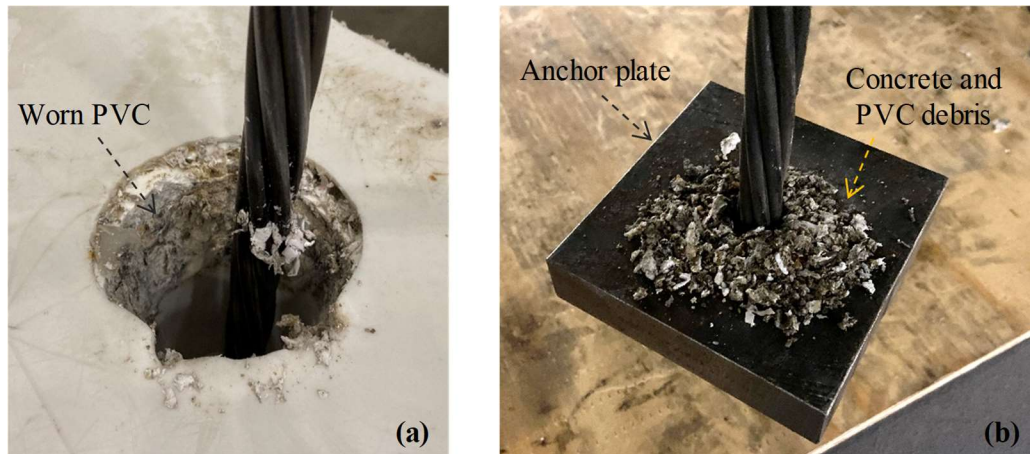
Figure 4-415. Phase IV, final damage inspection – debris of crushed/worn PVC, PTFE, and concrete: (a) duct adaptor on top of bottom column segment; (b) on strand anchor plate under foundation

Photos from the bottom surface of the bottom column segment are shown in Figure 4-416. The outside edge of the segment's cross section was fully crushed by rocking motion, exposing the spiral. However, the core concrete was not considerably damaged, except some cracks had appeared on its surface.

On the top surface of the same segment (Figure 4-417(a)) and the bottom surface of the middle segment (Figure 4-417(b)), between which sliding had happened, some PTFE wearing was observed, but the general condition of the pads was acceptable. The duct adaptors adjacent to the same sliding joint had got damaged due to the repeated movement of the strands on their edges. In particular, the entire thickness of the PVC pipes used as the duct adaptors in the bottom segment had been scraped up to 2 in. inside the segment by the strands, exposing the concrete. The remaining segment end surfaces were undamaged, as no sliding/rocking had occurred at Joints 3 and 4.
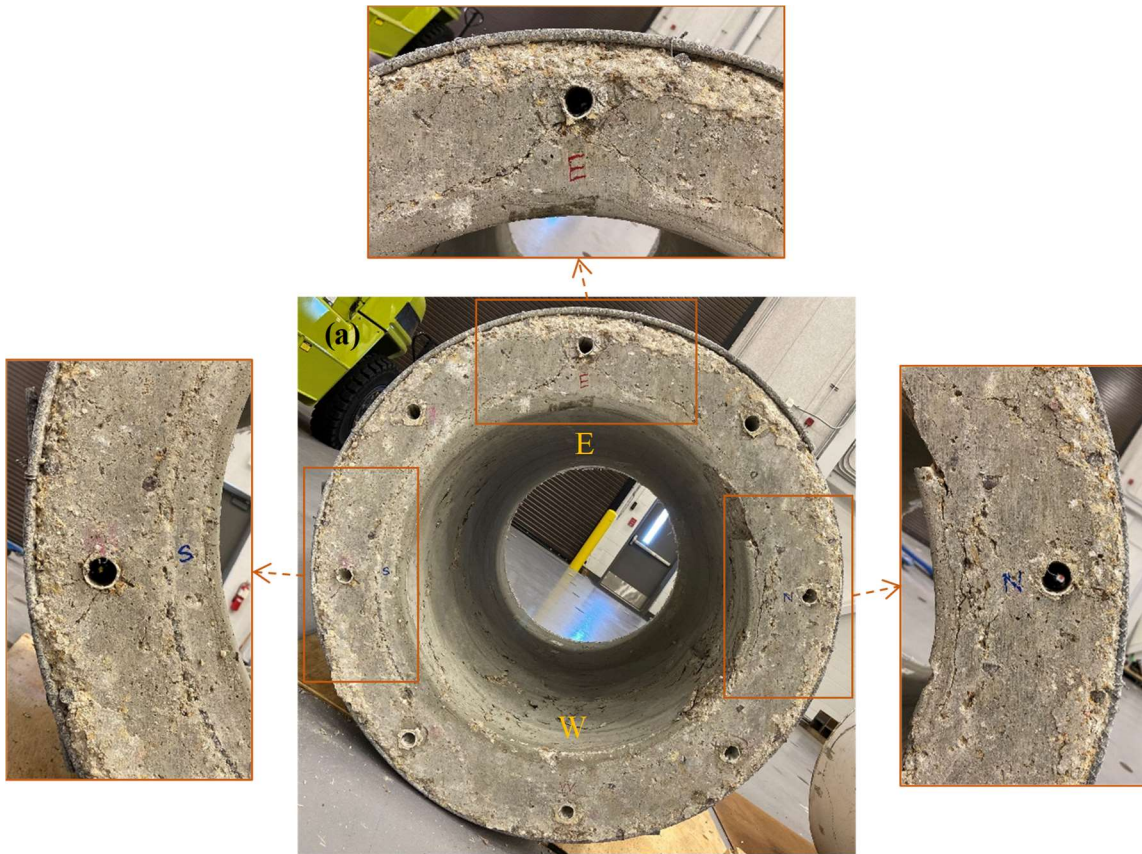
Figure 4-416. Phase IV, final damage inspection: bottom surface of bottom segment

4.7.4.6.3. Posttensioning Tendons

The posttensioning tendons extracted from the column specimen are displayed in Figure 4-418. None of the wires had broken, but plastic deformations were observed along the strands, wherever they would contact the duct adaptors or the ducts. The repeated contact of the strands with the duct-to-duct adaptor connection and their sliding against those had left three "shiny" areas on each of the strands, coinciding with the bottom end of the duct adaptor in the bottom segment (below Joint 2), Joint 2, and the top end of the lower duct adaptor in the middle segment (above Joint 2).
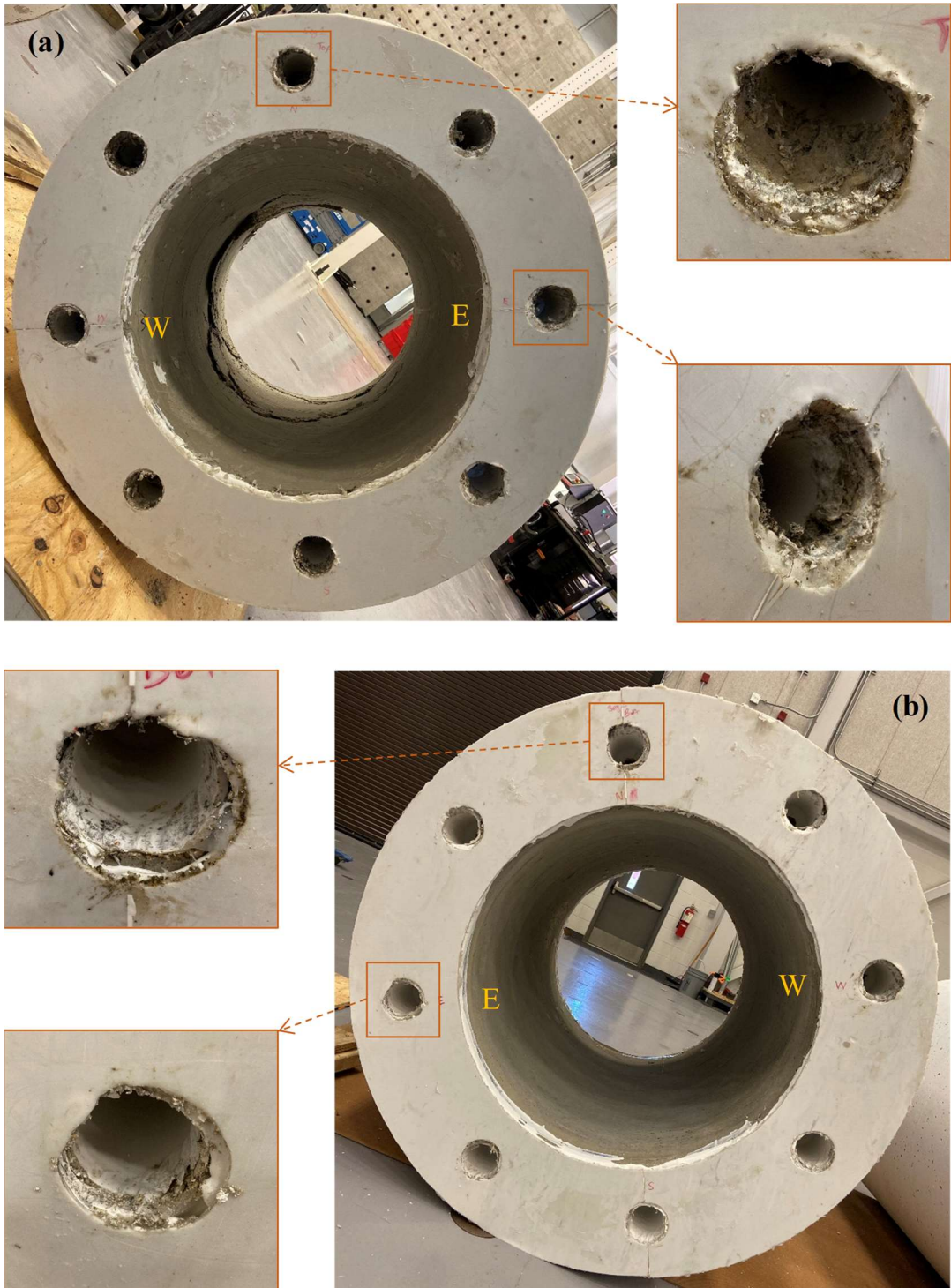
Figure 4-417. Phase IV, final damage inspection: (a) top surface of bottom segment; (b) bottom surface of middle segment

614
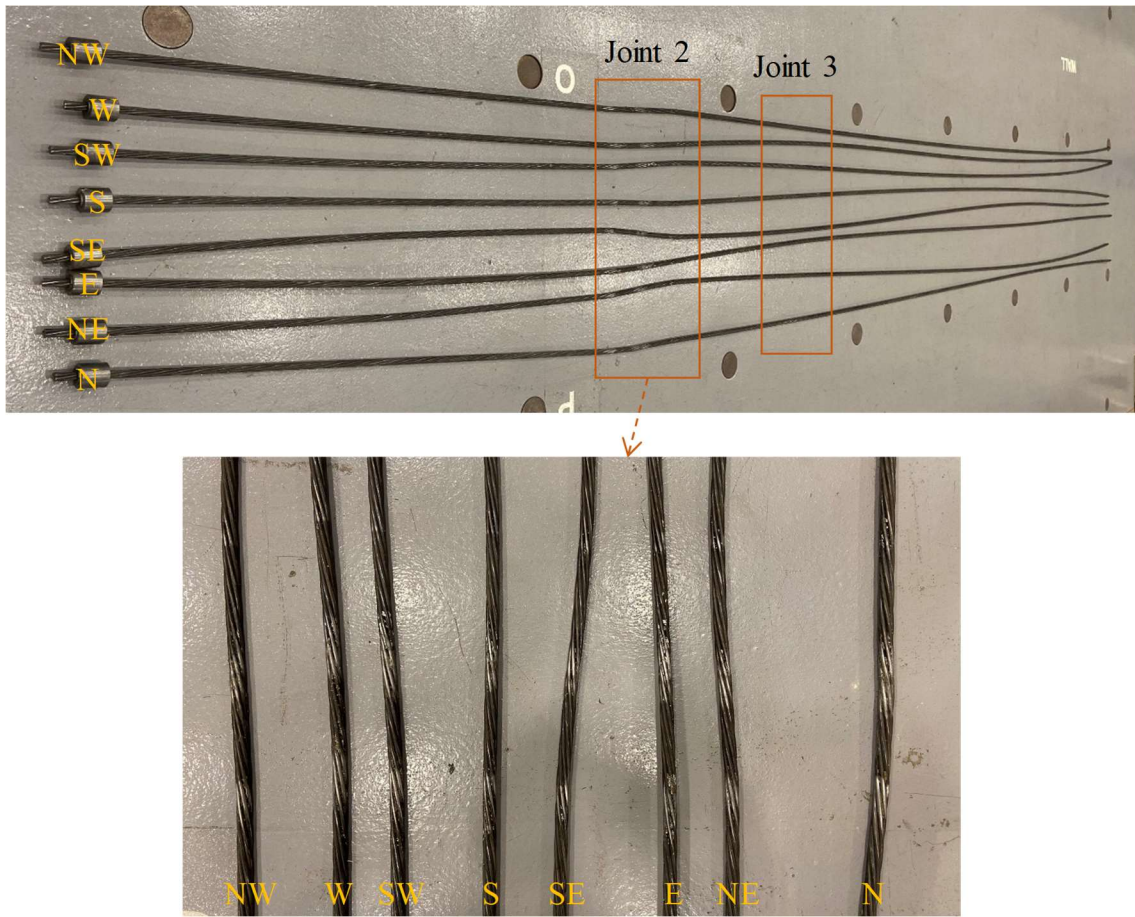
Figure 4-418. Phase IV, final damage inspection: posttensioning tendons

5. SIMULATION OF EXPERIMENTS

The objective of this chapter is to evaluate and refine the computational modeling approach proposed in Chapter 2 in predicting the responses of the HSR columns. This is achieved by comparing the experimental data of Chapter 4 with numerical simulation predictions. Only the column specimens tested under uniaxial lateral loading (i.e. in Phases I and III) are considered herein.

5.1. Finite Element Modeling

The finite element modeling of the HSR column specimens is carried out in OpenSees (McKenna et al. 2000) and on the basis of the methodology proposed in Chapter 2, with minor modifications. The element configurations, material models, and analysis methods are explained in the following.

5.1.1. Element Configuration

The finite element modeling approach used to model the tests performed in Phases I and III is schematically demonstrated in Figure 5-1 through Figure 5-4. All of the element formulations employ co-rotational geometric transformations in order to account for large displacements/rotations. According to Figure 5-1(a) and Figure 5-2, the column segments and their joints are modeled via four HSR elements and one GI element (as opposed to the element configuration considered in Chapter 2, where one GI element per segment was considered; Figure 2-1).
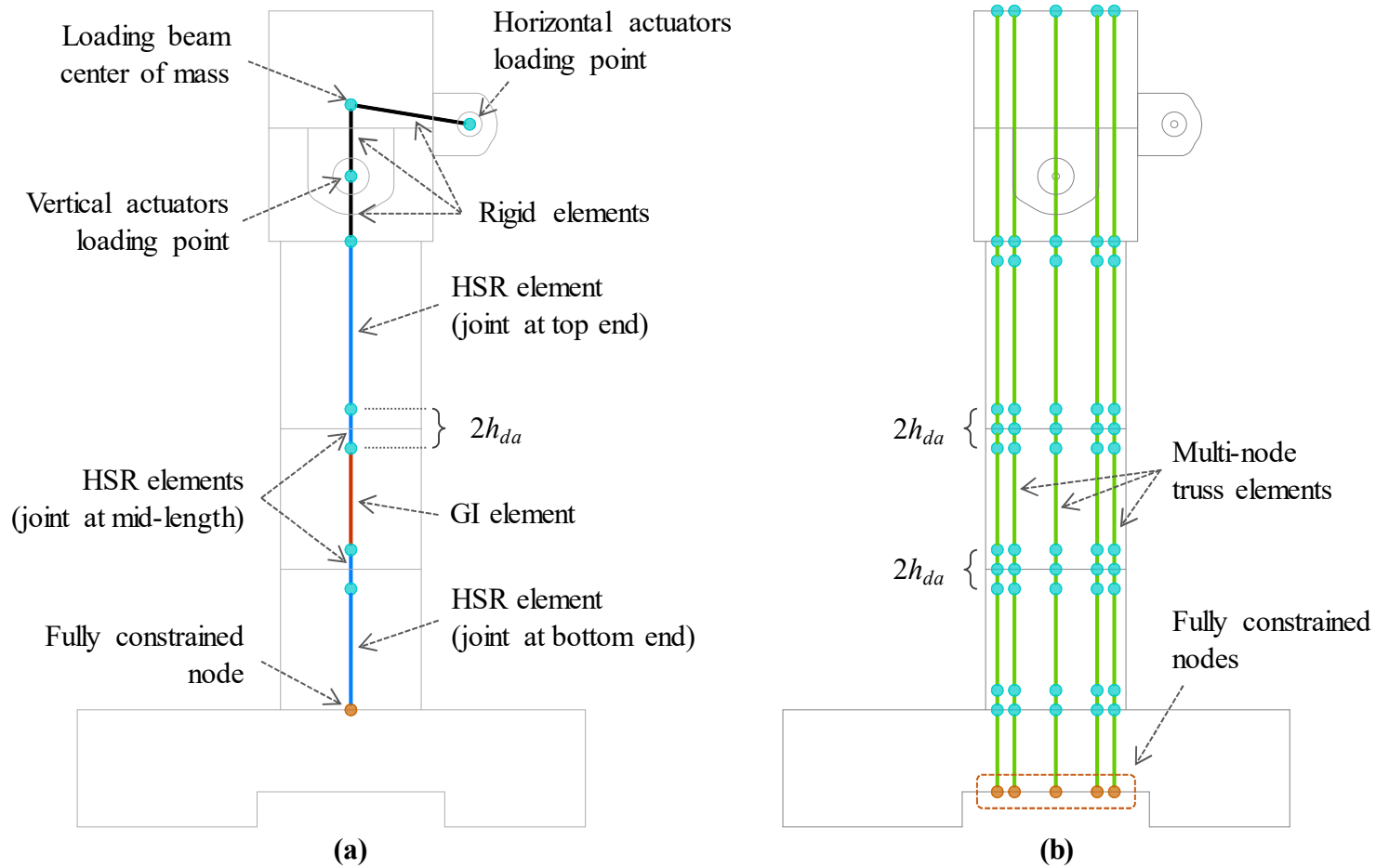
Figure 5-1. Element configuration used to simulate tests in Phase I: (a) beam-column elements representing concrete components and joints; (b) multi-node truss elements representing unbonded posttensioning tendons

617
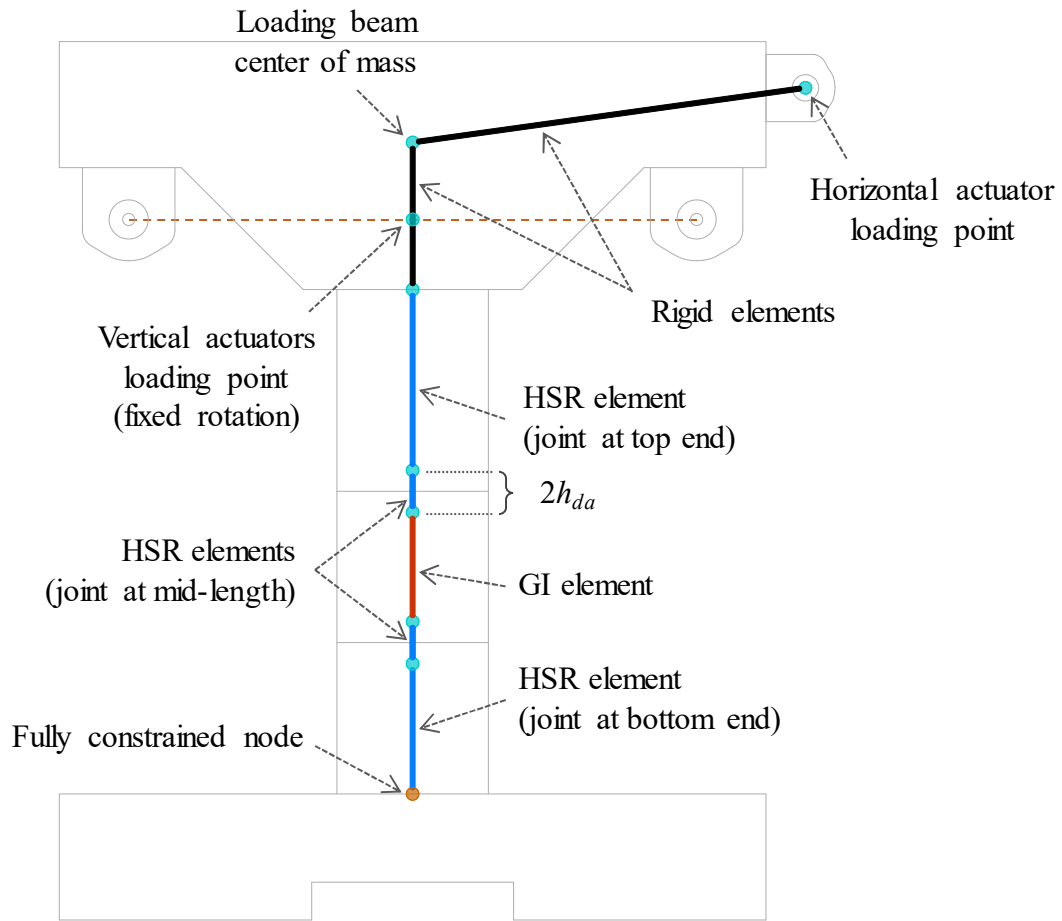
Figure 5-2. Element configuration used to simulate tests in Phase III
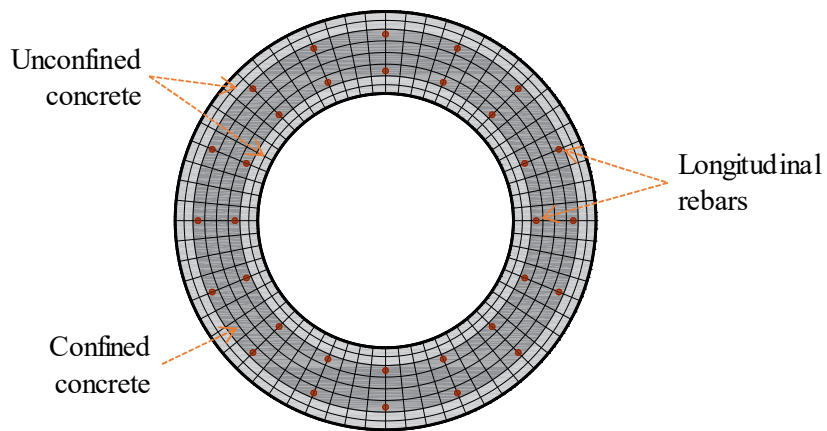
Figure 5-3. Fiber discretization of column cross section

618
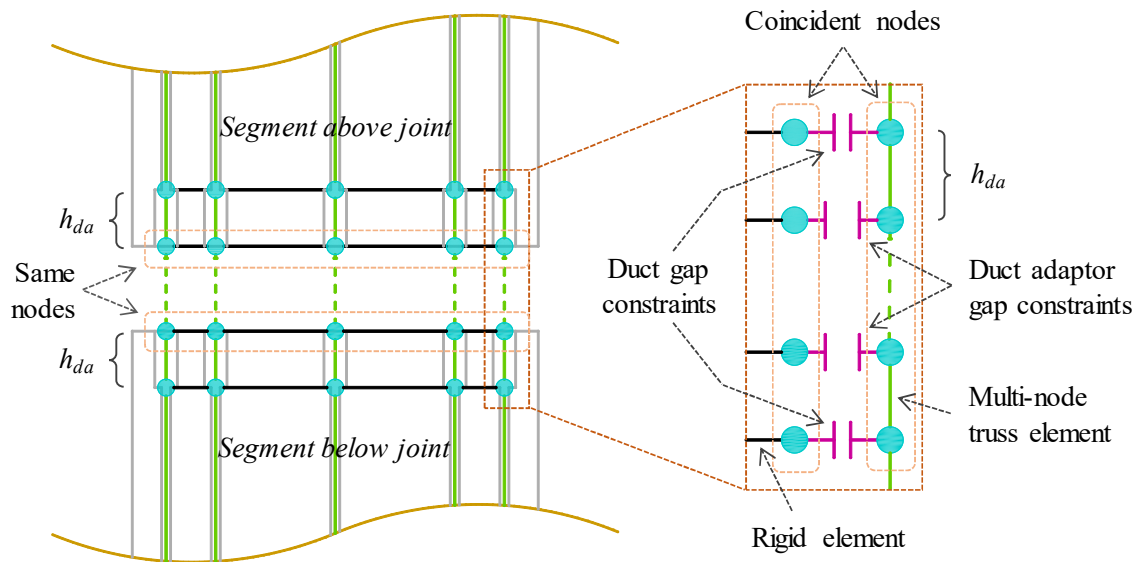
Figure 5-4. Arrangement of gap constraints representing ducts and duct adaptors

The bottom and top HSR elements are mainly expected to experience rocking and are longer than the middle two HSR elements. The middle HSR elements are twice as long as the duct adaptor height, h_{da}, and are centered at the sliding joints. A number of nodes are defined above the column to represent the loading beam's centroid – i.e. where the loading beam's weight is applied – as well as the actuators' swivel pins – i.e. where the actuator forces and weights act. As seen in Figure 5-1(a) and Figure 5-2, these nodes are connected to each other and the top end node of the top HSR element via rigid (highly stiff elastic) beam elements.

The joint sections in the bottom and top HSR elements are located at their bottom and top ends, respectively, where the rocking joints exist. In the middle two HSR elements, however, the joint sections are located at their mid-length, where the sliding joints exist. Each of the end and middle HSR elements have 7 and 5 IPs, respectively, while the GI

element has 5 IPs. Per Chapter 2, these numbers of IPs could ensure the objectivity of the elements' post-peak responses. The characteristic lengths, l_c, of the HSR elements and the GI element are taken equal to the cross section diameter and the cross section diameter, respectively.

The section constitutive relations used in the HSR and GI element formulations rely on the discretization of the cross sections into numerous uniaxial fibers representing confined concrete, unconfined concrete, and longitudinal rebar (Figure 5-3). The confined concrete is considered to cover the area enclosd by the spiral centerlines (Mander et al. 1988). The uniaxial material models representing these groups of fibers are described in the subsequent section. In order to partly account for the higher flexibility of the PTFE pads (see Appendix D) under compression compared to concrete, the stiffness of the concrete material models used at the fiber sections representing the sliding joints were reduced to 16% their original values. This factor was roughly calculated considering a series connection between the concrete and PTFE fibers at the sliding joint interfaces and assuming that they remain elastic. Furthermore, the cross section dimensions used to define the fiber sections correspond with the constructed column specimen measurements. Specifically, the inside and outside diameters of the hollow segments in Phases I and III were almost 11.25 in. and 18.5 in., respectively, while the concrete cover was almost 1.375 in., both outside and inside the segments.

As shown in Figure 5-1(b), the eight unbonded posttensioning tendons in each column specimen are modeled via five multi-node continuous truss elements formulated in Chapter 2. The nodes located at the bottom ends of all the truss elements are fully

620

constrained, whereas their top ends are connected to the other nodes defined over the loading beam through rigid beam elements. The rest of the intermediate nodes shown along the truss elements are located at the points of potential contact between the tendons and their ducts. These include three nodes adjacent to every sliding joint (two with h_{da} distances below and above the sliding joint and one at the joint height) and two nodes adjacent to every rocking joint (one with some distance above/below the rocking joint and one at the joint theight). As depicted in Figure 5-4, the intermediate nodes are used to constrain the tendons' movement in their ducts, through the zero-length constraint elements formulated in Chapter 2. Note that each of the nodes at the joint levels are connected through two constraint elements to the components below and above that joint (see Figure 5-4). The other ends of the constraint elements are nodes coincident with the tendons' intermediate nodes, but either connected to the elements representing the column segments and the loading beam, or fully constrained (i.e. at the foundation level). Considering that each of the three central truss elements in Figure 5-1(b) represent two tendons of the same location in the 2D plane, their cross section areas are double the area of a single monostrand. The initial prestress in the multi-node truss elements is enforced through an initial strain specified in their uniaxial material model, which is described subsequently.

5.1.2. Material Models

In accordance with the described finite element configuration, the following uniaxial material models are defined:

- *Unconfined and confined concrete*: The concrete constitutive models follow the Modified Kent and Park model (Scott et al. 1982) with minor modifications made to the softening part of its backbone curve such that its negative slope is not constant (Figure 5-6(a)). The parameters of the unconfined and confined concrete models are determined in accordance with Mander et al. (1988) and Karthik and Mander (2011). The unconfined concrete compressive strengths are assumed to be 85% the values obtained from the cyclinder tests at the times of testing (see Table 4-6) – the measured values are reduced because the concrete cylinders had been kept in the curing room before they were tested. The typical hysteretic responses achieved by these models are shown in Figure 5-5(a) and (b).

- *Mild steel*: The constitutive model representing the longitudinal steel bars follows the Giuffré-Menegotto-Pinto model (Giuffrè and Pinto 1970). In order to avoid the numerical convergence issues caused by the series material model incorporating the steel material model and a no-tension elastic material model, longitudinal steel is omitted at the fiber sections corresponding to the joint locations. The steel yield strength and strain hardening ratio are selected as 68 ksi (Caltrans 2013) and 1%, respectively (Figure 5-5(c)).

- *High-strength steel*: The high-strength steel material model used to simulate the prestressed strands is based on the model by Mattock (1979). This material model, which was advanced to incorporate tendon fracture through a damage factor and was implemented in OpenSees as part of this research, incorporates an initial strain to introduce prestressing into the strands and does not resist tension.

The model parameters are chosen per Sideris et al. (2014b) and Caltrans (2013). Per Sideris et al. (2014b), in order to account for the slippage of the strands in the wedges and the wedge seating into the barrel chucks without their explicit modeling, the modulus of elasticity of the high-strength steel material is reduced by 15% (Figure 5-5(d)). Note that modifying the modulus of elasticity instead of strands area would not affect the strands' yield/fracture strength.

- *Duct and duct adaptor gaps*: It is noted that the response of the zero-length constraint elements in transverse (horizontal) direction should emulate the gaps between the tendons and the ducts and duct adaptors, even if it does not account for the PVC pipes' bearing damage. Herein, the desired response is produced via the multi-linear elastic material model available in OpenSees. The material model parameters are selected such that it exhibits zero stiffness/resistance so long as the constraint's transverse deformation remains within the gap range, whereas the stiffness significantly increases beyond that range. The typical force-deformation responses of such material model defined to represent ducts and duct adaptors are shown in Figure 5-6. Note that in the models analyzed here, the duct adaptor gap ranges are adjusted per maximum sliding values measured in tests.
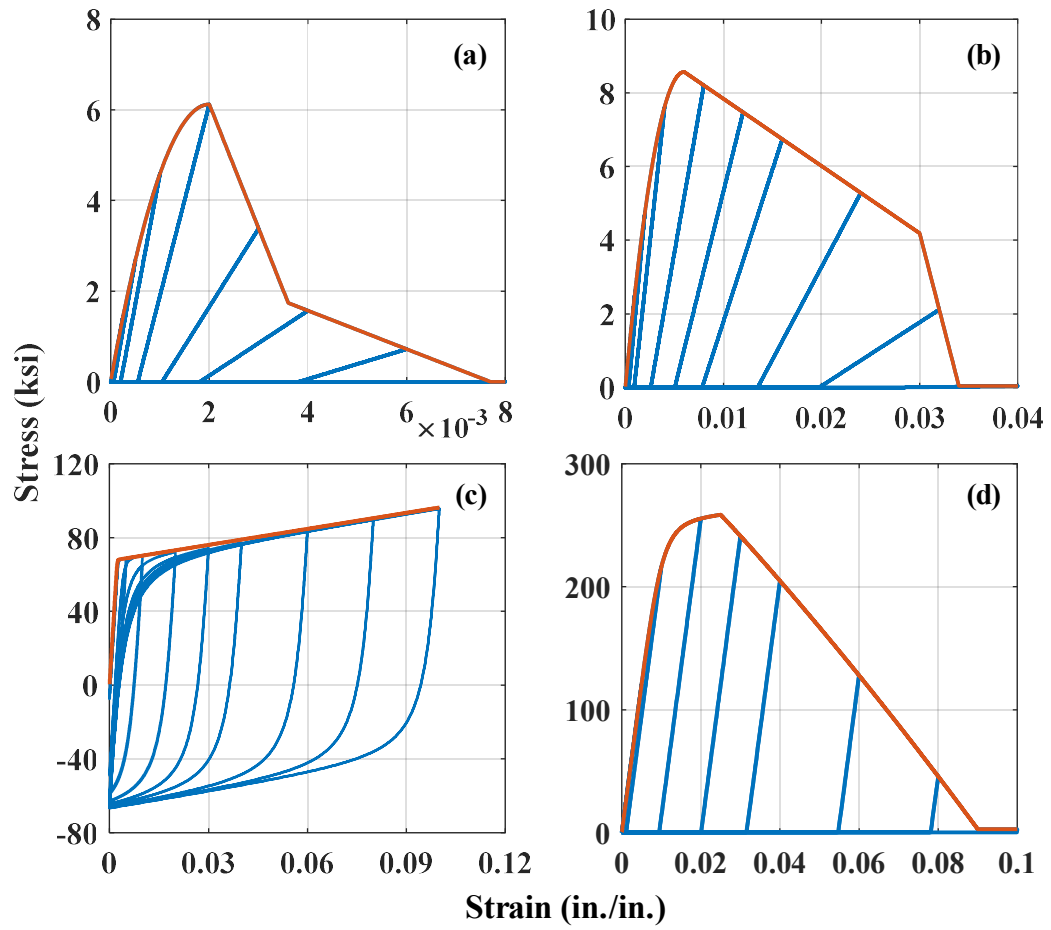
Figure 5-5. Hysteretic responses of material models: (a) unconfined concrete; (b) confined concrete; (c) mild steel; (d) high-strength steel
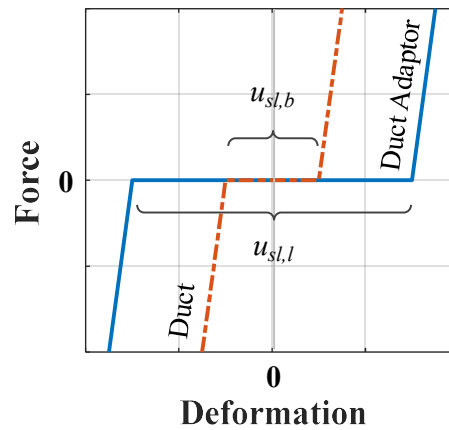
Figure 5-6. Typical force-deformation responses of constraint elements

5.1.3. Friction Model

The frictional shear stresses at the joint fiber sections are computed according to Eq. (2-36). In this equation, the function considered to determine the coefficient of friction, $f_\mu(.)$, is a simplified version of a model recently developed by Reddy Goli (2019) based on experiments on identical PTFE and grease materials. Although the model by Reddy Goli (2019) incorporates both pressure and velocity dependences of coefficient of friction, only the pressure dependence is considered here, because none of the simulated tests were performed under fast loading. According to the simplified model, the coefficient of friction, μ, is determined as:

$$\mu = \mu_P + \langle \mu_B - \mu_P \rangle exp\left(-\alpha_{BP}I_{BP}\right)$$

(5-1)

where $\langle . \rangle$ are the Macaulay brackets; μ_P and μ_B are the permanent (i.e. after sticky phase at interface terminates) and breakaway friction coefficients, respectively; α_{BP} is a calibration constant; and I_{BP} is the accumulated sliding. The breakaway friction coefficient, μ_B, is a function of contact pressure, σ, expressed as:

$$\mu_B = \mu_{B,min} + \left(\mu_{B,max} - \mu_{B,min}\right)exp\left(-\alpha_B\sigma\right)$$

(5-2)

where $\mu_{B,min}$ and $\mu_{B,max}$ are the breakaway friction coefficients at very high and zero contact pressure, respectively; and α_B is a calibration constant. Likewise, the permanent coefficient of friction, μ_P, depends on the contact pressure, σ, according to:

$$\mu_P = \mu_{P,min} + \left(\mu_{P,max} - \mu_{P,min}\right)exp\left(-\alpha_P\sigma\right)$$

(5-3)

where $\mu_{P,min}$ and $\mu_{P,max}$ are the permanent friction coefficients at very high and zero cotact pressure, respectively; and α_P is a calibration constant.

625

The values of the above model's parameters are chosen as listed in Table 5-1. These values are very close to those determined by Reddy Goli (2019) based on his experimental data. The resulting variations of breakaway and permanent coefficients of friction with contact pressure are displayed in Figure 5-7.

Table 5-1. Selected values for friction model parameters

Parameter	α_{BP}	$\mu_{B,min}$	$\mu_{B,max}$	α_B	$\mu_{P,min}$	$\mu_{P,max}$	α_P
Value	2.5 /in.	0.05	0.3	0.0016 /psi	0.015	0.135	0.0022 /psi
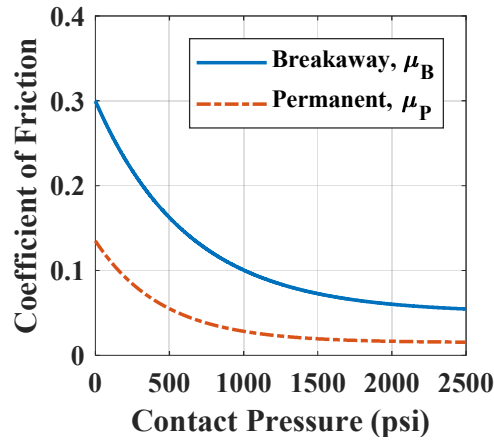
Figure 5-7. Variation of coefficient of friction with contact pressure

5.1.4. Load Application

The gravity loads due to the masses of the loading beam, the actuators, and the column segments are assigned as static point loads to the loading beam's center of mass, the actuators' connection nodes, and the nodes along the column segments, respectively. Although dynamic effects are negligible in the tests simulated herein, lumped masses consistent with the above gravity loads and the loading beam's mass moment of inertia

are assigned to appropriate nodes in the model. The total vertical load provided by the vertical actuators is applied to a node located at the same height as their swivel pins (see Figure 5-1(a) and Figure 5-2).

For each simulated test, the lateral displacement time histories obtained from the processing of the data obtained from the same test are imposed to the nodes representing the horizontal actuators' end swivel pins (see Figure 5-1(a) and Figure 5-2). This requires analysis of the model using a direct time integration method, which herein is the Newmark method. In order to allow sliding at the sliding joints, the inherent damping model used for all analyses is the Enhanced Rayleigh damping model (Salehi and Sideris 2020) with 3% critical damping ratio assigned to the first two modes.

5.2. Comparisons with Experiments

5.2.1. Simulation of Tests in Phase I

5.2.1.1. Under Cyclic Lateral Displacement

The tests simulated herein are Tests 1 to 3, which were executed under the loading protocols of Loading Set 1 (Table 4-14). Note that simulating the tests under very large displacements (e.g. those under the loading protocols of Loading Set 6) would require the incorporation of the additional confinement provided by the CFRP wrap (which was applied to the bottom column segment before those tests) in the simulation model. The selected loading protocols included cyclic lateral displacement and constant vertical load. In order to account for the damage caused by the tests prior to each test, the lateral displacement time histories of all the three tests are applied consecutively.

The column base shear vs. lateral displacement responses predicted by the simulation model are compared in Figure 5-8(a), (c), and (e). The column base moment vs. rocking responses are also compared in Figure 5-8(b), (d), and (f) – the rocking values in these plots are those predicted/measured for the bottom rocking joint (Joint 1).

It is observed the general hysteretic shear-displacement response of the tested HSR column is well captured by the simulation model. Specifically, the predicted stiffnesses in various stages of the response (e.g. before sliding initiation, after sliding initiation, and during tendon-duct interactions) are very close to their experimental counterparts.

Per Figure 5-8(a), the model predicts an earlier sliding initation than the test, but the corresponding base shear values (breakaway friction) are close, and similarly to the test, sliding onset is predicted to occur during the third displacement cycle. The energy dissipation observed during the first two displacement cycles of Test 1 (with a peak drift ratio of 0.43%, before sliding starts) is not captured by the model, as it neglects the tendon-to-duct friction. Also, the variation of friction with accumulated sliding during the initial cycles is not captured very well, but the permanent friction is found very close to that observed in the test data.

According to Figure 5-8(c) and (e), as expected, the simulation model does not capture the base shear drops at displacement reversals caused by the friction between the tendons and the ducts. The model does not exhibit any initial breakaway friction, because the analysis followed the analysis respective to the previous test and would not account for the friction built up at the sliding joint between the two tests. In terms of maximum base shear, however, the simulation model's predictions are in acceptable agreement with

the the experimental measurements. Specifically, the peak base shear values predicted by the model for Tests 1 to 3 are 7% lower, 5% higher, and 10% lower, respectively, than the experimentally measured values. The slightly higher peak strength obtained during the test could have occurred due to the tendon-duct friction and the friction at the rotating parts of the actuator swivels. The residual displacements predicted for the last displacement cycles (with a peak drift ratio of 4%) of Test 3 are also underestimated by the model (by 24%, Figure 5-8(e)). This difference is partly due to the inability of the model to capture the plastic compressive deformations of the duct adaptors by the tendons.

In terms of moment-rocking hysteretic responses at the bottom joint (Joint 1), the model predictions are overall acceptable. In all cases, the simulation model exhibits a higher stiffness against rotation than the actual column specimen. This is justified by the fact that the model assumes a full contact between the segments, the foundation, and the loading beam, while this was not the case in the tests. The predicted rocking values for the second two tests with larger rocking motion (Tests 2 and 3, Figure 5-8(d) and (f)) are maximum 30% larger than those measured during the tests. This is while the experimental column responses are not fully symmetric and measurement errors could affect them. The maximum moment values obtained from the tests and the simulation model are, however, as close as the peak base shear values were.
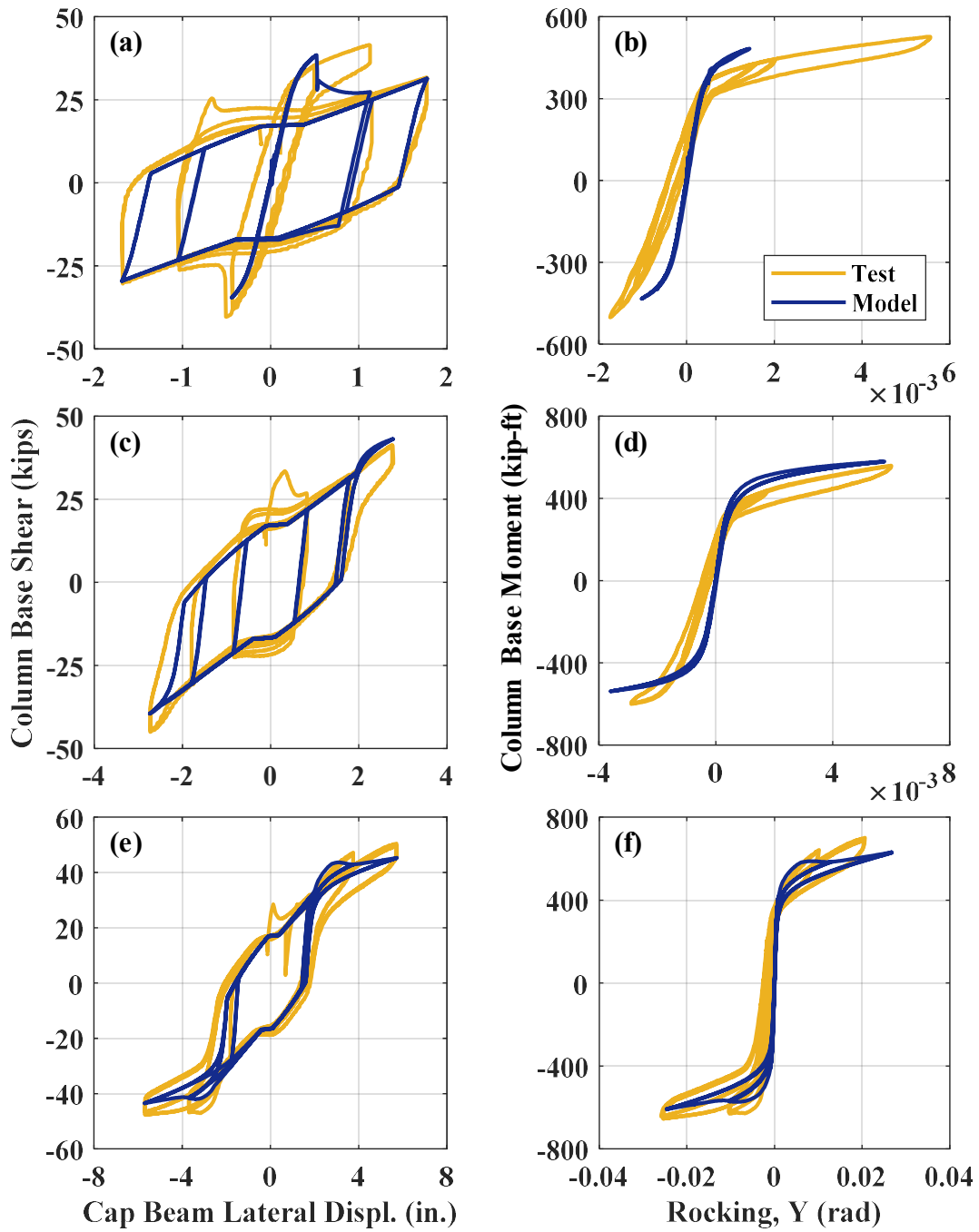
Figure 5-8. Comparison of base shear vs. lateral displacement and base moment vs. rocking responses obtained from experiment and simulation model: (a,b) Test 1; (c,d) Test 2; (e,f) Test 3

The shear vs. sliding responses of the sliding joints (Joints 2 and 3) obtained from the model are compared with those measured during the experiments in Figure 5-9. It is observed that the predicted responses are in a very good agreement with their experimental counterparts, both in terms of sliding and shear. The breakaway friction is only seen in the first test's simulation (Figure 5-9(a)), as the analyses related to all tests were run consecutively (as explained earlier).

The variations of total posttensioning force and moment with the loading beam's lateral displacement obtained from the tests and the numerical simulations are compared in Figure 5-10. Even though the general trends of the numerically predicted and experimentally measured responses resemble, the model overestimates the maximum PT forces by 8% (Figure 5-10(a), (c), and (e)). Also, the model does not capture the PT losses caused by phenomena other than yielding (e.g. tendon slippage and wedge seating in the anchorage hardware). That is, though the final total PT force after Test 3 was 124.5 kips, the corresponding value predicted by model was 132.5 kips, i.e. 6% higher.

The above findings shows that the mere reduction of the modulus of elasticity of the high-strength steel in the simulation model – as explained earlier in the modeling description – cannot sufficiently improve the accuracy of the tendon force predictions. It is also noted that the tendon forces reported herein were measured at the top ends of the tendons, while, because of the tendon-duct friction, the forces toward their bottom ends could be larger (see the discussion in Section 4.7.1.5.2).

As for the PT moments, a lack of symmetry is observed in the experimentally obtained responses, which is less significant in the model predictions (Figure 5-10(b), (d), and (f)).

This could partly have been caused by the inevitable inequality of the initial PT forces in the tested column specimen and also the duct misalignments.
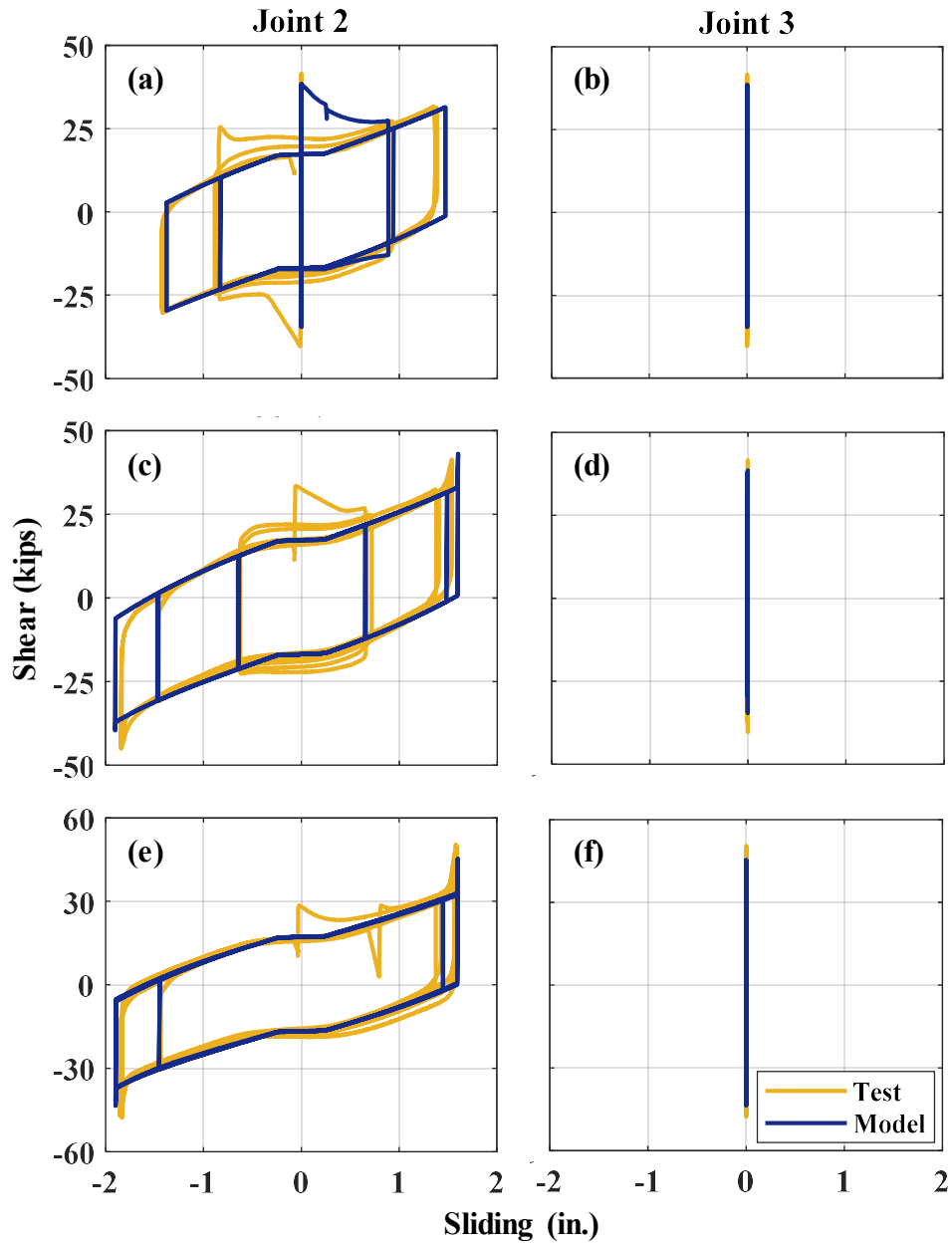
Figure 5-9. Comparison of joint shear vs. sliding responses obtained from experiment and simulation model: (a,b) Test 1; (c,d) Test 2; (e,f) Test 3
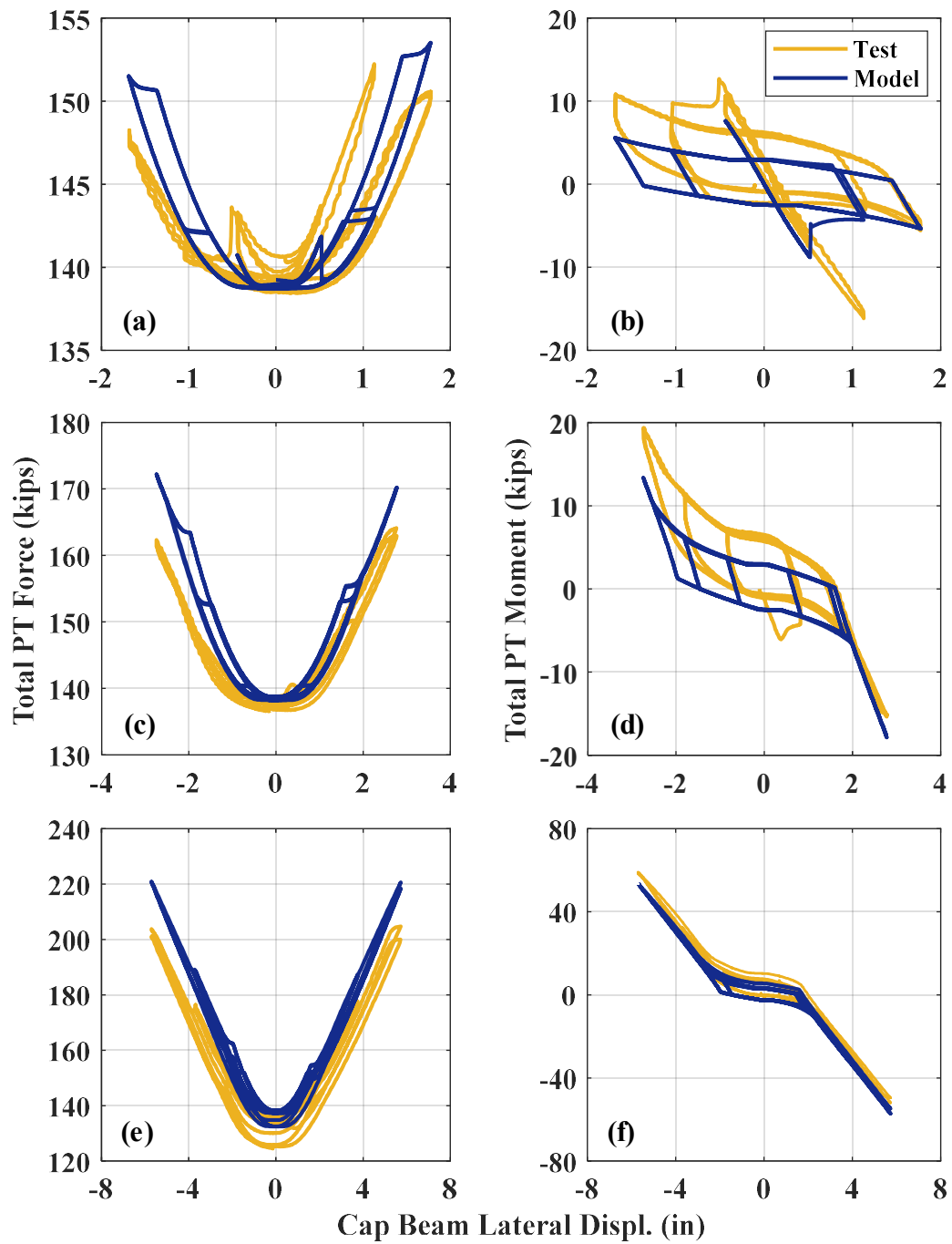
Figure 5-10. Comparison of total PT force and moment vs. lateral displacement responses obtained from experiment and simulation model: (a,b) Test 1; (c,d) Test 2; (e,f) Test 3

633

5.2.1.2. Under Arbitrary Lateral Displacement

The tests simulated in this section are Tests 18 and 20 from Loading Set 5 with two different levels of peak drift ratio (Table 4-18). Both these tests were conducted under a constant vertical load and arbitrary lateral displacement time histories. The two time history analyses are run individually, thereby ignoring the effects of the tests conducted prior to these tests on the column specimen. The initial total PT force considered in the model, however, matches that measured before running each of the tests in reality. Also, considering the low level of rocking in these tests, the impact of the additional confinement of the bottom column segment provided by the CFRP wrap on the response predeitions can be neglected.

The column base shear vs. lateral displacement response predictions are compared with those obtained from the respective tests in Figure 5-11. According to the graphs, while small differents are observed between the experimental and simulation results, the overall agreement of the results is acceptable. The differences between the results are attributed to four major factors, such as: (*a*) the exclusion of the inertia effects in the processing experimental data; (*b*) the absence of tendon-duct friction in the simulation model; (*c*) neglecting the prior tests' impact on the column and sliding joints (i.e. in terms of friction properties and residual sliding); and (d) disregarding the velocity dependence of coefficient of friction in the model.

Indeed, as also seen in in the joint responses (Figure 5-12), higher breakaway friction is observed in the simulation results in comparison with the test results, because the actual sliding joints had experienced several sliding cycles prior to these tests. Neglecting the

634

breakaway friction effects, however, the maximum base shear preditions for both tests are less than 5% different from the experimentally measured values (Figure 5-11). Likewise, the lateral displacements corresponding to zero base shear (characterizing the residual displacements) are very close in both directions for both simulated tests.
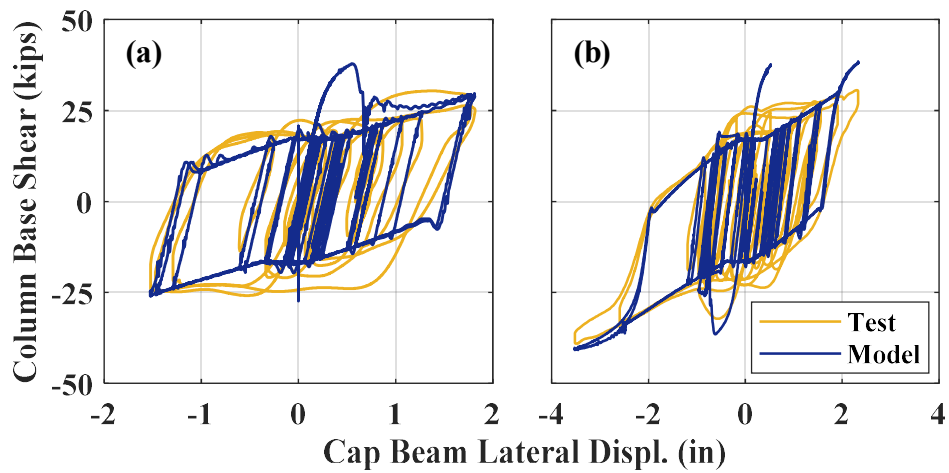
Figure 5-11. Comparison of base shear vs. lateral displacement responses obtained from experiment and simulation model: (a) Test 18; (b) Test 20
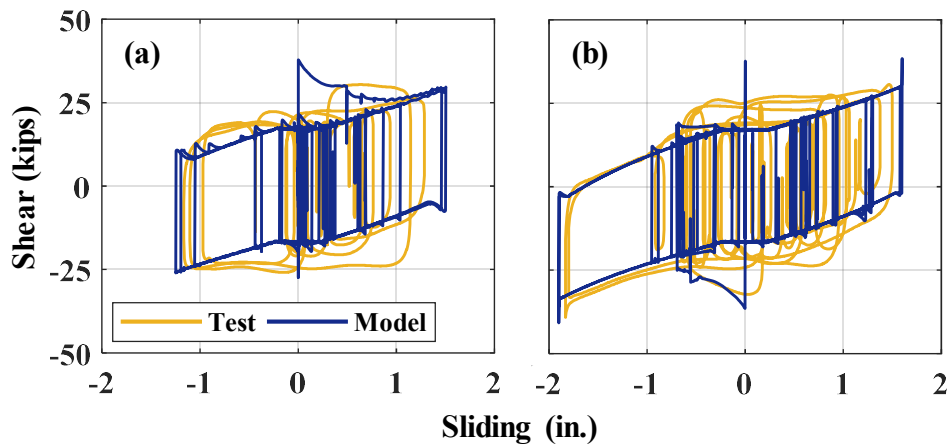
Figure 5-12. Comparison of shear vs. sliding responses of Joint 2 obtained from experiment and simulation model: (a) Test 18; (b) Test 20

As was the case during the actual tests, none of the the simulations predicted sliding at the second sliding joint (Joint 3), while the sliding time histories achieved for the first sliding joint (Joint 2) closely resemble the measured sliding time histories during the experiments (Figure 5-13). Specifically, the sliding initiation in both simulations coincides with the sliding initiation in the test data and the maximum sliding values are less than 15% different. It is also noted in these graphs that although the initial sliding in both tests was positive (from prior tests), the final predicted and measured residual sliding agree.
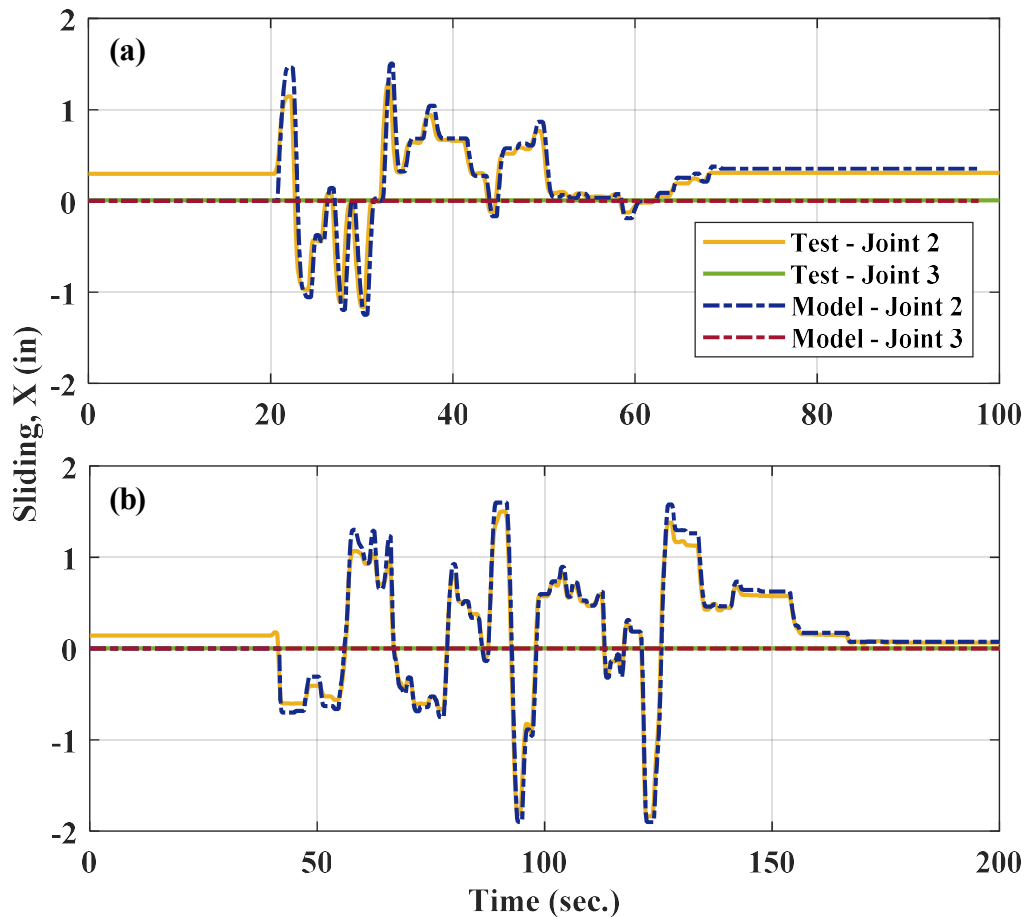
Figure 5-13. Comparison of joint sliding time histories obtained from experiment and simulation model: (a) Test 18; (b) Test 20

636

The next set of response time histories evaluated herein pertain to the total PT force. According to Figure 5-14, the general trends of the simulation predictions agree with the experimentally measured total PT forces, but they are overestimated. That is, the peak total PT forces obtained from the simulations of Tests 18 and 20 are 5% and 6% higher than those measured during those tests. As pointed out in Chapter 4, Section 4.7.1.5.2 (see Figure 4-75), tendon-to-duct friction contributes to the lower PT forces measured at the top ends of the tendons during the tests, while aside from that, neglecting the concrete damage resulted from the previous tests in the simulations could also increase the PT force predictions.
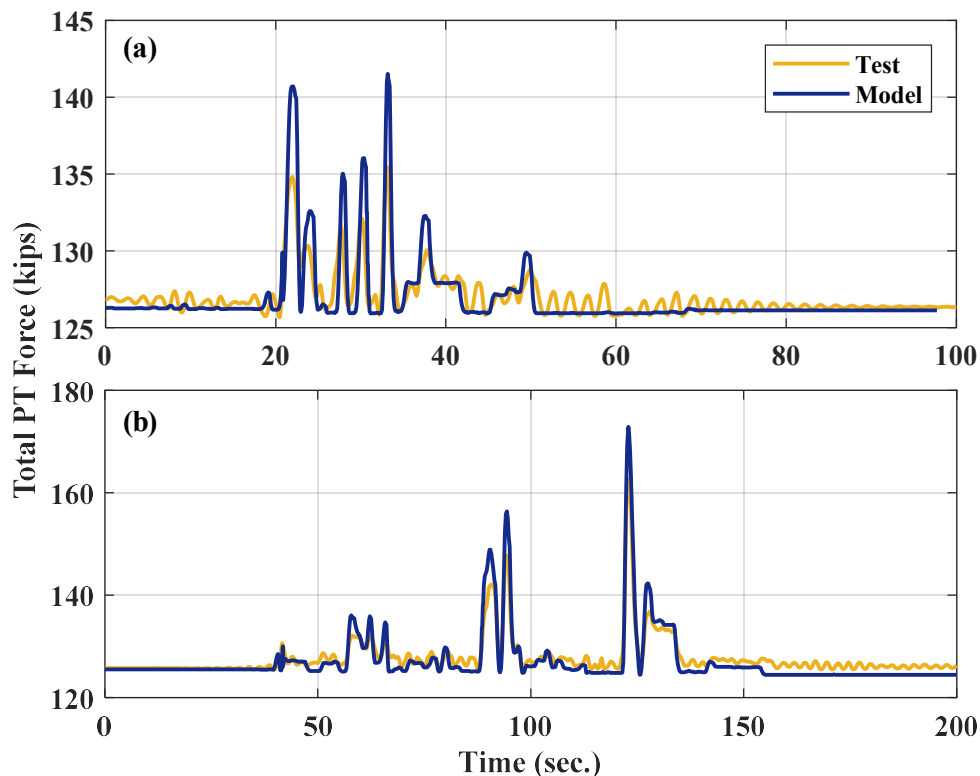
Figure 5-14. Comparison of total PT force time histories obtained from experiment and simulation model: (a) Test 18; (b) Test 20

Similarly to the total PT force time histories, the total PT moment time histories obtained from the model are in close agreement with the test data (Figure 5-15). Though the PT moment effects on the column itself are inconsequential (because of their low values), they can still be used to examine the model's accuracy. The maximum PT moment predictions for Tests 18 and 20 are about 14% higher than and equal to the measured maximum PT moment values, respectively. Note that the negative non-zero PT moment observed at the beginning of the simulated time histories are caused by the weight of the horizontal actuators applied to the nodes representing their swivel pins (see Figure 5-1).
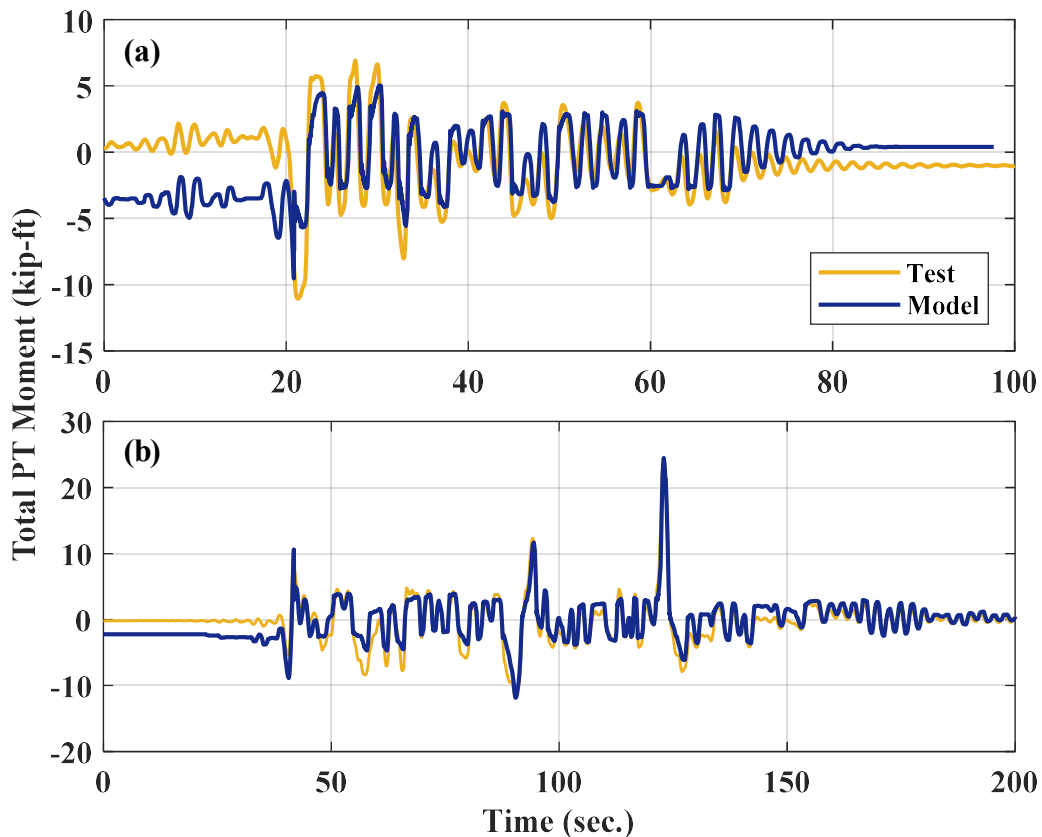
Figure 5-15. Comparison of total PT moment time histories obtained from experiment and simulation model: (a) Test 18; (b) Test 20

5.2.2. Simulation of Tests in Phase III

As seen ealier (e.g. Figure 4-320), significant duct adaptor damage was observed during the experimental tests in Phase III, which also observably influenced the column's response. Hence, compared to the model used to simulate the column specimen in Phase I, the secondary stiffness of the elastic multi-linear material model representing the transverse constraint of the tendons at the sliding joint heights (Figure 5-6) is reduced in the model used to simulate the tests in Phase III. Even though the constraint's response remains elastic and still does not simulate damage, its adjusted secondary stiffness (representing the tendon bearing force vs. duct adaptor indentation relationship) was found to improve the response predictions. According to the experimental test results, the value of this stiffness is selected to be 20 kips/in.

5.2.2.1. Under Cyclic Lateral Displacement

The tests simulated here are Tests 1 to 3 from Loading Set 1 (Table 4-39). All those tests were conducted under constant vertical load and cyclic lateral displacement. The analyses in this section are run individually, thereby neglecting the effects of prior tests on the column model before it is subjected to the next displacement time history. This approach is favored against running the analyses consecutively because, given the extent of damage during the first two tests was not significant (Figure 4-284 and Figure 4-285), prediction of the sliding joints' activation order during each test by itself is of more interest.

The predicted base shear vs. lateral displacement responses of the column specimen subjected to the displacement time histories of all three tests closely resemble the responses obtained from the experiments (Figure 5-16(a), (c), and (e)). Specifically, the

breakaway friction predicted by the model for the first test is 29% lower than its experimental counterpart (Figure 5-16(a)), while the breakaway friction values predicted for the second sliding joint (Joint 3) during the second two tests are higher than the experimentally observed values (Figure 5-16(c) and (e)). The former finding is justified by the miscalibration of the friction model used in the model, while the latter finding occurs because the second two simulations were run assuming no prior sliding had occurred at any of the sliding joints. As seen in Figure 5-16(e), showing the results for Test 3 (where the first sliding joint (Joint 2) became active for the first time in Phase III), the simulation model is capable of capturing the point where sliding initiated at Joint 2.

Disregarding the breakaway friction values, the simulation model is found capable of predicting the maximum base shear values with less than 7% difference. The predicted maximum residual displacements (defined here as the lateral displacement at which base shear reaches zero) corresponding to the maximum applied lateral displacements are also less than 20% higher than those obtained from the experimental data.

According to Figure 5-16(b), (d), and (f), despite capturing the general shapes of the total PT force vs. displacement responses obtained from the experiments, the simulation model overestimates the maximum PT forces. This overestimation exceeds 17% for the largest lateral displacement applied to the column during Test 3 (Figure 5-16(f)). The PT losses observed during the same test are also not captured by the model, as it does not predict yielding in the tendons, while the anchorage-related losses are also not simulated in the model.
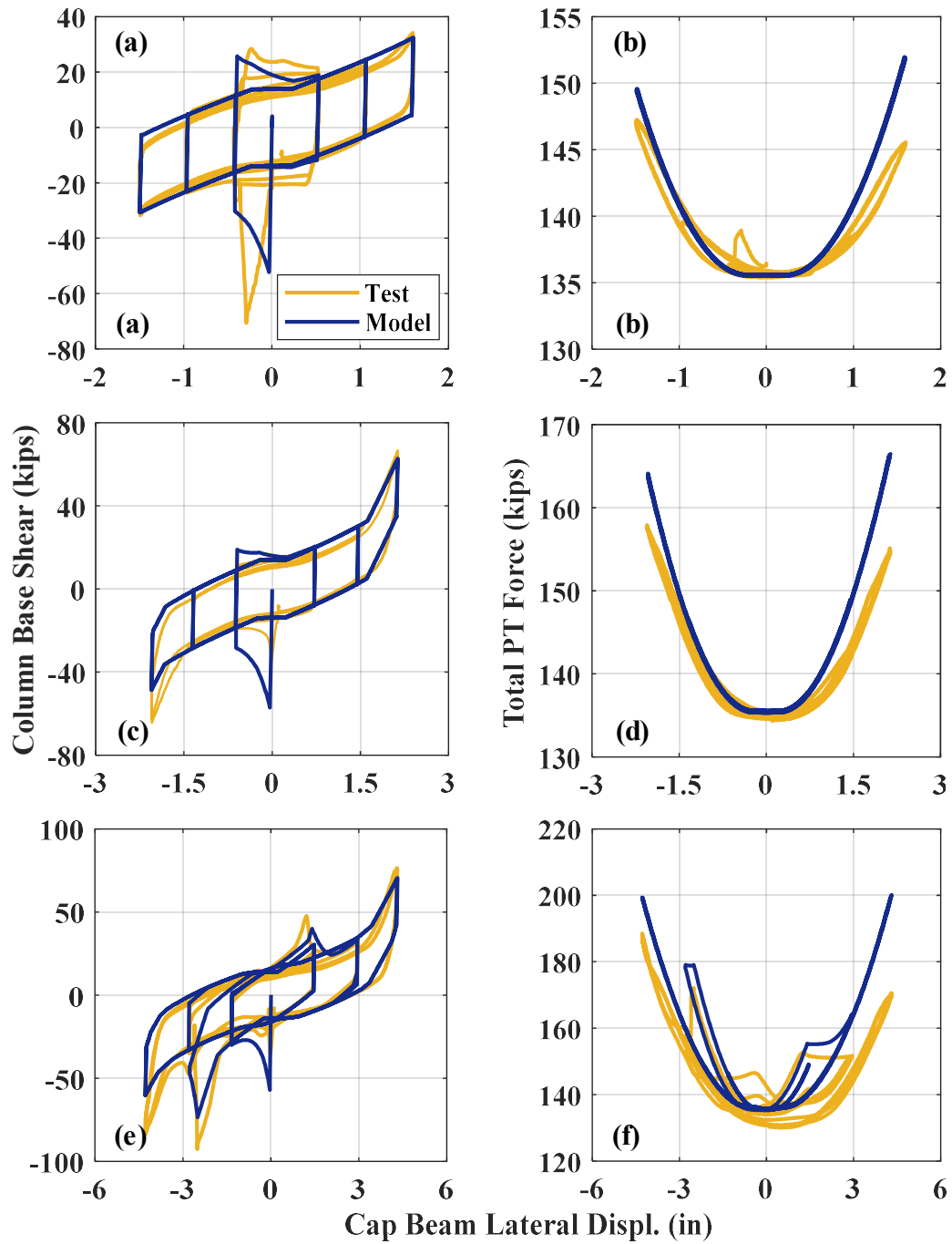
Figure 5-16. Comparison of base shear vs. lateral displacement and total PT force vs. lateral displacement responses obtained from experiment and simulation model: (a,b) Test 1; (c,d) Test 2; (e,f) Test 3

641

5.2.2.2. Under Arbitrary Lateral Displacement

In this section, Tests 11 and 14 under the loading protocols of Loading Set 4 (Table 4-42) are simulated through separate analyses – i.e. ignoring the effects of previous tests on the column. Note that the initial total PT forces applied in the model match those measured before running each of the tests.

The column's hysteretic responses obtained from the tests are generally similar to those obtained from the respective tests (Figure 5-17). Differences are, however, observed in the extents of breakaway friction, which is associated with the exclusion of the effects of previous tests on the sliding joints' responses.
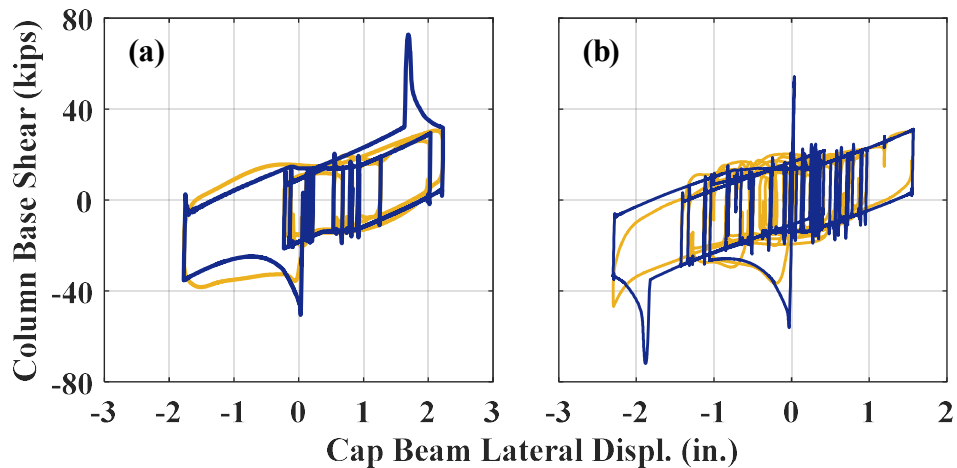
Figure 5-17. Comparison of base shear vs. lateral displacement responses obtained from experiment and simulation model: (a) Test 11; (b) Test 14

According to Figure 5-18, in both simulations, both sliding joints are activated, while the majority of sliding is concentrated in the second sliding joint (Joint 3) – this trend

generally agrees with the experimental tests, although Joint 2 did not exhibit sliding in Test 14, because of its initial negative residual displacement.
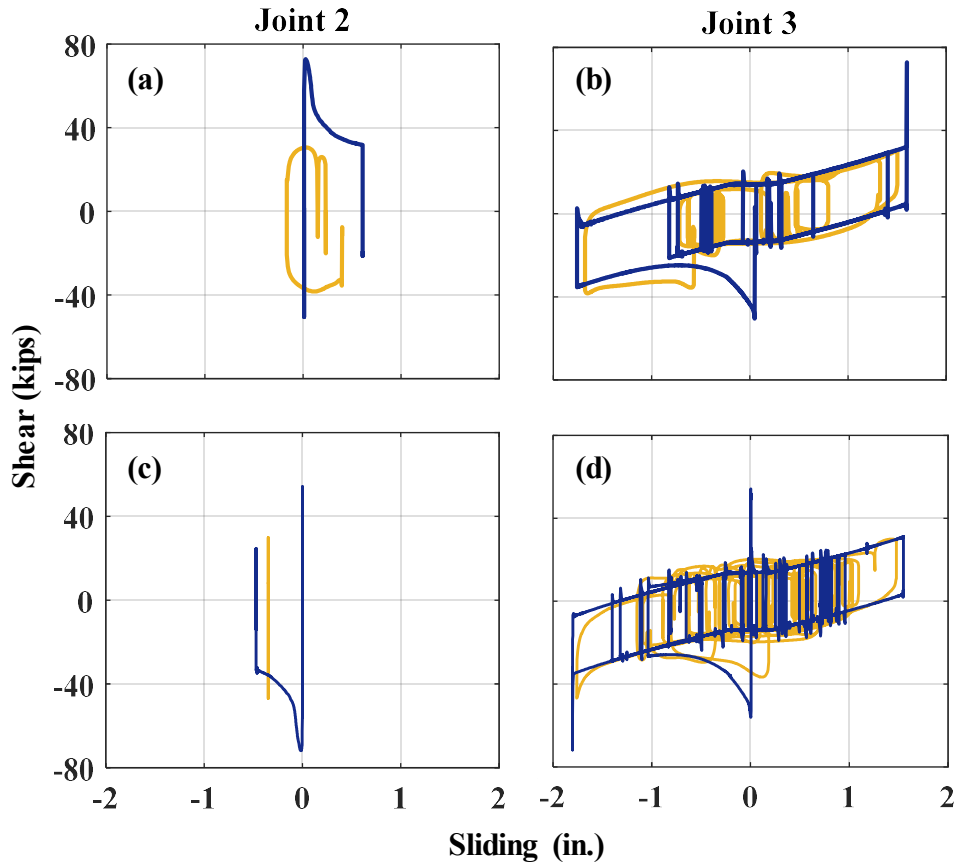
Figure 5-18. Comparison of joint shear vs. sliding responses obtained from experiment and simulation model: (a,b) Test 11; (c,d) Test 14

Although the residual sliding at the two joints from the previous tests are not considered in the simulation model, the joint sliding time histories obtained from the model and from the experiments are in a good agreement (Figure 5-19). The peak sliding values at Joint 3, which undergoes the most sliding, are only less than 5% different.
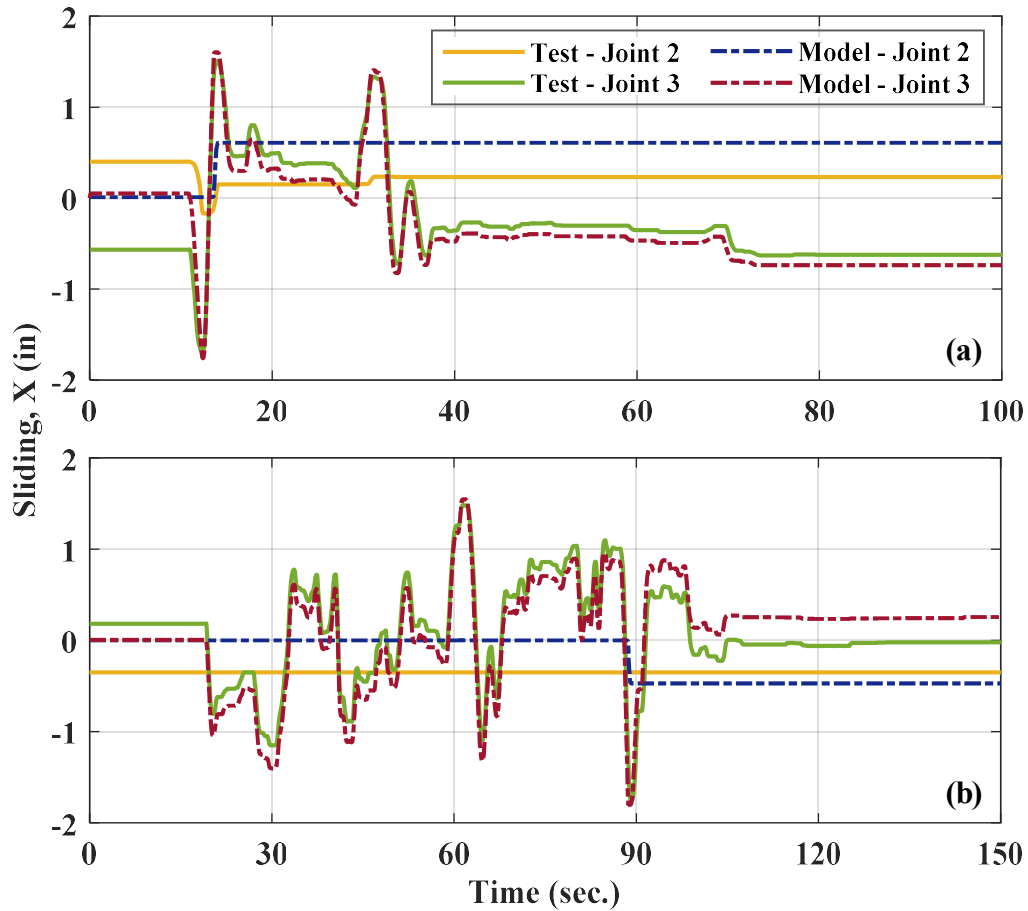
Figure 5-19. Comparison of joint sliding time histories obtained from experiment and simulation model: (a) Test 11; (b) Test 14

The total posttensioning force time histories obtained from the tests and simulation model are also compared in Figure 5-20. Consistently with the previous simulation results, the PT forces are generally overpredicted by the simulation model. However, the maximum total PT forces predicted and experimentally achieved in both tests are less than 3% different. The reason why the differences are smaller than the differences reported for the previous tests is the low level of lateral displacement applied to the column specimen during Tests 11 and 14.
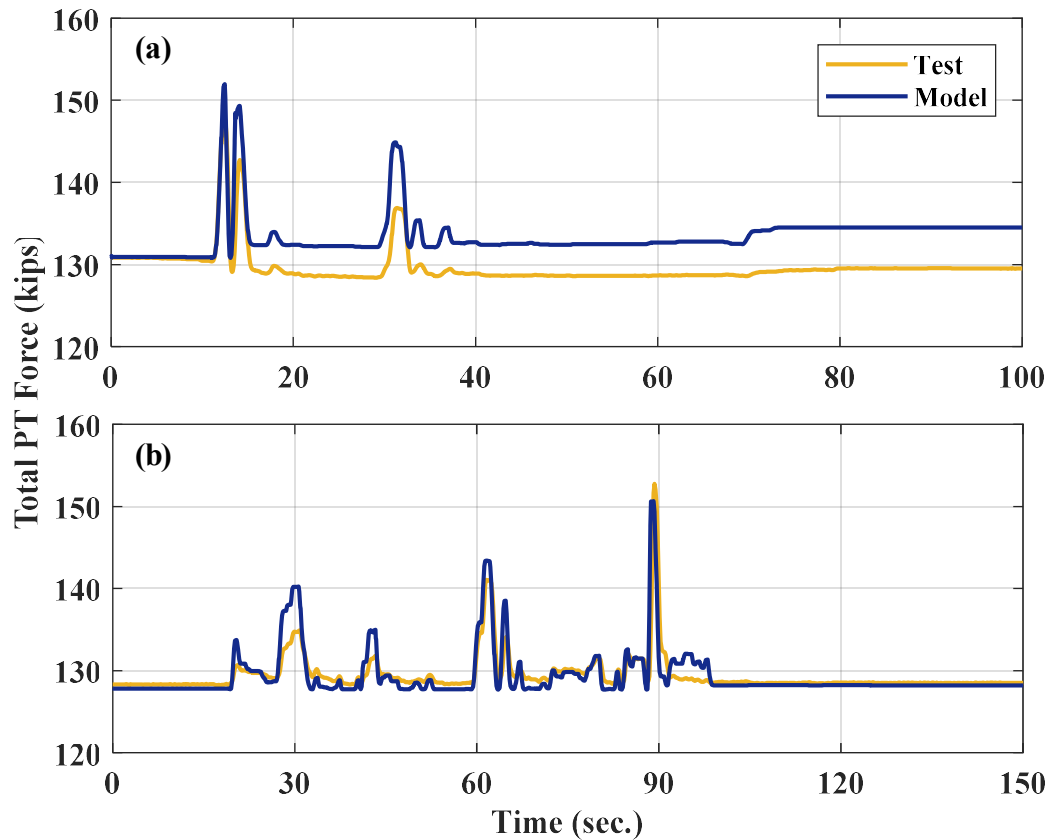
Figure 5-20. Comparison of total PT force time histories obtained from experiment and simulation model: (a) Test 11; (b) Test 14

5.3. Recommended Improvements

According to the simulation model evaluations made in the previous sections, the following is thought to significantly improve the HSR column model predictions:

- *Simulation of posttensioning tendon anchorage hardware*: Posttensioning tendon force overestimation and the inability to predict the PT losses were a constant observation throughout the model evaluations. Although other factors have contributed, too, it is expected that predictions could significantly improved by appropriately modeling the effect of the anchorage hardware on the response of

the PT strands. The explicit modeling of the strand slippage inside the wedges and the seating of the wedges into their enclosing components (e.g. barrel chucks) can improve the simulation results. For example, the model proposed by Sideris et al. (2014a) can be used for this purpose.

- *Simulation of friction between tendons and ducts*: The friction between the tendons and the ducts the duct-to-duct adaptor connections was found to be a source of discrepancies between the experimentally measured hysteretic responses and the computationally predicted responses. The presence of friction could increase both the column's lateral strength and energy dissipation capacity. These effects can become even greater in the presence of large sliding at the sliding joints, due to the tendons' bending deformations. This phenomenon may be incorporated in the simulation models by modifying the multi-node truss element formulation, such that it does not impose constant strain over its entire length and includes the friction effects at its intermediate nodes.

- *Simulation of duct/duct adaptor bearing damage*: Per the design philosophy of HSR columns, it is not desirable for the sliding joints to reach their nominal sliding capacities in order to avoid shear in the tendons at the sliding joints. In achieving this goal, bearing forces are applied by the tendons at the duct-to-duct adaptor connections. For strong earthquakes, thease forces are large and can damage the PVC material resulting in increased sliding amplitudes. The effects of such damage to the ducts and duct adaptors on the fixed-fixed HSR column's responses were found significant. As a result, it is recommended that the material

models used to represent the transverse constraints in the zero-length constraint elements be modified to simulate such inelastic response and the resulting damage.

6. SUMMARY, CONCLUSIONS, AND FUTURE RESEARCH

6.1. Summary

Considering their several proven advantages, such as fast construction, high durability and quality, low environmental impacts, and minimum traffic congestions, Accelerated Bridge Construction (ABC) technologies have become very popular during the last two decades. Precast concrete segmental bridge construction is one of the primary ABC technologies, per which concrete bridge components are cast off site and assembled on site. However, use of precast concrete segmental columns in seismic regions has been hindered by the lack of fundamental understanding of their seismic performance and design principles. For this reason, particularly during the last two decades, researchers have proposed several precast concrete substructure that could not only withstand intense seismic loads, but also sustain lower damage compared to conventional cast-in-place monolithic bridge columns.

Aiming at the same goals, the concept of hybrid sliding-rocking (HSR) bridge columns was recently proposed for applications in regions of moderate and high seismicity. HSR columns employ end (dry) rocking joints and unbonded posttensioning to produce self-centering capabilities, as well as intermediate sliding joints (positioned along the column height) to introduce energy dissipation into the system and increase the column's ductility. Even though quasi-static and shake table tests conducted in the past showed the low damage of HSR columns under seismic loads, a thorough understanding of their dynamic behavior and their design priciples is still not available. Advancements

in their computational modeling and further experimentation is essential to address this challenge.

In Chapter 2 of this dissertation, a simplified finite element modeling strategy was developed to enable simulating the nonlinear dynamic response of HSR columns subjected to earthquake excitations. The modeling strategy incorporated four finite element formulations that were developed herein, namely: (*i*) gradient inelastic (GI) force-based (FB) beam-column element formulation, which allowed simulation of reinforced concrete members prone to softening behavior without the strain localization issues encountered using the conventional FB elements; (*ii*) HSR FB element formulation, which represents the sliding/rocking joints and their close vicinity; (*iii*) multi-node continuous truss element formulation, which allows the tendons' (frictionless) sliding over control locations of the ducts by enforcing constant axial strain and stress over the entire length of the unbonded posttensioning tendons regardless of their deviations from the straight line; and (*iv*) zero-length constraint element formulation to simulate the duct-to-tendon interactions. The GI and HSR element formulations used fiber sections to produce section forces given section strains, thereby accounting for the axial force-moment interaction at all joints and axial force-moment-friction interactions at the sliding joints. All the element formulations were equipped with co-rotational geometric transformations to incorporate the effects of large rotations/displacements induced by the column segments' rocking and sliding in the simulations.

In order to allow performing nonlinear static and time history analyses on full bridge piers of HSR columns, the above element formulations and seleted material models were

implemented in the structural analysis software OpenSees. The element formulations were evaluated both individually and in conjunction with each other to model HSR columns. The proposed modeling strategy was then validated by comparing its predictions with those obtained from past quasi-static and shake table tests on an HSR column specimen and a single-span bridge specimen of HSR columns, respectively.

In Chapter 3 of this dissertation, the developed HSR column finite element models were used to computationally investigate the effects of various design variables, vertical excitations, and near-fault ground motions on the seismic performance of HSR piers. The seismic performance evaluations were primarily conducted through nonlinear time history analyses and using multiple ground motions. The design variables examined here were: (1) sliding joint distribution, i.e. the number and locations of sliding joints; (2) incipient sliding base shear ratio, quantifying the extent of shear needed to initate joint sliding relative to the column's peak lateral load resistance; (3) incipient bearing sliding amplitude, representing the amount of sliding that the sliding joints can undergo before the tendons contact their ducts; and (4) peak achievable sliding capacity, which is the maximum sliding that can be achieved under maximum lateral load resistance of the column. Design recommendations were made in regard to the selection of each of the above design variables in accordance with the results of the static and time history analyses.

In Chapter 4 of this dissertation, the effectiveness of HSR columns designed on the basis of the results of the computational studies was experimentally explored. In this part, first, a straightforward procedure was proposed for the design of HSR columns using the

criteria of the available AASHTO bridge design specifications and considering the specific features of the HSR columns. Accordingly, an HSR column specimen was designed as part of a single-column pier within a five-span bridge located in a highly seismic region to be tested under various loading conditions. The designed HSR column advanced the original design of HSR columns by reducing the number of sliding joints to two and using PTFE-based materials of low friction and high wearing resistance at the sliding joints. Four half-scale column specimens with identical design were constructed. Three of these specimens were tested in a cantilever condition under uniaxial lateral loading, combined uniaxial lateral and torsional loading, and biaxial lateral loading. The remaining column specimen was tested in a fixed-fixed condition and subjected to uniaxial lateral loading. Both quasi-static and quasi-dynamic, cyclic and arbitrary, lateral loads, as well as constant and variable vertical loads were imposed to the column specimens through a total of 87 tests. The maximum drift ratio applied to the columns was 10%. The general response of the HSR columns under the above loading conditions and their damage states were examined.

In Chapter 5 of this dissertation, selected tests performed on the cantilever and fixed-fixed HSR column specimens subjected to uniaxial lateral loading were simulated using the modeling strategy proposed in the first part of the dissertation. Comparing the test results and the model predictions, refinements were suggested for the numerical models.

6.2. Major Findings

The findings of four main chapters of this dissertation are summarized as follows.

6.2.1. Computational Modeling

- The proposed modeling strategy was capable of simulating the fundamental response mechanisms of HSR columns, namely, the sliding-rocking interactions at HSR joints, and interactions between the unbonded tendons and concrete segments in the vicinity of the duct adaptors.

- The GI and HSR element formulations eliminated strain localization and loss of objectivity, occuring in other FB element formulations in the presence of softening constitutive relations.

- Analyses with the HSR element eliminated chattering (i.e., high frequency fluctuations in the numerical solution) and eventual convergence failure of the solution algorithm; phenomena that often occur in structural models incorporating two-node contact sliders distributed over the cross section and subjected to large rapid variation of the contact pressure (as is the case for HSR joints).

- The multi-node continuous truss element formulation eliminated erroneous premature yielding/fracture predictions in the tendons due to their sliding-induced deviations by enforcing a constant strain/stress over the entire tendon lengths.

- Under quasi-static loading, the model accurately predicted the peak lateral strength (including softening) at all displacement amplitudes. However, residual deformations were underestimated, mostly because of a friction-type contribution from previously undetermined sources that appeared upon load

reversal during cycles of large displacement amplitudes and was not captured by the proposed modeling strategy. Such friction-type contributions were not observed during dynamic testing, for which the proposed modeling strategy provided more accurate results in terms of peak lateral strength and displacement, joint sliding demands, and residual deformations. This study found that these riction-type contributions resulted from friction between the tendon and the ducts.

6.2.2. Computational Investigations

- The number and location of sliding joints were found not to significantly affect the performance of HSR columns. Thus, no more than one or two sliding joints are recommended per HSR column. Slightly lower damage was obtained for sliding joints located towards the column bottom end, but far enough from it to avoid compression damage to the concrete.

- The coefficient of friction at the sliding joints and the column dimensions should be selected such that the incipient sliding base shear ratio is nearly identical to the incipient rocking base shear ratio, which yields larger effective damping ratio and lowers displacement demands.

- The incipient bearing sliding amplitude was found to have a small influence on the column response, as opposed to the peak achievable sliding capacity. The duct adaptor height should be selected such that the total peak achievable sliding capacity accounts for at least 75% the displacement demand of the HSR column at the design earthquake. Such a provision ensures that concrete (and tendon)

damage is alleviated. The peak achievable sliding capacity at each sliding joint should also be sufficiently smaller than its nominal sliding capacity to avoid tendon bearing and shearing damage.

- Columns with larger peak achievable sliding capacity exhibited higher effective damping, generally reducing their displacement demands.

- The performance of HSR columns was found to be practically unaffected by the vertical component of the earthquake excitation, mainly because the contribution of the vertical components on the contact pressure at the sliding joints remained small, even for large hazards.

- Likewise, near-fault ground motions with and without velocity pulses had no significant impact on the seismic performance of HSR columns.

- Deck displacements, concrete cover and core strains, and tendon strains were found to be much smaller for a HSR column compared to those for a rocking-only column of the same dimensions and material properties. Residual displacements were slightly higher for the HSR column, but they remained small (< 0.2% for the majority of motions). Base shear demands were also found to be smaller for the HSR column, which can result in cheaper foundation designs.

6.2.3. Experimental Testing

- Breakaway friction at the sliding joints was found to be crucial for the performance of the column specimens. Column damage was higher than expected when the second sliding joint did not become active (in Phases I and IV), because a larger displacement needed to be accommodated through rocking.

- In accordance with their design, none of the HSR column specimens tested under various loading conditions sustained minor damage under drift ratio demands representing DE and MCE hazard levels (i.e. up to 2%). The damage observed under such displacement demands was limited to hairline cracks.

- Due to the significant energy dissipation provided by the friction at the sliding joints, in cantilever condition, the effective damping ratio of the column ranged between 10% and 50% for a drift ratio range of 0.4% to 4%. The energy dissipation decreased with the peak drift ratio, as sliding joints reached their maximum sliding capacity.

- When subjected to larger drift ratios, particularly above 3%, the bottom segment of cantilever columns (i.e. in Phases I, II, and IV) sustained spalling near their rocking joint. Limited concrete crushing and longitudinal bar buckling were the severe damage states observed for drift ratios higher than 6%.

- The major damage mode in the fixed-fixed column was, however, concrete cone failures in the vicinities of duct adaptors, because of the tendons' significant bearing reactions on the duct adaptor edges. Signs of such failures appeared on the column surface at drift ratios above 3%. The fixed-fixed column also exhibited concrete spalling near both bottom and top rocking joints as the drift ratio reached 6%.

- The HSR column subjected to simultaneous effects of uniaxial lateral loading and torsion was found capable of effectively avoiding torsion-induced damage under a maximum twist of 0.09 rad.

- The HSR column specimen subjected to biaxial lateral loading (tested during Phase IV) was found more vulnerable than the rest of specimens tested in other Phases. Specifically, under 4% peak drift ratio, its bottom segment suffered from severe concrete spalling and wide vertical (compressive) cracks, and under 6% peak drift ratio, almost 75% of the bottom segment's cover was lost.

- In cantilever columns, tendon yielding started at the drift ratios over 6% and their wire fractures were observed for drift ratios above 8%, which represented unrealistically large earthquakes. Tendon wires were more prone to fracture at the locations of localized bending, i.e. where they contacted the duct edges (below or above sliding joints).

- Residual sliding was found to be a major source of residual displacements. Residual drift ratios up to 1.3% and 1.6% were resulted under peak drift ratios of about 4% when one and two sliding joints were active, respectively.

- The friction between the tendons and their ducts led to small sudden drops of column shear at load reversals. As rocking occurred, this friction also increased the tendon forces over their lengths below the foundation level compared to their forces inside the column.

- The effect of variable vertical load on the responses of the column specimens was minimal, as the resulting pressure variation at the joints was small (less than 20%). However, the overall effect of increasing axial load was a slight increase in the base shear. Under arbitrary lateral displacement, this effect was even less observable.

- Considering the maximum displacement rate applied to the columns was 8 in./sec., no meaningful difference was found between the column responses under cyclic loading and under arbitrary loading.

- In general, the sliding joint materials and the PVC pipes and fittings used to build ducts and duct adaptors were found to be effective. Although using steel pipes to make the duct adaptors could increase their resistance against the tendons' bearing damage, it could damage the tendons.

6.2.4. Simulation of Experiments

- The finite element models simulating the column specimens in Phases I and III (i.e. cantilever and fixed-fixed columns under uniaxial lateral loading) could reasonably capture the primary response characteristics of the tested HSR column specimens, namely, the joints' sliding and rocking responses, friction variations with pressure, and tendon-duct interactions.

- Overall, the predicted stiffness, maximum base shear, sliding time histories, and residual displacements for the simulated tests were in good agreement with the experimental data. However, the predicted cantilever column's stiffness against rocking at the bottom rocking joint was slightly higher than that observed in the experimental data.

- Due to the bearing-induced damage to the duct adaptors during the tests in Phase III, the ability of the respective simulation model in capturing the hysteretic behavior of the respective column specimen was compromised.

- Almost in all simulations, the predicted posttensioning forces were overestimated by the model, while the posttensioning losses were underestimated. This is attributed to the fact that the anchorage hardware was not explicitly simulated in the models.

6.3. Original Contributions

The major technical contributions made by this dissertation include:

- *Development of novel computational modeling tools*: As part of this research, the GI beam theory and a number of innovative finite element formulations, including the GI FB beam-column element, the HSR FB beam-column element, the continuous multi-node truss element, and the co-rotational zero-length constraint element, were developed. Not only did these element formulations make low-computational-cost high-fidelity modeling of HSR columns possible, but they could also be utilized to model other structural systems. The GI beam theory and its associated FB element formulation, which generate objective softening response, can be used in the analysis of any framed structure with potential material softening response. The GI beam theory can be employed to develop other structural element formulations, too. The analysis of HSR columns, especially under dynamic loads, required prohibitive computational resources before the development of the HSR element formulation. In addition, the HSR element formulation can be used to model frictional contact in systems other than HSR columns. The continuous multi-node truss element can be used in any system with unbonded cables, whether they are prestressed or not. The co-

rotational zero-length constraint element can also be used in various systems of considerable rotation, where zero-length constraints are needed. Note that all of the element formulations developed in this dissertation have been implemented in the open-source structural analysis framework of OpenSees (McKenna et al. 2000) and will be publically available.

- *Quantification of the effects of design variables and earthquake characteristics on seismic performance of HSR columns*: Although the concept of HSR columns had been previously developed, prior to this research, their seismic design was not fully understood. Also, the effects of vertical excitation and near-fault ground motions on the bridges with HSR columns had not been quantified. The above gaps in the knowledge about HSR columns could be filled after the development of suitable computational models in this dissertation. The extensive parametric study conducted in this dissertation allowed the identification of the key design variables affecting the response of HSR columns. Design recommendations were also made on the basis of the findings of the above investigations, which would potentially lower the seismic damage of HSR piers.

- *Development of a design procedure and effective construction methods for HSR columns*: It is noted that one of the obstacles to the use of innovative structural systems in industry is the lack of clear and straightforward design procedures. Therefore, in order to allow the design of HSR columns by other researchers or practitioners, a design procedure was put forth. Additionally, methods and materials were suggested for the construction of HSR columns meeting their

659

design objectives. The efficacy of the above design procedure and construction methods/materials was validated through a large number of large-scale experimental tests on four HSR columns.

- *Quantification of the performance of HSR columns subjected to a wide range of loading scenarios*: The seismic performance of the HSR columns designed and constructed based on the methods proposed in this dissertation was evaluated through an extensive experimental program. In this program, which consisted of testing four half-scale HSR columns, three different loading conditions – including uniaxial, biaxial, and torsional loading – and two boundary conditions – representing cantilever and fixed-fixed columns – were considered. This was the first time that HSR columns were subjected to biaxial displacement and torsion (i.e. outside shake table test setting), and were tested in a fixed-fixed condition. These tests allowed identification of all major damage mechanisms exhibited by HSR columns under the above loading/boundary conditions. The findings of these tests can support life-cycle performance assessments and further design optimization of HSR column design. The testing methods designed in this dissertation could be beneficial to other researchers working in similar areas, too.

6.4. Recommendations for Future Research

Further research on HSR bridges is recommended n the following areas:

1. *Advancement of computational models and analysis methods*: Despite the capabilities of the finite element modeling tools developed in this dissertation to enable nonlinear dynamic analysis of HSR columns, there are still advancements

that can be made to the finite element models and analysis methods. Considering the findings of the experimental tests, some possible important advancements are: (*a*) developing an element formulation that reproduces the inherent discontinuity of strains at rocking joints, but does not require cumbersome calibration; (*b*) modeling the friction between unbonded tendons and their ducts, which can affect the hysteretic response of HSR columns as a whole and the tendon damage predictions; (*c*) modeling the anchorage devices to account for the posttensioning losses and stiffness alterations caused by those; and (*d*) developing inherent damping models that are unaffected by the fast sliding and rocking at the sliding and rocking joints, respectively.

2. *Seismic performance assessment of bridges with HSR columns*: The majority of the numerical simulations in this dissertation were conducted using 2D models of single-column HSR bents. Though the superstructure mass and mass moment of inertia were incorporated in these models, the effects of superstructure vibration, higher modes, and superstructure boundary conditions were not accounted for neither implicitly nor explicitly. Such effects, especially in the bridges with skew-angled seat-type abutments, need to be considered to more realistically predict the seismic demands of bridges with HSR columns. It is also noted that, because of the pressure-dependence of the response of sliding joints, having more than one HSR column in a bent can influence their dynamic response through overturning effects. Given the foregoing, time history analyses

of bridges with single- and multi-column HSR bents using 3D finite element models would provide an insight into the overall response of such systems.

3. *Design improvement of sliding joints*: According to the observations made during the experimental tests, the performance of sliding joints could be improved in two respects. First, the residual sliding at the sliding joints can be large, necessitating its restoration after major earthquakes. That said, potential solutions may be sought to minimize the residual sliding, e.g. via shape memory alloys (SMA). Second, more suitable, yet cost-effective, sliding joint interface materials with low kinematic coefficient of friction and low breakaway friction in the dry condition (i.e. without lubrication) need to be explored.

4. *Shake table testing of new generation of HSR columns*: Although quasi-static tests of HSR columns under reversed loading provide invaluable insights into their behavior and damage states, still they cannot reveal the true performance of such systems under earthquake excitations. Specifically, because the displacement demands of such systems are predicted by numerical simulations, it cannot be guaranteed if the extent of damage observed under such imposed displacements resembles what would occur during the real earthquakes of the considered probability of exceedance. Also, dynamic response of systems with friction/sliding mechanisms can highly dependent on displacement rate (velocity), thereby making the observed performance of sliding joints during quasi-static tests questionable. Another important phenomenon that cannot be captured in quasi-static tests is the impact at rocking joints during column

rocking, which can both dissipate energy and cause damage at the column's compression toes. The above reasons justify the need for multi-directional shake table tests on either HSR piers or bridges with such piers.

5. *Development of durable construction specifications*: Similar to any emerging bridge technologies, before HSR columns can be utilized in practice, their constructability, durability, and repairability need to be ensured. One of the major durability challenges of any system of unbonded posttensioning is the protection of high-strength steel tendons against corrosion. Even though a number of solutions have been proposed to address this challenge (e.g. using flexible non-cementitious grouts or coated strands), adapting such solutions to fit the design of HSR columns is necessary. In addition, the accessibility of the tendon anchorage devices located in the foundation to allow their regular inspection or replacement is another construction challenge of HSR columns, as is the case for most column designs with unbonded posttensioning.

REFERENCES

AASHTO (2011). "Guide Specifications for LRFD Seismic Bridge Design." AASHTO, Washington, DC.

AASHTO (2014). "LRFD Bridge Design Specifications." AASHTO, Washington, DC.

Aifantis, E. C. (1992). "On the Role of Gradients in the Localization of Deformation and Fracture." *International Journal of Engineering Science*, 30(10): 1279-1299, DOI: 10.1016/0020-7225(92)90141-3.

Ala, N., Power, E. H., Azizinamini, A. (2016). "Experimental Evaluation of High-Performance Sliding Surfaces for Bridge Bearings." *Journal of Bridge Engineering*, 21(2): 04015034.

Ameli, M. J., Pantelides, C. P. (2017). "Seismic Analysis of Precast Concrete Bridge Columns Connected with Grouted Splice Sleeve Connectors." *Journal of Structural Engineering*, 143(2): .

ASCE (2010). "ASCE/SEI 7-10: Minimum Design Loads for Buildings and Other Structures." Reston, VA.

ASTM (2009). "A615/A615M: Standard Specification for Deformed and Plain Carbon-Steel Bars for Concrete Reinforcement." West Conshohocken, PA.

ASTM (2010). "A416/A416M: Standard Specification for Steel Strand, Uncoated Seven-Wire for Prestressed Concrete." West Conshohocken, PA.

ASTM (2014). "A36/A36M: Standard Specification for Carbon Structural Steel." West Conshohocken, PA.

ASTM (2018a). "A615/A615M: Standard Specification for Deformed and Plain Carbon-Steel Bars for Concrete Reinforcement." West Conshohocken, PA.

ASTM (2018b). "A416/A416M: Standard Specification for Low-Relaxation, Seven-Wire Steel Strand for Prestressed Concrete." West Conshohocken, PA.

ASTM (2018c). "C39/C39M: Standard Test Method for Compressive Strength of Cylindrical Concrete Specimens." West Conshohocken, PA.

ASTM (2019). "A513/A513M: Standard Specification for Electric-Resistance-Welded Carbon and Alloy Steel Mechanical Tubing." West Conshohocken, PA.

Berry, M., Eberhard, M. (2003). "Performance Models for Flexural Damage in Reinforced Concrete Columns." Pacific Earthquake Engineering Research Center, Berkeley, CA.

Billington, S. L., Yoon, J. K. (2004). "Cyclic Response of Unbonded Posttensioned Precast Columns with Ductile Fiber-Reinforced Concrete." *Journal of Bridge Engineering*, 9(4): 353-363.

Bondonet, G., Filiatrault, A. (1997). "Frictional Response of PTFE Sliding Bearings at High Frequencies." *Journal of Bridge Engineering*, 2(4): 139-148.

Cai, Z. K., Wang, Z. Y., Yang, T. Y. (2018). "Experimental Testing and Modeling of Precast Segmental Bridge Columns with Hybrid Normal- and High-Strength Steel Rebars." *Construction and Building Materials*, 166: 945-955, DOI: 10.1016/j.conbuildmat.2018.01.159.

Caltrans (2013). "Caltrans Seismic Design Criteria 1.7." California Department of Transportation, Sacramento, CA.

Chou, C. C., Chen, Y. C. (2006). "Cyclic Tests of Post-Tensioned Precast CFT Segmental Bridge Columns with Unbonded Strands." *Earthquake Engineering & Structural Dynamics*, 35(2): 159-175, DOI: 10.1002/eqe.512.

Coleman, J., Spacone, E. (2001). "Localization Issues in Force-Based Frame Elements." *Journal of Structural Engineering*, 127(11): 1257-1265.

Constantinou, M., Mokha, A., Reinhorn, A. (1990). "Teflon Bearings in Base Isolation .2. Modeling." *Journal of Structural Engineering*, 116(2): 455-474, DOI: Doi 10.1061/(Asce)0733-9445(1990)116:2(455).

CSI (2009). *CSI Analysis Reference Manual for SAP2000, ETABS, SAFE and CSiBridge*, Computers and Structures Inc. (CSI), Berkeley, CA.

Culmo, M. P. (2011). "Accelerated Bridge Construction - Experience in Design, Fabrication and Erection of Prefabricated Bridge Elements and Systems." FHWA, Springfield, VA.

Davis, P. M., Janes, T. M., Eberhard, M., Stanton, J. F. (2012). "Unbonded Pre-Tensioned Columns for Bridges in Seismic Regions." Pacific Earthquake Engineering Research Center, Berkeley, CA.

Dawood, H., ElGawady, M., Hewes, J. (2012). "Behavior of Segmental Precast Posttensioned Bridge Piers under Lateral Loads." *Journal of Bridge Engineering*, 17(5): 735-746.

Dawood, H. M., ElGawady, M. (2013). "Performance-Based Seismic Design of Unbonded Precast Post-Tensioned Concrete Filled GFRP Tube Piers." *Composites Part B-Engineering*, 44(1): 357-367.

de Souza, R. M. (2000). "Force-Based Finite Element for Large Displacement Inelastic Analysis of Frames." Ph.D. Dissertation, Department of Civil and Environmental Engineering, University of California, Berkeley, CA.

DS (2010). *Abaqus*, Dassault Systèmes, Providence, RI.

ElGawady, M., Booker, A. J., Dawood, H. M. (2010). "Seismic Behavior of Posttensioned Concrete-Filled Fiber Tubes." *Journal of Composites for Construction*, 14(5): 616-628, DOI: 10.1061/(Asce)Cc.1943-5614.0000107.

ElGawady, M. A., Sha'lan, A. (2011). "Seismic Behavior of Self-Centering Precast Segmental Bridge Bents." *Journal of Bridge Engineering*, 16(3): 328-339.

666

FEMA (2009). "Quantification of Building Seismic Performance Factors." Washington, DC.

Figg, L., Pate, W. D. (2004). "Precast Concrete Segmental Bridges - America's Beautiful and Affordable Icons." *PCI Journal*, 49(5): 26-39.

Freyermuth, C. L. (1999). "Ten Years of Segmental Achievements and Projections for the Next Century." *PCI Journal*, 44(3): 36-52.

Geren, K. L., Tadros, M. K. (1994). "The NU Precast/Prestressed Concrete Bridge I-Girder Series." *PCI Journal*, 39(3): 26-32.

Giuffrè, A., Pinto, P. E. (1970). "Il Comportamento Del Cemento Armato Per Sollecitazioni Cicliche Di Forte Intensità." *Giornale del Genio Civile*, 5(1): 391-408.

Golchin, A., Simmons, G. F., Glavatskih, S. B. (2012). "Break-Away Friction of PTFE Materials in Lubricated Conditions." *Tribology International*, 48: 54-62.

Guerrini, G., Restrepo, J. I., Massari, M., Vervelidis, A. (2015). "Seismic Behavior of Posttensioned Self-Centering Precast Concrete Dual-Shell Steel Columns." *Journal of Structural Engineering*, 141(4): 04014115

Haber, Z. B., Mackie, K. R., Al-Jelawy, H. M. (2017). "Testing and Analysis of Precast Columns with Grouted Sleeve Connections and Shifted Plastic Hinging." *Journal of Bridge Engineering*, 22(10).

Hewes, J. T., Priestley, M. J. N. (2002). "Seismic Design and Performance of Precast Concrete Segmental Bridge Columns." University of California, San Diego, La Jolla, CA.

Hieber, D. g., Wacker, J. M., Eberhard, M. O., Stanton, J. F. (2005). "State-of-the-Art Report on Precast Concrete Systems for Rapid Construction of Bridges." Washington State Transportation Center (TRAC), Seattle, WA.

Holombo, J., Priestley, M. J. N., Seible, F. (2000). "Continuity of Precast Prestressed Spliced-Girder Bridges under Seismic Loads." *PCI Journal*, 45(2): 40-63.

Hwang, J. S., Chang, K. C., Lee, G. C. (1990). "Quasi-Static and Dynamic Sliding Characteristics of Teflon - Stainless-Steel Interfaces." *Journal of Structural Engineering-Asce*, 116(10): 2747-2762.

Jeong, H., Sakai, J., Mahin, S. (2008). "Shaking Table Tests and Numerical Investigation of Self-Centering Reinforced Concrete Bridge Columns." Pacific Earthquake Engineering Research Center, Berkeley, CA.

Karthik, M. M., Mander, J. B. (2011). "Stress-Block Parameters for Unconfined and Confined Concrete Based on a Unified Stress-Strain Model." *Journal of Structural Engineering*, 137(2): 270-273.

Khoddamzadeh, A., Liu, R., Wu, X. J. (2009). "Novel Polytetrafluoroethylene (PTFE) Composites with Newly Developed Tribaloy Alloy Additive for Sliding Bearings." *Wear*, 266(7-8): 646-657.

Kwan, W. P., Billington, S. L. (2003a). "Unbonded Posttensioned Concrete Bridge Piers. I: Monotonic and Cyclic Analyses." *Journal of Bridge Engineering*, 8(2): 92-101, DOI: 10.1061/(Asce)1084-0702(2003)8:2(92).

Kwan, W. P., Billington, S. L. (2003b). "Unbonded Posttensioned Concrete Bridge Piers. Ii: Seismic Analyses." *Journal of Bridge Engineering*, 8(2): 102-111, DOI: 10.1061/(Asce)1084-0702(2003)8:2(102).

Lehman, D. E., Roeder, C. W. (2012). "Foundation Connections for Circular Concrete-Filled Tubes." *Journal of Constructional Steel Research*, 78: 212-225.

Li, T. T., Qu, H. Y., Wang, Z. Q., Wei, H. Y., Jiang, S. C. (2018). "Seismic Performance of Precast Concrete Bridge Columns with Quasi-Static Cyclic Shear Test for High Seismic Zones." *Engineering Structures*, 166: 441-453.

Madhusudhanan, S., Sideris, P. (2018). "Capacity Spectrum Seismic Design Methodology for Bridges with Hybrid Sliding-Rocking Columns." *Journal of Bridge Engineering*, 23(8), DOI: 10.1061/(Asce)Be.1943-5592.0001248.

Mander, J. B., Priestley, M. J. N., Park, R. (1988). "Theoretical Stress-Strain Model for Confined Concrete." *Journal of Structural Engineering*, 114: 1804-1826.

Mander, J. B., Cheng, C.-T. (1997). "Seismic Resistance of Bridge Piers Based on Damage Avoidance Design." National Center for Earthquake Engineering Research, Buffalo, NY.

Mantawy, I. M., Sanders, D., Eberhard, M., Stanton, J. F. (2019). "Modelling of Debonded Reinforcement in ABC Connections Designed for Seismic Zones." *Engineering Structures*, 198: 109351.

Marriott, D., Pampanin, S., Palermo, A. (2009). "Quasi-Static and Pseudo-Dynamic Testing of Unbonded Post-Tensioned Rocking Bridge Piers with External Replaceable Dissipaters." *Earthquake Engineering and Structural Dynamics*, 38: 331-354.

Marriott, D., Pampanin, S., Palermo, A. (2011). "Biaxial Testing of Unbonded Post-Tensioned Rocking Bridge Piers with External Replacable Dissipaters." *Earthquake engineering & structural dynamics*, 40(15): 1723-1741.

Marsh, M. L., Wernli, M., Garrett, B. E., Stanton, J. F., Eberhard, M. O., Weinert, M. D. (2011). "Application of Accelerated Bridge Construction Connections in Moderate-to-High Seismic Regions." Transportation Research Board of the National Academies, Washington, DC.

MathWorks (2019). "Matlab Documentation." <https://www.mathworks.com/help/>. (Accessed in).

Matsumoto, E. E., Kreger, M. E., Waggoner, M. C., Sumen, G. (2002). "Grouted Connection Tests in Development of Precast Bent Cap System." *Design of Structures 2002*, (1814): 55-64.

Matsumoto, E. E., Waggoner, M. C., Kreger, M. E., Vogel, J., Wolf, L. (2008). "Development of a Precast Concrete Bent-Cap System." *PCI Journal*, 53(3): 74-99, DOI: 10.15554/pcij.05012008.74.99.

Mattock, A. H. (1979). "Flexural Strength of Prestressed Concrete Sections by Programmable Calculator." *PCI Journal*, 24(1): 32-54.

McKenna, F., Fenves, G. L., Scott, M. H. (2000). "*Open System for Earthquake Engineering Simulation*", Version 2.2.2, Pacific Earthquake Engineering Research Center, Berkeley, CA.

McManus, K. J. (1980). "The Seismic Response of Bridge Structures Free to Rock on Their Foundations." Master of Science Dissertation, Civil Engineering Department, University of Canterbury, Christchurch, New Zealand.

Megally, S., Garg, M., Seible, F., Dowell, R. K. (2002a). "Seismic Performance of Precast Segmental Bridge Superstructures." University of California, San Diego, La Jolla, CA.

Megally, S., Seible, F., Garg, M., Dowell, R. K. (2002b). "Seismic Performance of Precast Segmental Bridge Superstructures with Internally Bonded Prestressing Tendons." *PCI Journal*, 47(2): 40-56.

Megally, S., Seible, F., Dowell, R. K. (2003a). "Seismic Performance of Precast Segmental Bridges: Segment-to-Segment Joints Subjected to High Flexural Moments and High Shears." *PCI Journal*, 48(3): 72-90.

Megally, S., Seible, F., Dowell, R. K. (2003b). "Seismic Performance of Precast Segmental Bridges: Segment-to-Segment Joints Subjected to High Flexural Moments and Low Shears." *PCI Journal*, 48(2): 80-96.

Megally, S., Veletzos, M. J., Burnell, K., Restrepo, J. I., Seible, F. (2009). "Seismic Performance of Precast Concrete Segmental Bridges: Summary of Experimental Research on Segment-to-Segment Joints." *PCI Journal*, 54(2): 116-142.

Mehrsoroush, A., Saiidi, M. S. (2016). "Cyclic Response of Precast Bridge Piers with Novel Column-Base Pipe Pins and Pocket Cap Beam Connections." *Journal of Bridge Engineering*, 21(4).

Mindlin, R. D. (1964). "Micro-Structure in Linear Elasticity." *Archive for Rational Mechanics and Analysis*, 16(1): 51-78.

Mokha, A., Constantinou, M., Reinhorn, A. (1988). "Teflon Bearings in a Seismic Base Isolation: Experimental Studies and Mathematical Modeling." National Center for Earthquake Engineering Research, Buffalo, NY.

Mokha, A., Constantinou, M., Reinhorn, A. (1990). "Teflon Bearings in Base Isolation .1. Testing." *Journal of Structural Engineering*, 116(2): 438-454.

Moustafa, A., ElGawady, M. A. (2018). "Shaking Table Testing of Segmental Hollow-Core FRP-Concrete-Steel Bridge Columns." *Journal of Bridge Engineering*, 23(5).

Muller, J. (1975). "10 Years of Experience in Precast Segmental Construction - Reply." *Journal Prestressed Concrete Institute*, 20(5): 85-85.

NCHRP (2003). "Prefabricated Bridge Elements and Systems to Limit Traffic Disruption During Construction." Transportation Research Board, Washington, DC.

Ou, Y. C., Chiewanichakorn, M., Aref, A. J., Lee, G. C. (2007). "Seismic Performance of Segmental Precast Unbonded Posttensioned Concrete Bridge Columns." *Journal of Structural Engineering*, 133(11): 1636-1647, DOI: 10.1061/(Asce)0733-9445(2007)133:11(1636).

Ou, Y. C., Wang, P. H., Tsai, M. S., Chang, K. C., Lee, G. C. (2010). "Large-Scale Experimental Study of Precast Segmental Unbonded Posttensioned Concrete Bridge Columns for Seismic Regions." *Journal of Structural Engineering*, 136(3): 255-264, DOI: 10.1061/(Asce)St.1943-541x.0000110.

Palermo, A., Pampanin, S., Calvi, G. M. (2005a). "Concept and Development of Hybrid Solutions for Seismic Resistant Bridge Systems." *Journal of Earthquake Engineering*, 9(6): 899-921, DOI: 10.1142/S1363246905002328.

Palermo, A., Pampanin, S., Carr, A. (2005b). "Efficiency of Simplified Alternative Modeling Approaches to Predict the Seismic Response of Precast Concrete Hybrid Systems." *fib Symposium "Keep Concrete Attractive"*, Budapest, Hungary, International Federation for Structural Concrete (*fib*).

Palermo, A., Pampanin, S., Marriott, D. (2007). "Design, Modeling, and Experimental Response of Seismic Resistant Bridge Piers with Posttensioned Dissipating Connections." *Journal of Structural Engineering-Asce*, 133(11): 1648-1661, DOI: 10.1061/(Asce)0733-9445(2007)133:11(1648).

Pang, J. B. K., Eberhard, M. O., Stanton, J. F. (2010). "Large-Bar Connection for Precast Bridge Bents in Seismic Regions." *Journal of Bridge Engineering*, 15(3): 231-239, DOI: 10.1061/(Asce)Be.1943-5592.0000081.

Pantelides, C. P., Ameli, M. J., Reaveley, L. D. (2017). "Evaluation of Grouted Splice Sleeve Connections for Precast Reinforced Concrete Bridge Piers." Mountain-Plains Consortium, Fargo, ND.

PCI (2003). *Precast Prestressed Bridge Design Manual*, Precast/Prestressed Concrete Institute, Chicago, IL.

Perez, F. J., Sause, R., Pessiki, S. (2007). "Analytical and Experimental Lateral Load Behavior of Unbonded Posttensioned Precast Concrete Walls." *Journal of Structural Engineering*, 133(11): 1531-1540.

Podolny, W. (1979). "Overview of Precast Prestressed Segmental Bridges." *Journal Prestressed Concrete Institute*, 24(1): 56-87.

Polizzotto, C. (2003). "Gradient Elasticity and Nonstandard Boundary Conditions." *International Journal of Solids and Structures*, 40(26): 7399-7423, DOI: 10.1016/j.ijsolstr.2003.06.001.

Priestley, M. J. N. (1991). "Overview of Presss Research Program." *PCI Journal*, 36(4): 50-57.

Reddy Goli, H. (2019). "Effects of Skewed Angle Abutments on the Seismic Response of a Bridge with Hybrid Sliding-Rocking Columns." M.S. Dissertation, Civil and Environmental Engineering, Texas A&M University, College Station, TX.

Restrepo, J. I., Tobolski, M. J., Matsumoto, E. E. (2011). "Development of a Precast Bent Cap System for Seismic Regions." NCHRP, Washington, DC.

Salehi, M., Sideris, P. (2016). "Nonlinear Dynamic Analysis of Hybrid Sliding-Rocking Bridges." *Geotechnical and Structural Engineering Congress 2016*, Phoenix, AZ, USA, 90-102, ASCE.

Salehi, M., Sideris, P., Liel, A. B. (2017). "Numerical Simulation of Hybrid Sliding-Rocking Columns Subjected to Earthquake Excitation." *Journal of Structural Engineering*, 143(11), DOI: 10.1061/(ASCE)ST.1943-541X.0001878.

Salehi, M., Sideris, P. (2017). "Refined Gradient Inelastic Flexibility-Based Formulation for Members Subjected to Arbitrary Loading." *Journal of Engineering Mechanics*, 143(9): 04017090.

Salehi, M., Sideris, P. (2018). "A Finite-Strain Gradient Inelastic Beam Theory and a Corresponding Force-Based Frame Element Formulation." *International Jounral for Numerical Methods in Engineering*, 116(6): 380-411, DOI: 10.1002/nme.5929.

Salehi, M., Sideris, P., Liel, A. B. (2020). "Effect of Major Design Parameters on the Seismic Performance of Bridges with HSR Columns." *Journal of Bridge Engineering*, under review.

Salehi, M., Sideris, P. (2020). "Enhanced Rayleigh Damping Model for Dynamic Analysis of Inelastic Structures." *Journal of Structural Engineering*, under review.

Scott, B. D., Park, R., Priestley, M. J. N. (1982). "Stress-Strain Behavior of Concrete Confined by Overlapping Hoops at Low and High Strain Rates." *Journal of the American Concrete Institute*, 79(1): 13-27.

Shen, Q., Kurama, Y., Weldon, B. D. (2006). "Seismic Analysis, Behavior, and Design of Unbonded Post-Tensioned Hybrid Coupled Wall Structures." University of Notre Dame, Notre Dame, IN.

Shim, C., Lee, S., Park, S., Koem, C. (2017). "Experiments on Prefabricated Segmental Bridge Piers with Continuous Longitudinal Reinforcing Bars." *Engineering Structures*, 132: 671-683, DOI: 10.1016/j.engstruct.2016.11.070.

673

Sideris, P. (2012). "Seismic Analysis and Design of Precast Concrete Segmental Bridges." Ph.D. Dissertation, Department of Civil, Structural, and Environmental Engineering, University at Buffalo, Buffalo, NY.

Sideris, P., Aref, A. J., Filiatrault, A. (2014a). "Effects of Anchorage Hardware on the Cyclic Tensile Response of Unbonded Monostrands." *PCI Journal*, 59(6): 60-77.

Sideris, P., Aref, A. J., Filiatrault, A. (2014c). "Large-Scale Seismic Testing of a Hybrid Sliding-Rocking Posttensioned Segmental Bridge System." *Journal of Structural Engineering*, 140(6): 04014025.

Sideris, P., Aref, A. J., Filiatrault, A. (2014d). "Quasi-Static Cyclic Testing of a Large-Scale Hybrid Sliding-Rocking Segmental Column with Slip-Dominant Joints." *Journal of Bridge Engineering*, 19(10): 04014036.

Sideris, P., Aref, A. J., Filiatrault, A. (2015). "Experimental Seismic Performance of a Hybrid Sliding-Rocking Bridge for Various Specimen Configurations and Seismic Loading Conditions." *Journal of Bridge Engineering*, 20(11): 04015009.

Sideris, P. (2015). "Nonlinear Quasi-Static Analysis of Hybrid Sliding-Rocking Bridge Columns Subjected to Lateral Loading." *Engineering Structures*, 101: 125-137.

Sideris, P., Salehi, M. (2016). "A Gradient-Inelastic Flexibility-Based Frame Element Formulation." *Journal of Engineering Mechanics*, 142(7): 04016039, DOI: 10.1061/(ASCE)EM.1943-7889.0001083.

Solberg, K., Mashiko, N., Mander, J. B., Dhakal, R. P. (2009). "Performance of a Damage-Protected Highway Bridge Pier Subjected to Bidirectional Earthquake Attack." *Journal of Structural Engineering-Asce*, 135(5): 469-478, DOI: 10.1061/(Asce)0733-9445(2009)135:5(469).

Spieth, H. A., Carr, A. J., Murahidy, A. G., Arnolds, D., Davies, M., Mander, J. B. (2004). "Modelling of Post-Tensioned Precast Reinforced Concrete Frame Structures with Rocking Beam-Column Connections." *2004 NZSEE Conference*, Auckland, New Zealand, New Zealand Society for Earthquake Engineering Inc.

Stanton, J. F., Hawkins, N. M., Hicks, T. R. (1991). "Presss Project 1.3: Connection Classification and Evaluation." *PCI Journal*, 36(5): 62-71.

Tazarv, M., Saiidi, M. S. (2016a). "Low-Damage Precast Columns for Accelerated Bridge Construction in High Seismic Zones." *Journal of Bridge Engineering*, 21(3).

Tazarv, M., Saiidi, M. S. (2016b). "Seismic Design of Bridge Columns Incorporating Mechanical Bar Splices in Plastic Hinge Regions." *Engineering Structures*, 124: 507-520.

Thonstad, T., Mantawy, I. M., Stanton, J. F., Eberhard, M. O., Sanders, D. H. (2016). "Shaking Table Performance of a New Bridge System with Pretensioned Rocking Columns." *Journal of Bridge Engineering*, 21(4), DOI: 10.1061/(Asce)Be.1943-5592.0000867.

Trono, W., Jen, G., Panagiotou, M., Schoettler, M., Ostertag, C. P. (2015). "Seismic Response of a Damage-Resistant Recentering Posttensioned-HYFRC Bridge Column." *Journal of Bridge Engineering*, 20(7), DOI: 10.1061/(Asce)Be.1943-5592.0000692.

Valanis, K. C. (1985). "On the Uniqueness of Solution of the Initial Value Problem in Softening Materials." *Journal of Applied Mechanics*, 52: 649.

Valigura, J. (2019). "Seismic Repair and Loss Assessment of Bridges with Hybrid Sliding-Rocking Columns." Ph.D. Dissertation, Department of Civil, Environmental, and Architectural Engineering, University of Colorado, Boulder, CO.

Valigura, J., Salehi, M., Liel, A. B., Sideris, P. (2020). "Seismic Repair Assessment of "ABC" Bridge Columns through Integrated Experimentation and Expert Panel Solicitation." *Journal of Structural Engineering*, under review.

Valipour, H. R., Foster, S. J. (2009). "Nonlocal Damage Formulation for a Flexibility-Based Frame Element." *Journal of Structural Engineering*, 135(10): 1213-1221.

Veletzos, M. J., Restrepo, J. I. (2009). "Influence of Vertical Earthquake Motion and Pre-Earthquake Stress on Joint Response of Precast Concrete Segmental Bridges." *PCI Journal*, 54(3): 99-128.

Wang, J. C., Ou, Y. C., Chang, K. C., Lee, G. C. (2008). "Large-Scale Seismic Tests of Tall Concrete Bridge Columns with Precast Segmental Construction." *Earthquake Engineering & Structural Dynamics*, 37(12): 1449-1465, DOI: 10.1002/eqe.824.

Wang, Z., Song, W., Wang, Y., Wei, H. (2011). "Numerical Analytical Model for Seismic Behavior of Prestressing Concrete Bridge Column Systems." *The Twelfth East Asia-Pacific Conference on Structural Engineering and Construction*, Hong Kong, China, Elsevier.

Weldon, B. D., Kurama, Y. C. (2007). "Nonlinear Behavior of Precast Concrete Coupling Beams under Lateral Loads." *Journal of Structural Engineering*, 133(11): 1571-1581.

Weldon, B. D., Kurama, Y. C. (2012). "Analytical Modeling and Design Validation of Posttensioned Precast Concrete Coupling Beams for Seismic Regions." *Journal of Structural Engineering*, 138(2): 223-233.

Wen, Y. K. (1989). "Methods of Random Vibration for Inelastic Structures." *Applied Mechanics Reviews*, 42(2): 39-52.

Zhu, Z. Y., Ahmad, I., Mirmiran, A. (2006). "Seismic Performance of Concrete-Filled FRP Tube Columns for Bridge Substructure." *Journal of Bridge Engineering*, 11(3): 359-370, DOI: 10.1061/(Asce)1084-0702(2006)11:3(359).

APPENDIX A

COLUMN SPECIMEN DESIGN

This appendix complements Sections 4.3.1 and 4.3.2 with providing more details as to the design of the column specimens without considering their sliding joints. The design of sliding joints is explained in Section 4.3.3.

A.1. Design Codes and Assumptions

The AASHTO LRFD Bridge Design Specifications (AASHTO 2014), the AASHTO Guide Specifications for LRFD Seismic Bridge Design (AASHTO 2011), and the PCI Bridge Design Manual (PCI 2003) are utilized as the guidelines for the design of the columns. That is, after the column are initially designed according to the force-based methodology of the AASHTO LRFD Bridge Design Specifications, its design is controlled against the AASHTO Guide Specifications for LRFD Seismic Bridge Design and is adjusted if necessary. The PCI Bridge Design Manual is merely used to estimate the prestress losses.

The bridge prototype and its deck cross section are shown in Figure A-2. Although no information existed in Megally et al. (2002a) on the substructure design, it is assumed here that the bent cap is integral with the deck and expands below the deck, so that the clear distance between the deck and the column's top end is 1.2 ft and the column itself is 20 ft tall. Assuming that the substructure is connected to the superstructure through an integral bent cap, the connections of the bents at the top end are assumed to be fixed for

the rotations around both transverse and longitudinal axes, as schematically shown in Figure A-1. It is noted that bearings are redundant in HSR bridges, as lateral movement can be accommodated by sliding of the HSR joints.
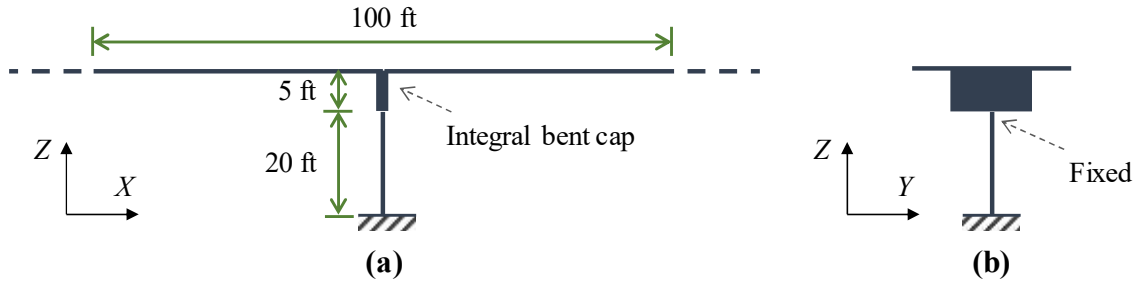
Figure A-1. Analyzed system: (a) bridge's longitudinal view; (b) column bent

A.2. Design Loads

The primary loads considered for the design of the column specimens are listed below:

- *DC*: dead load of structural components and nonstructural attachments

- *DW*: dead load of wearing surfaces and utilities

- *LL*: live load from vehicles

- *PS*: secondary loads, such as those imposed by prestressing

- *EQ*: earthquake load

A.2.1. Limit States and Load Combinations

The limit states examined for the column design are as follows:

- *Service I*: to control crack width in RC structures;

- *Strength I*: only basic load combinations caused by the use of bridge by normal vehicles and without any wind load effects;

- *Extreme Event I*: load combination including earthquake effects.

Each limit state is associated with one or more load combinations, expressed as:

$$Q_{ls} = \Sigma \eta_i \gamma_i Q_i \qquad \text{(A-1)}$$

where Q_{ls} is the magnified force effect used to check a limit state; η_i are the load modifiers, accounting for redundancy, ductility, and operational classification; γ_i are the load factors to account for different uncertainties pertinent to loading; these factors depend on the limit states; Q_i are the force effects coming from the analyses of member under various loads. Here the load modifiers, η_i, are set at 1. The load factors, γ_i, corresponding to the considered loads for each of the three limit states above are summarized in Table A-1, while γ_{EQ} is set at 0 to reduce the column cross section size.

Table A-1. Load factors for selected limit states

Limit State	DC		DW		PS	LL	EQ
	Min.	Max.	Min.	Max.			
Service I	1.0	1.0	1.0	1.0	1.0	1.0	0
Service III	1.0	1.0	1.0	1.0	1.0	0.8	0
Strength I	0.9	1.25	0.65	1.5	1.0	1.75	0
Extreme Event I	0.9	1.25	0.65	1.5	1.0	γ_{EQ}	1.0

(a)

(b)

Figure A-2. Prototype bridge: (a) elevation; (b) deck cross section (Megally et al. 2002a)

680

A.2.2. Dead Loads

Consistently with Megally et al. (2002a), the dead loads in the prototype domain are chosen to be 6.33 kips/ft, 0.78 kips/ft, and 0.97 kips/ft for deck, barriers, and future wearing, respectively. The first two of these loads comprise *DC* loads, while the last one is of *DW* load type. The bent reactions to balance these dead loads in the prototype domain are found to be P_{DC} = 711 kips and P_{DW} = 97 kips. In the model domain, however, these loads are scaled down by the force scale factor (Table 4-1) to P_{DC} = 178 kips and P_{DW} = 24 kips. The bent cap's weight is also approximated to be 20 kips in the prototype domain, which must be reduced to 5 kips for the model domain.

A.2.3. Live Loads

It is assumed that no pedestrian sidewalk exists on the bridge and the live loads are only caused by the vehicles. The number of lanes on the bridge are found as $w/12$, where w is the clear width of the deck (between the curbs and/or barriers) in feet. Since, in the prototype bridge, the deck is 27.8125 ft wide, 2 design lanes are considered.

To find the extreme live load effects, different combinations of occupied design lanes must be considered, while the resulting force effects are multiplied by appropriate multiple presence factors. The vehicular load on the bridge, designated as HL-93, must include combinations of design lane load and design truck or design tandem (not both concurrently). The loads are assumed to cover 10 ft of each design lane transversely. The design truck spacings and its associated loads in the prototype domain are shown in Figure A-3. The design tandem, however, consists of two 25-kip axles that are 4 ft apart, while the distance between the wheels in the transverse direction should be 6 ft. Both the truck

and tandem loads must be subjected to dynamic load allowance, which is achieved herein by multiplying their force effects by a factor of 1.33 ($1+IM/100$, with $IM = 33$). The design lane load of 0.64 kips/ft is uniformly distributed in the longitudinal direction, while it is assumed to cover 10 ft of width of each lane. The force effects resulting from the design lane load are not modified by dynamic load allowance.
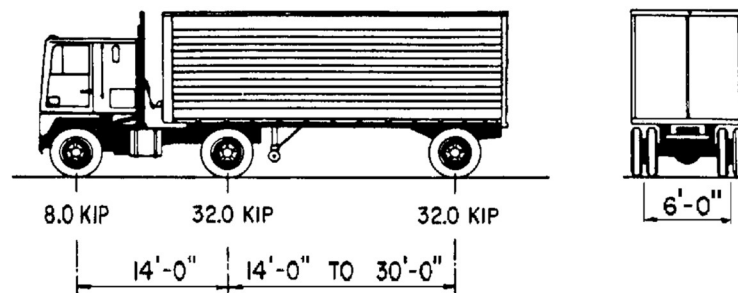
Figure A-3. HL-93 design truck

The live load scenario that causes the extreme axial forces in the piers combines 90 percent of the force effects of two design trucks with a minimum 50-ft spacing between their closest axles located along two adjacent spans and 90 percent of the force effects of a design lane. The distance between the design truck's 32-kip axles in this situation should be 14 ft. The critical scenario in the prototype domain is found to be as shown in Figure A-4(a); the extreme pier reaction due to the live loads is computed as 1.0 * 0.9 * (2.0 * (1.33 * 105 + 64)) = 366.58 kips, where 1.33 is the dynamic load allowance, 1.0 is the multiple presence factor, and 2.0 is for the presence of two design lanes). The value 105 kips was found via an ETABS model including all the five bridge spans and neglecting

the columns' flexural stiffness (conservative assumption). Hence, the column's axial reaction due to the live loads in the model domain is 92 kips.

In addition, the live load scenario causing the maximum moment at the bottom of the column (where maximum momet occurs) is found as demonstrated in Figure A-4(b). In the prototype domain, the maximum moment is found as 372 kips-ft (= 1.0 * 1.33 * (2.0 * 140), where 140 kips-ft is the moment obtained from the analysis of the ETABS model). Thus, the moment value used for the design of the columns in the model domain is 47 kips-ft. The corresponding shear forces are found to be very small and negligible.

A.2.4. Earthquake Loads

Per AASHTO (2014), the elastic seismic response coefficient, C_{sm}, for the mth mode is defined according to a design response spectrum that represents a seismic hazard with 7% probability of exceedance in 75 years (or approximately 1000-year return period). The design responses spectrum is determined on the basis of the location of the bridge and its supporting soil. Here, it is assumed that the prototype bridge is located in a highly seismic zone in central Los Angeles, California (Figure A-5(a)), where the peak ground acceleration (PGA), the short-period response spectral acceleration coefficient (S_s), and the long-period response spectral acceleration coefficient (S_1), are 0.6, 1.5, and 0.6, respectively. Additionally, the site class is assumed to be B, with the site factors $F_{PGA} = F_a = F_v = 1.0$. The design response spectrum computed based on these assumptions is displayed in Figure A-5(b). Since $0.5 < S_{D1}$, the bridge falls in Seismic Zone 4 per AASHTO (2014), or equivalently, Seismic Design Category D per AASHTO (2011).
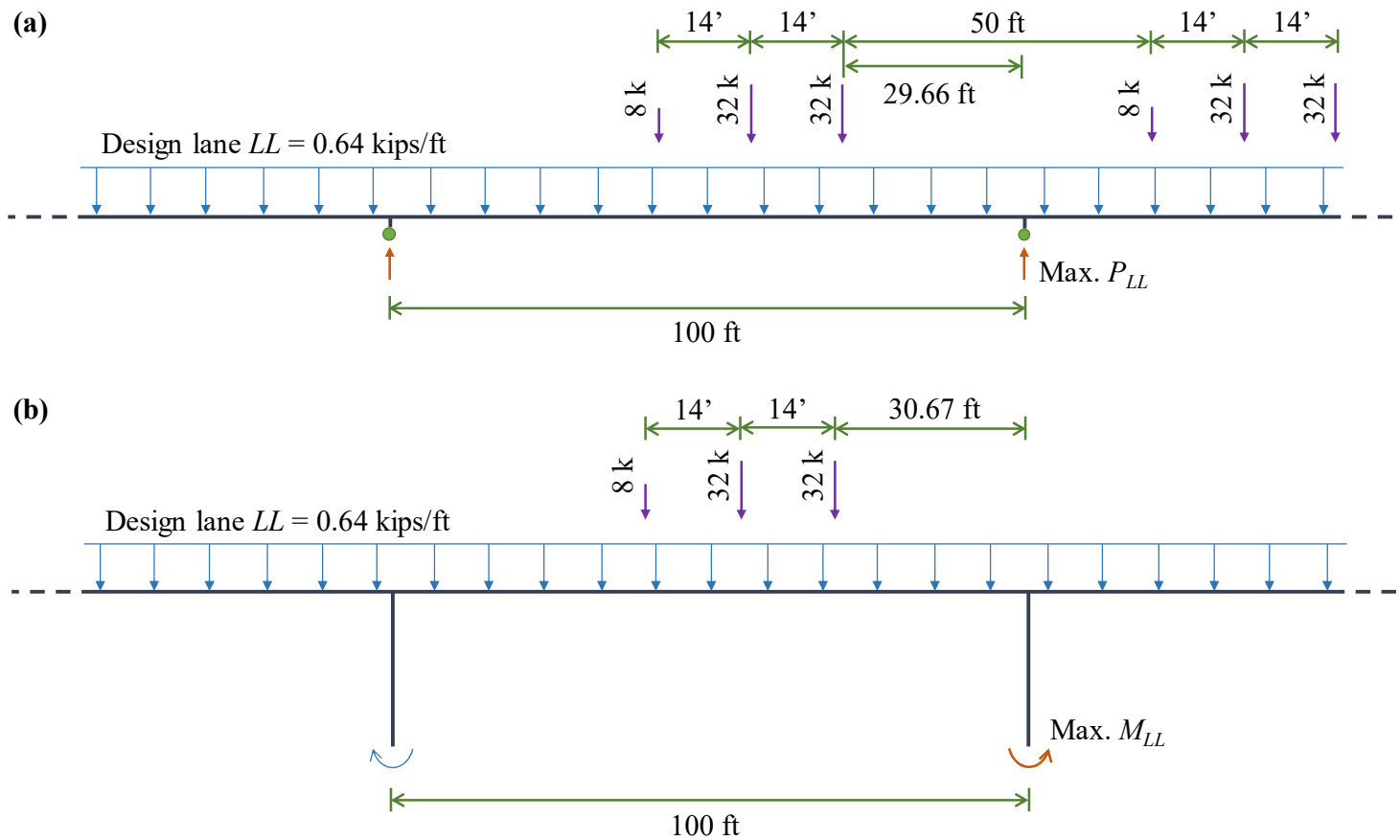
Figure A-4. Critical live load scenarios over one design lane for: (a) column axial reaction; (b) column base moment reaction

684
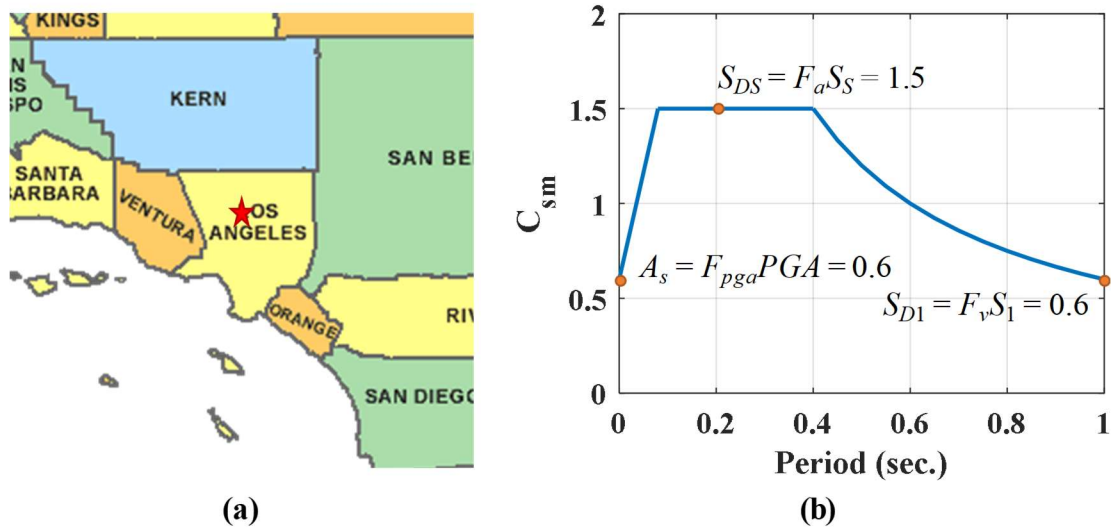
Figure A-5. (a) Prototype bridge location; (b) seismic design response spectrum

Any force effects determined due to the earthquake loads must be divided by appropriate response modification factor, R, depending on the importance category of the bridge. For the prototype bridge, which is considered to lie in the critical operational category, R equals 1.5. However, in order to intensify the inelastic response of the HSR columns under extreme loads, here, the R factor is increased to 8.

Given the prototype bridge is an essential multi-span bridge located in the Seismic Zone 4, according to AASHTO (2014), the earthquake force effects shall be obtained by time-history analysis. However, assuming that the bridge is long enough to design it in model domain for only one span, a single-mode elastic analysis method is deemed adequate. The single-mode method used here is of uniform load type. According to the uniform load method, first the fundamental periods of vibration in the longitudinal and transverse directions are approximated by elastic analysis of the bridge under uniformly distributed loads applied along its deck in the two respective directions, and then, the C_{sm}

values for those periods are computed. The C_{sm} values are subsequently utilized to approximate seismic loads in each direction and determine their corresponding force effects.

Considering the foregoing, before the vibration periods are computed, the seismic mass values and the stiffness values are required to be known. For this purpose, although the column cross section details are not still known, its dimensions are selected such that the axial stress due to the dead load does not exceed 10% of their axial load strength ($f'_c A_g$). That said and considering $f'_c = 5$ ksi, the column cross section in the prototype domain is chosen to be of a circular hollow shape with inside and outside diameters of 48 in. and 72 in., respectively.

Assuming that the superstructure's deformations caused by uniformly distributed loads along its two directions are negligible compared to the column displacements, only the stiffness values of the bent are used to approximate the periods. The stiffness of a single-column bent in the longitudinal direction, $k_{sc,x}$, is calculated as:

$$k_{sc,x} = \frac{12EI_{cr}}{L_{col}^{3}} = 2,593 \text{ kips/in} \quad \text{with} \quad I_{cr} = 0.7I \tag{A-2}$$

where E is the concrete modulus of elasticity, taken as 4,030 ksi; I is the cross section moment of inertia, which equals 1.059×10^{6} in^4; and L_{col} is the column height, i.e. 240 in. Note that, herein, the cross section moments of inertia are reduced by 30% to account for cracking. For the selected portion of the prototype bridge (see Figure A-1), the stiffness in the longitudinal direction, $K_{sc,x}$, is equal to the above value, i.e. 2,593 kips/in. In addition,

the stiffness of a single-column bent (assuming the deck and bent cap are rigid) in the transverse direction, $k_{sc,y}$, is calculated as:

$$k_{sc,y} = \frac{3EI_{cr}}{3L_{dck}{}^2 L_{col} - 3L_{dck} L_{col}{}^2 + L_{col}{}^3} = 335 \text{ kips/in} \tag{A-3}$$

where L_{dck} (height of deck centroid from foundation surface) is 25 ft and L_{col} is 20 ft. As a result, the stiffness of the isolated bridge portion with single-column bent in the transverse direction, $K_{sc,y}$, is equal to $k_{sc,y}$, i.e. 335 kips/in.

Additionally, the total seismic weight, W_s, of the considered bridge portion includes the dead loads of all its components, while the one-span superstructure's weight is 808 kips, the column's weight is 47 kips, and the bent cap is approximately 20 kips, leading to $W_s = 875$ kips. Finally, the fundamental period of the bridge in the two perpendicular horizontal directions are determined as:

$$T_{sc,x} = 2\pi \sqrt{\frac{W_s/g}{K_{sc,x}}} = 0.18 \text{ sec.}, \quad T_{sc,y} = 2\pi \sqrt{\frac{W_s/g}{K_{sc,y}}} = 0.51 \text{ sec.} \tag{A-4}$$

The C_{sm} values corresponding to the above periods in the prototype domain, before the application of R factor, can be found per Figure A-5(b), which are almost 1.5 and 1.18 in the longitudinal and transverse directions, respectively. After $R = 8$ is applied, these values are reduced to 0.188 and 0.148 in the longitudinal and transverse directions, respectively. Using the product of the seismic response coefficients and the seismic weight as the static seismic loads applied to the deck centroid in the two horizontal directions, the approximate earthquake force effects at the column's bottom end in the prototype domain are found to be as summarized in Table A-2. For the design in the model domain, the

scaled force effects of Table A-3 are utilized. Note that the moment arm for the moment

due to the seismic loads in the transverse direction is 25 ft (in prototype domain).

Table A-2. Earthquake force effects in prototype domain

Direction	Longitudinal			Transverse		
Force Effect	Axial (kips)	Shear (kips)	Moment (kips-ft)	Axial (kips)	Shear (kips)	Moment (kips-ft)
Value	0	±165	±1,645	0	±130	±3,238

Table A-3. Earthquake force effects in model domain

Direction	Longitudinal			Transverse		
Force Effect	Axial (kips)	Shear (kips)	Moment (kips-ft)	Axial (kips)	Shear (kips)	Moment (kips-ft)
Value	0	±41	±206	0	±33	±405

A.2.5. Secondary Loads

It is assumed that the total post-tensioning force applied to the column is almost 5% its

compressive strength, $f'_c A_g$. If f'_c = 5 ksi, the sum of the post-tensioning forces can be

estimated as 565 kips. In the model domain, this value equals 141 kips.

A.2.6. Combined Force Effects

A summary of the force effects caused by different loads at the bottom end of the column

in the model domain is presented in Table A-4. Using the load factors of Table A-1, the

minimum and maximum factored force effects resulted from different load combinations

for the bottom cross section of the column (i.e. the critical cross section) in the model

domain are computed. These force effects, which are subsequently used to design the

column, are not presented here for brevity, while the critical load combinations for each limit state are mentioned in the next sections.

Table A-4. Summary of force effects for column in model domain

Load Type		Axial (kips)	Shear (kips)	Moment (kips-ft)
DC		-183	0	0
DW		-24	0	0
PS		-141	0	0
LL		-92	0	47
EQ	Long.	0	±41	±206
	Trans.	0	±33	±405

A.3. LRFD Design

In order to design the column cross section and its reinforcement to resist the aforementioned force effects, two steps are iteratively taken. In the first step in each iteration, the column's cross section size, mild steel reinforcement, prestressing steel, and initial posttensioning are chosen according to the employed design codes. Then, the selected design is controlled against the force effects computed for various considered limit states. If the design is insufficient or uneconomical, it is adjusted accordingly and the second step is repeated. In the following, only the final final design is described. The same cross section assumed to estimate the earthquake force effects, i.e. a hollow circular cross section of inside and outside diameters of 24 in. and 36 in. (in model domain, Figure A-6), is considered in the final design.
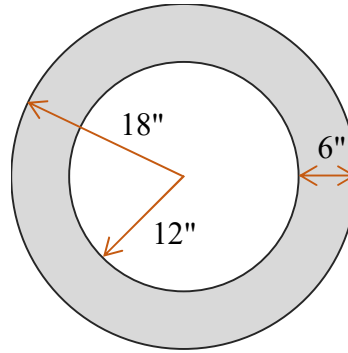
Figure A-6. Selected cross section dimensions for column specimen

A.3.1. Minimum Steel Reinforcement

A.3.1.1. Longitudinal Steel

The maximum areas of non-prestressed (mild) and prestressed longitudinal steel – A_s and

A_{ps}, respectively – in compressive members must satisfy the following inequalities:

$$\frac{A_s}{A_g} + \frac{A_{ps} f_{pu}}{A_g f_y} \leq 0.08 \quad \text{and} \quad \frac{A_{ps} f_{pe}}{A_g f_c'} \leq 0.30 \tag{A-5}$$

while their minimum area shall satisfy:

$$\frac{A_s f_y}{A_g f_c'} + \frac{A_{ps} f_{pu}}{A_g f_c'} \geq 0.135 \tag{A-6}$$

where f_y is the specified yield strength of mild steel, which is 60 ksi herein, and f_{pe} is the

effective stress of prestressing tendons. Also, in Seismic Zone 4, the mild longitudinal

reinforcement must range between 0.01 and 0.04 times the gross cross section area, i.e.:

$$0.01 \leq \frac{A_s}{A_g} \leq 0.04 \tag{A-7}$$

For precast hollow segmental piers, the longitudinal reinforcement should also meet the requirements for creep and shrinkage control, which prescribe the minimum steel areas below (in.²/ft) on each face and in each direction:

$$A_s \geq \frac{1.3 A_g}{Perimeter \cdot f_y} \quad \text{and} \quad 0.11 \leq A_s \leq 0.6 \tag{A-8}$$

where *Perimeter* is the total perimeter of cross section sides – including any holes in hollow section – in inches, A_g is in in.², and f_y is in ksi.

In terms of lateral spacing between longitudinal bars, it shall not exceed 8 in. to sufficiently confine concrete. Moreover, for hollow sections, the maximum spacing of longitudinal reinforcing bars must be limited to 1.5 times the wall thickness and 18 in., whichever is smaller.

Because the longitudinal non-prestressed reinforcement is not provided to contribute to the strength of the segmental columns, its minimum area is considered here. Satisfying all the conditions above, two layers of 16 #4 longitudinal bars are found sufficient for the designed column, one layer per face (interior and exterior) of the segments. The prestressed tendons are also chosen to constitute eight 0.6-in. diameter monostrands with an initial posttensioning force of 18 kips per tendon. This force results in an effective prestress, f_{pe}, of 83 ksi.

A.3.1.2. Transverse Steel

For the columns designed for SDC D, the spiral reinforcement volumetric ratio, ρ_s, (relative to the concrete core volume measured out-to-out of spirals) must exceed 0.005. It is also required that:

$$\rho_s \geq 0.45 \left(\frac{A_g}{A_c} - 1 \right) \frac{f_c'}{f_{yh}} \tag{A-9}$$

where A_c is the core area measured to the outside of hoop and f_{yh} is the transverse steel's specified minimum yield strength. Considering a cover concrete of 0.75 in. for the column specimens, the above requirement leads to $\rho_s \geq 0.0125$ for the selected column. If #3 rebar size is chosen, this minimum volumetric shear reinforcement ratio requires a maximum spacing of 4.25 in. However, the maximum center-to-center spacing of spirals is:

$$s_{max} = \min \left(D_{min}/5, 6d_b, 6 \text{ in} \right) \tag{A-10}$$

where D_{min} is the least dimension of cross section and d_b is the nominal diameter of longitudinal rebar. In the plastic hinge lengths of the columns, the requirement above becomes:

$$\rho_s \geq 0.12 \frac{f_c'}{f_{yh}} \tag{A-11}$$

which yields $\rho_s \geq 0.01$. The increased shear reinforcement must be provided over a length equal to the maximum of cross section depth, one sixth of column's clear height, and 18 in. The spacing of transverse reinforcement over these lengths cannot exceed one fourth of the cross section depth and 4 in. For SDC D, the minimum size of shear reinforcement is #4 (while for the test specimens in the model domain, probably #3 would be acceptable), and the spacing of transverse reinforcement must not exceed:

$$s_{max} = \begin{cases} 0.8d_v \leq 24 \text{ in} & v_u < 0.125 f_c' \\ 0.4d_v \leq 12 \text{ in} & v_u \geq 0.125 f_c' \end{cases} \tag{A-12}$$

where v_u is the shear stress on concrete, computed as:

$$v_u = \frac{|V_u - \phi V_p|}{\phi b_v d_v} \tag{A-13}$$

In the above equation, d_v is the effective shear depth, taken as the distance between the resultants of compressive and tensile forces acting on a section under nominal moment strength and b_v is the effective web width, which is assumed to be equal to the diameter of circular sections minus the hole diameters in their centerlines. Also, ϕ is the resistance factor for shear, i.e. 0.9, while V_p, the component of prestressing force in the direction of shear, is conservatively neglected. In addition, for the hollow cross sections, the center-to-center spacing of shear reinforcement shall not exceed 1.25 times the wall thickness and 12 in.

Considering the above requirements, #3 spirals with the spacing of 3 in. are provided both inside and outside the column segments, over their entire lengths. The final steel reinforcement chosen for the column specimens is demonstrated in Figure A-7.
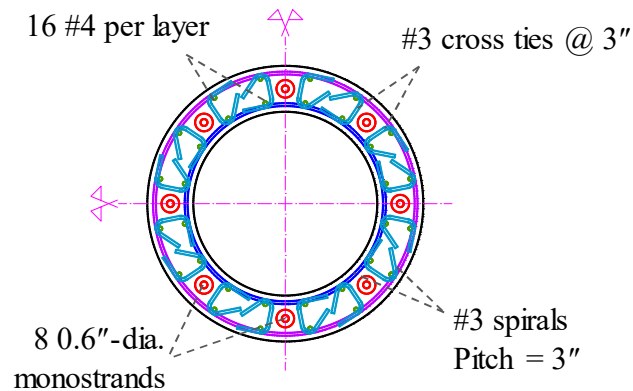
Figure A-7. Selected cross section dimensions and steel reinforcement

693

A.3.2. Control for Strength and Extreme Event Limit States

A.3.2.1. Axial Resistance

The pure axial resistance of a column with spirals, when no sliding exists, is determined as $P_r = \phi P_n$, with:

$$P_n = 0.85\left[0.85f_c'\left(A_g - A_s - A_{ps}\right) + f_y A_{st} - A_{ps}\left(f_{pe} - E_p \varepsilon_{cu}\right)\right] \tag{A-14}$$

where ε_{cu} is the failure strain of concrete in compression, which is taken as 0.003 here; and the resistance factor, ϕ, for compression-controlled sections with spirals is 0.75.

If the joints experience their maximum sliding capacities, the relationship above for nominal axial resistance can be modified as:

$$P_n = 0.85\left[0.85f_c'\left(A_{g,sl} - A_{st} - A_{ps}\right) + f_y A_{st} - A_{ps}\left(f_{pe} + E_p\left(\varepsilon_{p,sl} - \varepsilon_{cu}\right)\right)\right] \tag{A-15}$$

where $A_{g,sl}$ is the reduced contact area when complete sliding has occurred and $\varepsilon_{p,sl}$ is the strain caused by sliding in the tendons. $\varepsilon_{p,sl}$ is computed as:

$$\varepsilon_{p,sl} = \frac{\sqrt{\left(D_{da} - D_d\right)^2 + 4h_{da}^2} - 2h_{da}}{2h_{da}} \tag{A-16}$$

where D_{da}, D_d, and *had* are the duct adaptor diameter, the duct diameter, and the duct adaptor height, respectively. The axial resistance obtained from the above equation should be checked when the duct adaptor dimensions are chosen.

A.3.2.2. Flexural Resistance

The ultimate moment strengths of column is computed by assuming 0.003 as the concrete compressive failure strain and considering rectangular stress block of $0.85f'_c$ for the concrete under compression, over a depth of $\beta_1 c$, where β_1 varies linearly from 0.85 for f'_c

≤ 4 ksi to 0.65 for $f'_c \geq 8$ ksi and c is compression depth over cross-section. The stress in the ith unbonded posttensioned tendon, f_{ps}, is approximated as:

$$f_{ps,i} = f_{pe,i} + E_s \cdot \frac{l_p}{l_{t,i}} \cdot \begin{cases} \left(\varepsilon_o - \phi y_{t,i} \right) & \text{free top end} \\ 2\varepsilon_o & \text{fixed top end} \end{cases} \tag{A-17}$$

where f_{pe} is the initial posttensioning stress (after losses), l_p is the plastic hinge length, here assumed to be equal to 0.85 times the cross-section depth, l_t is the tendon's initial length, ε_o and ϕ are axial strain and curvature at bottom section, and y_t is the tendon's distance from cross-section centerline (where ε_o is computed). Likewise, the stress in each longitudinal reinforcing bar is found as:

$$f_{s,i} = E_s \cdot \left(\varepsilon_o - \phi y_{b,i} \right) \leq 0 \tag{A-18}$$

where $y_{b,i}$ is the ith longitudinal bar's distance form the cross-section centerline. It is noted that the steel bars in the rocking joints cannot bear tensile stress.

Given the above approximations and assumptions, the only unknown in finding moment strength corresponding to any external axial load is c, which can be found by seeking the equilibrium of axial forces acting on the bottom section. The equilibrium equation is found to have the following form:

$$P_c + P_s - P_{ps} - P_{ext} = 0 \quad \text{with} \quad \begin{cases} P_c = 0.85 f'_c A_{rec} \\ P_s = \sum f_{s,i} A_{s,i} \\ P_{ps} = \sum f_{ps,i} A_{ps,i} \end{cases} \tag{A-19}$$

where $A_{s,i}$ and $A_{ps,i}$ are the ith bar area and the ith tendon area, A_{rec} is the area included by the compressive stress block, and P_{ext} is the external axial load (positive if compressive).

Using the above equation, the P_n-M_n and ϕP_n-ϕM_n interaction diagrams obtained for the column are shown in Figure A-8. The axial force resistance in this graph refers to the external axial load and does not include the prestressing forces. It is noted that the resistance factor ϕ for flexure of columns with tie reinforcement designed for seismic zone 4 is taken 0.9, while under pure axial force it is 0.75. The critical load combination controlling the Extreme Event limit state was 0.9 DC + 0.65 DW + PS + 0.3 $EQ_{long.}$ + $EQ_{trans.}$, leading to the P-M pair indicated in Figure A-8.
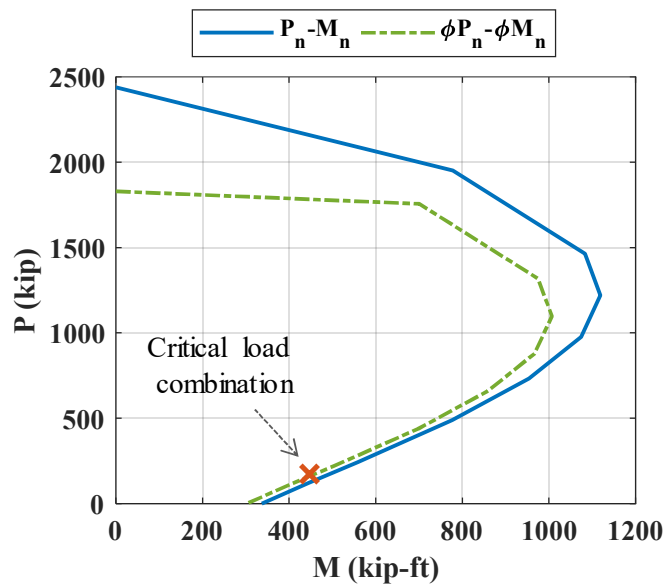
Figure A-8. *P-M* interaction diagram for designed column specimen

A.3.2.3. Shear Resistance

The factored shear resistance is determined as $V_r = \phi V_n$, where ϕ is 0.9, and assuming posttensioning tendons do not resist shear, V_n is computed as:

$$V_n = V_c + V_s \tag{A-20}$$

in which V_c and V_s are concrete and steel shear resistances, respectively. The concrete shear resistance can be found as:

$$V_c = v_c A_e \quad \text{with} \quad A_e = 0.8 A_g \tag{A-21}$$

For section under compression:

$$v_c = 0.032 \alpha' \left(1 + \frac{P_u}{2A_g}\right) \sqrt{f_c'} \leq \min \begin{cases} 0.11\sqrt{f_c'} \\ 0.047\alpha'\sqrt{f_c'} \end{cases} \tag{A-22}$$

where P_u is the ultimate axial force acting on section, while α' for circular sections with spirals is determined as:

$$\alpha' = \frac{f_s}{0.15} + 3.67 - \mu_D \quad \text{with} \quad f_s = \rho_s f_{yh} \leq 0.35 \tag{A-23}$$

Also, μ_D is the column's displacement ductility ratio demand, which is found as:

$$\mu_D = 1 + \frac{\Delta_{pd}}{\Delta_{yi}} \tag{A-24}$$

where Δ_{pd} is the plastic displacement demand for the column and Δ_{yi} is the idealized yield displacement of the column. Here, conservatively, μ_D is taken as 3.

The shear resistance provided by spirals is also computed as:

$$V_s = \frac{\pi}{2} \left(\frac{nA_{sp}f_{yh}D'}{s}\right) \tag{A-25}$$

where n is the number of individual interlocking spirals, A_{sp} is the area of spiral bar, s is the spiral pitch, and D' is the spiral diameter. For the hollow column with two spirals

697

(inside and outside), n may be taken as 1, but D' should be the sum of their diameters. The extent of shear reinforcement must be restricted such that:

$$V_s \le 0.25\sqrt{f_c'}A_e \qquad \text{(A-26)}$$

Using the above equations and considering the reinforcement chosen for the column cross section (Figure A-7), V_c and V_s are computed as 111 kips and 207 kips, respectively, for the critical load combination of Extreme Event limit state (i.e. simultaneously generating the lowest axial force and the highest shear force). As a result, the reduced shear resistance, V_r, of the column is found to be 286 kips, which is much larger than the maximum factored shear force effect for the Extreme Event limit state, i.e. 42 kips.

A.3.3. Control of Service Limit States

Before controlling the concrete/prestressing steel stress limits before and after losses, it is required to compute the initial post-tensioning needed to achieve the desired post-tensioning at the time of testing. The prestressing losses are determined as:

$$\Delta f_{pT} = \Delta f_{pF} + \Delta f_{pA} + \Delta f_{pES} + \Delta f_{pLT} \qquad \text{(A-27)}$$

where Δf_{pT} is the total loss, Δf_{pF} is the loss due to friction as the force is propagated from the jacking end to the dead end, Δf_{pA} is the loss due to anchorage set, Δf_{pES} is the sum of all losses (or gains) due to the elastic shortening (or extension) of the concrete member when prestress and other external loads are applied, and Δf_{pLT} is the long-term losses due to concrete creep and shrinkage of the concrete member as well as relaxation of the steel strands. Each of the above losses are determined as follows:

A.3.3.1. Immediate Losses

The immediate (or instantaneous) losses include the losses due to the anchorage set, friction, and elastic shortening. The anchorage set is assumed to be equal to 0.25 in. The prestress loss due to this anchorage set over the length of each tendon, which is approximated to be 200 in. in its final configuration, is $E_p \times (0.25 / 200) = 35.6$ ksi – note that E_p is the modulus of elasticity of the prestressing tendons, i.e. 28500 ksi.

The friction loss is computed as:

$$\Delta f_{pF} = f_{pj}\left(1 - e^{-(Kx - \mu\alpha)}\right) \tag{A-28}$$

where f_{pj} is the prestress at jacking, x is the length of prestressing steel from the jacking to the point of consideration in feet, K is the wobble friction coefficient (per foot of tendon), μ is the coefficient of friction, and α is the sum of angular changes over the length of tendon. The values of K and μ for the contact between strands and Polyethylene ducts are 0.0002 and 0.23, respectively, while x is approximately 16.5 ft and α is zero for straight tendons.

Assuming that the gravity loads are applied after the post-tensioning of the columns (using gravity tendons), the elastic shortening loss in the columns can be determined as:

$$\Delta f_{pES} = \frac{E_p}{E_{ci}} f_g \tag{A-29}$$

where E_{ci} is the modulus of elasticity of concrete when loaded and f_g is the average compressive stress in concrete caused by unfactored gravity loads (Service I). Considering 50% of maximum live load, the prestress losses due to elastic shortening for the column at the bottom ends of column are approximated as 3.2 ksi.

A.3.3.2. Long-Term Losses

The long-term losses consist of concrete creep and shrinkage as well as prestressing steel relaxation (PCI 2003). The concrete creep strain is computed by multiplying the concrete's compressive strain under service loads with the creep coefficient, C, which is defined as:

$$C(t,t_o) = \frac{(t-t_o)^{0.6}}{10+(t-t_o)^{0.6}} C_u \quad \text{with} \quad C_u = 1.88 k_c \tag{A-30}$$

where $k_c = k_{la} k_h k_s$, t and t_o are the concrete ages (in days) at the time of interest and when member is loaded, respectively, and k_{la}, k_h, and k_s are the correction factors for the loading age, relative humidity, and the size of member, respectively. Here, t and t_o are assumed to be 35 and 28 days, respectively. In addition, k_h is found to be 1.17 for an average humidity of 50%, k_{la} is taken as 0.84 for moist-cured concrete loaded after 28 days, and k_s is found to be 0.82 for the volume-to-surface ratio of 3 for the hollow column designed herein. Based on the above data, the creep coefficient for the column is determined to be 1.16. Also, the service compressive strain in the column is 0.00017, resulting in the creep strain loss of 0.00020.

The shrinkage strain, S, in a concrete component with the age of t days, after being moist-cured for 7 days, can be computed as:

$$S(t,t_o) = \frac{(t-7)}{35+(t-7)} S_u \tag{A-31}$$

where S_u is the ultimate shrinkage strain, with the average value of:

$$S_u = 545 k_{sh} \times 10^{-6} \quad \text{with} \quad k_{sh} = k_{cp} k_h k_s \tag{A-32}$$

In the last equation, k_{cp} is the correction factor for curing period, which is selected to be 1.0 (i.e. only 7 days of curing). As a result, the shrinkage strain after 35 days is 0.00023.

Overall, the long-term loss strain due to creep and shrinkage is 0.00043. This strain loss amounts to $\Delta f_{pLT} = 12.2$ ksi for the column. The steel relaxation loss – computed subsequently – must be added to the above value.

The stress relaxation of low-relaxation prestressing steel may be approximated as:

$$L_r = \frac{\log_{10}(24t)}{K_r}\left(\frac{f_i}{f_{py}} - 0.55\right)f_i \tag{A-33}$$

where t is the time over which the relaxation is approximated, K_r is equal to 45 for low-relaxation steel, f_i is the initial stress before relaxation starts, and f_{py} is the strand yield strength. Herein, t is taken as 7 days.

A.3.3.3. Staged Losses

The ultimate goal is to calculate the initial jacking force needed to achieve the desired post-tensioning forces when tests are carried out (F_{PT}), which is 18 kips per tendon (this value is chosen based on the Extreme Event limit state, as discussed in the next sections). That said, the tendon prestresses (f_{ps}) and corresponding concrete stresses (f_c) at different test set-up stages are found as summarized in Table A-5.

The prestress values and the concrete stresses presented above must be checked against the allowable stress limits. The prestressing stress limits for the low-relaxation PT tendons before and after anchor set are $0.9f_{py}$ and $0.7f_{pu}$, respectively, while after all losses, this limit is $0.8f_{py}$. Note that f_{py} and f_{pu} are the nominal yield and ultimate strengths of the prestressing steel, which are 243 ksi and 270 ksi for the selected prestressing steel,. All

these limits are met by the above approximated prestress values. The concrete compressive stress limits before and after losses are $0.6f'_{ci}$ and $0.45f'_c$, respectively (here, $f'_{ci} \approx f'_c$), which are also satisfied.

Table A-5. Prestress and concrete stresses at different stages

Stage	At Jacking	After Anchor Set	After Gravity Load	After Long-Term Losses
f_{ps}/f_{py}	0.55	0.40	0.39	0.34
f_{ps}/f_{pu}	0.50	0.36	0.35	0.31
f_c/f'_c	0.16	0.14	0.13	0.13

APPENDIX B

REINFORCEMENT LAYOUTS

B.1. Loading Beam Reinforcement

The reinforcement layouts for the designed loading beam are found in the following pages.

Top View & Section C-C

Front View & Section B-B
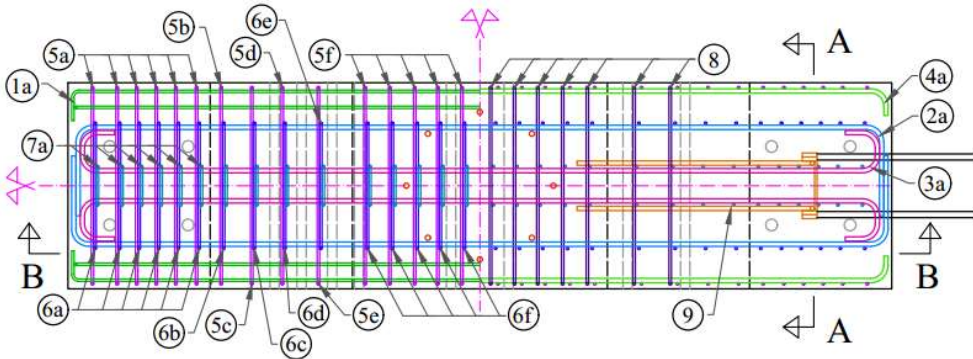
Side View & Section A-A
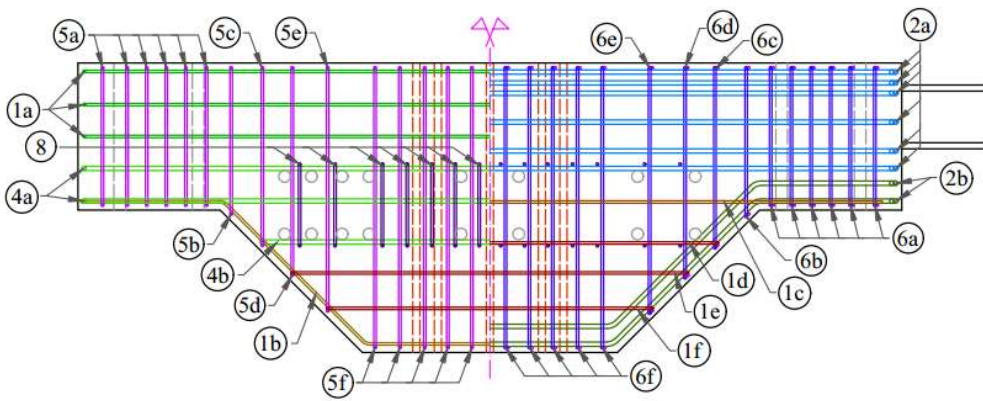
Section F-F & Bottom View
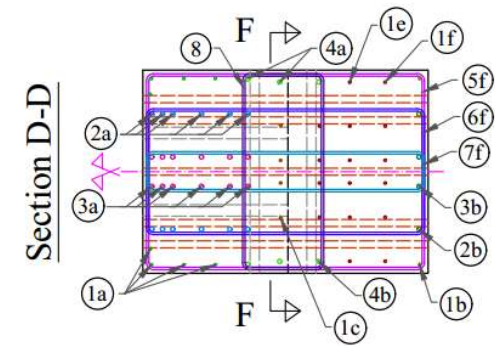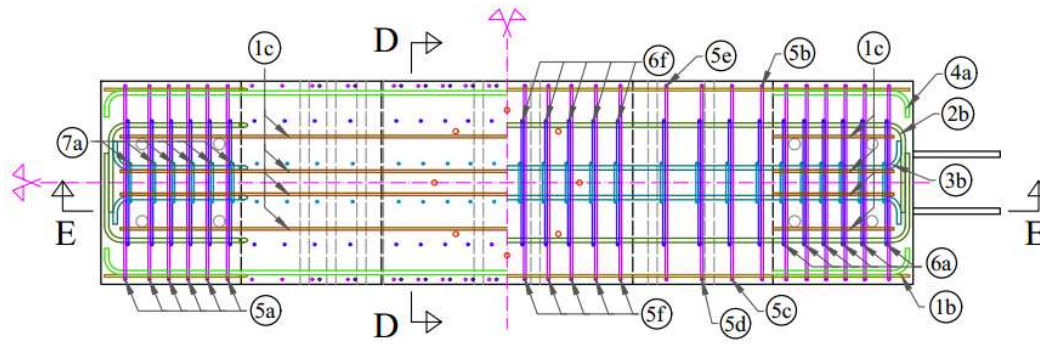
Section D-D
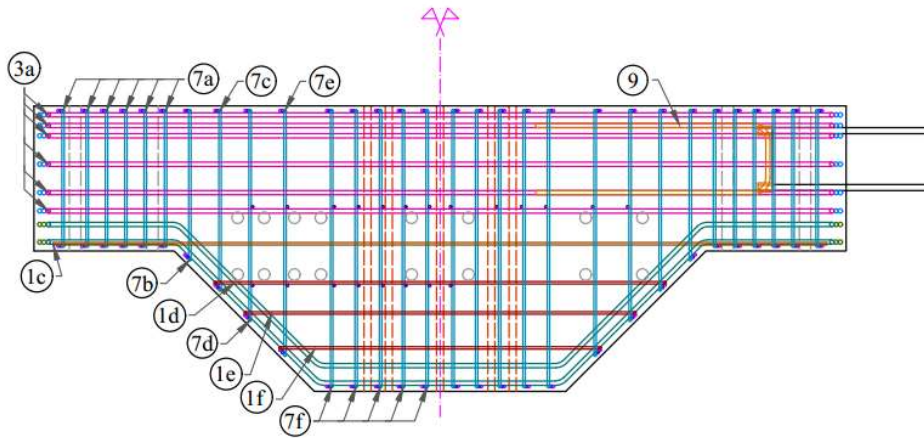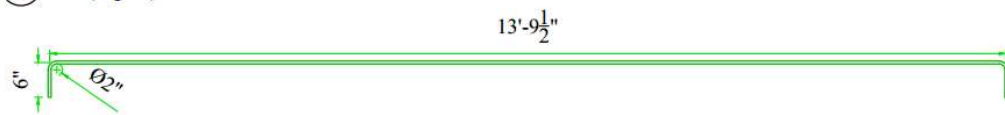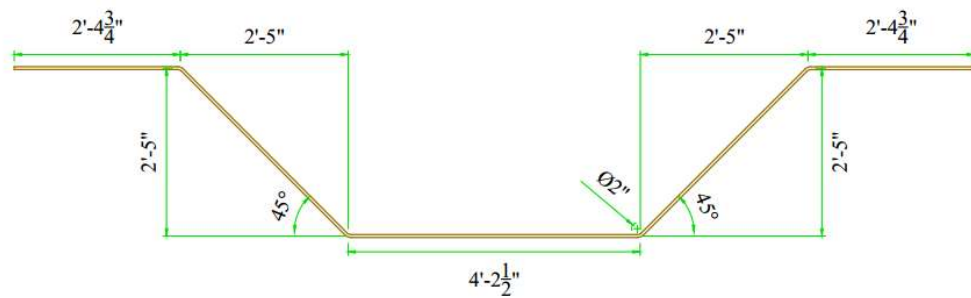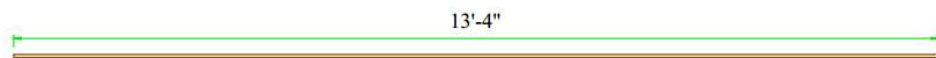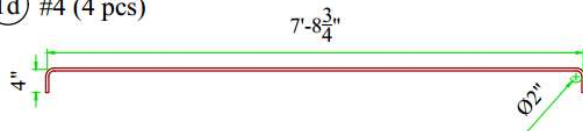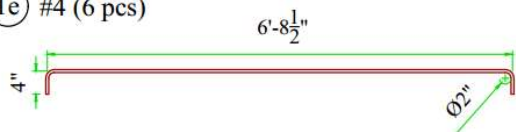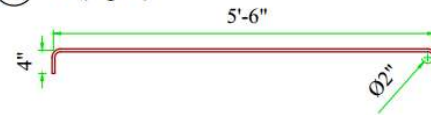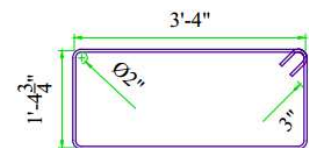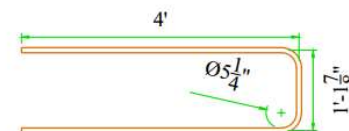
Section E-E

705

1a #4 (8 pcs)

13'-9½"

6"   Ø2"

1b #4 (2 pcs)

2'-4¾"   2'-5"   2'-5"   2'-4¾"

2'-5"   45°   Ø2"   45°   2'-5"

4'-2½"

1c #4 (4 pcs)

13'-4"

1d #4 (4 pcs)

7'-8¾"

4"   Ø2"

1e #4 (6 pcs)

6'-8½"

4"   Ø2"

1f #4 (6 pcs)

5'-6"

4"   Ø2"

8 #4 (14 pcs)

3'-4"

1'-4¾"   Ø2"   3"

9 #7 (2 pcs)

4'

Ø5¼"   7/8"   1'-1⅞"

706

2a #7 (12 pcs)

13'-8$\frac{3}{4}$"

1'-6"

Ø5$\frac{1}{4}$"

3a #7 (12 pcs)

13'-6"

7$\frac{3}{4}$"

3$\frac{1}{2}$"

Ø5$\frac{1}{4}$"

4a #7 (4 pcs)

13'-9$\frac{1}{2}$"

5"

Ø5$\frac{1}{4}$"

4b #7 (2 pcs)

7'-8$\frac{3}{4}$"

5"

Ø5$\frac{1}{4}$"

707

(2b) #7 (4 pcs)

Plan View

13'-8¾"

1'-6"

Ø5¼"

Elevation View

2'-4⅝" 2'-5¼" 2'-5¼" 2'-3¾"

2'-5¼" 2'-5¼"

45° 45°

Ø5¼"

4'-2"

3D View

(5a) #4 (12 pcs)

3'-4"

2'-4"

Ø2"

3"

(5b) #4 (2 pcs)

3'-4"

2'-5$\frac{7}{8}$"

Ø2"

3"

(5c) #4 (2 pcs)

3'-4"

3'-0$\frac{1}{4}$"

Ø2"

3"

(5d) #4 (2 pcs)

3'-4"

3'-6$\frac{3}{8}$"

Ø2"

3"

(5e) #4 (2 pcs)

3'-4"

4'-1$\frac{1}{2}$"

Ø2"

3"

(5f) #4 (10 pcs)

3'-4"

4'-9"

Ø2"

3"

6a #4 (12 pcs)
2'-1½"
Ø2"
3"
2'-4"

6b #4 (2 pcs)
2'-1½"
Ø2"
3"
2'-6⅞"

6c #4 (2 pcs)
2'-1½"
Ø2"
3"
3'-1¼"

6d #4 (2 pcs)
2'-1½"
Ø2"
3"
3'-7⅜"

6e #4 (2 pcs)
2'-1½"
Ø2"
3"
4'-2½"

6f #4 (10 pcs)
2'-1½"
Ø2"
3"
4'-9"

710

7a #4 (12 pcs)

$7\frac{3}{4}$"

2'-4"

3"

Ø2"

7b #4 (2 pcs)

$7\frac{3}{4}$"

$2'-6\frac{3}{8}$"

3"

Ø2"

7c #4 (2 pcs)

$7\frac{3}{4}$"

$3'-0\frac{3}{4}$"

3"

Ø2"

7d #4 (2 pcs)

$7\frac{3}{4}$"

$3'-6\frac{7}{8}$"

3"

Ø2"

7e #4 (2 pcs)

$7\frac{3}{4}$"

4'-2"

3"

Ø2"

7f #4 (10 pcs)

$7\frac{3}{4}$"

4'-9"

3"

Ø2"
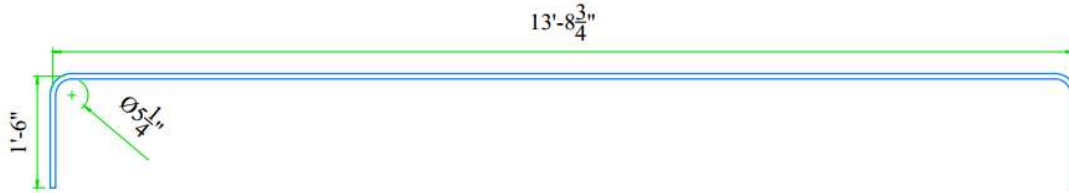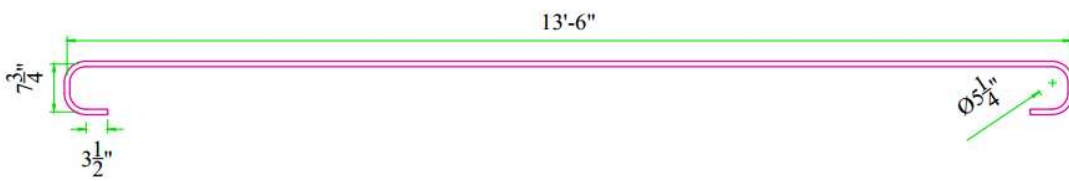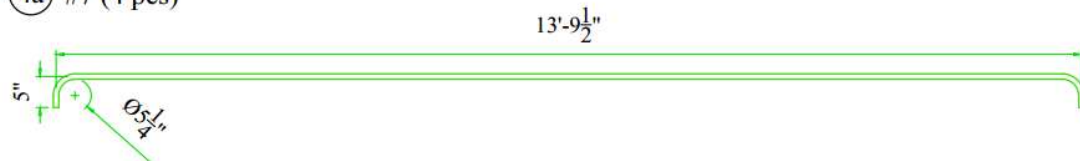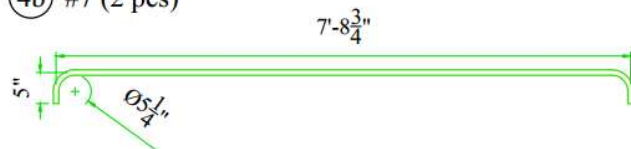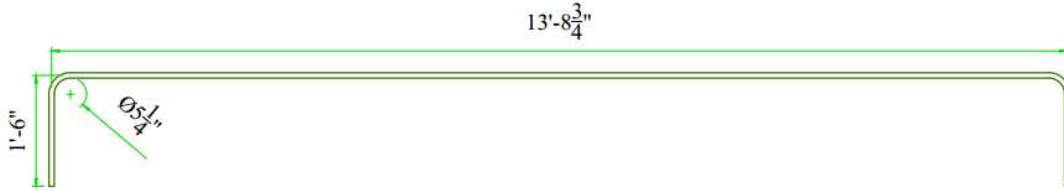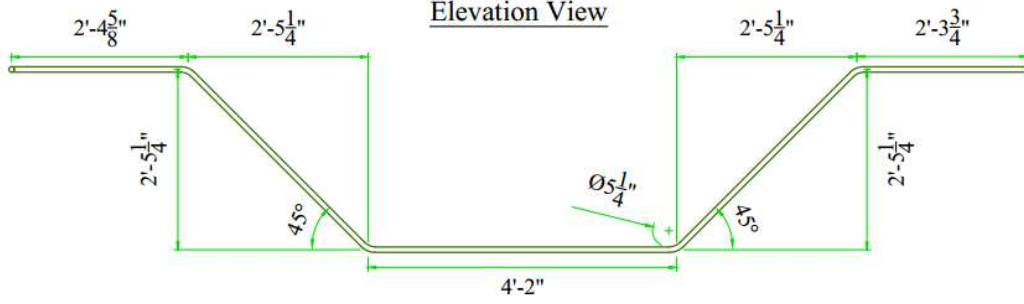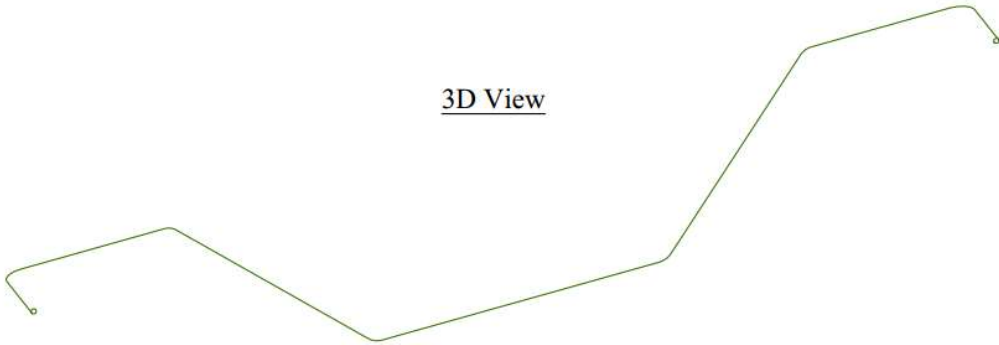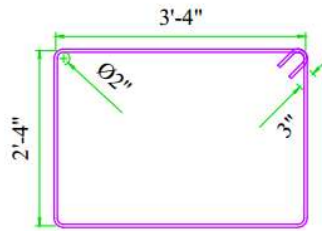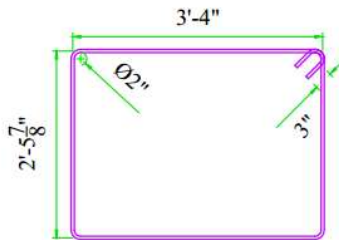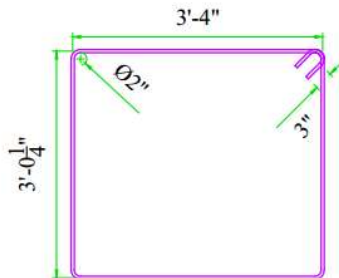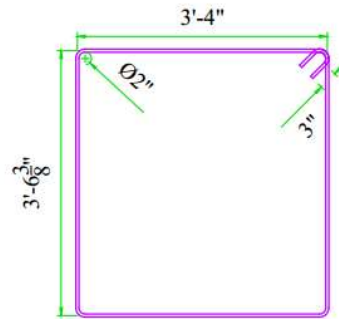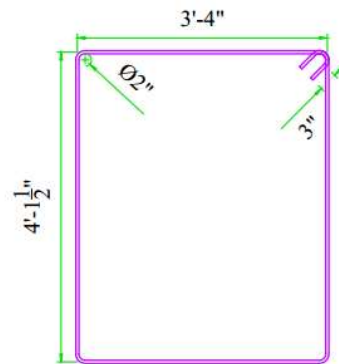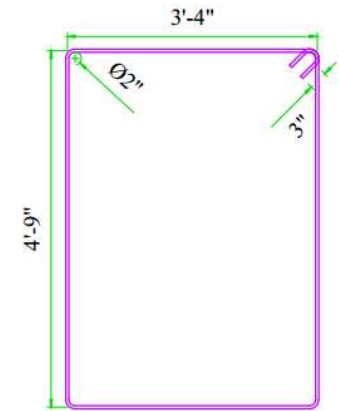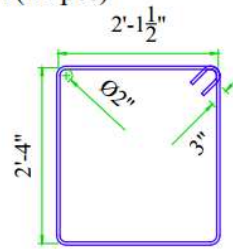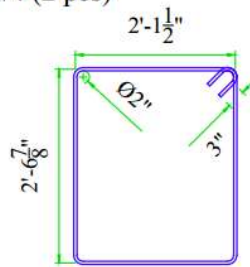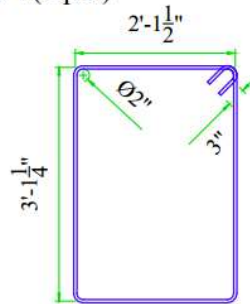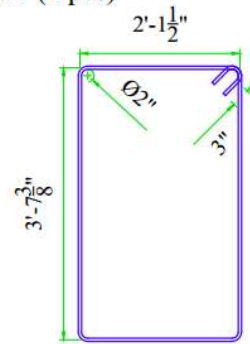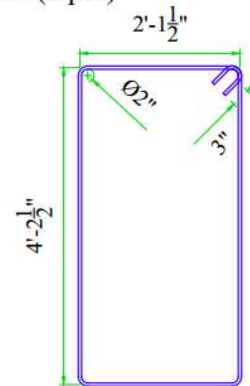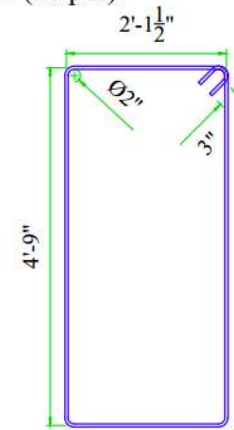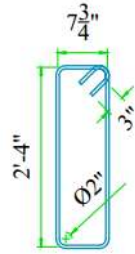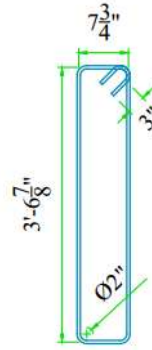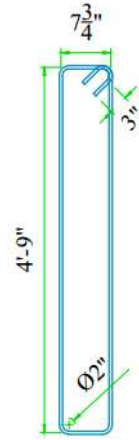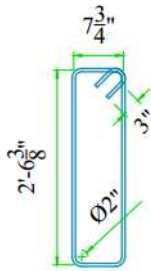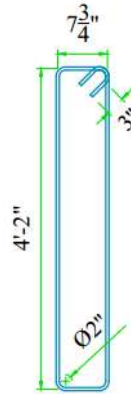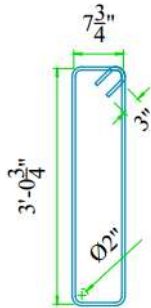
B.2. Foundation Block Reinforcement

The reinforcement layouts for the designed foundation block are found in the following pages.
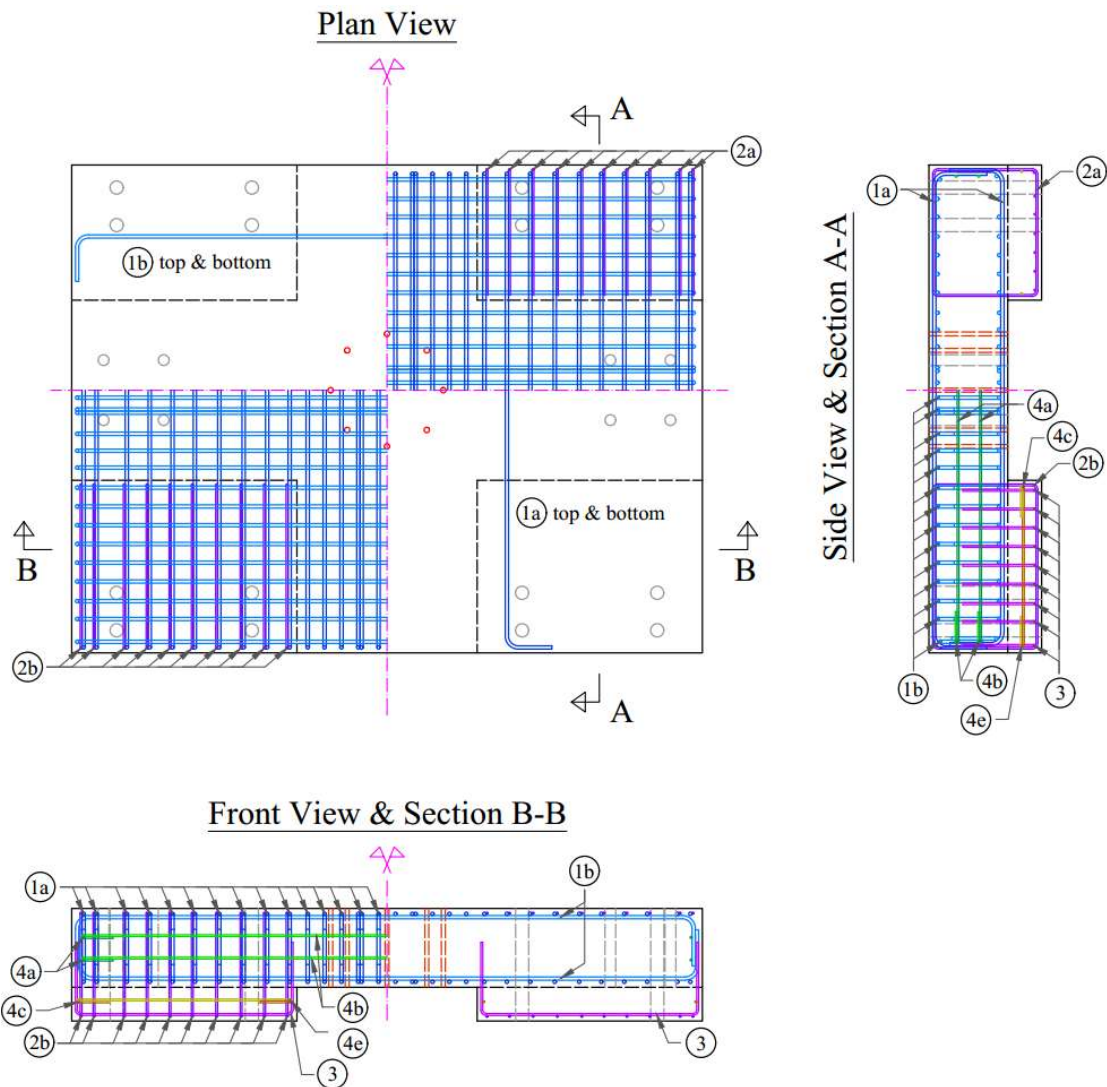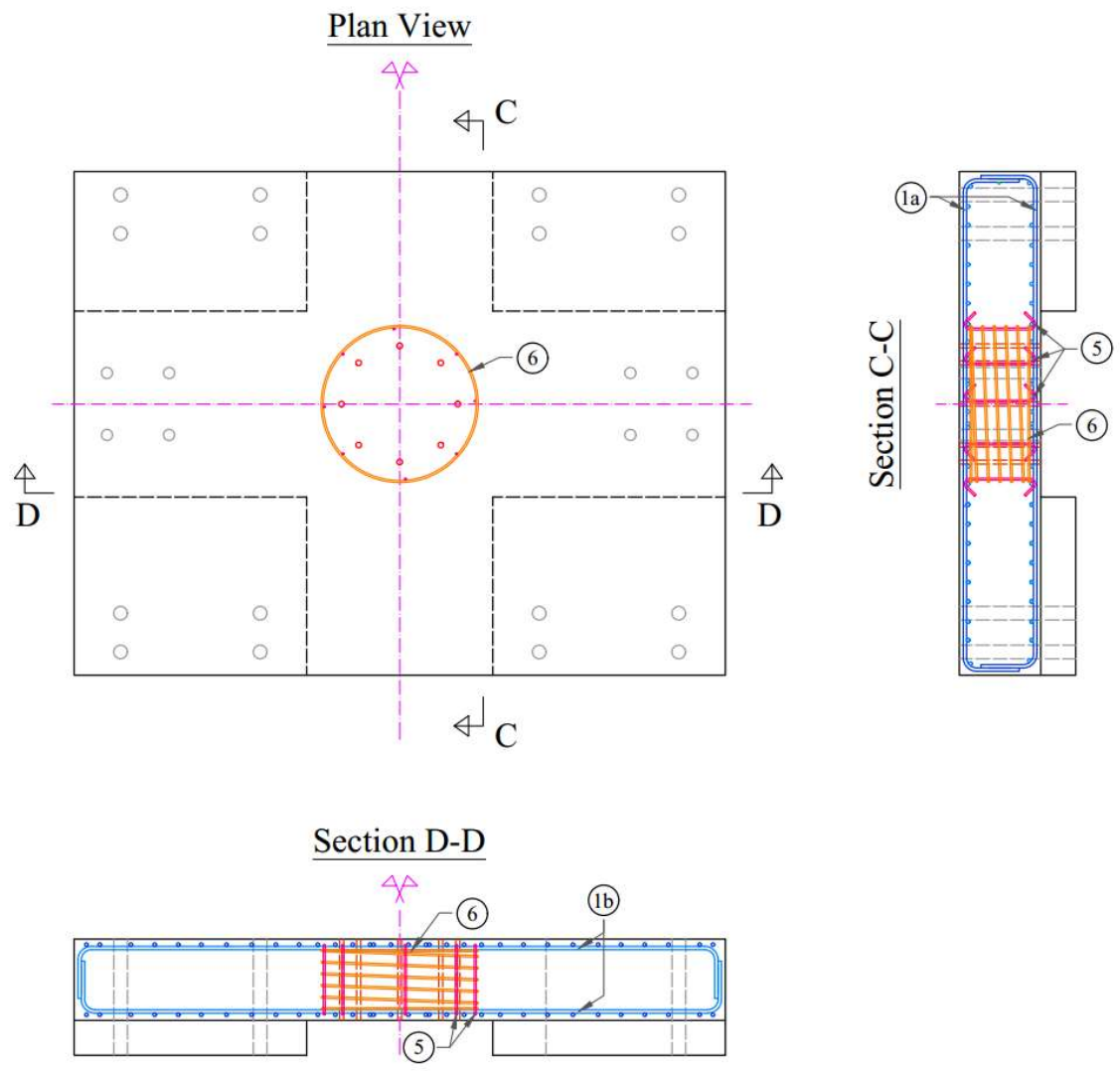
Plan View

Section C-C

Section D-D

713

(1a) #7 (64 pcs)

10'-6$\frac{1}{4}$"

1'-2"

Ø5$\frac{1}{4}$"

(1b) #7 (56 pcs)

13'-8$\frac{1}{4}$"

1'-1"

Ø5$\frac{1}{4}$"

(4a) #4 (4 pcs)

10'-4"

8"

Ø2"

(4b) #4 (4 pcs)

13'-6"

8"

Ø2"

(4c) #4 (4 pcs)

3'-6$\frac{1}{2}$"

8"

Ø2"

(4d) #4 (4 pcs)

2'-8$\frac{1}{2}$"

8"

Ø2"

(4e) #4 (8 pcs)

4'-8$\frac{1}{2}$"

8"

Ø2"

(2a) #4 (20 pcs)

2'-9½"

Ø2"

2'-3½"

3"

(2b) #4 (20 pcs)

3'-7½"

Ø2"

2'-3½"

3"

(3) #4 (32 pcs)

1'-7¼"

Ø2"

4'-9½"

(5) #4 (8 pcs)

3"

Ø2"

1'-5¾"
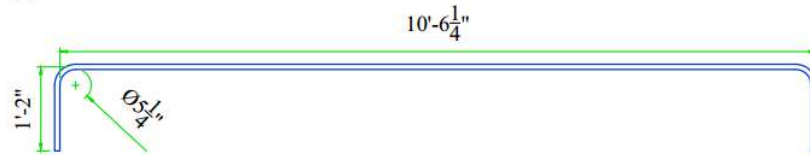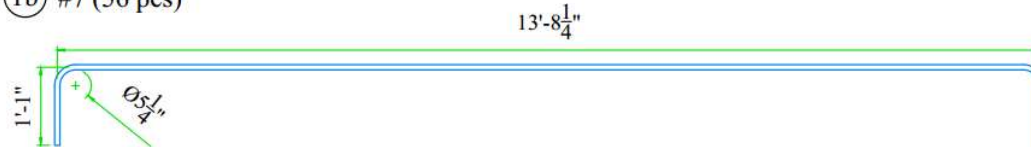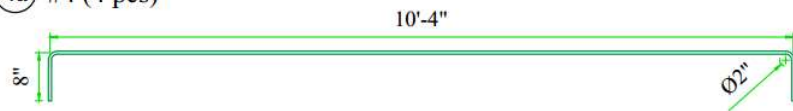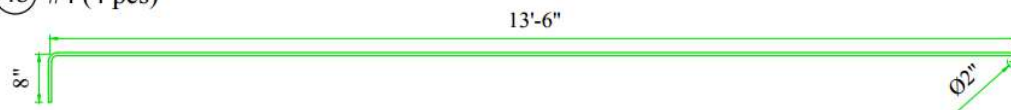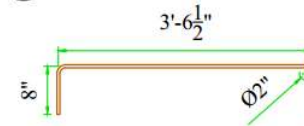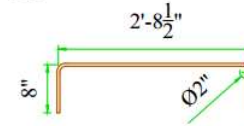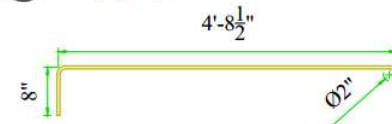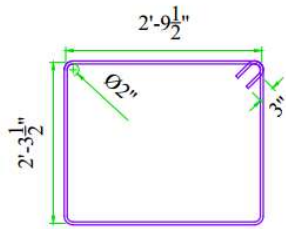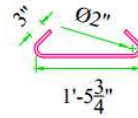
(6) #4 - Spiral
(Height = 1'-3" - Pitch = 3")

Ø3'-4"

715
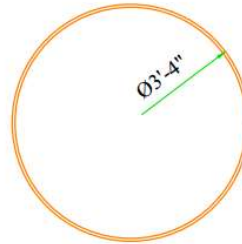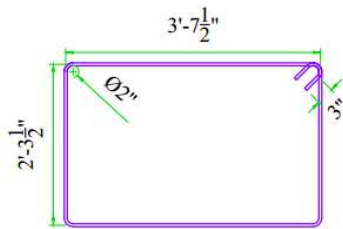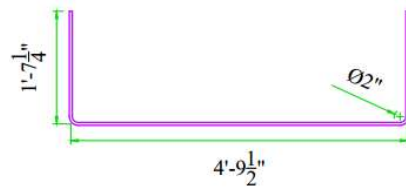
APPENDIX C

COLUMN SEGMENTS REPAIR

As mentioned in Section 4.6.1.4, the bottom and top segments of the column specimen tested in Phase II had large voids close to the bottom end of their formwork (Figure C-1 and Figure C-2). The top segment had more and larger voids close to its bottom surface. These voids were most likely caused by the low flowability of the concrete mixture and insufficient compaction while casting the concrete. Considering that these voids could compromise the strength of the respective column specimen, they needed to be filled with proper cementious material.

The product chosen for the repair of the column segments was the QUIKRETE non-shrink precision grout (Figure C-3(a)). Per the product's mixing instructions, the amount of water was chosen such that its highest flowability is achieved (Figure C-3(b)), while its nominal 28-day strength would remain above 8 ksi. The column voids were filled/patched with the prepared grout, as shown in Figure C-4 and Figure C-5 for the bottom and top segments, respectively. The grout was kept moist and covered by plastic sheating for a few days.

Figure C-1. Bottom segment of column tested in Phase II after formwork removal
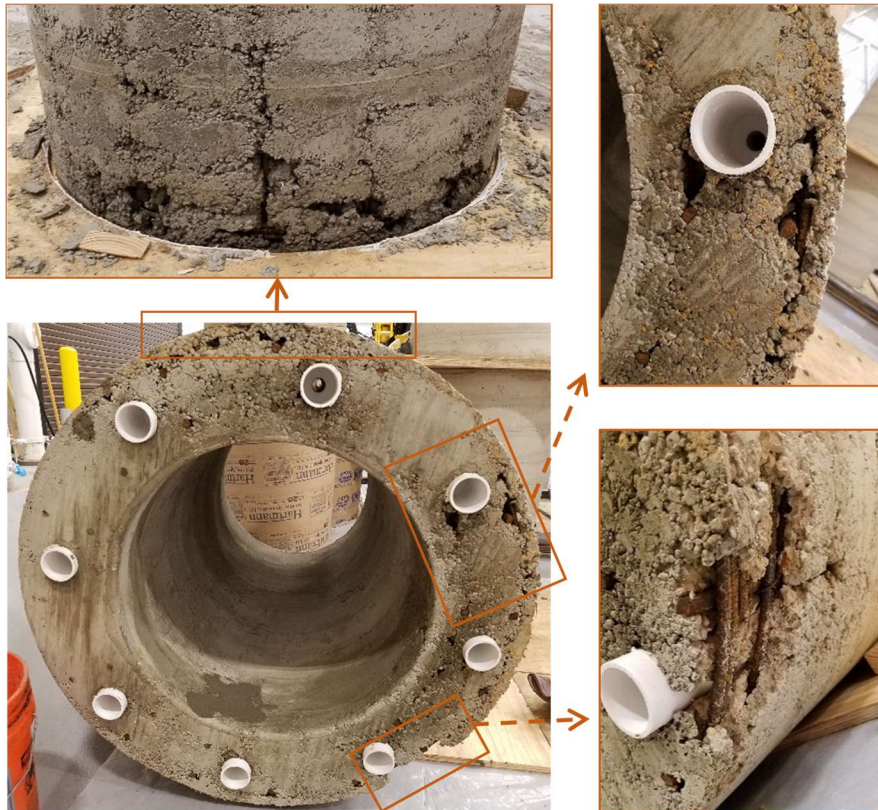
Figure C-2. Top segment of column tested in Phase II after formwork removal

717

Figure C-3. (a) Grout product used for repair; (b) flowability of mixed grout

Figure C-4. Repaired bottom column segment

Figure C-5. Repaired top column segment

APPENDIX D

SLIDING JOINT MATERIALS

The NA1525 PTFE material produced by Hanna Rubber was used one the sliding joints. 25% of the weight of this material was composed of glass. The properties of this material provided by the manufacturer are listed in Table D-1.

Table D-1. Properties of PTFE product

ASTM Test	Property		Value
D638-61T	Tensile Strength at 73°F		2000-3000 psi
D638-61T	Elongation		100-260%
D638-61T	Hardness Durometer		D55.5
D621-59	Deformation	73°F, 1500 psi, 24 hr.	1.73%
		100°F, 1500 psi, 24 hr.	1.91%
		200°F, 1500 psi, 24 hr.	4.57%
D570-59aT	Water Absorption		0.013%
-	Static Coefficient of Friction at 73°F		0.085%

The epoxy product used to bond the steel plates and PTFE pads on column segments was the two-part MT-13 adhesive produced by Smooth-On (Figure D-1). The mix-ratio of the parts A and B was 1:1 by volume and its cure time in the room temperature (73°F) was 16 hours. Other properties of the cured product provided by the manufacturer are listed in Table D-2.

The grease product used to lubricate sliding joints was the multipurpose synthetic NLGI Grade 2 grease manufactured by Super Lube (Figure D-2). This product is composed of synthetic base oil and PTFE thickener.

Table D-2. Properties of epoxy product

Property	Value
Tensile Strength	4.3 ksi
Modulus of Elasticity in Tension	285 ksi
Modulus of Elasticity in Compression	165 ksi
Compressive Yield Strength	8.7 ksi

Figure D-1. Epoxy product used for bonding sliding joint interface materials to column segment end surfaces

Figure D-2. Grease product used to cover sliding joint surfaces

APPENDIX E

TENDON LOAD CELL DESIGN AND FABRICATION

The tendon load cells are comprised from a small steel cylinder (round tube), which allows the tendon to pass through, along with four identical strain gauges connected to its outside periphery, at mid-height (to be far from the strain concentrations near the cylinder ends). The orientation of two of these strain gages needs to be aligned with the cylinder axis, while the other two need to be oriented normal to the axis (Figure E-1(a)). The strain gages attached to the opposite faces of the cylinder have the same orientation to compensate for the strain gradient caused by the flexure due to potential eccentric axial load. The strain gages, which are essentially electrical resistors, are connected to each other, an external source of electricity (E_{in}), and a voltage meter (E_{out}), in accordance with the so-called Wheatstone bridge circuit (Figure E-1(b)).

(a)   **(b)**
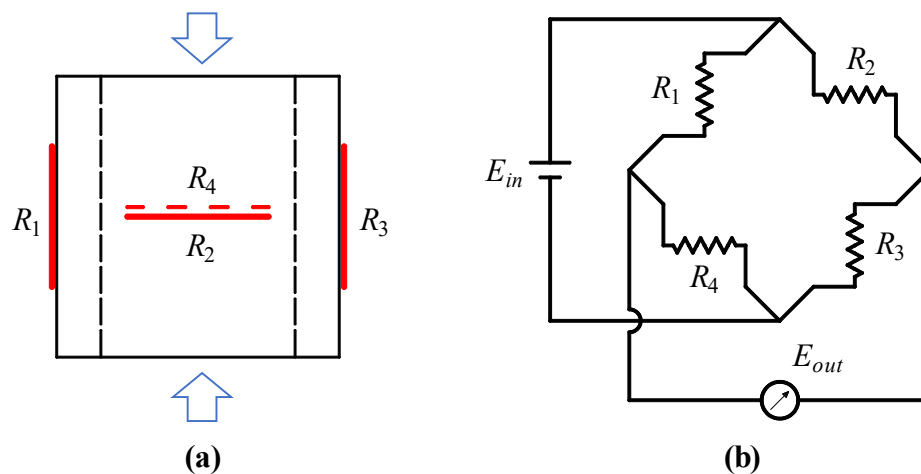
Figure E-1. (a) Strain gage layout on load cell; (b) Wheatstone bridge circuit

The strain in each strain gage is related to its resistance via equation below:

$$\frac{\Delta R}{R} = F_g \varepsilon \tag{E-1}$$

where R is the strain gage resistance, ΔR is its resistance change due to strain, ε, and F_g is named gage factor (a strain gage property). On the other side, the output voltage in Wheatstone bridge, E_{out}, is related to its input voltage, E_{in}, and the resistances of its resistors, as:

$$E_{out} = \frac{R_3 R_1 - R_4 R_2}{(R_2 + R_3)(R_1 + R_4)} E_{in} \tag{E-2}$$

According to Eq. (E-2), if no strain is imposed in the strain gages and their resistances remain equal, the output voltage of the circuit will be zero. Combining Eqs. (E-1) and (E-2) and recognizing that the strain in the transversely-oriented straing gages is $-v$ times the strain in the vertical ones, where v denotes the Poisson's ratio, the output voltage can be related to the axial strain as:

$$E_{out} = \frac{F_g E_{in}}{4}(2+v)\varepsilon \tag{E-3}$$

As a result, the load measured by the load cell, F, is obtained by measuring the output voltage according to:

$$F = EA\varepsilon = \frac{4EA}{F_g E_{in}(2+v)} E_{out} = C_c E_{out} \tag{E-4}$$

where C_c is a constant factor that can be obtained by calibration of the load cell.

The dimensions of the DOM round steel tubes used to build the load cells in this study, which conformed with ASTM 513/513M Grade 1020 (ASTM 2019) and had a yield

723

strength of 60 ksi, were selected such that it does not yield for double the ultimate strength of the monostrands (Figure E-2). The strain gages were Micro-Measurements Transducer Class strain gages of model N2A-06-T007R-350. The resistance of these strain gages was 350±0.15% ohms, which was large enough not to cause much temperature increase while in use.

Plan View
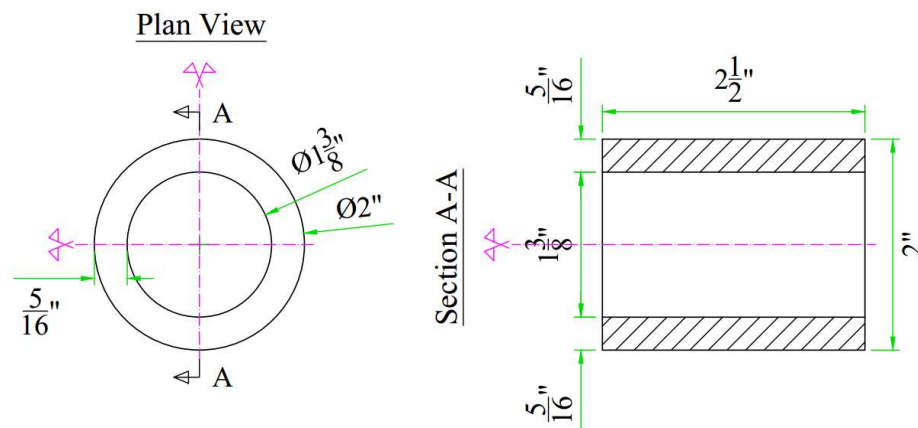
Figure E-2. Steel tube dimensions

The process of building the load cells is demonstrated in Figure E-3. In the first step, the strain gages were installed on the steel tubes (Figure E-3(a)) according to the manufacturer instructions and using their own installation products (Figure E-4). Once the strain gages were attached, they were connected through thin wires soldered on those and small connecting terminals between them (Figure E-3(b)). The connecting terminals used here were manufactured by Tokyo Measoring Instruments Lab (TML) and their type was TF-2M. The input and output wires were then connected to the terminals (Figure E-3(c)). Finally, in order to protect the gages and wires, hot glue was applied on the whole circuit

(Figure E-3(d)) and it was covered by duck tape. The cable connector used for each load cell was a 4-pin XLR connector (Figure E-5) that could accommodate all four wires coming out of the load cell (i.e. both input and output voltage wires).
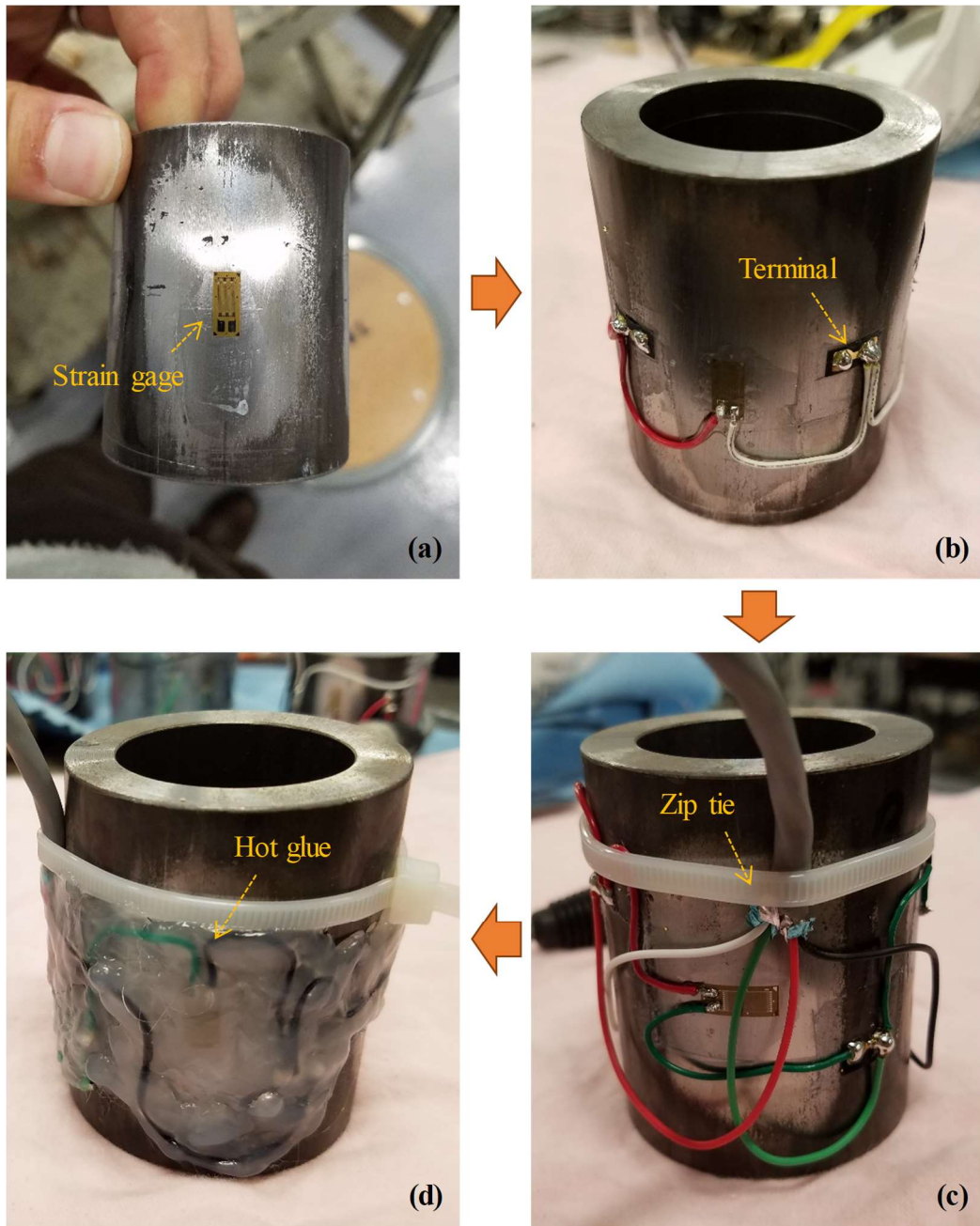
Figure E-3. Fabrication of tendon load cells: (a) installation of strain gage on steel tube; (b) completion of circuit wiring; (c) connection of output/input wires; (d) covering circuit with hot glue for protection
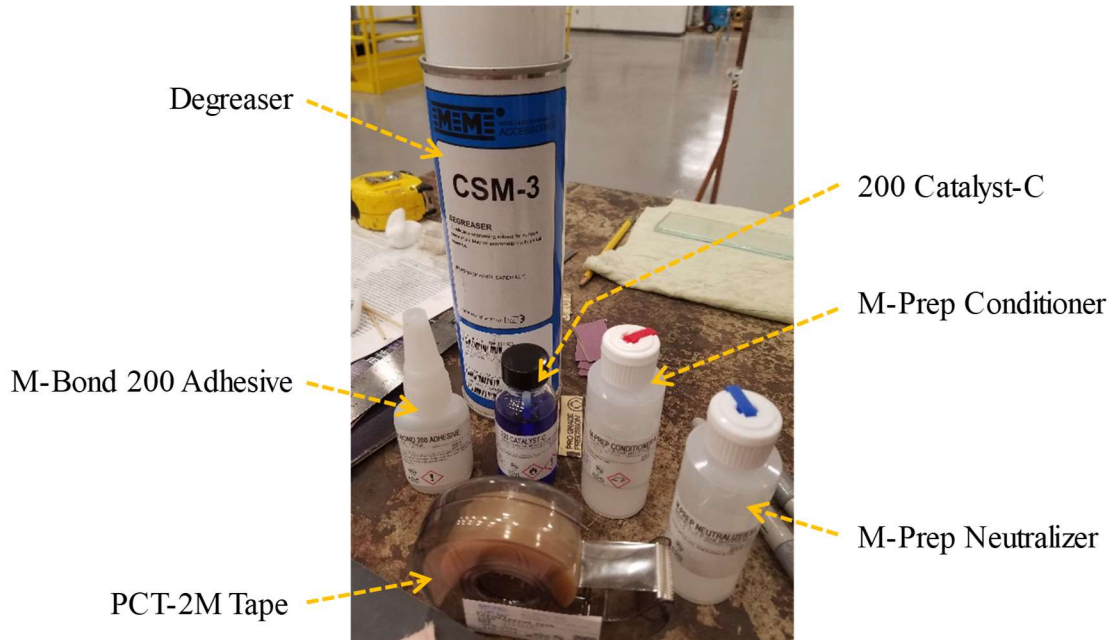
Figure E-4. Materials used for strain gage installation

Figure E-5. 4-pin XLR connector

APPENDIX F

COLUMN DAMAGE REPAIR

As pointed out in Section 4.7.1.4.4, the bottom segment of the column specimen tested in Phase I was repaired after Loading Set 3 was completed. This repair was necessary to achieve the objectives of a related study by Valigura (2019) and its pertinent calculations are found in the same reference. In this appendix, the repair materials and procedure are briefly described.

Considering the concrete spalling observed near the bottom rocking joint of the column specimen, the repair method recommended by practitioners was patching of the bottom segment and confining it with carbon fiber reinforced polymer (CFRP) wrap. For this purpose, the Sika products were used.

The product used to patch the column segment was SikaQuick VOH, which is a fast-setting one-component cementitious vertical and overhead repair mortar. Note that because it would eventually be confined by the CFRP wrap, the mortar's strength was not an important determinant in its selection, but its application convenience was. The mortar mixing was carried out in accordance with the manufacturer's instructions (Figure F-1(a)), resulting in a pretty thick and dry-looking mixture (Figure F-1(b)). Before patching the column segment with the mixed mortar, the loose concrete pieces were removed, the dust on the surface was cleaned by compressed air (Figure F-2(b)), and the surfaces were sprayed by water to enhance the bonding and reduce the mortar's water absorption by the underlying dry surface. After patching was completed (Figure F-2(c)), the patched areas

728

were water-sprayed and the column segment was covered by plastic sheating (Figure F-2(d)) to be set for a couple of days.
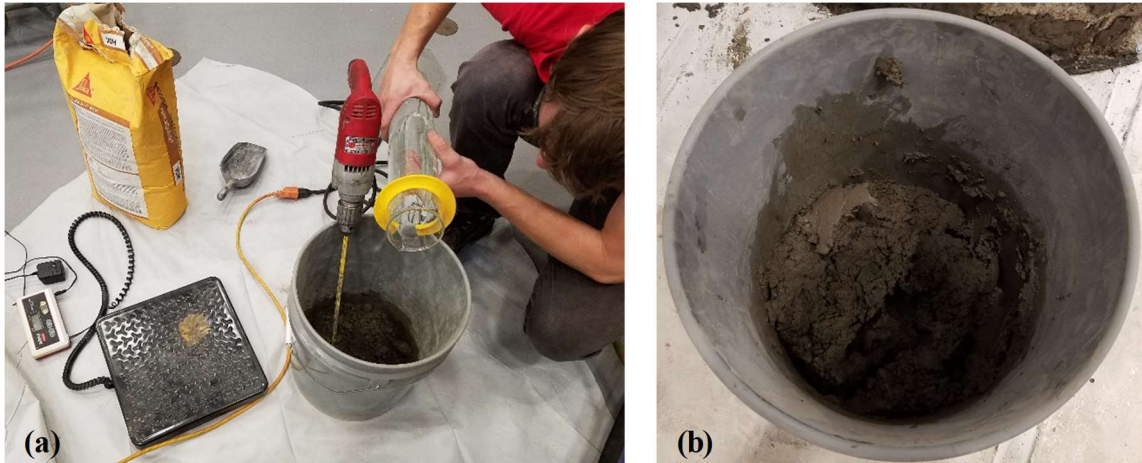
Figure F-1. (a) Mixing of mortar; (b) final consistency of mixed mortar

Once the patch was set and cured for a short time, the CFRP wrap could be installed. The wrap product used here was of the commercial name SikaWrap-103 C Pre-Saturated (Figure F-3(a)), which was a 2-ft wide, 0.035-in. thick, high-strength unidirectional carbon fiber fabric impregnated by a special resin. Some of the mechanical properties of this material are listed in Table F-1. In addition, the wrap installation required a two-part epoxy adhesive to be applied on the original concrete surface (i.e. as a primer) and on the edges of the wrap once it was installed (for sealing). The adhesive product used for this purpose was Sikadur-330 US (Figure F-3(b)). According to the design by Valigura (2019), six layers of the above CFRP wrap were placed on the segment.
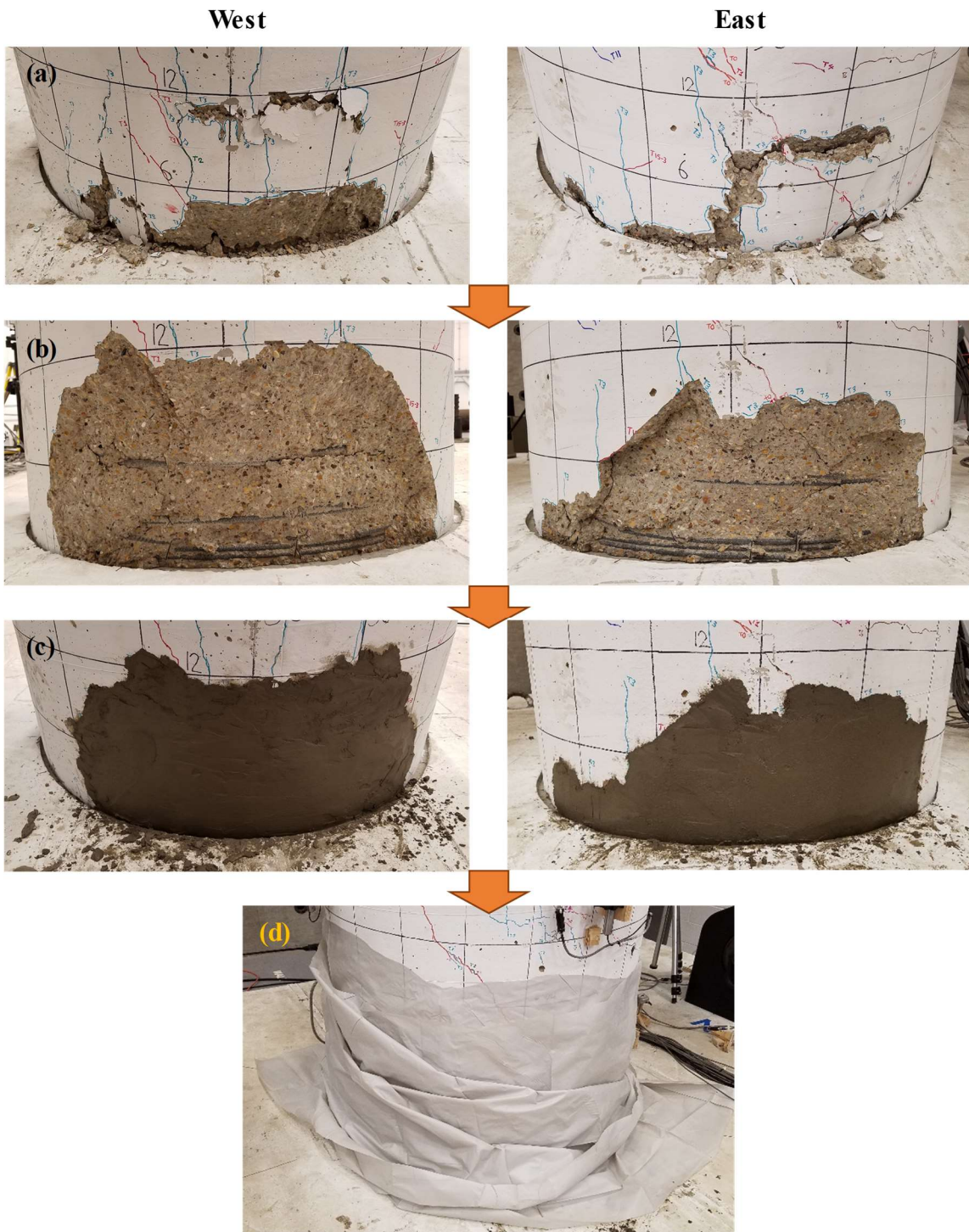
Figure F-2. Column repair process: (a) pre-repair condition; (b) removal of loose concrete; (c) patching by cementitious mortar; (d) plastic covering for moist curing

Figure F-3. Sika products: (a) CFRP wrap; (b) two-part epoxy
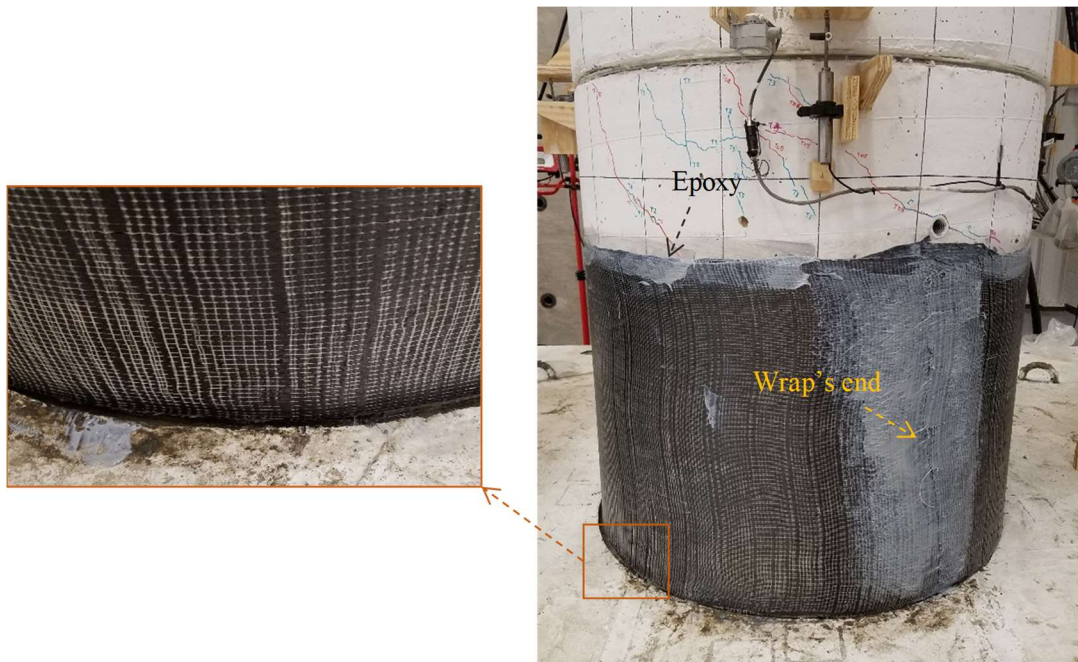
Figure F-4. Application of CFRP wrap

Table F-1. Properties of CFRP wrap at room temperature

Property	Value
Average Tensile Strength	~148 ksi
Tensile Modulus	12.32 msi
Average Ultimate Tensile Elongation	1.12 %